ADVANCED ANOMALY DETECTION TECHNOLOGIES AND APPLICATIONS IN ENERGY SYSTEMS

EDITED BY: Tinghui Ouyang, Yusen He, Xun Shen, Zhenhao Tang and Yahui Zhang

PUBLISHED IN: Frontiers in Energy Research

frontiers Research Topics

frontiers

ISSN 1664-8714
ISBN 978-2-83250-141-2
DOI 10.3389/978-2-83250-141-2

About Frontiers

Frontiers is more than just an open-access publisher of scholarly articles: it is a pioneering approach to the world of academia, radically improving the way scholarly research is managed. The grand vision of Frontiers is a world where all people have an equal opportunity to seek, share and generate knowledge. Frontiers provides immediate and permanent online open access to all its publications, but this alone is not enough to realize our grand goals.

Frontiers Journal Series

The Frontiers Journal Series is a multi-tier and interdisciplinary set of open-access, online journals, promising a paradigm shift from the current review, selection and dissemination processes in academic publishing. All Frontiers journals are driven by researchers for researchers; therefore, they constitute a service to the scholarly community. At the same time, the Frontiers Journal Series operates on a revolutionary invention, the tiered publishing system, initially addressing specific communities of scholars, and gradually climbing up to broader public understanding, thus serving the interests of the lay society, too.

Dedication to Quality

Each Frontiers article is a landmark of the highest quality, thanks to genuinely collaborative interactions between authors and review editors, who include some of the world's best academicians. Research must be certified by peers before entering a stream of knowledge that may eventually reach the public - and shape society; therefore, Frontiers only applies the most rigorous and unbiased reviews.
Frontiers revolutionizes research publishing by freely delivering the most outstanding research, evaluated with no bias from both the academic and social point of view. By applying the most advanced information technologies, Frontiers is catapulting scholarly publishing into a new generation.

What are Frontiers Research Topics?

Frontiers Research Topics are very popular trademarks of the Frontiers Journals Series: they are collections of at least ten articles, all centered on a particular subject. With their unique mix of varied contributions from Original Research to Review Articles, Frontiers Research Topics unify the most influential researchers, the latest key findings and historical advances in a hot research area! Find out more on how to host your own Frontiers Research Topic or contribute to one as an author by contacting the Frontiers Editorial Office: frontiersin.org/about/contact

ADVANCED ANOMALY DETECTION TECHNOLOGIES AND APPLICATIONS IN ENERGY SYSTEMS

Topic Editors:
Tinghui Ouyang, National Institute of Advanced Industrial Science and Technology (AIST), Japan
Yusen He, Grinnell College, United States
Xun Shen, Tokyo Institute of Technology, Japan
Zhenhao Tang, Northeast Electric Power University, China
Yahui Zhang, Yanshan University, China

Citation: Ouyang, T., He, Y., Shen, X., Tang, Z., Zhang, Y., eds. (2022). Advanced Anomaly Detection Technologies and Applications in Energy Systems. Lausanne: Frontiers Media SA. doi: 10.3389/978-2-83250-141-2

Table of Contents

frontiers | Frontiers in Energy Research

EDITORIAL
published: 23 August 2022
doi: 10.3389/fenrg.2022.965151

Editorial: Advanced Anomaly Detection Technologies and Applications in Energy Systems

Tinghui Ouyang[1], Xun Shen[2]*, Yusen He[3]*, Zhenhao Tang[4]* and Yahui Zhang[5]**

[1]National Institute of Advanced Industrial Science and Technology (AIST), Tsukuba, Japan, [2]Tokyo Institute of Technology, Meguro, Japan, [3]Grinnell College, Grinnell, AI, United States, [4]School of Automatic Engineering, Northeast Electric Power University, Jilin, China, [5]School of Mechanical Engineering, Yanshan University, Qinhuangdao, China

Keywords: anomaly detection, energy research, data mining, deep learning, machine learning

Editorial on the Research Topic

Advanced Anomaly Detection Technologies and Applications in Energy Systems

Anomaly detection is an important topic that has been well-studied in diverse research areas and application domains. It generally involves the detection of abnormal data, unhealthy statuses, and fault diagnosis, and is helpful to guarantee industrial systems' stability, security, and economy. With the development of intelligent industries and sensor systems, large amounts of data become easily available, but there are major challenges to industrial systems' anomaly detection. One typical case is the study on energy-related systems, like thermal energy, renewable energy (e.g., wind energy, photovoltaic), electric vehicles, and so on. These systems involve various data formats and more complex data structures making anomaly data detection a challenge. Currently, under the development of deep learning and big data analytics, many promising results have been achieved in energy systems' anomaly data detection. However, many challenging problems remain unsolved due to the complex nature of energy industries. New techniques and advanced engineering applications of anomaly detection in energy systems still appeal to a wide range of scholars and industries.

The objective of this Research Topic is to solicit papers on recent developments in anomaly detection techniques and advances in applications of energy-related systems. The topic can cover techniques related to anomaly detection algorithm development, such as machine learning, data mining, deep learning, graph theory, big data, and so on. Various aspects of energy applications can be addressed, like data cleaning, unhealthy evaluation of energy systems, condition monitoring, and faults diagnosis in energy-related industries. Special attention could be paid to energy-related systems, e.g., wind energy, photovoltaic, thermal energy, electric vehicle (EV) development, and so on.

After paper Research Topic and rigorous review, 63 high-quality articles contributed by 327 authors were finally accepted for their contributions to the study of condition monitoring and anomaly detection in power systems, renewable energy systems, and other industrial systems.

In the paper *Series Arc Fault Diagnosis Based on Variational Mode Decomposition and Random Forest*, Zhao et al. proposed a method based on variational mode decomposition and energy entropy to extract the characteristic quantity of series arc faults, and subsequently complete the fault detection.

In the paper *Sequential Detection of Microgrid Bad Data via a Data-Driven Approach Combining Online Machine Learning with Statistical Analysis*, Huang et al. proposed a sequential detection method to detect bad data in Energy Management Systems (EMS).

OPEN ACCESS

Edited and reviewed by:
David Howe Wood,
University of Calgary, Canada

****Correspondence:***
Tinghui Ouyang
ouyangtinghui@gmail.com
Xun Shen
shen.x.ad@cyb.sc.e.titech.ac.jp
Yusen He
heyusen@grinnell.edu
Zhenhao Tang
tangzhenhao@neepu.edu.cn
Yahui Zhang
zhangyahui@ysu.edu.cn

Specialty section:
This article was submitted to Wind Energy, a section of the journal Frontiers in Energy Research

Received: *09 June 2022*
Accepted: *24 June 2022*
Published: *23 August 2022*

Citation:
Ouyang T, Shen X, He Y, Tang Z and Zhang Y (2022) Editorial: Advanced Anomaly Detection Technologies and Applications in Energy Systems. Front. Energy Res. 10:965151. doi: 10.3389/fenrg.2022.965151

Abnormal detection data of fire accidents in power cable tunnels was studied by Guo et al. in the paper *Analysis of Abnormal Detection Data of Fire Accident in Power Cable Tunnel and Field Test Study on Characteristic Parameters of Tunnel Fire*.

In the paper *Research on Fire Prediction Method of High-Voltage Power Cable Tunnel Based on Abnormal Characteristic Quantity Monitoring*, Li et al. proposed a fire early warning method for a high-voltage power cable tunnel based on abnormal characteristic quantity monitoring.

In the paper *Data-Driven Traction Substations' Health Condition Monitoring via Power Quality Analysis*, Xie proposed a data-driven approach for recognizing anormal types of power quality problems, and developed a system with intelligent governance strategies.

In the paper *Monitoring and Identifying Wind Turbine Generator Bearing Faults Using Deep Belief Network and EWMA Control Charts*, a data-driven approach for condition monitoring of generator bearings using temporal temperature data was presented by Li et al.

In the paper *Invalid Data Rejection of Audible Noise on AC Transmission Lines Based on Moving Window Kernel Principal Component Analysis*, Cheng et al. proposed to detect outliers by using the moving window kernel principal component analysis (MWKPCA).

In the paper *Power Consumption Predicting and Anomaly Detection Based on Transformer and K-Means*, Zhang et al. combined the widely used deep learning model Transformer with the clustering approach K-means to estimate power consumption over time and detect anomalies.

In the paper *Heuristic Feature Selection for Wind Power Anomaly Events Study*, Yu and Lin took wind power ramp events as typical harmful anomaly events in wind engineering and detected them.

In the paper *Robust Vehicle Dynamics Control for a Sharp Curve with Uncertain Road Condition*, Miao et al. presented a robust control strategy for CAVs to preserve a precise tracking performance and maintain the stability of lateral dynamics.

In the paper *A Fault Signal Processing Method Based on An Improved Prony Algorithm*, Yang et al. proposed an improved adaptive Prony algorithm to detect faults in power systems.

In the paper *An Improved Solution to Generation Scheduling Problem Using Slime Mold Algorithm*, Zhu proposed a novel mathematical formulation that employs changeable weights to modify the sequence of both negative and positive propagation waves during oscillation.

Considering bird nests on transmission line towers pose a serious threat to the safe operation of power systems, in the paper *Recognition of Bird Nests on Power Transmission Lines in Aerial Images Based on Improved YOLOv4*, Zhang and He explored an effective method to detect bird nests taken by drone inspection.

In the paper *Research on STATCOM Mathematical Model of Battery Storage in HVDC Transmission System*, Xing et al. proposed research to study the possible imbalance of battery state of charge (SOC) in STATCOM/BESS.

In the paper *Power Grid Material Demand Forecasting Based on Pearson Feature Selection and Multi-Model Fusion*, a power grid material demand forecasting model based on feature selection and multi-model fusion was proposed by Dai et al. oriented to power grid analysis.

In the paper *Power Quality Data Compression and Disturbances Recognition Based on Deep CS-BiLSTM Algorithm with Cloud-Edge Collaboration*, Xia et al. proposed a hybrid model based on distributed compressive sensing and a bi-directional long-short memory network to classify power quality disturbances data.

In the paper *Numerical Analysis on the Sub-Span Oscillation of Iced Eight-Bundle Conductors During Galloping*, Yu et al. implemented a numerical analysis method to analyze the sub-span oscillation characteristics of the eight-bundle conductor during galloping.

In the paper *A New Grounding Resistance Reduction Method for Wind Turbines by Grounding Grid Connection in Limited Areas*, a new grounding resistance reduction method is proposed by Hu et al. and verified for wind turbines by connecting nearby wind turbine grounding grids.

In the paper *Acoustic-Electrical Joint Localization Method of Partial Discharge in Power Transformer Considering Multi-Path Propagation Impact*, Jia et al. proposed an acoustic-electrical joint method for partial discharge location in the power transformer with the full consideration of the multi-path propagation impact.

In the paper *Robust Unit Commitment for Minimizing Wind Spillage and Load Shedding With Optimal DPFC*, Zhu et al. presented a novel two-stage robust model to optimize the status of the generator and location-allocation of the distributed power flow controller (DPFC).

In the paper *Improved Electrogeometric Model of UHV Transmission Line Based on Long Gap Discharge and Its Application*, an improved EGM model was developed by Hu et al. and applied to evaluate the influence of tower type and slope steepness on the shielding failure tripping rate of UHV transmission lines.

In the paper *Traction Network Protection Based on Similarity of Transient Current Waveform*, a protection scheme for the traction network of the penetrating co-phase traction direct power supply system based on the waveform similarity at both ends of the line was proposed by Chen et al.

In the article *Numerical Simulation of Galloping Characteristics of Multi-Span Iced Eight-Bundle Conductors*, the numerical model of the multi-span iced eight-bundle conductor is established by Shunli et al.

In the paper *Research on Battery Energy Storage STATCOM Suppressing HVDC Commutation Failure*, a compensation method using battery energy storage STATCOM (STATCOM/BESS) to suppress commutation failure of the transmission system is proposed by Xing et al.

In the paper *Prediction of the 3D Distribution of NOx in a Furnace via CFD Data Based on ELM*, a novel method for the prediction of the three-dimensional (3D) spatial distribution of NOx in a furnace is proposed and evaluated by Lv et al.

In the paper *Accurate Modeling Simulation and Experimental Study of Hybrid Multi-Terminal UHVDC Transmission System*, Xing et al. proposed a simulation model of the control system

applicable to the hybrid multi-terminal UHVDC transmission system.

In the paper *Two-Stage Optimal Location Allocations of DPFC Considering Wind and Load Uncertainty*, Zhu et al. presented a novel two-stage stochastic model for optimal location allocations of the DPFC coupled with the interactions of DPFC to search for the optimal solutions.

In the paper *Simulation Study on Lightning Impulse Characteristics of Flexible Graphite Composite Grounding Materials Applied to Grounding Grid of Power System*, Hu et al. built a frequency domain electrical network model and an equivalent radius iterative algorithm to analyze the impulse characteristics of the graphite composite grounding electrode.

In the paper *Fuzzy Weighted Echo State Networks*, a novel echo state network (ESN) was proposed by Yao and Li, which uses the structural information of data sets to improve the performance of the classical ESN.

In the paper *Mechanism of Power Quality Deteriorating Caused by Multiple Load Converters for MVDC System*, Huang et al. discussed the mechanism of power quality deterioration caused by interfacing multiple load converters as anomalies in the MVDC system.

In the paper *An intelligent governance system for traction substations' power quality problems*, Xie proposed an advanced approach for detecting power quality problems in electrified railway traction substation systems.

In the paper *Multiterminal Hybrid DC Line Protection Based on Intrinsic Mode Energy Entropy*, the boundary frequency characteristics of the UHV multiterminal hybrid DC transmission system were analyzed by Xing et al.

In the paper *Energy-Efficiency-Oriented Vision Feedback Control of QCSP Systems: Linear ADRC Approach*, Li and Feng proposed a lightweight object detection network and a linear active disturbance rejection controller (LADRC) for the quadrotor with the cable-suspended payload (QCSP) system.

For the optimal size of a hybrid renewable energy system to meet the electrical load requirement of a specified distant location in the Haryana state of India, two intelligence techniques were proposed by Zhang in the paper *Optimal Allocation Of Hybrid Energy System For Competitive Electricity Market*.

In the paper *A Multi-Agent Game-Based Incremental Distribution Network Source–Load–Storage Collaborative Planning Method Considering Uncertainties*, Yang et al. proposed an incremental distribution network source–load–storage collaborative planning method with a multi-agent game.

In the paper *Grey Wolf Optimization–Based Deep Echo State Network for Time Series Prediction*, Chen and Zhang proposed a grey wolf optimization (GWO) algorithm introduced in this study to achieve the lowest learning error.

In the paper *A Study of Protection Method for Hybrid Multiterminal UHVDC Lines Based on CEEMDAN–Teager Energy Operator*, a protection scheme for hybrid multiterminal UHVDC lines based on the CEEMDAN and Teager energy operator is proposed by Xing et al.

In the paper *Study of Capacitive Coupling Sensor Fused with High Voltage XLPE Cable Joint*, Xia et al. proposed a capacitive coupling sensor for partial discharge detection with the fusion of high voltage XLPE cable joint.

In the paper *Bone Age Assessment Based on Deep Convolutional Features and Fast Extreme Learning Machine Algorithm*, Guo et al. proposed a new DL-based bone age assessment method based on the Tanner-Whitehouse method.

In the paper *Study on Dynamic Process Characteristics of CHP Unit with Variable Load Based on Working Point Linearization Modeling*, a CHP unit model based on working point linearization modeling was proposed by Huang et al. for the optimization scenario of an integrated energy system.

In the paper *Wind Power Prediction Based on a Hybrid Granular Chaotic Time Series Model*, Wang et al. proposed a hybrid model considering physical features of data for high-accuracy short-term wind power prediction.

In the paper *Operation State Evaluation Method of Smart Distribution Network Based on Free Probability Theory*, a method of operation state evaluation of smart distribution networks based on free probability theory was proposed by Zhang et al.

In the paper *Research on Dynamic Response of Slopes with Weak Interlayers Under Mining Blasting Vibration*, Zhang et al. constructed a slope model with a weak interlayer to investigate the influence of different factors of blasting on the internal dynamic response.

In the paper *Numerical Weather Prediction Correction Strategy for Short-Term Wind Power Forecasting Based on Bidirectional Gated Recurrent Unit and XGBoost*, Li et al. proposed a variational mode decomposition combined with bidirectional gated recurrent unit (VMD-BGRU) method for NWP wind speed correction and XGBoost forecasting model.

In the paper *Research on the Unstable Branch Screening Method for Power System With High-Proportion Wind Power*, Tang et al. proposed an unstable branch screening method for power systems with high-proportion wind power.

In the paper *Research on Conducted Disturbance to Secondary Cable Caused by Disconnector Switching Operation*, Chen et al. proposed a broadband equivalent circuit model of the potential transformer and the grounding grid based on the vector fitting method and the impedance synthesis method.

In the paper *The Influence of Humidity on Electron Transport Parameters and Insulation Performance of Air*, An et al. studied the microscopic process of electron–molecule collision in the air based on the Boltzmann equation.

In the paper *Intelligent Filling Method of Power Grid Working Ticket Based on Historical Ticket Knowledge Base*, An et al. proposed a method of intelligent filling in a power grid working ticket based on a historical ticket knowledge base.

In the paper *Lumped-Circuits Model of Lossless Transmission Lines and Its Numerical Characteristics*, aiming at the lumped-circuits model of the lossless transmission line in the digital simulation, Zhou et al. discussed and analyzed the unit step response generation of the lumped-circuits model.

In the paper *Tolerance of Electromagnetic Relay to Voltage Sags and Short Interruptions*, Zhang et al. studied the tolerance of electromagnetic relay (EMR) under voltage sag and short interruptions on the basis of response mechanism analysis and extensive tests.

In the paper *Ultra-Short-Term Wind Power Prediction Based on Bidirectional Gated Recurrent Unit and Transfer Learning*, an ultra-short-term prediction method based on multilayer bidirectional gated recurrent unit (Bi-GRU) and fully connected (FC) layer was proposed by Chen et al.

In the paper *Research on Combined Electricity and Heating System Scheduling Method Considering Multi-Source Ring Heating Network*, Ye et al. established an electrothermal coupling scheduling model and proposed a method of simplifying a multi-source cyclic heating network topology approximation.

In the paper *OC-SLAM: Steadily Tracking and Mapping in Dynamic Environments*, Wu et al. proposed an object detection and clustering assisted SLAM algorithm (OC-SLAM) to solve problems of SLAM systems.

In the paper *Research on Leakage Current Waveform Spectrum Characteristics of Artificial Pollution Porcelain Insulator*, to analyze the LC characteristics of porcelain insulators in the process of pollution flashover, artificial pollution flashover tests on porcelain insulators were conducted by Fang et al.

In the paper *Green Building Energy Cost Optimization With Deep Belief Network and Firefly Algorithm*, Liao et al. proposed a multi-objective optimization framework to minimize the energy cost while maintaining indoor air quality.

In the paper *Hosting Capacity Assessment in Distribution Networks Considering Wind–Photovoltaic–Load Temporal Characteristics*, Du et al. proposed a probabilistic assessment method of hosting capacity considering wind–photovoltaic–load temporal characteristics in distribution networks.

In the paper *Equivalent Firm Capacity Assessment of HDR-PV Hybrid Power System: A Distributionally Robust Approach*, Si et al. designed a flexible hot dry rock (HDR) hybrid power system (HPS), making full use of the potential of HDR for energy storage and power generation.

In the paper *Modeling the Heat-Hydrogen Balance Characteristic of Hydrogen Energy Storage and Cooperative Dispatch of Wind-Hydrogen Hybrid System*, Si et al. designed a hydrogen energy storage system (HESS), including waste heat utilization.

In the paper *Mapping Relation of Leakage Currents of Polluted Insulators and Discharge Arc Area*, Fang et al. carried out an experimental study on artificial pollution discharge of insulators.

In the paper *Short-Term Nacelle Orientation Forecasting Using Bilinear Transformation and ICEEMDAN Framework*, A tandem hybrid approach to improve the prediction accuracy of the wind direction data was developed by Li et al.

In the paper *Edge Intelligent Perception Method for Power Grid Icing Condition Based on Multi-Scale Feature Fusion Target Detection and Model Quantization*, Ma et al. proposed a lightweight intelligent recognition method of insulator icing thickness for front-end ice monitoring devices.

In the paper *Intelligent Frequency Control Strategy Based on Reinforcement Learning of Multi-Objective Collaborative Reward Function*, Zhang et al. constructed a multi-objective collaborative reward function by introducing a collaborative evaluation mechanism with multiple evaluation indexes.

In the paper *Insulator Contamination Perception Based on Feature Fusion of Infrared Image and Meteorological Parameters*, Wang et al. proposed a feature fusion model to perceive insulator contamination in different weather conditions.

It is seen that these papers in our Research Topic mainly involve anomaly detection in other industrial systems, as well as some advanced algorithms development, e.g., machine learning and data mining algorithms related to anomaly detection. From all contributions to this Research Topic, we see that anomaly detection in the energy system is meaningful and potential to be further developed in future research.

Finally, the guest editors would like to thank all authors for their interesting contributions and all the reviewers for their great effort in reviews. Special thanks go to the Editor-in-Chief and editorial members of the journal for their great support of this Research Topic.

AUTHOR CONTRIBUTIONS

All authors listed have made a substantial, direct, and intellectual contribution to the work and approved it for publication.

Conflict of Interest: The authors declare that the research was conducted in the absence of any commercial or financial relationships that could be construed as a potential conflict of interest.

Publisher's Note: All claims expressed in this article are solely those of the authors and do not necessarily represent those of their affiliated organizations, or those of the publisher, the editors and the reviewers. Any product that may be evaluated in this article, or claim that may be made by its manufacturer, is not guaranteed or endorsed by the publisher.

frontiers in Energy Research

ORIGINAL RESEARCH
published: 08 September 2021
doi: 10.3389/fenrg.2021.746378

Insulator Contamination Perception Based on Feature Fusion of Infrared Image and Meteorological Parameters

Hongxia Wang [1], Bo Wang [1], Min Li [2], Peng Luo [1], Hengrui Ma [3] and Fuqi Ma [1]*

[1]School of Electrical Engineering and Automation, Wuhan University, Wuhan, China, [2]School of Computer and Artificial Intelligence, Wuhan Textile University, Wuhan, China, [3]New Energy (Photovoltaic) Industry Research Center, Qinghai University, Xining, China

Polluted insulators seriously threaten the safe and stable operation of power grids, which attaches great significance to insulator contamination perception. Among the present methods, the non-contact approaches based on infrared images have gradually been widely used, as they are much more safe and are of low cost. However, the thermal effect of insulators is largely affected by meteorological conditions, which makes the infrared image-based methods less accurate. To solve the above problem, we take infrared image and meteorological parameters including humidity and temperature as input, and propose a feature fusion model to perceive insulator contamination in different weather conditions. Firstly, different feature extraction networks are used to perform feature extraction on the two types of data; secondly, the two features are concatenated to fuse together; thirdly, further feature extraction is performed and contamination is classified according to the pollution severity. Case studies show that the proposed method can better explore the relationship between humidity, temperature and pollution level of the insulators, thus can better separate the contamination grades and outperform the conventional infrared image based methods.

Keywords: insulator, contamination perception, feature fusion, infrared image, meteorological parameters

OPEN ACCESS

Edited by:
Xun Shen,
Tokyo University of Agriculture and Technology, Japan

Reviewed by:
Yahui Zhang,
Yanshan University, China
Fuguo Xu,
Sophia University, Japan

****Correspondence:***
Bo Wang
whwdwb@whu.edu.cn

Specialty section:
This article was submitted to Wind Energy, a section of the journal Frontiers in Energy Research

Received: *23 July 2021*
Accepted: *23 August 2021*
Published: *08 September 2021*

Citation:
Wang H, Wang B, Li M, Luo P, Ma H and Ma F (2021) Insulator Contamination Perception Based on Feature Fusion of Infrared Image and Meteorological Parameters. Front. Energy Res. 9:746378. doi: 10.3389/fenrg.2021.746378

1 INTRODUCTION

Functioning as electrical insulation and mechanical support, outdoor insulators play an important role in power systems (He et al., 2006). However, with the increasing pollution caused by gas emissions from factories and cars, bad weather like fog-haze, rain and snow conditions, the insulators are contaminated more severe and are more easily and frequently to flashover (Fofana et al., 2020; 3, 2020; Dong et al., 2014; Liu et al., 2020), which can seriously endanger the safe and stable operation of power grids, and even cause huge economic losses. Therefore, it is necessary to perceive the pollution level of insulators and take measures in time.

There are mainly two kinds of contamination perception methods for insulators: contact methods and non-contact methods (Jin et al., 2017). The contact ones include leakage current (Banik et al., 2016; Wang et al., 2019; Salem et al., 2020), surface conductivity (Wang et al., 2017; Zhong et al., 2018), ESDD (Equivalent Salt Deposit Density) (Cao et al., 2019) and so on. Generally speaking, the above approaches have clear physical meaning and are relatively accurate. However, they often require online monitoring equipments with large quantity and high prices, what's more, some of the equipments need to be implemented in power off situation. Based on the acoustic, discharge and heat phenomenon of polluted insulators in some cases, non-contact methods including infrared images

(Zhao et al., 2017), ultraviolet images (Zhao et al., 2017) and (Liu et al., 2021) photothermal radiometry are increasingly applied to insulator contamination perception, because of their advantages of safety and immunity to electromagnetic interference.

Among those non-contact approaches, the infrared image-based ones are mostly used because of their low costs. From the perspective of the elements they consider, these methods can be divided into two kinds: 1) those based on infrared images only; 2) those based on infrared images and meteorological parameters.

For contaminated insulators, the leakage current on their surfaces will increase under wet conditions, and the more severe the contamination, the greater the leakage current, which can be detected through infrared images. As a result, there are many methods perceiving insulator pollution based on infrared images. In Zhao et al. (2017), the authors analyze insulator contamination through the combination of infrared images shot in different angles—to deal with the limitations caused by angle diversification. In addition, to cope with the limitation of manually-designed features, they use Deep Convolutional Neural Networks (DCNNs) to automatically extract features. Jiang and Xia (2010) study the influence of contamination on deteriorated insulators, and conclude that the infrared image based methods are capable of detecting polluted deteriorated insulators in high-voltage. However, these methods lack the consideration of meteorological parameters, which can influence the temperature distribution of the contaminated insulators, to be specific, the same polluted insulator may behave differently in infrared images under different humidity.

The temperature distribution of infrared images depends on both contamination level and meteorological parameters, thus the methods consider both these two factors can be more generalized and accurate. Based on the color features extracted from infrared images and relative humidity, He et al. (2019) accomplish contamination level detection using Radial Basis Function Neural Network (RBFNN); For a contaminated insulator, its infrared images can give contamination information when it in wet conditions, while the visible images are valid to detect contamination level when it in dry conditions. Therefore, Jin et al. (2018) fuse the infrared and visible images to cope with the impact of humidity on non-contact methods. However, the above two kinds are both based on manually designed features, whose perception accuracy are highly dependent on expert experience.

In this study, taking both infrared image and meteorological conditions into consideration, we propose an end-to-end feature fusion method to detect pollution level of insulators in an automatic and accurate way, the contributions are as follows:

1. Considering the differences of infrared images under different weather conditions, the insulator pollution perception problem is mapped to a probability problem of pollution degree, infrared image and meteorological conditions. And the way to solve this problem is to calculate the conditional probability of each pollution severity under the corresponding inputs.

2. The insulator contamination perception methods based on infrared images largely depend on the meteorological conditions, to cope with this problem, we take both infrared image and meteorological parameters as input, and propose a feature fusion method to fuse these two types of data, from which the relationship between contamination grades, temperature and humidity is explored, and the contamination perception in different environmental conditions improves a lot.

3. Instead of manually designing features for inputs, the feature fusion method proposed can automatically extract features for the two kinds of data, which is more accurate and can be trained and tested in an end-to-end way.

The rest of this paper is organized as follows: Section II gives the basic principles of infrared image based contamination perception methods, based on this, the influences of meteorological parameters on infrared images are analyzed; Section III proposes the feature fusion method, which includes the feature extraction part, the feature fusion part and the contamination classification part; Section IV describes the data preparation, the model training and model testing process; Section V verifies the effectiveness of the proposed method from evaluation results and model comparison; and Section VI concludes this paper.

2 BASIC THEORY

Infrared images manifest infrared energy radiated from objects with temperature higher than absolute zero. Because of the abnormal temperature distribution caused by anomaly or faults of the objects, events can be detected through infrared image analysis, which has been widely used in biomedicine (Vainer, 2019), transportation control (Wang et al., 2020a), quality inspection (Tumas and Serackis, 2017), power systems (Wang et al., 2020b) and other fields.

For contaminated insulators in power systems, their pollution degrees can be detected through infrared images. To be specific, the infrared effect of a contaminated insulator is associated with the heat produced by leakage current on its surface, which is affected by the pollution on its surface and meteorological parameters, such as temperature and humidity. For example, even the same contaminated insulator can show different temperature distribution under different meteorological circumstances, which indicates the necessity to consider both thermal effect on infrared image and meteorological circumstance when analyzing the contamination degree of insulators. The factors affecting infrared effect are analyzed as follows:

2.1 Contamination Grade

In a humid atmosphere, the contamination grades of insulators are positively correlated with the heat they produce: The pollution on a polluted insulator absorbs moisture in the atmosphere, which causes a decrease in the surface resistance, and an increase in its conductivity. Therefore, the leakage current through the surface is significantly increased and thus causes thermal effect that can be detected by infrared images. In addition, when under a certain humidity condition, the higher the contamination grade, the larger the decrease of the surface resistance, and the larger the leakage current. While for a clean insulator without contamination, the leakage current is always

small and there are no obvious heating phenomenon even with very high humidity.

2.2 Humidity

A certain degree of humidity is necessary for contaminated insulators to produce leakage current: When the humidity is relatively small, both contaminated insulators and clean insulators produce small or even no leakage current, thus there are no clear differences between their corresponding infrared images; When subjected to a wet condition with relatively high humidity, however, the surfaces of the polluted insulators will become conductive, and the thermal effect caused by the leakage current will be reflected on the infrared images, while for the clean insulators, the increase in humidity does not affect their thermal effect. What's more, for the same contaminated insulator, it can present differently when in different wet condition, to be more specific, the higher the humidity value, the more heat it produces and the higher the temperature in infrared image.

2.3 Temperature

The environmental temperature affects both the leakage current and the infrared image: 1) The leakage current can be influenced in two ways: on the one hand, the change of the environmental temperature often yields change of the environmental humidity, which will indirectly affect the leakage current produced; on the other hand, it affects the evaporation rate of the contamination layer, and may affect the pollution grade of the insulators in the end. 2) The temperature distribution of infrared images can be affected by environmental temperature (Zou et al., 2014), which in turn can influence the contamination perception accuracy.

In short, there is a complicated nonlinear relationship between leakage current and pollution level, temperature and humidity. When using infrared images to perceive contamination grade, environmental humidity and temperature are necessary to be considered.

3 CONTAMINATION GRADE PERCEPTION BASED ON FEATURE FUSION METHOD

We model the pollution degree perception problem of insulators as a conditional probability function based on temperature, humidity and infrared image characteristics. In this paper, we divide the contamination degree into five classes according to the pollution severity, then under the interaction of humidity, temperature and the contamination on the insulator surface, the probability of the contaminated insulator belonging to each category can be characterized as

$$p(c = i \mid t, h, in)\ i = 1, 2, 3, 4, 5 \tag{1}$$

where c represents the contamination class, h, t represents humidity and temperature, respectively, and in is infrared image shoot under this environmental circumstance.

Based on **Eq. 1**, we convert the contamination perception problem into a conditional probability problem, and propose a feature fusion method to tackle this. In the following parts of this chapter, we firstly give the overall framework of the proposed method, and then illustrate the details of feature extraction, feature fusion and contamination perception.

3.1 Overall Framework

Figure 1 depicts the overall feature fusion framework consisting of four parts: 1) the input part, which includes two kinds of parameters—infrared image and meteorological parameters including humidity and temperature. What's more, the input data aligns in time, which means that they are collected at the same time; 2) the feature extraction part, where the two kinds of data are fed into different feature extraction networks—the meteorological parameters are extracted by an artificial neural network (ANN), and the infrared image is extracted by a convolutional neural network (CNN)—because of the differences in data format and physical meaning; 3) the data fusion part, where the two kinds of features are concatenated and fed into two fully connected layers to extract features further; 4) the output part, where and the contamination grade is outputted.

3.2 Meteorological Parameters Feature Extraction Network

Artificial Neural Network (ANN) is a highly nonlinear dynamic system with a directed graph as its topological structure. It learns features and processes information by adjusting the interconnection relationship between internal neurons, so it is of strong self-learning, self-adaptation and high fault tolerance (Kamesh and Rani, 2017; Hu et al., 2018; Bhatt and Gandhi, 2019; Shen et al., 2021).

For a polluted insulator, humidity and temperature can influence its infrared effect on infrared image, at the same time, the two meteorological parameters also interact and influence each other. Therefore, we take humidity and temperature parameters as a whole, and feed them into an ANN to extract the interaction between the two parameters, and learn the features with regard to the contamination grade. The reason we choose ANN to extract features of meteorological parameters is that the input is relatively simple—with only two parameters, in this way, we suppose that a rather simple network is enough to extract the information needed. Besides, ANN has been widely used in many scenes with meteorological parameters as parts of the inputs (Matsumoto et al., 1993; Bhatt and Gandhi, 2019; Madhiarasan, 2020), and the satisfactory results has provided intuitions to our problem.

The proposed feature extraction network is as shown in **Figure 2**, which consists of 2 1×10 fully connected layers and 1 1×5 fully connected layer (FC); and Relu is used to activate the fully connected layers. After the feature extraction, we get a 1×5 sized feature. What needs to be pointed out is that, we test the analysis results under different number of hidden layers and the neurons in each layer, and the structure of the proposed one can get relatively better performance when it used to fuse the two kinds of data.

Before feeding into the ANN, we use **Eq. 2** to normalize the two parameters, to solve the problem caused by their different scales.

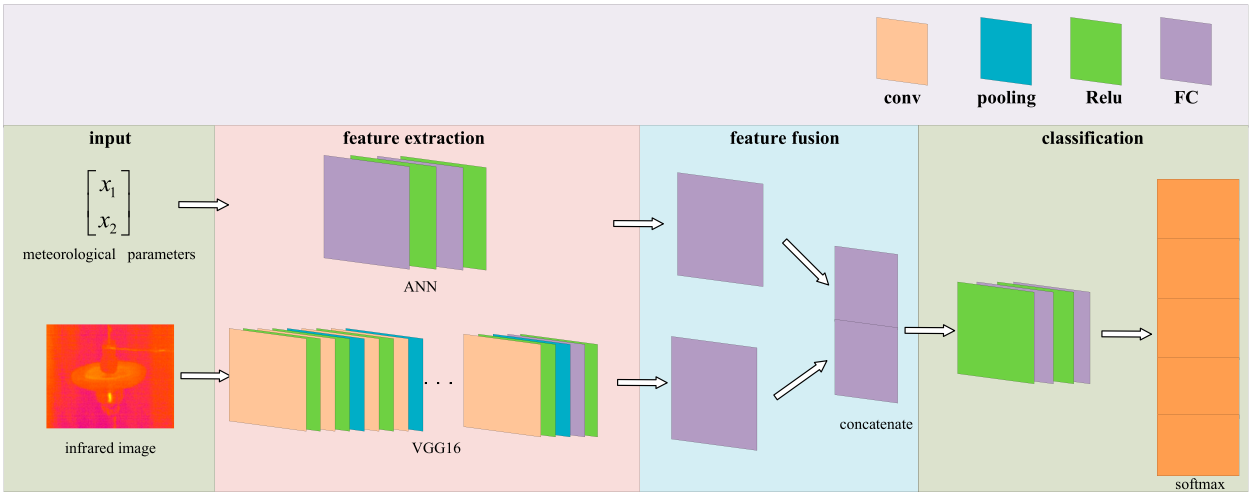

FIGURE 1 | The feature fusion based insulator contamination perception network.

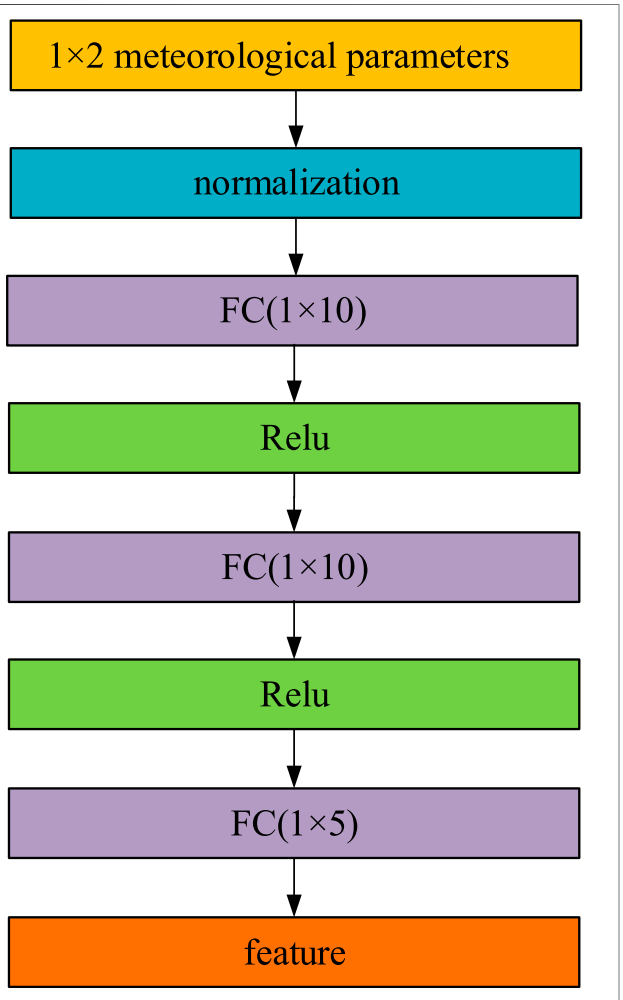

FIGURE 2 | Feature extraction of meteorological parameters.

$$x_{in} = \frac{x_{in} - \min(x_i)}{\max(x_i) - \min(x_i)} \tag{2}$$

where x_i represents the $i - th$ parameter, $i = 1, 2$; x_{in} is the $n - th$ parameter of x_i, which corresponds to the infrared image at the $n - th$ sampling moment; $\min(x_i)$ and $\max(x_i)$ are the minim and maxim of the two parameters.

3.3 Infrared Image Feature Extraction Network

One of the most popular image classification approaches today involves the convolutional neural network (CNN), which has been widely used in classification (Simonyan and Zisserman, 2014; He et al., 2016), object detection (Ren et al., 2017), segmentation (Long et al., 2015) and so on. Unlike traditional hand-crafted features, CNN unifies the feature learning and classification parts, and automatically and jointly solves the two problems together, which in turn greatly improves the accuracy of image classification (Hatami et al., 2017).

As is shown in **Figure 3**, in this paper, we take part of VGG-16 as feature extraction network of infrared images, for it is one of the classical classification networks with good results, and meets the contamination classification goal of this paper. In **Figure 3**, *conv* $(64 \times 3 \times 3) \times 2$ represents the same 2 convolutional layers, and each of them has 64 filters sized 3×3, and the same to *conv* $(128 \times 3 \times 3) \times 2$, *conv* $(256 \times 3 \times 3) \times 3$ and so on. *maxpooling* (2×2) is the max pooling layer sized 2×2. It can be seen that the convolutional layers are all sized 3×3, and the pooling layers are all sized 2×2. In addition, all the convolutional layers are activated by Relu.

We normalize the infrared images to $224 \times 224 \times 3$ before feeding them into the feature extraction network. During the feature extraction process, the width and height of a image are reduced to half of the original each time it passes through a pooling layer, and the channel size doubles every time it goes

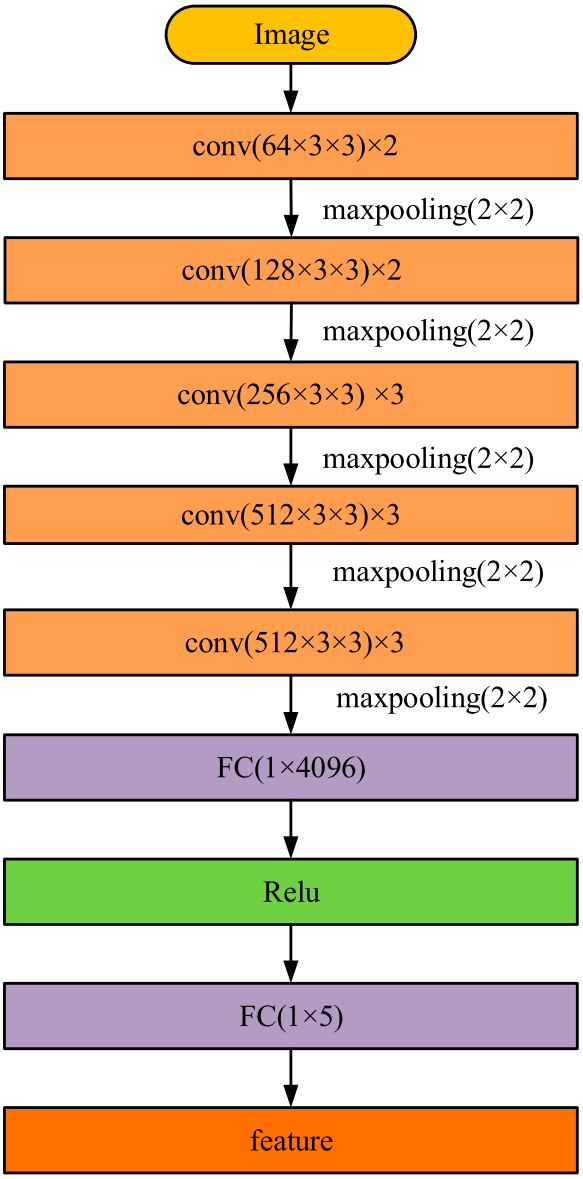

FIGURE 3 | Feature extraction of infrared image.

through the convolutional layer blocks (the network between two neighboring maxpooling represents a block). After the final maxpooling layer, we get a 7 × 7 × 512 sized feature, then it is fed into two fully connected layers activated by Relu function, to further feature extracted. Finally, a feature sized 1 × 5 is outputted.

3.4 Feature Fusion and Classification Network

As is shown in **Figure 4**, we fuse the two kinds of features by concatenating them. And after that, we get a 1 × 10 sized feature. To make the fusion effectively, it requires at least one nonlinear stage to successfully capture feature from the fused feature (Srivastava and Salakhutdinov, 2014; Ramachandram and Taylor, 2017). Therefore, we use two fully connected layers activated by Relu to further analyze the fused feature. Here, to avoid overfitting of the network, we set the dropout ratio of the FC layer followed by the concatenation layer to be 0.5.

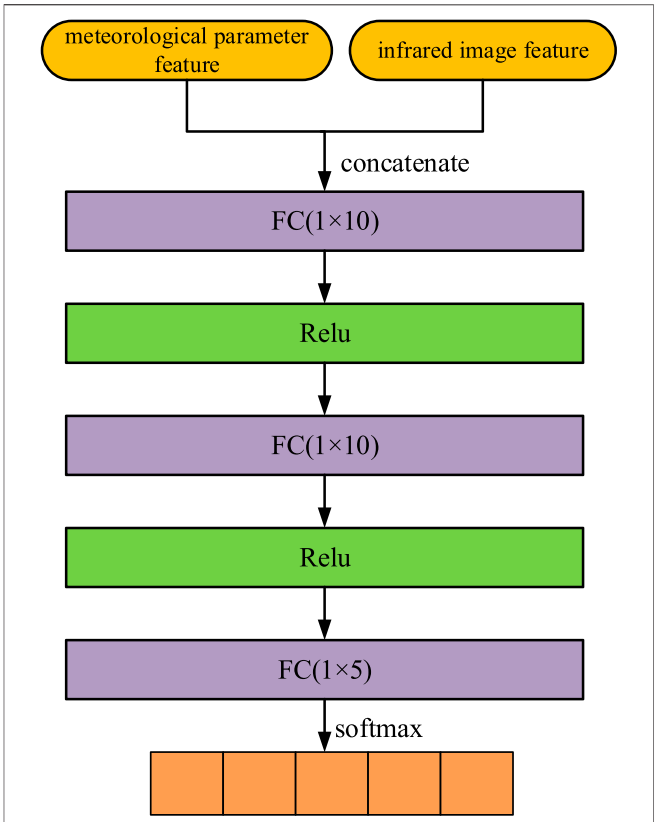

FIGURE 4 | Feature fusion and classification.

To classify the contamination, we divide the polluted insulators into five grades, and use softmax to calculate the probability that the input belonging to each class, as is shown in **Eq. 3**.

$$p(x) = \begin{bmatrix} p(y=1 \mid x) \\ p(y=2 \mid x) \\ \cdots \\ p(y=m \mid x) \end{bmatrix} = \frac{1}{\sum_{j=1}^{m} e^{x_j}} \begin{bmatrix} e^{x_1} \\ e^{x_2} \\ \cdots \\ e^{x_m} \end{bmatrix} \tag{3}$$

where $x = [x_1, x_2, \cdots x_m]$ is the input, which is determined by the network before the softmax; $p(x)$ represents the output of softmax, which is the conditional probability of the input belonging to each category; y is the label of the input; m represents the class number, which is 5 in this paper (we category the contamination into 5 classes). Finally, the grade with the biggest possibility is the class outputted.

4 EXPERIMENTAL SETUPS

As is shown in **Figure 5**, the implementation of the proposed method includes three parts: data acquisition and labeling, training phase and testing phase.

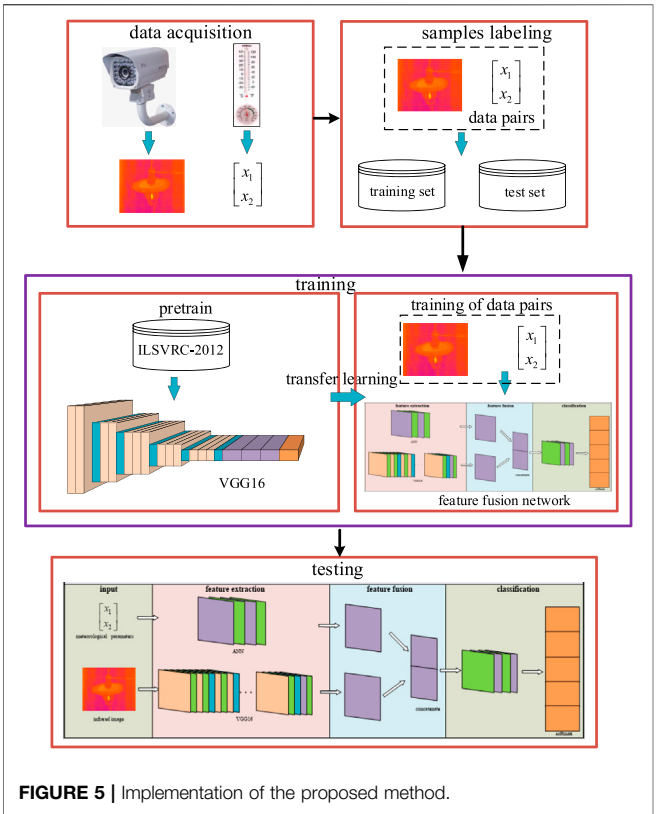

FIGURE 5 | Implementation of the proposed method.

4.1 Data Acquisition and Labeling

To collect polluted insulator image samples in different weather conditions, we use a mixture of NaCl and kaolin to contaminate the XP-70 insulators, and then, in a fog chamber, we shot infrared images in different humidity and temperature, where the relative humidity ranges from 60 to 100% in step of 5% each; and the temperature ranges from 0°C to 40°C in step of 5°C each. As is illustrated in 2.2, a ceratin value of humidity is a must for the polluted insulators to generate leakage current and radiate to show thermal effect. Therefore, we don't collect infrared images with the humidity less than 60%, as in that circumstance, the insufficient humidity will cause almost no leakage current generated by the contaminated insulators, and the contamination degree can't be perceived by the infrared images.

We use the equivalent salt deposit density (ESDD) (mg/cm^2) to discriminate the insulator contamination severity. According to Chinese national standard 'GB/T 5582–1993', the contamination can be classified into 5 grades according to the pollution content, as is shown in **Table 1**. In addition, we divide the data into a training and testing set according to 5 : 1, which are used to train the network and evaluate the performance of the proposed method, respectively.

4.2 Training Phase

During the training phase, we employ transfer learning to make the network converge faster and solve the problem of relatively small samples, which consists of two stages: In the first stage, we pretrain VGG-16 network based on the ILSVRC-2012 dataset, which contains more than 1 million training samples, and then the parameters of the network are saved. In the second stage, based on the shared parameters of the pretrained VGG-16, we retrain the feature fusion network taking both infrared and meteorological parameters pairs as input. The idea here is that, there are some similarities for the image classification problems, for example, they all have to extract some profile information based on the point and line characteristics, thus they can share some of the parameters for the same network regarding to different classification goals. Besides, the network has been trained to some extent and the loss function has arrived to a relatively small value, which leads to a relatively small modification compared with training from a completely new network. During the training process, we take the same training strategies as that in VGG-16 (Simonyan and Zisserman, 2014), and aim to make the loss function small enough, as is shown in **Eq. 4**.

$$L = -\sum_{i=1}^{n} p_i^* \log(p_i) \tag{4}$$

where L represents the loss; p_i is the probability from softmax, p_i^* represents the label of the input, which is the real class of the input data; n is the number of samples.

4.3 Testing Phase

After training process, the structure and parameters of the proposed network is frozen in the test stage. In this phase, we take testing set as input, and perceive the contamination grades of the polluted insulators, the evaluation indicators are as follows:

As is shown in **Eq. 5–8** — four indicators—including p (precision), R (recall), AP (average precision), and AR (average recall)— are used to evaluate the proposed approach.

$$\mathrm{P} = \frac{\mathrm{TP}}{\mathrm{TP} + \mathrm{FP}} \tag{5}$$

$$\mathrm{R} = \frac{\mathrm{TP}}{\mathrm{TP} + \mathrm{FN}} \tag{6}$$

$$\mathrm{AP} = \frac{1}{k}\sum_{i=1}^{m} \mathrm{P}_i \tag{7}$$

$$\mathrm{AR} = \frac{1}{k}\sum_{i=1}^{m} \mathrm{R}_i \tag{8}$$

The explanation of the parameters above are as follows:

TP (True Positive): the number of the positive samples predicted as positive; FP (False Positive): the number of the negative samples predicted as positive; TN (True Negative):

TABLE 1 | Contamination classification.

Grade	ESDD (mg/cm2)
1	< 0.03
2	0.03 ~ 0.06
3	0.06 ~ 0.1
4	0.1 ~ 0.25
5	0.25 ~ 0.35

TABLE 2 | Evaluation comparison between the two methods.

Input	AP (%)	AR (%)
Infrared images	68.96	71.08
Meteorological parameters and infrared images	78.75	83.54
Difference	9.79	12.46

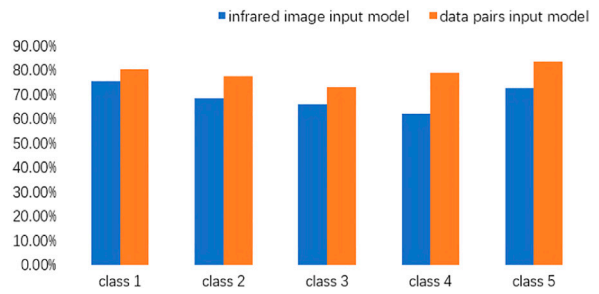

FIGURE 6 | Precision comparison between classes.

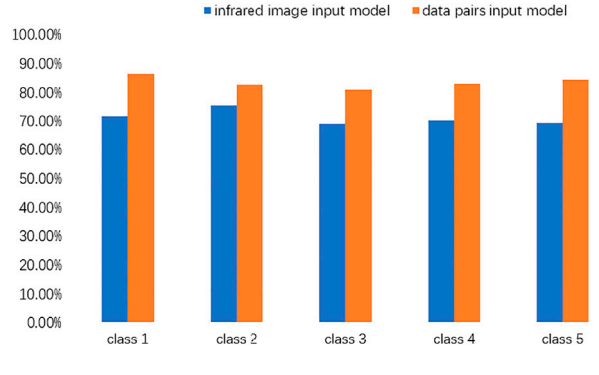

FIGURE 7 | Recall comparison between classes.

the number of negative samples predicted as negative; FN (False Negative): the number of positive samples predicted as negative.

m represents the class number, which equals to 5 in this paper.

5 CASE STUDIES

To validate the effectiveness of the proposed method, two insulator contamination perception methods are compared: 1) VGG-16; 2) feature fusion method proposed in this paper. For the two networks, we take the same training set to train them, and use the same test set to evaluate them. The only difference is that only infrared images are fed into VGG-16, while the data pairs (infrared image and meteorological parameters) are taken as input for the feature fusion network.

5.1 Evaluation Results

Table 2 tells the average results of the two methods, **Figure 6** and **Figure 7** illustrate the performance between five classes, from

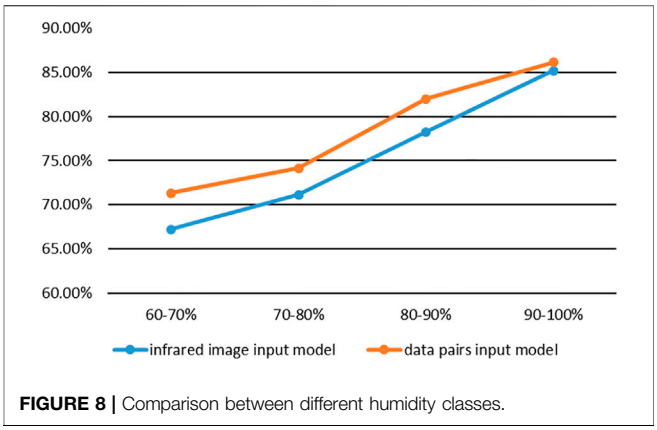

FIGURE 8 | Comparison between different humidity classes.

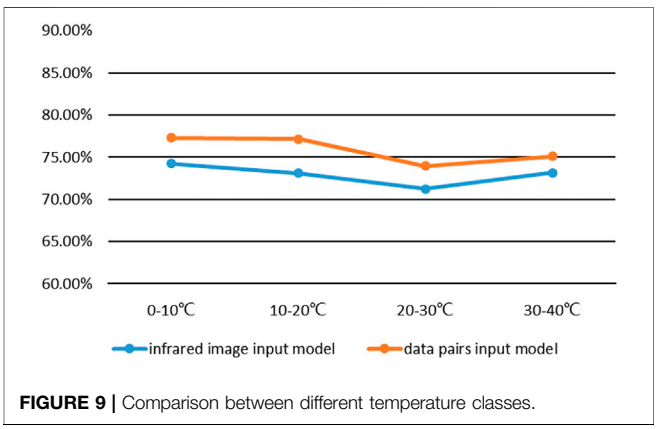

FIGURE 9 | Comparison between different temperature classes.

which we can see that, the fusion method proposed in this paper effectively improves the precision and recall (increases by 7.97 and 12.46% respectively), in addition, it has better results between different contamination classes.

To further analyze the necessity of considering meteorological parameters in insulator pollution perception, we divide humidity into four classes—60 ~ 70%, 70 ~ 80%, 80 ~ 90%, 90 ~ 100%—and compare the AP of the two methods, as is shown in **Figure 8**. And we also divide the temperature into four ranges—0 ~ 10°C, 11 ~ 20°C, 21 ~ 30°C, 31 ~ 40°C—and compare the AP of the two methods, as is shown in **Figure 9**.

From **Figure 8**, we get two conclusions: 1) both two methods perform better in high humidity. However, the data pairs input model is more balanced in each humidity range, while the infrared image input model is more dependent on humidity—the variance of AP of the former is 0.47%, while is 0.63% of the latter; 2) the method proposed in this paper outperforms the single-input method in all humidity levels.

From **Figure 9**, both two methods have relatively balanced performances in each temperature range, while the method proposed in this paper outperforms the single-input method in all the temperature classes.

The above phenomenons can be explained as follows: 1) Both humidity and temperature affect the leakage current of

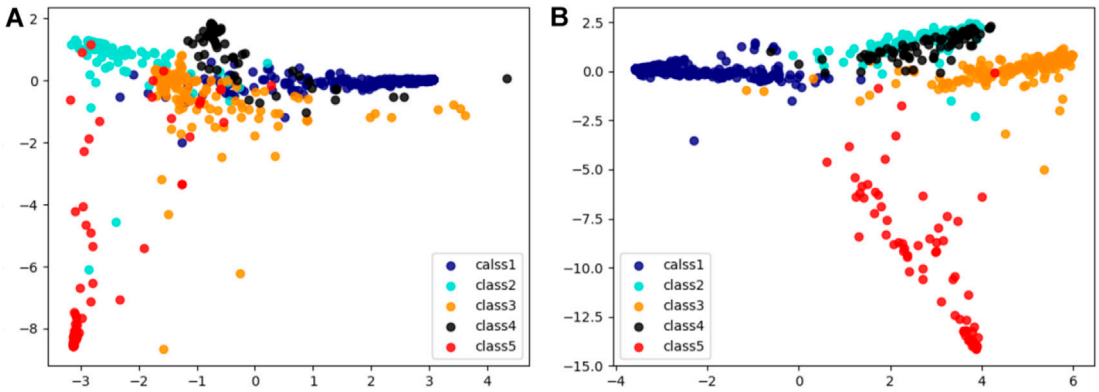

FIGURE 10 | Results of LDA feature reduction **(A)** is result of VGG-16 **(B)** is result of feature fusion model proposed in this paper.

the contaminated insulators, thus further influence the infrared image and the classification perception. When the infrared image alone is used as input, the model cannot explore the relationship between humidity, temperature and the pollution level of the insulator, so it has relatively low precision; While for the fusion method proposed in this paper, it takes humidity, temperature and infrared image as input, which can better explore the relationship between weather conditions and thermal radiation, so it can better judge the contamination level. 2) The temperature does not affect the performance between different contamination classes, as the two methods perform similar in the four temperature ranges within their own (the precision change for the two methods are within 5%). Still, it is still one of the key factors influencing the classification performance, as our method outperforms the single-input method in every temperature level, which may be explained by the influence of the temperature to the humidity.

5.2 Model Comparison

5.2.1 Class Separability Analysis

To reveal the ability of the proposed model to distinguish different levels of pollution, latent discriminant analysis (LDA) (Hussein Mouzannar and Awad, 2018) is performed on testing set to examine the separability of the two methods (the feature fusion model and VGG-16). We extract the features before softmax, and plot the distribution of the data after performing LDA, which reduces the dimensionality of the data to 2. As is shown in **Figure 10**, compared with VGG-16, the feature fusion method is more capable of distinguishing different levels of pollution, which is the reason of better classification ability.

5.2.2 Model Complexity Comparison

Compared with VGG-16, the feature fusion method is less complicated: Although it has more parameters in the meteorological parameters feature extraction part, the fused feature extraction part of the proposed network has much less parameters than VGG-16 — As the former has two 1×10 FC layers, while the latter has two 1×4096 FC layers.

6 CONCLUSION

The accuracy of infrared image based insulator contamination methods largely depend on weather conditions. In this paper, we take the constructed meteorological parameters and the unstructured infrared image as input, and propose a feature fusion model to classify insulator contamination in different meteorological conditions.

The two types of data are different in data form and physical meaning, which makes it difficult to fuse them. In this way, we extract the features of the two types of data, and represent them with the same data form, then two features are fused and further analyzed to classify the contamination. To be specific, the ANN and VGG-16 are used to extract features of meteorological parameters and infrared image, respectively. Then two features are fused by concatenation and further feature extracted by two nonlinear layers (Relu activated fully connected layers). In the end, the contamination level perception is performed by softmax, from which we get the probability of the input belonging to each contamination grade.

Compared with the infrared image input model, the method proposed in this paper can better separate the contamination classification, and perform better in different meteorological conditions. Besides, it has less parameters and is less complicated.

The model in this paper only test samples under the condition of humidity greater than 60%, while for those in the case of humidity less than 60%, there may be no obvious differences between the infrared images of each pollution level. In the future, we will focus on finding more features to make the method more applicable to different meteorological conditions.

DATA AVAILABILITY STATEMENT

The original contributions presented in the study are included in the article/supplementary material, further inquiries can be directed to the corresponding author.

AUTHOR CONTRIBUTIONS

HW: methodology, data collection, simulation, data analysis, writing original draft, recording image; BW: methodology,

recording image data, draft review and editing; ML: methodology, draft review and editing; PL: data collection, simulation; HM: writing review and editing; FM: writing review and editing.

FUNDING

This paper is supported by the State Grid Headquarters Technology Project (Grant No. 5400-202119145A-0-0-00).

REFERENCES

Author Anonymous (2020). *Ieee Draft Guide on the Selection of Transmission and Distribution Insulators with Respect to Cold Weather Conditions*. IEEE P1820/D12, 1–62.

Banik, A., Dalai, S., and Chatterjee, B. (2016). Autocorrelation Aided Rough Set Based Contamination Level Prediction of High Voltage Insulator at Different Environmental Condition. *IEEE Trans. Dielect. Electr. Insul.* 23, 2883–2891. doi:10.1109/tdei.2016.7736849

Bhatt, G. A., and Gandhi, P. R. (2019). "Statistical and Ann Based Prediction of Wind Power with Uncertainty," in 2019 3rd International Conference on Trends in Electronics and Informatics (ICOEI), Tirunelveli, India, April, 2019, 622–627. doi:10.1109/icoei.2019.8862551

Cao, B., Wang, L., and Yin, F. (2019). A Low-Cost Evaluation and Correction Method for the Soluble Salt Components of the Insulator Contamination Layer. *IEEE Sensors J.* 19, 5266–5273. doi:10.1109/jsen.2019.2902192

Dong, B., Jiang, X., Zhang, Z., Hu, J., Hu, Q., and Shu, L. (2014). Effect of Environment Factors on Ac Flashover Performance of 3 Units of Polluted Insulator Strings under Natural Fog Condition. *IEEE Trans. Dielect. Electr. Insul.* 21, 1926–1932. doi:10.1109/tdei.2014.004214

Fofana, I., N'cho, J. S., Betie, A., Hounton, E., Meghnefi, F., and Yapi, K. M. L. (2020). Lessons to Learn from post-installation Pollution Levels Assessment of Some Distribution Insulators. *Energies* 13, 4064. doi:10.3390/en13164064

Hatami, N., Gavet, Y., and Debayle, J. (2017). "Classification of Time-Series Images Using Deep Convolutional Neural networks*CoRR* abs/1710.00886, " Tenth International Conference on Machine Vision (ICMV 2017), Vienna, Austria (SPIE).

He, H., Luo, D., Lee, W.-J., Zhang, Z., Cao, Y., and Lu, T. (2019). A Contactless Insulator Contamination Levels Detecting Method Based on Infrared Images Features and Rbfnn. *IEEE Trans. Ind. Applicat.* 55, 2455–2463. doi:10.1109/tia.2018.2889835

He, K., Zhang, X., Ren, S., and Sun, J. (2016). "Deep Residual Learning for Image Recognition," in 2016 IEEE Conference on Computer Vision and Pattern Recognition (CVPR, Las Vegas, Nevada, USA), June, 2016, 770–778. doi:10.1109/CVPR.2016.90

He Wei, Wei., Yang Fan, Yang., Wang Jingang, Jingang., Yang Hao, Hao., Minyou, C., and Yao Degui, Degui. (2006). Inverse Application of Charge Simulation Method in Detecting Faulty Ceramic Insulators and Processing Influence from tower. *IEEE Trans. Magn.* 42, 723–726. doi:10.1109/tmag.2006.871393

Hu, Z., He, T., Zeng, Y., Luo, X., Wang, J., Huang, S., et al. (2018). Fast Image Recognition of Transmission tower Based on Big Data. *Prot. Control. Mod. Power Syst.* 3, 149–158. doi:10.1186/s41601-018-0088-y

Hussein Mouzannar, Y. R., and Awad, M. (2018). "Damage Identification in Social media Posts Using Multimodal Deep Learning," in ISCRAM 2018 Conference Proceedings—15th International Conference on Information Systems for Crisis Response and Management, Rochester NY, USA, May, 2018, 529–543.

Jiang, X., and Xia, Q. (2010). "Influence of Contamination on Deteriorated Insulators Detection with Infrared Imaging Method," in 2010 International Conference on High Voltage Engineering and Application, New Orleans, USA, October,2010, 457–460. doi:10.1109/ichve.2010.5640729

Jin, L., Ai, J., Tian, Z., and Zhang, Y. (2017). Detection of Polluted Insulators Using the Information Fusion of Multispectral Images. *IEEE Trans. Dielect. Electr. Insul.* 24, 3530–3538. doi:10.1109/tdei.2017.006516

Jin, L., Tian, Z., Ai, J., Zhang, Y., and Gao, K. (2018). Condition Evaluation of the Contaminated Insulators by Visible Light Images Assisted with Infrared Information. *IEEE Trans. Instrum. Meas.* 67, 1349–1358. doi:10.1109/tim.2018.2794938

Kamesh, R., and Rani, K. Y. (2017). Novel Formulation of Adaptive Mpc as Ekf Using Ann Model: Multiproduct Semibatch Polymerization Reactor Case Study. *IEEE Trans. Neural Netw. Learn. Syst.* 28, 3061–3073. doi:10.1109/tnnls.2016.2614878

Liu, L., Mei, H., Guo, C., Tu, Y., and Wang, L. (2021). Pixel-level Classification of Pollution Severity on Insulators Using Photothermal Radiometry and Multiclass Semisupervised Support Vector Machine. *IEEE Trans. Ind. Inf.* 17, 441–449. doi:10.1109/tii.2020.2984642

Liu, Y., Zong, Y., Zong, H., Gao, S., and Du, B. X. (2020). Contamination Deposition and Discharge Characteristics of Outdoor Insulators in Fog-Haze Conditions. *Int. J. Electr. Power Energ. Syst.* 121, 106176. doi:10.1016/j.ijepes.2020.106176

Long, J., Shelhamer, E., and Darrell, T. (2015). "Fully Convolutional Networks for Semantic Segmentation," in 2015 IEEE Conference on Computer Vision and Pattern Recognition (CVPR), Boston, USA, June, 2015, 3431–3440. doi:10.1109/cvpr.2015.7298965

Madhiarasan, M. (2020). Accurate Prediction of Different Forecast Horizons Wind Speed Using a Recursive Radial Basis Function Neural Network. *Prot. Control. Mod. Power Syst.* 5, 230–238. doi:10.1186/s41601-020-00166-8

Matsumoto, T., Kitamura, S., Ueki, Y., and Matsui, T. (1993). "Short-term Load Forecasting by Artificial Neural Networks Using Individual and Collective Data of Preceding Years," in [1993] Proceedings of the Second International Forum on Applications of Neural Networks to Power Systems, Yokohama, Japan, April, 1993, 245–250.

Ramachandram, D., and Taylor, G. W. (2017). Deep Multimodal Learning: A Survey on Recent Advances and Trends. *IEEE Signal. Process. Mag.* 34, 96–108. doi:10.1109/MSP.2017.2738401

Ren, S., He, K., Girshick, R., and Sun, J. (2017). Faster R-Cnn: Towards Real-Time Object Detection with Region Proposal Networks. *IEEE Trans. Pattern Anal. Mach. Intell.* 39, 1137–1149. doi:10.1109/tpami.2016.2577031

Salem, A. A., Abd-Rahman, R., Al-Gailani, S. A., Kamarudin, M. S., Ahmad, H., and Salam, Z. (2020). The Leakage Current Components as a Diagnostic Tool to Estimate Contamination Level on High Voltage Insulators. *IEEE Access* 8, 92514–92528. doi:10.1109/access.2020.2993630

Shen, X., Ouyang, T., Yang, N., and Zhuang, J. (2021). Sample-based Neural Approximation Approach for Probabilistic Constrained Programs. *IEEE Trans. Neural Netw. Learn. Syst.*, 1–8. doi:10.1109/tnnls.2021.3102323

Simonyan, K., and Zisserman, A. (2014). *Very Deep Convolutional Networks for Large-Scale Image Recognition*. CoRR abs/1409, 1556.

Srivastava, N., and Salakhutdinov, R. (2014). Multimodal Learning with Deep Boltzmann Machines. *J. Machine Learn. Res.* 15, 2949–2980.

Tumas, P., and Serackis, A. (2017). "Effective Background Subtraction Algorithm for Food Inspection Using a Low-Cost Near Infrared Camera," in 2017 Open Conference of Electrical, Electronic and Information Sciences (eStream), Vilnius, Lithuania, April, 2017, 1–4. doi:10.1109/estream.2017.7950322

Vainer, B. G. (2019). "Novel Measurement Methods in Biomedicine," in 2019 12th International Conference on Measurement, Smolenice, Slovakia, May, 2019. doi:10.23919/measurement47340.2019.8779955115–118

Wang, B., Benli, E., Motai, Y., Dong, L., and Xu, W. (2020a). Robust Detection of Infrared Maritime Targets for Autonomous Navigation. *IEEE Trans. Intell. Veh.* 5, 635–648. doi:10.1109/tiv.2020.2991955

Wang, B., Dong, M., Ren, M., Wu, Z., Guo, C., Zhuang, T., et al. (2020b). Automatic Fault Diagnosis of Infrared Insulator Images Based on Image Instance Segmentation and Temperature Analysis. *IEEE Trans. Instrum. Meas.* 69, 5345–5355. doi:10.1109/tim.2020.2965635

Wang, J., Xi, Y., Fang, C., Cai, L., Wang, J., and Fan, Y. (2019). Leakage Current Response Mechanism of Insulator String with Ambient Humidity on Days without Rain. *IEEE Access* 7, 55229–55236. doi:10.1109/access.2019.2910660

Wang, L., Cao, B., Mei, H., Zhao, C., and Guan, Z. (2017). Effects of Natural Contamination Components on the Surface Conductivity under Saturated Moisture. *IEEE Trans. Dielect. Electr. Insul.* 24, 2945–2951. doi:10.1109/tdei.2017.006558

Zhao, W., Liu, W., Hu, Y., An, Y., and Li, Y. (2017). "Extraction Method of Insulator Discharge Area in Ultraviolet Image and its Application," in 2017 4th International Conference on Systems and Informatics (ICSAI), Hangzhou, China, November, 2017, 857–961. doi:10.1109/icsai.2017.8248405

Zhao, Z., Fan, X., Qi, Y., and Zhai, Y. (2017). "Multi-angle Insulator Recognition Method in Infrared Image Based on Parallel Deep Convolutional Neural Networks," in *Computer Vision*. Editors J. Yang, Q. Hu, M.-M. Cheng, L. Wang, Q. Liu, X. Bai, et al. (Singapore: Springer Singapore), 303–314. doi:10.1007/978-981-10-7305-2_27

Zhong, R., Liu, C., and He, W. (2018). "Design and Verification of Contamination Insulator Conductivity Detecting System," in 2018 International Conference on Power System Technology (POWERCON), Guangdong, China, November, 2018, 3136–3141. doi:10.1109/powercon.2018.8602095

Zou, Z., Hu, Y., Gao, B., Woo, W. L., and Zhao, X. (2014). Temperature Recovery from Degenerated Infrared Image Based on the Principle for Temperature Measurement Using Infrared Sensor. *J. Appl. Phys.* 115, 0021–8979. doi:10.1063/1.4863783

Conflict of Interest: The authors declare that the research was conducted in the absence of any commercial or financial relationships that could be construed as a potential conflict of interest.

frontiers in Energy Research

CORRECTION
published: 18 October 2021
doi: 10.3389/fenrg.2021.773322

Corrigendum: Insulator Contamination Perception Based on Feature Fusion of Infrared Image and Meteorological Parameters

Hongxia Wang[1], *Bo Wang*[1]*, *Min Li*[2], *Peng Luo*[1], *Hengrui Ma*[3] *and Fuqi Ma*[1]

[1]School of Electrical Engineering and Automation, Wuhan University, Wuhan, China, [2]School of Computer and Artificial Intelligence, Wuhan Textile University, Wuhan, China, [3]New Energy (Photovoltaic) Industry Research Center, Qinghai University, Xining, China

Keywords: insulator, contamination perception, feature fusion, infrared image, meteorological parameters

A Corrigendum on

Insulator Contamination Perception Based on Feature Fusion of Infrared Image and Meteorological Parameters

by Wang, H., Wang, B., Li M., Luo, P., Ma, H., and Ma, F. (2021). Front. Energy Res. 9:746378. doi: 10.3389/fenrg.2021.746378

In the original article, there was an error. In the description of **Eq. 4**, the last part of the sentence that reads "which equals to 1,000 in the VGG-16 and 5 in the feature fusion network proposed." should be removed.

In addition, there was also an error in section 4 Experimental Setups, 4.2 Training Phase. The final sentence was incorrectly written as "where L represents the loss; pi is the probability from softmax, ppi represents the label of the input, which is the real class of the input data; n is the number of samples, which equals to 1,000 in the VGG-16 and 5 in the feature fusion network proposed." The sentence should read as follows: "where L represents the loss; p_i is the probability from softmax, p_i^* represents the label of the input, which is the real class of the input data; n is the number of samples."

Finally, there was also an error in the Funding statement. The original statement was incorrectly written as "This paper is supported by the National Natural Science Foundation of China (Grant No.51777142,51907096)". The statement should read as follows: "This paper is supported by the State Grid Headquarters Technology Project (Grant No.5400-202119145A-0-0-00)".

The authors apologize for this error and state that this does not change the scientific conclusions of the article in any way. The original article has been updated.

Conflict of Interest: The authors declare that the research was conducted in the absence of any commercial or financial relationships that could be construed as a potential conflict of interest.

OPEN ACCESS

Edited and reviewed by:
Xun Shen,
Tokyo University of Agriculture and Technology, Japan

***Correspondence:**
Bo Wang
whwdwb@whu.edu.cn

Specialty section:
This article was submitted to Wind Energy, a section of the journal Frontiers in Energy Research

Received: *09 September 2021*
Accepted: *17 September 2021*
Published: *18 October 2021*

Citation:
Wang H, Wang B, Li M, Luo P, Ma H and Ma F (2021) Corrigendum: Insulator Contamination Perception Based on Feature Fusion of Infrared Image and Meteorological Parameters. Front. Energy Res. 9:773322. doi: 10.3389/fenrg.2021.773322

frontiers in Energy Research

BRIEF RESEARCH REPORT
published: 30 September 2021
doi: 10.3389/fenrg.2021.760525

Intelligent Frequency Control Strategy Based on Reinforcement Learning of Multi-Objective Collaborative Reward Function

*Lei Zhang, Yumiao Xie, Jing Ye *, Tianliang Xue, Jiangzhou Cheng, Zhenhua Li and Tao Zhang*

College of Electrical Engineering and New Energy, China Three Gorges University, Yichang, China

Large scale wind power integration into the power grid will pose a serious threat to the frequency control of power system. If only Control Performance Standard (CPS) index is used as the evaluation standard of frequency quality, it will easily lead to short-term centralized frequency crossing, which will affect the effect of intelligent Automatic Generation Control (AGC) on frequency quality. In order to solve this problem, a multi-objective collaborative reward function is constructed by introducing a collaborative evaluation mechanism with multiple evaluation indexes. In addition, Negotiated W-Learning strategy is proposed to globally optimize the solution of the objective function from multi dimensions, it avoids the poor learning efficiency of the traditional Greedy strategy. The AGC control model simulation of standard two area interconnected power grid shows that the proposed intelligent strategy can effectively improve the frequency control performance and improve the frequency quality of the system in the whole-time scale.

Keywords: wind power grid-connected, intelligent frequency control strategy, multi-dimensional frequency control performance standard, Negotiated W-Learning algorithm, global optimization

OPEN ACCESS

Edited by:
Zhenhao Tang,
Northeast Electric Power University, China

Reviewed by:
Zhu Zhang,
Hefei University of Technology, China
Yuanchao Hu,
Shandong University of Technology, China

****Correspondence:***
Jing Ye
x1620730050@163.com

Specialty section:
This article was submitted to Smart Grids, a section of the journal Frontiers in Energy Research

Received: *18 August 2021*
Accepted: *14 September 2021*
Published: *30 September 2021*

Citation:
Zhang L, Xie Y, Ye J, Xue T, Cheng J, Li Z and Zhang T (2021) Intelligent Frequency Control Strategy Based on Reinforcement Learning of Multi-Objective Collaborative Reward Function. Front. Energy Res. 9:760525. doi: 10.3389/fenrg.2021.760525

1 INTRODUCTION

Automatic Generation Control (AGC) is an important means to realize the balance of active power-load supply and demand in the power system. Among them, the quality of frequency control strategy is an important factor that affects the performance of AGC control (Alhelou et al., 2018; Shen et al., 2021a; Shen and Raksincharoensak, 2021a). However, the control strategies applied in engineering, such as the threshold zone AGC control strategy that takes into account the combined effects of the proportional component, integral component and Control Performance Standard (CPS) control component of the regional control deviation (Arya and Kumar, 2017; Shen et al., 2020a; Xi et al., 2020; Shen and Raksincharoensak, 2021b), have been unable to adapt to the increasingly complex frequency control of interconnected power grids (Shen et al., 2017; Zhang and Luo, 2018).

In recent years, the intelligent frequency control strategy of reinforcement learning has received lots of attention (Yu et al., 2011; Abouheaf et al., 2019; Xi et al., 2019; Shen et al., 2020b; Liu et al., 2020), because it does not rely on models and does not require precise training samples or system prior knowledge (Watkins and Dayan, 1992; Yang et al., 2018; Li et al., 2020; Yang et al., 2021a; Shen et al., 2021b).

However, most intelligent control strategies are built on the CPS frequency control performance evaluation standard. The CPS index has low sensitivity for short-term inter-area power support

evaluation, and cannot take into account the short-term benefits of frequency control performance (Kumar and Singh, 2019; Yang et al., 2019; Zhu et al., 2019). In a system with large-scale wind power grid connection, the ability of each region to comply with CPS indicators is limited. The intelligent AGC control strategy that only considers the CPS control criteria can easily cause short-term concentrated frequency crossings, which seriously affects the control effect of the intelligent AGC control strategy (Wang and James, 2013; Xie et al., 2017; Yang et al., 2021b).

In fact, with the development of grid-connected new energy sources and smart grids, the grid frequency control evaluation standard is transitioning from single-scale evaluation to multi-time-scale and multi-dimensional evaluation. The North American Electric Reliability Council (NERC) proposed a new frequency evaluation performance index named Balancing Authority ACE Limits (BAAL), which is used to ensure the short-term frequency quality of the system by constraining the mean value of the frequency difference fluctuates in any 30 min not to exceed the limit. However, the intelligent AGC control strategy under both BAAL and CPS indicators is a kind of multi-objective control problem, and there is no relevant literature to study it.

In response to the above problems, this paper proposes an intelligent frequency control strategy for collaborative evaluation of multi-dimensional control standards. This strategy constructs and introduces a collaborative reward function that considers the CPS index and the BAAL index in the multi-objective reinforcement learning algorithm. Then, the Negotiated W-Learning strategy is used to learn the action space of the agent, which effectively solves the problem that the agent cannot fully explore the action (Nathan and Ballard, 2003; Liu et al., 2018; Wang et al., 2019). Simulation examples show that the proposed intelligent control strategy can effectively improve the overall frequency performance quality of the power system.

2 FREQUENCY CONTROL PERFORMANCE EVALUATION STANDARD OF INTERCONNECTED POWER GRID

2.1 CPS1 Frequency Control Performance Evaluation Standard

NERC uses the BAL (BAL-001) disturbance control series of indicators to evaluate the frequency control quality of the interconnected power grid. Among them, the CPS1 (BAL-001-2: R1) indicator is the most widely used in China, as shown in **Eq. 1**:

$$AVG_{1,T}\left[\left(\frac{ACE^{m}_{1\,\min}}{-10B_m}\cdot\Delta F_{1\,\min}\right)\right]\le\varepsilon^2 \tag{1}$$

where $\Delta F_{1\ \min}$ and $ACE^{m}_{1\ \min}$ are separately the average value of the frequency deviation and power deviation in the control area within 1 min, B_m is the frequency deviation coefficient of the area m, and represents the frequency adjustment responsibility assigned to area m. $AVG_{1,T}(\cdot)$ means calculate the average value for 12 months, ε is the upper limit of the area m in controlling the frequency deviation.

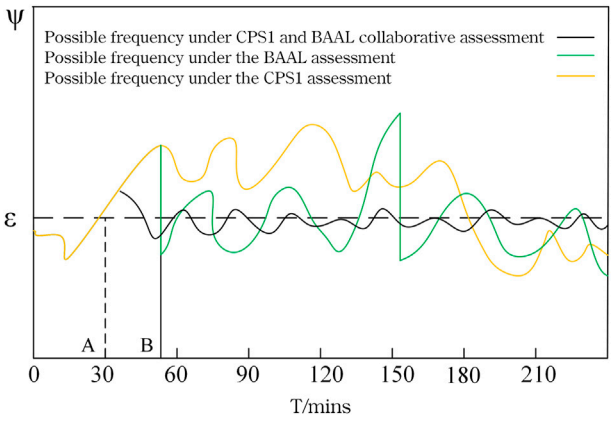

FIGURE 1 | The distribution curve of the integrated frequency deviation factor over time.

Taking the situation that the actual frequency is higher than the planned frequency as an example, expand **Eq. 1** as follows:

$$\frac{1}{T}\int_0^T\frac{\Delta F}{\varepsilon}*\left[\frac{\Delta P_{\text{tie}}}{-10B_m\varepsilon}+\frac{\Delta F}{\varepsilon}\right]dt\le 1 \tag{2}$$

where: T is the entire time period, $\Delta F/\varepsilon$ is the frequency deviation contribution of the region itself, $\Delta P_{\text{tie}}/-10B_m\varepsilon$ is the frequency contribution of other regions to this region, and $\Delta P_{\text{tie}}/-10\ \text{B}_m\varepsilon+\Delta F/\varepsilon$ is the comprehensive frequency deviation contribution. For the convenience of analysis, define $\Delta F/\varepsilon*[\Delta P_{\text{tie}}/-10\ \text{B}_m\varepsilon+\Delta F/\varepsilon]$ as the comprehensive frequency deviation factor, and denoted by ψ.

The CPS1 indicator statistically evaluates the rolling root mean square of the frequency difference time series during the T period in the evaluation area. When T is large enough, the system frequency deviation qualification rate is greater than 99.99%. Therefore, CPS1 is a long-term evaluation index reflecting the frequency quality of interconnected power grids.

2.2 BAAL Frequency Control Performance Evaluation Standard

NERC proposed the BAAL (BAL-001-2: R2) evaluation index in 2013 and began to implement it in 2016, as shown in **Eq. 3** ~4:

$$T\left[ACE^{m}_{1\,\min}\ge-10B_m\frac{\left(F_{FIL-high}-F_s\right)^2}{(F_A-F_S)_{1\,\min}}\right]\le T_v \tag{3}$$

$$T\left[ACE^{m}_{1\,\min}\le 10B_m\frac{(F_{FIL-low}-F_s)^2}{(F_A-F_S)_{1\,\min}}\right]\le T_v \tag{4}$$

where F_A is the actual frequency value; F_S is the planned frequency value; $F_{\text{FTL-high}}/F_{\text{FTL-low}}$ is the high/low frequency trigger limit; T_v is the specified allowable continuous time limit. $T[\cdot]$ is the continuous over-limit time.

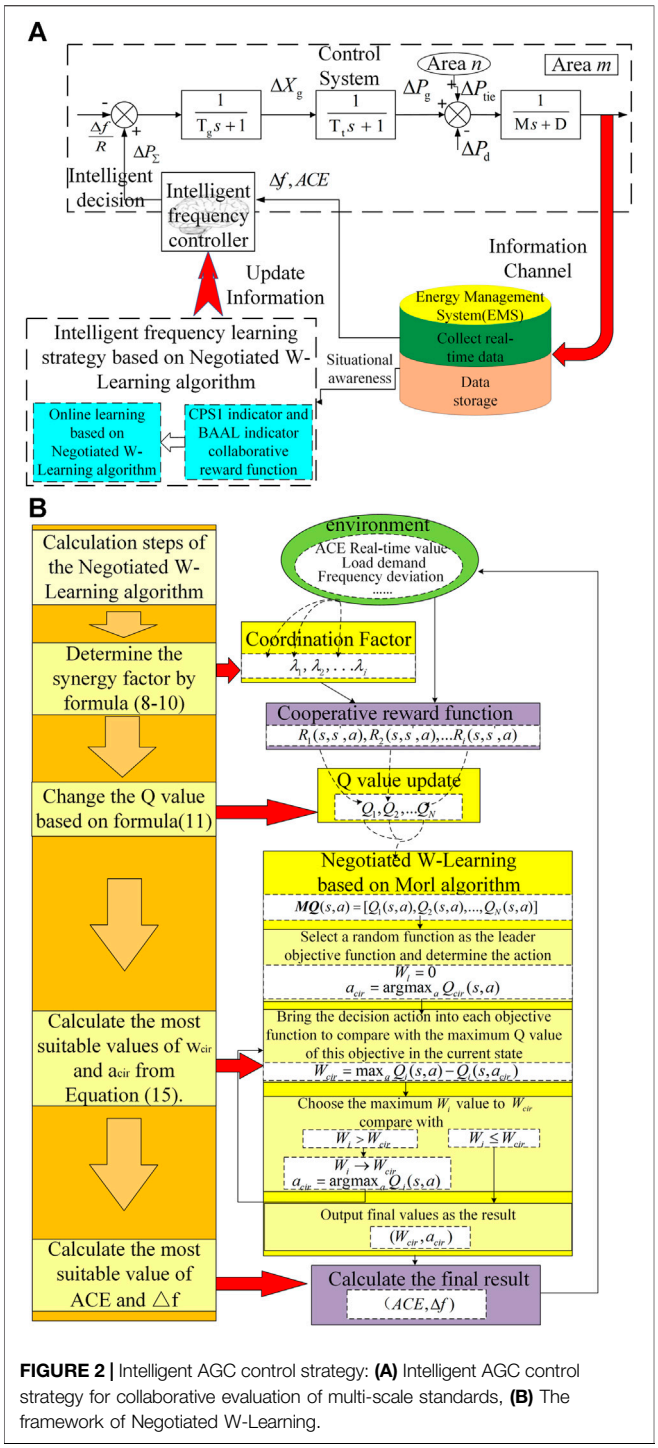

FIGURE 2 | Intelligent AGC control strategy: **(A)** Intelligent AGC control strategy for collaborative evaluation of multi-scale standards, **(B)** The framework of Negotiated W-Learning.

Taking the situation that the actual frequency is higher than the planned frequency as an example, **Eq. 3** can be transformed into the following form in the same way:

$$T\left[\frac{1}{T^n}\int_{T'}^{T'+T''}\frac{\Delta F}{\varepsilon}^{*}\left[\frac{\Delta P_{\text{tie}}}{-10\ \text{B}_m\varepsilon}+\frac{\Delta F}{\varepsilon}\right]dt\geq 1\right]\leq \text{T}_\text{v} \qquad (5)$$

2.3 Performance Analysis Under the Joint Control of BAAL Standard and CPS1 Standard

In order to further study the feature of the two index, **Figure 1** shows the change curve of the comprehensive frequency deviation factor ψ, which considers different performance indicators under the influence of the time dimension.

As shown in **Figure 1**, taking point A as the critical point of frequency line crossing, when only CPS1 is considered, the system frequency can still meet the requirements of control performance index, but it will affect the safe operation of various equipment in the system and cause the power quality reduced. If only the BAAL indicator is considered, the system frequency may appear "vertical dro" and "tip oscillatio," as shown in point B in **Figure 1**. At this time, the synchronous generator frequently receives the opposite frequency deviation signal that occurs in a short period of time. This situation will increase the wear of the unit. When considering the effects of CPS1 and BAAL indicators at the same time, the frequency will change into the reverse process under the influence of BAAL performance after short-term limit violation.

In summary, if CPS1 and BAAL indicators can be coordinated to constrain the system frequency closely, it can guarantee not only the long-term frequency quality but also the short-term frequency safety.

3 INTELLIGENT AGC CONTROL STRATEGY CONSIDERING COOPERATIVE EVALUATION OF MULTI-DIMENSIONAL CONTROL STANDARDS

Based on the analysis in **Section 2.3**, this paper constructs an AGC control model based on a multi-objective collaborative reward function reinforcement learning frequency control strategy. As shown in **Figure 2A**, it mainly consists of the following parts: system governor, equivalent module of the generator, dynamic model of system's frequency deviation, and intelligent brain controller. Where R, T_g, T_t, M, D are separately the equivalent unit adjustment coefficient, time constant of the governor, equivalent generator time constant, equivalent inertia coefficient and equivalent damping coefficient of the power system in area m; ΔP_{tie} is the exchange power deviation of the tie line in area m, ΔX_g, ΔP_g, ΔP_d are separately the change in the position of the regulating valve, in generator output power and in load disturbance, ΔP_Σ is the total adjustment command of the unit.

Frequency controller intelligent learning stage: This article uses a multi-objective collaborative reward function reinforcement learning strategy to learn and train the intelligent frequency controller. This strategy mainly includes two parts, namely CPS1 index and BAAL index cooperative reward function and Negotiated W-Learning based intelligent frequency control learning algorithm. First, use the MORL idea to construct the instant reward function of CPS1 index and BAAL

index, and use dynamic coordination factors to characterize the impact of different indicators on environmental changes. Then, the implementation rewards given under the MORL learning are used to update the respective state action sets of the CPS1 index and the BAAL index. Finally, Negotiated W-Learning conducts a global search to get the final action, which will meet the CPS1 and BAAL indicators and environmental feedback characteristic information.

Frequency controller online deployment stage: The learned and mature frequency controller receives the SCADA database in the Energy Management System (EMS) in each AGC control cycle to collect frequency deviation, ACE, CPS, BAAL, and other data in real time, and make real-time frequency control action.

3.1 Collaborative Reward Function of CPS1 Indicator and BAAL Indicator

This paper constructs a cooperative reward function based on the CPS1 indicator and the BAAL indicator, which is expressed as follows:

$$\begin{aligned} R_1(s,s',a) &= -\lambda_1 (ACE - BAAL)^2 \\ R_2(s,s',a) &= -\lambda_2 \left(CPS1^* - CPS1\right)^2. \end{aligned} \tag{6}$$

Among them: $R_i(s,s',a)$ is the instant reward value obtained when the ith goal is transferred from state s to state s' through action a; ACE (t) is the real-time value of the regional control deviation at the current moment; s is the system state $[ACE(t)]$ at time t, s' is the state $[ACE\ (t+1)]$ at time $t+1$, a is the system action $(\Delta P_{\Sigma}(t))$ when the system goes from s to state s'. $BAAL(t)$ is the instantaneous value of BAAL at time t, $CPS1$ (t) is the instantaneous value of $CPS1$ at time t, $CPS1^*$ is the target value, generally 200%.

λ_i is the dynamic coordination factor of the cooperative reward function, that is, λ_i changes dynamically with each state transition process. This paper adopts the method of comprehensive weighting and multiplicative weighting, comprehensively considers the preferences of decision makers and the inherent statistical law between the index data to determine the value of the dynamic coordination factor.

Firstly, Define parameter K as a parameter for evaluating the importance of frequency performance evaluation indicators. $K_{i,j}$ represents the importance degree of the evaluation index relative to another one in the frequency performance evaluation. When there is an out-of-bounds situation such as ACE < BAAL or $CPS1$ > 200, the importance of the corresponding indicators will increase accordingly. When the two indicators play equal or unimportant roles in the frequency evaluation process, the corresponding $K_{i,j}/K_{j,i}$ values are all 4 or 0. The relative importance of any index increases by one point, the corresponding $K_{i,j}/K_{j,i}$ value increases by 1, and the $K_{j,i}/K_{i,j}$ value decreases by 1. Then obtain the weighting factors of each target in each action cycle:

$$w_i = \frac{K_{j,i}}{K_{j,i} + K_{i,j}} \ (i \neq j) \tag{7}$$

In order to eliminate subjectivity, the entropy method is used to calculate the coefficient of difference between the two indicators β_i:

$$\beta_i = \frac{1 + \ln^{-1}(N) \sum_{y=1}^{K} P_{y,i} \ln\left(P_{y,i}\right)}{\sum_{i=1}^{N}\left(1 + \ln^{-1}(N) \sum_{y=1}^{K} P_{y,i} \ln\left(P_{y,i}\right)\right)} \tag{8}$$

$$P_{y,i} = x_{y,i} \Big/ \sum_{y=1}^{K} x_{y,i} \tag{9}$$

Where: $x_{y,i}$ is the standardized index value of the ith frequency control performance evaluation index at the yth time, K represents the number of the ith frequency control performance evaluation index from 0 to the current time t, and N represents the target number. $P_{y,i}$ is the proportion of $x_{y,i}$ to the total number of indicators from 0 to t.

At last, the final coordination factor is determined by multiplication weighted method. Therefore, the coordination factor can be obtained by combining 8 and 9:

$$\lambda_i = \frac{\sqrt{w_i \beta_i}}{\sum_{i=1}^{N} \sqrt{w_i \beta_i}} \tag{10}$$

3.2 Negotiated W-Learning Intelligent Frequency Control Learning Algorithm

The update formula of MORL is the same as the state-action value function update of traditional Q learning, as shown in **Eq. 11**. In order to facilitate the selection of the optimal action that satisfies each of the following goals, this paper uses the $\boldsymbol{MQ}(s,a)$ vector to represent the state-action value function Q value of the action a in the state s for the N goals, as shown in **Eq. 12**, and the optimal action strategy π^*_{MQ} for each target in the current state expressed in **Eq. 13**:

$$Q_i(s,a) \leftarrow Q_i(s,a) + \alpha\left(R_i(s,s',a) + \gamma \max_{a \in A} Q_i(s',a) - Q_i(s,a)\right) \tag{11}$$

$$\boldsymbol{MQ}(s,a) = [Q_1(s,a), Q_2(s,a), \ldots, Q_N(s,a)] \tag{12}$$

$$\pi^*_{MQ} = \arg\max_{a}\left\{\max_{i} \boldsymbol{MQ}(s,a)\right\} \tag{13}$$

In **Eq. 11**:α $(0 < \alpha < 1)$ is the learning rate, which is set to 0.01 in this article; γ is the discount coefficient, which is set to 0.9 in this article; Q_i (s, a) represents the Q value of the ith target's choice of action a in state s.

However, the above-mentioned optimal action selection strategy cannot guarantee that the agent fully explores the entire state-action space. In this paper, Negotiated W-learning strategy is used to optimize the $\boldsymbol{MQ}$ (s, a) vector space. This strategy defines variable W_i as a leader parameter. The operation steps are as follows, and **Figure 2B** is a reference flow chart:

Step 1: Choose an objective function in the $\boldsymbol{MQ}(s, a)$ vector space as the guide objective function. Its investigation parameter is expressed as W_i. The first guide objective function is uniformly set to $W_{cir} = 0$, and the guide action is obtained as follows:

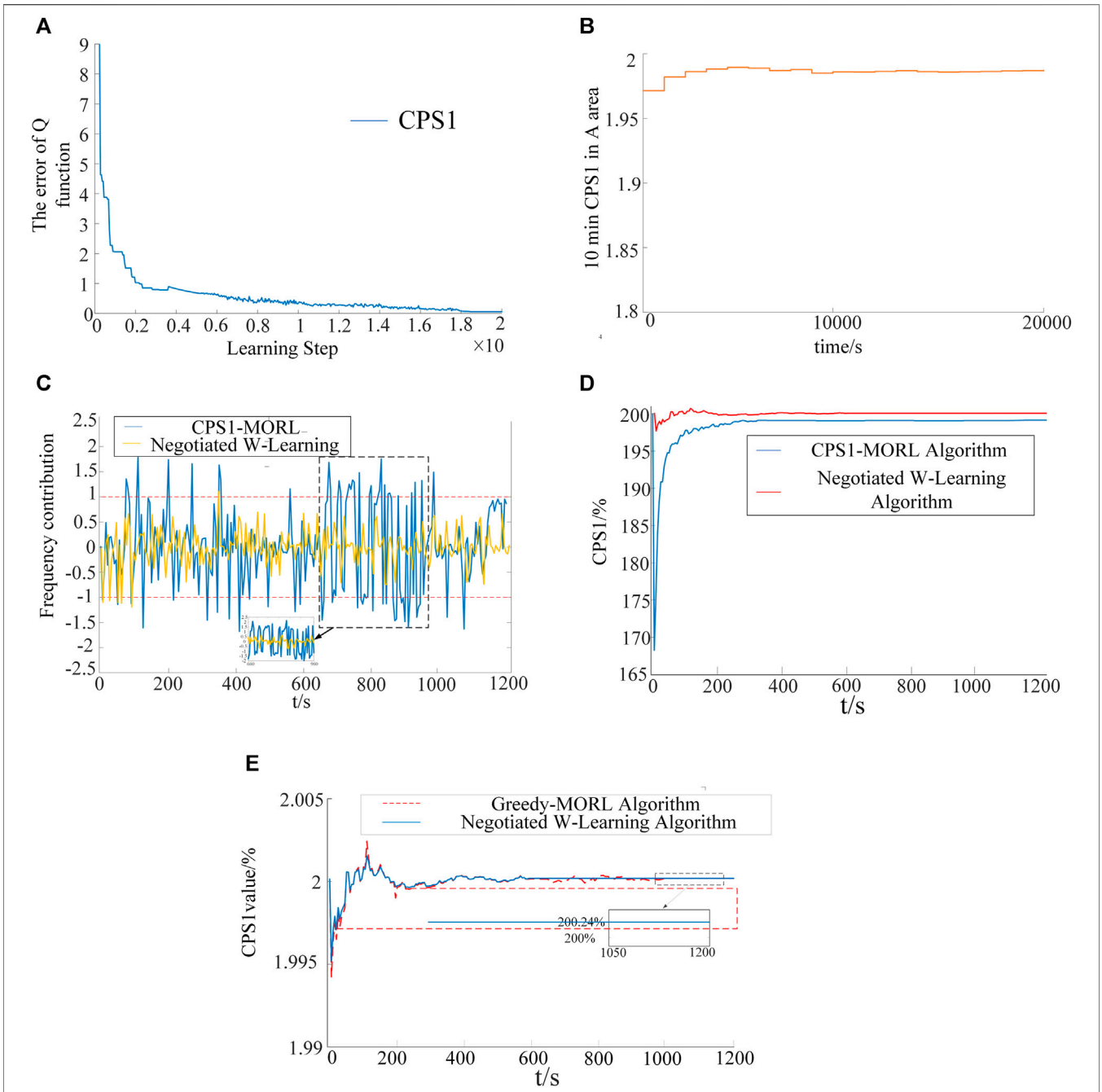

FIGURE 3 | Simulation results: **(A)** Differential convergence result of Q function under CPS1 objective, **(B)** $CPS1_{avg^{-}10-min}$ curve, **(C)** Self-contribution curve, **(D)** Curve reflecting the change of CPS1 value, **(E)** The curve of CPS1.

$$a_{cir} = \arg\max Q_{cir}(s, a) \tag{14}$$

Step 2: The remaining objective functions are calculated according to the following methods, as shown in 15:

$$W_i = \max Q_i(s, a) - Q_i(s, a_{cir}) \tag{15}$$

Step 3: Choose the maximum value of for other objective functions except the guide objective function, and compare it with W_{cir}. If $W_{i,\max} > W_{cir}$, the objective function which is corresponding to this maximum value of W_i should be selected as the new guidance objective function, the guidance value W_{cir} should be updated as the value of $W_{i,max}$, the corresponding action a should be made to be the new guidance action a_{cir}, and then go back to step 2 for repeated iterations until this condition is no longer met.

TABLE 1 | Simulation results under different algorithms.

Algorithms	Calculating time/s (pre-learning)	$\|\Delta f\|$/Hz	CPS1%	BAAL%
CPS1-MORL	12,031	0.0143	196	86.4
Coordinate Q-MORL	18,546	0.0132	197	96.2
Greedy-MORL	20,015	0.0129	199	97.2
Negotiated W-Learning	21,457	0.0064	200	98.5

If $W_i \le W_{cir}$ is obtained, record the guidance action a_{cir} and the guidance objective function at this time as the final value.

4 SIMULATION RESULTS

This paper builds a typical two-region interconnected power grid AGC model for controlling load frequency. The parameter settings of the two regions in the model system are the same, and the system base capacity is 1000 MW.

Figure 3A,B shows the pre-learning process of single CPS1 target and Negotiated W-Learning Algorithm. In the pre-learning stage, a continuous sinusoidal load disturbance with a period of 1,200 s, an amplitude of 100 MW and a duration of 20,000 s is applied to the A area, and a 2-norm Q function matrix $\|Q_t(s,a) - Q_{t-1}(s,a)\|^2 \le \zeta$ (ζ is a constant) is used as the standard for pre-learning to achieve the optimal strategy (Imthias Ahamed et al., 2002).

It can be seen from **Figure 3A** that after many iterations, the Q function tends to stabilize, reaching the optimal strategy for the CPS1 target. **Figure 3B** shows the average value of CPS1 ($CPS1_{\text{avg-10-min}}$) in area A every 10 min during the pre-learning process. It is found that the curve almost remains at a stable and acceptable value in the later stage, which shows that the Negotiated W-Learning algorithm has approached the optimal CPS1 control strategy. At the same time, the Q matrix corresponding to the target BAAL has also converged.

In addition, from the perspective of algorithm learning time, the four algorithms have been simulated for many times, and the average calculation time has been counted. See **Table 1** for details. Due to the difference in the number of optimization targets and the difficulty of calculating the coordination factor, the calculation time of the single target CPS1-MORL is the shortest. Since the CoordinateQ-MORL algorithm cannot fully explore the action set, its calculation time is the second. Compared with the global search algorithm Greedy-MORL, Negotiated W-Learning has gone through more search steps, so its time is the longest.

In order to further verify the adaptability of Negotiated W-Learning in the constantly changing power grid environment, this paper applies a random disturbance with a period of 1,200 s and an amplitude of 100 MW in area A. Four types of algorithms are set for comparison as follows.

Algorithm 1. Traditional single-objective reinforcement learning algorithm for intelligent frequency control based on CPS1 frequency control performance evaluation index (CPS1-MORL).

Algorithm 2. Multi-objective reinforcement learning algorithm for intelligent frequency control based on the traditional greedy strategy of multi-dimensional frequency control performance evaluation index and multi-objective Q function (Coordinate Q-MORL).

Algorithm 3. Under the traditional greedy strategy, this algorithm uses a cooperative reward function based on multi-dimensional frequency control performance evaluation indicators to achieve multi-objective reinforcement learning and intelligent frequency control algorithm (Greedy-MORL).

Algorithm 4. The Negotiated W-Learning algorithm proposed in this paper is based on the collaborative reward letter under the multi-dimensional frequency control performance evaluation index for multi-objective reinforcement learning and intelligent frequency control (Negotiated W-MORL).

4.1 Control Strategy Performance Analysis

Figure 3C shows the frequency deviation self-contribution degree ($\Delta f/\varepsilon$) and CPS1 index change curve of **Algorithm 1** and **Algorithm 4**. In this paper, the threshold is used for calculation, where $\mathcal{E}$ is 0.01. The frequency contribution degree has the ability to reflect the frequency quality of different algorithms. If the frequency contribution degree exceeds ± 1, it means that the frequency at this time has exceeded the prescribed limit 3ε. It can be seen that the frequency contribution curve of **Algorithm 1** exceeds the short-term index frequency continuous limit time specified in this article and has a steep drop in this interval, which will cause greater influence on system operation safety. However, the frequency contribution curve of **Algorithm 4** stays within the defined range. There are two main reasons for this phenomenon: One is that **Algorithm 4** controls the frequency by relaxing the weights of the two indicators in real time. If frequency fluctuations or "frequency drops" occur, the BAAL indicator will be given greater weight. If the frequency continuously exceeds the limit during the simulation period, CPS1 will be given a larger weight for regulation. The second is that **Algorithm 4** considers two indicators to participate in the evaluation of AGC control at the same time, while **Algorithm 1** only considers the impact of CPS1. At the same time, the CPS1 curve of **Algorithm 4** in **Figure 3D** fluctuates less throughout the simulation cycle, while the fluctuation of **Algorithm 1** is larger, which further proves that **Algorithm 4** is superior to **Algorithm 1** in terms of frequency control effect.

In summary, combining the BAAL and CPS1 indicators to constrain the system frequency can effectively improve the frequency quality of the system at the full time scale.

4.2 The Influence of Cooperative Reward Function on Frequency Control Performance

In order to verify the effectiveness of the collaborative reward function proposed in this paper, the control performance indicators of **Algorithm 2** and **Algorithm 3** can be compared. It can be seen that the control performance indicators of **Algorithm 3** are better than those of **Algorithm 2**. This is because the introduction of coordination factors between the multi-objective state-action value function may cause the agent to not fully explore the action set, leading to the omission of key actions, and the use of collaborative reward functions can effectively solve the above problems.

In summary, the introduction of a collaborative reward function can effectively improve the system frequency quality and various frequency performance indicators.

4.3 The Influence of Different Learning Strategies on Control Performance

In order to verify the effectiveness of **Algorithm 4** proposed in this paper, **Figure 3D** shows the CPS1 curve of **Algorithm 3** and **Algorithm 4**. It can be seen from **Figure 3E** that **Algorithm 4** has a faster convergence rate and a more stable fluctuation situation than **Algorithm 3** after the occurrence of load disturbance. This is because the Negotiated W-Learning strategy selects actions from global considerations, which effectively improves the traditional greedy strategy that is, easy to fall into the local optimal solution problem.

In summary, the global search strategy Negotiated W-Learning is more time-consuming than the local search strategies Greedy and CoordinateQ, but the search quality is higher.

5 CONCLUSION

This paper proposes a multi-intelligence frequency control strategy based on multi-dimensional evaluation criteria and cooperative reward function.

The simulation results show that: 1) Compared with the general algorithm, the Negotiated W-Learning algorithm can effectively improve the quality of the system frequency on the full time scale, and better explore the global action. 2) The collaborative reward function proposed in this paper can improve the linear weight of the traditional multi-objective Q function. In general, the intelligent AGC control strategy based on the collaboration of CPS1 and BAAL learning criteria proposed in this paper can effectively deal with the short-term power disturbance problem caused by the grid connection of new energy sources such as wind power, and improve the stability of the system.

DATA AVAILABILITY STATEMENT

The original contributions presented in the study are included in the article/Supplementary Material, further inquiries can be directed to the corresponding author.

AUTHOR CONTRIBUTIONS

LZ put forward the main research points; LZ, YX completed manuscript writing and revision; JY completed simulation research; TX collected relevant background information; JC, ZL, TZ revised grammar and expression.

FUNDING

This manuscript was supported in part by the National Natural Science Foundation of China 52007103.

REFERENCES

Abouheaf, M., Gueaieb, W., and Sharaf, A. (2019). Load Frequency Regulation for Multi-Area Power System Using Integral Reinforcement Learning. *IET Generation, Transm. Distribution* 13 (19), 4311–4323. doi:10.1049/iet-gtd.2019.0218

Alhelou, H. H., Hamedani-Golshan, M.-E., Zamani, R., Heydarian-Forushani, E., and Siano, P. (2018). Challenges and Opportunities of Load Frequency Control in Conventional, Modern and Future Smart Power Systems: a Comprehensive Review. *Energies* 11 (10), 2497. doi:10.3390/en11102497

Arya, Y., and Kumar, N. (2017). Optimal Control Strategy–Based Agc of Electrical Power Systems: A Comparative Performance Analysis. *Optimal Control. Appl. Methods* 38 (6), 982–992. doi:10.1002/oca.2304

Imthias Ahamed, T. P., Rao, P. S. N., and Sastry, P. S. (2002). A Reinforcement Learning Approach to Automatic Generation Control. *Electric Power Syst. Res.* 63 (1), 9–26. doi:10.1016/s0378-7796(02)00088-3

Kumar, A., and Singh, O. (2019). "Recent Strategies for Automatic Generation Control of Multi-Area Interconnected Power Systems," in 2019 3rd International Conference on Recent Developments in Control, Automation & Power Engineering (RDCAPE), Xi'an, China, April 25–27, 2019 (IEEE), 153–158. doi:10.1109/rdcape47089.2019.8979071

Li, Z., Jiang, W., Abu-Siada, A., Li, Z., Xu, Y., and Liu, S. (2020). Research on a Composite Voltage and Current Measurement Device for Hvdc Networks. *IEEE Trans. Ind. Electron.* 68, 8930-8941. doi:10.1109/tie.2020.3013772

Liu, H., Huang, K., Yang, Y., Wei, H., and Ma, S. (2018). Real-time Vehicle-To-Grid Control for Frequency Regulation with High Frequency Regulating Signal. *Prot. Control. Mod. Power Syst.* 3 (1), 1–8. doi:10.1186/s41601-018-0085-1

Liu, Y., Yang, N., Dong, B., Wu, L., Yan, J., Shen, X., et al. (2020). Multi-lateral Participants Decision-Making: A Distribution System Planning Approach with Incomplete Information Game. *IEEE Access* 8, 88933–88950. doi:10.1109/access.2020.2991181

Nathan, S., and Ballard, D. (2003). *Multiple-goal Reinforcement Learning with Modular Sarsa (0)*. Doctoral Dissertation Rochester: University of Rochester.

Shen, X., Ouyang, T., Yang, N., and Zhuang, J. (2021). Sample-based Neural Approximation Approach for Probabilistic Constrained Programs. *IEEE Trans. Neural Networks Learn. Syst.* 1-8. doi:10.1109/tnnls.2021.3102323

Shen, X., Ouyang, T., Khajorntraidet, C., Li, Y., Li, S., and Zhuang, J. (2021). Mixture Density Networks-Based Knock Simulator. *IEEE/ASME Trans. Mechatronics*, 1. doi:10.1109/tmech.2021.3059775

Shen, X., and Raksincharoensak, P. (2021). Pedestrian-aware Statistical Risk Assessment. *IEEE Trans. Intell. Transportation Syst.*, 1–9. doi:10.1109/tits.2021.3074522

Shen, X., and Raksincharoensak, P. (2021). Statistical Models of Near-Accident Event and Pedestrian Behavior at Non-signalized Intersections. *J. Appl. Stat.*, 1–21. doi:10.1080/02664763.2021.1962263

Shen, X., Zhang, Y., Sata, K., and Shen, T. (2020). Gaussian Mixture Model Clustering-Based Knock Threshold Learning in Automotive Engines. *IEEE/ASME Trans. Mechatronics* 25 (6), 2981–2991. doi:10.1109/tmech.2020.3000732

Shen, X., Zhang, X., Ouyang, T., Li, Y., and Raksincharoensak, P. (2020). Cooperative Comfortable-Driving at Signalized Intersections for Connected and Automated Vehicles. *IEEE Robotics Automation Lett.* 5 (4), 6247–6254. doi:10.1109/lra.2020.3014010

Shen, X., Zhang, Y., Shen, T., and Khajorntraidet, C. (2017). Spark advance self-optimization with knock probability threshold for lean-burn operation mode of si engine. *Energy* 122, 1–10. doi:10.1016/j.energy.2017.01.065

Wang, C., and James, D. M. C. (2013). Impact of Wind Power on Control Performance Standards. *Int. J. Electr. Power Energ. Syst.* 47, 225–234. doi:10.1016/j.ijepes.2012.11.010

Wang, H., Lei, Z., Zhang, X., Peng, J., and Jiang, H. (2019). Multiobjective Reinforcement Learning-Based Intelligent Approach for Optimization of Activation Rules in Automatic Generation Control. *IEEE Access* 7, 17480–17492. doi:10.1109/access.2019.2894756

Watkins, C. J. C. H., and Dayan, P. (1992). Q-learning. *Machine Learn.* 8 (3-4), 279–292. doi:10.1023/a:1022676722315

Xi, L., Lu, Y., Xu, Y., Wang, S., and Chen, X. (2019). A Novel Multi-Agent Ddqn-Ad Method-Based Distributed Strategy for Automatic Generation Control of Integrated Energy Systems. *IEEE Trans. Sustain. Energ.* 11 (4), 2417–2426. doi:10.1109/tste.2019.2958361

Xi, L., Zhou, L., Xu, Y., and Chen, X. (2020). A Multi-step Unified Reinforcement Learning Method for Automatic Generation Control in Multi-Area Interconnected Power Grid. *IEEE Trans. Sustain. Energ.* 12 (2), 1406–1415. doi:10.1109/tste.2020.3047137

Xie, Y., Zhang, H., Li, C., and Sun, H. (2017). Development Approach of a Programmable and Open Software Package for Power System Frequency Response Calculation. *Prot. Control. Mod. Power Syst.* 2 (1), 1–10. doi:10.1186/s41601-017-0045-1

Yang, N., Huang, Y., Hou, D., Liu, S., Ye, D., Dong, B., et al. (2019). Adaptive Nonparametric Kernel Density Estimation Approach for Joint Probability Density Function Modeling of Multiple Wind Farms. *Energies* 12 (7), 1356. doi:10.3390/en12071356

Yang, N., Liu, S., Deng, Y., and Xing, C. (2021). An Improved Robust Scuc Approach Considering Multiple Uncertainty and Correlation. *IEEJ Trans. Electr. Electron. Eng.* 16 (1), 21–34. doi:10.1002/tee.23265

Yang, N., Yang, C., Wu, L., Shen, X., Jia, J., Li, Z., et al. (2021). Intelligent Data-Driven Decision-Making Method for Dynamic Multi-Sequence: An E-Seq2seq Based Scuc Expert System. *IEEE Trans. Ind. Inform.* 1. doi:10.1109/tii.2021.3107406

Yang, N., Ye, D., Zhou, Z., Cui, J., Chen, D., and Wang, X. (2018). Research on Modelling and Solution of Stochastic Scuc under Ac Power Flow Constraints. *IET Generation, Transm. Distribution* 12 (15), 3618–3625.

Yu, T., Wang, Y. M., Ye, W. J., Zhou, B., and Chan, K. W. (2011). Stochastic Optimal Generation Command Dispatch Based on Improved Hierarchical Reinforcement Learning Approach. *IET generation, Transm. distribution* 5 (8), 789–797. doi:10.1049/iet-gtd.2010.0600

Zhang, Lei., and Luo, Yi. (2018). Combined Heat and Power Scheduling: Utilizing Building-Level thermal Inertia for Short-Term thermal Energy Storage in District Heat System. *IEEJ Trans. Electr. Electron. Eng.* 13 (6), 804–814. doi:10.1002/tee.22633

Zhu, B., Ding, F., and Don, M. V. (2019). Coat Circuits for Dc–Dc Converters to Improve Voltage Conversion Ratio. *IEEE Trans. Power Electron.* 35 (4), 3679–3687.

Conflict of Interest: The authors declare that the research was conducted in the absence of any commercial or financial relationships that could be construed as a potential conflict of interest.

Publisher's Note: All claims expressed in this article are solely those of the authors and do not necessarily represent those of their affiliated organizations, or those of the publisher, the editors and the reviewers. Any product that may be evaluated in this article, or claim that may be made by its manufacturer, is not guaranteed or endorsed by the publisher.

frontiers in Energy Research

ORIGINAL RESEARCH
published: 01 October 2021
doi: 10.3389/fenrg.2021.756733

Heuristic Feature Selection for Wind Power Anomaly Events Study

Peiwen Yu[1] *and Anping Lin*[2]*

[1]*Maritime College, Guangdong Ocean University, Zhanjiang, China,* [2]*School of Physics and Electronic Electrical Engineering, Xiangnan University, Chenzhou, China*

Wind power ramp events are typical harmful anomaly events in wind engineering, which bring new threat to the safety operation of power systems. To in-depth understand ramps and mitigate their harms, suitable ramp characteristics are crucial in many studies, e.g., ramp definition, classification, prediction and so on. However, due to ramps' specificity on event feature, more profound characteristics are needed besides basic ramp morphological characteristics. In this paper, an approach for extracting and selecting ramp characteristics is proposed for ramp study. First, according to ramps' causation on energy change, wavelet transformation is introduced to analyze ramp categories, and used to extract ramp energy characteristics. Then, heuristic feature selection methods are proposed to select ramp characteristics based on specific ramp application contexts. The objective of feature selection is to remove redundant characteristics, and to improve ramp studies' performance. Finally, combining basic ramp characteristics and wavelet characteristics, ramp studies on category classification and prediction of appointed characteristics are implemented on industrial data. The computational results validate the usefulness of wavelet characteristics, the feasibility of the proposed approach, and that performance of ramp study could be improved by using ramp characteristics in this paper.

Keywords: wind power ramp events, wavelet transform, feature selection, anomaly detection, feature exaction

OPEN ACCESS

Edited by:
Tinghui Ouyang,
National Institute of Advanced Industrial Science and Technology (AIST), Japan

Reviewed by:
Zhenhao Tang,
Northeast Electric Power University, China
Huangke Chen,
National University of Defense Technology, China

***Correspondence:**
Anping Lin
anping719@126.com

Specialty section:
This article was submitted to Wind Energy, a section of the journal Frontiers in Energy Research

Received: *11 August 2021*
Accepted: *14 September 2021*
Published: *01 October 2021*

Citation:
Yu P and Lin A (2021) Heuristic Feature Selection for Wind Power Anomaly Events Study. Front. Energy Res. 9:756733. doi: 10.3389/fenrg.2021.756733

INTRODUCTION

The generation of energy from wind is growing across the world, especially in China where large-scale and highly-concentrated wind projects prevail (Ouyang et al., 2017a). Due to the renewability feature, wind energy offered lots of opportunities, e.g., proving clean energy and reducing environment pollution. On the other hand, due to wind's fluctuation and intermittent, serious anomaly challenges threaten the safety and stability of power grid. For example, wind power ramp events are typical anomaly events bringing one of the greatest threat, which is namely the large and unexpected changes of wind power over a short time period (Wang et al., 2017). In 2008, a down-ramp event was reported in the State of Texas causing serious economic loss to the grid operated by Electric Reliability Council of Texas (ERCOT) (Francis, 2008). Therefore, it is significantly important to study ramp events for mitigating their negative impacts.

Ramp study mainly involves definitions, detection, prediction and classification. Generally, ramp definition and ramp detection are the basis of ramp study. While ramp events are usually detected by combining ramp definitions and specific detection methods. For example, dynamic programming recursion and the swinging door algorithm were proposed to detect ramp events from wind power data in (Florita et al., 2013; Sevlian and Rajagopal, 2013; Ouyang et al., 2017b). In (Xiong et al., 2017), a data mining method using affinity of weather data was also proposed for ramp detection. However, the mainstream definitions up to now mainly focus on three characteristics (Zha et al., 2016) (e.g.,

ramp amplitude, ramp duration, and ramp rate) which are superficial characteristics from ramp events' basic forms. Copying with complex power system operations in the future, more targeted and effective control strategies need to be made, which are essentially based on study of more profound ramp characteristics. On the other hand, ramp prediction and classification are two major objectives of ramp study. Generally, ramp prediction can be divided into event prediction and ramp's categories prediction which is actually ramp classification. Nowadays, ramp classification has been studied via many data mining algorithms, e.g., *k-means*, support vector machine (SVM), extrema learning machine (ELM), neural networks (NN) and so on (Couto et al., 2013; Florita et al., 2013; Tang et al., 2020; Shen et al., 2021). Ramp classification combined with weather regimes was also studied in (Chen et al., 2018). No matter ramp prediction or classification, proper input features are the premise of constructing high-performance models. However, most of these studies are based on superficial characteristics, no profound physical characteristics are considered to improve ramp studies' performance. Therefore, it is significant useful for studying extraction and selection of ramp characteristics in wind power ramp researches.

In modeling process, determination of input features is primarily based on original data points. Sometimes feature extraction, selection and transformation are involved according to specific criterions. For example, principal component analysis (PCA) is a commonly-used method to reduce dimension of feature space, which was also used in feature analysis for wind forecasting (He et al., 2013a). Other methods based on mathematical transforms were also useful to extract characteristics, e.g. wavelet-transform was utilized in wind power forecasting (Singh and Tewari, 2015). Moreover, Pearson correlation coefficient, Gini index, wavelet transformation and other intelligent tools were also applied to feature processing in engineering (Huang et al., 2018). Nowadays, with more industrial signals are collected from complicated systems and more un-researchable objects are analyzed, these situations lead to the urgent requirement of profound characteristics reflecting structural or physical features in modeling. Study on wind power ramp events is a representative problem among these issues. According to ramps' concept, ramp events involve a period of wind power values and variance, and they don't always have a unified time duration (Tang et al., 2021). Based on the traditional tools, basic characteristics (e.g., ramp amplitude, duration and ramp rate) could be obtained from wind power data. However, ramps' harmful effect on power grid is not just identified by ramp duration and amplitude. The difference of ramp amplitude, ramp rate, energy storage and other factors may also affect the stability of power system at different degree. Therefore, besides the basic ramp characteristics, how to acquire more profound characteristics is an urgent topic in ramp study, such as in ramp classification and prediction.

According to the outlined problems above, the objective of this paper is to propose an approach to extract and select ramp characteristics for wind power ramp study. Considering ramp events involves the variance of time series and energy change process of wind power, three basic ramp characteristics are extracted based on definitions firstly. These characteristics are able to distinguish ramps and non-ramp events. Then, a method transforming time series into energy forms is proposed to extract extra characteristics. Wavelet transformation has been applied for feature expression in literatures due to its superior description ability at both time and frequency domains. For example, the wavelet transform was utilized to analyze the features of ramp events in (Gallego et al., 2013). On the other hand, wavelet decomposition has the property of multiresolution which is helpful to study the allocation of ramp event's energy. Summarizing these two properties, wavelet transformation is proposed to extract profound characteristics for distinguishing refined ramp categories in depth. Moreover, for reducing dimension, mitigating noise's influence, improving computation efficiency, a heuristic intelligent algorithm is proposed in the feature selection. Finally, based on the refined characteristic vector, ramp studies (classification, prediction) on industrial datasets are discussed, and validate the approach in extracting and selecting ramp characteristics. The framework of the major work in this paper is sketched in the following figure.

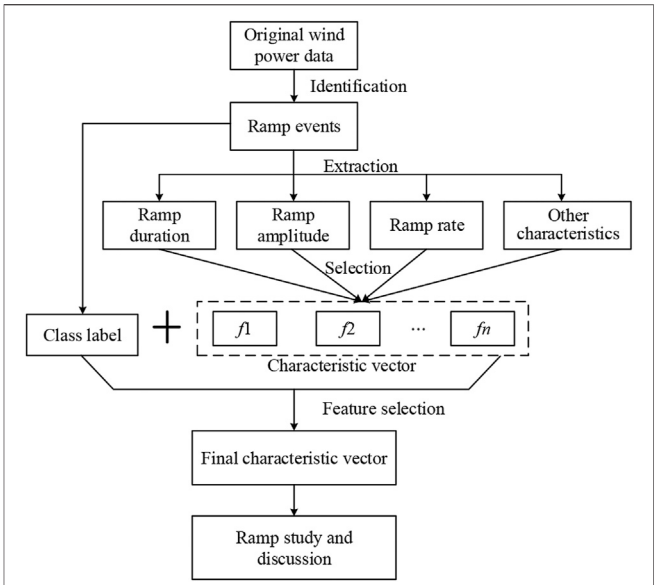

FIGURE 1 | Framework of the study in this paper.

In **Figure 1**, the identification of historical ramp events is implemented through ramp definitions and detection. Class labels of ramp events are determined by a given classification environment which could be based on weather sceneries, control requirement and so on. The other characteristics are energy characteristics extracted by wavelet transformation in this paper, and f_n represents the *nth* characteristic in the formed characteristic vector in **Figure 1**. According to the above description, we can conclude the novelties of this paper as following three points:

i) This paper proposes to consider characteristics of ramp events from multiple aspects, including the basic morphological characteristics from time domain and characteristics in frequency domain. Moreover, due to ramp events' specificity, characteristics are also extracted in terms of energy. This is the first time to consider ramp events' energy characteristics.

ii) Wavelet transformation is proposed to extract ramp characteristics. By utilizing the frequency and multiresolution properties in wavelet decomposition, ramp energy characteristics are expressed by energy at different frequency spaces. Meanwhile, these energy characteristics are selected and refined. Its purpose is to delete the energy of noise which may affect ramp classification.

iii) Heuristic intelligent algorithms are tried in the selection process, e.g., the sequential forward floating search (SFFS) and sequential backward floating search (SBFS) methods. The heuristic feature selection could refine the characteristic vector in related studies more effectively than unsupervised methods reducing dimension.

Besides the above introduction, rest of this paper is organized as follows. *Feature Extraction* addresses the processes of extracting ramp characteristics, including the basic ramp characteristics based on ramp definitions, and ramp energy characteristics based on wavelet transformation, for ramp studies are also extracted. *Feature Selection* proposes the feature selection approach which is based on dispersion matrix and heuristic method. The detailed processes are also presented in this section. *Ramp Anomaly Analysis and Evaluation* aims at designing ramp studies, e.g., ramp classification and ramp prediction. It also gives out some indicators for evaluating ramp study. In *Experiments and Discussion*, industrial wind power data is utilized in case study. Performance on ramp classification and prediction are compared with models using different feature sets and that using PCA for feature selection. Computational results validate the feasibility of wavelet characteristics and the proposed feature selection method. Finally, *Conclusion* concludes this paper.

FEATURE EXTRACTION

Basic Characteristics of Ramp Events

Wind power ramp events bring great harm to system operation as more and more wind power integrated into power grid. Copying with these new events, a series of studies has been carried out, such as ramp definition, ramp prediction and classification. Currently, there are four mainstream definitions widely used in ramp analysis (Zha et al., 2016). These definitions are defined as follows.

Definition 1. When the change of wind power in time duration Δt exceeds a given threshold Wp_{val}, there is a ramp event occurring, as expressed as below.

$$\left|Wp(t+\Delta t) - Wp(t)\right| \geq Wp_{val} \tag{1}$$

where: $Wp(t+\Delta t)$ and $Wp(t)$ are wind power values at time $t+\Delta t$ and t, respectively; Wp_{val} represents the threshold of ramp amplitude. When the criterion in **Eq. 1** meets under a given time period, a ramp event is identified.

Definition 2. When the largest difference of wind power in time duration Δt exceeds the given threshold Wp_{val}, then a ramp event is regarded as occurring.

$$\left|\max_{i\in[t,t+\Delta t]} Wp_i - \min_{i\in[t,t+\Delta t]} Wp_i\right| \geq Wp_{val} \tag{2}$$

where, $\max_{i\in[t,t+\Delta t]} Wp_i$ and $\min_{i\in[t,t+\Delta t]} Wp_i$ represent the maximum and minimum value of wind power in a time duration Δt.

Definition 3. When the average change of wind power in a given time duration Δt exceeds the given threshold Wp_{val}, a ramp event is identified.

$$\left(\sum_{i=1}^{h}\left|Wp(t+\Delta t+i) - Wp(t+i)\right|\right)/h \geq Wp_{val} \tag{3}$$

where, h is the time horizon in ramp identification.

Definition 4. When the ratio between the wind power change $|Wp(t+\Delta t)\text{-}Wp(t)|$ and time duration Δt exceeds a given threshold R_{val}, then a ramp event is regarded as occurring.

$$\left|Wp(t+\Delta t) - Wp(t)\right|/\Delta t > R_{val} \tag{4}$$

where, this definition in **Eq. 4** pays more attention on ramp rate while that in **Eq. 1** emphasizes only ramp amplitude. Summarizing the above four definitions, we can see they mainly focus on three major characteristics (Zha et al., 2016), such as ramp amplitude *Var*, ramp duration *T*, and ramp rate *R*. Based on these three characteristics, the variance of wind power in a given period could be determined as ramps or non-ramps. Therefore, they consist of the initial characteristic vector in ramp study, as $C_{v0} = [Var, T, R]$. As we know, sometimes ramp direction is also used in characteristic analysis. However, through above numerical definitions, ramp direction is not necessary, and could be expressed by sign of R when needed. Considering that ramp analysis in some cases needs the detailed information about power range rather than only fluctuation amplitude, so we replace ramp amplitude *Var* with maximum and minimum values. Assuming there are N studied ramp events in dataset, the initial characteristic matrix $\mathbf{X}_0$ is expressed as below.

$$\mathbf{X}_0 = \begin{bmatrix} Wp_{1,\max} & Wp_{1,\min} & T_1 & R_1 \\ Wp_{2,\max} & Wp_{2,\min} & T_2 & R_1 \\ \vdots & \vdots & \vdots & \vdots \\ Wp_{N,\max} & Wp_{N,\min} & T_N & R_N \end{bmatrix} \tag{5}$$

where, $Wp_{i,\min}$ and $Wp_{i,\max}$ represent the minimum and maximum value of wind power in the *ith* studied ramp event.

Wavelet Transformation and Characteristics Extraction

As the research on ramp events get more in depth, profound characteristics are needed to describe ramps' formation and categories. For example, the initial characteristics in **Eq. 4** is used to identify the basic formation of ramps and non-ramps. The detailed fluctuation inside ramps needs structural characteristics, and the essence of ramps' occurrence involves energy characteristics. In order to extract more profound information in ramp study, wavelet transformation is applied in this paper. Wavelet transformation is an advanced mathematical technique in signal analysis (Mohanty et al., 2015). It has advantages at decomposing a signal into various time and frequency domains, so it is useful to study the structural characteristics of ramps in different domains. Wavelet transformation also has advantages at detecting abrupt changed values (e.g., in edge detection) and analyzing signal in a specific time window. While ramp events certainly have large power charge in finite time durations, so it is relatively suitable to utilize wavelet transformation in ramp analysis (Escalante Soberanis and Mérida, 2015). On the other hand, due to the multiresolution feature of wavelet decomposition, energy of a given signal could be allocated into different frequency spaces. In this way, we are inspired to extract characteristics for expressing ramps' energy characteristics. This is also a key reason for considering wavelet transformation in extracting ramp characteristics.

The theory of discrete wavelet transformation is described as below. Assuming a discrete signal (e.g., wind power time series of a ramp event) is expressed as $\{x(t); t = 1,2,\cdots, T\}$, it could be reconstructed by elements of wavelet transformation, as expressed below.

$$x(t) = \sum_{j\in\mathbf{Z}} \sum_{k\in\mathbf{Z}} \delta_{j,k} \cdot \psi_{j,k}(t) \tag{6}$$

where: $x(t)$ is actually the signal of wind power; $\delta_{j,k}$ is the wavelet coefficient; $\psi_{j,k}$ is the child wavelet transformed from mother wavelet, denoted as follows.

$$\begin{cases} \psi_{j,k}(t) = a^{-j/2}\psi\left(a^{-j}\cdot t - kb\right) \\ \delta_{j,k} = \sum_{-\infty}^{\infty} \psi_{j,k}(t)\cdot x(t) \\ a > 1, b > 0 \end{cases} \tag{7}$$

where: j and k represent the scale and shift parameters of child wavelet $\psi_{j,k}$; $\psi(t)$ is the mother wavelet function; a and b are real parameters. From **Eqs 6**, **7** it implies that the reproduction of original signal could be realized by the weighted sum of wavelet components at different scales.

To in-depth explain the meaning of each wavelet component in **Eq. 6**, we could operate wavelet decompose step by step. Assuming the original signal with finite energy is projected on a space **L**, $x(t)$ with one-level-decomposition could be expressed as below.

$$x(t) = x_1(t) + \sum_k d_k \cdot \psi_k(x) \tag{8}$$

where, $x_1(t)$ is the estimation of the original signal reflecting variation in time domain; $\sum_k d(k)\cdot\psi_k(x)$ are detailed signals

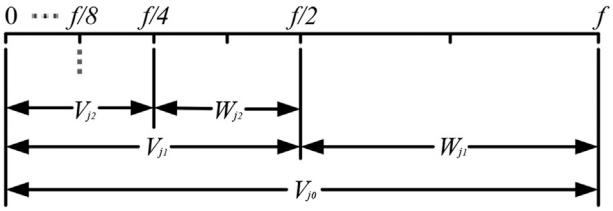

FIGURE 2 | The orthogonal decomposition of the space **L**.

expressed by wavelet functions which contain frequency-domain information. By estimating the approximate signal iteratively, $x_j(t)$ at the *jth* decomposition level is expressed as below.

$$x_j(t) = x_{j+1}(t) + \sum_k d_{j,k} \cdot \psi_{j,k}(t) \tag{9}$$

Similarly, we could utilize a series of wavelet functions to describe signal $x_j(t)$, as $\sum_k c_{j,k}\phi_{j,k}(t)$. Combining these formulas, transformation of the original signal in **Eq. 6** could be rewritten in details as below

$$x(t) = \sum_k c_{j_n,k}\phi_{j_n,k}(t) + \sum_{j=j_1}^{j_n}\sum_k d_{j,k}\psi_{j,k}(t) \tag{10}$$

where, the auxiliary function ϕ is called father wavelet; $c_{jn,k}$ is the coefficients of wavelets $\phi_{j_n,k}(t)$; $d_{j,k}$ are the coefficients of wavelets $\psi_{j,k}(t)$. The formula in **Eq. 10** is generally called as the multi-resolution analysis of wavelet transformation (Doucoure et al., 2016).

On the other hand, by corresponding each wavelet component to a frequency space, we could also divide the space **L** to series of energy subspaces. As shown in **Figure 2**, V_{j0} represents the original signal space **L** with a frequency band (0~f). According to **Eq. 10**, the frequency band is also divided step by step. For example, V_{j0} could be divided as orthogonal sum of a low-frequency space V_{j1} (0~f/2) and a high-frequency space W_{j1} (f/2~f). The relationship reflecting the division of frequency spaces in wavelet transformation is presented as below.

$$\begin{cases} \mathbf{V}_j \oplus \mathbf{W}_j = \mathbf{V}_{j-1} \\ \mathbf{L} = \mathbf{W}_{j1} \oplus \mathbf{W}_{j2} \oplus \cdots \oplus \mathbf{W}_{jn} \oplus \mathbf{V}_{jn} \end{cases} \tag{11}$$

where: $\oplus$ is a denoted operator calculating the orthogonal sum; n is the number of wavelet decomposition.

Considering signal's energy is generally expressed at frequency subspaces, therefore we could utilize the multi-resolution of wavelet decomposition to analyze the energy distribution of a signal (Ashrafian et al., 2017), as described in the following formula.

$$|P_{\{x\}}|^2 = \sum_k |c_{j_n,k}|^2 + \sum_j \sum_k |d_{j,k}|^2 \tag{12}$$

where: $|P_{\{x\}}|^2$ represent the energy of the given signal $\{x(t)\}$; $\sum_k |c_{j_n,k}|^2$ and $\sum_k |d_{j,k}|^2$ represent the energy of different subspaces. Since wind process generally involved atmosphere

movements (Mohanty et al., 2015), the occurrence of ramp events could be comprehensibly regarded as the speedy energy release or accumulation in atmosphere systems. Therefore, the energy expressions based on wavelet transform could be utilized to extract ramp energy characteristics which is meaningful in studying ramp's harms on power systems.

Moreover, when the number of decomposition levels is high (e.g., $j_n \to \infty$), the value of $c_{jn,k}$ is small, which implies the energy of V_{jn} becoming small to be ignored. In that case, the energy characteristics of W_j are mainly selected into the characteristic vector for ramp study in this paper.

$$\begin{cases} P_j = \sum_k \left| d_{j,k} \right|^2; \\ C_v = \left[W p_{\max}, W p_{\min}, T, R, P_j \right]; \\ j = 1, 2, \cdots, j_n; \end{cases} \tag{13}$$

where: P_j represents the *jth* energy characteristic and j is the decomposition level. C_v is the characteristic vector combining initial vector C_{v0} and P_j. By utilizing this vector including basic ramp characteristics and wavelet energy characteristics as inputs, some advanced ramp study could be implemented besides the identification of ramps and non-ramps.

FEATURE SELECTION

According to the above wavelet decomposition, j_n energy characteristics are extracted. Generally, the more the number of decomposition levels, the better the description ability of wavelet characteristics. In **Eq. 13**, the energy in frequency space V_{jn} is excluded since V_{jn} is the lowest frequency and its $c_{jn,k}$ is very small. However, when more fine-sorted energy characteristics P_j are generated, it is unavoidable to lead to many superfluous characteristics in a specific study case. Therefore, excluding basic ramp characteristics, feature selection is also necessary in ramp study.

Feature selection could not only select optimal energy characteristics for specific study, but also improve computing performance by reducing data dimension. Generally, feature selection methods are based on specific indicators or criterions to rank all characteristics, then realize selection through ranking scores. Most of these methods do not care about the application context in ranking. The other commonly used methods on dimension reducing is through feature transformation, such as PCA, LDA. This type of methods weakens the physical meaning of selected characteristics, and also ignore actual context. Therefore, in this paper we propose to utilize heuristic selection criterion which combining selection indicators and the application context (e.g., specific ramp study).

Dispersion Matrix

First, we propose to utilize dispersion matrix (Gu et al., 2017) to create selection indicator. Dispersion matrix is a mathematic tool based on feature distances of different classes, its elements are denoted as below.

$$\begin{cases} \mathbf{B} = \sum_{g=1}^{G} n_g \left(\boldsymbol{\mu}_g - \boldsymbol{\mu}_0 \right)^T \left(\boldsymbol{\mu}_g - \boldsymbol{\mu}_0 \right) \\ \mathbf{W} = \sum_{g=1}^{G} \sum_{k=1}^{n_g} \left(\mathbf{x}_{g,k} - \boldsymbol{\mu}_g \right)^T \left(\mathbf{x}_{g,k} - \boldsymbol{\mu}_g \right) \\ \left(k = 1, 2, \cdots, n_g; g = 1, 2, \cdots, G; \right. \\ \left. n_1 + n_2 + \cdots + n_g = N \right) \end{cases} \tag{14}$$

where: $\boldsymbol{W}$ and $\boldsymbol{B}$ are the dispersion matrix representing intra-class and inter-classes, respectively; $\boldsymbol{x}_{g,k}$ is characteristic vector of the *kth* ramp in the *gth* class; μ_g and μ_o represent the average vector of the *gth* class and all classes, respectively; n_g and N are the number of ramps the *gth* class and all classes, respectively; G is the number of classes. A Wilks criterion function λ_p could be selected as the reference indicator in feature selection, it is defined as below.

$$\lambda_p = |\mathbf{W}| / |\mathbf{T}| \tag{15}$$

where: $\boldsymbol{T}$ is total dispersion matrix, calculated as $\boldsymbol{T} = \boldsymbol{B} + \boldsymbol{W}$; p is the dimension of feature space. When the value of λ_p is small, implying a small value of $|\boldsymbol{W}|$ and a large value of $|\boldsymbol{T}|$, it illustrates that the characteristic is effective to distinguish different classes of samples. Generally, the statistical indicator λ_p is assumed to obey the Wilks distribution. By deciding a testing level α and its corresponding threshold $\lambda_{(\alpha)}$, the hypothesis testing of λ_p could be implemented. For the convenience of calculation, the value of Wilks distribution function could be estimated by the following two common distribution functions.

1) Bartlett approximation.

$$-\left(N - \frac{1}{2}(p - g) - 1 \right) \cdot \ln \lambda_p \sim \chi^2 \left(p(g - 1) \right) \tag{16}$$

2) Rao approximation.

$$\frac{N - (p - 1) - g}{g - 1} \cdot \left(\frac{\lambda_{p-1}}{\lambda_p} - 1 \right) \sim F\left(g - 1, N - (p - 1) - g \right) \tag{17}$$

Through the above two approximation methods, the hypothesis testing of Wilks distribution could be realized by formulas in **Eqs 16**, **17**.

Heuristic Selection

Combining the selected Wilks indicator λ_p and ramps' categories information, a supervised heuristic method could realize high-performance feature selection. In this paper, we propose to utilize SFFS (sequential floating forward search) and SFBS (sequential floating backward search) algorithms (Gan et al., 2014) which retain the strengths and improve the weakness of SFS (sequential forward selection) and SBS (sequential backward selection).

Considering the specificity of ramp studies, the basic characteristic vector C_{v0} contains basic ramp characteristics identifying ramps and non-ramps, so it is necessary included in the characteristic subset. Actually, the task of feature selection is to select optimal newly-extracted characteristics in ramp study.

Therefore, in this paper the initial subset is $\boldsymbol{X}_0$, the characteristics that need to be processed are wavelet energy

characteristics P_i (i = 1,2, ⋯, j_n). Assuming after the *mth* selection step, the feature subset is denoted as $\boldsymbol{X}_m$. If we consider to add a new characteristic x_r at the $(m+1)^{th}$ step by SFFS algorithm, the updated dispersion matrix could be calculated as below.

$$\begin{cases} \mathbf{W}' = \begin{pmatrix} \mathbf{W}_{11} & \mathbf{W}_{12} \\ \mathbf{W}_{21} & \mathbf{W}_{22} \end{pmatrix} \\ \mathbf{T}' = \begin{pmatrix} \mathbf{T}_{11} & \mathbf{T}_{12} \\ \mathbf{T}_{21} & \mathbf{T}_{22} \end{pmatrix} \end{cases} \tag{18}$$

where, $\boldsymbol{W}_{11}$ and $\boldsymbol{T}_{11}$ are the intra-class and the total dispersion matrix of $\boldsymbol{X}_m$, respectively; The rest of sub-matrix are newly introduced matrix related with x_r, calculated as the following formulas.

$$\begin{cases} \mathbf{W}_{12} = \left(w_{1r}, w_{2r}, \cdots, w_{pr}\right)^T; \mathbf{W}_{21} = \mathbf{W}_{12}^T; \mathbf{W}_{22} = w_{rr}; \\ \mathbf{T}_{12} = \left(t_{1r}, t_{2r}, \cdots, t_{pr}\right)^T; \mathbf{T}_{21} = \mathbf{T}_{12}^T; \mathbf{T}_{22} = t_{rr}; \end{cases} \tag{19}$$

Based on calculation of these sub-matrixes, the updated indicator λ_{m+1} could be calculated as below.

$$\begin{cases} \lambda_{m+1} = \dfrac{|\mathbf{W}'|}{|\mathbf{T}'|} = \dfrac{|\mathbf{W}_{11}|\left|\mathbf{W}_{22} - \mathbf{W}_{21}\mathbf{W}_{11}^{-1}\mathbf{W}_{12}\right|}{|\mathbf{T}_{11}|\left|\mathbf{T}_{22} - \mathbf{T}_{21}\mathbf{T}_{11}^{-1}\mathbf{T}_{12}\right|} = \lambda_m \cdot A_r \\ A_r = \dfrac{\left|\mathbf{W}_{22} - \mathbf{W}_{21}\mathbf{W}_{11}^{-1}\mathbf{W}_{12}\right|}{\left|\mathbf{T}_{22} - \mathbf{T}_{21}\mathbf{T}_{11}^{-1}\mathbf{T}_{12}\right|} \end{cases} \tag{20}$$

By substituting **Eqs 15–18**, the expression $\lambda_m/\lambda_{m+1} - 1$ could be replaced by $(1 - A_r)/A_r$. Then, the estimated value of testing x_r is denoted as F_{1r}, expressed as below

$$F_{1r} = \frac{1 - A_r}{A_r} \cdot \frac{N - p_m - g}{g - 1} \sim F\left(g - 1, N - p_m - g\right) \tag{21}$$

where: p_m is the number of characteristics in set $\boldsymbol{X}_m$. If $F_{1r} > F_\alpha(g\text{-}1, N\text{-}p_m\text{-}g)$ at given testing level α, then the hypothesis is correct and x_r is added into characteristic vector.

Similarly, if we utilize the SFBS algorithm to delete a characteristic x_r form the set $\boldsymbol{X}_m$, the final testing value is defined as F_{2r}, expressed as below

$$F_{2r} = \frac{1 - A_r}{A_r} \cdot \frac{N - \left(p_m - 1\right) - g}{g - 1} \sim F\left(g - 1, N - \left(p_m - 1\right) - g\right) \tag{22}$$

If the formula $F_{2r} \le F_\alpha(g\text{-}1, N\text{-}(p_m\text{-}1)\text{-}g)$ is satisfied at a given level α, then the variable x_r is regarded as invalid and removed from $\mathbf{X}_m$.

RAMP ANOMALY ANALYSIS AND EVALUATION

By taking the selected ramp characteristics as inputs and different types of data as output, we could construct models for different ramp study, e.g., ramp classification and ramp prediction. In this paper, we only do some simple experiments on these two studies for evaluating the selected ramp characteristics.

Ramp Classification

In ramp classification study, class labels of historical ramp events are taken as the output. The classification model can be constructed by data mining algorithms. To accurately classify ramp events, four data mining algorithms are applied to train ramp classification model, including support vector machine (SVM), neural networks (NN), random forests algorithm (RF) and boosted trees (BT) (Chen et al., 2017; Ouyang et al., 2017c; He et al., 2017; Ouyang, 2021). The optimal classification model could be determined by the comparison of their performance.

To evaluate the classification performance, the confusion matrix introduced from information retrieval (IR) field is widely applied (He et al., 2013b). The detailed expression is presented in the following table.

In **Table 1**, four types of events are defined, such as true positive event (TP), false negative event (FN), false positive event (FP) and true negative event (TN). Based on these events, several indicators could be defined to evaluate classification performance. Four representative indicators are defined as below.

$$\begin{cases} \mathrm{Rec} = num_{\mathrm{TP}}/\left(num_{\mathrm{TP}} + num_{\mathrm{FN}}\right) \\ \mathrm{Pre} = num_{\mathrm{TP}}/\left(num_{\mathrm{TP}} + num_{\mathrm{FP}}\right) \\ Acc = \left(num_{\mathrm{TP}} + num_{\mathrm{TN}}\right)/num_{\mathrm{All}} \\ Err = 1 - Acc \end{cases} \tag{23}$$

where, num_{X} represents the number of the specific event X; *Pre* represents precision indicator implying the percentage of TP in classified true events; *Rec* represents recall indicator implying the percentage of TP in observed true events; *Acc* is the classification accuracy, and *Err* is the classification error. By utilizing these four indicators, we could complete selection of the optimal classification model and the evaluation of classification performance.

Ramp Prediction

Ramp prediction is usually divided into two types: event prediction and regression prediction. Event prediction includes ramp detection and ramp classification study. Regression prediction mainly focus on utilizing traditional regression models to predict ramp characteristics, e.g., the ramp rate prediction in (Zheng and Kusiak, 2009). In this paper, we consider predicting two characteristics: ramp amplitude and ramp rate, which implies values of these two characteristics are taken as the output in modeling. Since the above study on ramp characteristics' extraction and selection are based on historical ramp events which randomly occur in wind power time series. Therefore, we propose to utilize these characteristics extracted from wind power in a given time window as inputs, then predict one appointed characteristic in the predicted time window, e.g., to predict ramp amplitude or ramp rate in the future 1-h horizon. Since this type of prediction is still based on regression models, the performance indicator could be decided by the commonly used root-mean-square error (RMSE), which is defined as below.

$$RMSE = \sqrt{\sum_{k=1}^{K} \left(\hat{y}_k - y_k\right)^2 / K} \tag{24}$$

where, y_k and $\hat{y}_k$ are the *kth* values predicted and observed of an appointed ramp characteristic; K is the number of tested samples.

TABLE 1 | Confusion matrix.

		Observation		Total
		True	False	
Classification	True	TP	FP	True classification
	False	FN	TN	False classification
Total		True observation	False observation	All

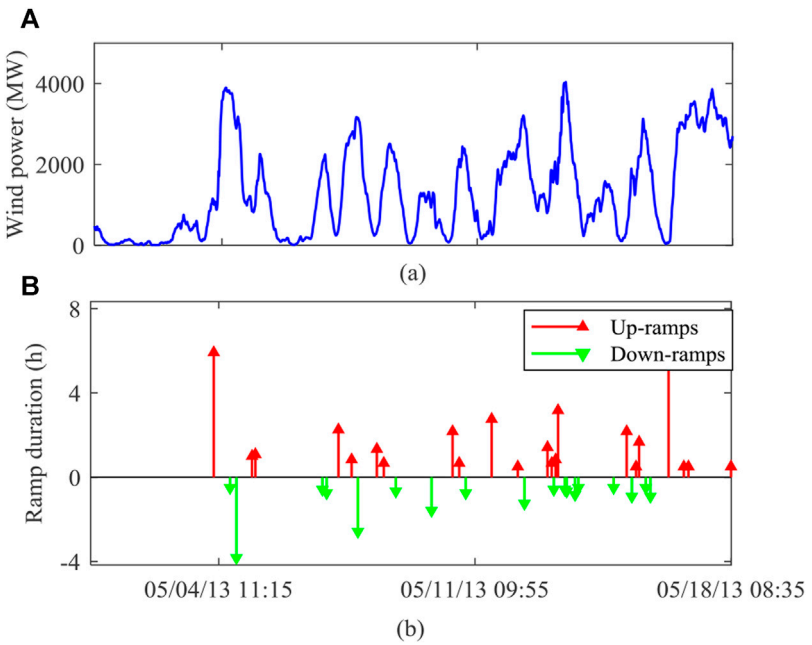

FIGURE 3 | Identification of **(A)** historical wind power **(B)** ramp events in May.

EXPERIMENTS AND DISCUSSION

In this paper, the industrial wind power data from Bonneville Power Administration (BPA) website (bpa.gov/transmission, 2013) is taken as the studied case. The data set spanning from 01/01/13 00:00 to 12/31/13 23:55 totally has 105,120 data points with a sampling interval of 5 min. First, we need to detect historical ramp events from wind power time series for the following ramp characteristics study. According to the definitions in **Eqs 1–4**, the forth definition can reflect three basic ramp characteristics more conveniently, so that it is selected to identify historical ramps in this paper. In (Tang et al., 2021), the value of R_{val} was chosen as 50% of the installed capacity within 4 h, so the value of R_{val} is computed by considering the capacity of 4,500 MW in the studied case, as below.

$$R_{val} = \frac{50\% \cdot P_{total}}{4hours} = \frac{50\%*4500MW}{4h} = 562.5\ MW/h \qquad (25)$$

Considering ramps always have a duration larger than 0.5 h, so we assume the minimum threshold as $\Delta t = 0.5$ h there are totally 526 ramp events are detected from data of former 6 months. One part of ramp identification results is shown in **Figure 3**. The subpicture 1) and 2) depict historical wind power and ramp events, respectively. In **Figure 3B**, up-ramps and down-ramps are expressed by lines above and below the X-axis, respectively, their durations are reflected by values in Y-axis. It is seen than most of ramps have duration around hours, some even reach 6 h.

Historical wind power and ramp events are depicted in **Figure 3A** and **Figure 3B**, respectively. In **Figure 3B**, up-ramps and down-ramps are expressed by lines above and below the X-axis, respectively, their durations are reflected by values in Y-axis.

Selection of Ramp Characteristics

Through analysis on ramp definitions, basic ramp characteristics (amplitude, duration, and ramp rate) could be extracted, as (5). These basic characteristics could be used to identify ramps and non-ramps, as two typical signals in **Figure 4**. To identify more detailed division of ramp categories, wavelet transformation is proposed to extract profound characteristics.

In order to illustrate the feasibility of wavelet characteristics, we firstly utilize wavelet coefficients as an index to qualitatively analyze ramps and non-ramps.

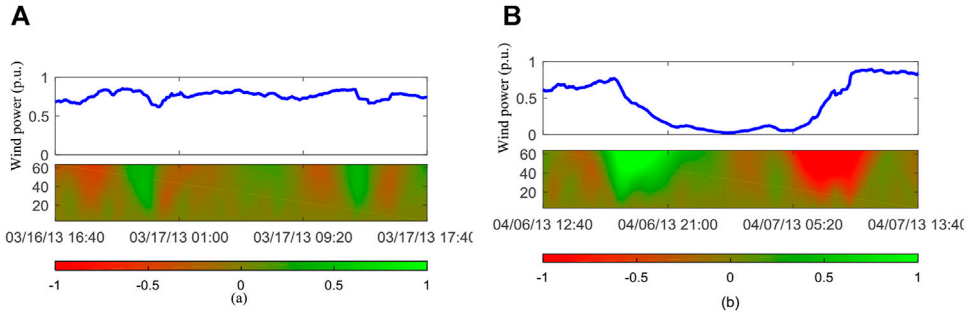

FIGURE 4 | Wavelet analysis of ramps and non-ramps; **(A)** non-ramp signal; **(B)** ramp signal.

In **Figure 4**, the two typical ramp and non-ramp events are identified by characteristics in **Eq. 5**. The function applied here is Haar wavelet which was validated useful in ramp analysis (Gallego et al., 2013). It is seen from **Figure 4** that wavelet coefficients which reflect signal's energy could obviously distinguish ramps and non-ramps. For example, ramps have larger coefficients than non-ramps. It verifies the validity of wavelet transformation in ramp characteristics analysis, therefore we could further extract more profound wavelet characteristics for ramp recognition.

According to the heuristic methods in selecting characteristics, the class labels are required. Therefore, we propose to construct ramp classification according to a specific context. Considering wind process are formed by different meteorological phenomena, so the categories of ramp events are related to division wind processes to some extent. In (Wang et al., 2013), five types of wind process are discussed, namely small wind, small fluctuation wind, large fluctuation wind, double peak wind and multi-peaks wind. However, there are a few ramp events attributed to the small wind. Double peaks wind can be regarded as a special type of multi-peaks wind. Based on these assumptions, we can group historical ramp events into the following category library **L,** denoted as below.

$$\mathbf{L}=\{\mathrm{A},\ \mathrm{B},\ \mathrm{C}\}\quad\begin{cases} A = small\ wind, small\ fluctuation\ wind; \\ B = large\ fluctuation\ wind; \\ C = double\ peaks\ wind,\ multi-peaks\ wind; \end{cases} \tag{26}$$

Combing with the description of wind process in (Wang et al., 2013) and the constructed library **L**, historical ramp events of training set are classified into three classes, as presented below.

Table 2 shows the statistical results of ramp events belonging to three categories in **L**, where number 1, 2 and 3 are defined as the class labels of A, B, C. It is seen that most ramp events are associated with the large fluctuation wind, a few of ramp events associated with the small wind and multi-peak wind. These results agree with the concept of ramp events involving a large change of wind power. Therefore, the constructed application context is reasonable for studying ramp characteristics. Based on the constructed library of ramp categories, then the extraction and selection of ramp characteristics could be implemented.

TABLE 2 | Number of ramps in three categories.

Class label	1	2	3
Number	101	378	47

TABLE 3 | Process of featue selection.

	P_1	P_2	P_3	P_4	P_5	Selection
Step 1	0.3064	0.3032	0.2969	0.2996	0.3146	P_3
Step 2	0.2963	0.2944	\	0.2917	0.2960	P_4
Step 3	0.2911	0.2901	\	\	0.2900	None

Assuming each signal is decomposed into five wavelet layers, the energy of each wavelet layer is extracted as ramp characteristics by **Eq. 13**, expressed as $\mathbf{P} = [P_1,P_2,P_3,P_4,P_5]$. Here, the number of decomposition layers is set as 5 since ramp events have only three categories in this paper. In other application context which requires more refined ramp classification, the level of decomposition could be higher. As the description in *Feature Selection*, the purpose of feature selection is to delete redundant characteristics, reduce dimension and computation cost. Combining ramp basic characteristics and extracted wavelet energy characteristics, the characteristic vector is expressed as $C_v = [Wp_{max}, Wp_{min}, T, R, P_1, P_2, P_3, P_4, P_5]$. For all historical ramp events, the feature set constructed by C_v is denoted as $\boldsymbol{X}_{p0}$. Then, according to the selection algorithm in *Feature Selection*, the process is shown in the following table.

At each step of **Table 3**, the value of λ_p is calculated for the rest characteristics P_i first. Then the minimum one is applied for F_r testing based on **Eqs 15**, **16**. If the result is satisfied, adding the corresponding characteristic into characteristic vector C_v. It is seen from **Table 3** that P_3 and P_4 is selected, so the final characteristic is re-written as $C_{vp} = [Wp_{max}, Wp_{min}, T, R, P_3, P_4]$, and the final feature set for all ramp events as $\boldsymbol{X}_p$.

Ramp Study and Discussion

By taking the feature set $\boldsymbol{X}_p$ as inputs and the class labels from **Table 2** as output, five data mining algorithms (SVM, NN, RF,

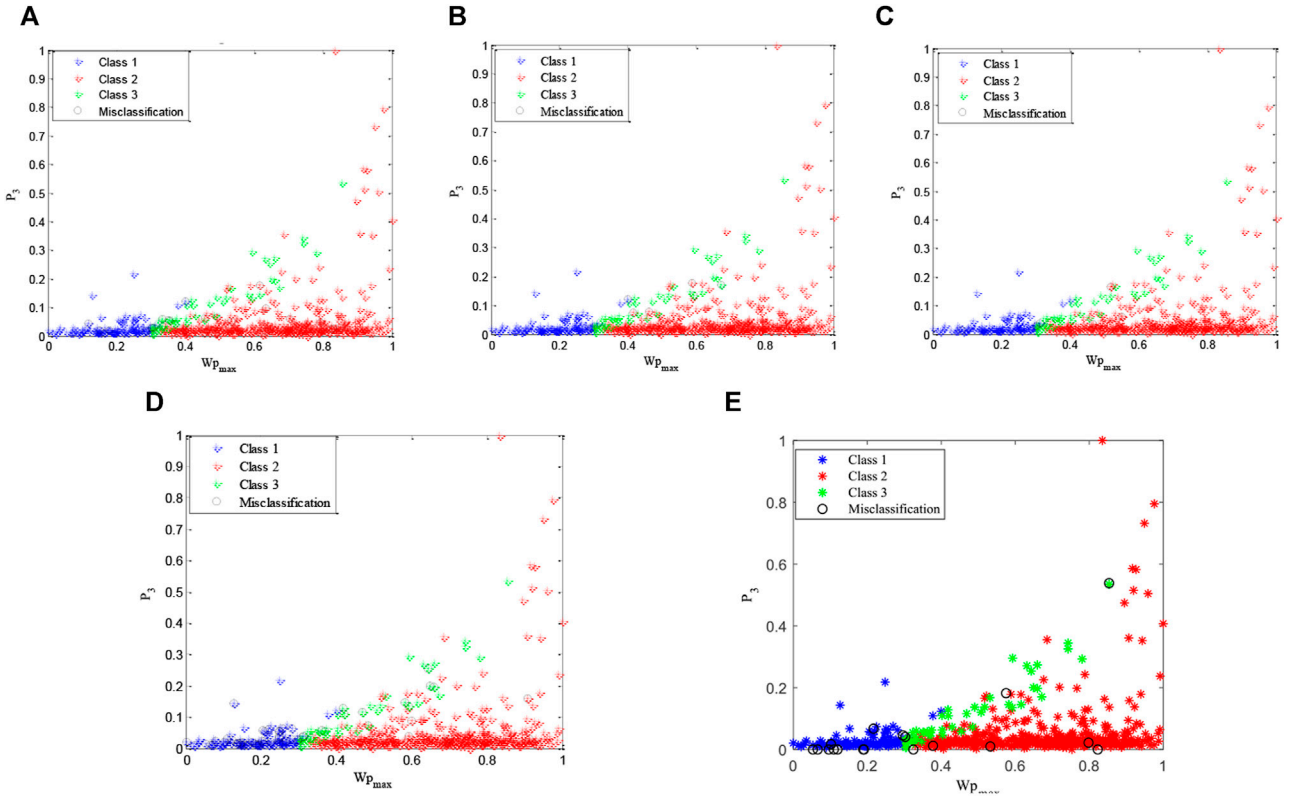

FIGURE 5 | Ramp classification based on four data mining algorithms; **(A)** SVM; **(B)** NN; **(C)** RF; **(D)** BT; **(E)** ELM.

TABLE 4 | Performance of ramp classification.

		Pre	*Rec*	*Acc*	*Err*
Class 1	SVM	0.9000	0.9802	0.9753	0.0247
	NN	1.0000	0.9714	0.9946	0.0054
	RF	1.0000	0.9683	0.9944	0.0056
	BT	1.0000	0.6126	0.9183	0.0817
	ELM	0.9381	0.9010	0.9696	0.0304
Class 2	SVM	0.9688	0.9868	0.9677	0.0323
	NN	0.9886	0.9886	0.9838	0.0162
	RF	0.9961	0.9846	0.9859	0.0141
	BT	0.8651	0.9729	0.8745	0.1255
	ELM	0.9739	0.9868	0.9715	0.0285
Class 3	SVM	0.8065	0.5319	0.9468	0.0532
	NN	0.8684	0.9167	0.9784	0.0216
	RF	0.8333	0.9677	0.9802	0.0198
	BT	0.7442	0.6957	0.9525	0.0475
	ELM	0.9565	0.9362	0.9905	0.0095

BT, ELM) are applied in ramp classification modeling. The classification results of three categories of ramps are shown in following figure.

For the convenience of presentation, **Figure 5** utilizes two characteristics (Wp_{max}×P_3) to show ramp classification results, as X-axis representing values of Wp_{max} and Y-axis representing values of P_3. Red, blue and green points represent ramps of Class1, Class2 and Class3, respectively. Black points represent ramp events classified into incorrect class. Based on these classification results, the performance indicators defined in **Eq. 23** could be calculated, as presented below.

Table 4 presents values of four performance indicators in classification of three ramp categories. According to the definitions of four matrixes, a classification system performs well with large value of Pre, Rec, Acc, and small value of Err. In **Table 4**, it is seen that NN, RF and ELM algorithms outperform on three classes, respectively. However, it is difficult to choose the best to classify all three ramp categories. To determine the final optimal model in ramp classification, the receiver operating characteristic curve (ROC) is introduced to compare performance further. ROC space is constructed by Recall (Rec) in the X-axis and false alarm (F) in the Y-axis. The definition of F is also based on **Table 1**, as expressed below.

$$F = num_{FP}/(num_{FP} + num_{TN}) \tag{27}$$

where, F calculates the percentage of FP in observed false events. According to these two indicators' definitions, it is easily comprehended that a classifier having a large Rec and a small F performs better, which implies the upper-left corner of the ROC space means the better performance. For a discrete classification system, a classifier is usually represented by a point in ROC space. Therefore, points representing all classifiers in **Table 4** are shown in the following figure.

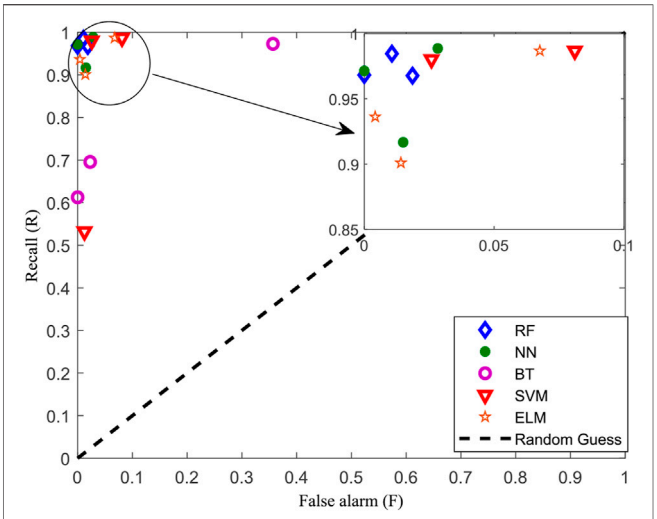

FIGURE 6 | Four data mining models in ROC space.

TABLE 5 | Classification performance of different feature sets.

		Pre	*Rec*	*Acc*	*Err*
Class1	$\boldsymbol{X}_0$	0.6111	1.0000	0.9157	0.0843
	$\boldsymbol{X}_{p0}$	0.6804	1.0000	0.9357	0.0643
	$\boldsymbol{X}_p$	0.6875	1.0000	0.9378	0.0622
	$\boldsymbol{X}_{\text{pca}}$	0.6735	1.0000	0.9398	0.0602
Class2	$\boldsymbol{X}_0$	0.9621	0.8945	0.9016	0.0984
	$\boldsymbol{X}_{p0}$	0.9914	0.8934	0.9157	0.0843
	$\boldsymbol{X}_p$	1.0000	0.8958	0.9137	0.0863
	$\boldsymbol{X}_{\text{pca}}$	0.9940	0.9089	0.8916	0.1084
Class3	$\boldsymbol{X}_0$	0.2813	0.1875	0.8574	0.1426
	$\boldsymbol{X}_{p0}$	0.3095	0.2708	0.8715	0.1285
	$\boldsymbol{X}_p$	0.3231	0.4375	0.8755	0.1245
	$\boldsymbol{X}_{\text{pca}}$	0.3088	0.4375	0.8514	0.1486

In **Figure 6**, three points having the same type present classifiers of three classes by a same algorithm. The points representing SVM and BT perform worse than the other three algorithms again. By comparing the points of NN, RF and ELM, it is seen that points of RF obviously are concentrated and closer to the upper-left corner, implying their classifiers have a better performance. Therefore, RF algorithm is finally chosen for modeling ramp classification in this paper.

Then, taking these trained RF models as ramp classifiers, 100 ramp events are selected from July to December as testing samples. To discuss the performance with and without wavelet characteristics in ramp classification, three different input sets are considered in the case study, such as initial feature set $\boldsymbol{X}_0$ consisting of vector C_{v0}, feature set $\boldsymbol{X}_{p0}$ consisting of vector $C_v = [C_{v0}, \boldsymbol{P}]$ which contains basic ramp characteristics and all wavelet characteristics, refined feature set $\boldsymbol{X}_p$ consisting of $C_{vp} = [C_{v0}, P_3, P_4]$ which reduces dimension by feature selection. Classification performance of testing data is presented in the following table.

Table 5 shows values of four indicators at classification of three ramp categories. Since three ramp categories have imbalance distribution as Table 2II, so the classification performance of Class 2 is the best. By comparing classification performance of using three feature sets, it is seen that using $\mathbf{X}_{p0}$ has better performance than using $\boldsymbol{X}_0$, having an average improvement of 10.17% (8.14% on Pre, 14.77% on Rec, 1.80% on Acc, 15.98% on Err). These results imply wavelet characteristics are useful in ramp classification. Also, using $\boldsymbol{X}_p$ improves a little again (with an average improvement of 6.05%) than using $\mathbf{X}_{p0}$, which implies that the proposed feature selection approach is feasible and effectual in ramp classification. While, for comparing with other feature selection methods, the commonly used PCA is applied. After the analysis of PCA on $\boldsymbol{P} = [P_1, P_2, P_3, P_4, P_5]$, two principal components are selected to keep a same dimension with $\boldsymbol{X}_p$, these two components contribute 84.00% explanation in classification, and consist of the feature set $\boldsymbol{X}_{\text{pca}}$. Table V also presents the performance of $\boldsymbol{X}_{\text{pca}}$. By comparing $\boldsymbol{X}_p$ and $\boldsymbol{X}_{\text{pca}}$, it is seen that using $\boldsymbol{X}_p$ has an average outperformance of 3.69% than using $\boldsymbol{X}_{\text{pca}}$. Summarizing all these results, the proposed approach on selecting wavelet characteristics is validated to be feasible.

TABLE 6 | Performance of ramp prediction.

		1 h	2 h	3 h	4 h	5 h
Var	$\boldsymbol{X}_0$	21.94	40.80	79.49	120.42	156.71
	$\boldsymbol{X}_{p0}$	19.02	38.05	81.63	115.94	151.46
	$\boldsymbol{X}_p$	18.68	35.31	86.21	113.93	149.46
	$\boldsymbol{X}_{\text{pca}}$	20.27	35.63	79.12	122.02	160.87
R	$\boldsymbol{X}_0$	1.8635	1.9418	2.4102	2.5717	2.6601
	$\boldsymbol{X}_{p0}$	1.7527	1.6638	2.0607	2.5032	2.4825
	$\boldsymbol{X}_p$	1.4786	1.4928	1.9097	2.3972	2.3897
	$\boldsymbol{X}_{\text{pca}}$	1.8355	1.8644	2.2158	2.5242	2.5728

On the other hand, by utilizing these selected ramp characteristics, we could do some try on the study of ramp prediction. Since ramp classification has validated the effectiveness on distinguishing different categories, so two basic ramp characteristics are taken as target output in prediction, such as ramp amplitude (*Var*) and ramp rate (*R*). As the design of ramp prediction in *Ramp Anomaly Analysis and Evaluation*, the historical feature extraction window and the predicted time window are set as the same for convenience. In this paper, ramp prediction is designed to predict two variables (*Var* and *R*) within future horizon of 1, 2, ⋯, 5 h, the prediction performance is presented in the following table.

Table 6 shows the performance of ramp prediction by RMSE of two ramp characteristics. In these two variables' prediction, a typical NN with three layers is used in modeling. For comparison study, four feature sets discussed in **Table 5** are also utilized as inputs of prediction models. It is seen from results of **Table 6** that models using feature sets containing wavelet characteristics (e.g., $\boldsymbol{X}_{p0}$, $\boldsymbol{X}_p$, $\boldsymbol{X}_{\text{pca}}$) outperforms than that only containing basic ramp characteristics (e.g., $\boldsymbol{X}_0$). Through the proposed feature selection in this paper, the model using $\boldsymbol{X}_p$ has an improvement of 5.97% than using $\boldsymbol{X}_0$, 1.29% than using $\boldsymbol{X}_{p0}$, and 2.70% than using $\boldsymbol{X}_{\text{pca}}$ on prediction of *Var*. Similarly, using $\boldsymbol{X}_p$ has an improvement of 16.30% than using $\boldsymbol{X}_0$, 8.24% than using $\boldsymbol{X}_{p0}$, and 13.07% than using $\boldsymbol{X}_{\text{pca}}$ on prediction of *R*. Through the discussion on results

of Table VI, it is concluded that the proposed approach on extracting and selecting ramp characteristics is also useful for constructing inputs of ramp prediction, and acquires good prediction performance.

CONCLUSION

The study in this paper focus on extracting and selecting profound ramp characteristics for in-depth ramp researches. First, based on wavelet transformation's properties on time-frequency domains and multiresolution, wavelet decomposition is validated useful in analyzing ramps and non-ramps, also different categories of ramps. Then, ramp characteristics are extracted based on the energy decomposition at different wavelet layers. Combining with given ramp categories from wind process, heuristic feature selection methods (e.g., SFFS, SFBS) are applied to select valid characteristics, to remove redundant characteristics and reduce feature dimension. Based on basic ramp characteristics and selected wavelet characteristics, ramp studies on classification and prediction acquire better performance than that without wavelet characteristics and that using PCA in feature selection. Therefore, the conclusion could be summarized in this paper that wavelet transformation is useful to extract profound ramp characteristics, and that selecting ramp characteristics by the proposed approach is feasible to improve performance of ramp studies.

However, besides the above conclusions, there is also a number of conceptual alternatives worth discussing and pursuing: 1) ramp categories in this paper are determined by wind process. Therefore, the selected wavelet characteristics are not completely applicable to other ramp contexts. The approach involving feature extraction and selection in this paper could be still referential. 2) Ramp events generally involve complicated weather movement, it is reasonable that considering meteorological variables in ramp studies could improve the performance. While, for the limitation of data sources in this paper, we only consider ramp characteristics from wind power data. More work on exogenous variables will be studied in future. 3) Based on the selected ramp characteristics and results of some ramp studies, power system's operation associated with ramp events could be studied further. Besides these points, more studies are needed to in-depth understand ramp events.

DATA AVAILABILITY STATEMENT

The original contributions presented in the study are included in the article/Supplementary Material, further inquiries can be directed to the corresponding author.

AUTHOR CONTRIBUTIONS

PY write the paper and implement the experiments. AL supervises the whole process.

FUNDING

This work is supported by Scientific Research Fund of Hunan Provincial Education Department (20A460).

REFERENCES

Ashrafian, A., Mirsalim, M., and Masoum, M. A. (2017). An Adaptive Recursive Wavelet Based Algorithm for Real-Time Measurement of Power System Variables during Off-Nominal Frequency Conditions. *IEEE Trans. Ind. Inform.* 14, 818–828. doi:10.1109/TII.2017.2727222

bpa.gov/transmission (2013). http://transmission.bpa.gov/Business/Operations/Wind/WindGenTotalLoadYTD_2013.xls.

Chen, Z., Zhang, L., Cao, Z., and Guo, J. (2018). Distilling the Knowledge from Handcrafted Features for Human Activity Recognition. *IEEE Trans. Ind. Inform.* 14, 4334. doi:10.1109/tii.2018.2789925

Chen, Z., Zhu, Q., Soh, Y. C., and Zhang, L. (2017). Robust Human Activity Recognition Using Smartphone Sensors via CT-PCA and Online SVM. *IEEE Trans. Ind. Inf.* 13 (6), 3070–3080. doi:10.1109/tii.2017.2712746

Couto, A., Costa, P., Rodrigues, L., Lopes, V. V., and Estanqueiro, A. (2013). "Impact of Weather Regimes on the Wind Power Ramp Forecast," in 12th International Workshop on Large-Scale Integration of Wind Power into Power Systems as well as on Transmission Networks for Offshore Wind Power Plants, London, United Kingdom, October 22–24, 2013.

Doucoure, B., Agbossou, K., and Cardenas, A. (2016). Time Series Prediction Using Artificial Wavelet Neural Network and Multi-Resolution Analysis: Application to Wind Speed Data. *Renew. Energ.* 92, 202–211. doi:10.1016/j.renene.2016.02.003

Escalante Soberanis, M. A., and Mérida, W. (2015). Regarding the influence of the Van der Hoven spectrum on wind energy applications in the meteorological mesoscale and microscale. *Renew. Energ.* 81, 286–292. doi:10.1016/j.renene.2015.03.048

Florita, A., Hodge, B. M., and Orwig, K. (2013). "Identifying Wind and Solar Ramping Events," in IEEE 5th Green Technologies Conference, Denver, CO, 4-5 April 2013 (IEEE). doi:10.1109/GreenTech.2013.30

Francis, N. (2008). *Predicting Sudden Changes in Wind Power Generation*, 58. Honolulu: North American Wind Power.

Gallego, C., Costa, A., Cuerva, Á., Landberg, L., Greaves, B., and Collins, J. (2013). A Wavelet-Based Approach for Large Wind Power Ramp Characterisation. *Wind Energy* 16 (2), 257–278. doi:10.1002/we.550

Gan, J. Q., Awwad Shiekh Hasan, B., and Tsui, C. S. L. (2014). A Filter-Dominating Hybrid Sequential Forward Floating Search Method for Feature Subset Selection in High-Dimensional Space. *Int. J. Mach. Learn. Cyber.* 5 (3), 413–423. doi:10.1007/s13042-012-0139-z

Gu, B., Sun, X., and Sheng, V. S. (2017). Structural Minimax Probability Machine. *IEEE Trans. Neural Netw. Learn. Syst.* 28 (7), 1646–1656. doi:10.1109/tnnls.2016.2544779

He, M., Vittal, V., and Zhang, J. (2013). Online Dynamic Security Assessment with Missing Pmu Measurements: A Data Mining Approach. *IEEE Trans. Power Syst.* 28 (2), 1969–1977. doi:10.1109/tpwrs.2013.2246822

He, S., Li, K., and Zhang, M. (2013). A Real-Time Power Quality Disturbances Classification Using Hybrid Method Based on S-Transform and Dynamics. *IEEE Trans. Instrum. Meas.* 62 (9), 2465–2475. doi:10.1109/tim.2013.2258761

He, Y., Kusiak, A., Ouyang, T., and Teng, W. (2017). Data-driven Modeling of Truck Engine Exhaust Valve Failures: a Case Study. *J. Mech. Sci. Technol.* 31 (6), 2747–2757. doi:10.1007/s12206-017-0518-1

Huang, H., Liu, F., Zha, X., Xiong, X., Ouyang, T., Liu, W., et al. (2018). Robust Bad Data Detection Method for Microgrid Using Improved ELM and DBSCAN Algorithm. *J. Energ. Eng.* 144 (3), 04018026. doi:10.1061/(asce)ey.1943-7897.0000544

Mohanty, S. R., Kishor, N., Ray, P. K., and Catalao, J. P. S. (2015). Comparative Study of Advanced Signal Processing Techniques for Islanding Detection in a Hybrid Distributed Generation System. *IEEE Trans. Sustain. Energ.* 6 (1), 122–131. doi:10.1109/tste.2014.2362797

Ouyang, T. (2021). Feature Learning for Stacked ELM via Low-Rank Matrix Factorization. *Neurocomputing* 448, 82–93. doi:10.1016/j.neucom.2021.03.110

Ouyang, T., Kusiak, A., and He, Y. (2017). Modeling Wind-Turbine Power Curve: A Data Partitioning and Mining Approach. *Renew. Energ.* 102, 1–8. doi:10.1016/j.renene.2016.10.032

Ouyang, T., Zha, X., and Qin, L. (2017). A Combined Multivariate Model for Wind Power Prediction. *Energ. Convers. Manag.* 144, 361–373. doi:10.1016/j.enconman.2017.04.077

Ouyang, T., Zha, X., Qin, L., and Kusiak, A. (2017). Optimisation of Time Window Size for Wind Power Ramps Prediction. *IET Renew. Power Generation* 11 (8), 1270–1277. doi:10.1049/iet-rpg.2016.0341

Sevlian, R., and Rajagopal, R. (2013). Detection and Statistics of Wind Power Ramps. *IEEE Trans. Power Syst.* 28, 3610–3620. doi:10.1109/tpwrs.2013.2266378

Shen, X., Ouyang, T., Yang, N., and Zhuang, J. (2021). Sample-Based Neural Approximation Approach for Probabilistic Constrained Programs. *IEEE Trans. Neural Netw. Learn. Syst.*, 1–8. doi:10.1109/TNNLS.2021.3102323

Singh, K., and Tewari, A. (2015). Classification of Power Quality Disturbances Using Wavelet Transform and Neural Network. *Int. J. Eng. Res. Tech.* 4 (05), 1423. doi:10.17577/ijertv4is051331

Tang, Z., Zhao, G., and Ouyang, T. (2021). Two-phase Deep Learning Model for Short-Term Wind Direction Forecasting. *Renew. Energ.* 173, 1005–1016. doi:10.1016/j.renene.2021.04.041

Tang, Z., Zhao, G., Wang, G., and Ouyang, T. (2020). Hybrid Ensemble Framework for Short-Term Wind Speed Forecasting. *IEEE Access* 8, 45271–45291. doi:10.1109/access.2020.2978169

Wang, L., Zhang, Z., Long, H., Xu, J., and Liu, R. (2017). Wind Turbine Gearbox Failure Identification with Deep Neural Networks. *IEEE Trans. Ind. Inf.* 13 (3), 1360–1368. doi:10.1109/tii.2016.2607179

Wang, Z., Wang, W., Liu, C., and Feng, S. (2013). Uncertainty Estimation of Wind Power Prediction Result Based on Wind Process Method. *Power Syst. Tech.* 37 (1), 242–247.

Xiong, Y., Zha, X., Qin, L., Ouyang, T., and Xia, T. (2017). Research on Wind Power Ramp Events Prediction Based on Strongly Convective Weather Classification. *IET Renew. Power Generation* 11 (8), 1278–1285. doi:10.1049/iet-rpg.2016.0516

Zha, X., Ouyang, T., Qin, L., Xiong, Y., and Huang, H. (2016). Selection of Time Window for Wind Power Ramp Prediction Based on Risk Model. *Energ. Convers. Manag.* 126, 748–758. doi:10.1016/j.enconman.2016.08.064

Zheng, H., and Kusiak, A. (2009). Prediction of Wind Farm Power Ramp Rates: A Data-Mining Approach. *J. solar Energ. Eng.* 131 (3), 031011. doi:10.1115/1.3142727

Conflict of Interest: The authors declare that the research was conducted in the absence of any commercial or financial relationships that could be construed as a potential conflict of interest.

Publisher's Note: All claims expressed in this article are solely those of the authors and do not necessarily represent those of their affiliated organizations, or those of the publisher, the editors and the reviewers. Any product that may be evaluated in this article, or claim that may be made by its manufacturer, is not guaranteed or endorsed by the publisher.

frontiers in Energy Research

ORIGINAL RESEARCH
published: 04 October 2021
doi: 10.3389/fenrg.2021.754335

Edge Intelligent Perception Method for Power Grid Icing Condition Based on Multi-Scale Feature Fusion Target Detection and Model Quantization

Fuqi Ma[1], Bo Wang[1], Min Li[2], Xuzhu Dong[1], Yifan Mao[3], Yinyu Zhou[4,1] and Hengrui Ma[5]*

[1]School of Electrical and Automation, Wuhan University, Wuhan, China, [2]School of Computer and Artificial Intelligence, Wuhan Textile University, Wuhan, China, [3]State Grid Shaanxi Electric Power Company, State Grid Xi'an Power Supply Company, Xi'an, China, [4]Guangdong Power Grid Corp, Huizhou Power Supply Bureau Co., Ltd., Huizhou, China, [5]Tus-Institute for Renewable Energy, Qinghai University, Xining, China

Insulator is an important equipment of power transmission line. Insulator icing can seriously affect the stable operation of power transmission line. So insulator icing condition monitoring has great significance of the safety and stability of power system. Therefore, this paper proposes a lightweight intelligent recognition method of insulator icing thickness for front-end ice monitoring device. In this method, the residual network (ResNet) and feature pyramid network (FPN) are fused to construct a multi-scale feature extraction network framework, so that the shallow features and deep features are fused to reduce the information loss and improve the target detection accuracy. Then, the full convolution neural network (FCN) is used to classify and regress the iced insulator, so as to realize the high-precision identification of icing thickness. Finally, the proposed method is compressed by model quantization to reduce the size and parameters of the model for adapting the icing monitoring terminal with limited computing resources, and the performance of the method is verified and compared with other classical method on the edge intelligent chip.

Keywords: intelligent perception, transmission line, icing monitoring, power depth vision, edge computing, model quantification, power grid safety

OPEN ACCESS

Edited by:
Xun Shen,
Tokyo University of Agriculture and Technology, Japan

Reviewed by:
Yuanchao Hu,
Shandong University of Technology, China
Nan Yang,
China Three Gorges University, China

****Correspondence:***
Bo Wang
whwdwb@whu.edu.cn

Specialty section:
This article was submitted to Smart Grids, a section of the journal Frontiers in Energy Research

Received: *06 August 2021*
Accepted: *15 September 2021*
Published: *04 October 2021*

Citation:
Ma F, Wang B, Li M, Dong X, Mao Y, Zhou Y and Ma H (2021) Edge Intelligent Perception Method for Power Grid Icing Condition Based on Multi-Scale Feature Fusion Target Detection and Model Quantization. Front. Energy Res. 9:754335. doi: 10.3389/fenrg.2021.754335

INTRODUCTION

The importance of safe and stable operation of power grid to the development of the national economy is self-evident. With the deepening of power grid interconnection and the gradual implementation of power market, the operation environment of power grid is more complex, which puts forward higher requirements for the stability and reliability of power grid (Ruszczak and Tomaszewski, 2015; Liu et al., 2020; Wang et al., 2020). Due to the vast territory, diverse climate, complex terrain and other factors, power grids in China are often damaged by various natural disasters, resulting in large-scale power outages. As an important equipment of transmission lines and substations, insulators have the functions of electrical insulation and mechanical fixation (Liu et al., 2017; Yang et al., 2019). Due to ice and snow condition, the external insulation performance of insulators will be significantly reduced. Severe icing may lead to the distortion of insulator potential distribution, flashover of insulator, line trip and outage, which brings great challenges to the safe and stable operation of power grid. In 2008, the south of China suffered extremely serious ice disaster,

which led to a large area of ice flashover of insulators in many transmission lines and substations, resulting in a series of serious accidents such as tripping and equipment damage (Tiannan and Dongxiao, 2016; Wang et al., 2021). Since then, although the degree of icing disaster is less than that in 2008, the destructive impact of ice disaster weather on insulators and even power grid has always existed. Therefore, it is urgent to carry out insulator icing perception research to guide the production, operation and maintenance, find and eliminate hidden dangers in time, so as to improve the safety and stability of the power grid operation (Wei and Caifei, 2019; Li et al., 2021).

At present, monitoring and restraining methods are mainly used for insulator icing control and management (Jiang et al., 2014; Li et al., 2019). The monitoring method can realize online monitoring of insulator icing state by installing sensors and cameras on electrical equipment, or find hidden dangers in key line inspection by manual inspection. Based on the monitoring results, various ice melting technologies have been adopted to eliminate the icing of insulators, mainly including mechanical de icing, laser de icing and manual de icing (Zhang et al., 2020a). The research on insulator icing monitoring and recognition mainly focuses on cloud centric computing mode, including environmental parameter monitoring (Junhua et al., 2018; Xingliang et al., 2018; Zhu et al., 2020) and image monitoring (Yan et al., 2013; Jingjing et al., 2017; Shen and Raksincharoensak, 2021a). The method based on environmental parameters is mainly fonded on experimental analysis, and the change of insulator icing thickness is often obtained through the change of environmental parameters and physical analysis. The limitation of insulator icing thickness calculate method based on environmental parameter monitoring is that all kinds of sensors installed on transmission lines will be affected by bad weather and complex electromagnetic interference, which may lead to large errors in icing monitoring results. In the image monitoring method, the video monitoring terminal installed on the transmission line tower to collect the insulator icing image regularly, and transmit the icing image to the monitoring center. Then use the rich computing resources and advanced images processing methods of the monitoring center to calculate the insulator icing thickness (Dongxiao et al., 2017; Yongsai et al., 2017). For the collected insulator icing image, the traditional image processing methods are mainly used for icing perception, such as image segmentation or edge detection to realize icing thickness level recognition (Yanpeng et al., 2017; Qiangliang et al., 2018). The processing mode and effect of traditional image methods are seriously affected by the quality and location of icing images. Different types of icing images usually need to be determined manually to select the best processing method, which shows the problems of insufficient generalization ability and low efficiency.

With the development of Graphics Processing Unit (GPU) and artificial intelligence (AI) technology, image processing method based on deep learning (Shen et al., 2020a; Shen et al., 2021a) is gradually applied to insulator icing monitoring (Zhuangli et al., 2018; Shen and Raksincharoensak, 2021b; Nan et al., 2018). Wang et al. (Gang et al., 2018) proposed a method of insulator icing thickness identification based on convolution neural network. Using the abundant computing resources of cloud computing center, a complex convolution neural network recognition model is established to identify the ice thickness level, which has strong generalization ability. Yang et al. (2021a); Yang et al. (2021b) first study SCUC problems and proposed an expanded sequence-to-sequence (E-Seq2Seq) based data-driven SCUC expert system for dynamic multiple-sequence mapping samples, it can accommodate the mapping samples of SCUC, and consider the various input factors that affect SCUC decision-making, possessing strong generality, high solution accuracy, and efficiency over traditional methods. However, the cloud computing model can not guarantee the reliable transmission, real-time analysis and recognition of insulator icing monitoring image in bad weather. But with the development of power Internet of things and the transformation of energy digitization (Shen et al., 2017; Haoyong et al., 2019), millions of power edge intelligent devices such as power sensors, state sensors and intelligent video monitoring system are connected to the power Internet of things, resulting in massive heterogeneous data (Zhang and Luo, 2018; Shen et al., 2020b; Nie et al., 2020; Ying et al., 2020). The traditional centralized data processing mode centered on cloud computing shows the problem of insufficient real-time, especially for the ice monitoring system with poor transmission conditions, the edge intelligent technology with edge computing as the core has been widely concerned. Therefore, the research on the intelligent identification method of front-end edge intelligent icing monitoring equipment has become the inevitable development trend of online icing monitoring (Chen et al., 2019; Zhou et al., 2019).

Ma et al. (2021) utilized the edge computing mode to identify icing thickness of transmission line in front-end monitoring equipment. Considering that the established ice thickness identification model is too complex to be suitable for the front-end ice monitoring device with limited computational resources, they use network channel pruning method for model lightweight compression. However, network channel pruning method requires a lot of manpower and computing power. In order to improve the engineering applicability of the edge intelligent icing thickness identification, this paper proposes a model quantization method for lightweight compression of icing thickness identification model, so as to realize the front-end localized identification of icing thickness in the icing monitoring device. And the ResNet network and FPN network are used to constructs a multi-scale feature extraction and fusion network framework to improve the detection accuracy of insulators. The main contributions of this paper are summarized as follows.

1) A edge intelligent perception method for power grid icing condition based on multi-scale feature fusion target detection and model quantization is proposed, so as to implement the front-end localization intelligent identification of insulator icing thickness.
2) The residual network ResNet and feature pyramid network (FPN) are fused to construct a multi-scale feature extraction network framework, so that the shallow features and deep

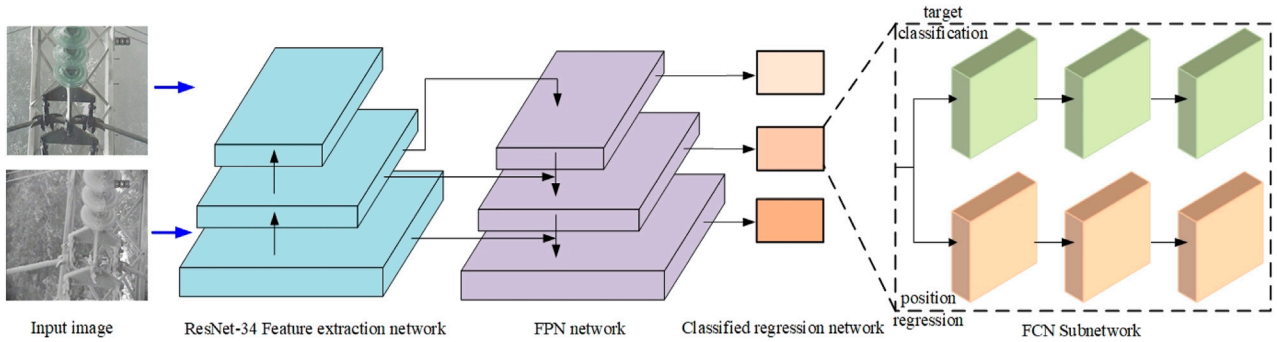

FIGURE 1 | Framework of insulator icing thickness identification method.

features are fused to reduce the information loss and improve the target detection accuracy.

3) The proposed method is compressed by model quantization, so as to reduce the size and parameters of the model to adapt to the icing monitoring terminal with limited computing resources.

The rest of the paper is organized as follows: Section II introduces the lightweight intelligent recognition method of icing thickness proposed in this paper for icing monitoring terminal, which is based on residual network ResNet, feature pyramid network (FPN), full convolutional network (FCN) and model quantification. In Section IV, the experiment results are presented to verify the proposed method, followed by conclusions.

PROPOSED METHOD

Considering that the actual transmission line icing usually faces various bad weather conditions, and different transmission line terrain and environment will lead to a variety of scene changes, such as strong wind, heavy rain and other scenes, the icing images collected by the actual icing monitoring system show the characteristics of complex background, low resolution and polymorphism. So the icing thickness identification model established in this paper is a combination of ResNet (Zhang et al., 2020b), FPN (Feature pyramid networks) (Zhao et al., 2019) and FCN (Full convolutional network) (Long et al., 2015). The residual network ResNet and feature pyramid network (FPN) are fused to construct a multi-scale feature extraction network framework to extract more icing image information. And full convolution network is used for insulator icing grading and position regression. The proposed method solves the multi-scale problem in target detection to a certain extent, and improves the detection accuracy of targets with different sizes. Especially, the shallow image features are introduced into the FPN network, which improves the detection sensitivity of small targets such as a small proportion of insulators. FCN network adopts the anchor frame generation mechanism to generate candidate regions with fixed size ratio and quantity, which is similar to YOLOv3 model. In this way, the speed of insulator icing detection is improved.

System Architecture

The network structure of ice thickness identification method proposed in this paper is mainly composed of feature extraction network, feature pyramid network (FPN network) and classification regression network (FCN sub network). In order to improve the recognition speed of insulator icing, its feature extraction network uses the ResNet-34 network with fewer layers than Faster RCNN to extract feature maps with different resolutions from the input image. Its target classification regression network uses the same candidate box generation mechanism as YOLOv3, the system architecture of our method is shown in **Figure 1**.

For the input insulator icing image, the high-level and low-level feature maps of the image are obtained under different resolutions by using the resnet-34 feature extraction network firstly. Then, the FPN network is used to connect the high-level and low-level features horizontally for feature fusion, and candidate boxes are generated on feature maps with different scales. Finally, the position information and icing thickness level information of the predicted insulator target frame are output by the classification regression sub network of FCN. The detailed process of intelligent recognition of insulator icing thickness as shown in **Figure 2**.

Multi-Scale Feature Extraction of Icing Image

The structure of multi-scale feature extraction network based on residual network ResNet-34 in this paper is shown in **Table 1**. When he sliding step of convolution kernel is set to 2, the feature map will shrink gradually in the form of two times. With the deepening of feature extraction network, the semantic information of insulator icing image is gradually enhanced (Shen et al., 2021b), but the location information is gradually blurred.

The feedforward calculation of ResNet-34 network is the bottom-up feature extraction process corresponding to the feature pyramid, which uses the feature activation of the last

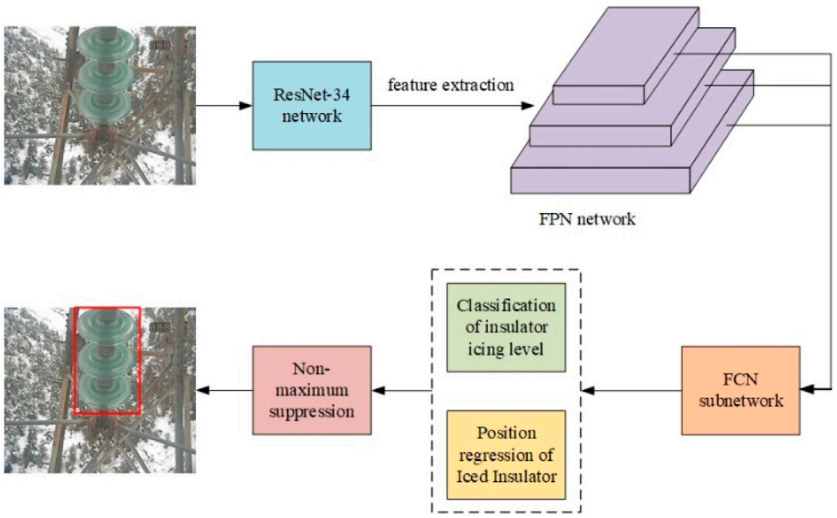

FIGURE 2 | Specific process of intelligent recognition of insulator icing thickness.

TABLE 1 | Feature extraction network architecture of ResNet-34.

Layer	Feature map size	Network structure
conv1	112 × 112	7 × 7, 64, Stride size: 2
conv2	56 × 56	3 × 3 max pool, Stride Size: 2
		$\begin{bmatrix} 3\times3, 64 \\ 3\times3, 64 \end{bmatrix}\times3$
conv3	28 × 28	$\begin{bmatrix} 3\times3, 128 \\ 3\times3, 128 \end{bmatrix}\times4$
conv4	14 × 14	$\begin{bmatrix} 3\times3, 256 \\ 3\times3, 256 \end{bmatrix}\times6$
conv5	7 × 7	$\begin{bmatrix} 3\times3, 512 \\ 3\times3, 512 \end{bmatrix}\times3$

TABLE 2 | The size and dimension of each feature in feature pyramid network.

Feature	Network	Size	Dimension
C2	ResNet-34	56 × 56	64
C3	ResNet-34	28 × 28	128
C4	ResNet-34	14 × 14	256
C5	ResNet-34	7 × 7	512
M2	FPN	56 × 56	256
M3	FPN	28 × 28	256
M4	FPN	14 × 14	256
M5	FPN	7 × 7	256
P2	FPN	56 × 56	256
P3	FPN	28 × 28	256
P4	FPN	14 × 14	256
P5	FPN	7 × 7	256

residual structure in each stage as the output. In this paper, the output of these residual modules is expressed as follows: {C2, C3, C4, C5}. Corresponding to the activation value of the last module of conv2, conv3, conv4 and conv5 in **Table 2**, the size dimensions of feature map are 56×56×64, 2,828,××128, 1,414,××256 and 7×7×512 respectively.

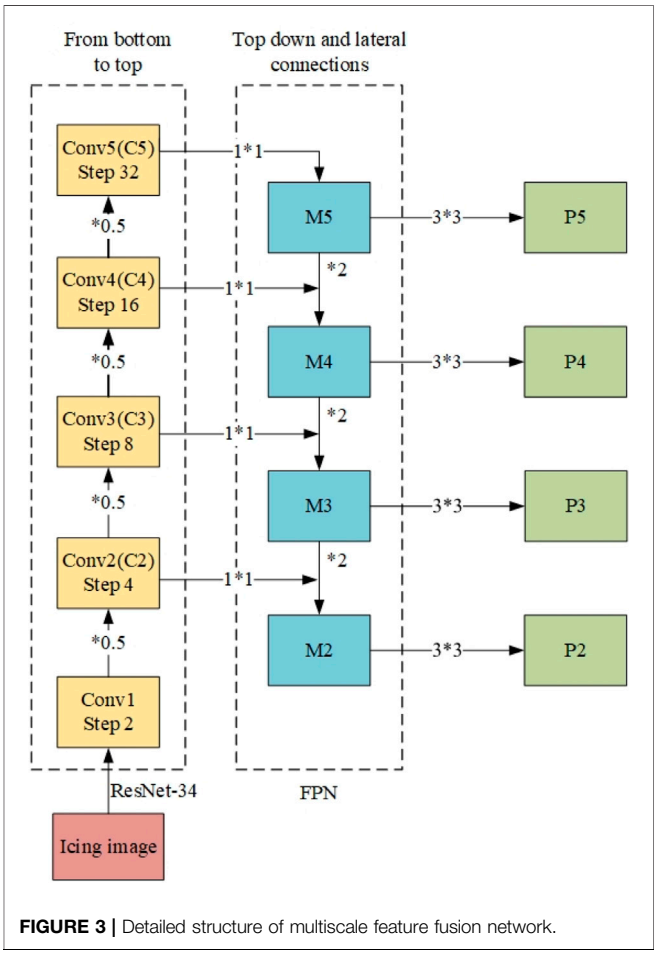

FIGURE 3 | Detailed structure of multiscale feature fusion network.

Multi Scale Feature Fusion

The semantic information of high-level feature map obtained by residual feature extraction network ResNet-34 is generally strong,

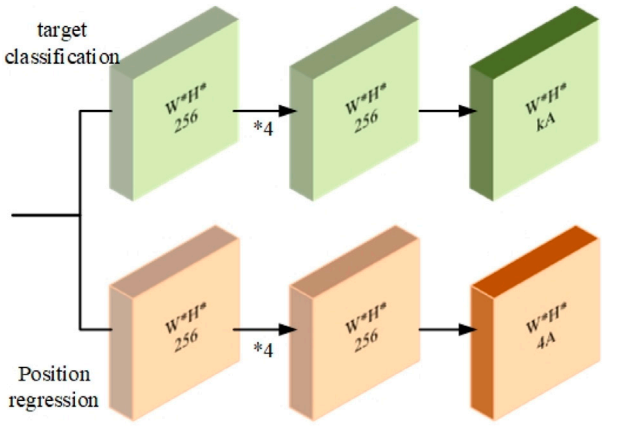

FIGURE 4 | FCN network structure diagram.

but the location information is fuzzy. The location information of low-level feature map is generally clear, but the semantic information is weak. Moreover, the top-down hierarchical structure of FPN network with horizontal connection helps to fuse the high-level strong semantic features of ResNet-34 network output with the low-level clear location features, so that the features of different scales have strong semantic information. The detailed structure of multi-scale feature fusion network is shown in **Figure 3**.

As shown in **Figure 3**, the output C5 of ResNet-34 changes to feature map M5 with 7×7×256 dimension size after a convolution 1×1×256. Then, a convolution operation with dimension 3×3×256 will be added to each feature map M to eliminate the aliasing effect between feature layers of different scales. For the construction of P4 in FPN network, the feature map of M5 is up sampled twice by nearest neighbor upsampling method, so as to double the size of the feature map. In this way, the feature map M5 becomes the same size dimension as M4 named M5'. And the feature map C4 becomes the same size dimension as M4 named C4′ after a convolution 1×1×256. Finally, the feature map M4 can be obtained by adding M5′ and C4'. Similarly, we can get the feature map M3, M2, M1, P3 and P2. The size and dimension of each feature map are shown in **Table 2**.

Classification of Icing Thickness and Location Regression

The target classification network of ice thickness recognition model is divided into two sub networks: target classification sub network and prediction box position regression sub network. The network structure of class sub network and box sub network used in feature map at different stages is related to the size of feature map, as shown in **Figure 4**.

In **Figure 4**, the sizes of *W* and *H* are the same as those feature maps (P2, P3, P4, P5) output by FPN. *K* represents the total number of categories to be predicted, and *A* represents the number of candidate boxes or anchors. In this paper, the idea of object classification regression of YOLOv3 is used to divide each feature map output by FPN into grids corresponding to the length and width of the feature map. For example, the feature map P5 with 7 × 7 size is divided into 7 × 7 grids. Then, three groups candidate frames are established from each grid center, the length width ratio of each group of candidate boxes is 1:1, 1:2 and 2:1 respectively. The ratio of the three groups of candidate boxes is 2^0:$2^{1/3}$:$2^{2/3}$. So the feature map P5 will be divided into 7 × 7×9 = 441 candidate boxes, as shown in **Figure 5** (in the figure, only one group candidate boxes are drawn in the center of the grid, and two groups with different proportions are not presented).

Class sub network uses 4-time 256 channel convolution and 1-time num_priors×num_classes convolution for feature extraction, num_priors refers to the number of candidate boxes owned by the feature layer. num_classes refers to how many kinds of targets are detected by the network. 4-times of 256 channel convolution and 1-time num_priors×4 convolution are used in box sub network. Where, four refers to the adjustment of the coordinates of the upper left corner and the lower right corner of the candidate box. Class sub network and box sub network can be used to modify the target category and location information of the initial candidate box. Finally, the confidence scores of candidate frames are sorted and the Non-maximum value is suppressed. The candidate frames with low scores are removed, and the candidate frames with more overlaps are combined to realize the classification of insulator icing level and position coordinate regression.

Model Compression Method Based on Quantization

The implementation of Quantization Compression for the model needs to convert the common operations (such as convolution, matrix multiplication, activation function, pooling, splicing, etc.) into the equivalent operation of the faster 8-bit integer (int8) version, and then add quantization and inverse quantization operations before and after the convolution operation. Quantization operation is convert input from high-precision floating-point operation (generally 32-bit floating-point or 16 bit floating-point) to low precision integer operation (generally 8-

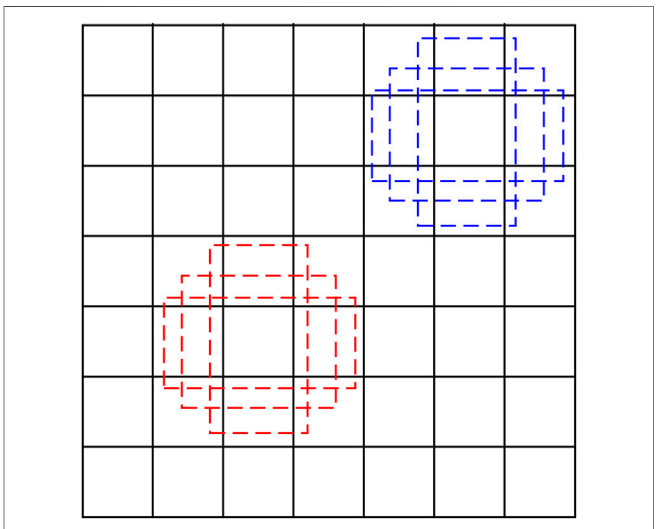

FIGURE 5 | Schematic diagram of grid and candidate box of feature map P5.

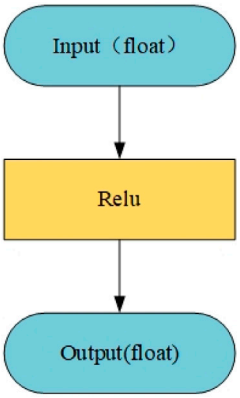

FIGURE 6 | Relu operation before quantization.

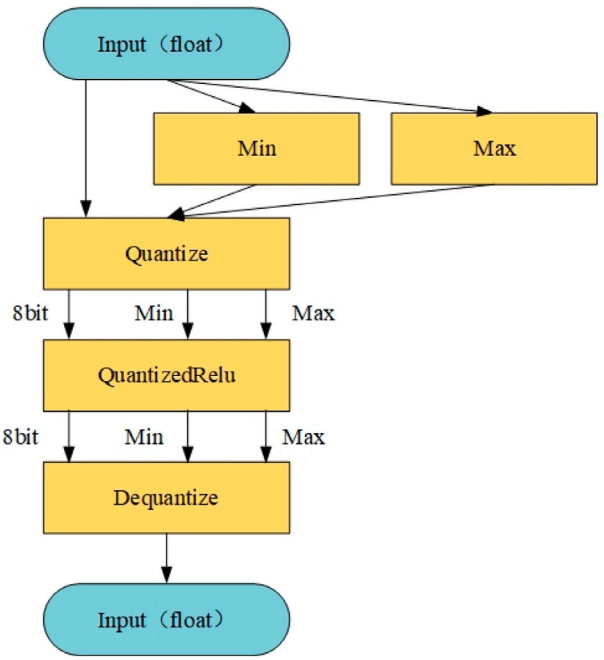

FIGURE 7 | Relu operation after quantization.

bit integer), while the inverse quantization operation is to transfer output from low-precision operation to high-precision operation. Taking the Relu activation function as an example, the relu operation before quantization is shown in **Figure 6**, and the relu operation after network quantization is shown in **Figure 7**.

For the quantization operation of converting floating numbers into 8-bit integers (0–255) in **Figure 7**, the core to find out the minimum value (Min) and maximum value (Max) of input data, and then the quantization value q of each input data can be obtained by using the following formula.

$$q = \frac{x - \min}{\max - \min} \cdot 255 \tag{1}$$

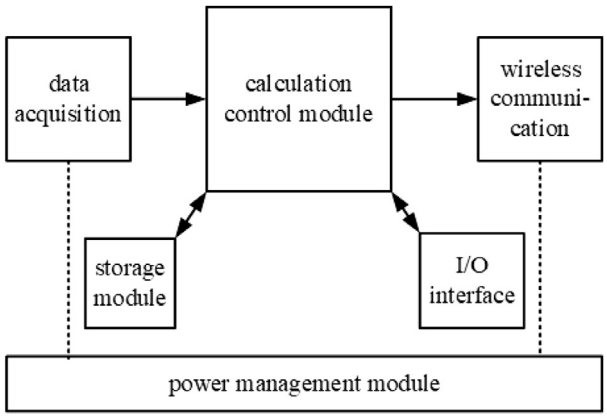

FIGURE 8 | Structure of the icing monitoring device.

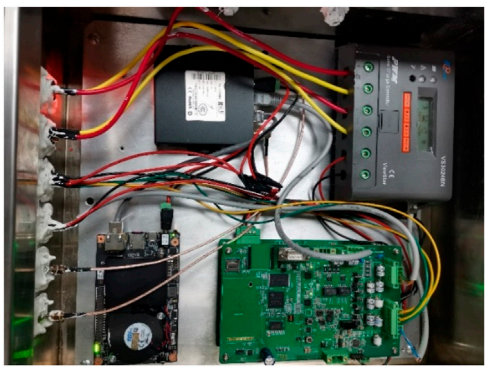

FIGURE 9 | Physical structure diagram of icing monitoring device.

On the contrary, the inverse quantization value x can also be obtained by using the following formula.

$$x = \frac{q \cdot (\max - \min)}{255} + \min \tag{2}$$

The quantization error after quantization is R.

$$R = \frac{\max - \min}{255} \tag{3}$$

Using the quantitative operation technology of neural network can reduce the memory occupation, the amount of calculation and the power consumption of the ice thickness identification model, which is not only conducive to the deployment of the established ice thickness identification model to the intelligent embedded system, but also can improve the operation efficiency of proposed model.

Structure Composition of Edge Intelligent Icing Monitoring Device

In order to realize the front-end localization identification of icing thickness, this paper designs an edge intelligent icing monitoring device based on edge artificial intelligent (AI) chip. The device

FIGURE 10 | The diagram of edge intelligent analysis module.

mainly includes six parts: data acquisition module, calculation control module, wireless communication module, storage module, power management module and I/O communication interface. The specific structural diagram of the device is shown in **Figure 8**, and the physical structure diagram of icing monitoring is shown in **Figure 9**. The icing monitoring with AI chip can be deployed to the transmission line tower for online monitoring of insulator icing thickness.

1) Data acquisition module. It is used to connect camera and other monitoring equipment or video monitoring system for data acquisition and coding processing of insulator icing image. Due to the slow change of insulator icing thickness, the device collects an icing image every 15 min.
2) Calculation control module. Huawei atlas 200 chip is used as the intelligent processing chip in the edge ice monitoring device, which can analyze and calculate the collected structured data such as insulator icing image and video, identify the icing thickness level of insulator, and control and coordinate the operation of each module.
3) Wireless communication module. Communication modes include 4G and WiFi, which can upload the identification results of insulator icing thickness to the cloud or server, so as to assist in transmission line maintenance and management.
4) Storage module. This module is used to store the operation system of the device, lightweight model of insulator thickness grade identification and other supporting software and algorithms.
5) Power management module. The icing monitoring device is powered by external photovoltaic panel and battery. Dual charging solar controller is used in icing monitoring device for power charging management and control.
6) I/O communication interface. Provide communication interface between modules.

EXPERIMENT RESULTS

This section introduces the experimental details and compares the performance of the proposed method for icing thickness recognition with other methods. In order to verify the performance of the lightweight icing intelligent recognition method proposed in this paper, under the same experimental conditions, classical single-stage method YOLOv3 and classical two stage method Faster RCNN are selected and quantized as the control group, and the detection accuracy and recognition speed are compared on the same experiment set. For the three methods, compare the performance of the methods on the server side firstly, and then compare the performance on the edge side through the model compression method. The model with suffix *-FP32* indicates that the model uses 32-bit floating-point full precision, It is experitmented on the server side. The model with suffix *-int8* indicates that the 8-bit integer precision is used after quantization and compression of the model, and it is experitmented on the edge intelligent ice monitoring device.

Construction of Image Sample Library for Insulator Icing Monitoring

The sample library constructed in this paper contains more than 4,000 insulator icing monitoring image. This paper divides the icing level based on icing and snow conditions of insulators and transmission lines, combined with the actual inspection experience and application requirements. The icing thickness of insulators is divided into five icing levels, including level_ 1, level_ 2, level_ 3, level_ four and level_ 5 (Ma et al., 2021). Each icing level represents a different insulator icing thickness range, as shown in **Table 3**.

Experiment Environment and Parameter Setting

In order to ensure that the performance indexes before and after model compression are compared under the same computing power as much as possible, the main configuration of the server side is 8-core CPU, 32 GB memory and an NVIDIA Tesla P4 graphics card with 8 GB video memory, its power consumption is 70*W*. Huawei atlas 200 DK chip is used as the intelligent processing chip in the edge ice monitoring device, which is shown in **Figure 10**. The experimental environment is deep learning framework Caffe under Ubantu system, and the power consumption is edge intelligence chip is 20 *W*. The 8-bit integer peak computing power of Tesla P4 graphics card and Atlas 200 DK chip is 22tops (trillion operations/s). To ensure the performance of the model under the same training and test conditions, the three methods use the same training set (including the verification set) in the cloud training. The number of iterations is 100, and the learning strategy is to

TABLE 3 | Classification of insulator icing thickness.

Icing level	Thickness	Describe
level_1	0 mm	No snow and ice
level_2	0~3 mm	Slight snow cover, no ice
level_3	3~6 mm	Snow is thick and slightly ice
level_4	6–10 mm	Heavy snow, moderate ice
level_5	>10 mm	Heavy snow cover, severe ice

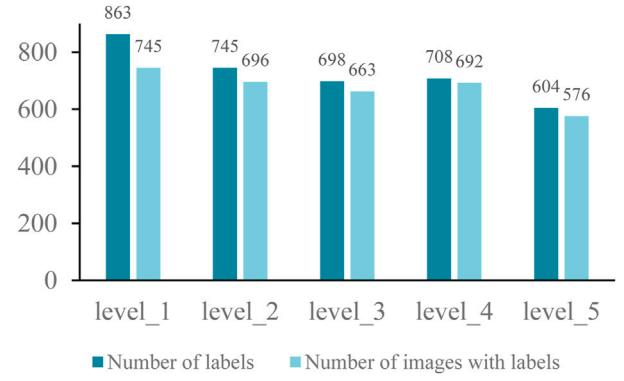

FIGURE 11 | Label and image distribution of various insulator icing levels in the training set.

automatically adjust the learning rate according to the verification accuracy, and the same test images in the insulator icing picture library are used for test comparison.

To ensure the sample balance of the test set, 135 images of each icing level are randomly selected from the insulator icing image library to form the test set. The number of images in the training set and the test set was 2,700 and 675, respectively, and the ratio is 8:2. The image distribution of training set on icing level of various insulator is shown in **Figure 11**, it can be seen that there is no sample imbalance in all kinds of icing levels of insulators in the images of training set and test set.

Comparative Analysis of Icing Identification Accuracy

This paper compares the models of Faster RCNN, YOLOv3 and our icing identification method before and after quantification compression, also compares them with the same test images. Firstly, the average precision (AP) is used to measure the performance of these methods. Average precision is achieved by averaging the precision at different recall points, which is generally calculated by the 11 point method. By setting a set of thresholds containing 11 recall points [0, 01, 0.2, 0.3, 0.4, 0.5, 0.6, 0.7, 0.8, 0.9, 1]. Each recall point corresponds to a maximum Precision. The average of these precision is the AP, and which can be obtained by the following equation.

$$AP = \frac{1}{11} \sum_{R\in\{0,0.1,\ldots\ldots,1\}} \max P(R) \tag{4}$$

Taking insulator icing level_1 as an example, the maximum accuracy and average precision of different recall thresholds are given, as shown in **Table 4**.

From **Table 4**, it can be seen that the Faster RCNN of the two-stage method has higher identification accuracy for icing thickness, which indicates that the RPN network of Faster RCNN model of can improve the detection accuracy. However, the detection accuracy of YOLOv3 based on integrated convolutional neural network is lower than that based on RPN, as there is no mechanism to generate target candidate domain. Besides, the accuracy of the proposed method is higher than that of the Faster RCNN model, which shows that the FPN network used in the proposed method is helpful to improve the accuracy of ice thickness identification. In addition, after the model compression, the Average precision (AP) of Faster RCNN, YOLOv3 and the method proposed in this paper presents a downward trend, which indicates that the identification accuracy for ice thickness will be reduced by the quantization compression.

Threfore, compared with the typical target detection methods, the multi-scale target detection method proposed in this paper has higher ice thickness identification accuracy for insulator icing level_1 under the server environment. But the accuracy of our method by model quantification is slightly lower than that of Faster RCNN under the edge intelligent equipment environment. In order to further measure the performance of those methods, we compare the model size, mean average precision (mAP). calculation speed and other indicators of those methods.

Average Precision Comparison and Performance Analysis

After calculating the average precision (AP) of YOLOv3, Fast RCNN and our method before and after compression for each

TABLE 4 | The detection accuracy of different method for insulator icing level_1 before and after compression.

Recall	The maximum precision of different models corresponding to different recall thresholds					
	YOLOv3-FP32	YOLOv3-int8	Faster RCNN-FP32	Faster RCNN-int8	Our method-FP32	Our method-int8
0	1.000	1.000	1.000	1.000	1.000	1.000
0.1	1.000	1.000	1.000	1.000	1.000	1.000
0.2	0.960	0.956	1.000	0.968	0.978	0.892
0.3	0.960	0.956	0.967	0.956	0.978	0.892
0.4	0.960	0.930	0.967	0.956	0.978	0.892
0.5	0.944	0.930	0.944	0.937	0.978	0.892
0.6	0.944	0.927	0.878	0.872	0.978	0.892
0.7	0.932	0.869	0.855	0.843	0.978	0.892
0.8	0.730	0.550	0.855	0.835	0.964	0.892
0.9	0.365	0.275	0.822	0.807	0.964	0.892
1	0.000	0.000	0.000	0.000	0.000	0.000
AP	0.800	0.763	0.844	**0.834**	**0.891**	0.831

TABLE 5 | The mean accuracy of different method before and after quantify compression.

Icing level	The average precision (AP) of different method each icing levels before and after quantify compression					
	YOLOv3-FP32	YOLOv3-int8	Faster RCNN-FP32	Faster RCNN-int8	Our method-FP32	Our method-int8
level_1	0.800	0.763	0.844	0.834	0.891	0.831
level_2	0.623	0.585	0.861	0.801	0.871	0.867
level_3	0.614	0.538	0.761	0.746	0.875	0.821
level_4	0.724	0.638	0.786	0.707	0.888	0.826
level_5	0.810	0.780	0.800	0.787	0.885	0.882
mAP	0.714	0.661	0.811	0.775	0.882	0.845

TABLE 6 | Performance comparison of model before and after quantization compression.

Method	Model size (MB)	Size change before and after compression	mAP	Map changes before and after compression	speed (ms/pic)	The change of recognition speed before and after compression
YOLOV3-FP32	235.97	−46.63%	0.714	−7.44%	50	64.40%
YOLOV3-int8	125.93		0.661		17.8	
FasterRCNN-FP32	445.24	−44.59%	0.811	−4.38%	180	−433.33%
FasterRCNN-int8	246.72		0.775		960	
Our method-FP32	139.67	−11.24%	0.882	−4.15%	112	−51.79%
Our method-int8	123.97		0.845		170	

insulator icing level, the mean average precision (mAP) of each method can be calculated, as shown in **Table 5**. The mean average precision (mAP) reflects the comprehensive detection accuracy performance of the target detection method for the insulators detection with different icing levels. It can be seen from **Table 5** that the mAP of our method is the highest on both the server side and the edge side. It shows that the comprehensive performance of the proposed method before and after quantization compression is better than that of YOLOv3 and Fast RCNN method.

In addition, for the icing online monitoring device with poor transmission conditions, it requires not only higher comprehensive detection accuracy performance, but also faster detection speed, whichs meet the real-time and reliability requirements of power grid condition monitoring. Therefore, this paper compares the changes of mAP, detection speed and model size of the three models before and after quantization compression, as shown in Tab 6.

It can be seen from **Table 6**, after quantization compression, the size and mAP of YOLOv3, Faster RCNN and our method are reduced, and the recognition speed of Faster RCNN model and our method also shows a downward trend, while the recognition speed of YOLOv3 is greatly improved. Besides, the sigle-stage method has the lowest mAP index for the method before and after the quantization compression. The mAP of our method combining the advantages of the single-stage method and the two-stage method is the highest, and the mAP of the Fast RCNN of the two-stage method is the middle. In addition, for the detection speed indicators before and after the quantization compression, the single-stage method YOLOv3 recognition speed is the fastest, the two-stage method Faster RCNN recognition speed is the slowest, and the ice recognition method proposed in this paper speed combining the advantages of the two methods is in the middle. At the same time, after the compression conversion and deployment to the edge, the recognition speed of YOLOv3 has been improved, while the speed of Faster RCNN to recognize a single image has reached 1 s, which can not meet the real-time requirements of power scene. Based on the above analysis, YOLOv3, Faster RCNN and our method all maintain a high mAP after quantitative compression. Although our method is slower than the single order Yolo V3 method, our method has the highest recognition accuracy in edge icing monitoring device. The speed of our method in the edge sideis up to 170 ms/pic, which can meet the actual needs of icing on-line monitoring. For the scene of insulator icing edge recognition in this paper, our method considering both detection accuracy and recognition speed can better meet the practical application requirements.

CONCLUSION

To implement the front-end high-precision identification of insulator icing thickness, a lightweight icing thickness identification method based on multi-scale feature fusion and model quantization is proposed in this paper, and the advantages of the proposed method are verified by experiments. Compared with other traditional image processing methods, our method can realize front-end intelligent recognition of icing thickness without manual adjustment and setting, which can avoid the long-distance transmission of icing image and show stronger generalization ability and higher efficiency for thickness monitoring. The specific conclusions are as follows.

1) Through multi-scale feature fusion of shallow and deep features of icing image, the accuracy of ice thickness identification can be effectively improved.
2) The quantification of the model will reduce the accuracy of the icing identification method. Under the condition of the same computational power, the mAP of our method proposed in this paper and classical target detection methods is only about 4–7% lower.
3) Compared to the classical methods YOLOv3 and Faster RCNN, the proposed method has higher recognition accuracy before and after model quantization compression.

However, due to the limitation that the icing image can only reflect two-dimensional information, our method can not realize the three-dimensional measurement of icing thickness. To impelment the comprehensive perception of insulator icing thickness, the ice thickness identification method based on multi-source data fusion, including image, mechanical sensor, space distance sensor and so on will be the focus of the next research.

DATA AVAILABILITY STATEMENT

The datasets presented in this article are not readily available because the requirements of the foundations. Requests to access the datasets should be directed to FM, whumfq@whu.edu.cn.

AUTHOR CONTRIBUTIONS

FM Drafting the manuscript, experimental analysis BW: Review and Supervision ML: Methodology and Formal analysis XD: Conceptualization and Revised YM: Data Curation and Resources YZ: Software HM: Resources.

FUNDING

This work was supported in part by the Guizhou Province Science and technology plan project (Gan ke he zhi cheng G.20202039).

REFERENCES

Chen, S., Wen, H., Wu, J., Lei, W., Hou, W., Liu, W., et al. (2019). Internet of Things Based Smart Grids Supported by Intelligent Edge Computing. *IEEE Access* 7, 74089–74102. doi:10.1109/ACCESS.2019.2920488

Dongxiao, N., Haichao, W., and Hanyu, C., (2017). The General Regression Neural Network Based on the Fruit Fly Optimization Algorithm and the Data Inconsistency Rate for Transmission Line Icing Prediction". *Energies* 10 (12), 1–20. doi:10.3390/en10122066

Gang, L., Bo, W., Hui, P., Siyuan, C., Biwu, P., and Yong, S., (2018). Identification of Icing Thickness of Transmission Line Based on Strongly Generalized Convolutional Neural Network". *Proc. CSEE* 38 (11), 3393–3401. doi:10.13334/j.0258-8013.pcsee.171057

Haoyong, C., Xiaojuan, W., and Zhihao, L., (2019). Distributed Sensing and Cooperative Estimation/detection of Ubiquitous Power Internet of Things. *Prot. Control. Mod. Power Syst.* 4, 2151–2158. doi:10.1186/s41601-019-0128-2

Jiang, X., Xiang, Z., Zhang, Z., Hu, J., Hu, Q., and Shu, L. (2014). Predictive Model for Equivalent Ice Thickness Load on Overhead Transmission Lines Based on Measured Insulator String Deviations. *IEEE Trans. Power Deliv.* 29 (4), 1659–1665. doi:10.1109/TPWRD.2014.2305980

Jingjing, W., Junhua, W., and Jianwei, S. (2017). Image Recognition of Icing Thickness on Power Transmission Lines Based on a Least Squares Hough Transform". *Energies* 10 (415), 1–15. doi:10.3390/en10040415

Junhua, W., Shiqi, L., and Jianwei, S. (2018). Study on Dual Pre-warning of Transmission Line Icing Based on Improved Residual MGM-Markov Theory". *IEEJ Trans. Electr. Electron. Eng.* 13 (4), 561–569. doi:10.1002/tee.22601

Li, H., Chen, Y., Zhang, G., Li, J., Zhang, N., Du, B., et al. (2019). Transmission Line Ice Coating Prediction Model Based on EEMD Feature Extraction. *IEEE Access* 7, 40695–40706. doi:10.1109/ACCESS.2019.2907635

Li, Z., Jiang, W., Abu-Siada, A., Li, Z., Xu, Y., and Liu, S. (2021). Research on a Composite Voltage and Current Measurement Device for HVDC Networks. *IEEE Trans. Ind. Electron.* 68 (9), 8930–8941. doi:10.1109/tie.2020.3013772

Liu, Y., Pei, S., Fu, W., Zhang, K., Ji, X., and Yin, Z. (2017). The Discrimination Method as Applied to a Deteriorated Porcelain Insulator Used in Transmission Lines on the Basis of a Convolution Neural Network. *IEEE Trans. Dielect. Electr. Insul.* 24 (6), 3559–3566. doi:10.1109/TDEI.2017.006840

Liu, Y., Yang, N., Dong, B., Wu, L., Yan, J., Shen, X., et al. (2020). Multi-Lateral Participants Decision-Making: A Distribution System Planning Approach with Incomplete Information Game. *IEEE Access* 8, 88933–88950. doi:10.1109/access.2020.2991181

Long, J., Shelhamer, E., and Darrell, T. (2015). "Fully Convolutional Networks for Semantic Segmentation[C]," in IEEE Conference on Computer Vision and Pattern Recognition (CVPR), Boston, MA, June 7–12, 2015, 3431–3440. doi:10.1109/CVPR.2015.7298965

Ma, F., Wang, B., and Dong, X., (2021). Receptive Field Vision Edge Intelligent Recognition for Ice Thickness Identification of Transmission Line. *Power Syst. Technol.* 45 (06), 2161–2169. 10.13335j.1000-3673.pst.2019.2382

Nan, Y., Di, Y., Zheng, Z., Jiazhan, C., Daojun, C., and Xiaoming, W. (2018). Research on Modelling and Solution of Stochastic SCUC under AC Power Flow Constraints. *IET Generation, Transm. Distribution* 12 (15), 3618–3625. doi:10.1049/iet-gtd.2017.1845

Nie, Z., Zhang, J., and Fu, H. (2020). Key Technologies and Application Scenario Design for Making Distribution Transformer Terminal Unit Being a Containerized Edge Node [J]. *Automation Electric Power Syst.* 44 (3), 154–161. doi:10.7500/AEPS20190524005

Qiangliang, G., Jin, X., and Xiaoguang, H. (2018). New Keypoint Matching Method Using Local Convolutional Features for Power Transmission Line Icing Monitoring". *Sensors* 18 (698), 1–15. doi:10.3390/s18030698

Ruszczak, B., and Tomaszewski, M. (2015). Extreme Value Analysis of Wet Snow Loads on Power Lines. *IEEE Trans. Power Syst.* 30 (1), 457–462. doi:10.1109/tpwrs.2014.2321008

Shen, X., Ouyang, T., and Li, Y. (2021a). Chanyut Khajorntraidet, "Mixture Density Networks-Based Knock Simulator". *IEEE/ASME Trans. Mechatronics, Early Access*. doi:10.1109/TMECH.2021.3059775

Shen, X., Ouyang, T., Yang, N., and Zhuang, J. (2021b). Sample-based Neural Approximation Approach for Probabilistic Constrained Programs. *IEEE Trans. Neural Netw. Learn. Syst.*, 1–8. doi:10.1109/TNNLS.2021.3102323

Shen, X., and Raksincharoensak, P. (2021a). Pedestrian-Aware Statistical Risk Assessment. *IEEE Trans. Intell. Transport. Syst.*, 1–9. doi:10.1109/TITS.2021.3074522

Shen, X., and Raksincharoensak, P. (2021b). Statistical Models of Near-Accident Event and Pedestrian Behavior at Non-signalized Intersections. *J. Appl. Stat. Early Access*, 1–21. doi:10.1080/02664763.2021.1962263

Shen, X., Zhang, X., Ouyang, T., Li, Y., and Raksincharoensak, P. (2020). Cooperative Comfortable-Driving at Signalized Intersections for Connected and Automated Vehicles. *IEEE Robot. Autom. Lett.* 5 (4), 6247–6254. doi:10.1109/LRA.2020.3014010

Shen, X., Zhang, Y., Sata, K., and Shen, T. (2020). Gaussian Mixture Model Clustering-Based Knock Threshold Learning in Automotive Engines. *Ieee/asme Trans. Mechatron.* 25 (6), 2981–2991. doi:10.1109/TMECH.2020.3000732

Shen, X., Zhang, Y., Shen, T., and Khajorntraidet, C. (2017). Spark advance Self-Optimization with Knock Probability Threshold for Lean-Burn Operation Mode of SI Engine. *Energy* 122, 1–10. doi:10.1016/j.energy.2017.01.065

Tiannan, M., and Dongxiao, N. (2016). Icing Forecasting of High Voltage Transmission Line Using Weighted Least Square Support Vector Machine with

Fireworks Algorithm for Feature Selection". *Applied Sci. Basel* 6 (12), 1–19. doi:10.3390/app6120438

Wang, B., Ma, F., Ge, L., Ma, H., Wang, H., and Mohamed, M. A. (2021). Icing-EdgeNet: A Pruning Lightweight Edge Intelligent Method of Discriminative Driving Channel for Ice Thickness of Transmission Lines. *IEEE Trans. Instrum. Meas.* 70, 1–12. Art no. 2501412. doi:10.1109/TIM.2020.3018831

Wang, Y., Zhao, W., and Zhang, J. (2020). Inheritance and Expansion Analysis of Research Topics between Energy Internet and Smart Grid. *Automation Electric Power Syst.* 44 (4), 1–7. doi:10.7500/AEPS20190710007

Wei, S., and Caifei, W. (2019). Staged Icing Forecasting of Power Transmission Lines Based on Icing Cycle and Improved Extreme Learning Machine". *J. Clean. Prod.* 208, 1384–1392. doi:10.1016/j.jclepro.2018.10.197

Xingliang, J., Xingbo, H., and Yuyao, H. (2018). Model for Ice Wet Growth on Composite Insulator and its Experimental Validation". *IET Generation Transmission Distribution* 12 (3), 556–563. doi:10.1049/iet-gtd.2017.0227

Yan, B., Chen, K., Guo, Y., Liang, M., and Yuan, Q. (2013). Numerical Simulation Study on Jump Height of Iced Transmission Lines after Ice Shedding. *IEEE Trans. Power Deliv.* 28 (1), 216–225. doi:10.1109/TPWRD.2012.2219324

Yang, N., Huang, Y., Hou, D., Liu, S., Ye, D., Dong, B., et al. (2019). Adaptive Nonparametric Kernel Density Estimation Approach for Joint Probability Density Function Modeling of Multiple Wind Farms. *Energies* 12, 1356. doi:10.3390/en12071356

Yang, N., Liu, S., Deng, Y., and Xing, C. (2021). An Improved Robust SCUC Approach Considering Multiple Uncertainty and Correlation. *IEEJ Trans. Elec Electron. Eng.* 16, 21–34. doi:10.1002/tee.23265

Yang, N., Yang, C., Wu, L., Shen, X., Jia, J., Li, Z., et al. (2021). Intelligent Data-Driven Decision-Making Method for Dynamic Multi-Sequence: An E-Seq2Seq Based SCUC Expert System. *IEEE Trans. Ind. Inf.*, 1. doi:10.1109/TII.2021.3107406

Yanpeng, H., Xiaolan, J., and Lin, Y. (2017). Evaluation of Natural Icing Condition for In-Service Insulators Based on Image Segmentation. *High Voltage Eng.* 43 (1), 285–292. doi:10.13336/j.1003-6520.hve.20161227037

Ying, J., Cai, Y., and Liu, M. (2020). Adaptive Access Method of Low Voltage Intelligent Terminal for Distribution Internet of Things". *Automation Electric Power Syst.* 44 (2), 22–27. doi:10.7500/AEPS20190827004

Yongsai, Z., Guangyuan, W., and Hong, Y. (2017). "Research on the Application of the Edge Detection Method for the UAVs Icing Monitoring of Transmis- Sion Lines"," in IEEE International Conference on Mechatronics and Automation (ICMA), Takamatsu, August 6–9, 2017, 1110–1114. doi:10.1109/ICMA.2017.8015972

Zhang, L., and Luo, Y. (2018). Combined Heat and Power Scheduling: Utilizing Building-Level thermal Inertia for Short-Term thermal Energy Storage in District Heat System. *IEEJ Trans. Elec Electron. Eng.* 13 (6), 804–814. doi:10.1002/tee.22633

Zhang, M., Pang, K., Gao, C., and Xin, M. (2020). Multi-Scale Aerial Target Detection Based on Densely Connected Inception ResNet. *IEEE Access* 8, 84867–84878. doi:10.1109/access.2020.2992647

Zhang, Y., Huang, X., Jia, J., Zhu, Y., Zhao, L., and Zhang, X. (2020). Detection and Condition Assessment of Icicle Bridging for Suspension Glass Insulator by Image Analysis. *IEEE Trans. Instrum. Meas.* 69 (10), 7458–7471. doi:10.1109/TIM.2020.2984965

Zhao, Y., Han, R., and Rao, Y. (2019). "A New Feature Pyramid Network for Object Detection," in International Conference on Virtual Reality and Intelligent Systems (ICVRIS), Jishou, September 14–15, 2019IEEE, 428–431. doi:10.1109/ICVRIS.2019.00110

Zhou, Z., Chen, X., Li, E., Zeng, L., Luo, K., and Zhang, J. (2019). Edge Intelligence: Paving the Last Mile of Artificial Intelligence with Edge Computing. *Proc. IEEE* 107 (8), 1738–1762. doi:10.1109/JPROC.2019.2918951

Zhu, B., Ding, F., and Vilathgamuwa, D. M. (2020). Coat Circuits for DC-DC Converters to Improve Voltage Conversion Ratio. *IEEE Trans. Power Electron.* 35 (4), 3679–3687. doi:10.1109/tpel.2019.2934726

Zhuangli, H., Tong, H., and Yihui, Z. (2018). Fast Image Recognition of Transmission tower Based on Big Data. *Prot. Control. Mod. Power Syst.* 3 (2), 149–158. doi:10.1186/s41601-018-0088-y

Conflict of Interest: Authors YM and YZ were employed by State Grid Shaanxi Electric Power Company, State Grid Xi'an Power Supply Company and Guangdong Power Grid Corp, Huizhou Power Supply Bureau Co., Ltd.

The remaining authors declare that the research was conducted in the absence of any commercial or financial relationships that could be construed as a potential conflict of interest.

Publisher's Note: All claims expressed in this article are solely those of the authors and do not necessarily represent those of their affiliated organizations, or those of the publisher, the editors and the reviewers. Any product that may be evaluated in this article, or claim that may be made by its manufacturer, is not guaranteed or endorsed by the publisher.

frontiers in Energy Research

BRIEF RESEARCH REPORT
published: 14 October 2021
doi: 10.3389/fenrg.2021.762246

Robust Vehicle Dynamics Control for a Sharp Curve With Uncertain Road Condition

Jing Miao[1,2,3], Yifan Dai[2], Ou Xie[1], Hao Chen[1], Fuzhou Niu[1], Yehu Shen[1], Yong Zhi Wu[1], Hui Sun[2], Xuemei Niu[1], Qixin Zhu[1] and Wenjiang Shen[3]*

[1]School of Mechanical Engineering, Suzhou University of Science and Technology, Suzhou, China, [2]Suzhou Automotive Research Institute, Tsinghua University, Suzhou, China, [3]Suzhou Institute of Nano-Tech and Nano-Bionics(SINANO), Chinese Academy of Sciences (CAS), Suzhou, China

Recently, more and more research has been conducted to develop Connected Autonomous Vehicles (CAVs) applications that ensures the safety driving of CAVs under some extreme situations. This brief presents a robust control strategy for CAVs to preserve a precise tracking performance and maintain the stability of lateral dynamics when passing a sharp curve with uncertain road friction coefficient changes. In the proposed robust lateral dynamics control, robust optimization-based lateral dynamics controller is designed to achieve the stability of the lateral dynamics with the consideration of the road friction coefficient uncertainty. Simulation validations are carried out to evaluate the proposed control strategy. The results show that the robust optimization-based lateral dynamics can improve the robustness even with the uncertainty of the road friction coefficient.

Keywords: model predictive conrol, robust optimisation, vehicle dynamic, uncertainty, stability

OPEN ACCESS

Edited by:
Yahui Zhang,
Yanshan University, China

Reviewed by:
Xun Shen,
Tokyo University of Agriculture and Technology, Japan
Yang Tian,
Yanshan University, China

****Correspondence:***
Jing Miao
jmiao@mail.usts.edu.cn

Specialty section:
This article was submitted to Wind Energy, a section of the journal Frontiers in Energy Research

Received: *21 August 2021*
Accepted: *08 September 2021*
Published: *14 October 2021*

Citation:
Miao J, Dai Y, Xie O, Chen H, Niu F, Shen Y, Wu YZ, Sun H, Niu X, Zhu Q and Shen W (2021) Robust Vehicle Dynamics Control for a Sharp Curve With Uncertain Road Condition. Front. Energy Res. 9:762246. doi: 10.3389/fenrg.2021.762246

1 INTRODUCTION

Autonomous vehicles will meet more emergency scenarios when leaving the research laboratory and entering public roads (Kritayakirana and Gerdes, 2012; Shen and Raksincharoensak, 2021). Vehicle stabilization under uncertain scenarios is one of the most important issues in the control of autonomous vehicles (Yue et al., 2019; Shen et al., 2020a; Guo et al., 2020). Recently, Model Predictive Control (MPC) has been used to improve the vehicle dynamics stability (Yuan et al., 2019). In (Taghavifar, 2019), neural network autoregressive with exogenous input system has been applied to obtain an accurate and explicit model in order to contribute to the control of the system over the prediction horizon. (Weiskircher et al., 2017). proposed a MPC-based predictive trajectory guidance and tracking control framework for autonomous and semiautonomous vehicles in dynamic public traffic. Moreover, a data-driven predictive control is proposed in (Li and Schutter, 2021) which is model-free predictive control method.

However, the normal MPC without considering the uncertainty is not able to address the problem caused by environment uncertainty. The state space model-based prediction has large variance and even mean bias if there are any uncertainties in disturbance or the system parameters (Shen et al., 2020b). If there is uncertain road friction changes when passing a sharp curve and the model used in MPC cannot reflect the uncertainty, MPC will lose some precise on the lateral dynamics control. To improve the robustness against uncertainty, it is necessary to design a robust controller. In (Heshmati-Alamdari et al., 2020), a robust predictive controller is designed for underwater robotic vehicles which forms a high robust closed-loop system against parameter uncertainties.

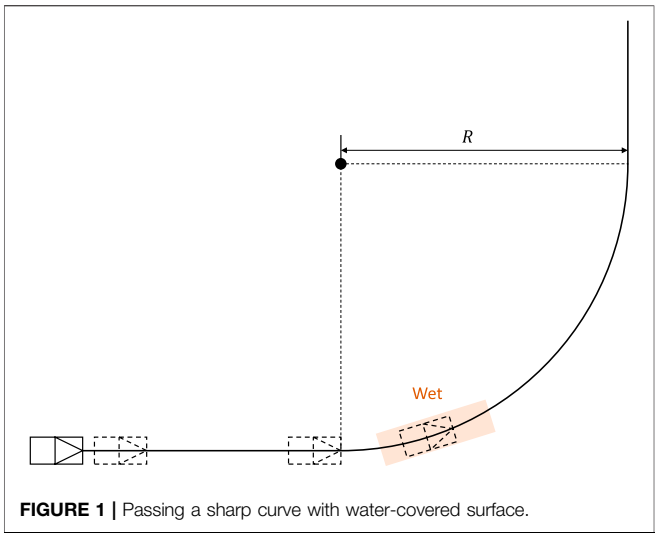

FIGURE 1 | Passing a sharp curve with water-covered surface.

Besides, (Gao et al., 2021), proposed a robust lateral trajectory following control for autonomous vehicles. Robust model predictive control is a potential solution to the issue caused by uncertain road friction in this research. In the problem formulation of robust model predictive control, the road friction is regarded as a uncertain variable. For all possible realizations of uncertain variable, a fixed control law has a cost. We focused on finding a control law that minimize the upper bound of the cost for all possible realizations of uncertain variable. In this way, the robustness of the control strategy is able to be attained. To achieve robust model predictive controller, it is essentially to solve a robust optimization problem or a chance constrained optimization problem in every time step (Nemirovski and Shapiro, 2006; Shen et al., 2019). Although it is NP-hard to solve a robust optimization problem or a chance constrained optimization problem (Hong et al., 2011; Geletu et al., 2017; Pena-Ordieres et al., 2020), the approximate solution can be obtained by formulating a solvable approximate problem of the original one (Luedtke and Ahmed, 2008; Shen et al., 2021; Campi and Garatti, 2019, 2011). Robust model predictive control was widely applied in water qulity management (Takyi and Lence, 1999) and other process control applications (Henrion and Moller, 2003). Recently, robust model predictive control has been applied to the automotive powertrain control to optimize the fuel efficiency with stochastic constraint on the knock (Shen et al., 2017; Shen and Shen, 2017) and the energy management system in hybrid electric vehicle (Shen et al., 2016). Robust model predictive control can also be applied to ensure the robustness for an autonomous vehicle when it passes a sharp curve with uncertain road condition.

This paper presents a novel robust model predictive control strategy for automated vehicles to preserve a precise tracking performance and maintain the stability of lateral dynamics. The optimal feedback control input is obtained in every step by solving a robust optimization problem. The robust optimization problem is solved by scenario approach introduced in (Calariore and Campi, 2006). Simulation validations are carried out to evaluate the proposed control strategy.

2 PROPOSED METHOD

2.1 Background and Problem Description

In **Figure 1**, the vehicle passed a sharp curve with water-covered surface. The water-covered surface is the area with orange color. The single track model of vehicle dynamics can be described by the following equations:

$$\dot{y}_c = \dot{y}_c, \tag{1}$$

$$\ddot{y}_c = -\frac{2\left(C_f + C_r\right)}{mV}\dot{y}_c + \frac{2\left(C_f + C_r\right)}{m}\phi + \frac{2\left(l_r C_r - l_f C_f\right)}{mV}\dot{\phi} + \frac{2C_f}{m}\delta_f, \tag{2}$$

$$\dot{\phi} = \dot{\phi}, \tag{3}$$

$$\ddot{\phi} = \frac{2\left(l_r C_r - l_f C_f\right)}{IzV}\dot{y}_c + \frac{2\left(l_f C_f - l_r C_r\right)}{IzV}\phi - \frac{2\left(l_f^2 C_f + l_r^2 C_r\right)}{IzV}\dot{\phi}. \tag{4}$$

Here, y_c is the lateral distance. $\dot{\phi}$ is the yaw rate. m is the mass of the vehicle. δ_f is the steer angle. V is the vehicle speed.

In order to apply MPC, the vehicle lateral dynamics model is transformed to the lateral deviation from the reference model. The used linear model is as

$$\begin{bmatrix} \dot{y}_{cr} \\ \ddot{y}_{cr} \\ \dot{\phi}_{cr} \\ \dot{\phi}_{cr} \end{bmatrix} = A \begin{bmatrix} y_{cr} \\ \dot{y}_{cr} \\ \phi_{cr} \\ \cdot\phi_{cr} \end{bmatrix} + B\delta_f + C\frac{1}{R} \tag{5}$$

Where

$$A = \begin{bmatrix} 0 & 1 & 0 & 0 \\ 0 & -\frac{2\left(C_f + C_r\right)}{mV} & \frac{2\left(C_f + C_r\right)}{m} & \frac{2\left(l_r C_r - l_f C_f\right)}{mV} \\ 0 & 0 & 0 & 1 \\ 0 & \frac{2\left(l_r C_r - l_f C_f\right)}{I_z V} & \frac{2\left(l_f C_f - l_r C_r\right)}{I_z V} & -\frac{2\left(l_f^2 C_f + l_r^2 C_r\right)}{I_z V} \end{bmatrix} \tag{6}$$

$$B = \begin{bmatrix} 0 \\ \frac{2C_f}{m} \\ 0 \\ \frac{2l_f C_f}{m} \end{bmatrix} \tag{7}$$

$$C = \begin{bmatrix} 0 \\ -V^2 + \frac{2l_r C_r - 2l_f C_f}{m} \\ 0 \\ -\frac{2l_f^2 C_f + 2l_r^2 C_r}{Iz} \end{bmatrix}. \tag{8}$$

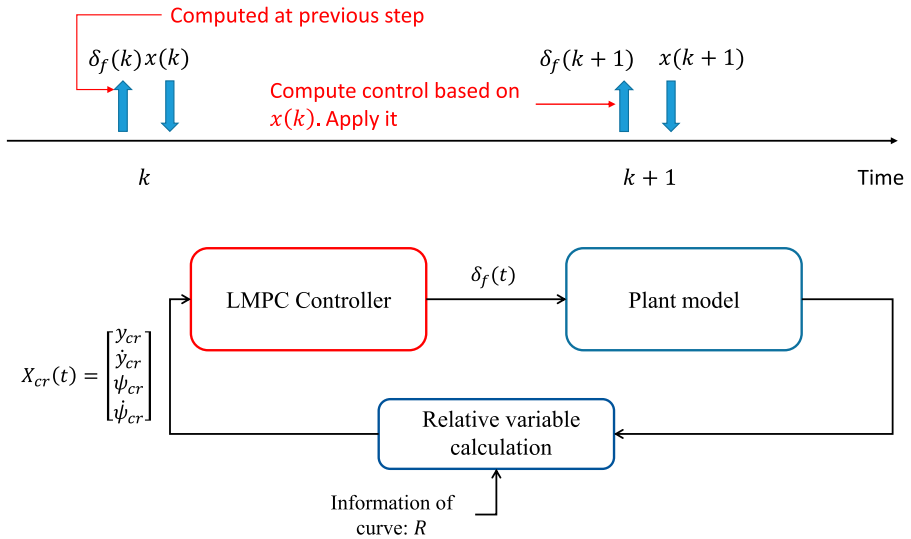

FIGURE 2 | Implementation of robust MPC.

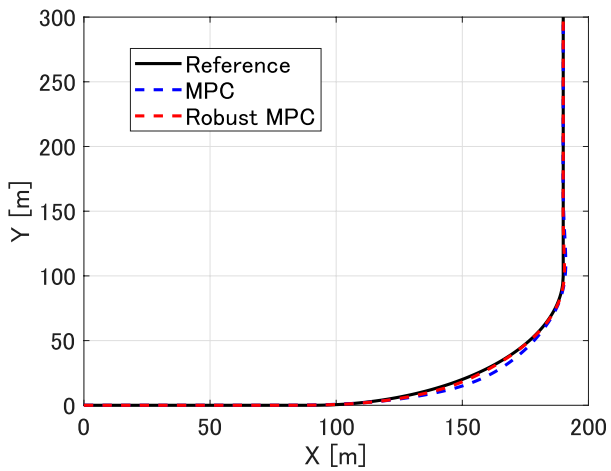

FIGURE 3 | Validation result.

Here, y_{cr} is the lateral deviation from the reference trajectory. $\dot{\phi}_{cr}$ is the yaw rate. R is the radius of the curve. m is the mass of the vehicle. δ_f is the steer angle. V is the vehicle speed.

Notice that C_f and C_r are both decided by the road friction coefficient. Since the road friction coefficient is uncertain, C_f and C_r are both uncertain variable as well.

Equation 5 is a continuous differential equation and can be transformed to a discrete state-space model by Euler method. Since at every time step, the state variable is decided by the input δ_f and the state variable in the previous step. The state variable at $k + 1$ can be expressed by the previous input sequence $\delta_f(0), \ldots, \delta_f(k)$ and the state variable at the initial step. Since the objective is to minimize the difference between the actual trajectory and the reference one, the cost function is a function of the input sequence and known state variable at initial step. To obtain the optimal input, a robust optimization problem should be solved. The problem can be formulated generally by

$$\begin{aligned} &\min_{u \in \mathcal{U} \subset \mathbf{R}^{n_u}} \quad J(u) \\ &s.t. \quad h(u, \delta) \leq 0, \ \delta \in \Delta \subset \mathbf{R}^{n_\delta}. \end{aligned} \tag{9}$$

Here, $u = [\delta_f(0), \ldots, \delta_f(K-1), E]^T$ if we consider K steps forward. δ is the uncertain variable. In our problem, it includes C_f and C_r. $J(u) = E$ and $h(u, \delta)$ is defined as

$$\sum_{k=1}^{K} y_{cr}(k) - E. \tag{10}$$

2.2 Scenario Approach

In scenario approach, independent samples $\delta^{(i)}$, $i = 1, \ldots, N$ is identically extracted from Δ randomly, a deterministic convex optimization problem can be formed as (Calariore, 2017; Campi et al., 2018; Campi and Garatti, 2018)

$$\begin{aligned} &\min_{u \in \mathcal{U} \subset \mathbf{R}^{n_u}} \quad J(u) \\ &s.t. \quad h\left(u, \delta^{(i)}\right) \leq 0, \ i = 1, \ldots, N \end{aligned} \tag{11}$$

which is a standard finitely constrained optimization problem. The optimal solution $\hat{u}_N$ of the program **Eq. 11** is called as the scenario solution for program **Eq. 9** generally. Moreover, since the extractions $\delta^{(i)}$, $i = 1, \ldots, N$ is randomly chosen, the optimal solution $\hat{u}_N$ is random variable. If $\hat{u}_N$ is expected to satisfy

$$\Pr^N\left\{\left(\delta^{(1)}, \ldots \delta^{(N)} \in \Delta^N : V(\hat{u}_N) \leq \alpha\right\} \geq 1 - \beta, \beta \in (0, 1), \tag{12}$$

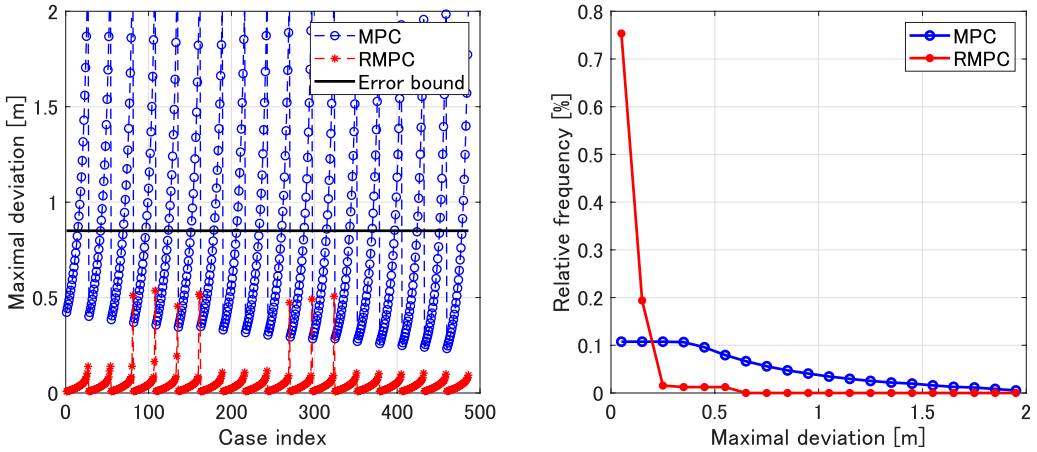

FIGURE 4 | Validation result.

then, N should have a lower limitation N_l

$$N \geq \frac{2}{\alpha}\ln\frac{1}{\beta} + 2n_u + \frac{2n_u}{\alpha}\ln\frac{2}{\alpha}. \tag{13}$$

Note that β is an important factor and choosing $\beta = 0$ makes $N_l = \infty$. Namely, if the number of chosen samples gets larger, the probability of satisfying the original probabilistic constraints approaches 1. Actually, when number of chosen samples becomes infinity, the samples cover the whole sample space. The feasible area determined by probabilistic constraints is only a subset of whole sample space. Then, it becomes a problem which requires total robustness. Therefore, the scenario approach conducts to a solution with total robustness which is more conservative than the probabilistic constraints require.

2.3 Implementation of Robust Model Predictive Control

The implementation of robust MPC is shown in **Figure 2**. At time step $k + 1$, it uses the first element of u calculated in time step k as the input. Namely, $\delta_f(k) = u\ (1)$. $x(k)$ denotes the state variable vector at time step k. Moreover, since the LMPC controller takes relative variable calculation as feedback, there will be a relative variable calculation. In the relative variable calculation, the relative variable is calculated based on the feedback state variable from plant model or real vehicle and the information of curve, for example, radius value R.

3 VALIDATION RESULTS AND CONCLUSTION

The validation is implemented by simulation. Since the real vehicle is not available, a plant model is established and used instead of the real vehicle. The plant model adopts the single track nonlinear model described by

$$\dot{v}_x - v_y\dot{\phi} = \frac{1}{m}\left(F_f^{x_T}\cos\delta_f + F_r^{x_T} - F_f^{y_T}\sin\delta_f\right), \tag{14}$$

$$\dot{v}_y + v_x\dot{\phi} = \frac{1}{m}\left(F_f^{y_T}\cos\delta_f + F_r^{y_T} + F_f^{x_T}\sin\delta_f\right), \tag{15}$$

$$I_{zz}\ddot{\phi} = l_f F_f^{y_T}\cos\delta_f - l_r F_r^{y_T} + l_f F_f^{x_T}\sin\delta_f, \tag{16}$$

$$\begin{bmatrix}\dot{p}_x\\ \dot{p}_y\end{bmatrix} = \mathcal{R}(\phi)\begin{bmatrix}v_x\\ v_y\end{bmatrix}. \tag{17}$$

The magic formula is used to model the friction forces which refers to (Yuan et al., 2019).

For the simulation conditions, the radius has six options: 100, 110, 120, 130, 140, and 150 m. For each R, three coefficients of friction for the wet road is randomly generated from (0.4,0.6). For each pair of a value of R and a value of coefficients of friction, the following longitudinal velocity values have be tested:

$$[0.4, 0.42, \ldots, 0.92] \times \sqrt{R\mu_{wet}g}. \tag{18}$$

Figure 3 shows one example of the validation results. The friction coefficient of dry road is $\mu_{dry} = 0.8$ which the one of wet road is $\mu_{wet} = 0.5$. The radius of the curve is 100 m. The middle part of the road is wet. The longitudinal velocity for passing the curve is $V = 65\,km/h$. If MPC is used by setting C_r and C_f according to $\mu_{dry} = 0.8$, the tracking error increases during the wet road. However, by considering $\mu \in [0.4, 0.9]$, the robust MPC keeps the tracking performance stable during the wet road.

Figure 4 shows a comprehensive statistical validation results of all cases. Obviously, the robust MPC succeeded to decrease the maximal deviation into the error bound. However, the normal MPC failed in most cases since the model has a very large bias compared to the real dynamics due to the uncertain friction coefficient.

DATA AVAILABILITY STATEMENT

The original contributions presented in the study are included in the article/Supplementary Material, further inquiries can be directed to the corresponding author.

AUTHOR CONTRIBUTIONS

All authors listed have made a substantial, direct, and intellectual contribution to the work and approved it for publication.

FUNDING

The authors appreciate the supports of Foundation of Natural Science Research in Colleges and Universities of Jiangsu Province (Grant: 18KJB510043), National Key R& D Program of China (Grant: 2018YFB0105201), Natural Science Foundation of China (Grant: 51975394; 61903269) and Natural Science Foundation of Jiangsu Province (Contract: BK20200271).

REFERENCES

Calariore, G. C., and Campi, M. C. (2006). The Scenario Approach Torobust Control Design. *IEEE Trans. Automatic Control.* 51 (5), 742–753. doi:10.1109/tac.2006.880951

Calariore, G. (2017). Repetitive Scenario Design. *IEEE Trans. Automatic Control.* 62 (3), 1125–1137. doi:10.1109/tac.2017.2788139

Campi, M. C., and Garatti, S. (2011). A Sampling-And-Discarding Approach to Chance-Constrained Optimization: Feasibility and Optimality. *J. Optimization Theor. Appl.* 148 (2), 257–280. doi:10.1007/s10957-010-9754-6

Campi, M. C., and Garatti, S. (2019). *Introduction to the Scenario Approach*. Philadelphia: MOS-SIAM Series on Optimization.

Campi, M. C., Garatti, S., and Ramponi, F. A. (2018). A General Scenario Theory for Nonconvex Optimization and Decision Making. *IEEE Trans. Automat. Contr.* 63 (12), 4067–4078. doi:10.1109/tac.2018.2808446

Campi, M. C., and Garatti, S. (2018). Wait-and-Judge Scenario Optimization. *Math. Program* 167, 155–189. doi:10.1007/s10107-016-1056-9

Gao, H., Kan, Z., and Li, K. (2021). Robust Lateral Trajectory Following Control of Unmanned Vehicle Based on Model Predictive Control. *Ieee/asme Trans. Mechatron.*, early access. doi:10.1109/TMECH.2021.3087605

Geletu, A., Hoffmann, A., Klöppel, M., and Li, P. (2017). An Inner-Outer Approximation Approach to Chance Constrained Optimization. *SIAM J. Optim.* 27, 1834–1857. doi:10.1137/15m1049750

Guo, N., Zhang, X., Zou, Y., Lenzo, B., and Zhang, T. (2020). A Computationally Efficient Path-Following Control Strategy of Autonomous Electric Vehicles with Yaw Motion Stabilization. *IEEE Trans. Transp. Electrific.* 6 (2), 728–739. doi:10.1109/tte.2020.2993862

Henrion, R., and Moller, A. (2003). Optimization of a Continuous Distillation Process under Random Inflow Rate. *Comput. Math. Appli.* 45, 13–30. doi:10.1016/s0898-1221(03)80017-2

Heshmati-Alamdari, S., Karras, G. C., Marantos, P., Kyriakopoulos, K. J., and Kyriakopoulos, K. J. (2020). A Robust Predictive Control Approach for Underwater Robotic Vehicles. *IEEE Trans. Contr. Syst. Technol.* 28 (6), 2352–2363. doi:10.1109/tcst.2019.2939248

Hong, L. J., Yang, Y., and Zhang, L. (2011). Sequential Convex Approximations to Joint Chance Constrained Programs: A Monte Carlo Approach. *Operations Res.* 59, 617–630. doi:10.1287/opre.1100.0910

Kritayakirana, K., and Gerdes, J. C. (2012). Autonomous Vehicle Control at the Limits of Handling. *Ijvas* 10 (4), 271–296. doi:10.1504/ijvas.2012.051270

Li, D., and De Schutter, B. (2021). Distributed Model-Free Adaptive Predictive Control for Urban Traffic Networks. *IEEE Trans. Contr. Syst. Technol.*, 1–13. early access. doi:10.1109/TCST.2021.3059460

Luedtke, J., and Ahmed, S. (2008). A Sample Approximation Approach for Optimization with Probabilistic Constraints. *SIAM J. Optim.* 19 (2), 674–699. doi:10.1137/070702928

Nemirovski, A., and Shapiro, A. (2006). Convex Approximations of Chance Constrained Programs. *SIAM J. Optimization* 17, 969–996. doi:10.1137/050622328

Peña-Ordieres, A., Luedtke, J. R., and Wächter, A. (2020). Solving Chance-Constrained Problems via a Smooth Sample-Based Nonlinear Approximation. *SIAM J. Optim.* 30 (3), 2221–2250. doi:10.1137/19m1261985

Shen, X., Ouyang, T., Yang, N., and Zhuang, J. (2021). Sample-Based Neural Approximation Approach for Probabilistic Constrained Programs. *IEEE Trans. Neural Netw. Learn. Syst.*, 1–8. early access. doi:10.1109/TNNLS.2021.3102323

Shen, X., Ouyang, T., Zhang, Y., and Zhang, X. (2020a). Computing Probabilistic Bounds on State Trajectories for Uncertain Systems. *IEEE Trans. Emerg. Top. Comput. Intell.*, 1–6. early access. doi:10.1109/TETCI.2020.3019040

Shen, X., and Raksincharoensak, P. (2021). Pedestrian-Aware Statistical Risk Assessment. *IEEE Trans. Intell. Transport. Syst.* 22, 1–9. early access. doi:10.1109/TITS.2021.3074522

Shen, X., and Shen, T. (2017). Real-Time Statistical Learning-Based Stochastic Knock Limit Control for Spark-Ignition Engines. *Appl. Therm. Eng.* 127, 1518–1529. doi:10.1016/j.applthermaleng.2017.08.150

Shen, X., Zhang, J., and Shen, T. (2016). "Real-time Scenario-Based Stochastic Optimal Energy Management Strategy for HEVs," in Proceedings of 2016 European Control Conference, Aalborg, Denmark, 29 June–1 July 2016, 631–636. doi:10.1109/ecc.2016.7810359

Shen, X., Zhang, X., and Raksincharoensak, P. (2020b). Probabilistic Bounds on Vehicle Trajectory Prediction Using Scenario Approach. *IFAC-PapersOnline* 53 (2), 2385–2390. doi:10.1016/j.ifacol.2020.12.038

Shen, X., Zhang, Y., Shen, T., and Khajorntraidet, C. (2017). Spark advance Self-Optimization with Knock Probability Threshold for Lean-Burn Operation Mode of SI Engine. *Energy* 122, 1–10. doi:10.1016/j.energy.2017.01.065

Shen, X., Zhuang, J., and Zhang, X. (2019). Approximate Uncertain Program. *IEEE Access* 7, 182357–182365. doi:10.1109/access.2019.2958621

Taghavifar, H. (2019). Neural Network Autoregressive with Exogenous Input Assisted Multi-Constraint Nonlinear Predictive Control of Autonomous Vehicles. *IEEE Trans. Veh. Technol.* 68 (7), 6293–6304. doi:10.1109/tvt.2019.2914027

Takyi, A. K., and Lence, B. J. (1999). Surface Water Quality Management Using a Multiple-Realization Chance Constraint Method. *Water Resour. Res.* 35, 1657–1670. doi:10.1029/98wr02771

Weiskircher, T., Wang, Q., and Ayalew, B. (2017). Predictive Guidance and Control Framework for (Semi-)Autonomous Vehicles in Public Traffic. *IEEE Trans. Contr. Syst. Technol.* 25 (6), 2034–2046. doi:10.1109/tcst.2016.2642164

Yuan, H., Sun, X., and Gordon, T. (2019). Unified Decision-Making and Control for Highway Collision Avoidance Using Active Front Steer and Individual Wheel Torque Control. *Vehicle Syst. Dyn.* 57 (8), 1188–1205. doi:10.1080/00423114.2019.169745610.1080/00423114.2018.1535125

Yue, M., Ning, Y., Zhao, X., and Zong, G. (2019). Point Stabilization Control Method for WIP Vehicles Based on Motion Planning. *IEEE Trans. Ind. Inf.* 15 (6), 3368–3378. doi:10.1109/tii.2018.2875048

Conflict of Interest: The authors declare that the research was conducted in the absence of any commercial or financial relationships that could be construed as a potential conflict of interest.

Publisher's Note: All claims expressed in this article are solely those of the authors and do not necessarily represent those of their affiliated organizations, or those of the publisher, the editors and the reviewers. Any product that may be evaluated in this article, or claim that may be made by its manufacturer, is not guaranteed or endorsed by the publisher.

frontiers in Energy Research

ORIGINAL RESEARCH
published: 22 October 2021
doi: 10.3389/fenrg.2021.779587

Power Consumption Predicting and Anomaly Detection Based on Transformer and K-Means

Junfeng Zhang[1], *Hui Zhang*[2], *Song Ding*[3]* *and Xiaoxiong Zhang*[2]

[1]Data Mining Laboratory, College of Mathematics and Information Technology, Hebei University, Baoding, China, [2]The Sixty-Third Research Institute, National University of Defense Technology, Nanjing, China, [3]School of Economics, Zhejiang University of Finance and Economics, Hangzhou, China

With the advancement of technology and science, the power system is getting more intelligent and flexible, and the way people use electric energy in their daily lives is changing. Monitoring the condition of electrical energy loads, particularly in the early detection of aberrant loads and behaviors, is critical for power grid maintenance and power theft detection. In this paper, we combine the widely used deep learning model Transformer with the clustering approach K-means to estimate power consumption over time and detect anomalies. The Transformer model is used to forecast the following hour's power usage, and the K-means clustering method is utilized to optimize the prediction results, finally, the anomalies is detected by comparing the predicted value and the test value. On real hourly electric energy consumption data, we test the proposed model, and the results show that our method outperforms the most commonly used LSTM time series model.

Keywords: power consumption prediction, anomaly detection, transformer, K-means, LSTM

OPEN ACCESS

Edited by:
Tinghui Ouyang,
National Institute of Advanced Industrial Science and Technology (AIST), Japan

Reviewed by:
Shinan Zhao,
Jiangsu University of Science and Technology, China
Dazhong Ma,
Northeastern University, China
Chao Li,
KU Leuven, Belgium

***Correspondence:**
Song Ding
dingsong1129@163.com

Specialty section:
This article was submitted to Smart Grids, a section of the journal Frontiers in Energy Research

Received: *19 September 2021*
Accepted: *06 October 2021*
Published: *22 October 2021*

Citation:
Zhang J, Zhang H, Ding S and Zhang X (2021) Power Consumption Predicting and Anomaly Detection Based on Transformer and K-Means. Front. Energy Res. 9:779587. doi: 10.3389/fenrg.2021.779587

1 INTRODUCTION

Modern power systems are evolving in a more sustainable path. The load demand for domestic electrical energy is gradually increasing as the number of household appliances and electric cars increases. Statistics show that residences and commercial buildings account for three-fifths of global electricity use (Desai, 2017). The power system has grown in complexity and intelligence, and more modern information transmission technology has been implemented, making grid processing more convenient and secure (Bayindir et al., 2016). Moreover, electric energy consumption in everyday living is also difficult and variable. Electric energy usage, for example, may vary significantly depending on the season, and consumption on working days and working days will fluctuate. At the same time, there will be anomalies in the electrical load, such as forgetting to turn off electrical appliances, failure of electrical appliances and even the theft of electricity, and so on, resulting in a much larger electrical demand than typical. As a result, detecting unusual consumption data is critical.

Abnormal detection can enhance abnormal electric energy consumption to achieve energy savings, remind users to discover malfunctioning electrical appliances or modify bad electricity usage patterns, lower users' energy consumption expenses, and promote electricity consumption safety awareness. The most crucial factor is that you can locate the source of the power theft (McLaughlin et al., 2009). According to the survey, power theft accounts for about half of the energy lost in some developing countries (Antmann,2009), and anomaly detection technologies can successfully combat this scenario.

Anomaly detection, as the name suggests, is the method of recognizing data that differs from the usual. Anomalies in data are situations that do not follow the specified usual behavior pattern

(Chandola et al., 2009). Anomalies are classified into three types: point anomalies, aggregate anomalies, and context anomalies. A point anomaly occurs when one point in the data is excessively high or too low in comparison to other points. The anomalous phenomena of a group of data compared to the full data set is referred to as a collection anomaly, and it only happens in the data set with the correlation between the data. Contextual abnormality refers to the abnormality when the data is combined with the context in the data set (Chandola et al., 2009). In this paper, abnormal power consumption means that if the difference between the power consumption predicted by the model and the real power consumption in a certain hour is greater than the threshold we set through the experiment, the current hour power consumption is considered abnormal, so the main task of this paper is to detect point anomalies.

Because the characteristics of variables are various, traditional models primarily focus on univariate prediction and anomaly detection (Hu et al., 2018). Univariate models are typically utilized in cases where there are too many other features or when vectorization is difficult, such as stock prediction (Hsieh et al., 2011). Various industries, such as speech recognition (Graves et al., 2013) and NLP (Natural Language Processing) (Nadkarni et al., 2011), have adopted deep learning technology and achieved remarkable success as a result of the rapid development of the field of deep learning. Time series analysis (Kuremoto et al., 2014), of course, has also a significant advancement. Traditional statistical methods such as ARIMA (Auto-Regressive Integrated Moving Average) (Yuan et al., 2016) and SARIMA (Seasonal ARIMA) (Ahn et al., 2015) were defeated by the proposed LSTM (Long and Short-Term Memory network) (Hochreiter and Schmidhuber,1997). For energy consumption prediction and anomaly detection, a lot of work on LSTM has been done.

However, with the introduction of Google's Transformer model (Vaswani et al., 2017), this model was first successfully used to the field of machine translation, and then it spread to other significant fields such as speech recognition (Wang et al., 2020), and so on. Since machine translation technology involves the processing of time series, we seem to be able to use the Transformer model for time series forecasting tasks. Transformer uses self-attention and multi-head self-attention for semantic extraction. When it comes to the long-distance dependence of features in time series, self-attention can naturally solve this problem, because there are connections between all features of time series when integrating features, and the relative position information between the input time series features is preserved through sinusoidal position encoding. It is not like RNN (Recurrent Neural Network) that needs to be gradually passed to the back through hidden layer node sequences, nor is it like CNN (Convolutional Neural Networks) that needs to be captured long distance features by increasing the network depth, Transformer has some advantages in processing time series features.

As a result, in this paper, we propose a new power consumption prediction and anomaly detection model that combines deep learning and clustering methods. The following are the contributions:

1) For time series prediction of power consumption, we merged the current popular Transformer deep learning model with K-means clustering. We reasoned that the historical time data contributes differentially to the expected value due to the regular behavior of household users. The K-means method can be used to locate data clusters that contribute more to the projected value, allowing the Transformer model prediction value to be optimized further.
2) In the experiment, we employed multi-dimensional data. The data dimension also incorporates auxiliary information data such as voltage, current, and the power consumption of various household appliances, in addition to the fundamental power consumption.
3) We compared the proposed method to the LSTM and only Transformer model's prediction performance. Experiments have revealed that the proposed combination method's error between predicted and true values is lower than those of LSTM and single Transformer.
4) To demonstrate the proposed method's superior performance in anomaly detection, we manually added anomalous data into the test data and treated it as a true anomaly.

The following is how we organize this paper. We introduce relevant research on power consumption and anomaly detection in **Section 2**. The data set used in the experiment, as well as the data set's preparation approach, are shown in **Section 3**. We describe our model's implementation approach and procedure in detail in **Section 4**. We compare the performance of model prediction and anomaly detection with different models in **Section 5**. This paper was summarized in the last section.

2 RELATED WORKS

Researchers have done a lot of research since power consumption prediction and anomaly detection are so crucial in the power energy system. Box et al. (2015) developed time series forecasting approaches like as Auto-Regressive (AR), ARIMA (Auto-Regressive Integrated Moving Average), and SARIMA (Seasonal ARIMA) in the economic sphere, and they had good results. To predict the value at a specific moment in the time series, the AR model primarily uses the weighting of all values preceding that time. ARIMA primarily employs the point before to the time to add a random vector in order to forecast the value at that time. SARIMA is mostly used for time series data with obvious seasonal differences. Ouyang et al. (2019b) improved the performance of wind power ramp prediction by combining the advantages of AR models and Markov chain. To detect anomalies, Yan et al. (2014) integrated the AR approach with SVM (Support Vector Machine) Ma and Guo (2014). ARIMA was used by Ediger and Akar (2007) to forecast fuel energy use in Turkey. The time series of ARIMA power consumption was utilized by Alberg and Last (2018) to estimate future power consumption, and Krishna et al. (2015) employed ARIMA for half-hour granular power consumption data. SARIMA was applied by Ahn et al. (2015) for long-term and mid-term load forecasting. The unsupervised K-means approach Münz et al. (2007) groups the data to identify anomalies that are outside of the cluster. Simultaneously, the autoencoder model has been a

TABLE 1 | Sample display of the data set used in this paper.

Datetime	Global_active_power (kW)	Global_reactive_power (kW)	Voltage (V)	Global_intensity (A)
2006-12-17 00:00:00	112.95	6.14	240.96	487.60
2006-12-17 01:00:00	200.96	8.22	240.45	854.80
2006-12-17 02:00:00	95.24	4.69	245.82	412.20
Sub_metering_1 (Wh)	**Sub_metering_2 (Wh)**	**Sub_metering_3 (W)h**	**Sub_metering_4 (Wh)**	
0.0	28.0	0.0	1854.47	
0.0	1,514.0	0.0	1835.40	
0.0	34.0	0.0	1,553.27	

huge success. The data is analyzed using unsupervised methods. The difference between input and output is utilized to detect whether the data is aberrant, from compression and abstraction to recovery and rebuilding. For anomaly detection, Al-Abassi et al. (2020) presented unsupervised stacked autoencoders for smart cyber-physical grids. Deb et al. (2015) developed an artificial neural network for predicting building energy usage in Singapore, and it was shown to be accurate.

The advancement of deep learning has improved the accuracy and performance of large data processing and prediction. Deep learning was used extensively in wind speed prediction (Khodayar et al., 2017), stock prediction (Rather et al., 2015), automated Vehicles (Shen et al., 2020) and other researches, and power grid technology has also incorporated the nerve of deep learning. The network is used to forecast and detect how much energy the user consumes. Ouyang et al. (2019a) proposed the use of Deep Belief Network (DBN) to predict hourly power load. According to Shi et al. (2017), predicting the electricity usage of a single customer in Ireland is the same as using a deep recursive network. For time series, LSTM can forecast and detect anomalies (Malhotra et al., 2016; Siami-Namini et al., 2018). Wang et al. (2019) proposed combining seasonal features with LSTM for power load forecasting and anomaly detection. However, because ARIMA requires time series data to be stationary and it can only capture linear relationships, but not non-linear relationships. For the LSTM model, its output at the current time requires not only the input at the current time, but also the output at the previous time. This makes the LSTM model unable to parallelize operations, resulting in too long training time when processing time series features. On the other hand, the Transformer model has had a lot of success in the field of speech recognition and natural language processing since it was introduced. As a result, we propose in this paper that we utilize the transformer model to estimate electric energy load, then apply the k-means approach to further improve the prediction results, and then compare the prediction results to the test data to look for anomalies.

3 DATASETS

For the experiment, we used hour-level electricity load data from a French family for 1,440 days (2006-12-17 to 2010-11-25). We selected 3 h of data for display, as shown in **Table 1**, except for "global_active_power" represents the total active power consumed by the household, and other data includes "global_reactive_power" representing the total reactive power consumed by the household, "voltage" representing the average voltage per hour, "global_intensity" representing the average current intensity, "sub_metering_1" representing the active electrical energy of the kitchen, "sub_metering_2" representing the active energy of the laundry, "sub_metering_3" representing the active energy of the climate control system, "sub_metering_4" representing other active energy. The hourly power load change diagram for 3 days which are all weekdays is shown in **Figure 1**. It can be seen that power consumption has increased significantly in the morning, noon and evening, and electricity consumption conforms to the law of electricity consumption in French households during workdays. To make the data more stable, we apply the Min-Max Normalization procedure. This will make the model's training easier and its convergence faster. We designed the model supervision task to estimate the following hour's electric energy usage based on multivariate data collected every 23 h, and we implemented it by using a 23-hour sliding window.

4 METHODOLOGY

We partitioned the data into 24-hour groups using a sliding window, then trained k-means clustering for the first 23 h of each group of real test data into k clusters, while also used the 23-hour real load data training Transformer model predicts the next hour's load data, then through the trained K-means to get the appropriate centroid as the final prediction result. **Figure 2** depicts the framework of our model.

4.1 Transformer Model

Initial and foremost, Positional Encoding is the first phase in the Transformer model utilized in this essay. Because Transformer does not have a cyclic structure like LSTM, it presents a new positional encoding strategy to capture the input time series information, as indicated in **Eqs 1, 2**. The basic idea is to add sine and cosine functions of various frequencies as position codes to the normalized input sequence, allowing the Transformer model's multi-head attention mechanism to fully capture time series data with more dimensions.

$$PE_{(pos,2i)} = \sin\left(pos/10000^{2i/d_{model}}\right) \quad (1)$$

$$PE_{(pos,2i+1)} = \cos\left(pos/10000^{2i/d_{model}}\right), i \in [0, \ldots, d_{model}/2) \quad (2)$$

where pos is the vector position of each time. For example, in the time series data in this paper, the pos of the first hour of each group is 0, and the pos of the second hour is 1, $2i$ and $2i + 1$ respectively represent the even position and the odd position.

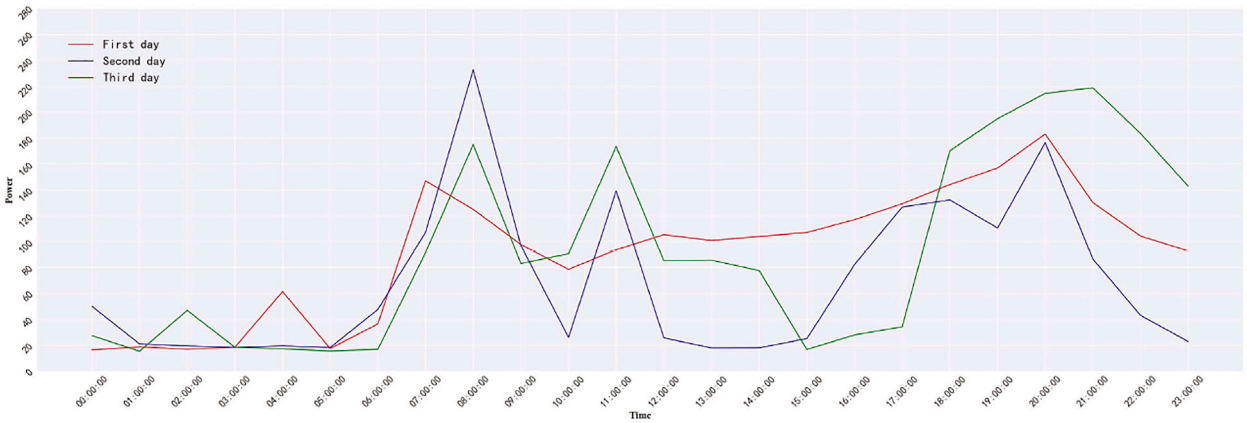

FIGURE 1 | Hourly household electric energy consumption change diagram for 3 consecutive days.

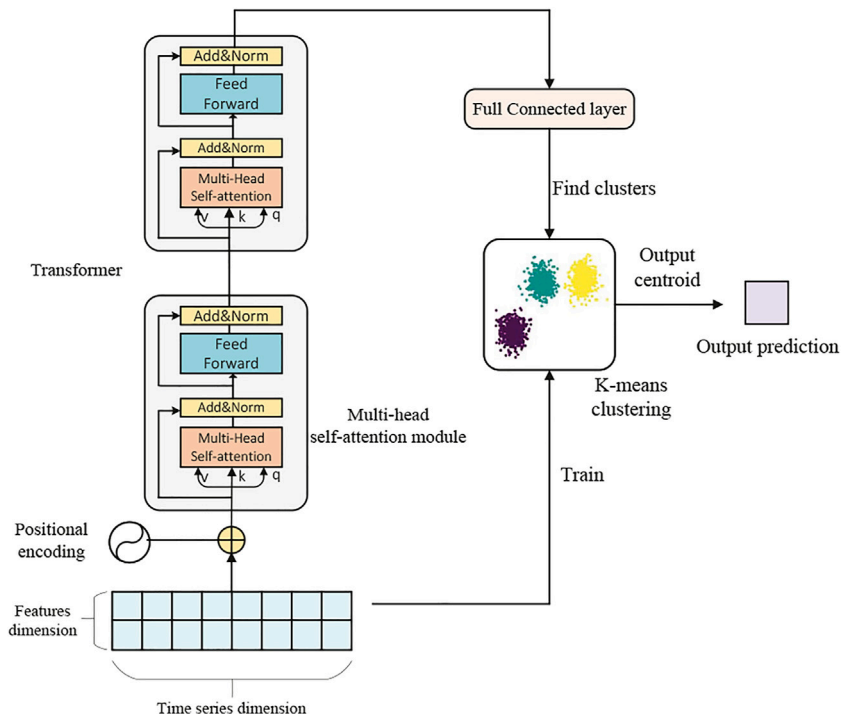

FIGURE 2 | The main framework of our model.

d_{model} represents the length of the feature vector per hour. Next, we use $X = [x_1, x_2, \ldots, x_n]$ to represent the input sequence combined with position encoding, and pass the multi-head self-attention of the Transformer model:

$$MultiHead(Q, K, V) = Concat(head_1, \ldots, head_i)W^o \quad (3)$$

$$head_i = Attention(QW_i^Q, KW_i^K, VW_i^V) \quad (4)$$

In the above formula, $Q = q_1 w^{q_1}, K = k_1 w^{k_1}, V = v_1 w^{v_1}$, $q_1 = k_1 = v_1 = X$. In the Transformer model, the Attention module first undergoes a linear transformation of Q (Query), K (Key), and V (Value). Each time Q, K, and V perform the linear transformation, the parameter W is different, and then input to Scaling dot product attention, the formula is as (5), note that it is necessary to do i times here, in fact, it is the so-called multi-head, and each time counts as one head. Then concatenate the attention results of the i times of scaling dot product, and then perform a linear transformation to obtain the value as the result of the multi-head attention. The advantage of this is that it allows the model to learn relevant information in different representation subspaces. The calculation of the Attention module uses Scaled Dot-product:

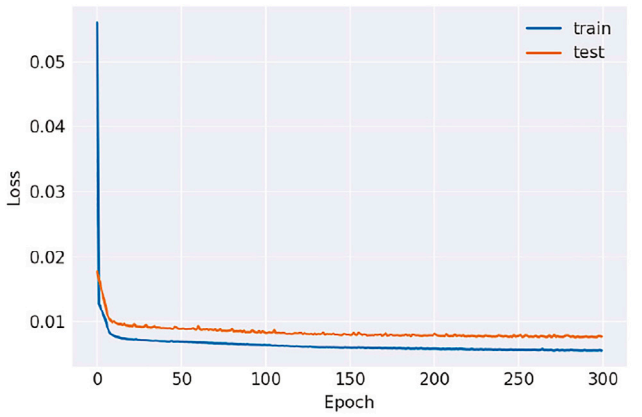

FIGURE 3 | Train and test loss over the 300 epochs of our model.

$$Attention(Q,K,V) = softmax\left(\frac{QK^T}{\sqrt{d_k}}\right)V \tag{5}$$

where d_k is the last dimension of the shape of Q, K, V, divided by $\sqrt{d_k}$ to prevent d_k from being too large and the softmax function's gradient becoming too tiny when QK^T is too large. The residual connection structure is then used to narrow the network's attention to solely the differences. In multi-layer network structures, it is frequently used:

$$L = LayerNorm(X + MultiHead(Q,K,V)) \tag{6}$$

where *LayerNorm* is Layer Normalization, which normalizes each neuron and adjusts the mean and variance of the input data to be the same, which will speed up the convergence. Then input L into the FeedForward layer, which is composed of two fully connected layers, the first layer uses the Relu activation function, and the second layer does not use the activation function:

$$s = \max(0, LW_1 + b_1)W_2 + b_2 \tag{7}$$

Similarly, use residual connection and Layer Normalization again to get the output S_E:

$$S_E = LayerNorm(L + s) \tag{8}$$

Our experiment uses a 2-layer Transformer multi-head attention module, which means that the output S_E needs to be re-input to the structure output S_{E2} described above. Finally, the output will be decoded and dimensionality reduction operations through the fully connected layer:

$$K = W_3 S_{E2} \tag{9}$$

4.2 K-Means Clustering Method

Clustering is the division of a sample set into several disjoint subsets (sample clusters), which is a typical unsupervised machine learning algorithm. When using clustering to classify samples, Euclidean Distance is used as the measurement criterion of sample similarity. The higher the similarity, the smaller the Euclidean Distance of the sample. K-means clustering is a well-known algorithm among clustering algorithms. It needs to determine the number of clusters k first when clustering, and k is given by the user. Each cluster passes through its centroid (the mean value of all elements in the cluster). The workflow of k-means is also very simple. First, randomly select k initial points as the initial centroids of each cluster, and then assign each point in the data set to the cluster closest to it. The distance calculation uses the Euclidean Distance mentioned above. The algorithm of k-means is shown in **Algorithm 1**:

Algorithm 1. *K*-means algorithm.

Data:
$D = \{x_1, x_2, ..., x_n\}$ //Set of elements
K //Number of desired clusters
Result:
K //Set of clusters
K-Means algorithm:
Initialize $\mu_1 ... \mu_K$ randomly
Repeat
Assign each data point to the closest centroid:
$c_i = j : d(x_j, \mu_i) \leq d(x_j, \mu_l), l \neq i, j = 1, ..., n;$
Recompute each μ_i as the centroids of all data points belonging to that cluster;
Until
The centroids no longer move.

4.3 Model Development

First, we divide the data set into a training set and a test set. Since the data set contains a total of 1,440 days of hourly data, we choose 1,240 days of data as the training set and 200 days of data as the test set. For the Transformer model, we choose two consecutive layers of multi-head self-attention modules, and each multi-head attention is set to 4 attention heads. The input data shape is 23 time steps and 8 features. For K-means clustering, we experimented with k = 2, 5, 8, 10, 11, and 15 respectively, and finally selected the cluster with k = 10. We choose the mean-square error of the predicted data and the original data, that is, MSE (Mean-Square Error) as the loss function, and Adam as the optimizer of the model. And set the epoch of the training model to 300, and the batch size to 200.

4.4 Model Prediction and Evaluation

We believed that the nearest neighbor of the real training data has the most impact on the forecast value, thus in the first 23 h of each group, we trained k-means clustering, partitioned the data into k categories, and provided the load K predicted by the Transformer model for the next hour as the final prediction output, then found the centroid in the trained K-means cluster. We analyzed the model's prediction ability by fitting the predicted value to the test value and calculating the RMSE (Root Mean Squard Error) of the forecasted value and the test value to measure the prediction's accuracy, and we compared it to the commonly used LSTM model.

4.5 Anomaly Detection

Because the model calculates the anticipated value based on a huge quantity of historical data, the forecasted values will generally follow the data's trend. If the test value differs significantly from the projected value, it indicates that the test value has deviated too far from the data trend and may be abnormal. The score between the predicted value

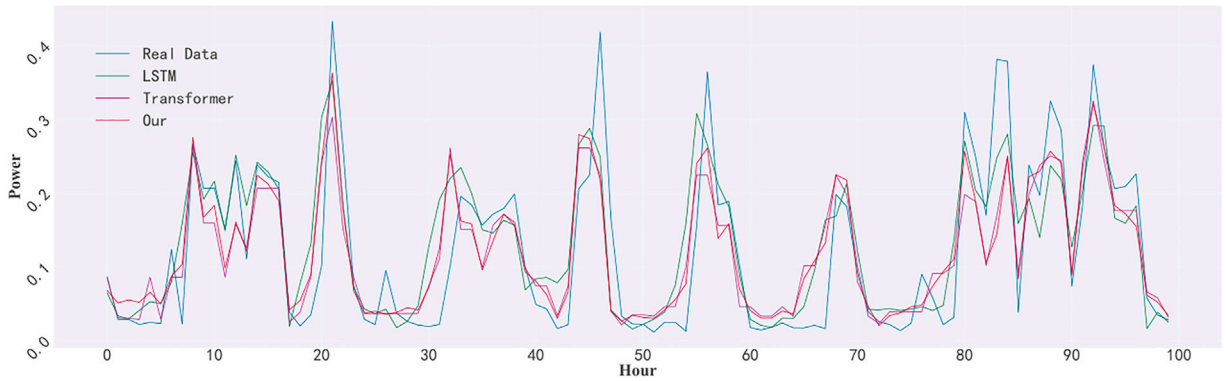

FIGURE 4 | Comparison of our model and LSTM predicted value fitting real data.

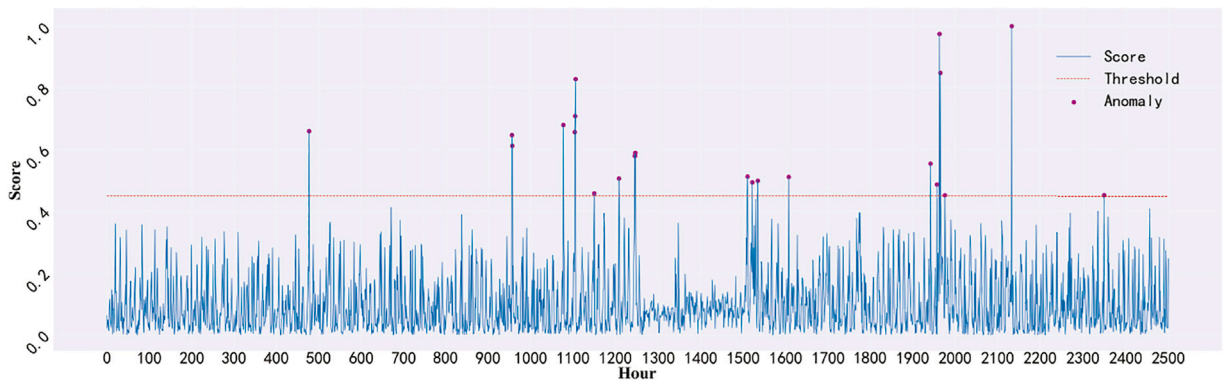

FIGURE 5 | Scores and anomalies exceeding the threshold for 2,500 h.

TABLE 2 | Comparison with some methods.

Method	Accurary	Precision	Recall	F1	RMSE(prediction)
K-means	0.96	0.82	0.28	0.42	—
LSTM	0.97	0.74	0.60	0.66	0.91
Our method	0.97	0.80	0.66	0.72	0.74

and the test value obtained after the Transformer model and k-means clustering is calculated in this research. The formula can be found in **Eq. 10**. In order to better analyze the difference, we normalized the score, the formula is as **Eq. 11**. The value of score collected from several experiments was used to determine a threshold. When the score between the predicted value and the test value exceeds the threshold, the test value is considered abnormal. The experiment can also evaluate whether the user is prone to having electricity theft by setting a time series window and a threshold for the number of anomalies. If the number of abnormalities in the time series data in a window is greater than the threshold, it means that the time series data are abnormal, and the user may have the suspicion of steal electricity. To better compare the accuracy of anomaly detection, we manually insert abnormal data points in the test data and compare our model with K-means and LSTM.

$$score_t = \frac{|predicted_t - test_t|}{avg_{i\epsilon T}(|predicted_i - test_i|)} \tag{10}$$

$$\widetilde{score_t} = \frac{score_t - \min(score)}{\max(score) - min(score)} \tag{11}$$

5 EXPERIMENT RESULTS

5.1 Consumption Prediction

We opted to compare the model against the most popular LSTM model for time series data prediction in order to test its performance. The LSTM is a variant of the recurrent neural network RNN. It is a unique RNN that incorporates three different types of gating to address the problem of gradient disappearance and explosion during lengthy sequence training. Simply put, LSTM outperforms standard RNNs in longer sequences, making it ideal for time series forecasting jobs.

Figure 3 shows how the training and test loss of the Transform model used in this paper changes at 300 epoch. It can be observed that the model converges quickly, and the figure shows that there is no overfitting in the model. All of this is achievable because of the Transformer model's benefits in time series processing.

Figure 4 depicts the test set's real-time power consumption data over 3 days, as well as a comparison of our model's and the LSTM model's prediction results on the test set. The blue line represents the actual data, the red line represents our model's predicted value, the green line represents the LSTM model's predicted value, and the purple line indicates the lone Transformer's predicted value. Our model's forecast data is more in accordance with the real test data, as can be shown. The RMSE of the model, on the other hand, are used to assess the model's fit. Our model has an RMSE of 0.73, the Transformer has an RMSE of 0.77, and the LSTM has an RMSE of 0.86. In terms of prediction accuracy, our model outperforms LSTM by 15%, while Transformer outperforms LSTM by just 10%. After our analysis, because the dimensionality of the feature vector of each time series in our time series data is too small, which leads to the failure of the full performance of the Transformer model.

5.2 Anomaly Detection

After a lot of testing and tweaking, we ultimately settled on 0.45 as the threshold. This means that any point with a score higher than 0.45 will be considered anomalous. The change in score data over 2,500 h is presented in **Figure 5**, with the red dashed line representing the threshold and the purple point representing the abnormal point. The data scores are primarily focused between 0 and 0.3, and there are relatively few aberrant spots, as can be shown. In practical applications, we can adjust the threshold size based on the scene being used, and lower or increase the threshold size based on the strictness of anomaly detection, a lower threshold is more stringent, allowing for the detection of more anomalies, on the other hand, a higher threshold is more tolerant, allowing for the detection of fewer anomalies.

We utilized the strategy of randomly inserting abnormal points in the test data to better compare and assess the model's anomaly detection capabilities because this experimental data set does not mark aberrant time points. In the 200 days (4,800 h) of the test set, we randomly selected a value every day and double it, and assume it is an outlier, so there are 200 outliers in the 4,800 data in the test set. For comparison, we separately used the clustering method K-means and the most popular depth method LSTM to detect abnormal points. Using the K-means approach, we discovered a total of 68 abnormal points, of which only 56 were the abnormal points we manually inserted into the data set. Using the LSTM model, we retrieved a total of 162 anomalies, 120 of which were the anomaly points we manually inserted into the data set. Our combined Transformer and K-means model found 165 anomalies, 132 of which were the abnormal points we manually added to the data set. The accuracy, precision, recall, and F1 of the three models are shown in **Table 2**. The predicted RMSE of LSTM and our model are also shown in the table.

6 CONCLUSION

The prediction of electric energy consumption and the identification of anomalies are critical in the functioning of the power grid, and the processing of multi-variable time series is a difficult challenge. We present a model that combines Transformer and K-means approaches in this article. Every 23 h of training data is separated into k clusters using K-means clustering. At the same time, this training data are used to train the Transformer model to predict the following hour's power usage, with the predicted value being placed into the trained K-means cluster and the cluster's centroid serving as the final predicted value. Finally, look for anomalies by comparing the anticipated value to the actual test results. The experimental results prove that the model achieves prediction accuracy with less error and high anomaly detection performance. In the future, we'll strive to improve prediction and anomaly detection accuracy, as well as study the differences between power consumption prediction and anomaly detection in different seasons, environments, and other scenarios, and other issues that need to be addressed.

DATA AVAILABILITY STATEMENT

The datasets presented in this study can be found in online repositories. The names of the repository/repositories and accession number(s) can be found below: https://archive.ics.uci.edu/ml/datasets/individual+household+electric+power+consumption.

AUTHOR CONTRIBUTIONS

JZ: conceptualization, methodology, data preprocessing, and writing-original draft preparation. HZ: visualization, investigation. SD: experimental training and testing. XZ: supervision and reviewing.

FUNDING

This work was supported in part by the National Natural Science Foundation of China under Grants 71901215, 71901191, the National University of Defense Technology Research Project ZK20-46, and the Outstanding Youth Talents Program of National University of Defense Technology.

REFERENCES

Ahn, B.-H., Choi, H.-R., and Lee, H.-C. (2015). Regional Long-Term/mid-Term Load Forecasting Using Sarima in south korea. *J. Korea Academia-Industrial cooperation Soc.* 16, 8576–8584. doi:10.5762/kais.2015.16.12.8576

Al-Abassi, A., Sakhnini, J., and Karimipour, H. (2020). "Unsupervised Stacked Autoencoders for Anomaly Detection on Smart Cyber-Physical Grids," in 2020 IEEE International Conference on Systems, Man, and Cybernetics (SMC) (IEEE), 3123–3129. doi:10.1109/smc42975.2020.9283064

Alberg, D., and Last, M. (2018). Short-term Load Forecasting in Smart Meters with Sliding Window-Based Arima Algorithms. *Vietnam J. Comput. Sci.* 5, 241–249. doi:10.1007/s40595-018-0119-7

Antmann, P. (2009). *Reducing Technical and Non-technical Losses in the Power Sector*.

Bayindir, R., Colak, I., Fulli, G., and Demirtas, K. (2016). Smart Grid Technologies and Applications. *Renew. Sustain. Energ. Rev.* 66, 499–516. doi:10.1016/j.rser.2016.08.002

Box, G., Jenkins, G. M., Reinsel, G. C., and Ljung, G. M. (20152015). *Time Series Analysis: Forecasting and Control*.

Chandola, V., Banerjee, A., and Kumar, V. (2009). Anomaly Detection. *ACM Comput. Surv.* 41, 1–58. doi:10.1145/1541880.1541882

Deb, C., Eang, L. S., Yang, J., and Santamouris, M. (2015). Forecasting Energy Consumption of Institutional Buildings in singapore. *Proced. Eng.* 121, 1734–1740. doi:10.1016/j.proeng.2015.09.144

Desai, B. H. (2017). 14. United Nations Environment Program (Unep). *Yearb. Int. Environ. L.* 28, 498–505. doi:10.1093/yiel/yvy072

Ediger, V. Ş., and Akar, S. (2007). Arima Forecasting of Primary Energy Demand by Fuel in turkey. *Energy policy* 35, 1701–1708. doi:10.1016/j.enpol.2006.05.009

Graves, A., Mohamed, A.-r., and Hinton, G. (20132013). *IEEE International Conference on Acoustics, Speech and Signal Processing*. IEEE, 6645–6649. doi:10.1109/icassp.2013.6638947Speech Recognition with Deep Recurrent Neural Networks

Hochreiter, S., and Schmidhuber, J. (1997). Long Short-Term Memory. *Neural Comput.* 9, 1735–1780. doi:10.1162/neco.1997.9.8.1735

Hsieh, T.-J., Hsiao, H.-F., and Yeh, W.-C. (2011). Forecasting Stock Markets Using Wavelet Transforms and Recurrent Neural Networks: An Integrated System Based on Artificial Bee colony Algorithm. *Appl. soft Comput.* 11, 2510–2525. doi:10.1016/j.asoc.2010.09.007

Hu, M., Ji, Z., Yan, K., Guo, Y., Feng, X., Gong, J., et al. (2018). Detecting Anomalies in Time Series Data via a Meta-Feature Based Approach. *Ieee Access* 6, 27760–27776. doi:10.1109/access.2018.2840086

Khodayar, M., Kaynak, O., and Khodayar, M. E. (2017). Rough Deep Neural Architecture for Short-Term Wind Speed Forecasting. *IEEE Trans. Ind. Inf.* 13, 2770–2779. doi:10.1109/tii.2017.2730846

Krishna, V. B., Iyer, R. K., and Sanders, W. H. (2015). "Arima-based Modeling and Validation of Consumption Readings in Power Grids," in International Conference on Critical Information Infrastructures Security (Springer), 199–210.

Kuremoto, T., Kimura, S., Kobayashi, K., and Obayashi, M. (2014). Time Series Forecasting Using a Deep Belief Network with Restricted Boltzmann Machines. *Neurocomputing* 137, 47–56. doi:10.1016/j.neucom.2013.03.047

Ma, Y., and Guo, G. (2014). *Support Vector Machines Applications*, Vol. 649. Springer.

Malhotra, P., Ramakrishnan, A., Anand, G., Vig, L., Agarwal, P., and Shroff, G. (2016). Lstm-based Encoder-Decoder for Multi-Sensor Anomaly Detection. arXiv preprint arXiv:1607.00148.

McLaughlin, S., Podkuiko, D., and McDaniel, P. (2009). "Energy Theft in the Advanced Metering Infrastructure," in International Workshop on Critical Information Infrastructures Security (Springer), 176–187.

Münz, G., Li, S., and Carle, G. (2007). "Traffic Anomaly Detection Using K-Means Clustering," in GI/ITG Workshop MMBnet, 13–14.

Nadkarni, P. M., Ohno-Machado, L., and Chapman, W. W. (2011). Natural Language Processing: an Introduction. *J. Am. Med. Inform. Assoc.* 18, 544–551. doi:10.1136/amiajnl-2011-000464

Ouyang, T., He, Y., Li, H., Sun, Z., and Baek, S. (2019a). Modeling and Forecasting Short-Term Power Load with Copula Model and Deep Belief Network. *IEEE Trans. Emerg. Top. Comput. Intell.* 3, 127–136. doi:10.1109/tetci.2018.2880511

Ouyang, T., Zha, X., Qin, L., He, Y., and Tang, Z. (2019b). Prediction of Wind Power Ramp Events Based on Residual Correction. *Renew. Energ.* 136, 781–792. doi:10.1016/j.renene.2019.01.049

Rather, A. M., Agarwal, A., and Sastry, V. N. (2015). Recurrent Neural Network and a Hybrid Model for Prediction of Stock Returns. *Expert Syst. Appl.* 42, 3234–3241. doi:10.1016/j.eswa.2014.12.003

Shen, X., Zhang, X., Ouyang, T., Li, Y., and Raksincharoensak, P. (2020). Cooperative Comfortable-Driving at Signalized Intersections for Connected and Automated Vehicles. *IEEE Robot. Autom. Lett.* 5, 6247–6254. doi:10.1109/lra.2020.3014010

Shi, H., Xu, M., and Li, R. (2017). Deep Learning for Household Load Forecasting a Novel Pooling Deep Rnn. *IEEE Trans. Smart Grid* 9, 5271–5280.

Siami-Namini, S., Tavakoli, N., and Namin, A. S. (2018). "A Comparison of Arima and Lstm in Forecasting Time Series," in 2018 17th IEEE International Conference on Machine Learning and Applications (ICMLA) (IEEE), 1394–1401. doi:10.1109/icmla.2018.00227

Vaswani, A., Shazeer, N., Parmar, N., Uszkoreit, J., Jones, L., Gomez, A. N., et al. (2017), Attention Is All You Need. *Advances in Neural Information Processing Systems*, 5998–6008.

Wang, X., Zhao, T., Liu, H., and He, R. (20192019). "Power Consumption Predicting and Anomaly Detection Based on Long Short-Term Memory Neural Network," in IEEE 4th international conference on cloud computing and big data analysis (ICCCBDA) (IEEE), 487–491. doi:10.1109/icccbda.2019.8725704

Wang, Y., Mohamed, A., Le, D., Liu, C., Xiao, A., Mahadeokar, J., et al. (2020). "Transformer-based Acoustic Modeling for Hybrid Speech Recognition," in ICASSP 2020-2020 IEEE International Conference on Acoustics, Speech and Signal Processing (ICASSP) (IEEE), 6874–6878. doi:10.1109/icassp40776.2020.9054345

Yan, K., Shen, W., Mulumba, T., and Afshari, A. (2014). Arx Model Based Fault Detection and Diagnosis for Chillers Using Support Vector Machines. *Energy and Buildings* 81, 287–295. doi:10.1016/j.enbuild.2014.05.049

Yuan, C., Liu, S., and Fang, Z. (2016). Comparison of China's Primary Energy Consumption Forecasting by Using ARIMA (The Autoregressive Integrated Moving Average) Model and GM(1,1) Model. *Energy* 100, 384–390. doi:10.1016/j.energy.2016.02.001

Conflict of Interest: The authors declare that the research was conducted in the absence of any commercial or financial relationships that could be construed as a potential conflict of interest.

Publisher's Note: All claims expressed in this article are solely those of the authors and do not necessarily represent those of their affiliated organizations, or those of the publisher, the editors and the reviewers. Any product that may be evaluated in this article, or claim that may be made by its manufacturer, is not guaranteed or endorsed by the publisher.

frontiers in Energy Research

ORIGINAL RESEARCH
published: 26 October 2021
doi: 10.3389/fenrg.2021.780928

Short-Term Nacelle Orientation Forecasting Using Bilinear Transformation and ICEEMDAN Framework

Huajin Li[1,2], Jiahao Deng[3], Peng Feng[1], Chuanhao Pu[2], Dimuthu D. K. Arachchige[3] and Qian Cheng[4]*

[1]School of Architecture and Civil Engineering, Chengdu University, Chengdu, China, [2]State Key Laboratory of Geo-hazard Prevention and Geo-environment Protection, Chengdu University of Technology, Chengdu, China, [3]College of Computing and Digital Media, DePaul University, Chicago, IL, United States, [4]College of Civil Engineering, Sichuan University of Science and Engineering, Zigong, China

To maximize energy extraction, the nacelle of a wind turbine follows the wind direction. Accurate prediction of wind direction is vital for yaw control. A tandem hybrid approach to improve the prediction accuracy of the wind direction data is developed. The proposed approach in this paper includes the bilinear transformation, effective data decomposition techniques, long-short-term-memory recurrent neural networks (LSTM-RNNs), and error decomposition correction methods. In the proposed approach, the angular wind direction data is firstly transformed into time-series to accommodate the full range of yaw motion. Then, the continuous transformed series are decomposed into a group of subseries using a novel decomposition technique. Next, for each subseries, the wind directions are predicted using LSTM-RNNs. In the final step, it decomposed the errors for each predicted subseries to correct the predicted wind direction and then perform inverse bilinear transformation to obtain the final wind direction forecasting. The robustness and effectiveness of the proposed approach are verified using data collected from a wind farm located in Huitengxile, Inner Mongolia, China. Computational results indicate that the proposed hybrid approach outperforms the other single approaches tested to predict the nacelle direction over short-time horizons. The proposed approach can be useful for practical wind farm operations.

Keywords: wind direction, bilinear transformation, ICEEMDAN, LSTM-RNN, error correction

OPEN ACCESS

Edited by:
Tinghui Ouyang,
National Institute of Advanced Industrial Science and Technology (AIST), Japan

Reviewed by:
Jirong Yi,
The University of Iowa, United States
Arian Dhini,
University Indonesia, Indonesia

****Correspondence:***
Jiahao Deng
jdeng5@depaul.edu

Specialty section:
This article was submitted to Wind Energy, a section of the journal Frontiers in Energy Research

Received: *22 September 2021*
Accepted: *12 October 2021*
Published: *26 October 2021*

Citation:
Li H, Deng J, Feng P, Pu C, Arachchige DDK and Cheng Q (2021) Short-Term Nacelle Orientation Forecasting Using Bilinear Transformation and ICEEMDAN Framework. Front. Energy Res. 9:780928. doi: 10.3389/fenrg.2021.780928

INTRODUCTION

Wind energy generation is expanding with about 12% of world's electricity to be supplied by 2020 (Kodama and Burls 2019). Compared with the traditional form of power generation, wind energy has the advantages of zero pollution and low operation cost. Hence, it has become one of the fastest growing renewable energy power supplies globally (Duan et al., 2021).

Although it has obvious advantages over others, wind energy still faces technical challenges due to the characteristics of chaos, randomness, and intermittence which make the wind data complex. The wind direction is one of the most complex aspect of the wind data due to its high dynamics in both spatial and temporal domains. To follow the wind direction, the nacelle of a wind turbine orientes the controlling of yaw and maximizes the energy output. For most efficient energy extraction, the nacelle

orientation of a wind turbine needs to agree with wind direction which calls for accurate and prediction of the wind direction (Hu et al., 2016).

According to literature review, statistical approaches based on meteorological and geographic information are widely applied to forecast wind direction (Mcwilliams and Sprevak 1982; Castino et al., 1998; Erdem and Shi 2011). Liu et al. (2010) applied a neural Kriging method to spacially estimate the distribubiton of wind directions. Erdem and Shi (2011) developed autoregressive moving average (ARMA) model to forecast the short-term wind directions. Masseran et al. (2013) used a mixture of Von Mises models to fit the wind direction series.

Therefore, machine learning adoptions for wind direction forecasting have evolved from the classic approach to deep learning, which is then improved in this study (Mohandes et al., 2004; Bilgili et al., 2007). In the wind direction forecasting sector, Zhou et al. (2011) selected least-square support vector machines (LS-SVM) to predict the wind directions. Tagliaferri et al. (2015) developed artificial neural networks to forecast the short-term wind directions. Khosravi et al. (2018) developed an adaptive neuro-fuzzy inference system to predict the wind directions. Amin et al. (2018) improved the wind direction forecasting using the echo state network (ESN) which is a deep-learning algorithm. Tang et al. (2021) integrated the ESN network with IFPA optimization algorithm and developed a two-step deep-learning wind direction framework.

Considering the complexity and high dynamics of the wind direction series, additional measures are essential to study in the pattern inside. Even though deep learning algorithms have achieved promising results in the field of time-series prediction, it is still challenging for a single deep-learning approach to adapt all wind direction patterns. To further improve the prediction performance, hybrid prediction models are considered to be the mainstream since last year. The signal decomposition is one of the most popular components within the hybrid models published. It contains wavelet decomposition (Liu et al., 2014), empirical mode decomposition (EMD) (Santhosh et al., 2018), complete ensemble empirical model decomposition (CEEMD) (Zhang et al., 2017), complete EEMD with adaptive noise (CEEMDAN) (Yang and Wang 2018), and the improved CEEMDAN (ICEEMDAN) (Rong et al., 2019). In particular, the ICEEMDAN has demonstrated its superior performance in decomposing a complex signal into a finite number of intrinsic mode functions with transient frequencies. The decomposed subseries contains the detailed characteristics of the signal and can essentially reflect the spatial and temporal patterns of the wind direction series (Kou et al., 2020).

Based on the above considerations, in this research, we propose a new hybrid approach combining ICEEMDAN and error correction methods for short-term wind direction forecasting. First, the angular wind direction data has been transformed *via* bilinear transformation. Then, the transformed wind direction series are decomposed into a series of relatively simple subseries by the ICEEMDAN modules. Next, the LSTM-RNN is established as the prediction module to predict each sub-series. After that, the prediction errors are obtained and decomposed by ICEEMDAN modules. The statistical ARIMA model is used to predict the error subsequence and compute the prediction error. In the last step, the final prediction of the wind direction is made by summing all predicted subseries together with current predicted error and then transformed into angular data by inverse bilinear transformation.

The major contribution of this research can be summarized as follows: First, the wind direction forecasting system based on ICEEMDAN decomposition, LSTM-RNN and error correction has been proposed; Second, the comparative analysis is performed against other benchmarking deep-learning algorithm; Third, the experiments were performed in different seasons to explore seasonal patterns of wind directions.

The remainder of the manuscript is configured as follows. In Section "dataset description and transformation", it summarizes the data collection process and patterns inside the wind direction dataset. In Section "methodologies", it introduces the ICEEMDAN decomposition, LSTM-RNN, error correction, benchmarking deep-learning algorithms, and error correction procedures. The experimental results are provided in Section "experimental results" and the Conclusion is made in Section "conclusions" respectively.

DATASET DESCRIPTION AND TRANSFORMATION

Data Analysis

In this study, the data has been collected during the year of 2020 from a wind farm namely Huitengxile wind power plant in Inner Mongolia, Northern China. It is one of the largest wind farms in Asian and it's located in the suburbs between Chaha'er youyi zhongqi and Ulanqab city. The whole wind farm has multiple wind turbines that are distributed in an open flat grassland which provides rich wind resources. The prevailing wind directions are northwest and southeast which are very stable in recent years. The location and the annual wind rose diagrams has been illustrated in **Figure 1** below.

According to **Figure 1B**, the two prevailing wind directions, around 180° and 315° are visible. The geographic center coordinate is 112°40′E and 41°05′N. It's annual average wind speed at 10 m height is 7.2 m/s and its annual average wind speed at 40 m height is 8.8 m/s. In the wind farm, the annual average air density is 1.07 kg/m and it contains an effective wind speed of 5–25 m/s with strong stability and high quality.

The data used in this research has been collected by the supervisory control and data acquisition (SCADA) system. Usually, data on more than 100 parameters at 10 s intervals is collected and stored in a SCADA system. The SCADA collected data of individual wind turbines is streamed to a central computer for condition monitoring, performance evaluation, and other forms of analysis.

In this research, the SCADA data collected at 20 wind turbines over the period of 2020 has been analyzed. According to **Figure 1B**, there are two annual prevailing wind directions and it can be partitioned into four seasons independently as illustrated with the wind roses in **Figure 2**. In the fall and spring,

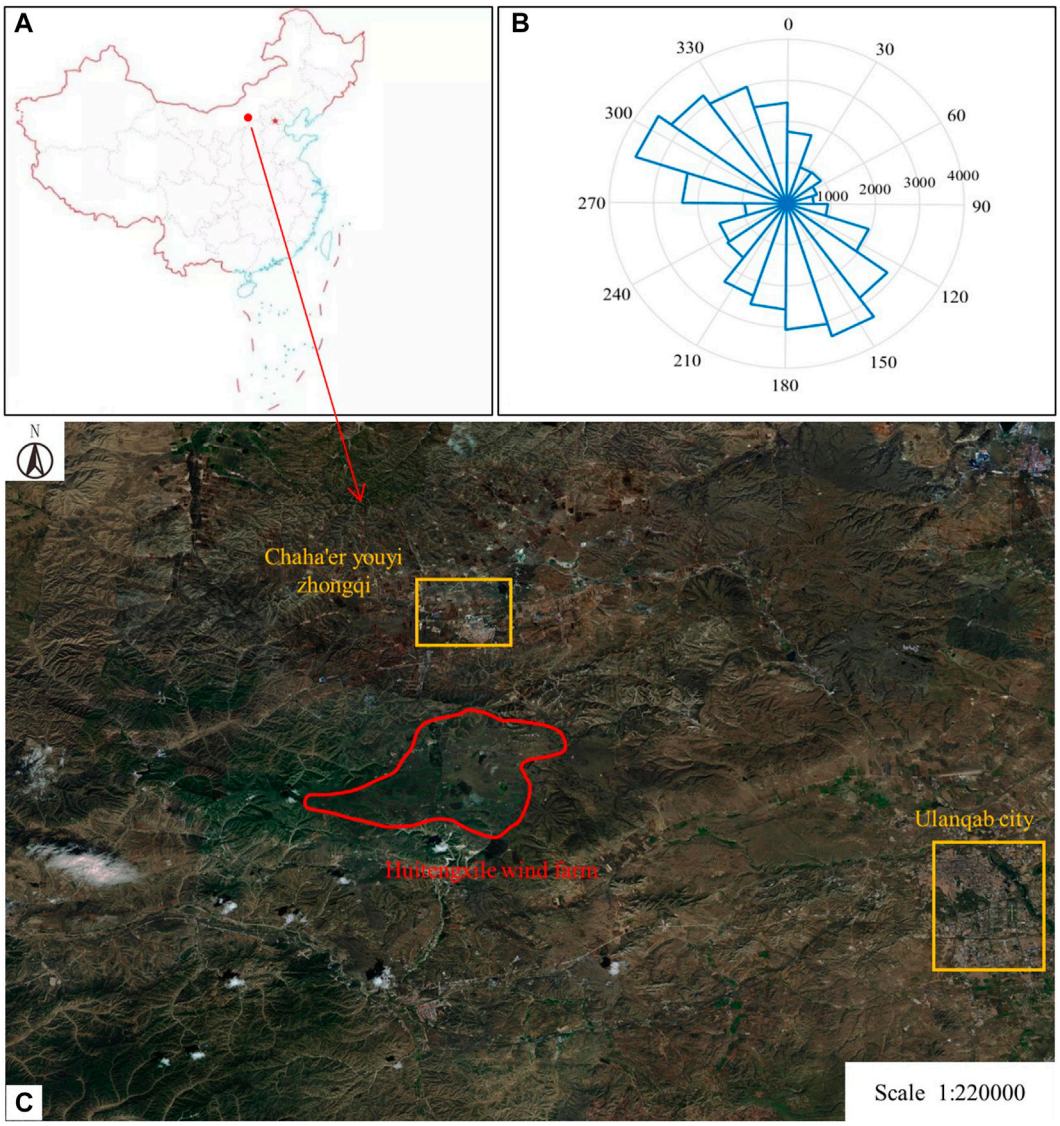

FIGURE 1 | Location of the Huitengxile wind farm.

two prevailing wind directions around 150° and 315°are observed. In the winter and summer, one prevailing wind direction is noted. Since the wind direction data is captured as a discrete angular variable, it needs to be transformed for modeling. A bilinear transformation of the angular wind direction is applied in the next section.

Bilinear Transformation of Angular Data

The value of wind direction ranges from 0° to 360°. It is likely that the wind direction may change from the interval, i.e (0°, 10°) to (350°, 360°). Practice shows that bilinear transformation is a better way for transforming discrete wind direction data to continuous data than the sine and cosine transformation (Peng et al., 2020). Geometrically, the two intervals are close to each other and therefore this change would lead to a large prediction error (Bilgili et al., 2007). To avoid such error, transformation of the discrete angular variable into a standardized continuous variable is essential. One option is to use a sine and cosine transformation which is not the best approach due to two variables needed for prediction which enlarges the prediction errors. A better option is to apply a bilinear transformation (Jury 1973).

The bilinear transformation maps the analog plane (s-plane) into the digital plane (z-plane) (Groutage et al., 2003) (see **Figure 3**). The transformation function, the ratio of two polynomials (Davies 1974), is expressed in **Eq. 1**.

$$H(s)_Z = \frac{1 + \frac{T}{2}s}{1 - \frac{T}{2}s} \tag{1}$$

where: s is the original value of angular variable in s-plane; T is the time interval of the transformation. The bilinear transformation expressed the angular variable between 0° and 360° as continuous

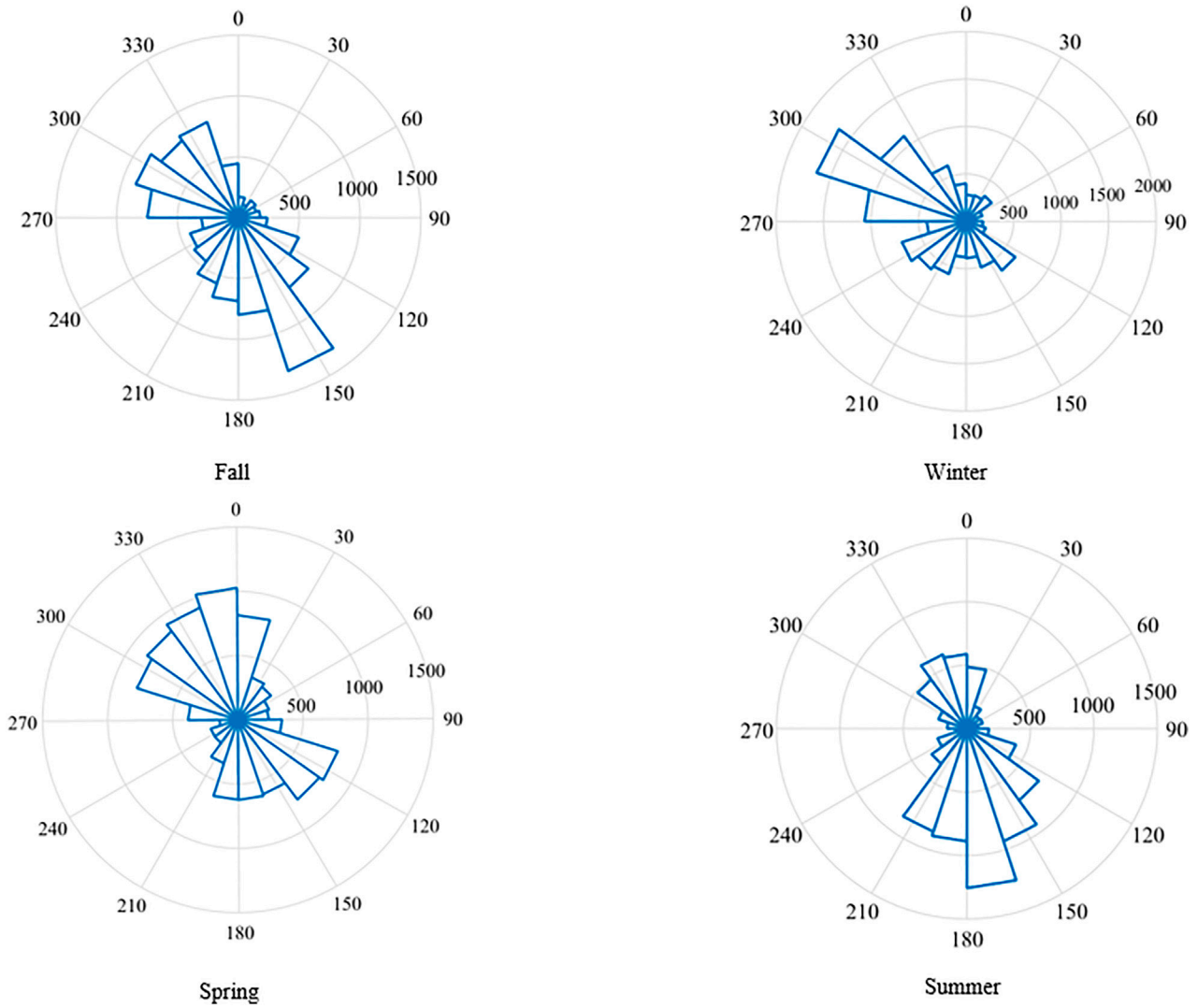

FIGURE 2 | Wind rose diagrams for four seasons.

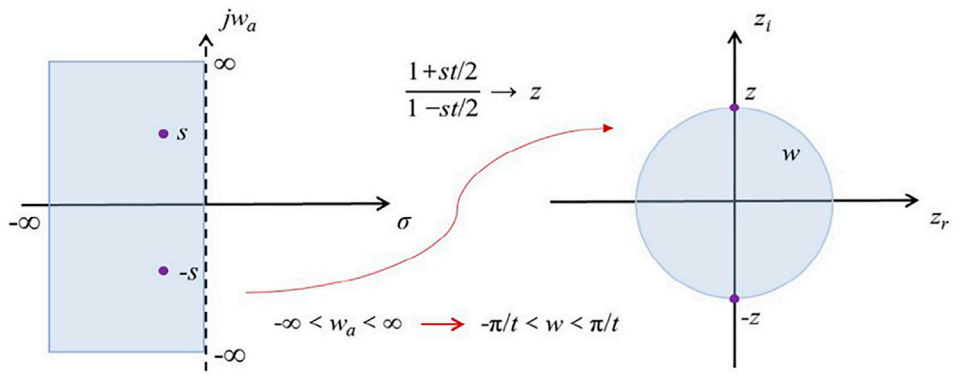

FIGURE 3 | Illustration of the bilinear transformation.

and normalized. The inverse bilinear transformation is expressed in **Eq. 2**.

$$s = \frac{1}{T}\frac{2 - 2H(s)_Z^{-1}}{2 + 2H(s)_Z^{-1}} \tag{2}$$

where: s is the inversed value of angular variable in s-plane; and $H(s)z$ is the transformed angular variable.

Since the wind direction data is noisy, a bilinear transformation function acting as a low-pass filter in the continuous-time domain reduces the noise (Davies 1974). A prediction model developed with the transformed data is more accurate than the model based on the discrete time-series angular data.

METHODOLOGIES

The use of deep learning algorithms in regression, multi-class classification, collaborative filtering, and graphic learning is growing (Lecun et al., 2015). The concept of deep learning originates from research in neural networks and it avoids the local optima dilemma. However, any single deep learning algorithms can offer limited extraction of patterns inside the dataset. Hybrid frameworks containing multiple deep learning algorithm is becoming the new mainstream in academia.

ICEEMDAN

In this research, the improved complete ensemble empirical mode decomposition with adaptive noise (ICEEMDAN) is served as the major module in the hybrid forecasting framework. It is considered as an improvement on empirical mode decomposition (EMD) which decomposes the wind directions in the temporal domain (Colominas et al., 2014).

The time-series of wind direction can be expressed as the sum of multiple IMFs and the residual after the ICEEMDAN decomposition which can be expressed in **Eq. 3** as follows:

$$H(t) = \sum_{j=1}^{n} IMF_j(t) + r(t) \tag{3}$$

The amplitude energy $E_1, E_2, \ldots, E_n$ of the IMFs is calculated as **Eq. 4**:

$$E_j = \sum_{k=1}^{N} \left|IMF_j(k)\right|^2 \tag{4}$$

where N denotes the total number of sampling points of the jth IMF. Assuming that the energy carried by $r(t)$ can be ignored, the total energy of the transformed direction series can be expressed as **Eq. 5** as follows:

$$E = \sum\nolimits_{j=1}^{n} \sum\nolimits_{k=1}^{N} \left|IMF_j(k)\right|^2 \tag{5}$$

To remain the data in the same magnitude, the amplitude of the IMFs is normalized to facilitate the subsequent calculations and the impact of singular data has been reduced. Hence, the energy entropy of the ICEEMDAN framework can be expressed as **Eq. 6** below:

$$E = -\sum_{i=1}^{n} p_j \ln p_j \tag{6}$$

Compared with other decomposition methods, the ICEEMDAN can not only reduce the noise in the original time-series data but also reduce the residual spurious pattern problems based by signal overlap. Thus, the decomposed subseries gains more orthogonality among each other and it can provide more accurate reconstruction of the original series.

Short-Term Wind Direction Forecasting Using ICEEMDAN

To integrate the wind direction series with the ICEEMDAN modules, the implementations are introduced as follows (Duan et al., 2021):

Step 1: Compute the local means of realizations using the EMD algorithm described in **Eq. 7**:

$$x^i = x + \beta_0 E_1\left(w^i\right) \tag{7}$$

where $\beta_0 = \varepsilon_0 \sigma(x)/\sigma(E_1(w^i))$; $\sigma()$ compute the standard deviation; and ε_0 is the reciprocal of the desired signal-to-noise ratio between the first added noise and the analyzed signal.

Step 2: Compute residual term R_1 in the first component using **Eq. 8**:

$$R_1 = M\left(x^i\right) \tag{8}$$

Step 3: Compute the first mode at the first stage (k = 1) using **Eq. 9**:

$$d_1 = x - R_1 \tag{9}$$

Step 4: Estimate the second residue as the average of local means of the realizations $R_1 + \beta_1 E_2(w^i)$ and then define the second mode using **Eq. 10** as follows:

$$d_2 = R_1 - M\left(R_1 + \beta_1 E_2\left(w^i\right)\right) \tag{10}$$

Step 5: For the other terms (k = 3, . . . ,K) of residuals, they can be computed by **Eq. 11**:

$$R_k = M\left(R_{k-1} + \beta_{k-1} E_k\left(w^i\right)\right) \tag{11}$$

Step 6: Compute the other terms (k = 3, . . . ,K) of the mode by **Eq. 12**:

$$d_k = R_{k-1} - R_k \tag{12}$$

Step 7: Implement step 4 for the next iteration.

For the transformed wind direction series, the IMF components are obtained *via* the above steps which can be illustrated by the diagram presented in **Figure 4**.

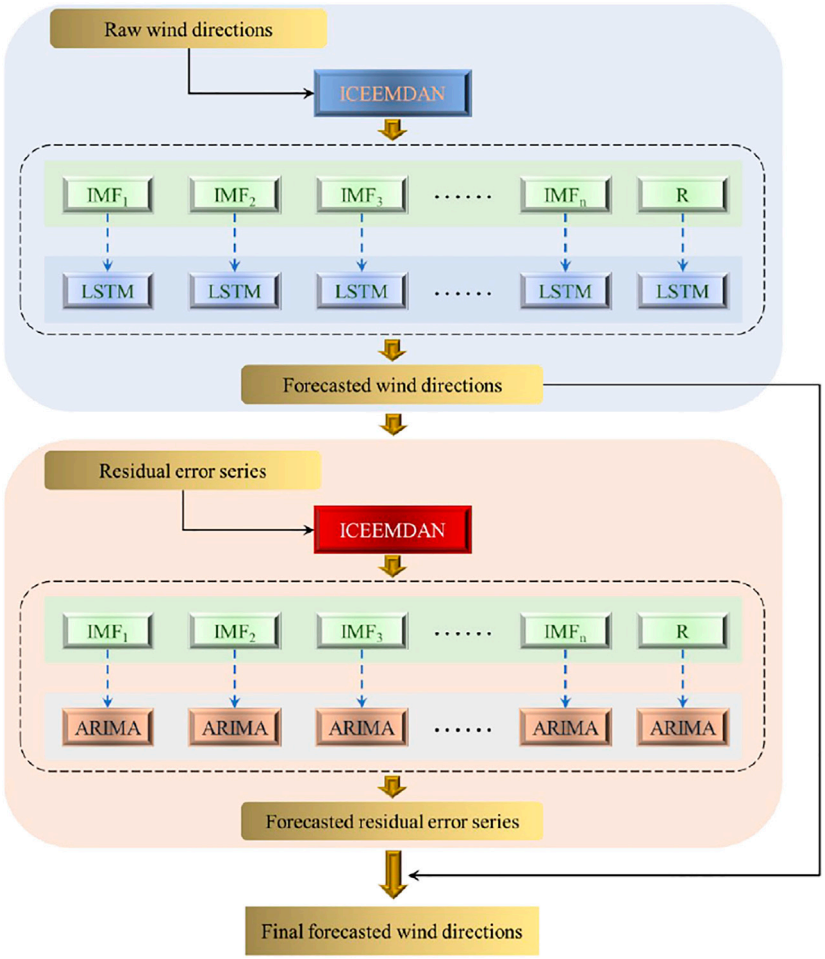

FIGURE 4 | Diagrams of ICEEMDAN modules.

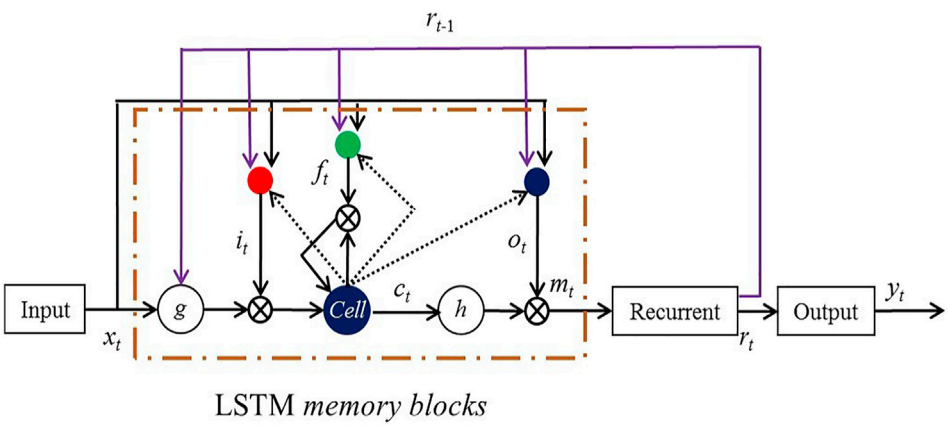

FIGURE 5 | Autocorrelation analysis of time-series wind direction data.

Long-Short-Term Memory Recurrent Neural Network

A major drawback of the classical deep neural networks is that they do not have memory of the past periods. The time series information such as the past clusters of seasonal patterns and seasonal trend may not be reflected (Lee et al. 1993). Introduced by Hochreiter and Schmidhuber (1997) and Gers et al. (2003), the long-short-term memory recurrent neural network (LSTM-RNN) matches the needs and it is used in this paper to predict wind direction.

The long-short-term memory recurrent neural network (LSTM-RNN) contains units called memory blocks composed of memory cells with self-connections storing temporal states. Each memory block includes an input and output gate. The input gate controls the flow of input data into the cell. The output gate controls the output data flow into the rest of the network (Sak et al. 2014). In addition, the LSTM-RNN has peephole connections (Gers et al. 2003) from its internal cells to the gates in the same cell to learn precise timing of the output. The architecture of LSTM-RNN is illustrated in **Figure 5**.

With a long-short-term memory recurrent neural network (LSTM-RNN) architecture, the mapping from an input to an output layer is iteratively computed from **Eqs 13–18** (Gers et al. 2003).

$$\boldsymbol{i}_t = sig(\boldsymbol{W}_{ix}\boldsymbol{x}_t + \boldsymbol{W}_{im}\boldsymbol{m}_{t-1} + \boldsymbol{W}_{ic}\boldsymbol{c}_{t-1} + \boldsymbol{b}_i) \tag{13}$$

$$\boldsymbol{f}_t = sig\left(\boldsymbol{W}_{fx}\boldsymbol{x}_t + \boldsymbol{W}_{fm}\boldsymbol{m}_{t-1} + \boldsymbol{W}_{ic}\boldsymbol{c}_{t-1} + \boldsymbol{b}_f\right) \tag{14}$$

$$\boldsymbol{c}_t = \boldsymbol{f}_t \circ \boldsymbol{c}_{t-1} + \boldsymbol{i}_t \circ g(\boldsymbol{W}_{cx}\boldsymbol{x}_t + \boldsymbol{W}_{cm}\boldsymbol{m}_{t-1} + \boldsymbol{b}_c) \tag{15}$$

$$\boldsymbol{o}_t = sig(\boldsymbol{W}_{ox}\boldsymbol{x}_t + \boldsymbol{W}_{om}\boldsymbol{m}_{t-1} + \boldsymbol{W}_{oc}\boldsymbol{c}_t + \boldsymbol{b}_o) \tag{16}$$

$$\boldsymbol{m}_t = \boldsymbol{o}_t \circ h(\boldsymbol{c}_t) \tag{17}$$

$$\boldsymbol{y}_t = \phi\left(\boldsymbol{W}_{ym}\boldsymbol{m}_t + \boldsymbol{b}_y\right) \tag{18}$$

where: W are the weight matrices (i.e., W_{ix} is the weight matrix from the input to the input layer; W_{ic}, W_{fc}, W_{oc} are diagonal weight matrices of the peephole connections (Gers et al., 2003)); b_i,b_f,b_o, and b_c are the bias vectors; m is the cell output activation vector; *sig* () is the sigmoid function; i, f, o, and c are the input gate, forget gate, output gate, and cell activation vectors, respectively, with all having the same size as the cell output activation vector m; $\circ$ is the element-wise product of the vectors; and g () and h () are the cell input and cell output activation functions, respectively.

Benchmarking Machine Learning Algorithms

Comparative analysis is performed in this research against the other benchmarking popular deep learning algorithms. All algorithms tested here are using the same ICEEMDAN framework as described in Section "Short-term Wind Direction Forecasting using ICEEMDAN". The benchmarking deep learning algorithms compared includes deep neural network (DNN) (Xu et al., 2018; Sun et al., 2020; Yi and Xu, 2020), deep belief network (DBN) (Ouyang et al., 2019; Li et al., 2020), kernel-based extreme learning machine (KELM) (Li et al., 2018; Ouyang et al., 2018), and gated recurrent unit network (GRU) (Pan et al., 2019; Tang and Zhang, 2019).

The DNN is a fully connected feedforward network that consists of a cascade of multiple layers and hidden units. It's structure with multiple processing layers enables it to handle highly nonlinear patterns inside the dataset. The deep temporal representations in the temporal domain can be effectively extracted by DNN.

Similar to DNN, the DBN consists of multiple layers of restricted Boltzmann machines (RBMs). It also contains a supervised regression layer stacked on the top of all RMBs for classification or regression tasks. Inside each RBM, it contains an input layer and a hidden layer with hidden-to-all-visible connections.

The ELM is a single hidden layer feedforward network. Instead of conventional back-propagation, it uses Penn-Moore pseudo-inverse to compute the wights between the hidden layer and output layer. The KELM is the improvement of vanilla ELM which uses the kernel matrix to replace the randomly initialized weights between the input layer and output layer. The most popular applied kernel functions include RBF, linear function, and polynomial function.

The GRU is another type of recurrent neural network other than LSTM-RNN proposed by Cho et al. (2014). In a typical GRU unit, it has one less gate than the LSTM unit and consists of two gates: the reset gate and the update gate. Hence, the GRU is also popular in modeling time-series dataset.

Measurement Matrices

To assess prediction accuracy of the proposed deep learning model, four metrics are computed: the MAE [Mean absolute error (**Eq. 19**)], the MAPE [Mean absolute percentage error (**Eq. 20**)], the MSE [Mean square error (**Eq. 21**)], and the RMSE [Root mean square error (**Eq. 22**)].

$$\mathrm{MAE} = \frac{1}{N}\sum_{i=1}^{N}\left|o_j - t_j\right| \tag{19}$$

$$\mathrm{MAPE} = \frac{1}{N}\sum_{i=1}^{N}\left|\frac{o_j - t_j}{t_j}\right| \tag{20}$$

$$\mathrm{MSE} = \frac{1}{N}\sum_{j=1}^{N} o_j - t_j^2 \tag{21}$$

$$\mathrm{RMSE} = \sqrt{\frac{1}{N}\sum_{j=1}^{N} o_j - t_j^2} \tag{22}$$

where: o_j is the jth predicted wind direction; t_j is the jth measured wind direction; and N denotes total number of samples.

Error Correction

To improve the forecasting accuracy, the error correction is implemented in this research. First, after the forecasting outcome produced by each LSTM-RNN, the error series E(t) of the training dataset can be computed by comparing the original transformed wind direction series. The step can be expressed in **Eq. 23** as follows:

$$E(t) = W_{LSTM}(t) - W_{Actual}(t) \tag{23}$$

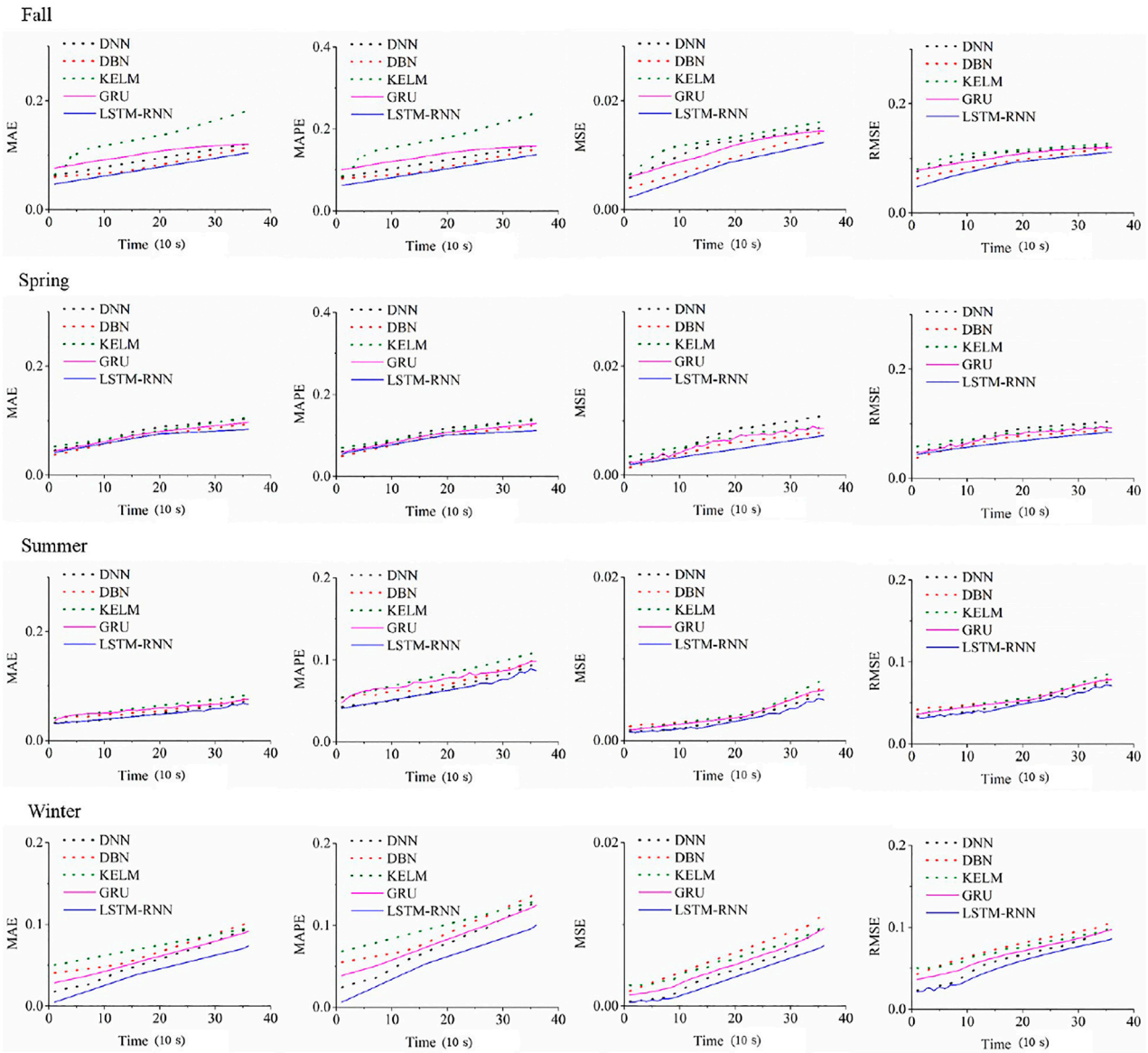

FIGURE 6 | Performance of all measurement metrices with various prediction horizons in four seasons.

where $W_{LSTM}(t)$ is the final forecasted transformed series in the first module; and $W_{Actual}(t)$ is the actual transformed wind direction series after bilinear transformation.

The forecasted errors of wind direction series E(t) are oscillatory in the time-series domain (Wasynczuk et al., 1981). The relationship between oscillatory and decaying property of the wind direction errors can be represented by an ARIMA model which predicts the errors. In detail, the ARIMA can be constructed by computing autocorrelation expressed with the autocorrelation factor (ACF) (See. **Eq. 24**) and the partial autocorrelation factor (PACF)) (See. **Eq. 25**). Here, Cov() denotes the covariance; Var() denotes the variance; and *Corr* () denotes the Pearson's correlation coefficient.

$$\rho_k = \frac{Cov(E(t), E(t-k))}{Var(E(t))} \tag{24}$$

$$\rho_k = Corr(E(t), E(t-k) | E(t-1), \ldots, E(t-k+1)) \tag{25}$$

For each IMF, an ARIMA model is developed and then all outcomes of each ARIMA are integrated to obtain the final error series. Last, as illustrated in **Figure 4**, the final prediction is achieved by **Eq. 26** as follows:

$$\widehat{W_{Final}(t)} = \widehat{W_{LSTM}(t)} + \hat{E}(t) \tag{26}$$

where $\widehat{W_{LSTM}(t)}$ denotes the forecasting results from the LSTMs; $\hat{E}(t)$ denotes the errors forecasted by ARIMA models; and $\widehat{W_{Final}(t)}$ is the final forecasting outcomes.

TABLE 1 | Mape of the five algorithms for 2020 before error correction.

Season	Resolution (s)	Algorithm	Prediction horizon				Season	Resolution (s)	Algorithm	Prediction horizon			
			2 min	5 min	10 min	1 h				2 min	5 min	10 min	1 h
Spring	10	DNN	0.082	0.106	0.133	0.211	Summer	10	DNN	0.047	0.057	0.092	0.181
		DBN	0.072	0.09	0.121	0.207			DBN	0.056	0.064	0.097	0.182
		KELM	0.081	0.098	0.137	0.224			KELM	0.062	0.074	0.106	0.186
		GRU	0.077	0.095	0.125	0.211			GRU	0.059	0.07	0.095	0.181
		LSTM-RNN	**0.072**	**0.091**	**0.108**	**0.195**			LSTM-RNN	**0.047**	**0.056**	**0.084**	**0.171**
	20	DNN	0.088	0.112	0.139	0.269		20	DNN	0.049	0.061	0.099	0.221
		DBN	0.077	0.093	0.127	0.252			DBN	0.056	0.065	0.105	0.227
		KELM	0.085	0.102	0.141	0.273			KELM	0.065	0.077	0.113	0.228
		GRU	0.082	0.101	0.131	0.264			GRU	0.064	0.073	0.104	0.227
		LSTM-RNN	**0.076**	**0.094**	**0.117**	**0.231**			LSTM-RNN	**0.049**	**0.058**	**0.096**	**0.214**
	30	DNN	0.096	0.114	0.15	0.33		30	DNN	0.052	0.066	0.112	0.278
		DBN	0.082	0.099	0.139	0.316			DBN	0.058	0.072	0.116	0.277
		KELM	0.089	0.109	0.153	0.328			KELM	0.068	0.083	0.125	0.29
		GRU	0.087	0.105	0.142	0.311			GRU	0.063	0.078	0.116	0.286
		LSTM-RNN	**0.081**	**0.096**	**0.128**	**0.305**			LSTM-RNN	**0.051**	**0.063**	**0.108**	**0.261**
Fall	10	DNN	0.094	0.112	0.154	0.239	Winter	10	DNN	0.049	0.069	0.125	0.212
		DBN	0.079	0.095	0.145	0.226			DBN	0.06	0.078	0.134	0.213
		KELM	0.14	0.163	0.232	0.302			KELM	0.077	0.091	0.125	0.213
		GRU	0.109	0.128	0.153	0.232			GRU	0.055	0.073	0.12	0.209
		LSTM-RNN	**0.075**	**0.092**	**0.133**	**0.211**			LSTM-RNN	**0.035**	**0.053**	**0.097**	**0.183**
	20	DNN	0.098	0.116	0.156	0.285		20	DNN	0.053	0.072	0.127	0.247
		DBN	0.082	0.101	0.147	0.279			DBN	0.064	0.084	0.136	0.264
		KELM	0.145	0.167	0.224	0.365			KELM	0.08	0.094	0.131	0.256
		GRU	0.113	0.131	0.158	0.285			GRU	0.059	0.077	0.124	0.243
		LSTM-RNN	**0.079**	**0.095**	**0.137**	**0.266**			LSTM-RNN	**0.041**	**0.057**	**0.102**	**0.234**
	30	DNN	0.102	0.124	0.168	0.364		30	DNN	0.058	0.084	0.14	0.314
		DBN	0.086	0.11	0.16	0.353			DBN	0.069	0.095	0.149	0.33
		KELM	0.149	0.179	0.237	0.459			KELM	0.083	0.101	0.142	0.313
		GRU	0.117	0.138	0.169	0.357			GRU	0.064	0.087	0.136	0.321
		LSTM-RNN	**0.083**	**0.104**	**0.149**	**0.332**			LSTM-RNN	**0.046**	**0.066**	**0.114**	**0.276**

Bold only shows the optimal solution results.

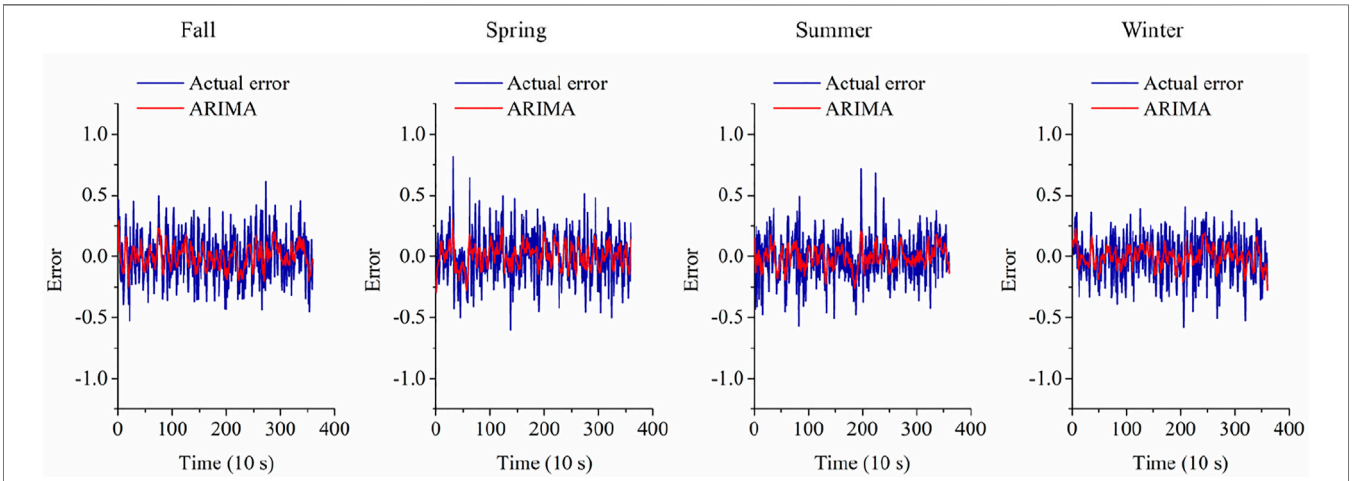

FIGURE 7 | Actual error versus forecasted error by ARIMA models.

EXPERIMENTAL RESULTS

Training Strategies

In this section, computational experience with models predicting wind direction is presented. Wind data from four seasons, spring, summer, fall, and winter are used. Prediction of wind direction is conducted using dataset at 10, 20, and 30 s resolution. The prediction horizons are 2, 5, 10 min, and 1 h. The prediction model is expressed in **Eqs 27–29**.

$$\boldsymbol{Y} = f(\boldsymbol{D}) \tag{27}$$

TABLE 2 | Mape of the five algorithms for 2020 after error correction.

Season	Resolution (s)	Algorithm	Prediction horizon				Season	Resolution (s)	Algorithm	Prediction horizon			
			2 min	5 min	10 min	1 h				2 min	5 min	10 min	1 h
Spring	10	DNN	0.082	0.106	0.133	0.211	Summer	10	DNN	0.047	0.057	0.092	0.181
		DBN	0.072	0.094	0.121	0.207			DBN	0.056	0.064	0.097	0.182
		KELM	0.081	0.098	0.137	0.224			KELM	0.062	0.074	0.106	0.186
		GRU	0.077	0.095	0.125	0.211			GRU	0.059	0.077	0.095	0.181
		LSTM-RNN	**0.072**	**0.091**	**0.108**	**0.195**			LSTM-RNN	**0.047**	**0.056**	**0.084**	**0.171**
	20	DNN	0.088	0.117	0.139	0.269		20	DNN	0.049	0.061	0.099	0.221
		DBN	0.077	0.093	0.127	0.252			DBN	0.056	0.065	0.105	0.227
		KELM	0.085	0.102	0.141	0.273			KELM	0.065	0.077	0.113	0.228
		GRU	0.082	0.146	0.131	0.264			GRU	0.064	0.073	0.104	0.227
		LSTM-RNN	**0.076**	**0.094**	**0.117**	**0.231**			LSTM-RNN	**0.049**	**0.058**	**0.096**	**0.214**
	30	DNN	0.096	0.114	0.154	0.332		30	DNN	0.052	0.066	0.112	0.278
		DBN	0.082	0.099	0.139	0.316			DBN	0.058	0.072	0.116	0.277
		KELM	0.089	0.109	0.153	0.328			KELM	0.068	0.083	0.125	0.294
		GRU	0.087	0.105	0.142	0.311			GRU	0.063	0.078	0.116	0.286
		LSTM-RNN	**0.081**	**0.096**	**0.128**	**0.305**			LSTM-RNN	**0.051**	**0.063**	**0.108**	**0.261**
Fall	10	DNN	0.071	0.096	0.117	0.204	Winter	10	DNN	0.036	0.056	0.092	0.181
		DBN	0.06	0.083	0.113	0.214			DBN	0.044	0.065	0.098	0.182
		KELM	0.107	0.142	0.176	0.254			KELM	0.056	0.076	0.092	0.179
		GRU	0.083	0.115	0.116	0.202			GRU	0.041	0.061	0.088	0.179
		LSTM-RNN	**0.057**	**0.079**	**0.101**	**0.185**			LSTM-RNN	**0.026**	**0.044**	**0.071**	**0.161**
	20	DNN	0.074	0.121	0.124	0.255		20	DNN	0.039	0.06	0.099	0.221
		DBN	0.062	0.086	0.117	0.243			DBN	0.047	0.071	0.106	0.234
		KELM	0.117	0.144	0.175	0.319			KELM	0.059	0.079	0.101	0.215
		GRU	0.086	0.114	0.125	0.239			GRU	0.044	0.064	0.097	0.212
		LSTM-RNN	**0.061**	**0.083**	**0.109**	**0.228**			LSTM-RNN	**0.03**	**0.048**	**0.081**	**0.205**
	30	DNN	0.077	0.107	0.135	0.305		30	DNN	0.043	0.074	0.111	0.275
		DBN	0.065	0.095	0.129	0.291			DBN	0.051	0.079	0.118	0.277
		KELM	0.113	0.155	0.187	0.387			KELM	0.061	0.084	0.113	0.285
		GRU	0.089	0.119	0.136	0.314			GRU	0.047	0.072	0.108	0.274
		LSTM-RNN	**0.063**	**0.089**	**0.122**	**0.282**			LSTM-RNN	**0.034**	**0.055**	**0.092**	**0.242**

Bold only shows the optimal solution results.

$$\boldsymbol{D} = [\boldsymbol{D}_{t-1}, \boldsymbol{D}_{t-2}, \boldsymbol{D}_{t-3}, \boldsymbol{D}_{t-4}, \boldsymbol{D}_{t-5}, \boldsymbol{D}_{t-6}] \tag{28}$$

$$\boldsymbol{D}_{t-i} = (\boldsymbol{x}_{t-i}, \ldots, \boldsymbol{x}_{t-i-359}) \tag{29}$$

where: f(D) represents the whole framework illustrated in **Figure 4**; $\boldsymbol{D}_{t-i}$ is the ith lagged vector containing 1 hour of the historical wind direction data; and $\boldsymbol{x}_{t-i}$ denotes the ith lagged transformed wind direction series.

The wind speed and wind direction are 10 s data. One hour of data (360 data points) is used as the input vector. The six-time lagged vectors containing 1 hour of the historical wind direction data are selected as the input vectors. The wind direction of the 2, 5, 10 min, and 1 h horizon is predicted. The input vector is normalized beforehand and the predicted values are inverse-normalized.

Short-Term Predictions

Based on the training strategy stated in Section "Training Strategies", experiments with the five selected algorithms have been performed. In all experiments, the wind direction has been predicted for the next 2, 5, 10 min, and 1 h. Experiments have been conducted in each of the four seasons of 2020.

The prediction accuracy results in **Figure 6** demonstrate that the long-short-term memory recurrent neural network (LSTM-RNN) performs better over short-term horizons than the other algorithms. Since the LSTM-RNN contains long/short term memory, it produces smaller prediction errors than the DNN, DBN, KELM, and GRU. For the short-term horizons (i.e., 2 and 5 min), prediction accuracy of all five algorithms is similar. However, the LSTM-RNN provides more promising results for longer-term predictions (i.e., 10 min and 1 h) of wind direction.

The prediction accuracy in four seasons varies. In the fall and spring season, the prediction errors are larger than the errors in the summer and winter season. This is due to a larger variability of the wind direction over short-term horizons. Hence, training specific prediction models in different seasons is necessary.

Table 1 provide the MAPE for different resolution data (i.e., 10, 20, 30 s) and different prediction horizons (i.e., 2, 5, 10 min, and 1 h) before the error correction. Obviously, the MAPE errors are smaller for the 10 s data than for 20 and 30 s. With the increase of the prediction horizon, the MAPEs increase. The LSTM-RNN algorithm has the smallest MAPE at all resolutions and all prediction horizons. Therefore, it is an effective algorithm for wind direction prediction at short-term horizons.

Error Correction

To correct the errors made by the ICEEMDAN modules, the ARIMA model has been developed to forecast the errors. In the

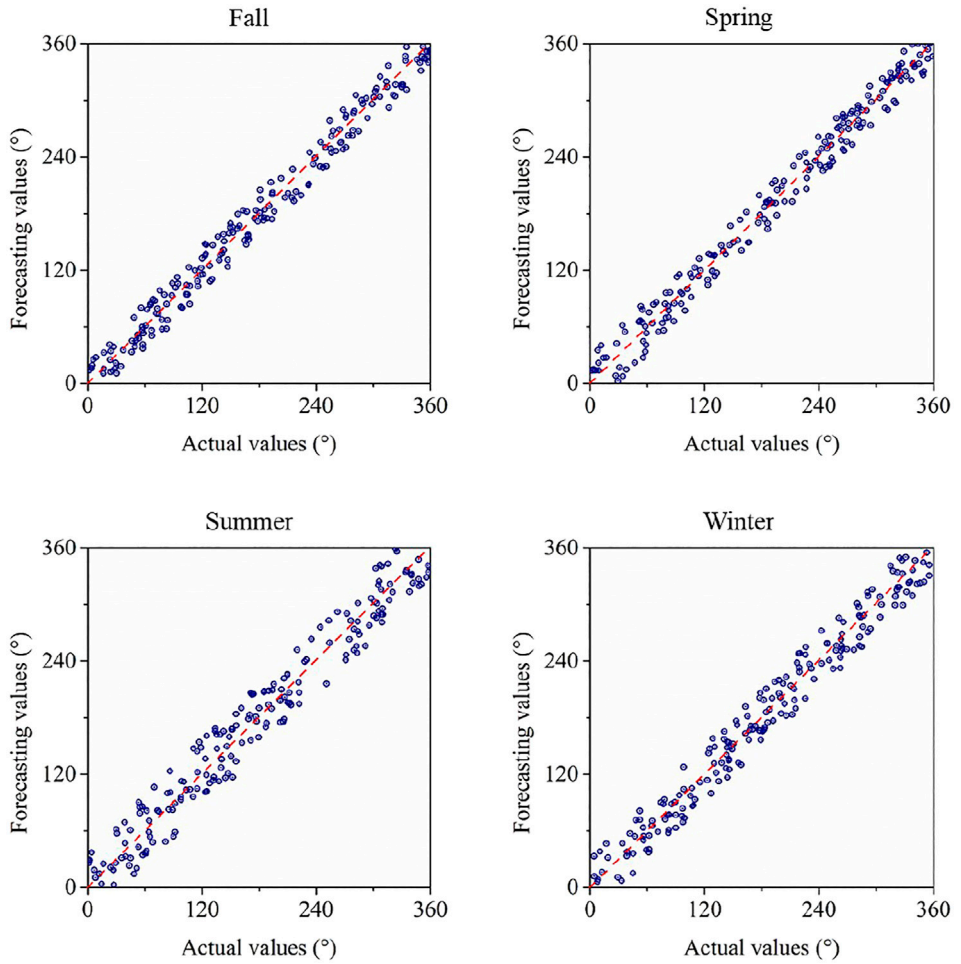

FIGURE 8 | Actual angular values versus forecasting angular values.

TABLE 3 | Angular prediction error at four seasons.

Season	Fall	Winter	Spring	Summer
MAE (2 min)	1.88°	1.67°	1.92°	1.65°
MAPE (2 min)	0.86%	0.79%	0.95%	0.74%
MAE (5 min)	5.18°	5.01°	5.57°	4.93°
MAPE (5 min)	2.37%	2.28%	2.75%	2.21%
MAE (10 min)	6.53°	6.25°	6.97°	6.10°
MAPE (10 min)	3.18%	3.01%	3.36%	2.96%
MAE (1 h)	10.64°	9.05°	10.58°	9.34°
MAPE (1 h)	5.62%	4.39%	5.29%	4.71%

second part of **Figure 4**, To illustrate this step, the forecasted errors using ARIMA versus the actual errors produced by LSTM-RNNs are visualized in **Figure 7**. It is obvious that the aggregated results from ARIMAs can represent the temporal trend of the forecasted errors produced from the first component of the proposed framework.

Table 2 provides the MAPE for different resolution data (i.e., 10, 20, 30 s) and different prediction horizons (i.e., 2, 5, 10 min, and 1 h) after the error correction. There exists significant performance for all algorithms tested with respect to the MAPE computed before and after error correction. It validates the effectiveness of implementing error correction in improving the forecasting accuracy of time-series dataset. Meanwhile, the LSTM produces the smallest errors which also demonstrates its superior performance in forecasting wind directions.

Error Analysis

The experiments reported in Section "Short-term Predictions" have been conducted using the transformed wind direction data from four seasons. An inverse bilinear transformation, expressed in **Eq. 2**, is applied to transform the predicted transformed wind direction into the original angular range [0°, 360°]. The actual angular values versus the forecasted angular values by the proposed framework using ICEEMDAN and LSTM-RNN are presented in **Figure 8**. It can be seen that the majority of the forecasted values fall within a relatively small range with respect

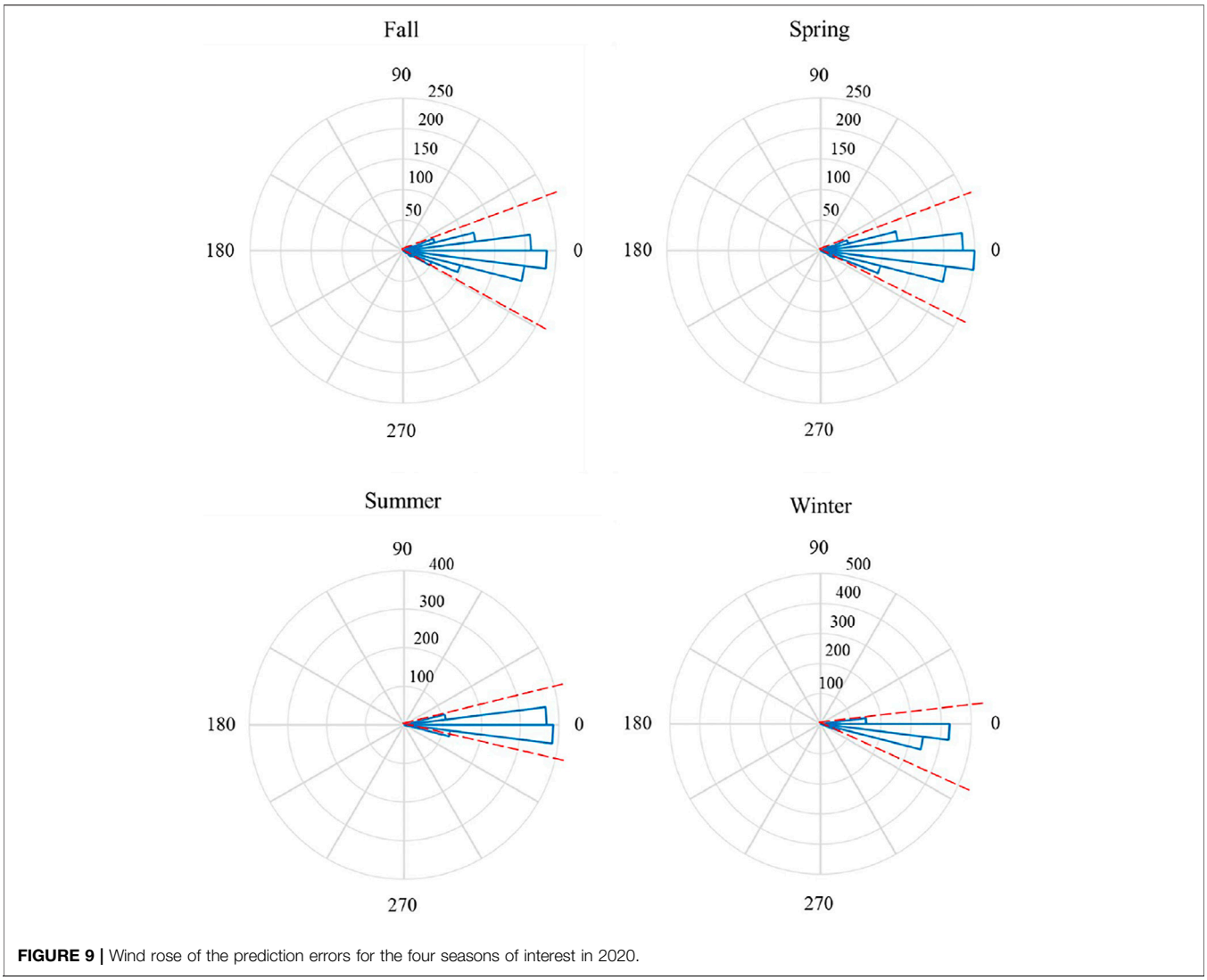

FIGURE 9 | Wind rose of the prediction errors for the four seasons of interest in 2020.

TABLE 4 | Angular prediction error at four seasons.

Season	Fall	Winter	Spring	Summer
MAE (2 min)	1.61°	1.63°	1.62°	1.59°
MAPE (2 min)	0.79%	0.78%	0.80%	0.76%
MAE (5 min)	4.94°	4.41°	5.19°	4.51°
MAPE (5 min)	2.08%	1.93%	2.58%	1.97%
MAE (10 min)	5.92°	5.86°	6.18°	5.94°
MAPE (10 min)	2.79%	2.78%	2.81%	2.71%
MAE (1 h)	9.81°	9.02°	9.75°	9.32°
MAPE (1 h)	4.77%	4.37%	4.92%	4.74%

to the actual values. It demonstrates the proposed framework can sufficiently provide accurate forecasting performances.

In this section, performance of the ICEEMDAN framework integrated with the long-short-term memory recurrent neural network (LSTM-RNN) for prediction of wind direction at four seasons is discussed. The prediction error of the inverse transformed wind direction at 2, 5, 10 min, and 1 h horizons are presented in **Table 3**. The mean absolute error (MAE) and mean absolute percentage error (MAPE) of wind direction are smaller in the summer and winter.

The wind direction error shows less variability over short horizons. The changes of a nacelle position are usually made within 5 min and the prediction error should be under 3% (Ouyang et al., 2017). A control chart is applied to monitor the prediction error and facilitate changing the nacelle position. A control chart with lower and upper limits enables monitoring the yaw error. Any prediction error that exceeds the bound (i.e., 3%) may trigger a change of the nacelle position. The final forecasting errors in the angular perspectives are illustrated in **Figure 9**.

Validation

The long-short-term memory recurrent neural network (LSTM-RNN) has been demonstrated to perform better than other algorithms. To validate the effectiveness and robustness of the LSTM-RNN, the data collected from another wind farm located

in Shandong Province in the year 2020 has been used. The experiments are conducted following the similar training strategies as described in Section "Data Analysis". The computational results are presented in **Table 4**.

The prediction error (see **Table 4**) in winter and summer seasons of 2020 from the wind farm in Shandong Province produced by the LSTM-RNN is similar to the one based on the 2020 data (see **Table 3**) in the wind farm in Inner Mongolia. More accurate performance has been observed in the fall and spring seasons with two prevailing wind directions. The favorable prediction error validates the effectiveness and robustness of the LSTM-RNN to predict the nacelle orientation.

CONCLUSION

A hybrid short-term forecasting framework to orient nacelle based on the predicted wind direction was presented. Industrial data collected from a wind farm in Inner Mongolia, China was utilized to train and validate the prediction models. A bilinear transformation was applied to transform the wind direction data from an angular variable into a continuous time-series. The forecasting framework was developed using ICEEMDAN integrated with LSTM-RNN. Also, the error corrections are implemented to improve the forecasting accuracy. The wind direction was predicted at short-term horizons, i.e., 2, 5, 10 min, and 1 h. Five algorithms, the deep neural network, deep belief network, kernel-based extreme learning machine, gated recurrent unit network, and long-short-term memory recurrent neural network were applied to predict wind direction at short-term horizons. The results of performance analysis of the five algorithms at four seasons were reported.

It was demonstrated that the long-short-term memory recurrent neural network outperformed the other four algorithms tested to predict wind direction. The results presented are of paramount importance in yaw control and can improve the efficiency of energy extraction process.

DATA AVAILABILITY STATEMENT

The raw data supporting the conclusions of this article will be made available by the authors, without undue reservation.

AUTHOR CONTRIBUTIONS

HL conceptualized the study, contributed to the study methodology, and wrote the original draft. JD contributed to the study methodology, data curation and investigation. PF contributed to data analysis and investigation. HL contributed to software and formal analysis. CP and DA contributed to investigation and writing-original draft. QC contributed to editing. All authors have read and agreed to the published version of the manuscript.

FUNDING

This research is supported by the "Miaozi project" of scientific and technological innovation in Sichuan Province, China (Grant No. 2021090), the National Key Research and Development Program of China (2018YFC1505105), the Opening fund of State Key Laboratory of Geohazard Prevention and Geoenvironment Protection (Chengdu University of Technology) (Grant No. SKLGP 2021K014), and the Project from Sichuan Mineral Resources Research Center (SCKCZY2021-YB009) the Project of remote sensing identification and monitoring of geological hazards in Sichuan province, CN (2020) (Grant No. 510201202076888).

REFERENCES

Amin, C. M., Sami, F. M., and Trzynadlowski, A. M. (2018). Wind Speed and Wind Direction Forecasting Using echo State Network with Nonlinear Functions. *Renew. Energ.* 131 (2), 879–889. doi:10.1016/j.renene.2018.07.060

Bilgili, M., Sahin, B., and Yasar, A. (2007). Application of Artificial Neural Networks for the Wind Speed Prediction of Target Station Using Reference Stations Data. *Renew. Energ.* 32 (14), 2350–2360. doi:10.1016/j.renene.2006.12.001

Castino, F., Festa, R., and Ratto, C. F. (1998). Stochastic Modelling of Wind Velocities Time Series. *J. Wind Eng. Ind. Aerodynamics* 74-76, 141–151. doi:10.1016/s0167-6105(98)00012-9

Cho, K., Van Merriënboer, B., Gulcehre, C., Bahdanau, D., Bougares, F., Schwenk, H., et al. (2014). *Learning Phrase Representations Using RNN Encoder-Decoder for Statistical Machine Translation*. doi:10.3115/v1/D14-1179

Colominas, M. A., Schlotthauer, G., and Torres, M. E. (2014). Improved Complete Ensemble EMD: A Suitable Tool for Biomedical Signal Processing.. *Biomed. Signal Proce. Contr.* 146, 19–29.

Davies, A. (1974). Bilinear Transformation of Polynomials. *IEEE Trans. Circuits Syst.* 21 (6), 792–794. doi:10.1109/tcs.1974.1083929

Duan, J., Zuo, H., Bai, Y., Duan, J., Chang, M., and Chen, B. (2021). Short-term Wind Speed Forecasting Using Recurrent Neural Networks with Error Correction. *Energy* 217, 119397. doi:10.1016/j.energy.2020.119397

Erdem, E., and Shi, J. (2011). ARMA Based Approaches for Forecasting the Tuple of Wind Speed and Direction. *Appl. Energ.* 88 (4), 1405–1414. doi:10.1016/j.apenergy.2010.10.031

Gers, F. A., Schraudolph, N. N., and Schmidhuber, J. (2003). Learning Precise Timing with Lstm Recurrent Networks. *J. Machine Learn. Res.* 3 (1), 115–143.

Groutage, F., Volfson, L., and Schneider, A. (2003). S-plane to Z-Plane Mapping Using a Simultaneous Equation Algorithm Based on the Bilinear Transformation. *IEEE Trans. Automatic Control.* 32 (7), 635–637. doi:10.1109/TAC.1987.1104664

Hochreiter, S., and Schmidhuber, J. (1997). Long Short-Term Memory. *Neural Comput.* 9 (8), 1735–1780. doi:10.1162/neco.1997.9.8.1735

Hu, Q., Zhang, R., and Zhou, Y. (2016). Transfer Learning for Short-Term Wind Speed Prediction with Deep Neural Networks. *Renew. Energ.* 85 (JAN), 83–95. doi:10.1016/j.renene.2015.06.034

Jury, E. (1973). Remarks on "The Mechanics of Bilinear Transformation". *IEEE Trans. Audio Electroacoust.* 21 (4), 380–382. doi:10.1109/tau.1973.1162485

Khosravi, A., Koury, R. N. N., Machado, L., and Pabon, J. J. G. (2018). Prediction of Wind Speed and Wind Direction Using Artificial Neural Network, Support Vector Regression and Adaptive Neuro-Fuzzy Inference System. *Sustainable Energ. Tech. Assessments* 25, 146–160. doi:10.1016/j.seta.2018.01.001

Kodama, K., and Burls, N. J. (2019). An Empirical Adjusted Enso Ocean Energetics Framework Based on Observational Wind Power in the Tropical pacific. *Clim. Dyn.* 53 (5), 3271–3288. doi:10.1007/s00382-019-04701-8

Kou, Z., Yang, F., Wu, J., and Li, T. (2020). Application of ICEEMDAN Energy Entropy and AFSA-SVM for Fault Diagnosis of Hoist Sheave Bearing. *Entropy* 22 (12), 1347. doi:10.3390/e22121347

Lecun, Y., Bengio, Y., and Hinton, G. (2015). Deep Learning. *Nature* 521 (7553), 436–444. doi:10.1038/nature14539

Lee, T.-H., White, H., and Granger, C. W. J. (1993). Testing for Neglected Nonlinearity in Time Series Models. *J. Econom.* 56 (3), 269–290. doi:10.1016/0304-4076(93)90122-l

Li, H., Xu, Q., He, Y., and Deng, J. (2018). Prediction of Landslide Displacement with an Ensemble-Based Extreme Learning Machine and Copula Models. *Landslides* 15 (10), 2047–2059. doi:10.1007/s10346-018-1020-2

Li, H., Xu, Q., He, Y., Fan, X., and Li, S. (2020). Modeling and Predicting Reservoir Landslide Displacement with Deep Belief Network and EWMA Control Charts: a Case Study in Three Gorges Reservoir. *Landslides* 17 (3), 693–707. doi:10.1007/s10346-019-01312-6

Liu, D., Niu, D., Wang, H., and Fan, L. (2014). Short-term Wind Speed Forecasting Using Wavelet Transform and Support Vector Machines Optimized by Genetic Algorithm. *Renew. Energ.* 62, 592–597. doi:10.1016/j.renene.2013.08.011

Liu, H., Shi, J., and Erdem, E. (2010). Prediction of Wind Speed Time Series Using Modified Taylor Kriging Method. *Energy* 35 (12), 4870–4879. doi:10.1016/j.energy.2010.09.001

Masseran, N., Razali, A. M., Ibrahim, K., and Latif, M. T. (2013). Fitting a mixture of von Mises distributions in order to model data on wind direction in Peninsular Malaysia. *Energ. Convers. Manag.* 72, 94–102. doi:10.1016/j.enconman.2012.11.025

Mcwilliams, B., and Sprevak, D. (1982). The Simulation of Hourly Wind Speed and Direction. *Mathematics Comput. Simulation* 24 (1), 54–59. doi:10.1016/0378-4754(82)90050-7

Mohandes, M. A., Halawani, T. O., Rehman, S., and Hussain, A. A. (2004). Support Vector Machines for Wind Speed Prediction. *Renew. Energ.* 29 (6), 939–947. doi:10.1016/j.renene.2003.11.009

Ouyang, T., He, Y., and Huang, H. (2018). Monitoring Wind Turbines' Unhealthy Status: a Data-Driven Approach. *IEEE Trans. Emerging Top. Comput. Intelligence* 3 (2), 163–172. doi:10.1109/TETCI.2018.2872036

Ouyang, T., He, Y., Li, H., Sun, Z., and Baek, S. (2019). Modeling and Forecasting Short-Term Power Load with Copula Model and Deep Belief Network. *IEEE Trans. Emerg. Top. Comput. Intell.* 3 (2), 127–136. doi:10.1109/tetci.2018.2880511

Ouyang, T., Kusiak, A., and He, Y. (2017). Predictive Model of Yaw Error in a Wind Turbine. *Energy* 123, 119–130. doi:10.1016/j.energy.2017.01.150

Pan, C., Yi, J., Yin, C., Yu, J., and Li, X. (2019). Joint 3D UAV Placement and Resource Allocation in Software-Defined Cellular Networks with Wireless Backhaul. *IEEE Access* 7, 104279–104293. doi:10.1109/access.2019.2927521

Peng, G., Si, C. A., Jc, B., and Di, C. (2020). Wind Direction Fluctuation Analysis for Wind Turbines. *Renew. Energ.* 162, 1026–1035. doi:10.1016/j.renene.2020.07.137

Rong, H., Gao, Y., Guan, L., Zhang, Q., Zhang, F., and Li, N. (2019). Gam-based Mooring Alignment for Sins Based on an Improved Ceemd Denoising Method. *Sensors* 19 (16), 3564. doi:10.3390/s19163564

Sak, H., Senior, A., and Beaufays, F. (2014). *Long Short-Term Memory Based Recurrent Neural Network Architectures for Large Vocabulary Speech Recognition*. arXiv preprint arXiv:1402.1128

Santhosh, M., Venkaiah, C., and Vinod Kumar, D. M. (2018). Ensemble Empirical Mode Decomposition Based Adaptive Wavelet Neural Network Method for Wind Speed Prediction. *Energ. Convers. Manag.* 168, 482–493. doi:10.1016/j.enconman.2018.04.099

Sun, Z., He, Y., Gritsenko, A., Lendasse, A., and Baek, S. (2020). Embedded Spectral Descriptors: Learning the point-wise Correspondence Metric via Siamese Neural Networks. *J. Comput. Des. Eng.* 7 (1), 18–29. doi:10.1093/jcde/qwaa003

Tagliaferri, F., Viola, I. M., and Flay, R. G. J. (2015). Wind Direction Forecasting with Artificial Neural Networks and Support Vector Machines. *Ocean Eng.* 97, 65–73. doi:10.1016/j.oceaneng.2014.12.026

Tang, Z., and Zhang, Z. (2019). The Multi-Objective Optimization of Combustion System Operations Based on Deep Data-Driven Models. *Energy* 182, 37–47. doi:10.1016/j.energy.2019.06.051

Tang, Z., Zhao, G., and Ouyang, T. (2021). Two-phase Deep Learning Model for Short-Term Wind Direction Forecasting. *Renew. Energ.* 173, 1005–1016. doi:10.1016/j.renene.2021.04.041

Wasynczuk, O., Man, D. T., and Sullivan, J. P. (1981). Dynamic Behavior of a Class of Wind Turbine Generators during Random Wind Fluctuations. *IEEE Power Eng. Rev.* PER-1 (6), 47–48. doi:10.1109/mper.1981.5511593

Xu, W., Yi, J., Dasgupta, S., Cai, J. F., Jacob, M., and Cho, M. (2018). "Sepration-free Super-resolution from Compressed Measurements Is Possible: an Orthonormal Atomic Norm Minimization Approach," in 2018 IEEE International Symposium on Information Theory (ISIT) (IEEE), 76–80.

Yang, Z., and Wang, J. (2018). A Hybrid Forecasting Approach Applied in Wind Speed Forecasting Based on a Data Processing Strategy and an Optimized Artificial Intelligence Algorithm. *Energy* 160, 87–100. doi:10.1016/j.energy.2018.07.005

Yi, J., and Xu, W. (2020). Necessary and Sufficient Null Space Condition for Nuclear Norm Minimization in Low-Rank Matrix Recovery. *IEEE Trans. Inform. Theor.* 66 (10), 6597–6604. doi:10.1109/tit.2020.2990948

Zhang, W., Qu, Z., Zhang, K., Mao, W., Ma, Y., and Fan, X. (2017). A Combined Model Based on CEEMDAN and Modified Flower Pollination Algorithm for Wind Speed Forecasting. *Energ. Convers. Manag.* 136, 439–451. doi:10.1016/j.enconman.2017.01.022

Zhou, J., Shi, J., and Li, G. (2011). Fine Tuning Support Vector Machines for Short-Term Wind Speed Forecasting. *Energ. Convers. Manag.* 52 (4), 1990–1998. doi:10.1016/j.enconman.2010.11.007

Conflict of Interest: The authors declare that the research was conducted in the absence of any commercial or financial relationships that could be construed as a potential conflict of interest.

frontiers in Energy Research

BRIEF RESEARCH REPORT
published: 05 November 2021
doi: 10.3389/fenrg.2021.775519

Invalid Data Rejection of Audible Noise on AC Transmission Lines Based on Moving Window Kernel Principal Component Analysis

Ziyi Cheng[1,2], *Zhenhua Li*[1]*, *Yuehua Huang*[1], *Weifang Yao*[3] *and Huichun Xie*[4]

[1]Electrical Engineering and New Energy, China Three Gorges University, Yichang, China, [2]State Grid Chongqing Electric Power Company Construction Branch, Chongqing, China, [3]State Grid Anhui Electric Power Corporation Research Institute, Hefei, China, [4]China Electric Power Research Institute Co., Ltd. Wuhan Branch, Wuhan, China

The statistical characteristics of the nighttime noise data of 1000 kV AC transmission lines were investigated, the noise data of the Huainan-Shanghai 1000 kV AC transmission line collected at night (0:00 to 6:00) from September 25, 2015, to February 16, 2016, were statistically analyzed using the nonparametric statistical K-S test, and the outliers were detected using the moving window kernel principal component analysis (MWKPCA). The results show that after the ineffective data are removed by MWKPCA, the 5, 50, and 95% values of the data are basically unchanged. To a certain extent, the method proposed in this paper can remove the invalid audible noise (AN) data of 1000 kV AC transmission lines without affecting the subsequent study of AN, we use various machine learning algorithms to predict the A weight sound level (Awsl) before and after the invalid data rejection, and the results show that the invalid data rejection has contributed to the improvement of the transmission line AN Awsl prediction accuracy.

Keywords: effective data, AC, UHV transmission lines, audible noise, MWKPCA

OPEN ACCESS

Edited by:
Xun Shen,
Tokyo University of Agriculture and Technology, Japan

Reviewed by:
Hengrui Ma,
Qinghai University, China
Guangzheng Yu,
Shanghai University of Electric Power, China

***Correspondence:**
Zhenhua Li
Lizhenhua1993@163.com

Specialty section:
This article was submitted to Smart Grids, a section of the journal Frontiers in Energy Research

Received: *14 September 2021*
Accepted: *27 September 2021*
Published: *05 November 2021*

Citation:
Cheng Z, Li Z, Huang Y, Yao W and Xie H (2021) Invalid Data Rejection of Audible Noise on AC Transmission Lines Based on Moving Window Kernel Principal Component Analysis Front. Energy Res. 9:775519. doi: 10.3389/fenrg.2021.775519

INTRODUCTION

Audible noise (AN) of transmission lines, as one of the design criteria of transmission lines, affects the conductor selection, corridor width, insulator string length, and conductor arrangement. However, in the process of collecting the transmission lines AN, there is a large amount of ambient noise, and the data collection is easily disturbed by the ambient noises. If the transmission lines AN is smaller than the ambient noises, then the ambient noises will probably become invalid data in the data set, and the invalid data will have an impact on the transmission line evaluation.

Previous research on transmission lines AN contains empirical formulas for transmission lines AN in various countries (Juette and Zaffanella, 1970; Trinh and Maruvada, 1977; Perry et al., 1979; Chartier and Stearns, 2007; Tang et al., 2010; Chen et al., 2012), analysis of transmission lines AN domain characteristics and frequency domain characteristics (Liu et al., 2018; Cheng et al., 2019), and transmission line design parameters, meteorological factors, environmental factors on transmission lines AN, and so on (Li et al., 2016; Guo et al., 2019; Zao et al., 2021; Xie et al., 2016; Du et al., 2016; Xie et al., 2017; Yang et al., 2016; Li et al., 2018; Pengfei et al., 2019). However, in order to solve the influence of ambient noises on data acquisition, Yuanqing Liu et al. studied the frequency spectrum of corona AN and ambient noises of positive and negative conductors of DC transmission lines at different voltages through corona cage test and studied the conversion relationship between

A-weighted sound level (Awsl) and 8 kHz component of DC transmission lines AN, so as to avoid the interference of ambient noises (Liu et al., 2014a). Yingyi Liu et al. studied the relationship between corona current and AN on transmission lines and summarized the empirical formula for calculating the A-weighted sound pressure level (Awsl) by corona current, so as to indirectly get the effective data of AN evading the ambient noises interference (Liu et al., 2019). Li Xebao et al. showed that, to accurately study the time-domain characteristics of the AN generated by single corona discharge, the ambient noise was removed by correlation analysis and impulse characteristics (Li et al., 2015). Liu Yuanqing et al. used a finite impulse response filter to reject the invalid data of AN on DC transmission lines. The above-mentioned research on the effective data of the AN of transmission lines is divided into two types: indirect acquisition of effective data and rejection of invalid data. The research on the rejection of invalid data uses methods for single-dimensional data, which directly process the original data of the sound signal or the Awsl, ignoring the connection between the individual octave components of the sound signal (Liu et al., 2014b). The above-mentioned studies on the effective data of AN on transmission lines are divided into two types: indirect acquisition of effective data and rejection of invalid data. The studies on the rejection of invalid data use methods for single-dimensional data, which directly process the original data of the sound signal and repair the sound pressure data disturbed by ambient noise, ignoring the connection between the individual octave band components of the sound signal. Therefore, this paper introduces a data-driven approach based on the determination of multidimensional data, and the data disturbed by environmental noise are directly eliminated.

Data-driven-based methods have more applications in power system stability, energy optimization and dispatch, voltage and current monitoring, transportation, etc. (Zhang and Luo, 2018; Zhu et al., 2019; Li et al., 2020; Yang et al., 2020; Shen and Raksincharoensak, 2021). In this paper, data consisting of 10 components of AN octave band from 16 Hz octave band to 8 kHz octave band and Awsl which are determined with moving window kernel principal component analysis (MWKPCA) by establishing the SPE statistic in the residual subspace of the principal component analysis with the T^2 statistic in the principal component subspace are used to evaluate AN invalid data, and the data that exceed the threshold of SPE statistic or T^2 statistic are excluded, so that the AN invalid data in the dataset are removed.

AN DISTRIBUTION CHARACTERISTICS

Noise data for a total of 69 days of the Huainan-Shanghai AC transmission line were collected at night (0:00 to 6:00) from September 25, 2015, to February 16, 2016. The conductor adopts 8×LGJ-630/45. Subconductor diameter is 33.6 mm. Subconductor spacing is 400 mm and the operating voltage is 1050 kV. The surface gradient of phase A, phase B, and phase C is 14.44, 14.82, and 14.73 kV/cm, respectively. The distribution characteristics of each octave band of AN and Awsl were analyzed using the K-S test (Kolmogorov-Smirnov test) one after another. The following hypothesis is made for the sample data H_0: the overall sample data is conformed to the normal distribution, and the alternative hypothesis H_1: the overall sample data from which the sample comes does not conform to normal distribution. The test statistic is defined as

$$D = \max\left(\left|f(x) - g(x)\right|\right) \tag{1}$$

where $f(x)$ is the cumulative probability of the sample value in the normal distribution and $g(x)$ is the actual cumulative probability.

Since the actual $f(x)$ and $g(x)$ are discrete values, **Equation 1** is modified to

$$D_m = \max_i\left(\left|f(x_{i-1}) - g(x_{i-1})\right|, \left|f(x_i) - g(x_i)\right|\right) \times \sqrt{n} \tag{2}$$

where n is the sample size. When the data size is large and the original hypothesis holds, D_M approximately conforms to the Kolmogorov distribution, and the distribution function is expressed as

$$Z(x) = \begin{cases} 0 & x < 0 \\ \sum_{j=-\infty}^{+\infty} (-1)^j \exp\left(-2j^2x^2\right) & x \geq 0 \end{cases} \tag{3}$$

Taking the significance level α as 0.05, calculate the test statistic Z values and the corresponding probability p values. If p is less than the significance level, then the original hypothesis H_0 is rejected and the distribution of the sample from the total is considered to be significantly different from the normal distribution. If p is greater than the significance level α, then the original hypothesis H_0 should not be rejected and the distribution of the total from which the sample comes is not significantly different from the normal distribution.

Normal distribution analysis in days for a total of 69 days of data: 16 Hz octave band of AN has the highest number of days conforming to the normal distribution with 46 days, the lowest octave band of AN has only 23 days conforming to the normal distribution, average 33 days conforming to the normal distribution. A test of 44 days in which the data size exceeded the average group size of 110 groups: 16 Hz octave band of AN has the highest number of days conforming to the normal distribution with 29 days, and the lowest octave band of AN has only 9 days conforming to the normal distribution, average 17.8 days conforming to the normal distribution.

AN INVALID DATA DETERMINATION

Correlation Analysis of Each Octave Band Component

When the electric field strength on the surface of AC transmission lines exceeds the critical strength, due to a large number of ionization effects, ionization zone will appear around the conductor, under the action of the electric field, positive ions in the positive zone and negative ions in negative zone are moved the radially outward movement, respectively. In the role of the alternating electric field around the conductor charged ions along

the conductor to do round-trip movement to produce "humming" sound, this noise is "pure tone," and its frequency is a multiple of the frequency of 50 Hz. At the same time, the rapid movement of these ions will produce corona current pulses around the conductor, while a large number of ions in the direction away from the conductor and air molecules collide to produce sound pressure pulses. The AN generated by the sound pressure pulses and corona current pulses together in the broadband noise belongs to the medium and high-frequency AN (Fa Yuan et al., 2016; Zelong et al., 2012; Cheng, 2020).

Both "pure tone" and broadband noise are periodic outward propagation of sound waves due to the pressure exerted on the air layer by ion motion under the effect of alternating electric fields (Di et al., 2012). There are many sound sources that produce various ambient noises during the acquisition of transmission lines AN. The frequency spectrum of different types of sound sources is not the same (Lu et al., 2010; Liu et al., 2018), and the final collected sound signal is the result of the joint action of the noise components belonging to different octave band. Therefore, it is necessary to consider the noise component data belonging to different octave band center frequency as a whole and to determine the invalid data for the data set composed of them. **Eqs 4**, **5** were used to calculate Pearson's correlation coefficient and gray correlation coefficient between each octave band component, respectively.

$$\rho_{X,Y} = \frac{E\left(\left(X_i - \mu\right)\left(Y_i - \nu\right)\right)}{\sqrt{\frac{\sum\left(X_i-\mu\right)}{N}\frac{\sum\left(Y_i-\nu\right)}{N}}} \tag{4}$$

where x_i and y_i are the sample observations of variable X and variable Y, respectively; μ and ν are the mean values of variables X and Y, respectively; N is the total number of samples.

$$\zeta_i(k) = \frac{\max\limits_i \max\limits_k \Delta_i(k) + \rho \cdot \max\limits_i \max\limits_k \Delta_i(k)}{\Delta_i(k) + \rho \cdot \max\limits_i \max\limits_k \Delta_i(k)} \tag{5}$$

where $\Delta_i(k)$ is the absolute value of the difference between the variable $y(k)$ and the corresponding element of the variable $x_i(k)$ and ρ is the resolution factor; usually ρ is 0.5.

A total of 55 pairs of correlation coefficients were obtained after calculating the Pearson correlation coefficients between each AN component by **Equation 4**, of which 33 groups had correlation coefficients less than 0.5 and 28 groups had correlation coefficients less than 0.4. A total of 55 pairs of gray correlation coefficients obtained after calculating the nonlinear relationship between the AN components by **Equation 5** are all greater than 0.7. It can be found that there is a strong nonlinear relationship between each octave band component, so it is necessary to consider each octave band component as a whole composed of multidimensional data. It has been proved that the data do not satisfy the normal distribution in most cases, the time span of the transmission line AN collection is long, and the meteorological factors change a lot during the data collection process, so MWKPCA is used to determine the invalid data day by day to reduce the influence of the change of meteorological factors on the determination results.

Algorithm Principle of MWKPCA

KPCA can be viewed as a principal component analysis in high-dimensional feature space (Li et al., 2018; Zhang and Luo, 2018; Zhu et al., 2021); compared with traditional PCA, it needs to project the dataset $X = [x_1, x_2 \cdots, x_N]$ into the high-dimensional feature space Γ through a nonlinear mapping b to obtain a new dataset:

$$\phi(X) = \left[\phi(x_1), \phi(x_2) \cdots \phi(x_N)\right] \tag{6}$$

where X is a matrix of N rows and M columns, $\phi(x)$ is a matrix of D rows and M columns, and $D > N$.

Then the covariance matrix in the higher dimensional space is C_Γ:

$$C_\Gamma == \frac{1}{N}\sum_{i=1}^{N}\phi(x_i)\phi(x_i)^T \tag{7}$$

The kernel matrix $K\epsilon\phi^{N\times N}$ is usually obtained in the high-dimensional feature space using the kernel function instead of the mapping function, followed by the calculation of the kernel matrix $\widetilde{K}$ after centering.

$$K = K - K\bullet 1_N - 1_N \bullet K + 1_N \bullet K \bullet 1_N \tag{8}$$

where k is a kernel matrix and 1_N is an $N \times N$ matrix where each element is $\frac{1}{N}$.

The eigenvectors $(P_1, P_2, \cdots, P_3)$ and the corresponding eigenvalues $(\lambda_1, \lambda_2, \cdots, \lambda_A)$ are obtained by the singular value decomposition of the covariance matrix R of the matrix $\widetilde{K}$, where A (A<N) is the number of principal elements obtained by the cumulative variance contribution, and the covariance matrix of the matrix $\widetilde{K}$ is shown in the following equation:

$$R = K^T K/(N-1) = [PP_e]\Lambda[PP]^T \tag{9}$$

where P is the principal component load matrix and P_e is the residual load matrix.

By building a good KPCA model, the T^2 statistic is used to determine the information of $\widetilde{K}$ projection into the principal component subspace, as the following equation:

$$\begin{aligned} T^2 &= K^T P \Lambda^{-1} P^T X \\ &= \sum\nolimits_{i=1}^{m} \frac{t_i^2}{\lambda_i} \sim \frac{p\left(n^2-1\right)}{n(n-p)} F\left(n, n-p\right) \end{aligned} \tag{10}$$

where $\Lambda = diag(\lambda_1, \lambda_2, \cdots \lambda_m)$ is the principal variance matrix, n is the number of samples, m is the number of principals, $F(n, n-p)$ is the F distribution with degrees of freedom n and n-p. Let the confidence coefficient be α; then the control threshold of the T^2 statistic is T^2_{UCL}.

$$T^2_{UCL} = \frac{\alpha\left(n^2-1\right)}{n-\alpha} F_\alpha(\alpha, n-\alpha) \tag{11}$$

The SPE statistics in the residual subspace are used to determine data anomalies. The SPE statistic is given in the following **Eq. 12**:

$$SPE = \left(XP_eP_e^T\right)\left(XP_eP_e^T\right)^T = XP_eP_e^TX^T \le SPE_{UCL} \tag{12}$$

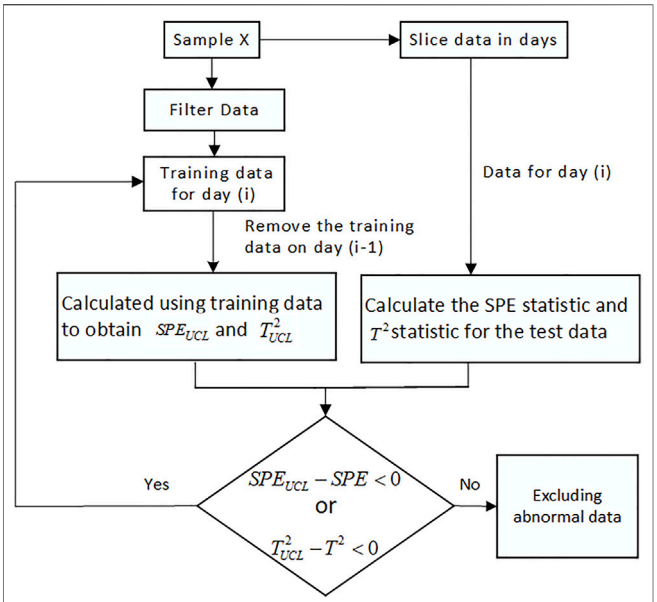

FIGURE 1 | Moving window kernel principal component analysis (MWKPCA) calculation process.

The control threshold SPE_{UCL} is given in the following **Equation 13**:

$$SPE_{UCL} = \theta_1 \left[\frac{C_\alpha \sqrt{2\theta_2 h_0^2}}{\theta_1} + 1 + \frac{\theta_2 h_0 (h_0 - 1)}{\theta_1^2} \right]^{\frac{1}{h_0}} \quad (13)$$

where α is the confidence level, C is the critical value of the normal distribution at the detection level of α,$h_0 = 1 - 2\theta_1\theta_3/3\theta_2^2$, and $\theta_i = \sum_{j=A+1}^{m}, i = 1, 2, 3$.

MWKPCA introduces the moving window function on the basis of KPCA, and for such cases as this paper where the time span is up to 6 months, the invalid data is determined in days, and the training data and test data are continuously updated with SPE_{UCL} and T^2_{UCL}, so as to reduce the negative impact of changes in meteorological factors on the results of invalid data determination.

The flow of MWKPCA calculation is shown in **Figure 1**.

Multidimensional Invalid Data Determination

The 484 sets of data for each octave band component which are close to the average value of that component are selected as the initial training data, and the training data are updated in the process of determining invalid data day by day, adding the data judged as normal on that day to the training data, and eliminating the corresponding number of data from the previous training data, so as to detect abnormal data for 7,658 sets of test data day by day. The computed significance level of the initial training modelα = 0.85, kernel width gamma = 16 for the radial basis function, corresponding to the control threshold SPE_{UCL} for the SPE statistic and the control threshold T^2_{UCL} for the T^2 statistic, and the corresponding number of principal elements is 9. The final outlier determination results are shown in **Figure 2**: the total number of groups that exceeded the threshold of SPE statistics or T^2 statistics was 1,013, the total number of groups that exceeded the threshold of T2 statistics was 703, and the final rejected data were 1,475.

PREDICTION OF AWSL EFFECTIVE DATA

Percentile Comparison

Table 1 shows the percentile of each octave band component of AN in the two stages of original data and after MWKPCA (Ln in the table indicates the values ranked in the top n% positions by arranging the data in descending order), and it can be found that most of the octave band components L5, L50, L95 do not change much after the removing of invalid data screening, so the elimination of invalid data using the method of this paper basically does not affect the study of AN data (Liu et al., 2014a).

Prediction Result Comparison

Direct collection of Awsl of transmission line AN is susceptible to ambient noises interference, while in the octave band 8 kHz component of sound ambient noises and AC transmission line AN, values differ significantly (IEEE Std 656-2018 Standard for the Measurement of Audible Noise from Overhead Transmission Lines., 2018; Lu et al., 2010); the collection of AN 8 kHz component is subject to less interference, while the collection of meteorological data is less subject to strong interference similar to that of ambient noises for AC transmission line AN. Therefore, this paper trains the algorithm model to predict the effective data of transmission line Awsl by the three features of octave band 8 kHz component, temperature, and visible range, so as to indirectly obtain the AC transmission line Aswl which is relatively less disturbed by ambient noises.

The three features of octave band 8 kHz component, temperature, and visible range are normalized by **Equation 14**, and the values are converted to between 0 and 1 to avoid the effect of the difference in magnitude between different features on the prediction accuracy.

$$S = \frac{s - s_{\min}}{s_{\max} - s_{\min}} \quad (14)$$

where S is the normalized result of each feature; s is the original data of each feature; $S_{max}$and S_{min} are the maximum and minimum values of each feature.

In order to prevent the influence of chance on the prediction results due to the random combination of data when dividing the train sets and test sets, this paper divides the data sets into 10 copies by 10-fold cross validation, taking one of them as the train sets and the remaining nine as the test sets, and quantifies the error of the model prediction results by root mean square error (RMSE), mean absolute error (MAE), Mean Absolute Percentage Error (MAPE), and Symmetric Mean Absolute Percentage Error (SMAPE) (as shown in **Eqs. 15–18**, the smaller the error, the better the

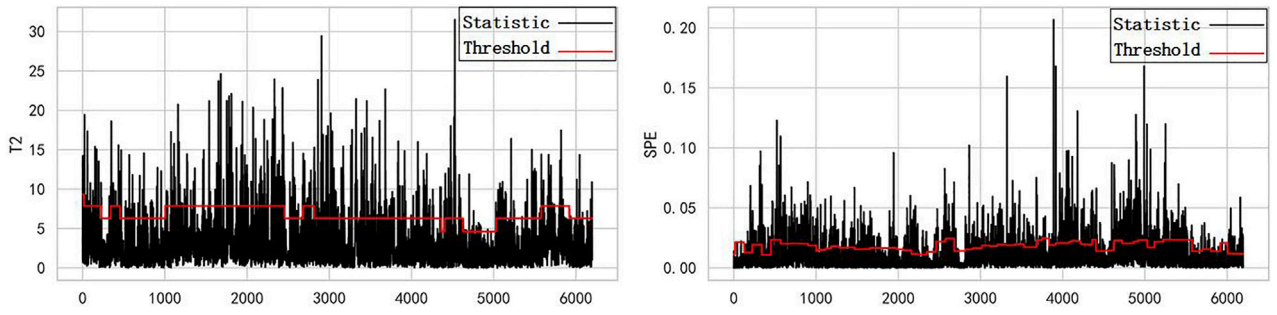

FIGURE 2 | Determination results based on MWKPCA.

TABLE 1 | Statistical values of audible noise (AN) in each frequency band before and after data processing.

	L95		L50		L5′	
	Original	**MWKPCA**	**Original**	**MWKPCA**	**Original**	**MWKPCA**
16 Hz	36.08	36.26	42.49	42.38	56.74	54.77
31.5 Hz	35.76	36.04	42.77	42.60	57.46	56.02
63 Hz	33.45	33.81	42.01	41.78	52.46	50.89
125 Hz	23.70	23.85	34.13	33.92	55.23	54.75
250 Hz	21.79	22.02	30.34	30.08	54.07	52.28
500 Hz	18.69	19.13	27.85	27.37	47.06	45.07
1000 Hz	17.08	17.59	27.86	26.99	45.97	44.77
2000 Hz	13.48	14.52	25.76	25.35	43.75	42.43
4000 Hz	14.59	15.20	27.74	27.33	41.99	41.20
8000 Hz	11.79	11.92	19.20	19.49	37.29	35.69
Awsl	27.75	28.01	37.41	37.15	53.75	52.75

TABLE 2 | Prediction errors.

	RMSE	**MAE**	**MAPE**	**SMAPE**
Original	6.60	4.97	12.95	12.78
MWKPCA	5.73	4.37	11.46	11.41
KPCA	6.10	4.42	11.97	11.71
IF	6.48	4.92	12.86	12.73
LOF	5.87	4.52	11.90	11.81
DBSCAN	6.02	4.54	11.93	11.83

prediction result, and the final result is taken as the average of 10 predictions).

$$\mathrm{RMSE} = \sqrt{\frac{1}{\mathrm{n}}\sum_{i=1}^{n}\left(y_i - \hat{y}_i\right)^2} \tag{15}$$

$$\mathrm{MAE} = \frac{1}{n}\sum_{i=1}^{n}\left|y_i - \hat{y}_i\right| \tag{16}$$

$$\mathrm{MAPE} = \frac{100\%}{n}\sum_{i=1}^{n}\frac{\left|\hat{y}_i - y_i\right|}{y_i} \tag{17}$$

$$\mathrm{SMAPE} = \frac{100\%}{n}\sum_{i=1}^{n}\frac{\left|\hat{y}_i - y_i\right|}{\left(\left|\hat{y}_i\right| + \left|y_i\right|\right)/2} \tag{18}$$

where y_i and $\hat{y}_i$ represent the true and predicted values; n represents the number of predicted versus true values.

In order to better reflect the improvement of the prediction accuracy by the outlier rejection algorithm, this paper uses LightGBM and XGBoost based on Boosting model, SVR based on hyperplane, KNN based on distance, and elastic network and linear regression to predict the Awsl, and the mean value of the final Awsl prediction result is shown in **Table 2**: predictions were made using the data sets before and after invalid data rejection in this paper, respectively. The mean error of the prediction results after invalid data rejection using MWKPA is lower than that of the original data, and the invalid data rejection has contributed to the improvement of the prediction accuracy.

Using the above six algorithms to predict the effective Awsl data after eliminating invalid data by IF, DBSCAN, LOF, KPCA, and MWKPCA, the comparison of the mean error values of the prediction results is shown in **Table 2**; the mean error values after eliminating invalid data by using MWKPCA are significantly lower than those of the other four methods.

CONCLUSION

A method is proposed to reject the invalid data of AN on transmission lines using MWKPCA. After using this method to reject the invalid transmission line AN data, there is no impact on the subsequent study of AN.

The multidimensional invalid data determination method MWKPCA proposed in this paper can improve the prediction accuracy of transmission lines AN Awsl to some extent, and the improvement of Awsl prediction accuracy on real data set is higher than IF, DBSCAN, and LOF.

DATA AVAILABILITY STATEMENT

The original contributions presented in the study are included in the article/Supplementary Materials; further inquiries can be directed to the corresponding author.

AUTHOR CONTRIBUTIONS

ZC completed thesis writing and coding, ZL and YH provided the idea and guide for the paper, WY and HX conducted experiments and provided data.

FUNDING

This work was supported by the Science and Technology Project of SGCC, grant no. 8100-202055158A-0-0-00.

REFERENCES

Chartier, V., and Stearns, R. (1981). Formulas for Predicting Audible Noise from Overhead High Voltage Ac and Dc Lines. *IEEE Trans. Power Apparatus Syst.* PAS-100 (1), 121–130. doi:10.1109/TPAS.1981.316894

Chen, Y., Xie, H., Zhang, Y., Xu, S., and Zhou, C. (2012). Audible Noise Prediction of Uhvac Transmission Lines Based on corona Cage. *High Voltage Eng.* 38 (9), 2189–2194. doi:10.3969/j.issn.1003-6520.2012.09.007

Cheng, L. (2020). *Analysis of Spectrum Characteristics of Audible Noise Generated by AC Corona Discharge*. BeiJing): Shool of Electrical and Electronic Engineering.

Cheng, L., Xuebao, L. I., Hao, M. A., Yingfei, L. I., Ti Eb Ing, L. U., and Liu, Y. (2019). Time-domain Correlation between Audible Noise and Radio Interference Caused by Single Positive corona Source on the Conductor. *High Voltage Eng.* 45 (12), 4088–4095. doi:10.13336/j.1003-6520.hve.20191125038

Fa Yuan, W. U., Liu, S. N., Wang, Y. C., Liu, P., Rui, X. U., and Cai, J. (2016). Audible Noise Characters Analysis of 220 Kv Xiang-tang Transmission Line. *Noise and Vibration Control* (01), 120–124.

Guo, T., Luo, R., Yang, Y., Shi, Z., and Wu, J. (2019). Research on Electromagnetic Environment of the 750 Kv/330 Kv Mixed Voltage Quadruple-Circuit Transmission Line on the Same tower. *High Voltage Apparatus* 55 (1), 157–164. doi:10.13296/j.1001-1609.hva.2019.01.024

Juette, G., and Zaffanella, L. (1970). Radio Noise Currents and Audible Noise on Short Sections of Uhv Bundle Conductors. *IEEE Trans. Power Apparatus Syst.* PAS-89 (5), 902–913. doi:10.1109/TPAS.1970.292653

Li, Z., Jiang, W., Abu-Siada, A., Li, Z., Xu, Y., and Liu, S. (2021). Research on a Composite Voltage and Current Measurement Device for Hvdc Networks. *IEEE Trans. Ind. Electron.* 68 (99), 8930–8941. doi:10.1109/TIE.2020.3013772

Li, Z., Li, C., and Zhang, Z. (2018). State Prediction of Electronic Voltage Transformer Based on Q-ARMA. *Sci. Sin.-Tech.* (12), 1401–1412. doi:10.1360/N092018-00226

Lingyan, L. I., Zhiye, D. U., Jiangjun, R., Chen, Y., Jian, L. I., and Huang, G. (2016). Electromagnetic Environment Analysis on ±800 Kv/±500 Kv Double-Circuit Dc Transmission Lines. *High Voltage Apparatus* (09), 26–33. doi:10.13296/j.1001-1609.hva.2016.09.005

Liu, Y., Guo, J., and Lu, J. (2014a). Audible Noise Spectrum Characteristics of Positive and Negative Wire in Uhv corona Cage. *Zhongguo Dianji Gongcheng Xuebao/Proceedings Chin. Soc. Electr. Eng.* 34 (18), 2976–2982. doi:10.13334/j.0258-8013.pcsee.2014.18.014

Liu, Y., Jiayu, L. U., Wenyu, L. I., Gao, C., and Zhang, J. (2018). Study on the Spectrum Characteristics of Dc corona Noise from Multi-Split Transmission Lines. *Noise and Vibration Control* (S2), 580–583. CNKI:SUN:ZSZK.0.2018-S2-048.

Liu, Y., Jiayu, L. U., Zhang, Q., and Guo, J. (2014b). Effectiveness Determination Method of Audible Noise Test Data for High Voltage Dc Transmission Lines. *High Voltage Eng.* 40 (9), 2728–2733. doi:10.13336/j.1003-6520.hve.2014.09.017

Liu, Y., Xv, J., Liu, Y., Yuan, H., and Cui, Y. (2020). A Method for the Indirect Detection of Audible Noise from High-Voltage Direct Current Transmission Lines. *IEEE Trans. Instrum. Meas.* 69 (99), 4358–4369. doi:10.1109/TIM.2019.2942251

Lu, Y., Qi, X. M., Zhang, G. Z., Wan, B. Q., and Ni, Y. (2010). Spectrum Characters of the Audible Noise from ±500 Kv Ge-Nan and Yi-Hua Transmission Line and Affecting Factors. *Gaodianya Jishu/High Voltage Eng.* 36 (11), 2754–2759. doi:10.1016/S1872-2040(09)60084-0

Ni, L. I., Zhang, B., Dai, S. J., Wan, H., Liu, J. B., Chen, Y. L., et al. (2018). Influence of Temperature and Humidity on Electromagnetic Environment of ±500kv Dc Transmission Lines. *Water Resour. Power* (10), 198–200. CNKI:SUN:SDNY.0.2018-10-050.

Pengfei, L. I., Zhang, Y., Zhang, T., Dai, K., Liu, Y., and Zhao, Z. (2019). Weather Factors and Prediction Method for "100 Hz" Pure Tone of Uhv Ac Transmission Lines. *High Voltage Eng.* (09), 2971–2979. doi:10.13336/j.1003-6520.hve.20190831033

Perry, D. E., Chartier, V. L., and Reiner, G. L. (1979). Bpa 1100 Kv Transmission System Development corona and Electric Field Studies. *IEEE Trans. Power Apparatus Syst.* PAS-98 (5), 1728–1738. doi:10.1109/TPAS.1979.319491

Shen, X., and Raksincharoensak, P. (2021). Pedestrian-Aware Statistical Risk Assessment. *IEEE Trans. Intell. Transportation Syst.* doi:10.1109/tits.2021.3074522

Sponsor (1985). *IEEE Standard for the Measurement of Audible Noise from Overhead Transmission Lines*. IEEE. doi:10.1109/IEEESTD.2018.8331395

Tang, J., Yang, Y. J., Li, Y. S., Zhang, G. Z., and He, J. L. (2010). Prediction of corona Effects Generated from Uhvac Transmission Lines, I: Audible Noise. *Gaodianya Jishu/High Voltage Eng.* 36 (11), 2679–2686. CNKI:SUN:GDYJ.0.2010-11-013.

Trinh, N. G., and Maruvada, P. S. (1977). A Method of Predicting the corona Performance of Conductor Bundles Based on Cage Test Results. *IEEE Trans. Power Apparatus Syst.* 96 (1), 312–325. doi:10.1109/T-PAS.1977.32339

Xie, H., Cui, X., Lu, Y., and He, W. (2016). Corona Audible Noise experiment of Uhv Ac Double-Circuit Line with Optimization of Insulator String Length. *High Voltage Eng.* (05), 1659–1666. doi:10.13336/j.1003-6520.hve.20160412056

Xie, Q., Ren, J., Zhiyu, L. I., Wang, Y., Huang, H., and Wang, N. (2017). Simulation Study on Electromagnetic Environment of Ac Double-Circuit Transmission Lines in Heavy Icing Area. *High Voltage Apparatus* (08), 9–16. doi:10.13296/j.1001-1609.hva.2017.08.002

Xuebao Li, X., Xiang Cui, C., Tiebing Lu, T., Donglai Wang, D., Wenzuo Ma, W., and Xingming Bian, X. (2015). Comparison between the Audible Noises Generated from Single corona Source under Dc and Ac corona Discharge. *CSEE Power Energ. Syst.* 1 (3), 23–30. doi:10.17775/CSEEJPES.2015.00031

Yang, N., Jia, J., Xing, C., Liu, S., and Deng, Y. (2020). Data-driven Intelligent Decision-Making Method for Unit Commitment Based on E-Seq2seq Technology. *Zhongguo Dianji Gongcheng Xuebao/Proceedings Chin. Soc. Electr. Eng.*

Yang, T., Zou, A., Chen, J., Luwen, X. U., Yongliang, J. I., and Long, Y. (2016). Simulation Analysis for Audible Noise Characteristics of ±800 Kv Transmission Lines Near the Complex Terrain. *High Voltage Apparatus* (08), 14–19. doi:10.13296/j.1001-1609.hva.2016.08.003

Zao, L., Xiao, B., Wang, B., Yue, S., and Gao, L. (2021). Experimental Research and Conductor Selection on Electromagnetic Environment of ±500 kV DC Transmission Line at High Altitude. *Power Syst. Tech.* (02), 794–801. doi:10.13335/j.1000-3673.pst.2020.0110a

Zelong, D. I., and Jiuhui, W. U. (2012). Mechanism and Theoretical Model for corona Audible Noise from High Voltage Ac Transmission Lines. *J. Xi an Jiaotong University* (08), 128–132.

Zhang, L., and Luo, Y. (2018). Combined Heat and Power Scheduling: Utilizing Building-Level thermal Inertia for Short-Term thermal Energy Storage in District Heat System. *IEEJ Trans. Elec Electron. Eng.* 13 (5), 804–814. doi:10.1002/tee.22633

Zhang, Z., Chen, Q., Hu, C., Li, H., and Chen, M. (2018). Evaluating the Metering Error of Electronic Transformers On-Line Based on VN-MWPCA. *Measurement* 130, 1–7. doi:10.1016/j.measurement.2018.07.083

Zhiye, D. U., Lingyan, L. I., Chen, Y., Jian, L. I., Jiangjun, R., and Huang, G. (2016). Conductor Selection of Double-Circuit Dc Transmission Lines with Mixed-Voltage ±800 Kv/±500 Kv on the Same tower. *High Voltage Eng.* (08), 2605–2611. doi:10.13336/j.1003-6520.hve.20160812031

Zhu, B., Ding, F., and Vilathgamuwa, D. M. (2020). Coat Circuits for Dc-Dc Converters to Improve Voltage Conversion Ratio. *IEEE Trans. Power Electron.* 35 (99), 3679–3687. doi:10.1109/TPEL.2019.2934726, PP

Zhu, X., Zhang, H., and Yang, S. (2021). MWPCA Blast Furnace Anomaly Monitoring Algorithm Based on Gaussian. *CIESC J.* 72 (03), 1539–1548.

Conflict of Interest: ZC was employed by State Grid Chongqing Electric Power Company Construction Branch and HX was employed by China Electric Power Research Institute Co., Ltd.

The remaining authors declare that the research was conducted in the absence of any commercial or financial relationships that could be construed as a potential conflict of interest.

Publisher's Note: All claims expressed in this article are solely those of the authors and do not necessarily represent those of their affiliated organizations or those of the publisher, the editors, and the reviewers. Any product that may be evaluated in this article or claim that may be made by its manufacturer is not guaranteed or endorsed by the publisher.

frontiers in Energy Research

ORIGINAL RESEARCH
published: 12 November 2021
doi: 10.3389/fenrg.2021.777230

Mapping Relation of Leakage Currents of Polluted Insulators and Discharge Arc Area

Chunhua Fang[1], Yuning Tao[1], Jianguo Wang[2], Can Ding[1], Li Huang[1], Mi Zhou[2], Yi Gu[3] and Yali Wang[3]*

[1]College of Electrical Engineering and New Energy, China Three Gorges University, Yichang, China, [2]School of Electrical Engineering, Wuhan University, Wuhan, China, [3]Department of Development and Planning, State Grid Corporation of China, Beijing, China

A fundamental parameter of polluted insulator online monitoring is the leakage current, which has already been shown to be well-related to the pollution discharge of insulators. In this article, in an effort to quantitatively reflect the discharge intensity and the discharge status by the leakage current, we carried out an experimental study on artificial pollution discharge of insulators. A high-speed photographic apparatus was utilized to capture the entire process of local arcs on a porcelain insulator surface, including the arc generation, the arc development, and the flashover, for which the associated leakage current of insulators was synchronously digitized. A comparative analysis of the relation between the two-dimensional discharge image and the leakage current waveform in the process of arc generation and development shows that if the arc area on the insulator surface is relatively small and the leakage current passes through zero, the arc might completely become extinct, whereas this phenomena will not occur if the arc area is larger. In addition, the amplitude of the discharge arc area is found to be roughly proportional to the square of leakage current over the range of leakage current amplitude from 0 to 150 mA. Our results can provide an important guidance for judgment of the discharge status and the discharge intensity on insulator surfaces using the leakage current of insulators.

Keywords: discharge arc, leakage current, mapping relation, polluted insulator, online monitoring

OPEN ACCESS

Edited by:
Xun Shen,
Tokyo University of Agriculture and Technology, Japan

Reviewed by:
Xiang Nianwen,
Hefei University, China
Xinjing Cai,
Shenyang University of Technology, China

****Correspondence:***
Yuning Tao
taoyuning12@163.com

Specialty section:
This article was submitted to Smart Grids, a section of the journal Frontiers in Energy Research

Received: *15 September 2021*
Accepted: *11 October 2021*
Published: *12 November 2021*

Citation:
Fang C, Tao Y, Wang J, Ding C, Huang L, Zhou M, Gu Y and Wang Y (2021) Mapping Relation of Leakage Currents of Polluted Insulators and Discharge Arc Area. Front. Energy Res. 9:777230. doi: 10.3389/fenrg.2021.777230

INTRODUCTION

Transmission line insulators are exposed to the natural environment during their long operation period, and the pollutants floating in the air are easily deposited on insulator surfaces under the influence of various external forces, leading to pollution of the insulators (Liu et al., 2020; Shen et al., 2020; Yang et al., 2021; Shen et al., 2021; Shen et al., 2021). Under severe weather conditions, such as fog, dew, and drizzle, the flashover might occur even at normal operating voltage, resulting in serious threats to the safe and stable operation of the power system (Yang et al., 2019; Yang et al., 2020; Shen and Raksincharoensak, 2021). Generally, the pollution flashover will experience four stages: the pollution deposition, the wetting, the dry band formation, and the local arc generation and flashover development. A discharge arc will be generated before flashover (Yang et al., 2019; Shen et al., 2020; Zhu et al., 2020; Noman et al., 2021; Shen and Pongsathorn, 2021). Meanwhile, the leakage current is associated with the whole operation process of insulators and is able to reflect the generation, development, extinction of the arc and, if possible, the full flashover. The leakage current, whose amplitude is affected by the pollution level, the humidity, the discharge strength, etc., may also be

TABLE 1 | Structure figure and parameters of the XP-70 insulator.

Type	XP-70
Configuration height (mm)	146
Disc diameter (mm)	255
Leakage distance (mm)	295
Surface area (cm^2)	1,591

used to reflect the insulator surface condition, the climatic condition, and the applied voltage condition. In recent years, many efforts have been devoted to determining the discharge status using the leakage current (Yang and Di, 2018; Zhang and Luo, 2018; Bakeer Abualkasim et al., 2021; Li et al., 2021; Nayak et al., 2021).

There is a belief that the leakage current waveform of insulators can be well-related to the arc condition (Gencoglu and Cebeci, 2009; Du et al., 2012; Cong and Li, 2014). The leakage current can be used to distinguish three different discharge statuses of insulators, namely, no discharge, arc discharge, and continuous arc discharge (Ahmadi–Joneidi et al., 2013). If the discharge is weak and invisible, the amplitude of leakage current, in a form of sine wave, is relatively small. When a filamentous discharge occurs, the leakage current is featured with small pulses with a triangular shape; furthermore, if there exists a small amount of weak arcs, a distorted triangular waveform will be presented. However, if the discharge becomes intense, the leakage current pulse will be larger in amplitude and will occur more frequently, the waveform being distorted as well, with a shape of an inhomogeneous sine wave (Kumagai and Yoshimura, 2004; Pylarinos et al., 2012; Moula et al., 2013). The length and strength of the resultant discharge arc will also periodically change along with the variation of the alternating leakage current flowing through the equipment surface, and hence, whether the arc quenches or reignites can be determined through the observation of the leakage current waveform (Claverie and Porcheron, 2007).

Although many studies have been carried out to correlate the discharge status of insulators with the leakage current, due in part to the complex relationship between each, this issue has not been fully solved. To our knowledge, until now, the discharge status of insulators is still in the stage of qualitative description, and the relations between the pollution discharge status, the discharge strength of the insulator, and the leakage current are not clear. Therefore, it is urgent to build a quantitative relation between the discharge strength and the leakage current.

In the present work, an experimental study on artificial pollution discharge is conducted in an artificial fog room. A high-speed photographic apparatus was utilized to capture the entire process of local arcs on a porcelain insulator surface, including the arc generation, the arc development, and the flashover, for which the associated leakage current of insulators was synchronously digitized. We discuss the relationship between the leakage current and the arc area.

TEST LAYOUT AND TEST METHOD

The structure and parameters of the test XP-70 insulator are presented in **Table 1**. The schematic diagram of the artificial pollution test is shown in **Figure 1**. The test is conducted in a pollution chamber with a width of 2 m, a length of 2 m, and a height of 4 m. The power supply of the test object, seven pieces of XP-70 insulators in this article, is supplied by a transformer cascade. The system frequency is 50 Hz. The transformer cascade, with a maximum output voltage and rated capacity of 500 kV and 1 MVA, respectively, is equipped with two test transformers of divided high voltage winding, and its primary voltage is adjusted by a regulating transformer. The voltage is applied to the test object via the bushings of the pollution chamber. For the measurement of the applied high voltage, a capacitive voltage divider, with a ratio of 1:1920, is used. Voltage and leakage current signals are simultaneously digitized in a leakage current measurement system, with a sampling rate of 100 kHz.

The predeposit method is adopted as the pollution procedure, as recommended in IEC 60507-2013 (IEC, 1991; IEC, 2004). This method is based on coating the test object with a conductive suspension of diatomite in water. The conductivity of the suspension is adjusted by salt (NaCl). Depending on the pollution class, the artificial pollution test is performed with different intensities of pollution. The pollution content required in each string of the test object was calculated according to the salt deposit density and the non-soluble deposit density required by the test object and surface area of the insulator. The test insulators were cleaned by washing with tap water and then the coating of the test insulators was made by flow coating. They were dried for 24 h to ensure a thermal equilibrium with the ambient conditions in the pollution chamber. Based on the IEC60507-1987 standard, equivalent salt deposit density (ESDD) = 0.3 mg/cm^2 is applied to the experiment, and the non-soluble deposit density (NSDD) is set to 1.0 mg/cm^2.

The test object was hanged in the center of the pollution chamber, which was closed during the test. Two pieces of diagonally arranged steam-fog equipment, of which the delivered fog amount can be adjusted, were used to produce cold fog to humidify the pollutants on the insulator surface. However, fog supply should be terminated when the water droplets appear on the insulator surface.

The relation between the leakage current flowing through the insulator surface and the discharge arc is investigated in this study. The discharge development process with the uniform step-up method is relatively faster than that with subsequent applications of the test voltage, which is held constant, and helpful for the synchronous monitoring of the leakage current and discharge phenomenon (Lambeth, 1988). As a result, the uniform step-up method was adopted in the test. Thus, the voltage was applied at uniform speed after the pollutants on the insulator surface were totally wetted until the full flashover occurred.

In the test, the self-developed leakage current measurement system was adopted to perform acquisition of the leakage current, with a sampling rate of 100 kS/s. High-speed video frames

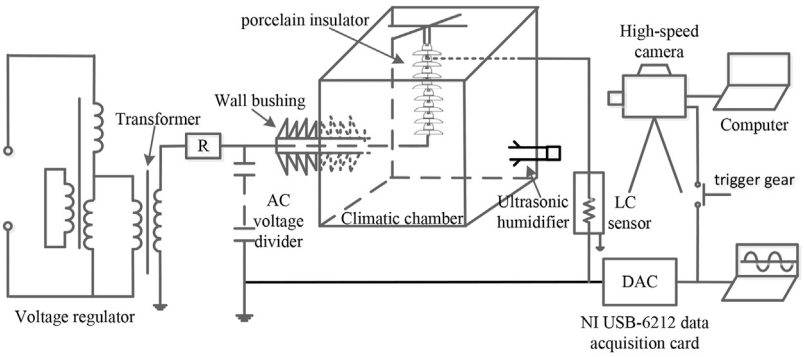

FIGURE 1 | Schematic diagram of the artificial pollution test.

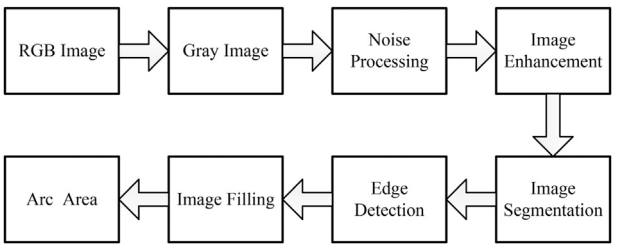

FIGURE 2 | Block diagram of image processing.

showing the development of the arc were recorded using a Photron SA1.1 high-speed camera operating at a framing rate of 1 kfps (kiloframes per second), with 640 pixels × 640 pixels. The high-speed camera was positioned approximately 1 m from the test object. Both the data acquisition card for measurement of the leakage current and the high-speed camera had external triggered function. In order to obtain synchronous recorded data, the synchronized trigger technology of the switch was used.

DISCHARGE ARC IMAGE PROCESSING AND AREA CALCULATION

The white part of the discharge arc image is arc, and its size changes with discharge strength. According to the aforementioned characteristics, image processing technology is utilized to quantify the discharge arc, and the image processing block diagram is shown in **Figure 2**. The arc image of the whole insulator surface collected by the high-speed camera is the RGB image. First, the RGB image is converted into a gray image and noise processing is performed on it. Second, arc information is enhanced with the image enhancement technique, and the image is converted into a binary image with threshold segmentation, thus extracting the arc area and segment arc from the image. As the edge of the segmented photo is not smooth, the edge detection operator is used to detect the arc edge. Finally, a filling algorithm is applied to fill the arc edge image to get the arc area (Chaou et al., 2015; Zhang et al., 2021).

The image through the foregoing processing is the binary image. It consists of 1 and 0, where 1 stands for the discharge arc and 0 for the background. The arc area can be obtained by calculating the number of points whose pixel is 1 in a 2D image. The mathematical expression of pixel point number calculation is as follows:

$$N = \sum_{i=1}^{m} \sum_{j=1}^{n} f''(i, j), \tag{1}$$

where, $f''(i, j)$ stands for the object with the value of 1 (Wang et al., 2014).

The area of the discharge arc is the number of pixel point, so the unit of area defined in this article is pixel (Chaou et al., 2015). In the formula, i and j represent the position coordinates of the pixel in the image.

A discharge RGB color image in **Figure 3A** is transformed to a gray image in **Figure 3B**; the discharge region is brighter than the background image. Next, noise processing and image enhancement technique are performed on it; the enhanced image is shown in **Figure 3C**. Then, the threshold segmentation algorithm is used to convert the gray image into a binary image, when the threshold value is set to 190; the binary image is shown in **Figure 3D**. The edge of the image is the place where the pixel gray scale changes, carrying a wealth of arc image information, in order to accurately depict the outline of the arc image. In order to accurately depict the contour of the arc image, the edge must be extracted accurately. A Canny operator is a multistage optimization operator with filtering, enhancement, and detection (Mason et al., 1975; Lambeth, 1988; Zhang et al., 2021). The Canny operator uses the Gaussian filter to smooth the arc image to reduce the influence of noise on the arc edge detection. In order to find the gradient magnitude maximum and suppress the non-maximum value, the finite difference of the first-order partial derivative is used to calculate the amplitude and direction of the gray gradient of the pixel point. The results of the edge detection using the Canny operator is shown in **Figure 3E**, which is filled with a connected region seed-filling algorithm for

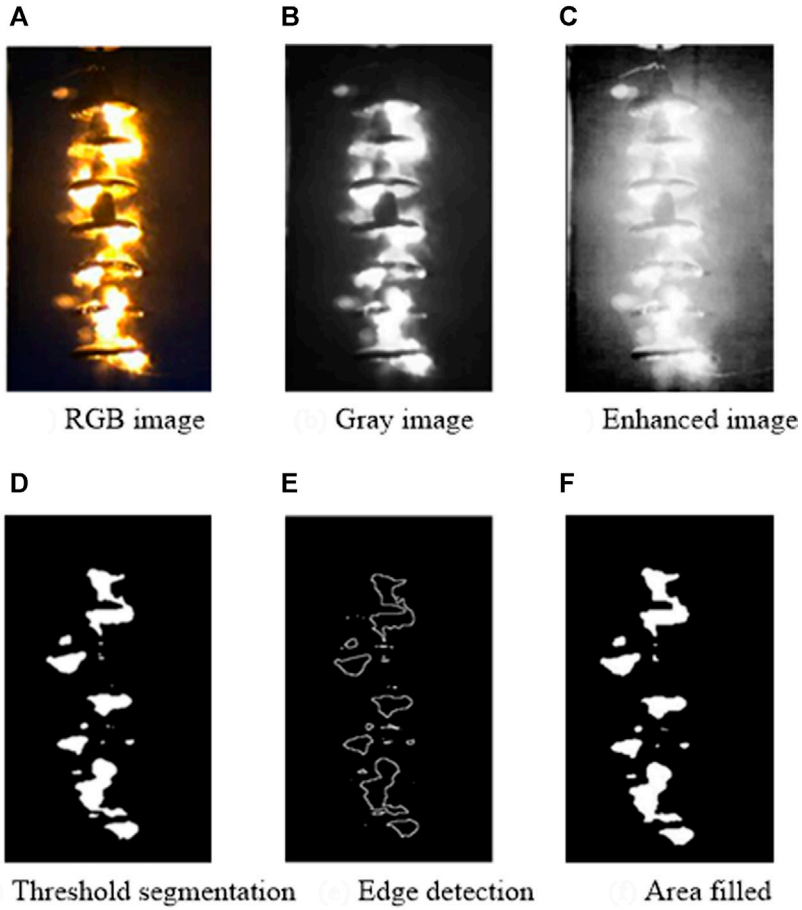

FIGURE 3 | Image after digital processing.

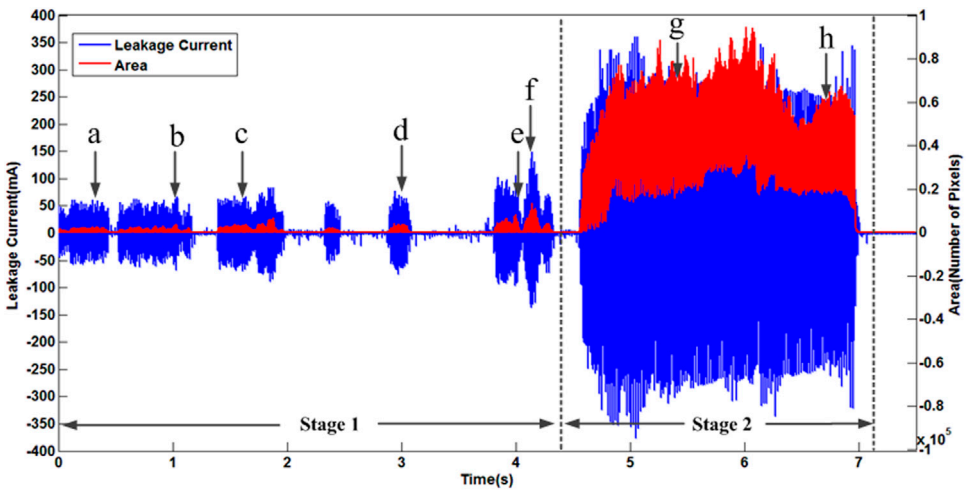

FIGURE 4 | Leakage current and the discharge area.

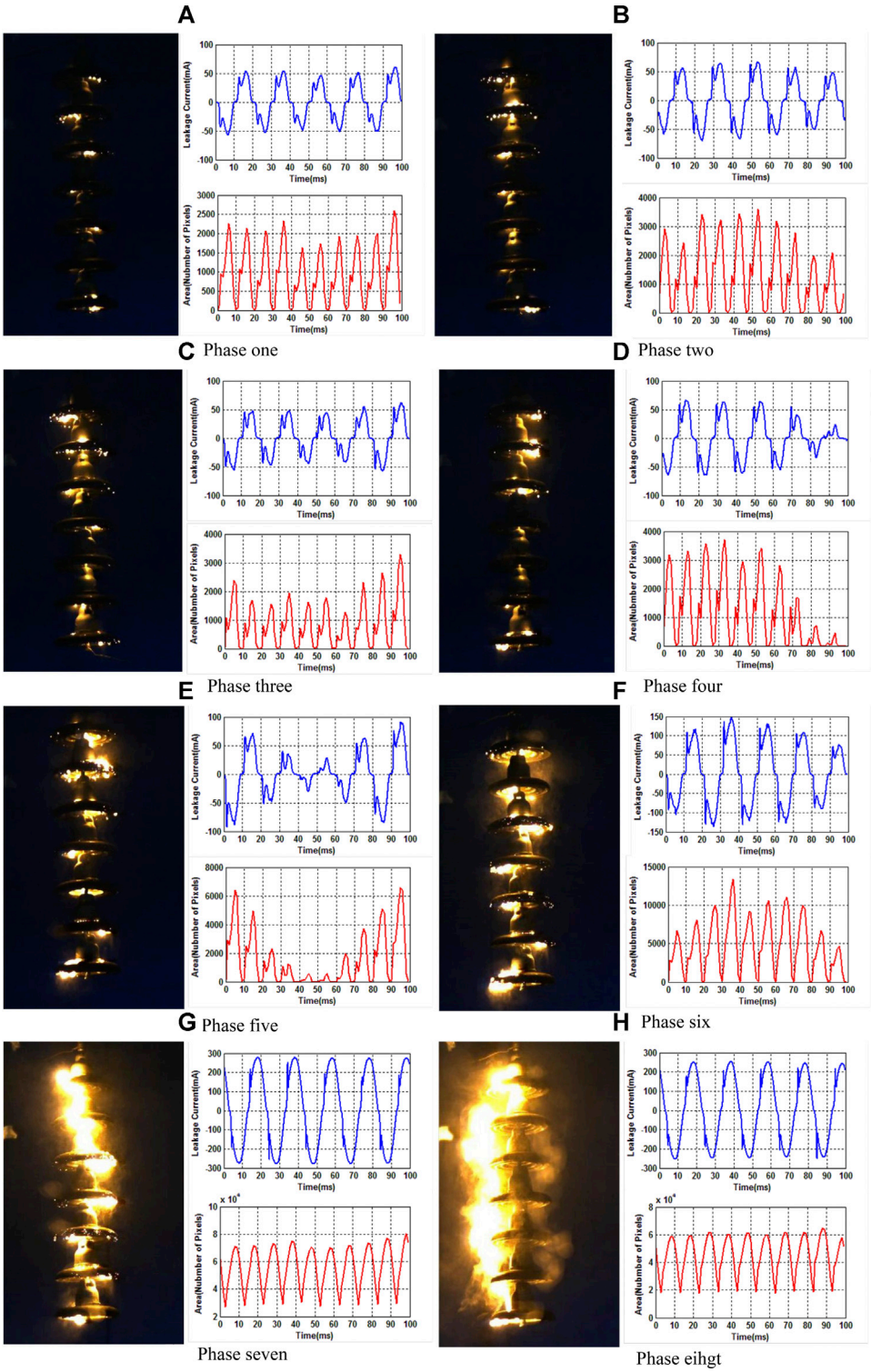

FIGURE 5 | Leakage current waveform and the arc area.

the closed bounded arc image. Starting from any pixel of the polymorphic interior, we judge the adjacent pixels from left to right and from top to bottom. If it is not the boundary pixel point and not been filled, it is filled up and its gray value is changed to 1. Then, the previous process is repeated until all pixels arc circle regions are filled. The filled image is shown in **Figure 3F**.

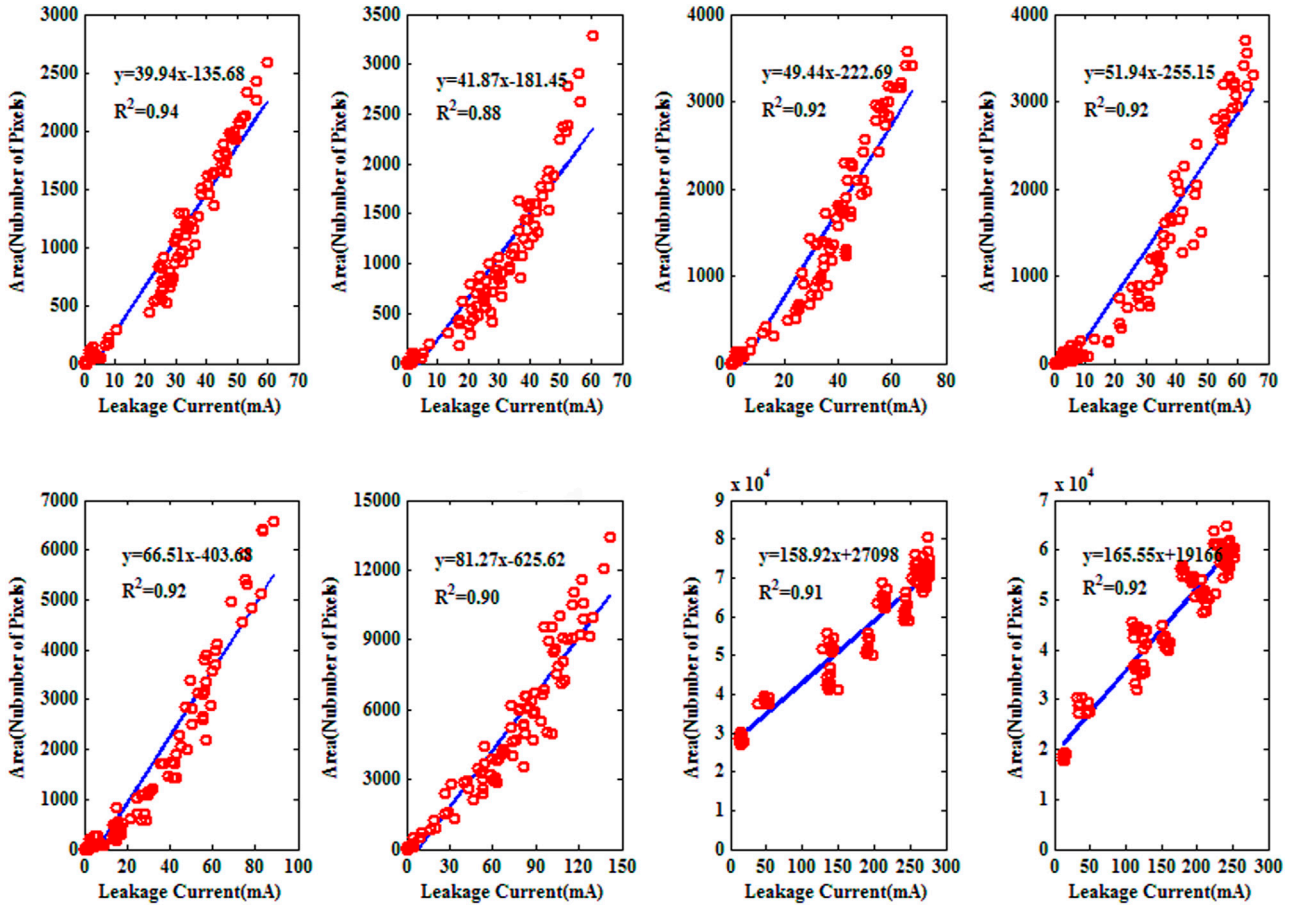

FIGURE 6 | Relation between leakage current and the arc area.

RESULTS AND ANALYSIS

Figure 4 shows the time-synchronized waveform of current and arc area variation for an entire arc discharge process, from the arc generation to the full flashover. During 0–0.447 s, 0.520–1.193 s, 1.39–1.974 s, 2.337–2.467 s, and 2.859–3.059 s, the amplitudes of leakage current were evenly above 50 mA, and the local arc, although relatively weak in luminosity, appeared on the insulator surface. During 3.809–4.334 s, the amplitude of the leakage current was averaged at 100 mA, with a maximum value of 150 mA, and the arc area increased accordingly. During 4.554–7.005 s, the amplitude of leakage current was suddenly increased, and the arc area was also featured with a sudden increase along with the leakage current. In other time however, the amplitudes of leakage current were generally small, and the insulator surface was not featured with any arc discharges. To the naked eye, it seems that there exists a good relationship between the leakage current and the associated arc area.

The leakage current waveforms and the corresponding arc discharge area variation at different times of the developing process of discharge were chosen to conduct a further analysis. To compare the arc area and current data with the same temporal resolution, the current record was preprocessed by a subsection average procedure, with a 1 ms window width. The corresponding current value with a temporal resolution of 1 ms was calculated by averaging 100 original current data.

The discharge arcs in **Figures 5A,B** sporadically disperse on the insulator surface. The amplitudes of the resultant leakage current were about 50 mA, with very slight variations in the first and second half waves in one period. The "zero-crossing" phenomenon is relatively weak, similar to the triangular waveform for which the two-side part is relatively large and the middle part is relatively small. The corresponding arc area also presents a feature of being relatively large in the two-side part and relatively small in the middle part. Compared with **Figures 5A,B**, the discharge strength in **Figure 5C** increases and the leakage current amplitudes are mostly above 50 mA. Accordingly, the arc area, to a certain degree, also increases. The "zero-crossing" phenomenon is quite weak for the leakage currents shown in **Figures 5A–C**, in which when the electrical degree is about 60°, a phenomenon of faint current flicker occurs, and the corresponding arc area decreases abruptly and then increases abruptly.

The discharge spark in **Figure 5D** becomes intense and bright in luminosity. For the second piece of the insulator, the arcs on its upper surface and those on the lower one have a tendency to

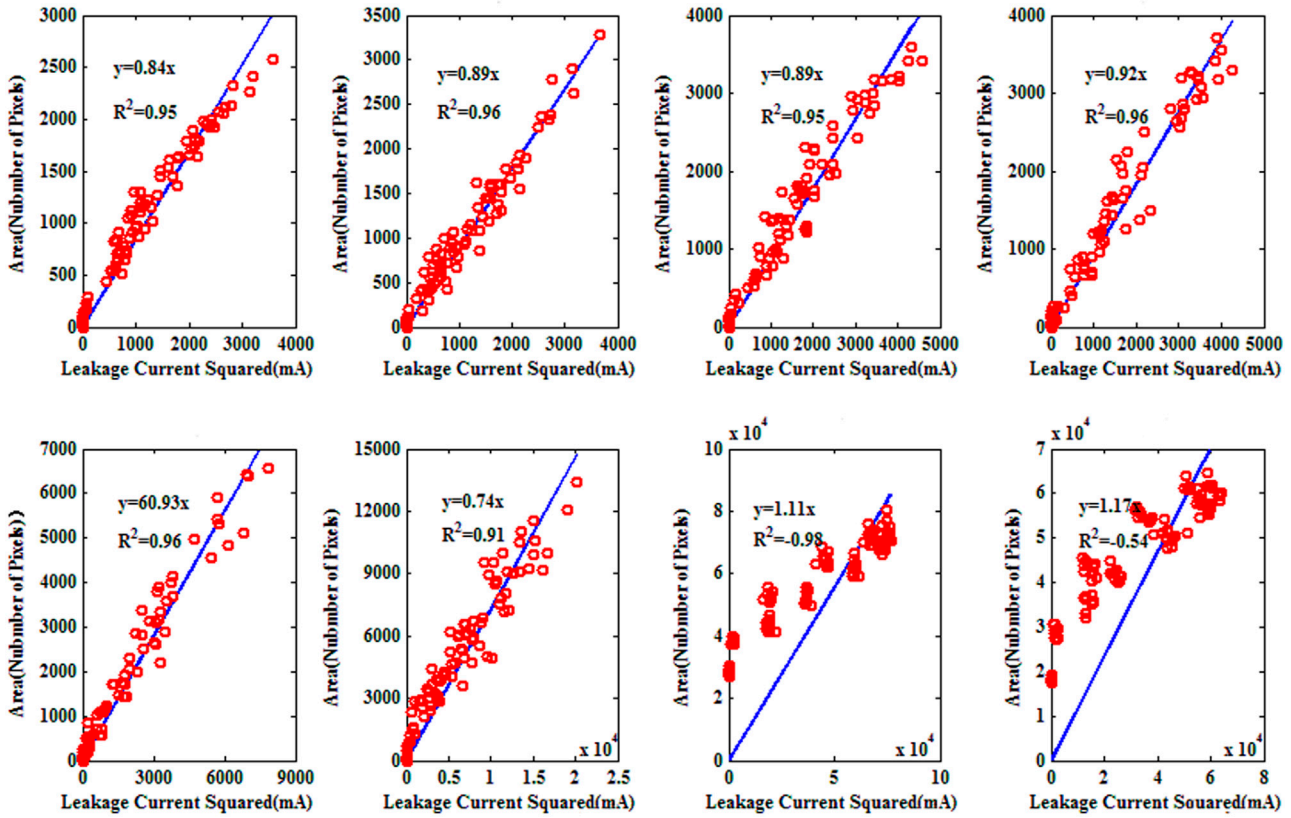

FIGURE 7 | Relation between leakage current squared and the arc area.

connect with each other. Meanwhile, the leakage current amplitude is mostly larger than 50 mA. The discharge spark in **Figure 5E** is larger in area, and the arcs in the upper surface and those in the lower one of the second piece of the insulator have been already connected. The discharges on the surface of several insulators between the top and bottom of the insulator are also obviously strengthened. In addition, the amplitudes of the first and second half waves in one period are featured with large variations, the maximum amplitude being about 100 mA. Waveforms in **Figures 5D,E** have severe distortion with the distinct "zero-crossing" phenomenon, and the discharge is quite weak when this current "zero-crossing" phenomenon occurs, the arc area being quite small.

A more intense discharge spark on the insulator surface is shown in **Figure 5F**. The amplitude of the corresponding leakage current is quite large, about 150 mA, and the amplitudes of the first and second half waves in one period are featured with large variations, with a trend of abrupt increase or of abrupt decrease. Compared with the last stage, the "zero-crossing" phenomenon is relatively weaker. However, the current flicker phenomenon is still obvious.

Comparing with **Figures 5A–F**, a sudden increase in the arc area can be found in **Figures 5G,H**. The arcs on most of the insulators in **Figure 5G** are connected, and those in **Figure 5H** are completely connected in two terminals. In this case, the leakage current rapidly increases, amplitudes being larger than 250 mA. The leakage current, with a waveform similar to the sine wave, has very slight variations in amplitudes of the first and second half parts in one period. In this case, the current "zero-crossing" phenomenon disappears, and the current flicker becomes weaker. The arc area also features with the sinusoidal variation trend, although the arc area variations do not pass zero. As is evident from the previous analyses, although the leakage current wave shapes for various discharge processes are different, a strong correlation can be found between the leakage current and the corresponding arc area. For example, when the leakage current reaches its positive or negative peak, the corresponding arc area will reach its maximum value, and when the leakage current passes through zero, the corresponding arc area will reach its minimum value. Moreover, it should be noted that the arc extinction occurs per half wave in one period in stage 1 (indicated in **Figure 4**). This can be probably interpreted as the fact that the smaller arc on the insulator surface, together with the smaller leakage current, corresponds to less stored energy and also shorter time required for the completion of deionization (Yang et al., 2014; Albano et al., 2016). In stage 2 (also indicated in **Figure 4**), possibly due to the fact that larger leakage current corresponds to more input energy and longer time required for deionization (Wang et al., 2014; Chaou et al., 2015), when the leakage current passes through zero, no arc extinctions will occur.

In the following analyses, the two simplest relationships, a linear correlation for the leakage current versus the arc area and for the leakage current squared versus the arc area, will be compared for the entire discharge process shown in **Figure 5**. **Figure 6** presents the scatterplots of the current versus the arc area for six discharge processes given in **Figure 5**. We first use the simplest linear model to correlate the leakage current and light intensity, as directly shown in **Figure 6**. The correlation coefficients for five cases, shown in **Figures 6A,C–H**, are larger than 0.9, and only one case, shown in **Figure 6B**, is lower than 0.9. Moreover, the slopes of the regression lines in **Figure 6** vary in a wide range, from 39.94 to 165.55. Furthermore, the intercepts of the regression lines also vary considerably. **Figure 7** shows the scatterplots of the instantaneous value of leakage current squared versus the arc area shown in **Figures 5A–H**. Note that the regression lines in **Figure 7** are constrained to pass through the origin. Although the resulting correlation coefficients in **Figure 7** are, to a certain degree, larger than those in **Figure 6**, we cannot tell which relationship is more compelling only by comparing the correlation coefficients. The slopes of the regression lines in **Figures 7A–F** with current amplitudes below 150 mA are however found to be more or less constant (around 0.8) for different discharge processes. If we combine the results from **Figures 7A–H**, it appears that when the leakage current is smaller than 150 mA, a rough linear relationship exists between the leakage current squared and the arc area. When the leakage current is larger than 150 mA, the relation between the arc area and leakage current becomes complicated. We choose to leave that analysis for a later study.

CONCLUSION

1) When the leakage current reaches its positive or negative peak, the corresponding arc area will reach to its maximum value, and when the leakage current passes through zero, the corresponding arc area will reach to its minimum value. A strong correlation can be found between the leakage current and the corresponding arc area.

2) In the case that the arc on the insulator surface is relatively small, if the leakage current passes through zero, complete arc extinction may occur. In the case when the arc is relatively larger, even if the leakage current passes through zero, complete arc extinction will not occur.
3) A rough linear relationship exists between the leakage current squared and the arc area if the leakage current is smaller than 150 mA. This conclusion can be used as a proxy for judging the discharge strength using the leakage currents of insulators.

DATA AVAILABILITY STATEMENT

The original contributions presented in the study are included in the article/Supplementary Material; further inquiries can be directed to the corresponding author.

AUTHOR CONTRIBUTIONS

CF, JW, and CD conceived the idea and designed the experiments. CF and CD led the experiments. YT, LH, and MZ contributed to data analysis and interpretation. CF, YT, YG, and YW wrote the manuscript. All authors read and approved the final manuscript.

FUNDING

This paper is supported by the National Natural Science Foundation of China (Grant No. 51807110).

REFERENCES

Ahmadi-Joneidi, I., Majzoobi, A., Shayegani-akmal, A. A., Mohseni, H., and Jadidian, J. (2013). Aging Evaluation of Silicone Rubber Insulators Using Leakage Current and Flashover Voltage Analysis. *IEEE Trans. Dielect. Electr. Insul.* 20, 212–220. doi:10.1109/TDEI.2013.6451360

Albano, M., Waters, R. T., Charalampidis, P., Griffiths, H., and Haddad, A. (2016). Infrared Analysis of Dry-Band Flashover of Silicone Rubber Insulators. *IEEE Trans. Dielect. Electr. Insul.* 23, 304–310. doi:10.1109/tdei.2015.005026

Bakeer, A., Salama, H. S., and Vokony, I. (2021). Integration of PV System with SMES Based on Model Predictive Control for Utility Grid Reliability Improvement. *Prot. Control. Mod. Power Syst.* 6. doi:10.1186/s41601-021-00191-1

Chaou, A. K., Mekhaldi, A., and Teguar, M. (2015). Elaboration of Novel Image Processing Algorithm for Arcing Discharges Recognition on HV Polluted Insulator Model. *IEEE Trans. Dielect. Electr. Insul.* 22, 990–999. doi:10.1109/TDEI.2014.00454910.1109/tdei.2015.7076800

Claverie, P., and Porcheron, Y. (1973). How to Choose Insulators for Polluted Areas. *IEEE Trans. Power Apparatus Syst.* PAS-92, 1121–1131. doi:10.1109/TPAS.1973.293679

Cong, W., and Li, T. (2014). Study of Composite Insulator Leakage Current Characteristics in Contamination and Humidity Conditions. 2014 IEEE Conference on Electrical Insulation and Dielectric Phenomena. doi:10.1109/ceidp.2014.6995783

Du, B. X., Han, T., Cheng, X. X., Li, J., and Ma, Z. L. (2012). Characterization of Surface Discharge as Indicator for Hydrophobicity Evaluation of Silicone Rubber Insulators. *IEEE Trans. Dielect. Electr. Insul.* 19, 1708–1714. doi:10.1109/TDEI.2012.6311519

Gencoglu, M. T., and Cebeci, M. (2009). Computation of AC Flashover Voltage of Polluted HV Insulators Using a Dynamic Arc Model. *Euro. Trans. Electr. Power* 19, 689–701. doi:10.1002/etep.249

IEC.(2004). 1991 Artificial Pollution Test of High Voltage Insulator for AC System.

IEC.(1991). 1991 Artificial Pollution Tests on High-Voltage Insulators to Be Used on AC Systems.

Kumagai, S., and Yoshimura, N. (2004). Leakage Current Characterization for Estimating the Conditions of Ceramic and Polymeric Insulating Surfaces. *IEEE Trans. Dielect. Electr. Insul.* 11, 681–690. doi:10.1109/TDEI.2004.1324357

Lambeth, P. J. (1988). Variable-voltage Application for Insulator Pollution Tests. *IEEE Trans. Power Deliv.* 3, 2103–2111. doi:10.1109/61.194022

Li, Z., Jiang, W., Abu-Siada, A., Li, Z., Xu, Y., and Liu, S. (2021). Research on a Composite Voltage and Current Measurement Device for HVDC Networks. *IEEE Trans. Ind. Electron.* 68, 8930–8941. doi:10.1109/TIE.2020.3013772

Liu, Y., Yang, N., Dong, B., Wu, L., Yan, J., Shen, X., et al. (2020). Multi-Lateral Participants Decision-Making: A Distribution System Planning Approach with

Incomplete Information Game. *IEEE Access* 8, 88933–88950. doi:10.1109/ACCESS.2020.2991181

Mason, D., Lauder, I., Rutovitz, D., and Spowart, G. (1975). Measurement of C-Bands in Human Chromosomes. *Comput. Biol. Med.* 5, 179–201. doi:10.1016/0010-4825(75)90004-9

Moula, B., Mekhaldi, A., Teguar, M., and Haddad, A. (2013). Characterization of Discharges on Non-uniformly Polluted Glass Surfaces Using a Wavelet Transform Approach. *IEEE Trans. Dielect. Electr. Insul.* 20, 1457–1466. doi:10.1109/TDEI.2013.6571469

Nayak, P. C., Prusty, R. C., and Panda, S. (2021). Grasshopper Optimization Algorithm Optimized Multistage Controller for Automatic Generation Control of a Power System with FACTS Devices. *Prot. Control. Mod. Power Syst.* 6. doi:10.1186/s41601-021-00187-x

Noman, M., Li, G., Wang, K., and Han, B. (2021). Electrical Control Strategy for an Ocean Energy Conversion System. *Prot. Control. Mod. Power Syst.* 6. doi:10.1186/s41601-021-00186-y

Pylarinos, D., Theofilatos, K., Siderakis, K., Thalassinakis, E., Vitellas, I., Alexandridis, A. T., et al. (2012). Investigation and Classification of Field Leakage Current Waveforms. *IEEE Trans. Dielect. Electr. Insul.* 19, 2111–2118. doi:10.1109/TDEI.2012.6396971

Shen, X., Ouyang, T., Khajorntraidet, C., Li, Y., Li, S., and Zhuang, J. (2021a). Mixture Density Networks-Based Knock Simulator. *Ieee/asme Trans. Mechatron.*, 1. doi:10.1109/TMECH.2021.3059775

Shen, X., Ouyang, T., Yang, N., and Zhuang, J. (2021b). Sample-Based Neural Approximation Approach for Probabilistic Constrained Programs. *IEEE Trans. Neural Netw. Learn. Syst.*, 1–8. doi:10.1109/TNNLS.2021.3102323

Shen, X., and Raksincharoensak, P. (2021). Pedestrian-aware Statistical Risk Assessment. *IEEE Trans. Intell. Transport. Syst.*, 1–9. doi:10.1109/TITS.2021.3074522

Shen, X., and Raksincharoensak, P. (2021). Statistical Models of Near-Accident Event and Pedestrian Behavior at Non-signalized Intersections. *J. Appl. Stat.*, 1–21. doi:10.1080/02664763.2021.1962263

Shen, X., Zhang, X., Ouyang, T., Li, Y., and Raksincharoensak, P. (2020b). Cooperative Comfortable-Driving at Signalized Intersections for Connected and Automated Vehicles. *IEEE Robot. Autom. Lett.* 5, 6247–6254. doi:10.1109/LRA.2020.3014010

Shen, X., Zhang, Y., Sata, K., and Shen, T. (2020a). Gaussian Mixture Model Clustering-Based Knock Threshold Learning in Automotive Engines. *Ieee/asme Trans. Mechatron.* 25, 2981–2991. doi:10.1109/TMECH.2020.3000732

Wang, S., Lv, F., and Liu, Y. (2014). Estimation of Discharge Magnitude of Composite Insulator Surface corona Discharge Based on Ultraviolet Imaging Method. *IEEE Trans. Dielect. Electr. Insul.* 21, 1697–1704. doi:10.1109/TDEI.2014.004358

Yang, H., Zhou, J., Li, Y., Pang, L., Yang, X., Zhang, Q., et al. (2014). Effect of Profiles on Ac Contamination Flashover Performance of Large-Tonnage Suspension Disc Insulators. *IEEE Trans. Dielect. Electr. Insul.* 21, 2476–2485. doi:10.1109/TDEI.2014.004530

Yang, N., and Di, Y. (2018). Research on Modelling and Solution of Stochastic SCUC under AC Power Flow Constraints. *IET Generation, Transm. Distribution* 12, 3618–3625. doi:10.1049/iet-gtd.2018.5151

Yang, N., Huang, Y., Hou, D., Liu, S., Ye, D., Dong, B., et al. (2019). Adaptive Nonparametric Kernel Density Estimation Approach for Joint Probability Density Function Modeling of Multiple Wind Farms. *Energies* 12, 1356. doi:10.3390/en12071356

Yang, N., Liu, S., Deng, Y., and Xing, C. (2020). An Improved Robust SCUC Approach Considering Multiple Uncertainty and Correlation. *IEEJ Trans. Elec Electron. Eng.* 16 (1), 21–34. doi:10.1002/tee.23265

Yang, N., Yang, C., Wu, L., Shen, X., Jia, J., Li, Z., et al. (2021). Intelligent Data-Driven Decision-Making Method for Dynamic Multi-Sequence: An E-Seq2Seq Based SCUC Expert System. *IEEE Trans. Ind. Inf.*, 1. doi:10.1109/TII.2021.3107406

Zhang, L., and Luo, Y. (2018). Combined Heat and Power Scheduling: Utilizing Building-Level Thermal Inertia for Short-Term Thermal Energy Storage in District Heat System. *IEEJ Trans. Elec Electron. Eng.* 13, 804–814. doi:10.1002/tee.22633

Zhang, L., Xie, Y., Ye, J., Xue, T., Cheng, J., Li, Z., et al. (2021). Intelligent Frequency Control Strategy Based on Reinforcement Learning of Multi-Objective Collaborative Reward Function. *Front. Energ. Res.* 9. doi:10.3389/fenrg.2021.760525

Zhu, B., Ding, F., and Vilathgamuwa, D. M. (2020). Coat Circuits for DC-DC Converters to Improve Voltage Conversion Ratio. *IEEE Trans. Power Electron.* 35, 3679–3687. doi:10.1109/TPEL.2019.2934726

Conflict of Interest: The authors declare that the research was conducted in the absence of any commercial or financial relationships that could be construed as a potential conflict of interest.

Publisher's Note: All claims expressed in this article are solely those of the authors and do not necessarily represent those of their affiliated organizations, or those of the publisher, the editors, and the reviewers. Any product that may be evaluated in this article, or claim that may be made by its manufacturer, is not guaranteed or endorsed by the publisher.

frontiers in Energy Research

ORIGINAL RESEARCH
published: 19 November 2021
doi: 10.3389/fenrg.2021.799039

Monitoring and Identifying Wind Turbine Generator Bearing Faults Using Deep Belief Network and EWMA Control Charts

Huajin Li[1,2], *Jiahao Deng*[3]*, *Shuang Yuan*[2], *Peng Feng*[1] *and Dimuthu D. K. Arachchige*[3]

[1]School of Architecture and Civil Engineering, Chengdu University, Chengdu, China, [2]State Key Laboratory of Geo-hazard Prevention and Geo-environment Protection, Chengdu University of Technology, Chengdu, China, [3]College of Computing and Digital Media, DePaul University, Chicago, IL, United States

Wind turbines are widely installed as the new source of cleaner energy production. Dynamic and random stress imposed on the generator bearing of a wind turbine may lead to overheating and failure. In this paper, a data-driven approach for condition monitoring of generator bearings using temporal temperature data is presented. Four algorithms, the support vector regression machine, neural network, extreme learning machine, and the deep belief network are applied to model the bearing behavior. Comparative analysis of the models has demonstrated that the deep belief network is most accurate. It has been observed that the bearing failure is preceded by a change in the prediction error of bearing temperature. An exponentially-weighted moving average (EWMA) control chart is deployed to trend the error. Then a binary vector containing the abnormal errors and the normal residuals are generated for classifying failures. LS-SVM based classification models are developed to classify the fault bearings and the normal ones. The proposed approach has been validated with the data collected from 11 wind turbines.

Keywords: bearing failure, condition monitoring, deep belief network, EWMA control chart, SCADA data analysis

OPEN ACCESS

Edited by:
Xun Shen,
Tokyo University of Agriculture and Technology, Japan

Reviewed by:
Zhiyu Sun,
The University of Iowa, United States
Heming Huang,
Wuhan University, China

***Correspondence:**
Jiahao Deng
jdeng5@depaul.edu

Specialty section:
This article was submitted to Wind Energy, a section of the journal Frontiers in Energy Research

Received: *21 October 2021*
Accepted: *01 November 2021*
Published: *19 November 2021*

Citation:
Li H, Deng J, Yuan S, Feng P and Arachchige DDK (2021) Monitoring and Identifying Wind Turbine Generator Bearing Faults Using Deep Belief Network and EWMA Control Charts. Front. Energy Res. 9:799039. doi: 10.3389/fenrg.2021.799039

1 INTRODUCTION

Wind energy is the fastest growing form of renewable energy. Continuous operations in all environmental conditions contribute to failures of wind turbine components, assemblies, and systems. The generator of a wind turbine is one of the most failure-prone assemblies due to the variable loads (Kusiak and Verma, 2012). Bearing failures account for more than 40% of the overall wind turbine generator failures leading to unexpected energy losses (Tavner et al., 2012). Hence, a solution for effective condition monitoring of generator bearings and early identification of failure symptoms is needed.

Deteriorating performance of a generator bearing manifests itself on abnormal changes of the vibration signal, torque, and bearing temperature (Yang et al., 2017; Feng et al., 2020). Vibration analysis and data-driven approaches have been applied for condition monitoring of generator bearings (Yang et al., 2018). The frequently used classical vibration analysis approaches include Fourier transformation (Klein et al., 2001), wavelet transform (Yan et al., 2014), Hilbert-Huang transform (Peng et al., 2005; Huang and Wu 2008), and empirical model decomposition (EMD) (Huang et al., 2008). Other models have been developed. Teng et al. (2016) utilized a complex

Gaussian wavelet to obtain the multi-scale enveloping spectrogram for extracting weak features. Lei et al. (2013) applied an ant colony algorithm to form adaptive stochastic resonance method for failure detection. Peeters et al. (2018) integrated automated spectrum editing procedure, band-pass filtering and envelop analysis to detect bearing failures based on the vibration signal. Vibration analysis approaches are valuable in monitoring and diagnosis of generator bearing failures. However, high frequency data from multiple vibration sensors is needed to perform such analysis. However, at present high frequency data is not available from industrial turbines due to the excessive cost and data sharing practices.

Most commercial wind turbines are equipped with the supervisory control and data acquisition (SCADA) systems collecting data that can be used to model behavior of generator bearings. Kusiak and Verma. (2012) applied a neural network to model bearing temperature for failure prediction and identification. Guo. (2012) introduced nonlinear state estimate technique (NSET) for temperature-based failure detection. Yang et al. (2013) applied correlation analysis and quantitative assessment based on the SCADA data. The published literature indicates that the data-driven methods provide robust bearing monitoring solutions for wind turbines.

Deep learning is a recent addition to the modeling suite with promising applications in multiple domains (Ouyang et al., 2017; Sun et al., 2020a; Sun et al., 2020b; Shen et al., 2021a; He et al., 2018; Li et al., 2018). The deep learning algorithms are capable of extracting in-depth features and patterns within the training dataset (Gritsenko et al., 2017; Ouyang et al., 2019; Li et al., 2020; Shen et al., 2021b; Shen and Raksincharoensak 2021). Within the wind energy sector, it has been applied in the prediction tasks of wind speed (Hu et al., 2016), wind power (Wang et al., 2017), and wind direction (Wang et al., 2016a; Li et al., 2021a). Extensive research has also been published using the deep-learning approaches: Wang et al. (2016b) developed deep auto-encoders to compress the time-series SCADA dataset and the blade breakages are extracted from the deep-learned features. Yang et al. (2018) applied stacked Restricted Boltzmann Machines (RBMs) to capture the system-wide patterns and then performed condition monitoring with promising results. Bach-Andersen et al. (2018) selected 1-dimensional convolutional neural networks (CNN) to extract temporal features to classify failures of gearbox bearings. Overall, deep-learning algorithms support development of higher complexity models.

In this research, a deep-learning approach is explored to monitor generator bearings. A deep belief network (DBN) integrated with back-propagation (B-P) fine-tuning and layer-wise training is developed to model normal generator bearing temperature using SCADA data. Four data-driven models predicting normal bearing temperature are constructed. Their performance is assessed with the absolute percentage error (APE), the mean absolute percentage error (MAPE) and the root mean square error (RMSE). The analysis of industrial SCADA data indicates that that bearing failure is preceded by the error shift. The exponentially weighted moving average (EWMA) control chart is applied to monitor the error shift. A temporal binary vector is generated in real-time, and a final failure classification model is developed. The benefits of the proposed approach are demonstrated with computational experiments.

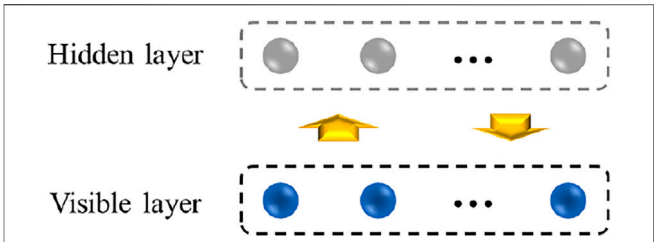

FIGURE 1 | The restricted Boltzmann machine.

2 RESEARCH METHODOLOGY

The use of deep-learning algorithms in prediction and condition monitoring is growing (LeCun et al., 2015). Deep learning originates from the research in neural networks. Deep-learning algorithms avoid the local optima dilemma and contains superior power in extracting globally robust features from the dataset (Deng and Yu 2013; Qiu et al., 2017).

2.1 Deep Belief Network

In this research, a deep belief network (DBN) is applied to model the generator bearing temperature. Proposed by Hinton et al. (2006), the classical DBN algorithm multilayers of restricted Boltzmann machines (RBMs) and a logistic regression layer (Wang et al., 2016c).

The restricted Boltzmann machine (RBM) is a commonly used generative stochastic neural network (Hinton et al., 2006). It includes a visible layer of binary-valued neurons and a hidden layer of Boolean neurons (see **Figure 1**). The connection between the hidden layer and the visible layer is bidirectional and symmetrical. There are no inter-connections between neurons in the same layer.

Training a single restricted Boltzmann machine (RBM) involves the weight matrix between the two layers. The configuration of weight matrix is based on the energy function expressed in **Eq. 1** (Wang et al., 2016c). The joint distribution of a visible layer vector and the hidden layer vector is expressed in **Eq. 2** (Hinton et al., 2006). The activation functions of neurons in the visible and hidden layer are presented in **Eqs 3**, **4** (Hinton et al., 2006

$$E(v,h) = -\sum_{i=1}^{n_v} a_i v_i - \sum_{j=1}^{n_h} b_j h_j - \sum_{i=1}^{n_v}\sum_{j=1}^{n_h} h_j w_{j,i} v_i, \qquad (1)$$

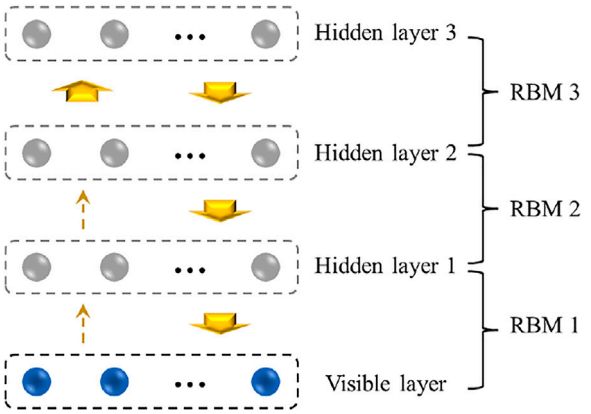

FIGURE 2 | Architecture of the deep belief network.

$$P(v,h) = \frac{e^{-E(v,h)}}{\sum_{v}\sum_{h} e^{-E(v,h)}}, \tag{2}$$

$$P(v_i = 1|h) = \mathrm{sig}\left(\alpha_i + \sum_{j=1}^{n_h} w_{j,i} h_j\right), \tag{3}$$

$$P(h_i = 1|v) = \mathrm{sig}\left(b_j + \sum_{i=1}^{n_v} w_{j,i} v_i\right), \tag{4}$$

where: v_i is the number of neurons in the visible layer; h_i is the number of Boolean neurons within the hidden layer; $w_{j,i}$ is the weight matrix between the visible layer and hidden layer; a_i and b_i are the biases of the two layers; and *sig*() denotes the logistic sigmoid function. Hence, the weight matrix and the layer biases are obtained in a layer-wise unsupervised pre-training described in the **Section 2.2**.

2.2 Layer-wise Pre-training

A deep belief network (DBN) includes multiple layers of restricted Boltzmann machines (RBMs) (Ouyang et al., 2019). **Figure 2** shows the architecture of the proposed DBN. The first RBM of the DBN model consisting of a visible and a hidden layer (hidden layer 1) is pre-trained as an independent RBM. Then, the weight matrix of the first RBM is computed. The output of the first RBM becomes the input to the second RBM that includes two layers. The first layer (hidden layer 1) is treated as a visible layer of the second RBM while the second layer (hidden layer 2) is treated as the hidden layer. The weight matrix of the second RBM is computed. Hence, the weight matrices between the remaining hidden layers are obtained iteratively.

Training each restricted Boltzmann machine (RBM) is accomplished with a stochastic gradient descent method (Hinton et al., 2006). Based on vector **Eq. 2** of the joint distribution function between the visible and hidden layer, the objective function of the stochastic gradient descend method is expressed in **Eq. 5** (Wang et al., 2016c).

$$L(a,b,w) = \sum \log P(v,h), \tag{5}$$

where: a is the bias vector of the visible layer; b is the bias vector of the hidden layer; and w is the weight matrix between the two layers. The parameters of the objective function (a, b, w) are updated based on the gradients of the function expressed in **Eqs 6–8**. The updating rules are formulated in **Eqs 9–11** (Hinton et al., 2006).

$$\frac{\partial \log P(v,h)}{\partial w_{j,i}} = \langle v_i h_i \rangle_{P(h|v)} - \langle v_i h_i \rangle_{\mathrm{recon}}, \tag{6}$$

$$\frac{\partial \log P(v,h)}{\partial a_i} = \langle v_i \rangle_{P(h|v)} - \langle v_i \rangle_{\mathrm{recon}}, \tag{7}$$

$$\frac{\partial \log P(v,h)}{\partial b_j} = \langle h_i \rangle_{P(h|v)} - \langle h_i \rangle_{\mathrm{recon}} \tag{8}$$

$$w_{i+1} = w_i + \eta\left(\langle v_i h_i \rangle_{P(h|v)} - \langle v_i h_i \rangle_{\mathrm{recon}}\right), \tag{9}$$

$$b_{i+1} = b_i + \eta\left(\langle v_i \rangle_{P(h|v)} - \langle v_i \rangle_{\mathrm{recon}}\right), \tag{10}$$

$$a_{i+1} = a_i + \eta\left(\langle h_i \rangle_{P(h|v)} - \langle h_i \rangle_{\mathrm{recon}}\right), \tag{11}$$

where: η is the learning rate; $\langle\rangle_{P(h|v)}$is the expectation of the conditional distribution with respect to the original input data; $\langle\rangle_{\mathrm{recon}}$ is the i-step reconstructed distribution obtained by the alternating Gibbs sampling scheme. The expectation of the reconstructed distribution is computed following the rules of contrastive divergence (Hinton, 2002).

2.3 Data-Driven Algorithms

Performance of the deep belief network (DBN) is compared with three algorithms, support vector regression machine (SVR), neural network (NN), and extreme learning machine (ELM).

The support vector regression machine (SVR) is considered in this study includes a Gaussian kernel function (Drucker et al., 1997). The values of the model parameters (c and γ) are selected based on the 10-fold cross-validation. The neural network (NN) contains two hidden layers. By testing on a small portion of the training data, the sigmoid activation function is selected based on the satisfactory performance. The extreme learning machine (ELM) algorithm (Liang et al., 2006) is utilized to model the normal bearing temperature. As a single-hidden layer feed-forward network, the ELM learning model is expressed in **Eqs 12, 13** (Liang et al., 2006).

$$f_L(x_j) = o_j, \forall j, \tag{12}$$

$$\sum_{i=1}^{L} \beta_i G(a_i, b_i, x_j) = t_j, j = 1, 2, ..., N, \tag{13}$$

where: x_j represents the input parameters; o_j represents the predicted output values; $f_L()$ is the non-linear function representing the ELM algorithm; a_i is the weight vector connecting the i^{th} hidden node and the input nodes; b_i is the threshold of the i^{th} hidden node; β_i is the weight vector connecting the i^{th} hidden node and the output nodes; and t_j is the actual output value.

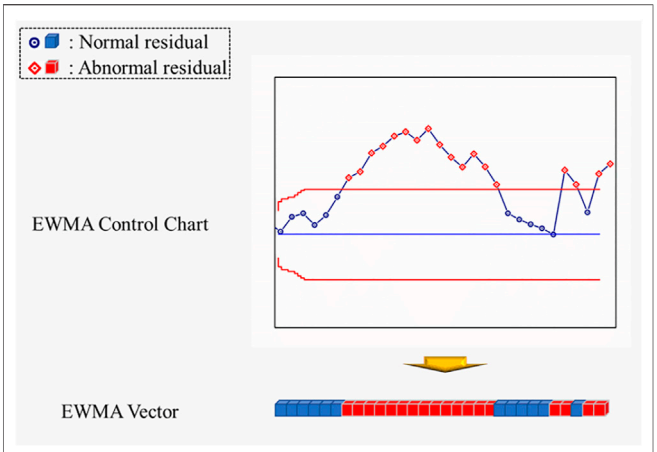

FIGURE 3 | Vectorization of residuals using EWMA control charts.

2.4 Performance Evaluation Metrics

To assess prediction accuracy of the deep belief network, three performance evaluation metrics are computed: the absolute percentage error (APE) **Eq. 14**, the mean absolute percentage error (MAPE) **Eq. 15**, and the root mean square error (RMSE) **Eq. 16**.

$$\mathrm{APE} = \left|\frac{o_j - t_j}{t_j}\right| * 100\%, \tag{14}$$

$$\mathrm{MAPE} = \frac{1}{N}\sum_{i=1}^{N}\left|\frac{o_j - t_j}{t_j}\right|, \tag{15}$$

$$\mathrm{RMSE} = \sqrt{\frac{1}{N}\sum_{j=1}^{N}\left\|o_j - t_j\right\|^2}, \tag{16}$$

where: o_j is the j^{th} predicted generator bearing temperature; t_j is the j^{th} actual generator bearing temperature; N denotes the number of data points.

2.5 Exponentially Weighted Moving Average Control Chart

The increasing value of the prediction bearing temperature error of a data-driven model reflects deterioration of the generator bearing conditions. In this research, an exponentially weighted moving average (EWMA) (Jones et al., 2001) control chart is applied to monitor the error. The weighted average of the past bearing temperatures reduces the noise and allows detecting small process shifts.

To compute the upper and lower confidence limits of the EWMA control chart, the $EWMA_t$ is obtained from **Eq. 17** (Wang et al., 2016b). The upper and lower confidence limits can be computed from **Eqs 18**, **19** (Horng Shiau and Ya-Chen 2005).

$$\mathrm{EWMA}_t = \lambda * \mathrm{APE}_t + (1-\lambda) * \mathrm{EWMA}_{t-1}, \tag{17}$$

$$\mathrm{UCL}(t) = \mu_{\mathrm{APE}} + L * \sigma_{\mathrm{APE}}\sqrt{\frac{\lambda\left[1-(1-\lambda)^{2t}\right]}{(2-\lambda)N}}, \tag{18}$$

$$\mathrm{LCL}(t) = \mu_{\mathrm{APE}} - L * \sigma_{\mathrm{APE}}\sqrt{\frac{\lambda\left[1-(1-\lambda)^{2t}\right]}{(2-\lambda)N}}, \tag{19}$$

where: μ_{APE} is the mean of absolute percentage error (APE); σ_{APE} is the standard deviation of APE; N denotes number of samples. According to Horng Shiau and Ya-Chen. (2005), the value of the parameter L is commonly set to 3 and λ is usually set to 0.2.

2.6 Binary Vectors Generated by Control Chart

The EWMA control charts used statistical thresholds to label the prediction error (residuals) as normal and abnormal. The normal residual usually denotes the bearing temperature is within the normal range and the wind turbine is at healthy status. On the other hand, the abnormal values often indicate abnormal bearing temperature change and it can be the warning signal for bearing failures. Hence, in this research, the normal and abnormal residuals identified by the EWMA control charts are transformed into binary vectors as described in **Figure 3** as follows.

According to **Figure 3**, the statistical thresholds classified the residuals into normal and abnormal ones. Each data point can be simply labeled as 0 (normal) and 1 (abnormal). Hence, the binary vectors can be generated in real-time and be utilized as the inputs for the final classification models introduced in the **Section 2.7**.

2.7 Classification Models

Using the real-time vectors generated by the EWMA control charts, the final failure classification models are constructed in this research. Here, the dimension of the input vector is determined as 20 which represents all normal/abnormal prediction residuals of bearing temperatures. In total of four state-of-art machine learning algorithms including support vector machine (SVM), least-square support vector machine (LS-SVM), extreme learning machine (ELM), and kernel-based extreme learning machine (KELM) are selected to classify the vectors representing generator bearing failures and vectors from normal bearing behaviors.

The SVM is the state-of-art supervised learning algorithm used for classification and function approximation (Cherkassky and Ma, 2004). It is based on kernel functions and it avoids the difficulty of using linear functions in the high dimensional parameter space, and the optimization problem is transformed into a dual convex quadratic programming problem.

The LS-SVM is developed based on statistical theory and considered as the improved version of SVM (Zhu et al., 2018). Compared with the vanilla SVM, the LS-SVM modifies the inequality constraint in the SVM to the equality constraint. Meanwhile, the training error square is used to replace the slack variable in order to transform quadratic programming problem into the linear equation problem for greatly improving the speed and accuracy of model parameters. The

TABLE 1 | Dataset description.

Turbine id.	Bearing temperature		Bearing failure	Failure times
	Min (°C)	Max (°C)		
A	14	68	No	
B	11	87	Yes	8
C	0	63	No	
D	3	68	No	
E	13	71	No	
F	13	69	No	
G	0	73	No	
H	6	90	Yes	2
I	9	86	Yes	5
J	14	71	No	
K	7	85	Yes	7

LS-SVM has the unique superiority in dealing with the small-sample learning problem.

The ELM is a feedforward neural network which contains the input layer, the output layer and one single hidden layer. Compared with other computationally expensive and time-consuming neural networks, the ELM adopts Penn Moore pseudo inverse to determine the weights and biases between the hidden layer and output layer (Li et al., 2021b). This method enables ELM to learn faster and attain higher generalization capability compared with other neural networks.

The KELM uses the kernel method over the vanilla ELM and it solves the problem of random initialization of ELM and has high classification accuracy (Pandey et al., 2018; Ouyang 2021), good generalization ability and high degree of robustness. The Gaussian kernel function is the most frequently used kernel function and thus is selected in this study.

3 COMPUTATIONAL ANALYSIS

The data used in this research has been collected from SCADA systems of a large wind farm. The data 10 min resolution data from 11 wind turbines is used to investigate failure of a generator bearing. Two bearing failure instances have been reported during the period covered by the dataset.

3.1 Dataset Description and Preprocessing

The ranges of the generator bearing temperature of the 11 turbines are provided in **Table 1**. The bearing failure incidents are also included in **Table 1**. Based on the maintenance records, Turbine B, H, I, and K have been affected by bearing failures and are not considered for modeling normal bearing behavior discussed in the **Section 3.2**. Rather they are selected to test abnormal behavior of the bearing temperature.

3.2 Parameter Selection

To capture the normal behavior of a generator bearing, 33 parameters relevant to the bearing temperature have been initially considered. Using domain expertise, the number of parameters of interest was reduced to 12. Next, three algorithms (i.e., the wrapper with genetic search (WGS) (Kohavi and John, 1997), boosting-tree algorithm (BTA) (Sbihi, 2007), and the relief algorithm (RA) (Liu et al., 2018) were applied to select the most relevant parameters for predicting the generator bearing temperature. The wrapper approach uses supervised learning to perform 10-fold cross validation in selecting relevant parameters. The boosting-tree algorithm evaluates the importance of parameters by constructing a sequence of decision trees and computing the prediction residuals. The relief algorithm selects the parameter set by detecting conditional dependence between the parameters. The eight most important parameters selected by the three data-mining algorithms are listed in **Table 2**.

TABLE 2 | Dataset description.

Parameter	BTA	WGS	RFA
Generator phase-1 winding temperature	100	10	0.1
Generator phase-2 winding temperature	98	10	0.1
Generator air temperature	97	10	0.09
Generator rear temperature	96	9	0.09
Generator phase-3 winding temperature	96	9	0.1
Water cooler temperature	91	8	0.11
Phase compensation panel temperature	78	7	0.07
Nacelle temperature	78	6	0.05

3.3 Modeling Bearing Behavior

Data from three wind turbines (i.e., Turbine C, Turbine D, Turbine E) have been merged to train the neural network, support vector regression machine, the extreme-learning machine presented in **Section 2.2**, and the proposed deep belief network (DBN). Data collected from Turbine A, B, F and G are used as validation dataset to validate prediction performance of the proposed DBN algorithm. Data from Turbine G, J, I and K are used as testing dataset respectively. To design the DBN, the number of hidden neurons in each layer is set at 10% of the training data (Mitchell, 1999). The data from the remaining 2 healthy turbines (i.e., Turbine 9 and 11) are designated as test datasets to evaluate performance of the four algorithms.

Table 3 presents prediction results produced by the four algorithms based for the test and validation datasets. The mean absolute percentage error (*MAPE*) and the root mean square errors (*RMSE*) produced by the DBN algorithm are the smallest which confirms the accuracy of the DBN model. This superior performance may be attributed to the layer-wise pre-training.

Figure 4 illustrates prediction error from testing and validation produced by the deep belief network (DBN). The *APEs* of healthy wind turbines and turbines with bearing failures demonstrate different behaviors. Hence, the emerging bearing failure is indicated by the *APE* of the DBN model.

3.4 Condition Monitoring

In this section, behavior of the prediction error associated with the bearing failure is discussed. The *APE* was monitored for

TABLE 3 | Performance evaluation of four algorithms.

Algorithm	Validation				Testing			
	Turbine B, H		Turbine A, F		Turbine G, J		Turbine I, K	
	MAPE (%)	RMSE	MAPE (%)	RMSE	MAPE (%)	RMSE	MAPE (%)	RMSE
SVR	1.27	0.93	0.96	0.56	4.95	4.27	4.46	3.98
NN	0.65	0.41	0.42	0.34	2.57	2.12	2.29	2.04
ELM	0.94	0.52	0.92	0.51	3.55	2.86	4.81	4.22
DBN	0.63	0.49	0.33	0.23	2.38	1.80	2.23	2.01

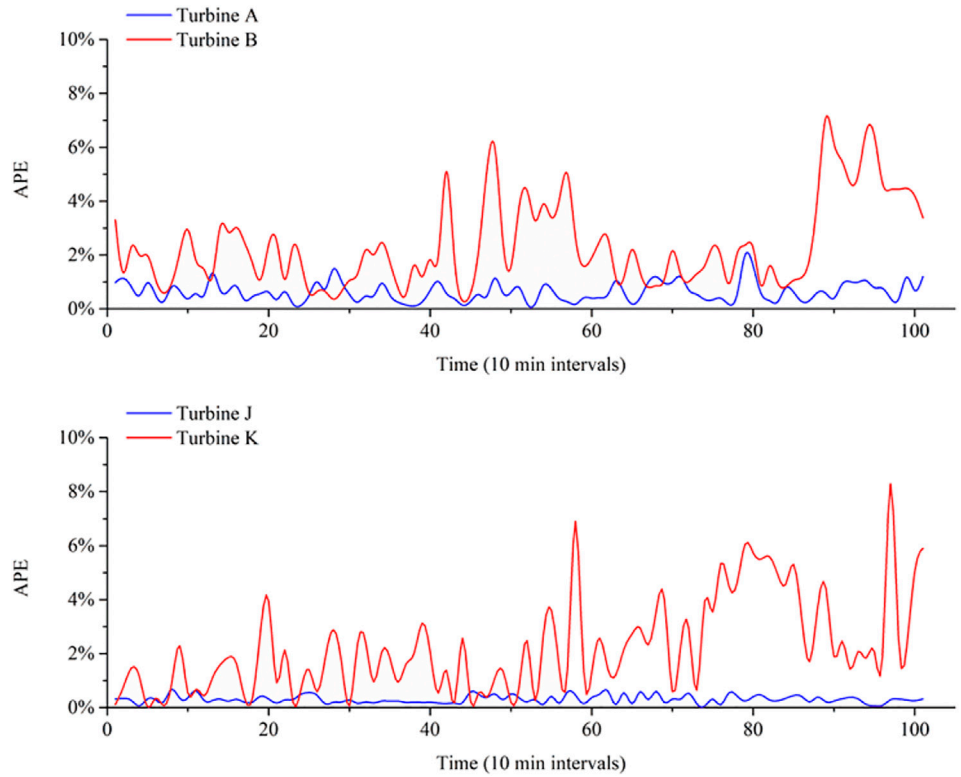

FIGURE 4 | The absolute percentage error produced by the deep belief network.

1 week prior to the bearing failure. The upper confidence limit (UCL) and the lower confidence limit (LCL) of the exponentially-weighted moving average (EWMA) control chart are computed from **Eqs 18**, **19** of **Section 2.4**. The monitored examples of healthy turbines and the turbines with emerging bearing failures are illustrated in **Figures 5**, **6**.

Figure 5 illustrates the EWMA charts of healthy turbines (Turbine G and J) while **Figure 6** shows the wind turbines (Turbine I and K) with problematic generator bearings of the same wind farm. In **Figure 5**, all statistics fall within the control limits which indicates normal bearing behavior. Meanwhile, outliers in **Figure 6** begin to emerge 1 week prior to the bearing failure and an early alarm is issued. According to the results presented in **Figure 6**, bearing failures are visible several days ahead of the occurrence. The proposed approach provides sufficient time to react and thus minimize power loss and downtime.

The outcomes of the EWMAs are transformed into the real-time binary vectors and then the bearing failure classification models are developed to classify the actual failures. However, in the temporal domain, the optimal size of the EWMA vectors are uncertain. Hence, this research performed several experiments by trying difference size of the EWMA vectors (i.e., $K = 10, 20, 30, 40$). All algorithms introduced in the **Section**

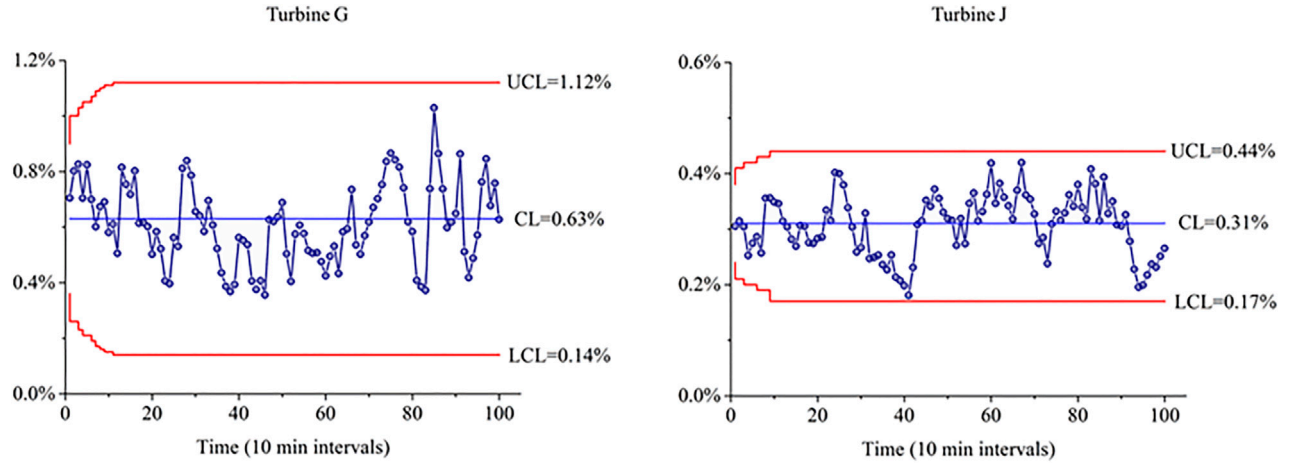

FIGURE 5 | The EWMA control charts of two healthy turbines.

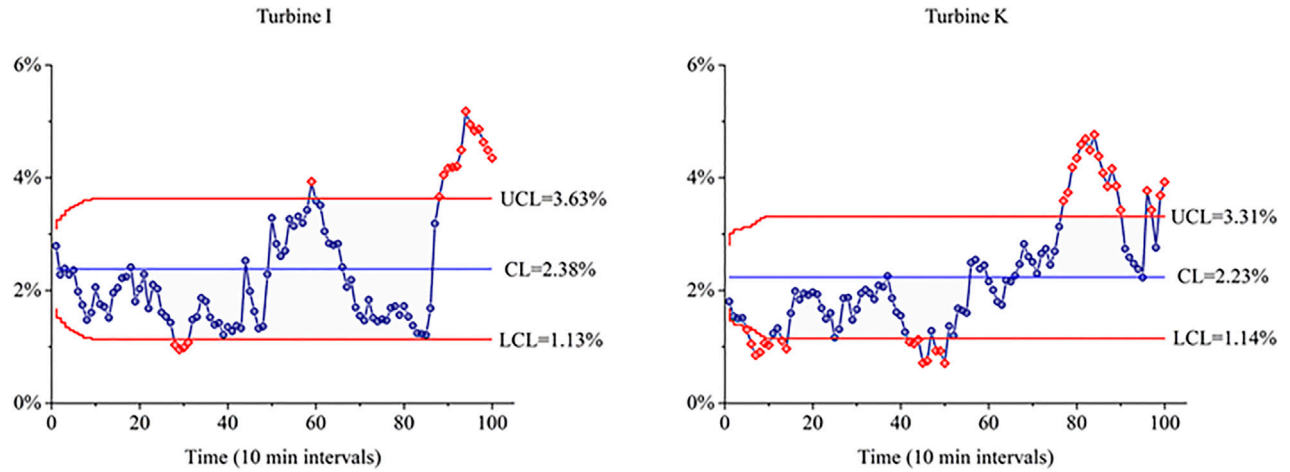

FIGURE 6 | The EWMA control charts of two turbines with bearing failures.

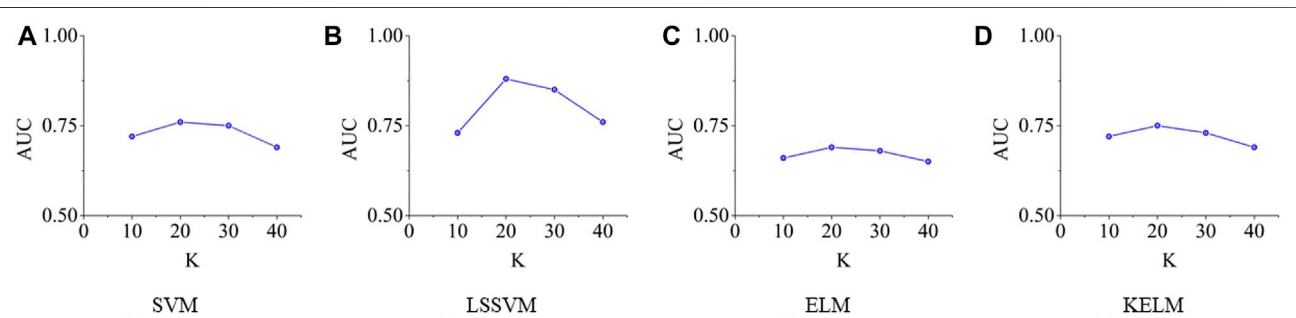

FIGURE 7 | The AUCs of all classification algorithms under different dimensions of EWMA vectors.

2.7 are tested and the computational results are illustrated in **Figure 7** below. The AUC is selected as the measurement It is obvious that all algorithms reached their peak classification performance when K = 20 and thus it is selected as the optimal setting for the dimension of the input EWMA vector in our study.

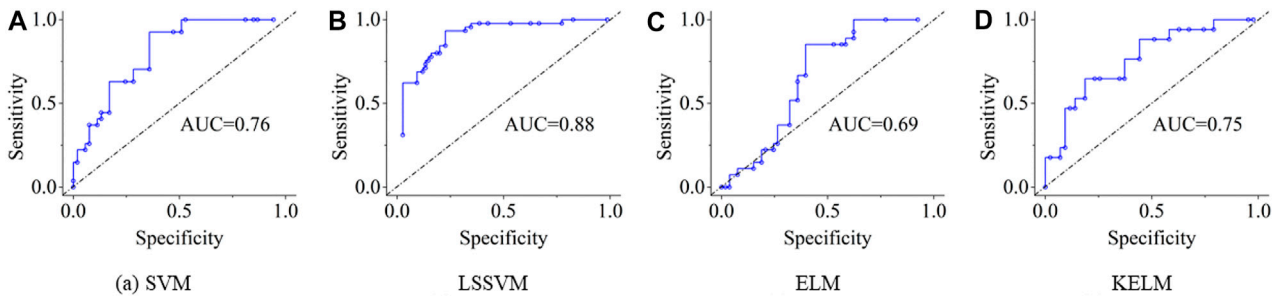

FIGURE 8 | ROC curves of the bearing failure classification outcome.

TABLE 4 | Summary of bearing fault classification results.

Classifier	Accuracy		Sensitivity		Specificity		AUC	
	Mean	95% C.I.	Mean	95% C.I.	Mean	95% C.I.	Mean	95% C.I.
SVM	0.74	(0.71–0.77)	0.64	(0.58–0.70)	0.87	(0.80–0.94)	0.76	(0.72–0.80)
LSSVM	0.83	(0.78–0.88)	0.77	(0.72–0.83)	0.94	(0.91–0.97)	0.88	(0.81–0.95)
ELM	0.71	(0.65–0.77)	0.64	(0.61–0.67)	0.79	(0.72–0.86)	0.69	(0.60–0.78)
KELM	0.76	(0.72–0.80)	0.71	(0.65–0.77)	0.82	(0.78–0.86)	0.75	(0.70–0.80)

As illustrated in **Figure 8** below, the ROC curves for the four state-of-art algorithms are obtained with respect to the testing dataset. Among them, the LS-SVM achieves the highest area under the ROC curve (AUC) as 0.88 which demonstrates its superior performance in classifying bearing failures from the binary vector mixed with normal and abnormal prediction residuals. Meanwhile, the other performance metrics including accuracy, sensitivity and specificity along with the 95% confidence intervals are also provided in **Table 4**. The LS-SVM still performs best among all algorithms tested according to all evaluation metrics. Hence, using the vectors generated from the DBN and EWMA control charts, the LS-SVM is capable of classify the majority of the bearing failures in the temporal domain.

4 DISCUSSION

The condition-monitoring framework proposed in this study has provided promising results using field SCADA data. Overall, the advantages of the proposed framework can be summarized into the following three points: First, it uses deep belief network as the backbone regressor. It has shown superior power in extracting temporal abnormal features from the dataset. Second, the framework is designed to be implemented on SCADA data which is the standard data collection system for almost all wind farms across the globe. Hence, it can be widely implemented on practice. Third, the classification part can save a lor of labor and time. Conventional control chart-based identification of mechanical failures requires humans to detect the statistical outliers. Instead, in this research, the machine-learning classifiers enables the automation of this process. In sum, it can be widely applied in wind farms for condition monitoring tasks.

On the other hand, there are also few shortcomings at current stage. For example, the sensor errors can be a misleading factor that cause false classification of mechanical failures. The reliability of the SCADA sensors is not considered in this framework. This can be a future direction of our current research.

5 CONCLUSION

In this research, a deep-learning based condition-monitoring framework to identify bearing failures was presented in this study. Historical data collected from healthy wind turbines was utilized to develop a model predicting bearing temperature with a deep belief network. Data from both healthy wind turbines and turbines to the bearing failures are served as the testing dataset. Comparative analysis demonstrated that the deep belief network model was more accurate in predicting generator bearing failures. An exponentially-weighted moving-average control chart was applied to capture shifts in prediction error. The control charts generated binary vectors lead to identification of the emerging bearing failure in real-time in the temporal domain.

Computational results reported in the paper validated accuracy of the deep-learning framework in condition monitoring of wind turbine generator bearings. In the future

research, analysis of high frequency vibration data may be coupled with the bearing temperature data for multi-scale condition monitoring.

DATA AVAILABILITY STATEMENT

The raw data supporting the conclusion of this article will be made available by the authors, without undue reservation.

AUTHOR CONTRIBUTIONS

HL conceptualized the study, contributed to the study methodology, and wrote the original draft. JD contributed to the study methodology, data curation and investigation. SY and PF contributed to data analysis and investigation. HL contributed to software and formal analysis. DA contributed to investigation and writing-original draft. All authors have read and agreed to the published version of the manuscript.

FUNDING

This research is supported by National Key Research and Development Program of China (2018YFC1505105), the Opening fund of State Key Laboratory of Geohazard Prevention and Geoenvironment Protection (Chengdu University of Technology) (Grant No. SKLGP2021K014), the "Miaozi project" of scientific and technological innovation in Sichuan Province, China (Grant No. 2021090), the Project from Sichuan Mineral Resources Research Center (SCKCZY2021-YB009), and the Open Research Subject of Key Laboratory of Fluid and Power Machinery (Xihua University), Ministry of Education (Grant No. LTDL2021-011).

REFERENCES

Bach-Andersen, M., Rømer-Odgaard, B., and Winther, O. (2018). Deep Learning for Automated Drivetrain Fault Detection. *Wind Energy* 21 (1), 29–41. doi:10.1002/we.2142

Cherkassky, V., and Ma, Y. (2004). Practical Selection of SVM Parameters and Noise Estimation for SVM Regression. *Neural networks* 17 (1), 113–126. doi:10.1016/s0893-6080(03)00169-2

Deng, L., and Yu, D. (2013). Deep Learning for Signal and Information Processing. *IEEE Signal. Process. Mag.* 28 (1), 145–154. doi:10.1109/MSP.2010.939038

Drucker, H., Burges, C., Kaufman, L., Smola, A., and Vapnik, V. (1997). Support Vector Regression Machines. *Adv. Neural Inf. Process. Syst.* 9, 155–161.

Feng, P., Wei, M., Dai, F., Tang, R., Qiu, H., and Gong, J. (2020). DEM Investigation on the Mechanical Behaviors of Flawed Specimens Subjected to Coupled Static-Dynamic Loads. *Soil Dyn. Earthquake Eng.* 135, 106–220. doi:10.1016/j.soildyn.2020.106220

Gritsenko, A., Sun, Z., Baek, S., Miche, Y., Hu, R., and Lendasse, A. (2017). "Deformable Surface Registration with Extreme Learning Machines," in *International Conference on Extreme Learning Machine* (Cham: Springer), 304–316. doi:10.1007/978-3-030-01520-6_28

Guo, P. (2012). Wind Turbine Generator Bearing Condition Monitoring with NEST Method," in Proceedings of the 2012 24th Chinese Control and Decision Conference (CCDC) (IEEE), Taiyuan, China, May 2012, 235–239. 10.1109/CCDC.2012.6244033.

He, Y., Fei, F., Wang, W., Song, X., Sun, Z., and Baek, S. (2018). "Predicting Manufactured Shapes of a Projection Micro-stereolithography Process via Convolutional Encoder-Decoder Networks," in Proceedings of the International Design Engineering Technical Conferences and Computers and Information in Engineering Conference (American Society of Mechanical Engineers (ASME)), V01BT02A033. doi:10.1115/detc2018-85458

Hinton, G. E., Osindero, S., and Teh, Y.-W. (2006). A Fast Learning Algorithm for Deep Belief Nets. *Neural Comput.* 18 (7), 1527–1554. doi:10.1162/neco.2006.18.7.1527

Hinton, G. E. (2002). Training Products of Experts by Minimizing Contrastive Divergence. *Neural Comput.* 14 (8), 1771–1800. doi:10.1162/089976602760128018

Horng Shiau, J.-J., and Ya-Chen, H. (2005). Robustness of the EWMA Control Chart to Non-normality for Autocorrelated Processes. *Qual. Technology Quantitative Management* 2 (2), 125–146. doi:10.1080/16843703.2005.11673089

Hu, Q., Zhang, R., and Zhou, Y. (2016). Transfer Learning for Short-Term Wind Speed Prediction with Deep Neural Networks. *Renew. Energ.* 85, 83–95. doi:10.1016/j.renene.2015.06.034

Huang, N. E., and Wu, Z. (2008). A Review on Hilbert-Huang Transform: Method and its Applications to Geophysical Studies. *Rev. Geophys.* 46 (2). doi:10.1029/2007rg000228

Huang, T. L., Ren, W. X., and Lou, M. L. (2008). "The Orthogonal Hilbert-Huang Transform and its Application in Earthquake Motion Recordings Analysis," in Proceedings of the 14th World Conference on Earthquake Engineering (Beijing, China, October 2008, 12–17.

Jones, L. A., Champ, C. W., and Rigdon, S. E. (2001). The Performance of Exponentially Weighted Moving Average Charts with Estimated Parameters. *Technometrics* 43 (2), 156–167. doi:10.1198/004017001750386279

Klein, R., Ingman, D., and Braun, S. (2001). Non-stationary Signals: Phase-Energy Approach-Theory and Simulations. *Mech. Syst. Signal Process.* 15 (6), 1061–1089. doi:10.1006/mssp.2001.1398

Kohavi, R., and John, G. H. (1997). Wrappers for Feature Subset Selection. *Artif. intelligence* 97 (1-2), 273–324. doi:10.1016/s0004-3702(97)00043-x

Kusiak, A., and Verma, A. (2012). Analyzing Bearing Faults in Wind Turbines: a Data-Mining Approach. *Renew. Energ.* 48, 110–116. doi:10.1016/j.renene.2012.04.020

LeCun, Y., Bengio, Y., and Hinton, G. (2015). Deep Learning. *nature* 521 (7553), 436–444. doi:10.1038/nature14539

Lei, Y., Li, N., Lin, J., and Wang, S. (2013). Fault Diagnosis of Rotating Machinery Based on an Adaptive Ensemble Empirical Mode Decomposition. *Sensors (Basel)* 13 (1-2), 16950–16964. doi:10.3390/s131216950

Li, H., Deng, J., Feng, P., Pu, C., Arachchige, D. D. K., and Cheng, Q. (2021a). Short-Term Nacelle Orientation Forecasting Using Bilinear Transformation and ICEEMDAN Framework. *Front. Energ. Res.* 9, 780928. doi:10.3389/fenrg.2021.780928

Li, H., He, Y., Yang, H., Wei, Y., Li, S., and Xu, J. (2021b). Rainfall Prediction Using Optimally Pruned Extreme Learning Machines. *Nat. Hazards* 108 (1), 799–817. doi:10.1007/s11069-021-04706-9

Li, H., Xu, Q., He, Y., and Deng, J. (2018). Prediction of Landslide Displacement with an Ensemble-Based Extreme Learning Machine and Copula Models. *Landslides* 15 (10), 2047–2059. doi:10.1007/s10346-018-1020-2

Li, H., Xu, Q., He, Y., Fan, X., and Li, S. (2020). Modeling and Predicting Reservoir Landslide Displacement with Deep Belief Network and EWMA Control Charts: a Case Study in Three Gorges Reservoir. *Landslides* 17 (3), 693–707. doi:10.1007/s10346-019-01312-6

Liang, N. Y., Saratchandran, P., Huang, G. B., and Sundararajan, N. (2006). Classification of Mental Tasks from EEG Signals Using Extreme Learning Machine. *Int. J. Neural Syst.* 16 (1), 29–38. doi:10.1142/S0129065706000482

Liu, W., Gao, P., Yu, W., Qu, Z., and Yang, C. (2018). Quantum Relief Algorithm. *Quan. Inf. Process.* 17 (10), 1–15. doi:10.1007/s11128-018-2048-x

Mitchell, T. M. (1999). Machine Learning and Data Mining. *Commun. ACM* 42 (11), 30–36. doi:10.1145/319382.319388

Ouyang, T. (2021). Feature Learning for Stacked ELM via Low-Rank Matrix Factorization. *Neurocomputing* 448, 82–93. doi:10.1016/j.neucom.2021.03.110

Ouyang, T., He, Y., Li, H., Sun, Z., and Baek, S. (2019). Modeling and Forecasting Short-Term Power Load with Copula Model and Deep Belief Network. *IEEE Trans. Emerg. Top. Comput. Intell.* 3 (2), 127–136. doi:10.1109/tetci.2018.2880511

Ouyang, T., Kusiak, A., and He, Y. (2017). Modeling Wind-Turbine Power Curve: A Data Partitioning and Mining Approach. *Renew. Energ.* 102, 1–8. doi:10.1016/j.renene.2016.10.032

Pandey, P., Patel, V., George, N. V., and Mallajosyula, S. S. (2018). KELM-CPPpred: Kernel Extreme Learning Machine Based Prediction Model for Cell-Penetrating Peptides. *J. Proteome Res.* 17 (9), 3214–3222. doi:10.1021/acs.jproteome.8b00322

Peeters, C., Guillaume, P., and Helsen, J. (2018). Vibration-based Bearing Fault Detection for Operations and Maintenance Cost Reduction in Wind Energy. *Renew. Energ.* 116, 74–87. doi:10.1016/j.renene.2017.01.056

Peng, Z., Peter, W., and Chu, F. (2005). An Improved Hilbert–Huang Transform and its Application in Vibration Signal Analysis. *J. sound vibration* 286 (1-2), 187–205. doi:10.1016/j.jsv.2004.10.005

Qiu, X., Ren, Y., Suganthan, P. N., and Amaratunga, G. A. J. (2017). Empirical Mode Decomposition Based Ensemble Deep Learning for Load Demand Time Series Forecasting. *Appl. Soft Comput.* 54, 246–255. doi:10.1016/j.asoc.2017.01.015

Sbihi, A. (2007). A Best First Search Exact Algorithm for the Multiple-Choice Multidimensional Knapsack Problem. *J. Comb. Optim* 13 (4), 337–351. doi:10.1007/s10878-006-9035-3

Shen, X., Ouyang, T., Khajorntraidet, C., Li, Y., Li, S., and Zhuang, J. (2021a). Mixture Density Networks-Based Knock Simulator. *IEEE/ASME Trans. Mechatronics*, 1. 10.1109/TMECH.2021.3059775..

Shen, X., Ouyang, T., Yang, N., and Zhuang, J. (2021b). Sample-Based Neural Approximation Approach for Probabilistic Constrained Programs. *IEEE Trans. Neural Networks Learn. Syst.*. doi:10.1109/tnnls.2021.3102323

Shen, X., and Raksincharoensak, P. (2021). Pedestrian-Aware Statistical Risk Assessment. *IEEE Trans. Intell. Transportation Syst.*. doi:10.1109/tits.2021.3074522

Sun, Z., He, Y., Gritsenko, A., Lendasse, A., and Baek, S. (2020a). Embedded Spectral Descriptors: Learning the point-wise Correspondence Metric via Siamese Neural Networks. *J. Comput. Des. Eng.* 7 (1), 18–29. doi:10.1093/jcde/qwaa003

Sun, Z., Rooke, E., Charton, J., He, Y., Lu, J., and Baek, S. (2020b). Zernet: Convolutional Neural Networks on Arbitrary Surfaces via Zernike Local tangent Space Estimation. *Computer Graphics Forum* 39 (6), 204–216. doi:10.1111/cgf.14012

Tavner, P. J., Greenwood, D. M., Whittle, M. W. G., Gindele, R., Faulstich, S., and Hahn, B. (2012). Study of Weather and Location Effects on Wind Turbine Failure Rates. *Wind Energy* 16 (2), 175–187. doi:10.1002/we.538

Teng, W., Ding, X., Zhang, X., Liu, Y., and Ma, Z. (2016). Multi-fault Detection and Failure Analysis of Wind Turbine Gearbox Using Complex Wavelet Transform. *Renew. Energ.* 93, 591–598. doi:10.1016/j.renene.2016.03.025

Wang, H.-z., Li, G.-q., Wang, G.-b., Peng, J.-c., Jiang, H., and Liu, Y.-t. (2017). Deep Learning Based Ensemble Approach for Probabilistic Wind Power Forecasting. *Appl. Energ.* 188, 56–70. doi:10.1016/j.apenergy.2016.11.111

Wang, H. Z., Wang, G. B., Li, G. Q., Peng, J. C., and Liu, Y. T. (2016c). Deep Belief Network Based Deterministic and Probabilistic Wind Speed Forecasting Approach. *Appl. Energ.* 182, 80–93. doi:10.1016/j.apenergy.2016.08.108

Wang, L., Zhang, Z., Long, H., Xu, J., and Liu, R. (2016a). Wind Turbine Gearbox Failure Identification with Deep Neural Networks. *IEEE Trans. Ind. Inform.* 13 (3), 1360–1368.

Wang, L., Zhang, Z., Xu, J., and Liu, R. (2016b). Wind Turbine Blade Breakage Monitoring with Deep Autoencoders. *IEEE Trans. Smart Grid* 9 (4), 2824–2833.

Yan, R., Gao, R. X., and Chen, X. (2014). Wavelets for Fault Diagnosis of Rotary Machines: a Review with Applications. *Signal. Process.* 96, 1–15. doi:10.1016/j.sigpro.2013.04.015

Yang, B., Liu, R., and Chen, X. (2017). Fault Diagnosis for a Wind Turbine Generator Bearing via Sparse Representation and Shift-Invariant K-Svd. *IEEE Trans. Ind. Inform.* 23 (5), 91–99. doi:10.1109/tii.2017.2662215

Yang, W., Court, R., and Jiang, J. (2013). Wind Turbine Condition Monitoring by the Approach of SCADA Data Analysis. *Renew. Energ.* 53, 365–376. doi:10.1016/j.renene.2012.11.030

Yang, W., Liu, C., and Jiang, D. (2018). An Unsupervised Spatiotemporal Graphical Modeling Approach for Wind Turbine Condition Monitoring. *Renew. Energ.* 127, 230–241. doi:10.1016/j.renene.2018.04.059

Zhu, X., Xu, Q., Tang, M., Li, H., and Liu, F. (2018). A Hybrid Machine Learning and Computing Model for Forecasting Displacement of Multifactor-Induced Landslides. *Neural Comput. Applic* 30 (12), 3825–3835. doi:10.1007/s00521-017-2968-x

Conflict of Interest: The authors declare that the research was conducted in the absence of any commercial or financial relationships that could be construed as a potential conflict of interest.

Publisher's Note: All claims expressed in this article are solely those of the authors and do not necessarily represent those of their affiliated organizations, or those of the publisher, the editors and the reviewers. Any product that may be evaluated in this article, or claim that may be made by its manufacturer, is not guaranteed or endorsed by the publisher.

frontiers in Energy Research

ORIGINAL RESEARCH
published: 22 November 2021
doi: 10.3389/fenrg.2021.791829

Modeling the Heat-Hydrogen Balance Characteristic of Hydrogen Energy Storage and Cooperative Dispatch of Wind-Hydrogen Hybrid System

Yang Si[1,2]*, *Laijun Chen*[1]*, *Linrui Ma*[1], *Mengyu Gao*[1], *Hengrui Ma*[1] and *Shengwei Mei*[1,2]

[1]Qinghai Key Lab of Efficient Utilization of Clean Energy (New Energy Photovoltaic Industry Research Center), Qinghai University, Xining, China, [2]State Key Lab of Control and Simulation of Power Systems and Generation Equipment (Tsinghua University), Beijing, China

The heat and hydrogen balance of the hydrogen energy storage system's intermittent operation becomes a key factor affecting the performance of the wind-hydrogen hybrid system (W-HHS). This work designed a hydrogen energy storage system (HESS), including waste heat utilization. Then, a dual state of charge (SOC) model is established, in which hydrogen and heat storage is considered. Furthermore, based on the distributionally robust method, an optimal dispatch method of W-HHS is proposed to reduce the operation cost of conventional units in the grid and increase the revenue of the W-HHS. The previously proposed dual SOC model of heat-hydrogen balance is regarded as a constraint in this cooperative dispatch. The effectiveness and efficiency of the dual SOC model were verified on the IEEE 30-bus system with an actual wind plant data set. The results show that the hydrogen-heat dual SOC model can fully reflect the influence of heat and hydrogen balance on the operation of the W-HHS. The cooperative dispatch method improves the reliability of the W-HHS operation under the premise of ensuring the heat-hydrogen balance. When the constraints of hydrogen balance SOC and heat balance SOC are met simultaneously, the available power of the wind plant is 6–8% lower than the ideal situation. Parameter analysis indicates that reducing the heat dissipation coefficient can reduce the influence of the SOC constraint of heat balance on the dispatch strategy and increase the power output of the wind plant. When the heat dissipation coefficient is less than 1/1,200, the heat balance SOC constraint fails.

Keywords: hydrogen energy storage, hybrid system, cooperative dispatch, distributionally robust method, heat balance, hydrogen balance

OPEN ACCESS

Edited by:
Zhenhao Tang,
Northeast Electric Power University, China

Reviewed by:
Xiao Wang,
Wuhan University, China
Bingke Yan,
State Grid Hubei Electric Power Company, China

***Correspondence:**
Yang Si
siyang@qhu.edu.cn
Laijun Chen
chenlaijun@qhu.edu.cn

Specialty section:
This article was submitted to Wind Energy, a section of the journal Frontiers in Energy Research

Received: *09 October 2021*
Accepted: *03 November 2021*
Published: *22 November 2021*

Citation:
Si Y, Chen L, Ma L, Gao M, Ma H and Mei S (2021) Modeling the Heat-Hydrogen Balance Characteristic of Hydrogen Energy Storage and Cooperative Dispatch of Wind-Hydrogen Hybrid System. Front. Energy Res. 9:791829. doi: 10.3389/fenrg.2021.791829

INTRODUCTION

With the change of energy structure, a new power system with a high proportion of renewable energy will become the mainstream for the development of energy system transformation in the future (Zhang and Chen, 2020). Wind and solar have become the primary power sources (Jiayu et al., 2021). However, the wide application of renewable energy raises many problems. The ensuing stability and security issues have become a critical bottleneck restricting the development of a high-proportion renewable power grid (Impram et al., 2020).

Wind power is one of the primary forms of renewable energy, and its participation in the power system dispatch has received extensive attention. Some researchers use stochastic optimization (Zhu et al., 2020), robust optimization (Yu et al., 2020), distributionally robust optimization (Guo et al., 2020), and other optimization methods to try to describe the existing uncertainties in the cooperative dispatch integrated with wind power. Among them, the distributionally robust method is a data-driven optimization method, which constructs the ambiguity set of uncertain parameter probability by using the information implicit in the actual data. Significantly, the distributionally robust method based on waister distribution has been developed rapidly. Ref. (Guo et al., 2020) compared and analyzed the adaptability of distributionally robust optimization methods based on Wasserstein divergence distribution. (Esfahani and Kuhn, 2018) demonstrated this method's performance guarantee and ease of treatment in detail. At the same time, it should also be pointed out that according to lemma 8 (HOTA et al., 2019), the premise of transforming the distributionally robust model of uncertainty into a set of CVar constraints is that the optimization problem studied is convex, which limits the application of this method to a certain extent. In (Yang et al., 2020), a distributionally robust chance constraint (DRCC) model is proposed for the optimal power gas flow (OPGF) problem with uncertain wind power. The DRCC-OPGF model is reformulated as a treatable mixed-integer convex programming problem.

Besides, some works focus on the different forms of hybrid systems with a wind plant. Different types of energy storage were considered to suppress the wind fluctuation, such as batteries (Xu et al., 2020), compressed air energy storage (Alirahmi et al., 2021), hot dry rock geothermal energy (Si et al., 2021), and hydrogen energy storage system (HESS) (Xiao et al., 2020), etc. constitute the optimal dispatch of the hybrid system. The cooperative dispatch strategy of these different hybrid systems was also well studied.

At present, the hybrid system formed by wind plants and energy storage has become an important form to realize the stable operation with a high proportion of wind power. On this basis, the research about reducing the operating costs of conventional units, increasing the power output of wind plants, and raising the operating efficiency of energy storage systems has become more and more popular. HESS has the advantages of fast response speed, large energy storage capacity, and cross-season energy storage. Also, it can adapt to the operating environment of cold climates and significant temperature differences between day and night (Petkov and Gabrielli, 2020). The application of HESS on the wind-storage hybrid system has attracted scholars' attention in recent years (Li et al., 2020).

In the existing works, some aim to suppress the uncertainty of wind power and improve the system economy. Ref. (Zhang and Wan, 2014) established a hydrogen energy storage model to reduce power curtailment and gave a scheme for wind/hydrogen production through water electrolysis. Ref. (Qiu et al., 2020) proposed a two-stage robust optimization method with stability constraints considering the HESS's safety and small disturbance stability and dynamic response characteristics. The power output range of the HESS was then determined. Ref. (Xu et al., 2020) further proposed a distributionally robust chance-constrained (DRCC) dispatch method for W-HHS in the day-ahead power market and transformed it into a standard second-order cone programming problem for a solution.

Other scholars regard the electrolyzer as an adjustable load and research from the perspective of demand response. Ref. (Mirzaei et al., 2018) proposed a safety constrained unit commitment model with high-proportion wind power in coordination with demand response. The HESS was used in this work to reduce energy consumption and improve system reliability. Ref. (Mansour-Saatloo et al., 2020) used the HESS in the energy hub to construct a robust dispatch method, which considered the demand response of the HESS and the characteristics of cogeneration.

The existing research shows that in the operation of the HESS, cogeneration can happen both in the hydrogen production and fuel cell generation stages. Its thermal characteristics have an important influence on the reliable and efficient operation of the HESS. On this basis, some work studied the future development of hybrid systems with ultra-high penetration of renewable energy. A thermoelectric hydrogen model with startup/shutdown constraints and a new seasonal hydrogen energy storage model was proposed (Wen et al., 2020). Ref. (Pan et al., 2020) studied the influence of heat load increase on the operation cost of the hybrid system and proposed a day-ahead dispatch scheme for the power system with high-proportion wind power and HESS. Ref. (Wei et al., 2021) further established a heat-hydrogen efficiency model for the intermittent operation of the electrolyzer by describing the heat exchange process in detail. Ref. (Kovač et al., 2021) carried out research on the thermal management of distributed photovoltaic-hydrogenation stations, put forward the optimized thermal management strategy, and improved the energy utilization efficiency. In order to ensure the energy efficiency of the renewable hydrogen energy system, the thermal management of the metal hydride tank is studied (Endo et al., 2021). Research shows that heat management can improve energy efficiency by 50%.

It can be seen that in the grid-connected operation of the hybrid system with renewable energy, the HESS can use the electrolyzer to transform the excess wind power into hydrogen to provide a down-reserves. At the same time. The fuel cell equipped in the HESS can consume hydrogen to generate power to provide an up-reserves for the hybrid system. The electrolyzer and the fuel cell work alternately and intermittently to suppress the power fluctuation. Notice that the electrolyzer and fuel cell's operation efficiency and response speed are closely related to their operating temperature. Therefore, the ability of HESS to respond to wind power fluctuations quickly, long-term, and efficiently is restricted by the following two factors. First, the balance between hydrogen production in the electrolyzer and the hydrogen consumption of the fuel cell should always be satisfied. Second, the balance between heat production under operation conditions and heat consumption under reserve mode should be held as well. Thus, the operation of W-HHS should meet both heat and hydrogen production-consumption balance simultaneously when it is connected to the grid.

Existing works have neglected the heat balance between electrolyzers and fuel cells in the reserve mode and the inherent relationship between hydrogen and heat balance. While maintaining heat balance and hydrogen balance is the key to ensuring the economic operation of the hybrid power

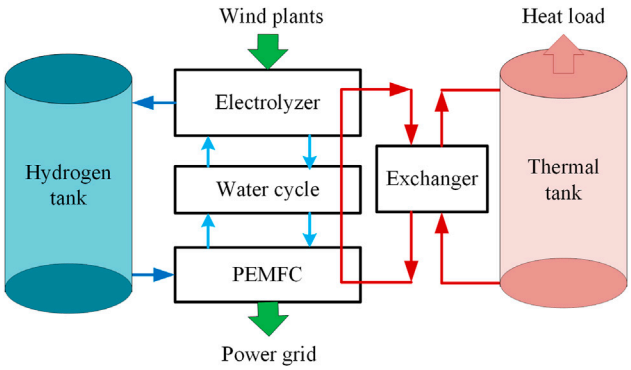

FIGURE 1 | Diagram of the wind-hydrogen hybrid system.

equipped with HESS. Therefore, based on the operating characteristics of the HESS, this paper first designs a brand new structure of the HESS, including the waste heat utilization system, and gives the heat-hydrogen state of charge (SOC) models. Furthermore, the distributionally robust optimization approach is used to model the uncertainty of wind plant power output. Then, an optimal dispatch method for the W-HHS considering the heat and hydrogen balance is proposed. The models and method are verified with the IEEE 30-bus system. The actual data set of a wind plant in Qinghai Province is used in this simulation. Finally, the key parameters are analyzed, and their impacts on system performance are well studied.

The rest of this article is organized as follows. *Mathematical Model of HESS With Waste Heat Utilization System* elaborates the overall design scheme and mathematical model of the HESS with waste heat utilization system. *Mathematical Models of the Wind Plant* introduces the mathematical models of wind plants. The cooperative dispatch method of W-HHS considering dual SOC constraints is proposed in *Cooperative Dispatch Method of W-HHS Considering Dual SOC Constraints*. *Case Study* verifies the effectiveness of the proposed method through a case consisting of actual data, followed by the disscusions in *Discussions*.

MATHEMATICAL MODEL OF HESS WITH WASTE HEAT UTILIZATION SYSTEM

Structure of HESS With Waste Heat Utilization System

The structure of a HESS with the waste heat utilization system is shown in **Figure 1**. The whole system consists of an electrolyzer, fuel cell, hydrogen storage system, and waste heat utilization system. This HESS adopts the alkaline electrolyzer as the water electrolysis device due to its mature technology and fast response speed. The electrolyzer is used to absorb the excess wind power to produce hydrogen. As for the fuel cell, the proton-exchange membrane fuel cell (PEMFC) is chosen to consume hydrogen and generate electricity considering the requirement of the operating temperature match.

The hydrogen storage system includes a hydrogen tank, an air/oxygen system, and a water supply cycle. The waste heat utilization system consists of a thermal tank, a heat storage exchanger, and a heat cycle system. The heat cycle system builds a heating/cooling cycle between the electrolyzer, PEMFC, water supply tank, and heat storage tank to stabilize the system temperature. The mathematical models of the various components of the HESS are given in the following sections.

Model of HESS With Waste Heat Utilization System

Model of Alkaline Electrolyzer and PEMFC

The alkaline electrolyzer has the advantages of short response time and mature technology. It is very suitable to be used in a HESS with wind plants. Its simplified model (Clua et al., 2018; Xiong et al., 2021) can be expressed as:

$$\begin{cases} P_{ele}^{t} = \dot{n}_{H2}^{t} H_{HV} + Q_{ele}^{t} \\ \eta_{ele} = \dfrac{\dot{n}_{H2}^{t} H_{HV}}{P_{ele}^{t}} \end{cases}, \tag{1}$$

where P_{ele}^{t} and Q_{ele}^{t}, respectively, represent the electricity consumed and the heat produced by the electrolyzer at time t. $\dot{n}_{H2}^{t}$ represents the rate of hydrogen production, and H_{HV} represents the higher heating value of hydrogen. η_{ele} represents the efficiency of the electrolyzer.

The operating temperature of the PEMFC should match that of the alkaline electrolyzer to facilitate the recovery and utilization of the waste heat of the HESS. Its model can be expressed as:

$$\begin{cases} \dot{m}_{H2}^{t} H_{HV} = P_{fuel}^{t} + Q_{fuel}^{t} \\ \eta_{fuel} = \dfrac{P_{fuel}^{t}}{\dot{m}_{H2}^{t} H_{HV}} \end{cases}, \tag{2}$$

where P_{fuel}^{t} and Q_{fuel}^{t} represent the electricity and heat produced by the fuel cell at time t, respectively. $\dot{m}_{H2}^{t}$ represents the hydrogen consumption rate of PEMFC. η_{fuel} represents the efficiency of PEMFC.

Dual SOC Model for Hydrogen and Heat Balance

The HESS stores the hydrogen produced by the electrolyzer in the hydrogen tank and supplies the hydrogen and oxygen to the PEMFC when electricity is needed. At the same time, water is supplied to the electrolyzer, and the electricity generation products of the PEMFC are collected through the water supply cycle. Taking the total energy stored in the hydrogen tank as the parameter to describe the hydrogen energy storage state, we establish SOC model of the hydrogen balance as:

$$SOC_{H2}^{t} = SOC_{H2}^{t-1} + \frac{1}{S_{H2}^{\max}} \left(\eta_{ele} P_{ele}^{t} - P_{fuel}^{t} / \eta_{fuel} \right) \Delta\tau, \tag{3}$$

where SOC_{H2}^{t} represents the SOC of hydrogen energy stored in the tank at time t. $S_{H2}^{\max}$ represents the maximum capacity of the hydrogen tank, and $\Delta\tau$ represents the time interval.

The waste heat utilization system provides thermal energy for each link and collects waste heat. On the one hand, the

waste heat is used to preheat the water entering the electrolyzer, and on the other hand, it is used to maintain the rated temperature of the PEMFC in reserve mode. Also, when the PEMFC is in operation mode, the waste heat needs to provide heat to the electrolyzer and recover the heat generated from the PEMFC. After meeting the heat balance requirements of the electrolyzer and PEMFC, the waste heat utilization system can also use the remaining thermal energy to provide heat for extra heat loads in the hybrid system. The SOC model of heat balance is:

$$SOC_{th}^{t} = SOC_{th}^{t-1} + \frac{1}{S_{th}^{\max}}\left[\eta_{ex}\left(Q_{ele}^{t} + Q_{fuel}^{t} - Q_{sys}^{t}\right) - Q_{load}^{t}\right]\Delta\tau, \tag{4}$$

where SOC_{th}^{t} represents the SOC of thermal energy stored in the thermal tank at time t. $S_{th}^{\max}$ represents the maximum thermal energy storage capacity of the thermal tank. Q_{ele}^{t} and Q_{fuel}^{t} represent the heat generated by the electrolyzer and the PEMFC, respectively. Q_{sys}^{t} and Q_{load}^{t} represent the heat consumed by the HESS and the heat provided for the extra heat loads, respectively. η_{ex} represents the efficiency of the heat exchanger.

In **Eq. 4**, Q_{sys}^{t} is composed of three losses: the heat dissipation of the electrolyzer, the heat dissipation of the fuel cell, and the preheating of the water supply cycle. Thus, Q_{sys}^{t} can be expressed as:

$$Q_{sys}^{t} = (T_{ele}^{t} - T_{atm}^{t})\lambda_{ele}P_{ele} + (T_{ele}^{t} - T_{atm}^{t})\lambda_{fuel}P_{fuel} + \dot{n}_{w}^{t}c_{p}\,(T_{ele}^{t} - T_{w}^{t}), \tag{5}$$

where T_{ele}^{t} and T_{fuel}^{t} represent the operating temperature of the electrolyzer and PEMFC. T_{atm}^{t} represent the ambient temperature. P_{ele} and P_{fuel} are the installed capacity of electrolyzer and PEMFC. $\dot{n}_{w}^{t}$, c_p, and T_{w}^{t} represent the molar mass flow rate, specific heat capacity and temperature of the water entering the electrolyzer. λ_{ele} and λ_{fuel} represent the heat dissipation coefficient of the unit capacity electrolyzer and PEMFC (Hwang, 2005), which are defined as the heat dissipation area per unit capacity A_{ele}/A_{fuel} to unit area thermal resistance R_{ele}/R_{fuel}. λ_{ele} and λ_{fuel} can be expressed as:

$$\lambda_{ele} = \frac{A_{ele}}{R_{ele}}; \lambda_{fuel} = \frac{A_{fuel}}{R_{fuel}}. \tag{6}$$

MATHEMATICAL MODELS OF THE WIND PLANT

Models of Wind Plant Output Power

The power output of a wind plant can be modeled with wind speed and installed power (Guo et al., 2020). By further equating the wind speed change as a power output impact factor λ_{W}^{t}, a simplified model of the wind plant output can be expressed as

$$\tilde{P}_{W}^{t} = \lambda_{W}^{t}P_{W}. \tag{7}$$

where P_W represents the installed power of the wind plant. $\tilde{P}_{W}^{t}$ represents the actual power output of the wind plant.

While, in an actual situation, the system operator usually uses the predicted wind plant output to determine the dispatch decisions and the dispatchable power. The predicted power output and dispatchable power can be expressed as:

$$\hat{P}_{W}^{t} = \hat{\lambda}_{W}^{t}P_{W}, \tag{8}$$

$$P_{W}^{t} = \delta\hat{P}_{W}^{t}, \tag{9}$$

where $\hat{\lambda}_{W}^{t}$ represents the predicted power output impact factor. $\hat{P}_{W}^{t}$ and P_{W}^{t} represent the predicted output and dispatchable power of the wind plant. $\hat{\lambda}_{W}^{t}$ reflects the availability of power grid dispatch with wind power forecasting. P_{W}^{t} represents the dispatchable power, forming the dispatching curve of the wind plant, which is the grid-connected power guaranteed by the wind plant. δ means availability factor of wind plant. Based on this, we can further define the dispatch tracking deviation index of the wind plant (Guo et al., 2020), which is:

$$\Delta_{W} = \left(\sum_{t=1}^{T}\tilde{P}_{W}^{t} - \sum_{t=1}^{T}P_{W}^{t}\right)/\sum_{t=1}^{T}\tilde{P}_{W}^{t}, \tag{10}$$

where Δ_W represents the total power deviation in the whole period of dispatch.

A Distributionally Robust Model of Wind Plant Output Uncertainty

Distributionally robust optimization is a data-driven analysis approach and has been widely studied and applied. This method does not require an accurate probability distribution to characterize the uncertainties. Its conservativeness lies between robust optimization and stochastic optimization. Therefore, the distributionally robust optimization approach is applied in this work. In this method, we adopt the Wasserstein divergence (Guo et al., 2020) as the ambiguous set to measure the uncertainties of wind power output. Hence, we have:

$$M^{\varepsilon} = \left\{P \in M(\Xi):\, d_{W}\left(P, \hat{P}\right) \le \varepsilon\right\}, \tag{11}$$

where P represents the probability distribution of the actual power output of the wind plant. $\hat{P}$ represents the empirical distribution of the power output. $M(\Xi)$ represents the set formed by all possible distributions satisfying Wasserstein divergence d_w, where ε is the radius of the ambiguous set. The calculation method of the parameters mentioned above can be found in (Esfahani and Kuhn, 2018).

COOPERATIVE DISPATCH METHOD OF W-HHS CONSIDERING DUAL SOC CONSTRAINTS

The optimal dispatch of the W-HHS should reduce the operation costs of conventional units in the grid as much as possible and then increase the grid-connected power generated by wind plants to make full use of clean energy and reduce carbon emissions. Hence, we try to optimize the dispatch strategy of the HESS to

ensure that the power output of the W-HHS can track the dispatchable power accurately, thereby reducing the impact of wind power fluctuation on the power grid.

Objective Function

In the cooperative dispatch, historical wind power data is commonly used to predict the wind plant output. The model that we establish combines the dispatchable power of wind plants with the availability coefficients to optimize the output of conventional units and increase the grid-connected output of wind plants. The operation cost of conventional units and carbon emissions can also be reduced. Therefore, the goal of the W-HHS's optimal dispatch is:

$$F = \max_{\tilde{P}_W^t} \min_{P_{gen}^{t,i},\delta} \sum_{t=1}^{T} \sum_{i=1}^{N} \left[a_i \left(P_{gen}^{t,i} \right)^2 + b_i P_{gen}^{t,i} + c_i \right] - c_e \delta \hat{P}_W^{t,i} + c_p \Delta_W P\left(\tilde{P}_W^t \right) \in M(\Xi), t \in T, i \in N, \tag{12}$$

where $P(\tilde{P}_W^t)$ represents the probability distribution of the actual wind plant output. c_e represents the on-grid power tariff. c_p represents the penalty coefficient. $P_{gen}^{t,i}$ represents the power output of the units. a_i, b_i, and c_i represent the operation cost coefficients of the conventional unit. i represents the bus index. N represents the set of all buses.

Constrains

Dual SOC Constrains

In order to ensure that the HESS can dispatch the electrolyzer and PEMFC to provide reserves for the hybrid system, the optimal dispatch strategy must meet the balance of the hydrogen production (generated by electrolyzer) and the hydrogen consumption (consumed by the PEMFC). Also, the strategy should hold the heat balance between heat production and consumption.

The hydrogen balance requires that the system does not need to supplement hydrogen from outside during the operation, and the hydrogen in the storage tank will never be lower than the lower bound of the rated value after operating for a period T. Thus, we have the hydrogen balance SOC constraint is:

$$\begin{cases} SOC_{H2}^t \geq 0 \\ SOC_{H2}^{ini} \leq SOC_{H2}^{T+1} \end{cases}, \tag{13}$$

where SOC_{H2}^{ini} is the initial value of the hydrogen tank.

Similarly, the heat balance requires that the waste heat utilization system supports the W-HHS to operate continuously and efficiently within the specified operation period without the input of external thermal energy. Its SOC constraint can be expressed as:

$$\begin{cases} SOC_{th}^t \geq 0 \\ SOC_{th}^{ini} \leq SOC_{th}^{T+1} \end{cases}, \tag{14}$$

where SOC_{th}^{ini} is the initial value of the thermal tank.

Besides of heat SOC constraint, heat balance also includes heat power balance constraint in operation.

$$Q_{ele}^t + Q_{fuel}^t = Q_{sys}^t + \left(Q_{load}^t + Q_{storage}^t \right) / \eta_{ex} \tag{15}$$

where $Q_{storage}^t$ represents the heat stored in the thermal tank.

Constraints for Grid

The constraints of power grid dispatch include power flow constraints, line capacity constraints, and power balance constraints. In this section, the linear AC power flow model is adopted. Then, we have the power flow constraints as follows:

$$\begin{cases} P_l^t = g_l \dfrac{V_i^t - V_j^t}{2} - b_l \left(\theta_i^t - \theta_j^t \right) + P_{Ll}^t \\ Q_l^t = -b_l \dfrac{V_i^t - V_j^t}{2} - g_l \left(\theta_i^t - \theta_j^t \right) + Q_{Ll}^t \end{cases}, \tag{16}$$

where P_l^t and Q_l^t represent the active and reactive power flow on line l at time t. V_i^t and θ_i^t represent the voltage magnitude and phase angle of bus i. P_{Ll}^t and Q_{Ll}^t represent the active and reactive power flow errors on line l (Guo et al., 2020).

The constraint of line capacity is:

$$\left(P_l^t \right)^2 + \left(Q_l^t \right)^2 \leq \left(S_l^t \right)^2, \tag{17}$$

where S_l^t represents the capacity of line l. **Eq. 17** can be linearized by the outer approximation approach as

$$\begin{cases} -S_l^t \leq P_l^t \leq S_l^t \\ -S_l^t \leq Q_l^t \leq S_l^t \\ -\sqrt{2} S_l^t \leq P_l^t + Q_l^t \leq \sqrt{2} S_l^t \\ -\sqrt{2} S_l^t \leq P_l^t - Q_l^t \leq \sqrt{2} S_l^t \end{cases}, \tag{18}$$

The power balance constraint is

$$\begin{cases} P_i^t = \sum_l P_l^t + V_i^t \sum_{j=1}^{N} G_{ij} = P_W^{t,i} + P_{gen}^{t,i} - P_{ld}^{t,i} \\ Q_i^t = \sum_l Q_l^t - V_i^t \sum_{j=1}^{N} B_{ij} = Q_{gen}^{t,i} - Q_{ld}^{t,i} \end{cases}, \tag{19}$$

where P_i^t and Q_i^t represent the active and reactive power injected into bus i, that is, the power generated by the generator connected to the bus minus the active/reactive load $P_{ld}^{t,i}/Q_{ld}^{t,i}$ on the same bus. G_{ij} and B_{ij} are the real and imaginary parts of elements in the network admittance matrix.

Model Solution

The problem established in **Eqs. 12–19** is a max-min optimization problem. The actual power output of the wind plant is modeled by the uncertain ambiguous set given in **Eq. 11**, which cannot be solved directly. To this end, we adopt the method proposed in (Guo et al., 2020) to transform the set into a set of linear chance constraints, which are:

$$\begin{cases} \varepsilon (1 - \Delta_W) + \dfrac{1}{K} \sum_{k=1}^{K} s_i^k - \gamma_i \alpha \leq 0 \\ s_i^k \geq (1 - \Delta_W) \sum_{t=1}^{T} \tilde{P}_{Wi}^{k,t} - \sum_{t=1}^{T} P_W^{k,t,i} + \gamma_i \\ s_i^k \geq 0 \end{cases}, \tag{20}$$

where K is the number of data samples. α is the confidence level. $\tilde{P}_{Wi}^{k,t}$ and $P_{Wi}^{k,t}$ are the actual wind plant output and dispatchable

TABLE 1 | System parameters.

Parameters	Value
Wind power installed capacityP_W MW	90
PEMFC installed capacity P_{fuel} MW	9
Electrolyzer installed capacity P_{ele} MW	9
Volume of hydrogen storage tank V_{H2} m^3	6.41
Pressure of hydrogen storage tank p_{H2}MPa	10
Efficiency of PEMFC η_{fuel} %	60
Efficiency of electrolyzer η_{ele} %	60
PEMFC operating temperature T^t_{fuel} °C	80
Electrolyzer operating temperature T^t_{ele} °C	80
Heat exchanger efficiency η_{ex}%	80
Ambient temperature T^t_{am}°C	20
Higher heating value of hydrogen H_{HV} kJ/mol	282
Heat dissipation coefficient of PEMFC λ_{fuel}°C^{-1}	1/800
Heat dissipation coefficient of electrolyzer λ_{ele}°C^{-1}	1/800
Water specific heat capacity c_pkJ/(kg·°C)	4.2
Availability coefficient δ	0.8–1
Confidence level α	0.05

grid-connected power represented by samples. s^t_i and γ_i are corresponding dual variables.

At this time, since we use samples to describe the uncertainties of the wind plants outputs, the power balance constraint of each line in **Eq. 19** can be rewritten as:

$$\begin{cases} P^{k,t}_i = \sum_l P^{k,t}_l + V^{k,t}_i \sum_{j=1}^{N} G_{ij} = P^{k,t,i}_W + P^{t,i}_{gen} + P^{k,t,i}_{fuel} - P^{k,t,i}_{ele} - P^{t,i}_{load} \\ Q^{k,t}_i = \sum_l Q^{k,t}_l - V^{k,t}_i \sum_{j=1}^{N} B_{ij} = Q^{t,i}_{gen} - Q^{t,i}_{load} \end{cases}, \quad (21)$$

The lower and upper bounds of each variable restricted by the limitations of technology and environment are all considered in modeling, which is not listed due to the space limitation. Besides, we notice that product terms of two decision variables exist in **Eq. 5**, making the model nonlinear. This term can be piecewise linearized by the Boolean expansion method (Pereira et al., 2005).

So far, the W-HHS proposed cooperative dispatch method is transformed into a mixed-integer linear program, which can be solved with matlab 2016b and Cplex12.6.

CASE STUDY

System Parameters

In this section, we test our models and method on the IEEE 30-bus testbed. The actual historical data obtained from the Qinghai Province's 90 MW wind plant is used as samples. The parameters of the system are shown in **Table 1**. The W-HHS is integrated on bus #12, which is also given in **Figure 2**. The capacity of HESS is selected according to the local energy storage configuration policy, equal to 10% of the wind plant capacity. The specific historical data is selected as the predicted value of the wind plant output. 20% prediction error is set according to the current wind power prediction level.

The Latin hypercube method generates 100 samples (Shu et al., 2014) to construct the proposed distributionally robust optimization model. The upper and lower bounds of predicted output, available power, and uncertainties of wind plants are shown in **Figure 3**.

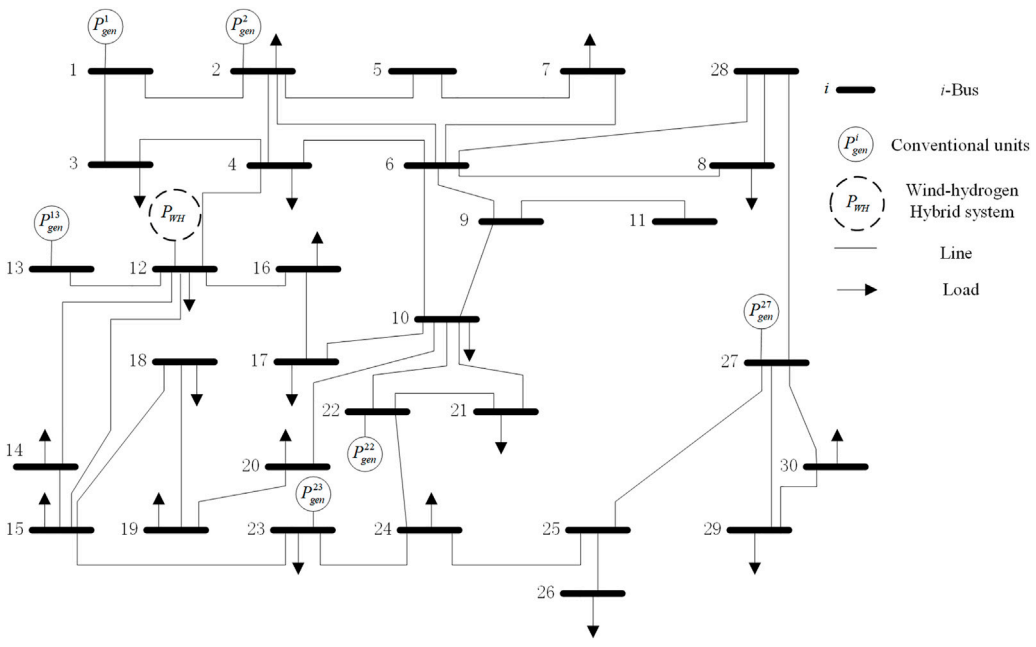

FIGURE 2 | Diagram of the IEEE 30 power system.

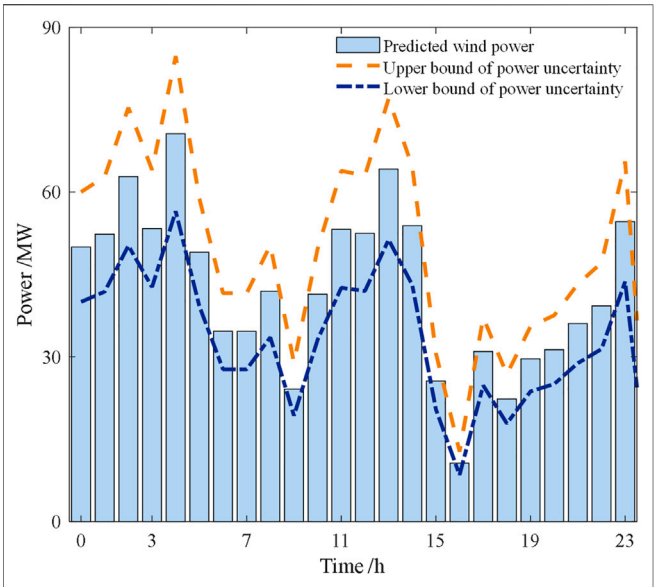

FIGURE 3 | Power chart of the wind plant.

Cooperative Dispatch Results of W-HHS

To analyze the influence of heat balance and hydrogen balance on the dispatch strategy of HPS, we study four different scenarios, which are listed as follows. The results are shown in **Table 2**.

Case 1: Heat and hydrogen balance constraints are not considered;

Case 2: Only heat balance constraints are considered;

Case 3: Only hydrogen balance constraints are considered;

Case 4: Both hydrogen and heat balance constraints are considered.

It can be seen from **Table 2** that where the hydrogen and heat balance constraints are ignored (Case 1), the dispatchable power of the wind plant is equal to the predicted value, and the operation cost of conventional units is the lowest. However, 25.04 kg extra hydrogen is needed to support the 24-h operation of the hybrid system. As constraints are added into the model, the availability coefficient of the wind plant decreases to meet hydrogen and heat balance requirements, and the cost of conventional units increases. Compared with Case 1, the wind plant availability coefficient in Case 4 has dropped by 6.33%, and the cost of conventional units has increased by 3.4%. The results of conventional unit dispatch in the four scenarios are shown in **Figure 4**.

According to the results in Case 2 and 3, we can figure out that the dispatch strategy that only satisfies the hydrogen balance or the heat balance requires the extra hydrogen or thermal supplement. It can be seen that when the system has sufficient day-ahead initial hydrogen storage or thermal storage, the corresponding dispatch strategy can also be adapted to increase the grid-connected power output of wind plants. When the initial hydrogen energy storage and the thermal storage are insufficient, the wind plant availability coefficient can only be reduced, and the dispatch strategy in Case 4 is adopted to maintain this efficient and economical operation of the HESS. **Figure 5** shows the operation of the HESS in the four Cases.

It can be seen from **Figure 5** that the PEMFC in Case 2 consumes extra hydrogen to provide an up-reserve for the hybrid system, improving the availability coefficient of wind power and meeting the heat balance constraints. In Case 3, the availability coefficient of the wind plant decreases. We can see that the probability of wind power curtailment increases while the probability of load curtailment decreases. The W-HHS calls the electrolyzer to increase hydrogen production, and the PEMFC is controlled to consume less hydrogen, thereby satisfying the hydrogen balance constraint. The SOC changes of hydrogen balance and heat balance are shown in **Figure 6**.

Figure 6 shows that only the dispatch strategy adopted in Case 4 can simultaneously satisfy the heat and hydrogen balance constraints. In this case, the hydrogen tank will have the remaining hydrogen. The remaining hydrogen can be used in the subsequent optimal dispatch to increase the grid-connected output of the wind plant, reflecting the character of hydrogen energy storage's cross-cycle energy storage. When the heat balance SOC shown in **Figure 6** is less than 0, it indicates that the hydrogen energy storage system must rely on additional supplementary heat energy to maintain the regular operation. This working condition means that the hydrogen energy storage system's thermal energy generated and stored is not enough to maintain the heat balance of intermittent work. In practice, the system's hydrogen production and power generation efficiency will decline to generate sufficient thermal energy.

Compared with Case 3, the optimal strategy in Case 4 further reduces the wind plant's available power and grid-connected power to satisfy the heat balance. It can be seen that the heat balance constraint reduces the profits of the hybrid system. Thus, the factors that affect the heat balance constraint should be

TABLE 2 | Cooperative dispatch results.

Scenarios	Operation cost of units ($\$\times10^6$)	Wind plant profits ($\$\times10^6$)	Residual hydrogen (kg)	Residual thermal energy (kW·h)	Wind plant availability coefficient
Case 1	0.14223	0.21934	−25.04	—	1
Case 2	0.14645	0.20951	−19.86	126.44	0.9552
Case 3	0.14564	0.20575	22.58	−489.15	0.9381
Case 4	0.14696	0.20546	22.50	135.95	0.9364

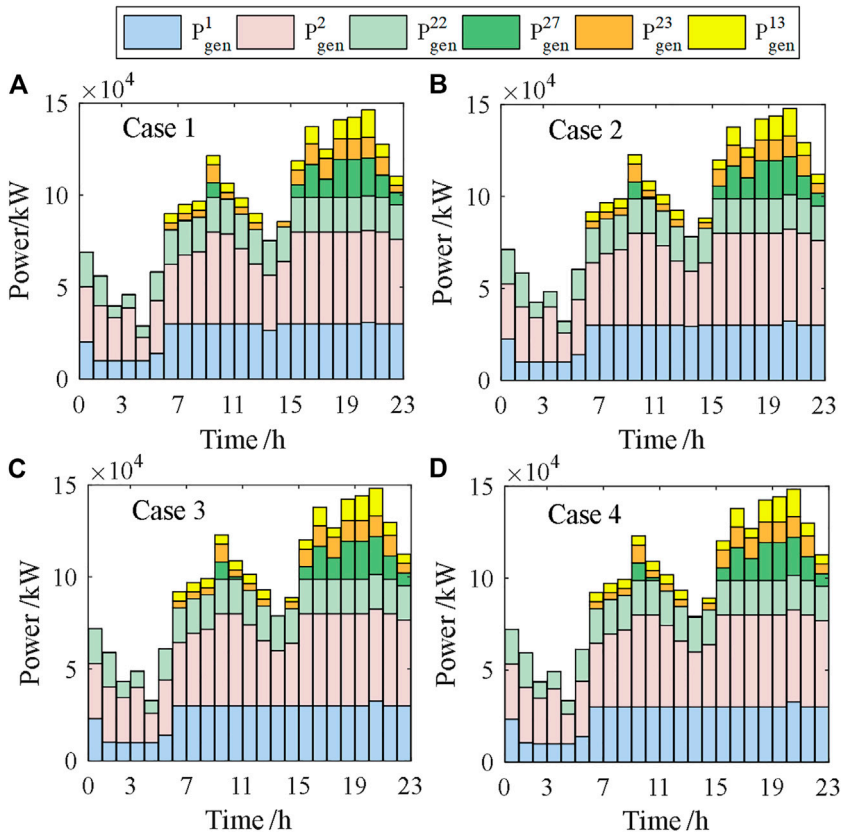

FIGURE 4 | Dispatch results of conventional units.

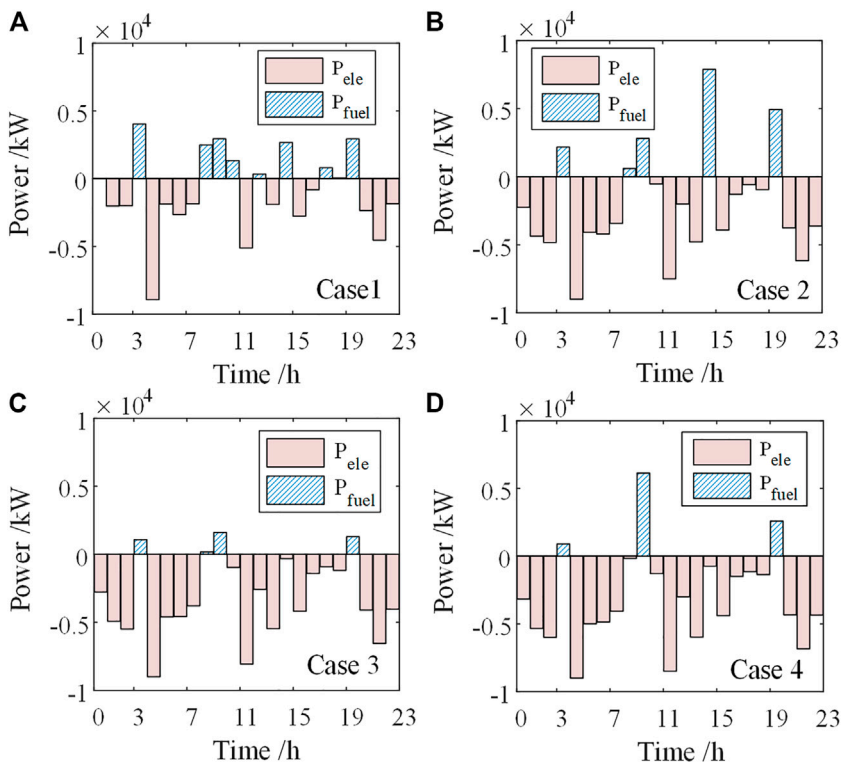

FIGURE 5 | Operation of hydrogen energy storage system.

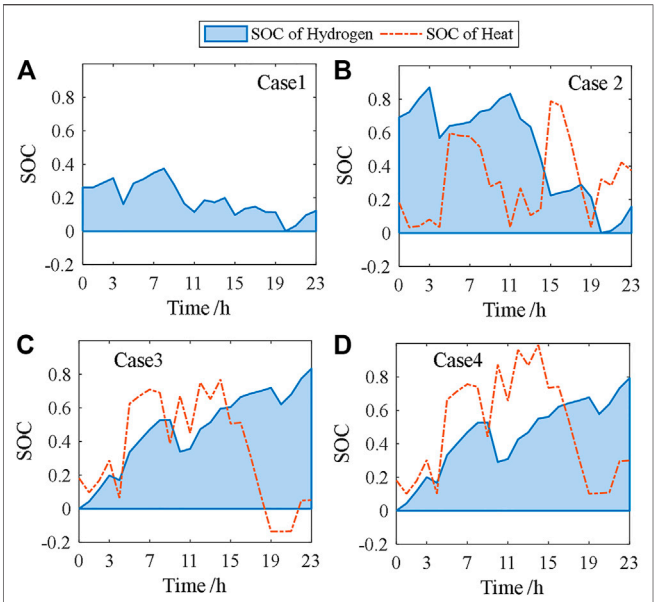

FIGURE 6 | SOC change of hydrogen energy storage system.

further analyzed to reduce the impact of heat balance on the operation of HESS.

Analysis of Impact Factors on Heat Balance

From the results in **Figures 5**, **6**, we can easily find out that when the W-HHS is in operation, the electrolyzer and PEMFC run intermittently. The electrolyzer cannot run at full power, and the PEMFC is always in reserve mode for a long time in an operation cycle. According to the heat balance model given in **Eq. 5**, **15**, whether the heat produced can meet the heat lost by the system mainly depends on the heat dissipation coefficient of the electrolyzer and PEMFC. Therefore, the influence of the heat dissipation coefficient on the heat balance SOC constraint should be analyzed. Thus, we take the heat dissipation coefficient in a range of [1/900, 1/1,500] to study the performance of the waste heat utilization system. The results are shown in **Table 3**.

Table 3 shows that as the heat dissipation coefficient decreases, the operation is less influenced by the heat balance constraints. The high availability coefficient of the wind plant results in a decreased operation probability of the electrolyzer and an increased working time of the PEMFC. Hydrogen storage drops accordingly. Also, due to the decrease of heat dissipation, the thermal energy stored in the thermal tank gradually increases.

When the heat dissipation coefficient is less than 1/1,200, Case 4 is equivalent to Case 3. The hybrid system is no longer affected by heat balance constraints. Thus, we can conclude that improving the heat insulation performance and reducing the heat dissipation power will help raise the system's operating efficiency. Meanwhile, the available grid-connected power of the wind plant increased, and the profit of the W-HHS improved.

DISCUSSION

According to the W-HHS energy storage system's electricity, hydrogen, and heat characteristics, this work designs a HESS with a waste heat utilization system. Then, the hydrogen and heat dual SOC constraints are established to describe the operation of the electrolyzer and PEMFC in the HESS. On this basis, a cooperative dispatch method for the W-HHS is proposed, aiming to reduce the operation cost of conventional units in the grid and increase wind plants' profit. The distributionally robust optimization approach models the uncertainties in the system. Then, the formulated model is transformed into a set of chance constraints and can be solved with an offline solver. Finally, we test our model with the IEEE 30-bus system, and actual wind power data from a Qinghai province wind plant is used.

The results show that without considering the hydrogen balance, the system has a significant wind power availability factor, which can improve the grid-connected power of the wind plant, but in practice, it needs to consume additional hydrogen to ensure fuel cell power generation. It can be seen that considering the hydrogen balance and heat balance will reduce the grid connection availability factor of the wind plant to generate enough hydrogen and thermal energy. In the operation of W-HHS, the available power of the wind plant is 6–8% lower than the ideal situation to meet the SOC constraints of hydrogen and heat balance. The heat dissipation coefficient of HESS has a significant influence on the SOC constraint of heat balance. When the heat dissipation coefficient is small enough, the SOC constraint of heat balance becomes invalid, and the SOC constraints of hydrogen balance only restrict the system operation strategy.

In addition, it should also be seen that after 24 h of continuous operation of the case4 in this paper, both hydrogen storage tank and heat storage tank have residual energy. This shows that in

TABLE 3 | Influence of heat dissipation coefficient.

Heat dissipation coefficient (°C^{-1})	Wind plant availability coefficient	Residual hydrogen (kg)	Residual thermal energy (kW·h)
1/900	0.9241	27.96	61.5
1/1,000	0.9346	22.5	135.95
1/1,100	0.9379	17.9	812.5
1/1,200	0.9431	13.98	996.9
1/1,300	0.9446	12.79	1,187.7
1/1,400	0.9446	12.79	1,365.8

multi-day dispatching scene when there is hydrogen and heat energy in the hydrogen storage tank and heat storage tank, the system dispatching can also adopt an optimistic availability factor to use the remaining hydrogen and heat energy to improve the grid-connected power of wind plant and reduce the generation cost of conventional units. This problem needs further research in the future.

DATA AVAILABILITY STATEMENT

The raw data supporting the conclusions of this article will be made available by the authors, without undue reservation.

AUTHOR CONTRIBUTIONS

YS: conceptualization, writing-original draft preparation, software. LC: funding acquisition, validation. LM: funding acquisition, conceptualization, methodology, and editing. HM: validation. MG: project administration. SM: supervision. All authors have read and agreed to the published version of the article.

FUNDING

This research was funded in part by the Joint Fund Project of National Natural Science Foundation of China (U1766203), in part by Key R and D and Transformation Plan of Qinghai Province (2021-GX-109), and in part by the Basic Research Project of Qinghai Province (2021-ZJ-948).

ACKNOWLEDGMENTS

The authors would like to thank Prof. Feng Liu and Wei Wei for very helpful discussions on the cooperative game, Dr. Xiaodai Xue and Xuelin Zhang for discussions on the HDR geothermal generator model, Dr. Zhongjie Guo and Jiayu Bai for suggestions on practical issues.

REFERENCES

Alirahmi, S. M., Razmi, A. R., and Arabkoohsar, A. (2021). Comprehensive Assessment and Multi-Objective Optimization of a green Concept Based on a Combination of Hydrogen and Compressed Air Energy Storage (CAES) Systems. *Renew. Sust. Energ. Rev.* 142, 110850. doi:10.1016/j.rser.2021.110850

Endo, N., Goshome, K., Tetsuhiko, M., Segawa, Y., Shimoda, E., and Nozu, T. (2021). Thermal Management and Power Saving Operations for Improved Energy Efficiency within a Renewable Hydrogen Energy System Utilizing Metal Hydride Hydrogen Storage. *Int. J. Hydrogen Energ.* 46 (1), 262–271. doi:10.1016/j.ijhydene.2020.10.002

Esfahani, P. M., and Kuhn, D. (2018). Data-driven Distributionally Robust Optimization Using the Wasserstein Metric: Performance Guarantees and Tractable Reformulations. *Math. Programming* 171 (1), 115–166. doi:10.1007/s10107-017-1172-1

García Clúa, J. G., Mantz, R. J., and De Battista, H. (2018). Optimal Sizing of a Grid-Assisted Wind-Hydrogen System. *Energ. Convers. Manag.* 166, 402–408. doi:10.1016/j.enconman.2018.04.047

Guo, Z., Wei, W., Chen, L., Xie, R., and Mei, S. (2020). Sizing Energy Storage to Reduce Renewable Power Curtailment Considering Network Power Flows: a Distributionally Robust Optimisation Approach. *IET Renew. Power Generation* 14 (16), 3273–3280. doi:10.1049/iet-rpg.2020.0354

Hota, A. R., Cherukuri, A., and Lygeros, J. (2019). Data-driven Chance Constrained Optimization under Wasserstein Ambiguity Sets. *Am. Control. Conf. (Acc).* doi:10.23919/ACC.2019.8814677

Hwang, J. J. (2006). Thermal-electrochemical Modeling of a Proton Exchange Membrane Fuel Cell. *J. Electrochem. Soc.* 153 (2), A216. doi:10.1149/1.2137652

Impram, S., Varbak Nese, S., and Oral, B. (2020). Challenges of Renewable Energy Penetration on Power System Flexibility: A Survey. *Energ. Strategy Rev.* 31, 100539. doi:10.1016/j.esr.2020.100539

Jiayu, B., Xingang, W., Chaoshan, X., Zhiyong, Y., Shoutao, T., and He, C. (2021). "Development Status and Measures to Promote the Development of Renewable Energy in China," in 2021 3rd Asia Energy and Electrical Engineering Symposium (Chengdu, China: AEEES), 1102–1107. doi:10.1109/AEEES51875.2021.9403132

Kovač, A., Marciuš, D., and Paranos, M. (2020). Thermal Management of Hydrogen Refuelling Station Housing on an Annual Level. *Int. J. Hydrogen Energ.* 46 (57), 29400–29410. doi:10.1016/j.ijhydene.2020.11.013

Li, Z., Zhang, W., Zhang, R., and Sun, H. (2020). Development of Renewable Energy Multi-Energy Complementary Hydrogen Energy System (A Case Study in China): A Review. *Energy Exploration & Exploitation* 38 (6), 2099–2127. doi:10.1177/0144598720953512

Mansour-Saatloo, A., Agabalaye-Rahvar, M., Mirzaei, M. A., Mohammadi-Ivatloo, B., Abapour, M., and Zare, K. (2020). Robust Scheduling of Hydrogen Based Smart Micro Energy Hub with Integrated Demand Response. *J. Clean. Prod.* 267, 122041. doi:10.1016/j.jclepro.2020.122041

Mirzaei, M. A., Yazdankhah, A. S., and Mohammadi-Ivatloo, B. (2018).Integration of Demand Response and Hydrogen Storage System in Security Constrained Unit Commitment with High Penetration of Wind Energy. In Electrical Engineering (ICEE), Iranian Conference on. IEEE, 1203–1208. doi:10.1109/ICEE.2018.8472631

Pan, G., Gu, W., Lu, Y., Qiu, H., Lu, S., and Yao, S. (2020). Optimal Planning for Electricity-Hydrogen Integrated Energy System Considering Power to Hydrogen and Heat and Seasonal Storage. *IEEE Trans. Sustain. Energ.* 11 (4), 2662–2676. doi:10.1109/tste.2020.2970078

Pereira, M. V., Granville, S., Fampa, M. H. C., Dix, R., and Barroso, L. A. (2005). Strategic Bidding under Uncertainty: a Binary Expansion Approach. *IEEE Trans. Power Syst.* 20 (1), 180–188. doi:10.1109/tpwrs.2004.840397

Petkov, I., and Gabrielli, P. (2020). Power-to-hydrogen as Seasonal Energy Storage: an Uncertainty Analysis for Optimal Design of Low-Carbon Multi-Energy Systems. *Appl. Energ.* 274, 115197. doi:10.1016/j.apenergy.2020.115197

Qiu, Y., Yang, H., Xu, Y., Chen, W., and Wang, P. (2020). Stability-constrained Two-Stage Robust Optimization for Integrated Hydrogen Hybrid Energy System. *Csee Jpes* 7 (1), 162–171. doi:10.17775/CSEEJPES.2020.00810

Shu, Z., Jirutitijaroen, P., Leite da Silva, A. M., and Singh, C. (2014). Accelerated State Evaluation and Latin Hypercube Sequential Sampling for Composite System Reliability Assessment. *IEEE Trans. Power Syst.* 29 (4), 1692–1700. doi:10.1109/TPWRS.2013.2295113

Si, Y., Chen, L., Zhang, X., Chen, X., Zheng, T., and Mei, S. (2021). Game Approach to HDR-TS-PV Hybrid Power System Dispatching. *Appl. Sci.* 11 (3), 914. doi:10.3390/app11030914

Wei, F., Sui, Q., Li, X., Lin, X., and Li, Z. (2021). Optimal Dispatching of Power Grid Integrating Wind-Hydrogen Systems. *Int. J. Electr. Power Energ. Syst.* 125, 106489. doi:10.1016/j.ijepes.2020.106489

Wen, T., Zhang, Z., Lin, X., Li, Z., Chen, C., and Wang, Z. (2020). Research on Modeling and the Operation Strategy of a Hydrogen-Battery Hybrid Energy Storage System for Flexible Wind Farm Grid-Connection. *IEEE Access* 8, 79347–79356. doi:10.1109/ACCESS.2020.2990581

Xiao, P., Hu, W., Xu, X., Liu, W., Huang, Q., and Chen, Z. (2020). Optimal Operation of a Wind-Electrolytic Hydrogen Storage System in the Electricity/hydrogen Markets. *Int. J. Hydrogen Energ.* 45 (46), 24412–24423. doi:10.1016/j.ijhydene.2020.06.302

Xiong, Y., Si, Y., Zheng, T., Chen, L., and Mei, S. (2021). Optimal Configuration of Hydrogen Storage in Industrial Park Integrated Energy System Based on Stackelberg Game. *Trans. China Electrotechnical Soc.* 36 (3), 507–516. doi:10.19595/j.cnki.1000-6753.tces.200576

Xu, X., Hu, W., Cao, D., Huang, Q., Liu, Z., Liu, W., et al. (2020). Scheduling of Wind-Battery Hybrid System in the Electricity Market Using Distributionally Robust Optimization. *Renew. Energ.* 156, 47–56. doi:10.1016/j.renene.2020.04.057

Yang, L., Xu, Y., Gu, W., and Sun, H. (2020). Distributionally Robust Chance-Constrained Optimal Power-Gas Flow under Bidirectional Interactions Considering Uncertain Wind Power. *IEEE Trans. Smart Grid* 12 (2), 1. doi:10.1109/TSG.2020.3029027

Yu, D., Zhang, T., He, G., Nojavan, S., Jermsittiparsert, K., and Ghadimi, N. (2020). Energy Management of Wind-PV-Storage-Grid Based Large Electricity Consumer Using Robust Optimization Technique. *J. Energ. Storage* 27, 101054. doi:10.1016/j.est.2019.101054

Zhang, G., and Wan, X. (2014). A Wind-Hydrogen Energy Storage System Model for Massive Wind Energy Curtailment. *Int. J. Hydrogen Energ.* 39 (3), 1243–1252. doi:10.1016/j.ijhydene.2013.11.003

Zhang, Q., and Chen, W. (2020). Modeling China's Interprovincial Electricity Transmission under Low Carbon Transition. *Appl. Energ.* 279, 115571. doi:10.1016/j.apenergy.2020.115571

Zhu, F., Zhong, P.-a., Xu, B., Liu, W., Wang, W., Sun, Y., et al. (2020). Short-term Stochastic Optimization of a Hydro-Wind-Photovoltaic Hybrid System under Multiple Uncertainties. *Energ. Convers. Manag.* 214, 112902. doi:10.1016/j.enconman.2020.112902

Conflict of Interest: The authors declare that the research was conducted in the absence of any commercial or financial relationships that could be construed as a potential conflict of interest.

Publisher's Note: All claims expressed in this article are solely those of the authors and do not necessarily represent those of their affiliated organizations, or those of the publisher, the editors and the reviewers. Any product that may be evaluated in this article, or claim that may be made by its manufacturer, is not guaranteed or endorsed by the publisher.

NOMENCLATURE

DRCC Distributionally robust chance-constrained

HESS Hydrogen energy storage system

PEMFC Proton-exchange membrane fuel cell

SOC State of charge

W-HHS Wind-hydrogen hybrid system

Variables

A_{ele} electrolyzer heat dissipation area per unit capacity

A_{fuel} PEMFC heat dissipation area per unit capacity

a_i,b_i,c_i operation cost coefficients of the conventional unit i

B_{ij} imaginary parts of elements in network admittance matrix

c_e on-grid power tariff

c_p penalty coefficient

d_w Wasserstein divergence

G_{ij} real parts of elements in network admittance matrix

H_{HV} higher heating value of hydrogen

K number of data samples

$\dot{m}_{H2}^t$ hydrogen consumption rate of PEMFC

$M(\mathbf{\Gamma})$ set formed by all possible distributions

$\dot{n}_{H2}^t$ rate of hydrogen production at time t

P probability distribution of the actual wind plant output

$\hat{P}$ empirical distribution of the wind plant output

P_{ele}^t electricity consumed by the electrolyzer at time t

P_{fuel}^t electricity consumed by the fuel cell at time t

$P_{gen}^{t,i}$ power output of the units i at time t

P_i^t active power injected into bus i

P_l^t active power flow on line l at time t

P_{Ll}^t active power flow errors on line l

$P_{ld}^{t,i}$ active load into bus i

P_W installed power of the wind plant

P_W^t dispatchable power of the wind plant at time t

$\hat{P}_W^t$ predicted output power of the wind plant at time t

$\tilde{P}_W^t$ actual power output of the wind plant at time t

$P(\tilde{P}_W^t)$ probability distribution of the actual wind plant output

Q_{ele}^t heat produced by the electrolyzer at time t

Q_{fuel}^t heat produced by the fuel cell at time t

Q_i^t reactive power injected into bus i

Q_l^t reactive power flow on line l at time t

Q_{Ll}^t reactive power flow errors on line l

$Q_{ld}^{t,i}$ reactive load into bus i

Q_{load}^t heat provided for extra heat loads

Q_{sys}^t heat consumed by the HESS

R_{ele} unit area thermal resistance of electrolyzer

R_{fuel} unit area thermal resistance of PEMFC

$S_{H2}^{\max}$ maximum capacity of the hydrogen tank

S_l^t capacity of line l

$S_{th}^{\mathbf{max}}$ maximum capacity of the thermal tank

SOC_{H2}^t SOC of hydrogen energy stored in the tank at time t

SOC_{th}^t SOC of thermal energy stored in the tank at time t

T_{atm}^t ambient temperature

T_{ele}^t operating temperature of the electrolyzer

T_{fuel}^t operating temperature of the PEMFC

T_w^t temperature of the water entering the electrolyzer

V_i^t voltage magnitude of bus i.

α confidence level

η_{ele} efficiency of the electrolyzer

η_{ex} efficiency of the heat exchanger

η_{fuel} efficiency of PEMFC

θ_i^t Phase angle of bus i

λ_{ele} heat dissipation coefficient of unit capacity electrolyzer

λ_{fuel} heat dissipation coefficient of unit capacity PEMFC

λ_W^t power output impact factor of wind plant

$\hat{\lambda}_W^t$ predicted power output impact factor of wind plant

γ_i,s_i^t dual variables

δ availability factor of wind plant

ε radius of the ambiguous set

$\mathbf{\Delta}_W$ total power deviation in the whole period of dispatch

$\mathbf{\Delta}\tau$ time interval

frontiers in Energy Research

ORIGINAL RESEARCH
published: 25 November 2021
doi: 10.3389/fenrg.2021.791818

Equivalent Firm Capacity Assessment of HDR-PV Hybrid Power System: A Distributionally Robust Approach

Yang Si[1,2], *Linrui Ma*[1], *Laijun Chen*[1]*, *Hengrui Ma*[1] *and Shengwei Mei*[1,2]

[1]New Energy Photovoltaic Industry Research Center, Qinghai University, Xining, China, [2]State Key Lab of Control and Simulation of Power Systems and Generation Equipment (Tsinghua University), Beijing, China

Aiming at the reliable grid connection of photovoltaic (PV) systems in frigid plateau regions, this work first designs a flexible hot dry rock (HDR) hybrid power system (HPS), making full use of the potential of HDR for energy storage and power generation. Based on the operation of HPS, a comprehensive energy system credible capacity assessment method considering the overall economy of the system and the reliability of the grid is established. In this method, the power allowable fluctuation rate of the grid as the equivalent firm capacity (EFC) constraint is considered. Then, the constraint is converted into a set of linear chance conditions through the distributionally robust method so that the capacity assessment of the HDR-PV HPS can be converted into a mixed-integer linear optimization problem for a solution. The proposed assessment method is verified by real HDR-PV HPS in the Gonghe Basin of Qinghai Province. The results show that the flexible HDR plant increases the credible capacity of the HPS by 113.38%. The profit of the flexible HDR plant was increased by 3.02% at the same time. The parameter analysis shows that the HDR-PV HPS obtains the most profit when the allowable fluctuation rate is 7%, but 10% can fully utilize the geothermal. The assessment method can effectively assess the credible capacity of the system under the premise of ensuring the overall economy of the HPS, thereby guiding power grid dispatching.

Keywords: hot dry rock, equivalent firm capacity, credible capacity assessment, distributionally robust method, hybrid power system

OPEN ACCESS

Edited by:
Xun Shen,
Tokyo University of Agriculture and Technology, Japan

Reviewed by:
Zhaojian Wang,
Shanghai Jiao Tong University, China
Sun Daming,
Zhejiang University, China

***Correspondence:**
Laijun Chen
chenlaijun@qhu.edu.cn

Specialty section:
This article was submitted to Wind Energy, a section of the journal Frontiers in Energy Research

Received: *09 October 2021*
Accepted: *08 November 2021*
Published: *25 November 2021*

Citation:
Si Y, Ma L, Chen L, Ma H and Mei S (2021) Equivalent Firm Capacity Assessment of HDR-PV Hybrid Power System: A Distributionally Robust Approach. Front. Energy Res. 9:791818. doi: 10.3389/fenrg.2021.791818

INTRODUCTION

As the concept of clean energy has reached a consensus worldwide, clean energy, such as photovoltaics (PV), has developed rapidly (Singh, 2013). The proportion of PV installed capacity in the power system is increasing year by year. At the same time, the proportion of conventional thermal power stations is decreasing year by year due to the requirements of environmental protection and carbon emission reduction. It can be seen that integrating PV plants into the grid reliably has become an urgent problem to be solved.

Abbreviations: EFC, Equivalent firm capacity; EGS, Enhanced geothermal system; ELCC, Effective load-carrying capability; ESS, Energy storage system; GMC, Geothermal mining cycle; HDR, Hot dry rock; HPS, Hybrid power system; HTO, Heat transfer oil; LOP, Loss of probability; MILP, Mixed-integer optimization problem; ORC, Organic Rankine cycle; PV, Photovoltaic; TOU, Time of use; TSGC, Thermal storage generation cycle.

The assessment of the credible capacity of grid-connected PV plants has attracted widespread attention worldwide (Islam et al., 2014). Some researchers have studied the optimal grid-connected capacity of different scales and multiple types of energy resources from the perspective of passive consumption by the grid (Injeti and Kumar, 2003) and modeled the uncertainties of renewable sources by robust optimization, stochastic optimization, and distributionally robust optimization (Guo et al., 2020). Ref (Yuan et al., 2012) studied the optimal capacity assessment of grid-connected PV plants by using the bus voltage threshold of the low-voltage side of the distribution transformer. Ref (Wang et al., 2019) put forward a method for calculating the credible capacity of PV plants in rural power systems considering the risk of overload. The distributionally robust method can balance conservatism and computational efficiency, which has attracted extensive attention in recent years. A method to transform the ambiguous set composed of Wasserstein divergence into chance constraints was addressed (Esfahani and Kuhn, 2018). Ref (Hota et al., 2019) further proved the performance of the distributionally robust method based on Wasserstein divergence.

Other researchers use existing PV plants and energy storage systems (ESSs) to form a hybrid power system (HPS) to improve the power quality with PV integration. From the perspective of power scheduling, different indicators, such as effective load-carrying capability (ELCC), equivalent firm capacity (EFC), loss of probability (LOP), are proposed to represent the credible capacity of the HPS in the sense of dispatchable grid. By optimizing the dispatch of ESSs, the HPS as a whole is equivalent to a dispatchable power source so that the overall power generation can meet the power fluctuation requirements (Zhang L. et al., 2014; Dent et al., 2014; Sulaeman et al., 2016). Further, the reliability of HPS is improved, and the cost is reduced at the same time (Esmaili and Nasiri, 2009; Tapetado and Usaola, 2019). Ref (Song et al., 2012) improved the dispatchable power through the coordinated operation of the PV plant and the electrochemical energy storage device, thereby increasing the credible capacity of the HPS. Ref (He et al., 2013) proposed a Markov-decision-process-based control strategy to evaluate the credible capacity of PV plants in an HPS. The results showed that ESSs could improve the PV system's reliability in weak solar irradiance and a high proportion of renewable energy. It can be seen that ESS plays a vital role in the stable operation of the power grid. Ref (Zhang et al., 2017) further used the EFC theory to optimize the configuration of a distributed HPS equipping with wind, solar, and storage, reducing the system investment cost. A method using EFC to estimate the equivalent energy storage capacity of grid-connected parking lots is proposed for the capacity assessment of electric vehicle urban virtual energy storage systems (Zeng et al., 2020). Moreover, EFC can also be used as the contribution index of electric field capacity to power supply security, and a market capacity value method for large-scale investment dispatching is proposed (Peter and Wagner, 2021).

For the grid, the grid dispatcher will make a dispatching plan according to the generation capacity of the connected plants to ensure a safe, stable, and economical operation. However, due to the uncertainty of the output power of renewable plants in HPS, the grid will not optimize the dispatching according to HPS's installed capacity. The grid must assess credible capacity to plan the dispatching curves. For HPS, accurate assessment of credible capacity is helpful to track the dispatching curves in actual operation, reduce the impact on the power grid, increase the grid-connected power and reduce the penalty. To sum up, the credible capacity assessment of HPS can provide an essential reference for the actual system operation. It can effectively reduce the cost of grid dispatching and improve system performance. Nowadays, the existing research mainly focuses on the HPS with electrochemical ESS and PV plants. When electrochemical ESSs are applied in plateau and frigid environments, they will face the problem of low cycle life and high self-consumption. These disadvantages limit the use of electrochemical ESSs on a large scale. Hence, insufficient energy storage makes some high-altitude areas equipped with high-proportion renewable sources lack dispatchable power sources. In this dilemma, new techniques are urgently needed to solve the reliable connection of large-scale PV plants in these frigid plateau regions.

The geothermal energy of hot dry rock (HDR) has the advantages of stable power generation, simple operation and maintenance, and complete cleanliness (Yan et al., 2019). It can replace electrochemical energy storage to build an HPS in frigid plateau regions. It has excellent potential for increasing the dispatchable capacity of the grid and improving reliability. Nevertheless, because of the geographical location restriction of resources, the long dynamic response time (Brown, 2009), and the high investment cost (Zhang Y.-J. et al., 2014), the existing HDR system can only be used as a base power source without participating in auxiliary services of the grid. Many studies have been proposed to improve the thermal process of the HDR geothermal power system and promote the comprehensive utilization of HDR geothermal energy. Ref (Zare, 2016) proposed an HDR-HPS that can realize a supply of cold, heat, and electricity to utilize the heating and cooling potential of HDR geothermal energy comprehensively. In order to improve the flexibility of the HDR system, Ref (Si et al., 2020). proposed a multi-energy HPS for HDR, wind, solar, and other renewable sources that were considered to meet the needs of cooling, heating, and electrical loads of independent microgrids. Further, a hybrid power system composed of an HDR plant heat storage plant was proposed and addressed the cooperative game dispatching model (Si et al., 2021).

The existing research has not paid attention to the influence of HDR geothermal energy on the credible capacity of the HPS. The HDR power system has its unique characteristics, and the operation mode of the HPS integrated with HDR is different from other systems. In the research on HDR power systems, the operation strategy of HDR is rarely considered to stabilize the fluctuation of the integrated PV plant, increase the credible capacity, and improve the system's reliability. To solve these problems, we first introduce the thermal storage generation cycle (TSGC) to improve the operational flexibility of the HDR power system. Then, the potential of HDR geothermal energy is explored, and a flexibly dispatchable HDR-PV HPS is designed. Moreover, the operation of this complex system is carefully studied.

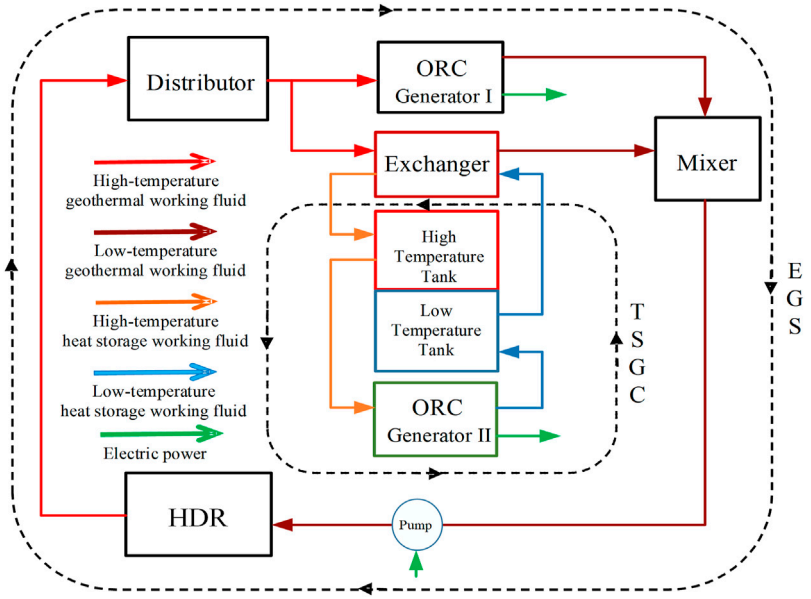

FIGURE 1 | Composition diagram of flexible HDR system.

Furthermore, combined with the EFC theory, taking power fluctuation requirements of the HPS's output as the EFC constraint, a credible capacity assessment method of the HDR-PV HPS considering the overall economy is established. The uncertainty of EFC constraints is modeled, and the corresponding solution method is given. The proposed model and method are verified with the actual weather and HDR resource data composition in the Gonghe Basin of Qinghai Province. The simulation results indicate the effectiveness and the efficiency of the proposed method.

The rest of this article is organized as follows. *HDR–PV Hybrid Power System Architecture* elaborates the overall design scheme of the flexible HDR system and the HDR-PV hybrid power system structure. *Mathematical Models of the HDR-PV HPS* introduces the mathematical models of the HDR-PV hybrid power system. The credible capacity assessment method for HDR-PV hybrid power system is proposed in *Credible Capacity Assessment Method Bbased on Distributionally Robust*. *Case Study* verifies the effectiveness of the proposed method through a case consisting of actual data of the Gonghe Basin, followed by the discussions in *Discussion*.

HDR–PV HYBRID POWER SYSTEM ARCHITECTURE

Flexible HDR System

The conventional HDR power system is not flexible enough to provide sufficient reserve for the HPS. Therefore, based on the conventional enhanced geothermal system (EGS), we design an HDR power system with flexible operation capabilities, a flexible HDR system. The composition of the flexible HDR system is shown in **Figure 1**.

The system consists of EGS and TSGC. In the system, EGS is composed of an HDR geothermal mining cycle (GMC) and organic Rankine cycle (ORC) power generation system. Geothermal working fluid distributor, ORC generator I, geothermal working fluid mixer, and reinjection pump are included, realizing geothermal energy for extraction, distribution, conversion, and reinjection. Brine often acts as a geothermal working fluid, forming the outer circle in **Figure 1**.

The TSGC consists of a heat exchange/storage system and an ORC power generation system, as shown in the inner circle of **Figure 1**. A heat storage/exchanger, a thermal storage tank, and an ORC generator II are included in the TSGC. The heat transfer oil (HTO) is always used as the heat storage medium to realize the time-sharing storage and utilization of continuous geothermal energy.

The performance of the ORC generator both in EGS and TSGC directly affects the operating characteristics of a flexible HDR plant. According to our previous work (Zhang et al., 2020), the subcritical ORC structure with dry steam can better adapt to the geothermal utilization scenario in the temperature zone of 180–200°C. Therefore, the results in (Zhang et al., 2020) are used in this paper, and butane is used as the organic working fluid for both ORC generator I and ORC generator II.

Structure of HDR-PV HPS

The HDR-PV HPS is formed with multiple PV plants and an HDR power system that serves as a storage to balance the energy exchange and eliminate the volatilities. The basic structure of HDR-PV HPS is shown in **Figure 2**.

In actual cases, due to the limitation of HDR resources and GMC capacity, the ability of the HDR power system to provide reserve is restricted. Also, the weather forecast accuracy cannot be guaranteed due to the uncertainties induced by different weather

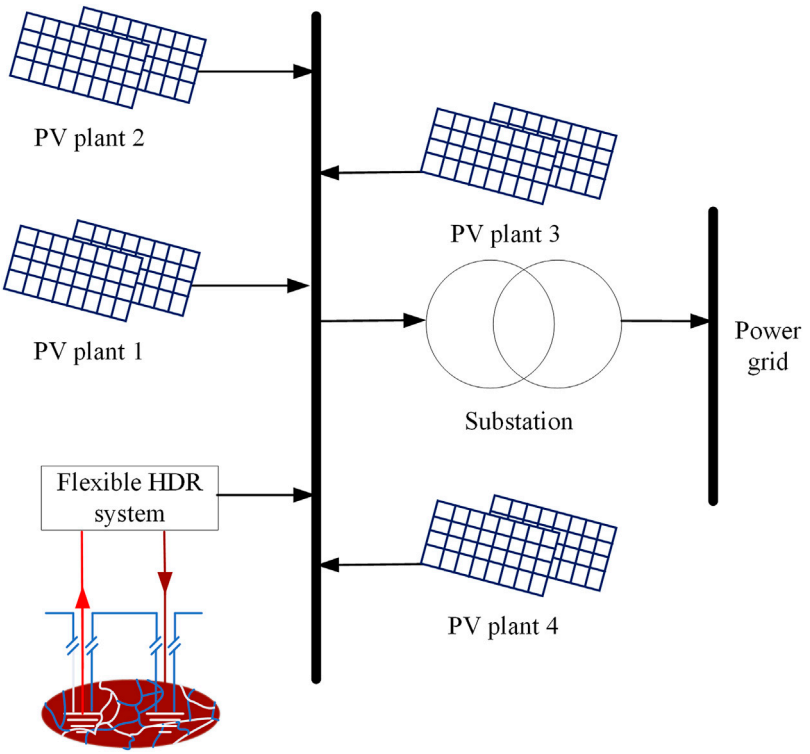

FIGURE 2 | Structure of HDR-PV HPS.

factors (Nespoli et al., 2019). Therefore, the credible capacity of HDR-PV HPS will also be affected by weather factors, and there is uncertainty in the assessment process of the credible capacity.

The HDR-PV HPS designed in this work uses an HDR power system as the ESS to provide energy reserves to the PV generation, increasing the overall credible capacity and improving system reliability while meeting economic efficiency. The key to realizing this target is establishing an operating model that considers the day-ahead forecast of PV generation and the HDR power system. Then, we can evaluate the maximum credible capacity of the system with EFC constraints. The assessment results lay the foundation for subsequently coordinated scheduling. Thus, the following work will focus on the operation and the credible capacity assessment of the HDR-PV HPS.

MATHEMATICAL MODELS OF THE HDR-PV HPS

Models of Flexible HDR System

As shown in **Figure 1**, the flexible HDR system consists of EGS and TSGC. EGS can be modeled through the GMC and the ORC power generation (Yao et al., 2018). The geothermal working fluid distributor realizes the flexible brine distribution between the ORC generator I and the heat exchanger. The ESG model can be expressed as follows:

$$m_{\alpha}^{t} + m_{\beta}^{t} = m_{r}^{t}, \tag{1}$$

where m_r^t represents the mass flow rate of brine in the GMC; m_{α}^{t} and m_{β}^{t} represent the brine mass flow rate for ORC generator I power generation and for heat exchange in the heat storage/exchanger, respectively.

The output $P_I^t$of ORC generator I can be modeled as

$$P_I^t = \eta_P m_{\alpha}^{t} c_{pr} (T_r - T_{\alpha}), \tag{2}$$

where η_P represents the power generation efficiency of the ORC generator; c_{pr} represents the specific heat capacity of the brine; T_r represents the initial temperature of the brine in the production well; T_{α} represents the residual heat temperature of the brine after passing through the power generation system. T_r and T_{α} can be considered as a fixed value during regular operation (Kaplanis and Kaplani, 2007).

The geothermal working fluid mixer model is as follows:

$$m_{\alpha}^{t} T_{\alpha} + m_{\beta}^{t} T_{\beta} = m_{t}^{t} T_{W}^{t}, \tag{3}$$

where T_{β} represents the residual heat temperature of the brine after exchanging heat through the heat storage/exchange system; T_W^t represents the reinjection temperature of the heat extraction cycle. Due to the long response time of the HDR GMC, m_r^t and T_r can be regarded as constants.

In TSGC, the heat storage/exchange system transfers the heat from the brine to the HTO through the heat storage/exchanger and stores the energy in the high-temperature tank. When power generation is needed, the system inputs high-temperature HTO into the ORC generator II to generate electricity, and

the cooled-down HTO after power generation flows back to the low-temperature tank.

The heat storage/exchanger model in the system can be expressed as

$$Q_{\beta}^{t} = m_{\beta}^{t} c_{pr}\left(T_{r} - T_{\beta}\right), \tag{4a}$$

$$Q_{c}^{t} = m_{c}^{t} c_{po}\left(T_{c} - T_{l}\right), \tag{4b}$$

$$Q_{c}^{t} = \eta_{ex} Q_{\beta}^{t}, \tag{4c}$$

where Q_{β}^{t} is the thermal power input from the geothermal working fluid distributor; Q_{c}^{t} is the heat charge power from the heat exchanger; η_{ex} is the efficiency of the heat exchanger; m_{c}^{t} is the mass flow of the HTO during heat storage; T_{c} is the temperature of the HTO after heat exchange; T_{l} is the initial temperature of the HTO; c_{po} is the specific heat capacity of the HTO.

TSGC uses ORC generator II to output electricity, and its model is

$$P_{II}^{t} = \eta_{P} Q_{dc}^{t}, \tag{5}$$

where P_{II}^{t} is the electric power output of the ORC generator II; Q_{dc}^{t} is the thermal power consumed by the ORC generator II when generating electricity, that is, the heat discharge power of the high-temperature tank.

The process of heat storage and heat power output of high-temperature tanks can be expressed as follows:

$$S_{h}^{t+1} = \eta_{h} S_{h}^{t} + \left(Q_{c}^{t} - Q_{dc}^{t}/\eta_{dc}\right)\Delta\tau, \tag{6a}$$

$$Q_{dc}^{t} = m_{dc}^{t} c_{po}\left(T_{c} - T_{l}\right), \tag{6b}$$

where S_{h}^{t} is the heat charged at the time t; η_{h} is the insulation coefficient; η_{dc} is the heat discharge efficiency; m_{dc}^{t} is the mass flow of the HTO when the high-temperature tank generates heat; and $\Delta\tau$ is the time interval of heat storage/heat release process.

In the heat charging and discharging process, the HTO is continuously exchanged between the high-temperature and the low-temperature tanks. Its quality state models are

$$M_{h}^{t+1} = M_{h}^{t} + m_{c}^{t}\Delta\tau - m_{dc}^{t}\Delta\tau, \tag{7a}$$

$$M_{l}^{t+1} = M_{l}^{t} - m_{c}^{t}\Delta\tau + m_{dc}^{t}\Delta\tau, \tag{7b}$$

where M_{h}^{t} and M_{l}^{t} denote the mass of HTO in the high-temperature tank and the low-temperature tank, respectively.

Considering that energy storage in TSGC can smooth power fluctuation, the HDR power system can set the operation interval in advance according to the power output prediction of the PV plant and provide reserves. The models for the reserve are

$$R^{t} = R_{I}^{t} + R_{II}^{t}, \tag{8a}$$

$$R_{I}^{t} = u_{I}^{+}\left(P_{I}^{\max} - P_{I}^{t}\right) + u_{I}^{-}\left(P_{I}^{t} - P_{I}^{\min}\right), \tag{8b}$$

$$R_{II}^{t} = u_{II}^{+}\left(P_{II}^{\max} - P_{II}^{t}\right) + u_{II}^{-}\left(P_{II}^{t} - P_{II}^{\min}\right), \tag{8c}$$

$$u_{I}^{+} + u_{I}^{-} \le 1, u_{II}^{+} + u_{II}^{-} \le 1, \tag{8d}$$

where R^{t} represents the total reserve; R_{I}^{t} and R_{II}^{t} represent the reserve provided by ORC generators I and II respectively; $P_{I/II}^{\max}$ and $P_{I/II}^{\min}$ are the power output's upper and lower bounds of ORC generators respectively; $u_{I/II}^{+/-}$ is a binary variable to ensure that the positive and negative reserves are not called at the same time.

Models of PV Plant

According to (Duan et al., 2018), the power output of a PV plant considering solar irradiance can be modeled as

$$P_{PV}^{t} = \lambda^{t} P_{PV}, \tag{9a}$$

$$\hat{\xi}_{PV}^{t} = \lambda_{\xi}^{t} P_{PV}, \tag{9b}$$

where λ^{t} is the PV power output coefficient according to the predicted value of solar irradiance; λ_{ξ}^{t} is the actual PV power output coefficient; P_{PV} is the credible capacity of the PV plant in the HPS; P_{PV}^{t} is the predicted value of the power output of the PV plant related to the trusted capacity P_{PV} of the PV plant and the predicted value of solar irradiance λ^{t}; $\hat{\xi}_{PV}^{t}$ is the actual power output corresponding to the credible capacity of the PV plant.

CREDIBLE CAPACITY ASSESSMENT METHOD BASED ON DISTRIBUTIONALLY ROBUST

The Formulation of the Assessment Method

The purpose of the credible capacity assessment of HDR-PV HPS is to determine the maximum credible capacity that meets the power grid's requirements for power volatilities. Sufficient credible capacity can enable the HPS to provide reserves by dispatching the HDR power system to deal with the uncertainty of the PV plant, thereby indirectly ensuring the reliable operation of the power grid. It can be seen that the credible capacity assessment of the HPS can be modeled as an optimization problem, including dispatchable power sources. This problem aims to maximize the system's generation profit and give full play to the regulating role of the HDR power system. The assessment model can be formed as:

$$\max \quad f(x) = \sum_{t=1}^{T} V_{HDR}^{t} + V_{PV}^{t}$$

$$s.t. \begin{cases} g_{r}^{t}(x, R^{t}) \le 0 \\ \forall R^{t}: \\ \quad g_{g}^{t}\left(x, R^{t}, \hat{\xi}_{PV}^{t}\right) \le 0 \\ \forall \hat{\xi}_{PV}^{t}: \\ \quad P\left(\hat{\xi}_{PV}^{t}\right) \in M(\Xi) \\ t \in T \end{cases}, \tag{10}$$

where x represents the decision variable, including the credible capacity P_{PV} of the PV plant, the brine mass flow m_{α}^{t} of the ORC generator I, the HTO mass flow m_{c}^{t} of the heat storage/exchanger, and the HTO mass flow m_{dc}^{t} of ORC generator II; V_{HDR}^{t} represents the profit of the flexible HDR system; V_{PV}^{t} represents the profit of the PV plant; $g_{r}^{t}(x, R_{t}) \le 0$ represents the operating constraint of the HDR power system; $g_{g}^{t}(x, R^{t}, \hat{\xi}_{PV}^{t}) \le 0$ represents the EFC constraint satisfying requirements of power fluctuation; $P(\hat{\xi}_{PV}^{t})$ represents the probability distribution of the PV power uncertainty, and

$M(\Xi)$ represents the ambiguous set of the probability of the photovoltaic power output.

$$V_{HDR}^t = c_e^t\left(P_I^t + P_{II}^t\right) - c_Q Q_{cur}^t, \tag{11}$$

where c_e^t represents the time-of-use electricity price, c_Q represents the penalty coefficient for abandonment of heat, and Q_{cur}^t represents the abandonment power that cannot be stored after heat exchange when taking the minimum reinjection temperature as a reference.

The profit of the PV plant can be modeled as

$$V_{PV}^t = c_e^t\left(P_{PV}^t - P_{PVcur}^t\right) - pc_e^t P_{PVal}^t, \tag{12}$$

where P_{PVcur}^t and P_{PVal}^t represent the PV and load curtailment of the PV plant's credible capacity; p is the penalty coefficient of load curtailment. For P_{PVcur}^t and P_{PVal}^t, they can be expressed as

$$P_{PVcur}^t = \max\left\{\hat{\xi}_{PV}^{k,t} - P_{PV}^t, 0\right\}, \tag{13}$$

$$P_{PVal}^t = \max\left\{P_{PV}^t - \hat{\xi}_{PV}^t, 0\right\}, \tag{14}$$

Distributionally Robust EFC Constrains

The HDR-PV HPS provides a reserve for the PV plant through the HDR power system. The whole HPS is equivalent to a dispatchable power source to meet the requirements of power fluctuation. Taking the predicted power output of the PV plant as the dispatchable power curve, we have the EFC constraint as follows:

$$(1-\sigma)P_{PV}^t \le \hat{\xi}_{PV}^t + R^t \le (1+\sigma)P_{PV}^t, \tag{15}$$

where represents the power fluctuation rate allowed by the grid. **Eq. 15** restricts the range of the sum of the PV plant's actual power output and the reserve provided by the HDR power system at any time. In such a case, the PV plant is equivalent to a dispatchable power source, thereby obtaining the credible capacity as

$$P_{sys} = P_I + P_{II} + P_{PV}, \tag{16}$$

where P_{sys} represents the credible capacity of the HPS; P_I and P_{II} represent the capacity of ORC power generation system I and II, respectively.

Due to the PV plant's power uncertainty, we adopt the distributionally robust method to model these uncertainties (Duan et al., 2018). The distributionally robust method uses the data-driven method to construct the uncertain probability distribution based on stochastic optimization. The method can ensure the robustness of the system under the worst probability distribution strategy within the confidence interval. It can be seen that the conservatism of the worst operation scenario described by the distributionally robust method is between robust optimization and stochastic optimization, which makes the system capacity assessment not only achieve the robustness within the full confidence interval but also reduce the system redundancy capacity to deal with extreme scenarios. The ambiguous set using Wasserstein divergence is used to measure the uncertainty measure and is given as follows:

$$M^\varepsilon = \left\{P \in M(\Xi):\ d_W\left(P, \hat{P}\right) \le \varepsilon\right\}, \tag{17}$$

where Prepresents the probability distribution of the actual power output of the PV plant; $\hat{P}$ represents the empirical distribution of the power output; $M(\Xi)$represents the space consisting of all probability distributions with the Wasserstein divergence; $\varepsilon$is the radius of the ambiguous set, which can be referred to as (Esfahani and Kuhn, 2018); and $d_w$represents Wasserstein divergence (Hota et al., 2019).

Then, we reformulate **Eq. 15** and consider the probability distribution of the power output in the worst case. The distribution should satisfy:

$$\inf_{P\in M^\varepsilon} P\left\{\left|\hat{\xi}_{PV}^t + R^t - P_{PV}^t\right| \le \sigma P_{PV}^t\right\} \ge 1-\alpha, \tag{18}$$

where α represents the confidence level, that is, the minimum probability that the derivation between $\hat{\xi}_{PV}^t + R^t$ (satisfying $M(\Xi)$) and P_{PV}^t does not exceed σ is greater than $1-\alpha$.

Reformulate **Eq. 18**, and we have:

$$\sup_{P\in M^\varepsilon} \Pr\left\{\left|\hat{\xi}_{PV}^t + R^t - P_{PV}^t\right| - \sigma P_{PV}^t \ge 0\right\} \le \alpha. \tag{19}$$

According to (Rockafellar and Uryasev, 2000). **Eq. 19** can be equivalent to the following risk condition constraint

$$\sup_{P\in M_i^\varepsilon} CVaR_{1-\alpha}^P\left(L\left(\hat{\xi}_{PV}^t, R^t\right)\right) \le 0, \tag{20a}$$

$$L\left(\hat{\xi}_{PV}^t, R^t\right) = \left|\hat{\xi}_{PV}^t + R^t - P_{PV}^t\right| - \sigma P_{PV}^t, \tag{20b}$$

In this work, we use the method proposed in (Fiaschi et al., 2017) to transform **Eq. 19** into a set of linear constraints, which is listed as follows:

$$\varepsilon H_L + \frac{1}{K}\sum_{k=1}^{K} s^{k,t} - \gamma^t \alpha \le 0, \tag{21a}$$

$$s^{k,t} \ge \xi_{PV}^{k,t} + R^{k,t} - (1+\sigma)P_{PV}^t + \gamma^t, \tag{21b}$$

$$s^{k,t} \ge -\xi_{PV}^{k,t} - R^{k,t} + (1-\sigma)P_{PV}^t + \gamma^t, \tag{21c}$$

$$s^{k,s} \ge 0, \forall k \in K, t \in T, \tag{21d}$$

where $\xi_{PV}^{k,t}$ represents the kth sample of PV power output $\hat{\xi}_{PV}^t$, i.e., $\xi_{PV}^{k,t} = \lambda_\xi^{k,t} P_{PV}$; K represents the number of samples, and T represents the whole scheduling period. Eq. 21 requires $L(\hat{\xi}_{PV}^t, R^t)$ to satisfy Lipschitz continuity while H_L represents the measure of Lipschitz continuity.

According to the actual operating conditions of the PV station, when the power output equals 0, the dispatched reserves should be equal to the dispatch value. Thus, there is $R^t = P_{PV}^t$ when $\hat{\xi}_{PV}^t = 0$. Then we have:

$$L\left(0, R^t\right) = -\sigma P_{PV}^t, \tag{22}$$

$$L\left(\hat{\xi}_{PV}^t, R^t\right) - L\left(0, R^t\right) = \left|\hat{\xi}_{PV}^t + R^t - P_{PV}^t\right|, \tag{23}$$

Since the actual power output of the PV plant is not less than the lower bound of the predicted value, $\hat{\xi}_{PV}^t \ge (1-\phi)P_{PV}^t$ satisfies ϕ represents the prediction error. Combining **Eqs 18d**–d**21d**, we can obtain

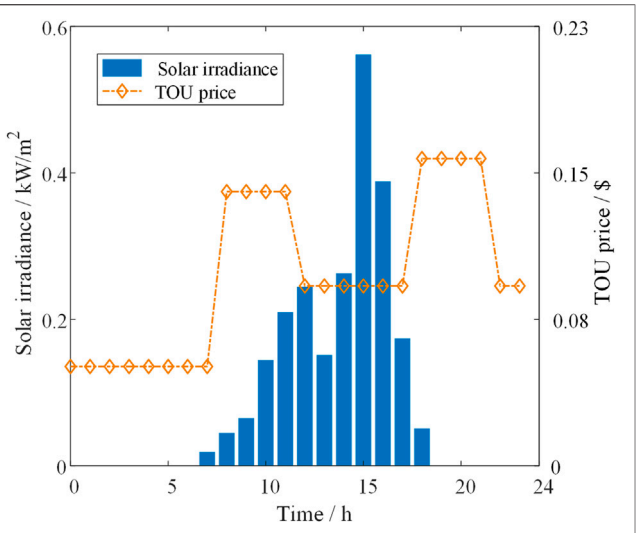

FIGURE 3 | Curve of solar irradiance and time-of-use power price.

TABLE 1 | The rated parameters of the HDR-PV hybrid power system.

Parameters	Value
Capacity of PV system P_{PV} MW	300
Brine temperature in production well T_r°C	200
Mass flow of brine in production wells m_r^t kg/s	75
Minimum brine reinjection temperature $T_W^{\min}$°C	40
Initial temperature of heat transfer oil T_l°C	25
Insulation coefficient η_h%	15
Specific heat capacity of heat transfer oil c_{po} kJ/(kg°C)	1.938
Specific heat capacity of brine c_{pr} kJ/(kg°C)	4.2
Efficiency of ORC generator η_P%	13.2 (Fallah et al., 2016)
Efficiency of heat exchanger η_{ex}%	90
Prediction error of PV power output φ%	20
Allowable power fluctuation rate of the grid σ %	≤10
Penalty for load curtailment p	3
Confidence level α	0.05

$$||L\left(\hat{\xi}_{PV}^t, R^t\right) - L\left(0, R^t\right)|| \le \frac{\sigma}{1-\phi}\hat{\xi}_{PV}^t. \tag{24}$$

Eq. 24 is used to prove that $L(\hat{\xi}_{PV}^t, R^t)$ satisfies Lipschitz continuity. To prove that, we can take $H_L = \sigma/(1-\phi)$. On this basis, Eqs 21a–d gives the EFC constraint for the PV plant with dispatchable reserves.

Operation Constraints

Considering the current technical conditions of HDR resources, the stable operation of the flexible HDR system should also meet the following upper and lower bounds:

$$P_r^{\min} \le P_{I/II}^t \le P_r^{\max}, \tag{25a}$$
$$0 \le m_c^t \le m_c^{\max}, \tag{25b}$$
$$0 \le m_{dc}^t \le m_{dc}^{\max}, \tag{25c}$$
$$S_h^{\min} \le S_h^t \le S_h^{\max}, \tag{25d}$$

where **Eq. 25a** is the capacity constraints of ORC generators I and II restricted by the GMC. **Eqs 25b**, **25c** are the constraints on the mass flow of HTO in the process of heat exchange. **Eq. 25d** is the constraint of heat storage. To satisfy the minimum power operation requirements of ORC generator II, the heat storage capacity of the high-temperature tank should be greater than $S_h^{\min}$.

The operation of HDR power system should also meet the following reliability and system safe operation constraints

$$m_\alpha^{\min} \le m_\alpha^t \le m_r^t, \tag{26a}$$
$$T_W^{\min} \le T_W^t, \tag{26b}$$
$$M_l^t + M_h^t = M_{\text{all}}, \tag{26c}$$
$$-(1-u^t)\mathrm{M} \le R_I^t \le u^t \mathrm{M}, \tag{26d}$$
$$-(1-u^t)\mathrm{M} \le R_{II}^t \le u^t \mathrm{M}, \tag{26e}$$

where **Eq. 26a** indicates that the brine used for ORC generator I is not less than the minimum value that guarantees the reliability of plant power. **Eq. 26b** restricts the reinjection temperature to ensure the stability of the underground thermal reservoir. **Eq. 26c** is the mass balance constraint of the thermal storage tank to ensure the safe operation of the high/low-temperature thermal storage tanks. **Eqs 26d**,**26e** are the constraints to ensure that the reserve dispatch of the two ORC power generation systems will not interfere with each other. Mis a sufficiently large positive number.

In addition, the product of variables m_β^t and T_β exists in **Eqs 3**, **4**, making the entire model non-linear. To simplify the model, the curtailed heat power Q_{cur}^t is used to represent this product term. At this time, the nonlinear model is transformed into a linear form. **Eqs 3**, **4a** can be rewritten as

$$m_\alpha^t T_\alpha + Q_{cur}^t / c_{pr} = m_r^t T_W, \tag{27}$$
$$Q_\beta^t = m_\beta^t c_{pr}\left(T_r - T_W^{\min}\right) + Q_{cur}^t, \tag{28a}$$
$$0 \le Q_{cur}^t. \tag{28b}$$

HDR-PV HPS's credible capacity assessment problem is transformed into a mixed-integer optimization problem (MILP) through the above reformulation, which can be directly solved with Matlab 2016b and CPLEX12.8.

CASE STUDY

System Parameters

The studied case is constructed based on the actual data of HDR and PV resources in the Gonghe Basin of Qinghai Province. The time-of-use (TOU) electricity price is adopted. Both solar irradiance data and time-of-use electricity prices are taken from local historical data, as shown in **Figure 3**.

In this case, the capacity of the PV plant is selected according to the local typical power station of 300 MWp. The operating parameters of the flexible HDR system are selected based on the local resources (Si et al., 2020). The capacity of the generator is selected based on the GMC parameters and the current status of geothermal development technology. The detailed parameters of the system are shown in **Table 1**.

TABLE 2 | Assessment results of each case.

Cases	EFC of PV (MW)	EFC of HDR (MW)	Mass of HTO (ton)	EGS profits ($/day)	TSGC profits ($/day)	PV profits ($/day)	Abandon heat (MWh/day)	Residual heat (MWh/day)
Case 1	52.95	6.6	—	13,338	—	64,127	78.844	—
Case 2	52.95	13.2	2,747	10,384	8,205	64,127	—	6.86
Case 3	77.44	13.2	2,937	10,150	7,541	65,828	—	45.64

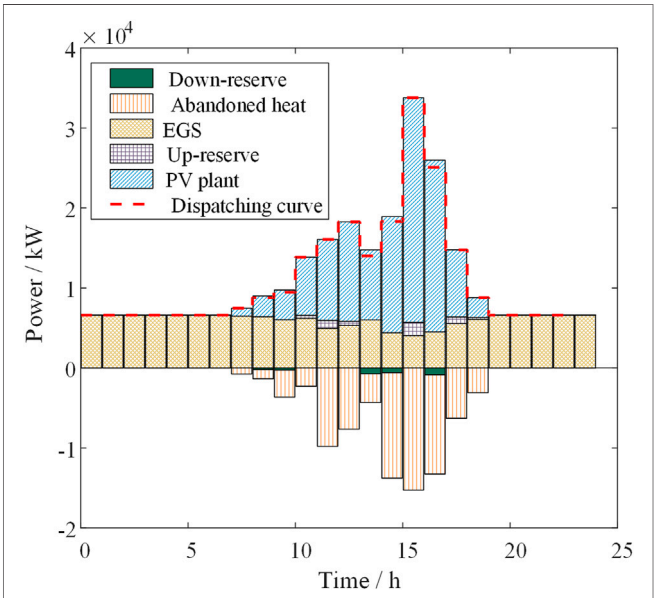

FIGURE 4 | System operation in case 1.

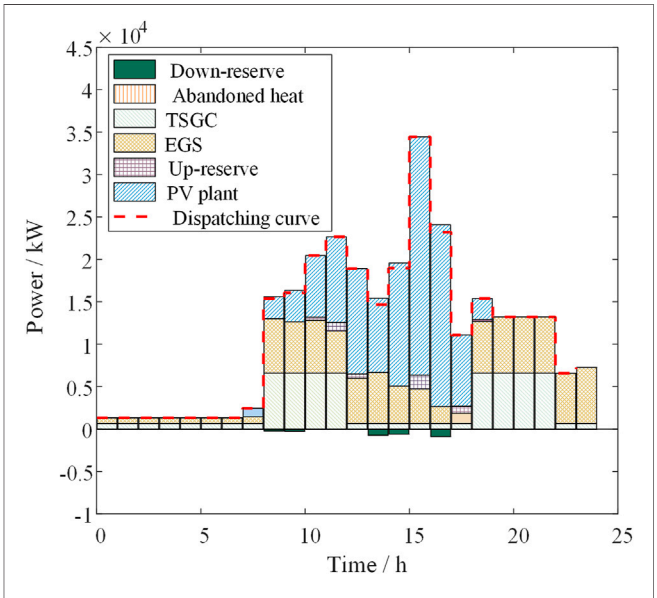

FIGURE 5 | System operation in case 2.

Simulation Results

We set up the following three cases to compare and analyze the capacity assessment results.

Case 1: Only the EGS with the HDR power system provides reserves for the PV plant; the TSGC is not used; Case 2: Based on the settings of scenario 1, the TSGC of the HDR power system is further configured to recover waste heat energy for power generation, but the TSGC provides no reserve; Case 3: Based on the settings of scenario 2, both EGS and TSGC provide reserves.

First, we set the allowable power fluctuation as 0% for the following analysis. The parameters of solar irradiance and TOU electricity price are the same in all scenarios.

The results in **Table 2** show that, with a 0% allowable power fluctuation, only using EGS to provide the reserve for the PV plant will generate a large amount of waste heat. The comparisons show that the HPS equipped with EGS realizes the dispatch ability of the PV plant by curtailing heat. To better illustrate the results, we give the power output of each part in Case 1 in **Figure 4**.

Due to the high investment cost of EGS (Zhang L. et al., 2014), the operation mode in case 1 is challenging to meet the financial requirements in practice. TSGC can store the curtailed heat well and then convert it back into electricity, improving the overall economic benefits and maintaining the credible capacity of the PV plant.

Figure 5 shows the power output of each part in case 2. The results show that TSGC plays a vital role in waste heat recovery. When the time-of-use electricity price is applied, the TSGC can store geothermal energy during the low electricity price from 00: 00 to 7:00 and generate electricity during the high electricity price, thereby achieving peak shaving. This has increased the profit of the flexible HDR system by 36.78%.

In case 3, when TSGC also participates in providing reserves, the credible capacity of the HPS is nearly doubled. Although the overall profit of the flexible HDR system decreased by 2.97%, the overall profit of the HPS increased due to the increased credible capacity. At the same time, it is also noticed that the thermal energy stored by TSGC was not fully utilized. After 24 h of operation, the remaining thermal energy in the thermal storage tank is 45.64 MWh, increasing 192.75% compared to case 2. In this case, geothermal energy is not fully utilized, so it is necessary to analyze the key parameters further. The operation curve of the HDR power system in the HPS is shown in **Figure 6**.

Figure 6 that, first of all, the flexible HDR system adopts the minimum power generation strategy during the low electricity price period (0:00–7:00) and in the high electricity price period (8:

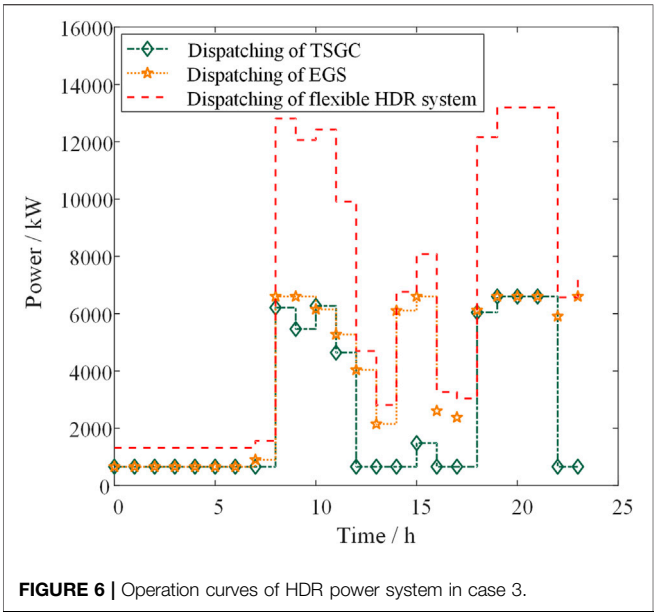

FIGURE 6 | Operation curves of HDR power system in case 3.

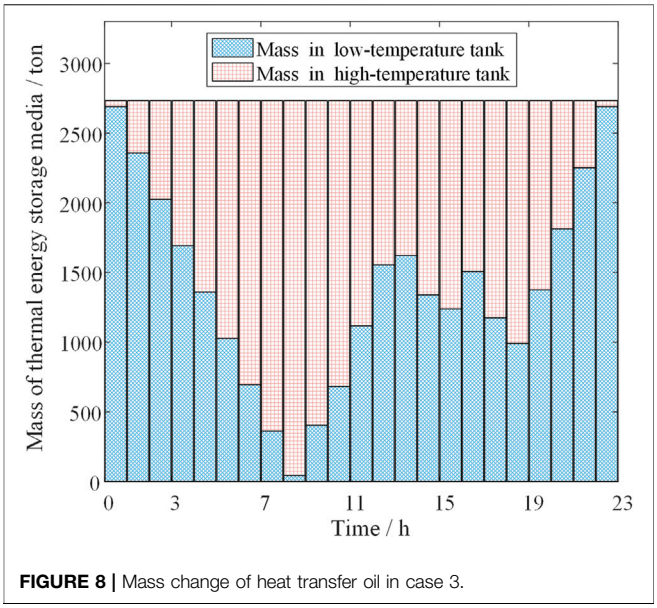

FIGURE 8 | Mass change of heat transfer oil in case 3.

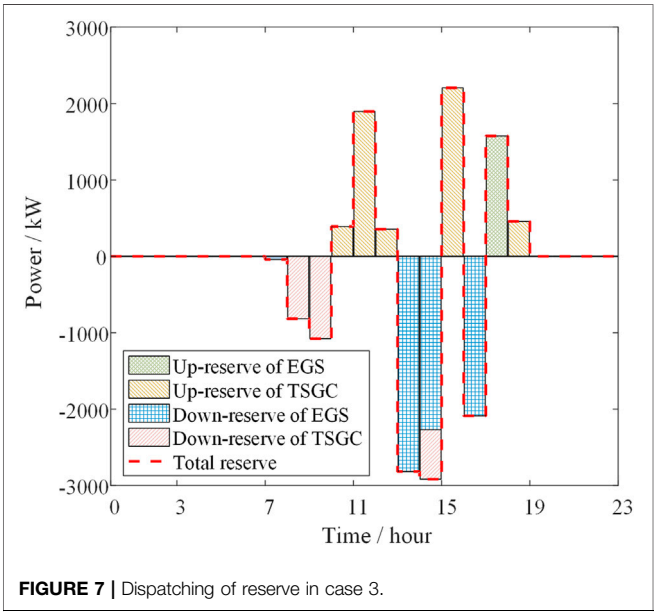

FIGURE 7 | Dispatching of reserve in case 3.

00–12:00, 18:00–22:00) adopt maximum power generation strategy to maximize profit. Secondly, during the PV plant power generation period (8:00–19:00), the output power of the HDR power system will be adjusted with the fluctuation of the actual PV power output according to EFC constraints. Especially during the period from 10:00 to 18:00, thanks to dispatchable reserves provided by the HDR power system, the PV plant's power output can meet the grid's dispatching requirements, thereby improving the reliability of HPS. **Figure 7** exhibits the reserve dispatch under a specific actual operation condition. It can be seen from the results that EGS mainly provides negative reserve, while TSGC mainly provides positive reserve. This is to minimize heat exchange and storage losses and maximize profit. Finally, the thermal energy stored in the high-temperature thermal storage tank will be converted into electrical energy by the ORC generator II during the high electricity price period from 20:00 to 22:00.

In the thermal storage tank, the mass of the HTO also changes with the power output fluctuation. **Figure 8** shows the mass change of the HTO between the high-temperature and the low-temperature tank in case 3. In the figure, the mass of the HTO in the high-temperature tank increases from 0: 00 to 7: 00, indicating that the geothermal energy is heated by the heat storage/exchanger and stored in the high-temperature tank. During the high electricity price period from 8:00 to 12:00, TSGC converts heat into electricity, and the mass of HTO in the high-temperature tank decreases. During the power generation period of the PV plant from 10:00 to 18:00, the HDR power system dispatches reserves to ensure that the system's output can meet the requirements of grid operation. In the same period, the mass of the HTO in the heat storage system fluctuates accordingly. After the PV plant power generation cycle ends, the heat stored in the storage will be converted into electricity during the high electricity price period from 20:00 to 22:00 to increase economic benefits.

Impact of Allowable Fluctuation rate on the Credible Capacity of the HPS.

With the parameter setting of case 3, we further study the influence of the allowable fluctuation rate of grid power on the credible capacity of the HPS. Take the allowable fluctuation rate as 3, 5, 7, and 10% for simulation, respectively. The comparison results are shown in **Table 3**.

The results in **Table 3** indicate that, as the grid's ability to withstand power fluctuation increases, the credible capacity of the HPS increases accordingly. Compared with the case with a 0% allowable fluctuation rate, the credible capacity of the PV plant is increased by 113% when the allowable fluctuation rate is equal to 10%. To increase the credible capacity of the HPS, the profit of the

TABLE 3 | Impact of allowable fluctuation rate on the credible capacity of HPS.

σ	EFC of PV (MW)	EFC of HDR (MW)	Capacity ratio	Mass of HTO (ton)	EGS profits ($/day)	TSGC profits ($/day)	PV profits ($/day)	Residual heat (MWh/day)
3%	93.96	13.2	7.12	2,747	10,459	8,053	65,990	6.1
5%	107.12	13.2	8.12	2,746	10,629	8,027	66,099	1.12
7%	124.56	13.2	9.44	2,746	10,737	7,968	66,291	0.62
10%	164.83	13.2	12.49	2,766	10,870	7,711	66,686	0

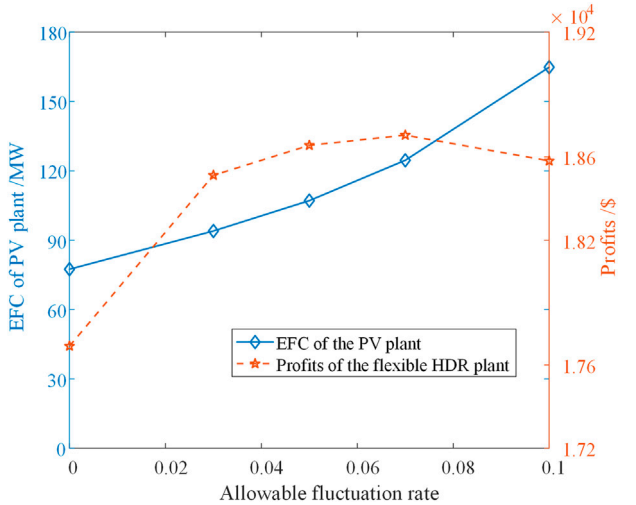

FIGURE 9 | Relationship of PV's credible capacity, HDR's profit, and allowable fluctuation rate.

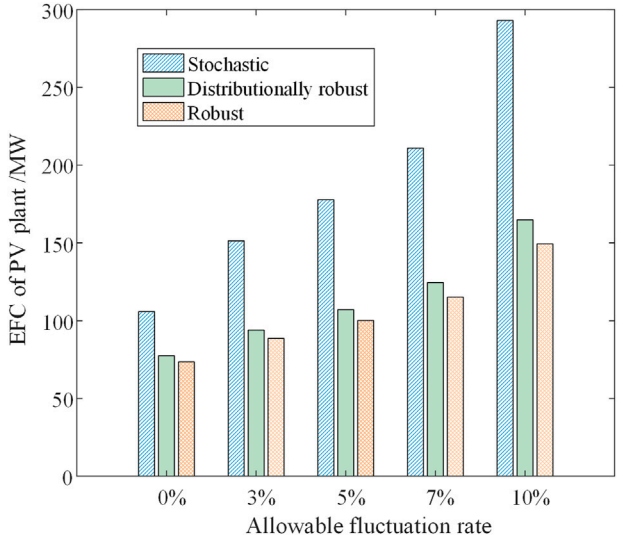

FIGURE 10 | Credible capacity assessment of PV plant based on different optimization methods.

flexible HDR system increased by 5.03%. This is because the geothermal energy stored in the thermal storage tank is fully utilized, which is reduced from 45.64 MWh to 0 MWh.Since the total geothermal energy obtained by the HDR geothermal extraction cycle remains stable quickly, the mass of the total HTO required from 3 to 10% is not much different. The relationship between the profit of the HDR power system, the PV plant's credible capacity, and the power fluctuation is shown in **Figure 9**.

As we can see, the PV plant's credible capacity increases monotonically with the increase in power fluctuation rate, and the profit of the flexible HDR system has a local maximum when the fluctuation rate is 7%. However, we obtain the minor remaining thermal energy of the thermal storage tank in **Table 3**, which shows that the geothermal energy is fully utilized with a 10% allowable fluctuation rate.

Influence of Uncertainty Modeling Method on Capacity Assessment

The distributionally robust method based on Wasserstein divergence is an optimization method driven by actual historical data. It can make full use of the implicit information of PV generation data and obtain a moderately conservative EFC assessment. Taking allowable fluctuation rate as 0%, 3 ,5, 7, and 10%, the credible capacity of the hybrid system is assessed by robust optimization, stochastic optimization to compare with the distributionally robust method, respectively. The EFC assessments of the PV plant are shown in **Figure 10**.

It can be seen from **Figure 10** that the credible capacity of PV plant obtained by stochastic optimization is the largest, followed by distributionally robust method, and the result obtained by robust optimization is the smallest. This further shows that the results obtained by stochastic optimization are too optimistic; The results obtained by the robust optimization are too conservative. In order to deal with the worst scenarios, its credible capacity is only 69.48–50.96% of the former compared with the stochastic optimization, and its conservatism becomes more and more evident with the increase of allowable fluctuation; The EFC assessment using the distributionally robust method proposed in this paper is between the results of stochastic optimization and robust optimization, which can ensure the robustness of the system in the sense of confidence.

DISCUSSION

To solve the problem of grid connection of large-scale PV plants in extreme-cold and high-altitude areas, we design a flexible HDR system consisting of an enhanced geothermal system and a thermal storage generation cycle. Then, a model of HDR-PV HPS is constructed with the HDR power system and PV plant. On this basis, a credible capacity assessment method of the proposed HPS with EFC constraint is proposed. This method can be transformed into a scheduling optimization problem of HPS to maximize profit. The EFC constraints are reformulated as a set of value-at-risk constraints by applying the distributionally robust method.

At last, the credible capacity assessment method is represented as a MILP with risk constraints for the solution. To verify the effectiveness of our work, we take the actual system in the Gonghe Basin of Qinghai Province as an example. The results show that the credible capacity assessment method can effectively assess the maximum credible capacity of the proposed HDR-PV HPS. Also, the HDR power system can enhance the reliability of connection between PV station and grid while increasing the overall profit of the HPS.

DATA AVAILABILITY STATEMENT

The raw data supporting the conclusion of this article will be made available by the authors, without undue reservation.

AUTHOR CONTRIBUTIONS

YS: conceptualization, writing-original draft preparation, software. LC: funding acquisition, validation. LM: funding acquisition, conceptualization, methodology, and editing. HM: validation. XC: project administration. SM: supervision. All authors have read and agreed to the published version of the manuscript.

FUNDING

This research was funded in part by the Joint Fund Project of National Natural Science Foundation of China (U1766203), in part by Key R and D and Transformation Plan of Qinghai Province (2021-GX-109), and in part by the Basic Research Project of Qinghai Province (2021-ZJ-948).

ACKNOWLEDGMENTS

The authors would like to thank Prof. Feng Liu and Wei for very helpful discussions on the cooperative game, Dr. Xiaodai Xue and Xuelin Zhang for discussions on the HDR geothermal generator model, Dr. Zhongjie Guo and Jiayu Bai for suggestions on practical issues.

REFERENCES

Brown, D. W. (2009). "February). Hot Dry Rock Geothermal Energy: Essential Lessons from Fenton Hill," in *Thirty-Fourth Workshop on Geothermal Reservoir Engineering* (Stanford: Stanford University), 9–11. Available at: https://pangea.stanford.edu/ERE/pdf/IGAstandard/SGW/2009/brown.pdf.

Dent, C. J., Hernandez-Ortiz, A., Blake, S. R., Miller, D., and Roberts, D. (2015). Defining and Evaluating the Capacity Value of Distributed Generation. *IEEE Trans. Power Syst.* 30 (5), 2329–2337. doi:10.1109/TPWRS.2014.2363142

Duan, C., Fang, W., Jiang, L., Yao, L., and Liu, J. (2018). Distributionally Robust Chance-Constrained Approximate AC-OPF with Wasserstein Metric. *IEEE Trans. Power Syst.* 33 (5), 4924–4936. doi:10.1109/TPWRS.2018.2807623

Esmaili, A., and Nasiri, A. (2009). "A Case Study on Improving ELCC by Utilization of Energy Storage with Solar PV," in 2009 35th Annual Conference of IEEE Industrial Electronics (IEEE), 3957–3962. doi:10.1109/IECON.2009.5415336

Fallah, M., Mahmoudi, S. M. S., Yari, M., and Akbarpour Ghiasi, R. (2016). Advanced Exergy Analysis of the Kalina Cycle Applied for Low Temperature Enhanced Geothermal System. *Energ. Convers. Manag.* 108, 190–201. doi:10.1016/j.enconman.2015.11.017

Fiaschi, D., Manfrida, G., Rogai, E., and Talluri, L. (2017). Exergoeconomic Analysis and Comparison between ORC and Kalina Cycles to Exploit Low and Medium-High Temperature Heat from Two Different Geothermal Sites. *Energ. Convers. Management* 154, 503–516. doi:10.1016/j.enconman.2017.11.034

Guo, Z., Wei, W., Chen, L., Xie, R., and Mei, S. (2020). Sizing Energy Storage to Reduce Renewable Power Curtailment Considering Network Power Flows: a Distributionally Robust Optimisation Approach. *IET Renew. Power Generation* 14 (16), 3273–3280. doi:10.1049/iet-rpg.2020.0354

He, J., Deng, C., Xu, Q., Liu, C., and Pan, H. (2013). Optimal Configuration of Distributed Generation System Containing Wind PV Battery Power Sources Based on Equivalent Credible Capacity Theory. *Power Syst. Technology* 37 (12), 3317–3324.

Hota, A. R., Cherukuri, A., and Lygeros, J. (2019). "Data-Driven Chance Constrained Optimization under Wasserstein Ambiguity Sets," in In 2019 American Control Conference (ACC) (IEEE), 1501–1506. doi:10.23919/ACC.2019.8814677

Injeti, S. K., and Prema Kumar, N. (2013). A Novel Approach to Identify Optimal Access point and Capacity of Multiple DGs in a Small, Medium and Large Scale Radial Distribution Systems. *Int. J. Electr. Power Energ. Syst.* 45 (1), 142–151. doi:10.1016/j.ijepes.2012.08.043

Islam, M. R., Guo, Y., and Zhu, J. (2014). A Multilevel Medium-Voltage Inverter for Step-Up-Transformer-Less Grid Connection of Photovoltaic Power Plants. *IEEE J. Photovoltaics* 4 (3), 881–889. doi:10.1109/JPHOTOV.2014.2310295

Kaplanis, S., and Kaplani, E. (2007). A Model to Predict Expected Mean and Stochastic Hourly Global Solar Radiation I(h;nj) Values. *Renew. Energ.* 32 (8), 1414–1425. doi:10.1016/j.renene.2006.06.014

Mohajerin Esfahani, P., and Kuhn, D. (2018). Data-driven Distributionally Robust Optimization Using the Wasserstein Metric: Performance Guarantees and Tractable Reformulations. *Math. Program* 171 (1), 115–166. doi:10.1007/s10107-017-1172-1

Nespoli, A., Ogliari, E., Leva, S., Massi Pavan, A., Mellit, A., Lughi, V., et al. (2019). Day-ahead Photovoltaic Forecasting: A Comparison of the Most Effective Techniques. *Energies* 12 (9), 1621. doi:10.3390/en12091621

Peter, J., and Wagner, J. (2021). Optimal Allocation of Variable Renewable Energy Considering Contributions to Security of Supply. *Ej* 42 (1). doi:10.5547/01956574.42.1.jpet

Rockafellar, R. T., and Uryasev, S. (2000). Optimization of Conditional Value-At-Risk. *Jor* 2, 21–41. doi:10.21314/jor.2000.038

Si, Y., Chen, L., Zhang, X., Chen, X., Zheng, T., and Mei, S. (2021). Game Approach to HDR-TS-PV Hybrid Power System Dispatching. *Appl. Sci.* 11 (3), 914. doi:10.3390/app11030914

Si, Y., Chen, L., Zhang, X., and Mei, S. (2020). Capacity Optimization of Micro Energy Network with Hot Dry Rock Enhanced Geothermal System. *Power Syst. Technol.* 44, 1603–1611.

Singh, G. K. (2013). Solar Power Generation by PV (Photovoltaic) Technology: A Review. *Energy* 53, 1–13. doi:10.1016/j.energy.2013.02.057

Song, J., Krishnamurthy, V., Kwasinski, A., and Sharma, R. (2012). Development of a Markov-Chain-Based Energy Storage Model for Power Supply Availability Assessment of Photovoltaic Generation Plants. *IEEE Trans. Sustainable Energ.* 4 (2), 491–500. doi:10.1109/TSTE.2012.2207135

Sulaeman, S., Benidris, M., Tian, Y., and Mitra, J. (2016). Modeling and Evaluating the Capacity Credit of PV Solar Systems Using an Analytical Method," in 2016 IEEE/PES Transmission and Distribution Conference and Exposition (T&D) (IEEE), 1–5. doi:10.1109/TDC.2016.7519949

Tapetado, P., and Usaola, J. (2019). Capacity Credits of Wind and Solar Generation: The Spanish Case. *Renew. Energ.* 143, 164–175. doi:10.1016/j.renene.2019.04.139

Wang, Y., Cheng, J., Fan, F., Chen, Z., Xiao, Z., and Deng, K. (2019). "Maximum PV Access Capacity Planning Method for Rural Power Grid Considering Overload Risk," in In 2019 IEEE 3rd Conference on Energy Internet and Energy System Integration (EI2) (IEEE), 387–391. doi:10.1109/EI247390.2019.9062179

Yan, X., Liu, Y., Wang, G., and Lu, Y. (2019). Optimal Injection Rate of Water in the Guide Basin Hot Dry Rock Mining Project. *Energy Exploration & Exploitation* 37 (2), 721–735. doi:10.1177/0144598718800729

Yao, J., Zhang, X., Sun, Z., Huang, Z., Liu, J., Li, Y., et al. (2018). Numerical Simulation of the Heat Extraction in 3D-EGS with thermal-hydraulic-mechanical Coupling Method Based on Discrete Fractures Model. *Geothermics* 74, 19–34. doi:10.1016/j.geothermics.2017.12.005

Yuan, Y., Liu, T. Q., and Cheng, D. W. (2012). Research on Maximum Access Capacity of Grid-Connected Photovoltaic Power. *Kezaisheng Nengyuan(Renewable Energ. Resources)* 30 (6), 9–14. doi:10.13941/j.cnki.21-1469/tk.2012.06.023

Zare, V. (2016). A Comparative Thermodynamic Analysis of Two Tri-generation Systems Utilizing Low-Grade Geothermal Energy. *Energ. Convers. Manag.* 118, 264–274. doi:10.1016/j.enconman.2016.04.011

Zeng, B., Sun, B., Wei, X., Gong, D., Zhao, D., and Singh, C. (2020). Capacity Value Estimation of Plug-In Electric Vehicle Parking-Lots in Urban Power Systems: A Physical-Social Coupling Perspective. *Appl. Energ.* 265, 114809. doi:10.1016/j.apenergy.2020.114809

Zhang, L., Wu, Y., Lou, S., Yang, Y., and Wang, Y. (2014a). "Photovoltaic Generation Capacity Credit Evaluation Method Considering its Daily Output Characteristics," in 2014 International Conference on Power System Technology (IEEE), 2763–2768. doi:10.1109/POWERCON.2014.6993726

Zhang, X., Zhang, T., Xue, X., Si, Y., Zhang, X., and Mei, S. (2020). A Comparative Thermodynamic Analysis of Kalina and Organic Rankine Cycles for Hot Dry Rock: a prospect Study in the Gonghe Basin. *Front. Energ.* 14 (4), 889–900. doi:10.1007/s11708-020-0704-1

Zhang, Y.-J., Li, Z.-W., Guo, L.-L., Gao, P., Jin, X.-P., and Xu, T.-F. (2014b). Electricity Generation from Enhanced Geothermal Systems by Oilfield Produced Water Circulating through Reservoir Stimulated by Staged Fracturing Technology for Horizontal wells: A Case Study in Xujiaweizi Area in Daqing Oilfield, China. *Energy* 78, 788–805. doi:10.1016/j.energy.2014.10.073

Zhang, Z., Chen, Y., Huang, S., and Zhang, X. (2017). IEEE, 1–5. doi:10.1109/PESGM.2017.8274181Credible Capacity Evaluation of a PV Plant with Energy Storages Governed by MDP Control StrategyIn 2017 IEEE Power & Energy Society General Meeting.

Conflict of Interest: The authors declare that the research was conducted in the absence of any commercial or financial relationships that could be construed as a potential conflict of interest.

Publisher's Note: All claims expressed in this article are solely those of the authors and do not necessarily represent those of their affiliated organizations, or those of the publisher, the editors and the reviewers. Any product that may be evaluated in this article, or claim that may be made by its manufacturer, is not guaranteed or endorsed by the publisher.

frontiers in Energy Research

ORIGINAL RESEARCH
published: 25 November 2021
doi: 10.3389/fenrg.2021.767610

Hosting Capacity Assessment in Distribution Networks Considering Wind–Photovoltaic–Load Temporal Characteristics

Nianchun Du[1], Fei Tang[1], Qingfen Liao[1], Chenxu Wang[2], Xin Gao[1], Jiarui Xie[1], Jian Zhang[3] and Runzhao Lu[3]*

[1]School of Electrical Engineering and Automation, Wuhan University, Wuhan, China, [2]Electric Power Research Institute, State Grid Zhejiang Electric Power Co., Ltd., Hangzhou, China, [3]China Electric Power Research Institute, Beijing, China

Under the background of clean and low-carbon energy transformation, renewable distributed generation is connected to the distribution system on a large scale. This study proposes a probabilistic assessment method of hosting capacity considering wind–photovoltaic–load temporal characteristics in distribution networks. First, based on time series of wind, photovoltaic, and load demands, a discretization–aggregation technique is introduced to generate and filter extreme combinations. The method can effectively reduce the scenarios that need to be evaluated. Then a holomorphic embedding method considering generation and load scaling directions is proposed. The holomorphic function of voltage about an embedding variable is established, and it is analytically expanded in the form of series. The hosting capacity restrained by the voltage violation problem is calculated quickly and accurately. Finally, the proposed stochastic framework is implemented to evaluate hosting capacity involving renewable energy types, penetration levels, and locations. The hosting capacity of single energy and hybrid wind–solar renewable energy systems is evaluated from the perspective of probability analysis. The results verify the outstanding performance of the hybrid wind–solar energy system in improving the hosting capacity.

Keywords: distributed renewable energy, hosting capacity, holomorphic embedding method, time series, voltage violation

OPEN ACCESS

Edited by:
Yahui Zhang,
Yanshan University, China

Reviewed by:
Lei Zhang,
China Three Gorges University, China
Yongxi Zhang,
Changsha University of Science and Technology, China
Guangzheng Yu,
Shanghai University of Electric Power, China

****Correspondence:***
Fei Tang
tangfei@whu.edu.cn

Specialty section:
This article was submitted to Smart Grids, a section of the journal Frontiers in Energy Research

Received: *31 August 2021*
Accepted: *11 October 2021*
Published: *25 November 2021*

Citation:
Du N, Tang F, Liao Q, Wang C, Gao X, Xie J, Zhang J and Lu R (2021) Hosting Capacity Assessment in Distribution Networks Considering Wind–Photovoltaic–Load Temporal Characteristics. Front. Energy Res. 9:767610. doi: 10.3389/fenrg.2021.767610

INTRODUCTION

In response to climatic deterioration and energy shortage, all countries are accelerating the process of new energy. Distributed renewable energy sources have become the mainstay to promote the development of new energy with the advantages of being clean, green, flexible, and efficient (IEA, 2019). Wind energy and solar energy are the most promising renewable energy sources. However, their access to the distribution network also brings uncertainty and intermittence. The booming development of distributed generation (DG) may lead to the violation of system operation constraints such as overvoltage (Ismael et al., 2019; Zhu et al., 2020), overloading of transformers and feeders (Shen et al., 2021), conductor thermal capacity (Zhang and Luo, 2018), and protection failure (Singh, 2017; Zobaa et al., 2020). In order to overcome the challenges of renewable energy source integration, it is of significant importance to evaluate the number of DGs that can be integrated into a given distribution network without violating the operating standards.

The concept of hosting capacity (HC) was first proposed by André Even in the context of distributed generation and improved by Bollen and Hassan (2011). The hosting capacity is defined as the maximum capacity of DGs that can be integrated into the distribution system, above which the performance of the system becomes unacceptable. Recently, many scholars have studied hosting capacity assessment in distribution networks. There are four main methods: the deterministic method, the stochastic method (Yang et al., 2019), the optimization-based method (Shen et al., 2017; Injeti and Thunuguntla, 2020), and the time series method (Abideen et al., 2020; Mulenga et al., 2020).

In earlier studies, the analysis methods were often used to calculate the HC at a specific DG access location by deriving the performance index of the system. In the study of Fan et al. (2017) and Li et al. (2021), the formula of voltage difference values at continuous buses of three-phase feeders is derived, and the maximum number of DGs at a specific bus is calculated. Ampofo et al. (2017) studied the impact of voltage rise and thermal loading on HC considering DG access to the end of feeders or the load center. HC is calculated in different scenarios by iteratively increasing the number/capacity of wind generation units and continuously calculating the power flow (PF) until one of the performance standards is violated (Papaioannou and Purvins, 2014; Gonzaga et al., 2019). It is evident that the deterministic method cannot consider the uncertainty of modern power systems, and its application range is limited.

When DGs with high uncertainty characteristics are connected to the distribution network, there are many unknown variables in the calculation of HC. Thus, the randomness of these variables needs to be considered; Monte Carlo simulation (MCS) is often used to generate different scenarios. Zio et al. (2015) proposed a probabilistic power flow method and simulated the variability of customer demand based on MCS but did not consider the variability of DG. The randomness of both DG access locations and load demand are considered (Kolenc et al., 2015; Shen and Raksincharoensak, 2021). In Al-Saffar et al. (2019), the probabilistic power flow is implemented under the scenarios with different photovoltaic (PV) penetration levels, and the HC of three real regions is determined, respectively. Mulenga et al. (2021) classify two types of uncertainties, namely, aleatory uncertainties and epistemic uncertainties. The HC is estimated by applying the transfer impedance matrix and the superposition principle to determine the voltage rise due to PV. In addition, using spatial and temporal uncertainties associated with PV, a new spatiotemporal probabilistic voltage sensitivity is proposed. It can calculate the probability distribution of voltage change at a specific bus, due to random change of PV power in the random position of the network (Munikoti et al., 2022).

The optimization-based method is also a common approach to determine the HC. The objective is to maximize the DG injection while constraints are met. In the study of Zou et al. (2016), Alturki et al. (2018), and Shen et al. (2020), based on deterministic optimization algorithms, the best access location is regarded as the main solution. But in fact, the inherent uncertainty of DG needs to be considered. Therefore, the trend is combining the stochastic method and the optimization-based method (Shen et al., 2021). A stochastic multi-objective optimization model was proposed in the study by Rabiee et al. (2017), which aims to maximize the HC for wind power and minimize the energy procurement costs, and then it is solved with the NSGA-II algorithm. Otherwise, the chance-constrained method was adopted, and the probabilistic power flow method was used to deal with the randomness problem (Sun et al., 2018; Wu et al., 2019). However, the optimization-based model is generally highly complex and non-linear, and for actual networks, the existing methods may not produce global optimal solutions.

Besides, in some studies (Khoshkbar-Sadigh et al., 2015; Fan et al., 2016; Shen and Raksincharoensak, 2021), the historical data of both demand and renewable production are used as the input, and it can provide a more realistic distribution network. Chen et al. (2018) considered temporal characteristics of wind power, PV, and load; the joint probability distribution method and the scene reduction technique were used to solve the DG capacity. Mulenga et al. (2021) studied the influence of time of day on the HC calculation results. However, the time series method considering time-varying renewables and demands are highly dependent on data, and a large amount of data enlarge the computing scale, which tends to be laborious or intractable. Some scholars study the security-constrained unit commitment (SCUC) (Yang et al., 2018; Liu et al., 2020; Yang et al., 2021). Yang et al., 2021 is a pioneer study for SCUC problems that proposes an expanded sequence-to-sequence (E-Seq2Seq)–based data-driven SCUC expert system. It can accommodate the mapping samples of SCUC and consider the various input factors that affect SCUC decision-making, possessing strong generality, high solution accuracy, and efficiency over traditional methods. To mitigate the excessive computational burden, Ochoa et al. (2010) proposed a processing technique for long-term time data, namely, the discretization–aggregation method. It can generate and screen out the reasonable combinations of renewables and demand to simplify data.

When excessive DG penetrates in the distribution network, the radial distribution system with the single power becomes a complex system with multiple power supplies. Then there are reverse power flows, which may lead to voltage rise (Mulenga et al., 2020; Shen et al., 2020; Wang et al., 2021). The studies have shown that the voltage rise is the main restriction considered in the research of HC (Torquato et al., 2018; Dong et al., 2019).

In this study, a stochastic framework of hosting capacity assessment is proposed considering the uncertainty of DG penetration levels, locations, and types, and extreme combinations are introduced to process wind–photovoltaic–load time series data. This effectively reduces the number of scenarios to be evaluated. Moreover, traditional methods of hosting capacity assessment are scenario-based and complex as they rely on the iterative PF algorithm. To avoid a large number of PF calculations, a novel holomorphic embedding method (HEM) based on the recursive algorithm is used to obtain the equivalent analytical formula of voltage (Trias. 2012). The HC corresponding to voltage violation can be directly solved without checking a large number of scenarios, which further significantly reduces the

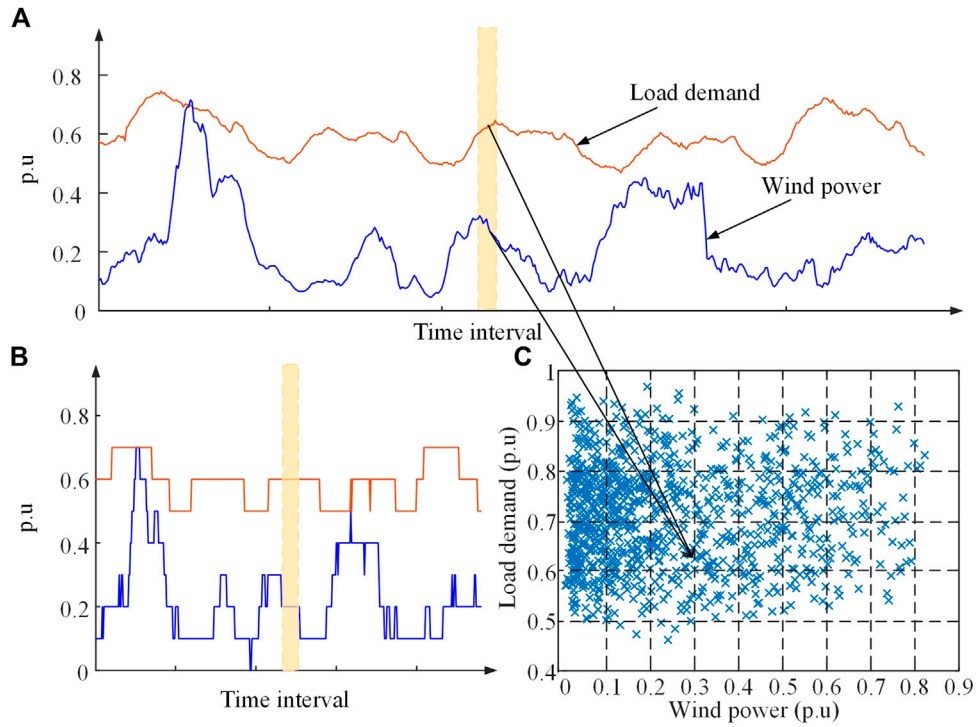

FIGURE 1 | Procedure of discretization and aggregation of time series data.

computational burden. In the simulation analysis, hosting capacity assessments of both single resource and hybrid cases are performed, and the results provide planners with a better understanding of the energy integration.

The rest of this article is organized as follows: *Processing of Renewables and Demand Data* discusses the processing technology of time series data of renewables and demand. *Holomorphic Embedding Method* introduces the holomorphic embedding method. Then the stochastic framework of the hosting capacity assessment is illustrated in *Framework for Hosting Capacity Assessment*. *Numerical Results* presents the results and discussions to evaluate the hosting capacity of single and hybrid cases on the IEEE 33-bus system. Finally, *Conclusion* summarizes the main conclusions.

PROCESSING OF RENEWABLES AND DEMAND DATA

Discretization–Aggregation Method

Due to the uncertainty and volatility of renewable generation and load, the temporal characteristics of both generation and load demand need to be considered in the hosting capacity assessment. However, long time series will bring a significant number of calculations. Therefore, the discretization–aggregation method is introduced to reduce the computational burden. The technology was first proposed by Ochoa et al. (2010), which only considers wind and load. Furthermore, if we consider the correlation between wind power, PV power, load demand, and time, each data point needs a multidimensional representation. The method has the potential to deal with the problems of multidimensionality.

The method mainly includes two steps: 1) in the discretization process, the historical data of renewables and demand are allocated into a series of bins covering the range between zero and the peak value; and 2) in the aggregation process, the bins of renewables and load demand are grouped into multiple combinations. To illustrate the approach, **Figure 1** presents the discretization–aggregation process with only two dimensions in the following example. **Figure 1A** shows a 5-day historical data sample of wind power and load with an interval of 15 min, and their values are normalized against respective peak values. **Figure 1B** shows the discrete time series. When the width of bins is set to 0.1 p.u, six load demand ranges (e.g., [0.4, 0.5], (0.5, 0.6], . . .) and nine generation ranges (e.g., [0, 0.1], (0.1, 0.2], . . .) are used. Then the time-varying data are allocated to a series of bins. **Figure 1C** presents the distribution with combinations of wind power and load. The combines of "similar" characteristics are aggregated into the same bin. For instance, the yellow block indicates the data where demand is 0.6 and wind is 0.2.

Extreme Combinations

The discretization–aggregation method allocates time series data into a finite number of combinations, which reduces the number of combinations to be evaluated, and retains the relevance between renewables and demand. Importantly, it does retain extreme characteristics. The "coincidence" between maximum

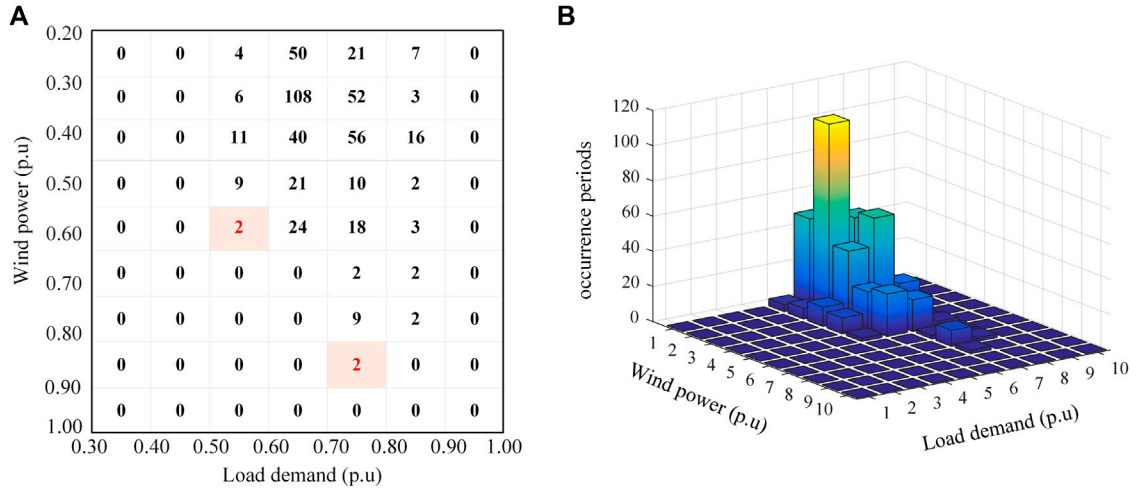

FIGURE 2 | (A) Occurrence periods for all combinations when the bin width is 0.1 p.u; **(B)** visualization of all wind–load aggregated combinations.

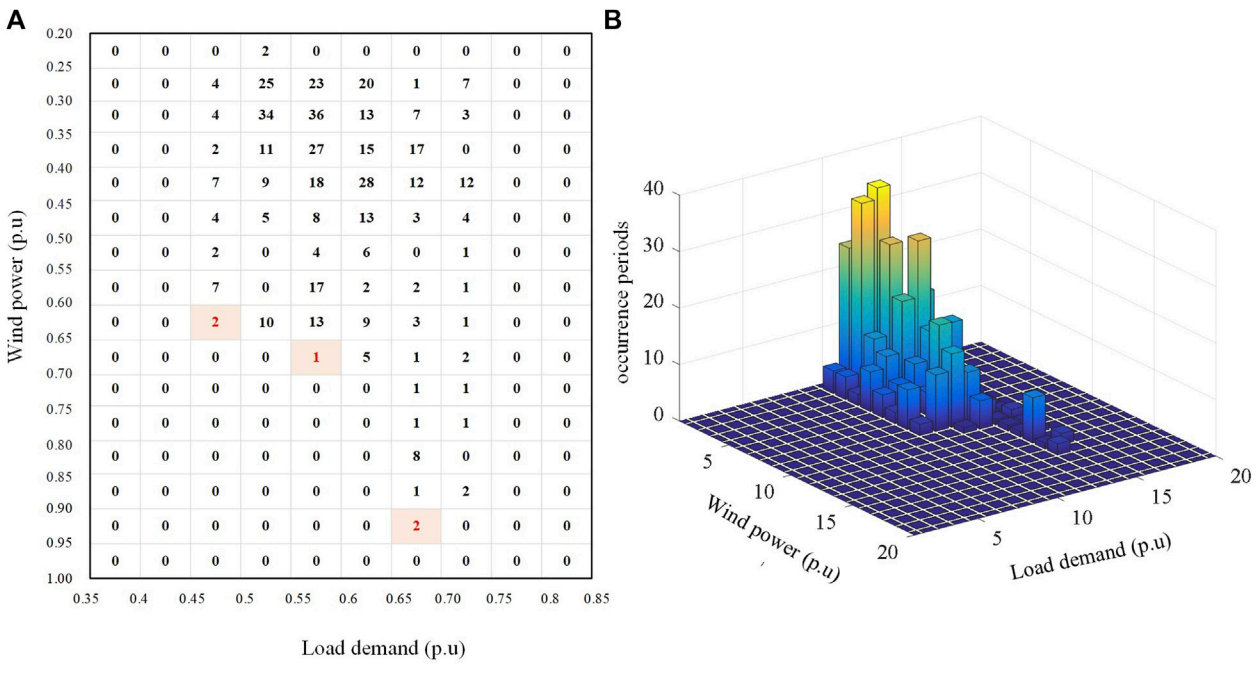

FIGURE 3 | (A) Occurrence periods for all combinations when the bin width is 0.05 p.u; **(B)** Visualization of all wind–load aggregated combinations.

generation and minimum demand is normally regarded as the extreme combination for voltage violation and the main constraint of the hosting capacity assessment.

The discretization–aggregation process goes through each possible combination and sums the occurrence periods, which captures the full range of generation and load. **Figure 2** presents all combinations of data above and their occurrence periods. The combinations labeled with red represent the extreme conditions of maximum power generation and minimum load demand. If the voltage constraint is not violated in these combinations, it is unlikely to be violated in other combinations.

It is obvious that different combinations will be obtained by selecting different widths. The smaller the width, the more detailed the bins to be evaluated. **Figure 3** shows the combinations of wind and load when the width is set to 0.05 p.u. The total number of combinations increases significantly, and the number of extreme combinations has only increased by one compared with the results in **Figure 2**. Therefore, the selection of bin width may affect the scale and accuracy of the

hosting capacity assessment. Moreover, when an additional PV power is added, the discretization–aggregation process remains unchanged, but the dimension is increased.

HOLOMORPHIC EMBEDDING METHOD

The holomorphic embedding method was applied to the PF problem by Dr. Antonio Trias for the first time (Trias, 2012), to avoid the non-convergence problem of the traditional iterative PF methods. In this study, the conventional HEM is improved considering the direction of generation and load change. The equivalent analytical formulations of voltage can be obtained by only one PF calculation. It can establish the dependence between the embedding parameter and the actual operation level.

Direction-of-Change Scaling Holomorphic Embedding Model

Consider an N-bus system, the power balance equation (PBE) can be expressed as follows:

$$\sum_{k=1}^{N} Y_{ik}\dot{V}_k = \frac{\dot{S}_i^*}{\dot{V}_i^*}, \tag{1}$$

where Y_{ik} is the (i, k) element of the bus admittance matrix, $\dot{S}_i$ and $\dot{V}_i$ are the complex power injection and voltage at bus i, respectively.

The non-holomorphic PBE is converted into holomorphic functions by embedding a complex parameter $\dot{s}$. Considering different types of buses, the improved holomorphic embedding formulas are given, where **Eq. 2** represents the voltage magnitude constraint for slack bus, **Eq. 3** represents the PBE for the PQ buses, **Eq. 4** represents the PBE for the PV buses, and **Eq. 5** represents the voltage magnitude constraint for the PV buses. The formulas allow the load at all buses and the real power generation at the PV buses to be scaled directionally.

$$\dot{V}_i(\dot{s}) = V_i^{sp}, i \in \mathbf{N}_{\text{slack}}, \tag{2}$$

$$\sum_{k=1}^{N} Y_{ik}\dot{V}_k(\dot{s}) = \frac{\dot{S}_{i0}^* + \dot{s}\Delta\dot{S}_i}{\dot{V}_i^*(\dot{s}^*)}, i \in \mathbf{N}_{\text{PQ}}, \tag{3}$$

$$\sum_{k=1}^{N} Y_{ik}\dot{V}_k(\dot{s}) = \frac{(P_{i0} + jQ_{Li0}) + \dot{s}(\Delta P_i + j\Delta Q_L) - jQ_{Gi}(\dot{s})}{\dot{V}_i^*(\dot{s}^*)}, i \in \mathbf{N}_{\text{PV}}, \tag{4}$$

$$\dot{V}_i(\dot{s})\dot{V}_i^*(\dot{s}^*) = \left|V_i^{sp}\right|^2, i \in \mathbf{N}_{\text{PV}}, \tag{5}$$

where P_{i0}, ΔSi, ΔP_{i}, ΔQ_{i} are given as follows:

$$P_{i0} = P_{Gi0} - P_{Li0}, \tag{6}$$

$$\Delta\dot{S}_i = k_{Li}\dot{S}_{i0}^*, \tag{7}$$

$$\Delta P_i = k_{Gi}P_{Gi0} - k_{Li}P_{Li0}, \tag{8}$$

$$\Delta Q_{Li} = k_{Li}Q_{Li0}, \tag{9}$$

where V_i^{sp} is the reference voltage amplitude; P_{Gi0} and Q_{Gi0} represent the active injection power and active load of bus i under the initial loading level, respectively; Q_{Li0} is the reactive load of bus i under the initial loading level; and k_{Gi} and k_{Li} are generation growth coefficient and load growth coefficient, respectively, which can represent the change direction of generation and load. $\mathbf{N}_{\text{slack}}$, $\mathbf{N}_{\text{PQ}}$, and $\mathbf{N}_{\text{PV}}$ represent the sets of slack bus, PQ buses, and PV buses, respectively.

Since $\dot{V}_i(\dot{s})$ and $Q_{Gi}(\dot{s})$ are holomorphic functions of the parameter $\dot{s}$, they can be expanded in the following Maclaurin series form:

$$\dot{V}_i(\dot{s}) = \sum_{n=0}^{\infty} \dot{V}_i[n](\dot{s})^n, \tag{10}$$

$$Q_{Gi}(\dot{s}) = \sum_{n=0}^{\infty} Q_{Gi}[n](\dot{s})^n, \tag{11}$$

where the voltage sequence coefficients $\dot{V}_i[n]$ are complex numbers, and the power sequence coefficient $Q_{gi}[n]$ are real numbers.

The Maclaurin series for $\dot{V}_i^*(\dot{s}^*)$ is given as follows:

$$\dot{V}_i^*(\dot{s}^*) = \sum_{n=0}^{\infty} \dot{V}_i^*[n](\dot{s})^n. \tag{12}$$

Additionally, let $W(s)$ represent the inverse of the voltage function $V(s)$, defined as follows:

$$\dot{W}(\dot{s}) = \frac{1}{\dot{V}(\dot{s})} = \dot{W}[0] + \dot{W}[1]\dot{s} + \cdots + \dot{W}[n]\dot{s}^n. \tag{13}$$

The relationship between $\dot{W}_i(\dot{s})$ and $\dot{V}_i(\dot{s})$ is shown as follows:

$$\dot{W}_i(\dot{s})\dot{V}_i(\dot{s}) = \left(\dot{W}_i[0] + \dot{W}_i[1]\dot{s} + \cdots + \dot{W}_i[n]\dot{s}^n\right)\bullet\left(\dot{V}_i[0] + \dot{V}_i[1]\dot{s} + \cdots + \dot{V}_i[n]\dot{s}^n\right) = 1. \tag{14}$$

The relationship between $\dot{W}_i[n]$ and $\dot{V}_i[n]$ is obtained as given in **Eq. 15** by equating the coefficients of the same order of s on both sides of **Eq. 14**.

$$\begin{cases} \dot{W}[0] = \dfrac{1}{\dot{V}[0]}, & n = 0\,(\text{a}) \\ \dot{W}[n] = -\dfrac{\sum_{\tau=0}^{n-1}\dot{W}[\tau]\dot{V}[n-\tau]}{\dot{V}[0]}, & n \geq 1\,(\text{b}) \end{cases}, \tag{15}$$

where **Eq. 15b** can also be formulated as follows:

$$\dot{V}[0]\dot{W}[n] + \dot{W}[0]\dot{V}[n] = -\sum_{\tau=1}^{n-1}\dot{W}[\tau]\dot{V}[n-\tau],\ n \geq 1. \tag{16}$$

By substituting **Eqs 10–13** into **Eqs 2–5**, we obtain the following:

$$\dot{V}_i[n] = 0\ \ n \geq 1,\ \ i \in \mathbf{N}_{\text{slack}}, \tag{17}$$

$$\sum_{k=1}^{N} Y_{ik}\dot{V}_k[n] - \dot{S}_i^*\dot{W}_i^*[n] = \Delta\dot{S}_i^*\dot{W}_i^*[n-1],\ \ i \in \mathbf{N}_{\text{PQ}}, \tag{18}$$

$$\sum_{k=1}^{N} Y_{ik}\dot{V}_k[n] - \left(P_{i0} + jQ_{Li0}\right)\dot{W}_i^*[n] + jQ_{Gi}[n]\dot{W}_i^*[0] + jQ_{Gi}[0]\dot{W}_i^*[n] = \left(\Delta P_i + j\Delta Q_{Li}\right)\dot{W}_i^*[n-1] - j\left(\sum_{\tau=1}^{n-1} Q_{Gi}[\tau]\dot{W}_i^*[n-\tau]\right), i \in \mathbf{N}_{\mathrm{PV}}, \tag{19}$$

$$\dot{V}_i[0]\dot{V}_i^*[n] + \dot{V}_i[n]\dot{V}_i^*[0] = -\sum_{\tau=1}^{n-1}\dot{V}_i[\tau]\dot{V}_i^*[n-\tau] \; n \geq 1, i \in \mathbf{N}_{\mathrm{PV}}. \tag{20}$$

Thus, we establish the recursion relationship from the aforementioned holomorphic embedding formulas to obtain the equations. Then $\dot{W}_i[n]$ and $\dot{V}_i[n]$ are divided into real parts and imaginary parts for calculation, respectively, and the voltage sequence is solved. Finally, the equivalent analytical expression of voltage can be obtained.

Reference State Calculation

To solve the system of equations above, the reference state at $s = 0$ is given as follows:

$$\dot{V}_i[0] = V_i^{sp}, i \in \mathbf{N}_{\mathrm{slack}}, \tag{22}$$

$$\sum_{k=1}^{N} Y_{ik}\dot{V}_k[0] = \frac{\dot{S}_{i0}^*}{\dot{V}_i^*[0]}, i \in \mathbf{N}_{\mathrm{PQ}}, \tag{23}$$

$$\sum_{k=1}^{N} Y_{ik}\dot{V}_k[0] = \frac{\left(P_{i0} + jQ_{Li0}\right) - jQ_{Gi}[0]}{\dot{V}_i^*[0]}, i \in \mathbf{N}_{\mathrm{PV}}, \tag{24}$$

$$\dot{V}[0] \cdot \dot{V}_i^*[0] = \left|V_i^{sp}\right|^2, i \in \mathbf{N}_{\mathrm{PV}}. \tag{25}$$

Notice that the meaning of the reference solution of the improved HEM is different from that of the conventional HEM (Rao et al., 2016). The reference solution of the conventional HEM represents the power system with no load and no generator, while the reference solution of the improved HEM represents the voltage and reactive power injections at the buses for the power system under the initial loading level. The solution process is as follows:

$\dot{V}_i[0]$ and $Q_{Gi}[0]$ are expressed as the holomorphic function, so a complex parameter $\dot{\sigma}$ is embedded in **Eqs 22–25**, and we obtain:

$$\dot{V}_{i\_0}(\dot{\sigma}) = 1 + \dot{\sigma}\left(V_i^{sp} - 1\right), i \in \mathbf{N}_{\mathrm{slack}}, \tag{26}$$

$$\sum_{k=1}^{N} Y_{ik}^{tr}\dot{V}_{k\_0}(\dot{\sigma}) = \frac{\dot{\sigma}\dot{S}_{i0}^*}{\dot{V}_{i\_0}^*(\dot{\sigma}^*)} - \dot{\sigma}Y_i^{sh}\dot{V}_{i\_0}(\dot{\sigma}), i \in \mathbf{N}_{\mathrm{PQ}}, \tag{27}$$

$$\sum_{k=1}^{N} Y_{ik}^{tr}\dot{V}_{k\_0}(\dot{\sigma}) = \frac{\dot{\sigma}\left(P_{i0} + jQ_{Li0}\right) - jQ_{Gi\_0}(\dot{\sigma})}{\dot{V}_{i\_0}^*(\dot{\sigma}^*)} - \dot{\sigma}Y_i^{sh}\dot{V}_{i\_0}(\dot{\sigma}), i \in \mathbf{N}_{\mathrm{PV}}, \tag{28}$$

$$\dot{V}_{i\_0}(\dot{\sigma})\dot{V}_{i\_0}^*(\dot{\sigma}^*) = 1 + \dot{\sigma}\left(\left|V_i^{sp}\right|^2 - 1\right), i \in \mathbf{N}_{\mathrm{PV}}, \tag{29}$$

where Y_i^{sh} corresponds to the shunt part of the admittance matrix, Y_{ik}^{tr} corresponds to the "non–shunt-branch" part of the admittance matrix, and $Y_{ik}^{tr} = Y_{ik} - Y_i^{sh}$.

To establish the recursive relationship of variables, a new variable δ_{ni} is defined as follows:

$$\delta_{ni} = \begin{cases} 1, & n = i \\ 0, & \text{else} \end{cases}. \tag{30}$$

For the slack bus, the power series coefficient expression is written as follows:

$$\dot{V}_{i\_0}^{re}[n] = \delta_{no} + \delta_{n1}\left(V_i^{sp} - 1\right), i \in \mathbf{N}_{\mathrm{slack}}. \tag{31}$$

The voltage power series coefficients of PQ bus and PV bus are solved, we can obtain the following equations:

$$\sum_{k=1}^{N} Y_{ik}^{tr}\dot{V}_{k\_0}[n] = -Y_i^{sh}\dot{V}_{i\_0}[n-1], i \in \mathbf{N}_{\mathrm{PQ}}, \tag{32}$$

$$\sum_{k=1}^{N} Y_{ik}^{tr}\dot{V}_k[n] + jQ_{Gi\_0}[0] = -j\left(\sum_{\tau=1}^{n-1} Q_{G\_i}[\tau]\dot{W}_{i\_0}^*[n-\tau]\right) - Y_i^{sh}\dot{V}_{i\_0}[n-1], i \in \mathbf{N}_{\mathrm{PV}}, \tag{33}$$

$$\dot{V}_{i\_0}^{re}[n] = \delta_{no} + \delta_{n1}\frac{\left(V_i^{sp}\right)^2 - 1}{2} - \frac{1}{2}\left(\sum_{\tau=1}^{n-1}\dot{V}_{i\_0}[\tau]\dot{V}_{i\_0}^*[n-\tau]\right), i \in \mathbf{N}_{\mathrm{PV}}, \tag{34}$$

where $\dot{V}_{i\_0}^{re}[n]$ is the real part of $\dot{V}_{i\_0}[0]$.

According to the recursive relationship of **Eqs 31–34**, let $\dot{\sigma} = 1$. $\dot{V}_i[0]$ and $Q_{Gi}[0]$ can be solved. Obviously, the process of solving the reference solution of the improved HEM is the same as that of the conventional HEM when the embedded variable is 1, which is actually the voltage solution of the traditional power flow equation (**Eq. (1)**). Therefore, the Newton–Raphson method can also be used to solve the PF at the initial loading level to obtain the reference solution.

Calculation Process

The process of using improved HEM to solve a PF problem and voltage violation is as follows:

1) The PBEs are embedded with the parameter $\dot{s}$, the voltage and the active power injections become the holomorphic function of $\dot{s}$, and the holomorphic embedding models are established.
2) Taking the direction of generation and load change into account, the growth coefficients kGi and kLi are defined, and then $\Delta\dot{S}_i$, ΔP_i, and ΔQ_i are calculated.
3) The function $\dot{V}_i(\dot{s})$ and $\dot{Q}_{gi}(\dot{s})$ are represented in Maclaurin series with coefficients to be solved.
4) Calculate the reference state $\dot{V}_i[0]$ and $Qg_i[0]$ when $\dot{s} = 0$.
5) Solve the recursive equations and calculate the coefficients of the series $\dot{V}_i[n]$ and $Qg_i[n]$.
6) Let $\dot{s} = 1$, the solution of PF is obtained under the initial loading level. Then judge whether the PF mismatch power error is less than the set tolerance, if so, continue the following step, otherwise return to step (4).
7) The voltage sequence coefficients and the voltage function $\dot{V}(\dot{s})$ can be obtained. Then solve the value of $\dot{s}$, which is only a real number when $\dot{V}(\dot{s}) = 1.05$ and s has a corresponding

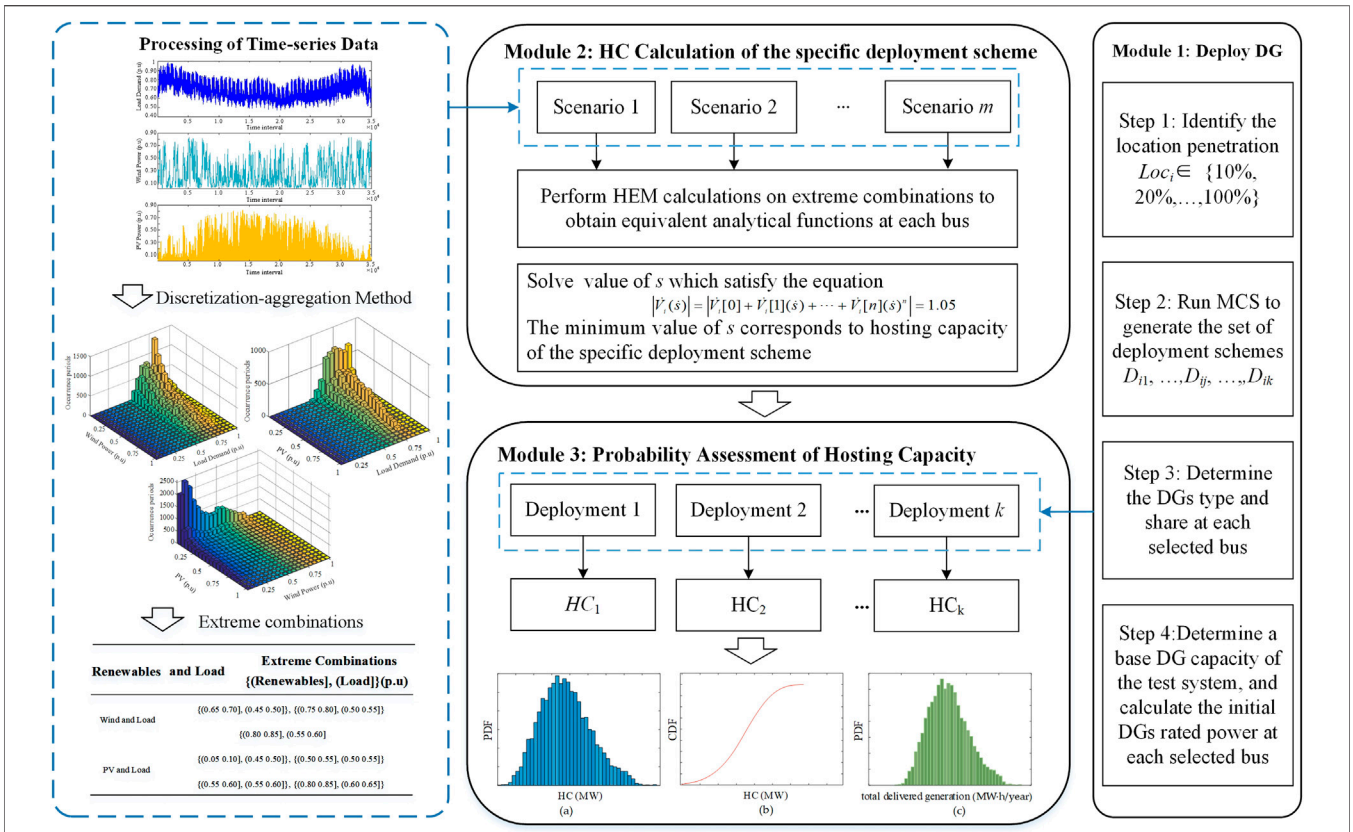

FIGURE 4 | Stochastic framework for the hosting capacity assessment.

relationship with the hosting capacity when the voltages exceed the restriction.

FRAMEWORK FOR HOSTING CAPACITY ASSESSMENT

Considering the temporal characteristics of renewable energy generation and load demand, this study proposes a framework for evaluating the hosing capacity in distribution networks with DGs. The framework consists of three modules, as shown in **Figure 4**.

1) Module 1: Deployment schemes of DGs.

This module generates multiple potential DG deployment schemes. The variables include DG location penetration, the locations of DGs, and the types of DGs. The steps are as follows:

Step 1: Identify the location penetration Loc_i. DG location penetration is defined as the ratio of the number of selected DG locations to the number of all potential locations. The location penetration is increased by a fixed step (e.g., 10%) from 0 to 100%. Let $Loc_i \in \{10\%, 20\%, \ldots, i \times 10\%, 100\%\}$, (i = 1, 2, . . ., 10).

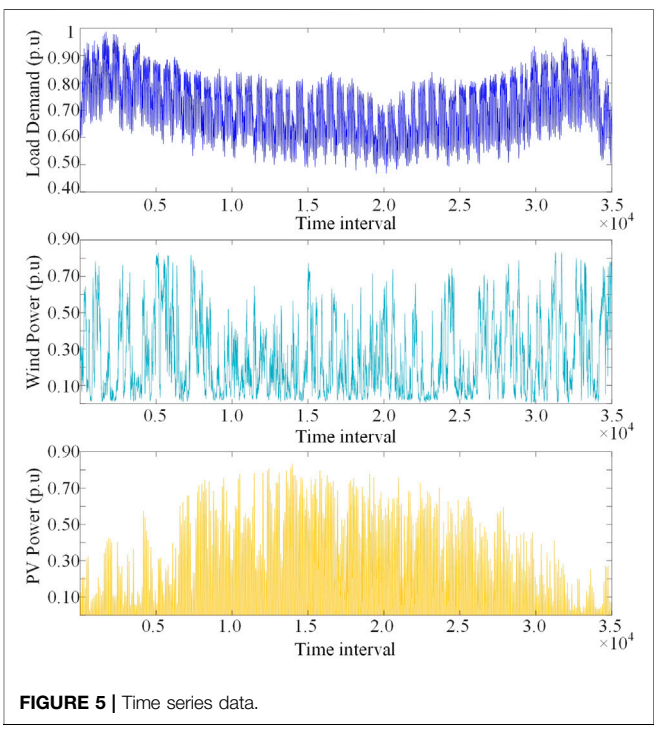

FIGURE 5 | Time series data.

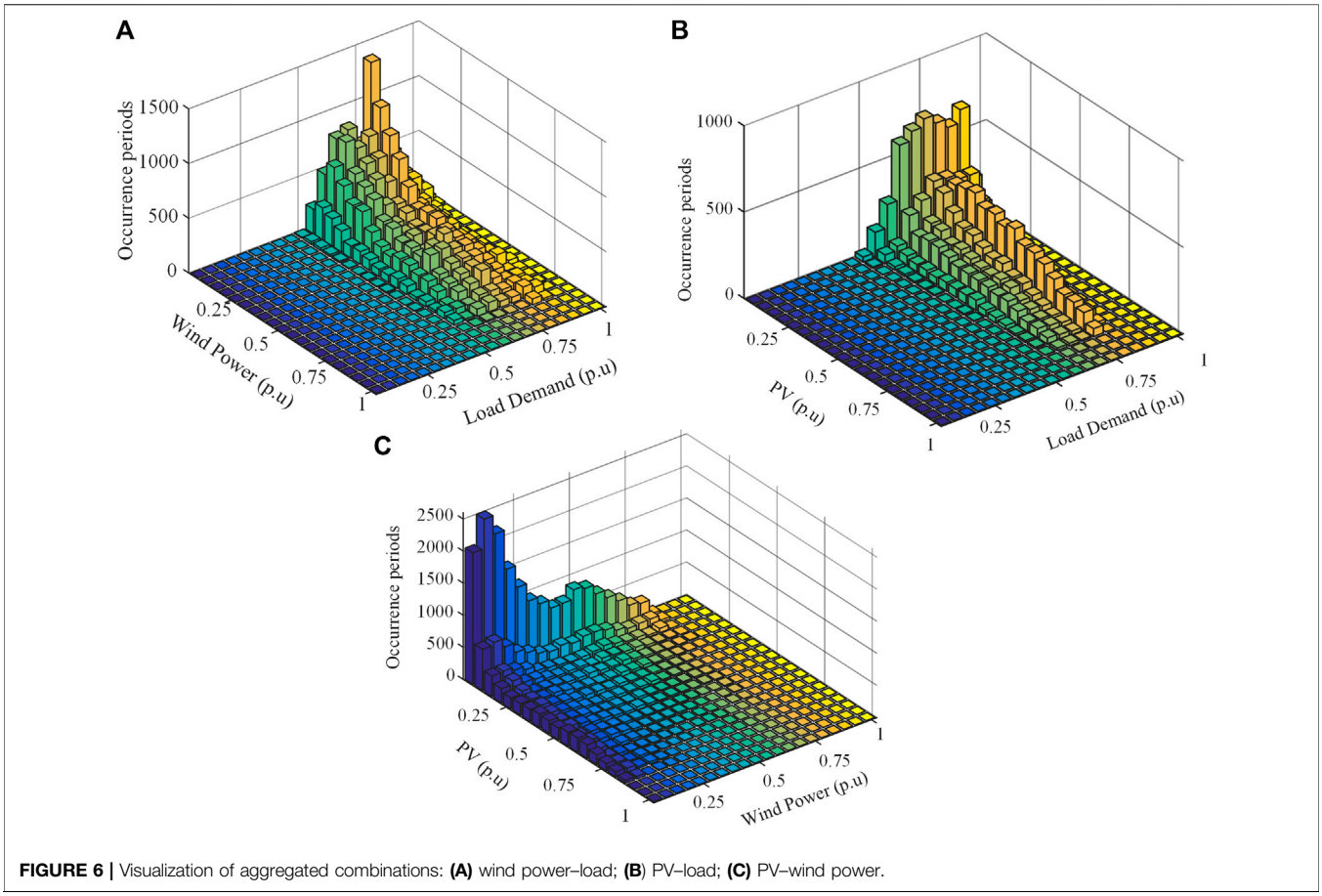

FIGURE 6 | Visualization of aggregated combinations: **(A)** wind power–load; **(B)** PV–load; **(C)** PV–wind power.

TABLE 1 | Results of extreme combinations.

Renewables and load	Extreme combinations {(renewables], (load]}(p.u)
Wind and load	{(0.65 0.70], (0.45 0.50]}, {(0.75 0.80], (0.50 0.55]} {(0.80 0.85], (0.55 0.60]
PV and load	{(0.05 0.10], (0.45 0.50]}, {(0.50 0.55], (0.50 0.55]} {(0.55 0.60], (0.55 0.60]}, {(0.80 0.85], (0.60 0.65]}

Step 2: Generate DG locations. For each location penetration level Loc_i, MCS is performed to generate k DG deployment schemes. Then the deployment scheme is represented as D_{ij} (j = 1, . . ., k).

Step 3: Set the types and shares of DGs. For example, 50% wind and 50% PV.

Step 4: Determine a base DG capacity (e.g., 1 MW). For each deployment scheme, the initial rated power of DGs is allocated based on the corresponding peak load.

2) Module 2: Calculation method of the hosting capacity. This module studies the calculation method of the hosting capacity based on the improved HEM, considering temporal characteristics of DGs and load demand. The steps are as follows:

Step 1: Process the historical data of wind, PV, and load. By the discretization–aggregation method, select the proper bin width and obtain m extreme combinations Sn (n = 1, . . ., m).

Step 2: For a specific deployment scheme Dij, perform HEM calculation on different extreme combinations, respectively. Then obtain the equivalent analytical function$V_i(\dot{s})$ of all buses on each combination.

Step 3: If none of the bus voltages exceed 1.05 p.u, let $|V_i(\dot{s})|$ = 1.05, and calculate the value of $\dot{s}$.

Step 4: Compare the minimum value of $\dot{s}$ on each extreme combination S_n, that is, $\dot{s}$ min corresponds to the maximum hosting capacity under deployment scheme D_{ij}.

3) Module 3: Analysis of hosting capacity results. Repeat steps in Module 2 to obtain the hosting capacity results for each deployment scheme D_{ij}, and obtain the hosting capacity results $\boldsymbol{HC}$ = {HC_1, . . . , HC_k}. Then perform statistical analysis for the obtained hosting capacity results. The steps are as follows:
   1) Histogram of HC is obtained based on the results $\boldsymbol{HC}$ = {HC_1, . . . , HC_k}, and the probability density function (PDF) based on Kernel density estimation is helpful to understand the probabilistic HC at a specific penetration level.

TABLE 2 | Hosting capacity results with different bin widths.

Bin width	Number of extreme combinations	HC results (MW)	Error (%)	Computational burden (s) (HEM)	Computational burden (s) (NR)
0.1	2	9.464	12.97	0.1107	0.6981
0.05	3	10.224	5.98	0.1362	0.8766
0.01	10	10.768	0.92	0.4082	1.5878
0.001	26	10.86	0.09	1.0365	2.7859

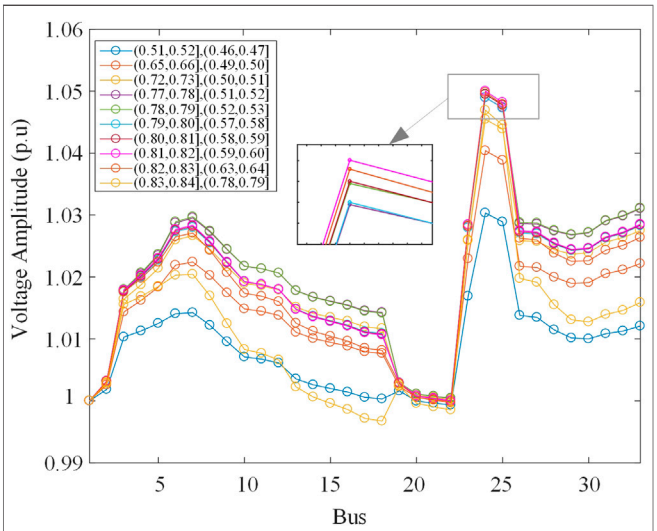

FIGURE 7 | Voltage violation scenarios.

2) Cumulative distribution function (CDF) curve of HC is helpful for planners to estimate the probability that the HC does not exceed a specific value.
3) Histogram of total delivered generation. The total delivered generation of DG is a valuable quantitative indicator of the use of renewable energy (Bawazir and Cetin, 2020). Therefore, some statistical data of total delivered generation in a year can provide the energy utilization of different types of renewable energy.

NUMERICAL RESULTS

The simulations are carried out on the IEEE 33-bus distribution system. The detailed parameters of the test system are available in Baran and Wu. (1989). Bus 1 is set as the slack bus and the voltage is set to 1.0 p.u. Other nodes are PQ buses. The reference voltage is 12.66 kV and the reference capacity is 10 MV A. The upper voltage limit of each bus is set to 1.05 p.u. Nodes 2–33 are candidate buses accessible to DG.

In this section, initially, the historical data of wind, PV, and load demand are processed by the discretization–aggregation method, and the extreme combinations are filtered. Then the proposed HEM is used to solve the voltage violation problem on extreme combinations. For a specific deployment scheme, the hosting capacity results with different bin widths are discussed. Finally, detailed hosting capacity assessments of both single resource and hybrid cases are performed.

Renewables and Demand Data

The simulations use the historical data of wind speed, solar irradiation, and load demand from a typical distribution system. The data of one year have a total of 35,040 data points with 15-min temporal resolution. The levels of load demand, wind, and PV output are normalized against peak values, as shown in **Figure 5**. It can be seen that load demand and PV have both obvious seasonal characteristics. The load in summer is relatively lower than that in winter, and the PV generation in summer is significantly higher than that in winter, but for wind power, the feature is not so obvious. It should be noted that different buses are close geographically in the test system, and the potential of renewable energy power generation is similar to a certain extent. So it is assumed that DGs follow the same time series curves.

The combinations of wind, PV, and load demand are obtained by the discretization–aggregation technology in *Introduction*. **Figure 6** shows the combinations and occurrence periods of renewable generation and load when the bin width is 0.05 p.u.

For the wind–load case, there are a total of 400 combinations, but only 175 contain non-zero occurrence periods. Similarly, for

TABLE 3 | Statistical results of HC with different penetration levels.

DG location penetration (%)	HC results of wind power (MW)		HC results of PV (MW)	
	Mean value	Standard deviation	Mean value	Standard deviation
30	7.086	3.987	7.381	4.203
50	7.671	1.925	7.979	1.974
70	7.775	0.794	8.104	0.860
90	7.843	0.247	8.160	0.276

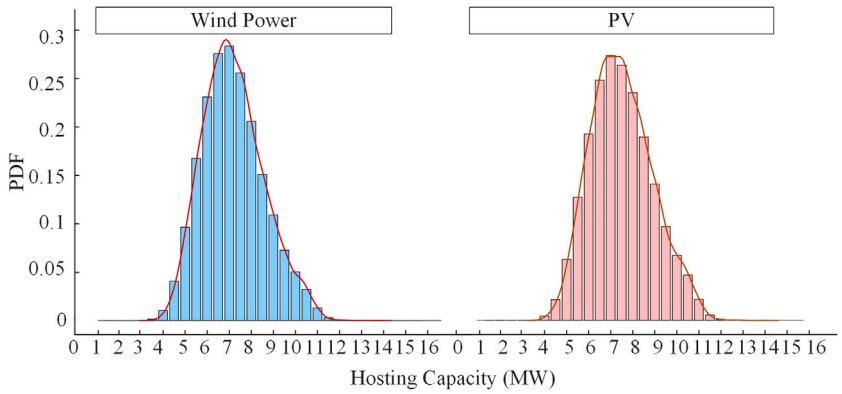

FIGURE 8 | PDF under 50% penetration level.

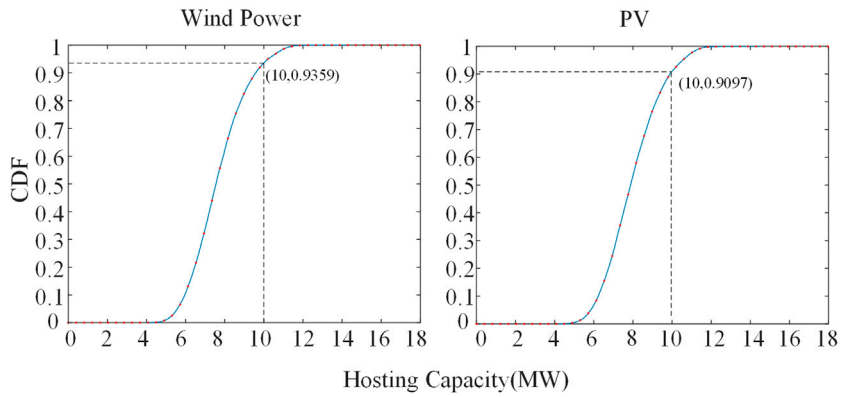

FIGURE 9 | CDF under 50% penetration level.

TABLE 4 | Statistical results of total delivered generation with different penetration levels.

DG location penetration (%)	Mean value of total delivered generation of wind power (MW·h/year)	Mean value of total delivered generation of PV (MW·h/year)
30	16,034.368	7,667.258
50	17,329.495	8,288.603
70	17,593.677	8,418.886
90	17,746.554	8,476.710

the PV–load case, the occurrence periods of only 133 combinations are non-zero. For renewable energy, wind power and PV are negatively correlated. PV generation mainly depends on solar radiation, and solar energy at night can be ignored. In contrast, the wind power during the day is usually less than that at night. Therefore, there is a certain complementarity between wind power and PV (Miglietta et al., 2017; Guozden et al., 2020).

The extreme cases of maximum generation and minimum demand are critical on the hosting capacity assessment restrained by voltage rise. The results of extreme combinations are given in **Table 1**. For the wind–load case and the PV–load case, only three and four extreme combinations need to be considered, respectively. For the wind–PV–load case, there are 2,567 combinations. It is difficult to show them in visual graphics, but 394 extreme combinations can be screened by the discretization–aggregation technique. Compared with the use of original historical data, the introduction of extreme combinations can significantly shrink the calculation scale of multidimensional problems.

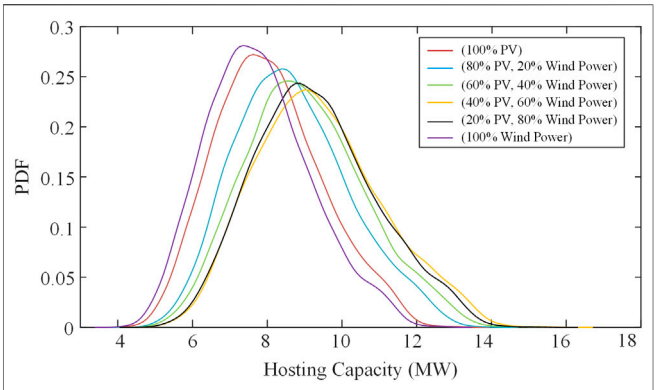

FIGURE 10 | PDF of the hosting capacity with different shares of wind and PV.

Hosting Capacity Assessment

Hosting Capacity Calculation of a DG-Specific Deployment Scheme

Taking a specific DG deployment scheme as an example, the influence of bin width is discussed. And the rapidity and effectiveness of the hosting capacity calculation method based on HEM are verified. Wind power is connected at Bus 2, 7, 24, and 33. Four widths are considered, namely, 0.1 p.u, 0.05 p.u, 0.01 p.u, and 0.001 p.u. The hosting capacity is calculated according to Module 2 in *Framework for Hosting Capacity Assessment*. For comparison, the Newton–Raphson power flow method is used to calculate the hosting capacity on each extreme combination, by increasing the total DG capacity until the upper voltage is violated. The hosting capacity result is 10.872 MW from all historical data, which is regarded as the accurate value. Using the calculation method based on HEM in this study, the results of extreme combinations and the hosting capacity with different bin widths are shown in **Table 2**.

The results in **Table 2** show that the method proposed in this study can greatly shorten the calculation time and improve the calculation efficiency. When the bin width is set to 0.1 p.u, the result is 12.97% smaller than the accurate value. Therefore, larger width may underestimate the hosting capacity and lead to conservative results. On the contrary, when the width is less than or equal to 0.01 p.u, the relative error is less than 1%. We can conclude that when the appropriate bin width is selected, the calculation scale can be simplified by using the proposed extreme combinations. More importantly, the hosting capacity calculation method based on HEM can further shorten the calculation time.

Figure 7 shows that the voltage violation occurs when the width is 0.01 p.u. Under the deployment scheme, when the extreme scenarios are {(0.81, 0.82], (0.59, 0.60]}, Bus 24 first exceeds the upper voltage limit.

Probability Assessment of the Hosting Capacity

In the test system, the number of DG candidate buses is 32. When the location penetration level is 50%, the total possible number of DG deployment schemes is more than 6×10^8. A large number of potential DG deployment schemes bring a significant computational burden. Therefore, MCS is used to simulate relatively few scenarios to obtain approximate results. In this context, we adopt the variance coefficient β (Prusty and Jena, 2017; Shen et al., 2020). $\beta \leq 0.5\%$ is set as the stopping criterion of MCS, and the results of MCS are considered to be accurate.

We performed the stochastic framework to access the hosting capacity of a single DG case in *Framework for Hosting Capacity Assessment*. The bin width is set as 0.01 p.u, and the location penetration level is increased from 10 to 100% by a fixed step of 10%. **Table 3** shows the statistical results of the wind system and PV system at location penetration levels of 30, 50, 70, and 90%.

The mean values of the hosting capacity increase with higher location penetration levels, while the standard deviations show the opposite trend. The reasons are as follows: first, with the increase of the location penetration level, DG locations increase and the capacity allocated to each location decreases, so the total hosting capacity of the system increases. Second, the higher penetration level reduces the uncertainty of DG locations, so the results of different deployment schemes are more concentrated.

Figure 8 shows the probability density distribution of the hosting capacity at 50% location penetration level. For the hosting capacity of the wind system, the minimum and maximum values are 3.995 and 14.224 MW, respectively. For the hosting capacity of the PV system, the results of the hosting capacity are 4.236 and 14.472 MW, respectively. The difference between extreme values is due to the location distribution of DGs.

Figure 9 shows the cumulative probability distribution of the hosting capacity, which can provide planners with the probability that the hosting capacity in distribution networks is lower than a specific value. For example, the probability of the hosting capacity, which is no more than 10 MW in the wind system, is 0.9359, while in the PV case, the result is 0.9097.

The total delivered generation can realistically reflect the energy utilization. Therefore, when planning the distributed system, not only the maximum hosting capacity of the system but also the total delivered generation is needed to be considered. The comparison of the mean values of total delivered generation of the wind system and the PV system is presented in **Table 4**. Although the hosting capacity of the PV system is slightly higher than that of the wind system, the total delivered generation of PV

TABLE 5 | Mean values of the hosting capacity and delivered generation.

	Mean value of the hybrid system	Mean value of wind power	Mean value of PV
HC results (MW)	9.396	7.040	2.356
Total delivered generation (MW·h/year)	17,999.262	15,617.893	2,381.369

is less than 50% of that of the wind system. The main reason for the difference is the higher correlation and capacity coefficient between wind resource and load demand.

There is complementarity between wind energy and photovoltaic energy, and their joint action may affect the hosting capacity of the system. However, the existing literature rarely discusses the hosting capacity of hybrid wind–PV energy systems. The proposed stochastic framework is used to analyze whether hybrid renewable energy helps improve the available hosting capacity.

A variety of deployment schemes are generated by MCS. **Figure 10** shows the probability distribution of HC results obtained with different shares of wind and PV at the 50% penetration level. It can be seen that the PDF curve of the single energy power generation hosting capacity is on the left side of the PDF curve of the hybrid energy hosting capacity. With the increase of wind power share, the PDF curve of the hosting capacity moves to the right until the share of wind power generation reaches 75%, and then the PDF curve of the hosting capacity moves to the left. It indicates that hybrid power generation has advantages in improving the level of the hosting capacity.

According to the results, when the wind power share reaches 75%, the hosting capacity of the hybrid wind–PV system reaches the maximum. **Table 5** shows the mean values of hosting capacity and delivered generation. The mean value of the total hosting capacity is 9.396 MW, while the mean values of wind and PV hosting capacity are 7.040 and 2.356 MW, respectively. Compared with the results of the single wind case and PV case, the hosting capacity increases by about 1.22 times and 1.18 times, respectively. Meanwhile, the mean value of total annual delivered generation is 17,999.262 MWh, of which wind power generation accounts for about 87% and PV accounts for about 13%. Compared with the single wind case and PV case, the total delivered generation increases by about 1.04 times and 2.17 times, respectively.

Wind power plays a leading role in hybrid wind–PV systems. PV accounts for a relatively small proportion, but as a supplement to energy, it is also essential to increase the total hosting capacity and total delivered generation. The results show that the complementarity between wind power and PV is conducive to distribution networks to accommodate more distributed renewable resources. It can leverage more renewable generation capacity to be utilized, thereby promoting higher energy export.

CONCLUSION

Due to the inherent uncertainty of renewable energy resources, the hosting capacity in distributed networks is not an immutable value. Meanwhile, it is important to consider the uncertainties of penetration levels, locations of DGs, and shares of wind and PV. Thus, HC needs to be expressed in some statistical ways. In this study, based on the wind–photovoltaic–load temporal characteristic, a stochastic framework for the hosting capacity is proposed. The main conclusions are as follows:

1) The uncertainty of wind power, PV, and load demand is considered through time series data. The discretization–aggregation method is introduced to process time series data and generate extreme combinations. It reduces the number of scenarios to be evaluated and significantly mitigates computational complexity.
2) The holomorphic embedding model is proposed considering the direction of generation and load change. The equivalent analytical formula of voltage establishes the corresponding relationship between the actual operation level and the embedding parameter. The improved HEM can improve the efficiency of the hosting capacity assessment.
3) Hosting capacity of the wind system, PV system, and hybrid wind–PV system is studied from a probabilistic view. Compared with the single resource case, the hybrid case has the advantage in power generation. Due to the complementarity between wind power and PV, the hybrid wind–PV system has the potential to increase the hosting capacity and energy production in distributed networks. The performance in promoting energy integration and improving utilization varies according to different shares of wind and PV.

From the development trend of the low-carbon goal, a large amount of distributed renewable energy will inevitably lead to more significant changes in distribution networks. This study proposes a method to quantify the hosting capacity in distribution networks with DGs based on the holomorphic embedding method. It offers assistance in understanding the level of renewable energy generation, making better use of the available renewable resources, and promoting the application of distributed hybrid power generation in the power grid. Furthermore, we will combine the optimization algorithm to plan the optimal access scheme of distributed generation with the method proposed in this study.

DATA AVAILABILITY STATEMENT

The original contributions presented in the study are included in the article/Supplementary Material, further inquiries can be directed to the corresponding author.

AUTHOR CONTRIBUTIONS

ND was responsible for methodology, formal analysis, validation, and editing of the manuscript. FT and QL were responsible for review and supervision. CW contributed to the conception and design of the study. XG and JX wrote sections of the manuscript. JZ and RL were responsible for part of data curation and project administration. All authors contributed, read, and approved the submitted version.

FUNDING

This work was supported by the Science and Technology Project of the State Grid Corporation of China (Research on the scale and the promotion of the hosting capacity of electronics power supply in power grids (5100-202116005A-0-0-00)).

REFERENCES

Al-Saffar, M., Zhang, S., Nassif, A., and Musilek, P. (2019). "Assessment of Photovoltaic Hosting Capacity of Existing Distribution Circuits," in Proceeding f the 2019 IEEE Canadian Conference of Electrical and Computer Engineering (CCECE), Edmonton, AB, Canada, May 2019 (IEEE), 1–4. doi:10.1109/CCECE.2019.8861957

Alturki, M., Khodaei, A., Paaso, A., and Bahramirad, S. (2018). Optimization-based Distribution Grid Hosting Capacity Calculations. *Appl. Energ.* 219, 350–360. doi:10.1016/j.apenergy.2017.10.127

Ampofo, D. O., Otchere, I. K., and Frimpong, E. A. (2017). "An Investigative Study on Penetration Limits of Distributed Generation on Distribution Networks," in Proceeding f the 2017 IEEE PES PowerAfrica, Accra, Ghana, June 2017 (IEEE), 573–576. doi:10.1109/PowerAfrica.2017.7991289

Baran, M. E., and Wu, F. F. (1989). Network Reconfiguration in Distribution Systems for Loss Reduction and Load Balancing. *IEEE Trans. Power Deliv.* 4, 1401–1407. doi:10.1109/61.25627

Bawazir, R. O., and Cetin, N. S. (2020). Comprehensive Overview of Optimizing PV-DG Allocation in Power System and Solar Energy Resource Potential Assessments. *Energ. Rep.* 6, 173–208. doi:10.1016/j.egyr.2019.12.010

Bollen, M., and Hassan, F. (2011). *Integration of Distributed Generation in the Power System*. Hoboken, USA: Wiley- IEEE Press. doi:10.1002/9781118029039

Chen, B., Bi, W., Li, X., and Li, C. (2018). Capacity Planning Strategies for Distributed Generation Considering Wind-Photovoltaic-Load Joint Time Sequential. *scenarios Power Syst. Technol.* 42, 755–761. doi:10.13335/j.1000-3673.pst.2017.1304

Dong, Y., Wang, S., and Yan, B. (2019). Review on Evaluation Methods and Improvement Techniques of DG Hosting Capacity in Distribution Network. *Power Syst. Technol.* 43, 2258–2266. doi:10.13335/j.1000-3673.pst.2019.0428

Fan, S., Li, C., Wei, Z., Pu, T., and Liu, X. (2017). Method to Determine the Maximum Generation Capacity of Distribution Generation in Low-voltage Distribution Feeders. *J. Eng.* 2017, 944–948. doi:10.1049/joe.2017.0470

Fan, S., Pu, T., Li, L., Yu, T., Yang, Z., and Gao, B. (2016). "Evaluation of Impact of Integrated Distributed Generation on Distribution Network Based on Time-Series Analysis," in Procedding of the 2016 China International Conference on Electricity Distribution (CICED), Xi'an, China, Aug. 2016 (IEEE), 1–5. doi:10.1109/CICED.2016.7576171

Gonzaga, R. M., Massigan, J. A. D., and London, J. B. A. (2019). "Analysis of the Hosting Capacity of a Real Distribution Feeder with Wind Generation," in Proceeding f the 2019 ISGT Latin America, Gramado, Brazil, Sept. 2019 (IEEE), 1–5. doi:10.1109/ISGT-LA.2019.8895318

Guozden, T., Carbajal, J. P., Bianchi, E., and Solarte, A. (2020). Optimized Balance between Electricity Load and Wind-Solar Energy Production. *Front. Energ. Res.* 8, 16. doi:10.3389/fenrg.2020.00016

IEA (2019). *Status of Power System Transformation*. https://www.iea.org/reports/status-of-power-system-transformation-2019 (Accessed August 24, 2021).]

Injeti, S. K., and Thunuguntla, V. K. (2020). Optimal Integration of DGs into Radial Distribution Network in the Presence of Plug-In Electric Vehicles to Minimize Daily Active Power Losses and to Improve the Voltage Profile of the System Using Bio-Inspired Optimization Algorithms. *Prot. Control. Mod. Power Syst.* 5, 3. doi:10.1186/s41601-019-0149-x

Ismael, S. M., Abdel Aleem, S. H. E., Abdelaziz, A. Y., and Zobaa, A. F. (2019). State-of-the-art of Hosting Capacity in Modern Power Systems with Distributed Generation. *Renew. Energ.* 130, 1002–1020. doi:10.1016/j.renene.2018.07.008

Khoshkbar-Sadigh, A., and Smedley, K. M. (2015). "The Necessity of Time-Series Simulation for Investigation of Large-Scale Solar Energy Penetration," in Procedding of the 2015 IEEE Power & Energy Society Innovative Smart Grid Technologies Conference (ISGT), Washington, DC, USA, Feb. 2015 (IEEE), 1–5. doi:10.1109/ISGT.2015.7131803

Kolenc, M., Papič, I., and Blažič, B. (2015). Assessment of Maximum Distributed Generation Penetration Levels in Low Voltage Networks Using a Probabilistic Approach. *Int. J. Electr. Power Energ. Syst.* 64, 505–515. doi:10.1016/j.ijepes.2014.07.063

Li, Z., Jiang, W., Abu-Siada, A., Li, Z., Xu, Y., and Liu, S. (2021). Research on a Composite Voltage and Current Measurement Device for HVDC Networks. *IEEE Trans. Ind. Electron.* 68, 8930–8941. doi:10.1109/TIE.2020.3013772

Liu, Y., Yang, N., Dong, B., Wu, L., Yan, J., Shen, X., et al. (2020). Multi-Lateral Participants Decision-Making: A Distribution System Planning Approach with Incomplete Information Game. *IEEE Access* 8, 88933–88950. doi:10.1109/ACCESS.2020.2991181

Miglietta, M. M., Huld, T., and Monforti-Ferrario, F. (2017). Local Complementarity of Wind and Solar Energy Resources over Europe: an Assessment Study from a Meteorological Perspective. *J. Appl. Meteorol. Climatol.* 56, 217–234. doi:10.1175/JAMC-D-16-0031.1

Mulenga, E., Bollen, M. H. J., and Etherden, N. (2020). A Review of Hosting Capacity Quantification Methods for Photovoltaics in Low-Voltage Distribution Grids. *Int. J. Electr. Power Energ. Syst.* 115, 105445. doi:10.1016/j.ijepes.2019.105445

Mulenga, E., Bollen, M. H. J., and Etherden, N. (2021b). Distribution Networks Measured Background Voltage Variations, Probability Distributions Characterization and Solar Pv Hosting Capacity Estimations. *Electric Power Syst. Res.* 192, 106979. doi:10.1016/j.epsr.2020.106979

Mulenga, E., Bollen, M. H. J., and Etherden, N. (2021a). Solar Pv Stochastic Hosting Capacity in Distribution Networks Considering Aleatory and Epistemic Uncertainties. *Int. J. Electr. Power Energ. Syst.* 130, 106928. doi:10.1016/j.ijepes.2021.106928

Munikoti, S., Abujubbeh, M., Jhala, K., and Natarajan, B. (2022). A Novel Framework for Hosting Capacity Analysis with Spatio-Temporal Probabilistic Voltage Sensitivity Analysis. *Int. J. Electr. Power Energ. Syst.* 134, 107426. doi:10.1016/j.ijepes.2021.107426

Nan, Y., Di, Y., Zheng, Z., Jiazhan, C., Daojun, C., and Xiaoming, W. (2018). Research on Modelling and Solution of Stochastic SCUC under AC Power Flow Constraints. *IET Generation, Transm. Distribution* 12, 3618–3625. doi:10.1049/iet-gtd.2017.1845

Ochoa, L. F., Dent, C. J., and Harrison, G. P. (2010). Distribution Network Capacity Assessment: Variable DG and Active Networks. *IEEE Trans. Power Syst.* 25, 87–95. doi:10.1109/TPWRS.2009.2031223

Papaioannou, I. T., and Purvins, A. (2014). A Methodology to Calculate Maximum Generation Capacity in Low Voltage Distribution Feeders. *Int. J. Electr. Power Energ. Syst.* 57, 141–147. doi:10.1016/j.ijepes.2013.11.04710.1016/j.ijepes.2013.11.047

Prusty, B. R., and Jena, D. (2017). A Critical Review on Probabilistic Load Flow Studies in Uncertainty Constrained Power Systems with Photovoltaic Generation and a New Approach. *Renew. Sustain. Energ. Rev.* 69, 1286–1302. doi:10.1016/j.rser.2016.12.044

Rabiee, A., and Mohseni-Bonab, S. M. (2017). Maximizing Hosting Capacity of Renewable Energy Sources in Distribution Networks: A Multi-Objective and Scenario-Based Approach. *Energy* 120, 417–430. doi:10.1016/j.energy.2016.11.095

Rao, S., Feng, Y., Tylavsky, D. J., and Subramanian, M. K. (2016). The Holomorphic Embedding Method_newline Applied to the Power-Flow Problem. *IEEE Trans. Power Syst.* 31, 3816–3828. doi:10.1109/TPWRS.2015.2503423

Shen, X., Ouyang, T., Khajorntraidet, C., Li, Y., Li, S., and Zhuang, J. (2021a). "Mixture Density Networks-Based Knock Simulator," in Proceeding of the IEEE/ASME Trans. Mechatron., February 2021 (Canada: IEEE), 1. doi:10.1109/TMECH.2021.3059775

Shen, X., Ouyang, T., Yang, N., and Zhuang, J. (2021b). Sample-based Neural Approximation Approach for Probabilistic Constrained Programs. *IEEE Trans. Neural Netw. Learn. Syst.*, 1–8. doi:10.1109/TNNLS.2021.3102323

Shen, X., and Raksincharoensak, P. (2021). "Pedestrian-Aware Statistical Risk Assessment," in Proceeding f the IEEE Trans. Intell. Transport. Syst., June 2021 (Canada: IEEE), 1–21. doi:10.1109/TITS.2021.3074522

Shen, X., and Raksincharoensak, P. (2021). Statistical Models of Near-Accident Event and Pedestrian Behavior at Non-signalized Intersections. *J. Appl. Stat.*, 1–21. doi:10.1080/02664763.2021.1962263

Shen, X., Zhang, X., Ouyang, T., Li, Y., and Raksincharoensak, P. (2020a). Cooperative Comfortable-Driving at Signalized Intersections for Connected and Automated Vehicles. *IEEE Robot. Autom. Lett.* 5 (4), 6247–6254. doi:10.1109/LRA.2020.3014010

Shen, X., Zhang, Y., Sata, K., and Shen, T. (2020b). Gaussian Mixture Model Clustering-Based Knock Threshold Learning in Automotive Engines. *Ieee/asme Trans. Mechatron.* 25 (6), 2981–2991. doi:10.1109/TMECH.2020.3000732

Shen, X., Zhang, Y., Shen, T., and Khajorntraidet, C. (2017). Spark advance Self-Optimization with Knock Probability Threshold for Lean-Burn Operation Mode of SI Engine. *Energy* 122, 1–10. doi:10.1016/j.energy.2017.01.065

Singh, M. (2017). Protection Coordination in Distribution Systems with and without Distributed Energy Resources- a Review. *Prot. Control. Mod. Power Syst.* 2, 27. doi:10.1186/s41601-017-0061-1

Sun, L., Zhao, M., and Wang, N., (2018). Research of Permitted Capacity of Distributed Photovoltaic Generation Based on Voltage Deviation Chance Constrained. *Trans. China Electrotechnical Soc.* 33, 1560–1569. doi:10.19595/j.cnki.1000-6753.tces.170185

Torquato, R., Salles, D., Oriente Pereira, C., Meira, P. C. M., and Freitas, W. (2018). A Comprehensive Assessment of PV Hosting Capacity on Low-Voltage Distribution Systems. *IEEE Trans. Power Deliv.* 33 (2), 1002–1012. doi:10.1109/TPWRD.2018.2798707

Trias, A. (2012). "The Holomorphic Embedding Load Flow Method," in Proceeding of the 2012 IEEE Power and Energy Society General Meeting, San Diego, CA, USA, July 2012 (IEEE), 1–8. doi:10.1109/PESGM.2012.6344759

Wang, J., Xu, Q., Su, H., and Fang, K. (2021). A Distributed and Robust Optimal Scheduling Model for an Active Distribution Network with Load Aggregators. *Front. Energ. Res.* 9, 646869. doi:10.3389/fenrg.2021.646869

Wu, H., Huang, R., Wang, Y., and Yuan, Y. (2019). "Chance-Constrained DG Hosting Capacity Assessment with Spatially Correlated Wind Speed," in Procedding of 2019 IEEE Innovative Smart Grid Technologies-Asia (ISGT Asia), Chengdu, China, May 2019 (IEEE), 1546–1551. doi:10.1109/ISGT-Asia.2019.8881689

Yang, N., Huang, Y., Hou, D., Liu, S., Ye, D., Dong, B., et al. (2019). Adaptive Nonparametric Kernel Density Estimation Approach for Joint Probability Density Function Modeling of Multiple Wind Farms. *Energies* 12, 1356. doi:10.3390/en12071356

Yang, N., Liu, S., Deng, Y., and Xing, C. (2021a). An Improved Robust SCUC Approach Considering Multiple Uncertainty and Correlation. *IEEJ Trans. Elec Electron. Eng.* 16, 21–34. doi:10.1002/tee.23265

Yang, N., Yang, C., Wu, L., Shen, X., Jia, J., Li, Z., Chen, D., Zhu, B., and Liu, S. (2021b). "Intelligent Data-Driven Decision-Making Method for Dynamic Multi-Sequence: An E-Seq2Seq Based SCUC Expert System," in IEEE Transactions on Industrial Informatics., August 2021 (Canada: IEEE), 1. doi:10.1109/TII.2021.3107406

Zain ul Abideen, M., Ellabban, O., and Al-Fagih, L. (2020). A Review of the Tools and Methods for Distribution Networks' Hosting Capacity Calculation. *Energies* 13, 2758. doi:10.3390/en13112758

Zhang, L., and Luo, Y. (2018). Combined Heat and Power Scheduling: Utilizing Building-Level thermal Inertia for Short-Term thermal Energy Storage in District Heat System. *IEEJ Trans. Elec Electron. Eng.* 13, 804–814. doi:10.1002/tee.22633

Zhu, B., Ding, F., and Vilathgamuwa, D. M. (2020). Coat Circuits for DC-DC Converters to Improve Voltage Conversion Ratio. *IEEE Trans. Power Electron.* 35 (4), 3679–3687. doi:10.1109/TPEL.2019.2934726

Zio, E., Delfanti, M., Giorgi, L., Olivieri, V., and Sansavini, G. (2015). Monte Carlo Simulation-Based Probabilistic Assessment of DG Penetration in Medium Voltage Distribution Networks. *Int. J. Electr. Power Energ. Syst.* 64, 852–860. doi:10.1016/j.ijepes.2014.08.004

Zobaa, A. F., Abdel Aleem, S. H. E., Ismael, S. M., and Paulo, F. R. (2020) . Hosting Capacity for Smart Power Grids. doi:10.1007/978-3-030-40029-3

Zou, H., Han, X., Liao, Q., and Liu, D. (2016). Penetration Capacity Calculation for Distributed Generation Considering Voltage Quality and Short Circuit Capacity. *Constraints Power Syst. Technol.* 40, 2273–2280. doi:10.13335/j.1000-3673.pst.2016.08.004

Conflict of Interest: Author CW is employed by Electric Power Research Institute, State Grid Zhejiang Electric Power Co., Ltd. Author JZ and author RL are employed by China Electric Power Research Institute.

The remaining authors declare that the research was conducted in the absence of any commercial or financial relationships that could be construed as a potential conflict of interest.

Publisher's Note: All claims expressed in this article are solely those of the authors and do not necessarily represent those of their affiliated organizations, or those of the publisher, the editors, and the reviewers. Any product that may be evaluated in this article, or claim that may be made by its manufacturer, is not guaranteed or endorsed by the publisher.

NOMENCLATURE

DG distributed generation

HC hosting capacity

HEM holomorphic embedding method

PDF probability density function

CDF cumulative distribution function

MCS Monte Carlo simulation

PV photovoltaic

frontiers in Energy Research

BRIEF RESEARCH REPORT
published: 01 December 2021
doi: 10.3389/fenrg.2021.805206

Green Building Energy Cost Optimization With Deep Belief Network and Firefly Algorithm

Yan Liao[1], *Yong Liu*[1]*, *Chaoyu Chen*[2] *and Lili Zhang*[3]

[1]Zunyi Vocational and Technical College, Zunyi, China, [2]College of Engineering, Zunyi Normal University, Zunyi, China, [3]College of Foreign Languages, Zunyi Normal University, Zunyi, China

In this research, we propose a multi-objective optimization framework to minimize the energy cost while maintain the indoor air quality. The proposed framework is consisted with two stages: predictive modeling stage and multi-objective optimization stage. In the first stage, artificial neural networks are applied to predict the energy utility in real-time. In the second stage, an optimization algorithm namely firefly algorithm is utilized to reduce the energy cost while maintaining the required IAQ conditions. Industrial data collected from a commercial building in central business district in Chengdu, China is utilized in this study. The results produced by the optimization framework show that this strategy reduces energy cost by optimizing operations within the HAVC system.

Keywords: green building, HVAC, feature selection, deep learning, multi-objective optimization

OPEN ACCESS

Edited by:
Yusen He,
Grinnell College, United States

Reviewed by:
Jiahao Deng,
DePaul University, United States
Ting Zeng,
Science and Technology for Development Research Center of Sichuan Province, China

***Correspondence:**
Yong Liu
mailto:yongliu_zvtc@outlook.com

Specialty section:
This article was submitted to Wind Energy, a section of the journal Frontiers in Energy Research

Received: *30 October 2021*
Accepted: *10 November 2021*
Published: *01 December 2021*

Citation:
Liao Y, Liu Y, Chen C and Zhang L (2021) Green Building Energy Cost Optimization With Deep Belief Network and Firefly Algorithm. Front. Energy Res. 9:805206. doi: 10.3389/fenrg.2021.805206

INTRODUCTION

The building industry is one of the largest sectors in creating jobs and has made great impact on the economy. Meanwhile, the buildings consume large amounts of natural resources such as water and electricity and its adverse environmental impacts are widely concerned. According to the World Business Council for Sustainable Development, buildings has contributed to more than 40% of total energy consumption (Mull, 1998) and 30% of greenhouse has emission (Payne et al., 2012). As a result, the high energy cost and environmental impacts from the buildings are becoming a major issue (Li et al., 2021a).

The new concept Green Building (GB) is conceived as an opportunity to reduce adverse impacts of buildings on the environment and energy cost. GB has been defined as a term that is interchangeable with buildings that has efficient energy utility and high sustainability. An increasing number of studies have been conducted on GB in the past decade and one major research direction is the reduction of the energy cost. Heating, ventilation, and air-conditioning (HVAC) systems are the major source of energy consumption in commercial buildings, and they account for more than 60% of annual total energy utility.

Previous literature has invested significant research efforts related to the modeling and optimization of the HVAC systems. They can be classified into two types of approaches: the physics-based approaches and the data-driven approaches. Physics-based approaches are generally developed over mathematical equations to depict the HVAC system modules and have been extensively utilized in HVAC related research. Sakulpipatsin et al. (2010) proposed extended physics-based models of HVAC systems and used TRNSYS software to perform the simulation for optimization studies. Zhang et al. (2013) introduced a novel physics-based model to study the HVAC energy consumption mechanism and a new model parameter namely entrants is included in the model. Teodosiu et al. (2003) developed an analytical model to

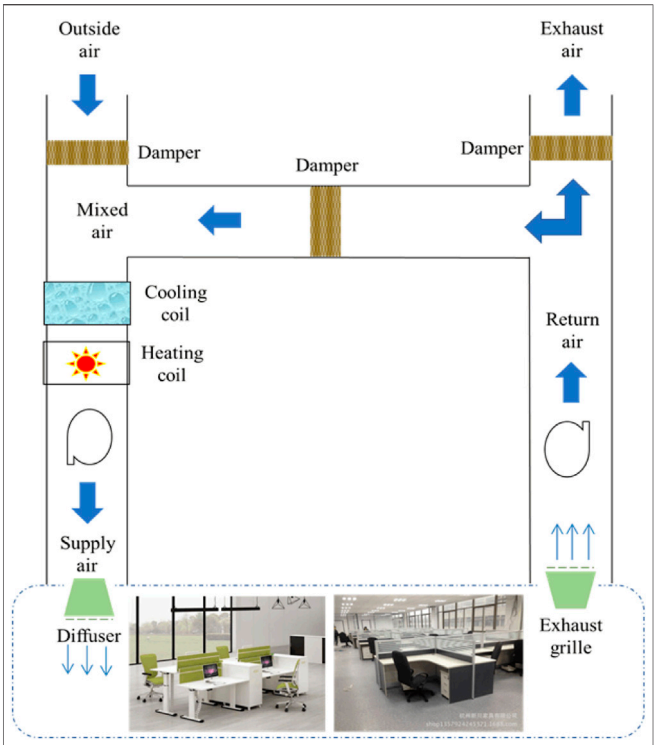

FIGURE 1 | Schematic diagram of an HVAC system.

evaluate thermal comfort by considering indoor air moisture and its transport by the airflow. Nassif et al. (2004) proposed a supervisory control strategy to optimize set points of controllers used in a multi-zone HVAC system.

The physics-based approaches are usually computationally complex and can be only applied under certain conditions. In comparison, data-driven approaches have reflected effectiveness in modeling complex, dynamic, and non-linear systems in many domains (He et al., 2017; He and Kusiak, 2017; Ouyang et al., 2017; Li et al., 2018; Ouyang et al., 2018; Li et al., 2020). Kusiak et al. (2011a) proposed a data-mining approach for the optimization of the HVAC units. Chang et al. (2009) constructed a Hopfield neural network to model the chilled water supply temperatures in chillers. Fong et al. (2006) used TRNSYS software to construct a data-driven model to optimize the settings of chilled water and supply air temperature. Lv et al. (2018) discussed various low carbon technologies and strategies to optimize the green building HVAC energy consumption. Kontes et al. (2013) proposed a stochastic optimization algorithm to maximize the utility of renewable energy proportion within the HVAC system. Lachheb et al. (2020) studied parametric models to investigate the impact of HVAC utility on the glazing size in various regions. Promising results from the data-driven approaches have demonstrated the effectiveness and robustness in modeling and optimizing the HVAC systems.

Inspired by the recent advent of deep learning algorithms, in this research, we would like to advocate a novel data-driven framework to modeling and optimizing the energy cost. In this modeling stage, the artificial neural network is constructed and trained on the HVAC energy consumption dataset to study the non-linear mapping between input features and energy cost. The algorithm with the top performance is selected as the benchmark for the following stage. In stage II, a firefly algorithm is utilized as the optimizer to reduce the total energy consumption while maintaining the air quality at an acceptable level.

HAVC SYSTEM AND PROBLEM FORMULATION

HVAC System

HAVC systems are widely installed in the commercial buildings located in the central business district (CBD). A schematic diagram of a typical HVAC system installed in the commercial buildings is illustrated in **Figure 1**. A typical HVAC system consists an air handling unit (AHU) and multiple thermal zones. For each thermal zone, a VAV (variable air volume) box is connected to the air handling unit to maintain the comfort temperature of the thermal zone.

The total energy utility by the HVAC system is consisted of the utility from the AHU and VAV. Three major resources including heat energy, fan energy, and pump energy, account for all energy consumptions in the AHU. For the VAV, the reheat load accounts for the maximum consumed energy (Kusiak et al., 2011b). The VAV box basically supplied the conditioned air for a specific thermal zone in order to satisfy the comfort temperature of the zone envelope. By tuning the dampers in the VAV box, the hot water flows through the coils adjusting to the actual requirements of the zone comfort.

Data Collection

The HVAC system discussed in this research as our case study is operated by a commercial building located in the central business district in Chengdu, China. This building has 33 floors and many big companies set their regional headquarter offices inside this building.

The dataset provided contains the hourly data of the HVAC system in the underlying building during the whole year of 2019. Multiple features that are relevant to our study is provided including total energy consumption, supply air temperature set point, supply air duct static pressure set point, system load, supply air humidity, barometric pressure, and outside air temperature. The in-detail description of the features utilized in this study has been summarized in **Table 1** as follows.

TABLE 1 | Introduction of the related features collected in the dataset.

Feature	Description	Unit
E_{Total}	Total energy consumption	KJ
x_{SAT}	Supply air temperature set point	°F
x_{SATPS}	Supply air static pressure set point	kPa
x_{Load}	System load	Discrete
x_{SAH}	Supply air humidity	%
x_{BP}	Barometric pressure	kPa
x_{OAT}	Outside air temperature	°F

Problem Formulation

In this research, the main goal is to develop a data-driven framework to minimize the total energy cost which ensuring the indoor air quality is maintained at a desirable level. The setting of the two controllable parameters namely the supply air temperature set point and the supply air static pressure set point play the essential role in impacting the total energy consumption of the HVAC system.

The total energy utility of an HVAC system comes from the AHU and VAV and it can be expressed in **eq. 1** as follows:

$$E_{Total} = E_{AHU} + E_{AVA} \tag{1}$$

Based on prior domain knowledge, the input features are associated with the AHU and VAV and we may re-formulate the problem as a regression problem as expressed in **eq. 2**:

$$E_{Total} = f(x_{SAT}, x_{SATPS}, x_{Load}, x_{SAH}, x_{BP}, x_{OAT}) \tag{2}$$

Among them, the x_{SAT} and the x_{SATPS} are controllable features and the rest are uncontrollable features.

In this research, the goal is to reduce the energy consumption while maintaining the indoor air quality. Hence, according to literature review (Kusial et al., 2011; Li et al., 2021b), we set the following constrains to our optimization model: the supply air temperature (x_{SAT}) should be between 50°F and 65°F; the supply air duct static pressure (x_{SATPS}) must be between 0.2 and 0.5 kPa; and the supply air humidity (x_{SAH}) should be controlled below 25%. Consequently, it can be formulated in the following non-linear optimization problem with the underlying constraints in **eq. 3** as follows:

$$\min f(x_{SAT}, x_{SATPS}, x_{Load}, x_{SAH}, x_{BP}, x_{OAT}) \tag{3}$$

subject to:

$$50 \le x_{SAT} \le 65$$
$$0.2 \le x_{SATPS} \le 0.5$$
$$x_{SAH} \le 25\%$$

METHODOLOGY

Deep Belief Network

The number of applications of deep learning architecture in regression, multi-class classification, collaborative filtering, and graphic learning tasks has experienced rapid growing in the recent decade (LeCun et al., 2015). In this section, a deep-learning based framework is presented to predict wind direction. The concept of deep learning originates from research on artificial neural networks and it alleviates the local optima problem in the non-convex objective function of a neural network (Ouyang et al., 2020). The success of deep learning architectures is contributed by three characteristics: a large number of hidden neurons, better learning algorithms, and better parameter initialization techniques (Deng and Yu, 2013).

In this paper, a widely utilized deep-learning algorithm namely deep belief network (DBN) is selected to construct the regression models to predict total energy consumption of the HVAC system. Originally proposed by Hinton et al. (2006), a typical DBN contains multiple restricted Boltzmann machines (RBMs) which are stacked in a hierarchically manner. Each RBM includes a visible layer and a hidden layer both are composed of Boolean neurons (see **Figure 2**). The connection between the hidden layer and the visible layer is bidirectional and symmetrical without any inter-connections between neurons in the same layer exists.

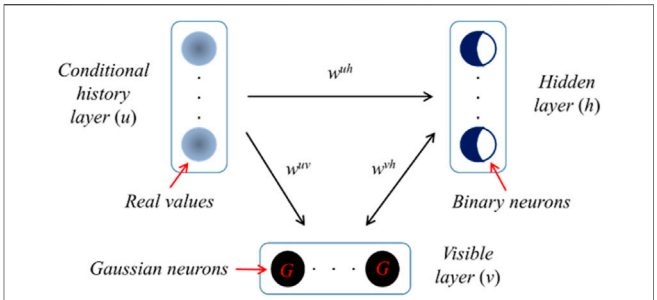

FIGURE 2 | Restricted Boltzmann Machine (RBM).

The optimization of the weight matrix between the two layers is the main target in the training process in order to construct a robust mapping. The configuration of weight matrix is based on the energy function expressed in **eq. 4** (Hinton et al., 2006). The joint distribution of a visible layer vector and the hidden layer vector is expressed in **eq. 5**. The activation functions of neurons in the visible and hidden layer are presented in **eqs. 6**, **7** (Hinton et al., 2006):

$$E(v,h) = -\sum_{i=1}^{n_v} a_i v_i - \sum_{j=1}^{n_h} b_j h_j - \sum_{i=1}^{n_v} \sum_{j=1}^{n_h} h_j w_{j,i} v_i \tag{4}$$

$$P(v,h) = \frac{e^{-E(v,h)}}{\sum_v \sum_h e^{-E(v,h)}} \tag{5}$$

$$P(v_i = 1|h) = sig\left(\alpha_i + \sum_{j=1}^{n_h} w_{j,i} h_j\right) \tag{6}$$

$$P(h_i = 1|v) = sig\left(b_j + \sum_{i=1}^{n_v} w_{j,i} v_i\right) \tag{7}$$

Layer-wise Training

Multiple layers of restricted Boltzmann machines (RBMs) are hierarchically stacked within the DBN algorithm. The first RBM is pre-trained as an independent RBM and the weight matrix of the first RBM is computed. The output of the first RBM is treated as the input to the second RBM. By training the RBMs iteratively following the above strategy, the DBN is trained and the weight matrices between the remaining hidden layers are obtained.

During the training process of RBMs, the optimization problem is formulated using a stochastic gradient ascent approach (SGA) (Hinton et al., 2006). Based on vector (5) of the joint distribution function between the visible and hidden layer, the objective function of the stochastic gradient ascend method is expressed in **eq. 8**:

$$L(a,b,w) = \sum \log P(v,h) \tag{8}$$

Benchmarking Algorithms

Three benchmarking algorithms including support vector regression machine (SVR), neural network (NN), and extreme learning machine (ELM).

The support vector regression machine (SVR) is a supervised classification/regression algorithm that includes a Gaussian kernel function (Drucker et al., 1996). The neural network (NN) is a machine-learning algorithm which contains the input layer, hidden layer and the output layer. The extreme learning machine (ELM) algorithm (Liang et al., 2006) is a single hidden layer feedforward network. The ELM learning model is expressed in **eqs. 9**, **10** (He and Kusiak 2017; Li et al., 2018; Ouyang et al., 2019; Li et al., 2021c).

$$f_L(x_j) = o_j, \forall j \tag{9}$$

$$\sum_{i=1}^{L} \beta_i G(a_i, b_i, x_j) = t_j, j = 1, 2, \ldots, N \tag{10}$$

Firefly Algorithm

The Firefly Algorithm (FA) (Bacanin et al., 2021) is a new swarm intelligence algorithm that simulates the social behavior of fireflies. In the nature, fireflies use flashing to attract mating partners and the movement of the fireflies is determined by the resulting attraction which is related to the intensity of the emitted light. Similar to the particle swarm optimization (PSO) algorithm, the FA algorithm is a population-based stochastic search algorithm. Each firefly member in the population represents a candidate solution in the search space. Fireflies move toward other directions and search potential candidate solutions. Overall, the attractiveness is determined by the intensity of the emitted light that is measured by the fitness value (Wang et al., 2017).

In detail, the attractiveness between the two fireflies X_i and X_j can be computed in **eqs. 11**, **12** as follows:

$$\beta(r_{ij}) = \beta_0 e^{-\gamma r_{ij}^2} \tag{11}$$

$$r_{ij} = \|X_i - X_j\| = \sqrt{\sum_{d=1}^{D} (x_{id} - x_{jd})^2} \tag{12}$$

where $d = 1,2,3, \ldots, D$ and D is the problem dimension; r_{ij} is the distance between X_i and X_j; x_{id} and x_{jd} are the dimension of X_i and X_j respectively. Each firefly X_i is compared with all other fireflies X_j, where $j = 1,2, \ldots, N$ and $j \neq i$. If X_j is brighter than X_i, the X_i will be attracted by X_j and move towards X_j. The movement of X_i can be computed by **eq. 13** as follows:

$$x_{id}(t+1) = x_{id}(t) + \beta_0 e^{-\gamma r_{ij}^2} (x_{id}(t) - x_{id}(t)) + S\epsilon_i \tag{13}$$

Therefore, the FA algorithm can be summarized into the following three steps as follows:

- Step 1: Initialization. Randomly generate N solutions as an initial population accordingly. Each individual solution (firefly) is X_i.
- Step 2: Movement (attraction). For each solution X_i, we compare with all other solutions X_j. If X_j is greater than X_i, X_i moves towards X_j and changes its position according to **eq. 13**.
- Step 3: Stopping. If the stopping criteria has been satisfied, we can stop the algorithm.

Measurement Metrices

In this research, the prediction output is the energy consumption and hence we may formulate this as a regression problem. Two widely utilized metrics namely mean absolute percentage error (MAPE) and root mean square error (RMSE) are selected in this study to measure the performance of different DBN architectures (Li et la. 2021b). The MAPE and RMSE are expressed in **eq. 8**, **9** as follows:

$$MAPE = \frac{\sum_{i=1}^{N} \left| \frac{\widehat{y_i} - y_i}{y_i} \right|}{N} \tag{8}$$

$$\text{RMSE} = \frac{\sqrt{\sum_{i=1}^{N} \left| \widehat{y_i} - y_i \right|}}{N} \tag{9}$$

EXPERIMENTAL RESULTS

Feature Analysis

In this research, the HAVC energy consumption dataset includes six predictor variables (features) and the energy utility is the dependent variable as indicated in Section "Data Collection". All features are continuous numerical features and the feature preliminary analysis with min-max scaling and histogram are performed in this section.

As illustrated in **Figure 4**, the histograms of the energy consumption are presented. In order to investigate the energy consuming behavior of the underlying commercial building in different seasons, the hourly energy consumption in summer season (Jun-Aug) and winter season (Dec-Feb) has been randomly sampled and plotted in **Figure 3**. It is obvious that the two energy distributions are right-skewed and are non-Gaussian distributed.

Meanwhile, the histograms of the input predictor features are also illustrated in **Figure 4** as follows. From **Figure 4**, almost all predictors follow a Gaussian-type of distribution and are symmetric in their empirical PDFs. The only exception is SAPTS which is left-skewed which indicate it may follow a non-Gaussian distribution. A log-transformation will be applied to further transform the distribution into a Gaussian shape distribution.

Predictive Modeling of Energy Cost

After data-preprocessing, the predictive modeling of energy consumption using DBN is provided in this section. The two hyper-parameters, the number of RBMs and the number of neurons within each RBM, directly impact the predicting performance of the energy prediction model. Hence, it is essential to tune the hyper-parameters to ensure the optimal setting of the DBN algorithm.

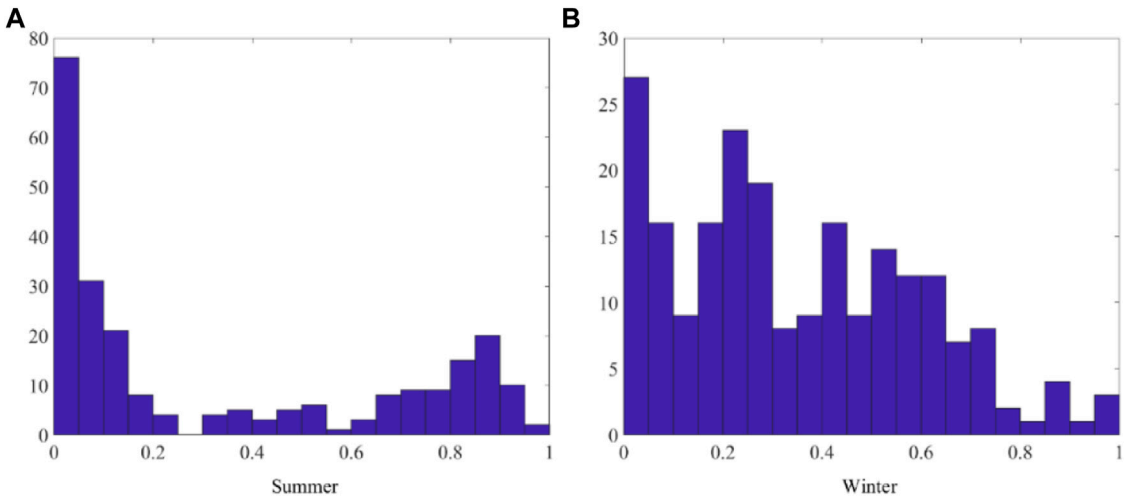

FIGURE 3 | Histogram of energy consumption in summer and winter.

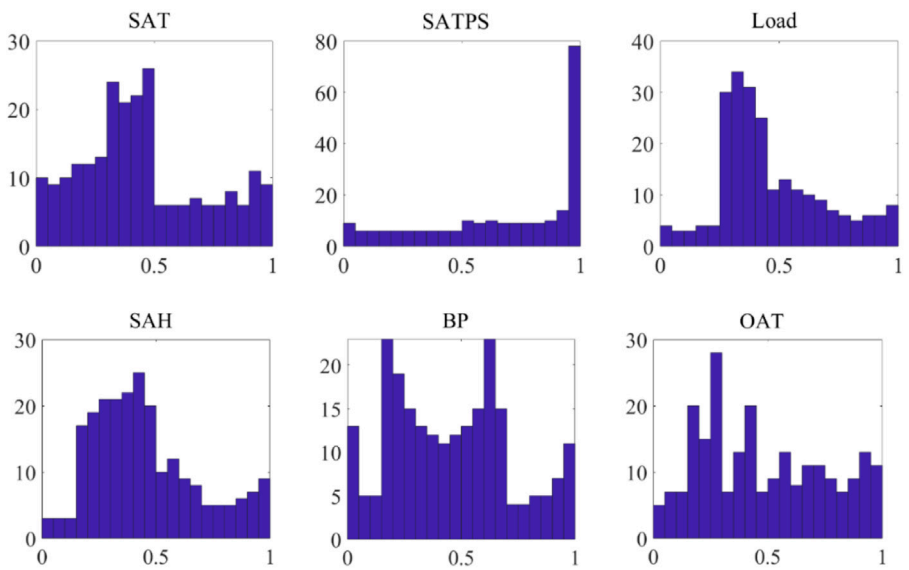

FIGURE 4 | Histogram of predictor variables.

In this research, a cross-validation based tuning process is implemented. As illustrated in **Figure 5**, we performed a series of experiments testing the average RMSE of various hidden layers as well as various hidden neurons in each hidden layer using an incremental manner. The dataset for such experiment are randomly sampled from the original dataset which contains a whole month hourly energy consumption records. It is obvious that the optimal number of RMBs within the DBN is 2 and the optimal number of hidden neurons in each RMB is 15.

Using the constructed optimal DBN algorithm, we performed training and testing experiments on two seasons: summer and winter. In each experiment, a whole month dataset has been used as the training dataset and the following weekly data has been used as the validation dataset. The prediction performance has been illustrated in **Figure 7** respectively. The prediction results of the testing dataset contain the actual energy consumption (blue) and the predicted energy consumption (red) of the two seasons. In summer, the RMSE is 5.51, and the MAPE is 11.77%. In winter, the RMSE is 5.25 and the MAPE is 10.81%. The prediction performance of the trained DBNs as well as the benchmarking machine learning algorithms on the testing dataset is presented in **Table 2** and **Figure 6** respectively.

In this section, the optimization of controllable features namely the supply air temperature set point (SAT) and the supply air static pressure set point (SATPS) in the temporal domain has been optimized by using the constructed DBN

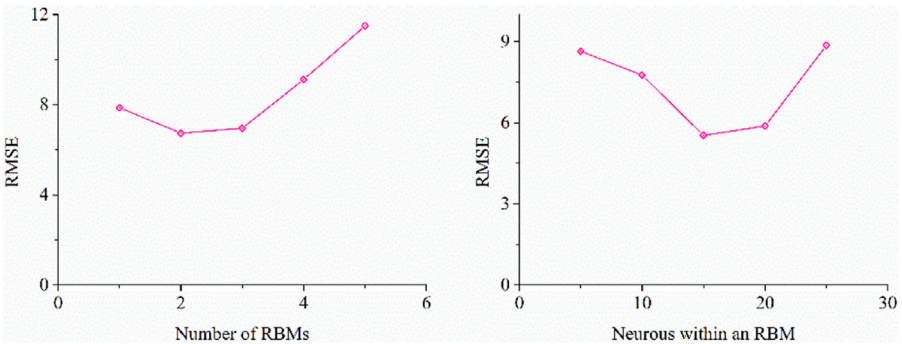

FIGURE 5 | Hyper-parameter tuning process.

TABLE 2 | Prediction performance of all algorithms tested.

Algorithm	MAPE (Summer)	R (%)MSE (Summer)	MAPE (Winter)	R (%)MSE (Winter)
SVR	13.37	6.02	14.42	6.92
NN	12.44	5.76	12.23	6.35
ELM	12.63	5.87	11.17	5.94
DBN	11.77	5.51	10.81	5.25

Optimization of controllable features.

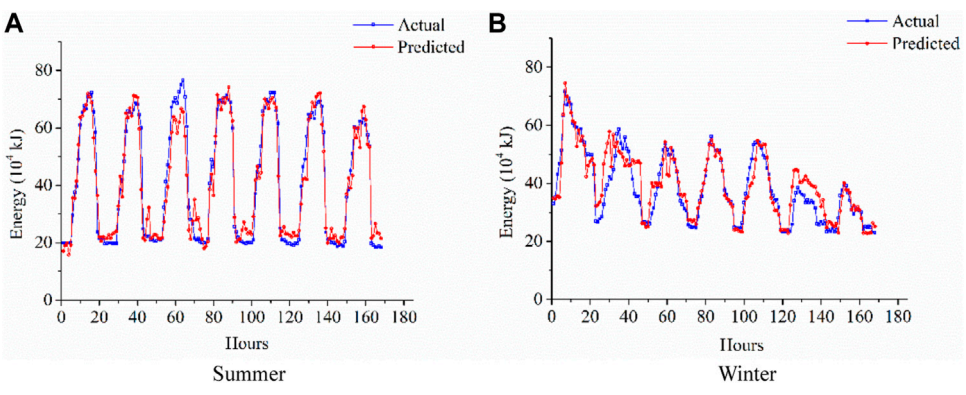

FIGURE 6 | Prediction performance of the testing dataset in Summer and Winter.

prediction models. The goal of the optimization is to reduce the energy consumption while maintaining the indoor quality. The formulation is expressed in **eq. 3** and the constrains for all predictor features are listed to ensure the indoor air quality. The firefly algorithm (FA) has been implemented in this section to reduce the energy consumption and the optimization experiments is illustrated in **Figure 7** as follows.

As illustrated in **Figure 7**, the fitness value of the FA algorithm has been plotted along with the iteration of the experiments. For the summer prediction model, the fitness value converges to near-zero zone after 20 epochs indicating the optimal solution has been numerically approached. For the winter prediction model, the fitness value converges to near-zero region after 30 epochs as it achieved its optimal solution. As it takes more epochs to approach the optimal solution, it indicates more complexity in the winter prediction model due to the challenges within the dataset provided.

Hence, using the feature settings computed by the FA algorithm, the two optimized feature outcomes are selected as new inputs in the pre-trained energy prediction models as discussed in Section "Predictive modeling of energy cost". The simulation results are presented in **Figure 8** that contains the actual energy consumption (blue), predicted energy consumption (red), and optimized energy consumption (purple) computed from the simulation outcome. For the summer season, the simulation results indicate the optimized energy consumption is 17% less than the predicted energy utility. For the winter season, the optimized energy is 14% less than the predicted energy utility.

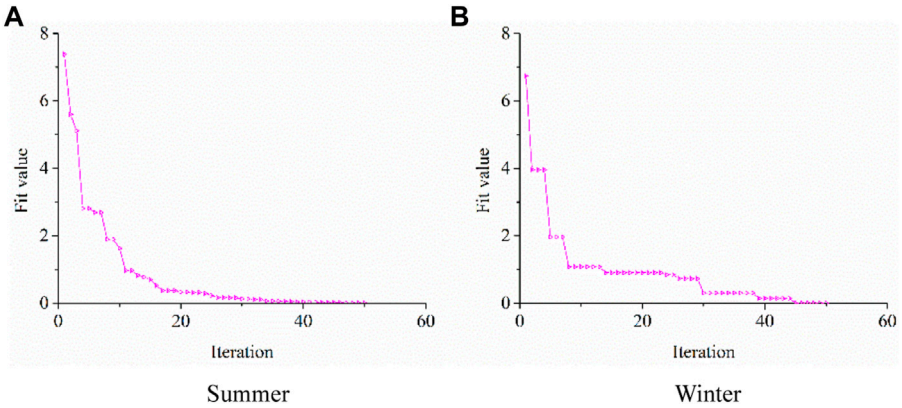

FIGURE 7 | Optimization experiment of firefly algorithm.

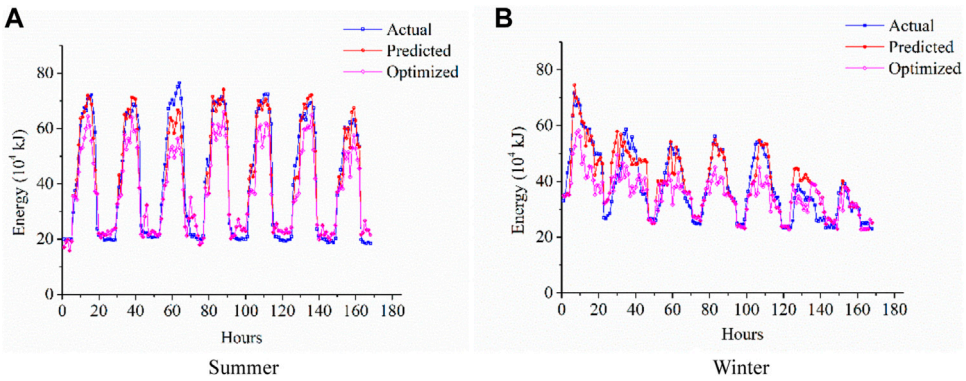

FIGURE 8 | Simulated energy consumption using the optimized controllable feature setting.

Based on the simulation results, we have achieved an optimized energy utility in our testing dataset. Considering the local electricity price, and total area within our underlying building, we have achieved a cost saving of 12.90 RMB/m^2 for our case study building in summer and 11.18 RMB/m^2 in winter from an economic perspective. If we incorporate this into the estimation of the total energy cost of the whole building, it would approximately achieve 16.6% of reduction in the total cost considering the savings in both winter and summer. Therefore, it achieved the standard Green Building concept and can be utilized as a sample for other local commercial buildings for larger scale energy saving projects.

CONCLUSION

The best performing neural network structure has been selected via cross-validation and gird-based search. In addition, an energy optimization problem has been formulated by incorporating the predictive neural network model and HVAC operational constraints. The formulated optimization problem has been successfully solved by the firefly algorithm. The optimal setting of the two controllable features including the supply air temperature set point and the supply air static pressure set point in the temporal domain has been computed. Computational results demonstrated that it can achieve the reduction of total energy cost by a significant portion. (Wang et al., 2016).

DATA AVAILABILITY STATEMENT

The original contributions presented in the study are included in the article/Supplementary Material, further inquiries can be directed to the corresponding author.

AUTHOR CONTRIBUTIONS

YL conceptualized the study, contributed to the study methodology, and wrote the original draft. YL contributed to the study methodology, data curation and investigation. CC contributed to data analysis and investigation. LZ contributed to investigation and writing-original draft. All authors have read and agreed to the published version of the manuscript.

REFERENCES

Bacanin, N., Bezdan, T., Venkatachalam, K., and Al-Turjman, F. (2021). Optimized Convolutional Neural Network by Firefly Algorithm for Magnetic Resonance Image Classification of Glioma Brain Tumor Grade. *J. Real-time Image Proc.* 18, 1085–1098. doi:10.1007/s11554-021-01106-x

Chang, Y.-C., and Chen, W.-H. (2009). Optimal Chilled Water Temperature Calculation of Multiple Chiller Systems Using Hopfield Neural Network for Saving Energy. *Energy* 34 (4), 448–456. doi:10.1016/j.energy.2008.12.010

Deng, L., and Yu, D. (2013). Deep Learning for Signal and Information Processing. *Microsoft Res. Monogr.*.

Drucker, H., Burges, C. J., Kaufman, L., Smola, A., and Vapnik, V. (1996). Support Vector Regression Machines. *Adv. Neural Inf. Process. Syst.* 9, 155–161.

Fong, K. F., Hanby, V. I., and Chow, T. T. (2006). HVAC System Optimization for Energy Management by Evolutionary Programming. *Energy and Buildings* 38 (3), 220–231. doi:10.1016/j.enbuild.2005.05.008

He, Y. Deng, J., and Li, H. (2017). Short-term Power Load Forecasting with Deep Belief Network and Copula Models. Proceeddings of the 9th International conference on intelligent human-machine systems and cybernetics (IHMSC). 26 August. 2017. Hangzhou, China, 1. IEEE, 191–194. doi:10.1109/ihmsc.2017.50

He, Y., and Kusiak, A. (2017). Performance Assessment of Wind Turbines: Data-Derived Quantitative Metrics. *IEEE Trans. Sustainable Energ.* 9 (1), 65–73.

Hinton, G. E., Osindero, S., and Teh, Y.-W. (2006). A Fast Learning Algorithm for Deep Belief Nets. *Neural Comput.* 18 (7), 1527–1554. doi:10.1162/neco.2006.18.7.1527

Kontes, G. D., Giannakis, G. I., and Rovas, D. (2013). Demand Shifting Using Model-Assisted Control. *Int. J. Energ. a Clean Environ.* 14 (1). doi:10.1615/interjenercleanenv.2014007281

Kusiak, A., Tang, F., and Xu, G. (2011a). Multi-objective Optimization of HVAC System with an Evolutionary Computation Algorithm. *Energy* 36 (5), 2440–2449. doi:10.1016/j.energy.2011.01.030

Kusiak, A., Xu, G., and Tang, F. (2011b). Optimization of an HVAC System with a Strength Multi-Objective Particle-Swarm Algorithm. *Energy* 36 (10), 5935–5943. doi:10.1016/j.energy.2011.08.024

Lachheb, A., Allouhi, A., Saadani, R., Jamil, A., and Miloud, R. A. H. M. O. U. N. E. (2020). Thermal and Economic Analysis of Different Glazing Systems for a Commercial Building in Various Moroccan Climates. *Int. J. Energ. a Clean Environ.* 22.

LeCun, Y., Bengio, Y., and Hinton, G. (2015). Deep Learning. *Nature* 521 (7553), 436–444. doi:10.1038/nature14539

Li, H., Deng, J., Feng, P., Pu, C., Arachchige, D. D. K., Cheng, Q., et al. (2021b). Monitoring and Identifying Wind Turbine Generator Bearing Faults Using Deep Belief Network and EWMA Control. *Front. Energ. Res.* 9, 799039. doi:10.3389/fenrg.2021.799039

Li, H., Deng, J., Feng, P., Pu, C., Arachchige, D. D. K., and Cheng, Q. (2021a). Short-Term Nacelle Orientation Forecasting Using Bilinear Transformation and ICEEMDAN Framework. *Front. Energ. Res.* 9, 780928. doi:10.3389/fenrg.2021.780928

Li, H., He, Y., Yang, H., Wei, Y., Li, S., and Xu, J. (2021c). Rainfall Prediction Using Optimally Pruned Extreme Learning Machines. *Nat. Hazards* 108 (1), 799–817. doi:10.1007/s11069-021-04706-9

Li, H., Xu, Q., He, Y., and Deng, J. (2018). Prediction of Landslide Displacement with an Ensemble-Based Extreme Learning Machine and Copula Models. *Landslides* 15 (10), 2047–2059. doi:10.1007/s10346-018-1020-2

Li, H., Xu, Q., He, Y., Fan, X., and Li, S. (2020). Modeling and Predicting Reservoir Landslide Displacement with Deep Belief Network and EWMA Control Charts: a Case Study in Three Gorges Reservoir. *Landslides* 17 (3), 693–707. doi:10.1007/s10346-019-01312-6

Liang, N.-Y., Saratchandran, P., Huang, G.-B., and Sundararajan, N. (2006). Classification of Mental Tasks from EEG Signals Using Extreme Learning Machine. *Int. J. Neur. Syst.* 16 (01), 29–38. doi:10.1142/s0129065706000482

Lv, Y., Bi, J., and Yan, J. (2018). State-of-the-art in Low Carbon Community. *Int. J. Energ. a Clean Environ.* 19 (3-4). doi:10.1615/interjenercleanenv.2018025415

Mull, T. E. (1998). *HVAC Principles and Applications Manual*. New York: McGraw-Hill.

Nassif, N., Kajl, S., and Sabourin, R. (2004). Evolutionary Algorithms for Multi-Objective Optimization in HVAC System Control strategyIEEE Annual Meeting of the Fuzzy Information. *Process. NAFIPS* 04 (1), 51–56. doi:10.1109/nafips.2004.1336248

Ouyang, T., He, Y., and Huang, H. (2018). Monitoring Wind Turbines' Unhealthy Status: A Data-Driven Approach. *IEEE Trans. Emerging Top. Comput. Intelligence* 3 (2), 163–172.

Ouyang, T., He, Y., Li, H., Sun, Z., and Baek, S. (2019). Modeling and Forecasting Short-Term Power Load with Copula Model and Deep Belief Network. *IEEE Trans. Emerg. Top. Comput. Intell.* 3 (2), 127–136. doi:10.1109/tetci.2018.2880511

Ouyang, T., Huang, H., He, Y., and Tang, Z. (2020). Chaotic Wind Power Time Series Prediction via Switching Data-Driven Modes. *Renew. Energ.* 145, 270–281. doi:10.1016/j.renene.2019.06.047

Ouyang, T., Kusiak, A., and He, Y. (2017). Predictive Model of Yaw Error in a Wind Turbine. *Energy* 123, 119–130. doi:10.1016/j.energy.2017.01.150

Payne, F. W., and McGowan, J. J. (2012). *Energy Management and Control Systems Handbook*. Springer Science & Business Media.

Sakulpipatsin, P., Itard, L. C. M., Van der Kooi, H. J., Boelman, E. C., and Luscuere, P. G. (2010). An Exergy Application for Analysis of Buildings and HVAC Systems. *Energy and buildings* 42 (1), 90–99. doi:10.1016/j.enbuild.2009.07.015

Teodosiu, C., Hohota, R., Rusaouën, G., and Woloszyn, M. (2003). Numerical Prediction of Indoor Air Humidity and its Effect on Indoor Environment. *Building Environ.* 38 (5), 655–664. doi:10.1016/s0360-1323(02)00211-1

Wang, H., Wang, W., Zhou, X., Sun, H., Zhao, J., Yu, X., et al. (2017). Firefly Algorithm with Neighborhood Attraction. *Inf. Sci.* 382-383, 374–387. doi:10.1016/j.ins.2016.12.024

Wang, H. Z., Wang, G. B., Li, G. Q., Peng, J. C., and Liu, Y. T. (2016). Deep Belief Network Based Deterministic and Probabilistic Wind Speed Forecasting Approach. *Appl. Energ.* 182, 80–93. doi:10.1016/j.apenergy.2016.08.108

Zhang, L., Liu, X., and Jiang, Y. (2013). Application of Entransy in the Analysis of HVAC Systems in Buildings. *Energy* 53, 332–342. doi:10.1016/j.energy.2013.02.015

Conflict of Interest: The authors declare that the research was conducted in the absence of any commercial or financial relationships that could be construed as a potential conflict of interest.

GLOSSARY

E_{Total} Total energy consumption

E_{AHU} Energy utility from the AHU

E_{VAV} Energy utility from the VAV

x_{SAT} Supply air temperature set point

x_{SATPS} Supply air duct static pressure

x_{Load} System load

x_{SAH} Supply air humidity

x_{BP} Barometric pressure

x_{OAT} Outside air temperature.

vi Number of neurons in the visible layer

hi Number of Boolean neurons within the hidden layer

wj,I Weight matrix between the visible layer and hidden layer

ai Weight vector connecting the *i*th hidden node and the input nodes

bi Threshold of the *i*th hidden node

sig() Logistic sigmoid function

a Bias vector of the visible layer

b Bias vector of the hidden layer

xj Input parameters

oj Output values

fL() Non-linear function representing the ELM algorithm

βi Weight vector connecting the *i*th hidden node and the output nodes

tj Actual output value

ϵ_i Random value uniformly distributed between [-0.5, 0.5]

s Step-factor between [0, 1]

$\widehat{y}_i$ Predicted value

y_i Actual value

N Total number of predicted values in the testing dataset

frontiers in Energy Research

ORIGINAL RESEARCH
published: 01 December 2021
doi: 10.3389/fenrg.2021.798048

Research on Leakage Current Waveform Spectrum Characteristics of Artificial Pollution Porcelain Insulator

Chunhua Fang[1], Yuning Tao[1], Jianguo Wang[2], Haixin You[1], Yan Cui[1] and Mi Zhou[2]*

[1]College of Electrical Engineering and New Energy, China Three Gorges University, Yichang, China, [2]School of Electrical Engineering, Wuhan University, Wuhan, China

The surface discharge development processes of polluted porcelain insulators for power transmission lines are tightly related with the development of leakage current (LC), the characteristics of LC, the insulating condition, and discharge intensity of the insulator surface have an important significance for revealing the contamination discharge state of insulators. In order to analyze the LC characteristics of porcelain insulators in the process of pollution flashover, artificial pollution flashover tests on porcelain insulators were conducted in the artificial fog cabinet, and the characteristics of LC waveforms in time-domain and frequency-domain were simultaneously measured and analyzed during the tests. The results indicated that the amplitude of LC, fundamental harmonic, the third harmonic, and fifth harmonic had a strong correlation, the maximum of LC(I_m), the rate of total harmonics (*THD*), and the phase difference of fundamental harmonic (θ) were used for the representation of the characteristics of the LC waveform. The LC has the characteristics of high amplitude, low proportion harmonic, and small phase difference between the fundamental harmonic and voltage before the flashover occurrence. The test results provide effective reference for porcelain insulators in pollution flashover forecasting.

Keywords: leakage current, insulator, pollution flashover, flashover voltage, transmission line

OPEN ACCESS

Edited by:
Yahui Zhang,
Yanshan University, China

Reviewed by:
Peng Yong,
China Electric Power Research Institute, China
Heming Deng,
Hubei University, China

****Correspondence:***
Yuning Tao
taoyuning12@163.com

Specialty section:
This article was submitted to Smart Grids, a section of the journal Frontiers in Energy Research

Received: *19 October 2021*
Accepted: *02 November 2021*
Published: *01 December 2021*

Citation:
Fang C, Tao Y, Wang J, You H, Cui Y and Zhou M (2021) Research on Leakage Current Waveform Spectrum Characteristics of Artificial Pollution Porcelain Insulator. Front. Energy Res. 9:798048. doi: 10.3389/fenrg.2021.798048

INTRODUCTION

Outdoor insulators have been exposed in severe environment since the birth of the power system (Yang et al., 2019; Liu et al., 2020; Shen and Raksincharoensak, 2021a; Shen and Raksincharoensak, 2021b). The airborne particles are deposited on the insulator surface and the pollution builds up gradually, which causes insulator flashover during wet weather conditions (Yang et al., 2019; Shen et al., 2021; Yang et al., 2021). So conditions monitoring of the insulator are important to know about insulator status of the insulator. The analysis of surface LC is necessary to know about the insulator condition (Miyake et al., 2010; Shen et al., 2020; Yang et al., 2020; Zhu et al., 2020; Noman et al., 2021).

A large number of research studies have dealt with LC, including the maximum value of the LC pulse under the operating voltage, the amplitude of the LC before the occurrence of flashover and the LC root-mean-square values (Li et al., 2010; Jiang et al., 2010). Besides, the number of the highest peak power-spectrum is also used as methods for pollution monitoring (Chandrasekar et al., 2009; Pylarinos et al., 2011; Pylarinos et al., 2012). Literature (Chaou et al., 2015) reported that the main frequency of the porcelain insulator LC waveform is 50, 150, and 250 Hz and the LC waveform is

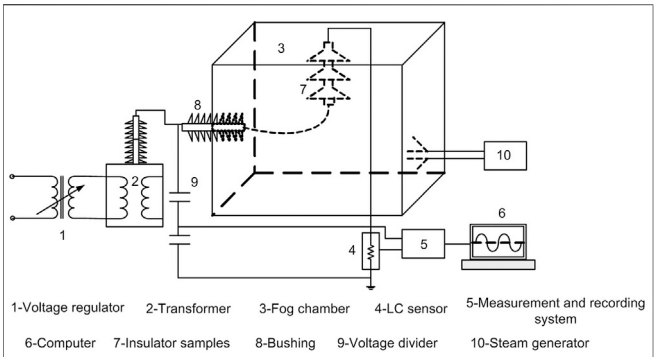

FIGURE 1 | Schematic diagram of the test device.

divided into six categories. Papers (Suda T, 2001; Bashir and Ahmad, 2010; Douar et al., 2010; Dhahbi-Megriche and Beroual, 2016) introduced the analysis of the variation characteristics of the LC in the frequency domain power spectrum during the entire process of the contamination flashover. But all these studies listed have not yet reached consensus on which spectrum parameters can represent contamination insulator surface state.

In this paper, while measuring polluted porcelain insulator LC data and shooting discharge pictures, the frequency spectrum characteristics of LC waveform is extracted during loading voltage process, analyzing the variation of LC characteristics carefully under various salt density, as well as the correlation between each feature quantity.

EXPERIMENTAL EQUIPMENT AND METHOD

Experimental Equipment

According to IEC60507 standard (IEC 60507, 1991), the solid layer method experiments are carried out in an artificial fog chamber. The schematic diagram of the test device is shown in **Figure 1**. The artificial fog chamber's dimensions are $5 \times 5 \times 5$ m. The power supply includes a shifting coil voltage regulator (150 kV/4A) and test transformer (1000 kV/2250 kVA). The high voltage supply is connected to the artificial fog chamber through a 220 kV wall bushing. The fog is generated by the automatic steam generator. Steam output remains at a fixed rate. The data acquisition system monitors and records LC and voltage waveforms using a LABVIEW program on the personal computer. The leakage current sensor is connected to the low-voltage circuit, the leakage current signal is obtained and the voltage signal is obtained through the capacitive voltage divider, which are then connected to the leakage current and voltage measurement system through the double-layer shielded coaxial cable, the sampling rate is 125kS/s, and then connected to the computer, the software of the leakage current measurement system finally completes the measurement of the leakage current and the pollution flashover voltage in the artificial pollution flashover test of the insulator.

TABLE 1 | Dimensions of test porcelain insulator.

Parameters	Dimensions in mm
Maximum diameter	255
Creepage distance	295
Axial height	146

Insulator Sample

The XP-70 porcelain insulator is used to measure the LC in the test. A sample insulator string includes seven pieces of porcelain insulator that are used for the experiments. The details of the dimensions of the porcelain insulator are in **Table 1**.

Test Methods

The solid layer method as described in IEC60507 is used in the test (IEC, 1991). NaCl is used as soluble salt. Kaolin powder is used as non-soluble salt. First, NaCl is mixed with Kaolin powder in a certain proportion in distilled water. Then the mixture is coated on the clean porcelain insulator surface. Finally, the pre-contaminated samples are hung in the laboratory until they naturally dry for more than 24 h before the experiment. Based on the IEC60507 standard, four levels of equivalent salt deposit density (*ESDD*) are applied to the experiment, respectively, 0, 0.1, 0.2, and 0.4 mg/cm^2. And the non-soluble deposit density (*NSDD*) is set to 1.0 mg/cm^2. The commonly used methods of artificial pollution test include constant pressure lifting method. During the test, when the wetness of the umbrella skirt surface reaches a fully saturated state, the pressure is immediately increased to flashover. The speed of the increase is not specified before 40% of the expected flashover voltage. Then the voltage is increased to flashover at a rate of 10–20% of the expected flashover voltage per second.

RESULTS AND DISCUSSION

Discharge Image and LC Waveforms and Frequency Spectrum

As shown in **Figure 2**, at the first stage of discharge, the weak filamentary discharge can be seen on the surface of the porcelain insulator. With the increase of voltage, the "squeak" sound can be heard.

Contaminant forms a layer on the surface of the insulator in combination with water, which causes the formation of conducting films, and that causes to flow the LC through the insulator surface under wet conditions. Evaporation of water layers in these areas forms dry bands. The appearance of dry bands on the insulator surface causes arcs. Such arcs may elongate until they bridge the two metal electrodes of the insulator, and total flashover occurs.

With the increase of voltage, partial arcs will enter into a stage of stability. Blue-violet partial arcs will appear on the surface of the porcelain insulator. For the whole insulator string, the development of partial arcs of each piece of porcelain insulator is relatively independent.

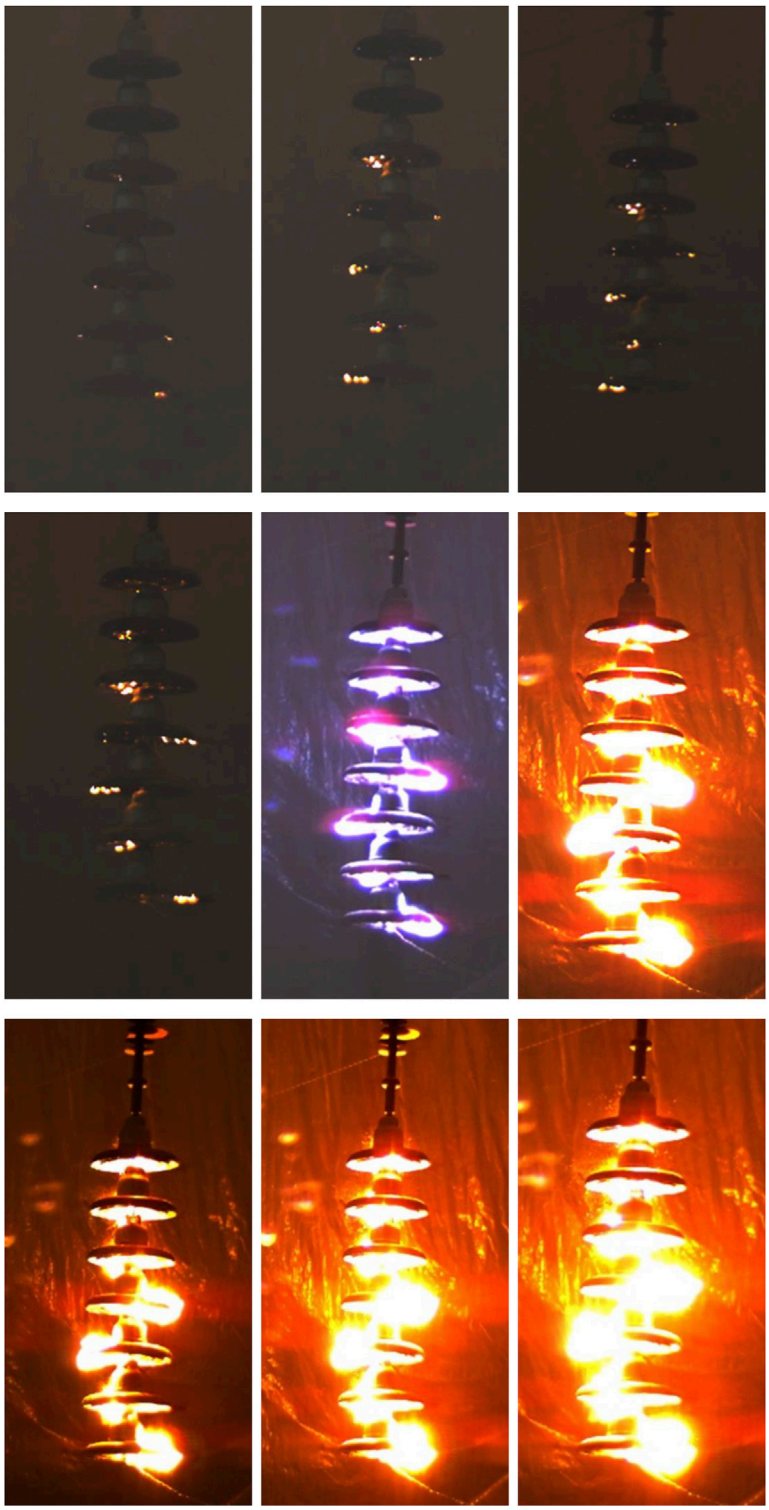

FIGURE 2 | The process of contamination discharge of insulators.

Bright blue-violet arcs are changed into light yellow, while the bright arcs are rotated around the axis of the porcelain insulator. A large number of small arcs get together to form the main arc and develop along the surface of the insulator. As voltage continues to increase, the partial arcs have a tendency to through the surface of an insulator, when they cross 70%

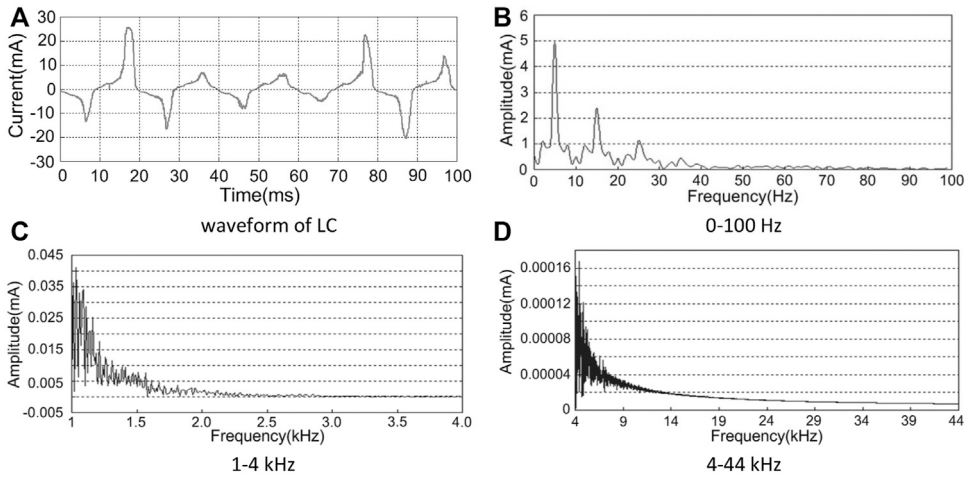

FIGURE 3 | The LC waveform and its Fourier transform.

creepage distance of the insulator, porcelain insulator string flashover.

Figure 3A shows a typical waveform of LC obtained at the test. **Figures 3B–D** show the frequency spectrum of **Figure 3A**. The frequency components of LC were studied within 0–100 Hz, 1–4, and 4–44 kHz. With the increase of frequency, the amplitude of LC decreases gradually. The maximum value of LC at 1 kHz is only 0.04 mA, which is more than that at 1.5 kHz. The amplitude of LC is less than 0.005 mA. It is only 0.1% of the fundamental harmonic. In **Figure 3A**, it is obvious that there is the third, fifth, and seventh harmonics, especially the third and fifth harmonics, expect the amplitude of the fundamental harmonic at 50 Hz.

A typical LC waveform and corresponding spectrum graph are shown in **Figure 4**. When the porcelain insulator surface is dry or extremely low contamination degree, there is LC waveform in **Figure 4A**. The waveform is a sine wave, but the phase difference is larger between the voltage and the fundamental harmonic, some even meet to 90°. When the insulator surface appears weak discharge current slowly, the LC waveform begins to distortion into symmetrical triangle waveform (**Figure 4B**), the odd harmonic increases sharply; when the discharge becomes more obvious and intense, the triangle wave will significantly increase, the peak of the LC waveform becomes more prominent, an asymmetric waveform is formed (**Figure 4C**); the strong arcs almost across insulator string before flashover occurs. The characteristics of LC are mainly decided by the nature of the arcs, a long arc represents resistance. As shown in **Figure 4D**, resistive current will appear again, but the amplitude of LC will increase tens to hundreds of mA.

LC Characteristic

The change curves of applied voltage and LC of porcelain insulator under different salt density are shown in **Figure 5**. With the increase of voltage, LC increases linearly, when the voltage rises to a certain value, the amplitude of LC begins to fluctuate, the value of salt density is higher, the discharge becomes more powerful and intense. The amplitude of LC increases sharply before the flashover is coming.

THD Variation Law of Polluted Insulators Under Wet Conditions

THD is the total harmonic distortion of LC (Khodsuz and Mizaie, 2015). The change curve of *THD* during loading voltage process is shown in **Figure 6**. The curve of *THD* of a clean insulator is shown in **Figure 6A**, the initial applied voltage is small, the LC of a clean insulator is also small, the interfering signals cause higher distortion. With the increase of voltage, the LC increases, the value of *THD* decreases gradually; a small number of arcs appear on the surface of the porcelain insulator. *THD* increases suddenly before the flashover is coming. As shown in **Figures 6B,C**, when the salt density is 0.1, and 0.2 mg/cm^2, *THD* changes greatly after the pressure for more than 20 s. With the salt density increased to 0.4 mg/cm^2, *THD* changes more intensely.

Phase Angel θ of Polluted Insulators LC Variation Law Under Wet Conditions

The θ is the phase difference between the applied voltage and LC. Change curves of phase difference under different salt densities are shown in **Figure 7**. The LC phase of clean porcelain insulators decreased gradually with the voltage increased, which decreased from 75 to 20°. The phase difference was mutated into a negative value before flashover occurs, which shows that there is a big arc, and following with insulator flashover.

LC contains resistive current and capacitive current, the proportion of resistive current is different from capacitive current, so the phase difference fluctuates between the positive and negative. With the increase of voltage, the porcelain insulator surface does not appear to discharge, the phase difference gradually decreases to negative, then the insulator begins to violently discharge and the phase difference begins to flounce between positive and negative.

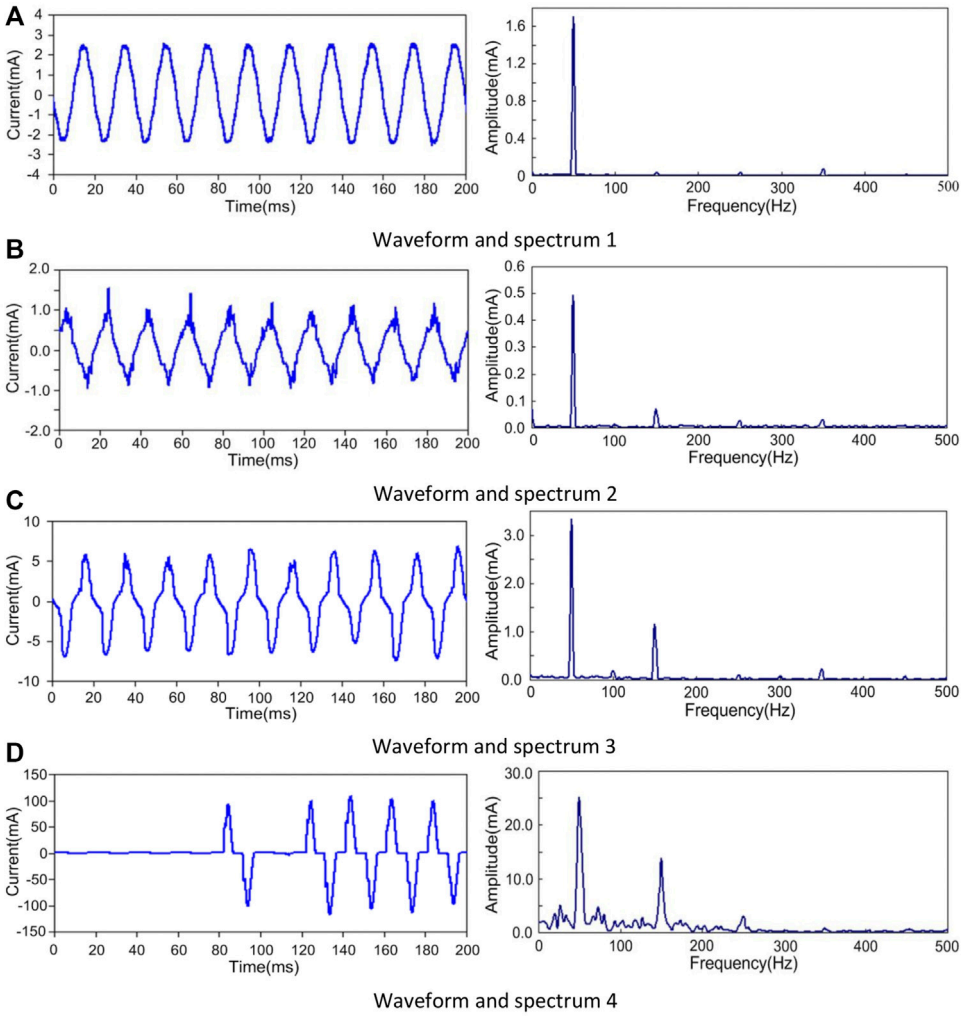

FIGURE 4 | LC waveforms and frequency spectrum of different discharging strength.

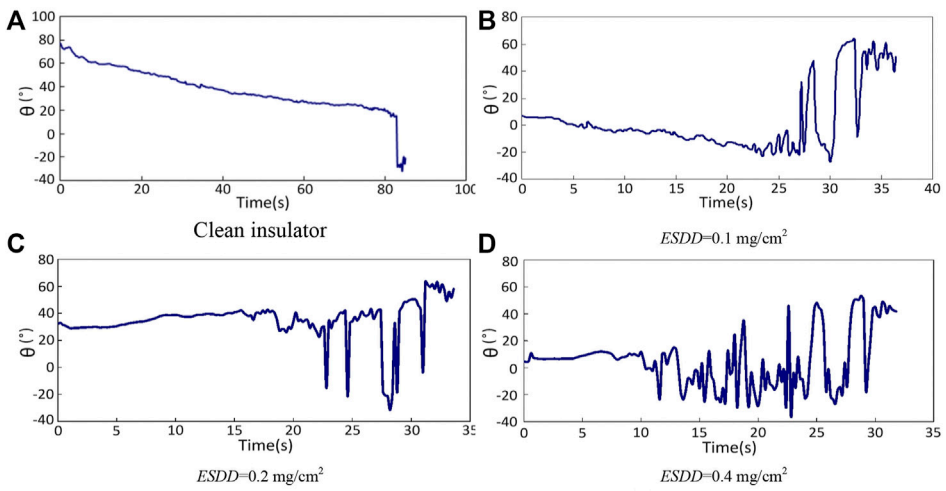

FIGURE 5 | Curves of LC with the increasing voltage.

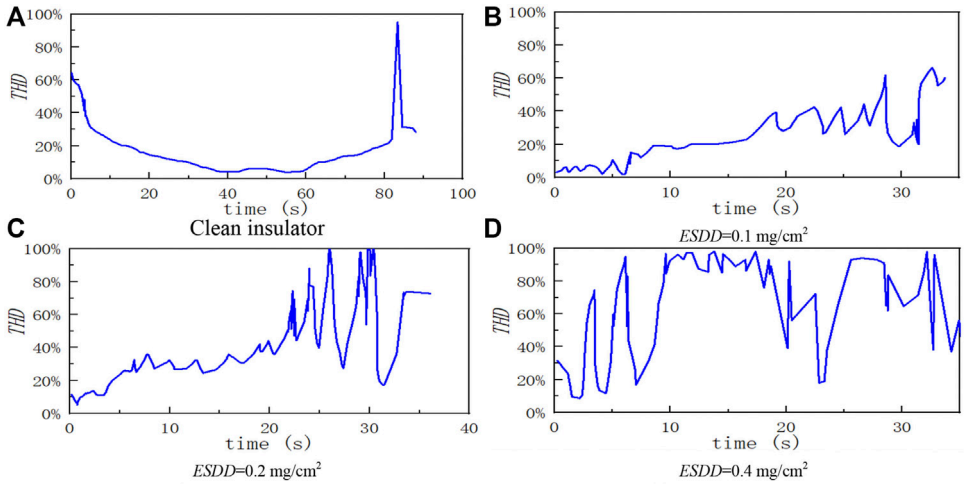

FIGURE 6 | Curves of *THD* of insulators under different pollution conditions.

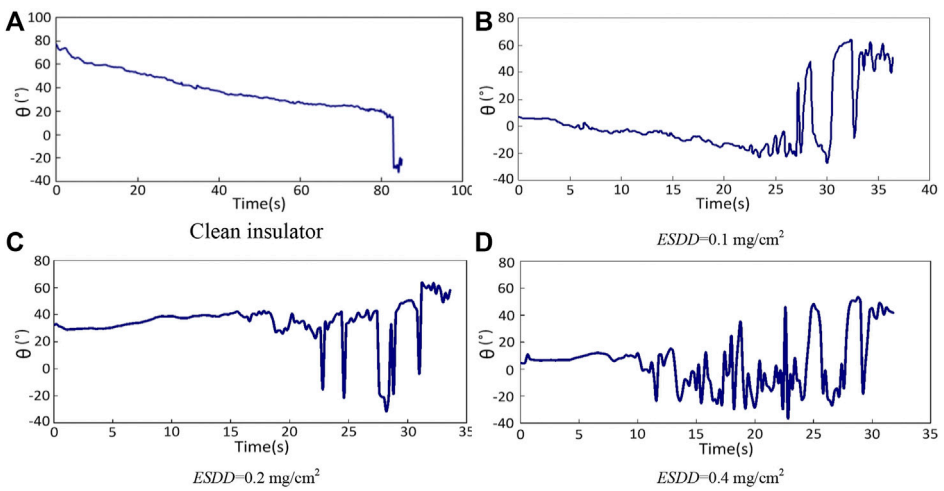

FIGURE 7 | Curves of θ of LC under different *ESDD*.

TABLE 2 | The coefficient of LC eigenvalues on clean insulator.

	I_m	I_{1m}	I_{3m}	I_{5m}	θ	*THD*
I_m	1.000	0.908	0.998	0.998	−0.229	0.418
I_{1m}	0.908	1.000	0.928	0.886	−0.461	0.285
I_{3m}	0.998	0.928	1.000	0.994	−0.252	0.431
I_{5m}	0.998	0.886	0.994	1.000	−0.197	0.425
θ	−0.229	−0.461	−0.252	−0.197	1.000	0.249
THD	0.418	0.285	0.431	0.425	0.249	1.000

TABLE 3 | The coefficient of LC eigenvalues (*ESDD*= 0.1 mg/cm^2).

	I_m	I_{1m}	I_{3m}	I_{5m}	θ	*THD*
I_m	1.000	0.971	0.865	0.917	−0.491	−0.061
I_{1m}	0.977	1.000	0.802	0.881	−0.402	−0.162
I_{3m}	0.865	0.804	1.000	0.958	−0.597	−0.021
I_{5m}	0.917	0.887	0.957	1.000	−0.565	−0.072
θ	−0.494	−0.407	−0.594	−0.564	1.000	0.094
THD	−0.061	−0.162	−0.022	−0.075	0.094	1.000

The Relationship LC Characteristics

LC fundamental harmonic, the third harmonic, the fifth harmonic, and the rate of total harmonic and the phase difference of the fundamental harmonic has carried on the correlation analysis.

From **Table 2** to **Table 3**, the correlation coefficient between the amplitude of LC and fundamental harmonic, the third harmonic, and the fifth harmonic is more than 0.800. The amplitude of the LC can be used to represent the fundamental wave, third, and fifth harmonic; current amplitude has a low

TABLE 4 | The coefficient of LC eigenvalues (*ESDD* = 0.2 mg/cm^2).

	I_m	I_{1m}	I_{3m}	I_{5m}	Θ	*THD*
I_m	1.000	0.969	0.861	0.934	−0.620	0.121
I_{1m}	0.969	1.000	0.823	0.924	−0.490	0.042
I_{3m}	0.861	0.823	1.000	0.938	−0.701	0.158*
I_{5m}	0.934	0.924	0.938	1.000	−0.655	0.135
θ	−0.620	−0.490	−0.701	−0.655	1.000	0.012
THD	0.121	0.042	0.158*	0.135	0.012	1.000

TABLE 5 | The coefficient of LC eigenvalues (*ESDD* = 0.4 mg/cm^2).

	I_m	I_{1m}	I_{3m}	I_{5m}	θ	*THD*
I_m	1.000	0.919	0.901	0.845	−0.368	−0.173*
I_{1m}	0.919	1.000	0.823	0.887	−0.204	−0.240
I_{3m}	0.901	0.823	1.000	0.965	−0.430	−0.155
I_{5m}	0.845	0.887	0.965	1.000	−0.444	−0.101
θ	−0.368	−0.204	−0.430	−0.444	1.000	−0.383
THD	−0.173*	−0.240	−0.155	−0.101	−0.383	1.000

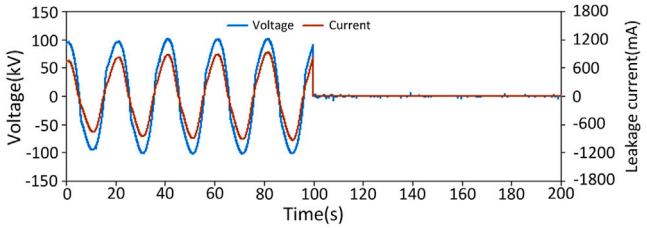

FIGURE 8 | The voltage and current waveform of flashover.

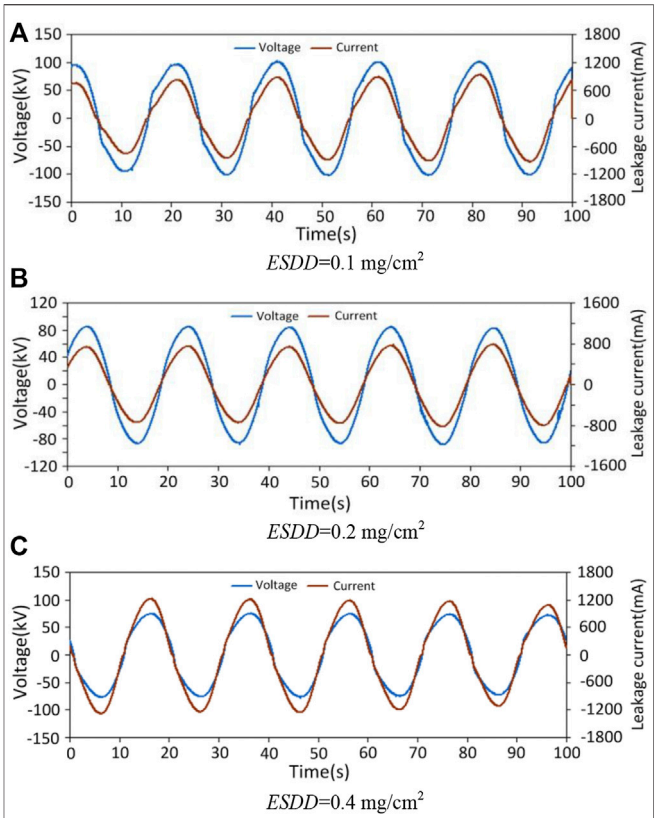

FIGURE 9 | The voltage and current waveform of pre-flashover.

correlation with θ, the maximum value is only −0.620 under four pollution levels, and all are negative. It is indicated that the value of LC is bigger. That θ is smaller; the correlation of THD and current amplitude is less than 0.44. Distortion degree of LC waveform and the value of LC lack of a strong linear relationship; there is no significant correlation between *THD* and θ.

The maximum value of LC is affected by the degree of pollution. The *THD* represents the degree of distortion of the LC waveform; the phase difference can distinguish effectively capacitive current and resistive current. Three characteristics describe the situation of LC of porcelain insulator surface from different aspects. The waveform of LC can be characterized by three features that are current amplitude, *THD,* and phase difference.

The LC Characteristics Before Flash

As shown in **Figure 8**, when the flashover occurs on the surface of the porcelain insulator, the voltage drops to zero rapidly. Before the flashover, the LC did not increase sharply, arcs almost throughout the whole string of the insulator, which lasted for a long time. The waveform of LC and applied voltage is shown in **Figure 9**, *NSDD* is 1.0 mg/cm^2, *ESDD* is 0.1, 0.2, 0.4 mg/cm^2, the amplitude of LC reached more than 700 mA before flashover. The total harmonic and phase differences are small, and the LC mainly is resistive current.

CONCLUSION

1) The correlation coefficient between the amplitude of LC and fundamental harmonic, the third harmonic, and the fifth harmonic is more than 0.800; the amplitude of the LC can be used to represent the fundamental waveform, the third harmonic, and the fifth harmonic; the correlation of *THD* and maximum value of LC is less than 0.44; the distortion degree of the LC waveform and the value of LC lack of a strong linear relationship; there is no significant correlation between *THD* and θ.
2) The maximum value of LC is affected by the degree of pollution. The *THD* represents the degree of distortion of LC waveform; the phase difference can distinguish effectively capacitive current and resistive current. Three characteristics describe the situation of LC of porcelain insulator surface from different aspects. The waveform of LC can be characterized by three features that are current amplitude, *THD,* and phase difference.
3) Test results can be used as an effective reference for porcelain insulators in pollution flashover forecasting.

DATA AVAILABILITY STATEMENT

The raw data supporting the conclusions of this article will be made available by the authors, without undue reservation.

AUTHOR CONTRIBUTIONS

C.F., J.W., and H.Y. conceived the idea and designed the experiments. C.F. and H.Y. led the experiments. Y.T., Y.C., and M.Z. contributed to data analysis and interpretation. C.F. and Y.T. wrote the paper. All authors read and approved the final manuscript.

FUNDING

This paper is supported by the National Natural Science Foundation of China (Grant No. 51807110).

REFERENCES

Bashir, N., and Ahmad, H. (2010). Odd Harmonics and Third to Fifth Harmonic Ratios of Leakage Currents as Diagnostic Tools to Study the Ageing of Glass Insulators. *IEEE Trans. Dielect. Electr. Insul.* 17 (3), 819–832. doi:10.1109/TDEI.2010.5492255

Chandrasekar, S., Kalaivanan, C., Cavallini, A., and Montanari, G. (2009). Investigations on Leakage Current and Phase Angle Characteristics of Porcelain and Polymeric Insulator under Contaminated Conditions. *IEEE Trans. Dielect. Electr. Insul.* 16 (2), 574–583. doi:10.1109/TDEI.2009.4815193

Chaou, A. K., Mekhaldi, A., and Teguar, M. (2015). Recurrence Quantification Analysis as a Novel LC Feature Extraction Technique for the Classification of Pollution Severity on HV Insulator Model. *IEEE Trans. Dielect. Electr. Insul.* 22 (6), 3376–3384. doi:10.1109/TDEI.2015.004921

Dhahbi-Megriche, N., and Beroual, A. (2015). Time-frequency Analyses of Leakage Current Waveforms of High Voltage Insulators in Uniform and Non-uniform Polluted Conditions. *IET Sci. Meas. Tech.* 9 (8), 945–954. doi:10.1049/iet-smt.2015.0116

Douar, M., Mekhaldi, A., and Bouzidi, M. (2010). Flashover Process and Frequency Analysis of the Leakage Current on Insulator Model under Non-uniform Pollution Conditions. *IEEE Trans. Dielect. Electr. Insul.* 17 (4), 1284–1297. doi:10.1109/TDEI.2010.5539701

IEC (1991). *Artificial Pollution Tests on High-Voltage Insulators to Be Used on A.C. Systems, IEC 60507*. Available at: https://webstore.iec.ch/publication/16401.

Jiang, X., Shi, Y., Sun, C., and Zhang, Z. (2010). Evaluating the Safety Condition of Porcelain Insulators by the Time and Frequency Characteristics of LC Based on Artificial Pollution Tests. *IEEE Trans. Dielect. Electr. Insul.* 17 (2), 481–489. doi:10.1109/TDEI.2010.5448104

Khodsuz, M., and Mirzaie, M. (2015). Harmonics Ratios of Resistive Leakage Current as Metal Oxide Surge Arresters Diagnostic Tools. *Measurement* 70, 148–155. doi:10.1016/j.measurement.2015.03.048

Li, J., Caixin Sun, C., Wenxia Sima, fnm., Qing Yang, fnm., and Jianlin Hu, fnm. (2010). Contamination Level Prediction of Insulators Based on the Characteristics of Leakage Current. *IEEE Trans. Power Deliv.* 25 (1), 417–424. doi:10.1109/TPWRD.2009.2035426

Liu, Y., Yang, N., Dong, B., Wu, L., Yan, J., Shen, X., et al. (2020). Multi-Lateral Participants Decision-Making: A Distribution System Planning Approach with Incomplete Information Game. *IEEE Access* 8, 88933–88950. doi:10.1109/ACCESS.2020.2991181

Miyake, T., Seo, Y., Sakoda, T., and Otsubo, M. (2010). Relationship between Leakage Current and Pollution Deposits on the Surface of Polymeric Insulator. *IEEJ Trans. FM* 130 (11), 1037–1041. doi:10.1541/ieejfms.130.1037

Noman, M., Li, G., Wang, K., and Han, B. (2021). Electrical Control Strategy for an Ocean Energy Conversion System. *Prot. Control. Mod. Power Syst.* 6 (1), 12. doi:10.1186/s41601-021-00186-y

Pylarinos, D., Siderakis, K., and Pyrgioti, E. (2011). Measuring and Analyzing Leakage Current for Outdoor Insulators and Specimens. *Rev. Adv. Mater. Sci.* 29 (1), 31–53. doi:10.2217/NNM.11.108

Pylarinos, D., Theofilatos, K., Siderakis, K., Thalassinakis, E., Vitellas, I., Alexandridis, A. T., et al. (2012). Investigation and Classification of Field Leakage Current Waveforms. *IEEE Trans. Dielect. Electr. Insul.* 19, 2111–2118. doi:10.1109/TDEI.2012.6396971

Shen, X., Ouyang, T., Khajorntraidet, C., Li, Y., Li, S., and Zhuang, J. (2021). Mixture Density Networks-Based Knock Simulator. *Ieee/asme Trans. Mechatron.*, 1. doi:10.1109/TMECH.2021.3059775

Shen, X., and Raksincharoensak, P. (2021b). Pedestrian-aware Statistical Risk Assessment. *IEEE Trans. Intell. Transport. Syst.*, 1–9. doi:10.1109/TITS.2021.3074522

Shen, X., and Raksincharoensak, P. (2021a). Statistical Models of Near-Accident Event and Pedestrian Behavior at Non-signalized Intersections. *J. Appl. Stat.*, 1–21. doi:10.1080/02664763.2021.1962263

Shen, X., Zhang, Y., Sata, K., and Shen, T. (2020). Gaussian Mixture Model Clustering-Based Knock Threshold Learning in Automotive Engines. *Ieee/asme Trans. Mechatron.* 25, 2981–2991. doi:10.1109/TMECH.2020.3000732

Suda, T. (2001). Frequency Characteristics of Leakage Current Waveforms of an Artificially Polluted Suspension Insulator. *IEEE Trans. Dielect. Electr. Insul.* 8 (4), 705–709. doi:10.1109/94.946726

Yang, N., Huang, Y., Hou, D., Liu, S., Ye, D., Dong, B., et al. (2019). Adaptive Nonparametric Kernel Density Estimation Approach for Joint Probability Density Function Modeling of Multiple Wind Farms. *Energies* 12, 1356. doi:10.3390/en12071356

Yang, N., Liu, S., Deng, Y., and Xing, C. (2020). An Improved Robust SCUC Approach Considering Multiple Uncertainty and Correlation. *IEEJ Trans. Elec Electron. Eng.* 16 (1), 21–34. doi:10.1002/tee.23265

Yang, N., Yang, C., Wu, L., Shen, X., Jia, J., Li, Z., et al. (2021). Intelligent Data-Driven Decision-Making Method for Dynamic Multi-Sequence: An E-Seq2Seq Based SCUC Expert System. *IEEE Trans. Ind. Inf.* 40, 1. doi:10.1109/TII.2021.3107406

Zhu, B., Ding, F., and Vilathgamuwa, D. M. (2020). Coat Circuits for DC-DC Converters to Improve Voltage Conversion Ratio. *IEEE Trans. Power Electron.* 35, 3679–3687. doi:10.1109/TPEL.2019.2934726

Conflict of Interest: The authors declare that the research was conducted in the absence of any commercial or financial relationships that could be construed as a potential conflict of interest.

Publisher's Note: All claims expressed in this article are solely those of the authors and do not necessarily represent those of their affiliated organizations, or those of the publisher, the editors, and the reviewers. Any product that may be evaluated in this article, or claim that may be made by its manufacturer, is not guaranteed or endorsed by the publisher.

frontiers in Energy Research

ORIGINAL RESEARCH
published: 06 December 2021
doi: 10.3389/fenrg.2021.803631

OC-SLAM: Steadily Tracking and Mapping in Dynamic Environments

Zhenyu Wu[1], *Xiangyu Deng*[2], *Shengming Li*[3] *and Yingshun Li*[4]*

[1]School of Innovation and Entrepreneurship of DUT, Dalian University of Technology, Dalian, China, [2]Faculty of Electronic Information and Electrical Engineering, Dalian University of Technology, Dalian, China, [3]School of Computer Science and Technology, Dalian University of Technology, Dalian, China, [4]School of Control Science and Engineering, Dalian University of Technology, Dalian, China

Visual Simultaneous Localization and Mapping (SLAM) system is mainly used in real-time localization and mapping tasks of robots in various complex environments, while traditional monocular vision algorithms are struggling to cope with weak texture and dynamic scenes. To solve these problems, this work presents an object detection and clustering assisted SLAM algorithm (OC-SLAM), which adopts a faster object detection algorithm to add semantic information to the image and conducts geometrical constraint on the dynamic keypoints in the prediction box to optimize the camera pose. It also uses RGB-D camera to perform dense point cloud reconstruction with the dynamic objects rejected, and facilitates European clustering of dense point clouds to jointly eliminate dynamic features combining with object detection algorithm. Experiments in the TUM dataset indicate that OC-SLAM enhances the localization accuracy of the SLAM system in the dynamic environments compared with original algorithm and it has shown impressive performance in the localizition and can build a more precise dense point cloud map in dynamic scenes.

Keywords: SLAM, dynamic environment, object detection, dense point cloud reconstruction, point cloud clustering

OPEN ACCESS

Edited by:
Xun Shen,
Tokyo University of Agriculture and Technology, Japan

Reviewed by:
Fengqiu Liu,
Ningbo University of Technology, China
Shi Zhang,
Northeastern University, China

***Correspondence:**
Yingshun Li
leeys@dlut.edu.cn

Specialty section:
This article was submitted to Smart Grids, a section of the journal Frontiers in Energy Research

Received: *28 October 2021*
Accepted: *08 November 2021*
Published: *06 December 2021*

Citation:
Wu Z, Deng X, Li S and Li Y (2021) OC-SLAM: Steadily Tracking and Mapping in Dynamic Environments. Front. Energy Res. 9:803631. doi: 10.3389/fenrg.2021.803631

1 INTRODUCTION

The indoor mobile robot is a robot system composed of multi-sensor fusion perception, autonomous decision making, mission planning, and control, etc. And from the perspective of the global mobile robot consumer market, its market scale is expanding, and various smart factories have great industrial demand for robots to complete various production tasks. For complex working environments, the first problem in autonomous mobile robots is the accuracy of localization and environmental map construction (Huang et al., 2019; Shen et al., 2020a). There has been a lot of outstanding work on SLAM research (Mur-Artal and Tardós, 2017; Engel et al., 2014; Qin et al., 2018), so we can build on these foundational frameworks to deal with tough issues.

In dynamic scenes, if the SLAM system fails to complete loop closure detection, the accuracy of pose estimation is seriously affected by dynamic features because the algorithm builds a map of the moving keypoints, resulting in poor system robustness and easily losing the tracking of camera pose. On the one hand, to solve these problems, some algorithms incorporate semantic segmentation or instance segmentation at the front-end of the visual odometry to obtain accurate edge information of moving objects, avoiding the influence of moving points from the feature extraction (Bescos et al., 2018; Kaneko et al., 2018; Runz et al., 2018; Yu et al., 2018; Zhong et al., 2018). Bescos *et al.* present a dynamic SLAM system based on ORBSLAM2 (Mur-Artal and Tardós, 2017) with Mask-RCNN semantic segmentation (Bescos et al., 2018), which contains monocular, binocular, and RGB-D inputs, and the extracted dynamic ORB features are rejected by invoking the Mask-RCNN model, but this

system is mainly time-consuming in the semantic segmentation algorithm and cannot achieve real-time pose estimation. Kaneko *et al.* present a monocular vision SLAM with a deep learning-based semantic segmentation method, using DeepLab v2 semantic segmentation of the mask to reject dynamic points and using CARLA simulator to provide new datasets for testing (Kaneko et al., 2018), but also faces the challenge of real-time. Runz *et al.* present RGBD-SLAM based on the aforementioned semantic segmentation and geometric segmentation, which can track dynamic objects and build corresponding 3D models that can be applied in AR (Runz et al., 2018). Yu *et al.* present a five threads dynamic SLAM system based on ORBSLAM2, adding a SegNet semantic segmentation thread and a semantic map thread to the original ORBSLAM2, and running in real-time with P4000 GPU (Yu et al., 2018). Doherty *et al.* build an IMU sensor based, semantic segmentation SLAM system which introduces data association into the SLAM system optimization process and performs land marker optimization, camera pose estimation and semantic information association simultaneously (Doherty et al., 2020). However, their approaches are fail to meet the demand for real-time operation and the single semantic segmentation algorithm does not guarantee the robustness of the SLAM system in the complex operating environment of the robot.

On the other hand, some notable results use the optical flow method for dynamic/static segmentation to highlight the dynamic semantics in the RGB images and provide the precise camera pose estimation and background reconstruction for robots (Alcantarilla et al., 2012; Jaimez et al., 2017; Zhang et al., 2020; Yu et al., 2021). Alcantara *et al.* present dense scene flow into visual SLAM, which performs scene flow calculation on images, and detects moving objects in the environment by comparing the scene flow changes of features (Alcantarilla et al., 2012), but the shortcomings of their method have been clearly recognized that time consumption severely affects the optical flow method, which is also restricted by the constant luminosity hypothesis. In addition to the aforementioned improvements to the front-end visual odometry, Henein *et al.* present a factor graph based back-end optimization method that incorporates moving point factors for dynamic objects to form constraints on feature observations, camera poses and dynamic object movement by semantic segmentation algorithms (Henein et al., 2020). Recently, some notable works focus their research on data association for dealing with the connection between semantic objects and RGB images in dynamic environments (Bowman et al., 2017; Doherty et al., 2019; Yu and Lee, 2018; Ran et al., 2021), and allow for better application of semantic techniques in SLAM algorithms. Furthermore, to deal with the uncertainty of environment, a potential approach is to improve SLAM algorithm by combining with various optimization-based algorithms (Wu and Shen, 2018; Shen et al., 2021; Shen et al., 2020b; Le et al., 2021; Wu et al., 2021; Toyoda and Wu, 2021) for scholastic systems.

Inspired by recent researches based on the semantic algorithm, we investigate the problem of real-time localization and dense map construction for the indoor mobile robots and propose a novel RGB-D SLAM framework which leverages a faster object detection method to obtain semantic information from RGB image and perform a dense map constuction with dynamic objects rejected.

Specifically, the main contributions of the SLAM framework presented in this paper are shown below:

- We design a real-time combined mismatch rejection algorithm based on the lightweight YOLO-Fastest object detection algorithm and Euclidean clustering method (OC-SLAM) where a robot can detect bad keypoints from dynamic objects through semantic information and point cloud clustering information. Especially, OC-SLAM is robust and computationally efficient in dynamic scenes.
- We present a dense point cloud reconstruction with dynamic objects rejected in OC-SLAM which leverages depth camera to directly obtain the depth image of scenes and remove dynamic objects in complex environments with Kd tree in order to create highly-precise dense maps.
- We evaluate OC-SLAM on a RGB-D benchmark dataset with the other state-of-the-art SLAM methods, and the proposed method achieves improved accuracy and robustness in dynamic scenes.

In the following section of this paper, we provide the framework of the proposed method OC-SLAM with the modules in the semantic object detection thread and dense mapping thread. Then **Section 3** includes experimental comparison with the original ORB-SLAM2 algorithm on TUM RGB-D dataset (Sturm et al., 2012). Ultimately, **Section 4** contains a brief discussion of the conclusions and results.

2 SYSTEM OVERVIEW

The dynamic objects in the robot operating environment will seriously affect the estimation of camera poses and mapping accuracy of the algorithm. Similarly, SLAM systems with monocular vision cameras cannot obtain real metric scale information in real complex environments. To accurately detect the dynamic features in the image, an improved algorithm is presented in this paper, whose overall framework is shown in **Figure 1**. Based on the original ORBSLAM2 (Mur-Artal and Tardós, 2017), a dense map reconstruction thread and an object detection thread are added in the system, and the identification of dynamic objects and the dense point cloud map reconstruction with dynamic objects removed is implemented by these two threads.

2.1 Dynamic Object Detection

You only look once (YOLO-Fastest) algorithm is now known to be the fastest and lightest improved version of the open-source YOLO universal object detection algorithm (Qiuqiu, 2021), which can run in real-time on the low-cost devices and consists of the convolutional neural network (CNN) (Long et al., 2015), so this paper utilizes the YOLO-Fastest detection algorithm and combines the geometric epipolar constraint

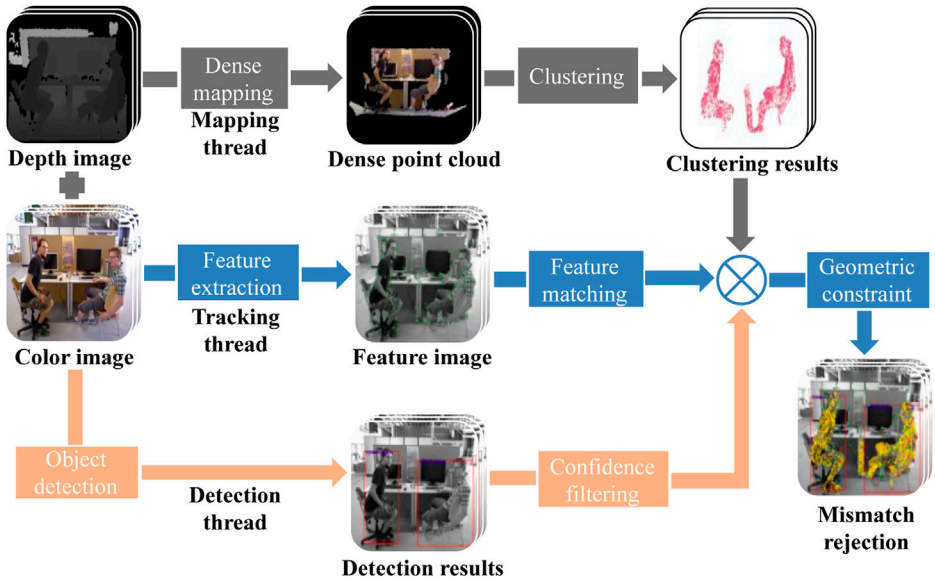

FIGURE 1 | The framework of the combined mismatch rejection algorithm, among which the tracking thread is as same as the original algorithm and the other two presented threads are added in the system.

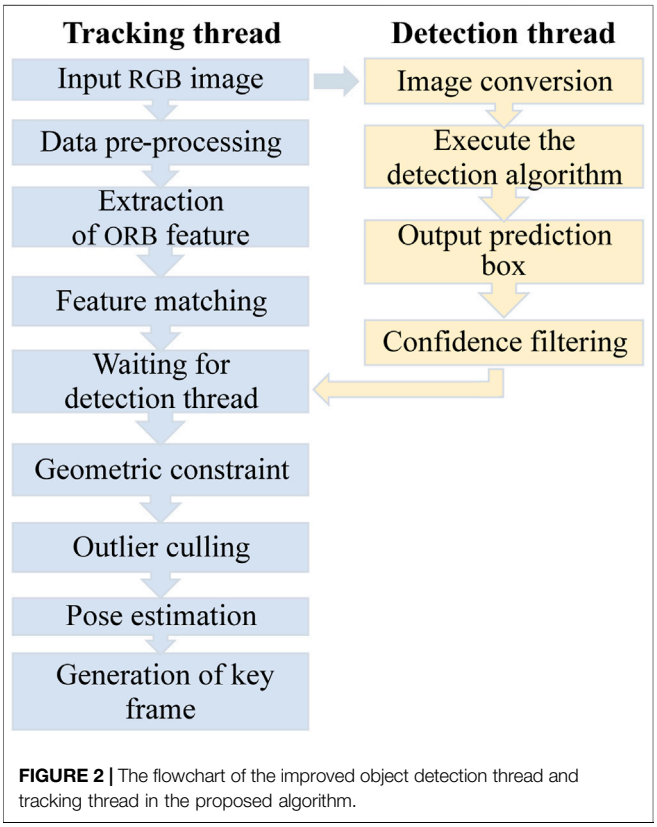

FIGURE 2 | The flowchart of the improved object detection thread and tracking thread in the proposed algorithm.

method for feature mismatch rejection, and further improves the original ORBSLAM2 system with three threads by adding the object detection thread for classification and localization of the original RGB image.

After the initialization of the SLAM system, the depth image is pre-processed to convert the depth map into real-scale depth data. As shown in **Figure 2**, The former thread is proposed to get the semantic information of the image and outputs the prediction box with confidence while the latter thread is improved to perform dynamic features rejection. The image is input to the YOLO algorithm for image detection after starting the object detection thread. While entering the main tracking thread, the extraction of image ORB features and the calculation of corresponding descriptors are started to complete the update of map points, and then the initial value of the camera pose is determined based on the working mode in which the main tracking thread is located, and the map points are reprojected and matched by the initial camera pose. The matching association between the map points and the current frame's features is discovered. When the system finishes feature matching, it exits the main tracking thread and waits for the YOLO object identification algorithm's detection result. Simultaneously, the prediction bounding box and confidence data are output by the object detection thread, where the results indicate the coordinates of the center point of a single prediction box, the width and height of the prediction box and the prediction confidence, and finally filter the information of the prediction boxes with confidence below 80, as shown in **Figure 3**, to obtain the prediction boxes of each target in the image.

2.2 Dynamic Geometrical Constraint

Therefore, when the object detection thread completes the image detection task, the matching feature pairs of the current frame are traversed within the main thread, and if the pixel coordinates of the features are within the prediction frame, the matching features outside the prediction frame are used to calculate the fundamental matrix F of the current frame and the previous

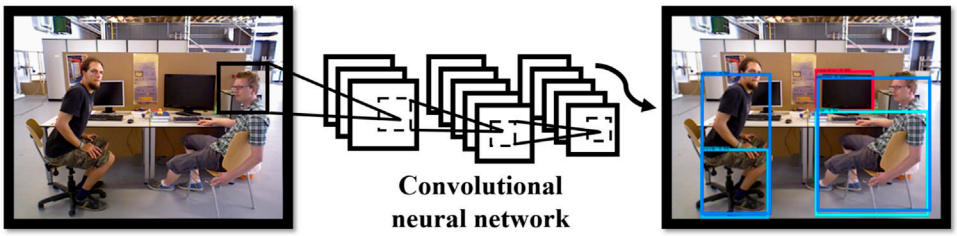

FIGURE 3 | The demonstration of YOLO-Fastest algorithm object detection for TUM dataset.

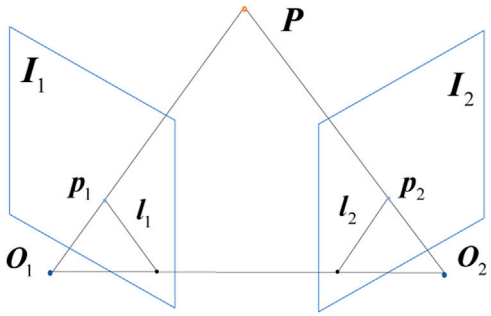

FIGURE 4 | The demonstration of epipolar geometry constraint.

images, and the distance from the reprojected epipolar lines to the corresponding matching features of the two adjacent frames is calculated by the method of geometric constraints (Andrew, 2001). If a point's distance error exceeds a threshold value set in a particular mode, the keypoint is considered an outlier, the corresponding map point matching association will be deleted. After the image feature extraction and matching process is completed, the camera pose estimation, local map establishment, and loop closure optimization process start implementation. As shown in **Figure 4**, p_1 and p_2 are the projection points of point P on the two camera images I_1 and I_2, respectively, the point p_1 should be in the projection of the epipolar lines l_1 under ideal circumstances. As shown in **Eq. 1**, the calculation of the fundamental matrix F between the current frame and the previous image can be defined as follows.

$$p_2^T F p_1 = 0, F = K^{-T} t \times R K^{-1}, \tag{1}$$

where K is the intrinsic matrix, t and R are the translation and rotation matrix, respectively. As a result, the distance between the keypoint and the reprojection line may be computed using the fundamental matrix, as shown in **Eq. 2**:

$$d = \frac{p_2^T F p_1}{\sqrt{A^2 + B^2 + C^2}}, \tag{2}$$

where d denotes the distance between points to lines, A, B and C denote the epipole line parameters. The minimum distance threshold is set based on the SLAM system's different modes (the distance threshold for the constant velocity motion model mode is smaller than the distance threshold for the keyframe mode), and if calculated distance exceeds threshold, the dynamic feature mismatch rejection is performed. Especially, the rejection of dynamic feature mismatch is not done when the SLAM system enters the relocalization mode because additional feature matching relationships are required for the initialization of the camera posture when the system enters the localization mode. Mismatch rejection is disabled in order to prevent the SLAM system from failing to initialize with insufficient features matching, which results in the loss of camera tracking. As shown in **Figure 5**, it depicts the result of dynamic feature rejection in the current frame

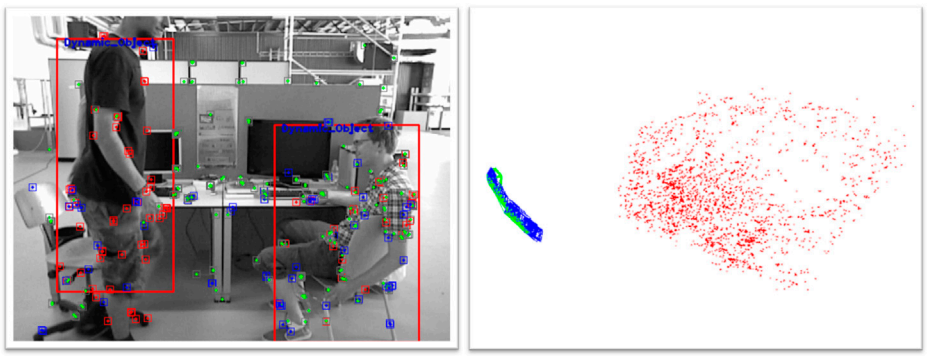

FIGURE 5 | Improved algorithm for current frame window with sparse point cloud map.

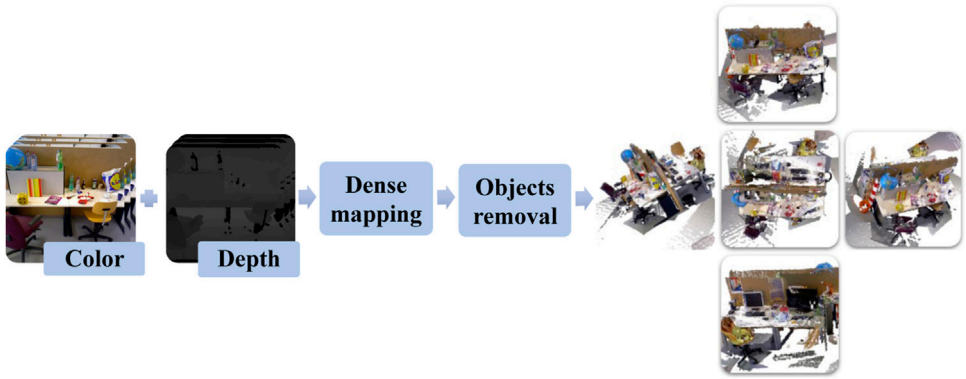

FIGURE 6 | The illustration of dense point cloud reconstruction thread in OC-SLAM system which is designed to perform the construction and clustering of dense point clouds without moving objects.

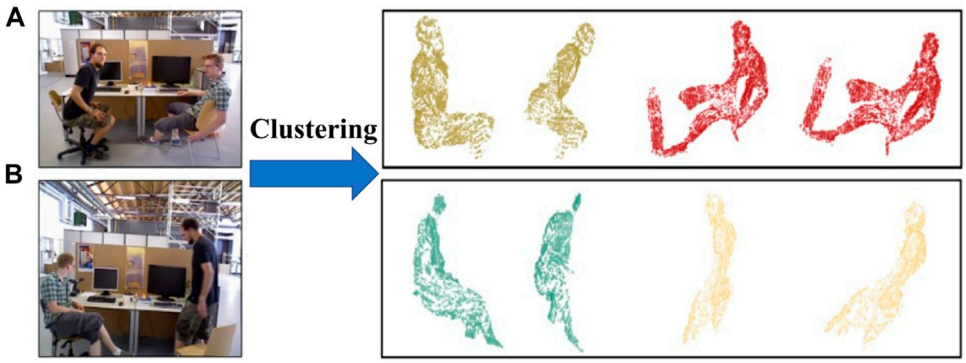

FIGURE 7 | Examples of Euclidean segmentation in TUM dataset, **(A)** is the point cloud segmentation with human bodies in the sitting posture, **(B)** are the clusters of the human body in the sitting and standing posture.

window with red dots indicating dynamic points and green dots indicating normal features, demonstrating that the enhanced method completes dynamic feature rejection properly. Moreover, the sparse point cloud generated from the features removes the map points from moving objects similarly in second image.

2.3 Dense Point Cloud Map Construction

Only sparse point cloud maps of features are built in the visualization thread of ORBSLAM2 system, which discards a large portion of the available map information. For this reason, sparse maps can not intuitively represent map information and are not available for other mission planning works such as navigation and obstacle avoidance by mobile robots that dense point cloud reconstruction is required. In this literature we introduce a new dense mapping thread to the ORBSLAM2 system, as shown in **Figure 6**, which is primarily utilized for dense point cloud reconstruction of the color and depth images Fernández-Madrigal (2012). If the coordinates of the picture sequence's points under the pixel coordinate $(\cdot)^P$ are $[u,v,1]^T$, then the coordinate values $[x,y,z]^T$ corresponding to those under the camera coordinate system $(\cdot)^C$ can be determined using **Eq. 3**:

$$\begin{cases} z = \dfrac{d}{s} \\ x = (u - c_x) \cdot \dfrac{z}{f_x} \\ y = (v - c_y) \cdot \dfrac{z}{f_y} \end{cases}, \tag{3}$$

where d is the depth value of the image and s is the depth metric scale of the camera. When the SLAM system inputs the depth map, its depth needs to be transformed to the real scale before it can be calculated. c_x, c_y, f_x and f_y are the camera intrinsic parameters. With the help of the camera extrinsic matrix, the pixel points can be converted from the coordinate system $(\cdot)^C$ to the real coordinates in the world coordinate system $(\cdot)^W$ as follows:

$$\begin{bmatrix} X \\ Y \\ Z \end{bmatrix} = (T \begin{bmatrix} x \\ y \\ z \end{bmatrix})_{1:3} = R \begin{bmatrix} x \\ y \\ z \end{bmatrix} + t, \tag{4}$$

where the coordinates $[X,Y,Z]^T$ represent the coordinate in the coordinate system $(\cdot)^W$, then the correspondence of points between the pixel coordinate and the world coordinate is

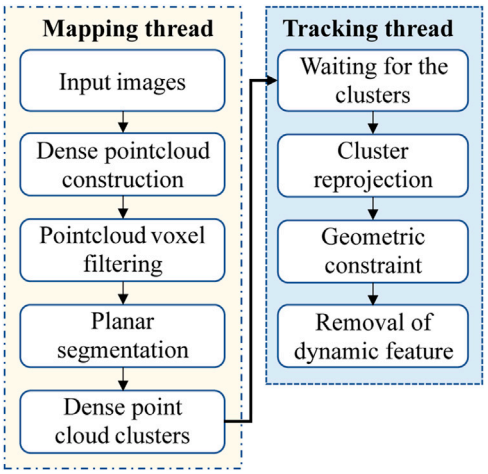

FIGURE 8 | The process of the rejection of dynamic objects. The presented mapping thread is illustrated in the yellow border which contains special operations on point clouds while the tracking thread is illustrated in the blue border which was improved to perform the task of dynamic keypoints rejection.

obtained, and the RGB value acquired from color image is set for each point cloud in the dense mapping thread, so that the basic dense point cloud is successfully constructed. However, in some practical applications, the pixel size of an image is usually 640 × 480, and the number of basic dense point clouds can be up to 300,000, so the point cloud voxel filtering and point cloud fusion are also needed for the basic point cloud.

2.4 Point Cloud Clustering Method

In this paper, the Euclidean Clustering method (Xiangyang et al., 2017) will be utilized to accomplish the point cloud segmentation task with the help of the YOLO-Fastest algorithm, which segments the point cloud data of the dense map into diverse single independent point cloud clusters. **Figure 7** illustrates the figures of two frames for 3D point cloud Euclidean clustering segmentation, when we input the depth image data from the dataset into the algorithm, a more accurate point cloud Euclidean segmentation result can be obtained with the assistance of semantic information from object detection method. Two point cloud clusters of human body in a sitting position with a well-defined point cloud profile extracted from the first image and the right corner of the table failed to remove through the filter since the human body is too close to the corner of table in Euclidean distance. In the second frame, a cluster of the human point cloud in sitting posture and a cluster of the human point cloud in standing posture are extracted, and the point cloud segmentation effect is better with no wrong clustering occurs.

2.5 Combined Mismatch Rejection Algorithm

The specified point cloud clusters in a frame are effectively separated after finishing the misson of Euclidean segmentation clustering of dense point cloud data. With this in mind, this paper presents a new mismatch rejection strategy algorithm for SLAM systems based on the Euclidean clustering method in OC-SLAM, which will be combined with an improved method based on the YOLO-Fastest object detection algorithm for jointly rejection of features of dynamic objects and ORB feature extraction in color image is carried out regularly on the main tracking thread, as shown in **Figure 8**. Moreover, feature matching is performed using different approaches depending on the incoming tracking mode and waits for the Euclidean clustering segmentation results in place once feature matching is accomplished. Accordingly, the dense mapping thread generates a sequence of independent point cloud clustering results by the use of the Euclidean clustering method, which includes point cloud dense reconstruction, voxel filtering and planar model segmentation. Afterwards, SLAM system set the dense build thread to idle. The tracking thread continues to implement after receiving the point cloud data from dense mapping thread, projecting each point cloud cluster into the pixel coordinate $(\cdot)^P$ using the equation:

$$\begin{cases} u = f_x \cdot x + c_x \\ v = f_y \cdot y + c_y \end{cases} . \tag{5}$$

The reprojection distance is calculated for the feature pairs contained in each point cloud according to the mismatching judgment method with respect to the epipolar constraint. Afterward, if more than half of the feature pairs fail to pass the geometrical constraint detection, the point cloud cluster is judged to be extracted from a moving object, and the features in the whole point cloud cluster and prediction box generated from the YOLO-Fastest algorithm are eliminated to perform the processing of moving objects removal in dynamic scenes.

2.6 Dynamic Object Rejection

Based on the previous work, the dense point cloud map is refined further and the clustered point cloud clusters of moving object in the base dense point cloud map are eliminated by constructing a Kd-Tree based on the results of point cloud Euclidean clustering, resulting in an environment map devoid of dynamic objects. As shown in **Figure 9**, two sets of color maps and depth images are input for dense construction: **Figure 9A** is the original color image, **Figure 9B** is the result of dense point cloud reconstruction and **Figure 9C** is the dense point cloud map with dynamic objects removed in which the point cloud clusters belonging to moving objects are essentially removed using the Euclidean clustering algorithm.

3 EXPERIMENTALS AND RESULTS

In this section, the improved algorithm is tested and validated on the TUM dataset from the Technical University of Munich, which collects image data in different experimental environments using Microsoft's Kinect camera and provides camera trajectory groundtruth for each dataset to evaluate the accuracy of the SLAM algorithm. In this research, dynamic and static

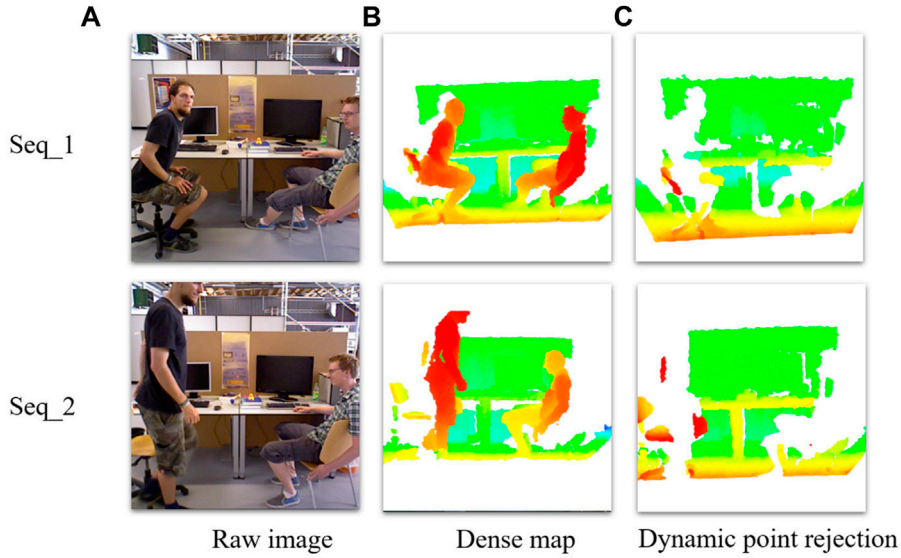

FIGURE 9 | (A) are the raw images, **(B)** are the point cloud dense reconstruction, (C) are the dense reconstruction with dynamic object rejection from which it can be seen that the clusters of moving human body in the dataset are removed by the improved algorithm.

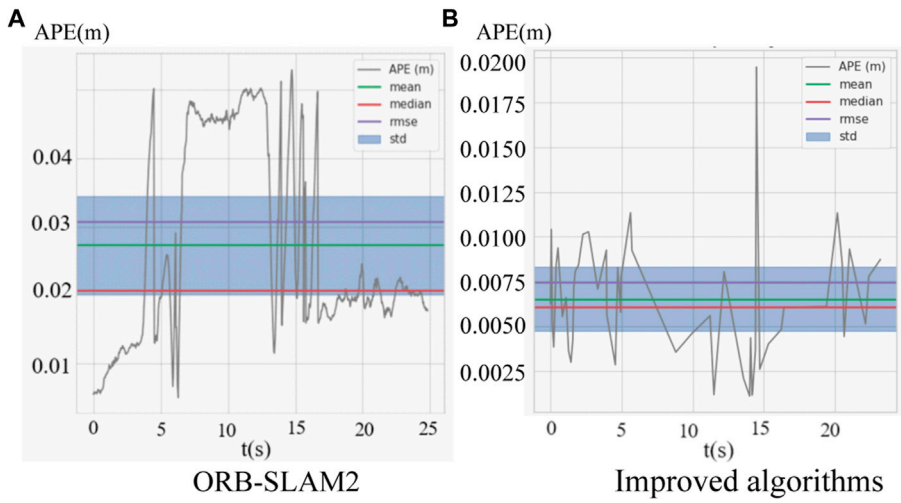

FIGURE 10 | (A) is the absolute trajectory error distribution of the combined improved algorithm, **(B)** is the absolute trajectory error distribution of the ORBSLAM2.

environment data are utilized to test the enhanced algorithm's accuracy of camera pose estimation and dense map construction performance.

3.1 Trajectory Estimation Experiments

In order to verify the robustness and accuracy of the improved algorithm's pose estimation, experiments under different complex environments are designed in this paper. The Root Mean Squared Error (RMSE) is used as the evaluation criterion for the absolute camera trajectory error (Sturm et al., 2012), and the RMSE of the estimated poses at all moments is calculated as follows:

$$RMSE(E) = \frac{1}{n}\sum_{t=1}^{n} \|trans(E_t)\|^2, \tag{6}$$

where error E_t denotes the absolute trajectory estimation error (ATE) of the SLAM system at moment t, which is obtained by the calculation of the difference between the estimated trajectory of the camera pose and the groundtruth of the dataset. $trans(\cdot)$ indicates the translation of absolute trajectory estimation error E_t and the enhancement effect in the experiment is calculated as the relative enhancement rate of the combined improved algorithm trajectory error with respect to the original algorithm. As shown in **Figure 10**, **Figure 10A** is the absolute trajectory error graph of the

TABLE 1 | The comparison of absolute trajectory error of pose estimation in TUM dataset.

Image sequence	ORB-SLAM2(m)			Proposed(m)			Improvements(%)		
	RMSE	Mean	Media	RMSE	Mean	Media	RMSE	Mean	Media
walking_static	0.325	0.284	0.213	0.007	0.006	0.006	97.8	97.8	97,1
walking_xyz	0.756	0.655	0.653	0.129	0.119	0.118	84.1	81.7	81.9
walking_half	0.426	0.433	0.414	0.083	0.085	0.080	80.4	80.3	80.6
sitting_static	0.008	0.008	0.007	0.008	0.008	0.007	−1.1	−3.7	2.6

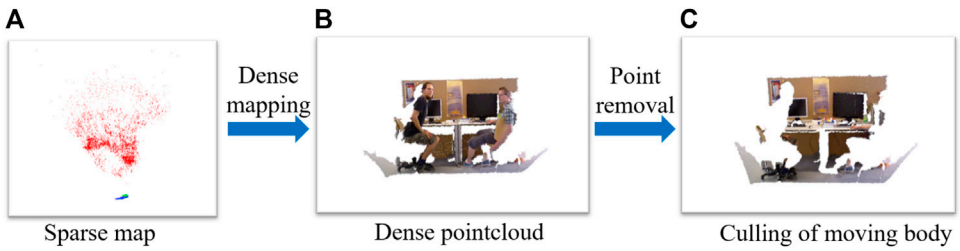

FIGURE 11 | The illustration of presented algorithm for dense point cloud map construction performance in the normal dataset, **(A)** is the sparse map, **(B)** is the dense point cloud map construction result, **(C)** is the dense map with moving body rejected.

FIGURE 12 | The illustration of presented algorithm for dense point cloud map construction performance in the dynamic dataset, **(A)** is the sparse map, **(B)** is the dense point cloud map construction result.

original algorithm without Loop closure and **Figure 10B** is the error evaluation graph of the combined algorithm, it can be seen that the majority of the time the error is below 0.01 m in the improved algorithm except for some extreme cases. Notably, at the moment of object detection algorithm failure, the Euclidean clustering module can continue to carry out the rejection of mismatch, which complements the object detection module to increase the robustness of the system and reduces the overall trajectory absolute error. Likewise, indicators of the median and mean trajectory error have significantly improved. Further, the error comparison between the improved algorithm and the original algorithm is shown in **Table 1**. And the evaluation indexes of the improved algorithm in the dynamic data sequences walking_static, walking_xyz, walking_half without loop closure are better than the original algorithm while the accuracy improvement effect is up to 97.8%, In spite of this, the accuracy in the image sequences in the static environment is approximately equal to that of the original algorithm in the static environment, indicating that the improvement modules in the algorithm do not lose too much algorithm performance. Importantly, the processing time per frame is only 97 ms on a low-performance processor, while the DynaSLAM (Bescos et al., 2018) algorithm takes 195 ms for the Mask R-CNN module alone using the Nvidia Tesla M40 GPU. Therefore, compared with the improved method using Mask R-CNN, the improved algorithm in this paper greatly improves the operation speed of the algorithm without excessive loss of accuracy.

3.2 Dense Reconstruction Experiment

Based on the successful detection and recognition of dynamic point cloud clusters, this paper performs point cloud dense building experiments on the improved algorithm, inputting normal image sequences in TUM dataset and image sequences in dynamic scenes to compare the dense building performance of the improved algorithm in two different dataset environments. As shown in **Figure 11**, in the

dense reconstruction experiment under the normal environment dataset, **Figure 11A** shows the sparse point cloud map established by the original system where the red points represent the map points successfully observed and the black points represent the map points observed in the current frame. Since the algorithm only calculates map points from the extracted features and performs fusion operation for redundant map points, only the sparse point cloud map is established. **Figures 11B,C** show the dense point cloud map built by the improved algorithm, which completely recovers the point cloud data in the dataset and further extracts more image information from the image sequence, making the mapping performance of the SLAM system more intuitive and the normal line of the map can be further calculated subsequently, thus reconstructing the network from the point cloud and converting the point cloud into a grid map. By contrast, as shown in **Figure 12**, in the dense reconstruction experiments under dynamic scene datasets, **Figure 12A** shows the sparse point cloud map built by the original system, which is built with low accuracy and fluctuating map updating with wrong map points due to the influence brought by fast-moving dynamic objects, thus leading to poor back-end nonlinear optimization of camera poses and map points. With this in mind, **Figure 12B** shows the dense point cloud map built by the improved algorithm, which not only recovers the specific scenes in the dataset completely but also uses the YOLO-Fastest object detection algorithm and the Euclidean clustering algorithm to eliminate the dynamic objects clusters in the dynamic scenes and retains the information of static objects in the point cloud map, which improves the robustness and accuracy of the dense point cloud mapping.

4 CONCLUSION

In this paper, we present an improved semantic SLAM algorithm (OC-SLAM) based on YOLO-Fastest object detection and Euclidean clustering method to reduce the impact of dynamic features on the accuracy of camera trajectory calculation by special processing of tricky issues in dynamic scenes to solve the problem of pose estimation and dense map construction. In comparison to Mask R-CNN and other semantic segmentation recognition methods, the proposed algorithm in this paper can greatly accelerate computation speed by leveraging the characteristics of the YOLO-Fastest algorithm to meet the algorithm's real-time requirements without sacrificing pose estimation accuracy. The absolute trajectory error(ATE) experiments in the TUM dataset indicate that this approach can increase accuracy on a low-performance embedded devices and build a dense point cloud map in the complex environment with dynamic objects eliminated.

DATA AVAILABILITY STATEMENT

The raw data supporting the conclusion of this article will be made available by the authors, without undue reservation.

ETHICS STATEMENT

Written informed consent was obtained from the individual(s) for the publication of any potentially identifiable images or data included in this article.

AUTHOR CONTRIBUTIONS

ZW and XD contributed to the conception or design of the work; or the acquisition, analysis or interpretation of data for the work; XD drafted the work or revised it critically for important intellectual content; SL provided approval for publication of the content; YL agrees to be accountable for all aspects of the work in ensuring that questions related to the accuracy or integrity of any part of the work are appropriately investigated and resolved.

FUNDING

This work was financially supported by the Department of Science and Technology of Liaoning Province on "Research on the key technology of distributed energy networking based on wireless energy transfer" (Grand No. ZX20180613).

SUPPLEMENTARY MATERIAL

The Supplementary Material for this article can be found online at: https://www.frontiersin.org/articles/10.3389/fenrg.2021.803631/full#supplementary-material

REFERENCES

Alcantarilla, P. F., Yebes, J. J., Almazan, J., and Bergasa, L. M. (2012). "On Combining Visual Slam and Dense Scene Flow to Increase the Robustness of Localization and Mapping in Dynamic Environments," in 2012 IEEE International Conference on Robotics and Automation, 1290–1297. doi:10.1109/ICRA.2012.6224690

Andrew, A. (2001). Multiple View Geometry in Computer Vision. *Kybernetes.* 30, 1333. doi:10.1108/k.2001.30.9_10.1333.2

Bescos, B., Facil, J. M., Civera, J., and Neira, J. (2018). Dynaslam: Tracking, Mapping, and Inpainting in Dynamic Scenes. *IEEE Robot. Autom. Lett.* 3, 4076–4083. doi:10.1109/LRA.2018.2860039

Bowman, S. L., Atanasov, N., Daniilidis, K., and Pappas, G. J. (2017). "Probabilistic Data Association for Semantic Slam," in 2017 IEEE International Conference on Robotics and Automation (ICRA), 1722–1729. doi:10.1109/ICRA.2017.7989203

Doherty, K., Fourie, D., and Leonard, J. (2019). "Multimodal Semantic Slam With Probabilistic Data Association," in 2019 International Conference on Robotics and Automation, Montreal, QC, Canada (ICRA), 2419–2425. doi:10.1109/ICRA.2019.8794244

Doherty, K. J., Baxter, D. P., Schneeweiss, E., and Leonard, J. J. (2020). "Probabilistic Data Association via Mixture Models for Robust Semantic Slam," in 2020 IEEE International Conference on Robotics and Automation (ICRA), 1432–1882. doi:10.1109/icra40945.2020.9197382

Engel, J., Schöps, T., and Cremers, D. (2014). "Lsd-slam: Large-Scale Direct Monocular Slam," in *Computer Vision – ECCV 2014*. Editors D. Fleet,

T. Pajdla, B. Schiele, and T. Tuytelaars (Cham: Springer International Publishing), 834–849. doi:10.1007/978-3-319-10605-2_54

Fernández-Madrigal, J.-A. (2012). *Simultaneous Localization and Mapping for Mobile Robots: Introduction and Methods: Introduction and Methods (IGI Global), Hershey, Pennsylvania, USA, IGI Global*.

Henein, M., Zhang, J., Mahony, R., and Ila, V. (2020). "Dynamic Slam: The Need for Speed," in 2020 IEEE International Conference on Robotics and Automation (ICRA), 2123–2129. doi:10.1109/ICRA40945.2020.9196895

Huang, B., Zhao, J., and Liu, J. (2019). A Survey of Simultaneous Localization and Mapping. arXiv preprint arXiv:1909.05214.

Jaimez, M., Kerl, C., Gonzalez-Jimenez, J., and Cremers, D. (2017). "Fast Odometry and Scene Flow from Rgb-D Cameras Based on Geometric Clustering," in 2017 IEEE International Conference on Robotics and Automation (ICRA), 3992–3999. doi:10.1109/ICRA.2017.7989459

Kaneko, M., Iwami, K., Ogawa, T., Yamasaki, T., and Aizawa, K. (2018). "Mask-slam: Robust Feature-Based Monocular Slam by Masking Using Semantic Segmentation," in 2018 IEEE/CVF Conference on Computer Vision and Pattern Recognition Workshops (CVPRW), 371–3718. doi:10.1109/CVPRW.2018.00063

Le, S., Wu, Y., Guo, Y., and Del Vecchio, C. (2021). "Game Theoretic Approach for a Service Function Chain Routing in Nfv with Coupled Constraints," in IEEE Transactions on Circuits and Systems II: Express Briefs, 1. doi:10.1109/TCSII.2021.3070025

Long, J., Shelhamer, E., and Darrell, T. (2015). "Fully Convolutional Networks for Semantic Segmentation," in Proceedings of the IEEE conference on computer vision and pattern recognition, 3431–3440. doi:10.1109/cvpr.2015.7298965

Mur-Artal, R., and Tardós, J. D. (2017). Orb-slam2: An Open-Source Slam System for Monocular, Stereo, and Rgb-D Cameras. *IEEE Trans. Robot.* 33, 1255–1262. doi:10.1109/TRO.2017.2705103

Qin, T., Li, P., and Shen, S. (2018). Vins-mono: A Robust and Versatile Monocular Visual-Inertial State Estimator. *IEEE Trans. Robot.* 34, 1004–1020. doi:10.1109/TRO.2018.2853729

[Dataset] Qiuqiu, D. (2021). Yolo-fastest: yolo-fastest-v1.1.0. Available at: https://github.com/dog-qiuqiu/Yolo-Fastest.

Ran, T., Yuan, L., Zhang, J., He, L., Huang, R., and Mei, J. (2021). Not only Look but Infer: Multiple Hypothesis Clustering of Data Association Inference for Semantic Slam. *IEEE Trans. Instrum. Meas.* 70, 1–9. doi:10.1109/TIM.2021.3074954

Runz, M., Buffier, M., and Agapito, L. (2018). "Maskfusion: Real-Time Recognition, Tracking and Reconstruction of Multiple Moving Objects," in 2018 IEEE International Symposium on Mixed and Augmented Reality (ISMAR), 10–20. doi:10.1109/ISMAR.2018.00024

Shen, X., Ouyang, T., Khajorntraidet, C., Li, Y., Li, S., and Zhuang, J. (2021). Mixture Density Networks-Based Knock Simulator. *Ieee/asme Trans. Mechatron.*, 10. doi:10.1109/TMECH.2021.3059775

Shen, X., Zhang, X., Ouyang, T., Li, Y., and Raksincharoensak, P. (2020a). Cooperative Comfortable-Driving at Signalized Intersections for Connected and Automated Vehicles. *IEEE Robot. Autom. Lett.* 5, 6247–6254. doi:10.1109/LRA.2020.3014010

Shen, X., Zhang, Y., Sata, K., and Shen, T. (2020b). Gaussian Mixture Model Clustering-Based Knock Threshold Learning in Automotive Engines. *Ieee/asme Trans. Mechatron.* 25, 2981–2991. doi:10.1109/TMECH.2020.3000732

Sturm, J., Engelhard, N., Endres, F., Burgard, W., and Cremers, D. (2012). "A Benchmark for the Evaluation of Rgb-D Slam Systems," in 2012 IEEE/RSJ International Conference on Intelligent Robots and Systems, 573–580. doi:10.1109/IROS.2012.6385773

Toyoda, M., and Wu, Y. (2021). Mayer-type Optimal Control of Probabilistic Boolean Control Network With Uncertain Selection Probabilities. *IEEE Trans. Cybern.* 51, 3079–3092. doi:10.1109/TCYB.2019.2954849

Wu, Y., Guo, Y., and Toyoda, M. (2021). Policy Iteration Approach to the Infinite Horizon Average Optimal Control of Probabilistic Boolean Networks. *IEEE Trans. Neural Netw. Learn. Syst.* 32, 2910–2924. doi:10.1109/TNNLS.2020.3008960

Wu, Y., and Shen, T. (2018). A Finite Convergence Criterion for the Discounted Optimal Control of Stochastic Logical Networks. *IEEE Trans. Automat. Contr.* 63, 262–268. doi:10.1109/TAC.2017.2720730

Xiangyang, C., Yang, Y., and Yunfei, X. (2017). Measurement of Point Cloud Data Segmentation Based on Euclidean Clustering Algorithm. *Bull. Surv. Mapp.* 0, 27–31. doi:10.13474/j.cnki.11-2246.2017.0342

Yu, C., Liu, Z., Liu, X.-J., Xie, F., Yang, Y., Wei, Q., et al. (2018). "Ds-Slam: A Semantic Visual Slam Towards Dynamic Environments," in 2018 IEEE/RSJ International Conference on Intelligent Robots and Systems (IROS), 1168–1174. doi:10.1109/IROS.2018.8593691

Yu, H. W., and Lee, B. H. (2018). "A Variational Feature Encoding Method of 3d Object for Probabilistic Semantic Slam," in 2018 IEEE/RSJ International Conference on Intelligent Robots and Systems (IROS), 3605–3612. doi:10.1109/IROS.2018.8593831

Yu, X., Wu, Y., Sun, X.-M., and Zhou, W. (2021). A Memory-Greedy Policy With Guaranteed Convergence for Accelerating Reinforcement Learning. *J. Autonomous Vehicles Syst.* 1, 011005–011012. doi:10.1115/1.4049539

Zhang, T., Zhang, H., Li, Y., Nakamura, Y., and Zhang, L. (2020). "Flowfusion: Dynamic Dense Rgb-D Slam Based on Optical Flow," in 2020 IEEE International Conference on Robotics and Automation (ICRA), 7322–7328. doi:10.1109/ICRA40945.2020.9197349

Zhong, F., Wang, S., Zhang, Z., Chen, C., and Wang, Y. (2018). "Detect-Slam: Making Object Detection and Slam Mutually Beneficial," in 2018 IEEE Winter Conference on Applications of Computer Vision (WACV), 1001–1010. doi:10.1109/WACV.2018.00115

Conflict of Interest: The authors declare that the research was conducted in the absence of any commercial or financial relationships that could be construed as a potential conflict of interest.

frontiers in Energy Research

BRIEF RESEARCH REPORT
published: 15 December 2021
doi: 10.3389/fenrg.2021.800906

Research on Combined Electricity and Heating System Scheduling Method Considering Multi-Source Ring Heating Network

Jing Ye, Danyang Zhao, Lei Zhang, Zhenghua Li and Tao Zhang*

College of Electrical Engineering and New Energy, China Three Gorges University, Yichang, China

Heating network constraint is one of the important factors that affect the scale of electro-thermal coupling scheduling. This paper first establishes an electrothermal coupling scheduling model considering the multi-source ring heating network pipe structure and then proposes a method of simplifying a multi-source cyclic heating network topology approximation. Second, the electrothermal coupling scheduling system is coordinated and solved. Finally, Through the simulation example results, the annular heating network topological approximate equivalent can simplify the model complexity of the original heating network while also retaining the thermal dynamic characteristics of the initial multi-source ring heating network. This study will greatly improve the efficiency of solving the electrothermal coupling system.

Keywords: combined electric and thermal dispatch system, multi-source combined heating ring network, model simplification, topological equivalent method, combined heat and power scheduling

OPEN ACCESS

Edited by:
Zhenhao Tang,
Northeast Electric Power University, China

Reviewed by:
Feng Zheng,
Fuzhou University, China
Zhu Zhang,
Hefei University of Technology, China

****Correspondence:***
Lei Zhang
leizhang3188@163.com

Specialty section:
This article was submitted to Smart Grids, a section of the journal Frontiers in Energy Research

Received: *24 October 2021*
Accepted: *12 November 2021*
Published: *15 December 2021*

Citation:
Ye J, Zhao D, Zhang L, Li Z and Zhang T (2021) Research on Combined Electricity and Heating System Scheduling Method Considering Multi-Source Ring Heating Network. Front. Energy Res. 9:800906. doi: 10.3389/fenrg.2021.800906

INTRODUCTION

The Combined Electricity and Heating System can realize the cascade utilization of different energy efficiency, which is an important way for the low-carbon economic operation of the power generation link. Considering the heat storage characteristics of the District Heating Network (DHN) can bring coordination and flexibility to the entire coupled electricity–heat energy system. In recent years, many scholars have studied the heat storage characteristics of heat network pipes (Li et al., 2021; Tang et al., 2021). The node method is effective to describe the temperature dynamic model of DHN (Li et al., 2017; Zheng et al., 2018; Wang et al., 2019; Yu et al., 2019; Shen et al., 2020; Shen et al., 2021; Shen and Raksincharoensak, 2021). The above study only considers the supply pipe network as a tree heating network structure which is harmful to the solution of the electrothermal coupling scheduling model. However, it does not match the structure of the multi-heat source combined with the multi-heat source, which will directly affect the applicability of the model.

Further, compared with the conventional tree heating network structure, the different heat sources of the multi-source cyclic heating network structure can be spared to each other, and the mutual coordination provides heat (Tian et al., 2017; Yang et al., 2019a; Shi et al., 2020; Yang, 2020). The heating network structure has been applied in some cities in the Nordics and China (Wu et al., 2019). Therefore, it is possible to further improve the flexibility between the electrothermal coupling system in the electrothermal coupling schedule. The scale and laying area of the actual heating pipe network are very huge, and it has brought difficulties to the solution of the model. In recent years, scholars have conducted research on reducing the complexity of scheduling models (Jiang et al.,

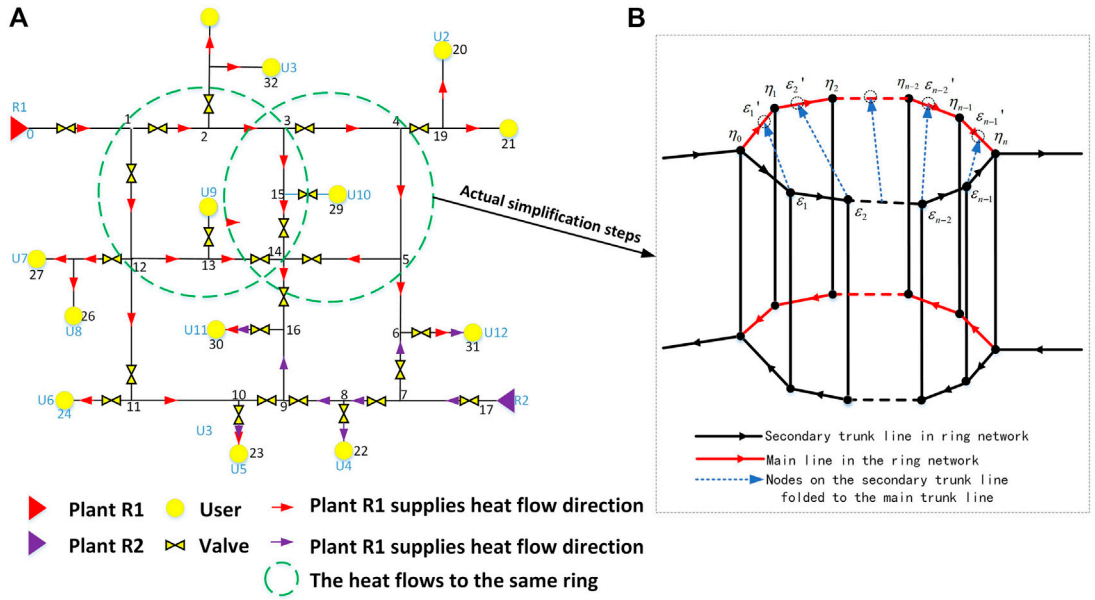

FIGURE 1 | (A) Two-heat source heating pipe network diagram under actual conditions. **(B)** Simplification process of general ring heating pipe network.

2019; Lu et al., 2019). Document (Larsen et al., 2002) is subtracted into a conventional tree heating network, but the actual multi-heat source combined heating network is more complex. The traditional simplification method cannot be applied to the actual operation of the current large-scale multi-heat source ring network.

In response to the questions raised above, this paper proposes a combined heat and power scheduling method based on ring heating network topological approximate equivalent. For the complex topology of the ring heating network, topology equivalent transformation and pipeline node aggregation are carried out on ring heating pipeline under the condition of ensuring accuracy, and the electric-thermal joint scheduling model is solved. There are many ways to solve the model (Yang et al., 2019b; Yang et al., 2021a; Yang et al., 2021b; Zhang et al., 2021). Finally, the effectiveness and accuracy of the method mentioned in this study is verified by example analysis.

TOPOLOGICAL EQUIVALENT METHOD OF LOOP REMOVAL FOR MULTI-HEAT SOURCE RING HEAT GRID

Topological Approximate Equivalent Method

In the actual multi-heat source heating ring network, due to the joint heating of multiple heat sources, the heat flow direction flowing through the same ring can be divided into the same direction and different direction, as shown in **Figure 1A**. On the basis of retaining most dynamic characteristics of the original pipe, this section will be used to topologically approximate the annular pipe network of the condition that satisfies the same flow direction and polymerizes the topology of the relatively simple tree network then use the node method to model the temperature dynamic model of DHN after the simplification. For heating networks and their models, the physical parameters of the pipe and the state variables of heat transfer process are very important. Its physical parameters are heating network topologies and pipeline parameters such as pipe mass flow m, pipe cross-sectional area S, pipe length L, pipe heat transfer coefficient u, etc. The state variable parameters are each load node temperature T_i, each node temperature T_x passed during water flow transfer, and the heat source to the time delay τ of each load node.

For the ring-shaped heating pipe network with the same heat flow (marked in green in **Figure 1A**), it can be equivalently simplified into a polymerization pipe. In order to ensure that the dynamic characteristics of heat transfer after the topological transformation of the heating network are equivalent, the heating network state variable needs to meet the following thermal equivalent conditions:

Assumption Condition 1: The total volume of water in the pipeline before and after the simplification of the model structure remains unchanged.

$$\sum_{x\in V^+} V_x' = \sum_{x\in V^+} V_x \tag{1}$$

In **Formula (1)**, x represents any pipe, and V_x represents the water volume of the conduit x. V^+ represents a collection of all pipes in the heating network, the tag $'$ represents the corresponding parameters after the heating network topology is equivalent.

Assumption Condition 2: The mass flow of each sub-branch flow into and out of each node remains unchanged.

$$m_x' = m_x \tag{2}$$

In **Formula (2)**, m_x represents the mass flow of water in the pipe.

Assumption Condition 3: The temperature of the node before and after polymerization does not change.

$$T_x' = T_x \tag{3}$$

In **Formula (3)**, T_x represents the temperature of any node before and after polymerization.

When the above three thermal equivalent conditions are met, the operating time of heating water in the pipe can be expressed as

$$\tau = \frac{V \cdot \rho}{m} \tag{4}$$

On the basis of preserving the thermal dynamic characteristics of the original pipe, the process of loop removal is essentially a topological approximate equivalent method which changes the original pipeline parameters to a tree-shaped heating pipe network, as shown in **Figure 1B**. Before the ring network is removed, this paper takes the starting point of the ring network shunting as the initial point and defines the ring heating network after shunting as the main line and secondary line. According to **Formula (4)**, the heat flow is obtained by the starting point to flow through the time required for each node, and the time delay flowing through the respective nodes on the main/secondary line is η_n/ε_n, where n represents the time set that flows through the main/secondary trunk nodes. The resulting time is arranged in size to obtain the time set sequence φ. φ is a time series consisting of ε and η. The nodes that have not alternated in the collection φ are considered a redundant node, such as $\varepsilon_{i-1}, \varepsilon_i$ in $\varepsilon_{n-3}, \eta_{i-2}, \varepsilon_{i-1}, \varepsilon_i, \eta_{i+1}, \varepsilon_{i+2}$, where i represents any node on the pipe. The redundant node is removed by conventional tree heating network simplification (Wu et al., 2019). After the redundant node is removed, the new φ is obtained as an alternating time sequence that occurs by ε and η.

$$\varphi: \left\{\tau_{\eta 0}, \tau_{\varepsilon 1}, \tau_{\eta 1}, \tau_{\varepsilon 2}, \tau_{\eta 2}, \cdots, \tau_{\eta \varepsilon - 1}, \tau_{\eta n - 1}, \tau_{\eta n}\right\} \tag{5}$$

The secondary trunk is aggregated to the main line. The mass flow of each pipeline after polymerization is

$$m_{\varepsilon_i}' = m_{\varepsilon_i} + m_{\eta_i} \tag{6}$$

$$m_{\eta_i}' = m_{\varepsilon_{i+1}} + m_{\eta_i} \tag{7}$$

In the above **Formulas (6) and (7)**, m_{η_i} and m_{ε_i} represent the mass flow of the main trunk and the secondary trunk polymerization.

The weighting average of the mass flow of each conduit on the secondary trunk and the weight of the mass flow corresponding to the main line can delay the flow of water flow through the new polymerization node time delay as follows:

$$\tau_{\varepsilon_i}' = \frac{m_{\eta_i}}{m_{\eta_i} + m_{\varepsilon_i}} \sum_{\theta=1}^{i} \tau_{\eta_\theta} + \frac{m_{\varepsilon_i}}{m_{\eta_i} + m_{\varepsilon_i}} \sum_{\theta=1}^{i} \tau_{\varepsilon_\theta} \tag{8}$$

$$\tau_{\eta_i}' = \frac{m_{\eta_i}}{m_{\eta_i} + m_{\varepsilon_{i+1}}} \sum_{\theta=1}^{i} \tau_{\eta_\theta} + \frac{m_{\varepsilon_i}}{m_{\eta_i} + m_{\varepsilon_{i+1}}} \sum_{\theta=1}^{i} \tau_{\varepsilon_\theta} \tag{9}$$

The equivalent water volume of each pipeline is obtained by **Formulas (4)**, **(8)**, and **(9)**.

$$V_{\varepsilon_i}' = \frac{1}{\rho}\left(m_{\varepsilon_i} + m_{\eta_i}\right)\left(\frac{m_{\eta_i}}{m_{\eta_i} + m_{\varepsilon_i}} \sum_{\theta=1}^{i} \tau_{\eta_\theta} + \frac{m_{\varepsilon_i}}{m_{\eta_i} + m_{\varepsilon_i}} \sum_{\theta=1}^{i} \tau_{\eta_\theta}\right) \tag{10}$$

$$V_{\eta_i}' = \frac{1}{\rho}\left(m_{\varepsilon_{i+1}} + m_{\eta_i}\right)\left(\frac{m_{\eta_i}}{m_{\eta_i} + m_{\varepsilon_{i+1}}} \sum_{\theta=1}^{i} \tau_{\eta_\theta} + \frac{m_{\varepsilon_i}}{m_{\eta_i} + m_{\varepsilon_{i+1}}} \sum_{\theta=1}^{i} \tau_{\varepsilon_\theta}\right) \tag{11}$$

The current flow rate of the original carrier in the main trunk line is the initial flow rate. By changing the volume of the pipeline before and after polymerization, the flow rate of the heating carrier in the pipeline polymerization is kept constant, then the tube length is determined based on the piping of the heat flow through the polymerization in the conduit and the ratio of the predecessor travel time during the pipeline. The equivalent length L of each pipe obtained by **Formula (8)** can be obtained.

$$L_{\varepsilon_i}' = \left(\sum_{\theta=1}^{i} \tau_{\varepsilon\theta} / \sum_{\theta=1}^{i} \tau_{\eta\theta}\right) L_{\eta_i} \tag{12}$$

$$L_{\eta_i}' = L_{\eta_i} - L_{\varepsilon_i}' \tag{13}$$

where $\sum_{\theta=1} \tau_{\varepsilon_\theta}$, $\sum_{\theta=1} \tau_{\eta_\theta}$ respectively represent the sum of the time it takes for the heat flow of all nodes in the secondary trunk line and the main trunk line to flow through the pipe 1 to pipe i.

Bring **Eqs (10)–(13)** to volume formula equivalent cross-sectional area:

$$S_{\varepsilon_i}' = \frac{\left(m_{\varepsilon_i} + m_{\eta_i}\right)\sum_{\theta=1}^{i} \tau_{\eta_\theta}}{\rho L_{\eta_i} \sum_{\theta=1}^{i} \tau_{\eta_\theta}}\left(\frac{m_{\eta_i}}{m_{\eta_i} + m_{\varepsilon_i}} \sum_{\theta=1}^{i} \tau_{\eta_\theta} + \frac{m_{\varepsilon_i}}{m_{\eta_i} + m_{\varepsilon_{i+1}}} \sum_{\theta=1}^{i} \tau_{\varepsilon_\theta}\right) \tag{14}$$

$$S_{\eta_i}' = \frac{\left(m_{\varepsilon_{i+1}} + m_{\eta_i}\right)}{\rho\left(L_{\eta_i} - L_{\varepsilon_i}'\right)}\left(\frac{m_{\eta_i}}{m_{\eta_i} + m_{\varepsilon_{i+1}}} \sum_{\theta=1}^{i} \tau_{\eta_\theta} + \frac{m_{\varepsilon_i}}{m_{\eta_i} + m_{\varepsilon_{i+1}}} \sum_{\theta=1}^{i} \tau_{\varepsilon_\theta}\right) \tag{15}$$

Thus, the equivalent model heat transfer coefficient u should be adjusted as follows:

$$\mu_{\varepsilon_i}' = \frac{c \cdot m_i'}{\pi \cdot d_i' \cdot L_i'^2} \cdot ln \frac{T_{i,in} - T^U}{T_{i,out}' - T^U} \tag{16}$$

$$\mu_{\eta_i}' = \frac{c \cdot m_i'}{\pi \cdot d_i' \cdot L_i'^2} \cdot ln \frac{T_{i,in} - T^U}{T_{i,out}' - T^U} \tag{17}$$

As can be seen from **Formula (3)**, the temperature of the node before and after the polymerization does not change. $T_{i,\mathrm{out}}'$ is the temperature of the terminal outlet after the tube i polymerization; $T_{i,\mathrm{in}}$ is the temperature of the exit before the piping i is polymerized, where c is a specific heat capacity of the heating flow, d_i' is a polymerized pipeline radius, and T^{U} is a natural ambient temperature.

After the above simplification, in the case of retaining most of the thermal dynamic characteristics, the multi-source annular DHN model completes the ring removal processing, which reduces the complexity of the original pipeline.

Multi-Source Ring Network Regional Heating System Model

1) CHP unit heating output

$$h_{i,t} = c \cdot m_j^{HS} \cdot \left(T_{n,t}^s - T_{n,t}^r\right), \forall i \in I^{CHP},\ j \in I^{HS},\ n = N_j^{HS},\ t \in T \tag{18}$$

$$\underline{T}_n^s \le T_{n,t}^s \le \bar{T}_n^s \tag{19}$$

where m_j^{HS} is the mass flow of the heating first station j; $h_{i,t}$ is the output of heat unit. N_j^{HS} is a node connected to the heating head j. $\underline{T}_n^s$, $\bar{T}_n^s$ is the upper and lower range limit for supplying pipe node temperatures. I^{CHP}, I^{HS}, and N_j^{HS} are connected to the CHP unit, and the tube collection of the heating first station and the collection of nodes belong to the heating.

2) Temperature station model:

In order to realize the exchange of heat load in the heating system, the heat transfer station model is constructed.

$$c^w \cdot m_l^{HES} \cdot \left(T_{n,t}^s - \tau_{n,t}^r\right) = H_{l,t}^{HES},\ \forall l \in I^{HES},\ n = N_l^{HES},\ t \in T_d \tag{20}$$

$$\underline{T}_n^r \le \tau_{n,t}^r \le \bar{T}_n^r \tag{21}$$

where m_l^{HES} is the mass flow of the heat exchange station (HES) l, $m_{l,t}^{HES}$ is the heat load $\underline{T}_n^r$ of the switch l at the period t, and $\bar{T}_n^r$ is the upper and lower range limit of the returns of the pipe node temperature.

3) Temperature mixing: Mass flowing into the same node is mixed, and the temperature of the mixed mass as a result of energy conservation is as follows:

$$\sum_{b \in V^-} \left(T_{b,t}^{s,out} m_b^s\right) = T_{i,t}^S \sum_{b \in \Omega_{V^-}} m_b^s,\ t \in T_d \tag{22}$$

$$\sum_{b \in V^+} \left(T_{b,t}^{r,out} m_b^r\right) = T_{i,t}^r \sum_{b \in \Omega_{V^+}} m_b^r,\ t \in T_d \tag{23}$$

where V^- indicates a set of pipelines at the end of the node V, and V^+ means a set of pipes that start with node V.

4) Temperature network pipeline dynamic model based on node method

It can be seen from **Formula (2)** that the mass flow does not change, and the amount of water flowing and flowing out does not change. The historical inlet temperature is used to estimate the outlet temperature without heat loss as follows:

$$T_{b,t}^{'x,out} = (1 - k_b) T_{b,t-\gamma_b-1}^{x,in} + k_b T_{b,t-\gamma_b}^{x,in},\ \forall b \in I^{pipe},\ x \in \{s, r\},\ t \in T_d \tag{24}$$

$$T_{b,t}^{x,out} = T_t^{am} + J_{b,t}\left(T_{b,t}^{'x,out} - T_{G,t}\right), \forall b \in I^{pipe},\ x \in \{s, r\},\ t \in T_d \tag{25}$$

$$\begin{cases} \gamma_b = \min_{n \in N}\{n:\ s.t.\ n\mu_b \Delta t \ge \rho A_b L_b\} \\ R_b = \gamma_b \mu_b \Delta t \\ k_b = \left(R_b - \rho A_b L_b\right)/\mu_b \Delta t \\ J_b = exp\left[- \dfrac{h_b \Delta t}{c^w \rho^w A_b}\left(\gamma_b + \dfrac{1}{2} - k_b\right)\right] \end{cases} \tag{26}$$

Among them, $T_{b,t}^x$ represents the mass flow temperature of the pipe b at the t hour. The superscript out and in respectively indicate the inflow end and outflow end of the pipe. I^{pipe} indicates a collection of heating networks. T_d represents the time collection of the scheduling cycle. $T_{b,t}^x$ represents the mass flow temperature flowing out of the t hour after the heat loss. $T_{G,t}$ represents the ambient temperature of the T moment. c^w indicates a specific heat capacity of water in the water flow in the pipeline.

MODELING AND SOLUTION OF ELECTROTHERMAL COUPLING SYSTEM

Objective Function

$$\min\left(C^{NC} + C^W + C^{CHP}\right) \tag{27}$$

C^{NC} denotes the operation cost of non-CHP thermal units, C^{W} denotes the penalty cost of wind power spillage, and C^{CHP} denotes the operation cost of CHP units. I represents a collection of units.

1) The operation cost of a non-CHP thermal unit is defined as a quadratic function of the generation dispatch

$$C^{NC} = \sum_{t=1}^{T} \sum_{i \in I^{NC}} \left(a_i P_{i,t}^2 + b_i P_{i,\mathrm{t}} + c_i\right) \tag{28}$$

a_i, b_i, and c_i are the cost factors of the conventional unit; T is the scheduling period; I^{NC} is a collection of conventional units; $P_{i,\mathrm{t}}$ is the electric power output of the unit i at time t.

2) Wind abandonment cost of wind farm

$$C^W = \sum_{t=1}^{T} \sum_{i \in I^W} \sigma_i \cdot \left(\bar{P}_{i,t}^w - p_{i,t}\right) \tag{29}$$

σ_i is the penalty factor for abandonment of wind farm i; $\bar{P}_{i,t}^w$ is forecasted output for wind farm i at time period t; I^W is the set for wind farms.

3) Operation cost of CHP unit

$$C^{CHP} = \sum_{t=1}^{T} \sum_{i \in I^{CHP}} \left(\gamma_1 P_{i,t}^2 + \gamma_2 P_{i,\mathrm{t}} + \gamma_3 h_{i,j}^2 + \gamma_4 h_{i,t} + \gamma_5 P_{i,\mathrm{t}} h_{i,t} + \gamma_6\right) \tag{30}$$

$\gamma_1, \gamma_2, \gamma_3, \gamma_4, \gamma_5, \gamma_6$ is the cost coefficient of i CHP unit. i^{CHP} is the set for CHP; $h_{i,t}$ is the thermal power output of unit i at time t.

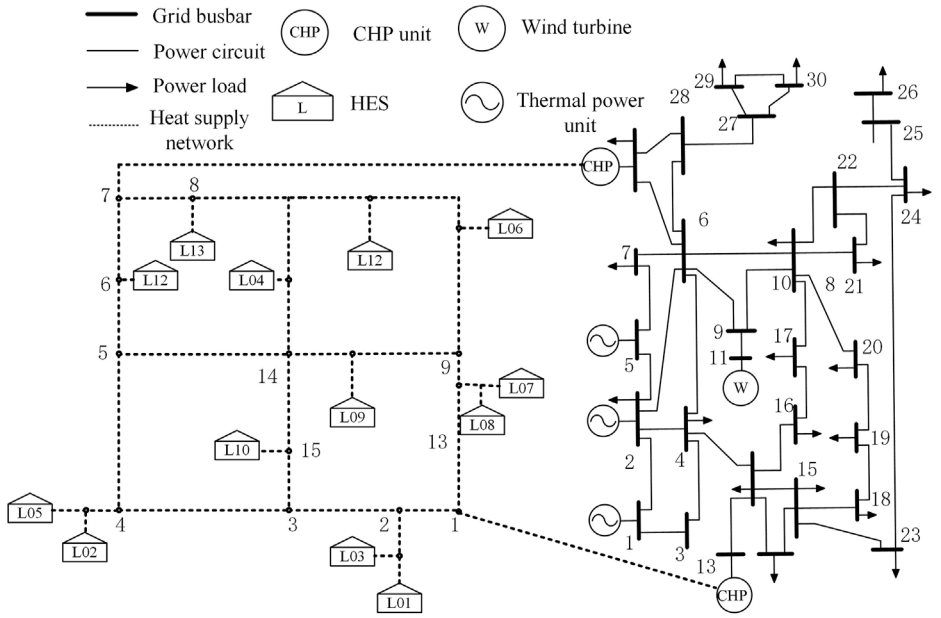

FIGURE 2 | Example model of combined electric heating system.

Constraint Condition

1) Power balance constraints:

$$\sum_{i\in I^{NC}} P_{i,t} + \sum_{i\in I^{CHP}} P_{i,t} + \sum_{i\in I^{W}} P_{i,t}^{W} = L_t \tag{31}$$

L_t is the electric load at time t.

2) Generation output constraints for non-CHP units:

$$P\bar{i} \le P_{i,t} \le \bar{P}_i,\ \forall i \in I^{NC} \tag{32}$$

$P\bar{i}$ and $\bar{P}_i$ represent the minimum and maximum output power of unit i.

3) Spinning reserve constraint for non-CHP units:

$$0 \le ru_{i,t} \le RAMP_i^{up} \tag{33}$$

$$0 \le rd_{i,t} \le RAMP_i^{down},\ rd_{i,t} \le p_{i,t} - P\bar{i} \tag{34}$$

$ru_{i,t}$ and $rd_{i,t}$ are reserved for the up/down rotation of the unit at time; $RAMP_i^{up}$ is upward ramping capability of generation unit i. $RAMP_i^{down}$ Downward ramping capability of generation unit i.

4) Operation constraints of wind power plant:

$$0 \le p_{i,t}^{w} \le \bar{p}_{i,t}^{w} \tag{35}$$

$p_{i,t}^{w}$ is wind farm output; $\bar{p}_{i,t}^{w}$ is predicted available wind energy of wind farm i at period t.

5) Ramping constraints:

$$-RAMP_i^{down} \le P_{i,t} - P_{i,t-1} \le RAMP_i^{up},\ \forall i \in I^{NC} \cup I^{CHP},\ t \in T \tag{36}$$

6) Feasible region constraint of CHP unit:

$$P_{i,t} \ge r_i h_{i,t}, i \in I^{CHP} \tag{37}$$

$$F_{i,\min} \le \rho_i^p P_{i,t} + \rho_i^q h_{i,t} \le F_{i,\max} \tag{38}$$

$$0 \le h_{i,t} \le h_{i,\max} \tag{39}$$

r_i is CHP unit electrothermal coupling coefficient, $F_{i,\min}$/ $F_{i,\max}$ is minimum/maximum fuel consumption, ρ_i^p is fuel consumption rate of electricity output, ρ_i^q is fuel consumption rate of heat output, and $h_{i,\max}$ is the maximum heat output of the CHP unit.

7) CHP unit constraints: Defined in **Eqs (18)** and **(19)**
8) HES constraints: Defined in **Eqs (20)** and **(21)**
9) Temperature mixing constraints: Defined in **Eqs (22)** and **(23)**
10) Temperature dynamics constraints: Defined in **Eqs (24)** and **(26)**

SIMULATION RESULTS

The structure of this calculation example adopts the combined heat and power system shown in **Figure 2**. The power supply type and unit parameters of the system are shown in **Supplementary Appendix Tables A1–A3**. The calculation example is day-ahead scheduling, and its scheduling period is 24 h which takes 1 h as the scheduling unit. The time resolution of the heat network model is 5 min. The electrical load of the system, the total heat

TABLE 1 | The pipeline simplification result of the model.

Model	Number of pipes/root	Degree of simplification (%)	Total length of pipe (m)	Time delay (h)	Total heat loss coefficient/H = h × L
1	35	0	20,917	6.576	8,573.42
2	32	91.42	18,992.556	6.544	8,573.42
3	29	82.85	16,348.762	6.625	8,573.42
4	12	34.29	8,374.645	6.637	8,573.42

load of the district heating system, and the predicted maximum output of wind power are shown in **Supplementary Appendix Tables B1–B3**, and the heating network pipeline parameters are shown in **Supplementary Appendix Table 1**.

Precision Analysis of the Ring Network After Loop Removal

To verify the accuracy of the proposed strategy, four different control modes are compared in the paper:

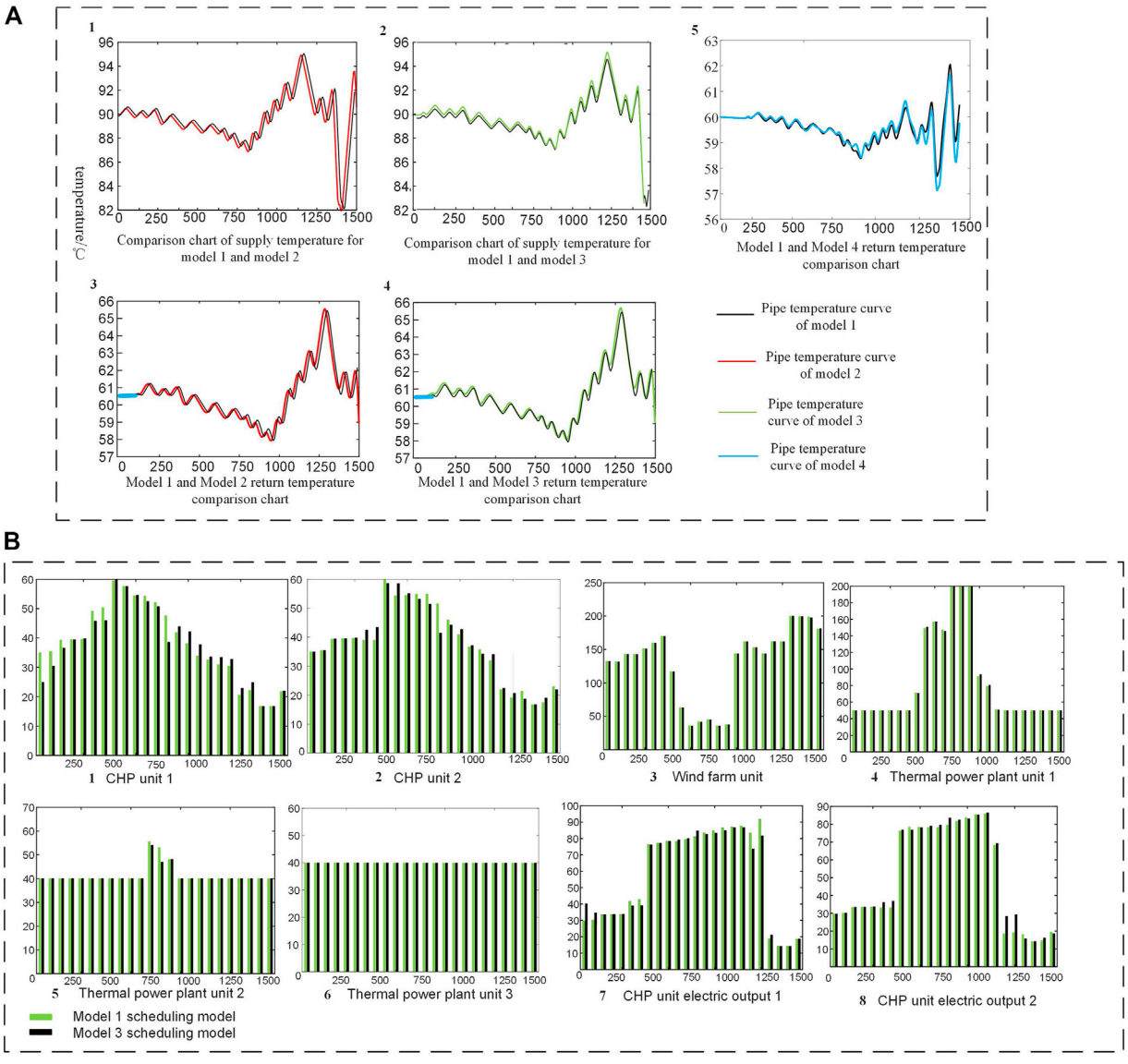

FIGURE 3 | (A) Temperature comparison curve after ring. **(B)** Each unit output dispatch plan.

Model 1: The initial model of the original 35-pipe multi-source ring heating network.
Model 2: After the first loop removal, model 1 is equivalent to an approximate equivalent model of 32 heating network pipes.
Model 3: After the second loop removal, model 2 is equivalent to the approximate equivalent model of 29 heating network pipes.
Model 4: Model 3 is further resolved into a topological equivalent heating network model of 12 heating pipes.

The pipe simplification results of the model are shown in **Table 1**, model 2, and model 3; the loop removal operation is carried out for the multi-source annular heating network model 1. After the loop removal, the total length of model 1 is reduced to a certain extent, and the loop structure is removed, which greatly reduces the complexity of the entire network. On the basis of model 3, model 4 further simplifies the model after loop removal and equivalence (using reference 14, traditional tree-shaped heating pipe simplification method), reducing the total number of pipes to 34.29% of the original network. The error of the time delay may be due to the loop structure of the heating pipeline; at least one node will have two different time delays when the loop is removed. This article only uses the weighted average of its time delay to calculate, which will cause a certain error. After the above steps, the topological de-ring of the multi-source ring heating network is approximately equivalent while ensuring that the total heat loss remains unchanged.

In addition to the above, we also need to consider the accuracy of different models after simplification. The initial water supply temperature is set in this paper. the return temperature and pipeline supply temperature curves of model 1 were compared with those of models 2, 3, and 4, respectively. The temperature of each model before and after simplification is compared and analyzed to verify whether the temperature is roughly the same before and after simplification.

For model 2 and model 3, the initial supply temperature and return temperature of the initial node and end point of loop removal were selected to compare with the temperature of the node before loop removal. It can be seen from **Figure 3**(A1, A2) that the supply temperature curve remains basically unchanged before and after the pipeline is simplified, and the return temperature is the same in **Figure 3**(A3, A4). The blue line in **Figure 3**(A3, A4) shows no significant change in temperature; because there is a time delay in the heat transfer process of the heating pipeline, the load node that is close to the heat source first feeds back the change of temperature, but the mass flow of a single load is limited, so the previous change is not obvious.

After removing the loop first and simplifying it later, the loop heating network of multi-heat source combined heating is gradually simplified, which reduces the complexity of the current multi-source loop heating pipeline model. Using the equivalent simplification method of multi-source heating network to get rid of loops, model 4 is obtained, and model 1 is equivalently simplified to 12 pipes. Compared with the initial loop heating network of 35 pipes, the heating network is simplified by 65.717%, and the heating network pipe constraints are reduced by 65.717% in the scheduling model, which greatly reduces the complexity of the model′s topology and the difficulty of solution. **Figure 3**(5) shows the accuracy comparison of the final pipeline simplification.

Analysis of the Result of Combined Electric and Heating Dispatching for Loop Heating Network

In order to verify the accuracy and validity of the combined electric heating dispatching results based on the approximate equivalent model of heat network after loop removal, in this section, the electrothermal scheduling results of model 1 and model 4 are compared. **Figures 3**(B1, B2) show the optimal electric output of units of the two models, where **Figures 3**(B1, B2) are the thermal output of CHP unit; **Figure 3B** shows the unit power output scheduling plan, where **Figure 3**(B3) is the output of wind farm. **Figures 3**(B4, B5, B6) are the output of three thermal power units, respectively, and **Figures 3**(B7, B8) are the thermal output of CHP units. It can be seen that the electrical and thermal outputs of the two models are basically the same, except that there is a large error between the thermal and electrical outputs of CHP unit 1 at the initial stage (1, 2 h).

The experimental results show that the scheduling costs of model 1 and model 4 are respectively 1,193,400 yuan and 1,190,300 yuan, indicating that the simplification of the model does not affect the scheduling costs. Moreover, the computation time of simplified model 4 is reduced by 60.11% compared with the scheduling time of model 1.

CONCLUSION

This paper proposes a method of simplifying a multi-source cyclic heating network topology approximation. The simulation results show that the multi-heat source ring heating network was first removed and then simplified. On the premise of ensuring accuracy, the topology complexity of the ring heating pipeline model was reduced by 65.717%, the complexity of calculation was reduced, and the solving time in the scheduling process was further reduced.

DATA AVAILABILITY STATEMENT

The raw data supporting the conclusions of this article will be made available by the authors, without undue reservation.

AUTHOR CONTRIBUTIONS

JY put forward the main research points. JY and DZ completed the manuscript writing and revision. LZ completed the simulation research. ZL collected the relevant background information. TZ revised the grammar and expression.

FUNDING

This manuscript was supported in part by the National Natural Science Foundation of China 52007103.

REFERENCES

Jiang, Y., Wan, C., Audun, B., and Song, Y. (2019). "Combined Heat and Power Dispatch Using Simplified District Heat Flow Model[C]," in 2019 IEEE Power & Energy Society General Meeting (PESGM) (Atlanta, GA, USA: IEEE). doi:10.1109/PESGM40551.2019.8973926

Larsen, H. V., Pálsson, H., Bøhm, B., and Ravn, H. F. (2002). Aggregated Dynamic Simulation Model of District Heating Networks. *Energ. Convers. Manag.* 43, 995–1019. doi:10.1016/s0196-8904(01)00093-0

Li, H., Zhang, X., and Zhou, H. (2021). Day-Ahead Economic Dispatch of Integrated Energy System Considering the Uncertainty of Source and Load [J]. *Sci. Tech. Eng.* 21 (18), 7.

Li, Z., Wu, W., Shahidehpour, M., Wang, J., and Zhang, B. (2017). "Combined Heat and Power Dispatch Considering Pipeline Energy Storage of District Heating Network[C]," in 2017 IEEE Power & Energy Society General Meeting (PESGM) (IEEE). doi:10.1109/TSTE.2015.2467383

Lu, S., Gu, W., Yu, W., and Zhou, S. (2019). High Resolution Modeling and Decentralized Dispatch of Heat and Electricity Integrated Energy System[J]. *IEEE Trans. Sust. Energ.* 99, 1451–1463. doi:10.1109/TSTE.2019.2927637

Shen, X., Ouyang, T., Khajorntraidet, C., Li, Y., Li, S., and Zhuang, J. (2021). Mixture Density Networks-Based Knock Simulator. *Ieee/asme Trans. Mechatron.* 2021, 1. doi:10.1109/TMECH.2021.3059775

Shen, X., and Raksincharoensak, P. (2021). Pedestrian-aware Statistical Risk Assessment. *IEEE Trans. Intell. Transport. Syst.* 2021, 1–9. doi:10.1109/TITS.2021.3074522

Shen, X., Zhang, Y., Sata, K., and Shen, T. (2020). Gaussian Mixture Model Clustering-Based Knock Threshold Learning in Automotive Engines. *Ieee/asme Trans. Mechatron.* 25 (6), 2981–2991. doi:10.1109/TMECH.2020.3000732

Shi, G., Yang, L., and Zhang, H. (2020). Multi-heat Source Dispatching Optimization Model for central Heating System[J]. *Therm. Power Generation* 049 (003), 68–75. doi:10.19666/j.rlfd.201909203

Tang, M., Luo, Y., and Hu, B. (2021). Summary of Electric and Heating Joint Dispatching Model [J]. *Power Syst. Prot. Control* 48 (23), 15.

Tian, Y., Song, J., and Li, S. (2017). Development Status and Trend of Multi-Heat Source Looped Pipe Network Operation Technology[J]. *SHANXI Architecture* 8, 142–143. doi:10.13719/j.cnki.cn14-1279/tu.2017.22.079

Wang, D., Zhi, Y.-q., Jia, H.-j., Hou, K., Zhang, S.-x., Du, W., et al. (2019). Optimal Scheduling Strategy of District Integrated Heat and Power System with Wind Power and Multiple Energy Stations Considering thermal Inertia of Buildings under Different Heating Regulation Modes. *Appl. Energ.* 240 (240), 341–358. doi:10.1016/j.apenergy.2019.01.199

Wu, C., Huang, S., Peng, X., and Liu, F. (2019). Optimal Design of Multi-Heat Source central Heating System [J]. *Reg. governance* 253 (27), 145–149. doi:10.1177/1687814018789504

SUPPLEMENTARY MATERIAL

The Supplementary Material for this article can be found online at: https://www.frontiersin.org/articles/10.3389/fenrg.2021.800906/full#supplementary-material

Yang, L. (2020). Optimal Analysis of Multi-Heat Source Dispatching in central Heating System[J]. *Process and Equipment* 07, 245–248. doi:10.3969/j.issn.1673-0038.2020.21.179

Yang, N., Huang, Y., Hou, D., Liu, S., Ye, D., Dong, B., et al. (2019). Adaptive Nonparametric Kernel Density Estimation Approach for Joint Probability Density Function Modeling of Multiple Wind Farms. *Energies* 12, 1356. doi:10.3390/en12071356

Yang, N., Liu, S., Deng, Y., and Xing, C. (2021). An Improved Robust SCUC Approach Considering Multiple Uncertainty and Correlation. *IEEJ Trans. Elec Electron. Eng.* 16, 21–34. doi:10.1002/tee.23265

Yang, N., Yang, C., Xing, C., Ye, D., Jia, J., Chen, D., et al. (2021). Deep Learning-Based SCUC Decision-Making: An Intelligent Data-Driven Approach with Self-Learning Capabilities. *IET Gener. Transm. Distrib.* 2021, 1–12. doi:10.1049/gtd2.12315

Yang, Z., Chang, W., and Xia, M. (2019). Research on Optimal Scheduling of Multi-Heat Source Combined Heating System[J]. *Energy and Energy Saving* 12, 56–58. doi:10.16643/j.cnki.14-1360/td.2019.12.024

Yu, Y., Chen, H., Chen, J., Chen, C., and Wu, J. (2019). Optimal Operation of the Combined Heat and Power System Equipped with Power-To-Heat Devices for the Improvement of Wind Energy Utilization. *Energy Sci Eng* 7, 1605–1620. doi:10.1002/ese3.375

Zhang, L., Xie, Y., Ye, J., Xue, T., Cheng, J., Li, Z., et al. (2021). Intelligent Frequency Control Strategy Based on Reinforcement Learning of Multi-Objective Collaborative Reward Function. *Front. Energ. Res.* 9, 1. doi:10.3389/fenrg.2021.760525

Zheng, J., Zhou, Z., Zhao, J., and Wang, J. (2018). Integrated Heat and Power Dispatch Truly Utilizing thermal Inertia of District Heating Network for Wind Power Integration. *Appl. Energ.* 211, 865–874. doi:10.1016/j.apenergy.2017.11.080

Conflict of Interest: The authors declare that the research was conducted in the absence of any commercial or financial relationships that could be construed as a potential conflict of interest.

Publisher's Note: All claims expressed in this article are solely those of the authors and do not necessarily represent those of their affiliated organizations or those of the publisher, the editors and the reviewers. Any product that may be evaluated in this article, or claim that may be made by its manufacturer, is not guaranteed or endorsed by the publisher.

frontiers in Energy Research

BRIEF RESEARCH REPORT
published: 17 December 2021
doi: 10.3389/fenrg.2021.808116

Ultra-Short-Term Wind Power Prediction Based on Bidirectional Gated Recurrent Unit and Transfer Learning

Wenjin Chen[1], Weiwen Qi[2], Yu Li[3], Jun Zhang[1], Feng Zhu[2], Dong Xie[2], Wei Ru[2], Gang Luo[2], Meiya Song[2] and Fei Tang[3]*

[1]State Grid Zhejiang Electric Power Company, Ltd., Hangzhou, China, [2]State Grid Shaoxing Power Supply Company, Shaoxing, China, [3]School of Electrical and Automation, Wuhan University, Wuhan, China

Wind power forecasting (WPF) is imperative to the control and dispatch of the power grid. Firstly, an ultra-short-term prediction method based on multilayer bidirectional gated recurrent unit (Bi-GRU) and fully connected (FC) layer is proposed. The layers of Bi-GRU extract the temporal feature information of wind power and meteorological data, and the FC layer predicts wind power by changing dimensions to match the output vector. Furthermore, a transfer learning (TL) strategy is utilized to establish the prediction model of a target wind farm with fewer data and less training time based on the source wind farm. The proposed method is validated on two wind farms located in China and the results prove its superior prediction performance compared with other approaches.

Keywords: bidirectional gated recurrent unit, transfer learning, target domain, wind power, wind power forecasting

OPEN ACCESS

Edited by:
Xun Shen,
Tokyo Institute of Technology, Japan

Reviewed by:
Aihong Tang,
Wuhan University of Technology, China
Yunyun Xie,
Nanjing University of Science and Technology, China

****Correspondence:***
Yu Li
2877630621@qq.com

Specialty section:
This article was submitted to Smart Grids, a section of the journal Frontiers in Energy Research

Received: *03 November 2021*
Accepted: *12 November 2021*
Published: *17 December 2021*

Citation:
Chen W, Qi W, Li Y, Zhang J, Zhu F, Xie D, Ru W, Luo G, Song M and Tang F (2021) Ultra-Short-Term Wind Power Prediction Based on Bidirectional Gated Recurrent Unit and Transfer Learning. Front. Energy Res. 9:808116. doi: 10.3389/fenrg.2021.808116

INTRODUCTION

The renewable energy problem is the focus of the 21st century (Zheng et al., 2017; Li et al., 2016). The transformation of the power grid is the key to solving this problem. The new form of the power grid with renewable energy as the main bulk is the ruling development trend of the future power grid (Li et al., 2021; Shen et al., 2021a). The Global Wind Energy Development Report 2019 shows that the newly installed capacity of global wind turbines in 2019 is 60.4 GW (Chen et al., 2021). However, the uncertainty existing in new energy, such as wind power, is not conducive to the safe and stable operation of the power grid. Therefore, accurate WPF is beneficial for enhancing system reliability (Shi et al., 2014).

There are three types of WPF methods including the physical method, statistical method, and artificial intelligence method. The first establishes a physical model that reflects the relationship between the wind power and numerical weather forecast (NWP) (Zhao et al., 2018), which is difficult to model and calculate. Yang proposes an expanded sequence-to-sequence (E-Seq2Seq) based data-driven SCUC expert system for dynamic multiple-sequence mapping samples, which is a pioneer study for SCUC problems (Yang et al., 2021a). The second (statistical method) is suitable for wind farms that have been built for a long time because it needs enough historical data. The representative algorithms of this method are Auto-Regression (AR) (Wu et al., 2014; Shen et al., 2021), Bayesian approach (Wang et al., 2019a), and Kalman filter (Yang et al., 2019). The final, AI method, such as support vector machine (Deo et al., 2016), artificial neural network (Wang et al., 2019b), extreme learning machine (Ali and Prasad, 2019), can deal with the complex nonlinear relationship between input and output and extract the deep features of input information, which has been widely used in recent years.

The ultra-short-term prediction of wind power is essentially a multi-variable time series prediction problem. In recent years, recurrent neural network (RNN) has developed rapidly. As the improved versions of RNN, long short-term memory (LSTM) network and gated recurrent unit (GRU) (Lin and Liu, 2020; Yang et al., 2021b) can efficiently extract the temporal correlation characteristics of wind power, and also mine the relationship between power and weather, which improves the performance of WPF. But there is a timing delay in actual prediction.

In addition, all deep learning approaches rely on a sufficient sample of data. However, newly built wind farms may not provide enough data, which makes WPF difficult. However, TL is a new method that breaks through traditional machine learning and is widely used in computer vision, text classification, and other fields (Wang et al., 2020; Shen and Raksincharoensak, 2021a; Yang et al., 2021; Yang et al., 2019; Shen et al., 2021b). It can finish pre-training of a model in the source domain with sufficient data and then transfer the pre-training model to the target domain after fine-tuning. On the one hand, TL can overcome the problem of few data, on the other hand, it can reduce the training time (Zhuang et al., 2020; Zhang et al., 2021). At present, there are few studies on the applications of TL in WPF.

In order to improve the prediction performance of RNN, the Bi-GRU method is proposed in this paper to enhance the and capacity and forecasting accuracy of the model by bidirectionality of the structure. The Bi-GRU enables the GRU to process the data in two directions including forward (future) and backward (past). Moreover, the TL strategy is used to forecast the wind power of newly built wind farms with few training data. The TL combined with Bi-GRU is used to ensure the power prediction accuracy and reduce the training time, which can guarantee model performance and reduce computational costs at the same time.

The rest of this paper is organized as follows. In *The Proposed BI-GRU Model and Transfer Learning Method*, the Bi-GRU model and transfer learning method are explained. Case studies and discussion are shown in *Case Studies*. *Conclusion* concludes this study by summarizing the key findings and contributions of this paper.

THE PROPOSED BI-GRU MODEL AND TRANSFER LEARNING METHOD

The Bi-GRU Prediction Model

RNN is widely used in time series prediction, but it has problems of gradients vanishing and exploding, and its memory ability for long series is limited (Liu et al., 2021). As the improved version of RNN, LSTM, and GRU effectively solve these problems and determine the sequential information to be forgotten and remembered through the gating mechanism. The gating mechanism of GRU is simpler than that of LSTM because it combines the forget gate and input gate of LSTM and reduces the computation while ensuring the prediction ability of the neural network. In addition, Bi-GRU is able to extract long-term dependencies before and after the current state, which means that Bi-GRU can extract more temporal features from sequential data, so Bi-GRU performs better than GRU. The structure diagram of Bi-GRU is shown in **Figure 1**.

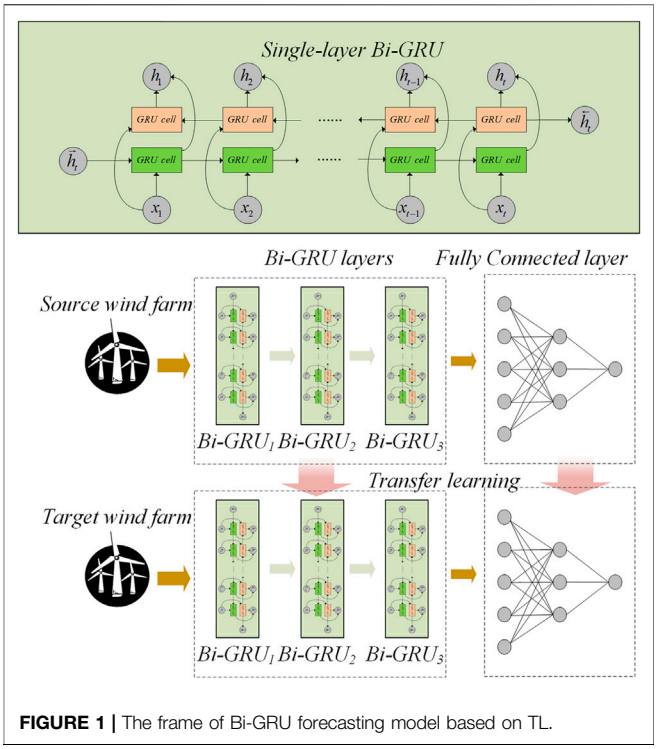

FIGURE 1 | The frame of Bi-GRU forecasting model based on TL.

The GRU cell has only two gates (an update gate z_t and a reset gate r_t). The update gate controls the extent to which the state information at the previous moment is retained into the current state, and the reset gate determines the extent to which the current state is combined with the previous information. The information flow is shown as follows in a GRU cell.

$$z_t = \sigma(W_z x_t + U_z h_{t-1} + b_z) \tag{1}$$

$$r_t = \sigma(W_r x_t + U_r h_{t-1} + b_r) \tag{2}$$

$$\tilde{h}_t = tanh(W x_t + U(r_t \dot{o} h_{t-1})) \tag{3}$$

$$h_t = z_t \dot{o} \tilde{h}_t + (1 - z_t) \dot{o} h_{t-1} \tag{4}$$

Where x_t, h_t are the input data and current state (also used as the output of a cell) at time t, respectively. h_{t-1} is the previous state. $\tilde{h}_t$ is the candidate state. W_r, U_r, W_z, U_z, W, U, and b_r, b_z represent weights and bias parameters, respectively. σ, tanh are activation functions and $\dot{o}$ denotes an element-wise product. But in Bi-GRU, the output h_t is concatenated by the outputs in two directions.

$$\vec{h}_t = \mathbf{GRU}\left(\vec{h}_{t-1}, x_t\right) \tag{5}$$

$$\overleftarrow{h}_t = \mathbf{GRU}\left(\overleftarrow{h}_{t-1}, x_t\right) \tag{6}$$

$$h_t = W_t \vec{h}_t + U_t \overleftarrow{h}_t + b_t \tag{7}$$

Where, $\vec{h}_t$, $\overleftarrow{h}_t$ represent the outputs in two directions, W_t, U_t, and b_t represent weights and bias parameters, respectively. In addition, FC neural network is used after Bi-GRU to fit the learned features to labels, which means achieving prediction by matching dimensions between inputs and outputs. The Rectified

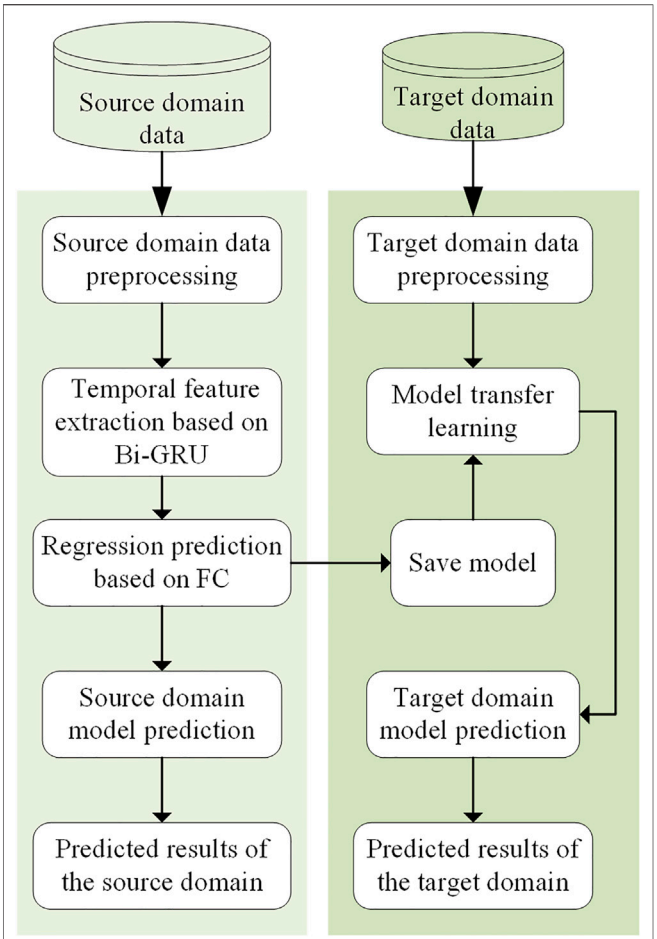

FIGURE 2 | The folw chart of propesed WPF.

Linear Unit (ReLU) activation function is utilized in the FC layer.

The Transfer Learning Method

The TL method is a machine learning concept that TL is used to improve the performance of target tasks on target domains by transferring the knowledge contained in different but similar source domains (Qureshi et al., 2017). Usually, the model is pre-trained in the source domain with sufficient data. Then the pre-trained model is fine-tuned in the target domain with small data, which makes full use of the source domain data to improve the performance of the model on the target domain data. TL methods can be divided into instance-based approach, feature-based approach, and parameter-based approach. The historical data of wind farms with short construction time or imperfect detection devices may not be enough to support the training of prediction models. In this paper, the parameter-based TL approach is used. The pre-training model trained by wind farms with sufficient data is fine-tuned by the target domain with insufficient data to accomplish the target tasks more efficiently. The basic idea of transfer learning can be expressed as follows.

$$DS_s = \{F_s, L_s\} \tag{8}$$

$$DS_t = \{F_t, L_t\} \tag{9}$$

Where DS_s, DS_t represent the data space of the source domain and target domain, respectively. F_s, L_s are the features of the source domain and target domain data spaces, respectively. F_t, L_t are the labels of the source domain and target domain data spaces, respectively. The tasks of the source domain and target domain are to find the optimal parameters W_s and W_t, to make that the predicted values P_s and P_t are as close as possible to the labels L_s and L_t. TL is to fine-tune the source domain model parameter W_s to make the target domain parameter as close as possible to the optimal target domain parameter W_t.

$$P_s = f_s(F_s, W_s) \tag{10}$$

$$P_t = f_t(F_t, W_t) \tag{11}$$

The prediction framework diagram of the method proposed in this paper is shown in **Figure 1**, and the processing flowchart is shown in **Figure 2**. The prediction process is mainly divided into two parts. In the first part, the wind farm power prediction model in the source domain is established. In the data pre-processing stage, the original data in the source domain are normalized to eliminate the scale difference of features and facilitate the use of gradient descent of loss function. First, the pre-processed data is fed into the three-layer Bi-GRU neural network. Then the FC layer matches the output dimension to achieve WPF to get the source-domain prediction results. The second part is to build the wind farm power prediction model in the target domain, and the data pre-processing is the same as the first part. The pre-trained source domain model is loaded and the parameters in the pre-trained model are transferred to the target domain as the initial parameters. Using a small amount of target-domain data to train the network, a fine-tuned target domain prediction model is obtained.

CASE STUDIES

In order to verify the effectiveness and superiority of the proposed prediction model and TL method, the experiment is divided into two parts. The first part compares the Bi-GRU with the AR, LSTM, and GRU. The second part uses the Bi-GRU prediction model and TL method to predict the power of wind farms in the target domain. The programming language used is Python3.8. The deep learning framework is PyTorch1.8.1.

Data Description

Two wind farms from Zhejiang Province in China are named ZJFD01 and ZJFD02 respectively. Each wind farm contains measured active power and meteorological data. The meteorological data contains wind speed, direction measured (sine and cosine of wind direction) at the hub, and air density. The time interval is 15 min. Since the running time of the two wind farms is different, the amount of historical data recorded is different. The wind farm ZJFD01 has recorded a large amount of data (including July 1, 2019–August 30, 2021) with an installed capacity of 90 MW, which is taken as the source-domain wind farm. The wind farm ZJFD02 (including January 1, 2021–August

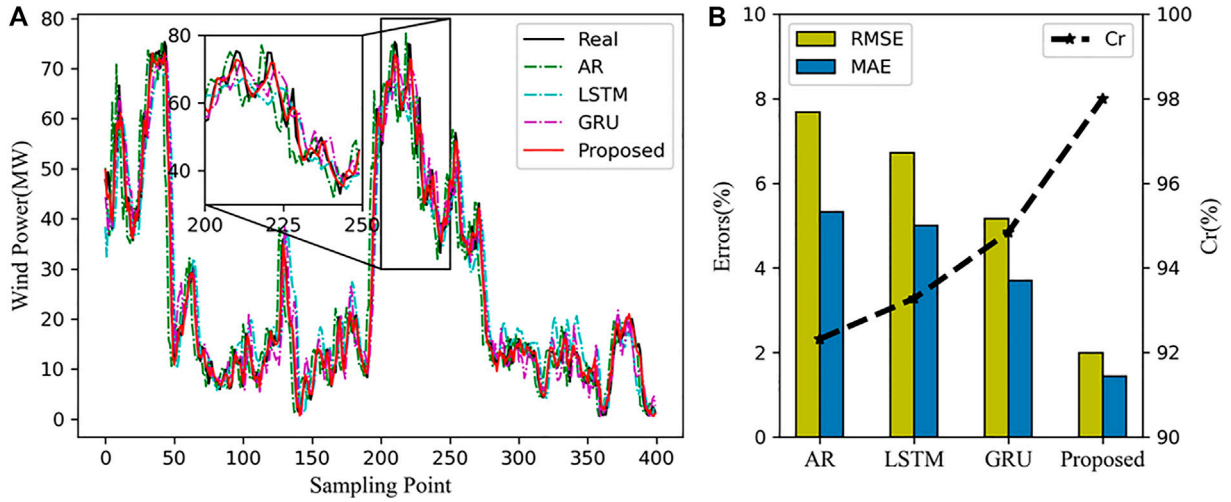

FIGURE 3 | The forecasting results of source-domain wind farm:**(A)** Foreacsting results; **(B)** Forecasting error.

25, 2021) has recorded a small amount of data with an installed capacity of 200 MW, which is taken as the target-domain wind farm. The relationship between input and output of samples in the target domain and source domain in these datasets is similar because the relationship of wind power and meteorological variables in different wind farms is semblable. Therefore, data domains can be positively transferred.

Evaluation Metrics

In order to evaluate the prediction performance of the prediction model, the root mean square error (RMSE), mean absolute error (MAE), and accuracy (Cr) are taken as evaluation metrics according to international standards. They are defined as follows. In addition, training time is introduced as a new evaluation index in the experiment of the target-domain wind farm.

$$\mathbf{RMSE} = \frac{1}{\sqrt{n}}\sqrt{\sum_{i=1}^{n}\left(\frac{P_{real,i} - P_{pred,i}}{C_i}\right)^2} \times 100\% \tag{12}$$

$$\mathbf{MAE} = \frac{1}{n}\sum_{i=1}^{n}\left|\frac{P_{real,i} - P_{pred,i}}{C_i}\right| \times 100\% \tag{13}$$

$$C_r = 1 - \mathbf{RMSE} \tag{14}$$

Where $P_{real,i}$, $P_{pred,i}$, and C_i are real output power, predicted output power, and capability of wind farm respectively. n is the total number of predicted samples.

The Experiment of Source-Domain Wind Farm

The source-domain prediction model, the Bi-GRU method, is established for the ZJFD01 wind farm. In the data pre-processing stage, the supervised learning dataset is constructed. The output power of the current time step y_t is selected as the label. The previous four timesteps (x_{t-1},x_{t-2}, . . . , x_{t-4}) are selected as features. A total of 70% of the dataset was used as the training set and the last 30% as the verification set.

For hyperparameters, set input size to 4, hidden size to 8, and the number of layers to 3. Then, the FC layer is connected to tag dimension matching, and the number of neuron nodes in the input layer is 64 (since the output of Bi-GRU is flattened), the hidden layer is 32, and the output layer is 1. In the model training stage, mean-squared loss is used as the loss function to measure the error between predicted power and actual output power, and the Adam optimization algorithm is used as the optimizer. In order to evaluate the superiority of the proposed method in wind farm prediction in the source domain, RMSE, MAE, and Cr are used as evaluation metrics.

The 400 sampling points of the test dataset are taken to verify the prediction effects of various methods. The power prediction results are shown in **Figure 3**. Compared with other methods, the power prediction curve of Bi-GRU is closer to the actual power output curve trend. As can be seen from **Figure 3**, the RMSE and MAE of the proposed method are significantly lower than those of other methods, and the accuracy is improved. Compared with LSTM and GRU, RMSE and MAE are reduced by 4.73 and 3.17% respectively. The prediction effect of GRU is better than that of LSTM because the same iteration times are set, but GRU has a simpler structure and fewer parameters to be optimized, so it has higher accuracy. There are two reasons why the proposed method is superior: 1) The Bi-GRU can excavate the relationship between historical meteorological data and current power data layer by layer through various gating mechanisms, and can also excavate the local and long-term correlation before and after the power data series; 2) The characteristics of both the forward and reverse time sequence of power and meteorological data are taken into account by the bidirectional mechanism, so it can effectively improve the accuracy of prediction. As seen from the local amplification figure, the forecasting curve trend of all methods is close to the actual power curve, but there are different levels of phase difference. However, the bidirectional mechanism of Bi-GRU solved this problem, making the prediction curve more closely fit the

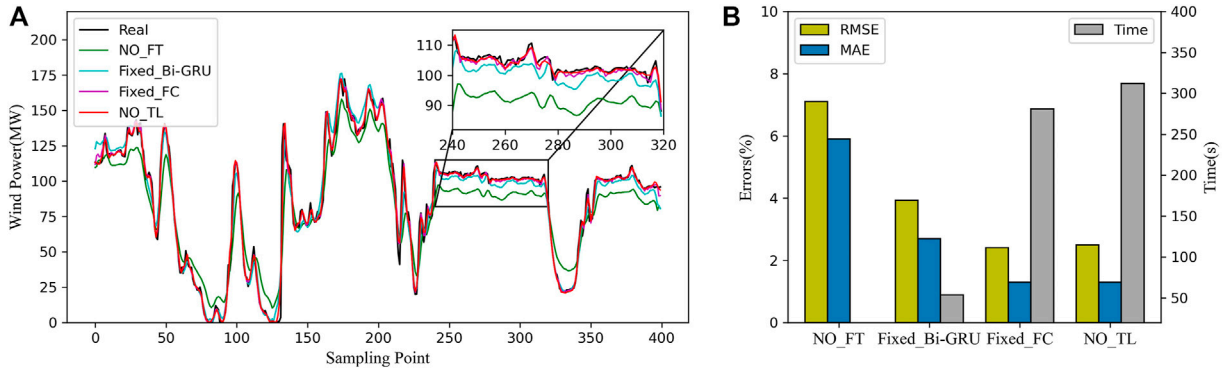

FIGURE 4 | The forecasiting results oftarget-domain wind farm:**(A)** Forcasting results; **(B)** Forcasting error and training time.

actual power curve, which is the important reason for its better prediction performance.

The Experiment of Target-Domain Wind Farm

In order to ensure the prediction accuracy and reduce the training time, the power prediction of the ZJFD02 wind farm in the target domain is based on transfer learning. The parameters and structure of the pre-trained model from ZJFD01 are migrated to the ZJFD02. The preprocessing method of the dataset is the same as that of source wind farm. In order to explore and verify the advantages of using transfer learning to predict power, the following cases are compared:

a) The pre-trained model in the source domain is directly loaded, and denoted as NO_fine-tunning (NO_FT);
b) The pre-trained model in the source domain is loaded and the parameters in Bi-GRU layers are frozen and the parameters of the FC layer are fine-tuned with target-domain data, which is named Fixed_Bi-GRU;
c) The pre-trained model in the source domain is loaded and the parameters in the FC layer are frozen and the parameters of Bi-GRU layers are fine-tuned with target-domain data, which is named Fixed_FC;
d) Redefine a prediction model whose structure is the same as that of the source-domain model but whose parameters are not trained at all. Then train it with target-domain data, which is named NO_TL.

In addition to RMSE and MAE, training time is added to the evaluation metrics to measure the improvement of computing speed caused by TL. Except for case (a), the number of iterations in other cases is set to 200.

By taking 400 sampling points, the prediction results and performance of the above cases can be compared, as shown in **Figure 4**. From the perspective of prediction accuracy, the prediction accuracy of case (a) and case (b) is lower than that of case (c) and case (d). RMSE and MAE of case (c) are 4.705 and 4.607%, respectively, lower than that of case (a), because there are still differences in the dataset of the source domain and target domain. If there is no parameter fine-tuning, it will cause a large prediction error. Case (b) and (c) fixed different parameters of the network layer, RMSE, and MAE were reduced by 1.533 and 1.404% respectively compared with case (b), because the number of three-layer network parameters of Bi-GRU was much more than that of FC layer. After fine-tuning in the target domain, case (b) changed the parameters of the model to a greater extent than case (b), so it is closer to the optimal target domain model; the prediction accuracy of case (c) and case (d) was similar, RMSE is 2.397 and 2.484%, MAE is 1.295%, and 1.298%, respectively. From the perspective of time-consuming, cases (b), (c), and (d) are compared. it is obvious that the training time of case (b) is less than that of (c). Most parameters of this prediction model are still Bi-GRU layers, so it saves training time to fine-tune FC layer parameters. The accuracy of (c) is similar to that of (d), but the training time of (c) is 9.9% shorter than that of (d). Therefore, using the transfer learning fine-tuning the pre-trained model can guarantee the prediction accuracy and save the training time to a certain extent compared with the training model starting from the beginning.

CONCLUSION

In this paper, a Bi-GRU prediction model based on the transfer learning method is presented for the ultra-short-term of wind power. According to the results of case studies, some conclusions are summed up as follows. On one hand, the Bi-GRU prediction model can extract the temporal features of wind power sequential data in two directions, which learns deeper historical information and realize higher accuracy of WPF than GRU and LSTM. On the other hand, the prediction model combined with the TL method saves training time and reduces the requirement for abundant data. In the future, more detailed research about how to balance training time and accuracy of prediction using TL will be completed. Moreover, more comprehensive evaluation metrics aimed at evaluating the TL method in WPF will be established (Shen and Raksincharoensak, 2021b).

DATA AVAILABILITY STATEMENT

The original contributions presented in the study are included in the article/supplementary material, further inquiries can be directed to the corresponding author.

AUTHOR CONTRIBUTIONS

WC: Data provision, Project administration, Methodology. WQ: Data Processing, Project administration, Supervision. YL: Methodology, Data Processing, Writing- Original draft preparation, Software. JZ: Conceptualization, Writing-Reviewing and Editing, Supervision. FZ: Validation, Investigation, Supervision. DX: Visualization, Supervision. WR: Investigation, Supervision. GL: Data Processing, Supervision. MS: Data Processing, Supervision. FT: Supervision, Writing-Reviewing and revising grammar and correct expression.

FUNDING

This study received funding from the Science and Technology Project of State Grid Zhejiang Electric Power Co., LTD. (5211SX2000ZM).

REFERENCES

Ali, M., and Prasad, R. (2019). Significant Wave Height Forecasting via an Extreme Learning Machine Model Integrated with Improved Complete Ensemble Empirical Mode Decomposition. *Renew. Sustain. Energ. Rev.* 104, 281–295. doi:10.1016/j.rser.2019.01.014

Chen, X., Zhang, X., Dong, M., Huang, L., Guo, Y., and He, S. (2021). Deep Learning-Based Prediction of Wind Power for Multi-Turbines in a Wind Farm. *Front. Energ. Res.* 9, 723775. doi:10.3389/fenrg.2021.723775

Deo, R. C., Wen, X., and Qi, F. (2016). A Wavelet-Coupled Support Vector Machine Model for Forecasting Global Incident Solar Radiation Using Limited Meteorological Dataset. *Appl. Energ.* 168, 568–593. doi:10.1016/j.apenergy.2016.01.130

Li, Z., Jiang, W., Abu-Siada, A., Li, Z., Xu, Y., and Liu, S. (2020). Research on a Composite Voltage and Current Measurement Device for HVDC Networks. *IEEE Trans. Ind. Electron.* 68 (9), 8930–8941. doi:10.1109/TIE.2020.3013772

Li, Z., Ye, L., Zhao, Y., Song, X., Teng, J., and Jin, J. (2016). Short-term Wind Power Prediction Based on Extreme Learning Machine with Error Correction. *Prot. Control. Mod. Power Syst.* 1 (1), 1. doi:10.1186/s41601-016-0016-y

Lin, Z., and Liu, X. (2020). Wind Power Forecasting of an Offshore Wind Turbine Based on High-Frequency SCADA Data and Deep Learning Neural Network. *Energy* 201, 117693. doi:10.1016/j.energy.2020.117693

Liu, X., Lin, Z., and Feng, Z. (2021). Short-term Offshore Wind Speed Forecast by Seasonal ARIMA - A Comparison against GRU and LSTM. *Energy* 227, 120492. doi:10.1016/J.ENERGY.2021.120492

Qureshi, A. S., Khan, A., Zameer, A., and Usman, A. (2017). Wind Power Prediction Using Deep Neural Network Based Meta Regression and Transfer Learning. *Appl. Soft Comput.* 58, 742–755. doi:10.1016/j.asoc.2017.05.031

Shen, X., Ouyang, T., Khajorntraidet, C., Li, Y., Li, S., and Zhuang, J. (2021a). Mixture Density Networks-Based Knock Simulator. *Ieee/asme Trans. Mechatron.*, 1. doi:10.1109/TMECH.2021.3059775

Shen, X., Ouyang, T., Yang, N., and Zhuang, J. (2021b). Sample-based Neural Approximation Approach for Probabilistic Constrained Programs. *IEEE Trans. Neural Netw. Learn. Syst.* 1, 8. doi:10.1109/TNNLS.2021.3102323

Shen, X., and Raksincharoensak, P. (2021a). Pedestrian-aware Statistical Risk Assessment. *IEEE Trans. Intell. Transport. Syst.*, 1–9. doi:10.1109/TITS.2021.3074522

Shen, X., and Raksincharoensak, P. (2021b). Statistical Models of Near-Accident Event and Pedestrian Behavior at Non-signalized Intersections. *J. Appl. Stat.* 1, 21. doi:10.1080/02664763.2021.1962263

Shi, J., Ding, Z., Lee, W.-J., Yang, Y., Liu, Y., and Zhang, M. (2014). Hybrid Forecasting Model for Very-Short Term Wind Power Forecasting Based on Grey Relational Analysis and Wind Speed Distribution Features. *IEEE Trans. Smart Grid.* 5 (1), 521–526. doi:10.1109/tsg.2013.2283269

Wang, J., Zhang, N., and Lu, H. (2019a). A Novel System Based on Neural Networks with Linear Combination Framework for Wind Speed Forecasting. *Energ. Convers. Manage.* 181, 425–442. doi:10.1016/j.enconman.2018.12.020

Wang, Y., Wang, H., Srinivasan, D., and Hu, Q. (2019b). Robust Functional Regression for Wind Speed Forecasting Based on Sparse Bayesian Learning. *Renew. Energ.* 132, 43–60. doi:10.1016/j.renene.2018.07.083

Wang, Z., Zhang, J., Zhang, Y., Huang, C., and Wang, L. (2020). Short-term Wind Speed Forecasting Based on Information of Neighboring Wind Farms. *IEEE Access* 8, 16760–16770. doi:10.1109/access.2020.2966268

Wu, B., Song, M., Chen, K., He, Z., and Zhang, X. (2014). Wind Power Prediction System for Wind Farm Based on Auto Regressive Statistical Model and Physical Model. *J. Renew. Sustain. Energ.* 6 (1), 013101. doi:10.1063/1.4861063

Yang, D. (2019). On post-processing Day-Ahead NWP Forecasts Using Kalman Filtering. *Solar Energy* 182, 179–181. doi:10.1016/j.solener.2019.02.044

Yang, N., Huang, Y., Hou, D., Liu, S., Ye, D., Dong, B., et al. (2019). Adaptive Nonparametric Kernel Density Estimation Approach for Joint Probability Density Function Modeling of Multiple Wind Farms. *Energies* 12 (7), 1356. doi:10.3390/en12071356

Yang, N., Liu, S., Deng, Y., and Xing, C. (2021a). An Improved Robust SCUC Approach Considering Multiple Uncertainty and Correlation. *IEEJ Trans. Elec Electron. Eng.* 16 (1), 21–34. doi:10.1002/tee.23265

Yang, N., Yang, C., Wu, L., Shen, X., Jia, J., Li, Z., et al. (2021b). Intelligent Data-Driven Decision-Making Method for Dynamic Multi-Sequence: An E-Seq2Seq Based SCUC Expert System. *IEEE Trans. Ind. Inf.*, 1. doi:10.1109/TII.2021.3107406

Yang, N., Yang, C., Xing, C., Ye, D., Jia, J., Chen, D., et al. (2021c). Deep Learning-based SCUC Decision-making: An Intelligent Data-driven Approach with Self-learning Capabilities. *IET Gener. Transm. Distrib.*. doi:10.1049/gtd2.12315

Zhang, L., Xie, Y., Ye, J., Xue, T., Cheng, J., Li, Z., et al. (2021). Intelligent Frequency Control Strategy Based on Reinforcement Learning of Multi-Objective Collaborative Reward Function. *Front. Energ. Res.*, 1–12. doi:10.3389/fenrg.2021.760525

Zhao, X., Liu, J., Yu, D., and Chang, J. (2018). One-day-ahead Probabilistic Wind Speed Forecast Based on Optimized Numerical Weather Prediction Data. *Energ. Convers. Manage.* 164, 560–569. doi:10.1016/j.enconman.2018.03.030

Zheng, D., Eseye, A. T., Zhang, J., and Li, H. (2017). Short-term Wind Power Forecasting Using a Double-Stage Hierarchical ANFIS Approach for Energy Management in Microgrids. *Prot. Control. Mod. Power Syst.* 2 (1), 13. doi:10.1186/s41601-017-0041-5

Zhuang, F., Qi, Z., Duan, K., Xi, D., Zhu, Y., Zhu, H., et al. (2021). A Comprehensive Survey on Transfer Learning. *Proc. IEEE* 109 (1), 43–76. doi:10.1109/JPROC.2020.3004555

Conflict of Interest: Author WC and JZ is employed by State Grid Zhejiang Electric Power Company, Ltd. Author WQ, FZ, DX, WR, GL, and MS are employed by State Grid Shaoxing Power Supply Company. This study received funding from the Science and Technology Project of State Grid Zhejiang Electric Power Co., LTD (5211SX2000ZM). The funder had the following involvement with the study: data collection and analysis.

The remaining author declare that the research was conducted in the absence of any commercial or financial relationships that could be construed as a potential conflict of interest.

frontiers in Energy Research

METHODS
published: 17 December 2021
doi: 10.3389/fenrg.2021.766472

Tolerance of Electromagnetic Relay to Voltage Sags and Short Interruptions

Huaying Zhang, Qing Wang and Yihong You*

New Smart City High-Quality Power Supply Joint Laboratory, China Southern Power Grid, Shenzhen, China

This paper studies the tolerance of electromagnetic relay (EMR) under voltage sag and short interruptions on the basis of response mechanism analysis and the extensive tests. First, it introduces the structure of EMR and proposes response mechanism of EMR under voltage sag. Then, a detailed test plan is presented, including the information of test platform, testing condition, EMRs used in test, list of test, test procedure, and the measured waveforms. Magnitude and duration of the sags are not only the characteristics to be considered to investigate EMR's tolerance. The other factors, which may have significance influence on tolerance of EMR, are considered here, including point-on-wave (POW), phase angle jump (PAJ), harmonic, magnitude variation in pre- and post-sag segments, two-stage sag, and slow recovery sag. Extensive tests results are presented in the form of voltage-tolerance curves (VTCs). Besides magnitude and duration, POW, PAJ, and two-stage sag have a significant influence on the tolerance of EMR. Other factors only have a tiny impact on the tolerance of EMR. The results show that the magnitude tolerance of EMR is 48–74% of U_{nom}, and duration tolerance is 5–28 ms; they are useful for the technical assessment of EMR's tolerance to voltage sags and short interruptions, and for the economic assessment of the industry process trip due to its disengagement. Test results also benefit for choosing proper EMR and mitigation device in the complicated operating environment.

Keywords: electromagnetic relay, power quality, short interruption, voltage sag, voltage-tolerance curve

OPEN ACCESS

Edited by:
Zhenhao Tang,
Northeast Electric Power University, China

Reviewed by:
P. Maadeswaran,
Periyar University, India
Karthik Balasubramanian,
Keppel Offshore and Marine Limited, Singapore

****Correspondence:***
Huaying Zhang
zhytgyx@163.com

Specialty section:
This article was submitted to Smart Grids, a section of the journal Frontiers in Energy Research

Received: *29 August 2021*
Accepted: *11 November 2021*
Published: *17 December 2021*

Citation:
Zhang H, Wang Q and You Y (2021) Tolerance of Electromagnetic Relay to Voltage Sags and Short Interruptions. Front. Energy Res. 9:766472. doi: 10.3389/fenrg.2021.766472

1 INTRODUCTION

Electromagnetic relay (EMR) is widely applied in industrial control system and communication as a kind of basic electric component, also playing a role in switching circuits, transferring signals, and eliminating interference. However, when a short-circuit fault occurs in the power system, it causes power quality issues, such as voltage sag and short interruption (Nagata et al., 2018; Wang et al., 2019; Ye et al., 2019), which affect the normal operation of EMR. Voltage sag even causes the malfunction and damage of EMR in severe cases (Wu and Fan, 2015; Jianbo and Qi, 2018), then leading to the failure of the whole industrial process and resulting in the huge economic losses (Mohammadi et al., 2017; De Santis et al., 2018; Gambôa et al., 2019). For example, (Bollen, 2000) records that the tripping of EMR under one voltage sag event "cause the shutdown of a large chemical plant, leading to perhaps $100,000 in lost production." However, the tolerance of EMR under voltage sag presented in Bollen (2000) is from IEEE Std. 1346 (IEEE, 1998) which published the sensitivity of EMR 20 years ago. The data in IEEE Std. 1346 may be not suited for the industry today, because of the improvement of the technique of EMR and the updating industry processes. It is important to understand the tolerance of EMR under voltage

sag nowadays to provide the voltage sag mitigation scheme and the EMR purchase plan for the industry users.

EMR is known as the sensitive equipment under voltage sag because of industrial users' complain (IEEE, 1998; Bollen, 2000; Zhai and Yang, 2008). IEEE Std. 1346 (IEEE, 1998) pays close attention to it and present that tolerance of EMR is 60–75% of rated voltage of magnitude, and is 10–30 ms of duration; however, this standard states that the presented tolerance "should not be considered typical for these types of devices but only a samples of what is available." It is difficult to provide the detailed guide for the users. The simulation was done to investigate the dynamic characteristics of EMR interfered by voltage sags and short interruptions to offer the qualitative understanding of the sensitivity of EMR (Zhai and Yang, 2008). It is a necessary way to get the tolerance information of sensitive equipment than conducting the extensive tests on equipment. The tolerance of other sensitive equipment is also obtained through test, for example, the tests on adjustable speed drive (ASD) (Xu et al., 2019a), programmable logic controller (PLC) (Xu et al., 2019b), AC coil contactor (ACC) (Djokic et al., 2004; Hardi et al., 2010; Weldemariam et al., 2016), and so on (Ouyang et al., 2015; Ouyang and Liu, 2017).

The different single-event characteristics of voltage sag is considered in the test. Magnitude and duration are the essential characteristics which should be included in the test. Furthermore, other characteristics should be included, such as point-on-wave (Alvaro et al., 2019; Wang et al., 2020) and phase angle jump (PAJ) (Wang et al., 2015). The former is also called phase angle, and the latter is called phase shift in IEC 61000-4-30 (IEC, 2021). POW is the phase angle of the fundamental voltage waveform at which the voltage sag occurs; PAJ is the change of phase angle during the voltage sag (Djoki et al., 2007; Wang et al., 2015; IEEE, 2017; Alvaro et al., 2019; Wang et al., 2020; Ren et al., 2021). There are two views about considering the other characteristics. For one thing, IEEE Std. 1346 recommends that "phase shift and point of initiation not be considered," since these "characteristics are not typically available in the sag environment data." However, for the improvement of the voltage sag generator and the monitor technical, the problem of "sag environment data" has not been the barrier of the testing. Another opinion is that POW and PAJ have significant impacts on electromagnetic equipment (Djoki et al., 2007; Wang et al., 2015; Alvaro et al., 2019; Wang et al., 2020; Ren et al., 2021); similar thinking is also recommended in the standards. IEC 61000-4-30 (IEC, 2021) states that for some equipment "drop-outs, the phase angle at which a voltage dip begins is an important characteristic"; IEEE Std. 1668-2017 (IEEE, 2017), which is the newest standard related to testing on the sensitive equipment under voltage sag, suggests that "...characteristics such as phase-shift, point-on-wave of initiation, and recovery of the instantaneous voltage waveform during the sag may have an effect on equipment performance as well." Thus, the various single-event characteristics of voltage sag are included in this paper to test the sensitivity of EMR.

This paper proposes a general test procedure and has done extensive tests to investigate the tolerance of EMR to get the quantitative results and support the voltage sag mitigation for EMR. The rest of this paper is organized as follows. **Section 2** describes the structure and response mechanism of EMR. Detailed test plan is elaborated in **Section 3**, including test principle, test procedure, equipment under test (EUT), and voltage sag generator. Test results are presented in the form of voltage tolerance curves in **Section 4**. **Section 5** discusses the potential application, and **Section 6** makes a conclusion of the test results.

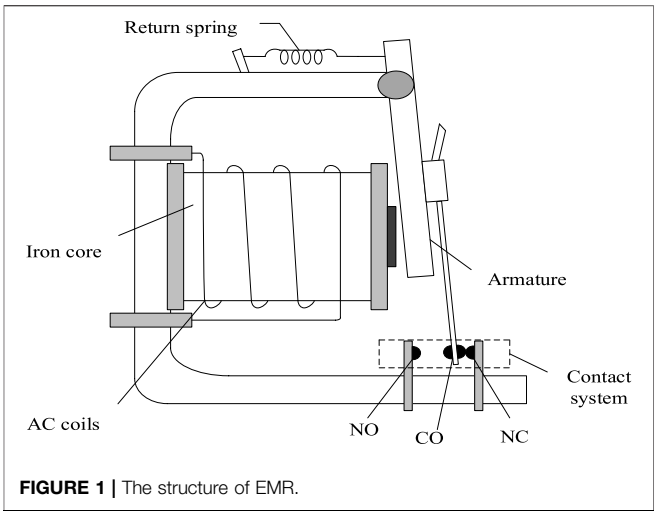

FIGURE 1 | The structure of EMR.

2 STRUCTURE AND RESPONSE MECHANISM

2.1 Structure of Electromagnetic Relay

The structure sketch of EMR is shown in **Figure 1** (Fan and Wu, 2014). It is mainly composed by an iron core, AC coils, an armature, return springs, and contact system, similar to the structure of ACC. Contact system contains three types of contacts: a normally open contact (NO), a normally closed contact (NC), and a common contact (CO); their positions are also shown in **Figure 1**.

When a certain voltage is supplied to the coil, an electromagnetic force (F_{mag}) is generated. Then, the armature is attracted toward to iron core as F_{mag} is greater than the force of spring (F_s). Then, the circuit is turned on. On the other hand, when the coil is de-energized, F_{mag} disappears but the F_s still exists. Then, armature returns to its original position, causing the circuit turned off. The whole working process is shown in **Figure 2**. Once a voltage sag occurs in the process, it causes EMR to work unnormal.

EMR and ACC are both basic electromagnetic equipment in the control systems, and their structures are similar. However, EMR is generally used for the control loop, whose operating current is small, only a few Amps; ACC is often used for main circuit control, commonly being used to control the start and stop of the motor, etc., and its rated current is greater, even up to several thousand Amps, so an arc extinguishing device is needed for ACC. The behaviors of EMR and ACC under

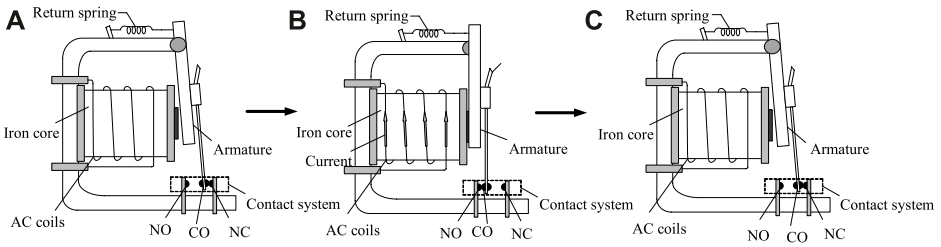

FIGURE 2 | Working principle of EMR. **(A)** EMR is not energized. **(B)** EMR is energized. **(C)** EMR is de-energized.

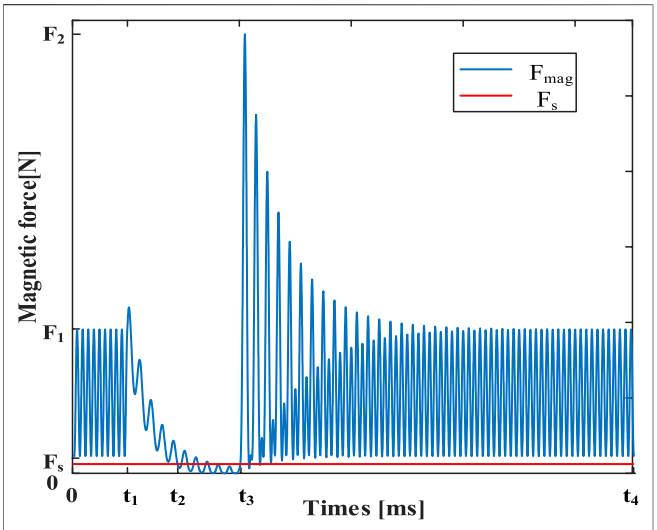

FIGURE 3 | The curves of the electromagnetic Force (F_{mag}) and the force of spring (F_s).

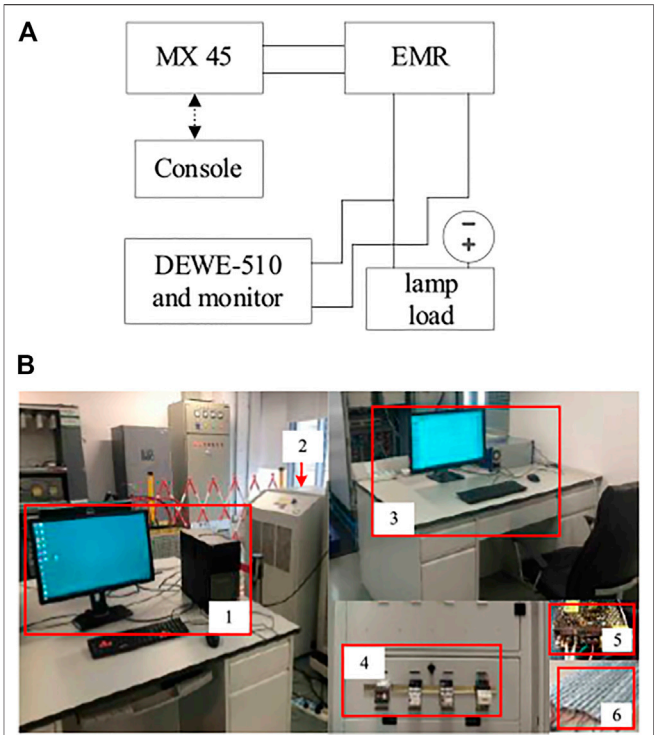

FIGURE 4 | Test circuit. **(A)** The connection of the test for EMR. **(B)** Test platform (1. console, 2. programmable power supply (MX45), 3. data acquisition device DEWE-510 and its Display, 4. EMR, 5. DC supply source, 6. lamp load).

voltage sag are different due to the arc extinguishing device, coil turn number, and so on. The research results on behavior of ACC under voltage sag cannot be used as the result of study on EMR, and the knowledge of behavior of EMR under voltage sag is limited.

2.2 Response Mechanism of Electromagnetic Relay to Voltage Sag

When the sinusoidal AC power is supplied, the main flux of the ac coil changes sinusoidally with time:

$$\Phi = \Phi_m \sin \omega t \tag{1}$$

The F_{mag} can be calculated by Maxwell's electromagnetic force formula:

$$F_{mag} = \frac{\Phi^2}{2\mu_0 S} \tag{2}$$

where S is magnetic attraction area at air gap, μ_0 is vacuum permeability.

Thus, according to **Eqs 1**, **2**, Fmag can be written as

$$F_{mag} = \frac{\Phi_m^2 \sin^2 \omega t}{2\mu_0 S} = \frac{\Phi_m^2}{4\mu_0 S} - \frac{\Phi_m^2 \cos 2\,\omega t}{4\mu_0 S} \tag{3}$$

Therefore, the F_{mag} is proportional to the square of the main flux. The F_{mag} changes versus time at twice voltage frequency.

Figure 3 shows the waveform of F_{mag} in blue and F_s in red during a voltage sag. In this case, the operation of EMR is influenced by the sag. Before sag starts, F_{mag} is greater than F_s, and EMR operates normally. When a sag occurs at time t_1, F_{mag} is gradually reduced; however, F_{mag} is still greater than F_s until time t_2, and EMR operates normally from t_1 to t_2. F_{mag} is less than F_s from t_2, and EMR is disengaged from t_2 to t_3. The sag ends at t_3, and EMR recovers to operate normally.

TABLE 1 | The main parameters of EUT.

EUT	Unom (V)	Inom (A)	Manufacturer
R1	220	5	OMRON
R2	220	5	OMRON
R3	230	5	ABB
R4	230	5	Schneider
R5	220	5	IDEC
R6	220	10	IDEC
R7	220	5	Chint
R8	220	5	DELIXI

It indicates that when the sag duration is too long, causing F_{mag} less than F_s, EMR trips (Wu and Fan, 2015). Of course, when voltage sag magnitude is above a certain level, F_{mag} keeps higher than F_s no matter how long the sag lasts, and the EMR can work steadily (Zhai and Yang, 2008). In other words, to ensure that the EMR works normally when powered, F_{mag} should be greater than F_s. Thus, it is necessary to know and quantify the EMR's tolerance to voltage sag.

Moreover, different POW and PAJ influence EMR's main flux, thereby affecting the change of F_{mag}. It means that POW and PAJ may influence EMR's tolerance, so this paper considers these characteristics in the test. According to **Eq. 3**, F_{mag} is related to voltage frequency, so harmonic and frequency fluctuation are also in consideration. In **Section 3**, a detailed schedule is presented to investigate the EMR's tolerance to various conditions.

3 TEST PLAN

3.1 Test Platform

Based on EMR's structure and its response mechanism, the test circuit is connected as shown in **Figure 4**. The test platform consisted of the console, voltage sag generator (programmable power supply MX45), the data acquisition device (DEWE-510), EUT, DC supply source, and the lamp load.

Programmable power supply MX45 (AMETEK, 2017), whose brand is AMETAK, is used as the sag generator here. The voltage output range is 0~400 V, and the maximum output power is 45 kVA; single and three phase mode are available. It meets the voltage sag generator requirements in IEEE 1668-2017 (IEEE, 2017), and MX45 can generate any voltage sag waveform designed by setting. In the test, the voltage waveform from MX45 is measured by the acquisition device. The measured single-event characteristics of the generated voltage sag are consistent with the setting value on the voltage sag generator.

The EUT is EMR, which is energized from one of the phases of MX45 (phase-A), since it is single-phase equipment. Thus, the test platform is a single-phase system.

3.2 Testing Condition and Equipment Under Test

The sensitivity is determined by two major factors: the design of the equipment and the physical characteristics of the voltage sag (IEEE, 2017). It suggests that different brands of the same equipment, and even different models of the same brand, often have different sensitivity to voltage sag. Eight EMRs from seven different manufactures are selected as EUT in the tests, in order to ensure a high degree of reliability and quantify the tolerance to voltage sag in the general way. The list of EUT is given in **Table 1**, with the information of EMR's nominal voltage (U_{nom}) and nominal current (I_{nom}).

EMRs are connected with a load circuit as a switch. A resistive lamp is used as the load here, supplied by a DC supply source (24 V). In all tests, EMR is supplied by MX45, 100% of U_{nom} is supplied to EMR during the pre-and post-sag segments, and a voltage sag is supplied to EMR during the sag segment. DEWE-510 was used to monitor the voltage on the lamp load. When a voltage sag causes EMR tripping, the voltage is about 0 V. The voltage indicates the behavior of EMR under voltage sag.

3.3 List of Test

The effect by rectangular and non-rectangular voltage sags is investigated.

EMRs are first tested against simple rectangular voltage sags, which are with different POW or PAJ, supplied from an ideal voltage source.

Then, another complicated voltage wave-forms, supplied from a non-ideal voltage source, is tested. These voltage sags include sags with a frequency variation up to ±2%, sags with a harmonic content (THD up to 12%), and sags with the magnitude variation up to ±10% in pre- and post-sag segments.

Lastly, the influence of various two-stage voltage sags, as well as the slow recovery sags, is investigated. **Table 2** summarizes the influence factor of this test.

3.4 Test Procedure

In order to get the accurate test results, the test is done according to the test procedure. The following procedure is used in tests with rectangular voltage sags, and it is presented as the general test procedure for the sensitive equipment under voltage sag.

3.4.1 Set the Influence Factors and the Ranges of Them for the Test

There are three main factors for EMR, including magnitude, duration, and POW; the non-main factors are PAJ, frequency variation, harmonic distortion, and magnitude variation. It is planned that the maximum and minimum magnitudes of voltage sag for testing are 90 and 0%; the two values are decided according to the definition of voltage sag. The maximum and minimum durations for testing are 2 and 0 ms, respectively; the tolerance of duration of all EUT in the current research is less than 2 s; thus, 2 s is as the maximum duration. The test step sizes are 2% and 2 ms for magnitude and duration, respectively. The step sizes for other influence factors are in **Table 2**.

The main and non-main factors for the different EUT can be different; it depends on the response characteristics of the different EUT under voltage sag. The factors in **Table 2** are suitable for most single-phase equipment; however, the type of voltage sag, which is not mentioned in **Table 2**, should be the important factor in the test for three-phase equipment.

TABLE 2 | Factors considered in the tests.

Test condition	Sag characteristics setting detailed
Rectangular voltage sag	Sag with POW (0° POW, 27° POW, 45° POW, 63° POW, 90° POW) Sag with PAJ (0° PAJ, 30° PAJ, 60° PAJ, 90° PAJ) Sag with a frequency variation up to ±2% Sag with a harmonic content (THD up to 12%) Sag with the magnitude variation in pre- and post-sag segments (up to ±10%)
Non-rectangular voltage sag	Two-stage voltage sags The slow recovery sags (voltage recovery gradient: 10, 20, 30, 40, 50 V/s)

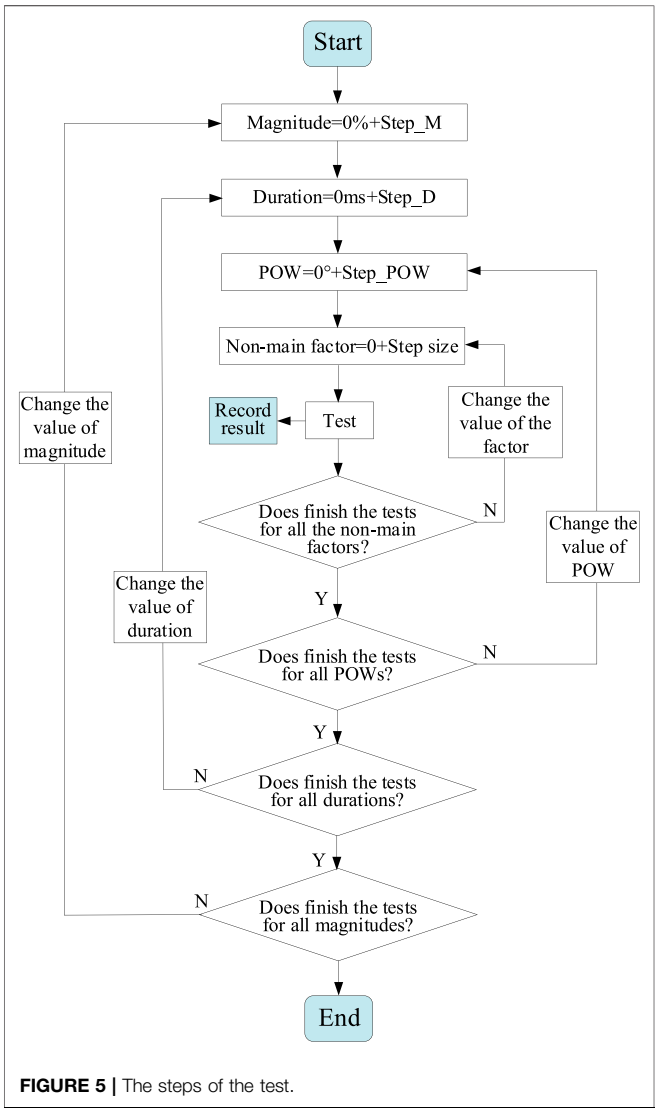

FIGURE 5 | The steps of the test.

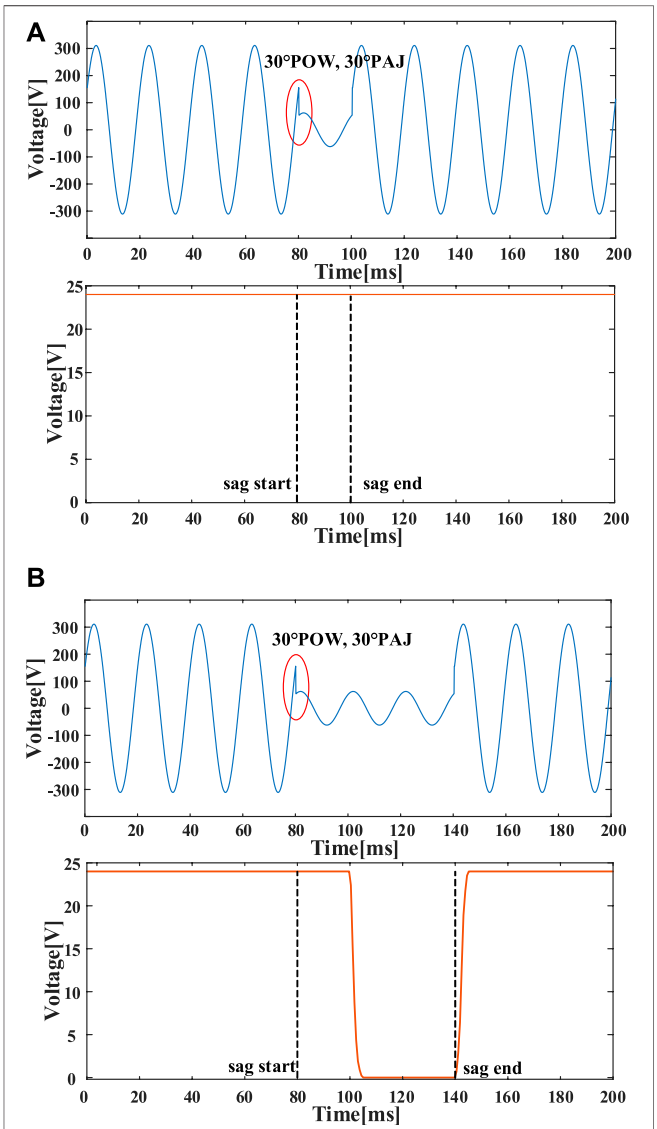

FIGURE 6 | The measured time-varying wave-forms. **(A)** EMR don't trip, **(B)** EMR trip.

3.4.2 Generate Voltage Sag and Test

The generated voltage sag is with the different single-event characteristics, as shown in **Figure 5**; the three main factors keep constant when changing the non-main factor. Take PAJ setting as example, when setting magnitude = 50%, duration = 100 ms, POW = 45°, the step is to set PAJ equals 0°, 30°, 60°, 90° in order, and record the test result. Then, change POW to 63° (magnitude and duration remain unchanged), and then test the EUT under the voltage sag with PAJ equals 0°, 30°, 60°, 90°, respectively. After finishing the test with considering the effect by PAJ, then do the tests considering the effect by the other non-

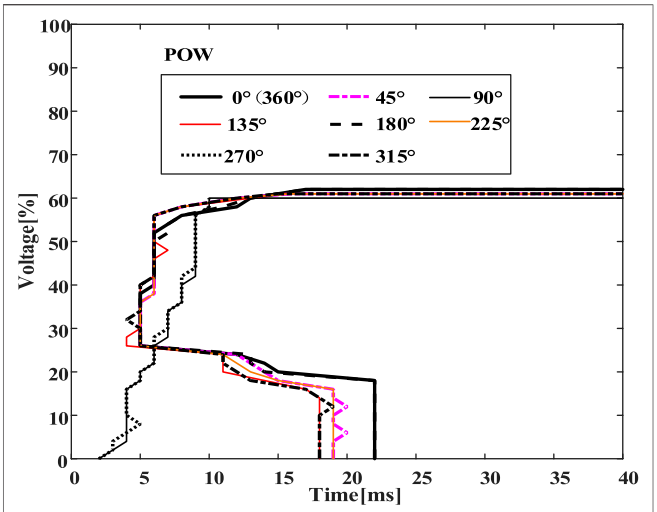

FIGURE 7 | Illustration of quarter-cycle symmetry (R1, 0° PAJ).

main factors. Considering all the factors in four loops in **Figure 5**, test the behavior of the EUT under the voltage sag with the different factors.

3.4.3 Tripping Criterion

The voltage sag generator generates voltage sag to supply EUT, and the states of EUT and the lamp load are recorded as the tripping criterion for EUT. The tripping criterion can be different for different EUT, for example, the dc voltage, current, or rotor speed can be options for tripping criterion of ASD. VTC can be drawn after all the tests were done.

The detailed test procedure may be different for the different EUT. The non-main factors are not necessary for all the EUT. It depends on the different structure and working condition.

3.5 The Measured Waveforms

The measured time-varying waveforms are shown in **Figure 6** as an example. The top panels of **Figures 6A,B** are the generated voltage sag waveforms; the bottoms are the voltage of the tested lamp. There is a voltage sag generated by MX45; the single-event characteristics of it are 20% of U_{nom} magnitude, 20 ms duration, 30° POW, and 30° PAJ; the voltage versus time is shown in the top of **Figure 6A**. The supplied voltage of lamp is recorded by the oscilloscope, which is about 24 V, shown in the bottom panel in **Figure 6A**; the lamp keeps working normally. EMR can tolerate this voltage sag. However, when the duration extends to 60 ms (shown in the top panel in **Figure 6B**), the other single-event characteristics of the voltage sag in **Figure 6B** are the same as the voltage sag in **Figure 6A**; the EMR fails in **Figure 6B**. EMR can tolerate about 20–25 ms, and then it fails; the load cannot keep working since the supply voltage of the load decrease to 0 V.

The two examples in **Figure 6** are the typical waveforms of the tests. The extensive tests show that the longer the duration or the lower magnitude of voltage sag, the greater probability of EMR tripping. The detailed results of the test are shown in **Section 4**.

4 TEST RESULTS

4.1 Testing of Electromagnetic Relay to Rectangular Voltage Sags

4.1.1 Quarter-Cycle Symmetry Respect to Point-on-Wave

The results of test are presented graphically by VTCs. The detailed test results for R1 are shown in **Figure 7**. VTCs of 0° POW, 180° POW, and 360° POW are quite close. VTCs of 90° POW and 270° POW are nearly the same. Furthermore, though there is a slight difference in VTCs of 45°, 135°, 225°, and 315° POW, they are almost coincident of the shape. It describes EMR's quarter-cycle symmetry. Thus, the sensitivity of EMRs is illustrated only for POW between 0° and 90° (0° POW, 27° POW, 45° POW, 63° POW, 90° POW are tested in this paper).

4.1.2 Sensitivity to Point-on-Wave

The sensitivity of EMR to POW is tested and shown in **Figure 8**. POW has a greater influence on the sensitivity of EMR.

It is obvious that the less POW, the stronger voltage sag tolerance of EMR, when the voltage sag is deep drop. Take R1 as example, when a short interruption occurs, the tolerance durations are 22 ms for 0° POW, 20 ms for 27° POW, 19 ms for 45° POW, 16 ms for 63° POW, and 3 ms for 90° POW, respectively. However, the greater POW, the stronger tolerance of EMR under voltage sag, when the voltage sag is shallow. R1 can tolerate 10 ms when 90° POW, but 5 ms when 0° POW, when the magnitude is 40%.

VTCs of 0° and 90° POW for all tested EMRs are shown in **Figure 8**. Overall, the shape of VTCs for the eight EMRs are similar; however, VTCs of different EMRs are with different "knee" parameter, due to the different type and different manufacturer. For example, R1 and R2 are two devices with the similar parameter (not the same model) from the same manufacturer; the results in **Figure 8** show that the VTCs of the two devices are different.

The sensitivity of the "flat" part for different POW is illustrated in **Figure 9**; "voltage threshold" means the maximum magnitude can be tolerated of a certain POW. In **Figure 9**, the larger POW, the smaller voltage threshold. Moreover, the variation of this threshold is between 2 and 10% of U_{nom} depending on the type of the EMR. For example, R5 will trip when the voltage drops below 54–62% of U_{nom}, depending on the POW, for voltage sags lasting more than 30 ms. This represents that the upper and lower limits of voltage magnitude threshold for the EMRs are tested.

4.1.3 Sensitivity to Phase Angle Jump

The test results of PAJ are showed in **Figure 10**. The tests of different PAJ are divided into two groups: one for 0° POW and another for 90° POW. The test of each group considers four PAJs, including 0° PAJ, 30° PAJ, 60° PAJ, and 90° PAJ.

From **Figure 10**, the tolerance of the complicated part ($t <$ 30 ms) of VTCs is clear. When voltage sag is starting at 0° POW, the larger PAJ, the stronger EMR's tolerance. For example, the duration is 24 ms of 90° PAJ when the voltage magnitude is 50% of U_{nom}, while the duration is only 8 ms of 0° PAJ under the same

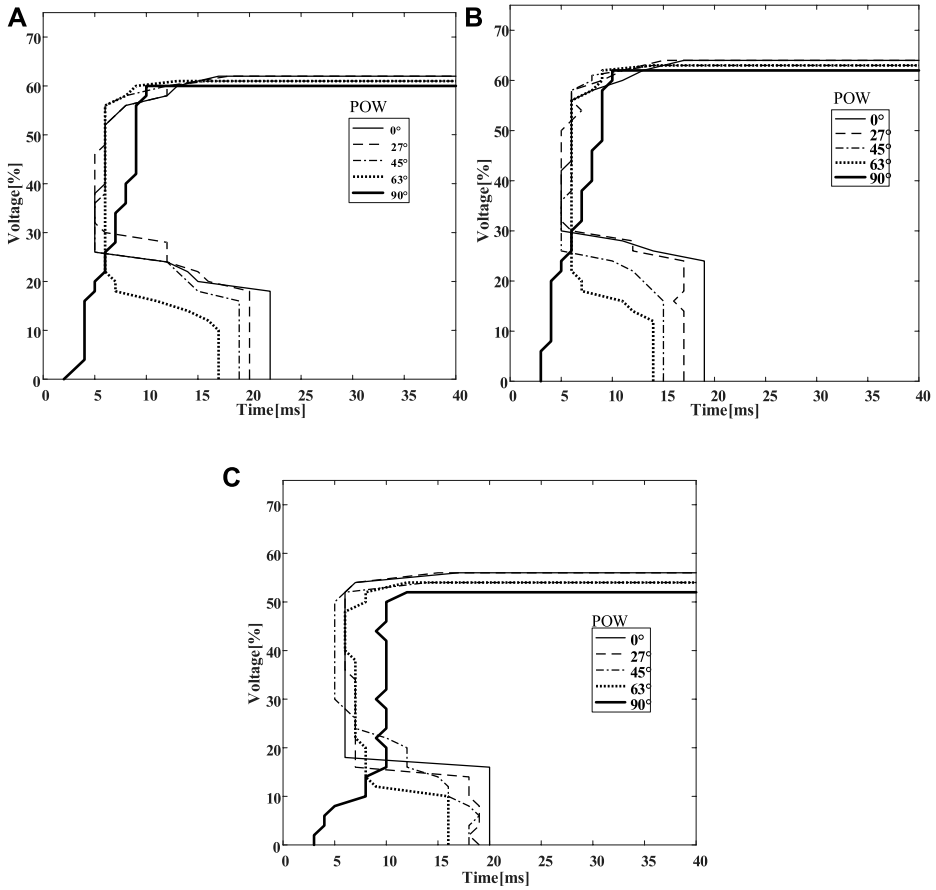

FIGURE 8 | Test results considering the different POW (0° PAJ). **(A)** Results for R1. **(B)** Results for R2. **(C)** Results for R7.

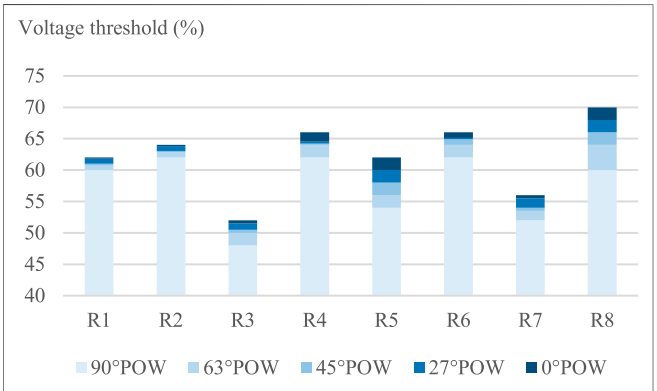

FIGURE 9 | Voltage threshold of different VTCs under different POW (0° PAJ).

condition. Instead, the larger PAJ, the weaker EMR's tolerance when the sag is starting at 90° POW.

For the two groups VTCs, the less PAJ, the stronger tolerance to the sags with shorter duration, which is with the obvious trend in the "vertical" part (t < 15–30 ms). In the "flat" part (t > 15–30 ms) of the VTCs, the less PAJ is also with the stronger tolerance; however, the trend is not as obvious as in the "vertical" part. Generally, PAJ effects on the tolerance of EMR, when a PAJ occurs, the tolerance of EMR is weaker.

4.1.4 Sensitivity to Frequency Variation

Test the tolerance of EMR to the sags with a frequency variation up to ±2%. The sags at 49, 50, and 51 Hz are considered. Frequency variation of ±2% of nominal frequency does not influence the sensitivity of the tested EMRs, since the VTCs at the three frequencies are almost coincident in **Figure 11A**.

4.1.5 Sensitivity to Harmonic Distortion

Test the tolerance of EMR to the sags with a harmonic content (THD up to 12%). It demonstrates that harmonic distortions of up to 12% of THD have only a slight influence on both EMR' sensitivity and the shape of VTCs, shown in **Figure 11B**. Test results show that the tolerance of EMR is slightly higher when the supply voltage contains harmonics.

4.1.6 Sensitivity to the Magnitude Variation in Pre- and Post-Sag Segments

The tolerance test results to the sags with variation in pre- and post-sag voltage magnitude (up to ±10%) is in

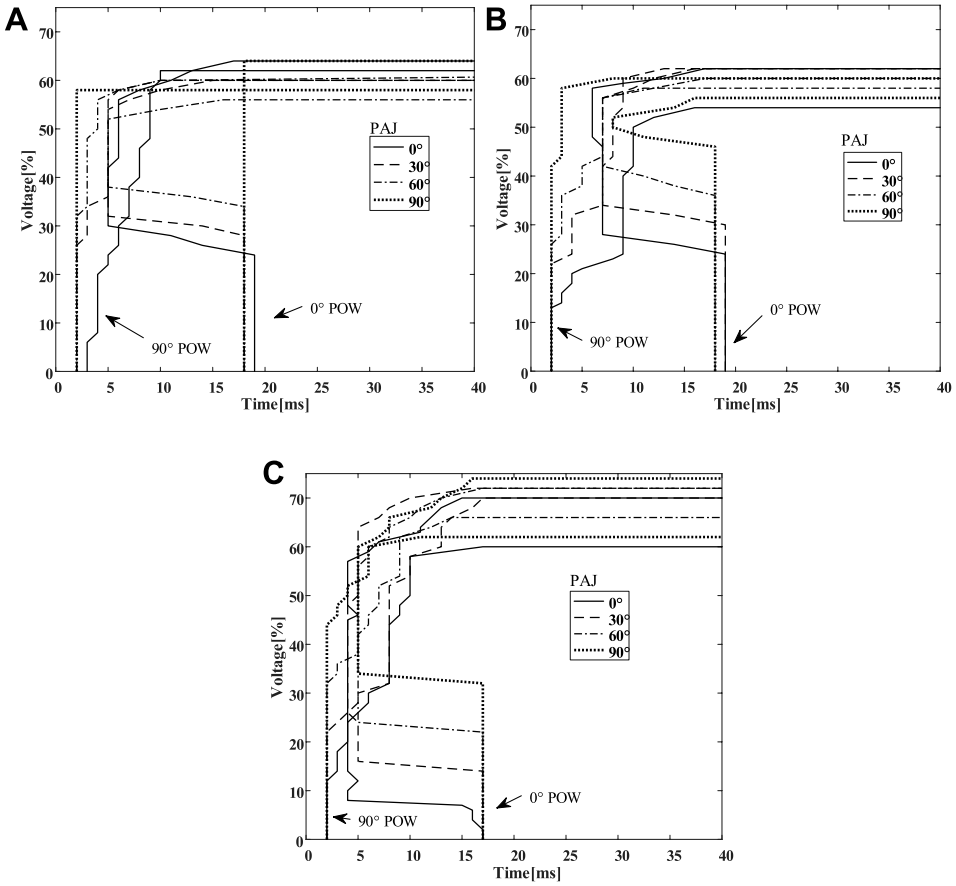

FIGURE 10 | Test results considering the different PAJ (0° POW and 90° POW). **(A)** Results for R2. **(B)** Results for R5. **(C)** Results for R8.

Figure 11C. It demonstrates that when the pre- and post-sag magnitude is 110% of U_{nom} (242 V), EMR's tolerance increases slightly. It can conclude that the slightly higher of the magnitude in pre- and post-sag segments, the stronger tolerance of EMR.

4.1.7 General Voltage-Tolerance Curves

Based on the test results obtained, the general VTC of all the tested EMR is shown in **Figure 12**. EMR can tolerate a voltage sag with the magnitude more than 74% of U_{nom}. When the sag magnitude is less than 48% of U_{nom}, EMR will trip when the sag duration exceeds 28 ms.

4.2 Testing of Electromagnetic Relay With Non-Rectangular Voltage Sags

4.2.1 Sensitivity to the Two-Stage Voltage Sags

In order to ensure the accuracy of the test results, the total duration of the two stages (**Figure 13**) must be less than the maximum tolerance duration (0% of U_{nom}) for a certain EUT. For example, the maximum tolerance duration of R4 is 24 ms when 0% of U_{nom}, 10% of U_{nom}, or 30% of U_{nom}; total duration of the two stage sags in this test for R4 should be less than 24 ms. All the tests to two-stage voltage sags are under the same conditions, both with the same total duration (20 ms), 0° POW and 0° PAJ.

The results of three groups tests are listed in **Table 3**. The tests of No. 1 group are to prove the tolerance of R4. R4 is exposed to a short interruption (0% of U_{nom}), a voltage sag (10% of U_{nom}), and a voltage sag (30% of U_{nom}); it remains engaged. It means R4 can operate normally to a sag or short interruption when the duration is less than 24 ms.

The tests of No. 2 group show that EMR is sensitive to the two-stage voltage sag. R4 is exposed to a combined two-stage voltage sag, different in respective sag duration, while both the states of R4 are disengaged. The sag in No. 1 is worse than the sag in No. 2; "two-stage" makes R4 disengaged.

The tests of No. 3 group show that EMR is sensitive to the order of the two-stage. R4 is exposed to two different sequential two-stage voltage sags. It works normally to the sag with first stage of 0% and second stage of 30%, and is disengaged to the sag with first stage of 30% and second stage of 0%.

4.2.2 Sensitivity to the Slow Recovery Voltage Sag

The slow recovery voltage sag is due to the starting of large motors or transformer energizing. In the tests, the voltage sag is

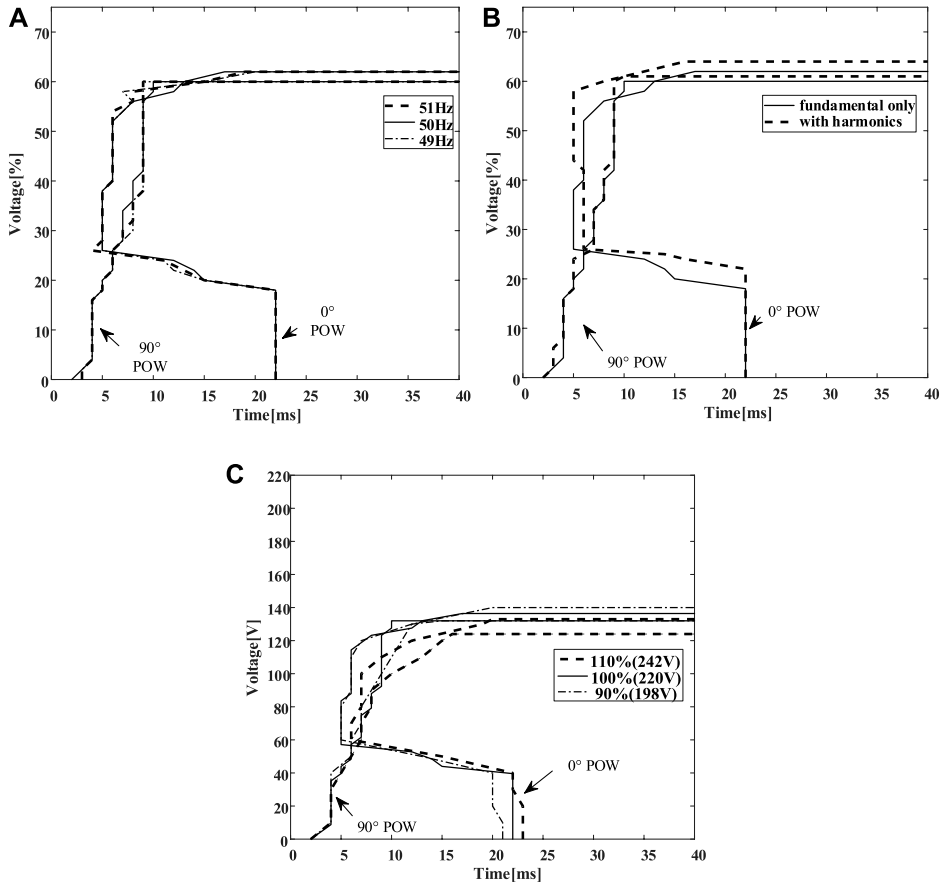

FIGURE 11 | Test results for R1 (0° PAJ). **(A)** Considering the frequency fluctuation. **(B)** Considering the harmonic distortion. **(C)** Considering the magnitude variation in pre- and post-sag segment.

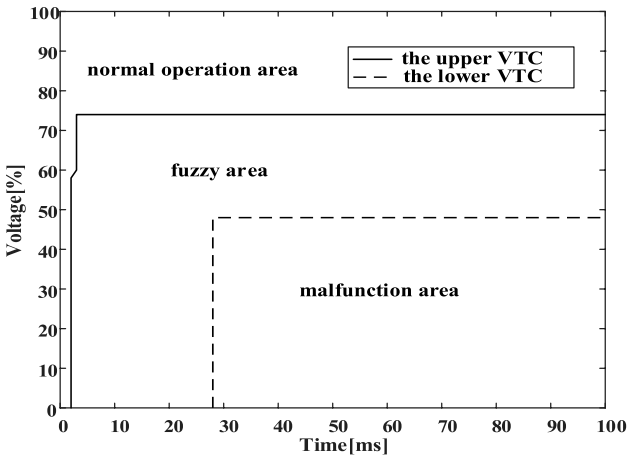

FIGURE 12 | Generic VTCs for EMR.

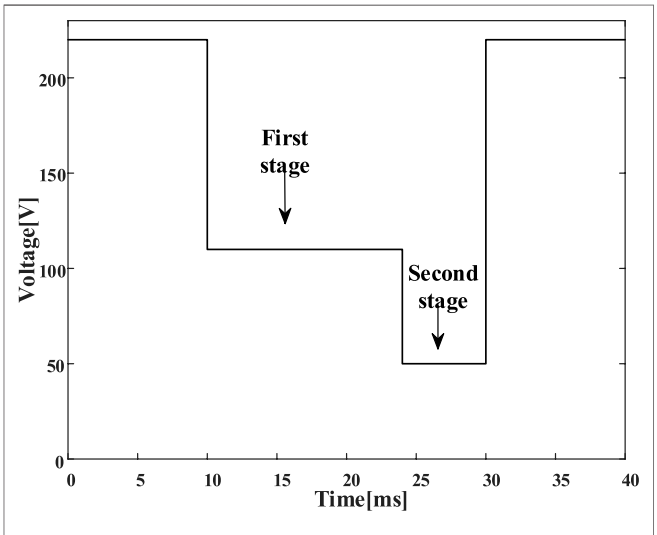

FIGURE 13 | An example of the two-stage voltage sag.

set as recovering progressively to the nominal voltage. Five voltage recovery gradient and two different POW are considered here.

Table 4 shows the duration of sag, which causes the disengagement of R4. From the test results, it can conclude that the disengagement time is increasing with the increasing

TABLE 3 | Test conditions and results to two-stage voltage sags for R4.

No	First stage		Second stage		State of R4
	Magnitude (%)	Duration (ms)	Magnitude (V%)	Duration (ms)	
1	0	20	—	—	Engaged
	10	20	—	—	Engaged
	30	20	—	—	Engaged
2	0	14	10	6	Disengaged
	10	6	0	14	Disengaged
3	0	14	30	6	Engaged
	30	6	0	14	Disengaged

TABLE 4 | Duration (ms) of the slow recovery voltage sag to disengage for R4 as a function of initial voltage drop and the voltage recovery gradient.

Initial drop to	Voltage recovery gradient				
	10V/s	20V/s	30V/s	40V/s	50V/s
(a) 0° POW (0° PAJ)					
0%	25	24	23	22	21
10%	25	24	24	23	21
20%	25	24	24	24	22
30%	25	24	24	24	22
40%	25	25	24	24	22
50%	7	7	7	8	10
60%	8	9	9	9	10
70%	—	—	—	—	—
(b)90° POW (0° PAJ)					
0%	5	5	4	4	4
10%	5	5	5	5	5
20%	6	6	6	5	5
30%	6	6	6	6	6
40%	10	10	10	9	9
50%	10	10	10	10	10
60%	12	12	12	13	14
70%	—	—	—	—	—

recovery gradient, for the shallower initial drop, while the opposite results would obtain for a deeper initial drop. Overall, difference of disengaged time is small of different recovery gradient if initial drop is a constant.

5 COMPARISON

This study proposes a general test procedure to improve the test effective and the accuracy. The comparisons of the effectiveness and the accuracy between the proposed test procedure and the test method proposed by IEEE standard (IEEE, 2017) are listed in **Table 5**.

The results in **Table 5** are the test results for R2, when 0° POW and 0° PAJ. The "real" critical points of the tolerance under the voltage sags with the different residual voltage are testing results by the traditional method, which is called "step by step" method. The step size is 1 ms; the small step size ensures the testing accuracy but with the heavy testing work. The real tolerances are 19, 19, 19, 6, 5, 6, and 14 ms when magnitudes are 0, 10, 20, 30, 40, 50, and 60%, respectively. However, the traditional method costs the extensive work, for example, it has to do 1,000 tests, when the critical point is 1,000 ms for a certain residual voltage.

IEEE test method (IEEE, 2017) is the fixed step test method. For example, the first step to the seventh step is testing the tolerance of EUT when duration is 0, 10, 20, 50, 100, 200, and 500 ms, respectively. The greater test step sizes result in the greater test errors. The example in **Table 5** is not with the great errors, because of the critical points are less than 20 ms, the step size in this range is small by IEEE method. The worse situation is that when the critical point is 300 or 400 ms, the test result should be 500 ms, leading the larger error.

The proposed method can decide the next test point automatically according to the test results of the two previous test points, can quickly approach the critical point. The errors of the testing results for R2 are less than 1 ms compared with the real tolerances. The test work is 8 times for a certain residual voltage, which is quite less than the test work by "step by step" method, whose testing works are 19, 19, 19, 6, 5, 6, and 14 times for the different residual voltage for R2. The proposed method is with the high efficiency and test accuracy.

6 APPLICATION OF THE TEST RESULTS

First, through numerous tests, it finds that POW and PAJ are the major affected factors, as well the two-stage sag. For the reason that, it can carry out a subset tests described in this paper to analyze the voltage tolerance of EMR, only considering magnitude, duration, POW, PAJ, and the two-stage sag.

Secondly, based on the test results got, the general VTC of EMR are obtained as shown in **Figure 12**. The general VTC is helpful for industry consumer to choose the proper EMR considering their own operating environment. Moreover, it is useful for the manufacturer to design the EMR with higher voltage tolerance for specific consumer. For example, EMR can work steadily in a longer duration environment.

Third, EMR can tolerate a voltage sag with the magnitude more than 74% of U_{nom} no matter how long the sag lasts from the general VTC in **Figure 12**. The result is profitable for providing appropriate sag countermeasures. For example, the voltage is only compensated to 74% of U_{nom} to ensure the EMR operate properly, and the entire industry process would not be

TABLE 5 | Comparisons between the proposed method and the IEEE method.

Magnitude (%)	The proposed method			IEEE method		
	Times	Results (ms)	Error (ms)	Times	Result (ms)	Error (ms)
0	8	19.063	0.0625	3	20	1.0000
10	8	19.063	0.0625	3	20	1.0000
20	8	19.063	0.0625	3	20	1.0000
30	8	5.3125	0.6875	2	10	4.0000
40	8	5.3125	0.3125	2	10	5.0000
50	8	6.5625	0.5625	2	10	4.0000
60	8	14.063	0.0625	3	20	1.0000

interrupted, accordingly. It means that industrial users can choose a voltage-compensating device with a smaller capacity to maintain the whole process and save money, more importantly.

7 CONCLUSION

This paper has performed a large number of tolerance tests on eight different EMRs, and the test results are presented graphically as VTCs. The tolerance to rectangular and non-rectangular voltage sag is investigated in the tests; the influence factors considered here include POW, PAJ, frequency variation, harmonic, magnitude variation in pre- and post-sag segments, two-stage sag, and slow recovery sag.

The obtained VTCs clearly show that the response of EMRs to voltage sag or short interruption can be rather complex. The magnitude and duration of sag are not the only parameters which influence EMR's sensitivity; POW and PAJ also have an important influence on the EMR's tolerance.

The following specific conclusions can be drawn from the tests performed.

1) From the tolerance test under rectangular voltage sag, the tolerance capability of EMR is obtained. Although the EMR's VTC is different depending on its type, the shapes of VTCs of all tested EMRs are basically similar. Through more than 10,000 tests on each EMR, EMR can tolerate a voltage sag with the magnitude more than 74% of U_{nom}. When the sag magnitude is less than 48% of U_{nom}, EMR will trip when the sag duration exceeds 28 ms.
2) A quarter-cycle symmetry of VTCs with respect to POW is proved. The POW has a significant influence on the behavior of EMRs. VTCs have different shapes for 0° and 90° POW. The tolerance of EMR is stronger at 0° POW than 90° POW, generally.
3) PAJ effects on the tolerance of EMR, when a PAJ occurs, the tolerance of EMR is weaker.
4) Two-stage voltage sags can decrease EMR's tolerance, making EMR easier to disengage. The sequence of the two-stage also has a significant influence on EMR's tolerance.
5) Other factors of frequency variation up to ±2%, harmonic (THD up to 12%), and the slow recovery voltage sag only have a not-noticeable impact on the tolerance of EMR. EMR can tolerate the slow recovery voltage sag with the magnitude more than 60–70% of U_{nom}.

The test results are useful to choose proper EMR with higher tolerance and to use subset tests to quantitatively analyze sensitivity of a new EMR. It is profitable to apply a voltage compensating device with a smaller capacity to keep the process unaffected using the general VTC.

DATA AVAILABILITY STATEMENT

The original contributions presented in the study are included in the article/supplementary material. Further inquiries can be directed to the corresponding author.

AUTHOR CONTRIBUTIONS

HZ contributed to the conception and design of the research. HZ design experiment. QW conducted a statistical analysis. YY wrote the first draft of the manuscript. HZ wrote part of the manuscript. All authors contributed to the revision of the manuscript and read and approved the submitted version.

FUNDING

This work was supported by the Science and Technology Project of China Southern Power Grid (090000KK52190169/SZKJXM2019669).

REFERENCES

Alvaro, F. B., Keng, W. L., Grazia, T., and Santoso, S. (2019). Accurate Identification of Point-on-Wave Inception and Recovery Instants of Voltage Sags and Swells. *IEEE Trans. Power Del.* 34 (4), 551–560. doi:10.1109/tpwrd.2018.2876682

AMETEK (2017). *MX Series Data Sheet, Technical Documentation*. Berwyn, USA: AMETEK.

Bollen, M. H. J. (2000). *Understanding Power Quality Problem: Voltage Sag and Interruptions, Ser. Series on Power Engineering*. NY, USA: IEEE Press.

De Santis, M., Noce, C., Varilone, P., and Verde, P. (2018). Analysis of the Origin of Measured Voltage Sags in Interconnected Networks. *Electric Power Syst. Res.* 154, 391–400. doi:10.1016/j.epsr.2017.09.008

Djoki, S., Milanovi, J. V., and Rowland, S. M. (2007). Advanced Voltage Sag Characterisation II: point on Wave. *IET Gener. Transm. Distrib.* 1 (1), 146–154. doi:10.1049/iet-gtd:20050434

Djokic, S. Z., Milanovic, J. V., and Kirschen, D. S. (2004). Sensitivity of AC Coil Contactors to Voltage Sags, Short Interruptions, and Undervoltage Transients. *IEEE Trans. Power Deliv.* 19 (3), 1299–1307. doi:10.1109/tpwrd.2004.824396

Fan, W., and Wu, S. (2014). "Ship Mechanical Environment Impact on the Performance of Electromagnetic Relay,"in 11th World Congress on Intelligent Control and Automation, Shenyang, China, June 24-July 4, 2014, 3702–3706. doi:10.1109/wcica.2014.7053332

Gambôa, P., Silva, J. F., Pinto, S. F., and Margato, E. (2019). Input-Output Linearization and PI Controllers for AC-AC Matrix Converter Based Dynamic Voltage Restorers with Flywheel Energy Storage: a Comparison. *Electric Power Syst. Res.* 169, 214–228. doi:10.1016/j.epsr.2018.12.023

Hardi, S., Daut, I., and Irwanto, M. (2010). "Testing of Contactors under Voltage Sag and Non-sinusoidal Voltage Conditions,"in 2010 IEEE International Conference and Power and Energy, Kuala Lumpur, Malaysia, November 29-December 1, 2010, 683–688. doi:10.1109/pecon.2010.5697667

IEC (2021). "IEC Electromagnetic Compatibility: Testing and Measurement Techniques-Power Quality Measurement Methods," in *IEC 61000-4-30, 2015* (Geneva: IEC).

IEEE (2017). "IEEE Recommended Practice for Voltage Sag and Short Interruption Ride-Through Testing for End-Use Electrical Equipment Rated Less Than 1000 V," in *IEEE Std. 1668, 2017. (Revision of IEEE Std. 1668-2014)* (Manhattan, NY: IEEE).

IEEE (1998). "IEEE Recommended Practice for Evaluating Electric Power System Compatibility with Electronic Process Equipment," in *IEEE Std. 1346, 1998* (Manhattan, NY: IEEE).

Ma, Z. Y., Xu, Z., Mo, W. X., Guo, W. Q., Wanf, J. H., Zhou, K., et al. (2018). "A New Method for Sensitive Single-phase Equipment Testing to Voltage Sag,"in 2018 18th International Conference on Harmonics and Quality of Power (ICHQP), Ljubljana, Slovenia, May 13-16, 2018, 1–6.

Mohammadi, Y., Moradi, M. H., and Chouhy Leborgne, R. (2017). Employing Instantaneous Positive Sequence Symmetrical Components for Voltage Sag Source Relative Location. *Electric Power Syst. Res.* 151, 186–196. doi:10.1016/j.epsr.2017.05.030

Nagata, E. A., Ferreira, D. D., Duque, C. A., and Cequeira, A. S. (2018). Voltage Sag and Swell Detection and Segmentation Based on Independent Component Analysis. *Electric Power Syst. Res.* 155, 274–280. doi:10.1016/j.epsr.2017.10.029

Ouyang, S., and Liu, L. (2017). Test and Study on Sensitivity of Electronic Circuit in Low-voltage Release to Voltage Sags. *IET Circuits, Devices Syst.* 11 (6), 529–534. doi:10.1049/iet-cds.2016.0222

Ouyang, S., Liu, P., Liu, L., and Li, X. (2015). Test and Analysis on Sensitivity of Low-voltage Releases to Voltage Sags. *IET Generation, Transm. Distribution* 9 (16), 2664–2671. doi:10.1049/iet-gtd.2015.0547

Ren, J., Xiao, X., Zheng, Z., Wang, Y., Ma, Z., and Liu, K. (2021). Impact of Phase Angle Jump on DFIG under LVRT Conditions: Challenges and Recommendations. *IEEE Trans. Power Deliv.*, 1. doi:10.1109/TPWRD.2020.3048434

Wu, S., and Fan, W. (2015). "A Method for Analyzing the Influence of Voltage Fluctuation on Pick-Up Characteristics of Electromagnetic Relay," in 2015 IEEE International Conference on Information and Automation, Lijiang, China, August 8-10, 2015, 2616–2620. doi:10.1109/icinfa.2015.7279726

Wang, Y., Bollen, M. H. J., and Xiao, X.-Y. (2015). Calculation of the Phase-Angle-Jump for Voltage Dips in Three-phase Systems. *IEEE Trans. Power Deliv.* 30 (1), 480–487. doi:10.1109/tpwrd.2014.2352358

Wang, Y., Deng, L.-F., Bollen, M. H. J., and Xiao, X.-Y. (2020). Calculation of the point-on-wave for Voltage Dips in Three-phase Systems. *IEEE Trans. Power Deliv.* 35 (4), 2068–2079. doi:10.1109/tpwrd.2019.2960524

Wang, Y., Luo, H., and Xiao, X.-Y. (2019). Voltage Sag Frequency Kernel Density Estimation Method Considering protection Characteristics and Fault Distribution. *Electric Power Syst. Res.* 170, 128–137. doi:10.1016/j.epsr.2019.01.009

Weldemariam, L. E., Gartner, H. J., Cuk, V., and Cobben, J. F. G. (2016). "Mitigation Strategies to Improve the Performance of AC Contactor against Voltage Dips,"in 2016 51st International Universities Power Engineering Conference (UPEC), Coimbra, Portugal, September 6-9, 2016, 1–6.

Xu, Y., Lu, W., Wang, K., Li, C., and Aslam, W. (2019). Sensitivity of Low-Voltage Variable-Frequency Devices to Voltage Sags. *IEEE Access* 7, 2068–2079. doi:10.1109/access.2018.2885402

Xu, Y., Wu, Y., Zhang, M., and Xu, S. (2019). Sensitivity of Programmable Logic Controllers to Voltage Sags. *IEEE Trans. Power Deliv.* 34 (1), 2–10. doi:10.1109/tpwrd.2018.2870086

Ye, J., Gooi, H. B., Wang, B., Li, Y., and Liu, Y. (2019). Elliptical Restoration Based Single-phase Dynamic Voltage Restorer for Source Power Factor Correction. *Electric Power Syst. Res.* 166, 199–209. doi:10.1016/j.epsr.2018.10.011

Zhai, G., and Yang, W. (2008). "3-D Finite Element Analysis of Dynamic Characteristics of Electromagnetic Relay Interfered by Voltage Dips and Short Interruptions,"in 2008 International Conference on Electrical Machines and Systems, Wuhan, China, October 17-20, 2008, 564–567.

Jianbo, Z., and Qi, W. (2018). "An Anti-misoperation Method for Intermediate Relay Used in DC System of Substation," in 2018 13th IEEE Conference on Industrial Electronics and Applications (ICIEA), Wuhan, China, May 31-June 2, 2018, 455–460. doi:10.1109/iciea.2018.8397760

Conflict of Interest: The authors declare that the research was conducted in the absence of any commercial or financial relationships that could be construed as a potential conflict of interest.

Publisher's Note: All claims expressed in this article are solely those of the authors and do not necessarily represent those of their affiliated organizations, or those of the publisher, the editors and the reviewers. Any product that may be evaluated in this article, or claim that may be made by its manufacturer, is not guaranteed or endorsed by the publisher.

frontiers in Energy Research

BRIEF RESEARCH REPORT
published: 22 December 2021
doi: 10.3389/fenrg.2021.809434

Lumped-Circuits Model of Lossless Transmission Lines and Its Numerical Characteristics

Huiyi Zhou, Tianlin Lu, Shuting Zhang and Xin Zhang*

College of Electrical Engineering and New Energy, China Three Gorges University, Yichang, China

Aiming at the lumped-circuits model of the lossless transmission line in the digital simulation, the article discusses and analyzes the unit step response generation of the lumped-circuits model by comparing the numerical simulation results of the implicit trapezoidal method, the implicit Euler method, and a multi-step formula. The root cause of numerical oscillations pointed out that using the L-stable numerical algorithm to indirectly simulate the dynamic response of the lumped-circuits model is a numerical method that does not truly reflect the original model, but it can directly reflect the true dynamic response of the lossless transmission line. In this study, a method for determining the chained number in the digital simulation of a lumped-circuits model is given. The simulation results prove the effectiveness of the method.

Keywords: lumped-circuits, digital simulation, lossless transmission line, numerical method, chained number

OPEN ACCESS

Edited by:
Zhenhao Tang,
Northeast Electric Power University, China

Reviewed by:
Kun Yu,
Changsha University of Science and Technology, China
Jun Wu,
Wuhan University, China

****Correspondence:***
Tianlin Lu
x136838207@163.com

Specialty section:
This article was submitted to Smart Grids, a section of the journal Frontiers in Energy Research

Received: *05 November 2021*
Accepted: *29 November 2021*
Published: *22 December 2021*

Citation:
Zhou H, Lu T, Zhang S and Zhang X (2021) Lumped-Circuits Model of Lossless Transmission Lines and Its Numerical Characteristics. Front. Energy Res. 9:809434. doi: 10.3389/fenrg.2021.809434

INTRODUCTION

In the digital simulation model of lossless transmission lines, the model using the circuit equivalent model to study the physical characteristics of transmission lines is called the lumped-circuits model, which is different from the classical finite-difference time-domain algorithm model. As the name suggests, the lumped-circuits is different from the distributed parameter circuit, which uses a partial differential equation to describe the voltage fluctuation process. The former uses lumped inductance and capacitance to approximate the physical characteristics of lossless transmission lines with distributed parameter characteristics. Cui (2018) pointed out that there are fundamental differences between the two, and they cannot be completely equivalent in physical characteristics. Therefore, only appropriate approximation methods (Shen et al., 2020; Shen et al., 2021; Shen and Raksincharoensak, 2021) can be found to ensure that the lumped-circuits of the transmission line can be approximately equivalent to the distributed parameter circuit.

The modeling of the transmission line transient response needs to select an appropriate physical model according to the frequency of the system research signal. The lumped-circuits model is a commonly used approximate model for physical simulation and digital simulation of transmission lines, but its significant problem in digital simulation is numerical oscillation (Ye et al., 2021). In order to solve this problem, various numerical algorithms are used to solve the transient response of transmission lines, but there are different defects in dealing with numerical oscillation. Root-matching techniques (Watson and Irwin, 1998) solve this problem well and are the main algorithm to solve the problem of numerical oscillation at present. Song et al. (2020) proposed an efficient electromagnetic transient simulation method based on the discrete similarity principle, which further expanded the application scope of root-matching techniques. Although the root-matching techniques can better solve the numerical oscillation problem, in a strict sense, these discrete calculation principles cannot ensure that the physical characteristics of the transmission line do not

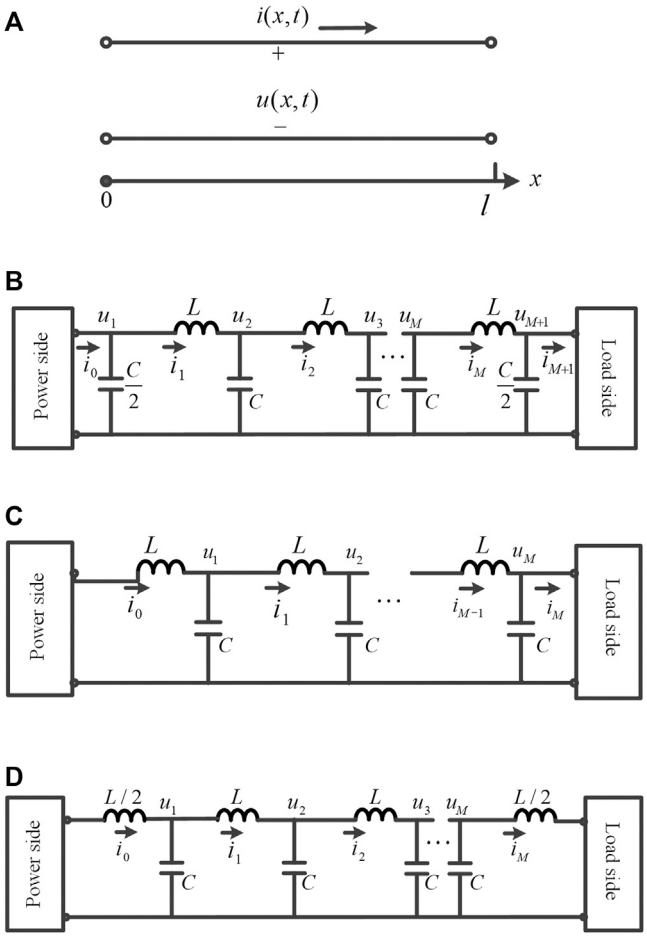

FIGURE 1 | Lossless transmission line and its three equivalent lumped-circuits. **(A)** Lossless transmission line. **(B)** Lumped-circuits consisted of M Π-type circuits. **(C)** Lumped-circuits consisted of M inverse Γ-type circuits. **(D)** Lumped-circuits consisted of M *T*-type circuits.

change. Therefore, the research on the numerical algorithm that can keep the physical structure of the transmission line from distortion has become a very important research subject.

In addition, the number of the chained circuits is a key parameter for the lumped-circuits of lossless transmission lines in physical analogy. Cui (2017) gives an estimation formula for determining the chained number of the lumped-circuits in the physical analogy of lossless transmission lines. This formula is also useful for the estimation (Yang et al., 2019a; Yang et al., 2019b; Yang et al., 2021a; Zhang et al., 2021) of the chained number in the digital simulation, but it can not be directly applied. The influence of the approximation error (Yang et al., 2018; Yang et al., 2021b) of the numerical algorithm needs to be considered.

For a long time, the lumped-circuits model of lossless transmission lines was often used as the electromagnetic simulation model of transmission lines (Paul, 1994; Min and Mao, 2007), but little is known about the numerical characteristics of the model. Starting from the characteristics of three lumped-circuits, the numerical characteristics of the lumped-circuits model, including its unit step response and sine excitation response, are studied in detail. The relevant conclusions can provide reference for the application range and method of the lumped-circuits model of lossless transmission lines. In addition, this study pointed out that the numerical algorithm of symplectic conservation can accurately simulate the physical characteristics of lossless transmission lines.

LUMPED-CIRCUITS MODEL OF LOSSLESS TRANSMISSION LINES

Basic Lumped-Circuits Model

Usually, the state space model is used to solve the dynamic response of lossless transmission lines. First, the lossless transmission lines need to be discretized in space to obtain blocks of *T*-type circuits, Γ-type or inverse Γ- type circuits, and Π-type circuits. As shown in **Figure 1**, it is a schematic diagram of a lossless transmission line, with an inductance per unit length of L_0 and a capacitance per unit length of C_0, and the total length of the line is recorded as l. If the transmission line is evenly divided into M segments, the inductance parameter of a single circuit segment is $L = L_0/M$ and the capacitance parameter is $C = C_0/M$.

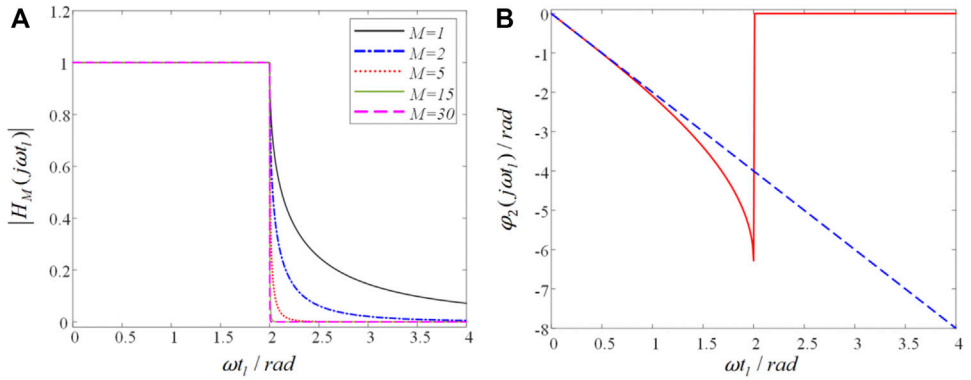

FIGURE 2 | Frequency response curve. **(A)** Amplitude-frequency response curve when M takes different values. **(B)** Phase-frequency response curve when $M = 2$.

According to the topological characteristics of the above lumped-circuits, it is not difficult to see that the lumped-circuits consisting of chained inverse Γ-type circuits is suitable for the situation where the ideal power supply is a unit step signal and the load is a pure capacitive load. The lumped-circuits composed of chained Π- type circuits are more suitable for the case that the power supply is a non-ideal power supply, that is, the power supply with internal impedance, and the load is pure capacitive load. However, for ideal power supply, such as the unit step signal, in order to facilitate the application of boundary conditions at the head end during simulation, a small resistance can be artificially inserted in series in the ideal power circuit, so that the step response characteristics of the circuit can be simulated. The lumped-circuit composed of chained T-type circuits is more suitable for ideal or non-ideal power supply, and the load is the pure inductance or resistance inductance series branch. It is worth noting that the above discussion is only based on not adding more system state variables. Without this limitation, the above three lumped-circuits are applicable to any form of load combination.

Dynamic Response of the Lumped-Circuits Model

When the lossless transmission line shown in **Figure 1A** is connected with the characteristic impedance Z_c, at this time, the head end voltage source u_{es} is transmitted to the terminal at the traveling wave velocity $v = (\sqrt{L_0C_0})^{-1}$, and there is no reverse traveling wave of the voltage, that is, the ending voltage amplitude has no attenuation, but the phase lags behind the head-end voltage wave by a delay time $t_L = l/v$. In this case, through the Fourier analysis of the ending voltage, it is obtained that the frequency response characteristic of the ending voltage transfer function when the terminal is matching is as follows:

$$H(l, j\omega) = e^{-j\omega t_L} \tag{1}$$

The amplitude-frequency characteristics and phase-frequency characteristics of **Eq. 1** are as follows:

$$|H(l, j\omega)| = 1 \tag{2}$$

$$\varphi(l, j\omega) = -\omega t_L \tag{3}$$

where ω is the angle frequency. **Eqs. 4**, **5** are the necessary conditions for digital simulation of the lossless transmission line and are also the key evaluation indexes to test the quality of the numerical algorithm.

For the lumped-circuits shown in **Figures 1B,D**, when the terminal is matched, the frequency response characteristic of the ending voltage transfer function is as follows (Cui, 2017; Cui, 2018):

$$|H_M(j\omega t_l)| = \begin{cases} 1, & \omega t_l \le 2rad \\ (\omega t_l)^{-2M}, & \omega t_l > 2rad \end{cases} \tag{4}$$

$$\varphi_M(j\omega t_l) = \begin{cases} -2M\, arscin\left(\dfrac{\omega t_l}{2}\right), & \omega t_l \le 2rad \\ 0, & \omega t_l > 2rad \end{cases} \tag{5}$$

where t_l represents the propagation time of the forward voltage traveling wave along the transmission line with length l/M.

As shown in **Figure 2A**, the amplitude-frequency response curve of the lumped-circuits when M is different is given. It can be seen that when M is greater than or equal to 5, the amplitude-frequency response characteristics of the lumped-circuits show the characteristics of an ideal low-pass filter, and the cut-off frequency is $\omega_c = 2/t_l$. In other words, if the frequency of the excitation source is greater than ω_c, the voltage signal transmitted to the transmission line terminal will be seriously distorted. In addition, in order to ensure that the phase error of the ending voltage signal is small, $\omega \le 1/t_l$ must be made. Therefore, when using the numerical method to analyze the lumped-circuits model of lossless transmission lines in the time domain, the frequency of the excitation source $\omega \le \omega_c$ must be met to ensure that the amplitude-frequency response is constant 1, $\omega \le \omega_c/2$ as far as possible to ensure a small phase error, so as to ensure the integrity of the signal in the transmission process.

Although it is theoretically possible to meet the property that the amplitude-frequency response of the lossless transmission line is always 1 and the phase relative error is 4.72% by physically controlling the frequency of the excitation source, it is inevitable to introduce numerical errors when using the numerical integration algorithm to solve the state space equation of the lumped-circuits (Lei et al., 2009). Therefore, reducing and

avoiding the amplitude and phase errors caused by numerical calculation is the problem to be solved in this study.

Numerical Characteristics of the Lumped-Circuits Model

Figure 3A shows an example of a double conductor lossless transmission line. The wave impedance of the lossless transmission line is Z_0, the wave velocity is c, the total length of the line is l, the ideal voltage source u_{es} at the head end of the transmission line is a 100-V step signal with time delay, and the load end is connected with a capacitor C_L of 1,000 pF. The lumped-circuits models shown in **Figures 1B,D** are used for numerical modeling, and the implicit trapezoidal integral formula, the implicit Euler method, and a linear multi-step method in the study by (Wang et al., 2019) are used for numerical simulation, and the respective characteristics of the model and the algorithm are compared and analyzed. The calculation formats of the three numerical algorithms are introduced as follows.

For the Following Initial Value Problems

$$\begin{cases} \dot{x} = f(x,t) \\ x(t=0) = x_0 \end{cases}$$

The approximate formula of the implicit trapezoidal integral formula (TR) for approximately solving the state variable $x(t)$ is as follows:

$$x_{j+1} = x_j + \frac{h}{2}\left[f\left(x_{j+1}, t_{j+1}\right) + f\left(x_j, t_j\right)\right]$$

where $x_{j+1} \approx x(t_{j+1}), t_{j+1} = t_j + h$, and h is the space between adjacent time grid points.

Similarly, the calculation format of the implicit Euler method (IE) is as follows:

$$x_{j+1} = x_j + hf\left(x_{j+1}, t_{j+1}\right)$$

The calculation format of the four-step method (FM) is as follows:

$$\frac{20-8\sqrt{2}}{11}hf\left(x_{j+4}, t_{j+4}\right) = \frac{1}{11}x_j + \frac{4\sqrt{2}-8}{11}x_{j+1} + \frac{4}{11}x_{j+2} - \frac{4\sqrt{2}+8}{11}x_{j+3} + x_{j+4}$$

Table 1 shows the comparison of the three numerical algorithms. It can be seen that the properties of the three algorithms are different, and the solution effect of the actual problem is also different. The time domain response results of a single lossless transmission line will be analyzed in detail below.

Taking the lumped model in **Figure 1B** as an example, a set of linear differential equations can be obtained according to the circuit law as follows:

$$\begin{cases} L\dfrac{di_k(t)}{dt} = u_k(t) - u_{k+1}(t) - ri_k(t), k \in (1, M) \\ C\dfrac{du_k(t)}{dt} = i_{k-1}(t) - i_k(t), \qquad k \in (1, M+1) \end{cases} \tag{6}$$

$$\begin{bmatrix} \boldsymbol{L} & 0 \\ 0 & \boldsymbol{C} \end{bmatrix}\begin{bmatrix} \dot{\boldsymbol{I}} \\ \dot{\boldsymbol{U}} \end{bmatrix} = \begin{bmatrix} -\boldsymbol{R} & \boldsymbol{P} \\ \boldsymbol{Q} & 0 \end{bmatrix}\begin{bmatrix} \boldsymbol{I} \\ \boldsymbol{U} \end{bmatrix} + \begin{bmatrix} \boldsymbol{\mu}_1(t) \\ \boldsymbol{\mu}_2(t) \end{bmatrix} \tag{7}$$

In **Eq. 7**, $\boldsymbol{I} = [i_1(t), i_2(t), \cdots, i_M(t)]^T$, $\boldsymbol{U} = [u_1(t), u_2(t), \cdots, u_{M+1}(t)]^T$, $\boldsymbol{R} = diag(r, r, \cdots, r)$, $\boldsymbol{C} = diag(C, C, \cdots, C)$, $\boldsymbol{L} = diag(L, L, \cdots, L)$, $\boldsymbol{\mu}_1(t) = [0, 0, \cdots, 0]^T$, $\boldsymbol{\mu}_2(t) = [i_0, 0, \cdots, 0]^T$.

$$\boldsymbol{P} = \begin{bmatrix} 1 & -1 & & & \\ & \ddots & -1 & & \\ & & 1 & -1 & \\ & & & 1 & -1 \end{bmatrix}_{M\times(M+1)}$$

$$\boldsymbol{Q} = \begin{bmatrix} -1 & & & \\ 1 & -1 & & \\ & \ddots & \ddots & \\ & & 1 & -1 \\ & & & 1 \end{bmatrix}_{(M+1)\times M}$$

Applying constraints to **Eq. 7**, we get the following:

$$\begin{cases} i_0 = \dfrac{u_{es} - u_1}{r_s} \\ \left(\dfrac{C}{2} + C_L\right)\dfrac{du_{M+1}}{dt} = i_M \end{cases} \tag{8}$$

In the simulation, the resistance in the ideal voltage source is $r_s = 0.000001\Omega$, the chained number of the lumped-circuits model is $M = 100$, and the simulation step size is $h = 1.0 \times 10^{-7}s$. The lumped-circuits consisted of chained Π-type circuits digitally simulated by using the implicit trapezoidal integral formula, the implicit Euler method, and the four-step method in the study by (Wang et al., 2019), as shown in **Figures 3B,D**. Since the four-step method cannot start the calculation by itself, the explicit Euler method needs to be used to calculate the header.

It can be seen from **Figures 3B,D** that under the Π-type lumped-circuits model, when the lossless transmission line is terminated with a capacitor, the ending voltage calculated using the three numerical algorithms with different properties has a certain time delay relative to the head-end voltage (Zhan et al., 2017). According to the research by (Cui, 2017; Cui, 2018), the calculation formula of the delay time is as follows:

$$t_M = \frac{M}{\omega}arccos\frac{2-\omega^2 t_l^2}{2} \tag{9}$$

Therefore, the relative phase error of the algorithm is defined as follows:

$$\varepsilon_{\varphi_M} = \left[\frac{t_{phase}}{t_M - 1}\right] \times 100\% \tag{10}$$

where t_{phase} represents the time delay of the ending voltage waveform calculated using the numerical algorithm.

The reason for the signal transmission delay under the lumped-circuits model is due to the charge discharge process of capacitance and inductance and the dissipative process of load energy in the lumped-circuits, which is obviously different from the wave process of lossless transmission lines.

In addition, the ending voltage calculated using the implicit trapezoidal method has obvious numerical oscillation. In order

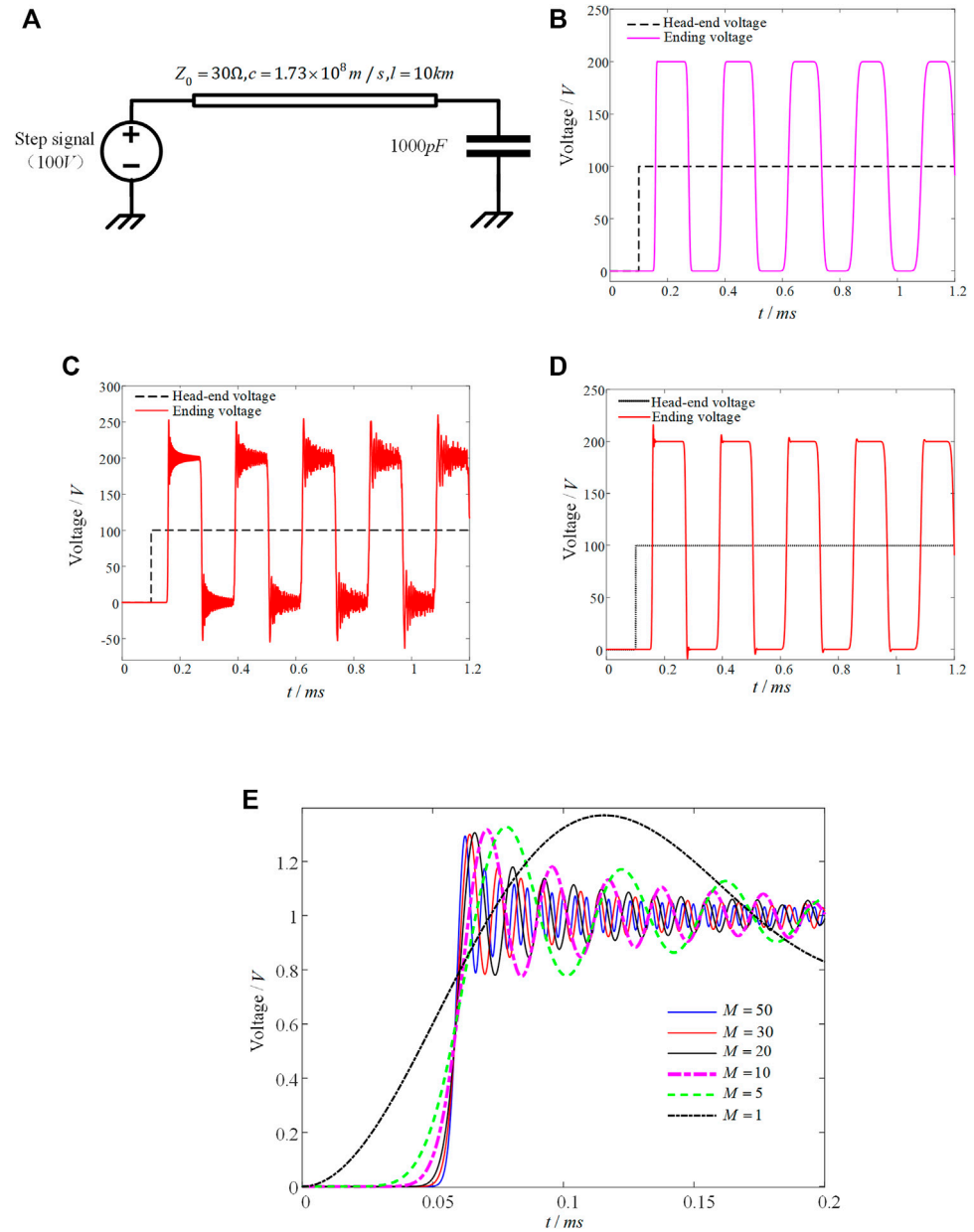

FIGURE 3 | Example analysis. **(A)** Step response model of the lossless transmission line. **(B)** Calculation results of the implicit Euler method. **(C)** Calculation results of the implicit trapezoidal method. **(D)** Calculation results of the four-step method. **(E)** Unit step response of the *T*-type lumped-circuits.

to further study the physical mechanism of numerical oscillation, this study uses the implicit trapezoidal method to solve the ending voltage response of different chained numbers M in the T-type lumped-circuits with the unit step signal connected at the head end without delay and characteristic impedance of the lossless transmission line at the end load. The simulation results are shown in **Figure 3E**, with the increase in the chained number M; the greater the step response overshoot of the ending voltage, the higher the frequency of voltage oscillation, the faster the attenuation of amplitude, the shorter the voltage rise time and dynamic time, and the overall waveform of the ending voltage is closer to the unit step voltage waveform in addition to the overshoot. This conclusion has the same physical characteristics as the step

TABLE 1 | Comparison of three numerical algorithms.

Algorithm	Principal coefficient of truncation error	Order	Stability
TR	−0.0833	2	A-stable
IE	−0.5	1	L-stable
FM	−0.1248	1	L-stable

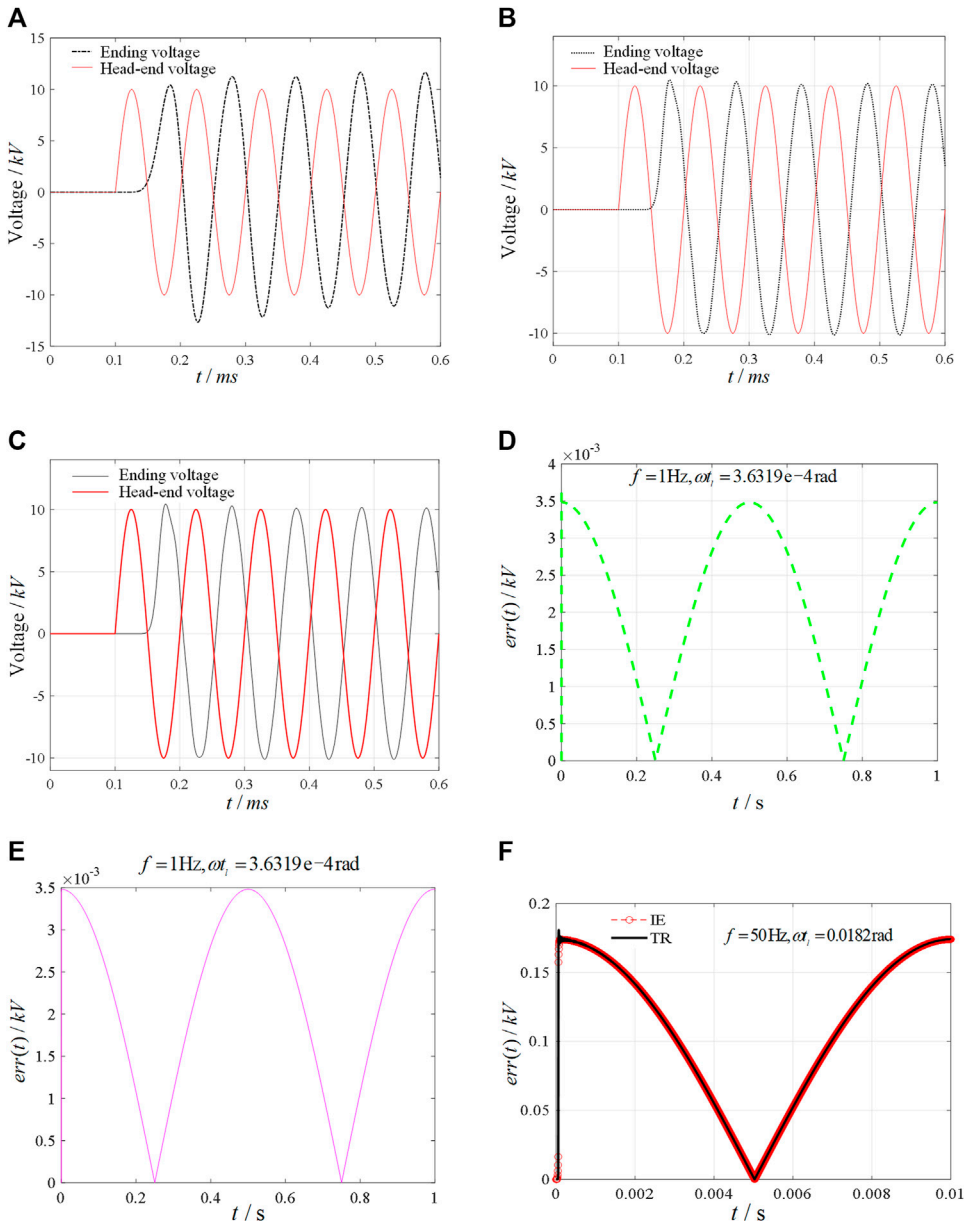

FIGURE 4 | Chained number and numerical algorithm analysis of lumped-circuits numerical simulation. **(A)** M = 4 (the terminal resistance is 30 Ω). **(B)** M = 12 (the terminal resistance is 30 Ω). **(C)** M = 12 (the terminal resistance is 29.65 Ω). **(D)** Amplitude-frequency response error curve of the TR algorithm. **(E)** Amplitude-frequency response error curve of algorithm IE. **(F)** Amplitude-frequency response error curve of algorithms TR and IE.

response of the lumped-circuits derived by inverse Fourier transform in the study by (Cui, 2018).

The above shows that the implicit trapezoidal integration method retains the dynamic response characteristics of the step response of the lumped-circuits because it does not have numerical L-stable (Noda et al., 2014; Chakraborty and Ramanujam, 2018), which just reflects the real numerical characteristics of the lumped-circuits. On the contrary, because of the L-stable of the implicit Euler method and the four-step method in the study by (Wang et al., 2019), the overshoot and oscillation characteristics of the unit step voltage waveform are suppressed and the details of the dynamic response process of the lumped-circuits are obliterated, so they are impossible for truly simulating the physical process (Wang and Yang, 2016).

The above conclusions show that whether the selection of the numerical algorithm is appropriate is very important to reflect the real dynamic response process of the lumped-circuits. Of course, this numerical oscillation is false for the lossless transmission line itself, which also shows that the lumped-circuits can not be completely equivalent to the lossless transmission line model. Therefore, the lumped-circuits is only a numerical approximation of the lossless

transmission line model. In order to truly reflect the numerical characteristics of the lossless transmission line model, it is suggested that the numerical algorithm with L-stable be used to simulate the lumped-circuits. Although the L-stable numerical algorithm dampens the overshoot and oscillation characteristics of the real waveform of the lumped circuit (Gao et al., 2021), it positively reflects the numerical characteristics of the lossless transmission line model.

SINE EXCITATION RESPONSE OF THE LUMPED-CIRCUITS MODEL

Different numerical algorithms have great differences in the numerical simulation results of the lumped-circuits, but this difference is not very obvious for the sine excitation response without the disturbance term. In addition, although the larger the chained number M is selected, the closer the ending voltage waveform is to the unit step voltage waveform as a whole, from the perspective of numerical calculation efficiency; how to select the appropriate chained number M directly determines the efficiency and accuracy of simulation. Besides, the simulation step size is limited by the accuracy of the numerical algorithm. Therefore, the efficiency of the lumped-circuits simulation depends on the chained number M and the accuracy and stability of the numerical algorithm adopted.

For the lossless transmission line shown in **Figure 3A**, according to the previous analysis, considering that the ending voltage phase delay is in the linear interval. Assuming that the angular frequency of the sinusoidal excitation source meets $\omega t_l \le 1$, the ending voltage phase delay approximately meets the following:

$$\varphi_M(j\omega) \approx -\omega M t_l,\ \omega = 2\pi f \tag{11}$$

According to **Eq. 11**, in order to reduce the phase transmission error of the lumped-circuits model and ensure that the amplitude-frequency response characteristic is constant 1, the chained number M should meet the following:

$$M \ge \left\lceil \frac{2\pi f_{max} l}{v} \right\rceil \tag{12}$$

where the square brackets indicate rounding up. f_{max} represents the maximum frequency of the excitation signal of the lossless transmission line during numerical simulation. l is the total length of the transmission line.

In order to verify the correctness of the above conclusions, the T-type lumped-circuits model of the lossless transmission line is considered. The simulation step size shall be less than or equal to the optimal step size as follows:

$$h < \frac{l}{Mv} \tag{13}$$

Using the numerical example shown in **Figures 3A**, a sine voltage excitation source with a frequency of $10\,kHz$ is considered, which has a delay of $0.1\,ms$ and a peak value of $10\,kV$. The terminal load is the characteristic resistance of the equivalent lumped-circuits. According to **Eq. 12**, the transmission line is divided into 4 equal parts. The implicit trapezoidal method is used to solve the model. According to the research by (Cui, 2017), the characteristic impedance of the T-type equivalent lumped-circuits is as follows:

$$Z_c^T = z_0\sqrt{1-\left(\frac{1}{2}\omega t_l\right)},\ t_l = \frac{l}{Mv} \tag{14}$$

As can be seen from **Figure 4**, when $M = 4$, there is an obvious difference in the amplitude of the head and end voltage waveform, which does not meet the characteristics of the transmission line. After increasing to $M = 12$, except for the obvious overshoot of the first wave peak, the subsequent amplitude error is basically stable. This shows that in the actual simulation, the value of N needs to be flexibly selected accordingly. Through a large number of simulations, it is found that M can be 2–3 times the calculated value of **Eq. 12**. In addition, the characteristics of the numerical algorithm are also one of the factors affecting the amplitude-frequency characteristics of the lumped-circuits model. How to choose an appropriate numerical algorithm is also a direction worthy of further research. Symplectic algorithms (Xing and Yang, 2007; Ye et al.) may be a better choice to accurately simulate the physical characteristics of lossless transmission lines. The amplitude frequency response error curve (absolute value of absolute error) of the commonly used TR and IE algorithms when $N = 12$ is calculated below, considering the sinusoidal voltage excitation source with frequency f, the excitation source has no delay and the end load is matched. The optimal time domain simulation step is taken according to **Eq. 13**.

As can be seen from **Figures 4D,E**, when the system frequency is small, that is, when ωt_l is close to 0, the amplitude frequency response error of algorithms TR and IE is also small. However, it can be seen from **Figure 4F** that the amplitude frequency response error of algorithms TR and IE increases sharply with the increase in system frequency. According to **Figure 2**, the error amplitude frequency response error caused by the model is almost 0, so the error at this time is mainly caused by the numerical algorithm, which also fully shows that it is very necessary to study the application of symplectic algorithms in the high-precision time-domain response simulation of lossless transmission lines.

CONCLUSION

Starting from the equivalent lumped-circuits model of lossless transmission lines, this article mainly studies the boundary condition application methods of three equivalent lumped-circuits models. Users can flexibly choose the type of the equivalent lumped-circuits model according to the type of excitation source and load. The causes of numerical oscillation in digital simulation of the equivalent lumped-circuits model are explained theoretically, and the L-stable numerical algorithm is proposed to avoid this situation. A determination method of chained number of the equivalent lumped-circuits model is studied, and a specific application example is given. In conclusion, the method proposed in this study can provide the basis for the selection of model and numerical algorithm for the

equivalent lumped-circuits model of lossless transmission lines in digital simulation.

DATA AVAILABILITY STATEMENT

The raw data supporting the conclusion of this article will be made available by the authors, without undue reservation.

AUTHOR CONTRIBUTIONS

HZ put forward the main research points and mathematical analysis; TL is responsible for the framework formation and revision; SZ collected relevant background information and completed simulation research; XZ completed manuscript writing.

REFERENCES

Chakraborty, S., and Ramanujam, R. (2018). New Numerical Integration Methods for Simulation of Electromagnetic Transients. *Int. J. Emerging Electric Power Syst.* 19 (4), 122. doi:10.1515/ijeeps-2018-0122

Cui, X. (2018). Notes on Lumped-Circuits for Physical Analogy of Transmission Lines[J]. *Zhongguo Dianji Gongcheng Xuebao/Proceedings Chin. Soc. Electr. Eng.* 38 (1), 1–11. doi:10.13334/j.0258-8013.pcsee.171699

Cui, X. (2017). Chained Number of Lumped-Circuits for Physical Analogy of the Lossless Transmission Lines. *Proc. Chin. Soc. Electr. Eng.* 37 (09), 2561–2571. doi:10.13334/j.0258-8013.pcsee.162633

Gao, S., Chen, Y., Song, Y., and Huang, S. (2021). Three-stage Implicit Integration for Large Time-step Size Electromagnetic Transient Simulation with Shifted Frequency-Based Modeling. *Electric Power Syst. Res.* 198 (11), 107356. doi:10.1016/j.epsr.2021.107356

Lei, L., Xiang, C., and Lei, Q. (2009). Simulation of Electromagnetic Transients of the Bus Bar in Substation by the Time-Domain Finite-Element Method[J]. *IEEE Trans. Electromagn. Compatibility* 51 (4), 1017–1025. doi:10.1109/TEMC.2009.2028691

Min, T., and Mao, J. (2007). A Precise Time-step Integration Method for Transient Analysis of Lossy Nonuniform Transmission Lines[J]. *IEEE Trans. Electromagn. Compatibility* 50 (1), 166–174. doi:10.1109/TEMC.2007.913222

Noda, T., Kikuma, T., and Yonezawa, R. (2014). Supplementary Techniques for 2S -DIRK - Based EMT Simulations[J]. *Electric Power Syst. Res.* (115), 87-93. doi:10.1016/j.epsr.2014.04.011

Paul, C. R . (1994). *Analysis of Multiconductor Transmission Lines[M*. New York: John Wiley & Sons.

Shen, X., Ouyang, T., Khajorntraidet, C., Li, Y., Li, S., and Zhuang, J. (2021). Mixture Density Networks-Based Knock Simulator. *Ieee/asme Trans. Mechatron.*, 1. doi:10.1109/TMECH.2021.3059775

Shen, X., and Raksincharoensak, P. (2021). Pedestrian-aware Statistical Risk Assessment. *IEEE Trans. Intell. Transport. Syst.*, 1–9. doi:10.1109/TITS.2021.3074522

Shen, X., Zhang, Y., Sata, K., and Shen, T. (2020). Gaussian Mixture Model Clustering-Based Knock Threshold Learning in Automotive Engines. *Ieee/asme Trans. Mechatron.* 25 (6), 2981–2991. doi:10.1109/TMECH.2020.3000732

Song, W., Yao, S., Chang, L., Zhang, X., and Han, M. (2020). The Research of Electromagnetic Transient Simulation Method Based on Discrete Similarity[J]. *Proc. Chin. Soc. Electr. Eng.* 40 (21), 9. doi:10.13334/j.0258-8013.pcsee.200249

Wang, F., and Yang, M. (2016). Fast Electromagnetic Transient Simulation for over - Voltages of Transmission Line by High Order Radau Method and V-Transformation [J]. *IET Generation Transm. Distribution 2016 10* (14), 3639–3645. doi:10.1049/iet-gtd.2016.0476

Wang, Y., Qiang, Li., Zhao, Wei., Zhang, Lei., and Chen, S. (2019). Electromagnetic Transient Simulation Algorithm Based on Improved Critical Damping Adjustment. *Automation Electric Power Syst.* (15), 180–185. doi:10.7500/AEPS20180413006

Watson, N. R., and Irwin, G. D. (1998). Electromagnetic Transient Simulation of Power Systems Using Root-Matching Techniques. *IEE Proc. Gener. Transm. Distrib.* 145 (5), 481–486. doi:10.1049/ip-gtd:19982173

Xing, Y., and Yang, R. (2007). Phase Errors and Their Correction in Symplectic Implicit Single-step Algorithm[J]. *Chin. J. Theor. Appl. Mech.* 39 (5), 4. doi:10.6052/0459-1879-2007-5-2006-561

Yang, N., Huang, Y., and Hou, D. (2019). Adaptive Nonparametric Kernel Density Estimation Approach for Joint Probability Density Function Modeling of Multiple Wind Farms[J]. *Energies* 12, 356. doi:10.3390/en12071356

Yang, N., Ye, Di., Zhou, Zh., Cui, J., Chen, D., and Wang, X. (2018). Research on Modelling and Solution of Stochastic SCUC under AC Power Flow Constraints [J. *].IET Generation, Transm. Distribution* 12 (15), 3618–3625. doi:10.1049/iet-gtd.2017.1845

Yang, N., Huang, Y., Hou, D., Liu, S., Ye, D., Dong, B., et al. (2019). Adaptive Nonparametric Kernel Density Estimation Approach for Joint Probability Density Function Modeling of Multiple Wind Farms. *Energies* 12, 1356. doi:10.3390/en12071356

Yang, N., Liu, S., Deng, Y., and Xing, C. (2021). An Improved Robust SCUC Approach Considering Multiple Uncertainty and Correlation. *IEEJ Trans. Elec Electron. Eng.* 16, 21–34. doi:10.1002/tee.23265

Yang, N., Yang, C., Xing, C., Ye, D., Jia, J., Chen, D., et al. (2021). Deep Learning-based SCUC Decision-making: An Intelligent Data-driven Approach with Self-learning Capabilities. *IET Gener. Transm. Distrib.* 1, 12. doi:10.1049/gtd2.12315

Ye, J., Zhao, D., and Zhang, L. (2021). Research on Combined Electricity and Heating System Scheduling Method Considering Multi-Source Ring Heating Network[J]. *Front. Energ. Res. Early Access*.

Ye, J., Xu, M., Wang, Y., Li, B., Zhang, L., Yi, Z., et al. (2021). Time Domain Response Analyses of Multiconductor Transmission Lines Using L-Stable Single Step Multistage Block Method[J]. *J. Xinyang Normal Univ. (Natural Sci. Edition)* 34 (4), 639697–640644. doi:10.3969/j.issn.1003-0972.2021.04.022

Zhan, R., Li, Y., Jiao, C., Yu, Y., Meng, J., and Wang, B. "Time Delay along a Chained Lumped-Circuits: for the Physical Analogy of Half-Wavelength Power Transmission Lines," in Proceedings of the 2017 IEEE 5th International Symposium on Electromagnetic Compatibility, EMC-Beijing), October 2017 (IEEE), 012044. doi:10.1088/1757-899x/231/1/012044

Zhang, L., Xie, Y., Ye, J., Xue, T., Cheng, J., Li, Z., et al. (2021). Intelligent Frequency Control Strategy Based on Reinforcement Learning of Multi-Objective Collaborative Reward Function. *Front. Energ. Res.* 9, 525. doi:10.3389/fenrg.2021.760525

Conflict of Interest: The authors declare that the research was conducted in the absence of any commercial or financial relationships that could be construed as a potential conflict of interest.

Publisher's Note: All claims expressed in this article are solely those of the authors and do not necessarily represent those of their affiliated organizations, or those of the publisher, the editors, and the reviewers. Any product that may be evaluated in this article, or claim that may be made by its manufacturer, is not guaranteed or endorsed by the publisher.

frontiers in Energy Research

BRIEF RESEARCH REPORT
published: 24 December 2021
doi: 10.3389/fenrg.2021.813855

Intelligent Filling Method of Power Grid Working Ticket Based on Historical Ticket Knowledge Base

*Zhiguo An[1], Mancheng Yi[1], Jing Liu[1], Ying Li[1], Zheng Peng[1], Sifan Yu[1], Jianxin Liu[1], Weirong Huang[1] and Chunhua Fang[2]**

[1]Guangzhou Power Supply Bureau, Guangzhou, China, [2]College of Electrical Engineering and New Energy, Three Gorges University, Yichang, China

The traditional power grid ticket filling method has a large workload, low efficiency, and cannot achieve comprehensive and effective reference of historical tickets. This paper proposes a method of intelligent filling in a power grid working ticket based on a historical ticket knowledge base. Firstly, the historical ticket data are preprocessed, then the historical ticket information is mined by the association rule algorithm, and the method of establishing the historical ticket knowledge base is proposed. Based on the improved word bag model, an intelligent grid work ticket filling model is established based on the historical ticket knowledge base, and the correctness of the method is verified by an example. The results show that the accuracy of the proposed method is at least 18% higher than that of the traditional model, and the matching efficiency is 50% higher than the evaluation results of the three models based on semantic expressions. The method enables the identification and extraction of similar and associated work tickets, improves the efficiency of filling work tickets for power grids, and promotes the intelligence of the safety procedures for power grid operations.

Keywords: work ticket, intelligent filling, the knowledge base, historical ticket, data mining

OPEN ACCESS

Edited by:
Zhenhao Tang,
Northeast Electric Power University, China

Reviewed by:
Zhibin Qiu,
Nanchang University, China
Xiaoyue Chen,
Wuhan University, China

****Correspondence:***
Chunhua Fang
45946866@qq.com

Specialty section:
This article was submitted to Smart Grids, a section of the journal Frontiers in Energy Research

Received: *12 November 2021*
Accepted: *06 December 2021*
Published: *24 December 2021*

Citation:
An Z, Yi M, Liu J, Li Y, Peng Z, Yu S, Liu J, Huang W and Fang C (2021) Intelligent Filling Method of Power Grid Working Ticket Based on Historical Ticket Knowledge Base. Front. Energy Res. 9:813855. doi: 10.3389/fenrg.2021.813855

1 INTRODUCTION

The historical work ticket of a power grid contains a lot of valuable information. The retrieval and utilization of the historical work ticket can effectively assist the filling of the power grid work ticket. The traditional power grid work ticket is mainly filled in by staff according to their tasks, who compare the grid wiring diagram, reference the maintenance equipment historical tickets, and combined them with their own experience. Among them, the retrieval process of historical tickets includes obtaining historical tickets with similar names by inputting the name of the maintenance equipment, and then the employees screen some work tickets based on their experience for reference. This retrieval method has a large workload, poor reliability, and low automation level. Therefore, it is of great significance to study the intelligent filling method of power grid work tickets (Liu et al., 2020; Gui et al., 2021).

Text mining, as a branch of data mining (Wang et al., 2016; Lin et al., 2017; Gao et al., 2019), can fully exploit the potential value of information and has been gradually applied to the field of electric power in recent years. An earlier study (Jiang et al., 2019) mined transformer operation and maintenance texts based on deep semantic learning, achieved text classification through text mining, and considered semantic factors in the text vectorization process to improve classification accuracy and achieve the assessment of transformer operation status. Other studies (Cao et al., 2017; Pang

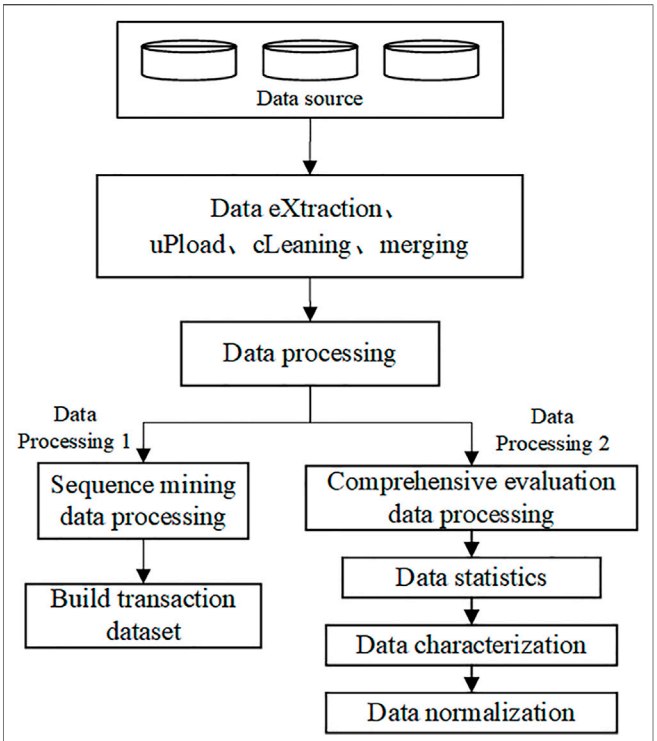

FIGURE 1 | Work ticket data preprocessing process.

et al., 2017) established a semantic framework-based text mining model to achieve classification and statistics of grid defect text. The study by Lynnette and David (2015) proposed a bag-of-words model based on FCM clustering to identify aerial targets, which improved the original "either/or" hard classification feature. The paper by Yuan and Zhou (2018) proposed a supervised bag-of-words model for multimedia information of different objects, and the text vector and retrieval results obtained by tagging the training samples were highly accurate compared with the traditional bag-of-words model. In this paper, according to the characteristics of the working ticket text, the original bag-of-words model was improved for problems such as multiple meanings of words and reversed order of words caused by irregular expressions, and an improved bag-of-words model containing both main words and auxiliary words was proposed.

Therefore, a method of intelligent filling of grid work tickets based on text mining of the historical ticket knowledge base is proposed. By analyzing the preliminary processing of historical ticket data and the establishment of a knowledge base, an improved two-layer bag-of-words model for intelligent filling of grid work tickets is constructed. The method uses Term Frequency-Inverse Document Frequency (TF-IDF) for feature extraction, and then uses cosine similarity to achieve multivariate matching between work tickets, after which the results are sorted in descending order, and finally the proposed method is proved to be more suitable for historical work tickets than other methods based on practical cases. The proposed method is finally proved to be more suitable for historical work ticket mining and work ticket filling than other methods. Therefore, the historical work tickets that have been stored in the long-term operation of the power grid can be fully utilized to effectively reduce the error rate of power system work and enhance the efficiency of filling work tickets in the power grid.

2 BIG DATA ANALYSIS OF WORK TICKETS

2.1 Data Sources of Work Tickets

Work ticket big data are mainly distributed in three information systems, including an Equipment Asset Management System, Production Scheduling and Managing System, and Distribution Automation System. Finally, the data are extracted and summarized in the intelligent verification system of the work ticket. When acquiring the working data, the historical data are firstly extracted from the Equipment Asset Management System, and then uploaded to the intelligent verification system of the working ticket. The data tables in the historical database are sorted out, the analysis objectives are clarified, and the corresponding data files are finally selected according to the objectives (Wu and Yu, 2021).

2.2 Work Ticket Data Preprocessing

In the data mining of a work ticket, the data sample of the work ticket should be preprocessed first. The workflow of preprocessing is shown in **Figure 1**, including data cleaning, data merging, comprehensive evaluation modeling data processing, and sequence mining models data processing.

2.2.1 Data cleaning

Work ticket data generally come from different information systems, so there are many differences in the integrity and format of data (Wu et al., 2015). To comprehensively investigate the basic situation of data, data cleaning occurs from the following four aspects:

2.2.1.1 Name normalization

The format of the work ticket type and the company field is unified. The format of "affiliated company" is "**power supply company". For example, after the format of the first kind of work ticket of B power supply company is unified, the fields are "B power supply company of the first kind of work ticket" and "B power supply company", respectively.

2.2.1.2 Time field specification and logical judgment

The time format is unified into "year/month/day hour/minute". Work ticket data contain the start time and end time. Generally, the end time is later than the start time, but the end time of some data is earlier than the start time, resulting in logical errors (Li, 2021). For this part of the data, the end time and start time are exchanged. If the system data only contain "operation time", the field is changed to "start time" and the "end time" is added.

2.2.1.3 Type and quantity of violation

Data processing is classified according to the type of violation and the name of the company, and each type of violation contains statistical quantity. Therefore, it is necessary to input all kinds of

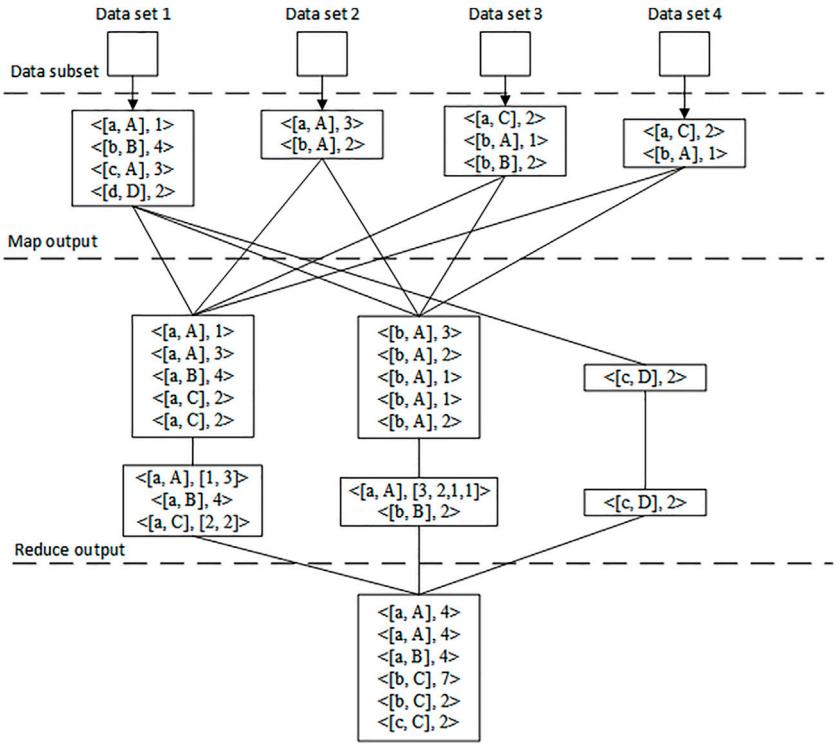

FIGURE 2 | MapReduce data statistics process diagram.

violation types into the system in a unified format to achieve accurate and rapid data classification.

2.2.1.4 Null data processing method

Because some important fields of data are null values, such as equipment name, line name, and sampling value, these null values will make it difficult for the system to carry out subsequent data mining, so these kinds of data will be screened out.

2.2.2 Data merging

After data cleaning, the data are combined to make data mining more convenient. Firstly, the fields of work ticket type, power supply company name, and planned time are extracted from the data (Zhu et al., 2003), then the fields of violation type and operating equipment are added, and the data are further divided. After data merging, the new data table contains the following five fields: work ticket type, name of power supply company, operating equipment, scheduled time, and violation type.

2.2.3 Comprehensive evaluation modeling data processing

Before the comprehensive evaluation of the data, the data need to be processed. The processing process includes: data statistics stage, data normalization, and data characterization.

2.2.3.1 Data statistics stage

In the map stage, we first define the input key value pair as < name, type >, and the intermediate key value pair generated after the map processing task as < (power supply company, violation type), quantity >, such as < [B, b] 2 >, indicating that there are two pieces of data for the violation type b of power supply company B. In the reduce phase, all key value pairs containing the same key are sent to the same reduce phase, and then the values corresponding to the same key are added to generate new key value pairs. Finally, the results are written into HDFS. The data statistics process based on MapReduce is shown in **Figure 2**. A, B, and C represent three different power supply companies, respectively, and A, B, and C represent different data indicators, respectively.

2.2.3.2 Data characterization

Due to the complexity of violation types of the work ticket, when evaluating the work ticket data, if the data preprocessing is carried out in a simple statistical detail way, it is easy to ignore the objective differences existing in the work ticket, which will affect the final evaluation results (Wang et al., 2016). Therefore, it is necessary to preprocess the data according to the characteristics of different data.

2.2.3.3 Data normalization

In order to avoid the impact of data-level differences on evaluation results, **Eq. 1** is used to normalize the data.

$$y_i = \frac{x_i - x_{\min}}{x_{\max} - x_{\min}} \tag{1}$$

In this formula, y_i is the normalized data; x_i is an attribute value of the original data; and $x_{\min}$ and $x_{\max}$ represent the minimum and maximum values for this property.

TABLE 1 | Serial transaction database.

Affair	Sequence
S1	[(a, c), b, e, f]
S2	(g, a, e)
S3	(g, a, b, f)
S4	(d, a)
S5	(a, b)

2.2.3.4 Sequence mining models data processing

In sequence mining, the corresponding transaction database should be established first. Then we use MapReduce to set up the transaction database. The setup steps are as follows:

1) Map input definition key value pair < name, type >, map function output key value pair < line, (begintime , name) >, the specific format is < name of power supply company, (operation equipment, violation type) >.
2) The reduce phase obtains key value pairs with the same key from the map task, and sorts the corresponding values in chronological order. For example, < Line1, list < (begintime1, Name2), (begintime2, name3), (begintime3, name1) >.
3) We use the map function to input key = name of power supply company, value = list, and output key = name of power supply company, value = violation type. Finally, we store the results. The above examples are: < Line1, (name2, name3, name, 1) >. The final sequence transaction database is shown in **Table 1**.

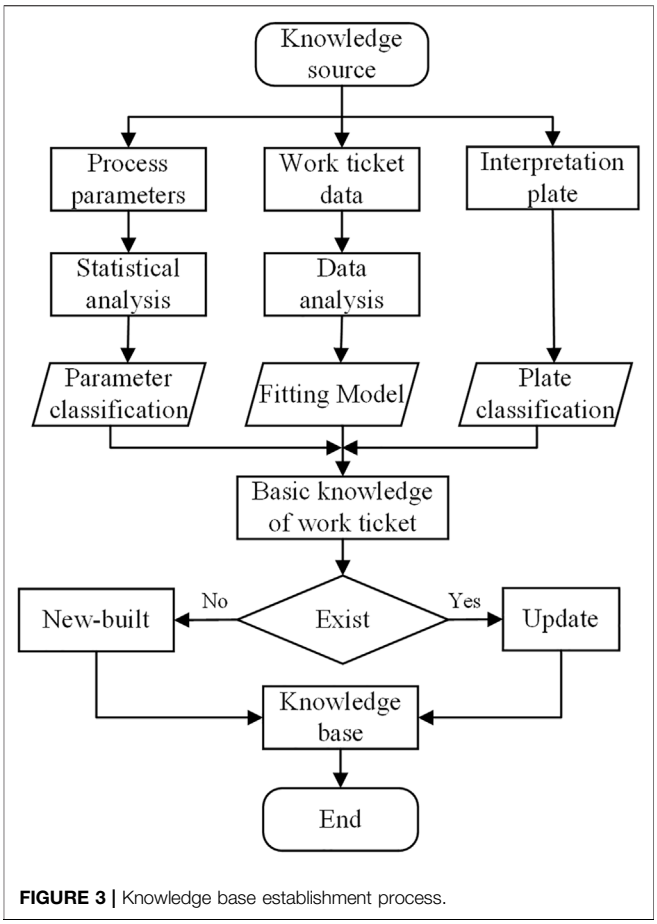

FIGURE 3 | Knowledge base establishment process.

3 INTELLIGENT FILLING MODEL OF WORK TICKETS

3.1 The Establishment of the Historical Ticket Knowledge Base

The establishment of the historical ticket knowledge base includes extracting historical ticket processing and interpretation information such as work ticket data, processing parameters, and interpretation templates from the knowledge source, converting them into specific computer code, and finally obtaining the preferred parameters for work ticket processing and interpretation (Jiang et al., 2019). Knowledge acquisition includes passive and active methods: 1) Active knowledge acquisition automatically obtains historical ticket processing interpretation rules based on accumulated ticket processing interpretation information and stores them in the knowledge base. For example, data fitting is carried out on the parameter frequency of the ticket, and the confidence interval method is used to statistically analyze the fitting results. 2) Passive knowledge acquisition uses the information base editor to store the logic rules of historical tickets in the knowledge base. When the working ticket processing and interpretation parameters are the knowledge source, the work ticket knowledge base conducts statistical analysis and classification of the parameters, and integrates the priority of the parameters. When the work ticket data are the knowledge source, the work ticket fitting model is established according to the work ticket data, and the classical formula parameters are obtained by using the work ticket data.

The establishment process of the knowledge base is shown in **Figure 3**. After preprocessing the knowledge source data, the data items are composed of a set $I = (I_1, I_2, \ldots I_n)$. The logical rules of the data can be expressed as follows:

$$\begin{cases} A \geq B \\ A \subset I, B \subset I, A \cap B = \Phi \end{cases} \tag{2}$$

In this formula, A is the antecedent of the logical rule, B is the consequent of the logical rule, and Φ is an empty set.

Support S is used to measure the applicability of logical rules, and reliability C is used to measure the accuracy of logical rules. P is the probability of logical rules, then:

$$\begin{cases} S(A \geq B) = P(A \cup B) \\ C(A \geq B) = P(A \cup B)/P(A) = P(B|A) \end{cases} \tag{3}$$

A frequent set is a set of items whose specified threshold is less than the support count. The information acquisition of the historical ticket includes two steps: 1) Finding all frequent sets of history tickets whose frequency is greater than or equal to the minimum support threshold. 2) The corresponding history ticket knowledge is generated by using frequent sets, and this

knowledge must meet the minimum trust threshold. The parameter model of the work ticket knowledge base is established by using the association rule algorithm, and the frequent set is calculated. For instance, in the process of obtaining information on historical tickets, the Archie formula can be chosen when the frequent set is less than 20%. Each item of the frequent set must be arranged according to the generated time order, and the specified time interval must be greater than the generated time difference (Zhu et al., 2003). In addition, minimum trust and minimum support must be set. Setting the minimum trust C_{min} to 70% and the minimum support S_{min} to 35%, the association rules of the model must meet the above conditions. If the logical association rule obtained during mining meets the following constraints, the association rule is acceptable.

$$\begin{cases} S(V_{sh} < 20\%, Archie) \geq 35\% \\ C(V_{sh} < 20\%, Archie) \geq 70\% \end{cases} \tag{4}$$

The significance of S in **Eq. 4** is that at least 35% of all model preferences exhibit behavior where both the frequent set of less than 20% and the Archie formula are used together, and the significance of C in this example is that at least 70% of the frequent set of less than 20% model preferences use the Archie formula together. Therefore, if there is a preference for an explanatory parameter with a frequency set of less than 20%, the knowledge base will be able to recommend that the user prefers the Archie formula.

3.2 Establishment of Intelligent Filling Model

Matching between texts is performed by relying on the similarity calculation of text features. Text vector feature extraction using the TF-IDF method, which has a wide range of applications in finding text, text classification, and other similar fields, has been called the most meaningful creation in information retrieval. In this paper, the multivariate similarity calculation between the feature vectors of query text and historical text is performed using the cosine function after deactivating words, splitting words, vectorization, and feature extraction of historical text and query text (Shang et al., 2015). The n-dimensional vector cosine similarity calculation formula is shown in **Eq. 5**.

$$S_{\cos}(a,b) = \frac{ab}{|a||b|} = \frac{\sum_{i=1}^{n} a_i b_i}{\sqrt{\sum_{i=1}^{n} a_i^2}\sqrt{\sum_{i=1}^{n} b_i^2}} \tag{5}$$

$a = (a_1\ a_2 \ldots a_n)$, $b = (b_1\ b_2 \ldots b_n)$ are the query text and historical text vectors, respectively, and a_i, b_i are the TF-IDF values corresponding to the i-th phrase in the text. The larger $Cos\theta$ is, the higher the similarity is. Since each variable in the vector is positive, the similarity takes values between 0 and 1.

In order to allow the computer to process text information, each word of the text is mapped into a number set. A word bag model is a common method of text processing. Firstly, the document set S is merged by **Eq. 6** to generate word bag T_0; then, the text vocabulary in the document is counted to obtain the text vector D_V composed of a number.

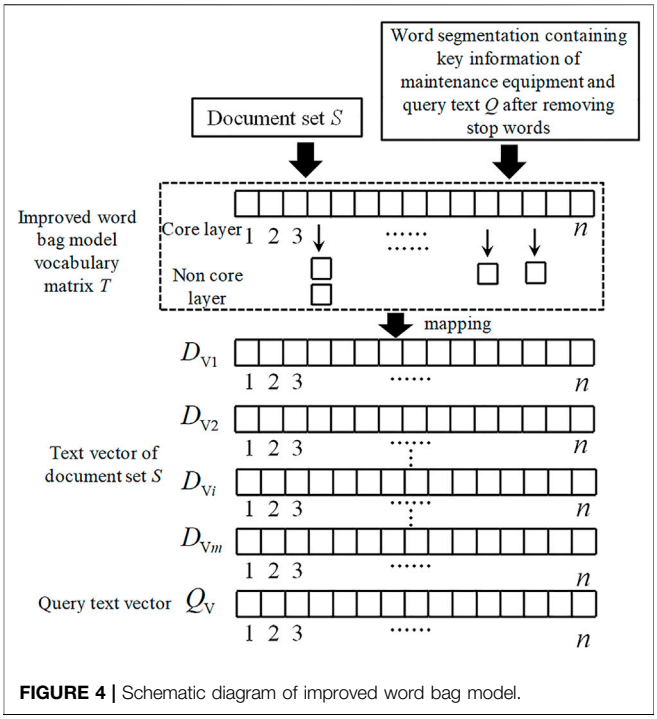

FIGURE 4 | Schematic diagram of improved word bag model.

$$T_0 = [t_{01}\ t_{02}\ t_{03} \cdots t_{0n}] \tag{6}$$

In this formula, t_{01}, $t_{02} \ldots t_{0n}$ are the words in D, respectively.

In the process of filling in work tickets, word order is often confused due to non-standard filling, which leads to the decrease of similarity (Han et al., 2016; Du et al., 2018). Therefore, this paper improves the original word bag model T_0 and adds a vocabulary relation expansion table on the basis of the original word bag model. The text is divided into a subject core layer and auxiliary non-core layer, and the vocabulary matrix T is expressed as:

$$T = \begin{bmatrix} t_{01} & t_{02} & \ldots & t_{0n} \\ t_{11} & t_{12} & \ldots & t_{1n} \\ \ldots & \ldots & \ldots & \ldots \\ t_{m1} & t_{m2} & \ldots & t_{mn} \end{bmatrix} \tag{7}$$

In this formula, the first line is the core layer of the subject, and the second line to the m line is the non-core layer of the auxiliary word.

In addition, on the basis of the original bag model, each text in S is successively mapped to n-dimensional vectors, as shown in **Eq. 8**:

$$\begin{cases} D_{V1} = [d_{11} d_{12} \ldots d_{1j} \ldots d_{1n}] \\ D_{V2} = [d_{21} d_{22} \ldots d_{2j} \ldots d_{2n}] \\ \ldots \\ D_{Vi} = [d_{i1} d_{i2} \ldots d_{ij} \ldots d_{in}] \\ \ldots \\ D_{Vk} = [d_{k1} d_{k2} \ldots d_{kj} \ldots d_{kn}] \end{cases} \tag{8}$$

In this formula, k is the number of power grid safety specification texts in the historical ticket knowledge base; d_{ij} is

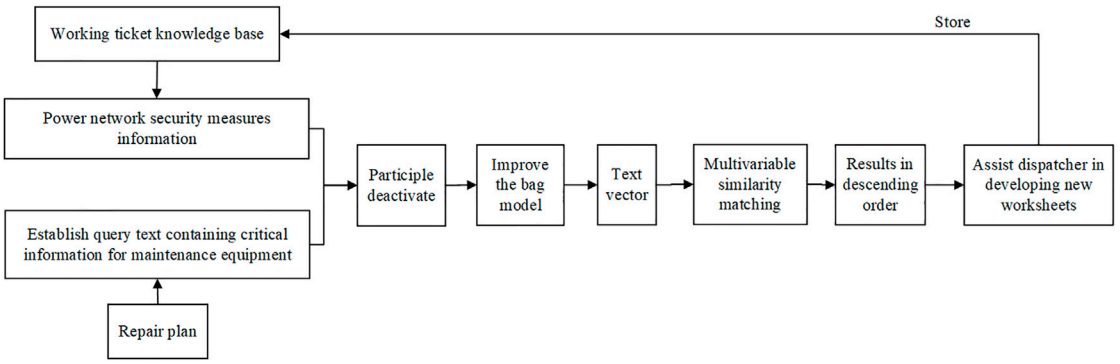

FIGURE 5 | The intelligent filling model of power grid work tickets.

the word frequency of the *j*-th word in the word bag model *i*; when the text contains an auxiliary word, we put the corresponding word frequency of the auxiliary word into the position of the subject word frequency, and add the word frequency. The working principle diagram is shown in **Figure 4**.

In order to improve the efficiency of power grid work ticket filling and promote the intelligent development of the power grid, an intelligent power grid work ticket filling model based on the historical ticket knowledge base is built on the basis of the improved word bag model. The process of the model is as follows:1) Analyze and obtain the text features of the work ticket, and mine the potential power grid security measures; 2) preprocess the unstructured text and segment the text according to the knowledge of the power field; 3) the improved model is applied to the vectorization of words after word segmentation; 4) extract the features of the text vector; and 5) cosine similarity is used to realize variable matching and descending arrangement of text. Employees can refer to the historical work ticket text at the top of the order. The intelligent filling model of the power grid work ticket is shown in **Figure 5**.

4 CASE ANALYSIS

4.1 Case Analysis 1

In order to demonstrate the accuracy of the proposed method for filling grid work tickets intelligently based on text mining of the historical ticket knowledge base. Taking the historical working tickets of power transmission and transformation equipment maintenance of a Power Supply Bureau in 2020 as an example, the work tickets are 2,542 in total. We take the key information of the equipment to be repaired as the query content, such as: "CT current rise of G02 cabinet of group junction no. 1 outdoor switch station of 10 kVA line, voltage withstand test of cable from group junction no. 1 outdoor switch station to no. 10 European style box transformer". After being segmented, it can be expressed as "10 kVA line, group junction, no. 1 outdoor switch station, G02 cabinet, CT upflow, group junction, no. 1 outdoor switch station, no. 10 European style box transformer, cable, voltage withstand test". The combination of historical ticket keyword association and plant station topology is used for analysis, the optimal parameters are obtained and returned to the work ticket application. The features of each text are extracted through the text similarity TF-IDF model, and the work ticket knowledge base is called to calculate the text similarity of the work task. The descending order of historical text similarity is obtained through intelligent matching, the top six texts are shown in the following table.

TABLE 2 | Top six historical texts in similarity ranking.

Text serial number	Similarity	Similarity ordering
36	0.956	1
53	0.901	2
18	0.874	3
79	0.793	4
3	0.705	5
48	0.608	6

In **Table 2**, the text with serial number 36 has the highest similarity, and the corresponding historical text is "voltage withstand test for cable from outdoor switch station no. 1 to switch room no. 14 of 10 kVA line ". The historical text of serial number 53 is "replace the transformer of no. 6 complex room of 10 kVA line", it is the same as the power failure line in the query content, so the power failure scope, power failure layout, and power failure time can be used as reference information to form a certain rule. The text no. 18 is "cable head made for cabinet G02 of Outdoor Switch Station no. 1 of 10 kVA Line Cluster". "Power cut line", "switch cabinet", and "power cut equipment" are similar to the query content, so the reference content can be filled in the corresponding column of the work ticket. The text of no. 79 corresponds to "voltage withstand test of newly laid cable from G02 cabinet in no. 2 switch room of 10 kVA line to newly installed G13 cabinet in this room". The work content in the historical text is also the cable withstand voltage test, which is similar to the work content in the text, and can be used as a reference when the staff arranges safety measures and precautions, and can be combined with the text no. 18 content, making the work ticket content more manageable. The text of no. 3 corresponds to "CT current rise test of G04

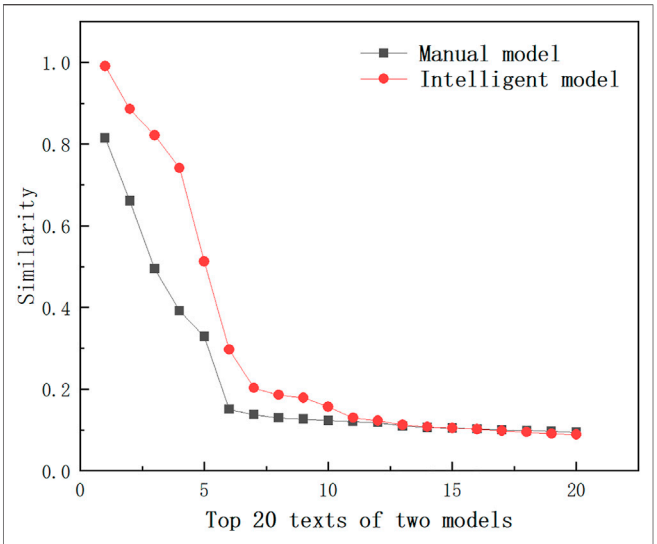

FIGURE 6 | Comparison of similarity between different models in the same text.

traditional model, and the accuracy is at least 18% higher than the traditional model.

4.2 Case Analysis 2

To prove that the proposed intelligent filling method of power grid work tickets based on historical ticket knowledge base text mining can improve the filling efficiency, the historical work tickets of transmission and substation equipment overhaul in a Power Supply Bureau in 2020 are analyzed as an example, with a total of 2,542 work tickets. The key information of five groups of overhaul equipment is selected as query items, where the average length of query items is 10 and the average length of documents is 500. Each query item will index the top five texts with similarity ranking, and after that, MAP (Mean Average Precision) and NDCG (Normalized Discounted cumulative gain), which are commonly used in the field of information retrieval, are used to match the text with the similarity ranking. Cumulative gain indexes commonly used in the field of information retrieval are used to evaluate the matching results, and the average of the five evaluation results is used as the final evaluation index, expressed as η. Where, the larger the average value, the more accurate the matching result is (Wang et al., 2014; Umagandhi and Senthil Kumar, 2015).

TABLE 3 | Results of the model in the matching of similar and correlated work tickets.

Category	Models	η (MAP)	η (NDCG)
Traditional features	BM25 model	0.23	0.4
Based on single semantics	DSMM model	0.08	0.2
Text expression	CDSSM model	0.06	0.14
Multi-semantic text-based representation	MV-LSTM model	0.12	0.18
Improving traditional features	The model proposed in the paper	0.28	0.47

standby cabinet in 10 kV 5 switchgear room", content similarity is "switchgear related tests", and the precautions for power failure can be used as an appropriate reference. The text of serial no. 48 is "switch room no. 11 of 10 kVA line is newly installed with 5 M busbar and four sides of newly installed open pressure cabinets (cabinets G11 to G14)", which has low similarity with the query content and is of no value.

According to the historical work ticket data of transmission and substation equipment maintenance in a Power Supply Bureau in 2020, 2,542 tickets were issued. Using the model proposed in the previous paper, the similarity comparison graph shown in **Figure 6** is drawn; the red curve is the similarity size under the improved model and the black curve is the similarity size under the traditional model. The similarity between the first four texts and the query text under the improved model is high and has a certain degree of connectivity; the similarity of the fifth text decreases sharply and continues to decrease in the latter. The similarity of the first two texts under the traditional model is higher.

It can be seen that the results under the traditional model have no obvious transition phase and are less accurate, while the text similarity results under the improved model have distinct boundaries. Dispatchers have clear targets when extracting work tickets, the similarity size is generally higher than the

The proposed model is compared with the traditional BM25 model, Deep Semantic Structured Model (DSSM) based on single-semantic text representation, and Convolutional Deep Semantic Structured Model (CDSSM). The Multi View-Long Short Term Memory (MV-LSTM) model based on multi-semantic representation is compared. The results of the evaluation metrics are shown in **Table 3**.

From **Table 3**, the MAP and NDCG index values of the model in this article are the largest among the average of the five evaluation results, the matching results are the best, and the effectiveness is the highest; the evaluation results of the three models based on semantic expression are very low, among which the MV-LSTM model has better evaluation results. Both MAP and NDCG values are lower than 50% of the models mentioned in the article.

5 CONCLUSION

By analyzing the preprocessing of work ticket data and the establishment of a knowledge base, this paper constructs an intelligent filling model of power grid work tickets based on

the historical ticket knowledge base, and verifies the specificity and effectiveness of the proposed method combined with an actual power grid case. The main conclusions are as follows:

1) Using the association rule algorithm to mine historical ticket knowledge, we can obtain the key words of historical ticket information effectively, and then assist the staff to carry out comprehensive referencing.
2) According to the non-standard expression of the work ticket text, the original word bag model is improved to reduce the similarity error caused by environmental noise and improve the matching accuracy.
3) The case study shows that the accuracy of the proposed model in the paper is at least 18% higher than that of the traditional model, and the matching efficiency is 50% higher than that of the evaluation results of the three models based on semantic expressions. Therefore, the work ticket management application module can be automated, saving time for filling and verifying tickets and improving work efficiency.

DATA AVAILABILITY STATEMENT

The original contributions presented in the study are included in the article/Supplementary Material, further inquiries can be directed to the corresponding author.

AUTHOR CONTRIBUTIONS

ZA, MY, and JL (3rd author) conceived the idea and designed the experiments. YL and ZP led the experiments. SY, JL (3rd author), and WH contributed to data analysis and interpretation. CF and ZA wrote the paper. All authors read and approved the final manuscript.

REFERENCES

Cao, J., Chen, L., Qiu, J., Wang, H., Ying, G., and Zhang, B. (2017). Semantic Framework-Based Text Mining Technique for Grid Defects and its Application. *Power Grid Technol.* 41 (02), 637–643. doi:10.13335/j.1000-3673.pst.2016.1044

Du, X., Qin, J., Guo, S., and Yan, D. (2018). Text Mining of Typical Fault Cases of Power Equipment. *High Voltage Technol.* 44 (04), 1078–1084. doi:10.13336/j.1003-6520.hve.20180329005

Gao, X., Chen, G., and Zhao, H. (2019). Data Mining-Based Cyber Security Posture Assessment of Electric Power Information Systems. *Electr. Meas. Instrumentation* 56 (19), 102–106. doi:10.19753/j.issn1001-1390.2019.019.017

Gui, Q., Yao, X., Wang, L., Shao, Z., Yang, H., Hao, Z., et al. (2021). Intelligent Error Prevention Technology of Maintenance Work Ticket Based on Layered Finite State Machine. *J. Hefei Univ. Technol. (Natural Sci. Edition)* 44 (04), 458–463.

Han, W., Fan, S., Wei, Z., and Wang, W. (2016). "A Method for Similarity Analysis of Power System State," in IEEE PES Asia-Pacific Power and Energy Engineering Conference (APPEEC), 2033–2036. doi:10.1109/appeec.2016.7779842

Jiang, Y., Li, L., Li, Z., Su, C., Wang, G., and Peng, S. (2019). A Deep Semantic Learning-Based Text Information Mining Method for Power Transformer Operation and Maintenance. *Chin. J. Electr. Eng.* 14, 4162–4172. doi:10.13334/j.0258-8013.pcsee.181457

Li, S. (2021). Intelligent Operation Ticket System for Power Grid Dispatch Based on Hierarchical Structure Knowledge Base and Reasoning Machine Technology. *Electric Age* 23 (04), 52–54.

Lin, S., Xie, C., Tang, B., Pan, A., and Zhou, J. (2017). Application of Data Mining in Power Quality Monitoring Data Analysis. *Electr. Meas. Instrumentation* 43 (09), 46–51.

Liu, T., Li, S., Gu, X., Wang, T., Wu, Y., and Wang, W. (2020). Research on Text Mining Based Power Grid Maintenance Work Ticket Assisted Decision Method. *Electr. Meas. Instrumentation* 57 (02), 39–45. doi:10.19753/j.issn1001-1390.2020.002.006

Lynnette, P., and David, S. (2015). Accounting Variables, Deception, and a Bag of Words: Assessing the Tools of Fraud Detection. *Contemp. Account. Res.* 32 (3), 1193–1223. doi:10.1111/1911-3846.12089

Pang, L., Lan, Y., Xu, J., Guo, J., Wan, S., and Cheng, X. (2017). A Review of Deep Text Matching. *J. Comput. Sci.* 40 (04), 985–1003. doi:10.27312/d.cnki.gshsu.2020.001431

Shang, F., Yuan, Y., Wang, C., Cao, M., and Feng, Z. (2015). A Knowledge-Base Based Method for Intelligent Preferential Logging Data Processing of Interpretation Models. *J. Pet.* 36 (11), 1449–1456.

Umagandhi, R., and Senthil Kumar, A. V. (2015). Evaluation of Reranked Recommended Queries in Web Information Retrieval Using NDCG and CV. *Int. J. Inf. Technol. Comput. Science(IJITCS)* 7 (8), 23–30. doi:10.5815/ijitcs.2015.08.04

Wang, S., Bi, S., Xu, Y., and Sun, Y. (2016). Short-term Load Forecasting Based on Data Mining Techniques and Support Vector Machines. *Electr. Meas. Instrumentation* 15 (10), 62–67.

Wang, Y., Huang, Y., Lu, M., Pang, X., Xie, M., and Liu, J. (2014). A Multi-Sorting Model Fusion Approach for Direct Optimization of Performance Metrics. *J. Comput. Sci.* 42 (08), 1658–1668.

Wu, J., and Yu, W. (2021). A Study of Text Clustering with Fused Knowledge Base Semantics. *J. Intelligence* 35 (05), 156–164. doi:10.3778/j.issn.1002-8331.2104-0286

Wu, K., Liu, W., Li, Y., Su, Y., Xiao, Z., Pei, X., et al. (2015). Cloud-based Power Big Data Analysis Technology and Application. *China Electric Power* 24 (02), 111–116+127.

Yuan, G., and Zhou, X. (2018). A Supervised Bag-Of-Words Model Based on Multimedia Information Retrieval. *Comput. Eng. Des.* 32 (09), 2873–2878. doi:10.16208/j.issn1000-7024.2018.09.031

Zhu, Y., Zhang, J., Yang, Z., Ji, X., and Yang, Y. (2003). An Object-Oriented General Expert System for Work Tickets and Operation Tickets in Agricultural Network Substations. *Power Grid Technol.* 24 (04), 27–30.

Conflict of Interest: ZA, MY, JL, YL, ZP, SY, JL, and WH were employed by the company Guangzhou Power Supply Bureau.

The remanining author declare that the research was conducted in the absence of any commercial or financial relationships that could be construed as a potential conflict of interest.

frontiers in Energy Research

BRIEF RESEARCH REPORT
published: 05 January 2022
doi: 10.3389/fenrg.2021.806595

The Influence of Humidity on Electron Transport Parameters and Insulation Performance of Air

Yunzhu An[1,2], Menghan Su[1], Yuanchao Hu[1], Shangmao Hu[3], Tao Huang[4], Baina He[1,2]*, Minghao Yang[1], Kaiqiang Yin[1] and Yitong Lin[1]*

[1]School of Electrical and Electronic Engineering, Shandong University of Technology, Zibo, China, [2]Key Laboratory of Special Machine and High Voltage Apparatus, Shenyang University of Technology, Shenyang, China, [3]Electric Power Research Institute, China Southern Power Grid, Guangzhou, China, [4]State Grid Jiangsu Power Engineering Consulting Limited Company, Nanjing, China

The environmental conditions affect the external insulation performance of power equipment. In order to study the physical characteristics of air discharge, the microscopic process of electron–molecule collision in the air based on the Boltzmann equation has been studied in this paper. The influence of humidity on the air gap insulation performance was also analyzed. The calculation results show that with the temperature 300 K and the pressure 1.0 atm, the electron energy distribution function and electron transport parameters varied with the air relative humidity. As the air relative humidity is increased by each 30%, the average electron energy decreases by about 0.2 eV, the reduced electron mobility decreases by about 0.25×10^{23} [1/(V·m·s)], the reduced electron diffusion coefficient decreases by about 0.2×10^{24} [1/(m s)], and the effective ionization coefficient decreases by about 4×10^{-24} m^2. As the air relative humidity increases from 0% to 60%, the critical breakdown electric field increases by 1.22 kV/cm.

Keywords: humidity, electronic energy distribution function, Boltzmann equation, critical breakdown field strength, electron transport parameters

OPEN ACCESS

Edited by:
Xun Shen,
Tokyo Institute of Technology, Japan

Reviewed by:
Jingshan Wang,
Shandong University, China
Shanpeng Zhao,
Lanzhou Jiaotong University, China

****Correspondence:***
Yuanchao Hu
huyuanchao3211@126.com
Baina He
114311366@qq.com

Specialty section:
This article was submitted to Wind Energy, a section of the journal Frontiers in Energy Research

Received: *01 November 2021*
Accepted: *22 November 2021*
Published: *05 January 2022*

Citation:
An Y, Su M, Hu Y, Hu S, Huang T, He B, Yang M, Yin K and Lin Y (2022) The Influence of Humidity on Electron Transport Parameters and Insulation Performance of Air. Front. Energy Res. 9:806595. doi: 10.3389/fenrg.2021.806595

1 INTRODUCTION

In order to transmit a large-capacity power supply by long transmission distance, a UHV power grid has been constructed and developed rapidly in China (Zhao et al., 2015; Xun et al., 2020a; Xun et al., 2021a). For high voltage level and large span of UHV transmission line, it inevitably leads to power loss, and noise pollution and equipment corrosion (Zhenya, 2005a; Zhenya, 2005b; Muniappan, 2021). The terrain conditions, altitude, and meteorological conditions along UHV transmission lines are complex and changeable, which may affect the external insulation characteristics (Xun et al., 2017; Xun et al., 2020b; Weichen et al., 2021). The characteristics of air discharge can be significantly affected by air humidity (Wenliang et al., 2007; Yang et al., 2021a; Yang et al., 2021b), which has become one of the focuses in the field of power system external insulation.

At present, most researches are committed to the development process of air discharge (Prasad and Craggs, 1960; Abdel-Salam, 1985; Xun et al., 2021b; Xun and Pongsathorn, 2021). Bian Xingming and other scholars (Xingming et al., 2010) studied the physical characteristics of negative DC corona in a rod-plate electrode. They applied the charge simulation method and surface photoelectron calculation method to achieve the inception voltage of negative DC corona, and to study the influence of humidity. Cai Xinjing and other scholars (Xinjing et al., 2015) used fluid model to simulate the propagation process of bi-directional streamer in air gaps with different water

vapor. It was concluded that humidity had little effect on the propagation characteristics of a streamer under the same background electric field, but the influence of air humidity on the inception characteristics of a streamer was not studied. To design the structure of EHV transmission lines in high altitude areas, Liu Youwei and other scholars (Liu et al., 1990) analyzed the characteristics of corona around the conductor with different humidity in detail. Their experimental results showed that humidity had a significant impact on the corona inception electrical field of the conductor. Li Kelin (Kelin, 2019) built the corresponding discharge chamber to simulate different climate conditions. The change of negative DC corona discharge mode under different humidity conditions was analyzed in detail, and the influence mechanism was analyzed combined with the simulation results. Yuke, (2017) used the self-designed experimental platform that can adjust humidity to study the influence of different air humidity on corona discharge with the internal electrode of converter valve as an example. The above studies were mostly focused on the influence of humidity on corona inception electric field and corona discharge process, and rarely considered the influence of humidity on electron transport parameters. The electron transport parameters are not only the basis for the plasma hydrodynamics model of air discharge but also can reflect the insulation performance of air gaps (Wen et al., 2016; Roostaee et al., 2017; Xinyu et al., 2018; Xun and Raksincharoensak, 2021; Yuanchao et al., 2021). The external insulation of power equipment exposed to air will be affected by air humidity. The variation of air humidity will affect the electronic transport parameters during air discharge that lead to different insulation performance of air gaps and may threaten the operation characteristics of external insulation of power equipment.

In this paper, the motion collision processes between electrons and molecules in air under different humidity are simulated in detail. The Boltzmann two approximation method is used to solve the electron transport parameters of air. The air electron transport parameters under different reduced electric fields are calculated and analyzed. The calculation results are compared with the results of Morrow (Morrow and Lowke, 1997) and Nikonov (Nikonov et al., 2001) to verify the model reasonability in this paper. The effect of humidity on electron energy distribution function (EEDF), reduced electron mobility (μ/N), reduced electron diffusion coefficient (D/N), and critical breakdown electric field are simulated and analyzed.

2 CALCULATION METHOD OF ELECTRON TRANSPORT PARAMETERS

2.1 Binomial Approximation Expansion

Electron energy distribution function is calculated by Boltzmann binomial approximation. The electron collision process plays a major role during the air discharge. In the numerical simulation of fluid dynamics of gas discharge, the accuracy of electron collision section data is the key to accurately solve the transport parameters using Boltzmann equation. In order to simplify the calculation, only four types of collision sections are considered in this paper, including elasticity, ionization, adhesion, and excitation (Su et al., 2019).

During air discharge, the electron distribution function can be described by Boltzmann **Eq. 1**:

$$\frac{\partial f}{\partial t}+\vec{v}.\nabla f-\frac{e}{m}\left(\vec{E}.\nabla\vec{v}.f\right)=C[f] \tag{1}$$

where f is the distribution function of electrons in the six-dimensional phase space; e is the amount of electron charge; v is an electron velocity vector; E is the field strength, V m^{-1}; ∇ is a velocity gradient operator; m is electronic quality; and C is a collision term, which represents the variation rate of distribution function.

Since it is very difficult to solve the Boltzmann equation directly, the equation can be expanded into spherical coordinates as **Eq. 2**.

$$\frac{\partial f}{\partial t}+v\cos\theta\frac{\partial f}{\partial z}-\frac{e}{m}E\left(\cos\theta\frac{\partial f}{\partial v}+\frac{\sin^2\theta}{v}\frac{\partial f}{\partial\cos\theta}\right)=C[f] \tag{2}$$

Based on the uniform spatial electric field, elastic collision plays a major role when the electric field intensity is not high (generally less than 1000Td). The binomial approximation method can be used to reduce the complexity. Here, f is expanded as **Eq. 3**.

$$f(v,t,z,\cos\theta)\approx f_0(v,t,z)+f_1(v,t,z)\cos\theta \tag{3}$$

where θ is the angle between the electron velocity vector and the direction of the electric field, and f_0 and f_1 correspond to the respective homogeneity and heterogeneity of the electron energy distribution function, respectively.

Take **Eq. 3** into **Eq. 2**, and the Legendre polynomial expansion is performed. Then the following two equations are obtained by integrating θ:

$$\begin{cases}\dfrac{\partial f_0}{\partial t}+\dfrac{\gamma}{3}\varepsilon^{\frac{1}{2}}\dfrac{\partial f_1}{\partial t}-\dfrac{\gamma}{3}\varepsilon^{\frac{1}{2}}\dfrac{\partial}{\partial\varepsilon}\varepsilon Ef_1=C_0\\ \dfrac{\partial f_1}{\partial t}+\gamma\varepsilon^{\frac{1}{2}}\dfrac{\partial f_0}{\partial t}-E\gamma\varepsilon^{\frac{1}{2}}\dfrac{\partial f_0}{\partial\varepsilon}=-N\sigma_m\gamma\varepsilon^{\frac{1}{2}}f_1\\ \sigma_m=\sum_k x_k\sigma_k,\gamma=(2e/m)^{0.5},\varepsilon=(v/\gamma)^2\end{cases} \tag{4}$$

Here, C_0 is the variation of f_0 caused by collision; σ_m and σ_k are the total collision cross section and the collision cross section of reaction k, where reaction k represents any collision reaction, m^2.

According to the separation variable method, **Eq. 4** can be combined as **Eq. 5**:

$$\begin{cases}\dfrac{\partial}{\partial\varepsilon}\left[\dfrac{\varepsilon}{3\sigma_m}\dfrac{\partial f_0}{\partial\varepsilon}\left(\dfrac{E}{N}\right)^2+\varepsilon^2\left(\mathrm{f}_0+\dfrac{k_bT}{e}\dfrac{\partial f_0}{\partial\varepsilon}\right)\right]=S\\ \mathrm{f}_1=\dfrac{E}{N}\dfrac{1}{\sigma_m}\dfrac{\partial f_0}{\partial\varepsilon},\sigma_\varepsilon=\sum 2\dfrac{\mathrm{m}}{M}\sigma_k,S=\sum_{\mathrm{k}=i_n}C_k-\gamma\lambda\varepsilon^{\frac{1}{2}}f\end{cases} \tag{5}$$

In **Eq. 5**, N denotes the number density of neutral gas molecules, m^{-3}; T represents temperature, K; k_b represents Boltzmann constant; M represents particle mass; σ_ε is the effective cross

TABLE 1 | Applied electron collision reactions.

Number	Specific reaction	Reaction type
1	e + N_2 = > e + N_2	Elasticity
2–23	e + N_2 = > e + N_2	Excitation
24	e + N_2 = > e + N + N	Excitation
25	e + N_2 = > e + e + N_2 +	Ionization
26–27	e + O_2 = > O_2-	Attachment
28	e + O_2 = > e + O_2	Elasticity
29–42	e + O_2 = > e + O_2	Excitation
43	e + O_2 = > e + e + O_2 +	Ionization
44	e + H_2O = > H_2 + O	Attachment
45	e + H_2O = > OH + H-	Attachment
46	e + H_2O = > e + H_2O	Elasticity
47–50	e + H_2O = > e + H_2O	Excitation
51	e + H_2O = > e + e + H_2O+	Ionization

section of the total elastic collision; $k = i_n$ represents all inelastic collision reactions, S represents loss term for inelastic collisions.

The electron energy distribution function can be obtained by solving f_0 and f_1, which provides the basis data for the subsequent solution of various electron transport parameters.

2.2 Calculation of Electronic Collapse Parameters

The electron energy distribution function in charged air is determined by the Boltzmann equation. According to its EEDF, the reduced ionization coefficient (α/N), reduced attachment coefficient (η/N), and effective ionization coefficient[$(\alpha$-$\eta)/N$] in air can be calculated. The reduced ionization coefficient and reduced attachment coefficient (Morrow and Lowke, 1997) are obtained by **Eq. 6**.

$$\begin{cases} \dfrac{\alpha}{N} = \sqrt{\dfrac{2e}{m}}\dfrac{1}{V}\displaystyle\int_{\varepsilon_i}^{\infty} \varepsilon Q_i(\varepsilon) F_0(\varepsilon) d\varepsilon \\ \dfrac{\eta}{N} = \sqrt{\dfrac{2e}{m}}\dfrac{1}{V}\displaystyle\int_{\varepsilon_a}^{\infty} \varepsilon Q_a(\varepsilon) F_0(\varepsilon) d\varepsilon \end{cases} \tag{6}$$

where, F_0 represents the stable energy distribution function by applying Boltzmann binomial approximation method to f; V represents the electron drift velocity; Q_i and ε_i represent the effective cross section and critical energy of ionization reaction, respectively; Q_a and ε_a represent the effective cross section and critical energy of the adhesion reaction, respectively; and ε is the electron energy, J.

2.3 Applied Reactions and Cross-Sectional Data

In order to simplify the calculation, air components are considered as 80% nitrogen and 20% oxygen, and H_2O is considered to study the effect of humidity on air gap discharge processes. The applied electron collision reactions are shown in **Table 1**. Their cross-sectional data are from the LAXCAT database. The parameters set in this paper are as follows:

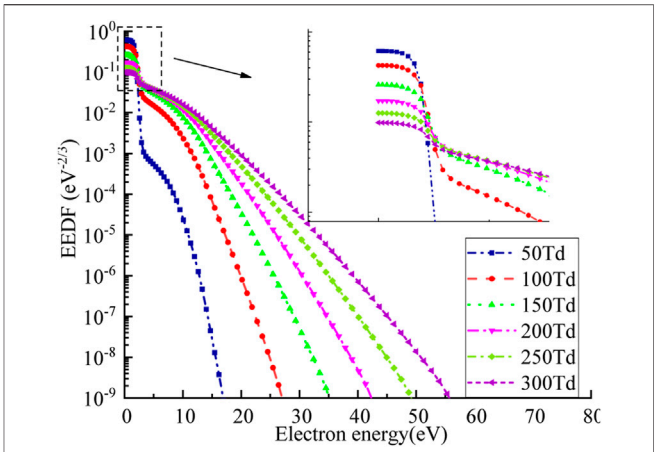

FIGURE 1 | Electron energy distribution function (EEDF) distribution of dry air.

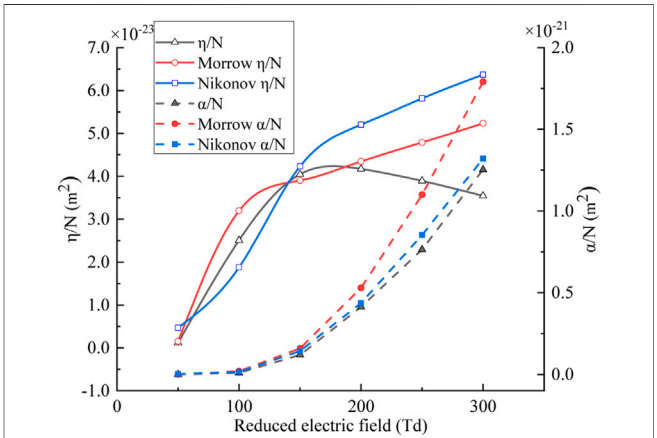

FIGURE 2 | The variation of ionization coefficient and attachment coefficient with reduced electric field.

standard atmospheric pressure, background temperature 300 K, and reduced electric field 50Td–300Td (1Td = 10^{-21} Vm^2).

3 ANALYSIS OF ELECTRON TRANSPORT PARAMETERS AND INSULATION PERFORMANCE OF AIR

3.1 Verification of Simulation Model in Dry Air

In this section, the dry air pressure is the standard atmospheric pressure, the relative humidity is 0%, and the air temperature is 300 K. The collision reactions include reactions 1–43 in **Table 1**.

3.1.1 Electron Energy Distribution Function Distribution

The calculated electron energy distribution is shown in **Figure 1**. The number of low-energy electrons is much higher than that of

high-energy electrons under the same electric field; the number of low-energy electrons decreases with reduced electric field while the number of high-energy electrons increases. When the electron energy is 0–3 eV, the average electron energy decreases with the reduced electric field; when the electron energy is greater than 3 eV, the average electron energy increases with the reduced electric field. The increase of electric field increases the electrons speed and their kinetic energy. Electrons are more likely to collide and ionize with molecules in the air.

3.1.2 Electron Transport Parameters Calculation

The reduced ionization coefficient and reduced adhesion coefficient calculated according to **Eq. 6** are shown in **Figure 2**. As shown in **Figure 2**, as the reduced electric field exceeds 100 Td, the reduced ionization coefficient increases exponentially with the reduced electric field, which has the same tendency with results by Morrow and Nikonov. The variation of ionization coefficient is mainly caused by the high electric field. The high electric field can greatly increase the number of high energy electrons in air that leads to the increasing number of collision ionization between electrons and molecules.

The reduced adhesion coefficient increases first and then decreases with the reduced electric field. As the reduced electric field is below 150 Td, the variation curve of attachment coefficient with reduced electric field calculated is between those obtained by Morrow and Nikonov. When the reduced electric field is below 200 Td, the adhesion coefficient increases with the reduced electric field. Hence, under the low reduced electric field, the energy of electrons is low, and the adhesion process is easy to occur. When the reduced electric field exceeds 200 Td, the adhesion coefficient decreases with the reduced electric field. The electrons are accelerated by obtaining more energy at such high electric field that make them difficult to be attached.

3.2 The Effect of Humidity on Electron Transport Parameters and Insulation Performance of Air

To study the effect of humidity on electron transport parameters and insulation performance of air, the relative humidity in the air is set as 0%, 30%, and 60%, respectively.

3.2.1 Effect of Humidity on Electron Transport Parameters

The reduced electron mobility (μ/N) and reduced electron diffusion coefficient (D/N) are important parameters during air discharges, which can be obtained from the electron energy distribution. **Figure 3** shows the variation of the approximate electron mobility and approximate electron diffusion coefficient with the approximate electric field under different relative humidity conditions calculated based on Boltzmann's equation.

As shown in **Figure 3**, μ/N decreases with the reduced electric field, and the reduction rate is faster with lower electric field. The increasing electric field can increase the kinetic energy of

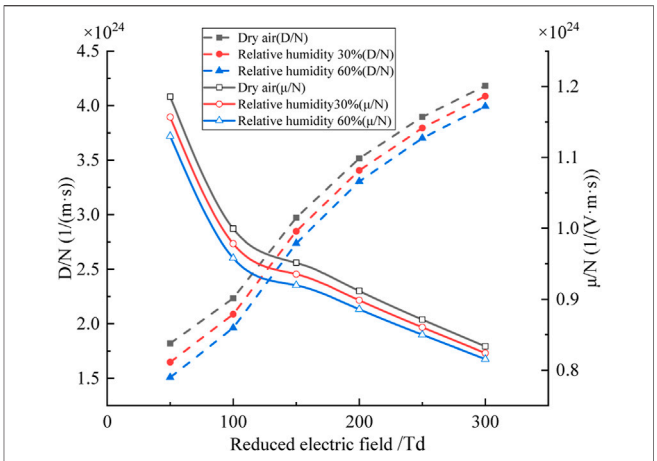

FIGURE 3 | The variation of electron transport parameters with reduced field strength under different humidity.

electrons, which accelerates the irregular movement of electrons and inhibits the directional migration of electrons. Thus, the reduced electron mobility decreases. Under the same reduced electric field, the reduced electron mobility decreases with the air humidity. For every 30% increase in relative humidity, the reduced electron mobility decreases by about 0.25×10^{23} [1/(V·m·s)] indicating that the presence of water molecules hinders the electron mobility. The influence of humidity on D/N is similar, the electron diffusion coefficient increases with the reduced electric field. Under the same reduced electric field, the reduced electron diffusion coefficient decreases with the air relative humidity. For every 30% increase in air humidity, the reduced electron diffusion coefficient decreases by about 0.2×10^{24} [1/(m.s)] showing that water molecules can weaken the diffusion of electrons.

3.2.2 Effect of Humidity on Effective Ionization Coefficient and Insulation Performance of Air

In the Thomson discharge theory, the ionization coefficient or the attachment coefficient is defined as the average number of ionizations or attachments per unit length of electrons moving along the electric field. It is used to characterize the collision ionization and electron adsorption ability of particles and electrons (Prasad, 1959; Chen, 2016). During air discharges, the Thomson ionization coefficient is mainly affected by the collision ionization between electrons and nitrogen molecules, and oxygen molecules and water molecules. The Thomson attachment coefficient is affected by the adhesion between electrons and molecules. Since the adsorption coefficient of N_2 approximately is equal to 0, the adsorption reaction here mainly considers the adsorption of electrons and O_2 molecules (Xingliang et al., 2009; Xiaobo et al., 2010).

Considering the effect of water molecules, the calculation of ionization coefficient and adhesion coefficient should be modified accordingly. The reduced ionization coefficient and adhesion coefficient in wet air can be calculated by **Eq. 7**.

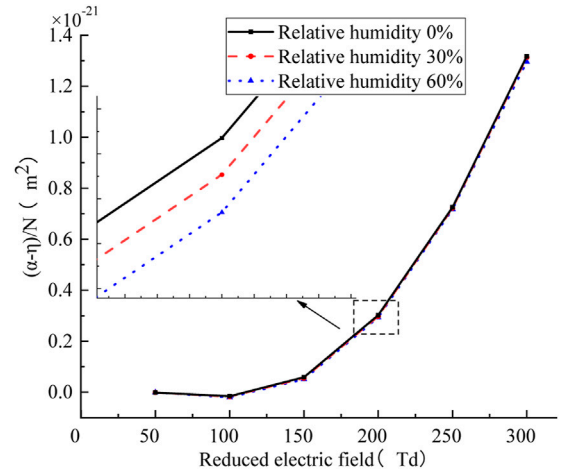

FIGURE 4 | Variation of effective ionization coefficient with reduced electric field under different humidity.

$$\begin{cases} \alpha = HP_w\left(0.001\left(\frac{E}{P}\right)^2 - 0.06\left(\frac{E}{P}\right) + 1.0\right) + P_d\left(4.7786e^{-211P/E}\right) \\ \eta = H\frac{P_w}{P}\eta_s + P_d\left(0.01298 - 0.54\times10^{-3}\left(\frac{E}{P}\right) + 0.87\times10^{-5}\left(\frac{E}{P}\right)^2\right) \end{cases} \tag{7}$$

Here, H represents the relative humidity in the air. P_d is dry air partial pressure, P_w is saturated vapor partial pressure, and unit is Torr. η_s is the adhesion coefficient of water vapor, in m^2. When $E/p \leq 37.6$ V/(cm.Torr), $\eta_s/p = 3.67 \times 10^{-5}$ $(E/P)^2 + 0.026$ $(E/P) - 0.273$. When $E/p \geq 37.6$ V/(cm.Torr), $\eta_s/p = -2.5 \times 10^{-5}$ $(E/P)^2 - 2.5 \times 10^{-4}$ $(E/P) + 0.23$. E is the electric field intensity, and the unit is V/cm.

According to the above formulas, the reduced ionization coefficient and the reduced attachment coefficient are mainly affected by the electric field, and the relative humidity has little effect on them. The density of water molecules in the air increases accordingly with the relative humidity. Collision ionization between electrons and water molecules in the air increases with humidity, resulting in an increasing reduced ionization coefficient. However, for the low electric field and low electron energy, the effect of humidity on ionization is not obvious. The water molecules adsorb electrons to form negative ions, which plays a leading role in the total collision process. The increase in relative humidity increases the density of water molecules in the air, and the adhesion will be more obvious. Therefore, the adhesion coefficient increases with the humidity.

Due to the adsorption effect of air, the ionization coefficient will be weakened in collision ionization process. The effective ionization coefficient is applied for the difference between the reduced ionization coefficient and the reduced attachment coefficient. **Figure 4** shows the effective ionization coefficient variation under different air relative humidity conditions. The effective ionization coefficient first decreases and then increases with the reduced electric field. The effective ionization coefficient decreases slightly with the relative humidity. Under the same reduced electric field, the effective ionization coefficient decreases about 4×10^{-24} m^2 for each 30% increase of air relative humidity.

TABLE 2 | Critical breakdown electric field under different humidity.

Relative humidity (%)	Critical breakdown electric field (V/cm)
0	29,889
30	30,375
60	31,104

As shown in **Table 2**, the critical breakdown electric field increases with the air relative humidity. This is caused by the increasing electron attachment velocity and the decreasing collision ionization velocity. More water molecules capturing free electrons in the air become negative ions, inhibiting the occurrence of collision ionization. Therefore, the increasing relative humidity of the air will increase the critical breakdown electric field and improve the air insulation performance.

4 CONCLUSION

According to the collision cross-section data of different electron collision reactions, the reduced ionization coefficient, reduced attachment coefficient, and effective ionization coefficient under different humidity are studied with Boltzmann equation. Conclusions are as follows:

1) The electron energy distribution is mainly affected by the reduced electric field. With the increasing reduced electric field, the proportion of low-energy electrons decreases, and the proportion of high-energy electrons increases, while the reduced ionization coefficient increases, and the reduced adhesion coefficient increases first and then decreases.
2) When the reduced electric field remains unchanged, the electron transport parameters are affected by the relative humidity of the air. As the air relative humidity is increased from 0% to 60%, the reduced electron mobility decreases by about 0.5×10^{23} [1/(V·m·s)], the reduced electron diffusion coefficient decreases by about 0.4×10^{24} [1/(m·s)], and the effective ionization coefficient decreases by about 8×10^{-24} m^2.
3) With the increasing relative humidity, the number of low-energy electrons increases and the number of high-energy electrons decreases, resulting in the increasing critical breakdown electric field of the air gap. The simulation results show that when the temperature is 300 K, the pressure is 1.0 atm, the relative humidity increases from 0% to 60%, and the critical breakdown electric field increases by 4%.

DATA AVAILABILITY STATEMENT

The raw data supporting the conclusion of this article will be made available by the authors, without undue reservation.

AUTHOR CONTRIBUTIONS

YA contributed to the conceptualization, preparation, writing, and preparation of the original draft and handled the software. MH was in charge of the software. SM ensured project administration. YH handled the funding acquisition and validation. TH and MY supervised the study. BH was involved in the revision of the manuscript. KY validated the study. YL handled the figures.

FUNDING

This manuscript was supported, in part, by the Natural Science Foundation of China under Grant 51807113 and, in part, by the Natural Science Foundation of Shandong Province under Grant ZR202103040796, the Natural Science Foundation of Jiangsu Province under Grant BK20200111, the Key Laboratory of Special Machine and High Voltage Apparatus (Shenyang University of Technology), and the Ministry of Education under Grant KFKT202111.

REFERENCES

Abdel-Salam, M. (1985). Positive Wire-To-Plane Coronas as Influenced by Atmospheric Humidity. *IEEE Trans. Ind. Applicat.* IA-21 (1), 35–40. doi:10.1109/tia.1985.349640

Chen, X. (2016). *Study on Micro-physical Characteristics and Propagation Law of corona Discharge Pulse in corona Cage*. Hubei: Wuhan University.

Kelin, L. I. (2019). *Study on the Influence of Humidity and Air Pressure on the Mode Conversion of DC corona Discharge*. Hunan: Hunan University.

Liu, Y., Jihong, L., and Bin, L. (1990). Influence of Air Density and Humidity on corona Characteristics of Conductor. *Power Syst. Tech.* 45 (4), 46–50.

Morrow, R., and Lowke, J. J. (1997). Streamer Propagation in Air. *J. Phys. D: Appl. Phys.* 30 (4), 614–627. doi:10.1088/0022-3727/30/4/017

Muniappan, M. (2021). A Comprehensive Review of DC Fault protection Methods in HVDC Transmission Systems. *Prot. Control. Mod. Power Syst.* 6 (1), 1–20. doi:10.1186/s41601-020-00173-9

Nikonov, V., Bartnikas, R., and Wertheimer, M. R. (2001). Surface Charge and Photoionization Effects in Short Air Gaps Undergoing Discharges at Atmospheric Pressure. *J. Phys. D: Appl. Phys.* 34 (19), 2979–2986. doi:10.1088/0022-3727/34/19/308

Prasad, A. N., and Craggs, J. D. (1960). Measurement of Ionization and Attachment Coefficients in Humid Air in Uniform fields and the Mechanism of Breakdown. *Proc. Phys. Soc.* 76 (2), 223–232. doi:10.1088/0370-1328/76/2/306

Prasad, A. N. (1959). Measurement of Ionization and Attachment Coefficients in Dry Air in Uniform Fields and the Mechanism of Breakdown. *Proc. Phys. Soc.* 74 (1), 33–41. doi:10.1088/0370-1328/74/1/306

Roostaee, S., Thomas, M. S., and Mehfuz, S. (2017). Experimental Studies on Impedance Based Fault Location for Long Transmission Lines. *Prot. Control. Mod. Power Syst.* 2 (1), 16. doi:10.1186/s41601-017-0048-y

Su, Z., Yunkun, D., Ruishuang, Z., and Dengming, X. (2019). The Synergistic Effect Analysis of CF_3I Mixed Gas Based on Boltzmann Equation. *Trans. China Electrotechnical Soc.* 34 (7), 1554–1557. doi:10.19595/j.cnki.1000-6753.tces.180373

Weichen, Y., Yunzhu, A., Yuanchao, H., Jiang, Z., Gao, X., and Zhou, L. (2021). Research on cylinder Flexible Graphite Earth Electrode (FGEE) Used to Reduce tower Earth Resistance. *Electric Power Syst. Res.* 196 (3), 107268. doi:10.1016/j.epsr.2021.107268

Wen, X., Yuan, X., Lan, L., Long, M., and Hao, L. (2016). Study on the Effective Ionization Rate of Atmospheric Corona Dicharge Plasmas by Considering Humidity. *IEEE Trans. Plasma Sci.*, 3386–3891. doi:10.1109/tps.2016.2623805

Wenliang, Z., Yongqing, Y., Guangfan, L., and Fan, J. B. (2007). Research on UHVDC Technology. *Proc. CSEE* 27 (22), 1–7. doi:10.3321/j.issn:0258-8013.2007.22.001

Xiaobo, M., Xingming, B., Zhao, X., and Cao, J. (2010). Influence of Environmental Factors on corona Inception Voltage of DC Overhead Conductors. *High Voltage Eng.* 36 (8), 1916–1922. doi:10.1016/j.puhe.2013.08.003

Xingliang, J., Rui, L., Qin, H., Zhijin, Z., and Jianlin, H. (2009). DC Positive Corona Inception Performances of Stranded Conductors and its Affecting Factors. *Proc. CSEE* 29 (34), 108–114.

Xingming, B., Jianfeng, H., Huang, H., and Wang, L.-M. (2010). Study on the Influence of Air Pressure and Humidity on the Characteristics of Negative DC corona. *Proc. CSEE* 30 (4), 118–123. doi:10.1021/j100398a017

Xinjing, C., Kaiqi, W., Xinxin, W., Xiaobing, Z., and Zhiwei, L. (2015). Flow Discharge Characteristics of Air under Different Humidity. *High Voltage Eng.* 41 (2), 633–638. doi:10.13336/j.1003-6520.hve.2015.02.041.org6

Xinyu, D., Xiaoyue, C., Wei, L., Guozhou, X., Lei, L., Xishan, W., et al. (2018). Study on Air Insulation Performance at Different Altitude Based on Boltzmann Equation. *Water Resour. Power* 36 (12), 167–170.

Xun, S., Ouyang, T., Khajorntraidet, C., Li, Y., Li, S., Zhuang, J., et al. (2021). Mixture Density Networks-Based Knock Simulator. *IEEE/ASME Trans. Mechatronics* (99), 1. doi:10.1109/TMECH.2021.3059775

Xun, S., Ouyang, T., Nan, Y., and Zhuang, J. (2021). Sample-based Neural Approximation Approach for Probabilistic Constrained Programs. *IEEE Trans. Neural Networks Learn. Syst.*, 1–8. doi:10.1109/TNNLS.2021.3102323

Xun, S., and Pongsathorn, R. (2021). Pedestrian-aware Statistical Risk Assessment. *IEEE Trans. Intell. Transportation Syst.*, 1–9. doi:10.1109/TITS.2021.3074522

Xun, S., and Raksincharoensak, P. (2021). Statistical Models of Near-Accident Event and Pedestrian Behavior at Non-signalized Intersections. *J. Appl. Stat.*, 1–21. doi:10.1080/02664763.2021.1962263

Xun, S., Zhang, X., Ouyang, T., Li, Y., and Raksincharoensak, P. (2020). Cooperative Comfortable-Driving at Signalized Intersections for Connected and Automated Vehicles. *IEEE Robotics Automation Lett.* 5 (4), 6247–6254. doi:10.1109/lra.2020.3014010

Xun, S., Zhang, Y., Kota, S., and Shen, T. (2020). Gaussian Mixture Model Clustering-Based Knock Threshold Learning in Automotive Engines. *IEEE/ASME Trans. Mechatronics* 25 (99), 2981–2991. doi:10.1109/TMECH.2020.3000732

Xun, S., Zhang, Y., Tielong, S., and Khajorntraidet, C. (2017). Spark advance Self-Optimization with Knock Probability Threshold for Lean-Burn Operation Mode of SI Engine. *Energy* 122 (MAR.1), 1–10. doi:10.1016/j.energy.2017.01.065

Yang, N., Yang, C., Wu, L., Shen, X., Jia, J., Li, Z., et al. (2021). Intelligent Data-Driven Decision-Making Method for Dynamic Multi-Sequence: An E-Seq2Seq Based SCUC Expert System. *IEEE Trans. Ind. Inform.*, 1. doi:10.1109/tii.2021.3107406

Yang, N., Yang, C., Xing, C., Yi, D., Jia, J., Chen, D., et al. (2021). Deep Learning-Based SCUC Decision-Making: An Intelligent Data-Driven Approach with Self-Learning Capabilities. *IET Generation, Transmation&Distribution*, 1–12. doi:10.1049/gtd2.12315

Yuanchao, H., Yitong, L., Yunzhu, A., Wen, X., Li, H., Su, M., et al. (2021). Laboratory Study on Negative Spark Inception Direction and Breakdown Characteristics in Rod–Rod Air Gaps. *Electric Power Syst. Res.* 201, 107498. doi:10.1016/j.epsr.2021.107498

Yuke, F. (2017). *Experimental Study on Influence of Air Pressure and Humidity on corona Characteristics of High Voltage Electrode under Compound Voltage*. Beijing: North China Electric Power University.

Zhao, M., Xiaoxin, Z., Yuwei, S., and Limei, Z. (2015). Form and Development Trend of Future Distribution System. *Proc. CSEE* 35 (6), 1289–1298. doi:10.13140/RG.2.1.3664.4004

Zhenya, L. (2005). *Special Album of Research Results of UHVDC Transmission Technology*. Beijing: China electric power Press.

Zhenya, L. (2005). *UHV Power Grid*. Beijing: China economic publishing house.

Conflict of Interest: TH was employed by the State Grid Jiangsu Power Engineering Consulting Limited Company.

The remaining authors declare that the research was conducted in the absence of any commercial or financial relationships that could be construed as a potential conflict of interest.

Publisher's Note: All claims expressed in this article are solely those of the authors and do not necessarily represent those of their affiliated organizations, or those of the publisher, the editors, and the reviewers. Any product that may be evaluated in this article, or claim that may be made by its manufacturer, is not guaranteed or endorsed by the publisher.

frontiers in Energy Research

ORIGINAL RESEARCH
published: 07 January 2022
doi: 10.3389/fenrg.2021.819021

Research on Conducted Disturbance to Secondary Cable Caused by Disconnector Switching Operation

Xiaoyue Chen[1], Zeyu He[2], Yanze Zhang[1], Junjie Si[1], Shuang Wang[1], Baoquan Wan[3] and Jianben Liu[3]*

[1]School of Electrical Engineering and Automation, Wuhan University, Wuhan, China, [2]State Grid Shaoxing Power Supply Company, Shaoxing, China, [3]State Key Laboratory of Power Grid Environmental Protection, Wuhan, China

The disconnector switching operation in GIS not only generates very fast transient overvoltage (VFTO) in primary equipment, but also couples to the secondary system, which affects normal operation of the secondary equipment. In this study, aiming at the conducted disturbance caused by the disconnector switching operation of the 1,000-kV UHV GIS test circuit on the secondary cable, a broadband equivalent circuit model of the potential transformer and the grounding grid is proposed based on the vector fitting method and the impedance synthesis method, and the accuracy of the model is tested. On the basis of this model, the conducted disturbance voltage of the secondary cable core is obtained by combining the measured typical disturbance source waveform. The research results of the influencing factors of conducted disturbance show that the amplitude of the disturbance voltage generated by the capacitive conduction is higher than that generated by the resistive conduction, but the main frequency of the resistive conducted disturbance voltage is higher. The amplitude of the conducted disturbance voltage will decrease with the increase of the length of the cable and the length of the grounding wire. The single-ended grounding of the secondary cable shield at the GIS side will cause serious disturbance voltage. The research results of this study will be beneficial to the protection of secondary cable electromagnetic disturbance in the intelligent substation and have reference significance for the implementation of secondary equipment protection measures in the intelligent substation.

Keywords: disconnector switching operation, broadband equivalent circuit model, finite integral method, overall electromagnetic disturbance, suppression measures

OPEN ACCESS

Edited by:
Xun Shen,
Tokyo Institute of Technology, Japan

Reviewed by:
Wangling He,
North China Electric Power University, China
Peng Li,
China Three Gorges University, China

****Correspondence:***
Xiaoyue Chen
chenxiaoyue@whu.edu.cn

Specialty section:
This article was submitted to Smart Grids, a section of the journal Frontiers in Energy Research

Received: *20 November 2021*
Accepted: *01 December 2021*
Published: *07 January 2022*

Citation:
Chen X, He Z, Zhang Y, Si J, Wang S, Wan B and Liu J (2022) Research on Conducted Disturbance to Secondary Cable Caused by Disconnector Switching Operation. Front. Energy Res. 9:819021. doi: 10.3389/fenrg.2021.819021

INTRODUCTION

Gas insulated switchgear (GIS) is widely used in substations due to its high reliability and small footprint. However, very fast transient overvoltage (VFTO) and transient enclosure voltage (TEV) appear when switching in GIS. Simulation and experiment show that the rise time of VFTO is only nanosecond grade, the frequency range mainly includes several to dozens of MHz, up to 100 MHz, and the amplitude range is generally between 1.5 p.u. and 2.8 p.u. The peak value of TEV can reach tens of kV, and it has higher frequency components than VFTO. In the development of a smart grid, there are new requirements for power system protection and control (Bo et al., 2016; Zhang et al., 2016). At present, intelligent equipment is widely used in the power system, especially in relay protection (Nan et al., 2018; Yang et al., 2021). The intelligent equipment on the secondary side is

vulnerable to electromagnetic disturbance, and the cable is the key to the transmission of electromagnetic disturbance to the intelligent equipment.

High-frequency and high-amplitude VFTO and TEV not only pose a threat to the insulation of GIS and winding equipment such as transformers and reactors connected to it, but also interfere with the normal operation of secondary equipment in a substation (D'Souza et al., 2020; Moreira et al., 2020). The VFTO and TEV transmitted in the primary equipment will be coupled to the secondary circuit through conduction and radiation. The disturbance voltage is generated on the secondary cable core, which will interfere with the sensitive secondary equipment of the cable terminal and may cause its misoperation. However, since the conducted disturbance in a substation is far more significant than the radiated disturbance, the radiated disturbance can be ignored when calculating the disturbance voltage of the secondary cable (Mahmood et al., 2015).

Some scholars have carried out corresponding research on the problem of electromagnetic disturbance source disturbing secondary equipment when operating a disconnector. The research methods mainly include field test, laboratory test, and numerical calculation (Cai et al., 2018). At the beginning of the 21st century, China has built a large number of GIS substations. In order to explain the mechanism and influencing factors of electromagnetic disturbance caused by disconnector switching operation, the China Electric Power Research Institute has combined several universities to build two disconnector test platforms with different operating speeds at the UHV AC test base of State Grid Corporation in Wuhan. The electromagnetic disturbance caused by the disconnector switching operation in GIS was systematically studied, and a large number of experimental measurement data were obtained (Chen et al., 2011; Zhang et al., 2013; Zhang et al., 2014; Hu et al., 2015; Ma et al., 2017).

Due to the complexity of field measurement and laboratory test method, the numerical calculation method has been widely used. In 1988, CIGRE Working Group 33/13.09 proposed in detail the equivalent circuit models of the main components of GIS equipment such as GIS bus, disconnector, circuit breaker, insulator, and bushing, but these models are only applicable to the calculation of internal transient field at low frequency, without considering the high-frequency response of components (CIGRE Working Group 33/13.09, 1988). Jiao et al. (2016) decomposed the specific structure of bushing into multiple parts, extracted and combined the parameters of different parts, and established the broadband equivalent circuit model of high voltage bushing. The model was in good agreement with the full-wave simulation results. Feng et al. (2014) modeled the specific structure of each component by HFSS (High Frequency Structure Simulator), obtained the parasitic parameters, and constructed the calculation model of conducted disturbance in the GIS substation. The simulation results are consistent with the experimental data. Hu (2016) uses the "black box method" to establish the high-frequency transmission function model of each component and establishes the broadband equivalent circuit model of grounding grid and grounding pillar by vector fitting method and impedance synthesis method, and embeds the data into EMTP to realize the calculation. In Wang and Yang (2016), the high-order Radau method is proposed to simulate the electromagnetic transient (EMT) of the power system. The corresponding high-dimensional linear algebraic equations are decoupled into blocks in time domain, and a multi-stage block recursive method is formed. This method avoids the numerical oscillation in calculation and has achieved good results in VFTO calculation of the 550-kV GIS system.

In summary, a large number of simulation studies have been carried out on the electromagnetic disturbance of the secondary cable caused by disconnector switching operation. However, most of the simulation uses a single numerical lumped parameter to model the components, which cannot reflect the broadband response characteristics of the components. In view of the above problems, this study deeply studies the establishment method of the broadband equivalent circuit model of each component in the simulation analysis of electromagnetic disturbance. The level and influencing factors of conducted disturbance voltage produced by the disconnector switching operation of the secondary cable are analyzed by simulation analysis, and the electromagnetic disturbance suppression measures of secondary cable are proposed. The research results of this study will be beneficial to the reasonable arrangement of secondary cables in the intelligent substation and have reference significance for the implementation of secondary equipment protection measures in the intelligent substation.

COUPLING MECHANISM OF CONDUCTED DISTURBANCE

In terms of the disturbance path, the electromagnetic disturbance caused by GIS disconnector switching operation to the secondary cable is mainly divided into conducted disturbance and radiated disturbance. However, usually the conducted disturbance in a substation far exceeds the radiated disturbance, so the radiated disturbance is often ignored when calculating the disturbance voltage of the secondary cable. The secondary equipment in a substation has low sensitivity to power frequency disturbance, but it has high sensitivity to high-frequency disturbance component, so it is prone to failure or damage under the high-frequency electromagnetic disturbance generated by disconnector switching operation.

Conducted disturbance refers to that in two circuits with electrical connection; the electrical signal (disturbance voltage or current) of one circuit is transmitted to another circuit through the common circuit, which is mainly divided into capacitive conduction and resistive conduction.

Capacitive conduction refers to the electromagnetic transient process in which the VFTO generated by the disconnector switching operation in the GIS bus is directly coupled to the core of secondary cable through stray capacitance between primary winding and secondary winding of a potential transformer. Due to the different response characteristics of the transformer port in case of high frequency, the modeling

method using a single numerical lumped element to describe the transformer will inevitably cause errors, so it is necessary to establish the broadband equivalent circuit model of the transformer.

Resistive conduction means that TEV generated by disconnector switching operation propagates along the enclosure in the form of a voltage wave. When it propagates to the grounding point of GIS enclosure, part of the voltage wave will couple to the grounding wire, and flow into the grounding grid along the grounding wire, causing the grounding grid potential to rise. Generally, the shield layer of the secondary cable is grounded at both ends. Therefore, under the effect of TEV, the potential of the shield layer of the secondary cable increases and the shielding effect decreases, and the voltage will be generated between the two grounding points, which will generate transient current on the shield layer of the secondary cable, and then couple to the core wire to generate disturbance voltage.

To sum up, capacitive conduction and resistive conduction are closely related to the potential transformer and grounding grid. The simple lumped element modeling cannot reflect its response characteristics in high frequency, and it will cause considerable errors under the excitation of VFTO and TEV disturbance sources with complex frequency components. Therefore, in order to ensure the accuracy of calculation, the broadband equivalent circuit model of the potential transformer and grounding grid should be established in the simulation of conducted disturbance caused by disconnector switching operation.

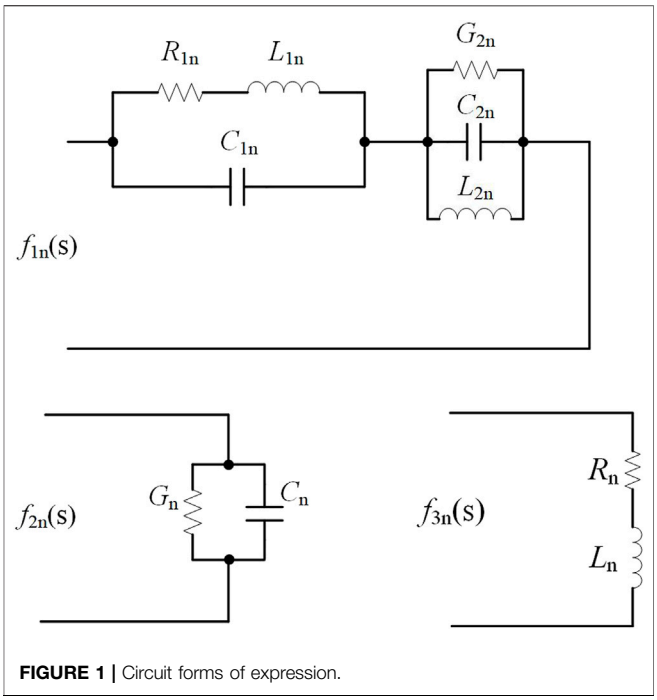

FIGURE 1 | Circuit forms of expression.

ESTABLISHMENT OF BROADBAND EQUIVALENT CIRCUIT MODEL

The Method of Modeling

The establishment of an equivalent circuit model can be generally divided into two methods: traditional equivalent circuit model and black box model. The traditional equivalent circuit model uses analytical formulas or simulation software to solve complex electromagnetic field problems based on physical factors such as the concrete structure and material of components. Every equivalent circuit element obtained by this method has actual physical meaning. The model meaning is intuitive, but it is necessary to know the detailed physical structure of each component, and the modeling and solving are more complex.

The black box model does not focus on the specific structure of the component to be tested, but obtains the frequency response of the component through actual measurement or simulation, and then determines the circuit expression of the element according to the numerical fitting method. The disadvantage of this method is that each component in the circuit model has no specific significance, but it avoids the complex electromagnetic field problem when using the traditional equivalent circuit model, and does not need to know the specific structure of each component.

In this study, the black box model is used to establish the broadband equivalent circuit model of the potential transformer and grounding grid. The specific method is used to obtain the broadband response characteristics of the potential transformer and grounding grid. Then, the stable and effective vector fitting method is used to fit the broadband response characteristics and the rational function expressions of the broadband response characteristics of the potential transformer and grounding grid are obtained. Finally, based on the analysis of the relationship between the time domain model and the complex frequency domain function, the broadband equivalent circuit model of the transformer and grounding grid is obtained.

Method of Establishing Broadband Equivalent Circuit

Based on the broadband response characteristics of the component, it can be assumed that its rational function expression is of the form of **Eq. 1** (Gustavsen and Semlyen, 1998; Deschrijver et al., 2008):

$$f(S) = \sum_{n-1}^{N} \frac{c_n}{s - a_n} + d + sh \tag{1}$$

Where n is the order of the pole, and a_n, c_n, d, and h are the unknowns in the expression, which are the poles, residue, constant term, and coefficient of first order term, respectively. These unknowns can be fitted by vector fitting method.

It is assumed that there are K pairs of conjugate complex poles after rational fitting of broadband response by vector fitting method, and the nth pair of conjugate complex poles is expressed as:

$$\begin{aligned} a_{2n-1} &= -p_{rn} + jp_{in} \\ a_{2n} &= -p_{rn} - jp_{in} \end{aligned} \tag{2}$$

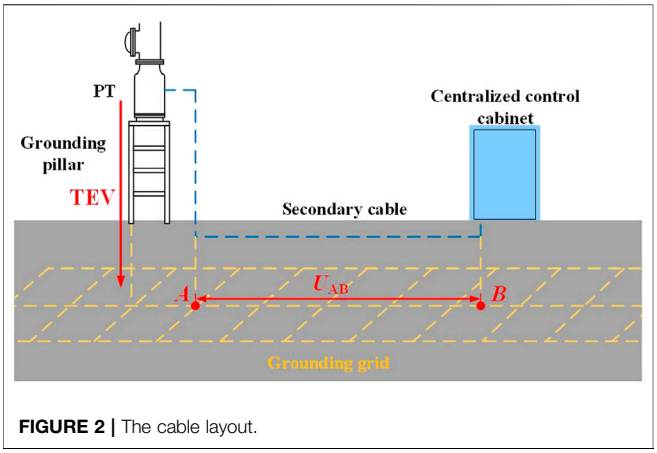

FIGURE 2 | The cable layout.

Where n = 1,2,. . .,k, and p_{rn} is the real part of the conjugate complex poles, and p_{rn} >0. It is assumed that the residue corresponding to the pair of complex poles:

$$\begin{aligned} c_{2n-1} &= -c_{rn} + jc_{in} \\ c_{2n} &= -c_{rn} - jc_{in} \end{aligned} \tag{3}$$

Combining **Eq. 2** and **Eq. 3**, **Eq. 1** can be divided into the following three parts:

$$\begin{aligned} f_{1n} &= \frac{2c_{rn}s + 2c_{rn}p_{rn} - 2p_{in}c_{in}}{s^2 + 2p_{rn}s + p_{rn}^2 + p_{in}^2} \\ f_{2n}(s) &= \frac{c_n}{s - a_n} \\ f_3(s) &= d + sh \end{aligned} \tag{4}$$

If f(s) is the expression of impedance, the above three parts can be represented by the circuit form in **Figure 1**.

The elements in the circuit are obtained according to the following formula:

$$\begin{aligned} R_{1n} &\frac{2(c_{rn}p_{rn} - c_{in}p_{in})}{p_{rn}^2 + p_{in}^2}, G_{2n} = \frac{2p_{rn}^2}{c_{rn}p_{rn} + p_{in}c_{in}} \\ L_{1n} &= \frac{c_{rn}p_{rn} - p_{in}c_{in}}{(p_{rn}^2 + p_{in}^2)p_{rn}}, L_{2n} = \frac{c_{rn}p_{rn} + p_{in}c_{in}}{(p_{rn}^2 + p_{in}^2)p_{rn}} \\ C_{1n} &= \frac{p_{rn}}{c_{rn}p_{rn} - p_{in}c_{in}}, C_{2n} = \frac{p_{rn}}{c_{rn}p_{rn} + p_{in}c_{in}} \end{aligned} \tag{5}$$

The final broadband equivalent circuit model can be established by connecting the above three parts in series.

If f(s) is the expression of admittance, the corresponding broadband equivalent circuit can be established by parallel connection in the same way.

Broadband Equivalent Circuit of Grounding Grid

This study takes the grounding grid of GIS test circuit at the UHV AC test base in Wuhan as the research object. The cable layout is shown in **Figure 2**, and the actual geometry of the ground grid is shown in **Figure 3**. The size of each grid is 0.8 m × 0.8 m, and the size of the small grid is 0.4 m × 0.4 m. It is assumed that the two conductors of the vertical grounding grid are the two grounding wires of the secondary cable shield layer. The grounding grid is set up with steel material, and the relative resistivity ρ_r is 10, relative permeability μ_r is 626 (relative to copper), the buried depth of ground grid is 0.8 m, and the conductor radius is 8 mm. Soil modeling is divided into two layers: the top soil resistivity is 28.43 Ω m and the thickness is 39.94 m; the bottom soil resistivity is 240,302 Ω m and the thickness is infinite.

By injecting current of different frequencies into the grounding point and measuring the response of each grounding point, the T-shaped two port equivalent circuit of the whole grounding grid can be established, as shown in **Figure 4A**.

Through the comparison of fitting effects of different pole orders, Z_A, Z, and Z_B are fitted with 4, 6, and 4 poles, respectively, and the fitting results are shown in **Figure 5**.

It can be seen from **Figure 5** that the error of the amplitude-frequency and phase-frequency errors of the results fitted by vector fitting method is less than 5%, which can meet the needs of calculation accuracy. The results of vector fitting are implemented in the circuit in **Figure 1**, and the overall broadband equivalent circuit model of the grounding grid can be established. The circuit model of the grounding grid is shown in **Figure 4B**.

Broadband Equivalent Circuit of a Potential Transformer

In this study, the simulation model of a potential transformer is established by using the measured S parameter matrix of broadband response of the potential transformer in Wang (2010). The measured S parameter matrix is converted into an admittance matrix, and the two-port equivalent π-shaped network of the potential transformer is shown in **Figure 4C**.

The broadband characteristics of each admittance in the circuit can be rationally fitted by the same method. According to the rational function, the broadband equivalent circuit model of the potential transformer can be established by the same method, as shown in **Figure 4D**.

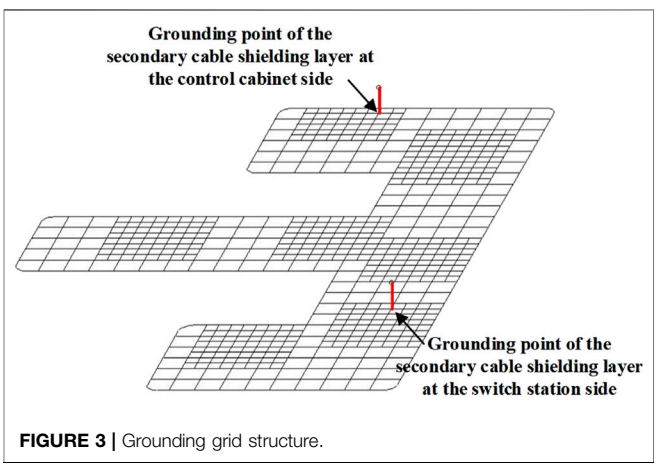

FIGURE 3 | Grounding grid structure.

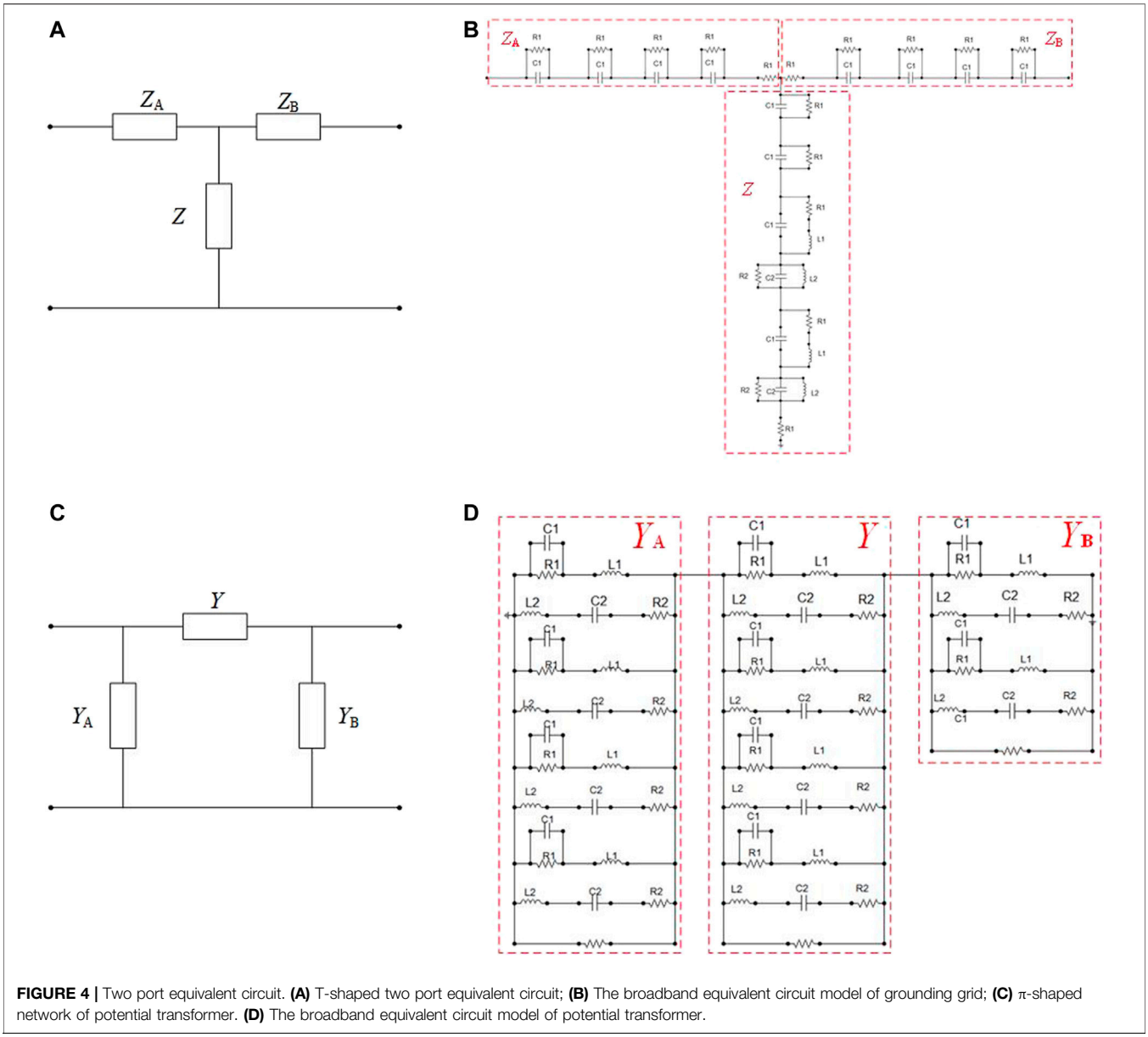

FIGURE 4 | Two port equivalent circuit. **(A)** T-shaped two port equivalent circuit; **(B)** The broadband equivalent circuit model of grounding grid; **(C)** π-shaped network of potential transformer. **(D)** The broadband equivalent circuit model of potential transformer.

SIMULATION OF CONDUCTED DISTURBANCE CAUSED BY DISCONNECTOR SWITCHING OPERATION

Research Objects

In this study, the GIS test circuit of the UHV AC test base (hereinafter referred to as the test circuit) shown in **Figure 6** is taken as the research object. The thickened real line represents the GIS bus, and the virtual line represents the secondary cable. DS and ES represent the disconnector and grounding switch in GIS, respectively.

The research team led by the China Electric Power Research Institute has conducted thousands of closing and opening tests of disconnectors in the test circuit, and obtained a large number of VFTO, TEV, and space electromagnetic field test data. Therefore, this study considers using the measured data of the test as the excitation to join the simulation model to calculate the disturbance voltage. The typical measurement waveforms of VFTO, TEV, and spatial electromagnetic field provided by the above research team in Chen et al. (2011) and Hu et al. (2015) are selected as the excitation sources of this study, and the waveform of the disturbance source is shown in **Figure 7**.

Simulation of Conducted Disturbance

KVVP2-22 quad cable is selected as the research object. In the modeling process, the J.Marti model suitable for the frequency conversion problem is used, and the corresponding simulation model is established combined with the geometric structure of the secondary cable.

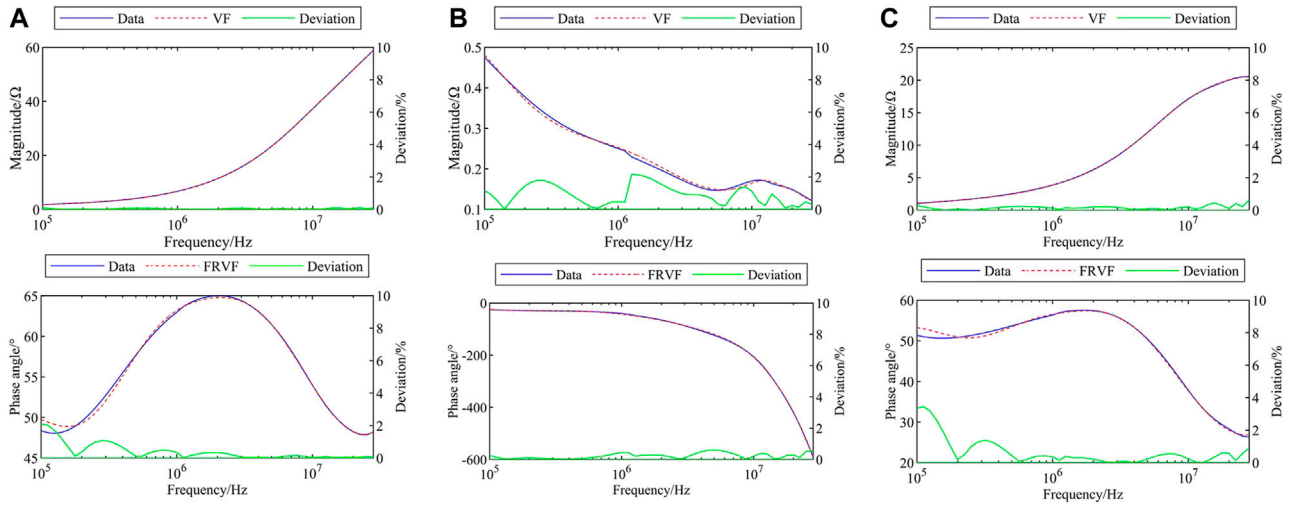

FIGURE 5 | Fitting results of grounding grid model. **(A)** Fitting results of Z_A. **(B)** Fitting results of Z. **(C)** Fitting results of Z_B.

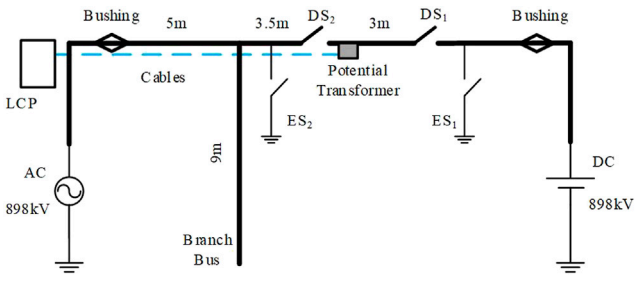

FIGURE 6 | UHV GIS test circuit.

The simulation model of conducted disturbance can be built in EMTP/ATP electromagnetic transient simulation software, as shown in **Figure 8**. Because the secondary cable shield layer is connected with the GIS enclosure in the GIS test circuit, the disturbance source TEV is directly loaded on the grounding point at the side of the GIS test circuit in the resistive conducted disturbance. In **Figure 8**, Z_{L1} and Z_{L2} represent the impedance of the grounding wire of the secondary cable shield layer. The terminal impedance R of core wire is 50 Ω.

The cable length is set to 20 m, the shield layer is grounded at both ends, the simulation step length is set to 0.5 ns, and the total calculation time is 0.6 μs. In 0.6 μs, the maximum amplitude of the disturbance source has passed, and the waveform has begun to decay, so it can meet the most serious conducted disturbance level in the whole disturbance process. By measuring the potential difference between the two ends of the load, the conducted disturbance voltage level under the action of typical disturbance sources can be obtained. The disturbance voltage level of the secondary cable core under the excitation of typical disturbance source is shown in **Figure 9**.

The calculation results show that under the excitation of typical disturbance source, the overall conducted disturbance voltage amplitude of the test circuit is about 2.5 kV, in which the capacitive conducted disturbance amplitude is about 1.5 kV, and the resistive conducted disturbance voltage amplitude is about 1.0 kV. From the perspective of frequency characteristics, the main frequency of the overall disturbance voltage is 6.7 MHz and below 5 MHz, and the main frequency of resistive conducted disturbance is higher than that of capacitive conducted disturbance. It can be seen that the capacitive transmission accounts for the main component in the conducted disturbance, accounting for 64% (Proportion of each disturbance voltage = Voltage area corresponding to each disturbance path/Total disturbance voltage area × 100%).

ANALYSIS OF FACTORS AFFECTING CONDUCTED DISTURBANCE

Cable Length

The disturbance voltage of the secondary cable also has high-frequency characteristics, so the propagation in the secondary cable needs to be considered by traveling wave. When the disturbance voltage wave propagates to both ends of the cable, the refraction and reflection will occur. The superposition of traveling waves may produce higher amplitude overvoltage, and the cable length directly affects the times of refraction and reflection in the whole transient process. In order to study the influence of cable length on the conducted disturbance voltage, the length L of cable is changed to 10, 20, 30, and 50 m, respectively. The time-domain waveform and frequency spectrum of terminal disturbance voltage under different cable lengths are calculated, as shown in **Figure 10**.

Figure 10 shows that with the increase of cable length, the disturbance voltage amplitude of the secondary cable core shows a downward trend. This is because when the cable length is short, the voltage wave will undergo multiple refraction and reflection in the propagation process. The continuous superposition of the incident wave and the reflected wave increases the disturbance voltage and has more high-frequency components. However, when the cable length is long, the number of refraction and reflection of voltage wave decreases significantly and attenuates continuously in the

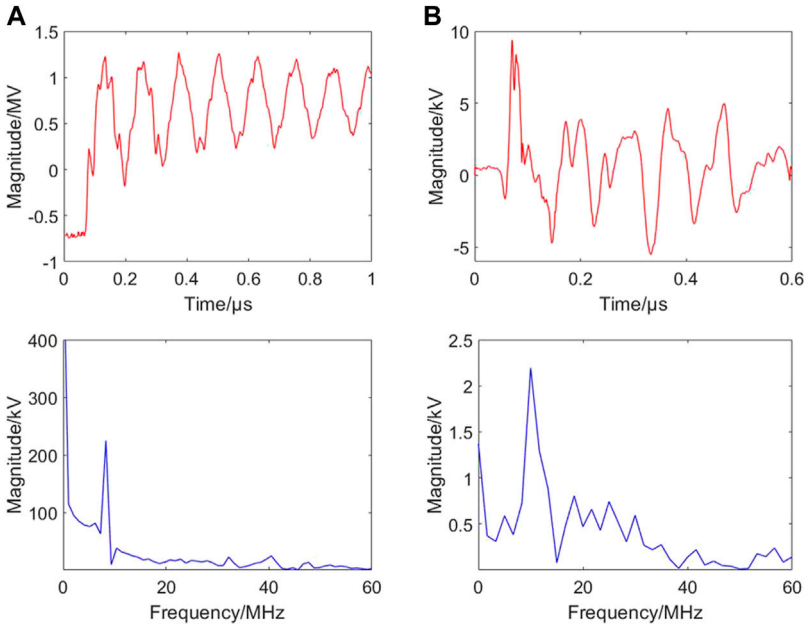

FIGURE 7 | Typical measured disturbance source waveform. **(A)** VFTO. **(B)** TEV.

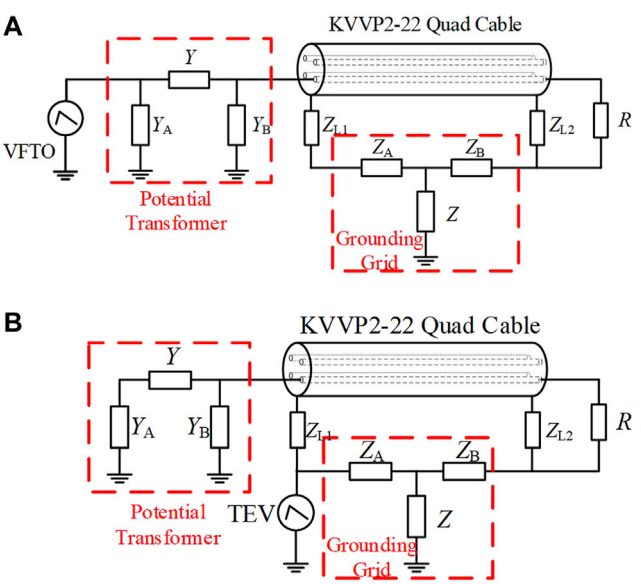

FIGURE 8 | Simulation diagram of conducted disturbance. **(A)** Calculation model of capacitive conducted disturbance voltage. **(B)** Calculation model of resistive conducted disturbance voltage.

propagation process, so the amplitude decreases and the high-frequency component decreases significantly.

Grounding Mode of Shield Layer

At present, it is generally recognized that shielded cables are used in GIS substations in the world. However, there are different opinions on the grounding mode of the secondary cable shield layer. IEEE believes that shielded cables should be grounded at one end (IEEE Std 1143™-2012, 2012), while IEC and State Grid believe that shielded cables should be grounded at both ends (IEC 61000, 1997). Therefore, this section studies the influence of three different grounding modes on conducted disturbance, including two-end grounding of the shield layer, single-end grounding of the GIS side, and single-end grounding of the control cabinet side. The calculation results are shown in **Figure 11**.

The calculation results show that the shield layer grounding mode has a great influence on the conducted disturbance, especially for the resistive conduction component. When the secondary cable shield layer is only grounded at the GIS side, the disturbance voltage is the most serious, and the amplitude is nearly 8 kV, which will seriously endanger the normal operation of the secondary equipment. When the shield layer is only grounded at the single end of the control cabinet side, the disturbance voltage level is the lowest, and the amplitude is only 1.3 kV. The reason is that TEV will lead to the increase of grounding grid potential. When the shield layer is grounded at the single end of the control cabinet, the grounding potential is low due to the distance from the GIS grounding wire, so it plays a good shielding effect on the core wire, and the resistive conduction component is in a very small value. When the shield layer is grounded at the single end of the GIS, due to the point close to the GIS grounding wire, the TEV will flow into the grid, and have a high potential. At this time, the whole shield layer will be in a high potential state, resulting in poor shielding effect of the cable and serious disturbance voltage on the core line.

Length of Grounding Wire

The grounding wire of secondary cable is usually inductive, and the voltage drop cannot be ignored when the high-frequency current

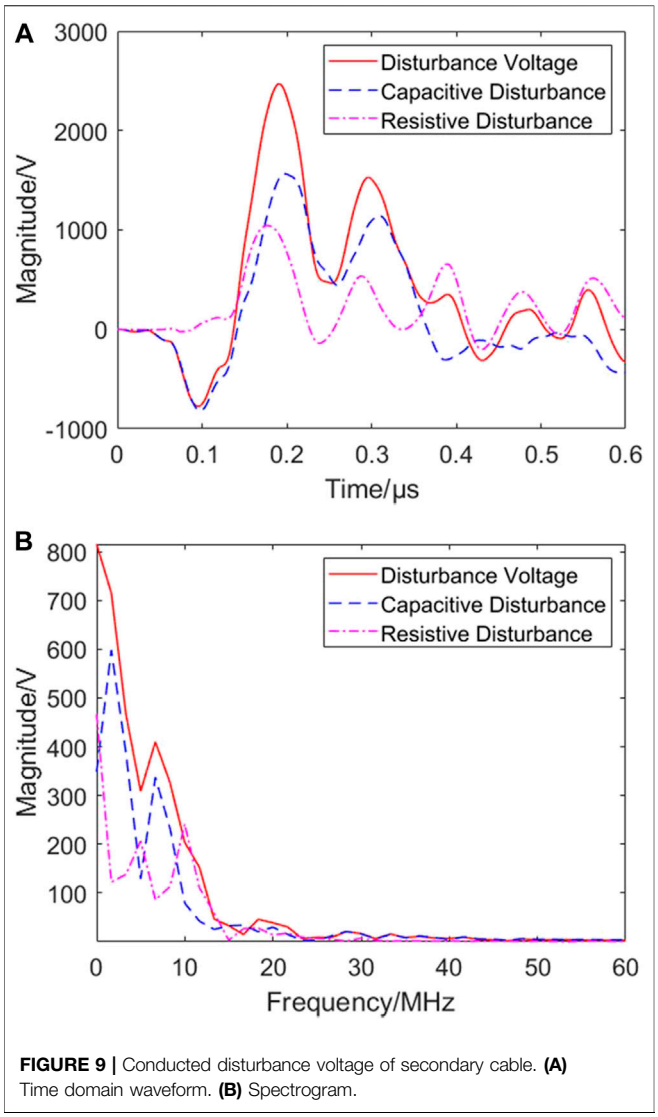

FIGURE 9 | Conducted disturbance voltage of secondary cable. **(A)** Time domain waveform. **(B)** Spectrogram.

flows. **Table 1** shows the level of conducted disturbance voltage when the grounding wire length is 1, 1.5, 2, and 2.5 m, respectively.

The calculation results show that the disturbance voltage level on the secondary cable will decrease with the increase of the length of the grounding wire. The reason is that the impedance of the grounding wire increases with the increase of the length of the grounding wire. When the resistive conduction source TEV is constant, the increase of the length of the grounding down lead will increase Z_{L1} and Z_{L2} in **Figure 8B**. Therefore, the partial voltage on the cable shielding layer decreases, the shunt of the grounding grid increases, the transient current on the shielding layer decreases, and the conducted disturbance voltage decreases.

Figure 12 shows the relationship between the voltage difference at the grounding point of the secondary cable shield layer and the transient current amplitude of the shield layer flowing through the grounding line length, which also proves the analysis in this study.

Terminal Impedance of Secondary Equipment

The terminal impedance of secondary equipment is usually 50 Ω or 100 Ω. The calculation results of the terminal impedance of 50 Ω are given in the preceding section, and the calculation results of the terminal impedance of 100 Ω are shown in **Figure 13**.

The calculation results show that the amplitude of conducted disturbance voltage increases with the increase of terminal impedance. The reason for the analysis is that when the terminal impedance amplitude increases, the difference between the wave impedance of the secondary cable and the terminal impedance is more significant, resulting in a more intense wave refraction and reflection process. In addition, the increase of terminal impedance has a more significant impact on capacitive conducted disturbance. When the terminal impedance increases from 50 to 100 Ω, the amplitude of capacitive conducted disturbance voltage increases by 0.3 kV, while the amplitude of resistive conducted disturbance voltage increases only by 0.1 kV.

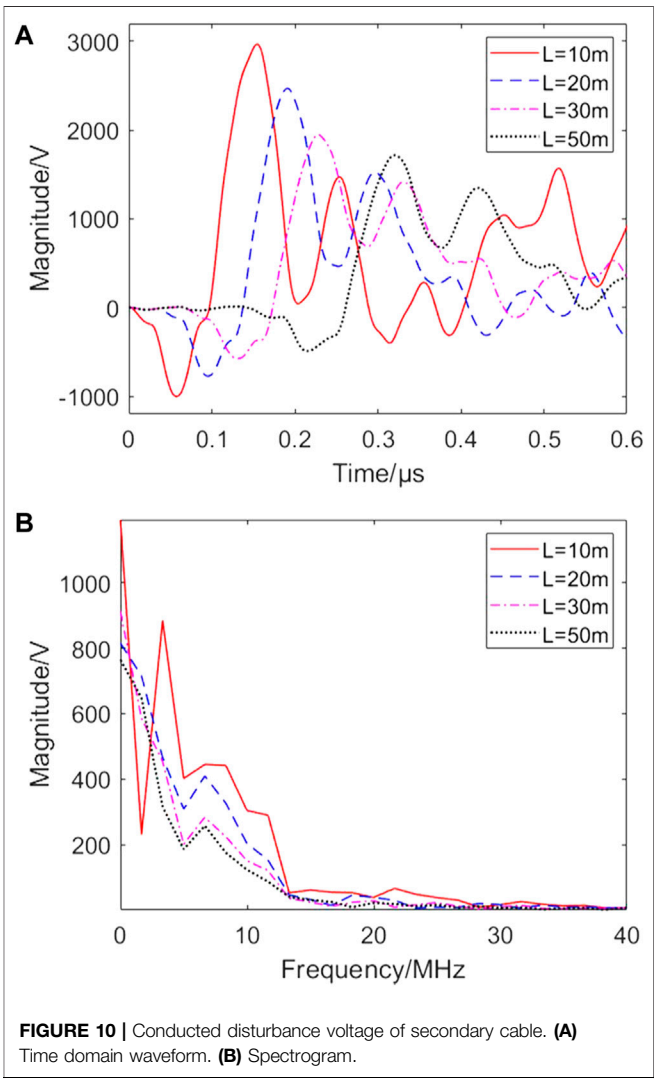

FIGURE 10 | Conducted disturbance voltage of secondary cable. **(A)** Time domain waveform. **(B)** Spectrogram.

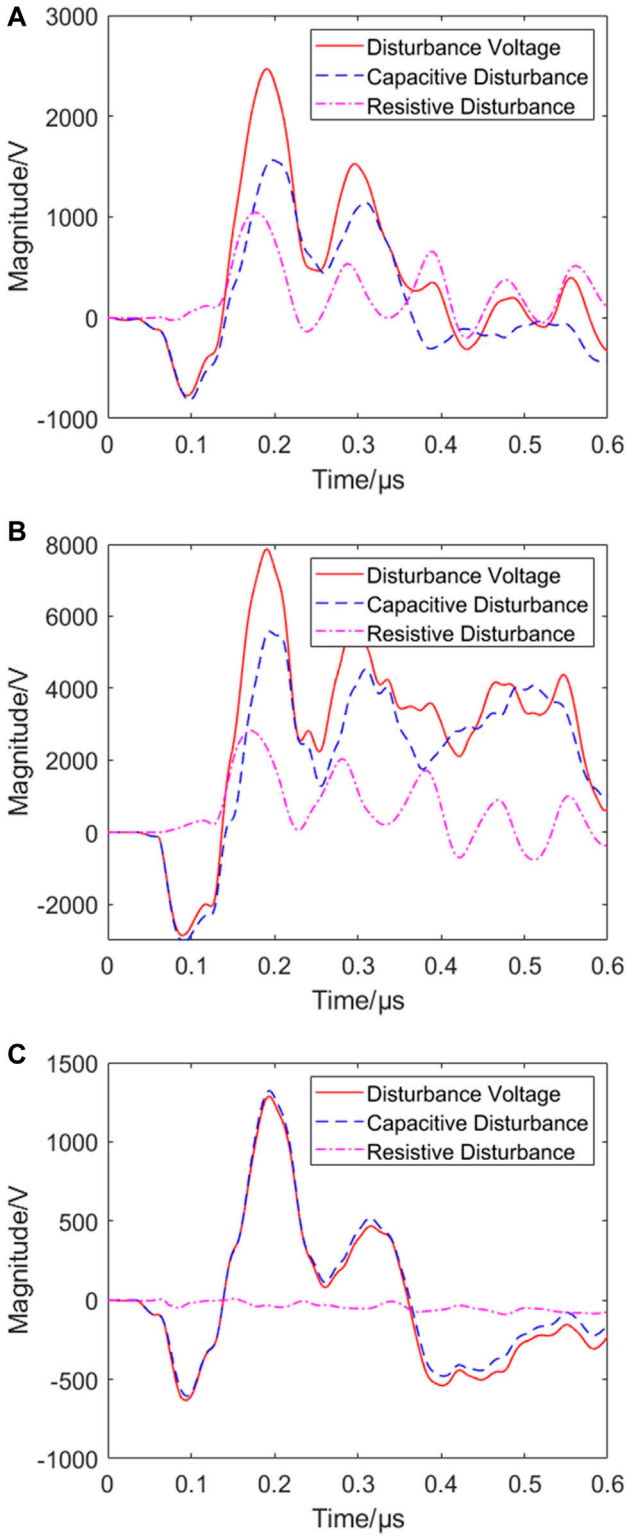

FIGURE 11 | Conducted disturbance voltage of secondary cable. **(A)** Two ends grounding. **(B)** Grounding of GIS side. **(C)** Grounding of control cabinet side.

TABLE 1 | Influence of grounding wire length on disturbance voltage.

Length/m	Capacitive conduction		Resistive conduction	
	Amplitude/V	proportion/%	Amplitude/V	proportion/%
1	1,441	64	916	36
1.5	1,214	56	692	44
2	1,039	61	536	39
2.5	901	64	424	36

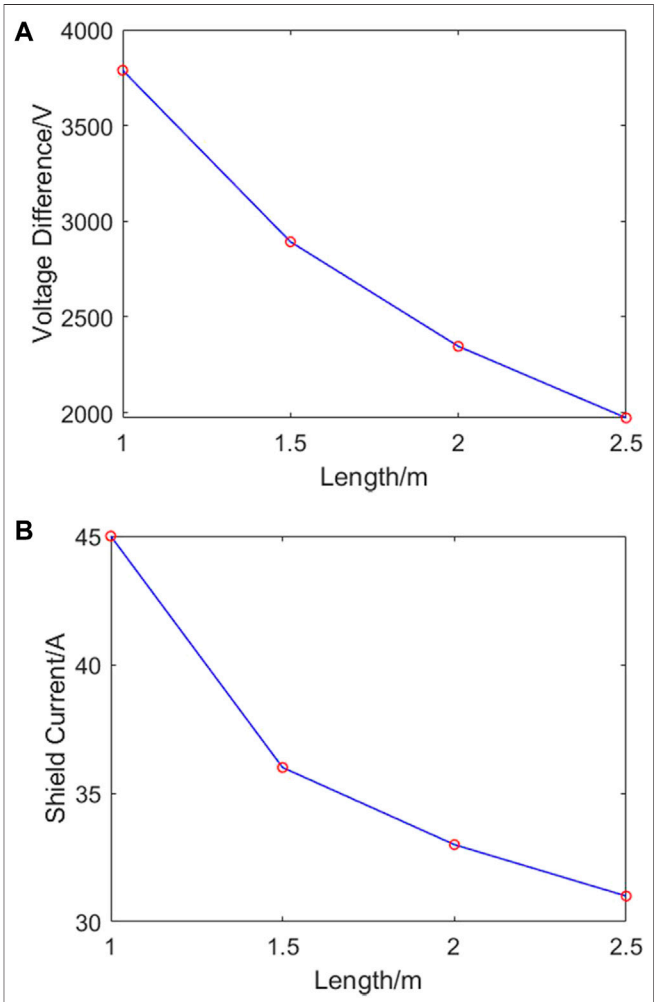

FIGURE 12 | Voltage and shield current of shield layer. **(A)** Voltage of shield layer. **(B)** Shield current of shield layer.

In Zhang et al. (2013), based on the 1000-kV GIS test circuit simulated in this study, UHV VFTO has measured the disturbance voltage of the secondary cable, and compared the disturbance voltage on the secondary cable core under three different grounding modes: grounding at both ends of the

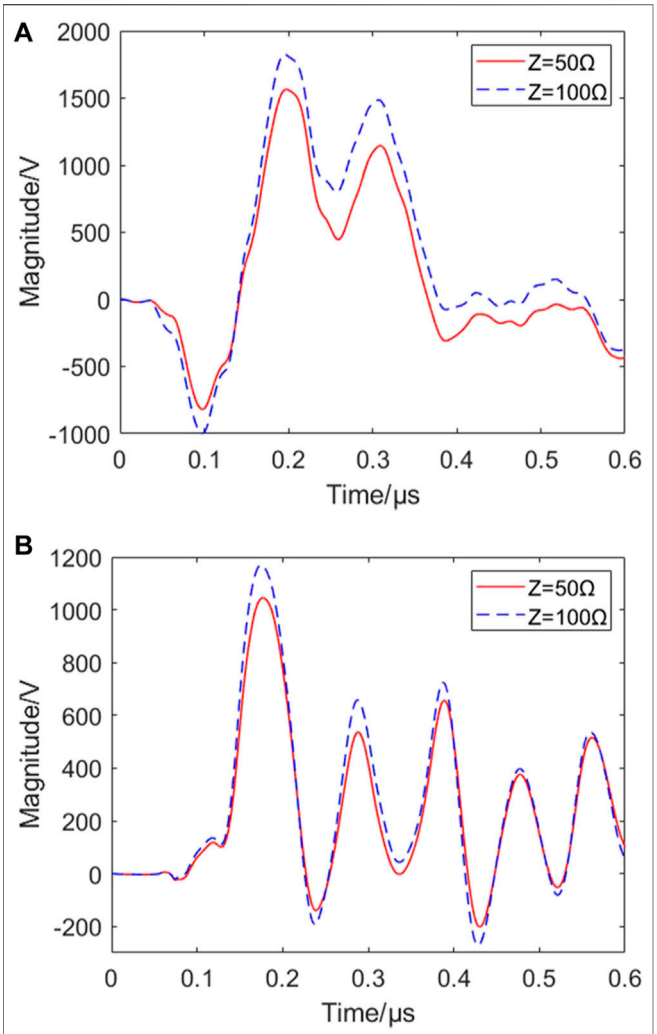

FIGURE 13 | Conducted disturbance voltage of secondary cable at different terminal impedance. **(A)** Capacitive conducted disturbance. **(B)** Resistive conducted disturbance.

secondary cable shield, single-end grounding at the side of the control cabinet, and single-end grounding at the side of the switch station, which are 395, 295, and 4557 V respectively. The following data are obtained during the simulation of the overall disturbance in this study: for the three different grounding methods of the two ends of the secondary cable shielding layer, the single-ended grounding on the control cabinet side, and the single-ended grounding on the switch station side, the overall disturbance voltages are 2.7, 1.5, and 8.0 kV respectively. Comparing the measurement results of the literature with the simulation results of this study, the following two points of analysis can be obtained:

1) Regardless of the measured voltage or the conducted disturbance voltage obtained by simulation in this paper, the disturbance voltage at the end of the secondary cable core is the highest when the shielding layer on the switchyard side is grounded at a single end, and the disturbance voltage is significantly lower than that on the switchyard side under the two methods of grounding at both ends and single-end grounding on the centralized control cabinet side.
2) The simulation results do not correspond to the measured results in the literature. The reasons are as follows: (a) The measured disturbance voltage includes conduction disturbance and radiation disturbance, and the simulation results in this paper only include conduction disturbance. (b) The simulation conditions in this paper are different from the measured conditions in the literature. In this paper, when analyzing the influence of different grounding modes on the conducted disturbance voltage of secondary cable, the cable length is 20 m, while the measured cable length in the literature is 100 m. Theoretically, the disturbance voltage measured at the end of the core wire will decrease with the increase of the cable length. (c) In the calculation, VFTO and TEV as excitation sources are the measured values under the most serious condition of the test circuit, so the simulation results are strictly considered.

Through the above analysis, it can be seen that although this study has some limitations in the verification of the secondary cable disturbance voltage value, the reasons for the difference between the measured value in the existing literature and the simulation value can be analyzed to verify the correctness of the simulation model establishment method in this study.

CONCLUSION

In this study, the electromagnetic disturbance to secondary cable caused by the disconnector switching operation in GIS is taken as the research object, and the conducted disturbance in the electromagnetic disturbance is mainly studied. The main research results are as follows:

1) The establishment method of the broadband equivalent circuit model based on the vector fitting method is proposed. The error of amplitude-frequency characteristics and phase-frequency characteristics is not more than 5%, which can meet the needs of calculation accuracy.
2) Under the calculation conditions in this study, the amplitude of conducted disturbance voltage is about 2.5 kV when the shield layer of the secondary cable is grounded at both ends. The amplitude of the capacitive component is higher than that of the resistive component, and the main frequency of the resistive component is higher than that of the capacitive component.
3) The research results of influencing factors of conducted disturbance show that with the increase of cable length, the amplitude of disturbance voltage will gradually decrease, and the high-frequency component will significantly decrease. The grounding mode of the cable shield layer has an obvious influence on conducted

disturbance, and it has a good shielding effect by way of single-end grounding on the side of the control cabinet or two-end grounding. With the increase of grounding wire length, the potential difference between the grounding point of the secondary cable shield layer and the transient current flowing through the shield layer gradually decreases, and the amplitude of conducted disturbance voltage also decreases.

DATA AVAILABILITY STATEMENT

The raw data supporting the conclusion of this article will be made available by the authors, without undue reservation.

AUTHOR CONTRIBUTIONS

XC: methodology and conceptualization; ZH: methodology, data analysis, writing original draft, and recording image; YZ: methodology, draft review, and editing; SW: data collection, draft review, and editing; JS: simulation, draft review, and editing; BW: funding acquisition; JL: funding acquisition.

FUNDING

This research was funded by Open Fund of State Key Laboratory of Power Grid Environment Protection (No. GYW51202001551).

REFERENCES

Bo, Z. Q., Lin, X. N., Wang, Q. P., Yi, Y. H., and Zhou, F. Q. (2016). Developments of Power System Protection and Control. *Prot. Control. Mod. Power Syst.* 1 (1). doi:10.1186/s41601-016-0012-2

Cai, Y., Guan, Y., Liu, W., and He, J. (2018). Study of Transient Enclosure Voltage Coupling to Secondary Cables in a Gas-Insulated Substation. *IEEE Trans. Power Deliv.* 33 (2), 761–768. doi:10.1109/tpwrd.2017.2688406

Chen, W., Li, Z., Sun, G., Dai, M., Liu, W., Li, C., et al. (2011). Experimental Research on the Characteristics of Very Fast Transient Overvoltage in Ultra High Voltage Gas Insulated Switchgear. *Proc. Chin. Soc. Electr. Eng.* 31 (31), 38–47. (In Chinese). doi:10.13334/j.0258-8013.pcsee.2011.31.009

CIGRE Working Group 33/13.09 (1988). *Very Fast Transients Phenomena Associated with Gas Insulated Substations*. France: CIGRE.

D'Souza, M., Dhara, R. S., and Bouyer, R. C. (2020). Modularization of High Voltage Gas Insulated Substations. *IEEE Trans. Ind. Applicat.* 56 (5), 4662–4669. doi:10.1109/tia.2020.3006463

Deschrijver, D., Mrozowski, M., Dhaene, T., and De Zutter, D. (2008). Macromodeling of Multiport Systems Using a Fast Implementation of the Vector Fitting Method. *IEEE Microw. Wireless Compon. Lett.* 18 (6), 383–385. doi:10.1109/lmwc.2008.922585

Feng, L., Wang, X., Jiang, X., Liu, H., Wang, J., Zhang, X., et al. (2014). Research on the EMC Modeling within the GIS in the EHV Substations. *High Voltage Apparatus* 50 (4), 97–102. (In Chinese). doi:10.13296/j.1001-1609.hva.2014.04.018

Gustavsen, B., and Semlyen, A. (1998). Application of Vector Fitting to State Equation Representation of Transformers for Simulation of Electromagnetic Transients. *IEEE Trans. Power Deliv.* 13 (3), 834–842. doi:10.1109/61.686981

Hu, R., Cui, X., Chen, W., Zhang, W., Li, Z., and Dai, M. (2015). Development of the Measuring Device of Transient Enclosure Voltage in Ultra High Voltage Gas Insulated Switchgear. *Proc. Chin. Soc. Electr. Eng.* 35 (23), 6235–6245. (In Chinese).

Hu, R. (2016). *Research on the Characteristics of Electromagnetic Transient Generated During Switching of Disconnector in AC Ultra High Voltage Gas Insulated Switchgear*. Beijing: North China Electric Power University Press. (In Chinese). doi:10.13334/j.0258-8013.pcsee.2015.23.032

IEC 61000 (1997). Electromagnetic Compatibility (EMC), Part 5: Installation and Mitigation Guidelines, Section 2: Earthing and Cabling, 1–72. BSI Standards Limited.

IEEE Std 1143™-2012 (2012). "IEEE Guide for the Design and Installation of Cable Systems in Substations," in *IEEE STD 525-2007 (Revision of IEEE Std 525-1992/Incorporates IEEE Std 525-2007/Cor1:2008)*, 1–138. doi:10.1109/IEEESTD.2008.7752756

Jiao, C., Li, M., and Cui, X. (2016). Broadband Equivalent Circuit Model of Bushing for Gas Insulated Switchgear in Ultra High Voltage Substation. *Trans. China Electrotechn. Soc.* 31 (20), 64–72. (In Chinese). doi:10.19595/j.cnki.1000-6753.tces.2016.20.006

Ma, G.-M., Li, C.-R., Li, X., Zhou, H.-Y., Chen, W.-J., Wang, H., et al. (2017). Time and Frequency Characteristics of Very Fast Transient Overvoltage in Ultra High Voltage Substation. *IEEE Trans. Dielect. Electr. Insul.* 24 (4), 2459–2468. doi:10.1109/tdei.2017.005687

Mahmood, F., Okamoto, K., and Takaya, K. (2015). "A Study on Conducted Disturbance below 150 kHz from Commercial Power-Conditioning System," in IEEE International Telecommunications Energy Conference (INTELEC)), Osaka, Japan, October 18–22, 2015.

Moreira, D. C., Nunes, M. V. A., Moreira, D. D. C., and Costa, D. K. D. (2020). Analysis of VFTO during the Failure of a 550-kV Gas-Insulated Substation. *Electric Power Syst. Res.* 189, 106825. doi:10.1016/j.epsr.2020.106825

Nan, Y., Di, Y., Zheng, Z., Jiazhan, C., Daojun, C., and Xiaoming, W. (2018). Research on Modelling and Solution of Stochastic SCUC under AC Power Flow Constraints. *IET Gener. Transm. Distrib.* 12 (15), 3618–3625. doi:10.1049/iet-gtd.2017.1845

Wang, F., and Yang, M. (2016). Fast Electromagnetic Transient Simulation for Over-voltages of Transmission Line by High Order Radau Method and V -transformation. *IET Gener. Transm. Distrib.* 10 (14), 3639–3645. doi:10.1049/iet-gtd.2016.0476

Wang, H. (2010). *Extraction of the Wide-Band Network Parameters and Transient Simulation of the Secondary cable in the Substation*. Beijing: North China Electric Power University Press. (In Chinese).

Yang, N., Yang, C., Wu, L., Shen, X., Jia, J., Li, Z., et al. (2021). Intelligent Data-Driven Decision-Making Method for Dynamic Multi-Sequence: An E-Seq2Seq Based SCUC Expert System. *IEEE Trans. Ind. Inf.*, 1. doi:10.1109/TII.2021.3107406

Zhang, B., Hao, Z., and Bo, Z. (2016). New Development in Relay protection for Smart Grid. *Prot. Control. Mod. Power Syst.* 1 (1). doi:10.1186/s41601-016-0025-x

Zhang, J., He, J., Zhao, J., Zhang, Y., and Zhang, W. (2014). "Characteristics Analysis of Switching Transient Disturbance to Secondary Equipment Port of 1,000 kV Substation," in International Conference on Power and Energy, Shanghai, China, November, 2014 (CRC Press/Balkema), 443–448.

Zhang, W., Chen, P., Chen, W., Cui, X., Wang, L., Huang, H., et al. (2013). Measurement and Simulation of Disturbance Voltage Generated by VFTO in UHV GIS Substation on the Secondary Cables. *Proc. Chin. Soc. Electr. Eng.* 33 (16), 187–196. (In Chinese). doi:10.13334/j.0258-8013.pcsee.2013.16.025

Conflict of Interest: ZH was employed by State Grid Shaoxing Power Supply Company.

The remaining authors declare that the research was conducted in the absence of any commercial or financial relationships that could be construed as a potential conflict of interest.

Publisher's Note: All claims expressed in this article are solely those of the authors and do not necessarily represent those of their affiliated organizations, or those of the publisher, the editors, and the reviewers. Any product that may be evaluated in this article, or claim that may be made by its manufacturer, is not guaranteed or endorsed by the publisher.

frontiers in Energy Research

BRIEF RESEARCH REPORT
published: 14 January 2022
doi: 10.3389/fenrg.2021.835440

Research on the Unstable Branch Screening Method for Power System With High-Proportion Wind Power

Fei Tang, Xiaoqing Wei, Yuhan Guo, Junfeng Qi, Jiarui Xie and Xinang Li*

School of Electrical Engineering and Automation, Wuhan University, Wuhan, China

The sooner the system instability is predicted and the unstable branches are screened, the timelier emergency control can be implemented for a wind power system. In this paper, aiming at the problem that the existing unstable branch screening methods are lack prejudgment, an unstable branch screening method for power system with high-proportion wind power is proposed. Firstly, the equivalent external characteristics model of the wind farm was deduced. And based on this, the out-of-step oscillation characteristics of the power system with high proportion wind power was analyzed. Secondly, based on the oscillation characteristics, line weak-connection index (LWcI) was proposed to quantify the stability margin of a branch. Then an instability prediction method and an unstable branch screening method were proposed based on LWcI and voltage phase angle difference. Finally, the rapidity and effectiveness of the proposed method are verified through the simulation analysis of IEEE-118 system.

Keywords: unstable branch, transient stability, line weak-connection index, wind power, out-of-step oscillation

OPEN ACCESS

Edited by:
Xun Shen,
Tokyo Institute of Technology, Japan

Reviewed by:
Yingbiao Li,
Huazhong University of Science and Technology, China
Aihong Tang,
Wuhan University of Technology, China

****Correspondence:***
Xiaoqing Wei
171820175@qq.com

Specialty section:
This article was submitted to Smart Grids, a section of the journal Frontiers in Energy Research

Received: *14 December 2021*
Accepted: *24 December 2021*
Published: *14 January 2022*

Citation:
Tang F, Wei X, Guo Y, Qi J, Xie J and Li X (2022) Research on the Unstable Branch Screening Method for Power System With High-Proportion Wind Power. Front. Energy Res. 9:835440. doi: 10.3389/fenrg.2021.835440

1 INTRODUCTION

With the proposal of "carbon peaks" and "carbon neutralization" goals, the penetration of renewable energy is increasing rapidly. However, different from synchronous generator, wind power and other renewable energy units have the disadvantages of low inertia and weak poor disturbance immunity, which have a profound impact on the stability of the grid (Liu et al., 2019; Shen and Raksincharoensak, 2021a). Power outage accidents (Nagpal et al., 2018; Alhelou et al., 2019; Liu, 2019; Yang et al., 2021c) in recent years indicate that due to the replacement of synchronous machines by renewable energy sources, the risk of power angle instability is greatly increased, and the development rate of chain fault is greatly accelerated. Therefore, how to prejudge the instability of the system and screen unstable branches as early as possible, so as to reserve more time to guarantee the implementation of emergency control, has become a research hotspot.

Currently, research results about instability criteria are mainly from traditional power systems. For example, Yang (Yang et al., 2006) proposed to use the extended equal area criterion (EEAC) to analyze the transient stability. Yan (Yan et al., 2011) used the maximal Lyapunov exponent (MLE) to prejudge the rotor angle stability. Saunders (Saunders et al., 2014) analyzed transient stability by constructing transient potential energy functions. Yang (Yang et al., 2021b) adopted data-driven method to study power system security and stability problem. This paper was the first study for SCUC problems, it can accommodate the mapping samples of SCUC, and consider the various input factors that affect SCUC decision-making, possessing strong generality, high solution accuracy, and efficiency over traditional methods. The above methods can prejudge the transient stability of the grid quickly using generator information such as rotor angle, but the further application in the

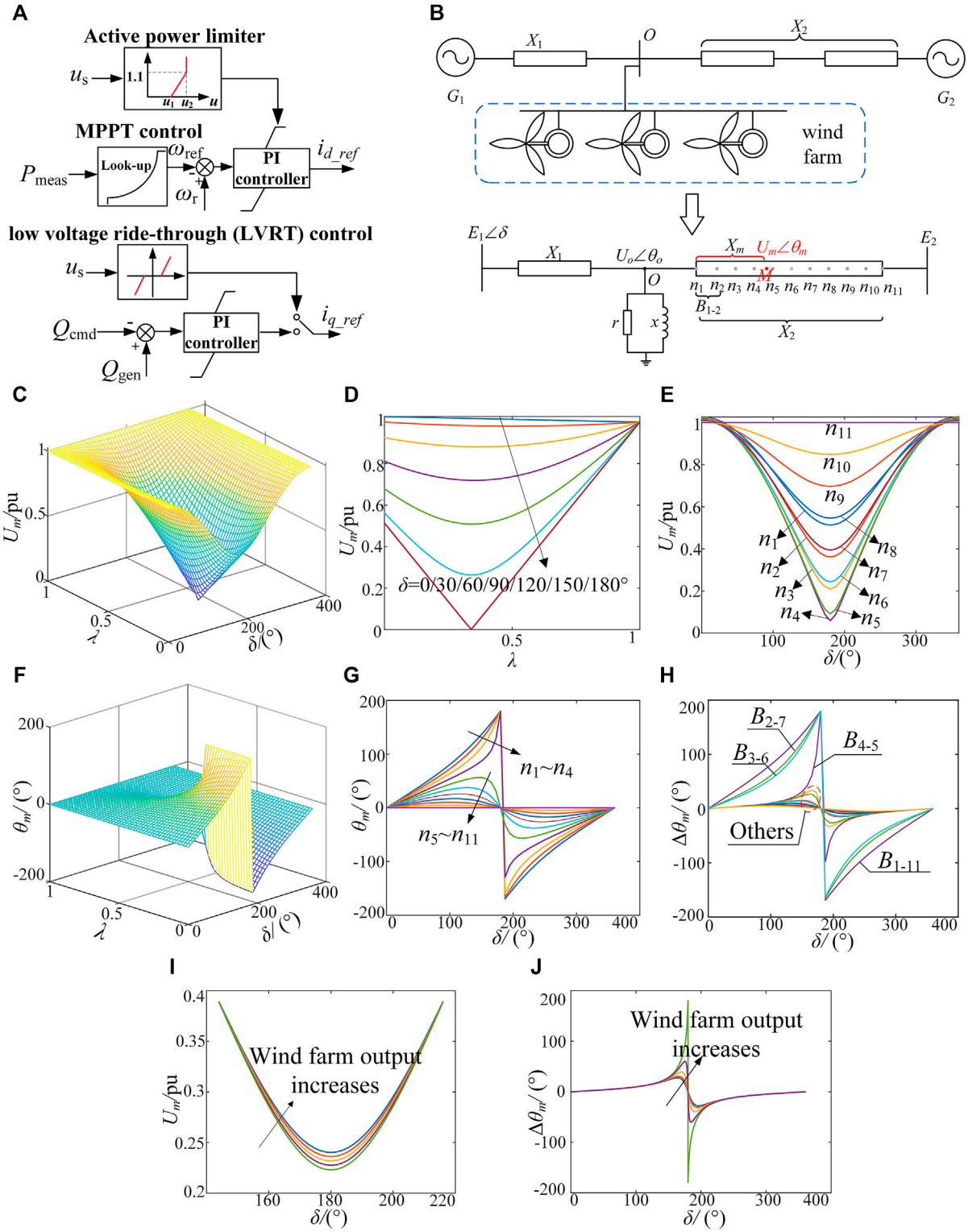

FIGURE 1 | Out-of-step oscillation characteristics of wind power system **(A)** is the control strategy of DFIG **(B)** is the equivalent two-machine system with DFIG integrated **(C)** is the distribution law of U_m in δ-λ space **(D)** is the variation law between U_m and λ **(E)** is the variation law between U_m and δ **(F)** is the distribution law of θ_m in δ-λ space **(G)** is the variation law of θ_m with δ at different position **(H)** is the variation law between $\Delta\theta_m$ and δ of different branches **(I)** is the variation law between U_m at point n_4 and δ when wind farm output changes **(J)** is the variation law between $\Delta\theta_m$ of $B_{5\text{-}6}$ and δ when wind farm output changes.

emergency control such as the splitting control is limited because the splitting section cannot be determined directly. Therefore, some scholars designed some new instability criterion using the branch response information, such as *ucosφ* criterion (Yang et al., 2013; Zhang et al., 2021), phase angle criterion (Regulski et al., 2018; Shen et al., 2021a), bus voltage frequency criterion (Zhang et al., 2019; Yang et al., 2022), apparent impedance differential method (Sreenivasachar, 2021; Shen and Raksincharoensak, 2021b) and so on. Compared with methods using generator response information, these methods can not only prejudge the unstable state of the system, but also accurately capture the unstable branches and the splitting section. However, the disadvantage is that these methods do not start until the instability accident has occurred (or approach to instability), thus it is difficult to reserve sufficient time for emergency control.

Research on the instability criterion of the high proportion renewable energy power system is still in the preliminary stage, and relevant work is mainly focused on the influence of wind power integration on transient stability (Ma et al., 2017; Liu et al., 2017; Zheng et al., 2019; Shen et al., 2021b). As for the research on the instability criterion, Wei (Wei et al., 2021; Yang et al., 2021a) and Qin (Li et al., 2021; Qin et al., 2021) respectively analyzed the influence of wind and photovoltaic power integration on oscillation center migration, but failed to propose oscillation center identification method and instability criterion. Chen (Chen et al., 2020; Li et al., 2021) proposed a new transient stability prediction method by defining a new stability index, but still failed to capture the unstable branch. Liu (Liu et al., 2020) proposed to use the slow coherency theory to study the coherency group of wind power system, but the impact of actual faults cannot be fully considered.

Therefore, aiming at the problem that the existing instability criterion lacks prejudgment, a system instability prediction method and an unstable branches screening method are proposed in this paper. which can predict power angle instability earlier and screen unstable branches accurately.

The rest of this paper is organized as follows. In **Section 2**, the out-of-step oscillation characteristics of the high proportion wind power system is analyzed. In **Section 3**, the line weak-connection index (LWcI) is proposed to quantify the stability margin, and the unstable branches screening method is proposed. Case study and discussion are shown in **Section 4**. **Section 5** concludes this study by summarizing key findings and contributions of this paper.

2 OUT-OF-STEP OSCILLATION CHARACTERISTICS OF WIND POWER SYSTEM

2.1 Equivalent External Characteristic Model of Wind Farm

Taking doubly-fed induction generator (DFIG) as an example, the control strategy is shown in **Figure 1A** (Wang et al., 2015). In steady state, DFIG adopts Maximum Power Point Tracking (MPPT) control strategy. When the system is disturbed, DFIG limits the active power output under the fault ride-through control, and outputs reactive power to support the grid. After the fault is cleared, DFIG switches back to MPPT control.

Obviously, without additional control, DFIG cannot actively respond to the disturbance of the system. When the system is disturbed, the output power of DFIG do not oscillate like a synchronous generator, but quickly return to the original state. Therefore, there is no power angle swing between DFIG and synchronous generator in electromechanical time scale. Thus, DFIG can be regarded as a power source without inertia, and its equivalent external characteristics can be equivalent to negative resistance and negative reactance in parallel:

$$\begin{cases} \boldsymbol{r} = -\dfrac{\boldsymbol{u}_s^2}{\boldsymbol{P}_{\mathrm{gen}}} \\ \boldsymbol{x} = -\dfrac{\boldsymbol{u}_s^2}{\boldsymbol{Q}_{\mathrm{gen}}} \end{cases} \tag{1}$$

Where the negative sign indicates the power injected into the bus.

In addition, if the system is still transient stable after the fault is cleared, DFIG can quickly recover to the pre-fault state and the output power also quickly resumes stability. So the equivalent impedance can be considered constant. If the system is already unstable, the output power of DFIG will oscillate due to the oscillation of the grid voltage. And the equivalent impedance also oscillates. Considering that there is a certain inertia in the system, it takes a certain amount of time from fault removal to complete instability, during which the output power of DFIG does not change dramatically, so it can be simply considered that the equivalent impedance during this period is constant.

2.2 Out-of-step Oscillation Characteristics of Wind Power System

Taking an equivalent two-machine system with a DFIG-based wind farm integrated as an example to analyze the out-of-step oscillation characteristics of wind power system. As shown in **Figure 1B**, bus O is the common coupling point of the wind farm, and the voltage vector can be expressed as $U_o\angle\theta_o$. r and x are equivalent resistance and reactance of the wind farm respectively. E_1 and E_2 are the equivalent potentials of generator G_1 and G_2 respectively, and δ is the rotor angle difference. X_1 and X_2 are equivalent resistance between G_1 and bus O, bus O and G_2, respectively. For convenience analysis, the X_2 is divided into 10 equivalents by points n_1~n_{11}, and each branch section is represented by $B_{1\text{-}2}$~$B_{10\text{-}11}$. The voltage vector of any point M between the bus O and G_2 is expressed as $U_m\angle\theta_m$, and its position function is $\lambda = X_m/X_2$, $\lambda\in[0,1]$.

Based on the node voltage method, the voltage vector of bus O can be expressed as:

$$\dot{\boldsymbol{U}}_{\boldsymbol{o}} = \frac{\boldsymbol{Z}_{\boldsymbol{\Sigma}}}{\boldsymbol{jX}_{\mathbf{1}}}\boldsymbol{E}_{\mathbf{1}}\boldsymbol{e}^{\boldsymbol{j\delta}} + \frac{\boldsymbol{Z}_{\boldsymbol{\Sigma}}}{\boldsymbol{jX}_{\mathbf{2}}}\boldsymbol{E}_{\mathbf{2}} \tag{2}$$

Where $Z_\Sigma = \frac{1}{G+\frac{1}{jX_1}+\frac{1}{jX_2}}$, $G = \frac{1}{r} + \frac{1}{jx}$.

Considering that the active power output of DFIG is limited under low voltage ride-through (LVRT) control, so the $\frac{1}{r}$ is very

small, and the real part of Z_Σ can be ignored. Thus, the expression of the voltage vector at bus O can be rewritten as:

$$\dot{U}_o = |Z_\Sigma|\left(\frac{E_1 e^{j\delta}}{X_1} + \frac{E_2}{X_2}\right) \tag{3}$$

As shown in **Eq. 3**, the integration of wind farm changes the amplitude of Z_Σ, thereby changing the voltage amplitude of the common coupling point. The larger the wind farm output power, the greater the Z_Σ, the greater the voltage amplitude of the common coupling point.

In addition, according to Yang (Yang et al., 2013), the unequal voltage on both sides of the branch is one of the reasons for the migration of out-of-step center. When the voltage amplitude on both sides of the branch is unequal, the out-of-step center migrates to the side where the voltage amplitude is smaller. Therefore, the integration of wind power increases the voltage amplitude of the common coupling point, resulting in the unequal voltage amplitude on both sides of the branch, which in turn leads to the migration of the out-of-step center to the side where the voltage amplitude is smaller.

Then, according to Ohm's law, the following equation exists:

$$\frac{\dot{U}_o - E_2}{jX_2} = \frac{\dot{U}_o - \dot{U}_m}{jX_m} \tag{4}$$

Therefore, based on **Equation 2** and **Equation 4**, the voltage vector of point M can be expressed as:

$$\dot{U}_m = \frac{Z_\Sigma}{jX_1}(1-\lambda)E_1 e^{j\delta} + E_2\left[\lambda + \frac{Z_\Sigma}{jX_2}(1-\lambda)\right] \tag{5}$$

Ignoring the real part of Z_Σ, the expression of voltage amplitude and phase angle at point M can be written as:

$$\begin{cases} U_m = \\ \sqrt{\left(\frac{Z_\Sigma(1-\lambda)}{Z_1}E_1\cos\delta + E_2\left[\lambda + \frac{Z_\Sigma(1-\lambda)}{Z_2}\right]\right)^2 + \left(\frac{Z_\Sigma(1-\lambda)}{Z_1}E_1\sin\delta\right)^2} \\ \theta_m = \arctan\dfrac{\frac{Z_\Sigma}{Z_1}(1-\lambda)E_1\sin\delta}{\frac{Z_\Sigma}{Z_1}(1-\lambda)E_1\cos\delta + E_2\left[\lambda + \frac{Z_\Sigma}{Z_2}(1-\lambda)\right]} \end{cases} \tag{6}$$

According to **Eq. 6**, the U_m and θ_m are related to the position function λ, the output power of wind farm, the power angle difference and so on. Thus, assuming that $E_1 = E_2 = 1.0$, $X_2 = 3X_1 = 0.3$, and the output power of the wind farm under LVRT control is $0.1 + j0.5$, the temporal and spatial distribution law of voltage amplitude U_m and θ_m are shown in **Figures 1C–H**.

Figures 1C–E show that with the increase of δ, the voltage U_m at any position on the branch decreases and then increases, getting the minimum value when $\delta = 180^\circ$. Meanwhile, the variation amplitude of U_m varies from location to location, so there is always a point where the variation is the most drastic, called the out-of-step center. According to **Figure 1E**, the out-of-step center is located between n_4 and n_5.

According to **Figures 1F–H**, when δ increases from 0° to 180°, for the node between the out-of-step center and G_1, θ_m changes monotonically in (0°, 180°). While for the node between the out-of-step center and G_2, θ_m firstly increases and then decreases, and the maximum value is no more than 90°. Therefore, only for the branch where the out-of-step center is located, the voltage phase difference $\Delta\theta_m$ variation rule is consistent with the power angle difference δ.

According to **Figures 1I,J**, as the output power of wind farm increases, the U_m at point n_4 increases, and the maximum value of $\Delta\theta_m$ at $B_{5\text{-}6}$ increases until the $\Delta\theta_m$ changes monotonically between (0°, 180°), indicating that the out-of-step center migrates from point n_4 to point n_5, until it completely enters into $B_{5\text{-}6}$.

In summary, the output power of wind farm changes the flow distribution and voltage level of the system, ultimately affecting the system transient stability and the out-of-step center position. However, the phenomenon that voltage amplitude drops sharply, and the voltage phase angle difference of the branch where the out-of-step center located increases monotonously are still exist, which can be used to predict the transient stability of the system and capture the unstable branch.

3 INSTABILITY PREJUDGMENT CRITERIA AND UNSTABLE BRANCH SCREENING METHOD

3.1 Line Weak-Connection Index (LWcI)

According to the conclusion in **Section 2**, when the out-of-step oscillation occurs, one or more branches loses stability, resulting in a sharp drop of voltage at each point of the branches. Considering that the voltage reduction at the oscillation center is the most severe (Yang et al., 2013), so the voltage of the oscillation center can be used to measure the stability margin of a branch. However, if the oscillation center is not on the branch due to the oscillation center migration, the voltage at one end of the branch is the minimum voltage, which is much greater than the oscillation center voltage. And the result can be conservative and misjudgment can occur. Therefore, in order to prevent misjudgment as the oscillation center migrates outside the branch, the terminal voltage can be used to correct the out-of-step center voltage. Thus, Line weak-connection Index (LWcI) is defined to reflect the stability margin of a branch:

$$LWcI = \begin{cases} \dfrac{U_A U_B|\sin\Delta\theta|}{\sqrt{U_A^2 + U_B^2 - 2U_A U_B\cos\Delta\theta}}, & U_{AB} > U_{hA} \text{ and } U_{AB} > U_{hB} \\ \min\{U_A, U_B\}, & U_{AB} < U_{hA} \text{ or } U_{AB} < U_{hB} \end{cases} \tag{7}$$

Where U_A and U_B are terminal voltage amplitude of a branch, $\Delta\theta$ is the voltage angle difference on both sides of a branch, all of which can be obtained through the WAMS system. $U_{AB} = \sqrt{U_A^2 + U_B^2 - 2U_A U_B\cos\theta}$, $U_{hA} = \sqrt{U_A^2 - U_h^2}$, $U_{hB} = \sqrt{U_B^2 - U_h^2}$.

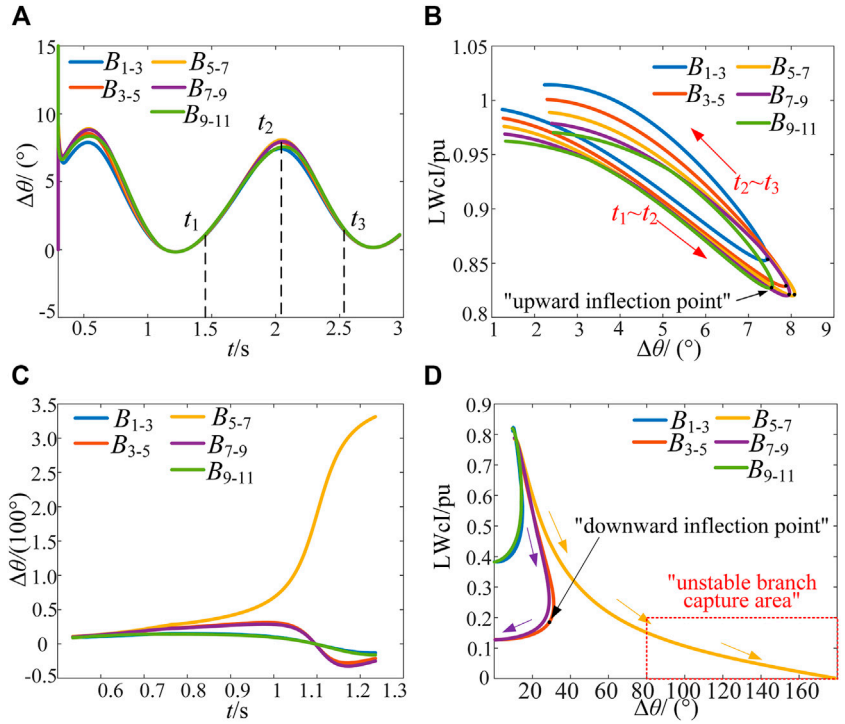

FIGURE 2 | Analysis of branch trajectory characteristics **(A)** is the $\Delta\theta$-t curve of different branches when the system is stable **(B)** is the LWcI-$\Delta\theta$ curve of different branches when the system is stable **(C)** is the $\Delta\theta$-t curve of different branches when the system is unstable **(D)** is the LWcI-$\Delta\theta$ curve of different branches when the system is unstable.

According to **Eq. 7**, there is a negative correlation between LWCI and $\Delta\theta$. The larger the $\Delta\theta$, the smaller the branch stability margin, the smaller the LWcI. Therefore, LWcI can be used to prejudge the transient stability of the wind power system.

Further, according to **Section 2.2**, only the $\Delta\theta$ of the unstable branch varies monotonously in (−180°, 180°). Thus, there are significant differences in the trajectories between the unstable branches and others in the plane with $\Delta\theta$ as the horizontal axis and LWcI as the vertical axis.

Taking the wind power system in **Figure 1B** as an example, the trajectory of each branch in LWcI-$\Delta\theta$ plane when the system is stable and unstable is shown in **Figure 2**.

As shown in **Figures 2A,B**, the $\Delta\theta$ of all branches constantly oscillate and decays when the power angle is stable. Taking one period as an example, during t_1~t_2, the $\Delta\theta$ increases, and the stability margin of all branches decreases, so the trajectories in LWcI-$\Delta\theta$ plane shows a monotonically decreasing trend, that is:

$$\begin{cases} \mathbf{LWcI}(t_i) - \mathbf{LWcI}(t_{i-1}) < \mathbf{0} \\ \boldsymbol{\Delta\theta}(t_i) - \boldsymbol{\Delta\theta}(t_{i-1}) > \mathbf{0} \end{cases} \tag{8}$$

During t_2~t_3, the $\Delta\theta$ of each branch decreases and the stability margin increases, as shown in **Eq. 9**. Therefore, an "upward inflection point" appears on the trajectory in LWcI-$\Delta\theta$ plane, indicating that there is no risk of instability in this cycle.

$$\begin{cases} \mathbf{LWcI}(t_i) - \mathbf{LWcI}(t_{i-1}) > \mathbf{0} \\ \boldsymbol{\Delta\theta}(t_i) - \boldsymbol{\Delta\theta}(t_{i-1}) < \mathbf{0} \end{cases} \tag{9}$$

As shown in **Figure 2C**, only the $\Delta\theta$ of $B_{5\text{-}7}$ exceeds 180°, which is the unstable branch. Corresponding to **Figure 2D**, only the trajectory of $B_{5\text{-}7}$ monotonically decreases, satisfying **Eq. 8**. While for a branch which is still stable, because the extreme value of $\Delta\theta$ exists, a "downward inflection point" appears. After crossing the "downward inflection point", as the system is already unstable, the voltage of each node is still decreasing, so the LWcI and $\Delta\theta$ both decrease, as shown in.

$$\begin{cases} \mathbf{LWcI}(t_i) - \mathbf{LWcI}(t_{i-1}) < \mathbf{0} \\ \boldsymbol{\Delta\theta}(t_i) - \boldsymbol{\Delta\theta}(t_{i-1}) < \mathbf{0} \end{cases} \tag{10}$$

Therefore, the "unstable branch capture area", which is shown in **Figure 2D**, can be used to prejudge the system instability and screen the unstable branch. If the trajectory of a branch always satisfies **Eq. 8** and enters into the "unstable branch capture area", which can be expressed as in **Eq. 11**, the stability margin of the branch is significantly reduced and the system is at risk of instability.

$$\begin{cases} \underline{\mathbf{LWcI}} < \mathbf{LWcI}(t_i) < \overline{\mathbf{LWcI}} \\ \underline{\boldsymbol{\Delta\theta}} < \boldsymbol{\Delta\theta}(t_i) < \overline{\boldsymbol{\Delta\theta}} \end{cases} \tag{11}$$

Where $\underline{\text{LWcI}}$ and $\overline{\text{LWcI}}$ represent the lower and upper limits of LWCI, respectively. $\underline{\Delta\theta}$ and $\overline{\Delta\theta}$ represent the lower and upper limits of $\Delta\theta$, respectively.

3.2 Unstable Branch Screening Process

The system instability prediction and unstable branch screening process proposed in this paper is shown in **Figure 3**. After the

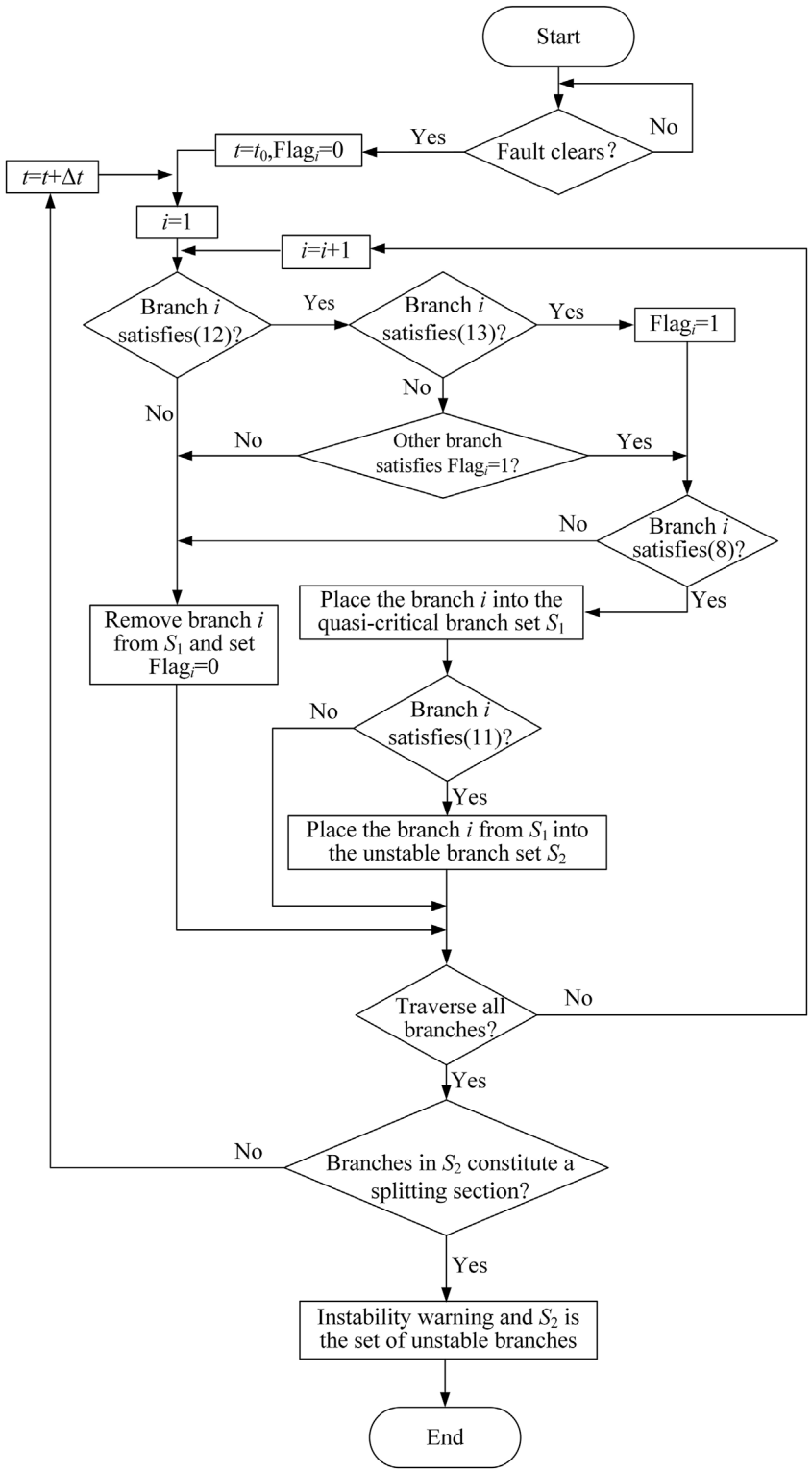

FIGURE 3 | Process of instability prediction and unstable branch screening.

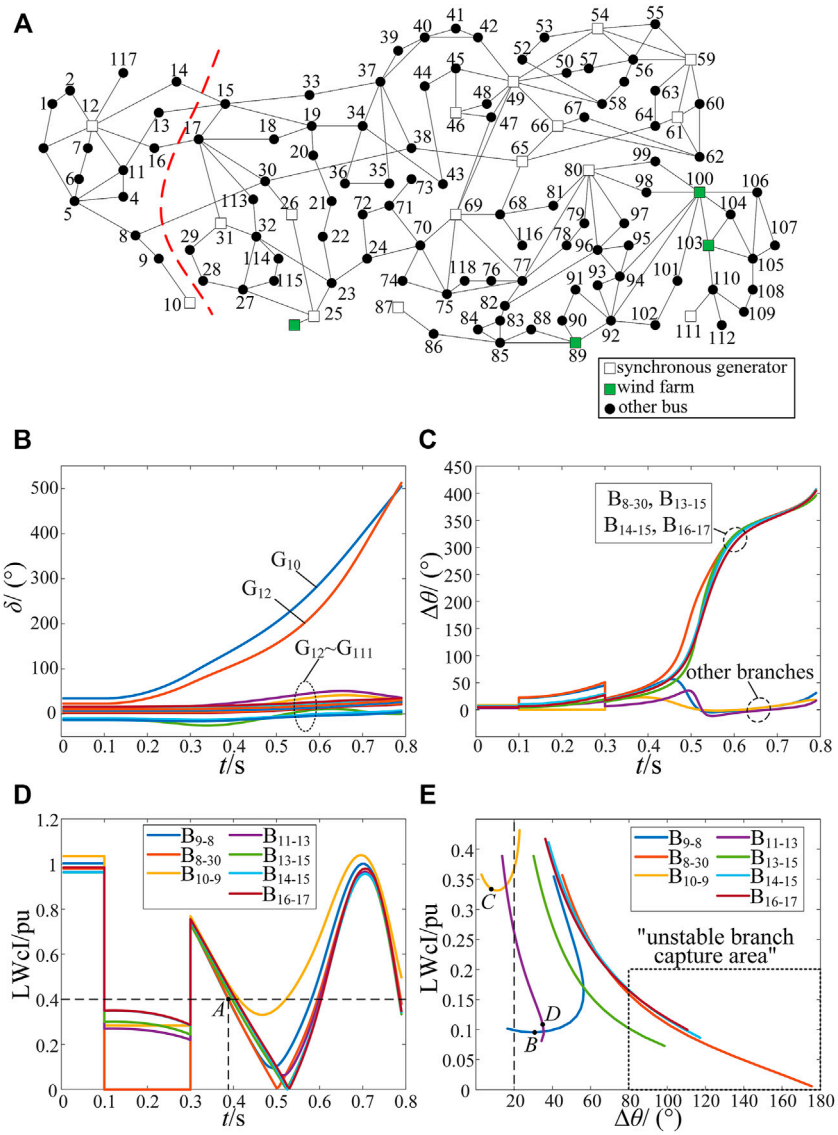

FIGURE 4 | The transient response of the IEEE-118 wind power system **(A)** is the diagram of IEEE-118 system with wind farms **(B)** is power angle curves of generators **(C)** is the voltage phase angle difference of branches **(D)** is the LWcI-*t* curve of different branches **(E)** is the LWcI-$\Delta\theta$ curve of different branches during the period of 0.39 and 0.51 s.

fault is cleared, the voltage phase angle difference of each branch is firstly calculated. As shown in **Eq. 12**, if it is greater than the threshold, the stability margin of the branch needs further analysis.

$$\boldsymbol{\Delta\theta_i > \Delta\theta_{th}} \tag{12}$$

Secondly, calculate LWcI of the branch which satisfies **Eq. 12**. If the value is lower than the threshold as shown in **Eq. 13**, the stability margin is already small, and it is necessary to monitor the trajectory in the LWcI-$\Delta\theta$ plane.

$$\mathbf{LWcI}_i \leq \mathbf{LWcI}_{th} \tag{13}$$

Thirdly, if the trajectory of the branch satisfying **Equation 12** and **Equation 13** in the LWcI-$\Delta\theta$ plane always satisfies **Eq. 8**, the stability margin of the branch keeps decreasing and the risk of instability keeps increasing. When the trajectory satisfies **Eq. 11**, that is, it enters into the "unstable branch capture area", the branch can be considered as an unstable branch.

Finally, traverse all branches in turn, and then repeat the steps above based on the data at the next sampling moment until all unstable branches constitute a splitting section.

4 CASE STUDY

In order to verify the effectiveness of the method proposed in this paper, the IEEE-118 system with wind farm integrated is built on the PSS/E platform. As shown in **Figure 4A**, the synchronous generators on the bus 89, 100 and 103 are replaced by wind farms,

the capacity of which is 450, 300 and 300 MVA, respectively. Meanwhile, another wind farm with capacity of 75MVA is integrated at the bus 25. Assume that the output power of wind farms equals to the rated power, and the load power is 4252 MW, so the penetration rate of wind power is 26.46%.

According to **Eq. 7**, when the voltage on both sides is equal and the $\Delta\theta$ is equal to 130°, LWcI = 0.41. Considering that the system is still stable at that time, so set $LWcI_{th} = 0.4, \theta_{th} = 20^{\circ}$. According to the variation rule of $\Delta\theta$ of an unstable branch, set $\underline{LWcI} = 0$, and $\overline{LWcI} = 0.2$, $\underline{\Delta\theta} = 80°$ and $\overline{\Delta\theta} = 180°$. It is worth mentioning that the setting parameters of the "unstable branch capture area" can be adjusted. The larger the $\Delta\theta_{\mathrm{m}}$ and the smaller the LWcI, the stronger the reliability of the criterion but the worse the speed.

Assume that a three-phase short circuit failure occurs on branch 8–30 at 0.1 s, and lasts 0.2 s. The transient response of the system is shown in **Figures 4B–E**. Considering that there are too many branches, only the branches whose voltage phase angle difference is greater than 20° are displayed. According to **Figures 4B,C**, the power angle of G_{10} and G_{12} increases rapidly after the fault is cleared, and the voltage phase angle difference of branch 8–30 13–15 14–15 and 16–17 continues to increase, indicating that G_{10} and G_{12} lose stability compared with other generators, and the out-of-step center is located on branch 8–30 13–15 14–15 and 16–17.

As shown in **Figure 4D**, the LWcI of each branch is monotonically decreasing when the fault is removed, indicating that the stability margin of each branch declines continuously. Around 0.39s, the LWcI of branch 8–30 firstly decreases to 0.4, satisfying **Eq. 13**. And the program begins to monitor the trajectory of each branch in the LWcI-$\Delta\theta$ plane to screen the unstable branches. Corresponding to **Figure 4E**, the trajectories of the branch 8–30 13–15 14–15 and 16–17 in the LWcI-$\Delta\theta$ plane are always monotonously decreasing, and enter into the " unstable branch capture area" at 0.45, 0.47, 0.48 and 0.49 s respectively. It indicates that the above branches are all unstable and constitute a splitting section, as shown by the red dashed line in **Figure 4A**. By contrast, at 0.49 s, the trajectories of the branch 9–8, 10–9, 11–13 are located at points B, C and D respectively. Obviously, there have been inflection points in the trajectories of branch 9–8 and 10–9, indicating that there is no out-of-step center on branch 9–8 and 10–9. For branch 11–13, the trajectory still drops monotonically, so it still needs to be monitored. But according to "upward inflection point" in the trajectory during the period of 0.49–0.51 s, it can be judged that branch 11–13 are not unstable branch, either.

In summary, the unstable status of the system can be prejudged and all unstable branches can be accurately screened at 0.49 s using the method in this paper. If the traditional method (Tang et al., 2015) is adopted, the complete splitting section cannot be obtained until the system is already unstable at 0.57 s. Therefore, compared with other methods, the method proposed in this paper can prejudge unstable status of the system and screen all the unstable branches earlier under the premise of ensuring correctness, and thus reserve more time for emergency control such as splitting control.

5 CONCLUSION

An instability prediction method and an unstable branch screening method are proposed in this paper. Some conclusions are summed up as follows. Firstly, when the wind power system loses stability, the bus voltage amplitude drops, and the voltage phase angle difference of the unstable branch increases, which are the key response information mapped on the branch. Secondly, according to the response information, an indicator called line weak-connection index (LWcI) is built to assess the stability margin of a branch. The smaller the LWcI, the smaller the stability margin of the branch. Thirdly, the trajectories of different branches are different in the plane composed of LWcI and voltage phase angle difference. Only the trajectory of the unstable branch shows a monotonically decreasing trend, while there are "upward inflection points" or "downward inflection points" in the trajectories of other branches. Depending on the difference of trajectory characteristics, the unstable branch can be accurately screened.

DATA AVAILABILITY STATEMENT

The original contributions presented in the study are included in the article/supplementary material, further inquiries can be directed to the corresponding author.

AUTHOR CONTRIBUTIONS

FT was responsible for methodology and revision of the manuscript. XW was responsible for writing the original draft. YG and JQ were responsible for data processing and supervision. JX and XL were responsible for visualization and supervision. All authors contributed, read, and approved the submitted version.

FUNDING

This work was supported by the National Natural Science Foundation of China under Grant 51977157.

REFERENCES

Alhelou, H., Hamedani-Golshan, M., Njenda, T., and Siano, P. (2019). A Survey on Power System Blackout and Cascading Events: Research Motivations and Challenges. *Energies* 12 (4), 682. doi:10.3390/en12040682

Chen, Y., Mazhari, S. M., Chung, C. Y., Faried, S. O., and Pal, B. C. (2020). Rotor Angle Stability Prediction of Power Systems with High Wind Power Penetration Using a Stability Index Vector. *IEEE Trans. Power Syst.* 35 (6), 4632–4643. doi:10.1109/TPWRS.2020.2989725

Li, Z., Jiang, W., Abu-Siada, A., Li, Z., Xu, Y., and Liu, S. (2021). Research on a Composite Voltage and Current Measurement Device for HVDC Networks. *IEEE Trans. Ind. Electron.* 68 (9), 8930–8941. doi:10.1109/TIE.2020.3013772

Liu, J., Tang, F., Zhao, J., Liu, D., and Kamwa, I. (2020). Coherency Identification for Wind-Integrated Power System Using Virtual Synchronous Motion Equation. *IEEE Trans. Power Syst.* 35 (4), 2619–2630. doi:10.1109/TPWRS.2020.2968294

Liu, J., Yang, D., Yao, W., Fang, R., Zhao, H., and Wang, B. (2017). PV-based Virtual Synchronous Generator with Variable Inertia to Enhance Power System Transient Stability Utilizing the Energy Storage System. *Prot. Control. Mod. Power Syst.* 2 (1), 39. doi:10.1186/s41601-017-0070-0

Liu, Y. (2019). "Analysis of Brazilian Blackout on March 21st,2018 and Revelations to Security for Hunan Grid," in 2019 4th International Conference on Intelligent Green Building and Smart Grid (IGBSG), Yichang, China, 06-09 Sep. 2019, 422–426. doi:10.1109/IGBSG.2019.8886219

Mosi, L., Zhiyuan, S., Guangshi, L., Mingpo, L., and Xiaoyin, Q. (2019). "Study on the Influence of Large-Scale Wind Power Integration on Transient Stability of Power System," in 2019 IEEE 8th International Conference on Advanced Power System Automation and Protection (APAP), Xi'an, China, 21-24 Oct. 2019, 1156–1159. doi:10.1109/APAP47170.2019.9224650

Ma, Z., Chen, H., and Chai, Y. (2017). Analysis of Voltage Stability Uncertainty Using Stochastic Response Surface Method Related to Wind Farm Correlation. *Prot. Control. Mod. Power Syst.* 2 (1), 20. doi:10.1186/s41601-017-0051-3

Nagpal, M., Martinich, T. G., Jiao, Z., Manuel, S.-H., Zhang, H. A., and Alimardani, A. (2018). Lessons Learned from a Regional System Blackout and Restoration in BC Hydro. *IEEE Trans. Power Deliv.* 33 (4), 1954–1961. doi:10.1109/TPWRD.2017.2768046

Qin, F., Tang, F., Zhang, T., Wei, X., and Li, Y. (2021). "Impact of Photovoltaic Grid-Connected on Distribution of Power System Disturbed Oscillation Center," in 2021 IEEE 4th International Electrical and Energy Conference (CIEEC), Wuhan, China, 28-30 May 2021. doi:10.1109/CIEEC50170.2021.9510601

Regulski, P., Rebizant, W., Kereit, M., and Herrmann, H.-J. (2018). "PMU-based Generator Out-of-step Protection," in 2018 10th IFAC Symposium on Control of Power and Energy Systems (CPES), Tokyo, Japan, 04-06 Sep. 2018, 79–84. IFAC-PapersOnLine51. doi:10.1016/j.ifacol.2018.11.681

Saunders, C. S., Alamuti, M. M., and Taylor, G. A. (2014). "Transient Stability Analysis Using Potential Energy Indices for Determining Critical Generator Sets," in 2014 IEEE PES General Meeting - Conference & Exposition, National Harbor, MD, USA, 27-31 July. 2014, 1–5. doi:10.1109/PESGM.2014.6939235

Shen, X., Ouyang, T., Khajorntraidet, C., Li, Y., Li, S., and Zhuang, J. (2021a). Mixture Density Networks-Based Knock Simulator. *Ieee/asme Trans. Mechatron.*, 1. doi:10.1109/TMECH.2021.3059775

Shen, X., Ouyang, T., Yang, N., and Zhuang, J. (2021b). Sample-Based Neural Approximation Approach for Probabilistic Constrained Programs. *IEEE Trans. Neural Netw. Learn. Syst.*, 1–8. doi:10.1109/TNNLS.2021.3102323

Shen, X., and Raksincharoensak, P. (2021a). Pedestrian-Aware Statistical Risk Assessment. *IEEE Trans. Intell. Transport. Syst.*, 1–9. doi:10.1109/TITS.2021.3074522

Shen, X., and Raksincharoensak, P. (2021b). Statistical Models of Near-Accident Event and Pedestrian Behavior at Non-signalized Intersections. *J. Appl. Stat.*, 1–21. doi:10.1080/02664763.2021.1962263

Sreenivasachar, K. (2021). Out-Of-Step Detection on Transmission Lines Using Apparent Impedance Differential Method. *IEEE Trans. Power Deliv.*, 1. doi:10.1109/TPWRD.2021.3125525

Tang, F., Yang, J., Liao, Q., Wang, Y., and Jia, J. (2015). Out-of-step Oscillation Splitting Criterion Based on Bus Voltage Frequency. *J. Mod. Power Syst. Clean. Energ.* 3 (3), 341–352. doi:10.1007/s40565-015-0140-0

Wang, Y., Hu, J., Zhang, D., Ye, C., and Li, Q. (2015). "DFIG WT Electromechanical Transient Behaviour Influenced by PLL: Modelling and Analysis," in International Conference on Renewable Power Generation (RPG 2015), Beijing, China, 17-18 Oct. 2015. doi:10.1049/cp.2015.0331

Wei, X., Tang, F., Li, Y., Qin, F., and Zhang, T. (2021). "Study on the Oscillation Center of DFIG-Based Wind Farm Power System," in 2021 IEEE 4th International Electrical and Energy Conference (CIEEC), Wuhan, China, 28-30 May 2021. doi:10.1109/CIEEC50170.2021.9510498

Xiaoming, Y., and Dichen, L. (2013). "Research on Dynamic Migration Mechanism of Out-of-step Oscillation center Based on Wide Area Measurement," in 3rd International Conference on Intelligent System Design and Engineering Applications (ISDEA), Hong Kong, China, 16-18 Jan. 2013. doi:10.1109/ISDEA.2012.275

Yan, J., Liu, C.-C., and Vaidya, U. (2011). PMU-based Monitoring of Rotor Angle Dynamics. *IEEE Trans. Power Syst.* 26 (4), 2125–2133. doi:10.1109/TPWRS.2011.2111465

Yang, J., Liao, Q. F., Tang, F., Wang, Y. F., Zhou, Y. T., and Tu, L. (2013). Study on Splitting Criterion Based on Improvement Ucosφ. *Amm* 433-435, 1313–1319. doi:10.4028/www.scientific.net/AMM.433-435.1313

Yang, N., Liu, S., Deng, Y., and Xing, C. (2021a). An Improved Robust SCUC Approach Considering Multiple Uncertainty and Correlation. *IEEJ Trans. Elec Electron. Eng.* 16 (1), 21–34. doi:10.1002/tee.23265

Yang, N., Qin, T., Wu, L., Huang, Y., Huang, Y., Xing, C., et al. (2022). A Multi-Agent Game Based Joint Planning Approach for Electricity-Gas Integrated Energy Systems Considering Wind Power Uncertainty. *Electric Power Syst. Res.* 204, 107673. doi:10.1016/j.epsr.2021.107673

Yang, N., Yang, C., Wu, L., Shen, X., Jia, J., Li, Z., et al. (2021b). Intelligent Data-Driven Decision-Making Method for Dynamic Multi-Sequence: An E-Seq2Seq Based SCUC Expert System. *IEEE Trans. Ind. Inf.*, 1. doi:10.1109/TII.2021.3107406

Yang, N., Yang, C., Xing, C., Ye, D., Jia, J., Chen, D., et al. (2021c). Deep Learning-based SCUC Decision-making: An Intelligent Data-driven Approach with Self-learning Capabilities. *IET Gener. Transm. Distrib.* doi:10.1049/gtd2.12315

Yang, W., Xue, Y., Song, X., Wu, D., Ge, F., and Xie, D. (2006). "Study on Stability Mechanism for a Typical Fault with EEAC Theory," in 2006 International Conference on Power System Technology, Chongqing, China, 22-26 Oct. 2006, 1–4. doi:10.1109/ICPST.2006.321621

Zhang, L., Xie, Y., Ye, J., Xue, T., Cheng, J., Li, Z., et al. (2021). Intelligent Frequency Control Strategy Based on Reinforcement Learning of Multi-Objective Collaborative Reward Function. *Front. Energ. Res.* 9, 587. doi:10.3389/fenrg.2021.760525

Zhang, S., and Zhang, Y. (2019). Characteristic Analysis and Calculation of Frequencies of Voltages in Out-of-step Oscillation Power System and a Frequency-Based Out-of-step Protection. *IEEE Trans. Power Syst.* 34 (1), 205–214. doi:10.1109/TPWRS.2018.2866022

Zheng, D., Ouyang, J., Xiong, X., and Li, M. (2019). Rotor Angle Stability Control for DFIG-integrated Power System Considering Phase-amplitude Characteristics of Transient-grid Voltage. *IET Generation, Transm. Distribution* 13 (16), 3549–3555. doi:10.1049/iet-gtd.2018.6960

Conflict of Interest: The authors declare that the research was conducted in the absence of any commercial or financial relationships that could be construed as a potential conflict of interest.

Publisher's Note: All claims expressed in this article are solely those of the authors and do not necessarily represent those of their affiliated organizations, or those of the publisher, the editors and the reviewers. Any product that may be evaluated in this article, or claim that may be made by its manufacturer, is not guaranteed or endorsed by the publisher.

frontiers in Energy Research

ORIGINAL RESEARCH
published: 17 January 2022
doi: 10.3389/fenrg.2021.836144

Numerical Weather Prediction Correction Strategy for Short-Term Wind Power Forecasting Based on Bidirectional Gated Recurrent Unit and XGBoost

Yu Li, Fei Tang, Xin Gao, Tongyan Zhang, Junfeng Qi, Jiarui Xie, Xinang Li and Yuhan Guo*

School of Electrical Engineering and Automation, Wuhan University, Wuhan, China

Accurate short-term wind power forecasting (WPF) plays a crucial role in grid scheduling and wind power accommodation. Numerical weather prediction (NWP) wind speed is the fundamental data for short-term WPF. At present, reducing NWP wind speed forecast errors contributes to improving the accuracy of WPF from the perspective of data quality. In this article, a variational mode decomposition combined with bidirectional gated recurrent unit (VMD-BGRU) method for NWP wind speed correction and XGBoost forecasting model are proposed. First, several NWP wind speed sub-series are divided by VMD to obtain more abundant multidimensional timing features. BGRU is applied to establish the potential relation between decomposed NWP wind speed sub-series and measured wind speed and get the proposed wind speed correction model. Then, a more clear regression forecasting model is trained based on XGBoost using historical measured wind speed and power. The corrected NWP wind speed is used to forecast wind power by XGBoost. Finally, the superiority of the proposed method is validated on a wind farm located in China. The results show that the proposed correction model and forecasting model outperform other compared models.

Keywords: short-term wind power forecasting, wind speed correction, bidirectional gated recurrent unit, variational mode decomposition, ensemble learning

OPEN ACCESS

Edited by:
Xun Shen,
Tokyo Institute of Technology, Japan

Reviewed by:
Yunyun Xie,
Nanjing University of Science and Technology, China
Lei Zhang,
China Three Gorges University, China

****Correspondence:***
Fei Tang
tangfei@whu.edu.cn

Specialty section:
This article was submitted to Smart Grids, a section of the journal Frontiers in Energy Research

Received: *15 December 2021*
Accepted: *24 December 2021*
Published: *17 January 2022*

Citation:
Li Y, Tang F, Gao X, Zhang T, Qi J, Xie J, Li X and Guo Y (2022) Numerical Weather Prediction Correction Strategy for Short-Term Wind Power Forecasting Based on Bidirectional Gated Recurrent Unit and XGBoost. Front. Energy Res. 9:836144. doi: 10.3389/fenrg.2021.836144

INTRODUCTION

Low-carbon economy is a worldwide problem of facilitating sustainable development (Li et al., 2021). In the past, coal, oil, and natural gas were the main primary energy, resulting in the rapid rise of carbon emissions, and global warming posed a threat to humans, directly or indirectly (Wang et al., 2019). Electrical energy is a vital form of energy. Constructing a new power system with a high penetration rate of new energy in the direction of low carbon is an effective way to reduce carbon emissions. In recent years, new energy power generation based on wind and solar energy has developed rapidly. According to the data released by Global Wind Report 2021, the global wind power installed capacity has reached 743 GW in 2020, of which 93 GW is newly installed (Global Wind Energy Council, 2021). It is widely recognized that wind power generation is one of the most potential and environmental energy resources (Okumus and Dinler, 2016). However, large-scale integration of wind power disrupts the balance of supply and demand in the power grid and brings huge challenges to safe and economic operation of the power grid (Zhang et al., 2021). Therefore,

accurate and reliable wind power forecasting (WPF) is an important segment for improving energy efficiency and ensuring safe operation of future power systems (Zhang et al., 2020; Zheng et al., 2017).

There are many kinds of classification methods. According to the timescales, very-short-term (Zhao et al., 2019), short-term (Yang et al., 2019), medium, and long-term prediction (Liu and Chen, 2019) are included. In general, there is no strict timescale. Ultrashort-term (from minutes to hours) prediction is used to balance load and control wind turbine in real-time; short-term (from hours to days) forecasting is utilized to formulate power generation plans and arrange reserve capacity; medium- and long-term prediction (from weeks to years) is vital for planning of windmills and site selection (Chen et al., 2017). Four types of modeling theory are grouped: physical method, traditional statistical method, artificial intelligence (AI) method, and hybrid method. The physical method requires detailed wind farm background data and numerical weather prediction (NWP), which shows better performance in medium- and long-term prediction with high-quality NWP (Hu et al., 2020). The traditional statistical method is represented by autoregressive integrated moving average (ARIMA) (Singh et al., 2021), seasonal autoregressive integrated moving average (SARIMA) (Liu et al., 2021), multilayer perceptron (MLP) (Deo et al., 2018; Shen et al., 2021b), and extreme learning machine (ELM) (Li et al., 2016), showing great accuracy in very-short-term prediction. And, many clustering methods are used (Shen et al., 2020). The AI method is popular for WPF under high-dimensional and big data conditions. (Shen and Raksincharoensak., 2021b). For example, an artificial neural network (ANN) (Song et al., 2018) such as back propagation neural network (BPNN), wavelet neural network WNN, and deep neural network (DNN) (Shen et al., 2021a), such as long short-term memory (LSTM) (Liu et al., 2018), gated recurrent unit (GRU) (Niu et al., 2020), and deep belief network (DBN) (Wang et al., 2018). The hybrid method can integrate the advantages of multiple methods, including a combination of the hyperparameter optimization algorithm and forecasting model (Khalid and Javaid, 2020; Zhu et al., 2020; Shen et al., 2017; Shen and Raksincharoensak., 2021a), weighted combination of prediction results of multiple models (Wu and Xiao, 2019; Yang et al., 2018), and stacked combination of multiple models (Liu et al., 2021, Yan et al., 2018). In recent years, cutting-edge AI technologies represented by ensemble methods have emerged, among which extreme gradient boosting (XGBoost) (Chen and Guestrin, 2016; Yang et al., 2021a) is the most typical. There are many applications in forecasting. Zheng and Wu, (2019) use the XGBoost model with weather similarity analysis and feature engineering to predict wind power. Liao et al., 2019 use XGBoost to evaluate similarity between the forecasting and historical days for load forecasting. Choi and Hur, (2020) use random forest (RF), XGBoost, and LightGBMs as ensemble models to forecast photovoltaic power. Besides, the forecasting objective can be grouped to wind turbine, single wind farm, and regional wind farm. This article concentrates on the short-term WPF for a single wind farm.

At present, lots of studies focus on optimization and refinement of the prediction model. However, the improvement of WPF accuracy depends more on data quality. NWP data, measured wind data and power data, are used for WPF. In general, measured data are more consistent with physical phenomena than historical forecast data, and it is important for very-short-term WPF to make full use of its time-series autocorrelation. NWP is the indispensable data source for short-term WPF since the time series recursion method causes error accumulation based on measured data. However, the resolution and accuracy of NWP are limited, and technical breakthroughs cannot occur in the short term. How to improve the power prediction accuracy under the current NWP accuracy level is a problem that needs to be studied. NWP wind speed correction is an effective way to improve the WPF accuracy from the perspective of the data, not the prediction model. Dong et al. (2013) use a linear correction model based on wavelet transform to correct the low-frequency stationary component of NWP wind speed, but it ignores the information on other frequencies. Zhang et al. (2019) propose a bias-correction method using an average, variance trend to correct the simulated wind speed based on historical data. Hu et al. (2021) propose a hybrid NWP wind speed correction model based on principal component analysis and improved deep belief network. Wang et al. (2019) propose a sequence transfer correction algorithm to correct the NWP wind speed and to obtain the correction results under different time steps, which is suitable for very-short-term WPF. Zhao et al. (2017) divide wind speed forecasting series into segments and combine the Cuckoo search optimized fuzzy clustering and *a priori* algorithm to correct weather research and forecasting (WRF) wind speed. Yang et al. (2021b) propose an expanded sequence-to-sequence (E-Seq2Seq)–based data-driven SCUC expert system for dynamic multiple-sequence mapping samples, which can accommodate the mapping samples of SCUC and consider the various input factors that affect SCUC decision-making as the first study about SCUC problems (Yang et al., 2021c; Yang et al., 2019). It has strong generality, high solution accuracy, and efficiency over traditional methods. Therefore, how to make full use of the potential relationship between NWP wind speed and historical measured wind speed and propose a method for short-term forecasting of wind speed correction are still worth studying.

This article proposes a variational mode decomposition and bidirectional GRU (VMD-BGRU) correction strategy for NWP wind speed and applies the optimized NWP wind speed to forecast wind power using the ensemble learning method XGBoost. First, in order to enrich the features of the input data, the VMD algorithm is used to decompose the NWP wind speed. The BGRU is used to correct the NWP wind speed based on the potential correlation between the multiple decomposed NWP wind speed sub-series and the measured wind speed. Then, the XGBoost algorithm is utilized to build the forecasting model according to the regression relationship between the measured wind speed and power, and the corrected NWP wind speed is input into the prediction model to obtain the short-term prediction results of wind power. Finally,

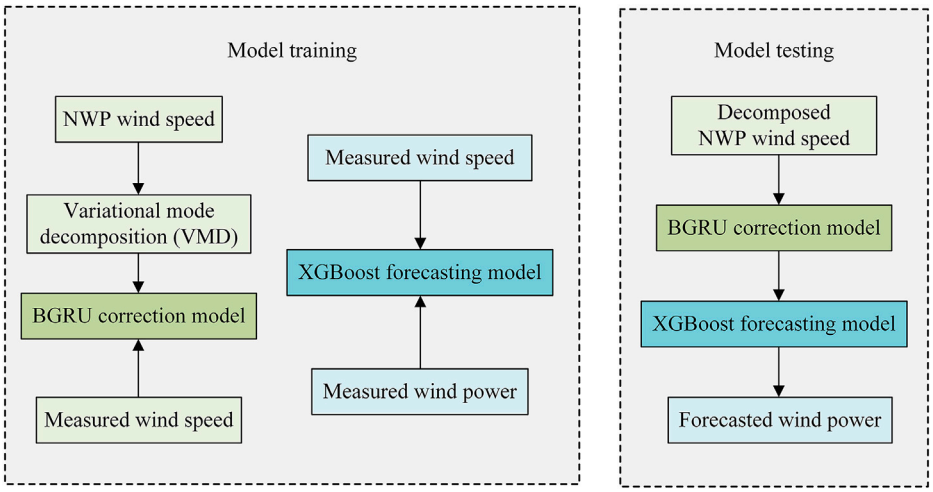

FIGURE 1 | Frame of short-term wind power forecasting.

the evaluation metrics is used to assess the performance of NWP wind speed correction and wind power forecasting.

The remainder of this article is organized as follows. In **Section 2**, the whole flowchart is simply generalized, and the basic theory of VMD, BGRU, and XGBoost is explained. Case study and discussion about the proposed method are shown in *Case Study*. *Conclusion* concludes this article.

METHODS

The framework of the proposed NWP wind speed correction strategy for short-term wind power forecasting is shown in **Figure 1**. First, the original NWP wind speed series is enriched by the VMD algorithm. The NWP wind speed is corrected with the measured wind speed as the target by the BGRU correction model. Then, the forecasting model based on XGBoost is trained with measured wind speed and power. Finally, improved forecasted wind power is obtained using corrected NWP wind speed as input.

The NWP Wind Speed Correction Strategy

In the wind farm operation, the measured data mainly include wind speed, wind direction, air pressure, humidity, and temperature from the wind tower and the active output power of the wind farm from the SCADA. NWP is a method used to predict the state of atmospheric movement and weather phenomena by solving the operating equations of atmospheric movement by means of large computers under given initial and boundary conditions of the atmosphere (Al-Yahyai et al., 2011). However, the NWP applied to wind power forecasting is provided by meteorological products purchased by third-party forecasting platforms, which contain meteorological information, such as wind speed and direction, at different heights in a specific area (Heppelmann et al., 2017; Shen et al., 2020). In this article, only the measured wind speed at the hub and the NWP wind speed at 70 m are considered.

As we all know, the atmosphere is full of chaos, and there is no absolutely accurate forecast of wind speed. The difficulty of wind power forecasting caused by the inaccuracy of wind speed forecast is mainly reflected in the regression characteristics of wind speed and power. Generally speaking, the power of wind turbines is proportional to the third power of wind speed (Xu et al., 2021). The power curve of the wind farm is slightly fuzzy compared with that of the wind turbine, as shown in **Figure 2**. However, if the measured wind speed is replaced by NWP wind speed, as shown in **Figure 3**, the regression characteristics will be seriously lost. Moreover, NWP wind speed is generally less than the measured wind speed. For example, the range of NWP wind speed is concentrated in 0–8 m/s, while the measured wind speed is concentrated in 3–12 m/s. Obviously, the measured wind speed cannot be predicted in advance, which will bring difficulties to the WPF. Therefore, it is necessary to correct NWP wind speed.

First, the VMD algorithm is used to enrich the original NWP wind speed series by decomposing it to several sub-series. Then, the correction model is established by BGRU based on decomposed NWP wind speed and measured wind speed. The VMD algorithm and BGRU are explained as 2.2.1 and 2.2.2, respectively.

The VMD Algorithm

VMD is a new signal decomposition estimation method proposed in 2014 (Konstantin and Dominique, 2014) which aims to decompose the original complex signal into K sub-series with different central frequencies. The VMD method uses non-recursive and variational modal decomposition to process the original signal, which has better robustness to the measurement noise.

It is assumed that f is the original NWP wind speed series. $\{u_k(t)\}, k = 1, 2, \ldots, K$ is the decomposed intrinsic modal

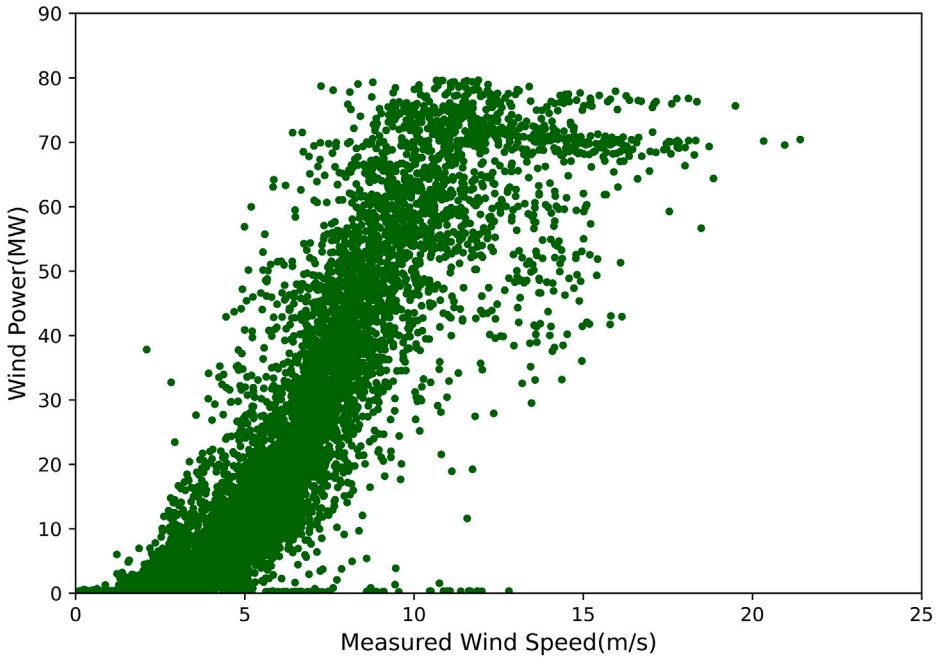

FIGURE 2 | Relation between measured wind speed and wind power.

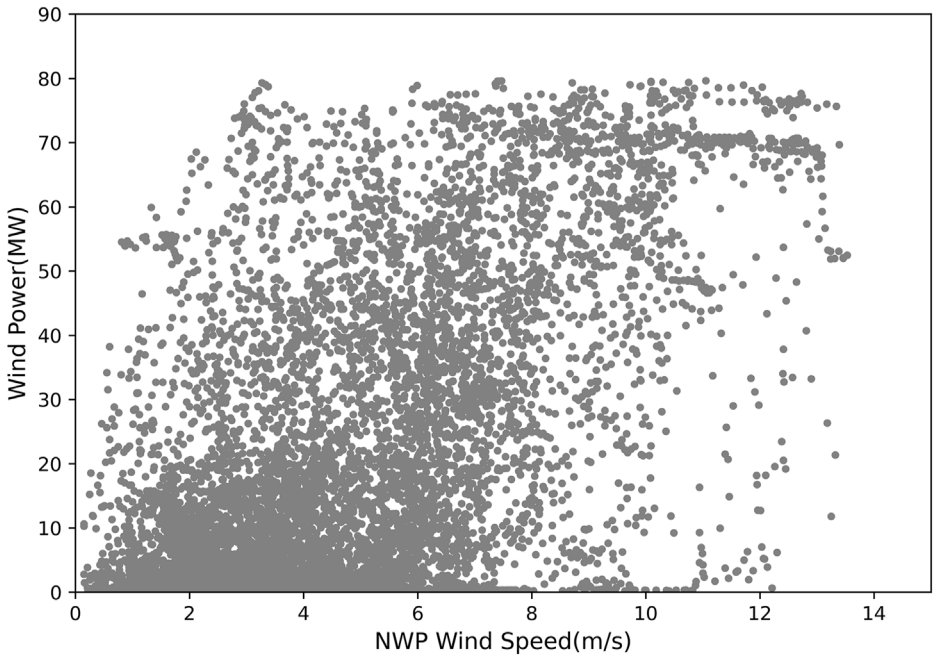

FIGURE 3 | Relation between NWP wind speed and wind power.

function (IMF) with finite bandwidth. First, for each IMF, the corresponding analytic signal is calculated by Hilbert transformation, so its unilateral spectrum is shown in **Eq. 1**. Then, the analytical signals of each IMF are mixed with the estimated central frequency $e^{-j\omega_k t}$, and the spectrum of each IMF is modulated to the corresponding baseband, as shown in **Eq. 2**. Finally, the Gaussian smoothing method of demodulated signals is used to estimate the bandwidth of

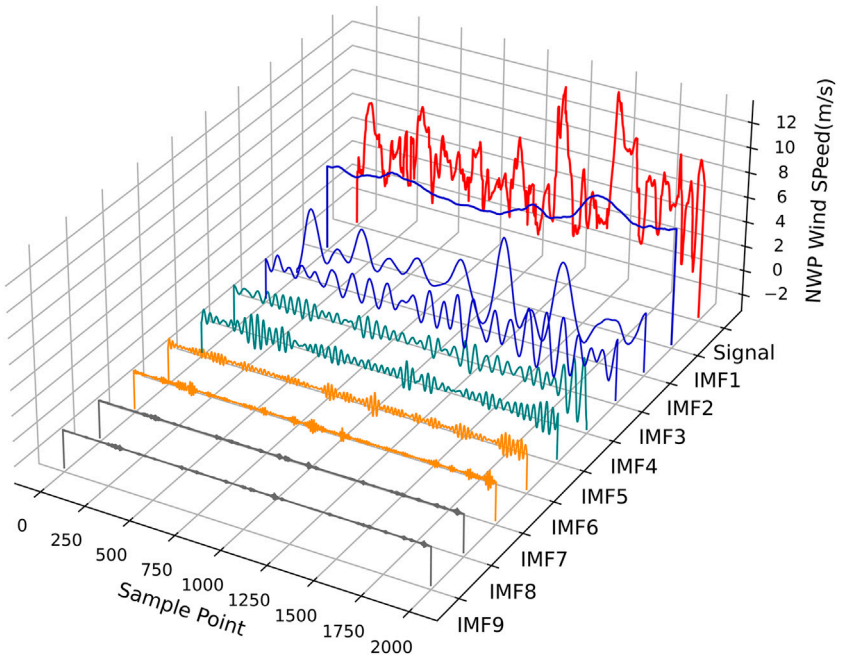

FIGURE 4 | Results of VMD.

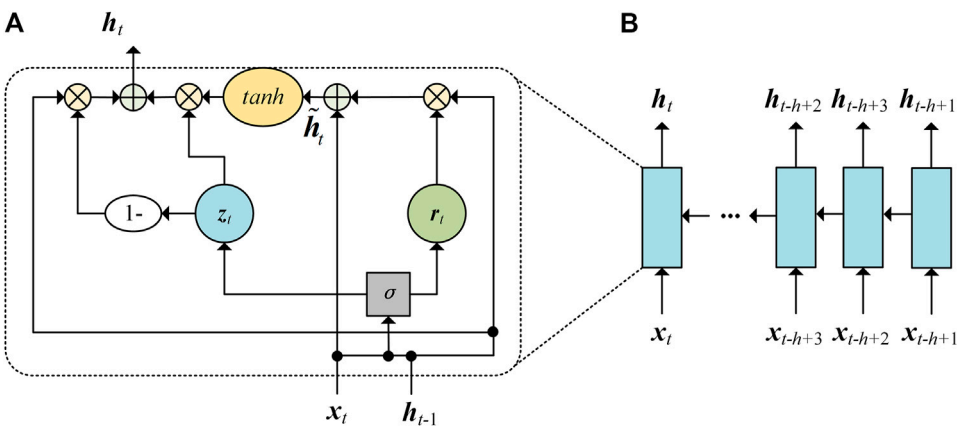

FIGURE 5 | (A) Structure of the GRU cell. **(B)** Structure of GRU.

each IMF and solve the variational problem with constraints. The optimization problem can be described preliminarily as **Eq. 3** shows.

$$\left[\delta(t)+\frac{j}{\pi t}\right]*u_k(t), \tag{1}$$

$$\left[\left(\delta(t)+\frac{j}{\pi t}\right)*u_k(t)\right]e^{-j\omega_k t}, \tag{2}$$

$$\begin{cases} \min\limits_{\{u_k\},\{\omega_k\}} \left\{ \sum\limits_k \left\| \partial_t \left[\left(\delta(t)+\frac{j}{\pi t} \right) * u_k(t) \right] e^{-j\omega_k t} \right\|^2 \right\} \\ s.t. \sum\limits_k u_k = f \end{cases} \tag{3}$$

where $\{u_k\}=\{u_1, u_2, \ldots, u_K\}; \{\omega_k\}=\{\omega_1, \omega_2, \ldots, \omega_K\}$. In order to solve this variational problem, there are two steps. First, the constrained variational problem is transformed into a non-constrained variational problem by introducing the quadratic penalty factor α and the Lagrange multiplication operator $\lambda(t)$, in which the quadratic penalty factor can guarantee the signal reconstruction accuracy in the presence of Gaussian noise, and the Lagrange operator keeps the constraint conditions strict. Then, the alternating direction method of multipliers is adopted to search the "saddle point" of the extended Lagrange expression by alternately updating $u_k^{n+1}, \omega_k^{n+1}, and\, \lambda^{n+1}$. The detailed derivation is available in

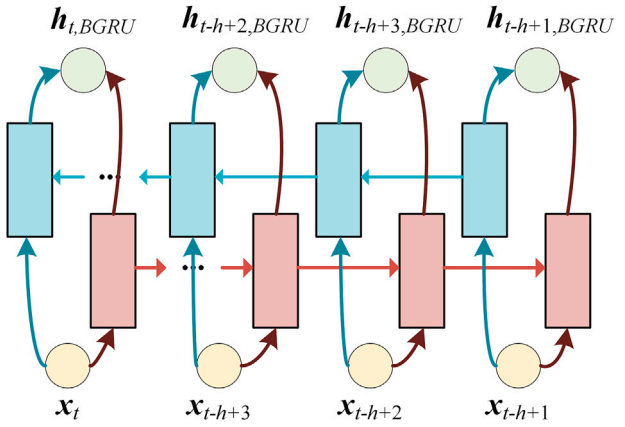

FIGURE 6 | Structure of BGRU.

the study by Konstantin and Dominique (2014). Finally, the solution $\hat{u}_k^{n+1}(\omega)$, central frequency ω_k^{n+1}, and λ^{n+1} are written as follows:

$$\begin{cases} \hat{u}_k^{n+1}(\omega) = \dfrac{\hat{f}(\omega) - \sum_{i\neq k}\hat{u}_i(\omega) + \dfrac{\hat{\lambda}(\omega)}{2}}{1 + 2\alpha(\omega - \omega_k)^2} \\ \omega_k^{n+1} = \dfrac{\int_0^\infty \omega|\hat{u}_k(\omega)|^2 d\omega}{\int_0^\infty |\hat{u}_k(\omega)|^2 d\omega} \\ \hat{\lambda}^{n+1}(\omega) = \hat{\lambda}^n(\omega) + \tau\left[\hat{f}(\omega) - \sum_k \hat{u}_k^{n+1}(\omega)\right] \end{cases} \tag{4}$$

In brief, the steps of the VMD algorithm are summarized as follows.

Step 1: Initializing $\{\hat{u}_k^1\}$, $\{\omega_k^1\}$, $\{\lambda_k^1\}$, and n and determining the number of IMF K.
Step 2: Updating u_k, ω_k, and λ according to **Eq. 4**.
Step 3: Stopping the iteration if given error $e > \sum_k ||\hat{u}_k^{n+1} - \hat{u}_k^{n2}||/\hat{u}_k^n||$; otherwise, returning to step 2.

Take the NWP wind speed series at 2000 sampling points for example. As **Figure 4** shows, IMF 1 to IMF 9 are the decomposed sub-series. There is no mode aliasing existed in all the IMFs. Therefore, VMD shows perfect performance in decomposing the non-stationary NWP wind speed signal. The selection of parameters, such as K and α, is discussed in the case study.

The BGRU Network

In this section, the correction model comprising BGRU is proposed. The basic building block GRU cell and its working scheme are presented at first. Then, BGRU is obtained by connecting two unidirectional GRUs.

The structure of a GRU cell and unidirectional GRU's working scheme are shown in **Figure 5**. An update gate $\boldsymbol{z}_t$ and a reset gate $\boldsymbol{r}_t$ contribute the basic function of the GRU cell. They are computed as **Eq. 5** shows. The GRU updates the hidden state $\boldsymbol{h}_t$ by calculating the hidden state $\boldsymbol{h}_{t-1}$ of the previous moment and the external input $\boldsymbol{x}_t$ of the current moment as **Eq. 6** shows. GRU has the ability of long-term memory of useful information because of the flexible control and coordination of these gates.

$$\begin{bmatrix} \boldsymbol{z}_t \\ \boldsymbol{r}_t \end{bmatrix} = \sigma\begin{bmatrix} \boldsymbol{W}_z & \boldsymbol{U}_z \\ \boldsymbol{W}_r & \boldsymbol{U}_r \end{bmatrix}\begin{bmatrix} \boldsymbol{x}_t \\ \boldsymbol{h}_{t-1} \end{bmatrix} + \begin{bmatrix} \boldsymbol{b}_z \\ \boldsymbol{b}_r \end{bmatrix}, \tag{5}$$

$$\tilde{\boldsymbol{h}}_t = \boldsymbol{tanh}\left(\boldsymbol{W}_{\tilde{h}_t}\boldsymbol{x}_t + \boldsymbol{U}_{\tilde{h}_t}(\boldsymbol{r}_t \odot \boldsymbol{h}_{t-1}) + \boldsymbol{b}_{\tilde{h}_t}\right), \tag{6}$$

$$\boldsymbol{h}_t = \boldsymbol{z}_t \odot \tilde{\boldsymbol{h}}_t + (\boldsymbol{1} - \boldsymbol{z}_t) \odot \boldsymbol{h}_{t-1}, \tag{7}$$

where $\boldsymbol{W}_z$, $\boldsymbol{W}_r$, $\boldsymbol{W}_{\tilde{h}_t}$, $\boldsymbol{U}_z$, $\boldsymbol{U}_r$, and $\boldsymbol{U}_{\tilde{h}_t}$ denote weight matrixes, respectively, $\boldsymbol{b}_z$, $\boldsymbol{b}_r$, $\boldsymbol{b}_{\tilde{h}_t}$ denote bias, respectively, $\tilde{\boldsymbol{h}}_t$ is the intermediate variable, σ denotes the activation function, and $\odot$ denotes the Hadamard operation.

For the abovementioned GRU, variables are updated from the past to the future, so there is monodirectional dependence between the hidden states. Specifically, as shown in **Figure 5**, $\boldsymbol{h}_t$ is related to all inputs ($\boldsymbol{x}_{t-h+1}$, $\boldsymbol{x}_{t-h+2}$, …, $\boldsymbol{x}_t$), while the hidden state at the last time $\boldsymbol{h}_{t-1}$ has nothing to do with $\boldsymbol{x}_t$. Therefore, only the final hidden state can fully utilize all input information, while the hidden state at other times does not consider the subsequent inputs for monodirectional GRU. To overcome this disadvantage, BGRU uses both forward and reverse GRUs with chronological relationship to make full use of all input information. **Figure 6** shows the structure of BGRU. The hidden state of BGRU $\boldsymbol{h}_{t,BGRU}$ is calculated as **Eq. 8**.

$$\boldsymbol{h}_{t,BGRU} = \left[\vec{\boldsymbol{h}}_t \oplus \overleftarrow{\boldsymbol{h}}_t\right], \tag{8}$$

where $\vec{\boldsymbol{h}}_t$ and $\overleftarrow{\boldsymbol{h}}_t$ represent the hidden state of forward and reverse GRU, respectively, and $\oplus$ denotes the sum of the corresponding elements.

The Ensemble Forecasting Method

The forecasting model is described in this section. XGBoost is a boosting ensemble learning algorithm which iteratively generates new trees by continuously fitting the residuals of the previous tree and constructs the tree model into a classifier with higher accuracy and stronger generalization ability (Chen and Guestrin, 2016), which is widely used in lots of Kaggle competitions and has achieved good results in recent years. Compared with GBDT, the XGBoost has the following advantages. The XGBoost algorithm uses Hessian matrix to expand the loss function Taylor to the second order, transforms the original optimization problem into convex function to obtain the optimal solution, and solves the distributed computing problem which is difficult to implement in the GBDT algorithm. In addition to this, XGBoost regularizes the complexity of the tree and reduces the possibility of overfitting the model. Therefore, wind and

power data can be better fitted by the XGBoost algorithm, and forecasting error is reduced, and higher prediction accuracy is achieved.

For the dataset $G = (\boldsymbol{x}_i,\ y_i)$ with n samples and m features, where $|G| = n$, $\boldsymbol{x}_i \in R^m$, and $y_i \in R$, the predicted value of the model is obtained from **Eq. 9**,

$$\hat{y}_i = \varnothing(\boldsymbol{x}_i) = \sum_{z=1}^{Z} f_z(\boldsymbol{x}_i), \tag{9}$$

where $f_z(\boldsymbol{x}) = w_q(\boldsymbol{x})$, $w_q(\boldsymbol{x})$ is the score of $\boldsymbol{x}$, $\hat{y}_i$ is the sum of all the scores. q is the structure of each tree, and Z is the number of the trees. Each f_z corresponds to an independent tree structure q and leaf weight w; the newly generated tree fits the residual of the last prediction. The iteration process is shown as follows.

$$\begin{cases} \hat{y}_i^{(0)} = 0 \\ \hat{y}_i^{(1)} = f_1(x_i) = \hat{y}_i^{(0)} + f_1(x_i) \\ \hat{y}_i^{(z)} = \hat{y}_i^{(z-1)} + f_z(x_i) \end{cases}, \tag{10}$$

where $\hat{y}_i^{(z)}$ is the forecasted value after z iterations of the ith sample, and $\hat{y}_i^{(0)}$ is the initial value of the ith sample. The objective function that needs to be minimized is shown as follows.

$$L_{obj} = \sum_{i=1}^{n} l(\hat{y}_i,\ y_i) + \sum_{z=1}^{Z} \Omega(f_z), \tag{11}$$

$$\Omega(f_z) = \gamma T + \frac{1}{2}\lambda ||w||^2, \tag{12}$$

where $l(\hat{y}_i,\ y_i)$ is a differentiable convex loss function between the prediction and target. $\Omega(f_z)$ is a regularization term, representing the complexity of the tree. The smaller the function value is, the stronger the generalization ability of the tree is. T is the number of middle nodes of the tree; w is leaf node fraction; γ is the penalty coefficient of the number of leaf nodes; and λ is the penalty coefficient of the L2 regularization term, which smoothen the learning weights of leaf nodes to avoid overfitting.

The iterative function based on additive training can be written as **Eq. 13**. Then, the second-order Taylor approximation of the original objective function is written as **Eq. 14**.

$$L_{obj}^{(z)} = \sum_{i=1}^{n} l\left(\hat{y}_i,\ \hat{y}_i^{(z-1)} + f_z(\boldsymbol{x}_i)\right) + \Omega(f_z), \tag{13}$$

$$\begin{aligned} L_{obj}^{(z)} \approx & \left(\sum_{i=1}^{n} l\left(\hat{y}_i,\ \hat{y}_i^{(z-1)}\right) + g_i f_z(\boldsymbol{x}_i) + \frac{1}{2} h_i f_z^2(\boldsymbol{x}_i)\right) \\ & + \left(\gamma T + \frac{\lambda}{2} j = 1 \sum_{j=1}^{T} w_j^2 + C\right), \end{aligned} \tag{14}$$

where $g_i = \partial l(y_i,\ \hat{y}_i^{(z-1)})/\partial \hat{y}_i^{(z-1)}$ and $h_i = \partial^2 l(y_i,\ \hat{y}_i^{(z-1)})/\partial (\hat{y}_i^{(z-1)})^2$. After removing all the constant terms, the objective function is rewritten as a function about the leaf node fraction as follows.

$$L_{obj}^{(z)} \approx \sum_{j=1}^{T}\left[\left(\sum_{i\epsilon I_j} g_i\right) w_j + \frac{1}{2}\left(\sum_{i\epsilon I_j} hi + \lambda\right) w_j^2\right] + \gamma T, \tag{15}$$

where j is the traversal on the leaf node; w_j is the score of the jth leaf node; and $I_j = \{i|q(\boldsymbol{x}_i) = j\}$ represents the samples on the jth leaf node. Finally, the optimal solution of the objective function is written as **Eq. 16**, where $G_j = \sum_{i\epsilon I_j} g_i$ and $H_j = \sum_{i\epsilon I_j} h_i$. The minimum of **Eq. 15** is rewritten as **Eq. 17**.

$$w_j^* = -\frac{G_j}{H_j + \lambda}, \tag{16}$$

$$L_{obj\_optim}^{(z)} = -\frac{1}{2}\sum_{j=1}^{T} \frac{G_j^2}{H_j + \lambda} + \gamma T. \tag{17}$$

Here, $L_{obj\_optim}^{(z)}$ represents the maximum gain loss when selecting a tree structure. The smaller the value is, the better the model is. During training, XGBoost greedily uses error functions to continuously improve the current model.

CASE STUDY

In this section, the actual wind farm data are utilized to support two experiments which are designed to verify the proposed NWP wind speed correction strategy and wind power forecasting method. The wind farm data include measured wind speed, measured wind direction, output wind power, and NWP from January to December 2019, which are sampled at a period of 15 min. However, only wind speed and power are used in this study since the relation between wind speed and wind power is mainly focused. This wind farm is located in eastern China, whose installed capacity is 85 MW.

The following experiments are implemented on a Windows 10 PC with AMD Ryzen 5 3550H, 2.1 GHz CPU, 16 GB of RAM and Python 3.8 with PyTorch 1.8.1.

The case study is divided into two parts, NWP wind speed correction and power forecasting. First, the NWP wind speed is corrected according to the measured wind speed by the VMD-BGRU correction strategy, which is to validate the effectiveness of the proposed wind speed correction strategy. And then, the forecasting model is trained by measured wind speed and wind power using the XGBoost algorithm since the measured data have clearer mapping. Finally, the corrected NWP wind speed is input to forecast wind power.

Performance Criterion

For the purpose of evaluating the correction and forecasting performance of the proposed strategy, the root mean square error (RMSE) and mean absolute error (MAE) are used as the performance criterions. In addition, the evaluation metrics of wind speed correction and WPF are a little bit different. Obviously, the smaller the value, the better the performance of the proposed model. These equations are defined as follows:

$$\begin{cases} \mathbf{RMSE}_{\mathrm{p}} = \sqrt{\frac{1}{N}\sum_{i=1}^{N}\left(\frac{P_i - \hat{P}_i}{C}\right)^2} \times 100\% \\ \mathbf{MAE}_{\mathrm{p}} = \frac{1}{N}\sum_{i=1}^{N}\left|P_i - \hat{P}_i\right| \end{cases} \tag{18}$$

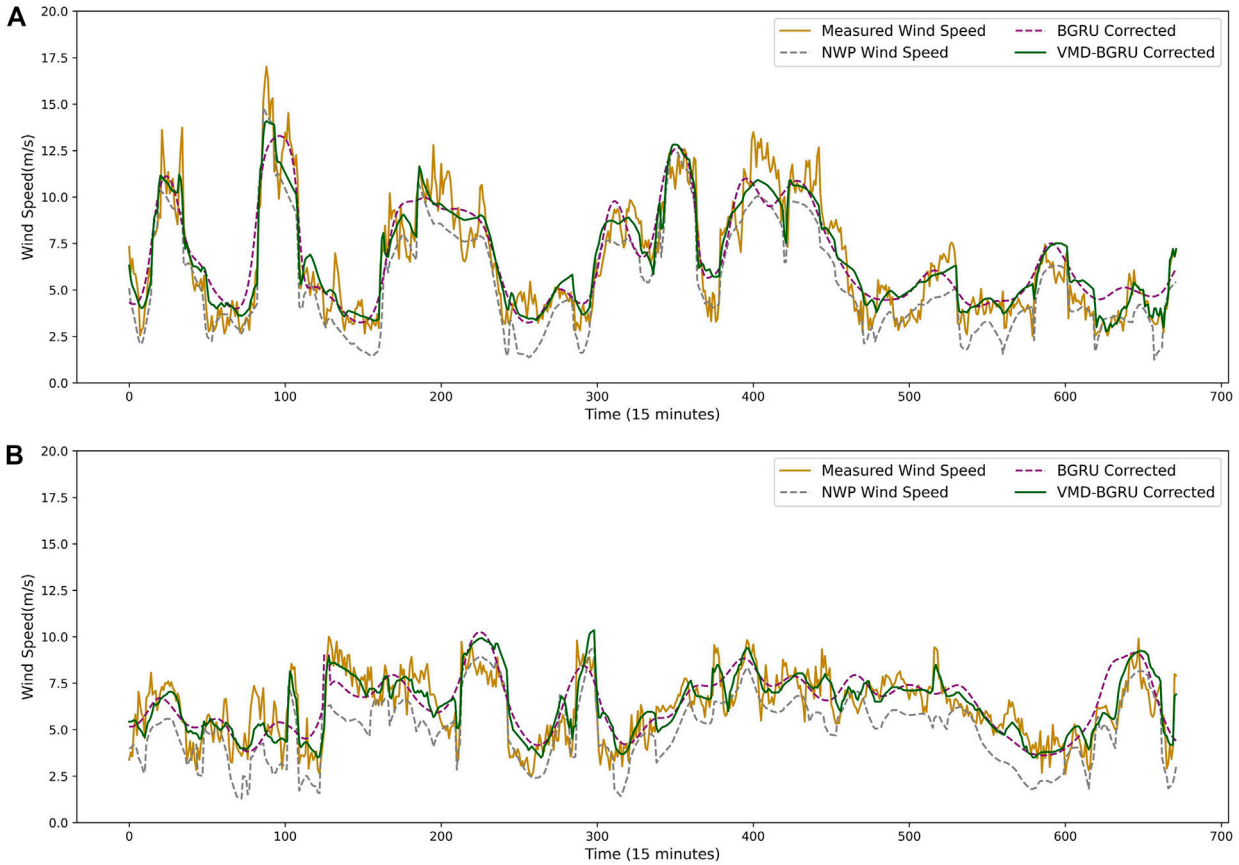

FIGURE 7 | Results of NWP wind speed correction. **(A)** Result for the first week of March. **(B)** Result for the first week of June.

TABLE 1 | Evaluation results of corrected wind speed.

		NWP		BGRU corrected		VMD-BGRU corrected	
		$RMSE_v$ (m/s)	**MAE_v (m/s)**	**$RMSE_v$ (m/s)**	**MAE_v (m/s)**	**$RMSE_v$ (m/s)**	**MAE_v (m/s)**
March	Day 1	1.351	1.014	1.791	1.461	1.788	1.408
	Day 2	1.851	1.547	1.265	0.956	1.193	0.944
	Day 3	1.748	1.408	1.181	0.92	1.089	0.882
	Day 4	1.415	1.186	1.308	1.128	1.16	0.964
	Day 5	1.939	1.666	1.582	1.278	1.313	1.07
	Day 6	1.37	1.153	1.021	0.828	0.912	0.743
	Day 7	0.997	0.771	0.963	0.721	0.948	0.677
June	Day 1	1.963	1.726	1.202	0.93	1.057	0.818
	Day 2	2.129	1.872	1.528	1.307	0.799	0.674
	Day 3	1.167	0.878	1.602	1.307	1.501	1.145
	Day 4	1.522	1.277	1.087	0.857	1.063	0.887
	Day 5	1.47	1.2	1.089	0.88	0.761	0.589
	Day 6	1.85	1.583	0.939	0.752	0.604	0.504
	Day 7	1.523	1.21	1.477	1.151	0.985	0.785

TABLE 2 | Hyper-parameter selection of XGBoost.

Hyper-parameter	Searching result	Search range and step
Number of estimators	15	{1,200,1}
Eta	0.35	{0.01,0.9,0.05}
Max depth	5	{1,10,1}
Min child weight	1	{1,10,1}

$$\begin{cases} \mathbf{RMSE_v} = \sqrt{\frac{1}{N}\sum_{i=1}^{N}\left(V_i - \hat{V}_i\right)^2} \\ \mathbf{MAE_v} = \frac{1}{N}\sum_{i=1}^{N}\left|V_i - \hat{V}_i\right| \end{cases}, \tag{19}$$

where P_i, $\hat{P}_i$ are ith actual wind power and forecasting power, V_i, $\hat{V}_i$ are ith measured wind speed and corrected wind speed, C is the installed capacity of the wind farm, $\mathbf{RMSE_v}$, $\mathbf{MAE_v}$, and $\mathbf{RMSE_p}$, $\mathbf{MAE_p}$ are the evaluation criterions of wind speed correction and wind power forecasting, respectively, and N is the total number of test samples.

Data Processing

For one thing, the wind farm data have some abnormal data caused by wind curtailment, power cuts, failure of measuring device, and so on, which should be deleted. For another, normalization is required to eliminate the different data ranges between wind speed and wind power to better meet the requirement of model training, which is expressed as follows:

$$x_i' = \frac{x_i - x_{min}}{x_{max} - x_{min}}, \tag{20}$$

where x_i' is the ith normalized value, x_i is the ith real value before normalization, and x_{max} and x_{min} are the maximum and minimum value in the dataset, respectively. The real value is also obtained by **Eq. 20** to calculate the evaluation metrics.

The Results of NWP Wind Speed Correction

In this section, the accuracy of NWP wind speed is improved through the VMD-BGRU correction strategy. To verify the superiority of the proposed correction strategy, the original NWP wind speed and corrected wind speed by BGRU is compared with VMD-BGRU. The result of the first week (a total of 672 sample points) in March and June is taken as a test dataset. Accordingly, the training dataset is the previous 3 months (a total of 8640 sample points). Besides, $\mathrm{RMSE_v}$ and $\mathrm{MAE_v}$ are used as evaluation metrics, whose units are m/s.

The number of IMF K is determined by observing central frequency. If the IMFs with close center frequency appear, it is considered to be over-decomposed. There are 8640 NWP wind speed samples that need to be decomposed in the testing set. The K is chosen as 6 by the traversal method. α is the default value 2000. τ is 1e-6 to ensure the fidelity of the actual signal decomposition. The number of BGRU layers is set to 2. The sub-series decomposed from NWP wind speed is fed into the BGRU network which extracts complex relation between multi-frequency domain signal and measured wind speed. Besides, a fully connected layer is used to transform the flattened vector to one dimension. The learning rate and epochs are set to 5e-3 and 300, respectively. Adam optimizer and MSELoss are used for model training.

The discussion about the experiment is described below. **Figure 7** shows the performance of the proposed correction strategy in the first 7 days in March and June. Obviously, the measured wind speed is higher than NWP wind speed most of the time. The average NWP wind speed and measured wind speed were 5.271 and 6.532 m/s in 2019, respectively. In addition, the fluctuation of measured wind speed is more severe than that of NWP wind speed. The 7 days' evaluation result is summarized in **Table 1.** Here are some findings summed from these statistical data.

(1) The proposed correction method performs better than NWP wind speed forecasting. Take these data for example. In March, the $\mathrm{RMSE_v}$ and $\mathrm{MAE_v}$ of VMD-BGRU corrected wind speed are smaller than that of NWP wind speed in test days except day 1. The NWP wind speed forecasting is not always inaccurate, and the correction model tends to raise it. Thus, a small amount of negative correction is inevitable, but it is beneficial to improve the accuracy of the forecast wind speed on the whole. The average $\mathrm{RMSE_v}$ and $\mathrm{MAE_v}$ of the VMD-BGRU model are 1.200 and 0.955 m/s in March, respectively, which reduced to 0.324 and 0.294 m/s compared with NWP wind speed, respectively. Moreover, the average $\mathrm{RMSE_v}$ and $\mathrm{MAE_v}$ of the proposed model are 0.967 and 0.780 m/s in June, respectively, which reduced to 0.693 and 0.612 m/s compared with NWP wind speed, respectively. Overall, the result confirms the efficiency of the proposed strategy.

(2) The VMD-BGRU also show a little advantage than BGRU. For instance, the average $\mathrm{RMSE_v}$ and $\mathrm{MAE_v}$ of the BGRU correction model are 1.302 and 1.042 m/s, respectively, while the average $\mathrm{RMSE_v}$ and $\mathrm{MAE_v}$ of the proposed model are 0.101 and 0.086 m/s less, respectively, in March. And, in June, the average $\mathrm{RMSE_v}$ and $\mathrm{MAE_v}$ of the BGRU correction model are 1.275 and 1.026 m/s, respectively, while the average $\mathrm{RMSE_v}$ and $\mathrm{MAE_v}$ of the proposed model are 0.308 and 0.246 m/s less, respectively. The result indicates that VMD can enrich the information of NWP wind speed signal by decomposing it to several sub-series in different frequencies. From this result, it is clear that the VMD-BGRU correction strategy shows better performance than compared strategies.

However, some limitations are found in this case. First, NWP wind speed is difficult to capture the abundant small-scale fluctuation information of measured wind speed, which is widely accepted. Even after the proposed wind speed correction, the measured wind speed fluctuation information is still hard to be described perfectly. In addition to this, the proposed wind speed correction does not always correct NWP wind speed positively. The complicated topography brings many uncertain factors to wind speed prediction, but there are always a few periods of accurate NWP forecasting. Inevitably, there will be negative corrections, for

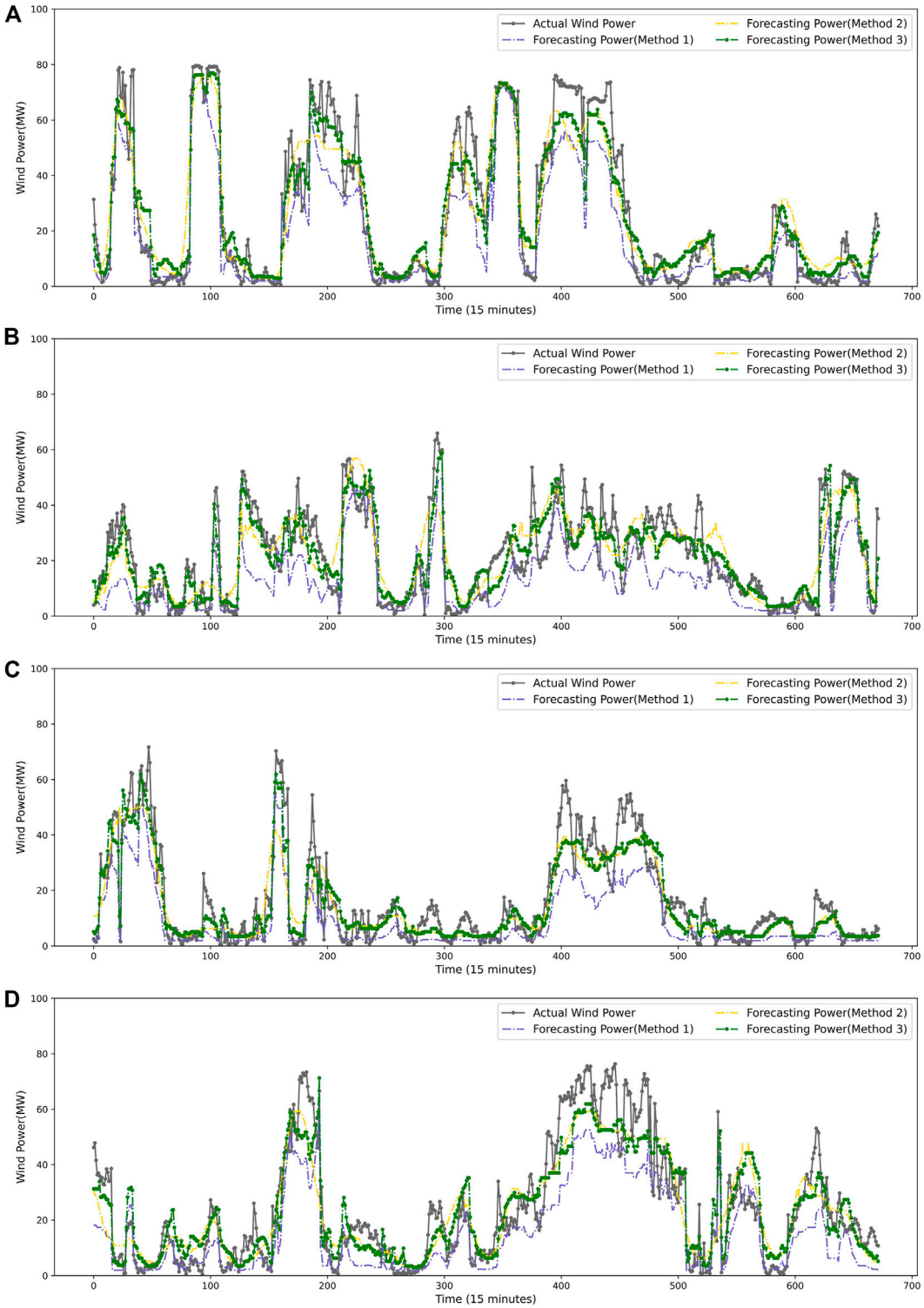

FIGURE 8 | Results of WPF. **(A)** Result for the first week of March. **(B)** Result for the first week of June. **(C)** Result for the first week of September. **(D)** Result for the first week of December.

example, NWP wind speed in day 3 of June and day 1 of March is incorrected. Despite the very low probability of negative correction, NWP wind speed can be effectively corrected most of the time.

The Results of WPF

In this section, the abovementioned NWP wind speed correction strategy is applied to WPF to further validate its advantage. First

TABLE 3 | Evaluation results of the corrected wind speed in March and June.

		Method 1		Method 2		Method 3	
		$RMSE_p$ (%)	MAE_p (MW)	$RMSE_p$ (%)	MAE_p (MW)	$RMSE_p$ (%)	MAE_p (MW)
March	Day 1	11.164	5.543	14.586	8.673	10.685	6.669
	Day 2	16.529	9.023	12.412	7.169	8.326	5.055
	Day 3	16.392	8.455	10.882	6.023	8.723	5.134
	Day 4	18.835	10.871	14.221	8.289	11.53	7.456
	Day 5	22.791	15.86	15.714	10.841	13.585	9.357
	Day 6	6.073	4.145	6.025	4.034	5.615	3.564
	Day 7	8.126	4.157	8.013	4.049	7.87	3.878
June	Day 1	14.486	8.533	9.391	6.346	6.68	4.458
	Day 2	20.908	13.628	14.881	9.26	8.151	5.292
	Day 3	10.572	5.728	13.734	8.522	9.233	5.874
	Day 4	14.653	8.627	14.085	8.248	11.48	7.802
	Day 5	18.385	11.797	12.278	8.293	9.542	6.999
	Day 6	16.432	10.775	9.985	7.512	7.826	5.676
	Day 7	14.089	7.425	14.045	7.359	8.322	4.39

TABLE 4 | Evaluation results of the corrected wind speed in September and December.

		Method 1		Method 2		Method 3	
		$RMSE_p$ (%)	MAE_p (MW)	$RMSE_p$ (%)	MAE_p (MW)	$RMSE_p$ (%)	MAE_p (MW)
September	Day 1	11.966	5.965	11.511	7.46	8.906	5.931
	Day 2	17.618	10.113	11.989	7.455	11.135	7.378
	Day 3	10.335	6.058	8.403	4.68	7.632	4.119
	Day 4	12.037	7.621	11.461	7.434	10.25	6.72
	Day 5	28.484	20.935	17.206	12.193	15.56	12.95
	Day 6	15.868	10.273	9.172	5.773	8.935	5.839
	Day 7	15.027	9.438	7.577	4.957	6.537	5.906
December	Day 1	16.085	9.217	12.439	6.309	9.207	5.388
	Day 2	13.558	7.313	13.442	7.124	13.228	7.017
	Day 3	7.818	4.534	7.747	4.239	7.063	4.001
	Day 4	6.939	4.039	5.075	3.231	5.062	3.109
	Day 5	23.333	16.491	12.901	8.627	12.664	8.561
	Day 6	8.26	4.954	7.795	4.715	7.116	4.61
	Day 7	7.54	4.566	4.36	2.475	4.354	2.354

of all, the power forecasting model is established according to the measured wind speed and power. Then, the different forecasting wind speed corrected by BGRU and VMD-BGU is utilized to forecast power. Also, the original NWP wind speed is used as a benchmark. Therefore, results are obtained to compare the differences between these forecasting power and analyze the reason. The design of the training set and testing set is the same as *The Results of NWP Wind Speed Correction*. More data are validated to enhance the wide availability in WPF. To be specific, the first 7 days of September and December are added for testing. Besides, RMSEp and MAEp are used as the evaluation metrics. Additionally, the proposed XGBoost method is compared with the traditional machine learning methods, such as support vector regression (SVR) and MLP.

The hyper-parameter of XGBoost is important to the performance of the forecasting model. Therefore, selecting the appropriate hyper-parameters is the key to optimize the mode. There are three types of hyper-parameters, including general parameters, booster parameters, and task parameters. In this task, some key hyper-parameters are tuned by grid searching, whose detail is shown in **Table 2.**

The experiment is discussed below. There are four pictures in different periods which are shown in **Figure 8**. For the sake of description, prediction result under NWP wind speed, BGRU corrected wind speed, and VMD-BGRU corrected wind speed are renamed as Method 1, Method 2, and Method 3, respectively. The daily forecast statistical results are shown in**Table 3** and **Table 4**. Here is the detailed discussion about these statistical data.

Method 3 outperforms well than other methods. For example, in the first week of March, the average $RMSE_p$ and MAE_p of Method 3 are 9.476% and 5.873 MW, respectively, which reduced to 4.797% and 2.420 MW than Method 1, respectively, and reduced to 2.217% and 1.138 MW than Method 2, respectively. In the first week of June, the average $RMSE_p$ and MAE_p of Method 3 are 8.748% and 5.784 MW, respectively, which reduced to 6.899% and 3.712 MW than Method 1, respectively, and reduced to 3.880% and 2.150 MW than Method 2, respectively. Also, the similar result can be obtained from September and December. It is worth noting that the forecasting performance is less effective than Method 1 in day 3 of June and day 1 of March, which corresponds to the negative wind speed correction. But, on the whole, the experiment indicates that the proposed NWP wind speed correction method is effective in improving the accuracy of WPF.

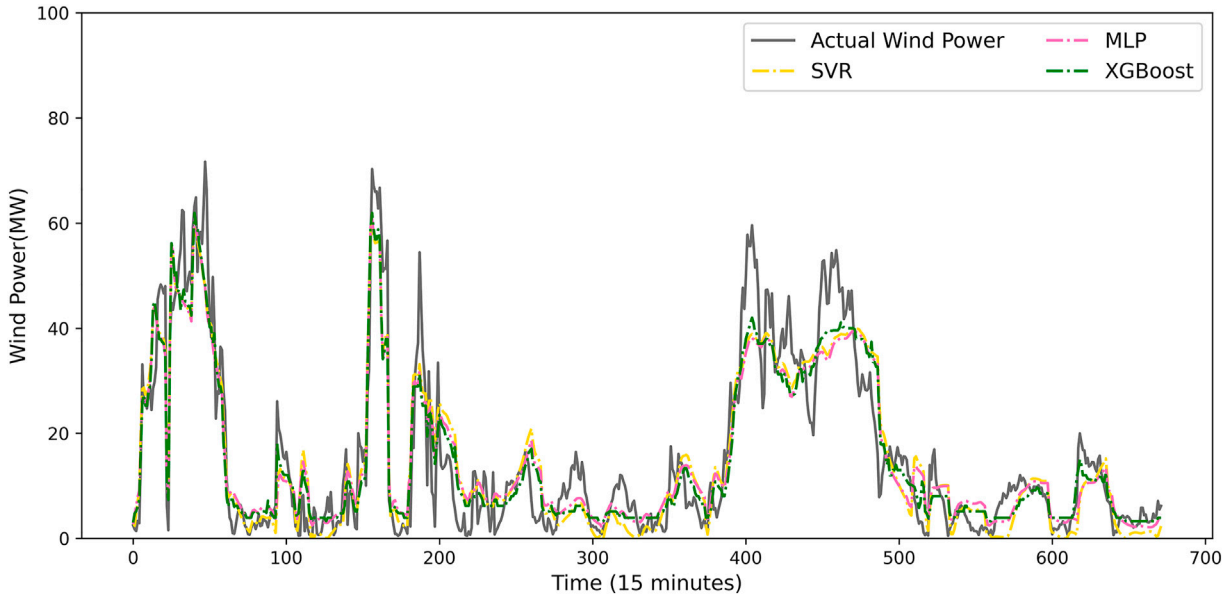

FIGURE 9 | Comparison of XGBoost, SVR, and MLP.

In order to verify the XGBoost forecasting method, MLP and SVR models, as the traditional machine learning methods, are compared with it. **Figure 9** shows the forecasted result. The $RMSE_p$ of the XGBoost is 7.532%, while that of SVR and MLP are 8.522 and 10.95%, respectively, which shows the superiority of the proposed prediction model.

CONCLUSION

This article proposes the VMD-BGRU method for the NWP wind speed correction and XGBoost forecasting model. First, the VMD algorithm is used to decompose the NWP wind speed to get abundant input features. The BGRU is used to correct the NWP wind speed based on decomposed NWP wind speed sub-series and the measured wind speed. Then, the XGBoost algorithm is utilized to establish the forecasting model using measured wind speed and power. Finally, the corrected NWP wind speed is input into the forecasting model to obtain the short-term prediction results of wind power. From the experimental results, some conclusions are drawn as follows. For NWP wind speed correction, the proposed method decreases the $RMSE_v$ and MAE_v by 0.324 and 0.294 m/s in the first week of March, respectively, and 0.639 and 0.612 m/s in the first week of June, respectively, compared with NWP. For WPF, using corrected NWP wind speed as input decreases the $RMSE_p$ and MAE_p by 3.54–6.89% and 2.29–3.71 MW on testing data, compared with NWP as input, respectively. Moreover, the XGBoost forecasting model outperforms than MLP and SVR. The results verify the effectiveness of the proposed wind speed correction method and WPF model.

DATA AVAILABILITY STATEMENT

The original contributions presented in the study are included in the article/Supplementary Material; further inquiries can be directed to the corresponding author.

AUTHOR CONTRIBUTIONS

YL: methodology, writing—original draft preparation, and software. FT: Writing—reviewing and editing, methodology, and supervision. XG: data processing, writing—reviewing and revising grammar and correct expression. TZ: conceptualization and software. FQ: validation and investigation. JX: visualization and data processing. XL: investigation and data processing. YG: investigation and visualization.

FUNDING

This study received funding from the National Natural Science Foundation of China under Grant 51977157.

REFERENCES

Al-Yahyai, S., Charabi, Y., Al-Badi, A., and Gastli, A. (2012). Nested ensemble NWP approach for wind energy assessment. *Renewable Energy* 37 (1), 150–160. doi:10.1016/j.renene.2011.06.014

Chen, T., and Guestrin, C. (2016). XGBoost. 22nd ACM SIGKDD International Conference on Knowledge Discovery and Data Mining (KDD). 785–794. doi:10.1145/2939672.2939785

Cheng, W. Y. Y., Liu, Y., Bourgeois, A. J., Wu, Y., and Haupt, S. E. (2017). Short-term wind forecast of a data assimilation/weather forecasting system with wind turbine anemometer measurement assimilation. *Renewable Energy* 107, 340–351. doi:10.1016/j.renene.2017.02.014

Choi, S., and Hur, J. (2020). An Ensemble Learner-Based Bagging Model Using Past Output Data for Photovoltaic Forecasting. *Energies* 13 (6), 1438. doi:10.3390/en13061438

Deo, R. C., Ghorbani, M. A., Samadianfard, S., Maraseni, T., Bilgili, M., and Biazar, M. (2018). Multi-layer perceptron hybrid model integrated with the firefly optimizer algorithm for windspeed prediction of target site using a limited set of neighboring reference station data. *Renewable Energy* 116 (A), 309–323. doi:10.1016/j.renene.2017.09.078

Dong, L., Ren, L., Gao, S., Gao, Y., and Liao, X. (2013). Studies on Wind Farms Ultra-short Term NWP Wind Speed Correction Methods. 25th Chinese Control and Decision Conference (CCDC). 25-27 May 2013. Guiyang, China, 1576–1579. doi:10.1109/ccdc.2013.6561180

Global Wind Energy Council (2021). Global Wind Report 2021. Available at: http://www.eqmagpro.com/gwec-global-wind-report-2021/.

Heppelmann, T., Steiner, A., and Vogt, S. (2017). Application of numerical weather prediction in wind power forecasting: Assessment of the diurnal cycle. *metz* 26 (3), 319–331. doi:10.1127/metz/2017/0820

Hu, J., Heng, J., Wen, J., and Zhao, W. (2020). Deterministic and probabilistic wind speed forecasting with de-noising-reconstruction strategy and quantile regression based algorithm. *Renewable Energy* 162, 1208–1226. doi:10.1016/j.renene.2020.08.077

Hu, S., Xiang, Y., Huo, D., Jawad, S., and Liu, J. (2021). An improved deep belief network based hybrid forecasting method for wind power. *Energy* 224, 120185. doi:10.1016/j.energy.2021.120185

Khalid, R., and Javaid, N. (2020). A survey on hyperparameters optimization algorithms of forecasting models in smart grid. *Sustainable Cities and Society* 61, 102275. doi:10.1016/j.scs.2020.102275

Dragomiretskiy, K., and Zosso, D. (2014). Variational Mode Decomposition. *IEEE Trans. Signal Process.* 62 (3), 531–544. doi:10.1109/TSP.2013.2288675

Li, Z., Ye, L., Zhao, Y., Song, X., Teng, J., and Jin, J. (2016). Short-term wind power prediction based on extreme learning machine with error correction. *Prot Control Mod Power Syst* 1 (1), 1–8. doi:10.1186/s41601-016-0016-y

Li, Z., Jiang, W., Abu-Siada, A., Li, Z., Xu, Y., and Liu, S. (2021). Research on a composite voltage and current measurement device for HVDC networks. *IEEE Trans. Ind. Electron.* 68 (9), 8930–8941. doi:10.1109/TIE.2020.3013772

Liao, X., Cao, N., Li, M., and Kang, X. (2019). Research on Short-term Load Forecasting Using XGBoost Based on Similar Days. International Conference on Intelligent Transportation, Big Data & Smart City (ICITBS). 12-13 Jan. 2019. Changsha, China. 675–778. doi:10.1109/ICITBS.2019.00167

Liu, H., and Chen, C. (2019). Data processing strategies in wind energy forecasting models and applications: A comprehensive review. *Applied Energy* 249, 392–408. doi:10.1016/j.apenergy.2019.04.188

Liu, H., Mi, X., and Li, Y. (2018). Smart multi-step deep learning model for wind speed forecasting based on variational mode decomposition, singular spectrum analysis, LSTM network and ELM. *Energy Conversion and Management* 159, 54–64. doi:10.1016/j.enconman.2018.01.010

Liu, X., Lin, Z., and Feng, Z. (2021). Short-term offshore wind speed forecast by seasonal ARIMA - A comparison against GRU and LSTM. *Energy* 227, 120492. doi:10.1016/j.energy.2021.120492

Liu, X., Zhou, J., and Qian, H. (2021). Short-term wind power forecasting by stacked recurrent neural networks with parametric sine activation function. *Electric Power Systems Research* 192, 107011. doi:10.1016/j.epsr.2020.107011

Niu, Z., Yu, Z., Tang, W., Wu, Q., and Reformat, M. (2020). Wind power forecasting using attention-based gated recurrent unit network. *Energy* 196, 117081. doi:10.1016/j.energy.2020.117081

Okumus, I., and Dinler, A. (2016). Current status of wind energy forecasting and a hybrid method for hourly predictions. *Energy Conversion and Management* 123, 362–371. doi:10.1016/j.enconman.2016.06.053

Shen, X., and Raksincharoensak, P. (2021a). Pedestrian-aware Statistical Risk Assessment. *IEEE Trans. Intell. Transport. Syst.* 1. 1–9. doi:10.1109/TITS.2021.3074522

Shen, X., and Raksincharoensak, P. (2021b). Statistical Models of Near-Accident Event and Pedestrian Behavior at Non-signalized Intersections. *Journal of Applied Statistics* 1, 1–21. doi:10.1080/02664763.2021.1962263

Shen, X., Zhang, Y., Shen, T., and Khajorntraidet, C. (2017). Spark advance self-optimization with knock probability threshold for lean-burn operation mode of SI engine. *Energy* 122, 1–10. doi:10.1016/j.energy.2017.01.065

Shen, X., Zhang, X., Ouyang, T., Li, Y., and Raksincharoensak, P. (2020). Cooperative Comfortable-Driving at Signalized Intersections for Connected and Automated Vehicles. *IEEE Robot. Autom. Lett.* 5 (4), 6247–6254. doi:10.1109/LRA.2020.3014010

Shen, X., Zhang, Y., Sata, K., and Shen, T. (2020). Gaussian mixture model clustering-based knock threshold learning in automotive engines. *IEEE/ASME Trans. Mechatron.* 25 (6), 2981–2991. doi:10.1109/TMECH.2020.3000732

Shen, X., Ouyang, T., Khajorntraidet, C., Li, Y., Li, S., and Zhuang, J. (2021a). Mixture Density Networks-Based Knock Simulator. *Ieee/asme Trans. Mechatron.* 1, 1. doi:10.1109/TMECH.2021.3059775

Shen, X., Ouyang, T., Yang, N., and Zhuang, J. (2021b). Sample-based Neural Approximation Approach for Probabilistic Constrained Programs. *IEEE Trans. Neural Netw. Learning Syst.* 1, 1–8. doi:10.1109/TNNLS.2021.3102323

Singh, P. K., Singh, N., and Negi, R. (2021). Short-Term Wind Power Prediction Using Hybrid Auto Regressive Integrated Moving Average Model and Dynamic Particle Swarm Optimization. *International Journal of Cognitive Informatics and Natural Intelligence (IJCINI)* 15 (2), 111–138. doi:10.4018/IJCINI.20210401.oa9

Song, J., Wang, J., and Lu, H. (2018). A novel combined model based on advanced optimization algorithm for short-term wind speed forecasting. *Applied Energy* 215, 643–658. doi:10.1016/j.apenergy.2018.02.070

Wang, K., Qi, X., Liu, H., and Song, J. (2018). Deep belief network based k-means cluster approach for short-term wind power forecasting. *Energy* 165 (A), 840–852. doi:10.1016/j.energy.2018.09.118

Wang, H., Han, S., Liu, Y., Yan, J., and Li, L. (2019). Sequence transfer correction algorithm for numerical weather prediction wind speed and its application in a wind power forecasting system. *Applied Energy* 237, 1–10. doi:10.1016/j.apenergy.2018.12.076

Wang, Y., Hu, Q., Li, L., Foley, A. M., and Srinivasan, D. (2019). Approaches to wind power curve modeling: A review and discussion. *Renewable and Sustainable Energy Reviews* 116, 109422. doi:10.1016/j.rser.2019.109422

Wu, Z., and Xiao, L. (2019). A structure with density-weighted active learning-based model selection strategy and meteorological analysis for wind speed vector deterministic and probabilistic forecasting. *Energy* 183, 1178–1194. doi:10.1016/j.energy.2019.07.025

Xu, K., Yan, J., Zhang, H., Zhang, H., Han, S., and Liu, Y. (2021). Quantile based probabilistic wind turbine power curve model. *Applied Energy* 296, 116913. doi:10.1016/j.apenergy.2021.116913

Yan, J., Zhang, H., Liu, Y., Han, S., Li, L., and Lu, Z. (2018). Forecasting the High Penetration of Wind Power on Multiple Scales Using Multi-to-Multi Mapping. *IEEE Trans. Power Syst.* 33 (3), 3276–3284. doi:10.1109/tpwrs.2017.2787667

Nan, Y., Di, Y., Zheng, Z., Jiazhan, C., Daojun, C., and Xiaoming, W. (2018). Research on modelling and solution of stochastic SCUC under AC power flow constraints. *IET Generation, Transmission & Distribution* 12 (15), 3618–3625. doi:10.1049/iet-gtd.2017.1845

Yang, N., Huang, Y., Hou, D., Liu, S., Ye, D., Dong, B., and Fan, Y. (2019). Adaptive Nonparametric Kernel Density Estimation Approach for Joint Probability Density Function Modeling of Multiple Wind Farms. *Energies* 12 (7), 1356. doi:10.3390/en12071356

Yang, N., Liu, S., Deng, Y., and Xing, C. (2021a). An Improved Robust SCUC Approach Considering Multiple Uncertainty and Correlation. *IEEJ Trans. Elec Electron. Eng.* 16 (1), 21–34. doi:10.1002/tee.23265

Yang, N., Yang, C., Wu, L., Shen, X., Jia, J., Li, Z., Chen, D., Zhu, B., and Liu, S. (2021b). Intelligent Data-Driven Decision-Making Method for Dynamic Multi-Sequence: An E-Seq2Seq Based SCUC Expert System. *IEEE Trans. Ind. Inf.* 1, 1. doi:10.1109/TII.2021.3107406

Yang, N., Yang, C., Xing, C., Ye, D., Jia, J., Chen, D., Shen, X., Huang, Y., Zhang, L., and Zhu, B. (2021c). Deep learning-based SCUC decision-making: An intelligent data-driven approach with self-learning capabilities. *IET Gener. Transm. Distrib.* 1. 1. doi:10.1049/gtd2.12315

Yang, J. (2019). A novel short-term multi-input-multi-output prediction model of wind speed and wind power with LSSVM based on improved ant colony algorithm optimization. *Cluster Comput* 22 (2), 3293–3300. doi:10.1007/s10586-018-2107-1

Zhang, T., Yan, P., Li, Z., Wang, Y., and Li, Y. (2019). Bias-correction method for wind-speed forecasting. *metz* 28 (4), 293–304. doi:10.1127/metz/2019/0950

Zhang, Y., Li, Y., and Zhang, G. (2020). Short-term wind power forecasting approach based on Seq2Seq model using NWP data. *Energy* 213, 118371. doi:10.1016/j.energy.2020.118371

Zhang, L., Xie, Y., Ye, J., Xue, T., Cheng, J., Li, Z., and Zhang, T. (2021). Intelligent frequency control strategy based on reinforcement learning of multi-objective collaborative reward function. *Front. Energy Res.* 9. doi:10.3389/fenrg.2021.760525

Zhao, J., Guo, Y., Xiao, X., Wang, J., Chi, D., and Guo, Z. (2017). Multi-step wind speed and power forecasts based on a WRF simulation and an optimized association method. *Applied Energy* 197, 183–202. doi:10.1016/j.apenergy.2017.04.017

Zhao, Y., Ye, L., Wang, Z., Wu, L., Zhai, B., Lan, H., and Yang, S. (2019). Spatio-temporal Markov chain model for very-short-term wind power forecasting. *J. eng.* 2019, 5018–5022. doi:10.1049/joe.2018.9294

Zheng, H., and Wu, Y. (2019). A XGBoost Model with Weather Similarity Analysis and Feature Engineering for Short-Term Wind Power Forecasting. *Applied Sciences* 9 (15), 3019. doi:10.3390/app9153019

Zheng, D., Eseye, A. T., Zhang, J., and Li, H. (2017). Short-term wind power forecasting using a double-stage hierarchical ANFIS approach for energy management in microgrids. *Prot Control Mod Power Syst* 2 (1), 1–10. doi:10.1186/s41601-017-0041-5

Zhu, B., Ding, F., and Vilathgamuwa, D. M. (2020). Coat Circuits for DC-DC Converters to Improve Voltage Conversion Ratio. *IEEE Trans. Power Electron.* 35 (4), 3679–3687. doi:10.1109/TPEL.2019.2934726

Conflict of Interest: The authors declare that the research was conducted in the absence of any commercial or financial relationships that could be construed as a potential conflict of interest.

Publisher's Note: All claims expressed in this article are solely those of the authors and do not necessarily represent those of their affiliated organizations, or those of the publisher, the editors, and the reviewers. Any product that may be evaluated in this article, or claim that may be made by its manufacturer, is not guaranteed or endorsed by the publisher.

frontiers in Energy Research

ORIGINAL RESEARCH
published: 17 January 2022
doi: 10.3389/fenrg.2021.812492

Research on Dynamic Response of Slopes With Weak Interlayers Under Mining Blasting Vibration

Xiaochao Zhang, Qingwen Yang, Xiangjun Pei and Ruifeng Du*

State Key Laboratory of Geohazard Prevention and Geoenvironment Protection, Chengdu University of Technology, Chengdu, China

As blasting technology starts to be used in a wide range of areas, blast loading has led to an increasing number of geological disasters such as slope deformation, collapses, and soil slippage. Slopes with weak interlayers are more likely to be deformed and damaged under the influence of blast loading. It is of great importance to study the evolution for the deformation of slopes with weak interlayers during blasting excavation. This study constructed a slope model with a weak interlayer to investigate the influence of different factors of blasting, including explosive charge, blast radius, blast origin, and multi-hole blasting, on the internal dynamic response. The deformation mechanism of slopes with weak interlayers under the influence of blast loading was analyzed. Test results show that each layer of the model had a different displacement response (uncoordinated dynamic response) to blasting with various factors. Explosive energy and the pattern of dynamic response of each layer varied depending on different settings of blasting factors such as explosive charge, blast radius, blast origin, and detonation initiation method. When the explosive energy produced under the influence of various factors was small, the change in the uncoordinated dynamic response between layers was significant, and the change gradually became less significant as the explosive energy increased. Therefore, this study has proposed the concept of critical explosive energy, and it is speculated that when the explosive energy produced with various factors is less than critical explosive energy, the dynamic response is mainly affected by the internal structure of the slope (property difference induced geologic layers). In other words, the uncoordinated motion of material's particles in each layer is caused by different limitations and the degree of movement of the particles, which leads to the uncoordinated dynamic response and uncoordinated deformation of each layer. If the explosive energy is greater than the critical value, the dynamic response of each layer is mainly affected by the explosive energy. The differences in the internal structure of the slope are negligible, and the incoordination of dynamic responses between layers gradually weakens and tends to synchronize.

Keywords: factors of blasting, dynamic response, uncoordinated dynamics, uncoordinated deformation, mining blasting vibration

OPEN ACCESS

Edited by:
Yusen He,
Grinnell College, United States

Reviewed by:
Jiahao Deng,
DePaul University, United States
Yi-Xiang Song,
Hebei University of Technology, China

****Correspondence:***
Qingwen Yang
yangqingwen1991@outlook.com

Specialty section:
This article was submitted to Wind Energy, a section of the journal Frontiers in Energy Research

Received: *10 November 2021*
Accepted: *29 November 2021*
Published: *17 January 2022*

Citation:
Zhang X, Yang Q, Pei X and Du R (2022) Research on Dynamic Response of Slopes With Weak Interlayers Under Mining Blasting Vibration. Front. Energy Res. 9:812492. doi: 10.3389/fenrg.2021.812492

HIGHLIGHTS

1) Blasting engineering often induces instability of surrounding slopes, especially slopes with weak interlayers.
2) Under the action of blasting vibration, the layers of slopes with weak interlayers presented uncoordinated dynamic response.
3) Uncoordinated dynamic response leads to uncoordinated deformation.
4) When the blasting energy is larger than the critical blasting energy, the uncoordinated dynamic response tends to be synchronized.

INTRODUCTION

In recent decades, as infrastructure and mine excavations continue to develop rapidly, blasting technology has been used in different types of large-scale engineering projects and mining engineering. While blasting technology brings great benefits to project construction, it also gives rise to an increasing number of issues in slope stability. Up to 25 landslides were induced by blasting in the Daye iron mine in Hubei province, China (Liu, 2009). Many landslides were caused by blasting excavation in a limestone mining area in Mount Emei in Sichuan province (Bai et al., 1995). At Pasir mine in Kalimantan, several slope failure accidents were caused by blasting in layered deposits with a high dip angle, resulting in considerable production interruption and economic losses (Deb et al., 2011). Some other slope failure accidents caused by blasting in different open-pit mines in China can also be found in the literature reports (Li et al., 2001; Luo et al., 2015; Song et al., 2017; Deng et al., 2018; He et al., 2021). Blasting-generated seismic waves were the main cause of disturbance to the overlaying open-pit slopes in triggering instability of slopes (Dvořák, 1977; Singh and Singh, 1995; Jiang et al., 2018; Adushkin, 2019; Hempen, 2019). Investigations into the effect of mine blast vibrations on the surrounding slopes are the key point to assess the effect of blasting on the stability of the nearby slopes. One of the most important studies is to obtain the propagation and attenuation of the blast vibration data in the rock slope by *in situ* monitoring of ground vibration (Ozcelik, 1998; Kesimal et al., 2008; Lu et al., 2015; Fan and Ge, 2020; Lu et al., 2020). Wang et al. (2007) studied the dynamic responses of continuous rock masses under blast loading and found blast tensile damage induced by wave propagation. It has been promoted that the level of rock fragmentation by blasting was largely affected by the distribution of structural planes (Ozcelik, 1998). Blasting acceleration was the main cause of plane shear failure inside the slope (Kesimal et al., 2008; Wang et al., 2019). Chang et al. (2007) conducted the study of numerical modeling of blast wave propagation through rock mass and effects of water and joints. With the development of computer technology, codes, such as DDA, FLAC3D, ANSYS/LS-DYNA, and GEO-SLOPE et al. are frequently adopted to study the influence of blast on rock slopes.

Excepting blasting, although many factors such as rainfall, geological conditions, and groundwater induce the loss of the slope stabilities, control over blasting in quarry should be more important since the geology of a pit cannot be changed. The adverse effects of blasting operations can be controlled by conducting optimization of the blast design. Blasting pattern, such as hole depth and diameter, explosive charge, bench geometry, blast timing, and position, is the key parameter within the control of the blasting risk. Besides the different blasting patterns having different influence on the dynamic response of slopes with weak interlayers, more complicated methods may be used for blasting, such as multi-hole blasting and blasting from different angles. Peak particle velocity, acceleration, and displacement are considered to be the reliable vibration monitoring parameters (Hakan et al., 2009; Li et al., 2021a; Li et al., 2021b).

The previous studies are mainly based on numerical or physical simulations of the patterns of dynamic responses of relatively homogeneous rock slopes under the influence of blasting. Some scholars point out that the vibration intensity caused by blasting is closely related to the lithology and structural characteristics of rock mass (Görgülü et al., 2013; González-Nicieza et al., 2014; Benchelha et al., 2017; Mohamad et al., 2018). Therefore, compared with normal rock slopes, the dynamic response of slopes with weak interlayers under blast loading is different from that of normal rock slopes because of their special geological structures. Under the influence of blasting vibration, slopes with weak interlayers are more prone to deformation and failure, and they can eventually cause geological disasters such as landslides. However, there are few research studies on the dynamic response of weak intercalated slopes under different blasting patterns.

The purpose of this study is to better study the patterns of dynamic response of slopes with weak interlayers in an actual blasting process and provide a reference for engineering practice. A typical blasting cracked slope in the Lingshi County of Shanxi province of China was chosen as the case, and physical model simulations of blast loading were constructed. Based on the proto-model, we investigated the dynamic response patterns of acceleration and strain of each layer of slope with a weak interlayer under the influence of blasting factors such as explosive charge, blast radius, blast directions, and multi-hole blasting. In addition, the study has analyzed the deformation mechanism of the slope with a weak interlayer under the effect of blasting, which provides a theoretical basis for studying the deformation and failure of slopes under blast loading.

PLANS OF BLASTING PHYSICAL SIMULATION TESTS

Model Design

The study area is located in Lingshi County, Shanxi Province, China. The area has rich mines in resources and has a long history of mining, especially in recent years where coal mining has become the main local industry. The unstable slope was selected as the research object, which is located in Beizhuang village, Lingshi County. The elevation of the rear edge of the slope is about 1,005 m, and the elevation of the leading edge is about 900 m. There is a slightly thick Quaternary mid-late

TABLE 1 | Similarity system for blasting physical model test.

Physical quantity	Similarity	Similarity coefficient (*controlled quantity)	
		Rock	Weak interlayer
Density ρ	C_ρ	1.2	1.2
Elastic modulus E	C_E	30*	30*
Poisson ratio μ	C_μ	1	1
Cohesion c	$C_c = C_E$	30	30
Internal friction angle Φ	C_Φ	1	1
Stress σ	$C_\sigma = C_E\, C_\varepsilon$	30	30
Strain ε	$C_\varepsilon = C_\rho C_g\, C_l\, C_E^{-1}$	8	8
Length l	C_l	200*	200
Displacement u	$C_u = C_l\, C_\varepsilon$	200	200
Time t	$C_t = C_\rho^{0.5}\, C_E^{0.5}\, C_l$	80	80
Frequency f	$C_f = Ct^{-1}$	0.0125	0.0125
Speed v	$C_v = C_\rho^{0.5}\, C_E^{0.5}$	6	6
Acceleration a	$C_a = C_\rho^{-1}\, C_l^{-1}\, C_E$	0.125	0.125
Acceleration of gravity g	C_g	1	1

TABLE 2 | Physical and mechanical parameters of blasting physical model and photo model.

Lithology		Density ρ (t/m^3)	Elastic modulus E (MPa)	Poisson ratio μ	Compressive strength σ_c (MPa)	Cohesion C (kPa)	Angle of internal friction φ (°)
Sandstone	Protomodel	2.57	12,000	0.28	58	2,200	45.8
	Theoretical value of the model	2.20	400	0.28	1.95	73	45.30
Mudstone	Protomodel	2.43	2,400	0.31	18.9	1,050	35.5
	Theoretical value of the model	2.02	80	0.31	0.63	35	35.5

Pleistocene loess on the top of the slope, bedrock exposed in the middle and upper slope, and an overburden composed of residual and slope sediments in the middle and lower part of the slope. The slope is composed of a soft- and hard-interbedded structure of sandstone and mudstone. Three groups of joints are developed: the first group is a rock layer (Sun et al., 2008; Wang, 2017), whose occurrence is 330–350° ∠ 5–10° (dip direction ∠ dip angle); the second group is a steeply inclined fissure J1, which is 330–340° ∠ 80–85°; and the third group is a steeply inclined fissure J2, whose occurrence is 50–55° ∠ 75–80°. There are 20 mining points within 1 km of the slope. The slope showed no signs of deformation before 2013. The closest to the slope is the ZL coalmine. In 2014, the coalmine was mined, and cracks appeared on the rear edge of the slope in June 2015. In 2016, the number of cracks increased to 12, and rift troughs appeared on the left and right sides of the slope. In 2017, 5 local rock avalanches occurred. By 2019, 18 cracks have been developed; the longest crack is about 35 m, and the widest crack is about 1 m. According to Google Earth images and a detailed visit to the study area, it was found that there was no deformation before mining in 2014. Therefore, we think that the effect of blasting vibration during the mining in the mining area may be the main reason for the deformation and damage of the slope.

The similarity between the test model and the prototype (**Table 1**), and physical and mechanical parameters (**Table 2**) were established based on the second theorem of similarity. The hard rock was semiarid by materials composed of quartz sand and barite powder. Gypsum and glycerin were used as the cementing agent for hard rock. Regarding soft rock similar materials, quartz sand and clay were used as aggregates for the simulation of soft rock. Gypsum and paraffin were chosen to cement other materials. Specific ratios and properties are listed in **Table 3**. The test model was designed as shown in **Figures 1**, **2**. It can be seen that the model consists of two parts. The bottom part was the base of the mode, which was made of cement mortar, and the upper part made of our similar materials for the soft layer and hard layer was the studied slope.

Blasting Equipment

The physical model test adopted the method of "explosive blasting energy approximation", and the test approximately meets the explosion dynamic criterion. Due to the lack of site blasting data, the explosive selected in this test is emulsion explosive to provide a certain equivalent blasting load for a similar model. This study aims to study the dynamic response of the slope model under different weights of explosive conditions. In addition, a plastic detonator with high safety performance is selected, as shown in **Figure 3**. The parameters of emulsion explosives are as follows: densityρ_c = 1.32 g/cm^3, detonation velocity D_v = 3,350 m/s, heat of explosion Q_v = 4200 k J/kg, and intensity $\triangle h$ = 11.5 mm. The specific amount of explosive charge is listed in **Table 4**. The method of decoupling charging was used for our tests. The upper part of the blast hole was filled with bentonite, and the soil bags were

TABLE 3 | Proportion of similar materials and related properties.

Similar materials	Ingredients (%)				Other ingredients (%)	Compressive strength	Elastic modulus	Density
	Barite powder (clay)	Quartz sand (40 mesh)	Gypsum	Glycerin (liquid paraffin)	Mixing water	MPa	MPa	g/cm^3
Hard layer	34.4	51.6	10.0	4.0	14.0	1.90	380.55	2.13
Soft layer	50.0	47.0	1.0	2.0	16.02	0.65	76.7	2.02

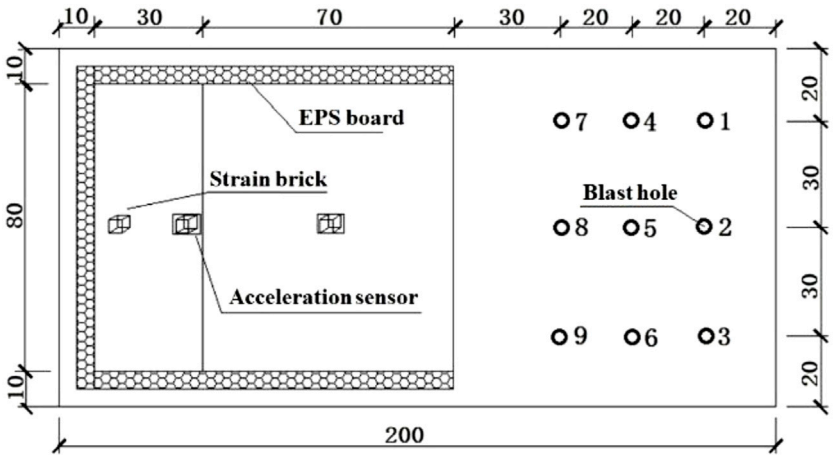

FIGURE 1 | Plan figure of the test model.

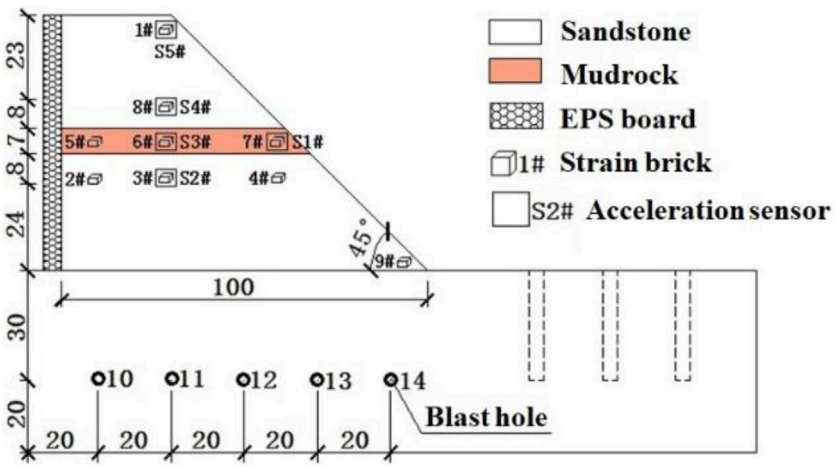

FIGURE 2 | Sectional view of the test model.

prepared and covered the hole. After that, the plastic detonator was detonated by using the high voltage spark.

Design of Testing

The factors of explosive charge, blasting radios, blasting directions, and multi-hole blasting were considered in our tests. The factor value shown in **Tables 4**, **5** was set according to the "approximate blasting energy of explosives" (Yuan, 2016). The value of 5, 7, and 10 g were used for the explosive charge factor. There were 14 blasting holes used in our tests; 1–9 blasting holes were used for the cases of explosive charge and blasting radius. The cases for blasting directions were involved with the 9

FIGURE 3 | Materials for blasting physical simulation test.

TABLE 4 | Design of blasting plans.

Plan	Factors of blasting	Blast holes	Charge (g/hole)	Detonation initiation method
1	Explosive charge	1, 2, and 3	7, 5, and 10	Single-hole blasting
		4, 5, and 6	7, 5, and 10	Single-hole blasting
		7, 8, and 9	7, 5, and 10	Single-hole blasting
2	Blast radius	2, 5, and 8	5	Single-hole blasting
		1, 4, and 7	7	Single-hole blasting
		3, 6, and 9	10	Single-hole blasting
3	Blast origin	9, 12	10	Single-hole blasting
4	Multi-hole blasting	1, 2, and 3	5	Simultaneous blasting
		4, 5, and 6	7	Simultaneous blasting
		10, 11, 12, 13, and 14	10	Simultaneous blasting

and 12 blasting holes. There were three cases involving 1–3, 4–6, and 10–14 blasting holes, respectively, for studying the effect of multi-hole blasting. These values were also used for the multi-hole blasting cases (**Table 4**). The blast radius of 100, 120, and 140 mm was used in our tests (**Table 5**).

TABLE 5 | Blast radius for each group of blast holes.

Blast holes in groups			Blast radius (cm)
①	②	③	
1	2	3	140
4	5	6	120
7	8	9	100

RESULTS

Analysis of Acceleration Response Characteristics

The time-series data of accelerations in the horizontal (X) and vertical (Z) directions measured in the upper hard layer, soft layer, and lower hard layer are shown in **Supplementary Figure S1**. The acceleration time-history curves showed an asymmetrical spindle shape. The blasting vibration was characterized by an instantaneous feature. The duration of acceleration violent fluctuations was very short. The main blasting vibration was concentrated in a limited period of time in all our cases of test, such as the duration of 0.013–0.03 s, in **Supplementary Figure S1A**. The curve of the main blasting vibration is enlarged and shown in **Supplementary Figure S1B**.

1) Analysis of acceleration characteristics of each layer with different explosive charges

This section analyzes the data obtained from the blasting holes 1, 2, and 3 in the first plan (**Table 4**). **Supplementary Figures 2–4** show the horizontal (X) acceleration characteristic curves of the upper and lower hard and soft layers with explosive charges of 5, 7, and 10 g, respectively.

It can be seen from the figures that when the amount of explosive charge was small (5 g), the difference in acceleration response of different layers was large. The acceleration response of the lower hard layer was the largest, that of the soft layer was second and the upper hard layer, the third. The peak acceleration of the three layers from the largest to the smallest was lower hard layer > soft layer > upper hard layer. The peak and minimum values of the accelerations for each layer were different, and there was a clear displacement. With the increase of the explosive charge (such as 7 and 10 g), the acceleration difference between each layer gradually decreased, and at the same time, the

displacement in peaks and valleys of each layer gradually disappeared and tended to synchronize. It can be seen that when the amount of the explosive charge was small, the explosive energy was small and the acceleration response between each layer was mainly affected by the material medium, which shows an uncoordinated dynamic variation, i.e., the lower hard layer > soft layer > upper hard layer. As the amount of explosive charge increased, it resulted in the increase of the explosive energy. The acceleration response due to the influence of the material medium in each layer decreased gradually, while the influence of the explosive energy on the acceleration response increases. It can be predicted that there might be a critical value of blasting energy. When the explosive charge reaches a certain critical value and the explosive energy reaches the critical explosive energy, the acceleration response will be mainly affected by the explosive energy. The uncoordinated dynamic response of different layers will also be disappeared and tend to change synchronously. The horizontal (X) acceleration characteristic curves between layers show similar response characteristics in the cases of blast holes 4, 5, 6, 7, 8, and 9.

Based on the analysis of the vertical (Z) acceleration characteristic curves (**Supplementary Figures S5–S7**), it can be seen that the response characteristics are slightly different from that of the horizontal (X) acceleration curves. Overall, the acceleration response characteristics in the vertical (Z) direction of each layer are as follows: lower hard layer > soft layer > upper hard layer. At the same time, the peaks and valleys in the acceleration trace for each layer still have displacement. However, the acceleration response of the soft layer in the vertical direction was more violent than that of the horizontal. The amplitude of the acceleration in the soft layer was even close to or exceeded that in the lower hard layer at a certain time. The displacement in the peaks and valleys of the acceleration trace of the soft layer and the lower hard layer at the same time was relatively small, but at the same time, the values at the peaks and valleys of acceleration were much larger than that of the upper hard layer. However, with the increase in the amount of the explosive charge, the displacement in the peaks and valleys for each layer gradually became more and more synchronized.

According to the horizontal (X) acceleration response characteristics of each layer, it can be seen that when the explosive charge was small, the movement of the medium particles of each layer was slightly limited in the horizontal direction, and the nature of the restricted motion of the medium particles of each layer was basically the same. Therefore, the acceleration response characteristics (lower hard layer > soft layer > upper hard layer) were more prominent, and the anomalies were not prominent. However, by analyzing the acceleration response characteristics in the vertical (Z) direction, it can be speculated that when the amount of the explosive charge was small, there were obvious differences in the limitation of the movement of the medium particles in different layers in the vertical direction.

Given different material properties in each layer, the particle density is different. The movement space of the media particles in each layer is then different. In addition, during blasting vibration, the density of the material medium increases with the depth. Considering all the above, the motion of the medium particles in the lower hard layer is more restricted in the vertical direction than in the soft layer. Therefore, the acceleration of the soft layer in the vertical direction responded more violently, and its variation even approached or exceeded that of the lower hard layer at a certain time. Theoretically, the motion limit of the medium particles in the upper hard layer is smaller than that of the lower hard layer, and its vertical acceleration response should be greater than that of the lower hard layer. However, in reality, the reflection or superposition cancellation occurred when the blasting wave reached the soft layer in the process of bottom-up propagation, leading to the weakest vertical acceleration response in the upper hard layer. It should be mentioned that when the amount of the explosive charge is sufficient and can generate energy more than the critical explosive energy, regardless of the horizontal or vertical acceleration of layers, the variation in the response will tend to synchronize. In other words, the uncoordinated dynamic variation of the dynamic response of different layers will be gradually weakened. In this regard, the dynamic response is mainly affected by the blasting energy and is little affected by the material medium.

2) Analysis of acceleration characteristics of each layer with different blast radii

Based on the analysis of the test data of the second group of blast holes (2, 5, and 8), the trend curve of the peak acceleration of each layer with the distance to the center of the blast was obtained, as shown in **Supplementary Figures S8, S9**. The influence of blast radius on the acceleration response characteristics of each layer can be summarized as follows:

① The acceleration response of each layer tended to decay with the increase in the blast radius. Specifically, at the same measurement point, the farther the distance to the explosion source, the smaller the acceleration. The peak acceleration value appeared to decline as the blast radius increased.
② Different levels of acceleration have different attenuation trends. The attenuation trend of the acceleration of the lower hard layer was the most significant, and the attenuation of the acceleration response of the soft layer and the upper hard layer was relatively slow.
③ Horizontal and vertical acceleration attenuation rates were different. The horizontal acceleration decay rate in the lower hard layer was less than the vertical acceleration decay rate; the horizontal acceleration decay rates in the soft layer and the upper hard layer were slightly greater than the vertical acceleration decay rates;
④ It can be predicted that when the blast radius is small and reaches a certain limit value and the explosive energy reaches the critical explosive energy, the acceleration response attenuation rate of each layer will tend to be consistent. Data analysis results of the first and third groups of blast hole tests were similar.

3) Analysis of acceleration characteristics of layers in different blast directions

TABLE 6 | Mean differences of the peak horizontal and vertical acceleration of each layer in different blast directions.

Mean difference of peak acceleration in different directions	Lower hard layer	Soft layer	Upper hard layer
Mean difference of peak horizontal acceleration	18.3376	21.8050	18.1285
Mean difference of peak vertical acceleration	27.1788	28.0374	30.9529

Based on the analysis of the test data of hole 12 at the bottom of the slope model and hole 9 at the leading edge of the slope, their characteristic acceleration curves are shown in **Supplementary Figures S10–15**. Specifically, **Supplementary Figures S10–12** are the horizontal acceleration characteristic curves in the lower hard layer, soft layer, and upper hard layer, respectively. **Supplementary Figures S13–15** are the vertical acceleration characteristic curves. Overall, the acceleration response of each layer is different in different blast directions. Specifically:

① The acceleration response of each layer during blasting at the bottom was stronger than that of the leading edge. As shown in **Supplementary Figures S10–12**, during blasting at the bottom of the slope, the maximum values of the peak horizontal acceleration in the lower hard layer, soft layer, and upper hard layer could reach 48.75332, 50, and 39.851071, respectively. During blasting at the leading edge of the slope, the maximum values of the peak horizontal acceleration in the above layers were 30.822168, 29.33868, and 17.92352, respectively. This pattern was more significant in the vertical acceleration response (**Supplementary Figures S13–15**).

② The vertical acceleration response of the same layer was more sensitive to blast directions than the horizontal acceleration. As shown in **Table 6**, when the location of the explosion source was different, the mean differences of the peak horizontal acceleration of the lower hard layer, soft layer, and upper hard layer were 18.3376, 21.8050, and 18.1285, respectively. The mean differences of the peak vertical acceleration of the above layers were 27.1788, 28.0374, and 30.9529, respectively. It is clear that when the blast directions were different, the vertical acceleration response of each layer was stronger.

③ Regarding the soft layer and the upper hard layer, the use of bottom blasting had a stronger effect on the acceleration than the leading edge blasting, mainly due to the different propagation methods of the blast wave.

(4) Analysis of acceleration characteristics of each layer during multi-hole blasting

Supplementary Figures S16, 17 show the time-history curves of horizontal and vertical acceleration of each layer when holes 1, 2, and 3 were simultaneously detonated. Unlike single-hole blasting, the acceleration response of each layer during multi-hole blasting exhibits two instantaneous violent fluctuations, which have been amplified separately in characteristic acceleration curves I and II (**Supplementary Figures S18–21**), respectively.

Based on the analysis of characteristic acceleration curves Ⅰ and Ⅱ, it can be known that the acceleration response characteristics of each layer during multi-hole blasting were still lower hard layer > soft layer > upper hard layer. At the same time, the peaks and valleys in the acceleration trace for each layer were different, and a clear displacement was observed. This result indicates that the acceleration response of each layer is in an uncoordinated dynamic change, indicating that there is an uncoordinated deformation characteristic between each layer. This pattern is more prominent in the vertical acceleration characteristic curve, but it gradually weakens in the horizontal acceleration characteristic curve. It is mainly related to the difference in the restricted nature of the movement of the medium particles in different directions in each layer and the reflection or superimposed cancellation of the blast wave from the bottom to the top. The principle is the same as explained before.

It is worth noting that even if the explosive charge, blast radius, and blast origin were the same, the explosive energy produced by multi-hole blasting was much larger than that produced by single-hole blasting. Therefore, during multi-hole blasting, the uncoordinated dynamics of the acceleration response between layers in the slope with weak interlayers is relatively weak.

Analysis of Strain Response Characteristics

In order to obtain effective strain wave waveforms and strain wave parameters (i.e., strain wave peak value and time) of each layer in the model, the data collection frequency was adjusted appropriately, and the clutter was filtered out to process the recorded signal in order to obtain strain time-history curves that can truly reflect the deformation characteristics of each layer in the model (**Supplementary Figures S22, S23**). A strain time-history curve is roughly divided into three parts: front, middle, and tail. The strain fluctuations in the front part were small, indicating that there was no major deformation in each layer. The severe strain fluctuations in the middle part indicate that the media in each layer were subjected to tensile or stamping under the action of stress waves, and tensile or compressive strains began to occur inside with large strain fluctuations. The strain fluctuation of the tail part was relatively stable, indicating that a certain degree of plastic creep appeared in each layer as the stress wave gradually disappeared. The middle and tail parts of the strain time-history curves were selected for analyzing the strain response characteristics of layers. The middle and tail parts of the strain time-history curves are referred to as the strain characteristic curve Ⅰ and the strain characteristic curve Ⅱ (**Supplementary Figures S24–S27**).

1) Analysis of strain response characteristics of each layer with different explosive charges

Supplementary Figures S22–S27 are the strain time-history curves and corresponding strain characteristic curves of each

layer during the single-hole blasting of holes 2 and 3 when the charges were 5 and 10 g, respectively.

Compared with the strain characteristic curve I, it can be seen that when the explosive charge was small (e.g., 5 g), the fluctuation of the strain response of each layer was violent and complex, and the duration was longer (about 0.2 s); the strain fluctuation of the soft layer was much greater than that of the upper and lower hard layers. The strain fluctuations of the upper and lower hard layers were basically synchronized. When the explosive charge was large (e.g., 10 g), the strain response fluctuations of each layer were gentle and simple, and the duration was short (only 0.007 s); the strain fluctuation of the soft layer was greater than that of the upper and lower hard layers. Similarly, the strain fluctuations of the upper and lower hard layers were basically synchronized. The above results suggest that when the explosive charge is small, the stress provided by the generated explosive energy is close to the yield strength of the soft layer and is far less than that of the upper and lower hard layers, resulting in severe yield deformation of the soft layer and further causing complex strain fluctuations in the upper and lower hard layers. When the explosive charge is large, the generated explosive energy can overcome the yield strength of each layer of the material medium, causing direct plastic deformation of each layer and regular strain fluctuations as the blasting vibration continues.

Based on the analysis of the strain characteristic curve II, it can be known that a certain plastic creep has occurred in each layer after blasting, and the creep continued to occur as the stress wave gradually disappeared. The difference between the two curves is that when the amount of the explosive charge was small, the plastic creep of the soft layer was the largest, followed by the lower hard layer and the upper hard layer, both of which were tensile strains. When the explosive charge was large, the plastic creep of the lower hard layer was the largest, followed by the upper hard layer and the soft layer, both of which were tensile strains, and the plastic creep of each layer presented a similar pattern of fluctuations. Following the same logic as before, when the amount of explosive charge is small, the soft layer has severe yield deformation, resulting in tensile fracture of the internal structure, and then large creep fluctuations occur. In addition, due to the severe yield deformation of the soft layer, small tensile deformation occurs inside the upper and lower hard layers, which leads to smaller creep fluctuations in the later period. When the explosive charge is large, each layer has direct plastic deformation. The upper and lower layers have brittle fractures, given the features of the material, while the soft layer has elastoplastic damage. Although the three layers have shown similar patterns of fluctuations, the strain values differed greatly in the tail section of the fluctuation, and the plastic deformation of the soft layer recovered to a certain extent. Therefore, the strain value of the soft layer was smaller than that of the upper hard layer and then the lower hard layer.

It should be noted that uncoordinated deformation characteristics of layers were observed regardless of the amount of explosive charge. In addition, the strain time-history curve and the strain characteristic curve obtained after the blasting of hole 1 with 7 g charge was similar to the curves obtained after the blasting of hole 3 with 10 g charge.

The vertical and radial strains of different layers have shown similar characteristics, but there were slight differences. This is mainly related to the limited nature of the movement of the medium particles, so it will not be further explained here.

2) Analysis of strain response characteristics of each layer with different blast radii

Supplementary Figures S28. S29 are the trend lines of the variation of the peak horizontal strain of each layer with the distance to the center of the blast during the single-hole blasting of holes 1, 4, and 7 (with 7 g charge) and holes 3, 6, and 9 (with 10 g charge). It can be seen from the figures that ①The strain response of each layer decreased with the increase of the blast radius; ②The peak strain of different layers shows a different degree of attenuation trend with the increase of the blast radius; the soft layer has the largest attenuation rate, followed by the lower hard layer and the upper hard layer; ③ It can be predicted that as the blast radius increases indefinitely, the peak strain attenuation rates of layers will tend to be consistent.

The pattern of variation of the peak vertical strain with the distance to the center of the blast is similar to that of the horizontal strain.

3) Analysis of the strain response characteristics of each layer in different blast directions

Based on the analysis of data about blasting holes 9 and 12 (with 10 g charge), the horizontal and vertical strain time-history curves of each layer during blasting from different origins are shown in **Supplementary Figures S30**. It is evident that the patterns of the strain response of each layer are different in different blast directions. Overall, the strain response of each layer was faster during blasting at the bottom of the slope model, and each layer had a certain plastic creep. The radial residual creep strain was larger than the vertical residual creep strain. However, during the blasting of the leading edge of the slope, the strain response of each layer was relatively slow, and the strong response occurred between 2 and 3 s without a large residual creep strain.

In the comparison of radial and vertical strains, the reason why the radial residual creep strain was greater than the vertical residual creep strain is mainly related to the limited nature of the motion of medium particles. The principle is the same as before, so it will not be analyzed again here.

It is worth noting that blast holes 9 and 12 have a small distance to the center of the blast and large charges, so the blasting of these holes can generate large blast energy. Therefore, the trend of the strain response of each layer was close to the same (**Supplementary Figures S31, S32**), but uncoordinated deformation could still be observed, which is consistent with the previous analysis. When the explosive energy reaches the limiting value, the dynamic response of each layer is mainly affected by the explosive energy, and the material medium has little effect on the response.

4) Analysis of response characteristics of each layer strain during multi-hole blasting

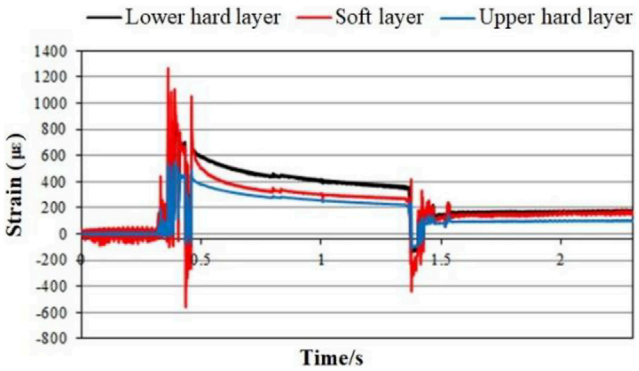

FIGURE 4 | Time-history curve of the radial strain of each layer during simultaneous blasting of Nos 1, 2, and 3.

As analyzed before, the acceleration response of each layer during multi-hole blasting fluctuated violently twice. Correspondingly, each layer also had two violent strain responses during multi-hole blasting. **Figures 4**, **5** are the radials and vertical strain time-history curves of each layer when the blast holes 1, 2, and 3 were simultaneously detonated (with 5 g charge). In a similar way as before, the two strain fluctuations in the acceleration time-history curve for multi-hole blasting were amplified and presented in strain characteristic curves I and II (**Figures 6**–**9**).

It can be seen from the figure: ① During multi-hole blasting, the strain response of each layer showed two violent fluctuations, of which the first fluctuation was greater than the second fluctuation; ② The overall strain response characteristics appear to follow the pattern of soft layer > lower hard layer > upper hard layer; ③ The patterns of strain response of different layers were approximately synchronous, but uncoordinated deformation still occurred, which was more obvious in the vertical strain characteristic curve. It can be seen that when the explosive charge, blast radius, and blast direction were the same, the explosive energy produced by multi-hole blasting was greater than that of single-hole blasting; each layer was more affected by the explosive energy, and the material medium has little effect on the response.

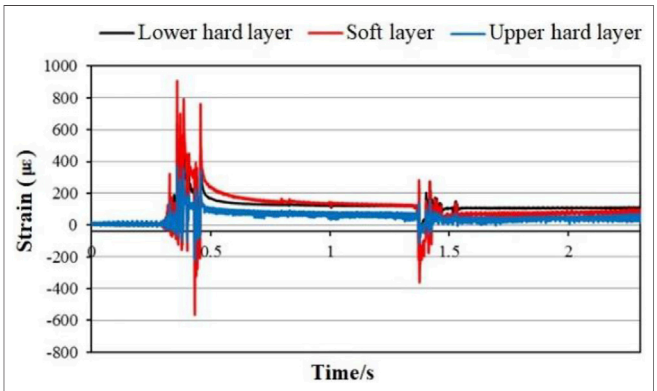

FIGURE 5 | Time-history curve of the vertical strain of each layer during simultaneous blasting of Nos 1, 2, and 3.

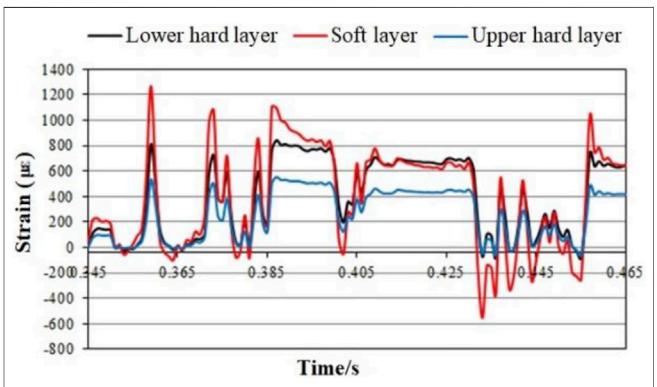

FIGURE 6 | Radial strain characteristic curve **I** of each layer during simultaneous blasting of Nos 1, 2, and 3.

ANALYSIS OF THE UNCOORDINATED DEFORMATION MECHANISM

Based on the above test results, it can be known that under the influence of blasting, there is certain incoordination in the dynamic response of each layer of the slope with weak interlayers. Specifically ① The incoordination of the particle movement of the material in each layer is reflected by the uncoordinated dynamics of the acceleration response of the layers; ② Due to the uncoordinated movements of particles, it will inevitably lead to the uncoordinated deformation inside the medium, which can be seen from the uncoordinated pattern of strain characteristics of different layers.

According to the test results, with large explosive charge, small blast radius, bottom blasting, and multi-hole blasting, the dynamic responses of different layers appeared to be synchronized, and the incoordination gradually weakened. From another perspective, this result suggests that when the explosive energy is small (less than the critical explosive energy), the dynamic response of each layer of the slope is

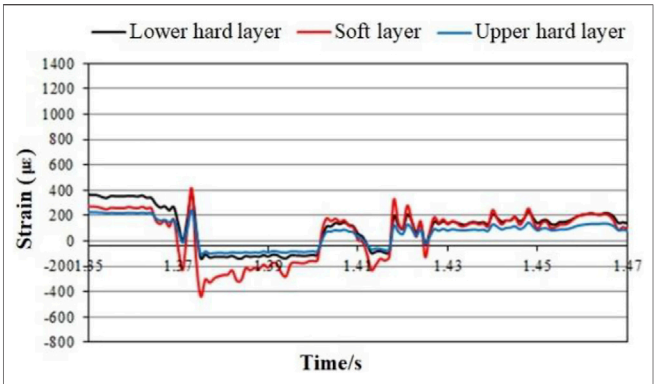

FIGURE 7 | Radial strain characteristic curve II of each layer during simultaneous blasting of Nos 1, 2, and 3.

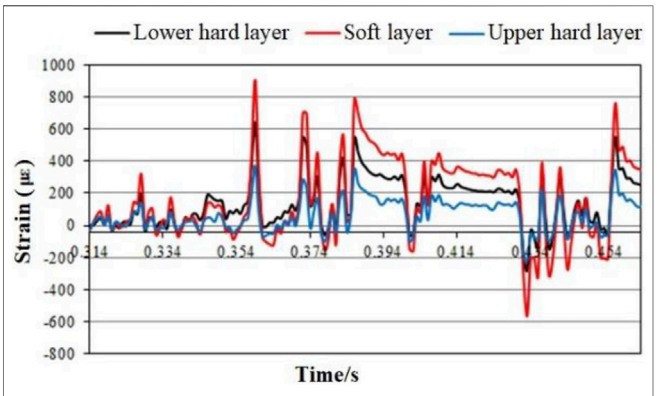

FIGURE 8 | Vertical strain characteristic curve I during simultaneous blasting of Nos 1, 2, and 3.

mainly affected by the internal structure of each layer under the effect of blasting. In reality, the surrounding slopes are often within the influence range of small explosive energy. Therefore, the deformation of the slope is mainly affected by the internal structure of each layer, which requires special attention.

Uncoordinated Particle Motion

Based on the analysis of the acceleration response characteristics, it can be known that there is an uncoordinated dynamic variation in the acceleration responses of different layers, and such variation is more significant between the horizontal and vertical directions. This may be related to the uncoordinated movement of medium particles in each layer during the blasting process.

In the blasting test, the acceleration sensor can be seen as a particle, and the vibration of the stress wave can be regarded as the movement of the particle. In each layer in a slope with a weak interlayer, the particle motion is not only affected by the stress wave but also by the size of the space it is located.

① Due to the different dielectric materials of the upper and lower hard layers and the soft layer, the density of the media in each layer and the movement space of the media particles are different. In addition, the stress wave is reflected, superimposed, and destructed during the propagation process from bottom to top, so the movement of the medium particles in each layer is different, presenting uncoordinated dynamic movements;

② As blasting vibration progresses, the density of the slope media particles increases with depth, which results in the vertical motion of the media particles in each layer being more restricted than the horizontal direction. Therefore, the vertical (Z) acceleration characteristic curve is slightly different from the horizontal (X) acceleration characteristic curve, but both of them have shown uncoordinated dynamic responses.

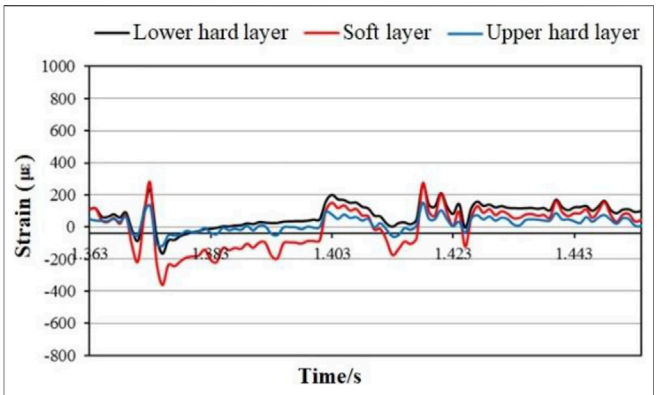

FIGURE 9 | Vertical strain characteristic curve II during simultaneous blasting of Nos 1, 2, and 3.

Uncoordinated Deformation

Considering the uncoordinated movements of medium particles in each layer and different yield strengths and ultimate strengths of the material, it will inevitably lead to uncoordinated deformation of the layers, which is mainly reflected by the difference in the plastic creep of the layers. When the explosive energy is small, the difference is particularly significant, indicating that the slope deformation is mainly affected by the internal structure of each layer. For example, when the explosive charge was small (5 g), the radial strain characteristic curve I of each layer under blasting of hole 2 shows that the strain fluctuation of the soft layer was much larger than that of the upper and lower hard layers, while the strain fluctuations of the upper and lower hard layers basically synchronized. This result suggests that when the explosive charge is small, the stress provided by the generated explosive energy is close to the yield strength of the soft layer and is far less than the yield strength of the upper and lower hard layers, resulting in severe yield deformation of the soft layer and further causing complex strain fluctuations in the upper and lower hard layers.

Since blasting vibration and seismic vibration have certain similarities to the deformation and destruction of engineering buildings, it can be inferred that during seismic vibration, there may be uncoordinated deformation characteristics of the layers of slopes with weak interlayers. This inference can be supported by a previous study (Cui et al., 2019; Cui 2017; Cui, et al., 2021).

SUMMARY

Based on blasting physical simulations, this study has investigated the influence of explosive charge, blast radius, blast directions, and multi-hole blasting on the dynamic response of a slope with a weak interlayer. The conclusions are as follows:

1) With a certain amount of the explosive charge, the acceleration response of each layer of the model showed a sharp fluctuation during single-hole blasting, and the overall performance of the three layers is as follows: lower hard layer > soft layer > upper hard layer. The peak and valley values of the acceleration curves of different layers appeared to be displaced, indicating that the dynamic responses of different layers were inconsistent, and their performance was slightly different in the vertical and horizontal directions. In addition, the smaller the explosive charge (such as 5 g), the more obvious the displacement of the peak and valley values of the acceleration curve and the more significant the uncoordinated dynamic responses. As the explosive charge increased (i.e., 7g, 10 g), the displacement of peak and valley values of the acceleration curve gradually decreased, and the incoordination of the dynamic responses of different layers gradually weakened and tended to synchronize. During multi-hole blasting, similar characteristics were observed as the above, but the acceleration response showed two sharp fluctuations, and the uncoordinated dynamic response gradually weakened.
2) The acceleration response of each layer decayed with the increase of the blast radius, and the acceleration response decay rate was different for different layers in different directions. As the blast radius further increased, the acceleration response decay rate of each layer gradually synchronized.
3) The acceleration response of each layer was different in different blast directions, and the acceleration response of each layer was more violent during bottom blasting than leading-edge blasting.
4) Under the effect of blasting, the strain waveform of each layer changed in three phases: front, middle, and tail. The strain curve of the middle phase fluctuated violently. The strain fluctuation of the tail phase was relatively stable but showed a certain degree of plastic creep. The uncoordinated deformation of each layer was obvious in the middle and tail phases. The uncoordinated deformation trend of different layers changed in varying degrees depending on the variation of blasting factors such as explosive charge, blast radius, blast direction, and blasting method.
5) The uncoordinated dynamic response of each layer has caused uncoordinated deformation. The uncoordinated dynamic change in the response was particularly significant when the explosive energy was less than the critical explosive energy, indicating that the change was mainly affected by the internal structure of the slope, i.e., the uncoordinated movement of medium particles. Furthermore, it is closely related to the strength of the material, propagation path of the blast wave, refraction, and the degree of superposition cancellation. When the explosive energy is large and exceeds the critical explosive energy, it can be speculated that the uncoordinated dynamic response of different layers would gradually weaken and tend to synchronize.

The physical model applied in this study is generalized from the geological prototype based on the similarity principle. Although our results were based on the scale test, the dynamic responses and basic laws of the slope model under blasting loading were effective. The blasting vibration in the mining area is very complex. It is difficult to fully meet the similarity. The obtaining of on-site blasting data is also difficult. In this study, the engineering analogy method was used to select blasting parameters. We argue that the test results can show the influence of the blasting dynamic load on the slope.

However, in actual working conditions, the surrounding slopes are mostly within the influence range of the smaller explosive energy. Our explosions are very close to the measurement points. It would be better to vary the physical model with blasts at distances farther away from those carried out. The deformation of the slope far away from the blasting position is mostly affected by the internal structure of the slopes. It is advised to pay special attention to this kind of situation and deploy appropriate measures to monitor any deformation. The critical explosive energy needs to be further studied, and it should be noted that the critical explosive energy varies with different lithology. Research is still required on how to establish the relationship between critical explosive energy and factors of blasting, such as the explosive charge and blast radius. In addition, the laws of motion for particles of different materials under blasting vibration still need to be explored to confirm the speculations in this study. It should be noted that more examples are needed to verify these results. Its validity for real cases should be supported by more research.

DATA AVAILABILITY STATEMENT

The original contributions presented in the study are included in the article/**Supplementary Material**; further inquiries can be directed to the corresponding author.

AUTHOR CONTRIBUTIONS

XZ designed the conceptualization, methodology, data curation, and the original draft preparation. QY performed data curation and formal analysis. XP was responsible for supervision and project administration. RD was responsible for resources, supervision, and reviewing and editing of the manuscript.

FUNDING

This project was partially supported by the National Key R&D Program of China (No. 2017YFC1501002), the National Science Foundation of China (No. 41907254 and 41931296), the Postdoctoral Foundation of China (No. 2020M683272).

ACKNOWLEDGMENTS

The authors particularly appreciate the valuable comments made by the editors and reviewers to make a substantial improvement to this manuscript.

SUPPLEMENTARY MATERIAL

The Supplementary Material for this article can be found online at: https://www.frontiersin.org/articles/10.3389/fenrg.2021.812492/full#supplementary-material

REFERENCES

Adushkin, V. V. (2019). Hill Slope Falls and Long-Runout Rockslides under Large-Scale Underground Blasting. *J. Min. Sci.* 55, 893–904. doi:10.1134/s1062739119066271

Bai, Z., Huang, S., and Lu, M. (1995). Effects of Blasting on Stability of Slope Rock Mass. *Subgrade Eng.*, 19–23. (in Chinese).

Benchelha, T., Remmal, T., El Hamdouni, R., Ejjaouani, H., Mansouri, H., El Kamel, F., et al. (2017). Combined Effects of Blasting and Geological Structure on Rock Mass Stability-A Case Study from the Marrakech-Agadir Highway, Morocco. *Bull. Eng. Geol. Environ.* 76, 815–828. doi:10.1007/s10064-016-0867-5

Chang, J. X., Song, Z., Tian, L., Liu, H., Wang, L., and Wu, X. (2007). Numerical Analysis of Effect of Water on Explosive Wave Propagation in Tunnels and Surrounding Rock. *J. Univ. China Min. Tech.* 17 (3), 368–371. doi:10.1016/S1006-1266(07)60107-2

Cui, S., Pei, X., Jiang, Y., Wang, G., Fan, X., Yang, Q., et al. (2021). Liquefaction Within a Bedding Fault: Understanding the Initiation and Movement of the Daguangbao Landslide Triggered by the 2008 Wenchuan Earthquake (Ms = 8.0). *Eng. Geol.* 295, 106455.

Cui, S., Pei, X., and Huang, R. (2019). Initiation Mechanism of Daguangbao Landslide: Uncoordinated Deformation of Sliding Zone and Dynamic Damage to Rock Mass during strong Earthquakes. *Chin. J. Rock Mech. Eng.* 38 (2), 237–253. (in Chinese). doi:10.13722/j.cnki.jrme.2018.1041

Cui, S. (2017). *Seismic Responses of Wake Interlayer and Initiation Mechanisms of Large Landslide during Strong Earthquake*. Ph.D. thesis. Chengdu (China): Chengdu University of Technology. (in Chinese).

Deb, D., Kaushik, K. N. R., Choi, B. H., Ryu, C. H., Jung, Y. B., and Sunwoo, C. (2011). Stability Assessment of a Pit Slope under Blast Loading: A Case Study of Pasir Coal Mine. *Geotech. Geol. Eng.* 29, 419–429. doi:10.1007/s10706-010-9387-4

Deng, E., Yang, W., Lei, M., Yin, R., and Zhang, P. (2018). Instability Mode Analysis of Surrounding Rocks in Tunnel Blasting Construction with Thin Bedrock Roofs. *Geotech. Geol. Eng.* 36, 2565–2576. doi:10.1007/s10706-018-0483-1

Dvořák, A. (1977). Landslides Caused by Blasting. *Bull. Int. Assoc. Eng. Geology* 16, 166–168.

Fan, C., and Ge, J. (2020). Dynamic Calculation Method of Vibration Response of Building Blasting Based on Differential Equation. *Environ. Technol. Innovation* 20, 101178. doi:10.1016/j.eti.2020.101178

Görgülü, K., Arpaz, E., Demirci, A., Koçaslan, A., Dilmaç, M. K., and Yüksek, A. G. (2013). Investigation of Blast-Induced Ground Vibrations in the Tülü boron Open Pit Mine. *Bull. Eng. Geol. Environ.* 72, 555–564. doi:10.1007/s10064-013-0521-4

González-Nicieza, C., Álvarez-Fernandez, M. I., Alvarez-Vigil, A. E., Arias-Prieto, D., López-Gayarre, F., and Ramos-Lopez, F. L. (2014). Influence of Depth and Geological Structure on the Transmission of Blast Vibrations. *Bull. Eng. Geol. Environ.* 73, 1211–1223. doi:10.1007/s10064-014-0595-7

Hakan, Ak., Melih, I., Mahmut, Y., and Adnan, K. (2009). Evaluation of Ground Vibration Effect of Blasting Operations in a Magnesite Mine. *Soil Dyn. Earthquake Eng.* 29 (4), 669–676. doi:10.1016/j.soildyn.2008.07.003

He, L., Zhong, D., Liu, Y., and Song, K. (2021). Prediction of Bench Blasting Vibration on Slope and Safety Threshold of Blasting Vibration Velocity to Undercrossing Tunnel. *Shock and Vibration* 2021, 1–14. doi:10.1155/2021/9939361

Hempen, G. L. (2019). "Reducing Impacts Potentially Triggered by Blasting," in IAEG/AEG Annual Meeting Proceedings, San Francisco, California, September 17–23, 2018. Editors A. Shakoor and K. Cato. 2018–Volume 6. doi:10.1007/978-3-319-93142-5_17

Jiang, N., Zhou, C., Lu, S., and Zhang, Z. (2018). Effect of Underground Mine Blast Vibrations on Overlaying Open Pit Slopes: A Case Study for Daye Iron Mine in China. *Geotech. Geol. Eng.* 36, 1475–1489. (in Chinese). doi:10.1007/s10706-017-0402-x

Kesimal, A., Ercikdi, B., and Cihangir, F. (2008). Environmental Impacts of Blast-Induced Acceleration on Slope Instability at a limestone Quarry. *Environ. Geol.* 54, 381–389. doi:10.1007/s00254-007-0825-4

Li, J., Zhang, L., and Yan, R. (2001). Mechanism of Rock Slope Unstability and Critical Vibration Velocity under Action of Blasting Seism Wave. *Mining Metall.* 10 (1), 11–15. (in Chinese).

Li, H., Deng, J., Feng, P., Pu, C., Arachchige, D. D. K., and Cheng, Q. (2021a). Short-Term Nacelle Orientation Forecasting Using Bilinear Transformation and ICEEMDAN Framework. *Front. Energ. Res.* 9, 780928. doi:10.3389/fenrg.2021.780928

Li, H., Deng, J., Yuan, S., Feng, P., and Arachchige, D. D. K. (2021b). Monitoring and Identifying Wind Turbine Generator Bearing Faults Using Deep Belief Network and EWMA Control Charts. *Front. Energ. Res.* 9, 799039. doi:10.3389/fenrg.2021.799039

Liu, Y. (2009). Study on the Failure Mechanism and Safety of Layered Rock Slopessubjected to Dynamic Loads. Ph.D. Dissertation. Chinese Academy of Science.

Lu, S., Zhou, C., Jiang, N., and Xu, X. (2015). Effect of Excavation Blasting in an Under-cross Tunnel on Airport Runway. *Geotech. Geol. Eng.* 33, 973–981. doi:10.1007/s10706-015-9879-3

Lu, S., Zhou, C., Zhang, Z., Ji, L., and Jiang, N. (2020). PPV Criterion of a Rock Slope Imbedded with a Fault Subjected to Blasting P-Waves. *Shock and Vibration* 2020, 1–7. doi:10.1155/2020/8865981

Luo, Z., Qin, Y., Xie, C., and Wang, W. (2015). Instability Process of the Cut Slopes under Complex Mining Environment. *Chin. J. Geol. Hazard Control.* 26 (03), 81–85. (in Chinese).

Mohamad, E. T., Yi, C. S., Murlidhar, B. R., and Saad, R. (2018). Effect of Geological Structure on Flyrock Prediction in Construction Blasting. *Geotech. Geol. Eng.* 36, 2217–2235. doi:10.1007/s10706-018-0457-3

Ozcelik, Y. (1998). Effect of Discontinuities on Fragment Size Distribution in Open–Pit Blasting-A Case Study. *Trans. Inst. Mining Metall.* 107 (A), 146–151.

Singh, V. K., and Singh, D. P. (1995). Controlled Blasting in an Open-Pit Mine for Improved Slope Stability. *Geotech. Geol. Eng.* 13, 51–57. doi:10.1007/bf00600523

Song, J., Hao, S., Yue, L., and Li, H. (2017). Analysis of the Dumping Deformation Mechanism of Jiangjunyayan Painting Area Caused by Mining and Control Measures. *Chin. J. Geol. Hazard Control.* 28 (04), 40–46. (in Chinese). doi:10.16031/j.cnki.issn.1003-8035.2017.04.07

Sun, J., Li, Z., Liu, G., Chen, M., and Jiang, Q. (2018). Dynamic Stress and Vibration Characteristics of Geomaterials in Slopes Induced by Blasting Vibration. *J. Vibration Shock* 37 (10), 141–148. doi:10.13465/j.cnki.jvs.2018.10.021

Wang, Z.-L., Li, Y.-C., and Shen, R. F. (2007). Numerical Simulation of Tensile Damage and Blast Crater in Brittle Rock Due to Underground Explosion. *Int. J. Rock Mech. Mining Sci.* 44 (5), 730–738. doi:10.1016/j.ijrmms.2006.11.004

Wang, W., Yuan, Q., Jiang, H., and Chen, P. S. (2019). Influence and Safety Control of Blasting Vibration on Existing Lining for Closely Tunnel Expansion. *IOP Conf. Ser. Earth Environ. Sci.* 351, 012043. doi:10.1088/1755-1315/351/1/012043

Wang, J. (2017). *Spread Regularity of Blasting Vibration on the Slope and the Influence on Slope Stability*. Mianyang (China): Southwest University of Science and Technology. (in Chinese).

Yuan, P. (2016). *Model-based Testing Research on Deep Rock Mass Rupture under Blast Loading*. Hefei (China): Anhui University of Science and Technology. (in Chinese).

Conflict of Interest: The authors declare that the research was conducted in the absence of any commercial or financial relationships that could be construed as a potential conflict of interest.

Publisher's Note: All claims expressed in this article are solely those of the authors and do not necessarily represent those of their affiliated organizations, or those of the publisher, the editors, and the reviewers. Any product that may be evaluated in this article, or claim that may be made by its manufacturer, is not guaranteed or endorsed by the publisher.

frontiers in Energy Research

ORIGINAL RESEARCH
published: 20 January 2022
doi: 10.3389/fenrg.2021.803010

Operation State Evaluation Method of Smart Distribution Network Based on Free Probability Theory

Jiaxin Zhang[1], Bo Wang[1], Hongxia Wang[1], Hengrui Ma[2], Fuqi Ma[1], Yifan Li[1] and Yingchen Zhang[1]*

[1]School of Electrical Engineering and Automation, Wuhan University, Wuhan, China, [2]Tus-Institute for Renewable Energy, Qinghai University, Qinghai, China

In view of the current situation that the new generation of smart grids with "double high" characteristics is in urgent need of effective state evaluation methods due to the characteristics of strong volatility and diverse demands, a method of operation state evaluation of smart distribution networks based on free probability theory is proposed, which is combined with high-order moment indexes to describe the operation trajectory of distribution networks from a data-driven perspective. First, the state assessment problem of smart distribution networks is modeled as a binary hypothesis testing problem, and the asymptotic free equation is established based on free probability theory to provide a framework for state assessment of distribution networks. Then, a high-order moment evaluation index is proposed, combined with the sliding time window processing, and the high-order moment sequence was obtained based on the high-dimensional data of the distribution network, which is used to describe the state evolution of the distribution network. Finally, this method is applied to a certain 110-kV distribution network. The analysis of an example shows that the proposed evaluation framework and indicators can effectively reflect the data changes in the distribution network and support the state assessment and evolution analysis of the distribution network.

Keywords: free probability theory, asymptotic spectral distribution, free convolution operation, distribution network status assessment, moments

OPEN ACCESS

Edited by:
Yusen He,
Grinnell College, United States

Reviewed by:
Lei Zhang,
China Three Gorges University, China
Tongmao Zhang,
The University of Manchester, United Kingdom

****Correspondence:***
Bo Wang
whwdwb@whu.edu.cn

Specialty section:
This article was submitted to Smart Grids, a section of the journal Frontiers in Energy Research

Received: *28 October 2021*
Accepted: *08 December 2021*
Published: *20 January 2022*

Citation:
Zhang J, Wang B, Wang H, Ma H, Ma F, Li Y and Zhang Y (2022) Operation State Evaluation Method of Smart Distribution Network Based on Free Probability Theory. Front. Energy Res. 9:803010. doi: 10.3389/fenrg.2021.803010

INTRODUCTION

As China proposes "to achieve carbon peak before 2030 and achieve carbon neutrality before 2060," improving overall energy utilization efficiency and focusing on developing renewable energy has become an inevitable choice. The power system is closely related to the production, transportation, and consumption of renewable energy, which also plays a key role in promoting energy transformation (Zhou et al., 2018). Moreover, the new generation smart grid has the characteristics of "double high": the high proportion of renewable energy and the high proportion of power electronic equipment. Distributed power supply, charging pile/station, and controllable load, along with other devices, are developing rapidly, and their large-scale access to the distribution network has brought strong uncertainties to the distribution network due to their characteristics of strong intermittent and diverse demands, making the operation mode of the distribution network increasingly complex and changeable.

As a pivotal link of energy, an intelligent distribution network is the key to the smooth operation of "the production-supply-marketing" of electric energy. The ultimate goal of the intelligent

distribution network is to build and form a panoramic real-time system covering the distribution network. The basis of supporting the panoramic real-time system of the distribution network is the collection, transmission, and storage of panoramic real-time data of the distribution network and the effective technology for rapid analysis of massive multi-source data (Liu, 2010; Yang et al., 2019; Shen and Raksincharoensak, 2021a; Yang et al., 2021a; Shen and Raksincharoensak, 2021b; Yang et al., 2021b; Zhang et al., 2021). The application of cloud computing, big data, Internet of Things, 5G information communication technology, and artificial intelligence in the power system provides a data basis for the realization of real-time state estimation and situation awareness of the smart distribution network (Yang et al., 2018; Shen et al., 2020a; Ma et al., 2020; Wang et al., 2020). However, the existing distribution network state estimation and situation awareness methods find it difficult to meet the requirements in many aspects of calculation accuracy, calculation speed, and visualization. Thus, it has become a hot topic for experts, scholars, and engineers at home and abroad to construct an effective state estimation and situation awareness system for the intelligent distribution network to support comprehensive, accurate, and real-time control of the operation situation of the distribution network.

In the field of power system state assessment, apart from the specific model method, classical research methods also include the analytic hierarchy process (AHP), the fuzzy comprehensive evaluation method, and principal component analysis (PCA). The literature (Cao et al., 2007) has proposed a comprehensive evaluation method for a new rural low-voltage distribution network based on the AHP and realized practical application. However, this method mainly solved the problems of distribution network construction planning and transformation in the near future and could not evaluate the real-time status. The literature (Sun et al., 2017) combined PCA and system clustering analysis to establish a comprehensive evaluation system of county power grids, which could evaluate the power grid from five aspects of security, economy, reliability, adaptability, and quality, but also could not evaluate the real-time state.

In recent years, data-driven state assessment has also been applied in the power field. The literature (Xu et al., 2016) proposed a correlation analysis method based on random matrix theory (RMT). Combining real-time separation window technology with RMT, the mean spectrum radius (MSR) index was used to evaluate the correlation of distribution network data. In the literature (Xu et al., 2018), the evaluation indexes of the hit ratio and the false alarm rate were proposed, and the vulnerability of the distribution network was evaluated based on RMT. The literature (He et al., 2017a) used the basic breakthrough of high-dimensional statistics in recent years to put forward the research framework of space-time big data of the distribution network based on the random matrix. For power system fault identification, the literature (Xu et al., 2019) proposed a feature self-learning method based on deep learning for high-dimensional space-time fault samples, which had fast calculation speed and strong robustness. However, the method itself had high requirements on source data but low comprehensibility. The literature (Wei et al., 2016) proposed a high-dimensional power data fusion method based on correlation mining in order to solve the key problem of online stability analysis of large power grids. This method mainly solved the problem of data fusion and did not directly evaluate the status of the large power grid.

The key of power system state evaluation based on high-dimensional big data should be the construction of an evaluation framework and an evaluation index system and identification of a power grid or equipment evolution situation. In this study, the free probability theory (FPT) is introduced into the electric power field for the first time in China, providing a complete and clear evaluation framework for the operation status of the smart distribution network, combining with sliding time window processing to solve the high-dimensional source data to obtain the time series of the index. In this study, the high-order moment index is also proposed to analyze the distribution network from the perspective of the state assessment and evolution trend and is applied to the state assessment of the 110-kV distribution network to verify the effectiveness of the proposed method.

FREE PROBABILITY THEORY AND BIG DATA PROCESSING METHODS

Introduction to Free Probability Theory

A random matrix is a matrix whose elements are random variables. Through the high-dimensional statistical analysis, important information can be extracted from massive disordered data in a random matrix.

Free probability theory can provide an effective analysis framework for the asymptotic spectrum distribution of high-dimensional random matrices. In the 1980s, Voiculescu proposed FPT to deal with abstract "non-commutative space," and the random matrix is a special case of "non-commutative space" (Dan, 1986; Voiculescu, 1987). The purpose of FPT is to introduce a concept similar to "independence" in classical probability theory, namely, "freedom," and make it applicable to non-commutative random variables such as random matrices and extend it to the case of large dimensions, namely, "asymptotic freedom."

Different from traditional mathematical theory, FPT defines some new operators, including additive-free convolution $\boxplus$ and its inverse operation additive-free deconvolution $\boxminus$, multiplicative-free convolution $\boxtimes$ and its inverse operation multiplicative-free deconvolution $\boxdot$, similar to the addition, subtraction, multiplication, and division operations in classical mathematics. Based on the asymptotic spectrum theory of RMT, combining the concept of asymptotic freedom with the above new operators, some difficult problems in classical mathematics can be solved. In traditional mathematics, if and only if two matrices are commutative, the eigenvalues of their sum matrix or product matrix can be obtained from their respective eigenvalues. In FPT, if two random matrices are asymptotically free and their respective asymptotic spectral distributions are known, the asymptotic spectral distributions of their sum matrix or product matrix can be obtained and *vice versa*. It is worth mentioning that in FPT, the semicircular law is similar to the classical Gaussian distribution, that is, the normalization of the free random matrix (given spectral distribution) and the spectral

distribution of matrix converge to the semicircular law; the Marchenk–Pastur law (M-P law) is similar to the classical Poisson distribution, that is, the normalization of those single-rank free random matrices and the spectral distribution of matrices converge to the M–P law (Tulino and Verdu, 2004).

FPT has become a powerful tool to describe the characteristics of wireless communication systems. Spectrum sensing algorithms based on FPT have fast convergence, which are also suitable for the limited number of samples, and have high sensing performance in the case of low signal-to-noise ratio (Tulino and Verdu, 2004). Domestic and foreign scholars have made great academic achievements in this field. This study is the first attempt to apply the FPT to the electric power field, which selects the operation of the smart distribution network as the application scenario and evaluates the operation status of the distribution network based on FPT, providing real-time and efficient support for intelligent operation and maintenance.

Free Probability Theory

Definition. 1 (Dan, 1986) The empirical spectrum distribution of an $N \times N$ random matrix B_N is defined as follows:

$$\mu_{B_N}(x) = \frac{1}{N}\sum_{i=1}^{N} I(\lambda_i(B_N) \le x), \tag{1}$$

where $\lambda_i(B_N), i = 1, 2, \ldots, N$ are the eigenvalues of B_N, $I(\cdot)$ is the indicator function.

In RMT, the asymptotic spectral distribution (ASD) is the empirical spectral distribution of B_N when $N \to \infty$, which is represented by the symbol μ_B, and can be expressed uniquely by the following moment:

$$m_k = \lim_{N\to\infty} \frac{1}{N} E\left\{tr\left(B_N^k\right)\right\} = \int x^k d\mu_B(x), \tag{2}$$

where $\mathrm{tr}(\cdot)$ represents the rank of the matrix and k represents the order of moments. In mathematics and statistics, moments can represent the distribution and morphological characteristics of variables. The specific moment algorithm of the method proposed in this study will be introduced in detail in *Calculation of High-Order Moment Index* section.

As mentioned above, Voiculescu proposed FPT in order to introduce the concept of "freedom" and summarize the law applicable to non-commutative variables such as random matrices, which is similar to the law in classical probability theory.

Random matrices are just one kind of non-commutative variable, and non-commutative variables are all elements of "non-commutative probability space." The concept of a non-commutative probability space is as follows.

Definition. 2 (Couillet and Debbah, 2011) Let B be a non-commutative algebraic system with unit element I; if ϕ is a linear function on B and meet $\phi(I) = 1$, then the order pair (B, ϕ) is called a non-commutative probability space.

For random matrices, the identity element I is the identity matrix I_N, and ϕ is defined as follows:

$$\phi(C) = \frac{1}{N}\sum_{i=1}^{N} E\{C_{ii}\} = \frac{1}{N} E\{tr(C)\}, \tag{3}$$

where $C \in B$, C_{ii} represents the ith row and the ith column element of C. It can be seen from **Eq. 3** that ϕ is the function of solving the moment. This kind of non-commutative probability space meets trace lemma, that is, $\phi(ab) = \phi(ba)$.

Definition. 3 (Couillet and Debbah, 2011) Let (B, ϕ) be a non-commutative probability space, and for all n-dimensional sequences $(b_1 b_2 \ldots b_n)$, if $\phi(b_1 b_2 \ldots b_n) = 0$ satisfies the following conditions:

1) $b_j \in B_{i_j}$, where $i_j \le K$
2) $i_1 \ne i_2, i_2 \ne i_3, \ldots, i_{n-1} \ne i_n$
3) for all $j \in \{1, \ldots n\}$, $\phi(b_j) = 0$

Then, a family of the subalgebra systems of B $\{B_1, \ldots, B_K\}$ is free.

Obviously, if $\{\{b_1\}, \ldots, \{b_n\}\}$ is free (each subalgebra system consists of only one of their elements), then random variables $\{b_1, \ldots, b_n\}$ are free.

Furthermore, let us extend the concept of "freedom" to "asymptotic freedom."

Definition. 4 (Couillet and Debbah, 2011) If the following two conditions are met

1) for all $k \in \{1, \ldots, K\}$, $X_{N,K}$ has an asymptotic spectral distribution;
2) for all $\{i_1, \ldots i_n\} \subset \{1, \ldots, K\}$, $i_1 \ne i_2, i_2 \ne i_3, \ldots, i_{n-1} \ne i_n$ and family of unary polynomials $\{P_1, \ldots, P_n\}$,

$$\lim_{N\to\infty} \phi\left\{P_j\left(X_{N,i_j}\right)\right\} = 0, j \in \{1, \ldots, n\} \tag{4}$$

and

$$\lim_{N\to\infty} \phi\left\{\prod_{j=1}^{n} P_j\left(X_{N,i_j}\right)\right\} = 0. \tag{5}$$

Then the $N \times N$ random matrix family $\{X_{N,1}, \ldots, X_{N,K}\}$ of non-commutative probability spaces (B_N, ϕ) is asymptotically free.

Based on the above definition of asymptotic freedom, combined with new operators such as additive-free convolution, the following illustration is made. If two random matrices $A_N \in \mathbb{C}^{N\times N}$ and $B_N \in \mathbb{C}^{N\times N}$ are asymptotically free, with their asymptotic spectral distributions denoted as μ_A and μ_B, respectively, and $A_N + B_N$ is known to have asymptotic spectral distribution μ_{A+B}, then

$$\mu_{A+B} = \mu_A \boxplus \mu_B, \tag{6}$$

where $\boxplus$ is called additive-free convolution, namely, μ_{A+B} is the additive-free convolution of μ_A and μ_B.

Furthermore, $\boxminus$ is defined as additive-free deconvolution, that is, if $\mu_C = \mu_A \boxplus \mu_B$, then $\mu_A = \mu_C \boxminus \mu_B$, and $\mu_B = \mu_C \boxminus \mu_A$. So additive-free convolution and additive-free deconvolution are inverse operations of each other.

Similarly, if $A_N B_N$ has an asymptotic spectral distribution μ_{AB}, then

$$\mu_{AB} = \mu_A \boxtimes \mu_B, \tag{7}$$

where $\boxtimes$ is called multiplicative-free convolution, namely, μ_{AB} is the multiplicative-free convolution of μ_A and μ_B.

Furthermore, $\boxdot$ is defined as additive-free deconvolution, that is, if $\mu_C = \mu_A \boxtimes \mu_B$, then $\mu_A = \mu_C \boxdot \mu_B$, and $\mu_B = \mu_C \boxdot \mu_A$. So multiplicative-free convolution and multiplicative-free deconvolution are inverse operations of each other. Both additive- and multiplicative-free convolution are commutative, namely, $\mu_A \boxplus \mu_B = \mu_B \boxplus \mu_A, \mu_A \boxtimes \mu_B = \mu_B \boxtimes \mu_A$. In this way, non-commutative variables (such as random matrices) can be exchanged in the operation.

DISTRIBUTION NETWORK STATE ESTIMATION METHOD BASED ON FPT

Data Pre-Processing

Supervisory Control and Data Acquisition (SCADA) is widely applied in the power system and collects the branch power, branch current amplitude, and node voltage amplitude in the system with high maturity, mainly through the remote terminal unit (RTU) and the feeder terminal unit (FTU) (Yang et al., 2020a; Shen et al., 2020b; Zhu et al., 2020; Li et al., 2021a; Shen et al., 2021a; Shen et al., 2021b; Qi et al., 2021; Xiang et al., 2021). The data collected by SCADA has the characteristics of mass and high dimension, so a high-dimension random matrix can be constructed according to the collected data. Combined with the sliding time window processing, the data characteristics of the distribution network can be analyzed based on FPT, and the distribution network state before and after can be compared in time to further realize the evolution of the distribution network operation state.

Assume that i nodes in the distribution network are equipped with measuring devices, and the sampling interval is 0.01 s. At the sampling time t_n, i nodes each generate a state data (which can be voltage, current, and power angle), and the state data of all nodes at this time constitute a column vector $x(t_n)$, as shown in the following formula:

$$x(t_n) = \left[x_{1t_n}, x_{2t_n}, \ldots, x_{it_n}\right]^T. \tag{8}$$

When there are a total of j sampling moments, the j column vectors are arranged to form a high-dimensional random matrix $X_{i\times j}$, as shown below:

$$X_{i\times j} = \begin{bmatrix} x_{11} & x_{12} & \ldots & x_{1j} \\ x_{21} & x_{22} & \ldots & x_{2j} \\ \vdots & \ldots & \ldots & \ldots \\ x_{i1} & x_{i2} & \ldots & x_{ij} \end{bmatrix}, \tag{9}$$

In the above formula, each row of $X_{i\times j}$ is the state data of the same node at different times, and each column is the state data of different nodes at the same time.

The normalization process is carried out according to **Eq. 10** below, and the normalized matrix $\tilde{X}$ with mean value $E = 0$ and variance $\sigma^2 = 1$ is obtained as follows:

$$\tilde{X}_l = \left(X_l - E(X_l)\right) \Big/ \sigma^2(X_l), l = 1, 2, \ldots, i, \tag{10}$$

where X_l is the lth row of X.

In statistical analysis of high-dimensional data, when the amount of data is large enough, the data as a whole will show certain random statistical characteristics after corresponding processing, such as the single ring theorem and the M–P law (Ling et al., 2018; Jain et al., 2019; Deepa et al., 2020; Xiong et al., 2020; Yang et al., 2020b; Li et al., 2021b; Li et al., 2021c; Yang et al., 2021c; Li et al., 2021d; Ye et al., 2021; Dong and Li, 2021; Liu et al., 2021; Mousavizadeh et al., 2021; Ouyang and Xu, 2021; Zhu et al., 2021). In the statistical analysis of high-dimensional power data, the corresponding linear eigenvalue statistics (LES) are constructed, such as MSR, high-order moment, etc., which can effectively represent the state of the distribution network. When there are only random fluctuations and measurement errors in the measured data, the data present a random statistical characteristic as a whole. If abnormal events occur in the power system, the original stable operation state of the system will be broken, and the measured data will change accordingly.

State Assessment Model Construction

The problem of distribution network operation state assessment is understood as a binary hypothesis testing problem, as follows:

$$y(n) = \begin{cases} v(n), & H_0 \\ x(n) + v(n), & H_1 \end{cases}, \tag{11}$$

where $y(n)$ represents the received sampled signal, $x(n)$ represents the event signal component, and $v(n)$ represents the noise component.

The above binary hypothesis testing problem is further explained. H_0 means that no abnormal events occur, and the received sampled signal only has randomly distributed noise components. H_1 indicates that abnormal events occur, event signals exist in the sampled signals, and the original stable operation state of the system is broken.

In this study, the basic idea of the distribution network state estimation method based on FPT is to estimate the asymptotic spectrum distribution of the event signal component $x(n)$ by establishing and solving the asymptotic free equation and then calculate the high-order moment index m_i ($i = 1, 2, \ldots, n$) of the event signal component $x(n)$. Thus, the high-order moment is the detection statistic of the algorithm.

Assuming that N received sampled signals y (1), y (2), . . ., y(N) are used for distribution network state estimation and each sampled signal is composed of M signal components, the sample covariance matrix of received sampled signals is as follows:

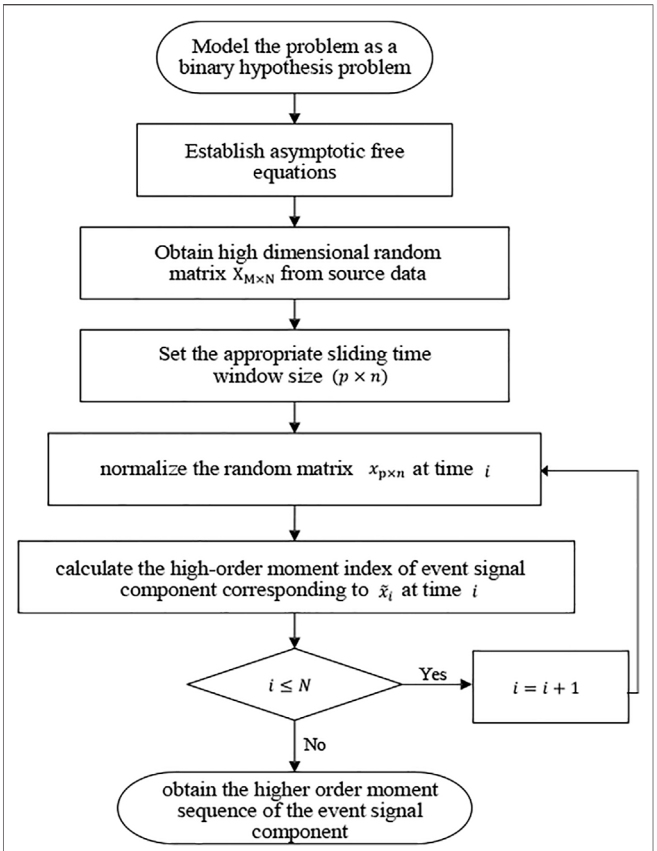

FIGURE 1 | Distribution network status evaluation process based on FPT.

$$\hat{\sum}_y = \frac{1}{N}\sum_{n=1}^{N} y(n)y(n)^H. \tag{12}$$

The sample covariance matrix of signal component $x(n)$ is as follows:

$$\hat{\sum}_x = \frac{1}{N}\sum_{n=1}^{N} x(n)x(n)^H. \tag{13}$$

In FPT, for the signal–noise model, the asymptotic spectral distributions of the above two sample covariance matrices $\hat{\Sigma}_y$ and $\hat{\Sigma}_x$ satisfy the following asymptotic free equation (Ryan and Debbah, 2007):

$$\mu_{\hat{\sum}_y} \boxdot \mu_c = \left(\mu_{\hat{\sum}_x} \boxdot \mu_c\right) \boxplus \mu_{\sigma^2 I}, \tag{14}$$

where $c = M/N$, and $\mu_{\sigma I}^2$ represents a probability distribution that has value only at point σ^2.

After rigorous mathematical derivation, the spectral distribution between the sample covariance matrix and the statistical covariance matrix of the event signal components can be obtained to satisfy the following relation:

$$\mu_{\hat{\sum}_x} = \mu_{\sum_x} \boxtimes \mu_{\frac{M}{N}}. \tag{15}$$

Substituted into **Eq. 10**, the asymptotic free equation becomes the following:

$$\mu_{\hat{\sum}_y} \boxdot \mu_c = \left(\mu_{\sum_x} \boxtimes \mu_{\frac{M}{N}} \boxdot \mu_c\right) \boxplus \mu_{\sigma^2 I}. \tag{16}$$

The asymptotic spectrum distribution of event signal component $x(n)$ can be obtained by solving the asymptotic free equation as follows:

$$\mu_{\hat{\sum}_x} = \left[\left(\mu_{\hat{\sum}_y} \boxdot \mu_{\frac{M}{N}}\right) \boxminus \mu_{\sigma^2 I}\right] \boxtimes \mu_c \boxdot \mu_{\frac{M}{N}}. \tag{17}$$

Based on the established asymptotic free equation and the sliding time window method, the high-order moment index of the continuous time window matrix is obtained to observe the state of the distribution network.

The state assessment process of the distribution network is shown in **Figure 1** below.

Calculation of High-Order Moment Index

From the above analysis, it can be seen that the calculation process of solving the high-order moment index is based on the asymptotic free equation, which involves new operators defined by FPT, namely, additive-free convolution and its inverse operation and multiplicative-free convolution and its inverse operation. It is a relatively simple calculation method to calculate additive-free convolution through the moment-cumulant formula (Ryan and Debbah, 2007).

1) Additive-free convolution

The moment-cumulant formula describes the relationship between the moments of a certain measure and the related R transformation. The R transformation of a probability distribution μ is defined as follows:

$$R_\mu = \sum_n \alpha_n^\mu z^n, \tag{18}$$

where α_n^μ is the nth order cumulant of μ. Based on R transformation, additive-free convolution can be realized, as shown in the following formula:

$$R_{\mu_A \boxplus \mu_B} = R_{\mu_A}(z) + R_{\mu_B}(z), \tag{19}$$

which is equivalent to that the cumulative measure has additivity under additive-free convolution. That is,

$$\alpha_n^{\mu_A \boxplus \mu_B} = \alpha_n^{\mu_A} + \alpha_n^{\mu_A}. \tag{20}$$

The moment-cumulant of the distribution μ is given as follows:

$$m_k^\mu = \sum_{n\le k} \alpha_n^\mu coef_{k-n}\left(\left(1 + m_1^\mu z + m_2^\mu z^2 + \ldots\right)^n\right), \tag{21}$$

where $coef_n(\cdot)$ is the coefficient of z^n.

The bidirectional conversion between the cumulant sequence and the moment sequence can be completed by using the above formula, that is, the first n-order cumulants can be obtained from the first n-order moments and *vice versa*.

This article gives a brief description of the use of the moment-cumulant formula in free convolution calculation, and the specific process is described as follows:

1) Taking the sequence of moments as input, vector f=(1,m_1,. . .,m_n) with length n+1 is formed, where m_1 is the first-order moment, and m_n is the nth-order moment. Then n vectors are obtained by convolution calculation according to the following formula:

$$F_1 = f, F_2 = f * f, ..., F_n = *_n f,$$

where * stands for the convolution operation, and *n stands for n-fold classical convolution with itself. With the accumulation of the convolution operation, the length of vector F increases gradually. Since only the first n+1 elements of M_1,. . .,M_n are used in subsequent operations, the length of vector F is uniformly trimmed to n+1 after the convolution operation in order to simplify calculation and reduce the storage space of the operation.

2) Calculate each cumulant iteratively. After the cumulants α_1, . . ., α_{n-1} are obtained by solving the moment-cumulant formula shown in **Eq. 21** for n-1 times, α_n can be obtained by solving the equation for the nth time. It should be added that the relation between each F vector in Step 1) and **Eq. 21** can be expressed by the following:

$$coef_{n-k}\left(\left(1 + \mu_1 z + \mu_2 z^2 + ...\right)^k\right) = F_k(n-k). \tag{22}$$

This equation can also be understood as writing the coefficients in the moment-cumulant formula as k-fold convolution. Based on this formula, it can be known that the kth cumulant is equivalent to the following expression:

$$\alpha_k = \frac{M_1(n+1) - \sum_{1 \le r \le k-1} \alpha_r M_r(k-r)}{M_k(0)}. \tag{23}$$

Thus, the additive-free convolution and additive-free deconvolution can be easily calculated by means of the moment-cumulant formula.

2) Multiplicative-free convolution

Computation involving multiplicative-free convolution and its inverse operation requires the transformation of boxed convolution, denoted as ⊠. Boxed convolution can be understood as a convolution operation acting on a power series polynomial, which involves the concept of non-cross partition not being repeated. Among the various forms of power series, the commonly used power series is *Zeta-series*, defined as $Zeta(z) = \sum z^i$. The sequence of moments under the deterministic measure^{i}is defined as $M(\mu)(z) = \sum_{k=1}^{\infty} m_k z^k$. The literature has proven that the above R transformation is equivalent to the following equation:

$$M(\mu) = R(\mu) \boxtimes Zeta. \tag{24}$$

It can be proven that the boxed convolution acting on the power series polynomial is the combination of multiplicative-free convolution on each measure, where the boxed convolution of power series $c^{n-1}Zeta$ represents the convolution of measure μ_c, as shown in the following formula:

$$M_{\mu \boxtimes \mu_c} = M_\mu \boxtimes \left(c^{n-1} Zeta\right) \tag{25}$$

also written as follows:

$$cM_{\mu \boxtimes \mu_c} = \left(cM_\mu\right) \boxtimes Zeta. \tag{26}$$

It can be found that, in fact, the above equation is the moment-cumulant formula, which is equivalent to **Eq. 21**. Thus, in the calculation process, the cumulant is replaced by the coefficient of cM_μ, and the moment is replaced by $cM_{\mu \times \mu_c}$. It is concluded that the calculation process of additive-free convolution is also applicable to multiplicative-free convolution operation.

CASE STUDIES

Data Sources

Based on Matlab, this study uses the voltage data of 40 buses under the maximum operation mode of the 110-kV distribution network in a certain province in the summer of 2020 to conduct simulation verification. The total duration of voltage data is 5s, the number of each sampled signal components is $M = 40$, and the sampling interval is $\Delta t = 0.01s$, so the high-dimensional random matrix $X_{40\times500}$ of source data can be obtained. The specific case description is shown in **Table 1**. In the following two cases, the high-order moments of the event signal component are obtained based on FPT, and the operation status of the distribution network is analyzed and compared with the classical PCA method (Rong et al., 2019) and the MSR indicator (Zheng et al., 2020) in the commonly used random matrix theory to further verify the effectiveness of the indicators proposed in this study.

Analysis of Cases

In this study, the high-dimensional random matrix of source data is $X_{40\times500}$, that is, $M = 40$ and $N = 500$, and the sliding time window size is set as 40×60, that is, $p = 40, n = 60$, so $c = p/n \in (0, 1)$. The index selected in the method based on FPT is the third-order moment m_3 of the event signal component $x(n)$. The classical PCA assessment indexes for abnormal state detection are T^2 statistics and SPE statistics. The control limit of T^2 statistics is T_α, and $T^2 < T_\alpha$ should be satisfied if the system runs normally; otherwise, it can be considered abnormal. The control limit of SPE statistics is Q_α. If the system is running properly, it should meet the $SPE < Q_\alpha$ requirement; otherwise, it can be considered abnormal. In the evaluation of the MSR index based on RMT, and the calculated inner ring radius is 0.52. If MSR falls below the threshold of the inner ring radius, it indicates the occurrence of abnormal events. As the width of the sliding

TABLE 1 | Case scenario description.

The serial number	Specific case description
Case 1	0–1 s: normal load 1–3 s: all loads are increased by 5% 3–5 s: the load of the whole network is maintained at 105%
Case 2	0–1 s: normal load 1–3 s: a certain line is set to continuously increase the impact load 3–5 s: maintain 3 times the original load

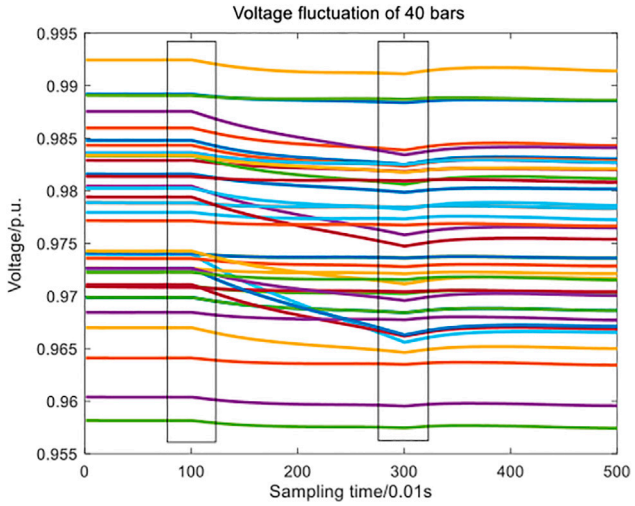

FIGURE 2 | Original voltage data of 40 buses in case 1.

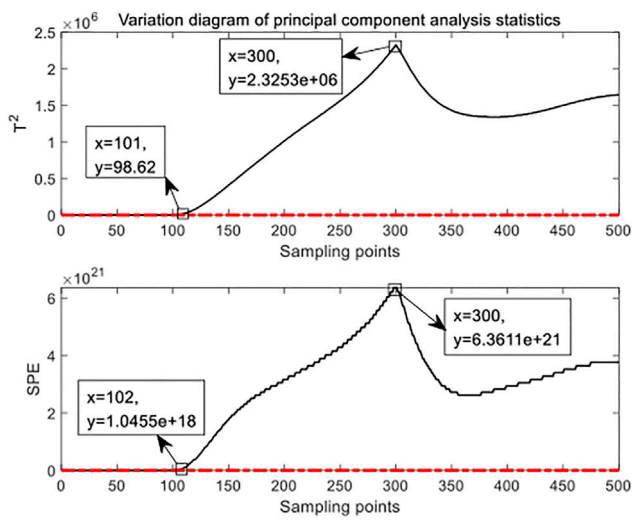

FIGURE 3 | T^2 and SPE indices of case 1.

time window is 60, all moments and MSR indicators in the following figures are 0 before the 60th sampling moment, as hereby stated.

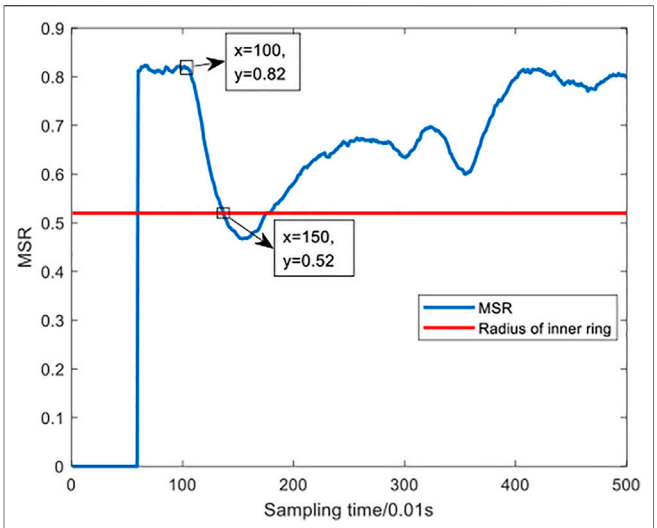

FIGURE 4 | MSR index of case 1.

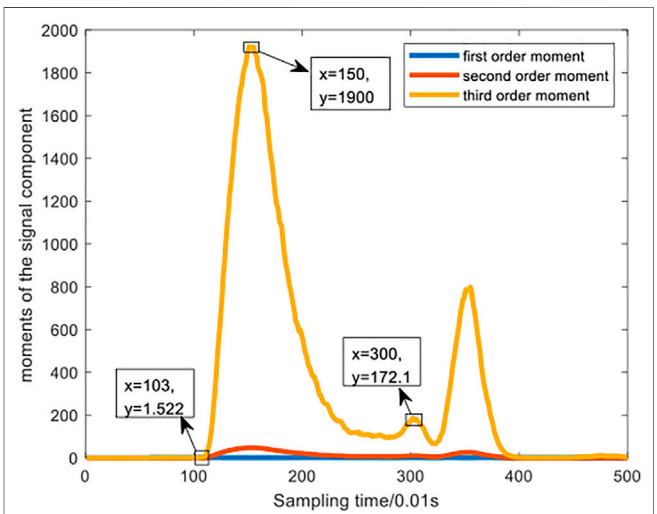

FIGURE 5 | Moments of the signal component in case 1.

In addition, in the power system, the voltage of each user must be kept at the rated value or within the allowable range of voltage offset. Currently, the percentage of voltage offset at the power supply end of 35 kV and above is defined as ±5% in China.

1) Case 1

By observing the voltage fluctuation of the 40 buses in **Figure 2** below, it can be seen intuitively that the voltage unit values of the 40 buses are initially distributed between (0.955,0.995), which are in a normal level, and obvious drops occur at about the 100th sampling time point, that is, the bus voltage drops at about 1s. Subsequently, the buses' voltage stops falling around the 300th

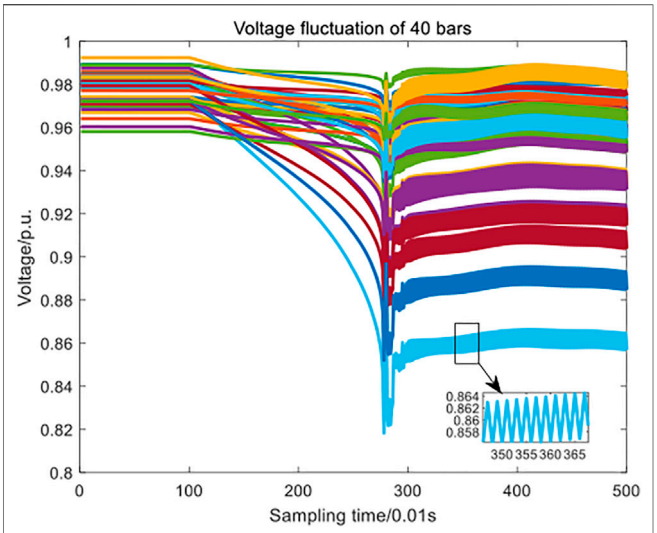

FIGURE 6 | Original voltage data of 40 buses in case 2.

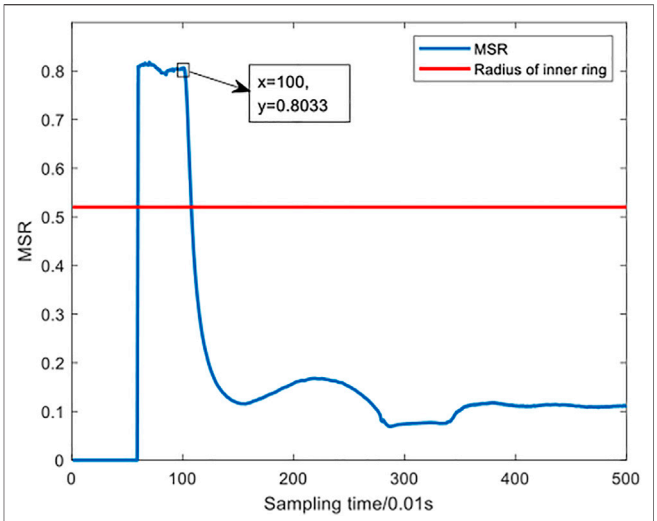

FIGURE 8 | MSR index of case 2.

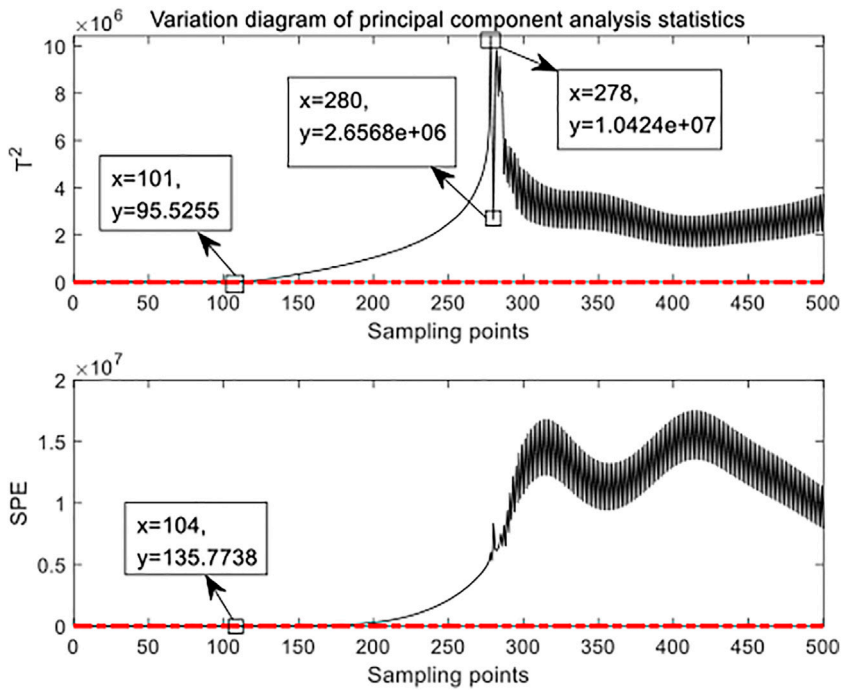

FIGURE 7 | T^2 and SPE indices of case 2.

sampling time point, that is, the bus voltage gradually stabilized after 3s and successfully reached a new stable state.

In **Figure 3**, the red dotted lines are control limits T_α and Q_α, which is the same in **Figure 7**. Observing various indicators in the figures of case 1 (i.e. **Figures 3**, **4**, **Figure 5**), the T^2 index in the PCA method changes dramatically at the 101th sampling point and exceeds T_α, indicating abnormal status. It climbs to the 300th sampling point and then begins to fall but fails to return to the control limit level, indicating that the power grid tried to re-establish a new balance after the third second, but it does not return to the normal state (not in line with the actual situation). Here, the SPE indicator is similar to the T^2 indicator. The MSR index begins to fall significantly at the 100th sampling point and falls below the inner ring radius at the 150th sampling point, indicating that the power grid is in an abnormal state (also not in line with the actual situation) and then gradually recovers to

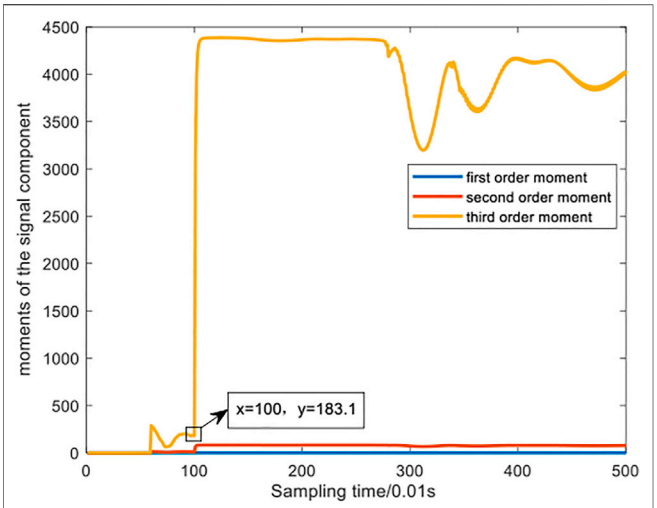

FIGURE 9 | Moments of the signal component in case 2.

above the inner ring radius at the 200th sampling point. In the moment index of each order, obviously, the first-order moment and the second-order moment are not sensitive to voltage changes, while the third-order moment is more sensitive to power grid fluctuations. Therefore, the third-order moment is selected as the final index in case 1, and the case of case 2 is the same as that of case 1. The third-order moment m_3 changes around the value of 1.5 under normal circumstances and changes dramatically at the 100th sampling point, almost climbing in a straight line. The value of m_3 reaches at 1900, which means that the event signal shows up during 1–1.5 s; so H_1 is true. After the 150th sampling point, m_3 begins to decline and shows a downward trend, indicating that the power grid tried to establish a new equilibrium state in this period. Then m_3 fluctuates at the 300th sampling point and recovers to the normal level after the 400th sampling point, representing that the power grid successfully establishes a new stable state, which means that H_0 is true. Based on the above analysis, in this case, the third-order moment index m_3 can reflect the original data more truly.

2) Case 2

By observing the voltage fluctuation of the 40 buses in **Figure 6**, it can be seen intuitively that the voltage unit values of the 40 buses are initially distributed between (0.95,1), which are in a normal level. After the 100th sampling point, as the impact load continues to increase, the voltage level drops sharply, and the minimum voltage unit value is as low as 0.82, which is at the abnormal operation level. After the 300th sampling point, the load level remains 3 times that of the original load, and the power grid tries to re-establish a stable state. It can be speculated that due to the limited capacity of the system, the new equilibrium state is not reached, and the voltage level is in continuous oscillation during 3–5 s.

By observing various indicators in the figures of case 2 (i.e. **Figures 7**, **8**, **9**), the $\boldsymbol{T}^2$ index in PCA begins to climb gradually at the 101th sampling point, exceeding T_α and indicating abnormal status. The violent fluctuation occurs at the 280th sampling point, showing that the power grid is in an extremely unstable state. Then the $\boldsymbol{T}^2$ index begins to fall and enters an oscillation state without returning to the control limit level, representing that the power grid tried to re-establish a new balance at about 3 s but failed to restore the normal state. Here, the trend of the SPE index and $\boldsymbol{T}^2$ index is slightly different after the 280th sampling point, but generally consistent, indicating that the power grid fails to return to the normal level and is in oscillation. The MSR index begins to decline at the 100th sampling point and then falls below the inner ring radius and remains below the threshold of the inner ring radius, failing to return to normal. The third-order moment m_3 changes dramatically at the 100th sampling point and remains at a high level, which means H_0 is true, and fluctuates near the 300th sampling point and then remains at a high level at about 4,000, indicating that the power grid tried to establish a new equilibrium in this period but failed, that is, H_1 is true.

Through the analysis of the above two cases, it can be found that the performance of the third-order moment index is better than that of the T^2 index, SPE index, and MSR index in the small disturbance monitoring of the power grid. When detecting abnormal events, all four indexes can reflect the operation state of the power grid effectively.

CONCLUSION

This study proposes a state evaluation method based on FPT, aiming to evaluate the operation of the distribution network according to high-order moment indexes. Through simulation cases, the following conclusions are obtained:

1) Based on the high-dimensional measurement data of the distribution network, the relevant asymptotic free equation is established, and the high-order moment index is proposed to evaluate the distribution network state, which verifies the feasibility of the proposed evaluation framework based on FPT, applied to the distribution network state analysis.
2) The free probability theory itself tends to be abstract. When calculating the high-order moment index, the moment-cumulant formula can effectively simplify the calculation process of the high-order moment. In addition, the evaluation index is the high-order moment. Theoretically, the index system can be extended to N-order moments, and the selection of specific indicators should be determined based on the actual application scenarios.
3) The proposed high-order moment index is compared with the classical T^2 index, SPE index, and the commonly used MSR index. The simulation results show that the above indexes can accurately detect the occurrence of abnormal events in the distribution network, and the high-order moment index performs better than other indexes mentioned in this article when only a small disturbance occurs in the distribution network.

In this study, the free probability theory is applied to the electric power field for the first time, and the proposed evaluation framework can be extended to high-dimensional electric power data processing, such as power dispatching, operation and maintenance control, new energy consumption, reliability

evaluation, and other scenarios to provide decision support. Based on the above analysis, the follow-up work of this study will focus on three aspects: the application of multiple power scenarios, internal performance comparison of high-order moment indicators, and further expansion as well as optimization of the evaluation index system (Xue and Lai, 2016, He et al., 2016, Liu et al., 2016, Wang et al., 2019, Chen et al., 2017, He et al., 2017b, Zhang et al., 2018, Xue, 2015).

DATA AVAILABILITY STATEMENT

The raw data supporting the conclusion of this article will be made available by the authors, without undue reservation.

AUTHOR CONTRIBUTIONS

JZ selected and studied the sources, designed the structure of the manuscript, and wrote the first draft of the manuscript. BW and HW contributed with supervision over the study of the literature and the writing of the manuscript. All authors contributed to manuscript revision and read and approved the submitted version.

FUNDING

This research is supported by a project from the National Natural Science Foundation of China (51907096).

REFERENCES

Cao, Y., Meng, H., Zhao, L., Wang, T., and Chen, S. (2007). Comprehensive Evaluation Method of New Rural Low-Voltage Distribution Network Based on ANALYTIC Hierarchy Process. *Power Grid Tech.* (08), 68–72. doi:10.3389/fenrg.2021.800906

Chen, P., Tao, S., and Xiao, X. (2017). Network Model for Correlation Analysis of Short-Term Electricity Consumption Behavior. *Automation Electric Power Syst.* 41 (03), 61–69. doi:10.7500/AEPS20160127014

Couillet, R., and Debbah, M. (2011). *Random Matrix Methods for Wireless Communications*. London: Cambridge University Press.

Dan, V. (1986). Addition of Certain Non-commuting Random Variables. *J. Funct. Anal.* 66 (3), 323–346. doi:10.1016/0022-1236(86)90062-5

Deepa, S. K., Savier, J. S., and Biju, S. S. (2020). Micro-synchrophasor Based Special protection Scheme for Distribution System Automation in a Smart City. *Prot. Control. Mod. Power Syst.* 5 (1), 97–110. doi:10.1186/s41601-020-0153-1

Dong, W., and Li, S. (2021). Reliability Sensitivity of Wind Power System Considering Correlation of Forecast Errors Based on Multivariate NSTPNT Method. *Prot. Control. Mod. Power Syst.* 6 (1), 136–146. doi:10.1186/s41601-021-00192-0

He, X., Ai, Q., Qiu, C., Zang, J., and Xu, X. (2017). Application of Stochastic Matrix Theory in Power System Cognition. *Power grid Technol.* 41 (04), 1165–1173. doi:10.13335/j.1000-3673.pst.2016.1956

He, X., Qiu, C., Ai, Q., Chu, L., and Ling, Z. (2017). Research on Spatial and Temporal Big Data of Distribution Network Based on Random Matrix Theory. *Power supply and consumption* 34 (06), 14–19+7. doi:10.19421/j.cnki.1006-6357.2017.06.003

He, X., Qiu, R. C., Ai, Q., Chu, L., Xu, X., and Ling, Z. (2016). Designing for Situation Awareness of Future Power Grids: An Indicator System Based on Linear Eigenvalue Statistics of Large Random Matrices. *IEEE Access* 4, 3557–3568. doi:10.1109/access.2016.2581838

Jain, T., Ghosh, D., and Mohanta, D. K. (2019). Augmentation of Situational Awareness by Fault Passage Indicators in Distribution Network Incorporating Network Reconfiguration. *Prot. Control. Mod. Power Syst.* 4 (4), 323–336. doi:10.1186/s41601-019-0140-6

Li, H., Deng, J., Feng, P., Pu, C., Arachchige, D. D., and Cheng, Q. (2021). Short-term Nacelle Orientation Forecasting Using Bilinear Transformation and ICEEMDAN Framework. *Front. Energ. Res.* 9, 697. doi:10.3389/fenrg.2021.780928

Li, H., Deng, J., Yuan, S., Feng, P., and Arachchige, D. D. Monitoring and Identifying Wind Turbine Generator Bearing Faults Using Deep Belief Network and EWMA Control Charts. *Front. Energ. Res.* 9, 770. doi:10.3389/fenrg.2021.799039

Li, Z., Jiang, W., Abu-Siada, A., Li, Z., Xu, Y., and Liu, S. (2021). Research on a Composite Voltage and Current Measurement Device for HVDC Networks. *IEEE Trans. Ind. Electron.* 68 (9), 8930–8941. doi:10.1109/tie.2020.3013772

Li, Z., Wan, J., Wang, P., Weng, H., and Li, Z. (2021). A Novel Fault Section Locating Method Based on Distance Matching Degree in Distribution Network. *Prot. Control. Mod. Power Syst.* 6 (2), 253–263. doi:10.1186/s41601-021-00194-y

Ling, Z., Qiu, R., and He, X. (2018). *A New Approach of Exploiting Self-Adjoint Matrix Polynomials of Large Random Matrices for Anomaly Detection and Fault Location*. arXiv:1802.03503v1.

Liu, W., Zhang, D., and Wang, X. (2016). Power System Transient Stability Analysis Based on Random Matrix Theory. *Proc. CSEE* 36 (18), 4854–4864. doi:10.13334/j.0258-8013.pcsee.160779

Liu, Y., Chen, S., Cong, Z., Jiang, Q., Yan, Y., and Jiang, X. (2021). Key Technology and Application Prospect of Digital Twin in Power Equipment Industry. *High Voltage Tech.* 47 (05), 1539–1554. doi:10.13336/j.1003-6520.hve.20210194

Liu, Z. (2010). *Modern Signal Processing*. Beijing: China Electric Power Press.

Ma, F., Wang, B., and Dong, X. (2020). Power Vision Edge Intelligence: Power Depth Vision Acceleration Technology Driven by Edge Computing. *Power Syst. Tech.* 44 (06), 2020–2029. doi:10.13335/j.1000-3673.pst.2019.2382

Mousavizadeh, S., Alahyari, A., Ghodsinya, S. R. M., and Haghifam, M. (2021). Incorporating Microgrids Coupling with Utilization of Flexible Switching to Enhance Self-Healing Ability of Electric Distribution Systems. *Prot. Control. Mod. Power Syst.* 6 (3), 300–310. doi:10.1186/s41601-021-00197-9

Ouyang, S., and Xu, W. (2021). Power Grid Fault Identification and Cause Identification Method Considering External Environmental Information. *High Voltage Tech.* 47 (03), 1075–1082. doi:10.13336/j.1003-6520.hve.20200106

Qi, B., Zhang, P., Zhang, S., Zhao, L., Wang, H., Huang, M., et al. (2021). Application Status and Development Prospect of Digital Twin Technology in State Evaluation of Power Transmission and Transformation Equipment. *High Voltage Tech.* 47 (05), 1522–1538. doi:10.13336/j.1003-6520.hve.20210093

Rong, Z., Qi, B., Zhang, P., Li, C., Yang, Y., Gu, C., et al. (2019). Fast Identification of Abnormal State of Oil Chromatography Online Monitoring Device Based on Nuclear Principal Component Analysis. *High voltage Technol.* 45 (10), 3308–3316. doi:10.13336/j.1003-6520.hve.20190624006

Ryan, Ø., and Debbah, M. (2007). "Free Deconvolution for Signal Processing Applications[C]," in Proceeding of the Information Theory, 2007. ISIT 2007. IEEE International Symposium on, Nice, France, June 2007 (IEEE), 1846–1850.

Shen, X., Ouyang, T., Khajorntraidet, C., Li, Y., Li, S., and Zhuang, J. (2021). "Mixture Density Networks-Based Knock Simulator," in Proceeding of the IEEE/ASME Trans. Mechatron., February 2021 (IEEE), 1. doi:10.1109/TMECH.2021.3059775

Shen, X., Ouyang, T., Yang, N., and Zhuang, J. (2021). "Sample-based Neural Approximation Approach for Probabilistic Constrained Programs," in Proceeding of the IEEE Trans. Neural Netw. Learning Syst., August 2021 (IEEE), 1–8. doi:10.1109/TNNLS.2021.3102323

Shen, X., and Raksincharoensak, P. (2021). "Pedestrian-aware Statistical Risk Assessment," in Proceeding of the IEEE Transactions on Intelligent Transportation Systems, June 2021 (IEEE), 1–9. doi:10.1109/TITS.2021.3074522

Shen, X., and Raksincharoensak, P. (2021). Statistical Models of Near-Accident Event and Pedestrian Behavior at Non-signalized Intersections. *J. Appl. Stat.*, 1–21. doi:10.1080/02664763.2021.1962263

Shen, X., Zhang, X., Ouyang, T., Li, Y., and Raksincharoensak, P. (2020). Cooperative Comfortable-Driving at Signalized Intersections for Connected

and Automated Vehicles. *IEEE Robot. Autom. Lett.* 5 (4), 6247–6254. doi:10.1109/LRA.2020.3014010

Shen, X., Zhang, Y., Sata, K., and Shen, T. (2020). Gaussian Mixture Model Clustering-Based Knock Threshold Learning in Automotive Engines. *Ieee/asme Trans. Mechatron.* 25 (6), 2981–2991. doi:10.1109/TMECH.2020.3000732

Sun, Y., Li, Q., Ding, Y., Quan, S., Guan, Z., Yang, D., et al. (2017). *Power System protection and Control*, 45, 30–36.

Tulino, A. M., and Verdu, S. (2004). *Random Matrix Theory and Wireless Communications*. Hanover, USA: Now Publishers Inc.

Voiculescu, D. (1987). Multiplication of Certain Non-commuting Random Variables. *J. Oper. Theor.* 18 (2), 223–235. doi:10.1016/0022-1236(86)90062-5

Wang, B., Ma, F., Ge, L., Ma, H., Wang, H., and Mohamed, M. A. (2020). Icing-EdgeNet: A Pruning Lightweight Edge Intelligent Method of Discriminative Driving Channel for Ice Thickness of Transmission Lines. *IEEE Trans. Instrum. Meas.* 70, 1–12. Art no. 2501412. doi:10.1109/TIM.2020.3018831

Wang, B., Wang, J., Liu, D., and Chen, S. (2019). Research on Evaluating Vulnerability of Power Network Based on High-Dimensional Random Matrix Theory. *Proc. CSE* 39 (06), 1682–1691+1864. doi:10.13334/j.0258-8013.pcsee.180284

Wei, D., Wang, B., Liu, D., Chen, D., Tang, F., and Guo, K. (2016). WAMS/SCADA Data Fusion Method Based on Time-Series Data Correlation Mining. *High voltage Technol.* 42 (01), 315–320.

Xiang, C., Zeng, X., Yan, P., Zhao, J., and Jia, B. (2021). Typical Application and Prospect of Digital Twin Technology in Power Grid Operation. *High Voltage Tech.* 47 (05), 1564–1575.

Xiong, S., Liu, Y., Fang, J., Cong, Z., Yan, Y., and Jiang, X. (2020). Detection Method of Incipient Faults of Power Distribution Lines. *High voltage technolo-gy* 46 (11), 3970–3976.

Xu, S., Qiu, C., Zhang, D., He, X., Chu, L., and Yang, H. (2019). Identification of Transmission Line Fault Type Based on Deep Learning. *Proc. CSEE* 39 (01), 65–74+321.

Xu, X., He, X., and Ai, Q. (2016). A Correlation Analysis Method Foroperation Status of Distribution Network Based on Random Matrixtheory. *Power Syst. Tech.* 40 (3), 5414–5420. doi:10.13335/j.1000-3673.pst.2016.03.018

Xu, Z., Han, Y., He, X., Zhuo, Y., and Shi, X. (2018). Design of Distribution Network Array Vulnerability Evaluation System Based on Random Matrix Theory. *Electr. Appliances Energ. Efficiency Manag. Tech.* 2018 (09), 54–59. doi:10.16628/j.cnki.2095-8188.2018.09.011

Xue, H. (2015). *Research on Spectrum Sensing Technology Based on Free Probability Theory*. Nanjing: Nanjing University of Posts and Telecommunications.

Xue, Y., and Lai, Y. (2016). The Integration of Big Energy Thinking and Big Data Thinking (I) Big Data and Power Big Data. *Automation electric Power Syst.* 40 (01), 1–8. doi:10.7500/AEPS20151208005

Yang, F., Wei, M., and Ling, Z. (2020). Brown Measure Based Spectral Distribution Analysis for Spatial-Temporal Localization of Cascading Events in Power Grids. *IEEE Trans. Smart Grid* 12 (99), 1805–1820. doi:10.1109/tsg.2020.3037542

Yang, N., Huang, Y., and Hou, D. (2019). Adaptive Nonparametric Kernel Density Estimation Approach for Joint Probability Density Function Modeling of Multiple Wind Farms. *Energies* 2019, 12. doi:10.3390/en12071356

Yang, N., Liu, S., Deng, Y., and Xing, C. (2020). An Improved Robust SCUC Approach Considering Multiple Uncertainty and Correlation. *IEEJ Trans. Elec Electron. Eng.* 16, 21–34. doi:10.1002/tee.23265

Yang, N., Qin, T., Wu, L., Huang, Y., Huang, Y., Xing, C., et al. (2021). A Multi-Agent Game Based Joint Planning Approach for Electricity-Gas Integrated Energy Systems Considering Wind Power Uncertainty. *Electric Power Syst. Res.* 2021, 107673, 2021 . ISSN 0378-7796. doi:10.1016/j.epsr.2021.107673

Yang, N., Yang, C., Wu, L., Shen, X., Jia, J., Li, Z., et al. (2021). "Intelligent Data-Driven Decision-Making Method for Dynamic Multi-Sequence: An E-Seq2Seq Based SCUC Expert System," in Proceeding of the IEEE Transactions on Industrial Informatics, August 2021 (IEEE), 1. doi:10.1109/TII.2021.3107406

Yang, N., Yang, C., Xing, C., Ye, D., Jia, J., Chen, D., et al. (2021). Deep Learning-Based SCUC Decision-Making: An Intelligent Data-Driven Approach with Self-Learning Capabilities. *IET Gener. Transm. Distrib.*, 1–12. doi:10.1049/gtd2.12315

Yang, N., Ye, D., Zhou, Z., Cui, J., Chen, D., and Wang, X. (2018). Research on Modelling and Solution of Stochastic SCUC under AC Power Flow Constraints. *IET Generation, Transm. Distribution* 12 (15), 3618–3625. doi:10.1049/iet-gtd.2017.1845

Ye, J., Zhao, D., and Zhang, L. (2021). Research on Combined Electricity and Heating System Scheduling Method Considering Multi-Source Ring Heating Network. *Front. Energ. Res.* 9. doi:10.3389/fenrg.2021.800906

Zhang, L., Xie, Y., and Ye, J. (2021). Intelligent Frequency Control Strategy Based on Reinforcement Learning of Multi-Objective Collaborative Reward Function. *Front. Energ. Res.* 9. doi:10.3389/fenrg.2021.760525

Zhang, L., Zhang, Z., and Gu, J. (2018). State Analysis and Disturbance Positioning Method of Power Grid Based on Random Matrix Theory. *Automation Electric Power Syst.* 42 (12), 93–99+126. doi:10.7500/AEPS20171106006

Zheng, K., Geng, Z., Wang, H., Ma, F., and Zhang, G. (2020). Detection and Location Method of Single-phase Grounding Fault in Distribution Network Based on Synchronous Measurement Data. *Power Grid Clean. Energy* 36 (09), 50–56. doi:10.3969/j.issn.1674-3814.2020.09.008

Zhou, X., Chen, S., and Lu, Z. (2018). Technology Features of the New Generation Power System in China. *Proc. CSEE* 38 (07), 1893–1904+2205. doi:10.13334/j.0258-8013.pcsee.180067

Zhu, B., Ding, F., and Vilathgamuwa, D. M. (2020). Coat Circuits for DC-DC Converters to Improve Voltage Conversion Ratio. *IEEE Trans. Power Electron.* 35 (4), 3679–3687. doi:10.1109/tpel.2019.2934726

Zhu, M., Xu, C., Dong, S., Tang, K., and Gu, C. (2021). An Integrated Multi-Energy Flow Calculation Method for Electricity-Gas-thermal Integrated Energy Systems. *Prot. Control. Mod. Power Syst.* 6 (1), 65–76. doi:10.1186/s41601-021-00182-2

Conflict of Interest: The authors declare that the research was conducted in the absence of any commercial or financial relationships that could be construed as a potential conflict of interest.

Publisher's Note: All claims expressed in this article are solely those of the authors and do not necessarily represent those of their affiliated organizations, or those of the publisher, the editors, and the reviewers. Any product that may be evaluated in this article, or claim that may be made by its manufacturer, is not guaranteed or endorsed by the publisher.

frontiers in Energy Research

BRIEF RESEARCH REPORT
published: 21 January 2022
doi: 10.3389/fenrg.2021.831347

A Fault Signal Processing Method Based on An Improved Prony Algorithm

Nan Yang[1], Yanming Lu[1], Jianmei Zhang[2], Zhenzhen Zhang[2], Li Ding[1], Cong Yang[1], Zhengqiang Dong[1], Songkai Liu[1], Wei Xiong[3], Binxin Zhu[1], Lei Zhang[1], Yuehua Huang[1] and Xin Zhang[4]*

[1]Hubei Provincial Engineering Research Center of Intelligent Energy Technology, China Three Gorges University, Yichang, China, [2]State Grid Gansu Electric Power Research Institution, Lanzhou, China, [3]State Grid Yichang Power Supply Company, Yichang, China, [4]CSG Power Generation Co., Ltd., Guangzhou, China

The fault of power systems introduces a severe challenge in terms of fault recording analysis, and the traditional Prony method cannot perform satisfactorily in the process of signal recordings fitting caused by faults. Therefore, an improved adaptive Prony algorithm is proposed in this article to study the characteristics of fault recordings. Specifically, the search step size is taken as an adaptive variable, and the mean square relative fitting error (MSRFE) is set as the criterion. Then, a large step is employed to rapidly determine an approximate segmentation point in the initial stage of the searching process, and its horizon is gradually reduced to establish an accurate subsegment point. Finally, the Prony algorithm is deployed to analyze the subsegment fitting original signal. The proposed approach has been simulated on an assumed fault signal, and the results validate the accuracy and efficiency of the method.

Keywords: power systems, fault recording, Prony algorithm, improved adaptive, signal fitting

OPEN ACCESS

Edited by:
Yahui Zhang,
Yanshan University, China

Reviewed by:
Zhengmao Li,
Nanyang Technological University, Singapore
Shaoyan Li,
North China Electric Power University, China

****Correspondence:***
Songkai Liu
skliu0120@163.com

Specialty section:
This article was submitted to Smart Grids, a section of the journal Frontiers in Energy Research

Received: *08 December 2021*
Accepted: *27 December 2021*
Published: *21 January 2022*

Citation:
Yang N, Lu Y, Zhang J, Zhang Z, Ding L, Yang C, Dong Z, Liu S, Xiong W, Zhu B, Zhang L, Huang Y and Zhang X (2022) A Fault Signal Processing Method Based on An Improved Prony Algorithm. Front. Energy Res. 9:831347. doi: 10.3389/fenrg.2021.831347

INTRODUCTION

An accurate assessment plays an indispensable role in the safety active control systems (Shen et al., 2021a; Shen and Raksincharoensak, 2021a; Shen and Raksincharoensak, 2021b). Similarly, it is significant to study an effective fault signal analysis method for safe and stable operation in power systems (WangJin et al., 2019; Yang et al., 2019; Yang et al., 2021a; Zhang et al., 2021). Although the technology of fault analysis has already been developed in the existing literature, there are still obstacles to fault identification using the electrical parameters of recording signals. In practice, the state of power systems is monitored using intelligent monitoring terminals in real time. In this way, the fault recording accuracy of the system can be guaranteed, but producing redundant data increases the difficulty of data storage. On the other hand, if only targeted data sampling is carried out for the power grid in case of fault, despite data redundancy can be cut down, it may lead to a lack of recording data and a decrease in recording accuracy. Therefore, the research on fault recording algorithms of power systems has theoretical and practical significance.

For research of signal recordings, it can be analyzed based on steady state and transient (Sajadi et al., 2019). However, the steady-state efficiency of fault identification is bounded. The main reason is that renewable energy to access power systems is becoming increasingly complicated in recent years, and fault analysis has to accord with the requirements of sensitivity, fast, and accurate at the same time (Liao et al., 2018; Zhu et al., 2019; Liu et al., 2020a; Zhu et al., 2020; Wang et al., 2021). These problems have been solved based on transient analysis, showing practical application (Saleh

et al., 2015; Yu et al., 2020). In addition, the demand for data is urgent with the rapid development of deep learning technology in power systems (Yang et al., 2018; Yang et al., 2021b). In this context, one of the most critical points is how to extract the characteristic information of transient electrical signals such as voltage, current, and frequency in the research of fault recording. For one thing, the random noise can lightly bury the transient with low energy and small amplitude due to the hybrid of transient and steady state. For another, although the extracted transient characteristics are directly applied in the fault research because the extracted data are massive and irregular (Xu et al., 2017; Shen et al., 2020a; Desai and Makwana, 2021), they still fail to achieve the goal of identifying specific faults. Therefore, the effective extraction of its feature information is crucial to the fault identification problem, which is directly related to the effectiveness and accuracy of fault identification and location.

Numerous works have studied methods to ensure the safety of power grids (Shen et al., 2017; Liu et al., 2020b; Shen et al., 2020b; Li et al., 2021a; Shen et al., 2021b; Hosseini et al., 2021). In the study of Li et al. (2021a), a combined high voltage direct current measurement method is present to improve the extraction accuracy of the measured signal. Besides, some traditional methods such as Hilbert–Huang transform, wavelet transform, and Fourier transform are used in signal processing (Borghetti et al., 2008; Satpathi et al., 2018; Li et al., 2021b). However, the previous methods only separate fault recordings and cannot realize the direct extraction of fault feature information. Its characteristics are obtained directly through the Prony algorithm. In Tawfik and Morcos. (2005), a fault location method integrating the Prony method and artificial neural networks is presented, and the modified scheme provided good accuracy. Yet, when the amplitude of the high-frequency component of the signal is small, the estimation is prone to errors in practice. In Ando. (2020), the difference algorithm is introduced to improve the characteristics of high-frequency components of signals, but its inherent defect has not been tackled. Later, a segmented Prony method is proposed (Jansen and Garoosi, 2000), which divides the signal into different subsegments to ensure good continuity and minor variation in each subsegment, improving the impact on signal characteristics. Nevertheless, the segmented method rarely focused on how to segment to obtain the best analysis results. Based on this, an adaptive Prony method is presented, taking MSRFE as the criterion to realize the adaptive segmentation of the fault signal (Bracale et al., 2007). However, the algorithm searches the subsegment boundary point by enumeration search with a fixed step, resulting in low efficiency. These methods also have the inadequacies of fault signal recognition accuracy for certain signals overall.

In this article, when a power system fault materializes, an improved adaptive Prony method is proposed to describe the accurate variation of electrical parameters. The point of the subsegment is searched by variable step-size strategy, and MSRFE is considered the criterion. The proposed approach has been simulated on an assumed fault signal, and results show that the improved Prony algorithm has higher accuracy and efficiency than the traditional method.

PRONY METHOD MODEL

The Prony method is formulated as a linear combination of exponential functions to describe the mathematical model of equal distance sampling data and linearized approximate solution. The amplitude, phase, frequency, and attenuation factor of the corresponding signal can be obtained directly by this method. The general solution procedure of the Prony algorithm is as follows.

The continuous signal $x(t)$ is equidistantly sampled according to the sampling frequency. There are N sampling data obtained and stated as $x(0), x(1), \ldots, x(N-1)$, and x_n can be stated in **Eqs 1**, **2**.

$$x_n = \sum_{i=1}^{p} b_i z_i^n, n = 0, 1, \ldots, N-1 \tag{1}$$

$$\begin{cases} b_i = A_i e^{j\theta_i} \\ z_i = e^{(a_i + j2\pi f_i)T_s} \end{cases} i = 1, 2, \cdots, p, \tag{2}$$

where A_i, θ_i, α_i, and f_i denote the amplitude, initial phase angle, attenuation factor, and frequency of the ith complex exponential function, respectively; N and p are the number of sampling points and the order, respectively; and T_s is the sampling period.

Then, obtain α_i and z_i by constructing the difference equation and its characteristic equation. The singular value decomposition and the least square method should be used to solve α_i, thereby improving the calculation accuracy (Liu et al., 2008).

Finally, the required parameter can be obtained from previous equations, respectively, as shown in **Eq.3**.

$$\begin{cases} A_i = |b_i|, \\ \theta_i = \arctan(\mathrm{Im}(b_i)/\mathrm{Re}(b_i)), \\ \alpha_i = \ln(z_i)/T_s, \\ f_i = \arctan(\mathrm{Im}(z_i)/\mathrm{Re}(z_i))/2\pi T_s, \end{cases} \tag{3}$$

IMPROVED PRONY ALGORITHM STRATEGY

The traditional Prony method has some practical limitations, which may lead to inaccurate fitting results of some specific signals under certain conditions, such as mutation signals when a fault occurs in power systems. Specifically, on the one hand, the search step size of the traditional Prony algorithm is performed with a fixed step. On the other hand, the accuracy of the fitting depends on the selected order. The order is selected artificially by using the traditional method. Although there will be an order to make the fitting accurate, it will take more time for an operation. At the same time, it will also bring extra components. Thus, the method proposed in this article is an improvement in these aspects. The steps involving the parameters of the analysis algorithm are explained as follows.

Step 1: Initialize the original data and parameters, including the signal information, search step k, minimum length of subsegment $L_{\min}$, sampling frequency, a maximum value of MSRFE E_m, and some remaining parameters.

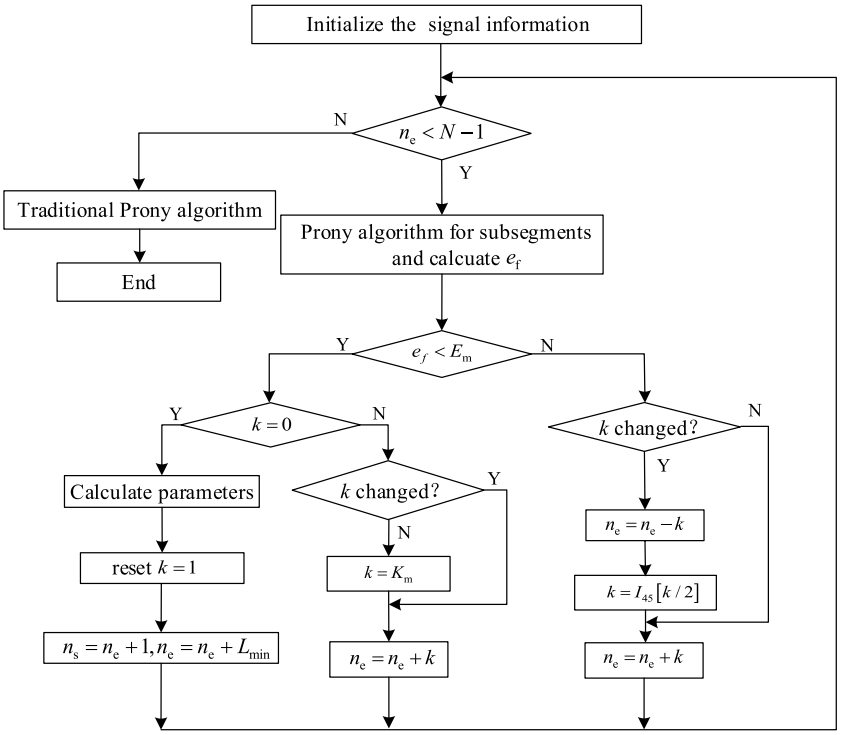

FIGURE 1 | Flowchart of the proposed, improved adaptive Prony method.

Step 2: Compare the number of sampling points and the sequence number at the end of the subsegment. When the number of sampling points is greater than the end sequence of the subsegment, the Prony algorithm is directly applied in the subsegment. Otherwise, proceed to step 3.

Step 3: Using the Prony algorithm for subsegments and calculating MSRFE e_f. According to MSRFE obtained from the subsegment, whether its value is lower than the maximum value assumed. If MSRFE is lower than its maximum value, proceed to step 4. Otherwise, proceed to step 5.

Step 4: Judge whether the step is equal to 0. If its value is 0, reset the step to 1. Otherwise, judge whether the step was changed, if not changed, then make it set the maximum search step K_m.

Step 5: Check the step was changed, and update the corresponding parameters, where I_{45} means rounding.

Step 6: Until the condition of step 2 is met, output the characteristic parameter of signal information.

The detailed procedure is shown in **Figure 1**, and the expression of MSRFE is shown in **Eq. 4**.

$$MSREF = \frac{1}{n_0} \sum_{n=n_s, x_n \neq 0}^{n_e} \frac{[x_1(n) - x(n)]^2}{x(n)^2}, \tag{4}$$

where $x(n)$ is the real value, $x_1(n)$ is the estimated value, n_0 is the total number of non-zero values in the subsegment, and n_s and n_e are the start sequence number and end sequence number, respectively.

To better evaluate the accuracy of fitting and real value, the root-mean-square error (RMSE) is introduced in this article, which is defined as **Eq. 5**.

$$RMSE = \sqrt{\frac{1}{L} \sum_{n=1}^{N} [x_1(n) - x(n)]^2}, \tag{5}$$

where L is the length of the signal.

CASE STUDY

Instance and Setup

In this article, two types of original voltage signals mimic recordings. The signals under the normal operation and fault are simulated by a smooth and a signal of mutational processes, respectively. The mathematical expression of the smooth voltage signal is shown in **Eq. 6**, and its parameters are shown in **Table 1**.

$$\begin{aligned} x(t) &= x_1(t) + x_2(t) + x_3(t) + x_4(t) \\ &= 110e^{-2.0t} \cos(2\pi \times 50t + \pi/3) \\ &\quad +220e^{-2.0t} \cos(2\pi \times 50t + \pi/6) \\ &\quad +220e^{-1.0t} \cos(2\pi \times 80t + \pi/6) \\ &\quad +330e^{-0.5t} \cos(2\pi \times 60t + \pi/6), \end{aligned} \tag{6}$$

Process Simulation Verification

The total number of sampling points, the sampling period, and the sampling frequency are set 1,000, 0.025 s, and 4 kHz in the

TABLE 1 | Specific parameters of the smooth signal.

Component	Frequency (Hz)	Amplitude (V)	Initial phase angle	Attenuation factor
1	50	110	60	-2.0
2	50	220	30	-2.0
3	80	220	30	-1.0
4	60	330	30	-0.5

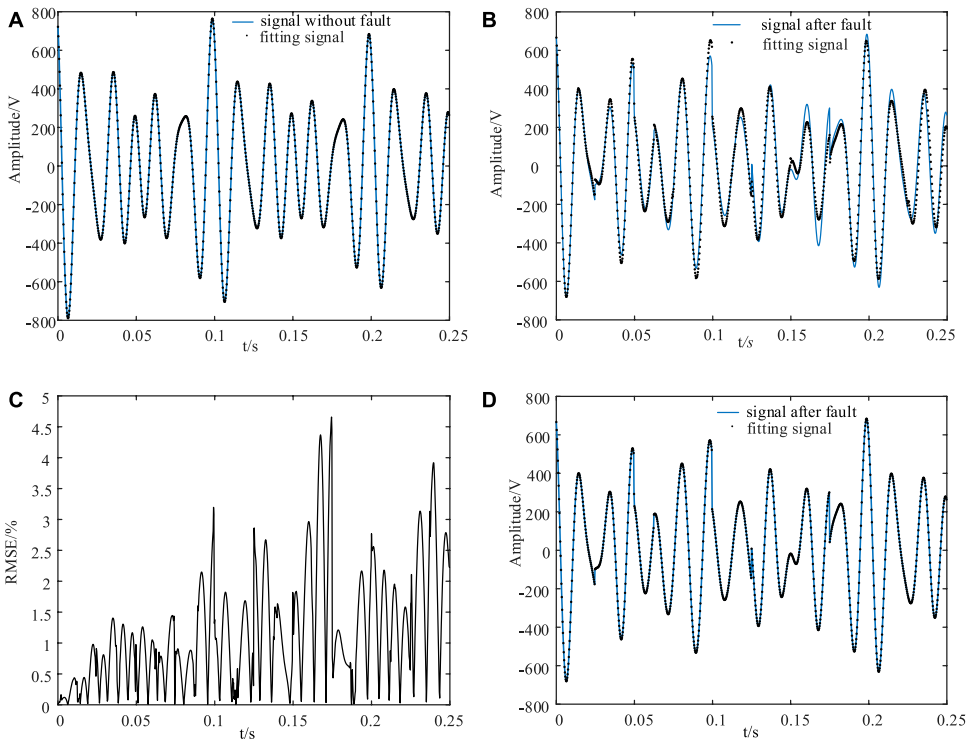

FIGURE 2 | Simulation results: **(A)** Smooth signal simulation based on the traditional Prony method. **(B)** Mutation signal simulation based on the traditional Prony method. **(C)** RMSE of the original and fitting signals based on the traditional Prony method. **(D)** Mutation signal simulation based on the proposed method in this article.

simulation, and the start sequence point and the end sequence point are defined as 1 and 20, respectively. The minimum length of the subsegment is 20, and the maximum search step is 20. **Figure 2A** is plotted to depict the fitting under the normal condition provided by known parameters. We can observe that the simulation results show an excellent agreement is consistent, the order is 230, and the RMSE is so tiny that it can be ignored.

Comparative Simulation Verification

In this case, based on the assumption of the smooth signal, $x_1(1{:}\ 200) = 0$, $x_2(100{:}\ 500) = 0$, $x_3(200{:}\ 500) = 0$, and $x_4(400{:}\ 700) = 0$ is set in the program to simulate the signal with sudden operation change, and the meaning of x_1 from 0 to 0.05 s, x_2 from 0.025 to 0.125 s, x_3 from 0.05 to 0.125 s, and x_4 from 0.1 to 0.175 s all failing to react. The traditional Prony method is used for the fault recording, and the comparison between fitting and the original signal is given in **Figure 2B**. We can see that the trend of the two signals is deviated. Furthermore, **Figure 2C** shows the maximum RMSE of both is around 4.5%, and the traditional method is intractable for fitting the signal. The reason for such a difference may be that the traditional method makes decisions by considering the original signal is always continuous and smooth without mutation, and it results in mutagenicity when a fault occurs. It is bound to skip some vital parts while fitting by this method, resulting in some information being ignored. Moreover, the order is often set in advance in the fitting process, and it takes a longer time to manually and continuously adjust the order to fit the original signal.

The previously assumed fault recording signal is analyzed by using the proposed method in this article, and the corresponding result is shown in **Figure 2D**. We can see that the performance of the proposed method is satisfying, overlapping with the original signal. The reason is that the search step, as a variable, will be segmented when encountering sudden change points in the search stage, avoiding some information being ignored at the critical moment of analysis. On the other hand, the time of fitting

TABLE 2 | Component parameters of subsegment based on simulation.

Subsegment	Frequency (Hz)	Amplitude (V)	Initial phase angle	Attenuation factor
1	50	220	30	-2.0
	80	220	30	-1.0
	60	330	30	-0.5
2	60	325.94	-150.4	-0.5
	80	214.62	29.8	-1.0

is decreased shorter than the traditional Prony method because the order of this method does not need to rule in advance. Meanwhile, to further illustrate the effectiveness of the proposed method, fitting dates are further analyzed. The signal is divided into eight subsegments in total, taking the first two segments of the total date as an example for analysis, as given in **Table 2**.

Table 2 indicates that the signal with a component frequency of 50 Hz and an amplitude of 110 V is not present in subsegment 1, so the corresponding data are missing, and the information of other components is accurately extracted. Similarly, the subsegment signal is not affected by components 1 and 2, so there is only relevant information of components 3 and 4 in the subsegment. More specifically, some data obtained through an attenuation process, such as amplitude and initial phase angle, do not get in line with **Table 1**. By taking the first line of subsegment 2 as an example, the sequence point of subsegment 2 ranges from 100 to 199. After 0.025 s, the accuracy of amplitude becomes $330 \times e^{-0.5*0.025} = 325.91$, and the initial phase angle transforms from 30 to $\arg[30 + (2*\pi \times 60 \times 0.025 \times 180)/\pi] = -150.0$.

CONCLUSION

The traditional Prony algorithm is improved in this article. First, the basic model of the Prony algorithm is constructed. On this basis, the mean square relative fitting error is set as the criterion, and the variable step method is used to search the subsegment boundary points. Finally, a fault recording signal processing with an improved adaptive Prony algorithm is proposed. The conclusions based on simulation analysis are as follows.

The improved adaptive Prony algorithm proposed in this article can not only fit the signal under normal conditions but also obtain higher accuracy after the signal characteristics change under abnormal conditions.

In the fault recording signal fitting, the proposed method does not need to set the order in advance. Compared with the traditional Prony algorithm, it can greatly reduce the fitting time and improve the calculation efficiency.

DATA AVAILABILITY STATEMENT

The original contributions presented in the study are included in the article/Supplementary Material, further inquiries can be directed to the corresponding author.

AUTHOR CONTRIBUTIONS

NY put forward the main research points; YL, JZ, and ZZ contributed to manuscript writing and revision; LD, CY, and ZD performed simulation research; SL, WX, and BZ collected relevant background information; LZ, YH, and XZ revised for grammar and expression. All authors contributed to manuscript revision and read and approved the submitted version.

FUNDING

This article was supported in part by the National Natural Science Foundation of China 51607104.

REFERENCES

Ando, S. (2020). Frequency-Domain Prony Method for Autoregressive Model Identification and Sinusoidal Parameter Estimation. *IEEE Trans. Signal. Process.* 68, 3461–3470. doi:10.1109/tsp.2020.2998929

Borghetti, A., Bosetti, M., Di Silvestro, M., Nucci, C. A., and Paolone, M. (2008). Continuous-Wavelet Transform for Fault Location in Distribution Power Networks: Definition of Mother Wavelets Inferred from Fault Originated Transients. *IEEE Trans. Power Syst.* 23 (2), 380–388. doi:10.1109/tpwrs.2008.919249

Bracale, A., Caramia, P., and Carpinelli, G. (2007). Adaptive Prony Method for Waveform Distortion Detection in Power Systems. *Int. J. Electr. Power Energ. Syst.* 29 (5), 371–379. doi:10.1016/j.ijepes.2006.10.005

Desai, J. P., and Makwana, V. H. (2021). A Novel Out of Step Relaying Algorithm Based on Wavelet Transform and a Deep Learning Machine Model. *Prot. Control. Mod. Power Syst.* 6, 40. doi:10.1186/s41601-021-00221-y

Hosseini, S. A., Taheri, B., Abyaneh, H. A., and Razavi, F. (2021). Comprehensive Power Swing Detection by Current Signal Modeling and Prediction Using the GMDH Method. *Prot. Control. Mod. Power Syst.* 6, 15. doi:10.1186/s41601-021-00193-z

Jansen, B. H., and Garoosi, V. (2000). Development and Evaluation of the Piecewise Prony Method for Evoked Potential Analysis. *IEEE Trans. Biomed. Eng.* 47 (12), 1549–1554. doi:10.1109/10.887935

Li, D., Ukil, A., Satpathi, K., and Yeap, Y. M. (2021). Hilbert-huang Transform Based Transient Analysis in Voltage Source Converter Interfaced Direct Current System. *IEEE Trans. Ind. Electron.* 68 (11), 11014–11025. doi:10.1109/tie.2020.3038056

Li, Z., Jiang, W., Abu-Siada, A., Li, Z., Xu, Y., and Liu, S. (2021). Research on a Composite Voltage and Current Measurement Device for HVDC Networks. *IEEE Trans. Ind. Electron.* 68 (9), 8930–8941. doi:10.1109/tie.2020.3013772

Liao, S., Xu, J., Sun, Y., Bao, Y., and Tang, B. (2018). Control of Energy-Intensive Load for Power Smoothing in Wind Power Plants. *IEEE Trans. Power Syst.* 33 (6), 6142–6154. doi:10.1109/TPWRS.2018.2834940

Liu, D., Hu, W., and Chen, Z. (2008). SVD-TLS Extending Prony Algorithm for Extracting UWB Radar Target Feature. *J. Syst. Eng. Electron.* 19 (2), 286–291. doi:10.1016/S1004-4132(08)60080-8

Liu, S., Liu, L., Fan, Y., Zhang, L., Huang, Y., Zhang, T., et al. (2020). An Integrated Scheme for Online Dynamic Security Assessment Based on Partial Mutual Information and Iterated Random Forest. *IEEE Trans. Smart Grid* 11 (4), 3606–3619. doi:10.1109/tsg.2020.2991335

Liu, Y., Yang, N., Dong, B., Wu, L., Yan, J., Shen, X., et al. (2020). Multi-Lateral Participants Decision-Making: A Distribution System Planning Approach with Incomplete Information Game. *IEEE Access* 8, 88933–88950. doi:10.1109/access.2020.2991181

Sajadi, A., Kolacinski, R. M., Clark, K., and Loparo, K. A. (2019). Transient Stability Analysis for Offshore Wind Power Plant Integration Planning Studies-Part I: Short-Term Faults. *IEEE Trans. Ind. Applicat.* 55 (1), 182–192. doi:10.1109/tia.2018.2868550

Saleh, S., Aljankawey, A., Errouissi, R., and Castillo-Guerra, E. (2015). Extracting the Phase of Fault Currents: A New Approach for Identifying Arc Flash Faults. *IEEE Trans. Ind. Applicat.* 52 (2), 1. doi:10.1109/tia.2015.2483698

Satpathi, K., Yeap, Y. M., Ukil, A., and Geddada, N. (2018). Short-Time Fourier Transform Based Transient Analysis of VSC Interfaced Point-to-Point DC System. *IEEE Trans. Ind. Electron.* 65 (5), 4080–4091. doi:10.1109/tie.2017.2758745

Shen, X., Ouyang, T., Khajorntraidet, C., Li, Y., Li, S., and Zhuang, J. (2021a). Mixture Density Networks-Based Knock Simulator. *Ieee/asme Trans. Mechatron.*, 1. doi:10.1109/tmech.2021.3059775

Shen, X., Ouyang, T., Yang, N., and Zhuang, J. (2021b). Sample-Based Neural Approximation Approach for Probabilistic Constrained Programs. *IEEE Trans. Neural Netw. Learn. Syst.*, 1–8. doi:10.1109/tnnls.2021.3102323

Shen, X., and Raksincharoensak, P. (2021). Pedestrian-aware Statistical Risk Assessment. *IEEE Trans. Intell. Transport. Syst.*, 1–9. doi:10.1109/tits.2021.3074522

Shen, X., and Raksincharoensak, P. (2021). Statistical Models of Near-Accident Event and Pedestrian Behavior at Non-signalized Intersections. *J. Appl. Stat.*, 1–21. doi:10.1080/02664763.2021.1962263

Shen, X., Zhang, X., Ouyang, T., Li, Y., and Raksincharoensak, P. (2020). Cooperative Comfortable-Driving at Signalized Intersections for Connected and Automated Vehicles. *IEEE Robot. Autom. Lett.* 5 (4), 6247–6254. doi:10.1109/lra.2020.3014010

Shen, X., Zhang, Y., Sata, K., and Shen, T. (2020). Gaussian Mixture Model Clustering-Based Knock Threshold Learning in Automotive Engines. *Ieee/asme Trans. Mechatron.* 25 (6), 2981–2991. doi:10.1109/tmech.2020.3000732

Shen, X., Zhang, Y., Shen, T., and Khajorntraidet, C. (2017). Spark advance Self-Optimization with Knock Probability Threshold for Lean-Burn Operation Mode of SI Engine. *Energy* 122, 1–10. doi:10.1016/j.energy.2017.01.065

Tawfik, M., and Morcos, M. (2005). On the Use of Prony Method to Locate Faults in Loop Systems by Utilizing Modal Parameters of Fault Current. *IEEE Trans. Power Deliv.* 20 (1), 532–534. doi:10.1109/tpwrd.2004.839739

Wang, C., Mei, S., Yu, H., Cheng, S., Du, L., and Yang, P. (2021). Unintentional Islanding Transition Control Strategy for Three-/single-phase Multimicrogrids Based on Artificial Emotional Reinforcement Learning. *IEEE Syst. J.* 15, 5464–5475. doi:10.1109/jsyst.2021.3074296

WangJin, Q. T., Jin, T., and Mohamed, M. A. (2019). An Innovative Minimum Hitting Set Algorithm for Model-Based Fault Diagnosis in Power Distribution Network. *IEEE Access* 7, 30683–30692. doi:10.1109/access.2019.2902598

Xu, Y., Sun, Y., Wan, J., Liu, X., and Song, Z. (2017). Industrial Big Data for Fault Diagnosis: Taxonomy, Review, and Applications. *IEEE Access* 5, 17368–17380. doi:10.1109/access.2017.2731945

Yang, N., Huang, Y., Hou, D., Liu, S., Ye, D., Dong, B., et al. (2019). Adaptive Nonparametric Kernel Density Estimation Approach for Joint Probability Density Function Modeling of Multiple Wind Farms. *Energies* 12 (7), 1356. doi:10.3390/en12071356

Yang, N., Liu, S., Deng, Y., and Xing, C. (2021). An Improved Robust SCUC Approach Considering Multiple Uncertainty and Correlation. *IEEJ Trans. Elec Electron. Eng.* 16 (1), 21–34. doi:10.1002/tee.23265

Yang, N., Yang, C., Wu, L., Shen, X., Jia, J., Li, Z., et al. (2021). Intelligent Data-Driven Decision-Making Method for Dynamic Multi-Sequence: An E-Seq2Seq Based SCUC Expert System. *IEEE Trans. Ind. Inf.* 1, 1. doi:10.1109/tii.2021.3107406

Yang, N., Ye, D., Zhou, Z., Cui, J., Chen, D., and Wang, X. (2018). Research on Modelling and Solution of Stochastic SCUC under AC Power Flow Constraints. *IET Generation, Transm. Distribution* 12 (15), 3618–3625. doi:10.1049/iet-gtd.2017.1845

Yu, J., Zhang, Z., Xu, Z., and Wang, G. (2020). An Equivalent Calculation Method for Pole-to-Ground Fault Transient Characteristics of Symmetrical Monopolar MMC Based DC Grid. *IEEE Access* 8, 123952–123965. doi:10.1109/access.2020.3006028

Zhang, L., Xie, Y., Ye, J., Xue, T., Cheng, J., Li, Z., et al. (2021). Intelligent Frequency Control Strategy Based on Reinforcement Learning of Multi-Objective Collaborative Reward Function. *Front. Energ. Res.* 9, 760525. doi:10.3389/fenrg.2021.760525

Zhu, B., Ding, F., and Vilathgamuwa, D. M. (2020). Coat Circuits for DC-DC Converters to Improve Voltage Conversion Ratio. *IEEE Trans. Power Electron.* 35 (4), 3679–3687. doi:10.1109/tpel.2019.2934726

Zhu, B., Zeng, Q., Chen, Y., Zhao, Y., and Liu, S. (2019). A Dual-Input High Step-Up DC/DC Converter with ZVT Auxiliary Circuit. *IEEE Trans. Energ. Convers.* 34 (1), 161–169. doi:10.1109/TEC.2018.2876303

Conflict of Interest: WX is employed by State Grid Yichang Power Supply Company. XZ is employed by CSG Power Generation Co., Ltd.

The remaining authors declare that the research was conducted in the absence of any commercial or financial relationships that could be construed as a potential conflict of interest.

Publisher's Note: All claims expressed in this article are solely those of the authors and do not necessarily represent those of their affiliated organizations, or those of the publisher, the editors, and the reviewers. Any product that may be evaluated in this article, or claim that may be made by its manufacturer, is not guaranteed or endorsed by the publisher.

frontiers in Energy Research

ORIGINAL RESEARCH
published: 04 February 2022
doi: 10.3389/fenrg.2022.836588

Research on Fire Prediction Method of High-Voltage Power Cable Tunnel Based on Abnormal Characteristic Quantity Monitoring

Chenying Li[1], Jie Chen[1], Ziheng Pu[2], Fengbo Tao[1], Jianjun Liu[1], Xiao Tan[1], Libin Hu[1] and Jingxing Cao[1]*

[1]Electric Power Research Institute of State Grid Jiangsu Electric Power Co., Ltd., Jiangsu Nanjing, China, [2]College of Electrical Engineering and New Energy, China Three Gorges University, Hubei Yichang, China

The proportion of cable lines in the urban distribution network is increasing. The fire hazard of important cable channels is prominent, which has a serious effect on the safety and stable operation of the power system. In recent years, intelligent mobile inspection and fire extinguishing devices have been applied in tunnels. The determination of firepower and location is conducive to the rapid and effective fire suppression of intelligent devices. Therefore, this study proposes a fire early warning method of a high-voltage power cable tunnel based on abnormal characteristic quantity monitoring. Based on the modified model of complex pyrolysis and combustion chemical reaction, the fire development of different fire source powers and fire locations is simulated. The temperature distribution and characteristic gas concentration under different simulation conditions are analyzed. The results show that the monitoring data of temperature, flue gas concentration, and CO and CO_2 concentration need comprehensive analysis to effectively reflect different fire conditions. The characteristic data set is selected and processed to form a total sample. The fire prediction model is trained and tested. The accuracy of the proposed prediction model is 92%.

Keywords: power cable tunnel, combustion simulation, complex pyrolysis, characteristic gas data, anomaly detection, fire early warning

OPEN ACCESS

Edited by:
Xun Shen,
Tokyo Institute of Technology, Japan

Reviewed by:
Hao Cui,
Southwest University, China
Jianli Yu,
Weifang University, China

****Correspondence:***
Ziheng Pu
pzhdq@ctgu.edu.cn

Specialty section:
This article was submitted to Smart Grids, a section of the journal Frontiers in Energy Research

Received: *15 December 2021*
Accepted: *10 January 2022*
Published: *04 February 2022*

Citation:
Li C, Chen J, Pu Z, Tao F, Liu J, Tan X, Hu L and Cao J (2022) Research on Fire Prediction Method of High-Voltage Power Cable Tunnel Based on Abnormal Characteristic Quantity Monitoring. Front. Energy Res. 10:836588. doi: 10.3389/fenrg.2022.836588

INTRODUCTION

With the growth of power demand, more and more power cables are laid intensively in cable tunnels. The cable insulation is aging with the increase of operation time, which may lead to insulation breakdown and further fire. Power cable tunnel is located underground, with a long and narrow structure, complex environment, and inconvenient communication. In case of fire, a large amount of toxic smoke accumulates in the tunnel, making it difficult for personnel to enter and extinguish the fire through the outside. The existing high-voltage cable tunnel monitoring system is imperfect, and the information means are insufficient. Monitoring alarm and fire extinguishing devices are only set in key areas such as intermediate joints of power cable, which is still impossible to fully monitor the situation of the whole tunnel (Fang et al., 2019; An et al., 2020b; Wu et al., 2020). With the development of artificial intelligence and information communication technology, intelligent mobile monitoring and fire extinguishing devices are developed and applied in tunnels. However, in practical application, due to the failure to accurately judge the fire source, the patrol fire extinguishing

device did not arrive at the fire point in time. The fire source is too large, and the fire develops rapidly. It did not extinguish the fire and caused damage to the intelligent patrol inspection and fire extinguishing device. It is necessary to predict the fire location and fire source power in combination with the monitored abnormal data.

In order to predict the fire situation combined with the monitoring data, it is necessary to analyze the development characteristics of a cable tunnel fire. Fire test is destructive and dangerous and has the disadvantages of high cost and being uncontrollable. In recent years, fire simulation research has developed rapidly, and a variety of fire conditions have been simulated and analyzed. Song et al. (2020) simulated the combustion of horizontal and triangular cables in the tunnel, respectively. The results show that the cable layout has little effect on the smoke concentration distribution and diffusion in a tunnel fire. However, horizontal cables can reduce the content of CO. Niu and Li (2012) simulated the fire process of the cable tunnel and obtained the smoke spread and section temperature change. The best fire extinguishing time is put forward, which provides a reference for formulating fire extinguishing measures and selecting a fire extinguishing system. An et al. (2020a) analyzed the influence of cable layout on fire through a cable combustion test. It shows that the fire risk and flame characteristics of the cable tunnel are affected by the distance between layers of cable support and the distance between cables on the same layer. The greater the distance between layers, the higher the flame height. The flame width decreases with increasing the distance between cables on the same layer. The influence of fire separation on the fire development of a power cable tunnel is simulated and analyzed in Zhang et al. (2018). When there is no fire separation, the smoke spreads rapidly, and the temperature of the whole tunnel increases significantly. The fire separation can effectively limit the fire smoke in the fire compartment. Different combination modes of the ventilation system, fire door, and sprinkler are compared in Mi et al. (2020). The optimal mode can effectively control the smoke propagation in the tunnel. The above studies aim mainly at medium- and low-voltage cables, and simple pyrolysis is mostly used in the simulation. A high-voltage power cable has a multi-layer structure, and its combustion effect is quite different. Appropriate simulation methods need to be proposed.

In order to deal with the fire hazards during cable tunnel operation and maintenance, a tunnel fire monitoring system is developed based on Internet of things technology (Wang et al., 2021). The test shows that the system can realize the automatic fire alarm of the power cable tunnel. Jing et al. (2019) proposed a multi-sensor network cable tunnel monitoring system, which integrates temperature, environment, security, and video monitoring. The system realizes information sharing and equipment intelligent linkage by considering the abnormal operation and maintenance requirements of a power cable tunnel. A fire early warning method based on camera monitoring image recognition is proposed by Li et al. (2021). This method first detects the flame and then analyzes the flame image based on the depth neural network of the convolutional neural network. In order to monitor the temperature state of cables in the whole tunnel, an intelligent inspection robot was developed by Qiu et al. (2018). The intelligent inspection robot can be linked with the fire-fighting equipment to improve the intelligent prevention and control level of the whole cable tunnel. The research of the cable tunnel monitoring systems continues to make breakthroughs and still has great development potential. Therefore, the key to the problem lies in how to make full use of the characteristic information contained in the monitoring data and use mathematical models and intelligent algorithms to analyze the relationship between various parameters (Shen et al., 2020; Shen et al., 2021; Shen and Raksincharoensak, 2021), through the information obtained to monitor and locate the fire in the cable tunnel, confirm the fire source information, and provide relevant information for the emergency dispatch of electric power (Yang et al., 2021a), to improve the level of fire prevention and control in cable tunnels. Emerging technologies such as artificial intelligence algorithms, especially deep learning, computer vision, and other related technologies, have developed rapidly (Yang et al., 2021b; Yang et al., 2021c; Yang et al., 2022). The above research mostly depends on image recognition. The intelligent inspection device may be far away from the fire source. Data such as temperature and flue gas are monitored first. It is necessary to analyze these data for prediction.

In this article, considering the complex structure of the high-voltage power cable, the cable combustion simulation method is proposed based on the definition of complex pyrolysis and combustion chemical reaction. According to the typical 110 kV cable tunnel structure, cable layout, and material properties, the fire development is simulated under different fire locations and fire source power. The data of temperature distribution, flue gas concentration, and generated gas content under different simulation conditions are obtained. Then, a variety of data in case of fire are analyzed based on the simulation results, and the characteristic data set is selected. The multi-dimensional nonlinear relationship between the size of the fire source, the location of the fire point, and the collected characteristic data set is analyzed. Finally, the fire early warning model based on support vector machine (SVM) is established. The data sets obtained under different simulation conditions are selected as the total samples. Some of them are used as training samples to train the early warning model and then use the test samples to test and verify the accuracy of the early warning model.

ANALYSIS ON FIRE DEVELOPMENT LAW OF CABLE TUNNEL

Simulation Method of Power Cable Combustion

The structure of a 110 kV high-voltage XLPE cable is quite different from that of the ordinary low-voltage communication cable. It mainly includes conductor, inner semi-conductive shielding layer, insulating layer, outer semi-conductive shielding layer, metal shielding, metal armor, outer sheath, and filler in relevant layers. The outer sheath is generally flame retardant, but it will still burn under open fire. The

insulating material XLPE is flammable and easy to melt and drip, which is easy to cause fire spread. High-voltage cable tunnel fire is generally caused by insulation breakdown and short circuits. In this case, both the internal insulating material and the outer sheath will be ignited by the arc. Studying the simulation method of different materials burning together in a cable multi-layer structure is necessary.

Cable combustion simulation is mainly divided into two processes: solid-phase reaction and gas-phase reaction. Firstly, the solid surface of the material is thermally pyrolyzed and gasified. Then, the pyrolyzed and gasified material reacts with oxygen to form combustion and release heat, which will further promote pyrolysis and ignition. The gas-phase reaction interacts with the solid-phase reaction. The pyrolysis reaction of each layer of the high-voltage XLPE cable is also different due to different materials of the multi-layer structure. If only simple pyrolysis is set, it does not involve the internal pyrolysis process of the solid, which may cause large errors. Herein, the complex pyrolysis method is used to simulate the combustion spread of the multi-layer cable structure. Set the pyrolysis kinetic parameters of the material and calculate the reaction rate using the following formula:

$$W_i = A_i\left(\frac{\rho_i(x,t)}{\rho o}\right)^N \exp\left(-\frac{E_i}{RT_S(x,t)}\right)X_{O_2}^{n_{O_2,n}} \quad (1)$$

,

where W_i is the ith pyrolysis reaction rate; A_i is the ith pre-exponential factor; E_i is the activation energy of the ith reaction; R is the general gas constant, with a value of 8.314 kJ/kmol•K; T_s is the reaction temperature (K); N is the reaction order; ρ_i is the mass concentration of the current solid-phase type; ρ_o is the initial density of the solid surface at the boundary; and X_{O2} is a simulated reaction rate, which is affected by local oxygen concentration.

The pyrolysis of power cables produces a variety of combustible gases, which undergo multiple chemical reactions with oxygen. If each gas reaction is simulated, the amount of calculation will be greatly increased. It will lead to non-convergence in the case of turbulent combustion. Therefore, the final material generated is considered in the simulation. The main material of the outer sheath is C_2H_3Cl. According to the corresponding generated substances measured by the combustion test, determine the substances and coefficients of the chemical reaction equation, as shown in **formula (2)**. The insulating layer material is cross-linked polyethylene (XLPE), and the corresponding chemical equation is shown in **formula (3)**. During the combustion process of the power cable, the combustion of the outer sheath and insulating layer needs to be determined according to the test. Combined with the combustion calorific value of solid materials obtained from the test, the mass of gas fuel required for the corresponding gas-phase reaction is converted. In other words, the dynamic process of pyrolysis gas is balanced by adjusting the generation rate of final gas fuel mass so that the combustion simulated by the gas-phase reaction is closer to the actual test value. According to the ratio of the outer sheath and insulating layer, the molecular formula of gas-phase fuel burned by the power cable is $C_2H_{3.6}Cl_{0.4}$, and the gas-phase reaction equation is shown in **formula (4)**:

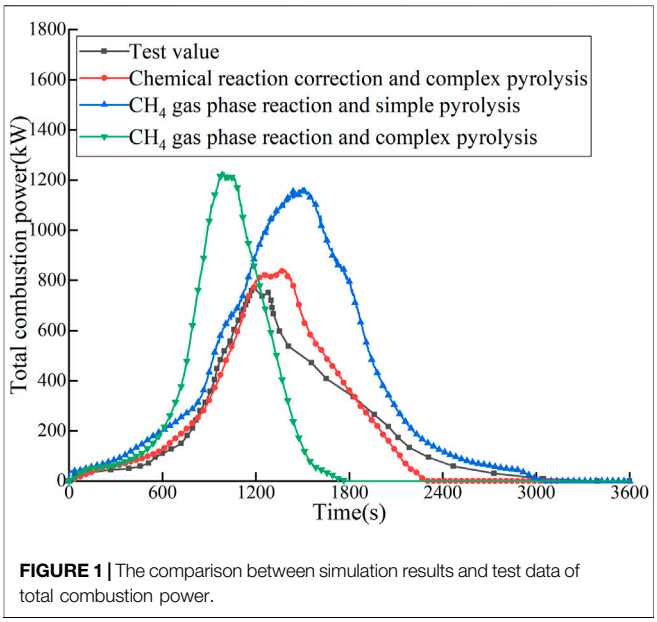

FIGURE 1 | The comparison between simulation results and test data of total combustion power.

$$C_2H_3Cl + 1.53O_2 \rightarrow 0.96CO_2 + 0.14CO + 0.9C + H_2O + HCl \quad (2)$$

$$C_2H_4 + 3O_2 \rightarrow 2CO_2 + 2H_2O \quad (3)$$

$$C_2H_{3.6}Cl_{0.4} + 2.39O_2 \rightarrow 1.42CO_2 + 0.34CO + 1.6H_2O + 0.4HCl + 0.24C \quad (4)$$

In order to verify the effectiveness of the improved simulation model, a comparative analysis is carried out combined with the combustion test of the high-voltage cable. Generally, CH_4 is used to simulate the gas-phase reaction. Pyrolysis reaction can be divided into simple pyrolysis and complex pyrolysis. The three combined simulation conditions are as follows: chemical reaction correction and complex pyrolysis, CH_4 gas-phase reaction and simple pyrolysis, and CH_4 gas-phase reaction and complex pyrolysis. The test measurement data are total combustion power. The comparison between simulation results and test data is shown in **Figure 1**. The results show that CH_4 in the gas-phase reaction will increase the total combustion power by about 50%. The rising rate of total combustion power of simple pyrolysis is slower than that of complex pyrolysis. It will also lead to the difference between the simulation results and the test data. The simulation results of the improved model proposed in this study are closest to the experimental results. The simulation is close to the rising stage of the test, and the error is about 2.3%. In the attenuation stage, the error between simulated combustion power and test power increases, and the maximum error is about 14%. The effectiveness of the improved model is verified.

Simulation Parameter Setting

The simulation model is established according to the typical 110 kV power cable tunnel layout. The length of each ventilation zone in the tunnel is 100 m. Three layers of 110 kV cables are arranged on the cable brackets. The height between layers is

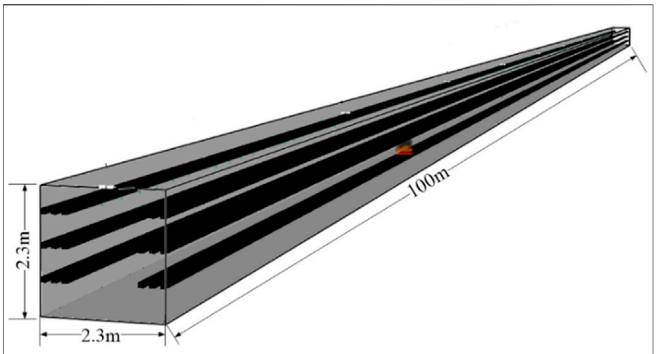

FIGURE 2 | The whole simulation model.

60 cm, and the spacing between three cables on each layer is 10 cm. A cable tunnel model is established with a length of 100 m and a cross section of 2.3 × 2.3 m, as shown in **Figure 2**. The calculation boundary is set to concrete properties. Probes of temperature, smoke concentration, and characteristic gas are set every 0.1 m at different model heights. Because the copper conductor cannot burn, the cable body is equivalent to the internal insulating layer and the external outer sheath. The insulating layer material is XLPE. The outer sheath material is PVC. The thermal performance parameters of the material are listed in **Table 1**.

The thermogravimetric analysis of PVC outer sheath material is carried out. The change law of temperature and weight of PVC during heating is obtained through the test. The research shows that a small amount of organic gas is produced when the cable is heated to 240°C. HCl gas begins to precipitate at 328°C. The reaction becomes an exothermic reaction at 385°C, and carbon oxides begin to precipitate in addition to HCl gas. The cable ignition temperature is set to the temperature at which the exothermic reaction occurs. The pyrolysis combustion parameters of corresponding cables are listed in **Table 2**.

The power of the fire source causing cable combustion needs to be analyzed and set in combination with the actual situation. When the outer sheath of the cable is damaged, the induced potential on the armor and metal shield can be grounded through the damaged point to form a circulating current. At this time, the current is small and the heating power is small. However, it will last for a long time to form smoldering. When the insulation layer of the power cable is aged and broken down, a short-circuit fault is formed. According to the capacity of the power cable system, there will be different short-circuit currents. The short-circuit current value is large, and the heating power is large, which can quickly ignite the cable insulation layer and outer protective layer. When the system suffers from overvoltage breakdown due to large short-time energy, the most serious joint explosion and fire may occur. At present, there is no clear fire classification of the power cable tunnel. Combined with the division regulations of urban fire alarm, the fire conditions are divided into smoldering fire, developing fire, and open fire. The fire caused by cable fire in different layers is different, so it is necessary to set simulation conditions for simulation research. Nine different simulation conditions are set in **Table 3**.

Analysis of Simulation Results

Analysis of Temperature Distribution in Cable Tunnel

The simulation results show that when the fire source power is 150 kW, it is difficult to spread the fire due to the small power. Combustion occurs only near the ground point where the outer sheath is damaged. When the fire source power is 600 and 1200 kW, the fire will spread along the cable. After the cable body is completely burned, the overall fire develops rapidly. For instance, the temperature distribution in the tunnel under the development fire of 600 kW is analyzed, as shown in **Figure 3**. In the process of cable combustion, the heat diffuses around with the flue gas flow, and the high-temperature airflow mainly spreads to the upper layer. Under the action of continuous high temperature, the cable material is rapidly pyrolyzed and then burned, and the upper cable is ignited. It shows that the high-temperature area in the early stage of development is mainly above the fire source. AS high-temperature gas accumulates in the upper cable and tunnel ceiling, the upper layer is easier to burn and develop. With the increase in combustion time, the upper cable gradually spreads and expands the combustion area. When the fire source is in the middle cable, it can still ignite the upper cable upward to achieve a certain combustion spread effect. When the fire source is located in the lower layer or middle layer, the tunnel temperature can reach 1000°C. When the fire source is located in the upper layer, as the temperature is mainly concentrated in the tunnel ceiling, the temperature rise on both

TABLE 1 | Thermal performance parameters of cable materials.

	Density g/cm^3	Thermal conductivity W/(m•K)	Specific heat kJ/(kg•K)	Thickness mm
Outer sheath	1.38	0.14	1.2	10
Insulating layer	0.92	0.4	2	20

TABLE 2 | Pyrolytic combustion parameters of cable materials.

	Pre-exponential factor A 1/s	Activation energy E kJ/kmol	Heat of combustion $\triangle H_c$ kJ/kg
Outer sheath	6.61×10^8	161,000	16,400
Insulating layer	6.5×10^{12}	218,000	43,600

TABLE 3 | Fire simulation conditions of power cable tunnel.

Simulation conditions	Risk level	Fire source type	Fire source power (kW)	Fire source location
No. 1	Warning	Smoldering fire	150	Upper layer
No. 2				Middle layer
No. 3				Lower layer
No. 4	Alarm	Developing fire	600	Upper layer
No. 5				Middle layer
No. 6				Lower layer
No. 7	Critical alarm	Open fire	1200	Upper layer
No. 8				Middle layer
No. 9				Lower layer

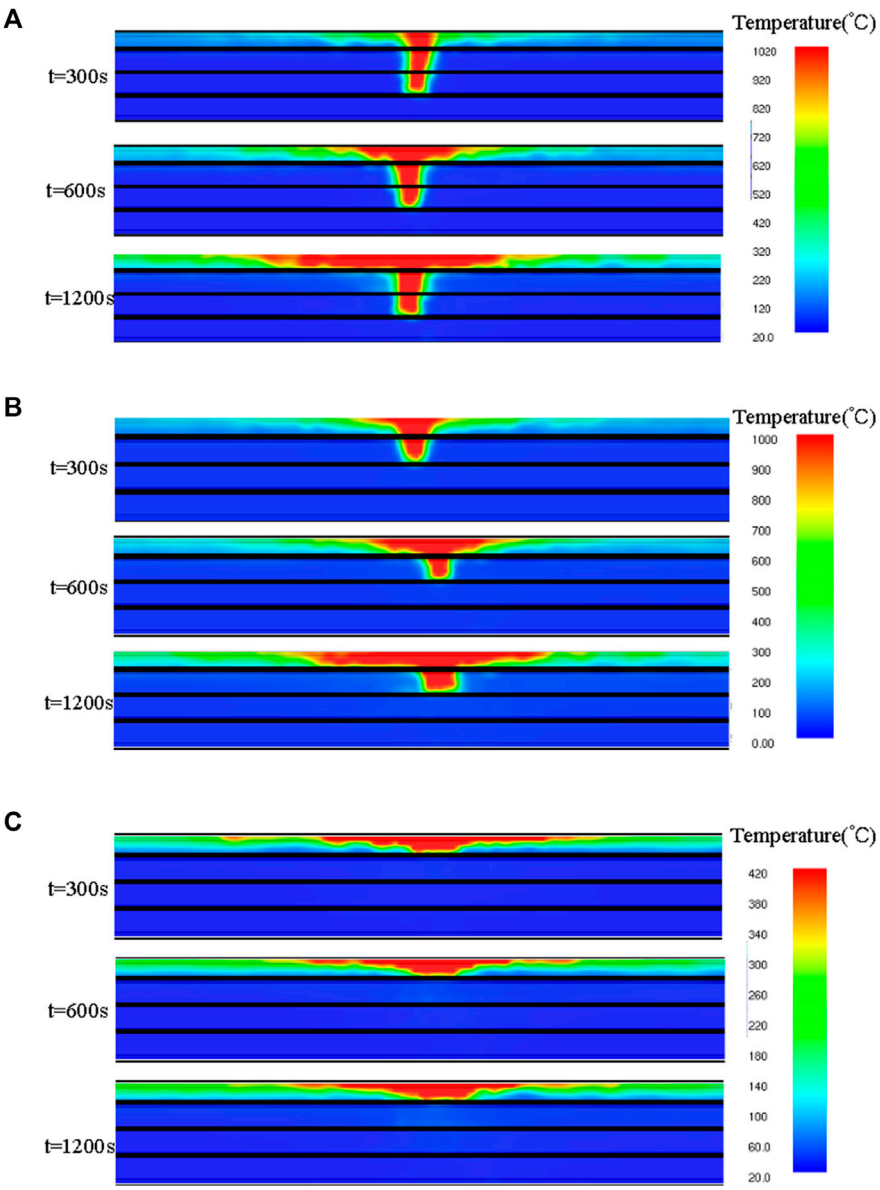

FIGURE 3 | Temperature distribution of cable tunnel when the ignition point is located in different layers. **(A)** At the lower layer. **(B)** At the middle layer. **(C)** At the upper layer.

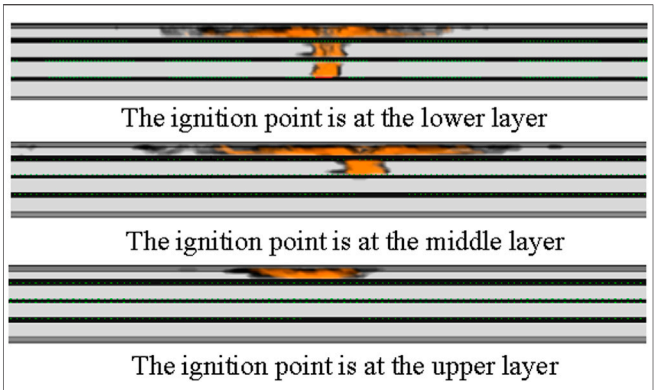

FIGURE 4 | Fire smoke spread at different ignition positions (fire source power 600 kW, t = 600 s).

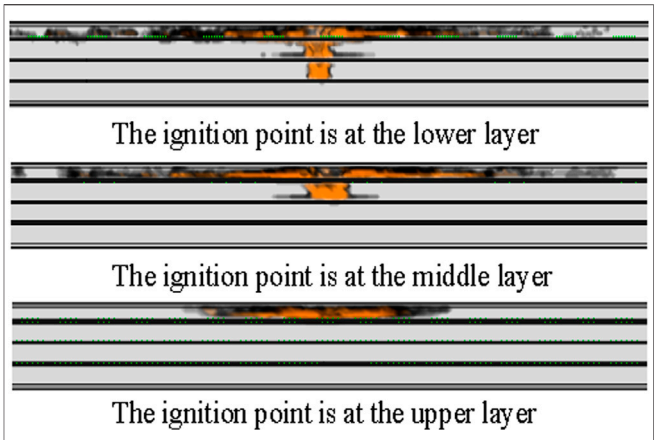

FIGURE 5 | Fire smoke spread at different ignition positions (fire source power 1200 kW, t = 600 s).

sides of the fire source of the cable body is not obvious, and the combustion is not easy to spread. The maximum temperature in the tunnel is about 420°C.

Analysis of Fire Smoke Spread

When the fire source power is 150 kW, the combustion range is small and the amount of smoke is less. When the fire source power is 600 kW, it can ignite the upper cable and spread continuously. With the expansion of the combustion spread range, the flue gas concentration increases gradually, as shown in **Figure 4**. With the expansion of the combustion spread range, the flue gas concentration increases gradually. The flue gas first reaches the top and then gradually diffuses to both sides. At 300 s, the flue gas has not completely diffused to the other end. At 1200 s, the flue gas has completely diffused to both sides and has sufficient concentration. When the ignition point of the cable is at the lowest layer, the total firepower is the largest. When the fire source power is 600 kW, the maximum total combustion power of the cable is about 5700 kW. When the fire source power is 1200 kW, the maximum total combustion power of the cable can exceed 16 MW. When the ignition point of the cable is at the lowest layer, it is easier to ignite the upper cable and is conducive to the flame extension of the middle layer cable. The overall combustion area is the largest, and the fire development is the most serious, as shown in **Figure 5**. When the flame develops close to the tunnel roof, the gas heat flow accumulates above. After reaching a certain degree, a fire flashover will occur. The cables on the top layer spread rapidly, and the burning rate is much higher than that of the lower two layers. When the ignition point of the cable is in the upper layer, the total firepower is the smallest. Because it cannot be fully ignited in this case, the total combustion power is much less than that in the lower two layers.

Characteristic Gas Analysis of Power Cable Combustion

Different fire source powers or locations will lead to the difference in combustion characteristic gas. Whether the combustion is sufficient directly affects the proportion of CO_2 and CO produced. Taking the fire source power of 600 kW for instance, the measured concentrations of CO_2 and CO with time and fire point distance are shown in **Figures 6**, **7**. The concentration distribution trend of the two gases in the tunnel is approximately the same. The concentration of CO_2 produced by fire is much higher than that of CO. At the beginning of the fire, the characteristic gas produced by combustion first accumulates and settles at the top. When the fire source is at the lower layer, the combustion rate is the highest. The concentrations of CO and CO_2 in the tunnel are generally high. The maximum concentration within 20 m from the fire source is 190 and 1050 ppm, respectively. When the fire source is located at the upper layer, the heat generated by combustion is mainly concentrated at the top of the tunnel. The cable body cannot be ignited, and the combustion is not easy to form and diffuse. The overall characteristic gas concentration in the tunnel is at a very low value.

CHARACTERISTIC DATA ANALYSIS AND EARLY WARNING METHOD OF CABLE TUNNEL FIRE

Basic Principle of Early Warning Method Based on Feature Anomaly Monitoring

The early warning of cable tunnel fire is based on real-time monitoring data such as temperature, smoke concentration, CO, and CO_2. However, considering the cost of installation, operation, and maintenance, it is impossible to arrange a variety of existing monitoring sensors in the whole line of the power cable. There is a blind area in the monitoring of tunnel fire. However, it is impossible to judge the power and relative position of the fire source. The simulation results show some differences in temperature change, smoke, and characteristic gas propagation of fires with different fire source sizes and relative positions. In case of a smoldering fire, the fire point temperature is low, the flue gas is large, and the characteristic gas concentration is easier to be monitored first. In case of insulation breakdown, short circuit, or even intermediate joint explosion, a large amount of heat will be generated rapidly, and high-temperature gas may spread faster. It is necessary to analyze a variety of abnormal monitoring data in case of fire in the cable

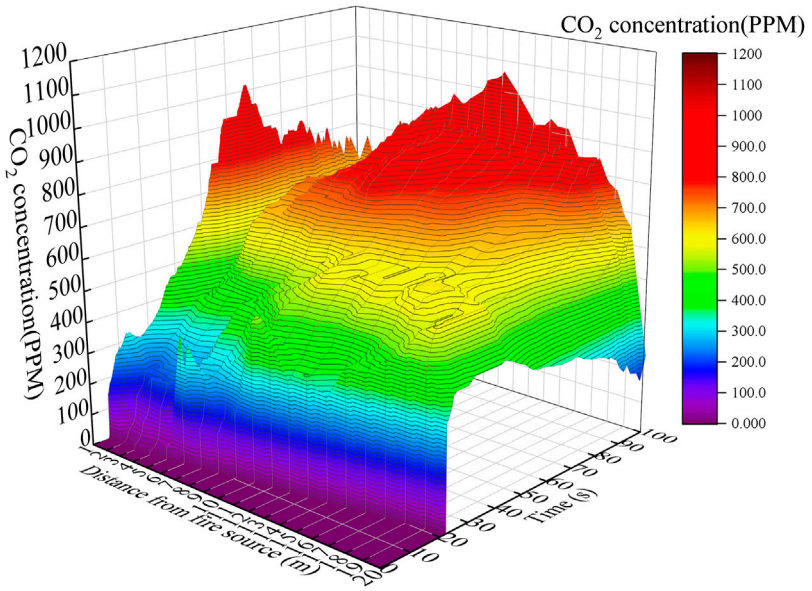

FIGURE 6 | Variation curve of CO_2 concentration (fire source power 600 kW).

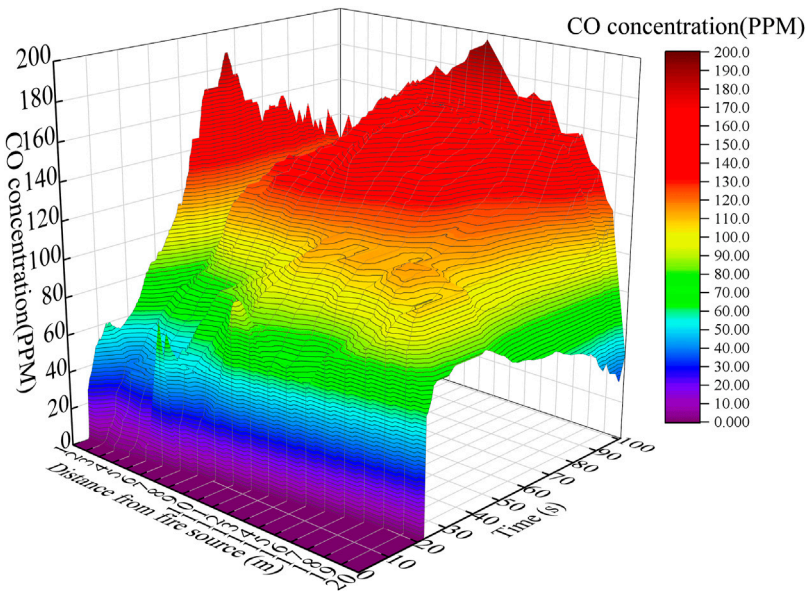

FIGURE 7 | Variation curve of CO concentration (fire source power 600 kW).

tunnel. The fire source level and relative position are predicted through the characteristic analysis of the collected data set.

The distance between the cable ignition point and the monitoring device is different, and the various characteristics of the combustion heat, smoke, and characteristic gas transmitted to the monitoring device are also different. It is necessary to select reasonable characteristic data for comparative analysis. Whether it is a fixed monitoring device or a mobile intelligent monitoring device, the measurement sensor has a minimum measurement threshold. When the threshold is triggered, the subsequent measured values can be continuously collected as a data set. The relationship between the size and relative position of the ignition source and the collected characteristic data set is a multi-dimensional nonlinear relationship. This multi-dimensional nonlinear relationship needs many data sets to be analyzed. Due to the high cost, low efficiency, and difficulty in controlling the actual tunnel test, it is not feasible to obtain a large amount of data through the test. The characteristic data can be obtained by

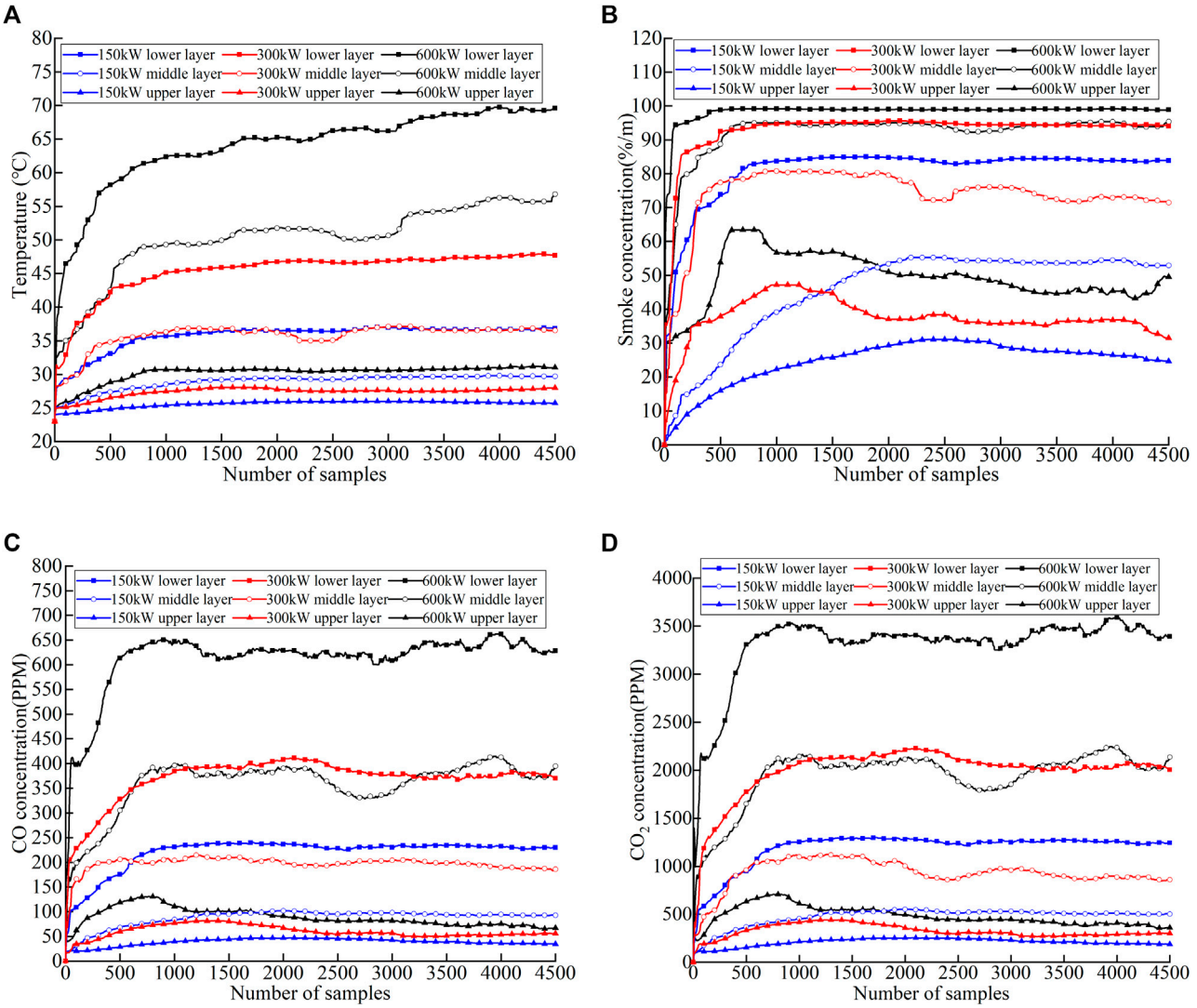

FIGURE 8 | The variation and comparison of sampling parameters. **(A)** Temperature, **(B)** smoke concentration, **(C)** CO, **(D)** CO_2.

simulating a variety of different situations. Under each condition, the amount of feature data is limited, and an appropriate intelligent algorithm needs to be used for prediction. It is difficult to directly predict the power value and accurate position of the fire source. In this article, the classification of fire source power and relative position is transformed into a classification problem. The SVM algorithm has certain advantages in solving small sample, nonlinear, and high-dimensional pattern classification problems. The kernel function is an important part of the support vector machine. Herein, the radial basis function kernel function is selected as follows:

$$K(x_i, y_i) = \exp(-\gamma \| x_i - y_i \|^2),$$

where γ is the kernel function parameters. The penalty coefficient C and kernel function parameters γ in SVM determine its recognition performance. The above parameters are optimized based on the genetic algorithm, which can avoid falling into a local minimum in the process of parameter optimization and quickly locate near the optimal solution.

Analysis and Selection of Fire Characteristic Parameters of Cable Tunnel

The temperature, flue gas concentration, and CO_2 and CO content under different fire source powers and fire locations are simulated. The intelligent mobile monitoring and fire extinguishing device is installed on the track in the middle of the top of the tunnel. The installation height of various sampling sensors is about 1.9 m. In order to simulate the actual sampling situation, the simulated sampling data points are also selected at the middle height of 1.9 m at the top of the tunnel. The data sets of characteristic parameters at monitoring points at different locations from the fire source are simulated and obtained.

TABLE 4 | Partial sampling data (300 kW, lower layer).

Sampling point	Temperature (°C)	Smoke concentration (%/m)	CO concentration (PPM)	CO_2 concentration (PPM)
1	32.91	72.70	243.12	1281.28
2	37.93	87.02	250.42	1303.27
3	38.89	87.81	228.15	1227.62
4	40.91	89.32	300.80	1630.79
5	42.20	92.64	355.00	1915.65
6	43.09	93.27	352.18	1904.47
7	43.35	93.38	380.16	2034.05
8	44.25	94.88	379.97	2015.69
9	44.25	94.57	380.88	2073.22
10	45.47	95.03	382.68	2133.56
11	45.39	94.72	375.01	1993.64
12	45.52	94.71	376.35	2018.54
13	45.86	95.07	383.83	2096.53
14	45.95	95.36	357.25	1988.37
15	46.06	95.57	420.28	2298.63

When the power is 150, 300, and 600 kW, the variation and comparison of sampling parameters at different ignition positions are shown in **Figure 8**. **Figure 8A** shows a little difference in change trend and amplitude between the temperature curve of 150 KW ignition point at the lower layer and that of the 300 kW ignition point at the middle layer. A similar situation exists in the comparison curve of flue gas concentration, CO, and CO_2. It shows that it is difficult to distinguish fire source power and fire location only by a single acquisition parameter.

Figures 8B,D show obvious differences in the changes of flue gas concentration and CO_2 content in the lower layer of 150 KW and the middle layer of 300 kW. **Figure 8B** shows that when the power is 300 kW and the ignition position is in the lower layer, the change law of flue gas is basically the same as that when the power is 600 kW and the ignition position is in the middle layer. However, the temperature curves in these two conditions are significantly different, as shown in **Figure 8A**. The above analysis shows that different fire source power and fire location can be distinguished using various characteristic parameters. Regardless of the distance from the ignition point, the same fire source power and ignition position have a similar change trend. Therefore, the data set of the above characteristic parameters can be used as the input sample for fire determination.

Prediction Method and Test Results of Fire Classification

For instance, when the power is 300 kW and the ignition position is in the lower layer, some sampling data sets are shown in **Table 4**. There are two main problems in using these sampling data sets directly as a sample unit. The numerical amplitudes of different physical quantities vary greatly, so the data need to be normalized first. Another problem is too much sampling data in the data set. If all of them are used for model training, there will be too many sample dimensions. It may lead to overfitting of the model and reduce the prediction accuracy. In order to simplify the redundancy of samples and reduce the data dimension, the sampling points in the stationary section are reduced in each physical quantity series in each group of samples. At the same time, the range, modulus, maximum value, and average value of each sequence value are added to ensure the overall characteristics.

If the regression prediction is carried out directly, it is difficult to predict the power value accurately. The classification prediction is carried out according to the fire grade. The fire source power is divided into five values on the basis of **Table 3** by classification: 150, 300, 600, 900, and 1200 kW. It is respectively set in three different layers of cables under different fire source powers. Fire sources are divided into 15 classifications according to the fire source power and fire location. In each classification, the monitoring sensors with different distances from the fire source are simulated to obtain data. Analog sampling of monitoring points is set every 2 m as a group of sample data, and a total of 40 groups of sample data are selected. A total of 600 samples were obtained. For each classification, 35 groups were randomly selected as training samples and the other five groups as test samples. A total of 525 groups of training samples and 75 groups of test samples were obtained. The training samples are used to train the fire classification and prediction model based on SVM, and then the test samples are input for prediction. The prediction accuracy of test samples is 92% (69/75), which verifies the effectiveness of the proposed detection method. The analysis of the samples with wrong prediction is mainly because the flue gas concentration, temperature, and CO and CO_2 concentration collected by some analog sensors at different distances in the two classification situations are relatively close. The samples with prediction errors are analyzed. This is mainly because after reducing the sampling data points for dimensionality reduction, the flue gas concentration, temperature, and CO and CO_2 concentration collected by some analog sensors with different distances in the two classification cases are relatively close. It is necessary to further analyze the correlation between characteristic parameters and study more appropriate dimensionality reduction methods to improve the accuracy of prediction.

CONCLUSION

This study presents an improved combustion model according to the structural characteristics of the high-voltage cable. The

variation characteristics of characteristic data in a cable tunnel under different fire conditions are analyzed, and a fire prediction model is proposed. The main conclusions are set as follows:

1) Through the comparison between simulation and experimental data, the cable model is established by defining chemical reactions and setting up complex pyrolysis. The total firepower obtained can be well consistent with the actual combustion.
2) The fire development under different fire source powers and fire locations is simulated. The results show that it is difficult to distinguish fire source power and fire location only by a single acquisition parameter. The different fire source powers and fire locations can be distinguished using a variety of characteristic parameters.
3) The accuracy of the fire classification and prediction model based on SVM is 92%. The effectiveness of the prediction model is verified. Fire can be put out more pertinently according to the prediction results of fire source power and fire location.

DATA AVAILABILITY STATEMENT

The original contributions presented in the study are included in the article/Supplementary Material. Further inquiries can be directed to the corresponding author.

AUTHOR CONTRIBUTIONS

CL put forward research ideas. JC guided the research methods. ZP wrote the original draft and is the corresponding author. FT reviewed the manuscript. JL provided relevant structural and material data. XT edited figures and tables. LH did the simulation. JCa did the data analysis. All authors have read and approved the submitted version of the manuscript.

REFERENCES

An, W., Tang, Y., Liang, K., Cai, M., Wang, T., and Wang, Z. (2020b). Study on Temperature Distribution and CO Diffusion Induced by cable Fire in L-Shaped Utility Tunnel. *Sust. Cities Soc.* 62, 102407. doi:10.1016/j.scs.2020.102407

An, W., Wang, T., Liang, K., Tang, Y., and Wang, Z. (2020a). Effects of Interlayer Distance and cable Spacing on Flame Characteristics and Fire hazard of Multilayer Cables in Utility Tunnel. *Case Stud. Therm. Eng.* 22, 100784. doi:10.1016/j.csite.2020.100784

Fang, H., Zhang, J., Huang, D., Lu, S., and Lo, S. M. (2019). "October)Simulation-Based Quantitative Risk Assessment of Fire in Urban Electrical Cable Tunnels," in 2019 9th International Conference on Fire Science and Fire Protection Engineering (ICFSFPE) (IEEE), 1–9.

Jing, Z., Li, C., Ren, G., Chi, Y., and Tian, F. (2019). October)Multi-Sensor Network Cable Tunnel Monitoring System Based on GISIOP Conference Series: Materials Science and Engineering. *IOP Conf. Ser. Mater. Sci. Eng.* 612 (3), 032178. doi:10.1088/1757-899X/612/3/032178

Li, C., Chen, J., Hu, L., Zhang, W., Cao, J., Tan, X., et al. (2021). Research on Cable Fire Detection and Early Warning Based on Deep Learning in 2021 IEEE International Conference on Electronic Technology, Communication and Information (ICETCI) (IEEE), 176–179. doi:10.1109/icetci53161.2021.9563399

Mi, H., Liu, Y., Jiao, Z., Wang, W., and Wang, Q. (2020). A Numerical Study on the Optimization of Ventilation Mode during Emergency of cable Fire in Utility Tunnel. *Tunnelling Underground Space Tech.* 100, 103403. doi:10.1016/j.tust.2020.103403

Niu, Y., and Li, W. (2012). Simulation Study on Value of cable Fire in the cable Tunnel. *Proced. Eng.* 43, 569–573. doi:10.1016/j.proeng.2012.08.100

Qiu, W., Huang, S., Pei, X., Cui, J., Ye, Y., and Meng, A. (2018). "November). Temperature Anomaly Location and Cable Equipment Recognition with an Improved Convolutional Neural Network Method and Transfer Learning," in 2018 International Conference on Power System Technology (POWERCON) (IEEE), 4555–4560.

Shen, X., Ouyang, T., Yang, N., and Zhuang, J. (2021). Sample-Based Neural Approximation Approach for Probabilistic Constrained Programs. *IEEE Trans. Neural Netw. Learn. Syst.*, 1–8. doi:10.1109/TNNLS.2021.3102323

Shen, X., and Raksincharoensak, P. (2021). "Pedestrian-Aware Statistical Risk Assessment," in IEEE Transactions on Intelligent Transportation Systems. doi:10.1109/tits.2021.3074522

Shen, X., Zhang, Y., Sata, K., and Shen, T. (2020). Gaussian Mixture Model Clustering-Based Knock Threshold Learning in Automotive Engines. *Ieee/asme Trans. Mechatron.* 25 (6), 2981–2991. doi:10.1109/TMECH.2020.3000732

Song, Z., Wang, X., Tan, Z., Miao, X., and Zou, L. (2020). "September)Analysis of Distribution Law of Fire Gas Concentration in Underground Cable Tunnel of Substation," in 2020 IEEE International Conference on High Voltage Engineering and Application (ICHVE) (IEEE), 1–4.

Wang, Y., Zheng, J., and Ding, B. (2021). "October)Fire Protection Monitoring System for Power Cabin in Utility Tunnel Based on IOT Technology," in 2021 IEEE 5th Information Technology, Networking, Electronic and Automation Control Conference (ITNEC) (IEEE), 5, 1366–1371.

Wu, J., Sun, H., Gao, J., Song, Z., Wang, X., and Zou, L. (2020). "September) Simulation of Fire Spread in Underground Cable Tunnel of Substation under Different Ventilation Conditions," in 2020 IEEE International Conference on High Voltage Engineering and Application (ICHVE) (IEEE), 1–4.

Yang, N., Liu, S., Deng, Y., and Xing, C. (2021b). An Improved Robust SCUC Approach Considering Multiple Uncertainty and Correlation. *IEEJ Trans. Elec Electron. Eng.* 16 (1), 21–34. doi:10.1002/tee.23265

Yang, N., Qin, T., Wu, L., Huang, Y., Huang, Y., Xing, C., et al. (2022). A Multi-Agent Game Based Joint Planning Approach for Electricity-Gas Integrated Energy Systems Considering Wind Power Uncertainty. *Electric Power Syst. Res.* 204, 107673. doi:10.1016/j.epsr.2021.107673

Yang, N., Yang, C., Wu, L., Shen, X., Jia, J., Li, Z., et al. (2021c). Intelligent Data-Driven Decision-Making Method for Dynamic Multi-Sequence: An E-Seq2Seq Based SCUC Expert System. *IEEE Trans. Ind. Inf.*, 1. doi:10.1109/TII.2021.3107406

Yang, N., Yang, C., Xing, C., Ye, D., Jia, J., Chen, D., et al. (2021a). Deep Learning-based SCUC Decision-making: An Intelligent Data-driven Approach with Self-learning Capabilities. *IET Gener. Transm. Distrib*. Transmission & Distribution. doi:10.1049/gtd2.12315

Zhang, J., Ji, K., Yan, B., Zhou, Z., Fan, M., and Zhang, B. (2018). July)Numerical Simulation on Smoke Propagation and Fire Separation in Electric Power cable Tunnel. *J. Phys. Conf. Ser.IOP Publishing* 1064 (No. 1), 012015. doi:10.1088/1742-6596/1064/1/012015

Conflict of Interest: CL, JC, FT, JL, XT, LH, and JCa were employed by Electric Power Research Institute of State Grid Jiangsu Electric Power Co., Ltd.

The authors declare that the research was conducted in the absence of any commercial or financial relationships that could be construed as a potential conflict of interest.

frontiers in Energy Research

BRIEF RESEARCH REPORT
published: 04 February 2022
doi: 10.3389/fenrg.2021.823786

Wind Power Prediction Based on a Hybrid Granular Chaotic Time Series Model

Yanyang Wang[1], Wei Xiong[1], Shiping E.[2], Qingguo Liu[1], Nan Yang[3], Ping Fu[1], Kang Gong[1] and Yu Huang[1]*

[1]State Grid Yichang Power Supply Company, Yichang, China, [2]State Grid Hubei Electric Power Co. LTD., Hubei, China, [3]China Three Gorges University, Yichang, China

For realizing high-accuracy short-term wind power prediction, a hybrid model considering physical features of data is proposed in this paper, with consideration of chaotic analysis and granular computing. First, considering the chaotic features of wind power time series physically, data reconstruction in chaotic phase space is studied to provide a low-dimensional input with more information in modeling. Second, considering that meteorological scenarios of wind development are various, complicated, and uncertain, typical chaotic time series prediction models and wind scenarios are analyzed correspondingly via granular computing (GrC). Finally, through granular rule-based modeling, a hybrid model combining reconstructed wind power data and different models is constructed for short-term wind power prediction. Data from real wind farms is taken for experiments, validating the feasibility and effectiveness of the proposed wind power prediction model.

Keywords: wind power prediction, hybrid model, time series, chaotic analysis, granular computing

OPEN ACCESS

Edited by:
Tinghui Ouyang, National Institute of Advanced Industrial Science and Technology (AIST), Japan

Reviewed by:
Davide Astolfi, University of Perugia, Italy
Lin Zhu, South China University of Technology, China

****Correspondence:***
Yanyang Wang
13972578420@163.com

Specialty section:
This article was submitted to Wind Energy, a section of the journal Frontiers in Energy Research

Received: *28 November 2021*
Accepted: *27 December 2021*
Published: *04 February 2022*

Citation:
Wang Y, Xiong W, E. S, Liu Q, Yang N, Fu P, Gong K and Huang Y (2022) Wind Power Prediction Based on a Hybrid Granular Chaotic Time Series Model. Front. Energy Res. 9:823786. doi: 10.3389/fenrg.2021.823786

INTRODUCTION

To mitigate the influence of global warming and energy crisis concerns, wind energy has been developed as one of the most potential energies around the world (Brouwer et al., 2016). Especially in areas with a large amount of wind sources (Li et al., 2017), e.g., Northwest of China, United States, and Europe, large-scale wind farms are being developed to provide more clear power to electricity industries. As more wind power is integrated into power systems with high concentration, the power grid also faces some great challenges caused by wind power generation. For example, the intermittency and variability of wind cause the uncertainty of wind power supply (Doostizadeh et al., 2017), which also causes the difficulties in scheduling wind power and threatens the security of the power grid. Therefore, an accurate wind power prediction system is eagerly required and improved by system operators to mitigate the harmful effects.

Currently, wind power prediction methods are mainly grouped into two categories: physics-based models and data-driven models (Yan et al., 2015). Physics-based models usually make use of meteorological data and physical laws to estimate wind speed, then wind speed is transformed into wind power, e.g. NWPs (Liu et al., 2012). Data-driven models, also called statistical models, utilize big data sets and artificial intelligence (AI) algorithms to train a mathematical model which could express the relationship between inputs and prediction output, e.g., auto-regressive and moving average models (ARMA), neural networks (NN), support vector machines (SVM), and so on (Liu et al., 2016; Shao et al., 2018). Generally, these data-driven models can achieve relatively satisfactory

performance on industrial data of wind farms in short-term forecasting. To further improve short-term wind power forecasting performance, hybrid models combining the advantages of several models are also proposed in literature. For example, in Ouyang et al. (2016), a hybrid model via switching models was proposed to obtain the optimal wind power prediction result, and the Markov chain was introduced as the switching regime. Moreover, many hybrid models usually utilize decomposed signals for prediction then combine these sub-predictions at last. For example, a hybrid model based on wind power time series decomposition was proposed for wind direction forecasting (Tang et al., 2020; Tang et al., 2021). Comparing these models, physical models usually explain the trend of the wind process meaningfully, because they govern the atmospheric behaviors in physics (Xiong et al., 2017). However, their precision in short-term prediction is generally low. On the other hand, those models involving data-driven algorithms may face two problems: one involves the subjective selection of AI algorithms; the other involves overfitting and under-fitting in many models, so the reliability and persuadability of these prediction models require more extra explanation.

Aiming at the mentioned problems above, this paper targets to propose a high-accuracy wind power prediction model combining the advantages of physical and data-driven models. First, as we know, the wind process is formed by atmospheric movement from the perspective of physics, namely, via the chaotic analysis of time series data (Lange and Focken, 2006; Lei et al., 2007). Based on chaotic analysis, the wind power time series could be reconstructed in a new phase space which could reflect both physical factors and statistical results of historical data. Second, if we analyze the wind process from a physical perspective, we would see that the pattern behind wind is variable, diversified, complicated, and uncertain. This is the reason why hybrid models with a switching regime and mode decomposition could succeed. Therefore, a hybrid prediction model considering wind patterns would also persuasively improve wind power prediction performance. Based on the above factors, the proposed method makes use of chaotic analysis and granular computing in wind power prediction and aims at realizing two contributions: 1) making use of chaotic analysis to reconstruct data, and to realize high effectiveness and efficiency with the reconstructed data in modeling; 2) considering the complexity and uncertainty of wind patterns, a hybrid model based on granular computing is proposed to reflect both physical and statistical factors. By taking industrial data from a wind farm as a studied case, the proposed approach is applied. Experiments and evaluation are discussed to validate the feasibility of the proposed wind power prediction model.

TIME SERIES RECONSTRUCTION

According to the above description, time series reconstruction is to extract effective inputs for modeling. Considering the wind speed time series is physically chaotic (Lei et al., 2007), it could be reconstructed based on physical features in a new space where large information is represented by refined features. Assuming a time series as $\{x\} = \{x_1, x_2, \cdots, x_N\}$, N is the length of the given data set, and it could be reconstructed into a new phase space according to the Takens embedding theory (Rand and Young, 1988). The reconstruction formula is expressed as below:

$$\mathbf{x}(i) = \left(x_i, x_{i+\tau}, \cdots x_{i+(m-1)\tau}\right) \in R^m, i = 1, 2\cdots, N_0 = N - (m-1)\tau \tag{1}$$

where $\{x\}$ is the wind power time series in this paper; $\mathbf{x}$ is the reconstructed data belonging to a space $\boldsymbol{R}^m$; and τ and m are the delay time and embedding dimension parameters in reconstruction. In this way, the reconstructed data could provide as much possible information with a limited number of dimensionalities, namely, improving effectiveness and efficiency in time series modeling (Tang et al., 2020). These two parameters can be calculated by the mutual information (MI) method (Fraser and Swinney, 1986) and false nearest neighbors (FNN) method (Abarbanel and Kennel, 1993), respectively. Through the selection of optimal delay time τ and embedded dimension m, a one-dimension time series could be reconstructed as $\mathbf{R^m}$ data by **Eq. 1**. In this way, the most relevant features could be included in the new data for modeling (Tang et al., 2020).

To judge if the reconstructed phase space is a chaotic system, some criteria are required. The Lyapunov exponent (Packard et al., 1980) was a useful metric to test a system's characteristic, as expressed in **Eq. 2**. If the value of Lyapunov exponent is positive, the given system could be considered as a chaotic system. When it equals 0, the system is considered as having bifurcation points or periodic solutions. When its value is negative, the system has stable and fixed solutions. To calculate the value of the Lyapunov exponent, firstly, choosing a start point in the reconstructed space and its nearest neighbor, their distance is defined as L_0. After the evolution of a given time T, two new points are obtained, and their new distance is defined as L'_0. Then, new data and new distance pair (L_1, L'_1) are calculated as the same principle. When the last point in the phase space is calculated, we could calculate the Lyapunov exponent as below:

$$\lambda = \frac{1}{MT}\sum_{i=0}^{M}\ln\frac{L_i^{'}}{L_i} \tag{2}$$

where M is the number of distance pairs. Through the calculation of the Lyapunov exponent in **Eq. 2**, we could judge if the reconstructed phase space and the original time series have chaotic features according to the above criterion.

WIND POWER PREDICTION MODEL BY GRANULAR COMPUTING

For chaotic time series, several prediction models are studied in the literature, e.g., local prediction models, global prediction methods, prediction methods based on the Lyapunov exponent, Volterra prediction models, and so on (Zhang and Liang, 2012). For wind power prediction, the meteorological regimes behind the wind process are various, so these models may just be suitable at specific time intervals. According to this

idea, the hybrid model with a regime switching the optimal models would achieve better performance. However, considering the uncertainty of wind development, the accuracy of meteorological regimes at a given period is complicated and uncertain. Therefore, a hybrid model considering more prediction models and uncertainty is a better choice to improve performance. This is also the reason for proposing a hybrid prediction model via granular computing.

Granular Computing for Dividing Scenarios

Granular computing (GrC) is actually a process of grouping objects which have the same or similar information (Ouyang et al., 2021) (e.g. shapes, sizes, or other features) and use information granules (IGs) to analyze the abstract objects in real world. Based on these ideas, we proposed to construct information granules of different wind development processes and utilized these granules to guide prediction.

Generally, IGs are constructed by two factors: prototype and granule size. To partition an original data set into different categories, the Fuzzy C-Means (FCM) is widely applied (Chuang et al., 2006). Assuming the set $\{\mathbf{x}\}$ having N data points with c clusters, the membership matrix of each data point based on FCM could be calculated by the following expression:

$$u_{ik} = \frac{1}{\sum_{j=1}^{c}\left(\frac{\|\mathbf{x}_k-\mathbf{v}_i\|}{\|\mathbf{x}_k-\mathbf{v}_j\|}\right)^{2/(m-1)}} \tag{3}$$

where, $\mathbf{x}_k \in \{\mathbf{x}\}$; u_{ik} is the membership to the ith cluster center, and m is a fuzzification coefficient and usually $m = 2$. Then, cluster centers could be selected as prototypes of granules, as below.

$$\mathbf{v}_i = \sum_{k=1}^{N} u_{ik}^m \mathbf{x}_k \Big/ \sum_{k=1}^{N} u_{ik}^m, i = 1, 2, \cdots, c \tag{4}$$

After the decision of these prototypes, a blueprint of IGs could be created. By concentrating on a prototype $\boldsymbol{v_i}$, a group of points could form a granule IG_i which could also be wind scenario in our study. Besides the position information, the sizes of IGs are also important in evaluating their description performance. Generally, coverage and specificity are two important metrics (Ouyang et al., 2019). Assuming a granule is constructed as a hypersphere granule via Euclidean distance, the coverage and specificity can be calculated as below:

$$\mathrm{cov}(\rho) = \frac{1}{N} \sum_{\substack{\mathbf{x}_k:\|\mathbf{x}_k-\mathbf{v}_j\|^2 \le \rho^2 \\ \mathbf{x}_k \in \Omega}} u_{ik} \tag{5}$$

$$sp(\rho) = 1 - \rho \tag{6}$$

where ρ is the size of granule, satisfying $\rho \in [0, 1]$. Ideally speaking, these two metrics are expected to maximum. For example, when dividing wind scenarios, a granule needs to cover as many similar scenarios as possible; meanwhile, it needs to reduce the overlap with other granules. However, it is seen from (**Eqs. 5–6**) that they are in conflict, namely, higher coverage will lead to lower specificity. To optimize the mentioned objective, a function $\mathrm{cov}(\rho)\mathrm{sp}(\rho)$ is proposed to be maximized. Finally, an optimal value of ρ, say ρ_{opt}, is returned. After the optimization of all granule sizes, the original data could be described by several constructed information granules, namely, scenarios.

Wind Power Prediction Modeling

According to the process of granular computing, data sets could be divided into several granules based on similarity. For reconstructed wind power data, to analyze the meteorological scenarios to which each data point belongs, we could also construct scenario granules based on reconstructed wind power data $\{\mathbf{x}\}$. While considering to utilize results of granular computing to improve the performance of wind power prediction, we propose to add the prediction errors into inputs in granular computing, defined as below:

$$input = [\mathbf{x}, e_1, e_2, e_3] \tag{7}$$

where $\mathbf{x}$ is the reconstructed chaotic data and e1, e2, and e3 are prediction errors of three models (Local linear model, Lyapunov model, Volterra model) forecasting wind power independently. By using these inputs in granular computing, three information granules IG_i (i = 1,2,3) reflecting the relationship of wind scenarios and prediction models could be constructed. Then, three fuzzy rules for determining a given data point's scenario could be given as below:

$$\mathrm{Rule}_i\text{: } IF \ input \text{ belongs to } \mathrm{IG}_i, \text{ THEN } \mathbf{x}_t \text{ is in the } i^{th} \text{ wind scenario; } (i = 1, 2, 3) \tag{8}$$

While the granular computing is based on fuzzy analysis, the uncertainty of the wind process is also considered. According to the above rules, for the current data point $\mathbf{x}_t$, its belonging degree to each wind scenarios could be calculated by **Eq. 3**. Considering the uncertainty of $\mathbf{x}_t$ belonging to wind scenarios, we propose to utilize the weighted hybrid model as the final prediction model, as below:

$$\mathbf{x}_{t+1} = \sum_{i=1}^{c} u_{it} \mathbf{x}_t \tag{9}$$

where the prediction model is regarded as a weighted model using fuzzy memberships as weights; $c = 3$ in this paper because only three chaotic time series models are considered.

EXPERIMENTS AND DISCUSSION

According to the above description, we could complete the chaotic analysis and prediction modeling of wind power data. In this paper, we take the industrial data from wind farms as studied cases. The collected data is from a wind farm of northwestern China, which has a sampling interval of 15 min. The objective of this research is to predict the wind power output from the studied wind farm that has a totally installed capacity of 603 MW. The data set has 34,080 data points, among of which 70% is taken as training set and the rest are for testing. Moreover,

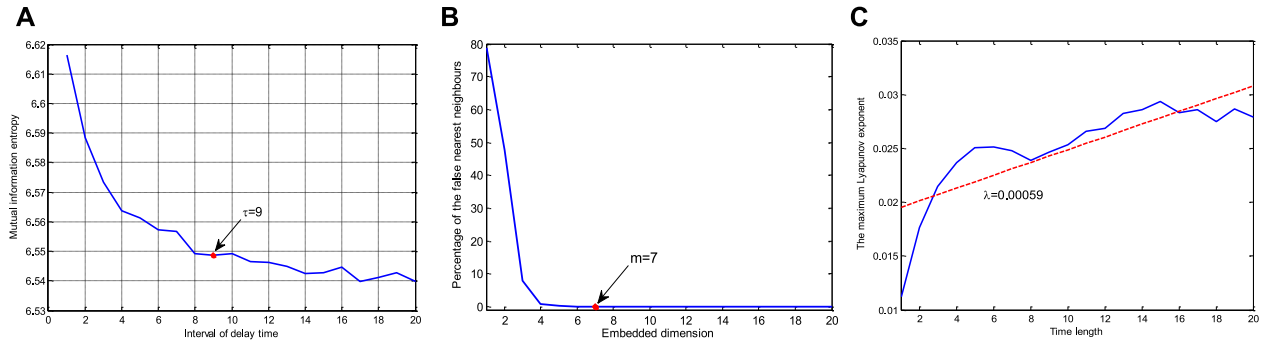

FIGURE 1 | Calculation of the delay time **(A)**, the minimum embedded dimension **(B)**, and the Lyapunov exponent **(C)**.

raw wind data often contains random noise and abnormal values; therefore, suitable data pre-processing is required before modeling, for example, wind power denoising and abnormality cleaning.

Wind Power Data Reconstruction

According to the above description, the proposed prediction model is based on chaotic analysis. Therefore, reconstruction of wind power data and verification of the chaotic system is the first step. As the processes are described in **Section 2**, we need to select the optimal delay time and embedded dimension for phase space reconstruction via the mutual information method and FNN method. Results are shown in **Figure 1**.

Figure 1A depicts the curve representing values of mutual information when the delay time τ increases. It is seen that the relevance becomes weak when delay time becomes large. Generally, the final delay time τ is decided when the value of mutual information reaches the first local minimum value. Therefore, the delay time of wind power is selected as $\tau = 9$. It means that the closet nine points, e.g. $x(t)$, $x\,(t\text{-}1)$, . . ., $x\,(t\text{-}8)$ have similar information, namely, dependent relation. In order to provide more information with lower dimensionality in modeling, two independent variables should be taken, such as $x(t)$ and x $(t\text{-}9)$. **Figure 1B** depicts the curve representing the number of false neighbor points when calculating the embedded dimension. When the value of the threshold is selected as ath = 10%, the percentage of false neighbors is 0% with reconstruction parameters $m = 7$. Combining with $\tau = 9$, it implies that the correlation will be ended at the 7*9 = 63 step, but the new phase space can be considered for the reconstruction of the most important seven points. Then, according to the calculation of the Lyapunov exponent in **Eq. 2**, the solution of the Lyapunov exponent is calculated as $\lambda = 0.00059$. It illustrates that wind power data belongs to a chaotic system ($\lambda > 0$) according to the above description of the Lyapunov exponent. Then, the prediction models based on chaotic time series are feasible in wind power prediction.

Wind Power Prediction

By taking 70% of the given data set as the training data, the remaining data is used for validation and testing. First, by applying the reconstruction parameters calculated above, the phase space of wind power data is reconstructed based on **Eq. 1**. Since the reconstructed wind power time series is verified to be chaotic, it is used to train and predict wind power based on three given chaotic models in **Section 3**, namely, the local linear model, Lyapunov prediction model, and Volterra prediction model, labeled as S_1, S_2, and S_3 respectively. Considering that each model has its best prediction performance at different time, we could consist of the reconstructed data and prediction errors of three models as inputs; three wind scenarios are analyzed by granular computing.

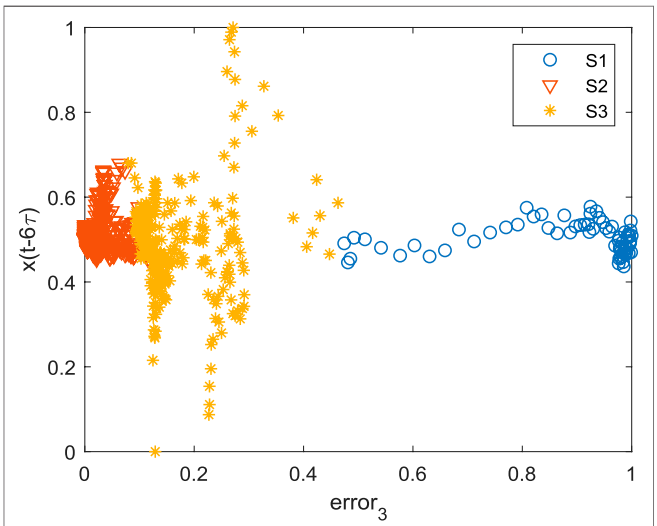

FIGURE 2 | Division of wind scenarios.

Figure 2 shows the division of three wind scenarios through granular computing. For convenience of presentation, only two elements [error3, **x** $(t\text{-}6\tau)$] are used in plot. It is seen from **Figure 2** that different scenarios for three chaotic time series models have clear division. Then, based on this division, fuzzy rules could be formed and the final hybrid model could be constructed by granular computing (**Eq. 9**). The performance of wind power prediction is expressed by four error metrics (Wu et al., 2014), namely, mean absolute error (MAE), root mean squared error

TABLE 1 | Four error metrics of different prediction methods

	MAE(MW)	RMSE(MW)	SDofAE	CC
S_1	20.578	28.477	19.694	0.9470
S_2	22.460	32.230	23.128	0.9354
S_3	17.907	21.556	18.431	0.9838
Proposed model	15.874	16.261	15.955	0.9938

TABLE 2 | Improvement coefficients of the proposed method vs. S_1, S_2, and S_3

	I_{MAE} (%)	I_{RMSE} (%)	I_{SDofAE} (%)	I_{CC} (%)	R^2 (%)
Proposed vs. S_1	22.86	42.90	18.99	4.94	67.39
Proposed vs. S_2	29.32	49.55	31.01	6.24	74.54
Proposed vs. S_3	11.35	24.56	13.43	1.02	43.09

(RMSE), standard deviation of absolute error (SDofAE), and correlation coefficients (CC), as presented in **Table 1**.

S_1, S_2, and S_3 represent three prediction models, respectively, and the proposed model is also compared. It is seen that the difference between the former three models is not large, and that S_1 has the worst prediction performance and S_3 has the best prediction performance according to the values of error metrics. In comparison, the performance of the proposed method is presented and improved greatly.

Comparison and Discussion

Moreover, based on the error metrics, some improvement coefficients were defined in (Wu et al., 2014), which are validated to be useful for studying performance improvement, as shown in **Eq. 10**.

$$I_{EM} = \frac{EM_{ref} - EM}{EM_{ref}} \cdot 100\% \tag{10}$$

where, I_{EM} is the improvement coefficient and EM represents a given error metric (e.g. MAE, RMSE, etc.). When the value of I_{EM} is larger than 0, it means the given model improves the performance w.r.t. the reference.

Table 2 shows the improvement coefficients of the proposed method by taking S_1, S_2, and S_3 as the reference models. The coefficient of determination R^2 is also proposed for analysis in **Table 2**. R^2 is actually the improvement coefficient of the mean square error (MSE) defined in **Eq. 11**.

$$MSE = \frac{1}{N}\sum_{i=1}^{N}(x_i - \hat{x}_i)^2 \tag{11}$$

It is seen that the proposed model has an improvement on longitudinal errors by an average of 21.18% on MAE, 39% on RMSE, and 21.14% on SDofAE, which means the proposed method can improve the prediction performance greatly. On the other hand, the value of I_{CC} is improved by an average of 4.07% since the value of CC is good.

Moreover, to compare the performance of other data-driven wind power prediction models, such as neural networks (NN), support vector machine (SVM), random forests (RF), boosting trees (BT), the MSAR model, and the generic linear combined model of S_1, S_2, and S_3, **Table 3** presents the improvement coefficients of the proposed method compared with these six models, as presented below.

TABLE 3 | Improvement coefficients of traditional prediction models

	I_{MAE} (%)	I_{RMSE} (%)	I_{SDofAE} (%)	I_{CC} (%)	R^2 (%)
NN	3.20	27.86	3.06	5.16	47.96
SVM	14.70	39.30	17.29	7.14	63.15
RF	19.22	41.69	19.41	6.19	65.99
BT	10.52	32.68	2.73	4.54	54.68
MSAR	4.72	16.77	5.20	0.85	30.73
Generic hybrid	4.07	9.09	10.64	1.74	17.35

It is seen that the proposed method still improves the prediction performance greatly, compared with traditional methods. By comparing with traditional AI algorithms, the improvements on errors have an average of 11.91% on MAE, 35.38% on RMSE, 10.62% on SDofAE, and 5.76% on CC. By comparing with two advanced hybrid models, the improvements are 4.4% on MAE, 12.93% on RMSE, 7.92% on SDofAE, and 1.3% on CC. It is seen that hybrid models have better performance than traditional AI models. Since all the values are positive, these results verify that the proposed model has indeed improved the wind power prediction performance when compared with both traditional models and hybrid models.

CONCLUSION

To improve the performance of short-term wind power prediction, this paper proposed a new hybrid model based on granular computing and chaotic data reconstruction. By reconstructing the wind power time series into chaotic phase space, more information could be provided with a low dimensionality for modeling. Then, considering the uncertainty and diversity of wind development scenarios, three chaotic models are constructed and their corresponding scenarios are constructed as information granules by granular computing. Finally, the proposed model is realized by granular computing and chaotic time series prediction models. Experiments on wind power prediction verify the superiority of the proposed model. Through the improvement coefficient shown in **Tables 2–3**, it is validated that the proposed method improves the accuracy of wind power prediction than most traditional models. Therefore, it is concluded that the proposed method is feasible and effective. It will be helpful for directing wind power scheduling and planning in the future.

DATA AVAILABILITY STATEMENT

The raw data supporting the conclusion of this article will be made available by the authors, without undue reservation.

AUTHOR CONTRIBUTIONS

YW put forward the main research points; WX completed the manuscript writing and revision; ES and QL completed the

simulation research; NY and PF collected relevant background information; KG and YH revised grammar and expression. All authors contributed to manuscript revision and read and approved the submitted version.

REFERENCES

Abarbanel, H. D. I., and Kennel, M. B. (1993). Local False Nearest Neighbors and Dynamical Dimensions from Observed Chaotic Data. *Phys. Rev. E* 47 (5), 3057–3068. doi:10.1103/physreve.47.3057

Brouwer, A. S., Van den Broek, M., Özdemir, Ö., Koutstaal, P., and Faaij, A. (2016). Business Case Uncertainty of Power Plants in Future Energy Systems with Wind Power. *Energy Policy* 89, 237–256. doi:10.1016/j.enpol.2015.11.022

Chuang, K.-S., Tzeng, H.-L., Chen, S., Wu, J., and Chen, T.-J. (2006). Fuzzy C-Means Clustering with Spatial Information for Image Segmentation. *computerized Med. Imaging graphics* 30 (1), 9–15. doi:10.1016/j.compmedimag.2005.10.001

Doostizadeh, M., Aminifar, F., and Lesani, H. (2017). Coordinated Multi-Area Energy and Regulation Joint Dispatch under Wind Power Uncertainty. *J. Renew. Sustain. Energ.* 9 (2), 023303. doi:10.1063/1.4978305

Fraser, A. M., and Swinney, H. L. (1986). Independent Coordinates for Strange Attractors from Mutual Information. *Phys. Rev. A.* 33 (2), 1134–1140. doi:10.1103/physreva.33.1134

Lange, M., and Focken, U. (2006). *Physical Approach to Short-Term Wind Power Prediction*. Berlin: Springer, 1–208.

Lei, D., Lijie, W., Shi, H., Shuang, G., and Xiaozhong, L. (2007). "Prediction of Wind Power Generation Based on Chaotic Phase Space Reconstruction Models," in Power Electronics and Drive Systems, 2007. PEDS'07. 7th International Conference on (IEEE), 744–748. doi:10.1109/peds.2007.4487786

Li, L., Teng, Y., and Wang, X. (2017). Dynamic Equivalent Modeling of Wind Farm Considering the Uncertainty of Wind Power Prediction and a Case Study. *J. Renew. Sustain. Energ.* 9 (1), 013301. doi:10.1063/1.4973445

Liu, K., Zhang, Y., and Qin, L. (2016). A Novel Combined Forecasting Model for Short-Term Wind Power Based on Ensemble Empirical Mode Decomposition and Optimal Virtual Prediction. *J. Renew. Sustain. Energ.* 8 (1), 013104. doi:10.1063/1.4939543

Liu, Y., Shi, J., Yang, Y., and Lee, W.-J. (2012). Short-Term Wind-Power Prediction Based on Wavelet Transform-Support Vector Machine and Statistic-Characteristics Analysis. *IEEE Trans. Ind. Applicat.* 48 (4), 1136–1141. doi:10.1109/tia.2012.2199449

Ouyang, T., Pedrycz, W., and Pizzi, N. J. (2019). Record Linkage Based on a Three-Way Decision with the Use of Granular Descriptors. *Expert Syst. Appl.* 122, 16–26. doi:10.1016/j.eswa.2018.12.038

Ouyang, T., Pedrycz, W., Reyes-Galaviz, O. F., and Pizzi, N. J. (2021). Granular Description of Data Structures: A Two-phase Design. *IEEE Trans. Cybern.* 51 (4), 1902–1912. doi:10.1109/tcyb.2018.2887115

Ouyang, T., Zha, X., Qin, L., Xiong, Y., and Xia, T. (2016). Wind Power Prediction Method Based on Regime of Switching Kernel Functions. *J. Wind Eng. Ind. Aerodynamics* 153, 26–33. doi:10.1016/j.jweia.2016.03.005

Packard, N. H., Farmer, J. P. J. D., Shaw, R. S., Farmer, J. D., and Shaw, R. S. (1980). Geometry from a Time Series. *Phys. Rev. Lett.* 45 (9), 712–716. doi:10.1103/physrevlett.45.712

Rand, D., and Young, L. S. (1988). Dynamical Systems and Turbulence. *lecture Notes Math.* 366381.

Shao, H., Deng, X., and Jiang, Y. (2018). A Novel Deep Learning Approach for Short-Term Wind Power Forecasting Based on Infinite Feature Selection and Recurrent Neural Network. *J. Renew. Sustain. Energ.* 10 (4), 043303. doi:10.1063/1.5024297

Tang, Z., Zhao, G., and Ouyang, T. (2021). Two-phase Deep Learning Model for Short-Term Wind Direction Forecasting. *Renew. Energ.* 173, 1005–1016. doi:10.1016/j.renene.2021.04.041

Tang, Z., Zhao, G., Wang, G., and Ouyang, T. (2020). Hybrid Ensemble Framework for Short-Term Wind Speed Forecasting. *IEEE Access* 8, 45271–45291. doi:10.1109/access.2020.2978169

Wu, B., Song, M., Chen, K., He, Z., and Zhang, X. (2014). Wind Power Prediction System for Wind Farm Based on Auto Regressive Statistical Model and Physical Model. *J. Renew. Sustain. Energ.* 6 (1), 013101. doi:10.1063/1.4861063

Xiong, Y., Zha, X., Qin, L., Ouyang, T., and Xia, T. (2017). Research on Wind Power Ramp Events Prediction Based on Strongly Convective Weather Classification. *IET Renew. Power Generation* 11 (8), 1278–1285. doi:10.1049/iet-rpg.2016.0516

Yan, J., Gao, X., Liu, Y., Han, S., Li, L., Ma, X., et al. (2015). Adaptabilities of Three Mainstream Short-Term Wind Power Forecasting Methods. *J. Renew. Sustain. Energ.* 7 (5), 053101. doi:10.1063/1.4929957

Zhang, X., and Liang, J. (2012). Chaotic Characteristics Analysis and Prediction Model Study on Wind Power Time Series. *Acta Phys. Sin.* 61 (19), 70–81. doi:10.7498/aps.61.190507

Conflict of Interest: SE is employed by State Grid Hubei Electric Power Co. LTD. YW, WX, QL, PF, KG, and YH is employed by State Grid Yichang Power Supply Company.

The remaining authors declare that the research was conducted in the absence of any commercial or financial relationships that could be construed as a potential conflict of interest.

frontiers in Energy Research

ORIGINAL RESEARCH
published: 04 February 2022
doi: 10.3389/fenrg.2021.815272

Study on Dynamic Process Characteristics of CHP Unit With Variable Load Based on Working Point Linearization Modeling

Yuehua Huang, Qing Chen, Jing Ye and Tianlin Lu*

College of Electrical Engineering and New Energy, China Three Gorges University, Yichang, China

In view of the difficulty of applying the refine modeling of combined heat and power (CHP) units to the optimization scenario of integrated energy system, a CHP unit model based on working point linearization modeling is proposed, and its variable load characteristics are analyzed. Firstly, the dynamic coupling relationship of CHP unit is analyzed, and the nonlinear dynamic model of the unit is constructed. Then, under the pure condensation and heating conditions, the linearized Laplace transform model of the working point is established, and the variable load capacity under the independent action of control variables is analyzed to test the availability of the Laplace model. On this basis, the dynamic adaptive particle swarm optimization algorithm is used for multivariable cooperative control to test the open-loop characteristics of the variable load capacity of the unit. At the same time, the control strategy of electrothermal cooperation and safety self-test is designed to adjust the control variables, and test the closed-loop characteristics of the unit's regulation ability. Finally, a 300-MW steam extraction CHP unit is taken as an example to verify the applicability of the unit model and the effectiveness of the control strategy.

Keywords: working point linearization, unit variable load, multivariable cooperative control, dynamic adaptive particle swarm optimization, dynamic regulation characteristics

OPEN ACCESS

Edited by:
Yahui Zhang,
Yanshan University, China

Reviewed by:
Yuanchao Hu,
Shandong University of Technology, China
Guangzheng Yu,
Shanghai University of Electric Power, China

****Correspondence:***
Qing Chen
chenqing20190808@163.com

Specialty section:
This article was submitted to Smart Grids, a section of the journal Frontiers in Energy Research

Received: *15 November 2021*
Accepted: *07 December 2021*
Published: *04 February 2022*

Citation:
Huang Y, Chen Q, Ye J and Lu T (2022) Study on Dynamic Process Characteristics of CHP Unit With Variable Load Based on Working Point Linearization Modeling. Front. Energy Res. 9:815272. doi: 10.3389/fenrg.2021.815272

INTRODUCTION

Clean, low-carbon, and efficient energy use plays an important role in realizing the strategic goal of "double carbon." Combined heat and power (CHP) plant is becoming the main energy supply source of the electrothermal integrated energy system (IES) with its superior comprehensive energy supply efficiency (Sun et al., 2021). The modeling of the CHP unit variable load capacity is very important for the optimal calculation of power dispatching, frequency regulation, and other scenarios of the IES (Ye et al., 2012; Zhang et al., 2021). However, its refined modeling mechanism is complicated, and the fast dynamic regulation characteristics after optimization control transformation are complex (Shen et al., 2017; Shen et al., 2020a), which makes it difficult to accurately describe the variable load capacity of the unit. Therefore, the research on the description method of the dynamic regulation characteristics of the CHP unit during the variable load process is of great significance to support the application of the CHP unit in the scenario of the IES.

The dynamic characteristics of the CHP unit are not only affected by its internal physical structure attributes but also related to the operation mode, the working condition, the external environment, and other factors (Wang, 2013). At present, it is difficult to obtain an accurate description of the

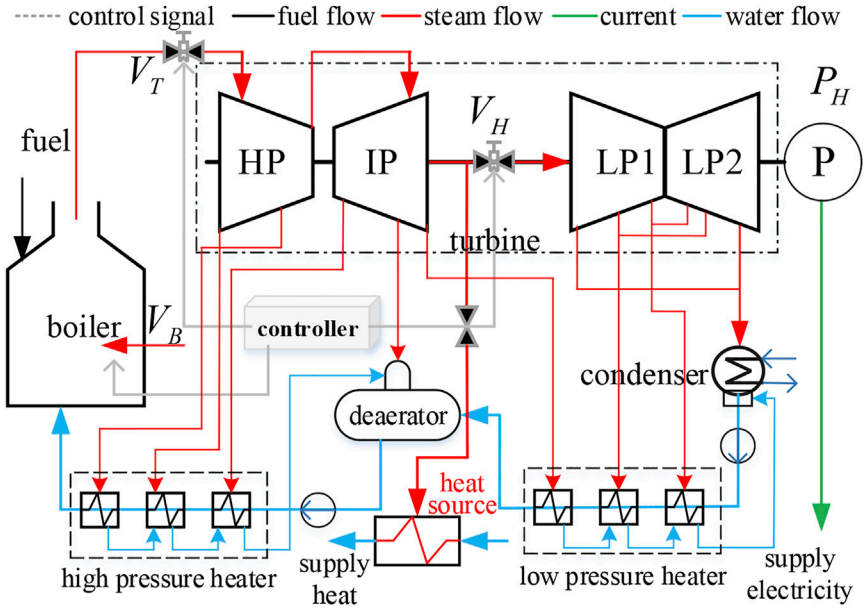

FIGURE 1 | Structure diagram of the CHP unit.

dynamic characteristics of the unit. A mathematical model that meets certain accuracy requirements and reflects the main dynamic characteristics of the unit is often established by reasonable simplification and approximation, combined with mechanism analysis and experimental modeling (Yang et al., 2018; Yang et al., 2019; Zhu et al., 2020; Li et al., 2021). Algebraic equations are usually used to describe the feasible region, climbing, and standby capacity of the CHP unit model (Liu et al., 2021). This model is mostly used in the calculation scenario of the unit participating in system long-time scale optimal dispatching (Zhang et al., 2018). The algebraic equation linearization model often ignores the continuous time variation characteristics of the unit output, and there is the assumption that the unit output power can change instantaneously. The model undoubtedly expands the rapid load changing capacity of the unit, which is easy to cause the possibility that the dispatching plan cannot be accurately realized, that is, there is the problem of energy nondeliverability (Gao and Yan, 2017). The mathematical description considering the internal characteristics of the unit is in the form of differential algebraic equations, which adopts the optimal control method to improve the short-term rapid regulation ability of the unit and participates in the system frequency modulation calculation scene (Wang et al., 2018; Yang et al., 2021). The constraints of differential algebraic equations will make the optimization problem a highly nonlinear dynamic optimization problem. This kind of an optimization problem is difficult to solve directly. Approximating differential variables through a discrete method will lead to the solution of large-scale optimization problems being easy to fall into a dimensional disaster (Wang, 2012), long solution time, and poor accuracy (Shen et al., 2021a; Shen and Raksincharoensak, 2021a), and cannot be solved online and in real time (Shen et al., 2020b; Shen et al., 2021b; Shen and Raksincharoensak, 2021b). The modeling of the dynamic characteristics of the unit variable load process faces the challenge of meeting the calculation accuracy and solution speed while taking into account the accurate description of unit dynamic characteristics.

Laplace-transform a real variable function and perform various operations in the complex number field, and then perform the inverse Laplace transform to obtain the corresponding results in the real number field, which is often much easier to calculate than directly obtaining the same results in the real number field (Beerends et al., 2003). Yang et al. (2020) proposed a generalized circuit modeling method based on Laplace transform, which transforms the complex transmission characteristics of multi-energy networks in the time domain into a simple algebraic problem in the Laplace domain. Laplace transform is particularly effective for simplifying differential equations, which can be transformed into easily solved algebraic equations (Hooman and Randolph, 2020), so as to simplify the calculation. The analysis and synthesis of the control system are based on Laplace transform. Gao and Tian (2020) linearized the nonlinear dynamic model of the heating unit with small deviation, obtained the transfer function matrix model, analyzed the coupling relationship of the unit, and studied the thermal power load decoupling control method of the unit. Liu et al. (2005) linearized the nonlinear model at different load/pressure operating points and studied the load pressure nonlinear characteristics of the 660-MW unit. After linearizing the small deviation of the dynamic model of the heating unit (Deng et al., 2017), the transfer function matrix model including the characteristics of the heating side is obtained, the thermoelectric coupling characteristics are analyzed, and the decoupler is designed. By introducing Laplace transform into linearization at different working points and using a transfer

function instead of a differential equation to describe the characteristics of the system, the whole characteristics of the control system can be determined intuitively and simply, the motion process of the control system can be analyzed, and the adjustment strategy of the control system can be provided. For the linearization of the CHP unit at the working point, it is rare to use Laplace transform modeling to make the model suitable for the flexible demand of the variable load capacity of the IES.

To solve the above problems, firstly, a simplified nonlinear dynamic model of the CHP unit is constructed. Then, the linearized Laplace transform model of the working point under pure condensation and heating conditions is established to analyze the variable load capacity of the unit when each control variable acts alone and cooperatively. Furthermore, the control strategy of electrothermal cooperation safety self-test is used to test the dynamic regulation ability of the unit in the variable load process. Finally, taking the 300-MW steam extraction CHP unit as an example, the dynamic characteristics of the variable load process of multivariable collaborative control are tested to verify the effectiveness of open-loop and closed-loop control strategies.

COMBINED HEAT AND POWER UNIT MODEL

Dynamic Relationship of Combined Heat and Power Unit

As shown in **Figure 1**, the fuel volume V_B of the unit directly controls the boiler combustion to produce high-temperature steam. The high-pressure regulating valve V_T of the steam turbine is connected with the high-pressure (HP) cylinder and the boiler, and the steam extraction regulating butterfly valve V_H is installed in the connecting pipe between the intermediate-pressure (IP) cylinder and the low-pressure (LP) cylinder. The steam exhaust of the IP cylinder of the steam turbine is divided into two parts. One part enters the LP cylinder of the steam turbine through the regulating butterfly valve to continue to work, and the other part enters the heat supply network heater to provide the heat source. After cooling, it is sent to the deaerator through the heat supply network drain pump. When the heating load is increased under the heating state, the V_H opening of the regulating butterfly valve will be reduced, and the exhaust pressure of the IP cylinder of the steam turbine will increase, so more steam will enter the heat network heater, the saturation temperature in the heat network heater will increase, and the outlet temperature of heating water will increase. If the system needs to reduce the heat supply, the operation is the opposite of the above steps. When the heating is stopped, the regulating butterfly valve V_H is fully opened and the heat supply shut-off valve is closed. At this time, the steam turbine works in the pure condensation state. By changing V_T and V_H , the proportion of heating and generating power of the unit is adjusted to provide heat source and power supply.

During the operation of the extraction type CHP unit, the electric power and thermal power are comprehensively determined by the fuel flow, main steam pressure, extraction steam flow, temperature, and other variables controlled by its valve. The load-pressure simplified nonlinear dynamic model of the pure condensing unit (Liu et al., 2014) is combined with the model in the study by Tian (2005), and the differential equation mathematical model of the dynamic coupling relationship between the electric power, thermal power, and control valve of the CHP unit is obtained. The simplified nonlinear dynamic model of the CHP unit is given by:

$$\begin{cases} \mathrm{r}_m = V_B(t-\tau) \\ T_f \dfrac{dr_B}{dt} = -r_B + r_m \\ C_b \dfrac{dp_d}{dt} = -K_3 p_t V_T - K_1 r_B \\ p_t = p_d - K_2 (K_1 r_B)^{\varepsilon} \\ T_t \dfrac{dN_E}{dt} = -N_E + K_4 K_3 p_t V_T + K_5 p_Z V_H \\ C_h \dfrac{dp_Z}{dt} = -K_6 q_x (96 p_z - t_i + 103) + K_3 p_t V_T (1-K_4) - K_5 p_Z V_H \\ q_H = K_7 K_6 q_x (96 p_Z - t_i + 103) \\ p_1 = 0.01 p_t V_T \end{cases} \tag{1}$$

where V_B is the coal supply mass flow of the unit; V_T is the opening of the steam inlet regulating valve of the HP cylinder of the steam turbine; V_H is the opening of the extraction regulating butterfly valve; q_x is the mass flow of circulating water; t_i is the return water temperature of circulating water, N_E is the generating power of the unit; p_d is the drum pressure; p_t is the front pressure of the steam turbine; p_z is the exhaust pressure of the intermediate pressure cylinder; p_1 is the first stage pressure of the steam turbine; q_H is the heating extraction steam flow; r_m is the actual amount of coal entering the pulverizer; r_B refers to the boiler combustion rate; K_1, K_2, K_3, K_4, K_5, K_6, and K_7 are the static parameters; τ is the delay time constant of the milling process; ε is constant-coefficient; T_f is the milling time constant of inertia; T_t is the inertia time constant of the steam turbine; C_b is the boiler heat storage coefficient; and C_h is the heat storage coefficient of the unit heater.

Linearization Model of Operating Point of Combined Heat and Power Unit

The nonlinear model is linearized at a certain working point, and the linearized model can accurately reflect the dynamic and static characteristics of each link of the system near the working point. The model described in **Eq. 1** is linearized to measure the action relationship between various inputs and outputs in the model and the influence of system nonlinearity on the controlled object. Firstly, write **Eq. 1** in incremental form. The linear model

near the equilibrium point is obtained by small deviation linearization:

$$\begin{cases} \mathrm{r}_m = \Delta V_B(t-\tau) \\ T_f \dfrac{d\Delta \mathrm{r}_B}{dt} = -\Delta \mathrm{r}_B + \Delta \mathrm{r}_m \\ C_b \dfrac{d\Delta p_d}{dt} = -K_3 p_t \Delta V_T - K_3 \Delta p_t V_T - K_1 \Delta \mathrm{r}_B \\ \Delta p_t = \Delta p_d - K_1 K_2 \sqrt{K_1 \mathrm{r}_B \Delta \mathrm{r}_B} \\ T_t \dfrac{d\Delta N_E}{dt} = -\Delta N_E + K_4 K_3 p_t \Delta V_T + K_4 K_3 \Delta p_t V_T + K_5 p_z \Delta V_H + K_5 \Delta p_z V_H \\ C_h \dfrac{d\Delta p_z}{dt} = -K_6 \Delta q_x (96 p_z - t_i + 103) - K_6 q_x (96 \Delta p_z - \Delta t_i) + K_3 \Delta p_t V_T (1-K_4) \\ \qquad + K_3 p_t \Delta V_T (1-K_4) - K_5 \Delta p_z V_H - K_5 p_z \Delta V_H \\ \Delta q_H = K_7 K_6 \Delta q_x (96 p_z - t_i + 103) + K_7 K_6 q_x (96 \Delta p_z - \Delta t_i) \\ \Delta p_1 = 0.01 p_t \Delta V_T + 0.01 \Delta p_t V_T \end{cases} \tag{2}$$

Secondly, the Laplace transform of the incremental equation is obtained. Assuming that the initial condition is zero, the Laplace transform is taken for the linear differential **Eq. 2** of the system, and the incremental symbol is omitted, the following can be obtained:

$$\begin{cases} \mathrm{r}_m(s) = e^{-\tau s} V_B(s) \\ T_f s \mathrm{r}_B(s) = -r_B(s) + r_m(s) \\ C_b s p_d(s) = -K_3 p_t V_T(s) - K_3 p_t(s) V_T - K_1 r_B(s) \\ p_t(s) = p_d(s) - K_1 K_2 \sqrt{K_1 r_B r_B}(s) \\ T_t s N_E(s) = -N_E(s) + K_4 K_3 p_t V_T(s) + K_4 K_3 p_t(s) V_T + K_5 p_z V_H(s) + K_5 p_z(s) V_H \\ C_h s p_z(s) = -K_6 q_x(s)(96 p_z - t_i + 103) - K_6 q_x (96 p_z(s) - t_i(s)) + K_3 p_t(s) V_T (1-K_4) \\ + K_3 p_t V_T(s)(1-K_4) - K_5 p_z(s) V_H - K_5 p_z V_H(s) \\ q_H(s) = K_7 K_6 q_x(s)(96 p_z - t_i + 103) + K_7 K_6 q_x (96 p_z(s) - t_i(s)) \\ p_1(s) = 0.01 p_t V_T(s) + 0.01 p_t(s) V_T \end{cases} \tag{3}$$

Then, the linear model is appropriately simplified and equivalent to obtain a set of linear equations describing the dynamic characteristics of the unit transfer process, and the system thermoelectric coupling relationship model after linearization of the working point can be obtained, which is expressed in the form of the transfer function matrix as follows:

$$\begin{bmatrix} p_t(s) \\ p_z(s) \\ N_E(s) \end{bmatrix} = \begin{bmatrix} G_{11}(s) & G_{12}(s) & G_{13}(s) \\ G_{21}(s) & G_{22}(s) & G_{23}(s) \\ G_{31}(s) & G_{32}(s) & G_{33}(s) \end{bmatrix} \cdot \begin{bmatrix} V_T(s) \\ V_B(s) \\ V_H(s) \end{bmatrix} \tag{4}$$

The elements of the thermoelectric coupling relationship matrix are

$$G_{11}(\mathrm{s}) = -\frac{M_2}{1+M_1 s} \tag{5}$$

$$G_{12}(\mathrm{s}) = \frac{\frac{K_1}{K_3 V_T}(1-M_3 s)}{\left(1+T_f s\right)(1+M_1 s)} e^{-\tau s} \tag{6}$$

$$G_{13}(\mathrm{s}) = 0 \tag{7}$$

$$G_{21}(\mathrm{s}) = \frac{\frac{1-K_4}{M_4} M_2 C_b s}{(1+M_1 s)\left(1+\frac{C_h}{M_4} s\right)} \tag{8}$$

$$G_{22}(\mathrm{s}) = \frac{\frac{K_1(1-K_4)}{M_4}(1-M_3 s)}{\left(1+T_f s\right)(1+M_1 s)\left(1+\frac{C_h}{M_4} s\right)} e^{-\tau s} \tag{9}$$

$$G_{23}(\mathrm{s}) = -\frac{\frac{M_6}{(M_4)^2}}{1+\frac{C_h}{M_4} s} \tag{10}$$

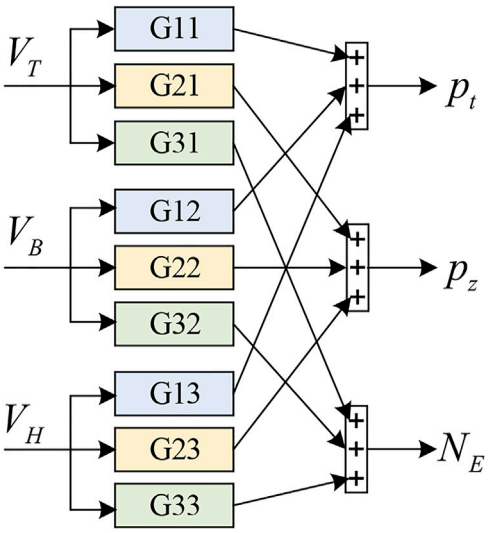

FIGURE 2 | Linearization function diagram of the CHP unit.

$$G_{31}(\mathrm{s}) = \frac{M_2 C_b s \frac{M_5}{M_4}\left(1+\frac{K_4 C_h}{M_5} s\right)}{\left(1+T_f s\right)(1+M_1 s)\left(1+\frac{C_h}{M_4} s\right)} \tag{11}$$

$$G_{32}(\mathrm{s}) = \frac{\frac{K_1 M_5}{M_4}(1-M_3 s)\left(1+\frac{K_4 C_h}{M_5} s\right)}{\left(1+T_f s\right)(1+M_1 s)(1+T_t s)\left(1+\frac{C_h}{M_4} s\right)} e^{-\tau s} \tag{12}$$

$$G_{33}(\mathrm{s}) = \frac{\frac{96 K_6 q_x M_6}{(M_4)^2}\left(1+\frac{C_h}{96 K_6 q_x} s\right)}{(1+T_t s)\left(1+\frac{C_h}{M_4} s\right)} \tag{13}$$

where $M_1 = C_b/(K_3 V_T)$, $M_2 = K_1 V_B/(K_3 V_T^2)$, $M_3 = 1.5 K_2 C_b \sqrt{K_1 V_B}$, $M_4 = 96 K_6 q_x + K_5 V_H$, $M_5 = 96 K_4 K_6 q_x + K_5 V_H$, $M_6 = K_5[K_6 q_x t_i - 103 K_6 q_x + K_1 V_B(1-K_4)]$.

Under different input operating points, the transfer function of the CHP unit will be different. This nonlinearity only changes the model parameters, and the model structure is unchanged. The Laplace transform model with a linearized working point takes into account the advantages of simplicity, being in real time, and high precision. In this paper, the variable load characteristics of the CHP unit under pure condensation and heating conditions will be studied.

ANALYSIS METHOD OF VARIABLE LOAD CHARACTERISTICS OF COMBINED HEAT AND POWER UNIT

Open-Loop Variable Load Characteristic Test and Multicontrol Variable Synergy Method

Variable Load Characteristic Test With Independent Action of Control Variables

The functional relationship between control variables and output variables is shown in **Figure 2**. The pure condensation condition

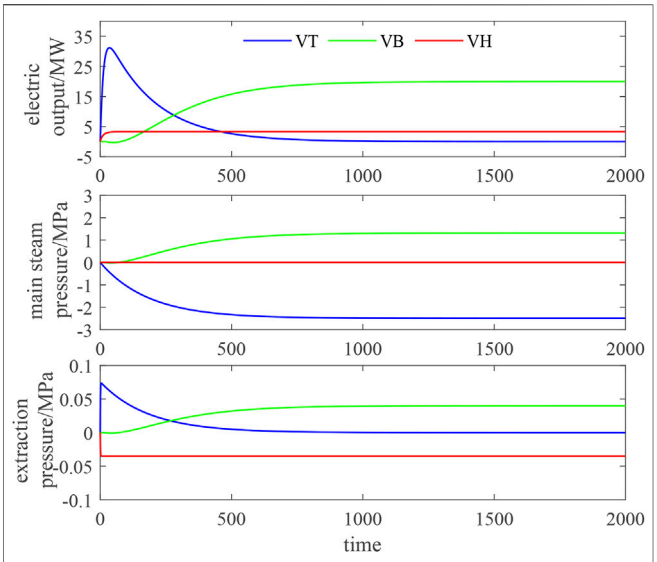

FIGURE 3 | Effect of independent action of control variables under the heating condition.

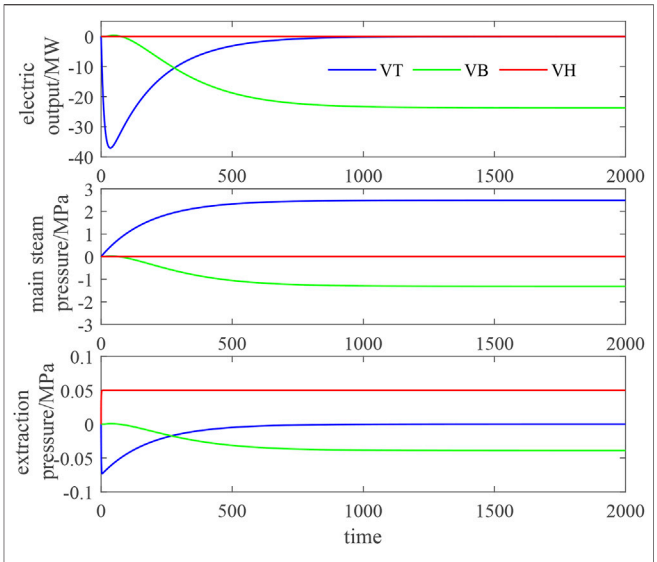

FIGURE 4 | Effect of control variables acting alone under the pure condensation condition.

and heating condition are modeled in Simulink to test and analyze the input–output relationship between variable load process variables. See **Supplementary Appendix SB** for the parameters of the working condition model. The dynamic characteristics of the boiler steam turbine heating system and the variable load capacity are obtained by analyzing the output change when the control variables act alone. Under the heating condition, apply step changes of 10 t/h, 10, and 10% on V_B, V_T, and V_H commands, respectively, and under the pure condensation condition, apply step changes of -10 t/h, −10%, and −10%, respectively. The response curves of electric power, main steam pressure, and extraction pressure under different working conditions are shown in **Figures 3**, **4**.

Figure 3 shows the change of the object output under the step disturbance of boiler fuel V_B, turbine high regulating valve V_T opening, and heating extraction regulating butterfly valve V_H opening. When V_B increases, the front pressure of the unit, the electric power of the unit, and the exhaust pressure of the IP cylinder (heating extraction flow) all rise. When V_T opening increases, the pressure in front of the unit decreases, the boiler releases heat storage, the electric power of the unit first increases and then returns to the original level, and the exhaust pressure (heating extraction flow) of the IP cylinder first increases and then returns to the original level. When V_H increases, the pressure in front of the turbine will remain unchanged, the electric power of the unit will increase due to the increase in the work share of some steam in the LP cylinder, the IP exhaust pressure will decrease, and the heating extraction flow will decrease due to the decrease in steam extraction from the turbine.

Figure 4 shows the object output changes under the step disturbance of boiler fuel volume V_B, turbine high regulating valve V_T opening, and heating extraction regulating butterfly valve V_H opening. When V_B is lowered, the pressure of the front engine, the power of the generating unit, and the exhaust pressure of the IP cylinder are all decreased. Because V_H is fully opened, the extraction flow of heating is zero and remains unchanged, which is no different from the traditional pure condensing unit. When V_T opening decreases, the pressure in front of the unit increases, the boiler releases heat storage, and the electric power of the unit decreases first and then returns to the original level. The variation law of the exhaust pressure of the IP cylinder is similar to that of the electric power. Because V_H is fully open, the heating extraction flow is zero and remains unchanged. When V_H opening decreases, because the heating state of the unit is not actually turned on, the electric power of the unit remains unchanged, the exhaust pressure of the IP cylinder increases, and the heating extraction flow is zero.

The dynamic characteristics of the linearized model after univariate action are basically consistent with the original model (Wang, 2013). Therefore, it can be considered that the linearized model has good reproducibility. It is feasible to analyze and study the dynamic regulation characteristics of the variable load process according to the linearized model.

The independent action test of control variables under the two working conditions shows that the control variable regulation has different effects on the load change of the CHP unit. V_B has obvious effect on the change of electric power, V_T has a great impact on the change of main steam pressure, and V_H mainly affects the change of extraction pressure. Although the control variables acting alone have a certain variable load capacity, the regulation time is long and the regulation is differential. The actual system is controlled by pressure, temperature, flow, and other factors, and the final control effect is the superposition of many influencing factors. The control effects of the reverse superposition of influencing factors offset each other, while the control effects of the positive superposition strengthen each other. The multicontrol variable synergy effect of the work point linearization model needs to be further tested and verified.

Multicontrol Variable Synergy Method

In this paper, the optimization algorithm is used to determine the three control variables of V_T, V_B, and V_H to analyze the change of the system output when the three control variables work together. Compared with other optimization algorithms, dynamic adaptive particle swarm optimization (DAPSO) has relatively excellent convergence ability and solution accuracy (Fu et al., 2017), which is suitable for the variable optimization problem of the control system in this paper. Its mathematical description is as follows:

$$\begin{cases} v_{id}^{t+1} = \omega_i^t v_i^t + \rho_1 r_1 \left(P_i^t - x_i^t\right) + \rho_2 r_2 \left(G_i^t - x_i^t\right) \\ x_i^{t+1} = x_i^t + x_i^{t+1}, \qquad i = 1, 2, \ldots, n \\ \omega_i^t = \begin{cases} \beta s_2, & s_2 > a \text{ and } s_2 < b \\ 1 - \gamma h_i^t + \beta s_1, & \text{other} \end{cases} \end{cases} \tag{14}$$

$$\begin{cases} h_i^t = 1 - \left|\dfrac{\min\left(F\left(P_i^{t-1}\right), F\left(P_i^t\right)\right)}{\max\left(F\left(P_i^{t-1}\right), F\left(P_i^t\right)\right)}\right| \\ s_1 = \left|\dfrac{\min\left(F_t, \bar{F}_t\right)}{\max\left(F_t, \bar{F}_t\right)}\right| \\ s_2 = 1 - \dfrac{1}{NL}\sum_{i=1}^{N}\sqrt{\sum_{d=1}^{D}\left(p_{id} - \bar{p}_d\right)^2} \end{cases} \tag{15}$$

where v_i^t is the velocity of the i-th particle in the t-th iteration; x_i^t is the position of the i-th particle in the t-th iteration, and ρ_1 and ρ_2 are the acceleration coefficients; generally, $\rho_1 = \rho_2 = 2$. r_1 and r_2 are two random numbers varying in [0,1]. P_i^t is the best location for the i-th particle to be searched in t iterations; G_i^t is the best location for the whole population to search in t iterations; ω_i^t is the inertial weight of the i-th particle in the t-th iteration; γ and β are selected in [0,1]; generally, $\gamma = \beta = 0.5$. a and b are the thresholds for controlling the aggregation factor; generally, $a = 0.9$ and $b = 0.5$; h_i^t is the rate factor of evolution; s_1 is the fitness aggregation factor; s_2 is the spatial aggregation factor. $F(P_i^t)$ is the fitness value of P_i^t; F_t is the best fit in the t-th iteration; $\bar{F}_t$ is the average fitness value in the t-th iteration; N is the population size; L is the longest radius of the search space; D is the dimension of the solution space; p_{id} is the d-dimensional coordinate of the i-th particle; $\bar{p}_d$ is the average of the d-dimensional coordinates of all particles.

Given the electric power variable load demand, the optimization algorithm flow of the synergy of the three control variables is shown in **Figure 5**. The connection between DAPSO and the Simulink model is through the particle (i.e., control variables V_T, V_B, and V_H) and the corresponding fitness value of the particle (i.e., the performance index of the matching degree between the output value and the expected value). The optimization process is as follows: DAPSO generates particle swarm optimization (initial particle swarm optimization or updated particle swarm optimization), assigns the particles in the particle swarm to the model parameters V_T, V_B, and V_H in turn, and then runs the Simulink model under a certain working condition of the unit to obtain the performance index corresponding to the group of parameters, which is transmitted to DAPSO as the fitness value of the particle. Finally, judge whether the algorithm can be exited.

Thermal System Constraints

CHP unit control shall be able to realize accurate variable load tracking, reliable heat supply, and safe pressure fluctuation. Heating and power generation are affected by boiler fuel volume V_B, turbine high regulating valve V_T opening, and heating extraction regulating butterfly valve V_H opening. Based on the PID optimization control method, three control variables are matched, and the PID controllers of $V_T(t)$, $V_B(t)$, and $V_H(t)$ are designed, respectively (Chen et al., 2014):

$$\begin{cases} V_T(t) = K_{PT}E_T(t) + K_{IT}\int_0^t E_T(t)dt + K_{DT}\dfrac{dE_T(t)}{dt} \\ V_B(t) = K_{PB}E_B(t) + K_{IB}\int_0^t E_B(t)dt + K_{DB}\dfrac{dE_B(t)}{dt} \\ V_H(t) = K_{PH}E_H(t) + K_{IH}\int_0^t E_H(t)dt + K_{DH}\dfrac{dE_H(t)}{dt} \end{cases} \tag{16}$$

Control scheme I:

$$\begin{cases} E_T(t) = p_t^{sp}(t) - p_t(t) \\ E_B(t) = p_z^{sp}(t) - P_z(t) \\ E_H(t) = N_E^{sp}(t) - N_E(t) \end{cases} \tag{17}$$

where K_{PT}, K_{IT}, K_{DT}, K_{PB}, K_{IB}, K_{DB}, K_{PH}, K_{IH}, and K_{DH} are parameters of variables associated with the PID. In the control optimization cycle, p_t^{sp}, N_E^{sp}, and p_z^{sp} are the set values for the main steam pressure, the electric power of the unit, and the IP extraction pressure, respectively. PID parameter commissioning method is determined by engineering experience method, as shown in **Supplementary Table S3**.

In order to ensure the safe and stable operation of the unit, the influence of output variable fluctuation shall be considered in the regulation process, and the control system path constraint (Tian et al., 2017) shall be met, as shown in **Eq. 18a**. The steady-state value of each output variable shall not exceed the allowable error range, and the system final value constraint shall also be satisfied (Tian et al., 2015), as shown in **Eq. 18b**.

$$\begin{cases} \left|p_t^{sp} - p_t(t)\right| \le M_{p_t} \\ \left|N_E^{sp} - N_E(t)\right| \le M_{N_E} \\ \left|p_z^{sp} - p_z(t)\right| \le M_{p_z} \end{cases} \tag{18a}$$

$$\begin{cases} \left|p_t(t_e) - p_t^{sp}\right| \le m_{p_t} \\ \left|N_E(t_e) - N_E^{sp}\right| \le m_{N_E} \\ \left|p_z(t_e) - p_z^{sp}\right| \le m_{p_z} \end{cases} \tag{18b}$$

where m_{p_t}, m_{N_E}, and m_{p_z} are the error range of the main steam pressure, electric power, and IP extraction pressure, respectively; M_{p_t}, M_{N_E}, and M_{p_z} are the fluctuation range of the main steam pressure, electric power, and IP extraction pressure, respectively.

According to the above control process requirements and the optimization control strategy proposed in the study by Wang et al. (2019), the control concepts of disturbance compensation and multivariable coordination are further adopted. Through the design of three key control modules: electrothermal coordination, thermal state reconstruction, and accurate energy balance, and

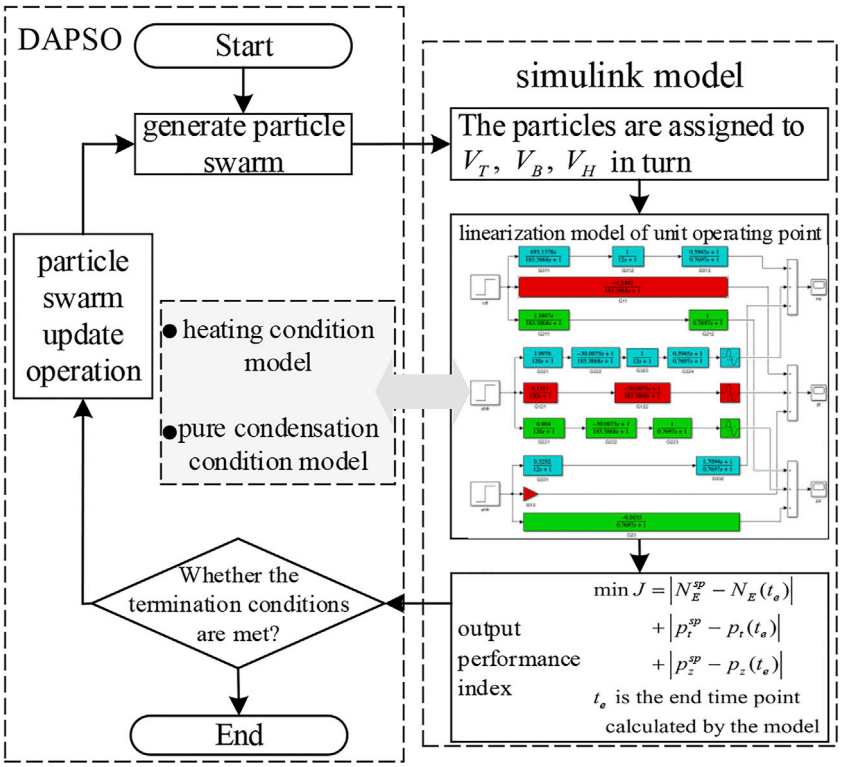

FIGURE 5 | Structure diagram of the control variable optimization algorithm.

considering the main influencing factors of main steam fluctuation, a new electrothermal power coordinated distribution and pressure safety self-test control strategy is proposed. The parameters of the control system are manually set by an empirical method to realize the three key functions of the CHP unit control system: accurate electric power tracking, rapid thermal power recovery, and safe and stable operation of the system. The structure of the control system is shown in **Figure 6**.

Control scheme II:

$$\begin{cases} E_T(t) = p_t^{sp} - \dfrac{K_1 e^{-t/T_1}}{T_1} p_t(t) \\ E_B(t) = \left(N_E^{sp} - p_z^{sp}\right) - \left[N_E(t) - \dfrac{K_2 e^{-t/T_2}}{T_2} p_z(t)\right] \\ E_H(t) = N_E^{sp} - N_E(t) \end{cases} \tag{19}$$

Among them, K_1, T_1, K_2, and T_2 are the parameters of the pressure safety self-test and electrothermal power coordinated distribution control strategy, as shown in **Supplementary Table S3**.

The variable load regulation process of the CHP unit will lead to large changes in the heating capacity of the unit in a short time, and the heat transfer is delayed. The increase or decrease in long-term accumulated heat will lead to the change of the ambient temperature of the heat load, thus affecting the comfort of users.

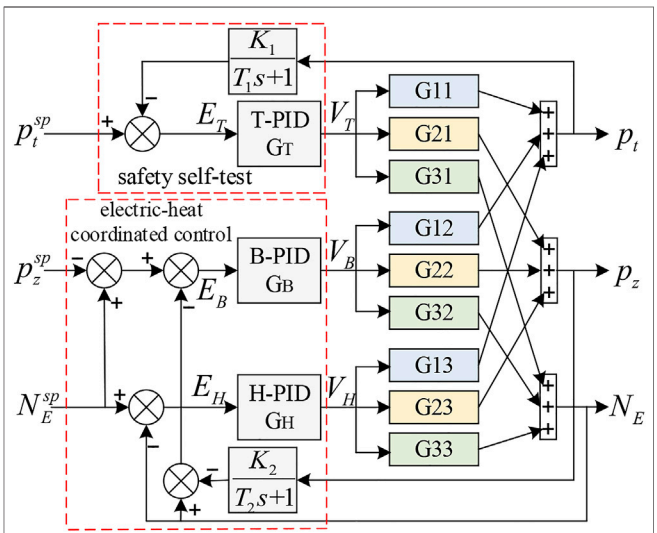

FIGURE 6 | Structure diagram of the CHP unit control system.

Therefore, after the step signal of variable load disturbance is given for the dynamic model of the CHP unit, it is necessary not only to test the changes of main steam pressure and electric power but also to further analyze the change process of extraction steam flow in the optimal control cycle. The influence of heat change caused by extraction steam flow fluctuation on heat load demand

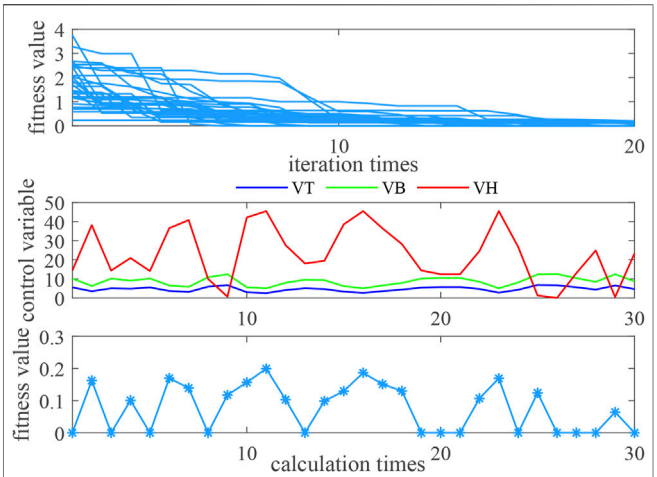

FIGURE 7 | Convergence of DAPSO and optimization results of control variables under the heating condition.

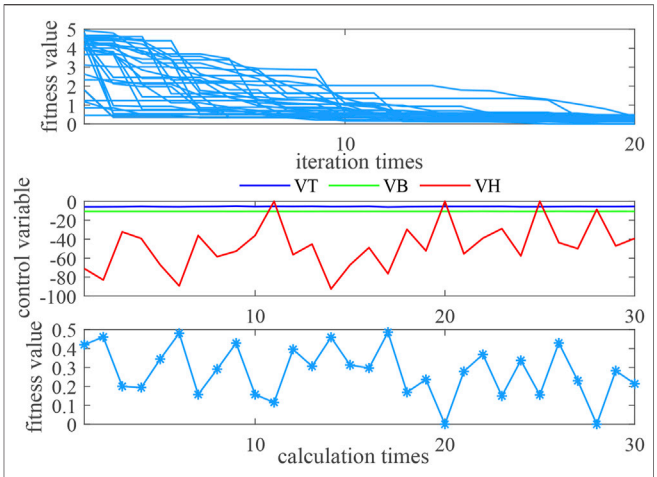

FIGURE 8 | Convergence of DAPSO and optimization results of control variables under the pure condensation condition.

is quantitatively analyzed, and calculate it according to the following method (Wang et al., 2019) (**Supplementary Table S2**):

$$q_H(t) = K_7 K_6 q_x \left(96 p_z(t) - t_i + 103\right) \tag{20}$$

$$q_{H,equ} = \frac{\int_{t_0}^{t_e} q_H(t)dt}{t_e - t_0} \tag{21}$$

$$Q_{H,equ} = q_{H,equ} \cdot \Delta h \tag{22}$$

where $Q_{H,equ}$ is the thermal power of the equivalent CHP unit, Δh is the enthalpy drop of heating extraction ($\Delta h = 2.3637 \times 10^3$), $q_{H,equ}$ is the average equivalent flow of the regulation process, and t_0 and t_e are the starting and ending points of optimal control of the CHP unit, respectively.

The CHP unit model has obvious system nonlinearity. The object transfer function parameters contain the input variable information that determines the operating point, so the transfer function has different nonlinear characteristics at different operating points. By using the same PID controller setting parameters to test the control quality of the unit system under different working conditions of heating and pure condensation, how strong the nonlinearity of the CHP unit is measured. Through the analysis of simulation results to determine the method that setting controller parameters can ensure the system control quality under common working conditions, guide the coordinated control system structure or controller parameters to make some adjustment, so as to adapt to the changes of controlled object parameters.

EXAMPLE ANALYSIS

In order to verify the effectiveness of the models and methods proposed in this paper, a 300-MW steam extraction heating unit is used to build a model on a MATLAB/Simulink platform for simulation. The variable load open-loop characteristics of the unit are tested by controlling variable disturbance, and the variable load closed-loop dynamic characteristics of the unit are tested by designing control strategy. The response curves of each output are simulated to verify the reproducibility of the linearized model, and the effectiveness of the control method and strategy is analyzed. Relevant parameters of the unit and operating point parameters under pure condensation and heating conditions are shown in **Supplementary Appendix SA, SB**.

Open-Loop Characteristic Analysis

Under the heating condition, when the electric load is given a step signal of 25 MW, the regulation index performance of the system and the optimization process of three control variables are shown in **Figure 7**. After setting 20 populations of parameters and 20 iterations, the optimization algorithm can stably calculate three control variables after 30 simulation calculations, and the performance fitness value of the regulation index of the system can stably converge to less than 0.2. The V_T regulation range is [2.5,7]%; the V_B regulation range is [5.0,13.0]t/h, and they act in the same direction. The V_H regulation range is widely distributed and opposite to the former two.

When the step signal of -25 MW is given for the electric load under the pure condensation condition, the regulation index performance of the system and the optimization process of three control variables are shown in **Figure 8**. With the same algorithm parameter setting as the heating condition, the adjustment index performance fitness value of the system can stably converge to less than 0.5. The V_T regulation range is [5.0,6.0]%, the V_B regulation range is [10.5,10.6]t/h, and the V_H regulation range is widely distributed and inversely correlated with the fitness value.

Under the heating condition and the pure condensation condition, the output changes of the system under the synergistic action of control variables are shown in **Figures 9**, **10**. Under the heating condition, given the step signal and adjusting the control variables (5.52%, 10.15 t/h, 14.39%), after about 1,500 s, the output power of the system accurately meets the 25 MW required for the variable load, the main steam pressure is adjusted back to −0.04 MPa, and the extraction pressure is

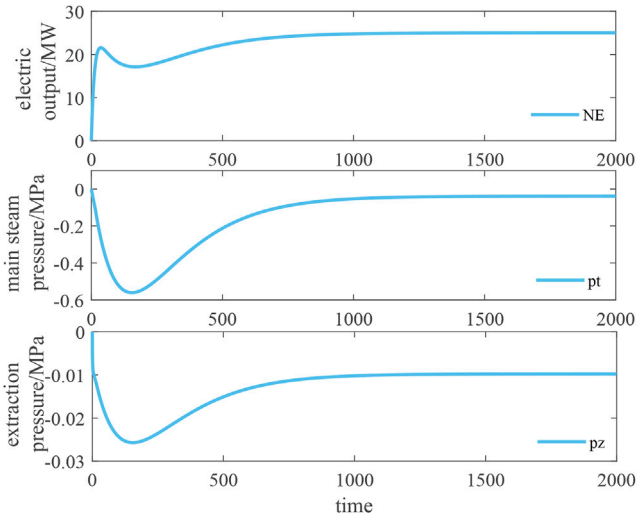

FIGURE 9 | Synergistic regulation effect of three control variables under the heating condition.

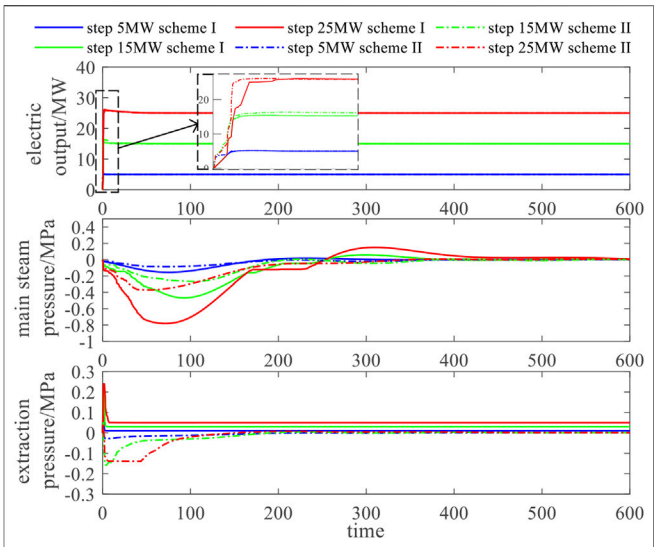

FIGURE 11 | Control effect diagram of scheme I and scheme II under the heating condition.

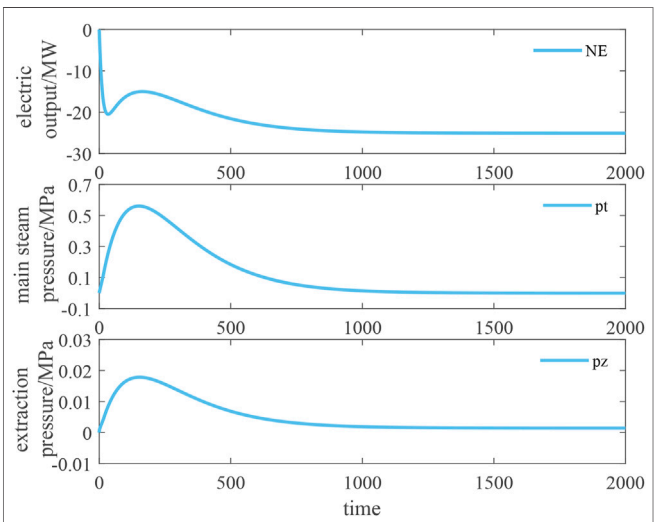

FIGURE 10 | Synergistic regulation effect of three control variables under the pure condensation condition.

stabilized to −0.01 MPa. Under the pure condensation condition, given the step signal and the regulated control variable (−5.59%, −10.58 t/h, −8.54%), after about 1,500 s, the system output power accurately reaches −25 MW required by the variable load, the main steam pressure is adjusted back to 0.0007 MPa, and the extraction pressure is stabilized to 0.0015 MPa.

The open-loop regulation eliminates the complex PID setting work and can accurately complete the electric power regulation. However, there is a difference between the safe main steam pressure involved in the variable load process and the extraction pressure of heating, and the calculation time of one-time optimization is about 5 min, which is a long adjustment time.

Closed-Loop Characteristic Analysis

Based on the established s-domain system simulation model of the CHP unit, the step signals of the electric load are given as 5, 15, and 25 MW, respectively. The closed-loop control simulation analysis is carried out by using control scheme I and control scheme II. The changes of electric power, main steam pressure, and extraction pressure of the CHP unit are shown in **Figure 11**.

Under the two control schemes, the electric power of the unit increases rapidly. In the three variable load scenarios, it takes 10, 35, and 80 s, respectively, to accurately reach the step expected steady-state value. The stronger the variable load, the longer the regulation time. Specifically, the response speed and climbing rate of scheme II are slightly better than scheme I in the first 30 s of regulation.

The dynamic fluctuation of the main steam pressure regulation process is directly related to the safe and stable operation of the unit. It can be seen from the figure that the larger the variable load, the more intense the main steam pressure fluctuation. Scheme II improved by the pressure safety self-test control strategy effectively reduces the pressure fluctuation in the control process. Compared with scheme I, the peak value of pressure fluctuation in scheme II is reduced by about 50%, and all indexes of the control system can return to the steady-state value within 350 s.

In control scheme I, the extraction pressure cannot be adjusted back to the steady-state value (0 MPa, which does not affect heating), and the stronger the variable load capacity, the greater the steady-state deviation of the extraction pressure (the greater the impact on heating). Scheme II improved by the electrothermal cooperative control strategy can realize the rapid recovery function of heating. It can be seen from the

TABLE 1 | Influence of steam extraction pressure variation of different heating schemes on heating.

Variable load (MW)	Scheme	Average value within 600 s			600 s heat change/kJ
		$\Delta p_{z,equ}$	$\Delta q_{h,equ}$	$\Delta Q_{h,equ}$	
5	I	0.0121	6.94	4.56	2,734.82
	II	−0.0044	−2.54	−1.67	−1,001.28
15	I	0.0334	19.25	12.64	7,582.85
	II	−0.0157	−9.01	−5.92	−3,550.21
25	I	0.0541	31.17	20.47	12,279.48
	II	−0.0205	−11.79	−7.74	−4,643.11

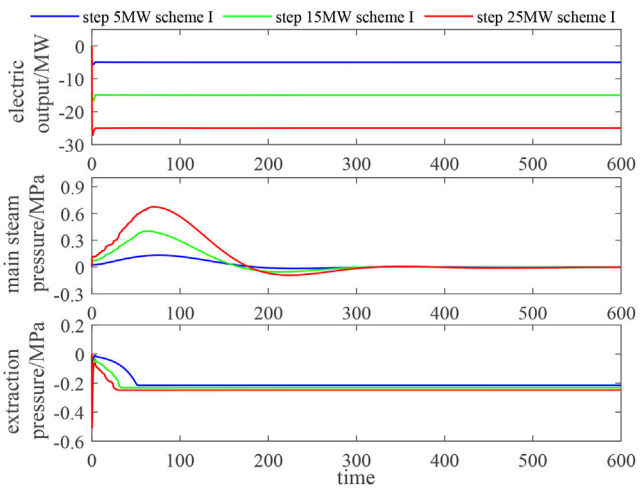

FIGURE 12 | Control effect diagram of scheme I with the same PID parameters under the pure condensation condition.

figure that scheme II can recover the extraction steam pressure closer to the steady-state value after 100-s dynamic adjustment. The influence of steam extraction pressure change on heating in the two schemes (compared with rated heating conditions $p_z = 0.35$, $q_h = 400$, $Q_h = 262.63$) can be calculated by **Eqs 20–22**.

The data in **Table 1** shows that, compared with scheme I, the control strategy of scheme II has less impact on the heating power output of the unit, and the heat change in the optimization cycle is reduced by about 60% (reference value: 0 kJ), which can ensure the stability of the thermal output of the unit when the electric power changes to load.

The working point linearization model is established under the pure condensation condition, and the same PID parameters as the control strategy of scheme I of the heating condition are used to analyze the robustness of the control system and the universality of PID parameters. As shown in **Figure 12**, the control quality of the pure condensation condition is acceptable as a whole, which shows that although the object has system nonlinearity, the robustness of the existing conventional controller is strong enough to overcome the impact caused by this nonlinearity. It also shows that the controller parameters set at any working point of the unit can adapt to the normal load variation range of the unit. However, there are still problems similar to those under rated heating conditions. The control effect of the main steam pressure and the extraction pressure is slightly insufficient. The main steam pressure regulation process fluctuates, and the extraction pressure cannot be adjusted without error. In the simulation test, the control strategy of scheme II cannot be applied to the pure condensation condition, and the safety self-test and electrothermal coordination parameters need to be reset.

CONCLUSION

In this paper, the dynamic characteristic simulation model of the CHP unit based on working point linearization is established, and the open-loop characteristics of the variable load process are analyzed by using the cooperation of improved particle swarm optimization control variables. Through the control strategy based on electrothermal cooperation and safety self-test, the closed-loop characteristics of unit dynamic regulation are studied, and the following conclusions are obtained:

1) When the control variable acts alone, V_B has an obvious effect on the change of electric power, V_T has a great effect on the change of main steam pressure, and V_H mainly affects the change of extraction steam pressure. When the three control variables work together, the electric power can be adjusted accurately, but the safe main steam pressure involved in the variable load process and the extraction steam pressure of heating are adjusted with difference, and the adjustment time is long.
2) The closed-loop characteristic simulation of the control strategy based on electrothermal coordination and safety self-test shows that the electric power response speed and climbing rate are better, the peak value of pressure fluctuation is reduced by about 50%, and the recovery of extraction pressure closer to the steady-state value has less impact on heating.
3) Experiments on pure condensing and heating conditions with the same PID parameter show that the robustness of the conventional controller is strong enough to overcome the influence of modeling nonlinearity at different working points and adapt to the normal load variation range of the unit.

DATA AVAILABILITY STATEMENT

The original contributions presented in the study are included in the article/**Supplementary Material**; further inquiries can be directed to the corresponding author.

AUTHOR CONTRIBUTIONS

YH put forward the main research points. QC completed manuscript writing and mathematical analysis. JY contributed to the framework formation and revision. TL completed the simulation research.

FUNDING

This work was supported by the National Natural Science Foundation of China (52007103) and Research Fund for Excellent Dissertation of China Three Gorges University (2021BSPY013).

SUPPLEMENTARY MATERIAL

The Supplementary Material for this article can be found online at: https://www.frontiersin.org/articles/10.3389/fenrg.2021.815272/full#supplementary-material

REFERENCES

Beerends, R. J., ter Morsche, H. G., van den Berg, J. C., and Van de Vrie, E. M. (2003). Fourier and Laplace Transforms. Cambridge: Cambridge University Press.

Chen, Z., Yuan, X., Ji, B., Wang, P., and Tian, H. (2014). Design of a Fractional Order PID Controller for Hydraulic Turbine Regulating System Using Chaotic Non-dominated Sorting Genetic Algorithm II. *Energ. Convers. Manage.* 84, 390–404. doi:10.1016/j.enconman.2014.04.052

Deng, T., Tian, L., and Liu, J. (2017). Thermal and Electric Load Coupling Analysis and Decoupling Coordinated Control in Heat Supply Units. *J. Syst. Simulation* 29 (10), 2593–2599. doi:10.16182/j.issn1004731x.joss.201710046

Fu, W., Li, J., Wang, L., Shi, Y., and Yang, Y. (2017). Optimal Design for Thermodynamics System of Double Reheat Coal-Fired Power Plants with post-combustion Carbon Capture Based on Dynamic Adaptive Particle Swarm Optimization. *Proc. CSEE* 37 (9), 2652–2659. doi:10.13334/j.0258-8013.pcsee.161456

Gao, Y., and Tian, L. (2020). Thermal and Electric Load Decoupling Control of Heat Supply Units. *J. North China Electric Power Univ. (Natural Sci. Edition)* 47 (1), 87–95.

Gao, Y., and Yan, P. (2017). Dynamic Economic Dispatch of Wind Power Integrated System with Fully Developed Supply Responses of thermal Units. *Proc. CSEE* 37 (9), 2491–2499. doi:10.13334/j.0258-8013.pcsee.160468

Hooman, F., and Randolph, R. (2020). A Method for Inverting the Laplace Transforms of Two Classes of Rational Transfer Functions in Control Engineering. *Alexandria Eng. J.* 59 (6), 4879–4887. doi:10.1016/j.aej.2020.08.052

Li, Z., Jiang, W., Abu-Siada, A., Li, Z., Xu, Y., and Liu, S. (2021). Research on a Composite Voltage and Current Measurement Device for HVDC Networks. *IEEE Trans. Ind. Electron.* 68 (9), 8930–8941. doi:10.1109/tie.2020.3013772

Liu, J., Tian, L., Zeng, D., and Liu, X. (2005). Analysis on the Nonlinearity of Load-Pressure Characteristics of a 660MW Unit. *J. Power Eng.* 25 (4), 533–540. doi:10.3969/j.issn.1674-7607.2005.04.017

Liu, S., Zhou, C., Guo, H., Shi, Q., Song, T. E., Schomer, I., and Liu, Y. (2021). Operational Optimization of a Building-Level Integrated Energy System Considering Additional Potential Benefits of Energy Storage. *J. Prot. Control. Mod. Power Syst.* 6 (1), 1–10. doi:10.1186/s41601-021-00184-0

Liu, X., Tian, L., Wang, Q., and Liu, J. (2014). Simplified Nonlinear Dynamic Model of Generating Load-Throttle Pressure-Extraction Pressure for Heating Units. *J. Chin. Soc. Power Eng.* 34 (2), 115–121. doi:10.3969/j.issn.1674-7607.2014.02.006

Shen, X., Ouyang, T., Khajorntraidet, C., Li, Y., Li, S., and Zhuang, J. (2021). Mixture Density Networks-Based Knock Simulator. *Ieee/asme Trans. Mechatron.*, 1. doi:10.1109/TMECH.2021.3059775

Shen, X., Ouyang, T., Yang, N., and Zhuang, J. (2021). Sample-based Neural Approximation Approach for Probabilistic Constrained Programs. *IEEE Trans. Neural Netw. Learn. Syst.*, 1–8. doi:10.1109/TNNLS.2021.3102323

Shen, X., and Raksincharoensak, P. (2021). Pedestrian-aware Statistical Risk Assessment. *IEEE Trans. Intell. Transport. Syst.*, 1–9. doi:10.1109/TITS.2021.3074522

Shen, X., and Raksincharoensak, P. (2021). Statistical Models of Near-Accident Event and Pedestrian Behavior at Non-signalized Intersections. *J. Appl. Stat.*, 1–21. doi:10.1080/02664763.2021.1962263

Shen, X., Zhang, X., Ouyang, T., Li, Y., and Raksincharoensak, P. (2020). Cooperative Comfortable-Driving at Signalized Intersections for Connected and Automated Vehicles. *IEEE Robot. Autom. Lett.* 5 (4), 6247–6254. doi:10.1109/LRA.2020.3014010

Shen, X., Zhang, Y., Sata, K., and Shen, T. (2020). Gaussian Mixture Model Clustering-Based Knock Threshold Learning in Automotive Engines. *Ieee/asme Trans. Mechatron.* 25 (6), 2981–2991. Dec. doi:10.1109/TMECH.2020.3000732

Shen, X., Zhang, Y., Shen, T., and Khajorntraidet, C. (2017). Spark advance Self-Optimization with Knock Probability Threshold for Lean-Burn Operation Mode of SI Engine. *Energy* 1223, 1–10. doi:10.1016/j.energy.2017.01.065

Sun, H., Pan, Z., Sun, Y., Li, B., and Guo, Q. (2021). Reflection and Understanding of Application of Transboundary Thinking in Energy Internet. *Automation Electric Power Syst.* 45 (16), 63–72. doi:10.7500/AEPS20210323008

Tian, L., Lian, H. Q., Liu, X. P., and Liu, J. (2017). Coupling Characteristics of Steam Pressure and Intermediate Point Temperature for Once-Through Boiler. *Proc. CSEE* 37 (4), 1142–1150. doi:10.13334/j.0258-8013.pcsee.152321

Tian, L., Liu, F., Liu, X., and Liu, J. (2015). Parameter Optimization on Coordinated Control System of Thermal Power Units in High Rate Variable Load Operation Mode. *J. Syst. Simulation* 27 (7), 1532–1540. doi:10.16182/j.cnki.joss.2015.07.017

Tian, L. (2005). Research of Unit Plant Nonlinearity Dynamic model. Beijing: North China Electric Power University.

Wang, Q. (2013). Research on Optimization Control for Heating Units under the Condition of Large-Scale Integration of Wind power. Beijing: North China Electric Power University.

Wang, W., Sun, Y., Liu, J., et al. (2018). Load-change Control Strategy for Combined Heat and Power Units Adapted to Rapid Frequency Regulation of Power Grid. *Automation Electric Power Syst.* 42 (21), 63–69.

Wang, W., Jing, S., Sun, Y., Liu, J., Niu, Y., Zeng, D., et al. (2019). Combined Heat and Power Control Considering thermal Inertia of District Heating Network for Flexible Electric Power Regulation. *Energy* 169, 988–999. doi:10.1016/j.energy.2018.12.085

Wang, Z. Q. (2012). Fast Solving Strategies for Dynamic Optimization with Differential-Algebraic equations. Hangzhou: Zhejiang University.

Yang, J., Zhang, N., and Kang, C. (2020). Analysis Theory of Generalized Electric Circuit for Multi-Energy Networks—Part One branch Model. *Automation Electric Power Syst.* 44 (9), 21–32.

Yang, N., Ye, D., Zhou, Z., Cui, J., Chen, D., and Wang, X. (2018). Research on Modelling and Solution of Stochastic SCUC under AC Power Flow Constraints [J]. *IET Generation, Transm. Distribution* 12 (15), 3618–3625.

Yang, N., Huang, Y., Hou, D., Liu, S., Ye, D., Dong, B., et al. (2019). Adaptive Nonparametric Kernel Density Estimation Approach for Joint Probability Density Function Modeling of Multiple Wind Farms. *Energies* 12, 1356. doi:10.3390/en12071356

Yang, N., Liu, S., Deng, Y., and Xing, C. (2021). An Improved Robust SCUC Approach Considering Multiple Uncertainty and Correlation. *IEEJ Trans. Elec Electron. Eng.* 16, 21–34. doi:10.1002/tee.23265

Ye, J., Zhao, D., Zhang, L., Li, Z., and Zhang, T. (2012). "Research on Combined Electricity and Heating System Scheduling Method Considering Multi-Source Ring Heating Network," in *Front. Energy Res.* 9:800906. doi:10.3389/fenrg.2021.800906

Zhang, L., Xie, Y., Ye, J., Xue, T., Cheng, J., Li, Z., et al. (2021). Intelligent Frequency Control Strategy Based on Reinforcement Learning of Multi-Objective Collaborative Reward Function. *Front. Energ. Res.* 9. doi:10.3389/fenrg.2021.760525

Zhang, W., Wang, X., Li, Y., and Qian, T. (2018). An Analysis Model of Multi-Area Interconnected Power Systems with Large-Scale Wind Power Involved in Comprehensive Heating and Power System Scheduling. *Power Syst. Tech.* 42 (1), 154–161. doi:10.13335/j.1000-3673.pst.2017.1559

Zhu, B., Ding, F., and Vilathgamuwa, D. M. (2020). Coat Circuits for DC-DC Converters to Improve Voltage Conversion Ratio. *IEEE Trans. Power Electron.* 35 (4), 3679–3687. Apr. doi:10.1109/TPEL.2019.2934726

Conflict of Interest: The authors declare that the research was conducted in the absence of any commercial or financial relationships that could be construed as a potential conflict of interest.

Publisher's Note: All claims expressed in this article are solely those of the authors and do not necessarily represent those of their affiliated organizations, or those of the publisher, the editors and the reviewers. Any product that may be evaluated in this article, or claim that may be made by its manufacturer, is not guaranteed or endorsed by the publisher.

frontiers in Energy Research

ORIGINAL RESEARCH
published: 14 February 2022
doi: 10.3389/fenrg.2021.813650

Bone Age Assessment Based on Deep Convolutional Features and Fast Extreme Learning Machine Algorithm

Longjun Guo, Juan Wang, Jiaqi Teng and Yukun Chen*

Beijing Rehabilitation Hospital, Capital Medical University, Beijing, China

Bone age is an important metric to monitor children's skeleton development in pediatrics. As the development of deep learning DL-based bone age prediction methods have achieved great success. However, it also faces the issue of huge computation overhead in deep features learning. Aiming at this problem, this paper proposes a new DL-based bone age assessment method based on the Tanner-Whitehouse method. This method extracts limited and useful regions for feature learning, then utilizes deep convolution layers to learn representative features in these interesting regions. Finally, to realize the fast computation speed and feature interaction, this paper proposes to use an extreme learning machine algorithm as the basic architecture in the final bone age assessment study. Experiments based on publicly available data validate the feasibility and effectiveness of the proposed method.

Keywords: bone age assessment, deep convolution learning, ELM, RoIs extraction, hybrid prediction

OPEN ACCESS

Edited by:
Zhenhao Tang,
Northeast Electric Power University, China

Reviewed by:
Heming Huang,
Wuhan University, China
Junfeng Zhang,
Hebei University, China

****Correspondence:***
Longjun Guo
dalong531@126.com

Specialty section:
This article was submitted to Smart Grids, a section of the journal Frontiers in Energy Research

Received: *12 November 2021*
Accepted: *29 November 2021*
Published: *14 February 2022*

Citation:
Guo L, Wang J, Teng J and Chen Y (2022) Bone Age Assessment Based on Deep Convolutional Features and Fast Extreme Learning Machine Algorithm. Front. Energy Res. 9:813650. doi: 10.3389/fenrg.2021.813650

INTRODUCTION

In pediatrics, bone age is a significant metric to evaluate the development of child's skeleton (Manzoor Mughal et al., 2014). Generally, the discrepancy between bone age (skeletal development age) and chronological age (physical age calculated from birth date) can suggest abnormalities in skeletal development. For example, illness may cause the delayed or accelerated appearance of ossification centers. Moreover, a child's bone age is useful to predict an individual's final height (Creo and Schwenk, 2017). Therefore, assessing a child's bone age has become a very common examination in pediatrics. It is helpful to not only monitor growth hormone therapy but also to diagnose endocrine disorders.

Usually, bone age assessment (BAA) is based on a hand-wrist radiograph which is straightforward to obtain and contains all relevant regions of interest (ROI) within the hand and wrist. Then, it is realized by recognizing the maturity of the bones through the changes of radiographic appearance. There exist two most typical methods for BAA, namely the Greulich-Pyle (GP) method and the Tanner-Whitehouse (TW) method (Lee et al., 2021; Shah et al., 2021). The former one is based on the hand atlas, and its reference dataset consists of a series of left-hand X-ray images derived from the middle socioeconomic class of Caucasian children from the Midwest region of the US from 1931 to 1942. If a patient's X-ray image is collected and compared with this reference dataset, the closest matching will determine the final bone age of the patient. This method is simple and fast (2–5 min for one case), but difficult to assess precise bone age with large variations, since this reference data is unchanged and contains only template bone age data from 6 months to 1 year. The latter one aims at evaluating the maturity levels of specific bones within hand and wrist instead of all bones in GP. Several ROIs, actually ossification centers (Spampinato et al., 2017), are selected and assigned some

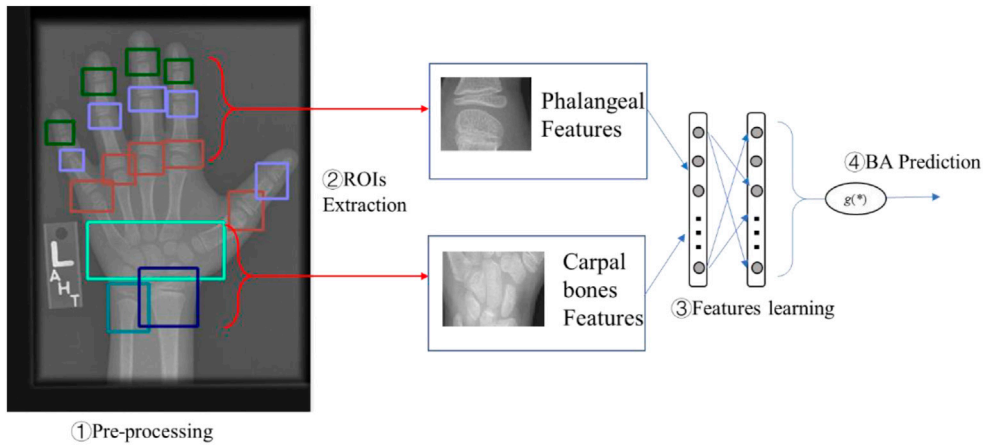

FIGURE 1 | Framework of the proposed new BAA system.

developmental scores according to their maturity level. Then, a patient's bone age can be derived from the sum of all these ROIs' scores. The TW methods have several versions, like TW1, TW2, and TW3 (Son et al., 2019). While, compared with the GP methods, TW methods are relatively complicated and time consuming, so they are rarely used in practice. However, as the rapid development of deep learning (DL) (Yu et al., 2013), DL-based methods can effectively solve the above-mentioned problems. For example, DL-based image analysis techniques have achieved great success in the past decade, especially in medical image analysis like breast cancer recognition, brain lesion segmentation, and so on (Ritter et al., 2011; Xu et al., 2014). Correspondingly, DL-based BAA has also attracted several scholars' attention, for example, CNN and their variants are widely used for automating BAA and show positive performance. In (Lee et al., 2017), a GP-based CNN network called BoNet was proposed to use the X-ray images of the left hand and wrist for BAA and was validated as effective in bone age prediction. In (Chen, 2016), a DL model inheriting the existing models (e.g., GoogLeNet and VGGNet) for weight initialization and fine-tuning was constructed to predict bone age, in which L_2-based loss function was leveraged for training. This model finally achieved competent performance close to a radiologist's readings. More other successful BAA models based on DL were also found in the literature (Thodberg et al., 2008; Kim et al., 2017).

However, besides the advantages of DL-based models in TW-based BAA, one of the important problems with which we are always concerned is the high computation overhead, especially involving the process of learning deep features from images with back-propagation parameters tuning (Tang et al., 2021). Aiming at these issues in the DL-based BAA study, this paper proposes a new automated BAA system with fast bone age estimation speed. The proposed BAA system consists of four major parts, such as data processing, ROIs extraction, feature learning, and fast BAA estimation, as shown in **Figure 1**.

Figure 1 shows the framework of the proposed BAA method. First, the raw radiological images require some necessary pre-processing steps, for example, background noise cleaning, orientation, and so on. Then, according to the TW-based BAA method, important ROIs are extracted for the subsequent study instead of the whole radiological images. Next, based on the extracted ROIs, this paper proposes to learn deep convolutional features from those ROI images. Finally, this paper proposes to combine deep convolutional features and fast extreme learning machine (ELM) (Huang et al., 2006) algorithm for the final BAA. The novelties and contributions of the proposed method are summarized as follows: 1) inheriting the advantages of TW-based methods, only representative ROIs are selected to realize efficient and effective BAA. For example, this paper only considers phalangeal ROIs and carpal bones ROIs for features learning. In this way, not only the most important features in BAA could be considered, but also the dimensionality of inputs can be reduced to lower computation cost. 2) Convolutional features are learned separately for each ROI region. To make use of DL's ability on feature learning, this paper proposes to use the CNN architectures to extract the important features from each ROI. 3) To further realize the fast learning speed and to improve the efficiency of DL-based BAA, ELM is considered as the architecture at the last layer. In this way, the proposed method could not only make use of ELM's fast learning ability, but also consider the interactions between different ROIs fast. Based on the proposed method, an end-to-end system is developed to realize the automatic bone age estimation. Experiments from a publicly available dataset are implemented to validate the performance of the proposed method.

The rest of this paper is organized to describe each part in the proposed BAA system. *Related work on data processing in BAA* introduces some necessary preprocessing steps for the radiological images in the BAA study, such as orientation correction, background removal, and ROIs selection. *Methodology of the proposed DL-based BAA* describes the methodology of the proposed DL-based method for BAA, including parts of convolutional features learning and fast bone age estimation via ELM. *Experiments and discussion* implements some experiments based on real hand-wrist

radiographs, and some quantitative analyses are discussed. *Conclusions* concludes the work of this paper.

RELATED WORK ON DATA PROCESSING IN BAA

In order to obtain accurate bone age estimation from hand-wrist radiographs, generally the quality of input images is an important factor. According to the proposed BAA method, the first part is to pre-process the raw data (hand-wrist radiographs) to improve data quality. Based on requirements of different applications, various preprocessing operations can be implemented, including file format transformation (Ratib et al., 1991), correction of image orientation (McNitt-Gray et al., 1992), window/level values, and look-up-tables for enhancing image brightness and contrast. This paper mainly introduces three operations required in the proposed BAA system, such as orientation correction, background removal, and ROIs selection.

Orientation Correction

First, the operation of orientation correction aims at guaranteeing a standard hand position within the image. Generally, the standard orientation of hand position should be anteroposterior, upright, and left-hand wrist according to the expert experience of radiologists. While abnormal positions are commonly detected for various reasons in the real pediatric examination, e.g., a child's hand may diverge from the standard position, or phosphor plates and cassette are placed in an abnormal direction based on the examination conditions. These lead to 35–40% of the collected raw hand-wrist radiographs required for orientation correction in radiology (McNitt-Gray et al., 1992). Therefore, it is necessary to orient images before the BAA study.

Background Removal

In radiological image processing, the background can contain two kinds of definitions (Kaur et al., 2018). The first type is referred to as an area outside the radiation field, for example, white borders caused by blocking of the collimator surrounding the radiation field. The second type is referred to as the area within the radiation field but outside the patient's body (hand-wrist), e.g., landmarks or other labels reflecting just the patient's information like name, birthday, ID number, etc.

Targeting at removing the former type of background, algorithms blacking the unexposed background have been successfully applied in clinical picture archiving and communication system (PACS) (Yan et al., 2018), particularly in pediatric radiology. It can reduce the amount of unwanted light as well as transparent borders without losing any pertinent information. On the other hand, targeting at removing the latter type of background, the algorithm aims at increasing the hand-to-background ratio, then improves the performance on ROIs segmentation and detection.

To estimate bone age in BAA, removing the second type of background needs more attention because extracting phalanges is significantly important in processing under- or overexposed

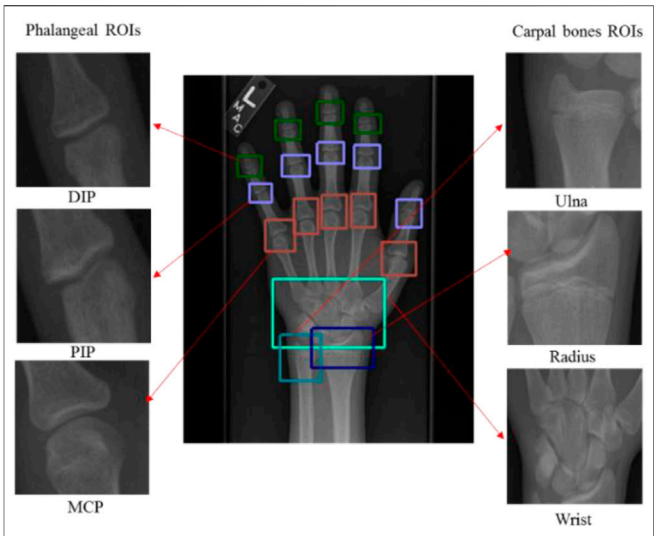

FIGURE 2 | Locations of six ROIs in BAA.

hand-wrist radiographs. Moreover, if the phosphor plates are not closed to the cassette tightly, background non-uniformity might happen and further affect the accuracy of bone age estimation. Therefore, background suppression with dynamic thresholds is necessarily adopted in BAA to solve these issues (Yuan et al., 2018). The procedure of selecting dynamical thresholds is performed separately in both directions (horizontal and vertical) according to the local background value. Its realization can be described as follows: first, on the top part of a studied image, a window with a given size representing the average phalangeal width slides in the vertical direction, and several statistical metrics (e.g., mean, variance) are calculated for windows at each step. Then, two windows from both sides having the lowest values of mean and variance can determine the background area and ranking the mean values of all these windows referring to their variances can be used to calculate the threshold in the studied rows. Similarly, the lower part of the images also can be processed to result in another threshold value. Once this calculation process is completed, the threshold value of each row can be generated by using linear interpolation in the vertical direction, as well as the interpolation in the horizontal direction for generating the threshold value of each column. Applying these threshold values, the background suppression can be realized as the following form.

$$\hat{p} = \begin{cases} p, & \text{if } p \geq v_{\text{th}} \\ 0, & \text{if } p < v_{\text{th}} \end{cases} \quad (1)$$

where p and $\hat{p}$ represent the original and processed pixel values in the image; and *vth* is the calculated threshold. When the pixel value is lower than the threshold value, then it is set as zero, and vice versa keeping its value. Furthermore, the processing in **Eq. 1** can be developed to remove all small noisy elements in the background. For example, to remove noise between phalanges, the threshold for erosion can be metamorphosed from a pixel to a *3*3* structuring element, and all elements smaller than the threshold would be turned to zero.

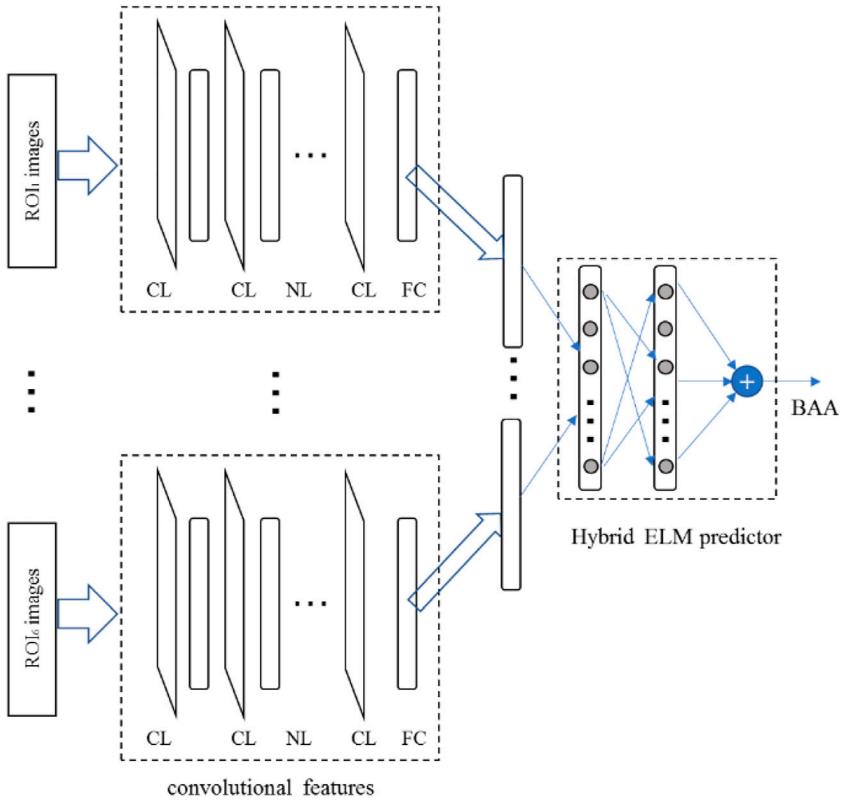

FIGURE 3 | Architecture of the proposed bone age prediction model.

ROIs Selection, Annotation, and Determination

Based on the TW-based methods, several ROIs are required for assessing the maturity of bone. While there are not only several regions of the hand verified important by radiologists, but also various methods to select ROIs for modelling the BAA system to estimate the bone age.

In this paper, six most important ROIs (Kim et al., 2018) are chosen for bone age assessment, such as DIP regions reflecting epiphyseal growth locating between the distal and the intermediate phalanges, PIP regions between the intermediate and the proximal phalanges, MCP regions between the proximal phalanges and the metacarpals, the wrist region covering the carpal bones, the ulna region, and the radius region. The detailed locations of these ROIs are shown in **Figure 2**, **Figure 3**.

Based on the given requirements for ROIs selection, annotating these ROIs is a necessary and important step in data preprocessing. In order to make the annotation process comfortable, several operations can be applied. First, the number of ROIs in each hand-wrist radiograph and that of samples for each ROI should always be the same. This can guarantee the data balance of each class of ROI, and also affect the TW-based BAA. Second, an annotation candidate was regarded as the template to speed up the annotation process. Third, considering the size differences between radiographs, a scaling operation can be implemented to unify datasets. Furthermore, the extracted ROIs also require scaling in each class for uniformities. Fourth, there also exists differences on the brightness of radiographs, a contrast enhanced view seems necessary in data preprocessing, especially to detect the regions of DIP and PIP which are usually very dark. Finally, ROIs should be detected before the prediction of bone age in automated BAA systems. This paper also utilizes the commonly applied Faster-RCNN (Girshick, 2015) architecture for ROIs detection. Since no pre-trained Fast-RCNN is available for detecting the defined ROIs above, it should be trained first based on those annotated data. Then, it would be used to extract ROIs for modeling bone age prediction models.

METHODOLOGY OF THE PROPOSED DL-BASED BAA

Framework of the Proposed Algorithm

This section aims at describing the methodology of the proposed bone age prediction model in detail. First, defined ROIs in *Related work on data processing in BAA* are detected by Faster RCNN. Then, by taking these ROIs as inputs, the proposed hybrid bone age prediction model is realized as the following framework.

According to the description in *Introduction*, the proposed bone age prediction method is based on deep learning. It mainly contains two stages, namely convolutional feature learning and

hybrid fast bone age prediction. At the first stage, the size of each class of ROI should be scaled uniformly first. Then, a CNN model is constructed with several convolutional layers and a full-connection layer. The full-connection layer targeted at the final bone age and flatten features of the final convolutional layer represent features of the studied ROI related to bone age prediction. At the second stage, combining independent convolutional features of all classes of ROIs, a model for predicting bone age is further constructed. The reason for the combination aims at learning the interaction between different ROIs which can enhance the performance of predicting bone age, e.g., interaction of DIP, PIP, and MCP, and interaction of wrist, ulna, and radius regions. While considering the dimensionality of all these convolutional features is huge, a deep learning model can be used but it is not necessary. Therefore, here we propose to apply the ELM algorithm having fast learning speed (Huang et al., 2011) to model the final hybrid bone age prediction. Details of these two stages are described as below.

Convolutional Feature Learning

As described above, convolutional features of each ROI are learned based on CNN networks which mainly consist of convolutional layers. To describe the convolution learning in detail, here the process is divided into four sequential steps, such as convolution, normalization, pooling operations, and feature representation.

(1) Convolution operation

First, in a convolutional layer, convolutions are implemented between feature maps of the previous layer and a series of filters. Then, a non-linear activation function g (.) is applied in the sum of results of the convolutions and an additional bias, and the ReLU nonlinear function is usually used in CNN. At last, the output of activation function represents a learned feature. Assuming v_{ij}^{mn} as the value of the pixel position (m, n) in the *jth* feature map of the *ith* layer, it can be expressed as:

$$v_{ij}^{mn} = g\left(\sum_{k} \sum_{p=0}^{P_i-1} \sum_{q=0}^{Q_i-1} w_{ijk}^{pq} v_{(i-1)k}^{(m+p)(n+q)} + b_{ij} \right) \tag{2}$$

where b_{ij} is the bias; k indexes over all data of the feature maps in the $(i-1)^{\text{th}}$ layer for convolution; w_{ijk}^{pq} is the weight value of the pixel position (p, q) in the filter kernel; and P_i and Q_i represent the height and width of the filter kernel, respectively.

Through the convolutions, it realizes a nonlinear transformation from images with low-level representation to the high-level semantic representation. For the convenience of computing, the equation in **Eq. 2** can be simplified as:

$$v_j = g\Big(\sum w_{ij} \otimes v_{(i-1)} \Big) \tag{3}$$

where ⊗ is denoted as the convolutional operator; w_{ij} is still denoted as the weight which will be randomly initialized and trained via the iterative BP algorithm; and v_i represents the features of the *ith* layer. Generally, the size of the feature maps reflects the resolution affecting the accuracy finally. If the size of a feature map is large, it implies more good features can be learned, but correspondingly with the high cost of computing. Vice versa, the small size reduces the computation cost as well as the model's accuracy.

(2) Contrast normalization

There are several methods realizing the normalization process in convolutional networks. In this paper, the contrast normalization is inspired by the idea of computational neuroscience (Sermanet and LeCun, 2011). It aims at enhancing the local competition between neurons and their neighbors, as well as forcing features of different feature maps at the same location to be computed. Here, two normalization operators, namely subtractive and divisive, are proposed to realize these objectives. First, assuming v_{mnk} represents the value of the pixel position (m, n) in the *kth* feature map this time, it can be calculated by the following form:

$$z_{\text{mnk}} = v_{mnk} - \sum_{p=-(P_i-1)/2}^{(P_i-1)/2} \sum_{q=-(Q_i-1)/2}^{(Q_i-1)/2} \sum_{j=1}^{J} \varepsilon_{pq} v_{(m+p)(n+q)j} \tag{4}$$

where ε_{pq} is defined as a normalized Gaussian kernel; z_{mnk} is the output of the subtractive normalization operation, which will also be input to the divisive normalization operation expressed as below.

$$v_{mnk} = \frac{z_{mnk}}{\max(E, E(m,n))} \tag{5}$$

where

$$E(m,n) = \sqrt{\sum_{p=-(P_i-1)/2}^{(P_i-1)/2} \sum_{q=-(Q_i-1)/2}^{(Q_i-1)/2} \sum_{j=1}^{J} \varepsilon_{pq} v_{(m+p)(n+q)j}^2} \tag{6}$$

$$E = \frac{\left(\sum_{m=1}^{s1} \sum_{n=1}^{s2} E(m,n) \right)}{(s_1 \times s_2)} \tag{7}$$

While in both the subtractive and divisive operations above, the Gaussian kernel ε_{pq} is operated with zero-padded edges to guarantee the sizes of output and input keeping the same. Then, through the introduced contrast normalization operations, features from the convolution layers can be normalized.

(3) Pooling operation

Generally, the dimensionality of features in an image is high, and not all features are meaningful in decision-making. To reduce the irrelevant information, pooling is proposed in CNN. It operates like the subsampling to transform the joint features into a novel representation, but keeps the crucial information. Generally, the max pooling operation is implemented on each feature map, e.g., the value at the pixel position (m, n) in the *jth* feature map and the *ith* layer calculated as below:

$$v_{ij}^{mn} = \max\left\{ v_{(i-1)j}^{mn}, v_{(i-1)j}^{(m+1)(n+1)}, \cdots, v_{(i-1)j}^{(m+P_i)(n+Q_i)} \right\} \tag{8}$$

The max pooling operation detects the maximum representations of the learned feature map and meanwhile reduces the resolution. In this subsampling process, pooling can realize not only the position invariance over larger local regions, but also built-in invariance to small shifts and distortions.

(4) Feature representation

Through implementing the mentioned three operations sequentially, convolutions can be completed. To learn the most representative convolutional features for BAA, features are flattened and directly connected to the output which aims at estimating the target bone age. Therefore, the convolution features of each ROI for BAA can be learned through the following objective:

$$\min_{w} \sum_{i=1}^{N} \left\| y_i - \hat{y}_i \right\|^2 \tag{9}$$

where y_i is the target bone age; and $\hat{y}_i$ is calculated via convolution features of the given ROI, expressed as below:

$$\hat{y} = g\left(\sum_{k} \sum_{i} \sum_{j} w_{ijk} v_{ijk} + b \right) \tag{10}$$

where $\boldsymbol{V} = \{v_{ijk}\}$ is the convolution feature vector. Through the minimization of **Eq. 9** and the back-propagation learning, optimal convolutional features of each ROI can be learned to estimate bone age.

Hybrid Fast BAA Estimation

According to the above convolution feature learning, it is seen that these convolutional features of each ROI aim at estimating the target bone age optimally. This implies that features of each ROI can be used directly for BAA, which is also the conventional way in the literature. While considering ROIs from the same radiograph has tight correlation between each other, features of an individual ROI may not completely express the target bone age. Therefore, this paper proposes to construct a hybrid estimation with consideration of interactions between features of all ROIs. Moreover, considering the dimensionality of feature vectors in each ROI is large, the hybrid BAA model should adopt a fast-learning architecture. Therefore, the ELM network is proposed for hybrid BAA estimation here.

ELM was first proposed by Huang et al. (Huang et al., 2004; Huang et al., 2018), which is a kind of single-hidden-layer feedforward neural network (SLFN). Its input weights and hidden layer biases are randomly assigned for feature learning, then the output weights are learned according to the target. Due to these features, ELM has the advantages at fast feature learning ability when faced with high-dimensional inputs. The implementation of ELM could be expressed as below.

Assuming the input consists of N samples as $(\boldsymbol{x}_i, t_i)$, $i = 1,2, \ldots N$, where $\boldsymbol{x}_i$ is the input vector and t_i is the target. In BAA, the target is the bone age, therefore the ELM model for bone age prediction can be written as

$$y_i = \sum_{j=1}^{L} \beta_j g_j(x_i) = \sum_{j=1}^{L} \beta_j g\left(w_j x_i + b_j\right),\ i = 1, 2, \cdots, N \tag{11}$$

where β_j represents the weight between the *jth* hidden node and the output; $\boldsymbol{w}_j = [w_{1j}, w_{2j}, \ldots, w_{nj}]^T$ is the randomly generated input weights to the *jth* node, and b_j is the corresponding bias. Then y_i is denoted as the output (predicted bone age) from the ELM.

To train the ELM model's parameters, the output of ELM can be approximated to predict the target with zero error, namely as

$$\sum_{i=1}^{N} \left\| y_i - t_i \right\| \approx 0 \tag{12}$$

If expressing these expressions in ELM as a matrix format, then the above equation can be simply expressed as

$$\boldsymbol{H}\boldsymbol{\beta} = \boldsymbol{T} \tag{13}$$

where H is the hidden layer output matrix. The complete elements of these three matrices are written as follows:

$$H = \left[h_{\mathrm{ij}}\right] = \begin{bmatrix} g(\boldsymbol{w}_1 x_1 + b_1) & \cdots & g(\boldsymbol{w}_L x_1 + b_L) \\ \vdots & \ddots & \vdots \\ g(\boldsymbol{w}_1 x_N + b_1) & \cdots & g(\boldsymbol{w}_L x_N + b_L) \end{bmatrix} \tag{14}$$

and

$$\boldsymbol{\beta} = \begin{bmatrix} \beta_1 & \beta_2 & \cdots & \beta_L \end{bmatrix}^T,\ T = \begin{bmatrix} t_1 & t_2 & \cdots & t_L \end{bmatrix}^T \tag{15}$$

After that, the least-squares minimization is applied to optimize the output weights $\boldsymbol{\beta}$ as

$$\hat{\boldsymbol{\beta}} = \boldsymbol{H}^{\dagger}\boldsymbol{T} \tag{16}$$

where $H^{\dagger}$ is the Moore–Penrose inverse (Wu and Zheng, 2020) of the matrix $\boldsymbol{H}$. Then, the output of ELM for predicting bone age can be expressed as

$$y(x) = h(x)\boldsymbol{\beta} = h(x)\boldsymbol{H}^{\dagger}\boldsymbol{T} \tag{17}$$

EXPERIMENTS AND DISCUSSION

In this section, a publicly available dataset containing radiological images is taken for the BAA study, such as its statistical features, training the proposed DL models, and evaluating the performance on predicting bone ages. Here, the dataset is taken from the Pediatric Bone Age Challenge (RSNA, 2017) organized by the Radiological Society of North America (RSNA) as the foundation of research in this paper. This dataset contains 12,611 images with labels, which consists of 54.2% male and 45.8% female infants' hand images. To construct the BAA model and discussion, the raw dataset is divided as a training set (70%) and a testing set (30%). Then some related analysis can be implemented subsequently.

Statistical Analysis

First, according to this given dataset, some statistical analysis can be implemented to study the distribution of the original dataset.

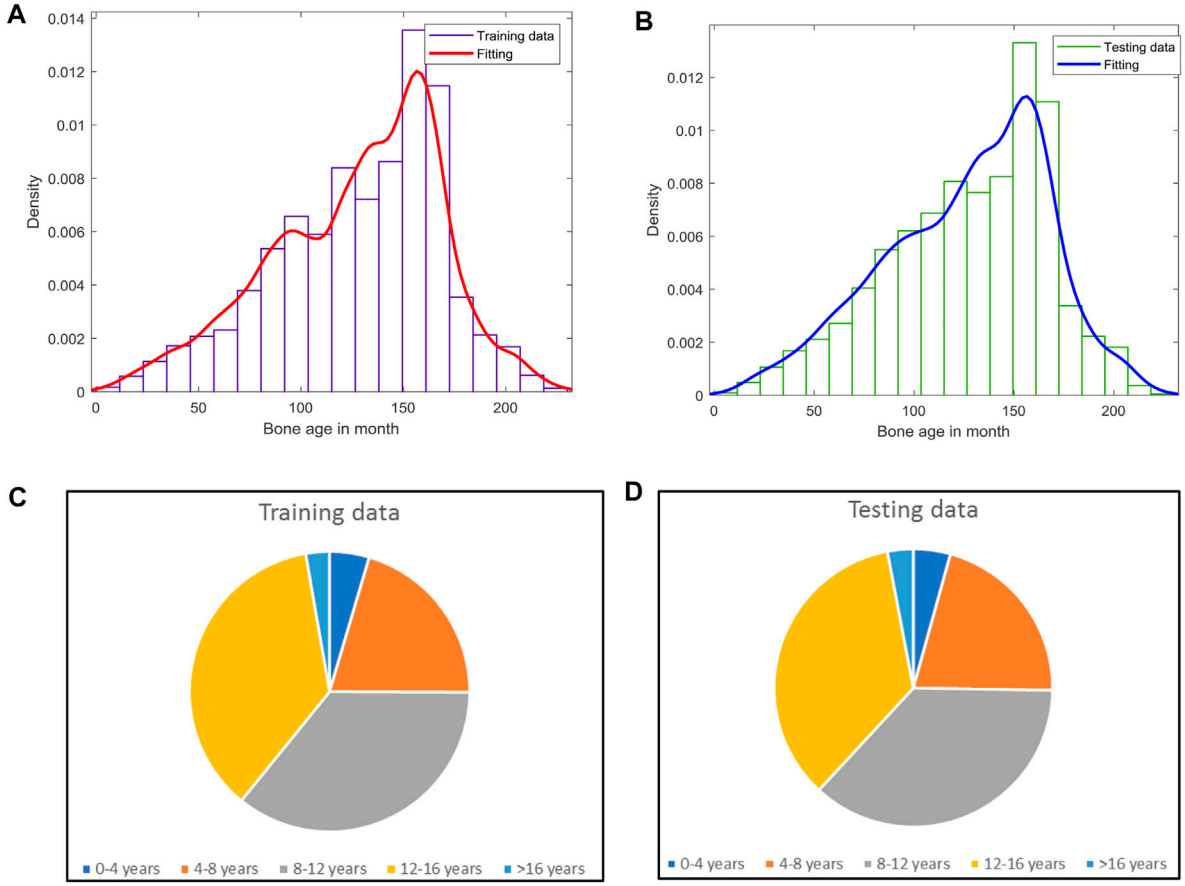

FIGURE 4 | Distribution of bone ages. The distribution of ages based on training data **(A)** and testing data **(B)**. **(C)** and **(D)** plot the ratio of different age phases in training data and testing data, respectively.

Figure 4 shows the distribution of ages based on training data (a) and testing data (b). It can be found that training data and testing data are a match with each other even though both do not satisfy the normal distribution. Moreover, the highest ratio of bone age is located between 12 and 18 years, which means the given dataset collected the data from teenagers. By dividing ages of 4 years as a phase, the detailed distribution of different age phases is also shown in **Figure 4** (c)-(d).

Figure 4 (c) and (d) plot the ratio of different age phases in training data and testing data, respectively. It is seen that ages between 8 and 16 years occupy almost 70% in both training and testing data. Therefore, this dataset for BAA research is better to orient to study the growing development of teenagers.

ROI Extractions

According to the idea of TW-based BAA methods, ROIs in hand-wrist radiological images are the basis of DL-based BAA. As the description in *ROIs selection, annotation and determination*, two kinds of ROIs are extracted, such as phalangeal and carpal bones ROIs should be extracted, and in total six ROIs are annotated as DIP, PIP, MCP, ulna, radius, and wrist as **Figure 2** shows. Then, based on this information, a Faster RCNN model is trained for extracting these ROIs in the testing data automatically. The experiment is implemented on the platform of Tensorflow, and the Inception-ResNet-V2 architecture is chosen in the construction of Faster RCNN. Then, running training and testing, the ROIs extraction results are shown in **Figure 5**.

In **Figure 5**, there are 10 sample images shown in each of six defined ROIs. While considering these ROI images have different sizes, they are all resized as 128*128 in **Figure 5**. In order to guarantee the extracted ROIs could provide useful information for the BAA study, the performance of ROIs extraction by Faster R-CNN requires evaluation. By taking the annotation as the ground truth, the performance of six ROIs is presented in **Table 1**.

In **Table 1**, four metrics are given out to evaluate the performance of detected ROIs, such as Precision, Recall, F1-score, and AP@0.5IoU. The former three performances are based on the central points of ROIs annotated by expert, the last one means the average precision under overlapping ROIs with an IoU larger than 50%. Here, since there exist some random factors in the extraction of ROIs, the results may have some fluctuation at each time. Therefore, multiple experiments are required, and the average values and variance of all metrics are calculated in **Table 1**. It is seen from these results that Faster RCNN achieve good performance on detecting the annotated ROIs to provide confident information for BAA study subsequently.

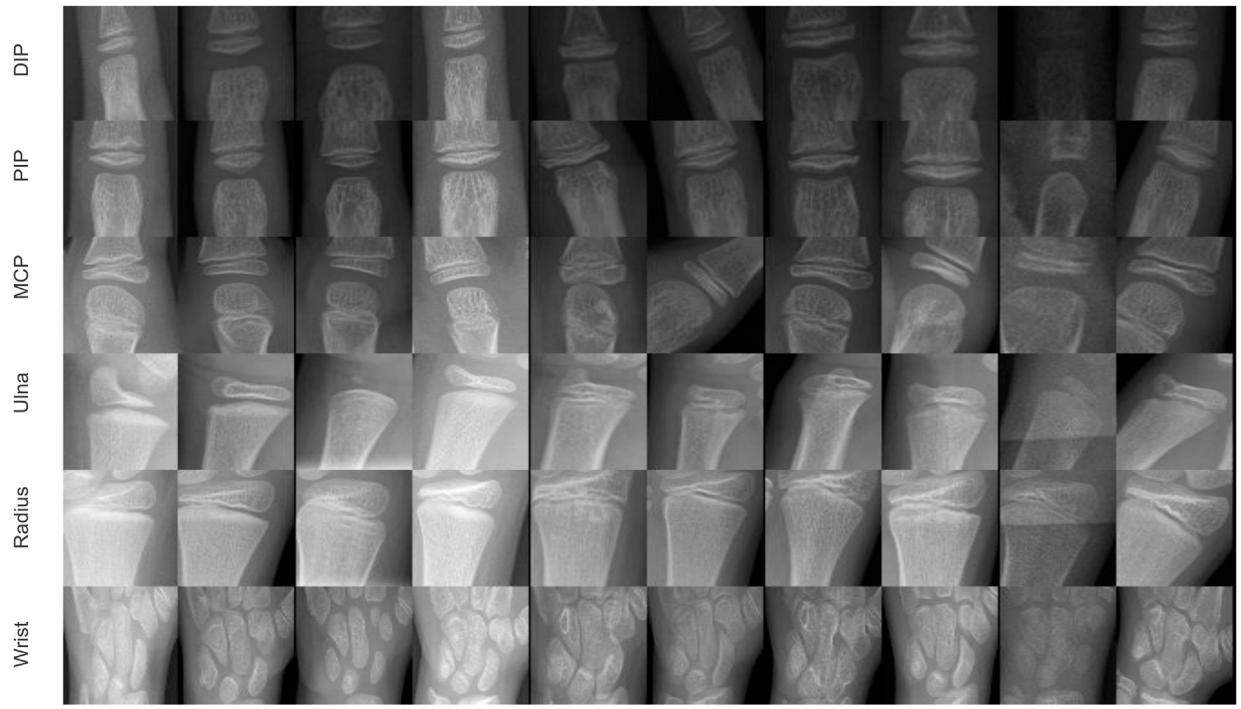

FIGURE 5 | Extracted annotated ROIs in the testing data.

TABLE 1 | Evaluation of ROIs detection by using Faster R-CNN.

	DIP	PIP	MCP	Ulna	Radius	Wrist
Precision	98.78 ± 0.72	98.29 ± 0.22	98.73 ± 0.46	98.63 ± 0.56	99.41 ± 0.52	98.13 ± 1.31
Recall	95.46 ± 1.50	97.03 ± 0.46	97.31 ± 0.71	91.07 ± 1.02	97.38 ± 1.69	96.69 ± 1.28
F1-Score	97.85 ± 0.49	97.79 ± 0.37	97.74 ± 0.48	98.22 ± 0.94	98.40 ± 0.82	97.87 ± 0.82
AP@0.5IoU	89.62 ± 5.10	88.27 ± 4.12	92.17 ± 1.44	87.78 ± 3.59	97.32 ± 1.67	98.36 ± 0.26

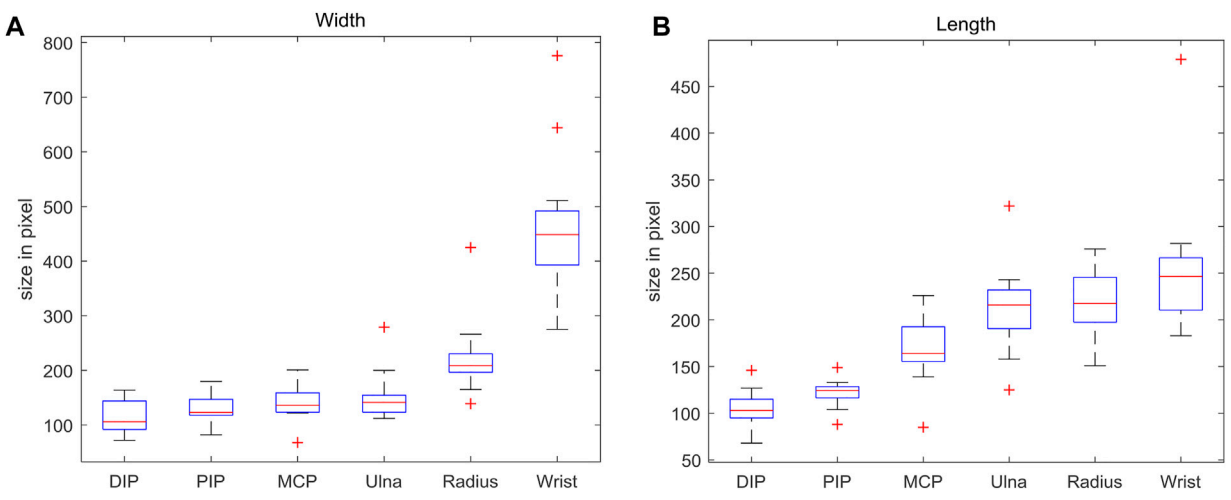

FIGURE 6 | The bounding box sizes of extracted ROIs in testing dataset. **(A)** Width; **(B)** length.

TABLE 2 | BAA performance based on different ROIs.

	Training		Testing	
	MAE	MAPE	MAE	RMSE
DIP	11.9839	34.8812	13.3639	31.1543
PIP	8.8644	19.7156	9.9487	22.6017
MCP	7.2890	18.2744	7.8430	18.8568
Ulna	7.2482	19.5226	7.7967	18.3828
Radius	6.5820	13.9685	7.6778	12.6105
Wrist	5.5849	15.7875	6.7924	15.4450
Hybrid	**5.4150**	**8.9073**	**6.0737**	**11.4836**

TABLE 3 | Comparison analysis on performance of different models.

	MAE	RMSE	Training times(s)
Model1	5.8324	10.9134	53,975
Model2	7.1478	15.2785	329
The proposed method	6.0737	11.4836	21,648

Bone Age Prediction

Based on the extracted ROIs, useful features could be learned to model a prediction model for bone age estimation. While before modeling a DL model for BAA, some issues should be paid attention. First, it is found that images of different ROIs have different qualities and brightness, e.g., the DIP and PIP regions are usually very dark, so the brightness of these ROIs could be further adjusted to enhance their performance in the subsequent modeling. The second issue is the image size of different ROIs. **Figure 6** gives out the statistical results of six ROIs' size parameters.

In **Figure 6**, the bounding box sizes of each class of ROI are visualized. Based on these two figures, it is seen that Wrist has the widest ROI, the other ROIs have relatively smaller width values. From **Figure 6B**, DIP, PIP, and MCP ROIs have smaller lengths than that of Radius, Ulna, and Wrist. Based on their mean values, the sizes of ROI bounding boxes could be unified in order to learn convolutional features conveniently. By making a comprehensive consideration of ROIs sizes in feature learning, those extracted ROIs could be set with a unified size. For example, resizing all extracted ROIs as 128*128 images, then input into the convolution layers for feature learning, as shown in **Figure 3**. Then, based on the Tensorflow platform, set the filters of convolutional layers as 3*3, and the filter in the pooling layers as 2*2. Considering the memory requirements and computation cost in the training process, set the learning rate as 0.0001 and 5,000 as the stop step. Aiming at the final BAA, the convolutional features are learned from each class of ROIs. Finally, a full-connection layer containing two layers is constructed to flatten the learned convolutional features, and output 100 features for each class of ROI. According to the proposed hybrid fast BAA method in **Figure 3**, all these learned features are combined as inputs of an ELM regressor. The final bone age prediction will be obtained from ELM with consideration of the interaction between features of all extracted ROIs.

Considering BAA is actually a kind of regression analysis, the generic regression metrics are introduced to evaluate the performance of BAA, e.g., mean absolute error (MAE) and root mean square error (RMSE) (Chai and Draxler, 2014). The definitions of these two typical metrics are presented as below.

$$MAE = \frac{1}{n}\sum_{j=1}^{n}\left|y_j - \hat{y}_j\right| \tag{18}$$

$$RMSE = \sqrt{\frac{1}{n}\sum_{j=1}^{n}\left(y_j - \hat{y}_j\right)^2} \tag{19}$$

where y_j and $\hat{y}_j$ denote the target bone age and predicted ones; and n is the number of test data samples. To compare the performance of the proposed method on the BAA study, here features of each ROI are considered for bone age prediction directly. The results of all models are presented in **Table 2**.

From the results in **Table 2**, some conclusions can be found. First, by using the features learned from each ROI to predict bone age independently, Wrist has the best performance. This implies that Wrist as the major carpal bone region can represent better characteristics related to bone age development. By combining features from all ROIs, including phalangeal and carpal bones regions, the hybrid BAA performance can be improved compared with independent predictions.

On the other hand, the proposed method can be studied via comparison with conventional models. For example, to study the influence of ROIs extraction, a model based on CNN without ROIs extraction is constructed, denoted as Model1. For studying the effectiveness of convolutional features, a model based on ELM directly is constructed, denoted as Model2. Their performances are presented in **Table 3**.

From the results of **Table 3**, some further studies could be implemented. It is seen that, among these three models, Model2 (full ELM) has the fast learning speed, but its performance is worst due to no deep features are learned in the training process. Model1 performs the best accuracy; however, it cost a lot on the iterative computation and learning features of a whole radiograph without ROIs extraction. Compared with these two, the proposed method could achieve good performance with a relatively lower cost, since it reduces the computation complexity of feature learning in only several ROIs as well as makes use of ELM's fast learning ability. Therefore, summarizing all the results above, it is concluded that the proposed method could realize both effectiveness and efficiency in developing a good BAA system for business requirements.

CONCLUSION

To realize fast and valid feature learning for BAA study, based on traditional TW-based methods, this paper proposed a hybrid model combining deep convolutional features learning and fast ELM algorithms. First, faced with real hand-wrist radiographs, this paper introduced several necessary preprocessing steps, such as background removal, orientation, and useful ROIs extraction

and annotations. Two kinds of ROIs are mainly considered in this paper for BAA study, such as phalangeal and carpal bone regions. Then, extracted ROIs are resized uniformly and input to a multiple-layers convolution network for learning useful features for predicting bone age. Finally, combining the convolutional features of all ROIs, an ELM regression model is constructed to fast predict the bone age. Experiments based on data from RSNA are implemented, the comparable discussion is valid, the proposed hybrid is feasible and effective to obtain good performance on the BAA study.

DATA AVAILABILITY STATEMENT

Publicly available datasets were analyzed in this study. This data can be found here: https://www.rsna.org/education/ai-resources-and-training/ai-image-challenge/rsna-pediatric-bone-age-challenge-2017.

AUTHOR CONTRIBUTIONS

Conceptualization, LG and JW; methodology, JT; writing—original draft preparation, LG and JW.; writing—review and editing, JT and YC.

FUNDING

The research is supported by the Scientific Research Fund of Beijing Rehabilitation Hospital, Capital Medical University (No. 2019-012).

REFERENCES

Chai, T., and Draxler, R. R. (2014). Root Mean Square Error (RMSE) or Mean Absolute Error (MAE)? - Arguments against Avoiding RMSE in the Literature. *Geosci. Model. Dev.* 7 (3), 1247–1250. doi:10.5194/gmd-7-1247-2014

Chen, M. (2016). "Automated Bone Age Classification with Deep Neural Networks," in *Technical Report* (USA: Stanford University).

Creo, A. L., and Schwenk, W. F. (2017). Bone Age: a Handy Tool for Pediatric Providers. *Pediatrics* 140 (6), e20171486. doi:10.1542/peds.2017-1486

Girshick, R. (2015). "Fast R-Cnn," in Proceedings of the IEEE international conference on computer vision, Santiago, Chile, Dec. 2015 (IEEE), 1440–1448. doi:10.1109/iccv.2015.169

Huang, G. B., Zhou, H., Ding, X., and Zhang, R. (2011). Extreme Learning Machine for Regression and Multiclass Classification. *IEEE Trans. Syst. Man. Cybern B Cybern* 42 (2), 513–529. doi:10.1109/TSMCB.2011.2168604

Huang, G. B., Zhu, Q. Y., and Siew, C. K. (2004). "Extreme Learning Machine: a New Learning Scheme of Feedforward Neural Networks," in Proceedings of the 2004 IEEE international joint conference on neural networks (IEEE Cat. No. 04CH37541), Budapest, Hungary, July 2004 (IEEE), 985–990.

Huang, G. B., Zhu, Q. Y., and Siew, C. K. (2006). Extreme Learning Machine: Theory and Applications. *Neurocomputing* 70 (1-3), 489–501. doi:10.1016/j.neucom.2005.12.126

Huang, H., Liu, F., Zha, X., Xiong, X., Ouyang, T., Liu, W., et al. (2018). Robust Bad Data Detection Method for Microgrid Using Improved ELM and DBSCAN Algorithm. *J. Energ. Eng.* 144 (3), 04018026. doi:10.1061/(asce)ey.1943-7897.0000544

Kaur, B., Sharma, M., Mittal, M., Verma, A., Goyal, L. M., and Hemanth, D. J. (2018). An Improved Salient Object Detection Algorithm Combining Background and Foreground Connectivity for Brain Image Analysis. *Comput. Electr. Eng.* 71, 692–703. doi:10.1016/j.compeleceng.2018.08.018

Kim, J. R., Shim, W. H., Yoon, H. M., Hong, S. H., Lee, J. S., Cho, Y. A., et al. (2017). Computerized Bone Age Estimation Using Deep Learning Based Program: Evaluation of the Accuracy and Efficiency. *Am. J. Roentgenology* 209 (6), 1374–1380. doi:10.2214/ajr.17.18224

Kim, S., Ji, Y., and Lee, K. B. (2018). "An Effective Sign Language Learning with Object Detection Based ROI Segmentation," in Proceeding of the 2018 Second IEEE International Conference on Robotic Computing (IRC), Laguna Hills, CA, USA, 2018-January (IEEE), 330–333. doi:10.1109/irc.2018.00069

Lee, H., Tajmir, S., Lee, J., Zissen, M., Yeshiwas, B. A., Alkasab, T. K., et al. (2017). Fully Automated Deep Learning System for Bone Age Assessment. *J. Digit Imaging* 30 (4), 427–441. doi:10.1007/s10278-017-9955-8

Lee, K. C., Lee, K. H., Kang, C. H., Ahn, K. S., Chung, L. Y., Lee, J. J., et al. (2021). Clinical Validation of a Deep Learning-Based Hybrid (Greulich-Pyle and Modified Tanner-Whitehouse) Method for Bone Age Assessment. *Korean J. Radiol.* 22, 2017–2025. doi:10.3348/kjr.2020.1468

Manzoor Mughal, A., Hassan, N., and Ahmed, A. (2014). Bone Age Assessment Methods: A Critical Review. *Pak J. Med. Sci.* 30 (1), 211–215. doi:10.12669/pjms.301.4295

McNitt-Gray, M. F., Pietka, E., and Huang, H. K. (1992). Image Preprocessing for a Picture Archiving and Communication System. *Invest. Radiol.* 27 (7), 529–534. doi:10.1097/00004424-199207000-00011

Ratib, O., Ligier, Y., Appel, R., and Jean, R. (1991). *PAPYRUS: A Portable Image File Format[M]. Picture Archiving and Communication Systems (PACS) in Medicine*. Berlin, Heidelberg: Springer, 91–94. doi:10.1007/978-3-642-76566-7_12

Ritter, F., Boskamp, T., Homeyer, A., Laue, H., Schwier, M., Link, F., et al. (2011). Medical Image Analysis. *IEEE pulse* 2 (6), 60–70. doi:10.1109/mpul.2011.942929

RSNA (2017). *RSNA Pediatric Bone Age Challenge*. Available From: https://www.rsna.org/education/ai-resources-and-training/ai-image-challenge/rsna-pediatric-bone-age-challenge-2017.

Sermanet, P., and LeCun, Y. (2011). "Traffic Sign Recognition with Multi-Scale Convolutional Networks," in Proceedings of the 2011 International Joint Conference on Neural Networks, San Jose, CA, USA, 2011-July (IEEE), 2809–2813. doi:10.1109/ijcnn.2011.6033589

Shah, N., Khadilkar, V., Lohiya, N., Prasad, H. K., Patil, P., Gondhalekar, K., et al. (2021). Comparison of Bone Age Assessments by Gruelich-Pyle, Gilsanz-Ratib, and Tanner Whitehouse Methods in Healthy Indian Children. *Indian J. Endocrinol. Metab.* 25 (3), 240–246. doi:10.4103/ijem.IJEM_826_20

Son, S. J., Song, Y., Kim, N., Do, Y., Kwak, N., Lee, M. S., et al. (2019). TW3-based Fully Automated Bone Age Assessment System Using Deep Neural Networks. *IEEE Access* 7, 33346–33358. doi:10.1109/access.2019.2903131

Spampinato, C., Palazzo, S., Giordano, D., Aldinucci, M., and Leonardi, R. (2017). Deep Learning for Automated Skeletal Bone Age Assessment in X-ray Images. *Med. image Anal.* 36, 41–51. doi:10.1016/j.media.2016.10.010

Tang, Z., Zhao, G., and Ouyang, T. (2021). Two-phase Deep Learning Model for Short-Term Wind Direction Forecasting. *Renew. Energ.* 173, 1005–1016. doi:10.1016/j.renene.2021.04.041

Thodberg, H. H., Kreiborg, S., Juul, A., and Pedersen, K. D. (2008). The BoneXpert Method for Automated Determination of Skeletal Maturity. *IEEE Trans. Med. Imaging* 28 (1), 52–66. doi:10.1109/TMI.2008.926067

Wu, W., and Zheng, B. (2020). Improved Recurrent Neural Networks for Solving Moore-Penrose Inverse of Real-Time Full-Rank Matrix. *Neurocomputing* 418, 221–231. doi:10.1016/j.neucom.2020.08.026

Xu, Y., Mo, T., Feng, Q., Zhong, P., Lai, M., Eric, I., et al. (2014). "Deep Learning of Feature Representation with Multiple Instance Learning for Medical Image Analysis," in Proceeding of the 2014 IEEE international conference on acoustics, speech and signal processing (ICASSP), Florence, ItalyMay-2014 (IEEE), 1626–1630. doi:10.1109/icassp.2014.6853873

Yan, K., Wang, X., Lu, L., and Summers, R. M. (2018). DeepLesion: Automated Mining of Large-Scale Lesion Annotations and Universal Lesion Detection with Deep Learning. *J. Med. Imaging (Bellingham)* 5 (3), 036501. doi:10.1117/1.JMI.5.3.036501

Yu, K., Jia, L., Chen, Y., and Xu, W. (2013). Deep Learning: Yesterday, Today, and Tomorrow. *J. Comput. Res. Dev.* 50 (9), 1799.

Yuan, X., Li, D., Mohapatra, D., and Elhoseny, M. (2018). Automatic Removal of Complex Shadows from Indoor Videos Using Transfer Learning and Dynamic Thresholding. *Comput. Electr. Eng.* 70, 813–825. doi:10.1016/j.compeleceng.2017.12.026

Conflict of Interest: The authors declare that the research was conducted in the absence of any commercial or financial relationships that could be construed as a potential conflict of interest.

Publisher's Note: All claims expressed in this article are solely those of the authors and do not necessarily represent those of their affiliated organizations, or those of the publisher, the editors and the reviewers. Any product that may be evaluated in this article, or claim that may be made by its manufacturer, is not guaranteed or endorsed by the publisher.

frontiers in Energy Research

BRIEF RESEARCH REPORT
published: 15 February 2022
doi: 10.3389/fenrg.2022.813643

Study of Capacitive Coupling Sensor Fused With High Voltage XLPE Cable Joint

Rong Xia[1], Yang Zhao[2], Benhong Ouyang[1], Yuli Wang[1], Chunhua Fang[3] and Yao Xu[3]*

[1]State Key Laboratory of Power Grid Environmental Protection, China Electric Power Research Institute Co., Ltd., Wuhan, China, [2]Cable Branch of State Grid Beijing Electric Power Co., Ltd., Beijing, China, [3]College of Electrical Engineering and New Energy, Three Gorges University, Yichang, China

A capacitive coupling sensor for partial discharge detection with the fusion of high voltage XLPE cable joint is designed in this paper. The sensor is to address partial discharge signals leading to transmission attenuation and external interference causing poor field detection sensitivity. First, a coaxial waveguide transmission model was established of high-frequency electrical signals in the body and joint. The result showed that the signal transmission attenuation was minimized while the sensor electrodes were closely attached to the outer semi-conductive layer of the body. Second, the equivalent circuit model was constructed of the capacitive coupling sensor fused with the 110 kV straight passing joint. The specific installation location, main structure size, detection bandwidth, and sensitivity of the sensor in the joint area were determined, which was to maximize the coupling output signal amplitude and transfer function amplitude. Finally, a lightning surge voltage test was carried out with the integration of the fusion of the joint voltage thermal cycling. Simulation and measurement show the following: while the sensor is installed in the cable metal sleeve break and the electrodes are closed to the overall semi-conductive layer, there is excellent performance for partial discharge detection in the frequency range of 1–300 MHz, with a sensitivity of 5 pC.

Keywords: partial discharge detection, capacitive coupling, fusion, sensitivity, frequency band range

OPEN ACCESS

Edited by:
Yahui Zhang,
Yanshan University, China

Reviewed by:
Shuo Jin,
Hubei University of Technology, China
Li Cai,
Wuhan University, China

****Correspondence:***
Chunhua Fang
45946866@qq.com

Specialty section:
This article was submitted to Smart Grids, a section of the journal Frontiers in Energy Research

Received: *12 November 2021*
Accepted: *05 January 2022*
Published: *15 February 2022*

Citation:
Xia R, Zhao Y, Ouyang B, Wang Y, Fang C and Xu Y (2022) Study of Capacitive Coupling Sensor Fused With High Voltage XLPE Cable Joint. Front. Energy Res. 10:813643. doi: 10.3389/fenrg.2022.813643

INTRODUCTION

The power grid may have abnormal operating events including insulation breakdown and line shutdown if the high voltage cable insulation defects cannot be detected in time (Zhou et al., 2014; Fang, 2018). Of the operational faults of high-voltage cable lines, 70% are caused by the joint according to statistics (Luo et al., 2003; Li et al., 2004; Jiang, 2007). Partial discharge is one of the main factors causing insulation deterioration and triggering joint faults. Therefore, partial discharge detection is an important technical means to discover potential insulation defects of high voltage XLPE cable joint in an efficient manner.

Researchers had developed various principles of partial discharge detection methods for a series of physicochemical phenomena accompanying the partial discharge (Liang, 2019). There are mainly electromagnetic coupled, capacitance coupling, ultrasonic, and UHF methods (Meng et al., 2015; Wang, 2017; Shu et al., 2018; He J. et al., 2020). Meanwhile, many achievements have been made in cables and accessories in the transmission law of PD

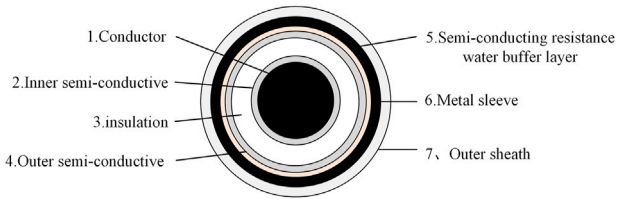

FIGURE 1 | Schematic cross-sectional structure of the body of the 110 kV cable.

(partial discharge) signals, signals spectrum identification, and PD source location (Chen, 2017; Shen, 2018; Wang et al., 2019; Wu et al., 2020). However, PD detection still faces the problems of weak signals, complex and variable waveforms, and susceptibility to external electromagnetic interference (Zhao, 2018; Xie et al., 2019). These problems hamper the accurate sensing and effective identification of PD signals.

Many efforts have been made to solve the problem of significant attenuation of PD signals in transmission. A capacitive coupling sensor with a response band of 500 MHz built into the body was developed (Tang et al., 2008). A simulated field defect PD test using a patch type partial discharge sensor built into both sides of the joint shield was conducted (Luo et al., 2018). The experiments could obtain a good PD detection effect and better shield the external interference. A built-in partial discharge detection system based on a differential capacitance sensor was designed in reference (He N. et al., 2020). The detection system had a good detection effect on the three types of defect models constructed (Yang et al., 2021a; Yang et al., 2021b). The built-in PD sensor is designed and optimized by using the integrated model of the built-in sensor in the cable intermediate joint (Ge, 2016). Several built-in sensor capacitance coupling charged correction technologies were studied and found that based on the equivalent circuit simulation of built-in cable capacitance coupling sensor of charged highest accuracy calibration method (Wang et al., 2017).

The sensor needs to be close to the outer semi-conducting layer of the cable to get a better coupling effect because the semi-conductive layer of the cable will accelerate the attenuation of PD signals. Therefore, this study designs a capacitive coupling sensor fused with high voltage XLPE cable joint, based on the principle of capacitive coupling, and combining with the characteristics of high partial discharge at the joint. The corresponding relationship was analyzed between the circuit components and the physical structure by establishing the equivalent circuit model of the built-in coupling sensor. The influence of the circuit component parameters on the detection performance and frequency response characteristics of the sensor was calculated. The ring electrode width and the insulating pad thickness were determined by combining the numerical calculation and experimental test results. The installation position and structural dimensions of the sensor were optimized. Experiments were conducted to verify the performance of the fused sensor in terms of safety and partial discharge detection.

HIGH VOLTAGE XLPE CABLE JOINT PARTIAL DISCHARGE SIGNALS COUPLING METHOD AND SENSOR DESIGN

Design of Partial Discharge Signal Coupling

The internal structure of the cable joint is much more complex than that of the cable body, therefore, taking the cable model YJLW03-Z 64/110 1 × 800 as an example, high frequency partial discharge signal is analyzed with distance transmission in the cable body. Its structure is shown in **Figure 1**.

The high frequency electrical signals in high voltage XLPE cable can be considered as a coaxial waveguide in the form of a uniform transmission line. Its equivalent model is shown in **Figure 1**.

The series impedance in **Figure 2** can be expressed as:

$$Z(\omega) = \frac{1}{2\pi r_1}\sqrt{\frac{j\omega\mu_0}{\sigma_1}} + j\omega\frac{\mu_0}{2\pi}\ln\left(\frac{r_6}{r_1}\right) + \frac{1}{2\pi r_6}\sqrt{\frac{j\omega\mu_0}{\sigma_6}} \quad (1)$$

where r_1 is the radius of the first layer structure (conductor) of the cable body from inside out, r_6 is the inner radius of the sixth layer structure (metal sleeve), σ_1 is the conductivity of copper, σ_6 is the conductivity of aluminum, and μ_0 is the permeability in vacuum.

The cable parallel admittance consists of insulating layer and semi-conductive layer, which can be expressed as:

$$Y(\omega) = 1\Big/\sum_{2}^{5}\frac{1}{Y_i(\omega)} \quad (2)$$

$$Y_i(\omega) = j\omega\frac{2\pi\varepsilon_0\varepsilon_i^*}{\ln(r_i/r_{i-1})} \quad (3)$$

where

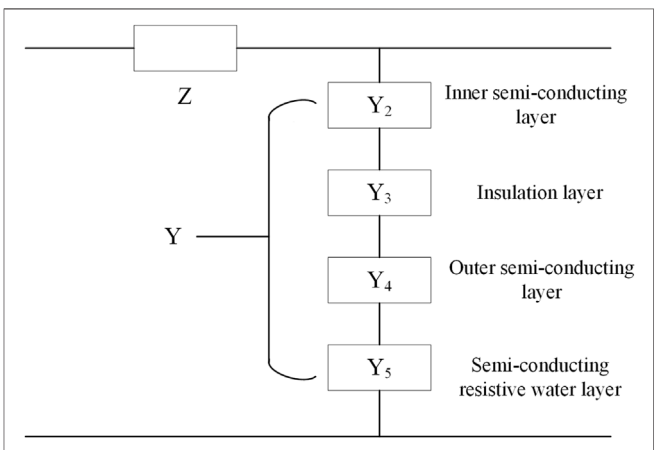

FIGURE 2 | 110 kV cable uniform transmission line model.

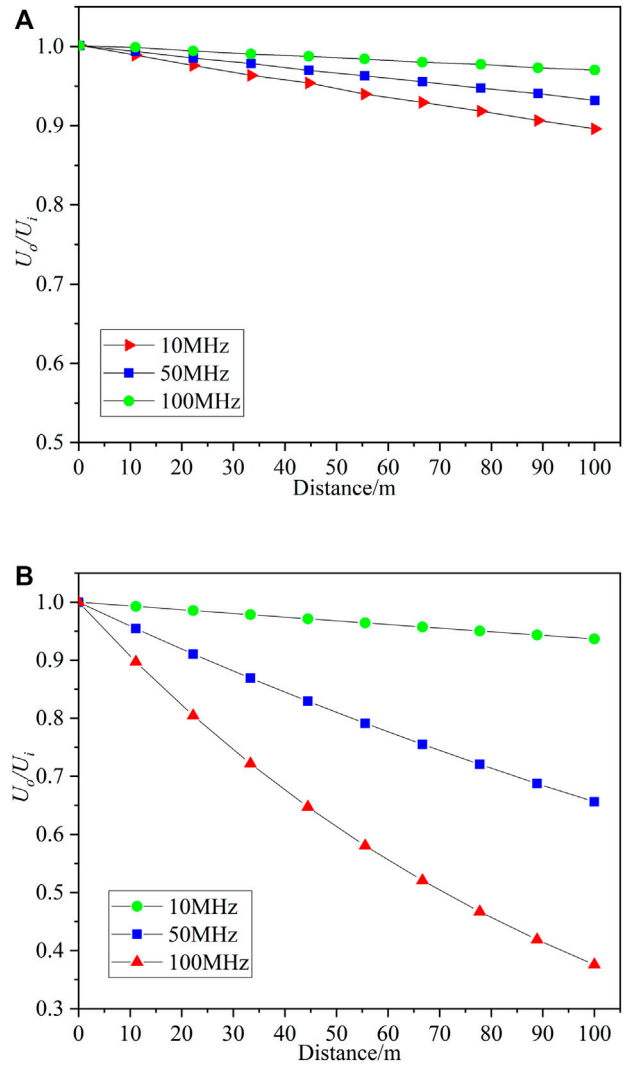

FIGURE 3 | Variation of transmission attenuation of signal amplitude at different frequencies with axial distance of high-voltage cable. **(A)** Without semi-conductive layer. **(B)** With semi-conductive layer.

ε_0 is the vacuum dielectric constant with a value of 8.85×10^{-12} F/m,

$\varepsilon_i^* = \varepsilon_i^{'} - j\varepsilon_i^{''}$ is the relative complex dielectric coefficient of the structural material of layer i,

$Y_i(\omega)$ is the parallel admittance of the structure of layer i.

The value of $Y_i(\omega)$ is related to the relative complex dielectric constant of the structural material of the layer and the internal and external radii of the structural layer.

The propagation coefficient of the uniform transmission line model for high voltage XLPE cable can be deduced from the series impedance and parallel admittance expressions as:

$$\gamma(\omega) = \sqrt{Z(\omega) \cdot Y(\omega)} = \alpha(\omega) + j\beta(\omega) \tag{4}$$

where

α is the attenuation coefficient, and β is the phase constant.

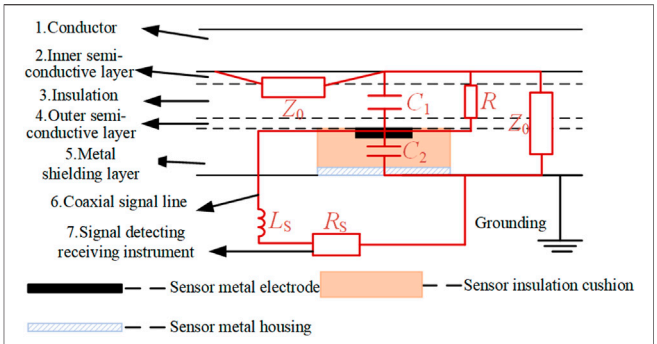

FIGURE 4 | Schematic of the capacitive coupling principle of the local amplifier signal in the connector.

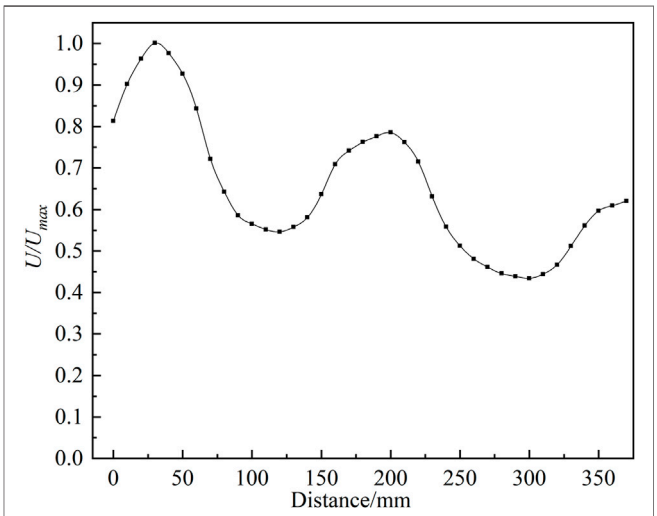

FIGURE 5 | Average values of coupling signals for different installation positions of sensors in the long end zone of the protection tail pipe.

ATP-EMTP software was used to establish a uniform transmission model of high voltage XLPE cable, which was to investigate the influences of the inner and outer semi-conductive layer on the transmission characteristics of high frequency signals. Sine waves U_i were injected from the beginning of the model ($x = 0$) with the same amplitude and frequencies of 10, 50, and 100 MHz. The variation of the U_i amplitude attenuation values was calculated and analyzed with axial distance transmission in the model with or without the inner and outer semi-conducting structural layers. The result is shown in **Figure 3**.

Signal amplitude decays faster than low frequency signals with the increase in transmission distance for high frequency signals, which can be seen from **Figure 3**. The signal amplitude decay is faster than the case without considering the influence of the semi-conductive layer while the influence of the semi-conductive layer is considered. The higher the frequency, the greater the influence of the semi-conductive layer on the signal decay.

The coupling of the PD signals is achieved by the sensor through the principle of capacitive voltage division. The equivalent circuit is shown in **Figure 4**.

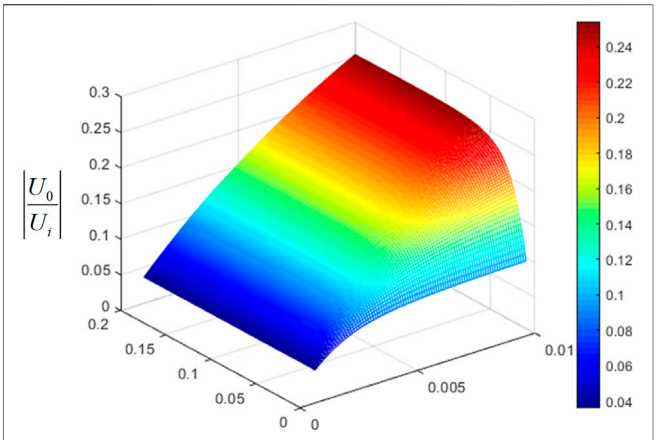

FIGURE 6 | Variation curve of transfer function amplitude with electrode width and insulation pad thickness.

where Z_0 is the cable characteristic impedance, C_1 is the coupling capacitance between the cable core and the metal enclosure of the sensor, C_2 is the stray capacitance between the metal electrode of the sensor and the metal enclosure, R is the cable insulation resistance of the joint area, L_s is the stray inductance on the coaxial signal cable, and R_S is the coupling output resistance.

Selection of Sensor Location

A 110-kV combined prefabricated straight passing joint is used as the research object. The protection tail pipe of high voltage XLPE cable joint is divided into a long end and a short end. The sensor can only be installed on the break side of the metal enclosure due to the short end area has limited space.

To determine the appropriate installation position of the sensor in the long end area of the protection liner, the following numerical calculation model was established: The joint center to the long end of 515 mm was taken as the origin. From the origin, the sensor was moved with a step of 10 mm from the origin. The excitation source was injected at the short end of the joint with the amplitude of 1 A and the frequencies of 37, 105, and 148 MHz, respectively. The average value of the voltage coupled to the sensor under the action of the three frequency excitation sources at the same installation position is shown in **Figure 5**.

The amplitude of the coupling signal is not monotonically decaying with increasing distance which can be seen from **Figure 5**. The sensors in both long end and short end areas are chosen to be installed at the metal enclosure break of the body considering the factors of sensor coupling signal amplitude attenuation, installation convenience, and fusion reliability at various locations.

Design of Sensor Structure

The transfer function of the sensor in the frequency domain is given by:

$$H(\omega) = \frac{U_i(\omega)}{U_0(\omega)} = \frac{j\omega RR_s(C_1 + C_2) - \omega^2 L_s R(C_1 + C_2) + j\omega L_s + R + R_s}{j\omega C_1 RR_s + R_s} \tag{5}$$

As can be seen from **Equation 5**, while frequency is low, R and R_S mainly affect the power frequency voltage division. So, the power frequency high voltage is mainly in R, and the detection system only has a small voltage drop. The main influence on the transfer function is determined by the ratio of C_1 and C_2 for the high frequency PD signal. C_1 and C_2 are correlated with the sensor structure parameters, electrode width, and insulation pad thickness. The relationship can be expressed as:

$$C_1 = \frac{2\pi\varepsilon_0\varepsilon_r W}{\ln(D_1/D_0)} \tag{6}$$

$$C_2 = \frac{2\pi\varepsilon_0\varepsilon_{r2}\cdot W}{\ln((r_4 + d_1 + d)/(r_4 + d_1))} \tag{7}$$

where

ε_0 is the vacuum dielectric constant, ε_{r1} is the relative dielectric constant of the insulation material, being 2.3 for XLPE, D_1 is the overall diameter of the cable insulation layer, D_2 is the inner diameter of the cable insulation layer, W is the sensor electrode width, ε_{r2} is the relative dielectric constant of the insulation pad layer, and the insulation pad layer uses silicone rubber material with relative dielectric constant 2.6,

d is the thickness of the insulation pad layer,

d_1 is the sensor electrode thickness with a value of 1 mm, r_4 is the overall diameter of the semi-conducting layer.

Equations 6 and **7** are taken into **Equation 5**. The stray inductance L_s takes the value of 10 mH, and the frequency is taken as the center frequency of the designed detection band. The above parameters are taken into the transfer function to obtain

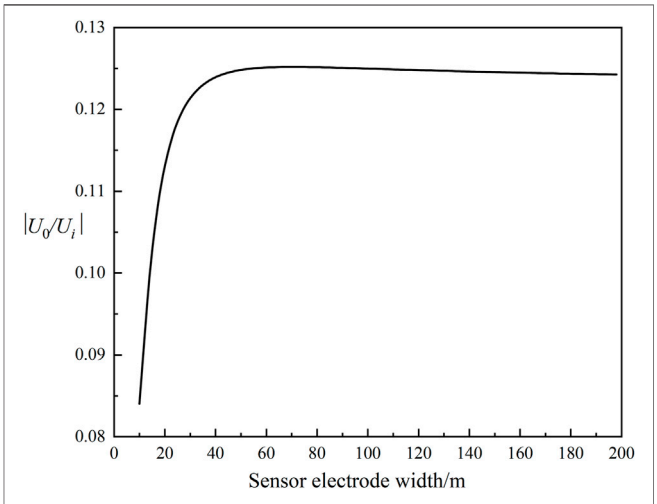

FIGURE 7 | Variation curve of transfer function amplitude with electrode width.

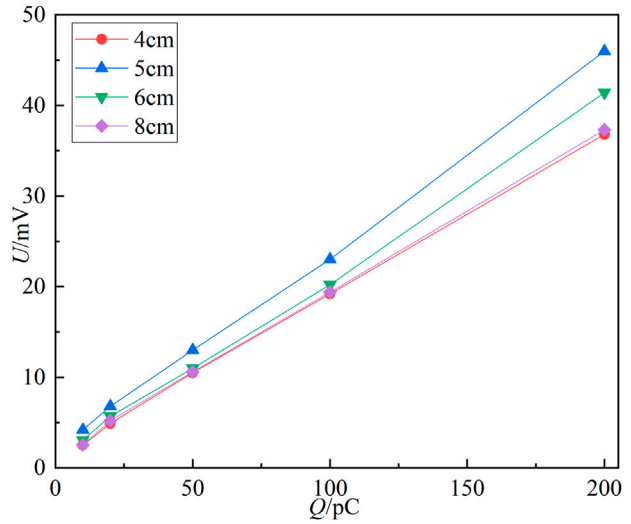

FIGURE 8 | Impulse response curves of electrode sensors with different widths.

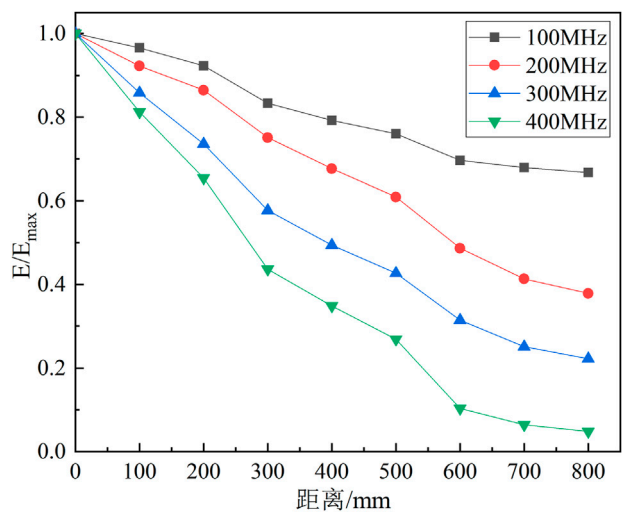

FIGURE 9 | Four kinds of frequency variable electromagnetic field in the joint electric field component with distance transmission attenuation change curve.

the relationship between amplitude change, sensor electrode width, and insulation layer thickness, as shown in **Figure 6**.

The greater the thickness of the sensor insulation pad layer and the transfer function amplitude, the better the detection performance, which can be seen from **Figure 5**. While the thickness of the insulation pad layer is less than 4 mm, the sensor electrode width has less influence on the transfer function amplitude. While the insulation pad layer thickness is greater than 4 mm, the sensor electrode width gradually increases the influence on the transfer function amplitude. The sensor shell is designed to be at the same level as the cable metal sleeve and the

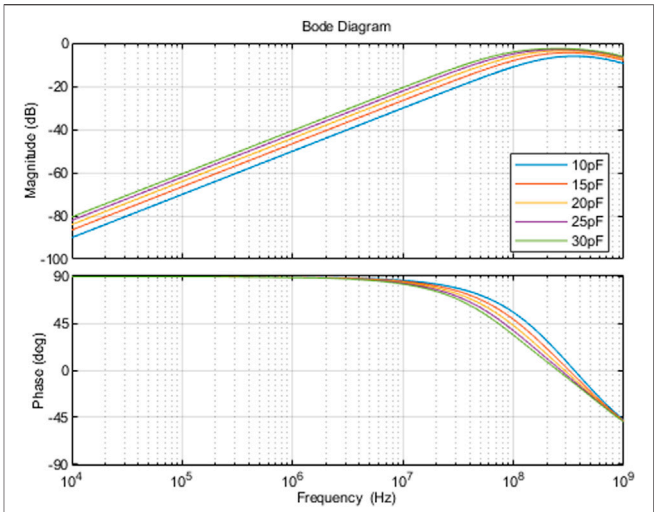

FIGURE 10 | Frequency response characteristic curve of the sensor with different coupling capacitance.

thickness of the insulation pad layer is 6 mm, which is to ensure the installation reliability and is for facilitating its lap with the cable metal sleeve and achieving equipotential to shield and protect the sensor.

The transfer function amplitude and sensor electrode width are obtained while the thickness of the sensor insulation pad layer is 6 mm, as shown in **Figure 7**. The transfer function amplitude remains relatively high while the sensor electrode width is between 40 and 80 mm.

The sensor was designed with electrode widths of 40, 50, 60, and 80 mm to further determine the optimal width of the circular electrode of the capacitive coupling sensor. The same square wave signal was injected at one end of the cable to simulate the partial discharge source. The response signals of the sensor were tested under four different electrode widths, with the results shown in **Figure 8**. The signal works best while the electrode width is 50 mm. So, the sensor electrode width is designed to be 50 mm.

STUDY OF SENSOR KEY PERFORMANCE

Setting of Sensor Bandwidth

Ansoft HFSS software was used to analyze the electric field component distribution of electromagnetic waves with frequency of 100, 200, 300, and 400 MHz in the joint, which was to determine the design range of the sensor detection band.

The higher the signal frequency, the faster the signal decays with transmission distance increasing as can be seen from **Figure 9**. While the frequency reaches 400 MHz and the distance from the signal source is above 600 mm, the signal will decay to less than 10% of the initial value. Therefore, the sensor bandwidth is set to (1–300) MHz to strike a balance between the signal amplitude and the detection bandwidth.

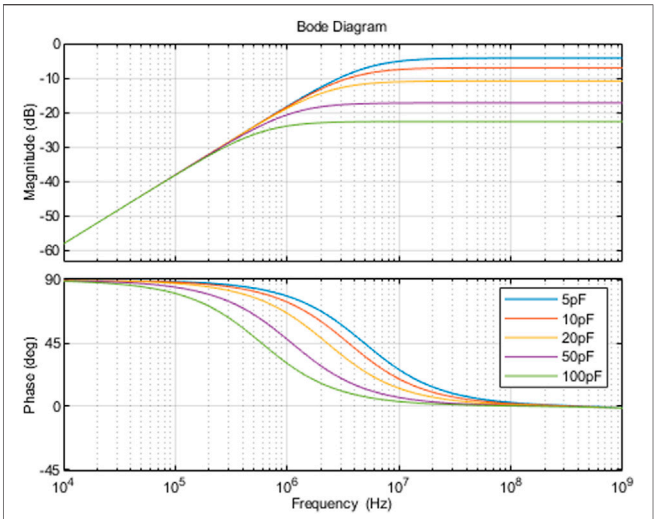

FIGURE 11 | Frequency response with different stray capacitance.

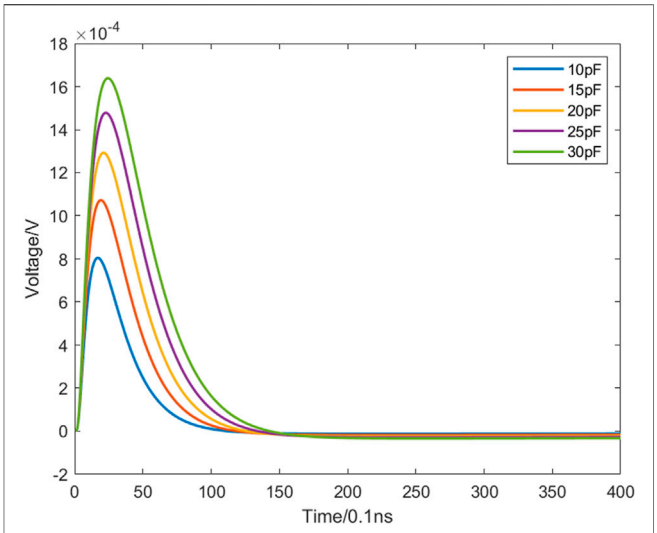

FIGURE 13 | Effect of C_1 on sensor detection performance.

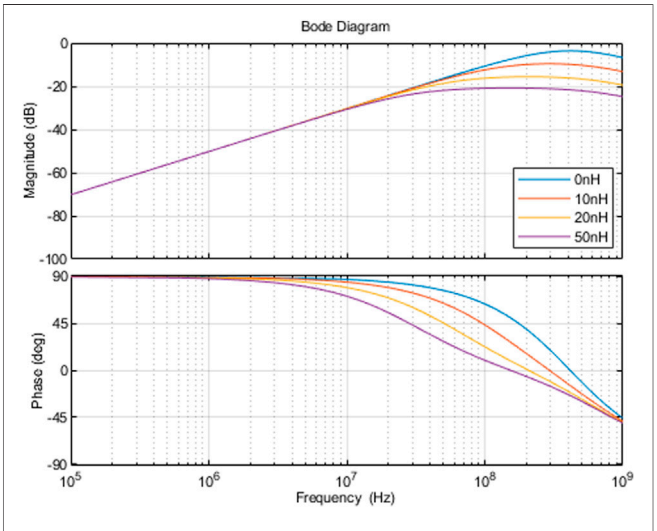

FIGURE 12 | Frequency response with different stray inductance.

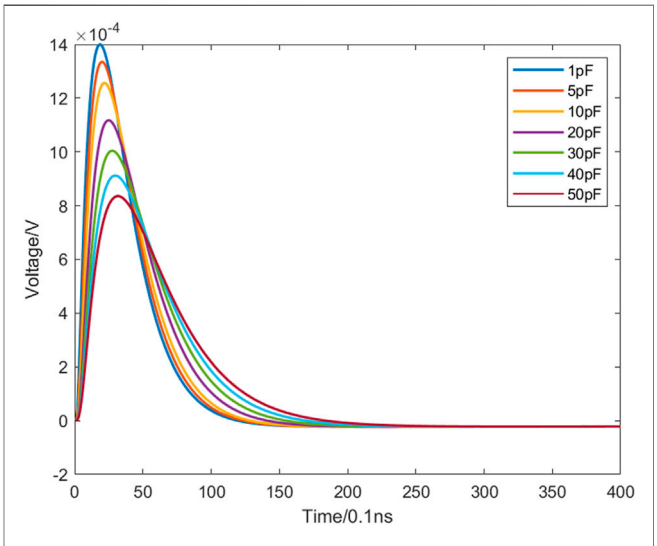

FIGURE 14 | Effect of C_2 on sensor detection performance.

Analysis of Sensor Frequency Response Characteristics

The values of C_2, R_S, and L_s in the circuit were set to 10, 50, and 10. Respectively, C_1 is increased from 10 to 30. Calculate the frequency response characteristic curve of the built-in capacitive coupling sensor under different coupling capacitances, as shown in **Figure 10**.

C_1 has a relatively significant impact on the sensor frequency response. While C_1 increases, the sensor frequency response gain also increases. But the increase will be reduced. While the frequency is less than 100 MHz, the effect of C_1 on the frequency response of the sensor decreases as the frequency increases while the frequency is greater than 100 MHz. Therefore, C_1 should be kept within an appropriate range.

C_2 was increased from 5 to 100 pF and other conditions remained the same. The frequency response characteristic curves of the built-in capacitively coupled sensor with different stray capacitance is calculated, as shown in **Figure 11**.

The stray capacitance C_2 has negligible effect on the sensor frequency response gain while the frequency is less than 300 kHz. However, as the frequency increases, while the frequency is more than 1 MHz, the increase of C_2 will greatly reduce the frequency response gain, which will weaken the sensor detection effect.

The stray inductance L_S was set to 0, 10, 20, and 50 nH, respectively, and kept other conditions constant. The frequency response characteristics of the built-in capacitively coupled sensor are shown in **Figure 12**.

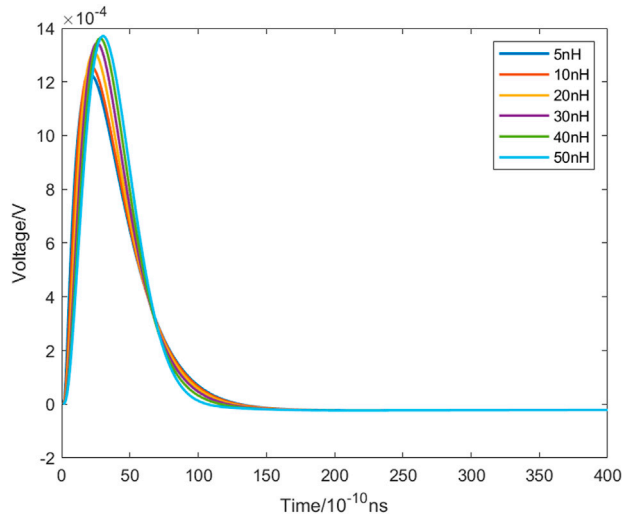

FIGURE 15 | Effect of L_s on sensor detection performance.

The effect of stray inductance L_S on the frequency response gain of the sensor is small, with the increase of frequency, the influence gradually increases, while the frequency is less than 20 MHz. The increase of L_s significantly reduces the frequency response gain, further weakening the detection ability while the frequency is more than 100 MHz.

Analysis of Sensor Signal Coupling Characteristics

The influence of C_1, C_2, and L_s circuit parameters on sensor detection effect was analyzed by observing the change of sensor output waveform.

The C_1 was gradually increased from 10 to 30 pF, and the values of other parameters remained unchanged. The output waveform corresponding to each capacitance value is shown in **Figure 13**. The amplitude of the waveform detected by the capacitance sensor increases significantly and the rise time of the waveform increases.

The C_2 was gradually increased from 1 to 50 pF with the values of other parameters unchanged. The detected waveform of the capacitive sensor is shown in **Figure 14**. As can be seen, the increase in C_2 results in a significant decrease in the amplitude of the waveform and an increase in the rise time of the waveform.

The value of L_s was gradually increased from 5 to 50 nH with the values of other parameters unchanged. The detected waveform of the capacitive sensor is shown in **Figure 15**.

The value of *Ls* has a smaller effect on the waveform amplitude detected by the capacitive sensor, after comparing to C_2. But as the value of stray inductance increases, the rise time increases and oscillations occur in the wave tail, which can have an impact on the detection accuracy of the sensor.

ELECTRICAL PERFORMANCE TEST OF HIGH-VOLTAGE CABLE JOINTS INCORPORATING CAPACITIVELY COUPLED SENSORS

Analysis of Sensor Signal Coupling Characteristics

The frequency sweep test of a 110-kV combined prefabricated straight passing joint with capacitive coupling sensor was carried out to analyze the frequency response characteristics of the sensor. The swept-frequency signal was injected from one end of the cable between the conductor and the metal shield, and the frequency range of the swept signal was set to 1 GHz. The spectrum analysis of the sensor-coupled swept signals was performed by Anglient9320B spectrum analyzer. The frequency response of the sensor is better within 300 MHz.

High frequency pulse signal injection tests were performed on the sensor under laboratory conditions to determine the ability of the sensor to couple signals. The sensor was mounted on the connector, and the signal generator output a square wave signal with a rising edge of 5 ns. A 10-pF capacitor was connected in series at the output, and a charge of 5 pC was injected into the cable end while the amplitude of the pulse square wave was 500 mV, the sensor can effectively couple the analog discharge pulse of 5 pC in the cable by comparing the amplitude of the signal and the baseband.

Thermal Cycling Voltage Test

The cable specimen consisted of a 6-m 110 kV cable with a prefabricated straight passing joint containing a capacitive coupling sensor. One segment of the specimen was bent into a U shape with a diameter of less than 25 (d + D) × 1.05. Heat the specimen by conductor current for at least 8 h and ensure that the conductor temperature exceeded the maximum temperature for normal cable operation for at least 2 h during each heating cycle (the actual temperature was maintained at 95–98°C). Next, the specimen was naturally cooled for at least 16 h until the conductor temperature was cooled to less than 30°C or cooled to within 15 K above ambient temperature, taking the higher of the two, but not higher than 45°C (the actual temperature was controlled at 22–32°C). The above experiments were referred to 12.4.6 in GB/T 18,890.1.

- Heating and cooling cycles 20 times
- Voltage applied to cable specimen $2U_0$
- The upper limit of AC voltage output 600 kV
- The upper limit of current output 20 A
- The upper limit of analog load current output in FKGB thermal cycle intelligent control system 5000 A
- Analog load current output step ±5 A
- Conductor temperature measurement accuracy ±0.5°C

The cable joint had good electrical performance while fused with the capacitive coupling sensor, and the joint and sensor had stable performance throughout the test, without breakdown phenomenon.

Lightning Surge Voltage Test

CDYH-4800 kV/960 kJ lightning surge voltage tested system; the purpose is to verify the sensor safety detection performance.

- The upper limit of lightning impulse voltage output ±4800 kV
- The upper limit of lightning impulse power 960 kJ

The shock voltages of positive and negative polarity are applied to the specimen during the test. The lightning surge voltage amplitude was 550 kV, with a wavefront time of 5 μs and a half-wave peak time of 54 μs. No damage was found to the connector or the sensor during or after the test.

CONCLUSION

1) The sensor is installed at the break in the metal sleeve of the cable and the electrode close to the outer semi-conductive layer because the overall semi-conductive layer of the cable can cause severe attenuation to high frequency signal transmission.
2) The frequency band of the sensor is designed at (1–300) MHz, while the frequency of the electromagnetic wave exceeds 300 MHz, the signal in the joint decays rapidly with the propagation distance.
3) The sensor electrode width is designed to be 50 mm, and the insulation layer thickness of 6 mm is achieved by the reliable installation of the sensor, which obtains a good signal coupling effect.
4) The sensor has a good response in the (1–300) MHz band range, and the local discharge signal detection sensitivity reaches 5 pC in the design of the sensor band response and sensitivity tests.
5) The joint and the sensor are unaffected by frequency voltage and lightning shock, and no damage is found in the connector body and the sensor after the field lightning shock tests.

DATA AVAILABILITY STATEMENT

The original contributions presented in the study are included in the article/Supplementary Material. Further inquiries can be directed to the corresponding author.

AUTHOR CONTRIBUTIONS

CF, BO, YZ, and RX conceived the idea and designed the experiments. CF and RX led the experiments. CF, BO, RX, and YW contributed to data analysis and interpretation. CF, YZ, YW, and YX wrote the paper. All authors read and approved the final manuscript.

FUNDING

This study received funding from research and application of key technologies of perceptual integration and edge enabling of high voltage cable lines in an urban power grid (Science and Technology Project No. 5500-202111118A-0-0-00 of State Grid Co., Ltd.). The funder was not involved in the study design, collection, analysis, interpretation of data, the writing of this article, or the decision to submit it for publication.

REFERENCES

Chen, T. (2017). "Research on Propagation of Partial Discharges in HV XLPE Cable System," (Beijing: North China Electric Power University). dissertation/master's thesis.

Fang, Y. (2018). "Method for Detecting Crimp Defects of Cable Joint Based on Temperature Measurement and its Application," (Chongqing: Chongqing University). dissertation/master's thesis.

Ge, Z. (2016). "Study on Partial Discharge Sensor of Intermediate Joint of High Voltage XLPE cable," (Beijing: North China Electric Power University). dissertation/master's thesis.

He, J., Tian, T., Song, X., Wang, H., Chen, R., and Zhu, X. (2020a). Research on Partial Discharge Identification Method of Switchgear Based on UHF Method. *High Voltage Apparatus* 56, 11. doi:10.13296/j.1001-1609.hva.2020.11.015

He, N., Ren, Z., Chen, P., Shi, L., Li, H., Wu, C., et al. (2020b). Research on Partial Discharge Characteristics of Typical Defects in XLPE cable. *Electr. Technol.* 13, 6. doi:10.19768/j.cnki.dgjs.2020.13.041

Jiang, P. (2007). Analysis and Assessment of the Breakdown Fault of Homemade XLPE Power Cables. *Electric Wire & Cable* 002, 1–5. doi:10.3969/j.issn.1672-6901.2007.02.001

Li, H., Zhou, Z., and Chen, P. (2004). Fault Analysis of 110 kV and above High Voltage XLPE cable System. *Electr. Equipment* 3 (08), 9–13.

Liang, Y. (2019). "On Online Measurement of the Power Cable's Partial Discharge," (Xi'an: Xi'an University of Electronic Science and technology). dissertation/master's thesis.

Luo, J., Qiu, Y., and Yang, L. (2003). Operation Fault Analysis of CLPE Power Cable above 10kV. *High Voltage Eng.* 06, 14–16. doi:10.13336/j.1003-6520.hve.2003.06.007

Luo, J., Wang, J., Gao, F., and Fang, J. (2018). Application of Built-In Partial Discharge Sensor in 110 kV cable Joint. *Electromechanical Inf.* 24, 46–47. doi:10.19514/j.cnki.cn32-1628/tm.2018.24.024

Meng, S., Wang, Y., Xia, R., and Yang, D. (2015). Online Correction of Partial Discharge On-Site Detection for Power Cables Based on Capacitance Coupling Method. *High Voltage Eng.* 41 (11), 3766–3774. doi:10.13336/j.1003-6520.hve.2015.11.034

Shen, C. (2018). "Design and Development of XLPE Cable Partial Discharge Data Analysis System Based on Feature Map and Recognition Technology," (Shanghai: Shanghai Jiao Tong University). dissertation/master's thesis.

Shu, B., Li, Y., Zhao, H., Xu, Y., Qian, Y., and Sheng, G. (2018). Design of a High-Frequency Current Sensor Used for Detection of Cable Partial Discharge. *Electr. automation* 40 (03), 105–108. doi:10.3969/j.issn.1000-3886.2018.03.031

Tang, J., Deng, Z., Gong, N., Zhang, X., and Wei, G. (2008). Performance Analysis of Inner Sensors Used for Partial Discharge Detection in cable Accessories. *J. Chongqing Univ.* 11 (07), 760–765. doi:10.11835/j.issn.1000-582x.2008.07.011

Wang, M. (2017). "Research on High Voltage Switchgear Partial Discharge On-Line Monitoring Based on Ultrasonic Sensor," (Guangzhou: South China University of Technology). dissertation/master's thesis.

Wang, T., Gu, X., Xu, Y., Xia, R., Shao, Y., and Ma, D. (2017). Research on Calibration Technology of XLPE cable Built-In Sensor for Detecting Partial Discharge. *High Voltage Apparatus* 53 (06), 129. doi:10.13296/j.1001-1609.hva.2017.06.022

Wang, X., Zhou, K., Xie, M., Huang, Y., Rao, X., and Li, R. (2019). Research on Partial Discharge Source Location for Power Cables Based on Time Reversal Phase Method. *Power Syst. Tech.* 44 (02), 783–790. doi:10.13335/j.1000-3673.pst.2019.0434

Wu, S., Zheng, S., Zhong, A., Dai, W., and Sohail, S. (2020). Location Method of Multiple Partial Discharges Sources in Substation Space by UHF Method Based on Intelligent Clustering Algorithm. *High Voltage Eng.* 46 (12), 4309–4318. doi:10.13336/j.1003-6520.hve.20200787

Xie, J., Liu, Y., Liu, L., Liu, L., Tang, G., and Li, X. (2019). A Partial Discharge Signal Denoising Method Based on Adaptive Weighted Framing Fast Sparse Representation. *Proc. CSEE* 39 (21), 6428–6439. doi:10.13334/j.0258-8013.pcsee.190142

Yang, N., Yang, C., Wu, L., Shen, X., Jia, J., Li, Z., et al. (2021b). Intelligent Data-Driven Decision-Making Method for Dynamic Multi-Sequence: An E-Seq2Seq Based SCUC Expert System. *IEEE Trans. Ind. Inf.*, 1. doi:10.1109/TII.2021.3107406

Yang, N., Yang, C., Xing, C., Ye, D., Jia, J., Chen, D., et al. (2021a). Deep Learning-based SCUC Decision-making: An Intelligent Data-driven Approach with Self-learning Capabilities. *IET Gener. Transm. Distrib.*, 1–12. doi:10.1049/gtd2.12315

Zhao, Y. (2018). "Partial Discharge Signal Denoising of Synchronous Wavelet Transform Based on Iterative Layered Threshold," (Wuhan: Wuhan University of Science and Technology). dissertation/master's thesis.

Zhou, Y., Zhou, J., Liu, R., Chen, Z., and Zhang, Y. (2014). Key Technical Analysis and Prospect of High Voltage and Extra-high Voltage Power Cable. *High Voltage Eng.* 40 (9), 2593–2612. doi:10.13336/j.1003-6520.hve.2014.09.001

Conflict of Interest: Authors RX, BO and YW are employed by the State Key Laboratory of Power Grid Environmental Protection, China Electric Power Research Institute Co., Ltd., author YZ is employed by Cable branch of State Grid Beijing Electric Power Co., Ltd.

The remaining authors declare that the research was conducted in the absence of any commercial or financial relationships that could be construed as a potential conflict of interest.

frontiers in Energy Research

ORIGINAL RESEARCH
published: 21 February 2022
doi: 10.3389/fenrg.2022.840967

A Study of Protection Method for Hybrid Multiterminal UHVDC Lines Based on CEEMDAN–Teager Energy Operator

Chao Xing[1,2], *Long Wang*[2,3], *Guihong Bi*[3], *Shilong Chen*[3], *Jingye Gao*[2,3] *and Yanbo Che*[1]*

[1]Key Laboratory of Smart Grid of Education Ministry, Tianjin University, Tianjin, China, [2]Electric Power Research Institute of Yunnan Power Grid Co., Ltd., Kunming, China, [3]College of Electric Power Engineering, Kunming University of Science and Technology, Kunming, China

In the research, a protection scheme for hybrid multiterminal UHVDC lines based on the CEEMDAN and Teager energy operator is proposed. The fault direction criterion is proposed according to the polarity difference of the sudden variable of the mode component of the current line on both sides of the T-zone after the fault of the EHV multiterminal hybrid DC system. When the fault is located on the left or right side of the T-zone, CEEMDAN is used to decompose the mode component of the fault transient current and obtain the intrinsic mode function (IMF component) at different local characteristic time scales. Then, the Teager energy operator is used to calculate the instantaneous energy of the current high-frequency IMF1 component. Finally, the faults inside and outside the line are judged by comparing the maximum value of current high-frequency IMF1 instantaneous energy with the setting value. When the fault is located in the T-zone, it is determined as a fault outside the line zone. The protection scheme of hybrid multiterminal UHVDC lines is given. The simulation model of the Kunliulong hybrid multiterminal UHVDC line system is built in a PSCAD/EMTDC simulation platform, and the proposed protection method is verified. A large number of simulation results show that the protection scheme has certain anti-transition resistance ability and high reliability.

Keywords: hybrid multiterminal UHVDC system, line protection, CEEMDAN, Teager energy operator, PSCAD/EMTDC simulation

OPEN ACCESS

Edited by:
Xun Shen,
Tokyo Institute of Technology, Japan

Reviewed by:
Hardeep Singh,
Sophia University, Japan
Sandeep Kumar,
Lovely Professional University, India

***Correspondence:**
Yanbo Che
lab538@163.com

Specialty section:
This article was submitted to Smart Grids, a section of the journal Frontiers in Energy Research

Received: *21 December 2021*
Accepted: *24 January 2022*
Published: *21 February 2022*

Citation:
Xing C, Wang L, Bi G, Chen S, Gao J and Che Y (2022) A Study of Protection Method for Hybrid Multiterminal UHVDC Lines Based on CEEMDAN–Teager Energy Operator. Front. Energy Res. 10:840967. doi: 10.3389/fenrg.2022.840967

INTRODUCTION

The hybrid multiterminal UHVDC system integrates the traditional grid commutated converter–based high voltage direct current (LCC-HVDC) and modular multilevel flexible DC transmission system (MMC-HVDC) with the advantages of large transmission capacity, low transmission losses, and low cost; the receiving end can supply weak AC systems and passive systems, and there is no phase change failure, flexible operation, etc. The long-distance, large-capacity transmission has a wide range of application prospects (Zheng et al., 2016; Tian et al., 2021; Chen et al., 2019).

The development of a hybrid multiterminal UHVDC system faces many technical challenges, and DC line protection is one of the important technical challenges (Li et al., 2019). At present, traditional DC transmission line main protection generally uses traveling wave protection, under voltage sensing protection, etc. The traveling wave protection has fast action speed but poor transition

resistance and anti-interference ability, and it is easy to refuse to move in case of high-resistance ground fault (Boussaadia, 2019; Li et al., 2016). There is an adaptability problem when applying the traditional DC line protection to the hybrid multiterminal UHVDC line protection. For the line protection of hybrid multiterminal UHVDC systems, domestic and foreign experts have conducted relevant studies. Gao et al. (2021) studied the T-zone protection of multiterminal hybrid DC transmission lines and constructed the T-zone protection criterion using the mode mutation of the current line and Hausdorff distance algorithm on both sides of the T-zone; Wang et al. (2019) calculated the analysis of traveling wave protection for flexible DC networks, but the analysis method is very computationally intensive; Lin et al. (2020) constructed the fault direction criterion based on the difference between the amplitude of the forward and reverse traveling waves at the near ends of the converter station on both sides. However, this method requires accurate detection of the first wave head of the traveling wave, and the transition resistance needs to be improved; Li Haifeng et al. (2019) used the attenuation of the low-frequency component of the fault transient current in the T-zone to construct a directional criterion for fault area discrimination in parallel-type multiterminal hybrid DC lines and discriminate the fault location, but in the wavelet transform, the decomposition gradient of the signal sampling frequency needs to be set in advance before the analysis so that it cannot fully reflect the information of the signal itself followed by the pre-selection of the wavelet change basis function, so the resulting error directly affects the correct analysis of the signal itself (Toyoda and Wu, 2021).

The CEEMDAN algorithm is a complete ensemble empirical mode decomposition with the adaptive noise algorithm, which is widely used in the field of mechanical fault diagnosis, and the algorithm achieves complete decomposition of the signal by adding zero-mean Gaussian white noise to the original signal; Wang and Shao (2020) and Vanra et al. (2017) used complete ensemble empirical mode decomposition with adaptive noise (CEEMDAN) to extract the fault characteristic signal of faulty rotating machinery; the decomposition method has better decomposition effect than the traditional method, does not need to select the basis function, and is subject to less interference; domestic experts have combined the CEEMDAN algorithm with other algorithms to apply in the fields of harmonic detection, ultrashort-term load prediction, etc. Ren et al. (2017) used the CEEMDAN algorithm and Teager energy operator for harmonic signal detection; Li and Li, (2015) combined the CEEMDAN algorithm, alignment entropy, and leakage integral echo state network (LIESN) method for load prediction; Gao et al. (2020) used the Teager energy operator to calculate the transient energy magnitude of transient voltage of DC lines to construct the longitudinal protection criterion to improve the reliability and quick action of the protection, (He et al., 2020) but the method directly uses the value of the outer voltage of the flat-wave reactor, and the protection may be misactivated when there is an error in the measurement.

This study combines two algorithms, the CEEMDAN algorithm and the Teager energy operator, for DC line fault diagnosis. The protection principle is simple and is constructed using the attenuation characteristics of boundary elements to high-frequency quantities of faults. Compared to the time domain–type protection, the method is a frequency domain–type protection, which improves the quick-action and high reliability of the UHV multiterminal hybrid DC line protection. The method uses CEEMDAN to completely decompose the fault transient current signal, accurately extract the high-frequency component of the fault current, calculate the fault high-frequency component amplitude using the simplicity and speed of the Teager energy operator algorithm, and thus determine the fault location.

In this study, we propose a protection scheme based on the CEEMDAN–Teager energy operator for hybrid multi–terminal UHVDC lines. There is an analysis of the attenuation characteristics of fault transient current signals at the rectifier side boundary and the inverter side boundary at the end of the line for ultrahigh voltage multiterminal hybrid DC transmission; the fault direction is discerned according to the polarity of the sudden change in the mode component of the fault current line on both sides of the T-zone; the maximum value of the instantaneous energy of the high-frequency component of the fault transient current is used to construct the in-zone and out-zone criterion to discern the fault inside and outside its zone. Finally, the PSCAD/EMTDC simulation platform is used to build the UHV multiterminal hybrid DC transmission model, and MATLAB is used to write the protection algorithm for verification. The extensive simulation results show that the proposed protection method has good reliability.

INTRODUCTION TO THE TOPOLOGY OF THE HYBRID MULTITERMINAL UHVDC SYSTEM

The topology of the Kunliulong hybrid multiterminal UHVDC system is analyzed, which adopts the traditional type line-commutation converter (LCC) and full half-bridge modular multilevel converter (FHMMC) for the converter station (FHMMC) (Le et al., 2021; Zhu et al., 2020), where the sending end of the converter station uses the LCC-type converter, the receiving end used the FHMMC-type converter, the system's transmission lines are overhead lines, its voltage level of the system is ±800 kV, and line 1 length and line 2 length are marked according to the actual and the system's topology and fault location, respectively, as shown in **Figure 1**.

ANALYSIS OF BOUNDARY FREQUENCY CHARACTERISTICS OF THE HYBRID MULTITERMINAL UHVDC SYSTEM

The boundary of the conventional DC transmission system and flexible DC transmission system is symmetrical structure. The boundary of the rectifier side and the boundary of the inverter side at the end of the line of the Kunliulong hybrid multiterminal UHVDC system are asymmetrical, so the frequency characteristics of the boundary of the rectifier side and the

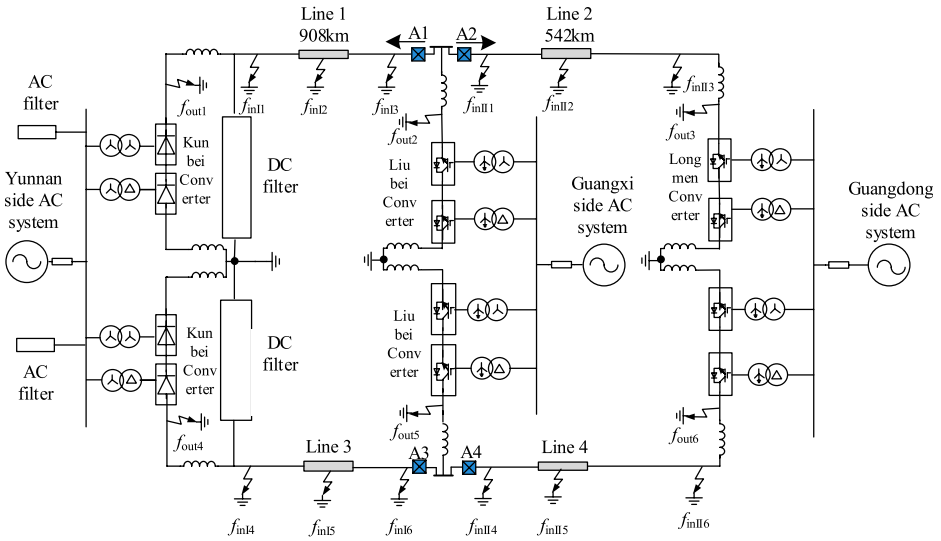

FIGURE 1 | Topology diagram of the Kunliulong hybrid multiterminal UHVDC system.

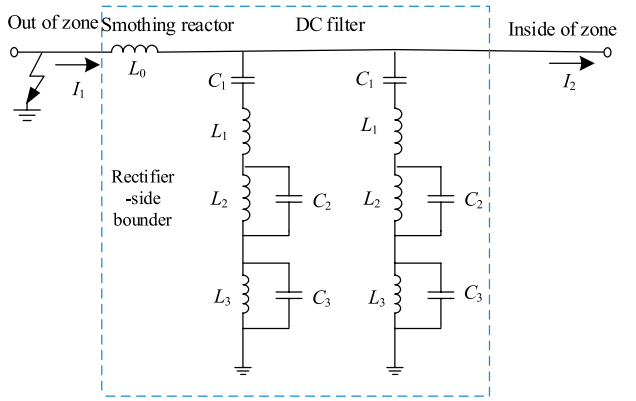

FIGURE 2 | Rectifier-side boundary elements.

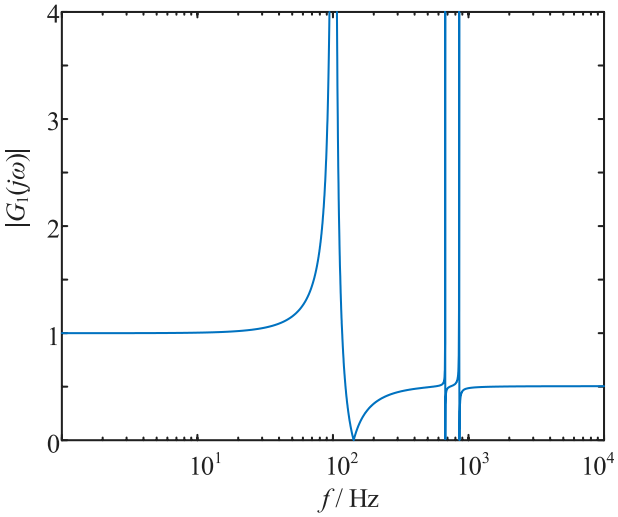

FIGURE 3 | Frequency characteristics of transfer function of the rectifier side of the boundary.

frequency characteristics of the boundary of the inverter side at the end of the line need to be analyzed separately.

Frequency Characteristics of the Boundary of the Rectifier Side

The rectifier-side line boundary of the Kunliulong hybrid multiterminal UHVDC system comprises both the DC filter and smoothing reactor, and the rectifier-side line boundary of this system is shown in **Figure 2** (Chen et al., 2013; Yang et al., 2018; Yang et al., 2019; Yang et al., 2021b).

The rectifier-side line transfer function of the Kunliulong hybrid multiterminal UHVDC system is defined as $G_1(j\omega)$; from the circuit theory, it can be introduced that $G_1(j\omega)$ is as follows:

$$G_1(j\omega) = \frac{I_2(j\omega)}{I_1(j\omega)} = \frac{Z_1(j\omega) + Z_2(j\omega)}{2Z_1(j\omega) + Z_2(j\omega)}. \quad (1)$$

The $Z_1(j\omega)$ in the formula is the impedance of the DC filter; $Z_2(j\omega)$ is the impedance of the smoothing reactor. Smoothing reactor parameters: L_0 = 300mH; DC filter parameters: C_1 = 2μF; L_1 = 11.773mH; L_2 = 10.266mH; C_2 = 3.415μF; L_3 = 4.77mH; and C_3 = 11.773μF; when they are brought into **Eq. 1**, we can get the amplitude frequency characteristics of transfer function of the rectifier side of the boundary shown in **Figure 3**.

As can be seen from **Figure 3**, when 0Hz < f < 100Hz, $|G_1(j\omega)| \approx 1$; when 100Hz < f < 192Hz, $|G_1(j\omega)| > 1$; when f = 102Hz, 、 f = 673Hz, and f = 854Hz, $|G_1(j\omega)|$ takes a great value; and when the frequency f > 1000Hz, $|G_1(j\omega)| \approx 0.5$. It can be seen that the rectifier side of the boundary

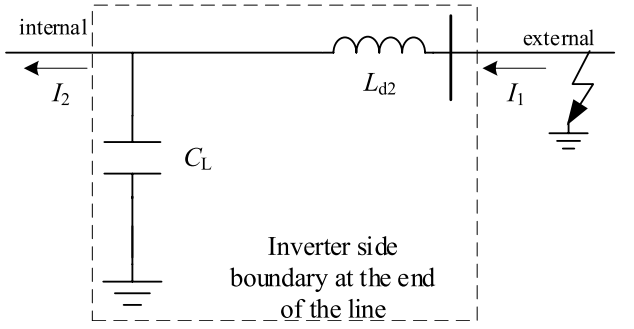

FIGURE 4 | Inverter-side boundary at the end of the line.

has a significant attenuation characteristic on the high-frequency components of the fault transient fault current signal. When a fault occurs on the outside of the rectifier side, the high-frequency component of the fault current signal needs to go through the dual attenuation of the rectifier side of the boundary and line 1 to reach the installation protection A1. Therefore, the high-frequency component of the fault signal detected by protection A1 has small amplitude; when the fault occurs in line 1, the fault current signal high-frequency components only need to go through the attenuation of line 1 to reach the installation protection A1, so protection A1 detects a larger high-frequency component energy of the transient fault current. Therefore, based on the size of the high-frequency component energy of the fault current signal detected by protection A1, we can discriminate faults inside and outside on the left side of the T-zone.

Inverter-Side Boundary Frequency Characteristics at the End of the Line

The Kunliulong UHV multi-end hybrid DC transmission system is equipped with a smoothing reactor at the end of the transmission line, and there is ground capacitance to the ground, so it is proposed to use a section of overhead line ground capacitance and smoothing reactor at the end of the line to form the inverter side boundary at the end of the line, and the boundary components are shown in **Figure 4**.

The transfer function of the inverter side boundary at the end of the line is defined as G_2, which can be introduced by the circuit theory as follows (Song et al., 2020; Yang et al., 2022; Yang et al., 2021c; Yang et al., 2021a):

$$G_2(j\omega) = \frac{I_2(j\omega)}{I_1(j\omega)} = \frac{Z_1(j\omega) + Z_2(j\omega)}{2Z_1(j\omega) + Z_2(j\omega)}. \quad (2)$$

$Z_1(j\omega)$ is a section of overhead line impedance to the ground, $Z_1(j\omega) = \frac{1}{j\omega C_L}$, C_L is a section of the overhead line to ground capacitance, $Z_2(j\omega)$ is the impedance of the smoothing reactor $Ld2$, and $Z_2(j\omega) = j\omega L_{d2}$; substituting $C_L = 0.1\mu F, L_{d2} =$ 150mH into **Eq. 2** yields the amplitude–frequency characteristics of the inverter-side boundary transfer function at the end of the line as shown in **Figure 5**.

From **Figure 5**, the transitory current transfer function $|G_2(j\omega)|$ at the inverter side boundary at the end of the line has high resistance to the high-frequency component of the fault transient current; when in the DC and low-frequency band $0\text{Hz} < f < 400\text{Hz}$, $|G_2(j\omega)| \approx 1$; when $400\text{ Hz} < f < 1050\text{ Hz}$, $|G_2(j\omega)| \geq 1$; and when $f > 3k\text{Hz}$, $|G_2(j\omega)| \approx 0.45$. It can be seen that the inverter side of the boundary of the line end on the fault current high-frequency signal has a strong attenuation characteristics. When the fault occurs outside the inverter side area of the line section, the fault current signal high-frequency component after double attenuation of the line end inverter-side boundary and line 2 reaches the installation protection A2, and the high-frequency component energy of the fault current signal detected by protection A2 is less; when the fault occurs in line 2, fault current high-frequency signal only after the attenuation of line 2 can reach the installation protection A2, and the high-frequency component energy of the fault current signal detected by protection A2 is less. Based on the size of the high-frequency component energy of the fault current detected by protection A2, the fault can be discerned inside and outside the right side of the T-zone.

PRINCIPLE OF THE CEEMDAN–TEAGER ENERGY OPERATOR ALGORITHM

Basic Principle of the CEEMDAN Algorithm

The CEEMDAN algorithm is improved on the basis of EEMD, which effectively solves the modal mixing phenomenon of EMD and also avoids the problem of unequal number of IMFs after each EMD decomposition in EEMD and CEEMD so that the reconstructed signal is almost identical to the original signal. The algorithm, compared with wavelet decomposition, does not require the selection of basic functions and can achieve

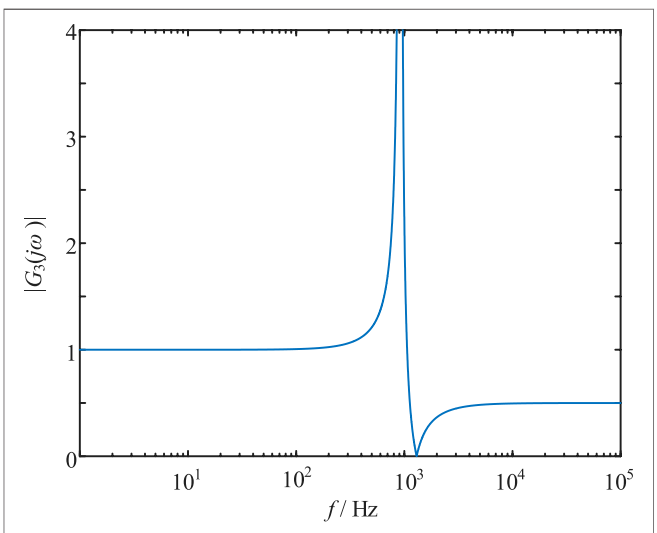

FIGURE 5 | Amplitude–frequency characteristics of the inverter-side boundary transfer function at the end of the line.

complete decomposition of the signal, which is suitable for the processing of nonlinear and nonstationary signals. The specific steps of the algorithm are as follows (Colominas et al., 2013; Wu et al., 2021; Zhang et al., 2021).

(1) ε_{i-1} is defined as the adaptive coefficient in solving $\overline{\text{IMF}}$, $w^i(n)$ as the ith addition of zero-mean white noise, and $E_k(\cdot)$ and IMFk as the k$^{\text{th}}$ modal component obtained by the decomposition of EMD and CEEMDAN algorithms, respectively. The noise component $\varepsilon_0 w^i(n)$ is added to the original signal $x(n)$ and then the EMD decomposition is performed, and the first IMF component $\overline{\text{IMF1}(n)}$ is decomposed by adding noise for the ith time:

$$\overline{\text{IMF1}(n)} = \frac{1}{I}\sum_{i=1}^{I}\overline{\text{IMF1}^i}(n). \tag{3}$$

(2) The first-order residuals of CEEMDAN are calculated:

$$r_1(n) = x(n) - \overline{\text{IMF1}(n)}. \tag{4}$$

(3) After adding adaptive white noise $\varepsilon_1 E_1(w^i(n))$ to the residual $r_1(n)$ shown in **Eq. 3**, EMD decomposition is performed to obtain the second-order IMF component $\overline{\text{IMF2}(n)}$:

$$\overline{\text{IMF2}(n)} = \frac{1}{I}\sum_{i=1}^{I}E_1\left(r_1(n) + \varepsilon_1 E_1\left(w^i(n)\right)\right). \tag{5}$$

(4) Steps (2) and (3) are repeated to obtain the k$^{\text{th}}$ residual signal $r_k(n)$ and (k+1)$^{\text{st}}$ order IMF components $\overline{\text{IMF}k+1(n)}$ as shown in **Eqs 6**, **7**.

$$r_k(n) = r_{k-1}(n) - \overline{\text{IMF}k(n)}. \tag{6}$$

$$\overline{\text{IMF}k+1(n)} = \frac{1}{I}\sum_{i=1}^{I}E_1\left(r_k(n) + \varepsilon_k E_k\left(w^i(n)\right)\right). \tag{7}$$

(5) Step (4) is repeated until the end of the residual signal $r_k(n)$ is not available for EMD decomposition.

The CEEMDAN algorithm finally decomposes the k IMF components with a final residual of $R(n)$:

$$R(n) = x(n) - \sum_{k=1}^{k}\overline{\text{IMF}k(n)}. \tag{8}$$

The original signal $x(n)$ is as follows:

$$x(n) = \sum_{k=1}^{k}\overline{\text{IMF}k(n)} + R(n). \tag{9}$$

From **Eq. 9**, the CEEMDAN algorithm decomposes the original signal into a series of IMF components with instantaneous frequencies ranging from high to low and one residual to achieve complete decomposition of the signal by adding zero-mean white noise.

Teager Energy Operator

The Teager energy operator is a nonlinear difference operator, and compared with the traditional energy operator, instantaneous energy of the Teager energy operator is related to both amplitude and frequency, with obvious local characteristics, which can quickly perform DC line fault analysis.

The Teager energy operator for the nonlinear signal $\alpha(t)$ is defined as in the study by Karimian and Hosseinian, (2020):

$$\psi[\alpha(t)] = \dot{\alpha}^2(t) - \alpha(t)\ddot{\alpha}(t), \tag{10}$$

where $\dot{\alpha}(t)$ and $\ddot{\alpha}(t)$ are the first-order derivative function and the second-order derivative function of the signal $\alpha(t)$, respectively.

When the signal is discrete, the Teager energy operator is defined as

$$\psi_d[\alpha(i)] = \alpha^2(i) - \alpha(i-1)\alpha(i+1). \tag{11}$$

The relationship between ψ and ψ_d is as follows:

$$\psi[\alpha(t)] = \frac{\psi_d[\alpha(i-1)]}{T^2}, \tag{12}$$

where T is the sampling period.

Extraction of High-Frequency Transient Energy of Fault Current Based on the CEEMDAN–Teager Energy Operator

The CEEMDAN algorithm can achieve complete decomposition of the fault current signal, and the IMF components are arranged in the order from highest to lowest frequency band, that is, 2 has the highest frequency band. When the frequency of IMF1(n) is greater than the attenuation frequency of the boundary, the occurrence of out-of-zone fault, the IMF1 component through the double attenuation of the line boundary and the line to reach the protection device installation, and the protection device to detect the fault transient current IMF1 component of the energy is smaller; on the contrary, the discovery of the in-zone fault, the component only through the line attenuation to reach the protection installation, and the energy of the high-frequency component IMF1 of the fault transient current detected by the protection device is larger.

Therefore, the DC transmission line protection can be constructed based on the energy magnitude of the high-frequency IMF1(n) component of the fault transient current.

The steps to extract the high-frequency transient energy of the fault transient current based on the CEEMDAN-Teager energy operator are as follows:

(1) The fault current signal is obtained and decoupled using phase mode transformation, and the fault current line mode component is obtained.
(2) The mode components of the fault current line obtained in step (1) are decomposed using CEEMDAN to obtain the kth IMF components.
(3) The instantaneous energy of the high-frequency IMF1(n) component of the fault transient current is calculated using the Teager energy operator.
(4) The rectified value and maximum value of the instantaneous energy of the high-frequency IMF1(n) component of the

fault transient current are compared to discriminate the fault location. When the maximum value of the transient energy of the high-frequency IMF1(n) component of the fault transient current is greater than the value of the rectification, the fault is judged to be within the zone; conversely, the fault is judged to be outside the zone.

HYBRID MULTITERMINAL UHVDC LINE PROTECTION SCHEME

Protection Triggering Criterion

When the DC line fault occurs, the voltage amplitude of the line on both sides of the T-zone changes (Li et al., 2021), the amplitude of the transient voltage can be used as the triggering criterion; in order to improve the protection sensitivity, the side of line with large voltage fluctuation on both sides of the T-zone is selected as the triggering criterion; the triggering criterion is as follows:

$$max\left(|\Delta u_1|, |\Delta u_2|\right) > K_{\Delta u}, \tag{13}$$

where Δu_1, Δu_2 represent line voltage change line 1 and line 2, respectively; a $K_{\Delta u} = 0.2U_{ref}$; U_{ref} for line mode voltage of normal operation is required in order to prevent frequent false starts of protection; when $max\left(|\Delta u_1|, |\Delta u_2|\right)$ for three consecutive points is greater than the start value, protection is triggered.

Protection Direction Criterion

When a fault occurs in the DC line, it is necessary to judge the direction of the fault, and the DC current has definite size and direction (Liu et al., 2020; Muniappan, 2021). For the Kunliulong hybrid multiterminal UHVDC system, under working condition, DC current always flows from Kunbei converter station to Liubei converter station and Longmen converter station, and the specified current reference direction is the bus pointing to the line, as shown in **Figure 1**.

When the fault occurs on the left side of the T area, the Kunbei-side LCC converter station, the Liubei-side converter station MMC1, and the Longmen-side converter station MMC2 all inject short-circuit current into the short-circuit point; at this time, for protection A1, fault current direction is positive, and protection A1 detects the current increase; for protection A2, the fault current is opposite to the reference direction, so the fault current direction detected by protection A2 is negative, and the current detected by protection A2 becomes smaller; Similarly, when the fault occurs in the right side of the T-zone, protection A1 detects a decrease in current and protection A2 detects an increase in current; when the fault occurs in the T-zone, both protection A1 and protection A2 detect a decrease in current. When the fault occurs in the T-zone, both protection A1 and protection A2 detect a decrease in current.

Analysis of the fault occurred at simulation f_{inI2}, f_{inII2}, and f_{out2}, respectively, that is, simulation of the fault occurred at the left side of the T-zone, the right side of the T-zone, and within the T-zone; mode component mutation amount of the fault current line detected by protection A1 and protection A2 is shown in **Figure 6**.

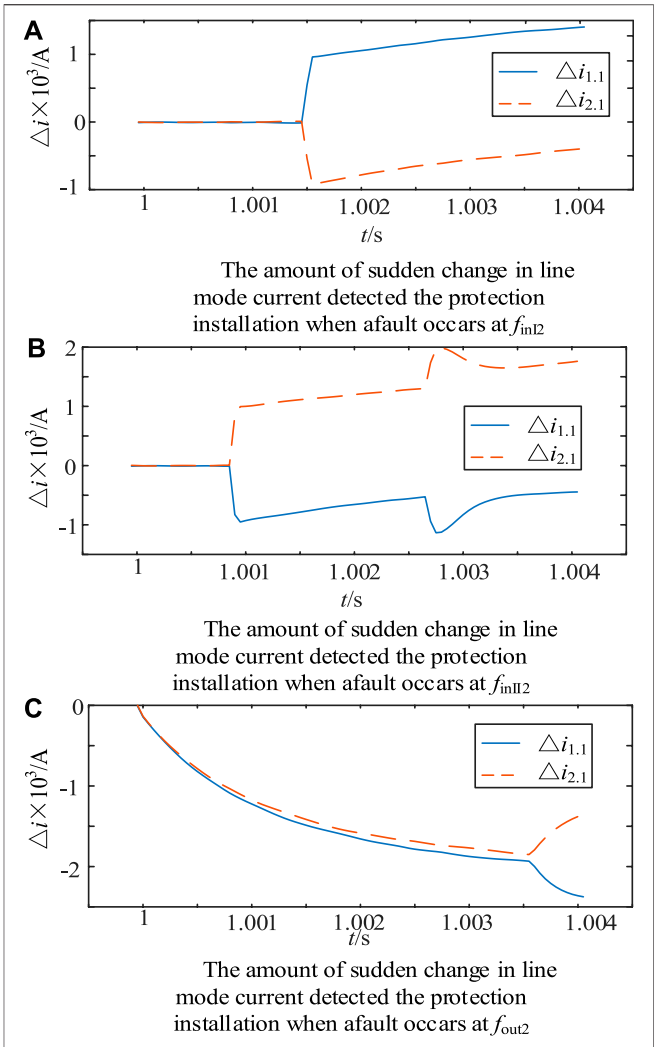

FIGURE 6 | Mode component mutation of the fault current line.

As can be seen in **Figure 6**, when the left side of the T-zone is fault, protection A1 detects the mode component mutation $\Delta i_{1.1}$ of the fault current line in line 1 and is positive, protection A2 detects the mode component mutation $\Delta i_{2.1}$ of the fault current line in line 2 and is negative; when the right side of the T-zone is fault, protection A1 detects the mode component mutation $\Delta i_{1.1}$ of the fault current line in line 1 and is negative, protection A2 detects the mode component mutation $\Delta i_{2.1}$ of the fault current line in line 2 and is positive; when the T-zone is fault, protection A1 detects the mode component mutation $\Delta i_{1.1}$ of fault current line in line 1 and is negative, protection A2 detects the mode component mutation amount $\Delta i_{2.1}$ of fault current line in line 2 and is negative; Therefore, the construction fault direction criterion is as follows:

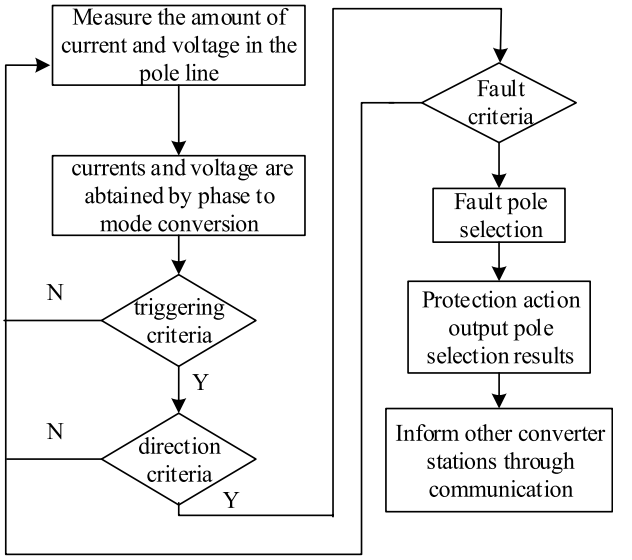

FIGURE 7 | Protection flow chart.

$$\begin{cases} K_1 > 0, K_2 < 0 & \text{T} - \text{zone left side failures} \\ K_1 < 0, K_2 > 0 & \text{T} - \text{zone right side failures} \\ K_1 < 0, K_2 < 0 & \text{failures in T} - \text{zone} \end{cases}, \quad (14)$$

where K_1 indicates the integral of the change in the mode component of the current line at the end of line 1 calculated by protection A1 over the time window.

K_2 denotes the integral over the time window of the change in the mode component of the current line at the first end of line 2 calculated by protection A2. The calculation formula of k1 and k2 is as follows:

$$K_x = \sum_{t_0}^{t_0+k\Delta t} \Delta i_{x.1}(t_0 + n\Delta t), \quad (15)$$

where "x" is taken as 1 or 2, $\Delta i_{1.1}$, $\Delta i2.1$ are mode change amount of the current line at the end of line 1 and the first end of line 2, t_0 is the initial moment of the fault, Δt is the sampling interval, and $n\Delta t$ indicates the length of the time data window.

In- and Out-of-Zone Fault Criterion

After achieving fault direction discrimination, it is also necessary to determine whether the fault occurs in the protection range. When the fault is located in the left side of the T-zone, protection A1 is required to determine the location of the fault; if the fault is located in line 1, protection A1 acts. If the fault is located outside the rectifier side area, protection A1 does not act; when discriminating the fault located in the right side of the T-zone, protection A2 is required to determine the location of the fault, when the fault is located in line 2, protection A2 acts; when the fault is located outside the inverter side area at the end of the line, protection A2 does not act; when the fault is located in the T-zone, this type of fault belongs to the line outside the fault area; hence, protection A1 and protection A2 do not act.

In- and Out-of-Zone Fault Criterion for the Left Side of the T-Zone

Section 2.1 analysis results show that the rectifier side boundary has strong attenuation characteristics for the high-frequency component of the fault current. When the fault is located in the left side of the T-zone, the rectifier-side boundary is used to discern the fault location for the attenuation characteristics of the high-frequency component of the fault transient current. When the fault is located in line 1, the high-frequency signal of the fault current only needs to go through the line attenuation, so the high-frequency component transient energy of the fault current signal is larger; when the fault is located outside the rectifier-side zone, the high-frequency signal of the fault current needs to go through the double attenuation of the rectifier-side boundary and line 1, and the high-frequency component transient energy of the fault current signal is smaller. In order to improve the sensitivity of the protection, the maximum value of the high-frequency component transient energy of the fault current signal is extracted to construct the protection criterion, so the construction of the left side of the T-zone inside and outside the zone fault criterion is as follows:

$$\begin{cases} T_1 > T_{set1} & \text{Fault inside the left the T} - \text{zone} \\ T_1 \le T_{set1} & \text{Fault outside the left the T} - \text{zone} \end{cases}, \quad (16)$$

where T_1 is the maximum value of the instantaneous energy of the high-frequency component of the fault current calculated by protection A1, and T_{set1} is the rectification value of protection A1. In order to reliably distinguish between the left side of the T-zone inside and outside the zone fault, the value should be selected in accordance with the most serious fault situation X. The principle of the rectification is that high-resistance ground fault occurs at the head-end of line 1 to avoid metallic ground fault outside the rectifier side area. Therefore T_{set1} is as follows:

$$T_{set1} = K_{rel} \times T_{max\_out1}, \quad (17)$$

where K_{rel} is a reliable coefficient, K_{rel} take 1.5, and $T_{\max\_out1}$ is the maximum value of the instantaneous energy of the high-frequency component of the fault current when a metal ground fault occurs on the outside of the rectifier-side smoothing reactor. Through simulation experiments, it is calculated that T_{set1} is 1.82×10^3. When the fault is located in the left side of the T-zone, using **Eq. 16** can accurately discern the fault in the left side of the T-zone; when the fault is located outside the left side of the T-zone, protection A1 does not act; and when the fault is located in the left side of the T-zone, protection A1 acts.

Internal and External Faults in the Right-Hand Area of the T-Zone

Section 2.2 analysis results show that the inverter side boundary at the end of the line also has a strong attenuation effect on the high-frequency signal of the fault current. Similarly, the attenuation characteristics of the high-frequency component of the fault current from the inverter side boundary at the end of the line are used to discriminate between internal and external faults in the right-hand side of the T-zone. Fault judgment inside and outside the right side of the T-zone is as follows:

TABLE 1 | Main parameters of the simulation system.

Converter station	Kunbei converter station	Liubei converter station	Longmen converter station
Rated power	8,000 MW	3,000 MW	5,000 MW
Rated voltage	800 kV	800 kV	800 kV
Rated current	5 kA	1.875 kA	3.125 kA
Flat-wave reactor	300 mH	150 mH	150 mH

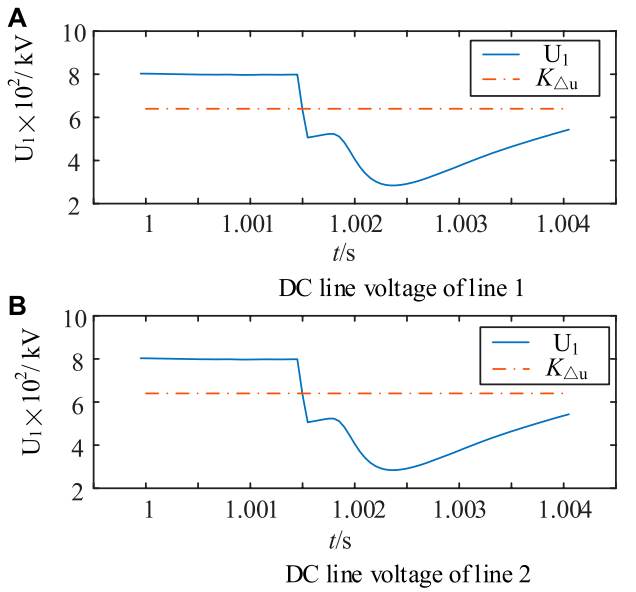

FIGURE 8 | Voltage of DC lines.

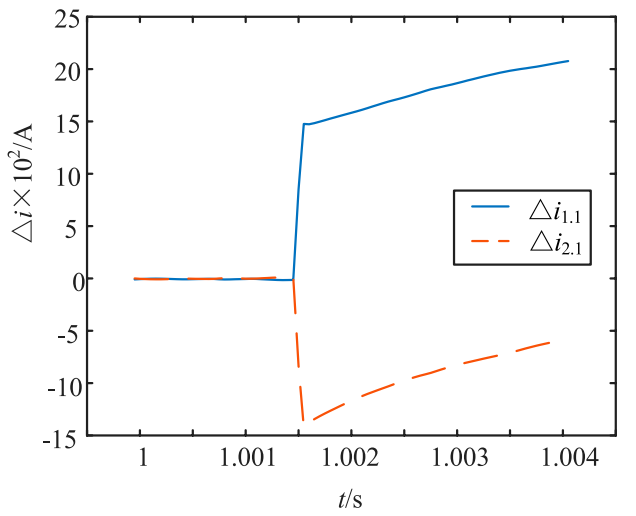

FIGURE 9 | Sudden change amount of the fault current line mode component.

$$\begin{cases} T_2 > T_{set2} & \text{Fault inside the right the T} - \text{zone} \\ T_2 \le T_{set2} & \text{Fault outside the right the T} - \text{zone} \end{cases}, \quad (18)$$

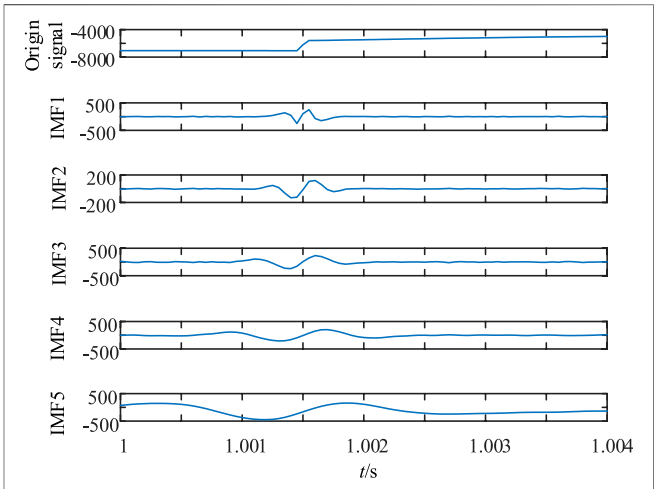

FIGURE 10 | Decomposition results of CEEMDAN.

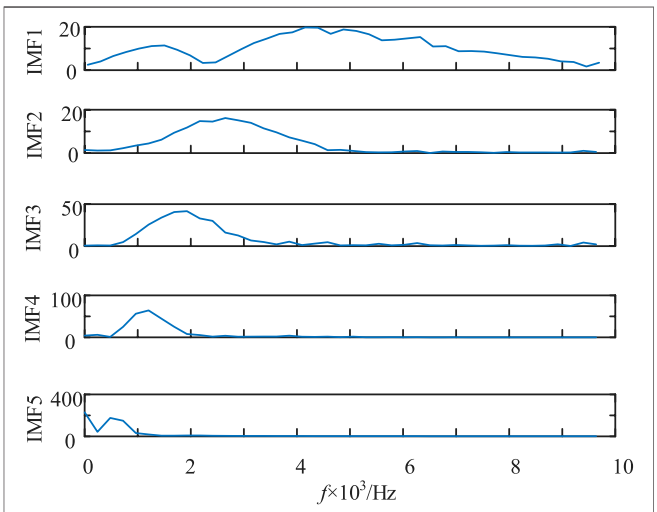

FIGURE 11 | Frequency spectrum of CEEMDAN modal components.

where T_2 is the maximum value of the transient energy of the high-frequency component IMF1(n) of fault transient current calculated by protection A2, and T_{set2} is the rectification value of the protection A2. In order to reliably distinguish between the right side of the T-zone inside and outside the zone fault, T_{set2} should be selected in accordance with the most serious fault situation. The principle of the rectification is that high-resistance ground fault occurs at the head-end of line 1 to avoid metallic

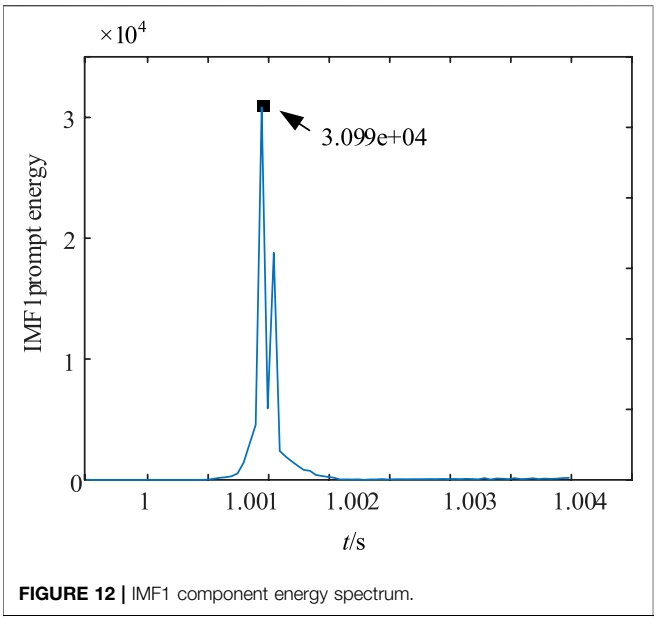

FIGURE 12 | IMF1 component energy spectrum.

ground fault outside the rectifier side area. Therefore T_{set2} is calculated as follows:

$$T_{set2} = K_{rel} \times T_{max\_out3}, \tag{19}$$

where K_{rel} is the reliability factor, taken as 1.5; and $T_{\max\_out3}$ is the maximum value of the instantaneous energy of the high-frequency component of the fault when a metal ground fault occurs on the outside of the inverter-side flat-wave reactor. Through simulation experiments, it is calculated that T_{set2} is 9.834×10^3. When the fault is located in the right side of the T-zone, **Eq. 18** can be used to discern the fault in the right side of the T-zone. When the position is located within the right side of the T-zone, protection A2 is operated, and when the fault is located outside the right side of the T-zone, protection A2 is not operated.

Criterion of Fault Pole Selection

When judging the fault within the left side of the T-zone or within the right side of the T-zone, in order to make the protection act accurately on the fault pole and ensure normal operation of the non-fault pole, the fault pole discrimination is required, and the fault pole criterion is defined as follows:

$$\begin{cases} P \geq 1.5 & \text{positive pole fault} \\ 0.8 < P < 1.5 & \text{double pole fault} \\ P \leq 0.8 & \text{negtive pole fault} \end{cases}. \tag{20}$$

P is the pole selection factor, and the calculation formula is as follows:

$$P = \frac{\sum_{i=1}^{N_s} |\Delta i_P(i)|}{\sum_{i=1}^{N_s} |\Delta i_N(i)|}, \tag{21}$$

where $\Delta i_P(i)$ and $\Delta i_N(i)$ are the positive and negative current change, respectively; and N_s is the number of current sampling within 4 ms; when the fault initiating element is activated, the sampling starts.

Protection Flow

The protection device starts when the start-up criterion of any of the protection installations on both sides of the T-zone is satisfied. The current data of the 2-ms time window of the line on both sides of the T-zone are taken and decoupled after phase mode transformation and then polarity of the mode component change of the fault current line is calculated, and fault direction discrimination is carried out. When discriminated as the left side of the T-zone fault, protection A1 calculates the maximum value of the instantaneous energy of the high-frequency component of the current line mode at the end of the fault line 1 and judges the fault inside and outside the left side of the T-zone; when discriminated as the right side of the T-zone fault, protection A2 calculates the maximum value of the instantaneous energy of the high-frequency component of the fault current line mode at the first end of the line 2 and discriminates the fault inside and outside the right side of the T-zone; when discerning a fault within the T-zone, A1 and A2 judge the fault to be outside the line zone, where protection A1 and protection A2 are not operating. The current data of fault line 4 ms for fault pole judgment are calculated, the final fault pole protection device action. The protection flow is shown in **Figure 7**.

SIMULATION VERIFICATION

On the PSCAD/EMTDC simulation platform, the Kunliulong hybrid multiterminal UHVDC system model shown in **Figure 1** is built. The Kun-North side adopts the traditional grid phase–shifting type converter with constant DC current and minimum trigger angle control; the Liu-North converter station adopts a hybrid full-bridge and half-bridge modular multiterminal flat converter with constant active power and reactive power control. Longmen converter station uses a full-bridge and half-bridge hybrid modular multiterminal flat converter. Control mode uses fixed DC voltage and reactive power control. Line 1 and line 2 are overhead lines, line model using Frequency Dependent (Phase) Model Options model, the length of 908 km and 542 km, respectively. System parameters are shown in **Table 1**. The main parameters of the system are shown in **Table 1**.

In **Figure 1**, f_{out1}, f_{out4} are the faults occurring on the outside of the positive and negative Kun-north side of the flat-wave reactor, respectively, which is outside the left zone of the line T-zone; $f_{\text{inl1}} \sim f_{\text{inl3}}$ are first end, midpoint, and end fault of positive line 1; $f_{\text{inl4}} \sim f_{\text{inl6}}$ are the first end, midpoint, and end failure of negative line 1. Line 1 faults are intrazone faults on the left side of the T-zone; $f_{\text{inlI1}} \sim f_{\text{inlI3}}$ are first end, midpoint, and end failure of positive line 2, $f_{\text{inlI4}} \sim f_{\text{inlI6}}$ are the first end, midpoint, and end fault of negative line 2; line 2 fault is an intrazone fault on the right side of the T-zone; f_{out2}, f_{out5}, respectively, for the positive and negative Longmen side of the flat-wave reactor outside the fault, the fault for the right side of the T-zone outside the fault; f_{out3}, f_{out6} are faults occurring on the outside of the positive and negative Longmen-side flat-wave reactors respectively, which are faults outside the right side of the T-zone; f_{out2}, f_{out5} are faults occurring on the outside of the positive and negative Liubei-side flat-wave reactors, respectively, which are faults within the T-zone.

TABLE 2 | Simulation of the positive fault.

Location of the fault	Transition resistance value/Ω	K_1	K_2	Direction of failure	T_1	T_2	P	Judgment results of A1	Judgment results of A2
f_{out1}	0	67	−52	Left side of the T-zone	$1.647*10^3$	—	1.6624	Outside the left side of the positive T-zone	—
	100	49	−37	Left side of the T-zone	$7.12*10^2$	—	1.6949	Outside the left side of the positive T-zone	—
	200	37	−27	Left side of the T-zone	$3.10*10^2$	—	1.7224	Outside the left side of the positive T-zone	—
	300	30	−21	Left side of the T-zone	$1.95*10^2$	—	1.7481	Outside the left side of the positive T-zone	—
	500	21	−14	Left side of the T-zone	$1.52*10^2$	—	1.799	Outside the left side of the positive T-zone	—
f_{inl1}	0	256	−187	Left side of the T-zone	$2.42*10^5$	—	1.7315	Inside the left side of the positive T-zone	—
	100	121	−89	Left side of the T-zone	$4.12*10^4$	—	1.6946	Inside the left side of the positive T-zone	—
	200	78	−57	Left side of the T-zone	$1.34*10^4$	—	1.69	Inside the left side of the positive T-zone	—
	300	58	−42	Left side of the T-zone	$5.88*10^3$	—	1.6917	Inside the left side of the positive T-zone	—
	500	37	−26	Left side of the T-zone	$2.27*10^3$	—	1.6923	Inside the left side of the positive T-zone	—
finl2	0	459	−236	Left side of the T-zone	$3.15*10^5$	—	3.2431	Inside the left side of the positive T-zone	—
	100	308	−159	Left side of the T-zone	$1.31*10^5$	—	3.2563	Inside the left side of the positive T-zone	—
	200	232	−119	Left side of the T-zone	$6.98*10^4$	—	3.2548	Inside the left side of the positive T-zone	—
	300	186	−95	Left side of the T-zone	$4.45*10^4$	—	3.2468	Inside the left side of the positive T-zone	—
	500	133	−67	Left side of the T-zone	$2.11*10^4$	—	3.2305	Inside the left side of the positive T-zone	—
finl3	0	1,591	−671	Left side of the T-zone	$9.07*10^5$	—	4.7264	Inside the left side of the positive T-zone	—
	100	810	−316	Left side of the T-zone	$3.84*10^5$	—	4.6185	Inside the left side of the positive T-zone	—
	200	539	−202	Left side of the T-zone	$2.1*10^5$	—	4.651	Inside the left side of the positive T-zone	—
	300	402	−147	Left side of the T-zone	$1.32*10^5$	—	4.6757	Inside the left side of the positive T-zone	—
	500	266	−94	Left side of the T-zone	$6.68*10^4$	—	4.75	Inside the left side of the positive T-zone	—
finll1	0	−796	1751	Right side of the T-zone	—	$9.8*10^5$	4.7264	—	Inside the right side of the positive T-zone
	100	−391	885	Right side of the T-zone	—	$4.06*10^5$	4.6185	—	Inside the left side of the positive T-zone
	200	−256	593	Right side of the T-zone	—	$2.22*10^5$	4.6504	—	Inside the left side of the positive T-zone
	300	−190	445	Right side of the T-zone	—	$1.36*10^5$	4.6757	—	Inside the left side of the positive T-zone
	500	−125	297	Right side of the T-zone	—	$6.97*10^4$	4.75	—	Inside the left side of the positive T-zone
finll2	0	−322	660	Right side of the T-zone	—	$8.44*10^5$	4.5303	—	Inside the right side of the positive T-zone
	100	−216	447	Right side of the T-zone	—	$3.64*10^5$	4.3115	—	Inside the right side of the positive T-zone
	200	−162	338	Right side of the T-zone	—	$1.99*10^5$	4.1887	—	Inside the right side of the positive T-zone
	300	−130	272	Right side of the T-zone	—	$1.31*10^5$	4.1107	—	Inside the right side of the positive T-zone
	500	−93	195	Right side of the T-zone	—	$6.39*10^4$	4.0138	—	Inside the right side of the positive T-zone

(Continued on following page)

TABLE 2 | (*Continued*) Simulation of the positive fault.

Location of the fault	Transition resistance value/Ω	K_1	K_2	Direction of failure	T_1	T_2	P	Judgment results of A1	Judgment results of A2
finII3	0	−328	569	Right side of the T-zone	—	$7.98*10^5$	6.1925	—	Inside the right side of the positive T-zone
	100	−198	354	Right side of the T-zone	—	$4.11*10^5$	5.7473	—	Inside the right side of the positive T-zone
	200	−140	254	Right side of the T-zone	—	$2.63*10^5$	5.1994	—	Inside the right side of the positive T-zone
	300	−108	198	Right side of the T-zone	—	$1.84*10^5$	4.8146	—	Inside the right side of the positive T-zone
	500	−74	137	Right side of the T-zone	—	$1.01*10^5$	4.3354	—	Inside the right side of the positive T-zone
fout3	0	−270	444	Right side of the T-zone	—	$8.94*10^3$	6.3299	—	Outside the right side of the positive T-zone
	100	−151	264	Right side of the T-zone	—	$7.72*10^3$	6.357	—	Outside the right side of the positive T-zone
	200	−100	182	Right side of the T-zone	—	$7.07*10^3$	5.1923	—	Outside the right side of the positive T-zone
	300	−73	138	Right side of the T-zone	—	$6.27*10^3$	4.467	—	Outside the right side of the positive T-zone
	500	−47	93	Right side of the T-zone	—	$7.64*10^3$	3.7292	—	Outside the right side of the positive T-zone
fout2	0	−615	−560	T-zone	—	—	4.3946	—	—
	100	−282	−244	T-zone	—	—	4.6647	—	—
	200	−177	−146	T-zone	—	—	4.6524	—	—
	300	−128	−102	T-zone	—	—	4.7011	—	—
	500	−83	−63	T-zone	—	—	4.8375	—	—

According to the protection scheme proposed in *Principle of the CEEMDAN–Teager Energy Operator Algorithm*, the protection algorithm is written in MATLAB, and the simulation data are imported. This study uses the CEEMDAN algorithm to decompose the first IMF component after the fault transient current; it can be achieved when the center frequency is greater than the boundary decay frequency. Considering the CEEMDAN decomposition principle and Shannon's theorem to engineering practical impact factors, this study involves simulation sampling frequency using 20 kHz, and the data window length is 4 ms (Shen et al., 2021a; Shen et al., 2021b; Shen and Raksincharoensak, 2021a; Shen and Raksincharoensak, 2021b).

The intra-area fault in the left area of the T-zone is taken as an example. If the center point of line 1 is metallic ground, the moment of fault occurrence is 1 s, the fault duration is 0.1 s, and the amount of line voltage change on both sides of the T-zone is shown in **Figure 8**.

It can be seen from **Figure 8** that when the midpoint of line 1 metal ground fault and line 1 and line 2 voltage are down to reach the protection of the start value, the protection process is started. According to the protection process to discriminate the fault direction, line 1 and line 2 current line mode change amount is as shown in **Figure 9**.

From **Figure 9**, it can be seen that when the line 1 of the midpoint of a metallic ground fault protection A1 detecting the mode change amount of the current line at the end of line 1 is positive, protection A2 detecting the mode change amount of the current line at the first end of line 2 is negative. According to **Eq. 18**, it can be determined that the fault occurred on the left side of the T-zone. According to the protection process, the location can be determined. The mode components of the fault transient current line for CEEMDAN decomposition can be obtained for each order IMF component as shown in **Figure 10**, and the FFT transform of each order IMF component to find its spectrum, as shown in **Figure 11**.

As seen in **Figures 10**, **11**, the mode signal of the fault transient current line is decomposed by CEEMDAN to obtain IMF1~IMF5, which is FFT-transformed to find the center frequency of IMF1 as 5.3 kHz, and the center frequency is greater than the boundary decay frequency, and the energy spectrum of IMF1 is calculated by using the Teager energy operator, and the energy spectrum of IMF1 is shown in **Figure 12**.

From **Figure 12**, we can see that the maximum value of the instantaneous amplitude of the IMF1 component is $2.925 \times 10^5 > T_{set1} = 7.82 \times 10^3$; this value satisfies the T internal fault criterion of the left side of T-zone and is judged to be an internal fault in the left zone of the T-zone, that is, line 1 is faulty. According to the protection process, we need to determine the pole line of the fault, that is, the fault pole selection; according to **Eq. 21**, the pole selection factor P is calculated as 3.2431; according to **Eq. 20**, the fault occurred in the positive pole is determined. In summary, the fault occurred in the positive T-zone left zone, that is, the positive line 1 fault, and protection A1 issued operation instructions.

In order to verify the impact of different fault locations and different transition resistances on the protection, (shen et al., 2020a; shen et al., 2020b) this study selected $f_{\text{inl1}} \sim f_{\text{inl6}}$, $f_{\text{inlI1}} \sim f_{\text{inlI6}}$, and $f_{\text{out1}} \sim f_{\text{out6}}$ where the fault occurred; the transition resistance is in the value range of 0 ~ 500Ω, and the simulation results are shown in **Tables 2**, **3**.

From **Tables 2**, **3**, it can be seen that when the fault occurs at $f_{\text{inl1}} \sim f_{\text{inl6}}$, $f_{\text{inlI1}} \sim f_{\text{inlI6}}$, and $f_{\text{out1}} \sim f_{\text{out6}}$, the transition

TABLE 3 | Simulation of the negative fault.

Location of the fault	Transition resistance value/Ω	K_1	K_2	Direction of fault	T_1	T_2	P	Judgment results of A1	Judgment results of A2
fout4	0	67	−53	Left side of the T-zone	$2.58*10^2$	—	0.6972	Outside the left zone of the negative T-zone	—
	100	49	−38	Left side of the T-zone	$1.76*10^2$	—	0.7191	Outside the left zone of the negative T-zone	—
	200	38	−28	Left side of the T-zone	$1.67*10^2$	—	0.7415	Outside the left zone of the negative T-zone	—
	300	30	−22	Left side of the T-zone	$1.85*10^2$	—	0.766	Outside the left zone of the negative T-zone	—
	500	21	−15	Left side of the T-zone	$1.46*10^2$	—	0.776	Outside the left zone of the negative T-zone	—
finI4	0	259	−190	Left side of the T-zone	$2.48*10^5$	—	0.605	Inside the left zone of the negative T-zone	—
	100	123	−91	Left side of the T-zone	$4.30*10^4$	—	0.6435	Inside the left zone of the negative T-zone	—
	200	80	−59	Left side of the T-zone	$1.25*10^4$	—	0.6706	Inside the left zone of the negative T-zone	—
	300	59	−43	Left side of the T-zone	$6.49*10^3$	—	0.6954	Inside the left zone of the negative T-zone	—
	500	38	−28	Left side of the T-zone	$2.28*10^3$	—	0.7447	Inside the left zone of the negative T-zone	—
finI5	0	455	−235	Left side of the T-zone	$2.97*10^5$	—	0.2953	Inside the left zone of the negative T-zone	—
	100	305	−157	Left side of the T-zone	$1.23*10^5$	—	0.2876	Inside the left zone of the negative T-zone	—
	200	229	−118	Left side of the T-zone	$6.73*10^4$	—	0.2818	Inside the left zone of the negative T-zone	—
	300	183	−94	Left side of the T-zone	$4.61*10^4$	—	0.2765	Inside the left zone of the negative T-zone	—
	500	131	−67	Left side of the T-zone	$2.26*10^4$	—	0.2658	Inside the left zone of the negative T-zone	—
finI6	0	1,586	−673	Left side of the T-zone	$5.63*10^5$	—	0.2116	Inside the left zone of the negative T-zone	—
	100	810	−317	Left side of the T-zone	$1.96*10^5$	—	0.2169	Inside the left zone of the negative T-zone	—
	200	539	−202	Left side of the T-zone	$1.21*10^5$	—	0.2184	Inside the left zone of the negative T-zone	—
	300	402	−147	Left side of the T-zone	$7.29*10^4$	—	0.2255	Inside the left zone of the negative T-zone	—
	500	266	−94	Left side of the T-zone	$3.74*10^4$	—	0.2415	Inside the left zone of the negative T-zone	—
finII4	0	−798	1711	Right side of the T-zone	—	$5.15*10^5$	0.2116	—	Inside the right zone of the negative T-zone
	100	−393	886	Right side of the T-zone	—	$2.29*10^5$	0.2169	—	Inside the right zone of the negative T-zone
	200	−258	594	Right side of the T-zone	—	$1.25*10^5$	0.2184	—	Inside the right zone of the negative T-zone
	300	−191	446	Right side of the T-zone	—	$7.54*10^4$	0.2255	—	Inside the right zone of the negative T-zone
	500	−126	298	Right side of the T-zone	—	$3.99*10^4$	0.2415	—	Inside the right zone of the negative T-zone
finII5	0	−323	658	Right side of the T-zone	—	$8.13*10^5$	0.2165	—	Inside the right zone of the negative T-zone
	100	−216	445	Right side of the T-zone	—	$3.28*10^5$	0.2192	—	Inside the right zone of the negative T-zone
	200	−163	337	Right side of the T-zone	—	$1.87*10^5$	0.2222	—	Inside the right zone of the negative T-zone
	300	−131	271	Right side of the T-zone	—	$1.27*10^5$	0.2235	—	Inside the right zone of the negative T-zone
	500	−94	195	Right side of the T-zone	—	$5.93*10^4$	0.2233	—	Inside the right zone of the negative T-zone

(Continued on following page)

TABLE 3 | (*Continued*) Simulation of the negative fault.

Location of the fault	Transition resistance value/Ω	K_1	K_2	Direction of fault	T_1	T_2	P	Judgment results of A1	Judgment results of A2
finll6	0	−326	567	Right side of the T-zone	—	$7.37*10^5$	0.1734	—	Inside the right zone of the negative T-zone
	100	−196	353	Right side of the T-zone	—	$4.24*10^5$	0.1832	—	Inside the right zone of the negative T-zone
	200	−138	254	Right side of the T-zone	—	$2.73*10^5$	0.2013	—	Inside the right zone of the negative T-zone
	300	−106	198	Right side of the T-zone	—	$1.82*10^5$	0.2177	—	Inside the right zone of the negative T-zone
	500	−72	137	Right side of the T-zone	—	$1.09*10^5$	0.2438	—	Inside the right zone of the negative T-zone
fout6	0	−270	442	Right side of the T-zone	—	$6.88*10^3$	0.1686	—	Outside the right zone of the negative T-zone
	100	−151	263	Right side of the T-zone	—	$6.08*10^3$	0.1622	—	Outside the right zone of the negative T-zone
	200	−100	182	Right side of the T-zone	—	$5.26*10^3$	0.1878	—	Outside the right zone of the negative T-zone
	300	−74	138	Right side of the T-zone	—	$5.39*10^3$	0.2141	—	Outside the right zone of the negative T-zone
	500	−48	92	Right side of the T-zone	—	$5.39*10^3$	0.2518	—	Outside the right zone of the negative T-zone
fout5	0	−617	−246	Inside of the T-zone	—	—	0.2255	—	—
	100	−283	−216	Inside of the T-zone	—	—	0.2143	—	—
	200	−177	−147	Inside of the T-zone	—	—	0.2181	—	—
	300	−129	−103	Inside of the T-zone	—	—	0.2273	—	—
	500	−82	−63	Inside of the T-zone	—	—	0.2434	—	—

resistance changes in the range of 0 ~ 500Ω; protection A1 and protection A2 can correctly determine fault direction and fault location, correctly determine the fault pole line, and have high sensitivity in the occurrence of high-resistance ground fault. The protection method was found to be 100% correct for different fault locations and transition resistances.

SUMMARY

In this study, a protection scheme for hybrid multiterminal UHVDC lines based on the CEEMDAN–Teager energy operator is proposed, which uses the protection principle to discriminate the fault direction by the polarity of the sudden change in the line mode component of the fault current when a fault occurs on both sides of the T-zone, and then according to the rectifier-side boundary or line end inverter-side boundary on the fault transient current high-frequency signal attenuation characteristics, to determine the left side of the T area inside and outside the fault area or the right side of the T area inside and outside the fault area. The protection principle has the following advantages:

1) When the fault occurs, because the normal operation of DC current has a clear direction and size, the current on both sides of the line will be obvious to sudden changes, and one can use the polarity of the current line mode component of the sudden change in the construction of the direction of the criterion.
2) The adaptive nature of CEEMDAN decomposition and accurate identification ability of the Teager energy operator are used to determine the faults inside and outside the left side of the T-zone and the right side of the T-zone, respectively.
3) The method in this study does not require high sampling frequency and has strong resistance to transition resistance, and the time window is 4 ms, which can quickly and accurately determine the faults inside and outside the zone.

DATA AVAILABILITY STATEMENT

The original contributions presented in the study are included in the article/Supplementary Material; further inquiries can be directed to the corresponding author.

AUTHOR CONTRIBUTIONS

CX was responsible for providing ideas and methods and providing an experimental platform. YC was responsible for deriving formulas, reviewing, and verifying. LW was responsible for model building, simulation, data analysis, and manuscript writing. GB, SC, and JG wrote sections of the manuscript. All authors participated in the reading and approved the submitted version.

FUNDING

The research is funded by the National Natural Science Foundation of China (52067009).

REFERENCES

Boussaadia, F . (2019), Reliability Analysis of Transmission Lines protection Systems of the SONELGAZ Power System[C]//Algerian Large Electrical Network Conference. 0. doi:10.1109/CAGRE.2019.8713173

Chen, S., Shu, H., Xie, J., Cai, Z., and Zhang, W. (2013). Frequency Characteristics of UHVDC Transmission Line and its Boundary[J]. *Electric Power Automation Equipment* 33 (11), 134–139+153. doi:10.3969/j.issn.1006-6047.2013.11.024

Chen, Z., Zhou, Z., and Wang, X. (2019). Research on protection Scheme of Hybrid Multi-Terminal DC Transmission Lines[J]. *Power Syst. Tech.* 43 (07), 2617–2622. doi:10.13335/j.1000-3673.pst.2018.2400

Colominas, M. A., Schlotthauer, G., Torres, M. E., and Flandrin, P. (2013). Noise-Assisted Emd Methods in Action[J]. *Adv. Adaptive Data Anal.* 4 (04). doi:10.1142/S1793536912500252

Gao, S., Gao, Yue., and Song, G. (2020). A protection Method Based on Instaneous Engery of Teager Operator for Modular Multilevel Converter Multiterminal Flexible Direct Current Grid[J]. *J. Xi'an Jiaotong Univ.* 54 (09), 40–48. doi:10.7652/xjtuxb202009004

Gao, S., Zeng, Z., and Song, G. (2021). A Differential protection Scheme for Hybrid Three-Terminal DC System[J]. *J. Xi'an Jiaotong Univ.* 55 (01), 17–26. doi:10.7652/xjtuxb202101003

He, J., Chen, K., Li, M., Luo, Y., Liang, C., and Xu, Y. (2020). Review of protection and Fault Handling for a Flexible DC Grid. *Prot. Control. Mod. Power Syst.* 5, 15. doi:10.1186/s41601-020-00157-9

Karimian, A., and Hosseinian, S. H. (2020). Online Tracking of Voltage Flicker for Inverter-based Distributed Generation Using Teager Energy Operator [J]. *Int. Trans. Electr. Energ. Syst.* 30 (4). doi:10.1002/2050-7038.12292

Le, S., Wu, Y., Guo, Y., and Vecchio, C. D. (2021). Game Theoretic Approach for a Service Function Chain Routing in NFV with Coupled Constraints. *IEEE Trans. Circuits Syst.* 68, 3557–3561. Published online. doi:10.1109/TCSII.2021.3070025

Li, B., He, J., Feng, Y., Li, Y., Li, G., and Qiu, H. (2016). Key Techniques for Protection of Multi-Terminal Flexible DC Grid[J]. *Automation Electric Power Syst.* 40 (21), 2–12. doi:10.7500/AEPS20160601011

Li, H., Zhang, K., and Wang, G., Fault Area Discrimination Method for Parallel Multi-Terminal Hybrid HVDC DC Line[J]. *Automation Electric Power Syst.*, 2019, 43(04): 119–125.±179+126-128. doi:10.7500/AEPS20180615004

Li, J., and Li, Q. (2015). Medium Term Electricity Load Forecasting Based on CEEMDAN-Permutation[J]. *Electric Machines and Control* 19 (008), 70–80. doi:10.15938/j.emc.2015.08.011

Li, S., Chen, W., Yin, X., Chen, D., and Teng, Y. (2019). A Novel Integrated Protection for VSC-HVDC Transmission Line Based on Current Limiting Reactor Power[J]. *IEEE Trans. Power Deliv.* 35 (1), 226–233. doi:10.1109/tpwrd.2019.2945412

Li, Z., Jiang, W., Abu-Siada, A., Li, Z., Xu, Y., and Liu, S. (2021). Research on a Composite Voltage and Current Measurement Device for HVDC Networks. *IEEE Trans. Ind. Electron.* 68 (9), 8930–8941. doi:10.1109/tie.2020.3013772

Lin, X., Qi, L., and Fan, L. (2020). Blocking Pilot protection Based on Ratio of Superimposed Energy for VSC-MTDC Grid[J]. *Automation Electric Power Syst.* 40 (04), 2–8+16. doi:10.16081/j.epae.202004024

Liu, Y., Yang, N., Dong, B., Wu, L., Yan, J., Shen, X., et al. (2020). Multi-Lateral Participants Decision-Making: A Distribution System Planning Approach with Incomplete Information Game. *IEEE Access* 8, 88933–88950. doi:10.1109/access.2020.2991181

Muniappan, M. (2021). A Comprehensive Review of DC Fault protection Methods in HVDC Transmission Systems. *Prot. Control. Mod. Power Syst.* 6 (1), 1–20. doi:10.1186/s41601-020-00173-9

Ren, Z., Cheng, J., and Xing, Q. (2017). A Harmonic Detection Method Based on CEEMDAN and Teager Energy Operator Algorithm[J]. *Power Syst. Prot. Control.* (9), 56–62. doi:10.7667/PSPC160634

Shen, X., Ouyang, T., Khajorntraidet, C., Li, Y., Li, S., and Zhuang, J. (2021a). Mixture Density Networks-Based Knock Simulator. *Ieee/asme Trans. Mechatron.*, 1. doi:10.1109/TMECH.2021.3059775

Shen, X., Ouyang, T., Yang, N., and Zhuang, J. (2021b). Sample-based Neural Approximation Approach for Probabilistic Constrained Programs. *IEEE Trans. Neural Netw. Learn. Syst.*, 1–8. doi:10.1109/TNNLS.2021.3102323

Shen, X., and Raksincharoensak, P. (2021a). Pedestrian-aware Statistical Risk Assessment. *IEEE Trans. Intell. Transport. Syst.*, 1–9. doi:10.1109/TITS.2021.3074522

Shen, X., and Raksincharoensak, P. (2021b). Statistical Models of Near-Accident Event and Pedestrian Behavior at Non-signalized Intersections. *J. Appl. Stat.*, 1–21. doi:10.1080/02664763.2021.1962263

Shen, X., Zhang, X., Ouyang, T., Li, Y., and Raksincharoensak, P. (2020a). Cooperative Comfortable-Driving at Signalized Intersections for Connected and Automated Vehicles. *IEEE Robot. Autom. Lett.* 5 (4), 6247–6254. doi:10.1109/LRA.2020.3014010

Shen, X., Zhang, Y., Sata, K., and Shen, T. (2020b). Gaussian Mixture Model Clustering-Based Knock Threshold Learning in Automotive Engines. *Ieee/asme Trans. Mechatron.* 25 (6), 2981–2991. doi:10.1109/TMECH.2020.3000732

Shen, X., Zhang, Y., Shen, T., and Khajorntraidet, C. (2017). Spark advance Self-Optimization with Knock Probability Threshold for Lean-Burn Operation Mode of SI Engine. *Energy* 122 (3), 1–10. doi:10.1016/j.energy.2017.01.065

Song, G., Hou, J., Guo, B., Chen, Z., et al. (2020). Pilot protection of Hybrid MMC DC Gridbased on Active Detection. *J. Prot. Control. Mod. Power Syst.* V5 (1), 82–96. doi:10.1186/s41601-020-0152-2

Tian, P., Wu, Q., and Huang, j. (2021). Research on protection Strategy of a Hybrid Multi-Terminal DC System Based on LCC and FHMMC[J]. *Power Syst. Prot. Control.* 49 (01), 170–177. doi:10.19783/j.cnki.pspc.200211

Toyoda, M., and Wu, Y. (2021). Mayer-type Optimal Control of Probabilistic Boolean Control Network with Uncertain Selection Probabilities. *IEEE Trans. Cybern.* 51, 3079–3092. doi:10.1109/tcyb.2019.2954849

Vanra, J., Dhami, S. S., and Pabla, B. S. (2017). Non-Contact Incipient Fault Diagnosis Method of Fixed-Axis Gearbox Based on CEEMDAN. *R. Soc. Open Sci.* 4 (8), 170616. doi:10.1098/rsos.170616

Wang, L., and Shao, Y. (2020). Fault Feature Extraction of Rotating Machinery Using a Reweighted Complete Ensemble Empirical Mode Decomposition with Adaptive Noise and Demodulation Analysis[J]. *Mech. Syst. signal Process.* 138 (Apr), 1065451–1106545.20. doi:10.1016/j.ymssp.2019.106545

Wang, Y., Fan, X., and Zhang, B. (2019). The Analytical Analysis and Protection Setting of Traveling Wave Protection in VSC-HVDC Grid[J]. *Proc. CSEE* 39 (11), 3201–3212. doi:10.13334/j.0258-8013.pcsee.181633

Wu, Y., Guo, Y., and Toyoda, M. (2021). Policy Iteration Approach to the Infinite Horizon Average Optimal Control of Probabilistic Boolean Networks. *IEEE Trans. Neural Netw. Learn. Syst.* 32 (6), 2910–2924. doi:10.1109/TNNLS.2020.3008960

Yang, N., Ye, D., Zhou, Z., Cui, J., Chen, D., and Wang, X. (2018). Research on Modelling and Solution of Stochastic SCUC under AC Power Flow Constraints [J]. *IET Generation, Transm. Distribution* 12 (15), 3618–3625. doi:10.1049/iet-gtd.2017.1845

Yang, N., Huang, Y., Hou, D., Liu, S., Ye, D., Dong, B., et al. (2019). Adaptive Nonparametric Kernel Density Estimation Approach for Joint Probability Density Function Modeling of Multiple Wind Farms. *Energies* 12, 1356. doi:10.3390/en12071356

Yang, N., Liu, S., Deng, Y., and Xing, C. (2021b). An Improved Robust SCUC Approach Considering Multiple Uncertainty and Correlation. *IEEJ Trans. Elec Electron. Eng.* 16, 21–34. doi:10.1002/tee.23265

Yang, N., Qin, T., Wu, L., Huang, Y., Huang, Y., Xing, C., et al. (2022). A Multi-Agent Game Based Joint Planning Approach for Electricity-Gas Integrated Energy Systems Considering Wind Power Uncertainty. *Electric Power Syst. Res.* 204, 107673. ISSN 0378-7796. doi:10.1016/j.epsr.2021.107673

Yang, N., Yang, C., Wu, L., Shen, X., Jia, J., Li, Z., et al. (2021c). Intelligent Data-Driven Decision-Making Method for Dynamic Multi-Sequence: An E-Seq2Seq Based SCUC Expert System. *IEEE Trans. Ind. Inf.*, 1. doi:10.1109/TII.2021.3107406

Yang, N., Yang, C., Xing, C., Ye, D., Jia, J., Chen, D., et al. (2021a). Deep Learning-based SCUC Decision-making: An Intelligent Data-driven Approach with Self-learning Capabilities. *IET Gener. Transm. Distrib.*, 1–12. doi:10.1049/gtd2.12315

Zhang, Lei., Xie, Y., Ye, J., Xue, T., Cheng, J., Li, Z., et al. (2021). Intelligent Frequency Control Strategy Based on Reinforcement Learning of Multi-Objective Collaborative Reward Function[J]. *Front. Energ. Res. Early Access*. doi:10.3389/fenrg.2021.760525(SCI)

Zheng, X., Wang, S., Li, N., Xiao, H., and Jiang, W. (2016). A LCC and MMC Series Hybrid HVDC Topology Suitable for Bulk Power Overhead Line Transmission[J]. *Power Syst. Tech.* 40 (01), 55–63. doi:10.13335/j.1000-3673.pst.2016.01.008

Zhu, B., Ding, F., and Vilathgamuwa, D. M. (2020). Coat Circuits for DC-DC Converters to Improve Voltage Conversion Ratio. *IEEE Trans. Power Electron.* 35 (4), 3679–3687. doi:10.1109/TPEL.2019.2934726

Conflict of Interest: Author CX is studying for his doctor's degree in Tianjin University and employed by the Electric Power Research Institute, Southern Power Grid Yunnan Electric Power Co., Ltd. Author YC works at the Key Laboratory of Smart Grid of Education Ministry of Tianjin University.

The remaining authors declare that the research was conducted in the absence of any commercial or financial relationships that could be construed as a potential conflict of interest.

Publisher's Note: All claims expressed in this article are solely those of the authors and do not necessarily represent those of their affiliated organizations, or those of the publisher, the editors, and the reviewers. Any product that may be evaluated in this article, or claim that may be made by its manufacturer, is not guaranteed or endorsed by the publisher.

frontiers in Energy Research

ORIGINAL RESEARCH
published: 11 March 2022
doi: 10.3389/fenrg.2022.858518

Grey Wolf Optimization–Based Deep Echo State Network for Time Series Prediction

Xiaojuan Chen and Haiyang Zhang*

School of Electronic Information Engineering, Changchun University of Science and Technology, Changchun, China

The Echo State Network (ESN) is a unique type of recurrent neural network. It is built atop a reservoir, which is a sparse, random, and enormous hidden infrastructure. ESN has been successful in dealing with a variety of non-linear issues, including prediction and classification. ESN is utilized in a variety of architectures, including the recently proposed Multi-Layer (ML) architecture. Furthermore, Deep Echo State Network (DeepESN) models, which are multi-layer ESN models, have recently been proved to be successful at predicting high-dimensional complicated non-linear processes. The proper configuration of DeepESN architectures and training parameters is a time-consuming and difficult undertaking. To achieve the lowest learning error, a variety of parameters (hidden neurons, input scaling, the number of layers, and spectral radius) are carefully adjusted. However, the optimum training results may not be guaranteed by this haphazardly created work. The grey wolf optimization (GWO) algorithm is introduced in this study to address these concerns. The DeepESN based on GWO (GWODESN) is utilized in trials to forecast time series, and therefore the results are compared with the regular ESN, LSTM, and ELM models. The findings indicate that the planned model performs the best in terms of prediction.

Keywords: time series prediction, deep echo state network, grey wolf optimization, network structure optimization, combined cycle power plant

OPEN ACCESS

Edited by:
Yusen He,
Grinnell College, United States

Reviewed by:
Rui Yin,
Dalian University of Technology, China
GL Feng,
Dalian University of Technology, China

****Correspondence:***
Xiaojuan Chen
cxj001@cust.edu.cn

Specialty section:
This article was submitted to Smart Grids, a section of the journal Frontiers in Energy Research

Received: *21 January 2022*
Accepted: *01 February 2022*
Published: *11 March 2022*

Citation:
Chen X and Zhang H (2022) Grey Wolf Optimization–Based Deep Echo State Network for Time Series Prediction. Front. Energy Res. 10:858518. doi: 10.3389/fenrg.2022.858518

1 INTRODUCTION

Time series appear in every facet of life, and one of the current research topics is time series forecasting. Time series prediction may be aided by the development of new methodologies. The time series, on the other hand, is frequently created by a chaotic system and is untidy or non-linear. As a result, time-series forecasting research is extremely difficult. Furthermore, time series prediction requires models with high prediction accuracy.

Over the two past decades, several researchers proposed various models for time series forecasting that involve scientific prediction based on historical time-stamped data. Among these researchers, Liu (2017) presented a time-series prediction approach based on an online sequential extreme learning machine (OS-ELM). This approach was later updated to include an adaptive forgetting factor and a bootstrap to improve the prediction accuracy and stability. Guo et al. (2016) used differential evolution (DE) to optimize the model parameters in an efficient extreme learning machine (EELM) that is utilized to anticipate chaotic time series. Lukoseviciute et al. (2018) used evolutionary algorithms and Bernstein polynomials to develop a short-term time-series prediction model. For chaotic time series, Ma et al. (2004) suggested a mixed model based on neural networks and wavelets. Milad et al. (2017) proposed a model of adaptive decayed brain emotional learning

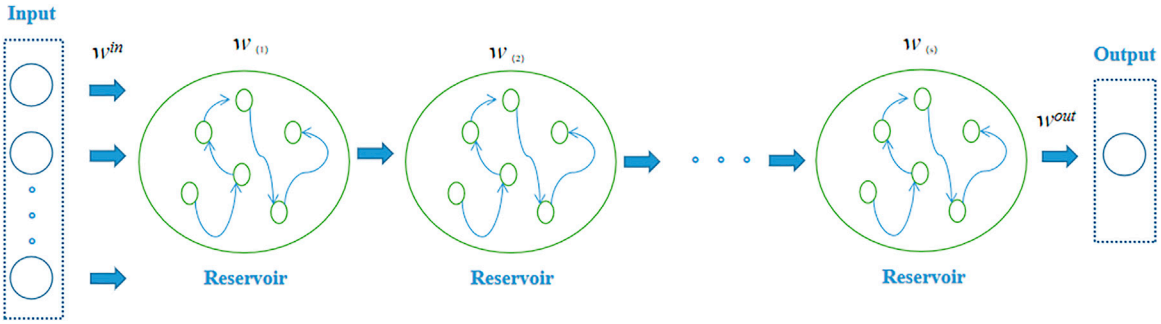

FIGURE 1 | Architecture of a DeepESN.

(ADBEL) to better handle online forecasting of time series through a neuro-fuzzy network architecture. Miranian and Abdollahzade (2013) proposed a local neuro-fuzzy (LNF) scheme combined with least-square support vector machines (LSSVMs) for non-linear and chaotic modeling and forecasting. Tang et al. (2020) proposed a LSSVM model to model NOx emissions. Chai and Lim (2016) constructed a discriminative model of a neural network architecture equipped with weighted fuzzy membership functions (NEWFM) for identifying patterns of economic time series. Li et al. (2016) proposed an adaptive Volterra-type prediction model with matrix factorization for chaotic time-series analysis. Su and Yang (2021) proposed a brain emotional network in conjunction with an adaptive genetic algorithm (BEN-AGA) model for predicting time series of chaotic behavior. Nevertheless, the aforementioned methods have several limitations. First, an adequate structure must be pre-specified for the conventional neural networks, and the convergence rate of these networks is slow. Also, the ELM method exhibits weak generalization and robustness. Also, the LSSVM method is greatly affected by time delays.

Recently, recurrent neural networks (RNNs) have been introduced to handle problems with temporal dynamics. The RNN architectures have been successfully utilized for time-series detection (Li et al., 2021a) and forecasting (Li et al., 2021b). However, the overall RNN weights should be learned through backpropagation, and this imposes a significant computational burden. To enhance the operational efficiency, Echo State Networks (ESNs) were proposed by Jaeger and Haas (2004) as a novel RNN variant that can be efficiently utilized for time series forecasting. For example, Han et al. (2021) proposed an optimized ESN model with adaptive error compensation for network traffic prediction. Liu et al. (2020) proposed a hybrid time-series prediction approach with the binary grey wolf algorithm and echo state networks (BGWO-ESN). Beyond time series forecasting, the echo state networks have also been applied in other problems, including mainly classification (Stefenon et al., 2022), detection (Steiner et al., 2021), and image segmentation (Abdelkerim et al., 2020). However, the conventional ESN architectures still lack the ability to handle complicated tasks. To address this limitation, a DeepESN model is introduced in this paper, where a grey wolf optimization (GWO) algorithm is used to optimize the DeepESN model parameters. Our proposed DeepESN architecture is evaluated on the Lorenz system, the Mackey–Glass (MG) model, and the non-linear autoregressive moving average (NARMA) model. The proposed method was evaluated with a real-time series representing full-load electrical power outputs. The simulations demonstrate promising performance of the proposed forecasting strategy.

The main contributions of this paper are highlighted as follows: first, the effort made in the paper represents one of the first few attempts to construct DeepESN to forecast times series. Then, compared with ESN, LSTM, and ELM models, the proposed GWODESN outperforms in terms of forecast accuracy.

The remainder of this work is arranged as follows. A detailed overview of the DeepESN and GWO algorithms is presented in **Section 2**, while **Section 3** provides the details of the proposed GWODESN model. The simulation outcomes are analyzed in **Section 4**. Then, **Section 5** gives final conclusions.

2 METHODOLOGY

2.1 Deep Echo State Networks

Following the conventional ESN model, the DeepESN model is made up of multiple dynamical reservoir components. Specifically, the DeepESN reservoir is organized into stacked repetitive layers. For each layer, the output is the input of the next layer, as outlined in **Figure 1** (Gallicchio and Micheli, 2017). In our work, *NU* indicates the number of the input measurements, *NL* indicates the reservoir layer count, *NR* denotes the number of the recurrent units, and *t* indicates time. Moreover, $u(t)$ denotes the model input at time *t*, whereas $\mathrm{x}^{(i)}(t)$ represents the state for the *ith* reservoir layer at time *t*. The DeepESN reservoir dynamics are mathematically modeled as follows. The dynamics of the primary DeepESN layer can be expressed as

$$\mathrm{x}^{(1)}(t) = \left(1-\mathrm{a}^{(1)}\right)\mathrm{x}^{(1)}(t-1) + \mathrm{a}^{(1)}\,\mathrm{f}\left(\mathrm{W}^{(1)}\,\mathrm{u}(t) + \hat{\mathrm{W}}^{(1)}\,\mathrm{x}^{(1)}(t-1)\right) \quad (1)$$

When $i > 1$, the DeepESN state is computed as

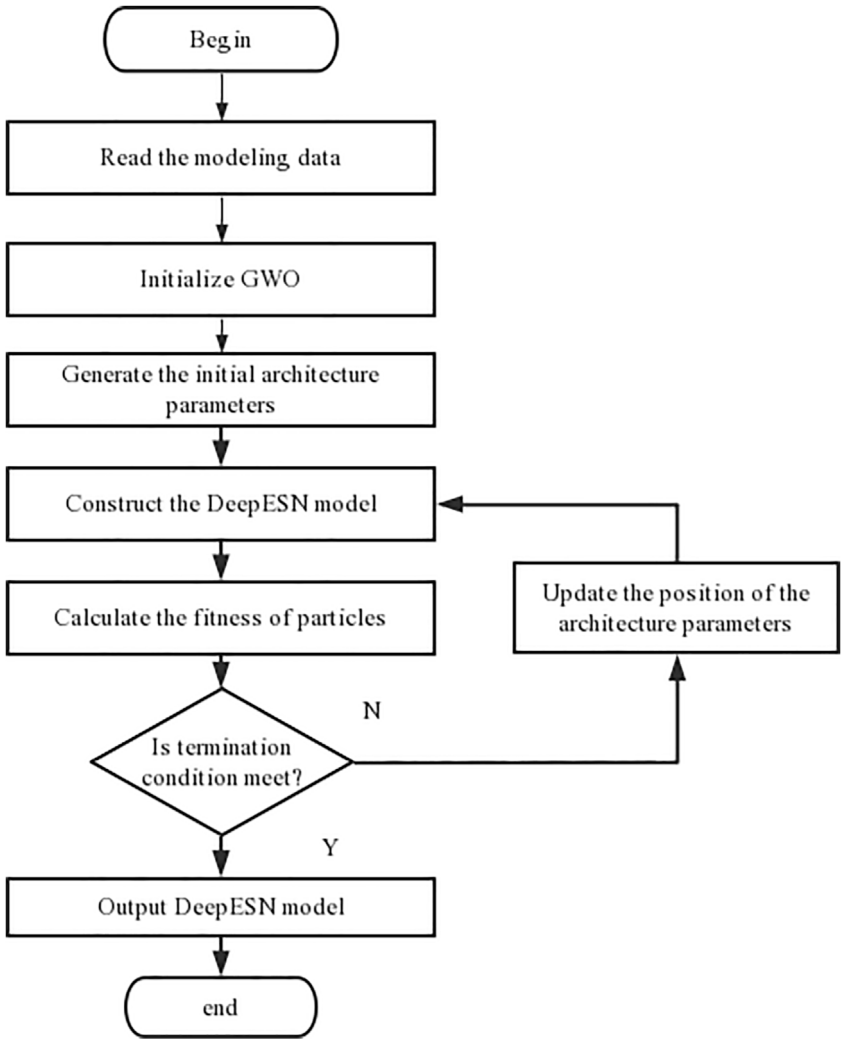

FIGURE 2 | A flowchart of the proposed modeling approach.

$$\mathrm{x}^{(i)}(t) = \left(1 - \mathrm{a}^{(i)}\right)\mathrm{x}^{(i)}(t-1) + \mathrm{a}^{(i)}\,\mathrm{f}\left(\mathrm{W}^{(i)}\,\mathrm{x}^{(i)}(t) + \hat{\mathrm{W}}^{(i)}\,\mathrm{x}^{(i)}(t-1)\right) \tag{2}$$

where $\mathrm{W}^{(1)}$ indicates the input weight matrix, $\mathrm{W}^{(i)}$ indicates the weights of the connections between the $(i-1)^{th}$ and *ith* layers, $\hat{\mathrm{W}}^{(i)}$ indicates the recurrent weights of the *ith* layer, $\mathrm{a}^{(i)} \in [0, 1]$ indicates the leakage rate of the *ith* layer, and f represents the employed activation function (regularly chosen as the tanh function).

2.2 Grey Wolf Optimizer

GWO could be a nature-inspired algorithm that imitates the chain of command of administration and daily routine (Mirjalili et al., 2014). The wolves have four conceivable sorts: alpha, beta, delta, or omega. The pioneers of the pack (called alphas), which may be recognized by the leading administration abilities instead of the most grounded body, make choices almost every day exercises for the whole pack. The beta wolf helps alpha to make a choice. The omega wolf position is most reduced among wolves, but it plays a key part in keeping up a prevailing structure. The delta wolf is auxiliary to the alpha and beta, but it has the upper hand over the omega within the previously mentioned chain of command. The GWO algorithm can be mathematically represented as follows:

$$\vec{D} = \left|C \cdot \overrightarrow{X_p}(t) - \vec{X}(t)\right| \tag{3}$$

$$\vec{X}(t+1) = \overrightarrow{X_p}(t) - A \cdot \vec{D} \tag{4}$$

where t is utilized to mean the current iteration, $\overrightarrow{X_p}$ to mean the prey position vector, and $\vec{X}$ to represent the wolf position vector. Meanwhile, A and C can be represented as

$$A = 2a \cdot r_1 - a \tag{5}$$

$$C = 2 \cdot r_2 \tag{6}$$

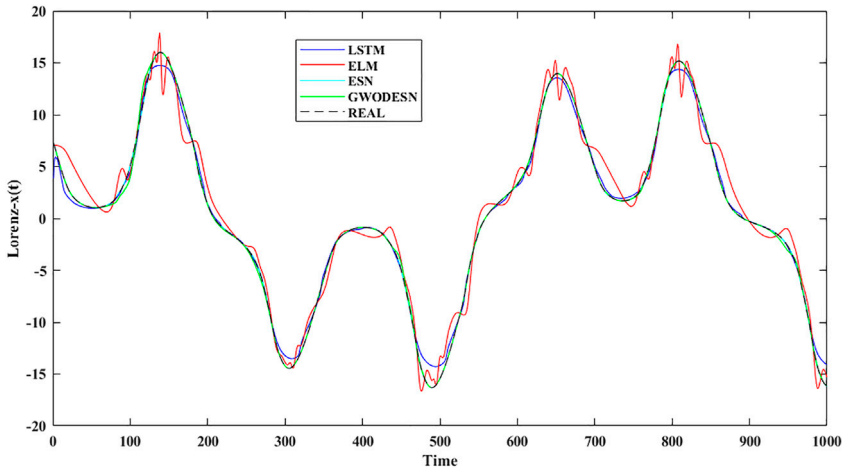

FIGURE 3 | The real value and the anticipated value for Lorenz x(*t*).

TABLE 1 | The performance comparison of GWODESN, ESN, ELM, and the LSTM for Lorenz x(*t*)

Model	MAPE	MAE	RMSE	R^2
GWODESN	0.00010737	0.008402	0.012598	1
ESN	0.0018053	0.099649	0.22953	0.99923
LSTM	0.028958	0.36154	0.55374	0.99758
ELM	0.17571	1.0301	1.3047	0.977

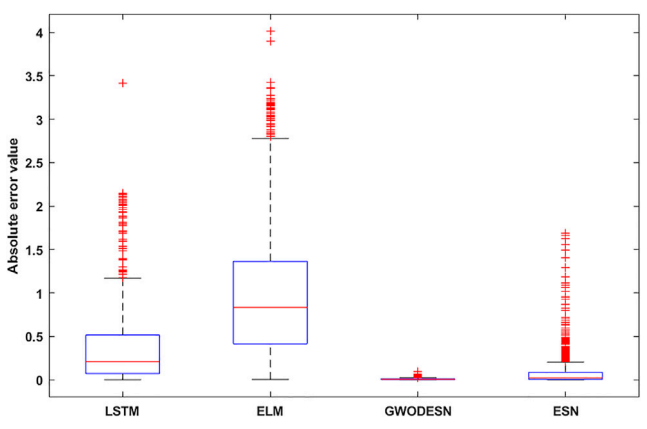

FIGURE 4 | The absolute error box diagram for Lorenz x(*t*).

where a is diminished in a straight design from 2 to 0. r_1, r_2 are haphazardly created from the unit interval [0,1]. The wolf pack chasing design is driven by the alpha wolves and frequently by the beta and delta ones. This design may be scientifically sculptural as takes after

$$\begin{aligned}\overrightarrow{D_\alpha} &= \left|C_1 \cdot \overrightarrow{X_\alpha} - \vec{X}\right| \\ \overrightarrow{D_\beta} &= \left|C_2 \cdot \overrightarrow{X_\beta} - \vec{X}\right| \\ \overrightarrow{D_\delta} &= \left|C_3 \cdot \overrightarrow{X_\delta} - \vec{X}\right|\end{aligned} \tag{7}$$

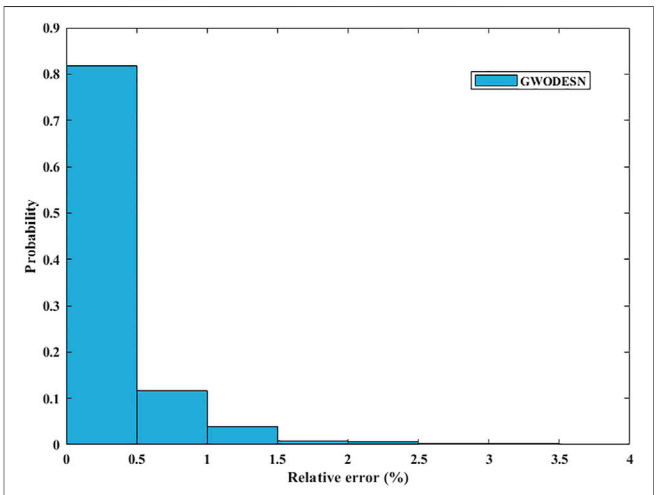

FIGURE 5 | Relative error distribution for Lorenz x(*t*).

$$\begin{aligned}\overrightarrow{X_1} &= \overrightarrow{X_\alpha} - A_1 \cdot \overrightarrow{D_\alpha} \\ \overrightarrow{X_2} &= \overrightarrow{X_\beta} - A_2 \cdot \overrightarrow{D_\beta} \\ \overrightarrow{X_3} &= \overrightarrow{X_\delta} - A_3 \cdot \overrightarrow{D_\delta}\end{aligned} \tag{8}$$

$$\vec{X}\,(t+1) = \left(\overrightarrow{X_1} + \overrightarrow{X_2} + \overrightarrow{X_3}\right)\Big/3 \tag{9}$$

3 GREY WOLF OPTIMIZER–BASED DEEP ECHO STATE NETWORK

As the same as simple ESN model, we must appropriately indicate network parameters of DeepESN for getting palatable comes about. We might rehash the tests trusting to secure great plan scenarios. Be that as it may, we can never be sure that the best solution has been achieved. To address it, the GWO algorithm ought to be utilized to

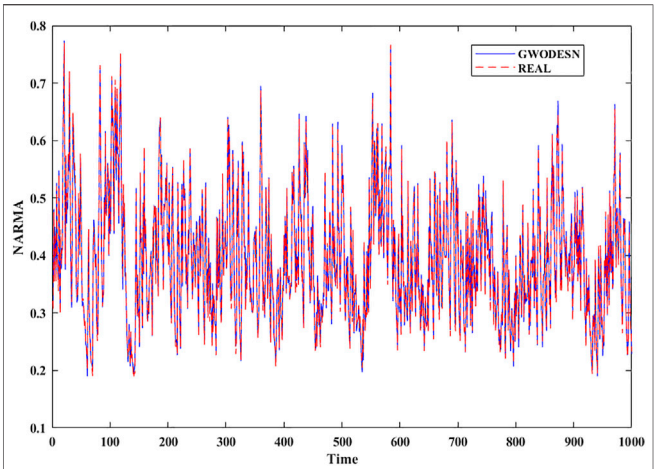

FIGURE 6 | The real value and the anticipated value for NARMA.

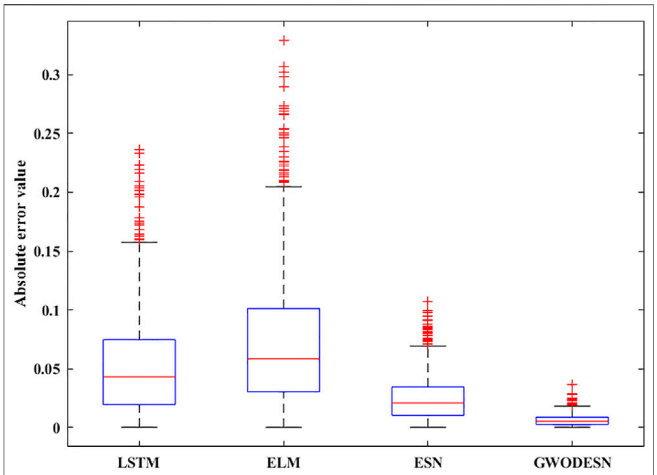

FIGURE 7 | The absolute error box diagram for NARMA.

TABLE 2 | Prediction performance comparison for NARMA

Model	MAPE	MAE	RMSE	R^2
GWODESN	0.016684	0.006208	0.0078925	0.99487
ESN	0.067969	0.024812	0.031407	0.91423
LSTM	0.13112	0.052137	0.067306	0.66642
ELM	0.19488	0.072871	0.093292	0.24624

optimize a couple of parameters including *NR*, *NL*, ρ, and *IR*. The spectral radius ρ is one in all the foremost central parameters characterizing the reservoir's weight matrix W. And to take care of the echo state property (ESP), ρ should be scaled to equal or less than one. **Figure 2** shows a flowchart of the proposed GWODESN. The taking after steps depict the particular modeling strategy:

Step 1. Read time series file as the input data.

Step 2. Initialize the GWO algorithm containing the a, A, and C.

Step 3. Set initial population representing *NR*, *NL*, ρ, and *IR*.

Step 4. Use initial population to establish the DeepESN model.

Step 5. Calculate the mean absolute error of various population as the corresponding fitness value.

Step 6. Obtain initial optimum value having least fitness values in population.

Step 7. If the fitness value obtained meets the accuracy requirements of the model, skip to Step 9. Something else, proceed.

Step 8. Update the population applying **Eq. 9**, the number of iterations $t = t+1$, and then return to Step 4.

Step 9. Output the best *NR*, *NL*, ρ, and *IR*.

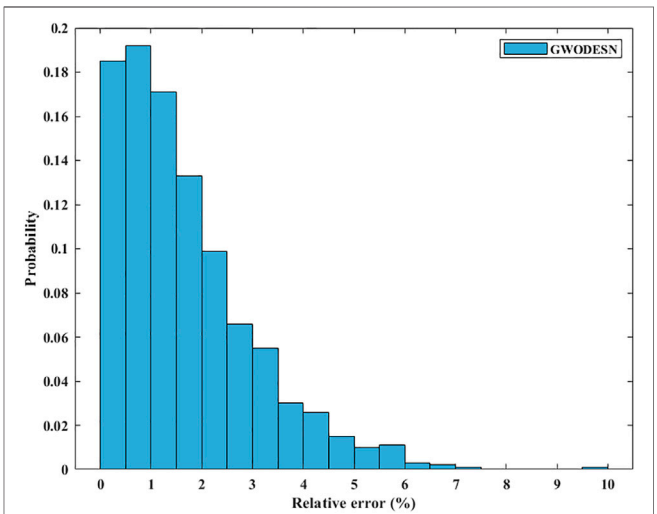

FIGURE 8 | Relative error distribution for NARMA.

4 EXPERIMENTAL SETUP, RESULTS, AND DISCUSSION

In this pondering, three benchmark datasets and one real-world illustration are embraced to confirm the execution of diverse models. One-step ahead expectation is examined in this segment. To assess the created demonstration, 4 standard records (Tang et al., 2020; Li et al., 2021a; Li et al., 2021b) including the mean absolute error (MAE), the mean absolute percentage error (MAPE), the root-mean-square error (RMSE), and the coefficient of determination (R^2) are characterized as takes after

$$MAE = \frac{1}{M}\sum_{j=1}^{M}\left|y_j - \hat{y}_j\right| \tag{10}$$

$$MAPE = \frac{1}{M}\sum_{j=1}^{M}\frac{\left|y_j - \hat{y}_j\right|}{y_j} \tag{11}$$

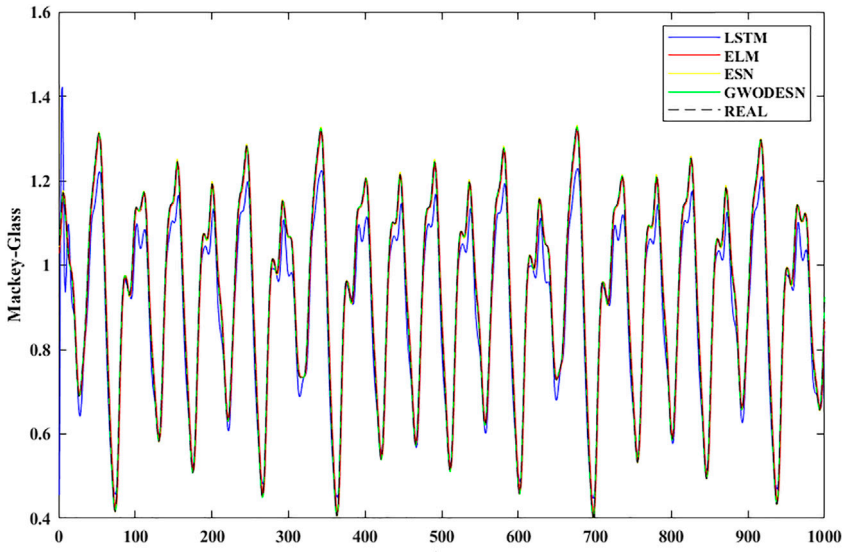

FIGURE 9 | The real value and the anticipated value for MG.

TABLE 3 | Prediction performance comparison for MG

Model	MAPE	MAE	RMSE	R^2
GWODESN	1.52E−06	1.34E−06	8.74E−06	1
ESN	0.0022983	0.0019566	0.0023502	0.99989
LSTM	0.049911	0.047476	0.059318	0.96962
ELM	0.035191	0.029265	0.03455	0.97677

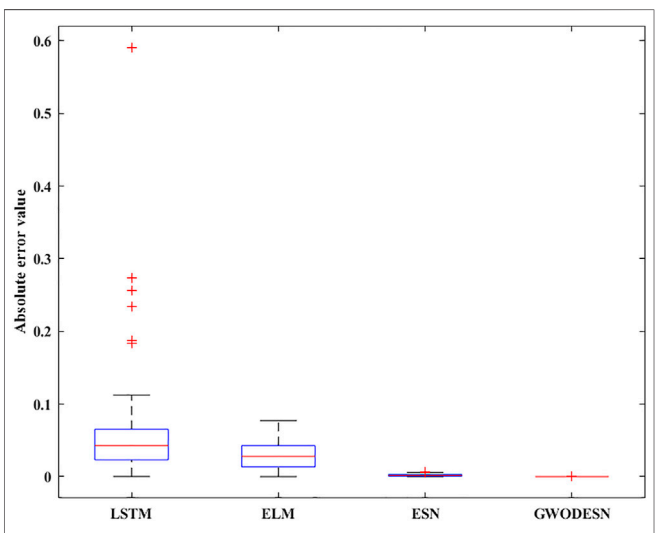

FIGURE 10 | The absolute error box diagram for MG.

$$RMSE = \sqrt{\frac{1}{M}\sum_{j=1}^{M}\left(y_j - \hat{y}_j\right)^2} \tag{12}$$

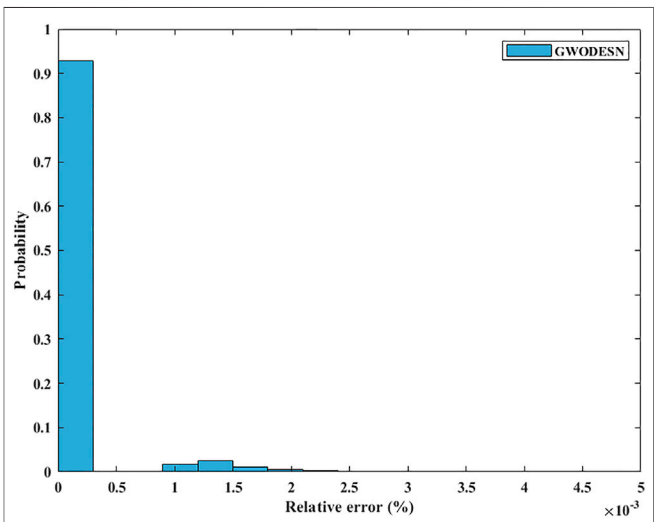

FIGURE 11 | Relative error distribution for MG.

$$R^2 = 1 - \frac{\sum_{j=1}^{M}\left(y_j - \hat{y}_j\right)^2}{\sum_{j=1}^{M}\left(y_j - \bar{y}_j\right)^2} \tag{13}$$

Within the equations, M is utilized to represent sample size, y_j to represent the true value, $\bar{y}_j$ to represent mean true value, and $\hat{y}_j$ to represent the forecast value. All experiments were carried out in MATLAB on a Windows 10 operating system, with a 2.50-GHz Intel CPU, and a memory of 8.0 GB. The performance outcomes of our approach were compared with those based on the conventional ESN, ELM, and LSTM architectures.

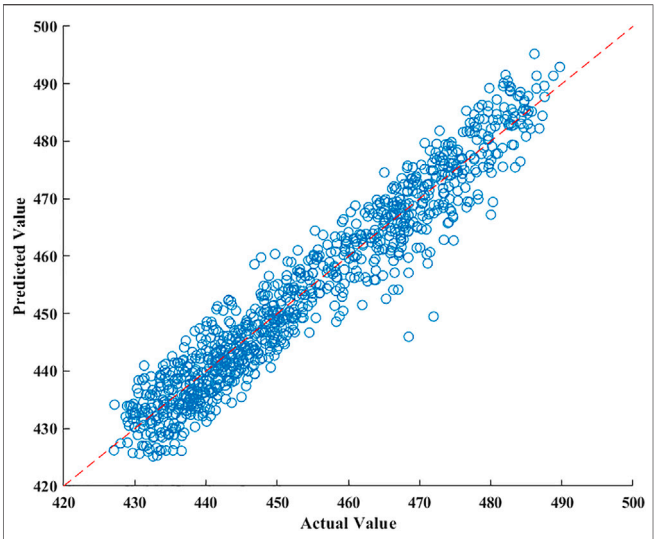

FIGURE 12 | Scatter diagram of the real value and the anticipated value for CCPP.

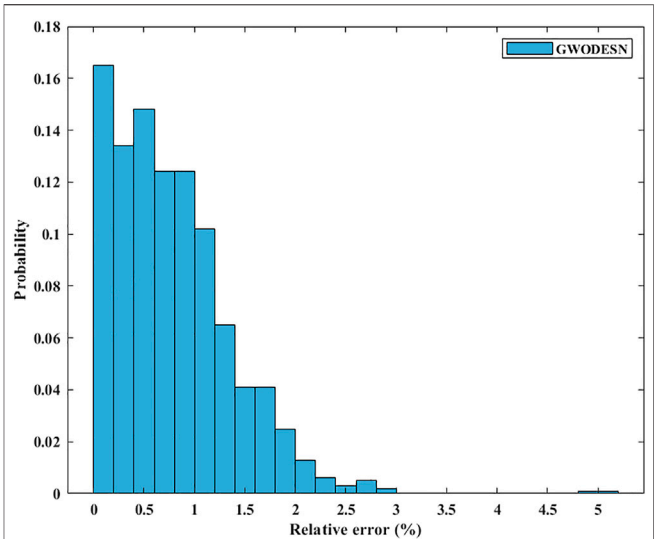

FIGURE 13 | Relative error distribution for CCPP.

4.1 Lorenz System

The Lorenz dynamical system (Wu et al., 2021) is a key benchmark of time series forecasting and is mathematically defined as

$$\begin{aligned} \frac{dx}{dt} &= a(-x+y) \\ \frac{dy}{dt} &= bx - y - xz \\ \frac{dz}{dt} &= xy - cz \end{aligned} \tag{14}$$

where t expresses time, while the model coefficients a, b, and c are respectively chosen as 10, 28, and 8/3. Model training and testing were carried out with time series lengths of 4,000 and 1,000, respectively. For x-dimensional forecasting, past information of $x(t-1)$, $y(t-1)$, and $z(t-1)$ is utilized in the prediction of the present $x(t)$ values. In the arrangement to assess the viability and preferences of this proposed GWODESN, the conventional ESN, ELM, and the LSTM are chosen as benchmarks. The real value and the anticipated value of GWODESN, ESN, ELM, and the LSTM to begin with appeared in **Figure 3**, and the expectation exactness is recorded in **Table 1**. It is clear that GWODESN is superior than others, showing the adequacy of this approach. In expansion, the yield of ELM cannot coordinate the real esteem, particularly at a few emphasis focuses. It moreover outlines the justification of RNN. The expectation mistakes of GWODESN, ESN, ELM, and the LSTM are advance compared in **Figure 4**. **Figure 4** shows the box graph of absolute error recorded for 30 runs of diverse models. It can be seen that the GWODESN shows superior forecast exactness and solidness than other models. The absolute error box graph of the ELM demonstration is long, and it is known that the supreme mistake values are scattered, showing that the forecast performance of the ELM model is not as steady as in other models. The box chart of the GWODESN model is the most brief. Most of the absolute error values are smaller than other comparison models. **Figure 5** gives the relative error distribution of the testing information by the GWODESN. Among the 1,000 testing cases, 93.3% of the relative errors were less than 1%. In general, the prediction accuracy of the GWODESN model is relatively high and relatively stable. In common, the expectation precision of the GWODESN model is moderately high and generally steady.

4.2 NARMA system

NARMA (Chouikhi et al., 2017), which is featured with a very high rate of chaos in its behavior, could also be an accepted studied benchmark. The flow of this benchmark is produced by **Eq. 15**:

$$y(t+1) = c_1 y(t) + c_2 y(t) \sum_{i=1}^{k} y(t-i) + c_3 x(t-(k-1)) x(t) + c_4 \tag{15}$$

where $y(t)$ and $x(t)$ are the yield and input of the framework at time t, separately. The consistent c is set as 0.3, 0.05, 1.5, and 0.1, separately. The k, which decides the intricacy of NARMA, is set to 10. As the same as the past simulation, the real value and the anticipated value of GWODESN are shown in **Figure 6**, and the desired precision is recorded in **Table 2**. It is evident that GWODESN can take after the

TABLE 4 | Prediction performance comparison for CCPP

Model	MAPE	MAE	RMSE	R^2
GWODESN	0.0071209	3.2268	4.1052	0.93981
ESN	0.0078012	3.5345	4.4278	0.93013
LSTM	0.0085425	3.8767	4.9317	0.91412
ELM	0.0079702	3.6098	4.4885	0.92832

real esteem ideally. The desired botches of GWODESN, ESN, ELM, and the LSTM are developed and compared in **Figure 7**. It can be seen in **Figure 7** that the GWODESN appears to have a more predominant estimate precision and solidness than other models. The absolute error box graph of the ELM is long, and it is known that the incomparable botch values are scattered, appearing that the figure execution of the ELM is not as steady as other models. The box chart of the GWODESN show is the foremost brief. Most of the absolute error values are more diminutive than other comparison models. **Figure 8** gives the relative error dispersion of the testing data by the GWODESN. Among the 1,000 testing cases, 90.1% of the relative error distribution were less than 3.5% as appeared in **Figure 8**.

4.3 Mackey–Glass System

The MG (Mackey and Glass, 1977) may be a normal chaotic framework, which is known by its non-linear behavior. Thus, learning the designs appears to be a troublesome errand. It is portrayed by **Eq. 16**.

$$\frac{dx(t)}{dt} = \frac{0.2x(t-\tau)}{1+x^{10}(t-\tau)} - 0.1x(t) \tag{16}$$

where τ is a vital parameter of the MG system, which is regularly set to 17. In total, 4,000 tests were utilized as training data sets and 1,000 tests were utilized for testing. The forecast that comes about appears in **Figure 9** and **Table 3**. The conventional utilized ESN can be seen to have superior forecast execution than the ELM and the LSTM and can fit the original data well. Be that as it may, the execution of the GWODESN is superior than that of the conventional ESN. **Figure 10** appears that the GWODESN show has superior forecast precision and soundness than other models. Among the 1,000 testing cases, 99% of the relative mistakes were less than 1% in **Figure 11**.

4.4 Combined Cycle Power Plants

CCPPs generally contain steam turbines (STs) and gas turbines (GTs), as well as heat recovery steam generators (HRSGs). For a CCPP, power generation is jointly performed by the steam and gas turbines, and is exchanged between each turbine and the others (Tüfekci, 2014). Here, we use CCPP data to evaluate the single-step prediction performance. The utilized dataset includes four input factors and one target variable, where this dataset was collected from 2006 to 2011. **Figure 12** outlines both the GWODESN-predicted and measured electrical power outputs. The specked reddish straight line represents the ideal relationship of the predicted and measured values. The blue line demonstrates the GWODESN predicted outcomes. Almost all of the predictions are scattered around the ideal line. **Figure 13** gives the relative error distribution of the GWODESN model on the test data. Among the 1,000 test samples, 90.3% of the relative errors are less than 1.6%. Obviously, the GWODESN model outperforms the other three competing models. The adequacy of the proposed model is shown by the results in **Table 4**.

5 CONCLUSION

In this paper, the GWODESN is created for time series expectation. The four primary parameters of the DESN were optimized by utilizing the GWO algorithm. Four ordinary time series, counting Lorenz, MG, NARMA, and CCPP, are chosen as the simulation objects. Comparative test that comes about on four time-series forecast assignments clearly illustrates that the proposed GWODESN outflank the ELM, LSTM, and ESN benchmarks. The expectation strategy is basic and effective, and has certain hypothetical centrality and commonsense esteem. Hyper-parameter optimization and the topology of the networks are all the common optimization strategies. Within the future, we will center on progressing the network topology and apply the model in other domains, such as wind energy prediction.

DATA AVAILABILITY STATEMENT

The raw data supporting the conclusion of this article will be made available by the authors, without undue reservation.

AUTHOR CONTRIBUTIONS

XC designed the research and the article structure, and revised the article. HZ carried out the experiments and revised the article.

REFERENCES

Abdelkerim, S., Amma, B., Zoubir, A. F., and Elhadj, B. H. (2020). Echo State Network-based Feature Extraction for Efficient Color Image Segmentation. *J. Concurrency Computation: Pract. Experience* 32 (21), 1. doi:10.1002/cpe.5719

Chai, S. H., and Lim, J. S. (2016). Forecasting Business Cycle with Chaotic Time Series Based on Neural Network with Weighted Fuzzy Membership Functions. *Chaos, Solitons & Fractals* 90 (1), 118–126. doi:10.1016/j.chaos.2016.03.037

Chouikhi, N., Ammar, B., Rokbani, N., and Alimi, A. M. (2017). PSO-based Analysis of echo State Network Parameters for Time Series Forecasting. *Appl. Soft Comput.* 55, 211–225. doi:10.1016/j.asoc.2017.01.049

Gallicchio, C., and Micheli, A. (2017). *Deep Echo State Network (DeepESN): A Brief Survey Statistics*, 1–15.

Guo, W., Xu, T., and Lu, Z. (2016). An Integrated Chaotic Time Series Prediction Model Based on Efficient Extreme Learning Machine and Differential Evolution. *Neural Comput. Applic* 27 (4), 883–898. doi:10.1007/s00521-015-1903-2

Han, Y., Jing, Y. W., Dimirovski, G. M., and Zhang, L. (2021). *Multi-step Network Traffic Prediction Using echo State Network with a Selective Error Compensation Strategy [J]*. Transactions of the Institute of Measurement & Control, 1. doi:10.1177/01423312211050296

Jaeger, H., and Haas, H. (2004). Harnessing Nonlinearity: Predicting Chaotic Systems and Saving Energy in Wireless Communication. *science* 304 (5667), 78–80. doi:10.1126/science.1091277

Li, H., Deng, J., Feng, P., Pu, C., Arachchige, D. D., and Cheng, Q. (2021). Short-Term Nacelle Orientation Forecasting Using Bilinear Transformation and ICEEMDAN Framework. *Front. Energ. Res.* 9, 1–14. doi:10.3389/fenrg.2021.780928

Li, H., Deng, J., Yuan, S., Feng, P., and Arachchige, D. D. (2021). Monitoring and Identifying Wind Turbine Generator Bearing Faults Using Deep Belief Network and EWMA Control Charts. *Front. Energ. Res.* 9, 1–10. doi:10.3389/fenrg.2021.799039

Li, Y., Zhang, Y., Wang, J., Huang, B., and Liu, W. (2016). The Volterra Adaptive Prediction Method Based on Matrix Decomposition. *J. Interdiscip. Maths.* 19 (2), 363–377. doi:10.1080/09720502.2015.1113692

Liu, J. Z. (2017). Adaptive Forgetting Factor OS-ELM and Bootstrap for Time Series Prediction. *Int. J. Model. Simulation, Scientific Comput. [J]* 8 (3), 1–19. doi:10.1142/s1793962317500295

Liu, J., Sun, T., Luo, Y., Yang, S., Cao, Y., and Zhai, J. (2020). Echo State Network Optimization Using Binary Grey Wolf Algorithm. *Neurocomputing* 385, 310–318. doi:10.1016/j.neucom.2019.12.069

Lukoseviciute, K., Baubliene, R., Howard, D., and Ragulskis, M. (2018). Bernstein Polynomials for Adaptive Evolutionary Prediction of Short-Term Time Series. *Appl. Soft Comput.* 65 (1), 47–57. doi:10.1016/j.asoc.2018.01.002

Ma, J. H., Chen, Y. S., and Xin, B. G. (2004). Study on Prediction Methods for Dynamic Systems of Nonlinear Chaotic Time Series [J]. *Appl. Math. Mech.* 25 (6), 605–611.

Mackey, M. C., and Glass, L. (1977). Oscillation and Chaos in Physiological Control Systems. *Science* 197 (4300), 287–289. doi:10.1126/science.267326

Milad, H. S. A., Farooq, U., El-Hawary, M. E., and Asad, M. U. (2017). Neo-Fuzzy Integrated Adaptive Decayed Brain Emotional Learning Network for Online Time Series Prediction. *IEEE Access* 5, 1037–1049. doi:10.1109/access.2016.2637381

Miranian, A., and Abdollahzade, M. (2013). Developing a Local Least-Squares Support Vector Machines-Based Neuro-Fuzzy Model for Nonlinear and Chaotic Time Series Prediction. *IEEE Trans. Neural Netw. Learn. Syst.* 24 (2), 207–218. doi:10.1109/tnnls.2012.2227148

Mirjalili, S., Mirjalili, S. M., Lewis, A., and Grey Wolf Optimizer [J] (2014). Grey Wolf Optimizer. *Adv. Eng. Softw.* 69, 46–61. doi:10.1016/j.advengsoft.2013.12.007

Stefenon, S. F., Seman, L. O., Neto, N. F. S., Meyer, L. H., Nied, A., and Yow, K. C. (2022). Echo State Network Applied for Classification of Medium Voltage Insulators. *Int. J. Electr. Power Energ. Syst.* 134, 1–11. doi:10.1016/j.ijepes.2021.107336

Steiner, P., Jalalvand, A., and Birkholz, P. (2021). Unsupervised Pretraining of Echo State Networks for Onset Detection. *Lecture Notes Comp. Sci.* 12895, 59–70. doi:10.1007/978-3-030-86383-8_5

Su, L., and Yang, F. (2021). Prediction of Chaotic Time Series Based on BEN-AGA Model. *Complexity* 2021, 1–16. doi:10.1155/2021/6656958

Tang, Z., Li, Y., Chai, X., Zhang, H., and Cao, S. (2020). Adaptive Nonlinear Model Predictive Control of NOx Emissions under Load Constraints in Power Plant Boilers. *J. Chem. Eng. Jpn.* 53 (1), 36–44. doi:10.1252/jcej.19we142

Tüfekci, P. (2014). Prediction of Full Load Electrical Power Output of a Base Load Operated Combined Cycle Power Plant Using Machine Learning Methods [J]. *Electr. Power Energ. Syst.* 60, 126. doi:10.1016/j.ijepes.2014.02.027

Wu, Z., Li, Q., and Zhang, H. (2021). Chain-Structure Echo State Network with Stochastic Optimization: Methodology and Application. *IEEE Trans. Neural Netw. Learn. Syst.*, 1–12. doi:10.1109/tnnls.2021.3098866

Conflict of Interest: The authors declare that the research was conducted in the absence of any commercial or financial relationships that could be construed as a potential conflict of interest.

Publisher's Note: All claims expressed in this article are solely those of the authors and do not necessarily represent those of their affiliated organizations, or those of the publisher, the editors and the reviewers. Any product that may be evaluated in this article, or claim that may be made by its manufacturer, is not guaranteed or endorsed by the publisher.

frontiers in Energy Research

BRIEF RESEARCH REPORT
published: 14 March 2022
doi: 10.3389/fenrg.2022.803716

A Multi-Agent Game-Based Incremental Distribution Network Source–Load–Storage Collaborative Planning Method Considering Uncertainties

Nan Yang[1], Ye He[1], BangTian Dong[2], Tao Qin[1], Li Ding[1], XingLei Yang[3], JunWei Yao[3], YueHua Huang[1], ShuoHao Wang[1], Lei Zhang[1], BinXin Zhu[1], Wei Xiong[3] and YuLun Ren[4]*

[1]Hubei Provincial Engineering Research Center of Intelligent Energy Technology, China Three Gorges University, Collage of Electrical Engineering and New Energy, Yichang, China, [2]Substation Transportation Inspection Branch State Grid Huangshi Power Supply Company, Huangshi, China, [3]State Grid Yichang Electric Power Company, Yichang, China, [4]Economic and Technological Research Institute, State Grid Hubei Electric Power Company, Wuhan, China

OPEN ACCESS

Edited by:
Yusen He,
Grinnell College, United States

Reviewed by:
Yushuai Li,
University of Oslo, Norway
Haitao Li,
Shandong University of Technology, China

***Correspondence:**
Nan Yang
ynyyayy@ctgu.edu.cn

Specialty section:
This article was submitted to Smart Grids, a section of the journal Frontiers in Energy Research

Received: *28 October 2021*
Accepted: *14 February 2022*
Published: *14 March 2022*

Citation:
Yang N, He Y, Dong B, Qin T, Ding L, Yang X, Yao J, Huang Y, Wang S, Zhang L, Zhu B, Xiong W and Ren Y (2022) A Multi-Agent Game-Based Incremental Distribution Network Source–Load–Storage Collaborative Planning Method Considering Uncertainties. Front. Energy Res. 10:803716. doi: 10.3389/fenrg.2022.803716

How to obtain the optimal decision-making scheme based on the investment behavior of various stakeholders is an important issue that needs to be solved urgently in incremental distribution network planning. To this end, this article introduces the virtual player "Nature" to realize the combination of the game theory and robust optimization and proposes an incremental distribution network source–load–storage collaborate planning method with a multi-agent game. First, the planning and decision-making models of a DG investment operator, a distribution network (DN) company, power consumers, and a distributed energy storage (DES) investment operator are constructed, respectively. Then the static game behaviors between the DG investment operator and distribution network company, as well as the DG investment operator and the DES investment operator, are analyzed based on the transfer relations between these four participants. At the same time, robust optimization is used to deal with the uncertainty of the DG output, and the virtual player "Nature" is introduced to study the dynamic game behavior between the DG investment operator and the distribution company. Finally, a dynamic–static joint game planning model is proposed. The simulation results verify the correctness and effectiveness of the proposed method.

Keywords: multi-agent planning, robust optimization, dynamic–static joint game, iterative search method, collaborative planning

1 INTRODUCTION

With the steady progress of pilot reform, incremental distribution business in China began to become open to social capital (Liu and Yang, 2021). At the same time, distributed generation (DG) investors, power consumers participating in demand side response (DSR), and distributed energy storage (DES) investors, in the role of independent entities, started to participate in the investment and operation of the distribution network. The diversification of investors has become one of the most significant characteristics of China's incremental distribution network (Ma and Wang, 2017; Liu et al., 2020; Shen and Raksincharoensak, 2021a; Ma et al., 2021). Additionally, more uncertainties have been injected into it. Therefore, it is of great theoretical and practical significance to study the

incremental distribution network planning method considering multiple independent participants and uncertainties (Li et al., 2020; Li et al., 2021a; Shen and Raksincharoensak, 2021b).

At present, distribution network planning considering multiple investment entities have attracted increasing research attention among investment operators and academic communities (Su et al., 2016; Li et al., 2017; Zhu et al., 2020; Li et al., 2021b). Su et al. (2016) analyzed the cost–benefit relationship between DG investment operators and distribution network companies after the access of DGs, establishing the model of optimizing DG capacity. Li et al. (2017) proposed a three-layer planning model of an active distribution network considering the interests of distribution network companies, DG operators, and consumers. Although the benefits or costs of different entities are modeled independently in the aforementioned article, the whole planning model is based on the overall rationality, aiming for optimizing the weighted sum, rather than the independent optimization of each investment entity. This cannot inflect the market mechanism of the actual incremental distribution network, deteriorating its economic performance (Liao et al., 2018). Therefore, it is a promising way to construct an incremental distribution network planning model based on individual rationality and game theory, improving the planning decision efficiency (Li and Xu, 2020a; Shen et al., 2022a).

Currently, the game issue in distribution network planning has been widely studied (Mei et al., 2011; Lu et al., 2014; Wen et al., 2016). Based on the complete information from the dynamic game theory, Mei et al. (2011) took photovoltaic, energy storage, and power grid as game participants, analyzed the game relationship between them in the market environment, and established a coordinated planning model of the optical storage network. According to the possible alliance relationship between wind power generation, photovoltaic power generation, and energy storages, Wen et al. (2016) proposed five non-cooperative and cooperative game planning modes and obtained the optimal capacity allocation scheme under them. The aforementioned references analyzed the game relation between each participant, establishing various game models from the perspective of dynamic and static and cooperative and non-cooperative. However, the uncertainties of distribution network are not considered, and the accuracy of planning cannot be guaranteed in the large-scale access of distributed power (Lu et al., 2014).

In this article, the main contributions are summarized as follows:

(1) By introducing the virtual player "Nature," the deep integration of the game theory and robust optimization was realized.
(2) Considering multi-agent dynamic and static game, a source–load–storage collaborative planning method for incremental distribution networks was proposed.
(3) The uncertainty of DG output is fully considered. The network topology is actively changed to enhance robustness in large fluctuations of the DG output, and the planning result is more reasonable.

The correctness and effectiveness of the proposed method are verified in a modified IEEE 33-bus distribution network system.

2 PLANNING MODEL OF EACH INVESTMENT ENTITY

2.1 DG Investment Operator

2.1.1 Objective

The objective is to maximize the total operation cost of DG investment operators while satisfying prevailing physical constraints (Shi et al., 2016; Li and Xu, 2020b). The details can be generally described as follows:

$$\max C^{DG}(x_i, N_i) = C_S^{DG} + C_C^{DG} - \left(C_I^{DG} + C_{OM}^{DG}\right), \tag{1}$$

$$\begin{cases} C_S^{DG} = \sum_{t=1}^{\Omega_t} \theta_{es1} \cdot P_t^{DG} + \sum_{t=1}^{\Omega_t} \theta_{es2} \cdot P_{qt}^{DG} \\ C_C^{DG} = \sum_{t=1}^{\Omega_t} \theta_{gc} \cdot P_t^{DG} \\ C_I^{DG} = \left(\theta_{sg} \cdot \sum_{i=1}^{\Omega_i} x_i \cdot P_{sg}^{DG} \cdot N_i\right) \cdot \dfrac{r(1+r)^{LT}}{(1+r)^{LT}-1} \\ C_{OM}^{DG} = \sum_{t=1}^{\Omega_t} \theta_{om} \cdot P_t^{DG} \end{cases}. \tag{2}$$

2.1.2 Constrains

The constraint conditions of the DG investment operator planning model mainly include the restriction of the number of nodes to be selected in DG and the constraint of the DG output (Jin et al., 2017; Shen et al., 2020a; Shen et al., 2020b).

$$N_{i.\min} \le N_i \le N_{i.\max}, \tag{3}$$

$$P_{\min}^{DG} \le P_t^{DG} \le P_{\max}^{DG}. \tag{4}$$

2.2 Distribution Network Company

2.2.1 Objective

The objective is to maximize their income of DN company, and the mathematical expression of the model can be expressed as follows:

$$\max C^{DN}(y_i) = C_S^{DN} - \left(C_I^{DN} + C_L^{DN} + C_{B1}^{DN} + C_{B2}^{DN} + C_{B3}^{DES}\right). \tag{5}$$

$$\begin{cases} C_S^{DN} = \sum_{t=1}^{\Omega_t} \psi_{es} \cdot \left(P_t^{load} - \left(P_t^{it} + P_t^{out} - P_t^{in}\right)\right) \\ C_I^{DN} = \left(\psi_{sg} \cdot \sum_{j=1}^{\Omega_j} y_j \cdot l_j\right) \cdot \dfrac{r(1+r)^{LT}}{(1+r)^{LT}-1} \\ C_L^{DN} = \sum_{t=1}^{\Omega_t} \psi_{es} \cdot P_t^{loss} \\ C_{B1}^{DN} = \sum_{t=1}^{\Omega_t} \psi_{eb1} \cdot \left(P_t^{load} - P_t^{DG} - P_t^{DES} - \left(P_t^{it} + P_t^{out} - P_t^{in}\right)\right) \\ C_{B2}^{DN} = \sum_{t=1}^{\Omega_t} \psi_{eb2} \cdot P_t^{DG} \cdot T_t \\ C_{B3}^{DES} = \sum_{t=1}^{\Omega_t} \psi_{eb3} \cdot P_t^{DES} \cdot T_t \end{cases}. \tag{6}$$

2.2.2 Constrains

The constraint conditions of the distribution network company planning model mainly include new line investment constraint, branch flow constraint, and safety constraint.

$$\sum_{k=1}^{\Omega_k} y_{j,k} = 1, \tag{7}$$

$$\begin{cases} P_{i.t} = U_{i.t} \cdot \sum_{j \in i} U_{j.t} \cdot \left(G_{ij} \cdot \cos\theta_{ij} + \mathrm{B}_{ij} \cdot \sin\theta_{ij}\right) \\ Q_{i.t} = U_{i.t} \cdot \sum_{j \in i} U_{j.t} \cdot \left(G_{ij} \cdot \sin\theta_{ij} - \mathrm{B}_{ij} \cdot \cos\theta_{ij}\right) \end{cases}, \tag{8}$$

$$\begin{cases} U_{i.\min} \le U_{i.t} \le U_{i.\max} \\ P_{ij.t} \le P_{ij.\max} \end{cases}. \tag{9}$$

2.3 Power Consumers

2.3.1 Objective

The objective function of the power consumer planning model is C^{US}. The details are as follows:

$$C^{US}\left(P^{it}, P^{out}, P^{in}\right) = C_B^{US} + C_C^{US}, \tag{10}$$

$$\begin{cases} C_B^{US} = \sum_{t=1}^{\Omega_t} \omega_{eb} \cdot \left(P_t^{it} + P_t^{out} - P_t^{in}\right) \\ C_C^{US} = \sum_{t=1}^{\Omega_t} \omega_{gc} \cdot P_t^{it} \end{cases}. \tag{11}$$

2.3.2 Constrains

The constraints of the power consumer planning model mainly include transfer load power constraints and interruptible load power constraints according to the demand-side response mode (Guo and Liu, 2017; Shen et al., 2021b).

$$\begin{cases} \lambda_{\min} P_t^{load} \le P_t^{out} \le \lambda_{\max} P_t^{load} \\ \mu_{\min} P_t^{load} \le P_t^{in} \le \mu_{\max} P_t^{load} \end{cases}, \tag{12}$$

$$\sum_{t=1}^{\Omega_t} P_t^{out} = \sum_{t=1}^{\Omega_t} P_t^{in}, \tag{13}$$

$$P_{\min}^{it} \le P_t^{it} \le P_{\max}^{it}. \tag{14}$$

2.4 DES Investment Operator

2.4.1 Objective

The objective function C^{DES} of distributed energy storage investment operators mainly includes the profit of energy price difference C_S^{DES}, government daily subsidy C_C^{DES}, DES investment cost C_I^{DES}, and energy storage equipment operation and maintenance cost C_{OM}^{DES}. The details are as follows:

$$\max C^{DES} = C_S^{DES} + C_C^{DES} - \left(C_I^{DES} + C_{OM}^{DES}\right), \tag{15}$$

$$\begin{cases} C_S^{DES} = \sum_{t=1}^{\Omega_t} \psi_{eb3} P_t^{DES} T_t - \sum_{t=1}^{\Omega_t} \theta_{es2} P_t^{DG} T_t - \sum_{t=1}^{\Omega_t} \lambda_{es} P_t^{DN} T_t \\ C_C^{DES} = C_I^{DES} \times 15\% / (365 \cdot N) \\ C_I^{DES} = \left(K_{in} C_{AC} + K_P P_{\max}\right) \cdot \dfrac{r(1+r)^{LT}}{(1+r)^{LT} - 1} \\ C_{OM}^{DES} = K_O P_{\max} + K_M E_{dis.year} \\ C_{day} = C_I^{DES} / (N \cdot 365) + K_O \cdot P_{\max} / 365 + K_M \cdot E_{dis.day} \end{cases}. \tag{16}$$

2.4.2 Constrains

The constraint conditions of the DES investment operator planning model mainly include the active power output constraint and residual capacity constraint of energy storage equipment.

$$\begin{cases} P_{cha.\min} \le P_{cha} \le P_{cha.\max} \\ P_{dis.\min} \le P_{dis} \le P_{dis.\max} \end{cases}, \tag{17}$$

$$SOC_{\min} \le SOC \le SOC_{\max}. \tag{18}$$

3 MULTI-AGENT GAME BEHAVIOR IN INCREMENTAL DISTRIBUTION NETWORK PLANNING

3.1 Transfer Relation Among Entities

The planning investment entities of this study are the DG investment operator, DN company, power consumer, and the DES investment operator. After the access of DG, the uncertainty of its output would affect the security operation of the DN. Therefore, the output of DG is considered as a special decision variable to characterize its uncertainty, and "Nature" is introduced as a virtual entity (Shen et al., 2017; Wang et al., 2021; Zhang et al., 2021; Yang et al., 2022a).

The DG investment operator selects the location and capacity under the current grid structure, transmitting the information to the DN companies, "Nature," and the DES investment operator. Thereby, the DES investment operator would determine its decision result according to DG's location and capacity.

The active response measures are formulated by power consumers after receiving time-of-use price information and interruptible load incentive information, that is, it determines the power of transfer load and interruptible load, feeding back to DN companies in the form of an equivalent load.

After the DN company knowing the location of DG and the current power grid structure, its planning would be interfered by "Nature." Therefore, when the output of DG is transmitted to the DN company, it would accept the transmission information from other entities and decide to establish a new line to form a new power grid structure.

TABLE 1 | DG relevant parameters.

Investment cost per of DG unit capacity(w/kW)	**1**
Rated capacity of single DG (/kW)	50
Unit selling electricity price of DG(yuan/kW•h)	0.4
Operation and maintenance cost per unit of DG(yuan/kW•h)	0.2
Government subsidy for power generation(yuan/kW•h)	0.2

TABLE 2 | DES relevant parameters.

Rated capacity of single DES/kWh	**180**
Coefficient of DES investment cost per unit capacity K_{in} (yuan/kW)	1,200
Coefficient of DES power related cost K_p (yuan/kW)	300
Coefficient of DES maintenance cost K_m (yuan/kW)	0.05
Coefficient of DES annual operating cost K_o (yuan/kW)	0.03
Operation and maintenance cost per unit of DES(yuan/kW)	1,200
Government subsidy for power generation(yuan/kW•h)	0.2

3.2 Dynamic and Static Combined Game Analysis

In this study, considering four entities and "Nature," a dynamic–static joint game pattern was put forward. The static game behaviors were formed between the DG investment operator and distribution network company, as well as the DG investment operator and the DES investment operator. At the same time, a dynamic game was formed between the distribution network company and "Nature."(Mei et al., 2016).

The final game equilibrium state is described as follows:

$$\begin{cases} \boldsymbol{f}^* = \arg\max C^{DG}(\boldsymbol{f}, \boldsymbol{y}^*, \boldsymbol{p}^*) \\ \boldsymbol{y}^* = \text{argmax} C^{DN}(\boldsymbol{f}^*, \boldsymbol{y}, \boldsymbol{p}^*) \\ \boldsymbol{p}^* = \arg\max C^{DES}(\boldsymbol{f}^*, \boldsymbol{y}^*, \boldsymbol{p}) \end{cases}, \tag{19}$$

where $\boldsymbol{f}^*$, $\boldsymbol{y}^*$, and $\boldsymbol{p}^*$ are the planning strategies of the DG investment operator, DN company, and the DES investment operator under an equilibrium state, respectively, and $\arg\max(\cdot)$ represents the set of variables when the objective is maximized.

4 CASE STUDY

4.1 Instance and Setup

In this study, we test the performance of the proposed approach using a case study based on the modified IEEE 33-bus distribution system (Li et al., 2021c; Li et al., 2021d; Yang, 2021; Yang et al., 2021; Yang et al., 2022b). Its structure is shown in **Figure 1**. The system consists of 37 branches. A total load of 3715 kW + 2700 kvar and a reference voltage of 12.66 kV are considered in this system.

DG is considered as photovoltaic power generation. At the same time, the optional access position of photovoltaic power generation is {7, 20, 24, and 32}. Other relevant parameters of DG are shown in **Table 1**. Meanwhile, the relevant parameters of DES are shown in **Table 2**. No. 33 ~ 37 is the new load node, and the total capacity is 460 kW. In this study, the planned cycle is 5 years, and the new capacity of original load nodes is 5% at the planned level. The solid lines indicate the existing lines, and the dotted line indicates the line to be selected for new load access. Other relevant parameters of DN are shown in **Table 3**. The specific parameters are as follows.

4.2 Simulation Results and Analysis

4.2.1 Planning Results

The following two cases are studied to validate the effectiveness of the proposed approach.

Case 1: Incremental distribution network planning without game theory.
Case 2: Incremental distribution network planning using game theory without considering the uncertainty of DG output.
Case 3: Incremental distribution network planning using game theory with considering the uncertainty of DG output, that is, the game model established in this study.

The planning results under the two cases are shown in **Table 4**.

The results of the three cases are compared in **Table 4**. It can be seen that optimal planning schemes of the DG investment operator and the DES investment operator are the same in Cases 2 and 3 but different from those in Case 1, and the planning results of the distribution network company in the three scenarios are disparate.

4.2.2 Necessity Analysis of Multi-Agent Game

Under Cases 1 and 2, the necessity of considering a multi-agent game by comparing the costs and benefits of the DG investment operator, DN company, and DES investment operator is illustrated. The specific results are shown in **Table 5**.

As can be seen from **Table 5 (A),** the DG electricity sale revenue, DG investment cost, DG operation, maintenance cost, and government subsidies in Case 2 are, respectively, 140 yuan, 200 yuan, 81,500 yuan, 70,000 yuan, and 70,000 yuan higher than those of Case 1. The reason is that the installed capacity of DG expands after considering the multi-agent game, making the investment cost increase. Meanwhile, with the rapid development of DG output, other costs and benefits would increase.

As shown in **Table 5 (B),** in Case 2, the electricity sales revenue, investment cost, and government subsidy of the DES investment operator are all increased, compared with Case 1. This is because after considering the multi-agent game, the DES investment operator can adjust its investment decision according to the increase in DG installed capacity to maximize the overall benefit.

From **Table 5 (C),** compared with Case 1, the increase in electricity sales revenue is lesser than that enhanced in other costs. Therefore, Case 2 has no advantage in the net income of the DN company. The main reason is that after the multi-agent game is considered in Case 2, the length of new lines is longer, which makes the investment cost and network loss increase. At the same time, the installed capacity of DG is increased. Based on the principle of preferential absorption of DG and DES, the DN

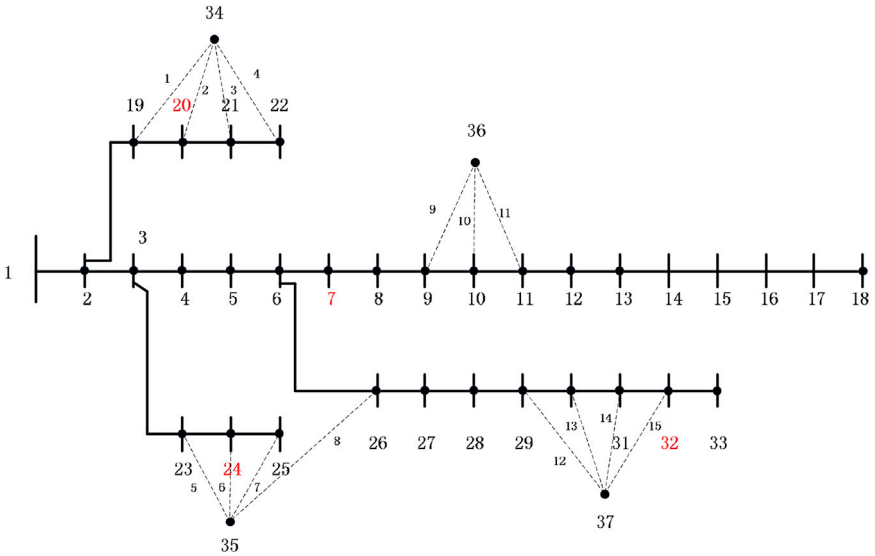

FIGURE 1 | IEEE33 node distribution system.

TABLE 3 | Distribution network relevant parameters.

Cost per unit length of new line(w/km		**20**	
Sell electricity prices of DN company(yuan/kW•h)	peak:0.9	flat:0.6	valley:0.3
Electricity price purchased from the main network(yuan/kW•h)	peak:0.6	flat:0.4	valley:0.3

TABLE 4 | Planning results of different market participants in the two cases.

	DG investment operator	**DN company**	**DES investment operator**
Case 1	7(2),20(0),24(3),32(2)	34–21,35–24,36–10,37–30	7(1),20(0),24(2),32(2)
Case 2	7(2),20(1),24(4),32(1)	34–20,35–24,36–10,37–31	7(2),20(1),24(2),32(1)
Case 3	7(2),20(1),24(4),32(1)	34–19,35–26,36–11,37–32	7(2),20(1),24(2),32(1)

TABLE 5 | Costs, benefits, and net income of each entity.

A. Costs, benefits, and net income of DG investment operator

	C_S^{DG} (w)	C_I^{DG} (w)	C_C^{DG} (w)	C_{OM}^{DG} (w)	C^{DG} (w)
Case 1	98.11	57.04	49.06	49.06	41.07
Case 2	112.13	65.19	56.06	56.06	45.73

B. Costs, benefits, and net income of DES investment operator

	C_S^{DES} (w)	C_I^{DES} (w)	C_C^{DES} (w)	C_{OM}^{DES} (w)	C^{DES} (w)
Case 1	114.87	57.20	28.08	40.37	45.38
Case 2	129.34	76.27	35.21	37.44	50.84

C. Costs, benefits, and net income of DN company

	C_S^{DN} (w)	C_I^{DN} (w)	C_L^{DN} (w)	C_E^{DN} (w)	C_{B1}^{DN} (w)	C_{B2}^{DN} (w)	C_{B3}^{DN} (w)	C^{DN} (w)
Case 1	1,437.91	77.51	73.34	2.50	962.30	85.85	52.63	183.78
Case 2	1,443.26	87.69	75.75	2.49	947.46	98.11	67.54	164.22

TABLE 6 | Costs, benefits, and net income of DN company.

	C_S^{DN}(w)	C_I^{DN} (w)	C_L^{DN} (w)	C_E^{DN} (w)	C_{B1}^{DN} (w)	C_{B2}^{DN} (w)	C_{B3}^{DN} (w)	C^{DN} (w)
Case 2	1,443.26	87.69	75.75	2.49	947.46	98.11	67.54	164.22
Case 3	1,453.83	97.17	80.39	2.54	962.15	85.85	66.31	152.85

TABLE 7 | Robustness check.

	C_L^{DN} (w)		C_E^{DN} (w)		Flow off-limit ratio (%)
	Mean value	Maximum value	Mean value	Maximum value	
Case 2	75.75	76.89	2.49	2.56	11.78
Case 3	80.39	81.23	2.54	2.55	0

company purchases more power from the investment operators of DG and DES. When the total purchased power is certain, the purchase power from main network is cut down. Moreover, the available power supply increases on fault and the expected power shortage decreases. Therefore, the failure cost is reduced.

From tab 5, the sum of net income of the DG investment operator, DN company, and DES investment operator in Case 2 is less than that of Case 1 by 94,400 yuan, but the net income of the DG investment operator and DES investment operator is more than that of Case 1 by 46,600 yuan and 54,600 yuan, respectively. The reason is that in Case 1, the optimization goal of planning is to maximize the overall benefits of the DG investment operator, DN company, and DES investment operator. However, the overall benefit maximization is at the expense of the DG investment operator and DES investment operator. In Case 2, the planning scheme is obtained after the continuous game of multiple entities. The decision combination of each entity forms a Nash equilibrium point, that is, no participant can obtain better results by independent strategy change. This approach is more in line with market mechanisms, as well as the benefits of all market participants would be taken into account.

4.2.3 The Necessity Analysis of Considering Uncertainty in Multi-Agent Game Model

The decision of the DN company would only be affected by considering the uncertainty of the output of the DG. However, the planning results of the DG investment operator and DES investment operator in Cases 2 and 3 are the same, as well as the costs and benefits remained unchanged. Therefore, by comparing the costs and benefits of the DN company in Cases 2 and 3, it could illustrate the necessity of adopting robust optimization to deal with the uncertainty of the DG output.

From **Table 6**, compared with Case 2, the electricity sale revenue, investment cost, network loss cost, failure cost, and power purchase cost from the main network increase by 105,700 yuan, 94,800 yuan, 46,400 yuan, 500 yuan, and 146,900 yuan, respectively. This is because the uncertainty of the DG output is taken into account in Case 3. As well as the DN company would make a decision after observing the worst interference in the DG output. Therefore, the investment decision-making is more conservative. This leads to a longer length of the new line and increased investment costs. At the same time, the system load is bigger in the worst scenario. However, the DG output is smaller, and more load need to be supplied from the main network. The load cannot be absorbed locally to the maximum extent, thus resulting in increased costs.

In order to further verify the robustness of the grid scheme in Case 3, Monte Carlo simulation is used in this study to randomly select 10,000 sample data within the uncertain interval of the DG output. The specific results are shown in **Table 7**.

It can be seen from **Table 7** that the mean and maximum value of the network loss cost in the sample data of Case 2 are higher than 757,500 yuan, and the maximum value of the failure cost is higher than 24,900 yuan. The situation of flow off-limit ratio accounts for 11.78%. However, the mean and maximum value of the network loss cost in the sample data of Case 3 are lower than 8,123,000 yuan, and the mean and maximum value of the failure cost are lower than 25,600, There is no power flow exceeding the limit.

Since the method in this study is based on robust optimization, the worst possible scenario of photovoltaic power output is fully considered. Therefore, the grid scheme in Case 3 could ensure that the operating cost would not increase and security constraints would not be violated, when the output of DG fluctuates within the uncertainty interval.

5 CONCLUSION

In this study, the game theory and the thought of robust optimization are integrated into the planning of incremental distribution network, and a multi-agent game based incremental distribution network source–load–storage collaborative planning method considering uncertainties is proposed. The simulation results are as follows:

1) Compared with the traditional method, by accurately simulating the game behavior of market entities, it can be ensured to continuously optimize their own decisions in the

process of game, maximizing their own benefits and improving the market vitality and the effectiveness of planning decisions.

2) By introducing virtual game player "Nature," the planning model based on the game theory can fully consider the influence of uncertain factors on planning decisions, optimizing the planning decisions actively to improve the benefits of the system.

The future study mainly focuses on the following two points. First, the uncertainty of the new energy output is only studied in this study. However, the safety risk of the power grid and other important uncertain factors does not consider. How to introduce the aforementioned uncertain factors into the game planning model has the value of further research. Second, for energy storage systems, the lithium battery is only selected as the energy storage device. Therefore, to improve the overall economic benefit of new energy stations, the influence of more types of energy storage device needs to be considered.

DATA AVAILABILITY STATEMENT

The raw data supporting the conclusion of this article will be made available by the authors, without undue reservation.

AUTHOR CONTRIBUTIONS

NY: conceptualization, methodology, validation, formal analysis, investigation, writing—review and editing, supervision, and project administration. YH: methodology, software, validation, formal analysis, investigation, data curation, writing—original draft, and visualization. BD: methodology, software, and validation. TQ: writing—review and editing, supervision, and project administration. LD: writing—review and editing, supervision, and project administration. XY: data curation and project administration. JY: data curation and project administration. YH: validation, investigation, and funding acquisition. SW: validation, investigation, and funding acquisition. LZ: investigation and funding acquisition. BZ: investigation and funding acquisition. WX: supervision and project administration. YR: supervision and project administration

FUNDING

This work was supported by the National Natural Science Foundation of China under Grant 51607104. (Corresponding author: NY.).

REFERENCES

Guo, T., and Liu, Y. (2017). Game Theory Based Reconfiguration Optimization for Distribution Network with Distributed Generations. *Power Syst. Prot. Control.* 45 (7), 28. doi:10.7667/PSPC160488

Jin, Q., and Cheng, W., (2017). *Coordinated Planning Model for Photovoltaic Station, Storage Battery and Grid Based on Complete Information Dynamic GameAutomation of Electric Power Systems*. 41.

Li, H., Deng, J., Feng, P., Pu, C., Arachchige, D. D., and Cheng, Q. (2021d). Short-Term Nacelle Orientation Forecasting Using Bilinear Transformation and ICEEMDAN Framework. *Front. Energ. Res.* 68 (9), 8930–8941. doi:10.3389/fenrg.2021.780928

Li, H., Deng, J., Yuan, S., Feng, P., and Arachchige, D. (2021c). Monitoring and Identifying Wind Turbine Generator Bearing Faults Using Deep Belief Network and EWMA Control Charts. *Front. Energ. Res.*, 770. doi:10.3389/fenrg.2021.799039

Li, Y., Gao, D. W., Gao, W., Zhang, H., and Zhou, J. (2020). Double-Mode Energy Management for Multi-Energy System via Distributed Dynamic Event-Triggered Newton-Raphson Algorithm. *IEEE Trans. Smart Grid* 11, 5339–5356. doi:10.1109/TSG.2020.3005179

Li, Y., Gao, W., Yan, W., Huang, S., Wang, R., Gevorgian, V., et al. (2021a). Data-driven Optimal Control Strategy for Virtual Synchronous Generator via Deep Reinforcement Learning Approach. *J. Mod. Power Syst. Clean Energ.* 9 (no. 4), 919–929. doi:10.35833/MPCE.2020.000267

Li, Z., Jiang, W., Abu-Siada, A., Li, Z., Xu, Y., and Liu, S. (2021b). Research on a Composite Voltage and Current Measurement Device for HVDC Networks. *IEEE Trans. Ind. Electron.* 68, 8930–8941. doi:10.1109/TIE.2020.3013772

Li, Z., Lei, X., and Qiu, S. (2017). Coordinated Planning of Active Distribution Network Considering "Source-Grid-Load" Benefits. Powver System Technology. *2017* 41 (2), 378–386. doi:10.1109/TPWRS.2020.3039538

Li, Z., and Xu, Y. (2020a). A Risk-Averse Adaptively Stochastic Method for MultiEnergy Ship Operation under Diverse Uncertainties. *IEEE Trans. Power Systems*. doi:10.1109/TPWRS.2020.3039538

Li, Z., and Xu, Y. (2020b). Optimal Deployment of Heterogeneous Energy Storage System in a Residential Multi-Energy Microgrid with Demand Side Management. *IEEE Trans. Ind. Inform. Early access* 17 (2), 991–1004. doi:10.1109/TII.2020.2971227

Liao, S., Xu, J., Sun, Y., Bao, Y., and Tang, B. (2018). Control of Energy-Intensive Load for Power Smoothing in Wind Power Plants. *IEEE Trans. Power Syst.* 33, 6142–6154. doi:10.1109/TPWRS.2018.2834940

Liu, L.-N., and Yang, G.-H. (2021). Distributed Optimal Economic Environmental Dispatch for Microgrids over Time-Varying Directed Communication Graph. *IEEE Trans. Netw. Sci. Eng.* 8, 1913–1924. doi:10.1109/TNSE.2021.3076526

Liu, Y., Yang, N., Dong, B., Wu, L., Yan, J., Shen, X., et al. (2020). "Multi-Lateral Participants Decision-Making: A Distribution System Planning Approach with Incomplete Information Game," in *IEEE Access*, 8, 88933–88950. doi:10.1109/ACCESS.2020.2991181

Lu, Q., Chen, L., , and Mei, S. (2014). Typical Applications and Prospects of Game Theory in Power System. *Proc. CSEB* 34, 8013. doi:10.13334/j0258-8013

Ma, H., Zheng, K., Jiang, H., and Yin, H. (2021). A Family of Dual-Boost Bridgeless Five-Level Rectifiers with Common-Cor Inductors. *IEEE Trans. Power Electron*, 12565–12578. doi:10.1109/TPEL2021.3078533

Ma, Q., and Wang, Y. (2017). Investment Risk Analysis of Power Grid Enterprises under Incremental Distribution Businesses Opening. *Electric Power Construction* 38 (09), 139. doi:10.3969/j.issn.1000-7229.2017.09.020

Mei, S., Liu, F., and Wei, W. (2016). *Engineering Game Theory Foundation and Power System Application [M]*, 2016. Beijing: Science Press, 216.

Mei, S., Wang, Y., and Liu, F. (2011). A Game Theory Based Planning Model and Analysis for Hybrid Power System With Wind Generators-Photovoltaic Panels-Storage Batteries. *Automation Electric Power Syst.* 35 (20), 13–19. doi:10.1097/MCC.0b013e328344b397

Shen, X., Ouyang, T., Khajorntraidet, C., Li, Y., Li, S., and Zhuang, J. (2022a). Mixture Density Networks-Based Knock Simulator. *Ieee/asme Trans. Mechatron.* 27, 159–168. doi:10.1109/tmech.2021.3059775

Shen, X., Ouyang, T., Yang, N., and Zhuang, J. (2021b). Sample-Based Neural Approximation Approach for Probabilistic Constrained Programs. *IEEE Trans. Neural Netw. Learn. Syst.*, 1–8. doi:10.1109/tnnls.2021.3102323

Shen, X., and Raksincharoensak, P. (2021). Pedestrian-Aware Statistical Risk Assessment. *IEEE Trans. Intell. Transport. Syst.*, 1–9. doi:10.1109/TITS.2021.3074522

Shen, X., and Raksincharoensak, P. (2021). Statistical Models of Near-Accident Event and Pedestrian Behavior at Non-signalized Intersections. *J. Appl. Stat.*, 1–21. doi:10.1080/02664763.2021.1962263

Shen, X., Zhang, X., Ouyang, T., Li, Y., and Raksincharoensak, P. (2020a). Cooperative Comfortable-Driving at Signalized Intersections for Connected

and Automated Vehicles. *IEEE Robot. Autom. Lett.* 5 (4), 6247–6254. doi:10.1109/lra.2020.3014010

Shen, X., Zhang, Y., Sata, K., and Shen, T. (2020b). Gaussian Mixture Model Clustering-Based Knock Threshold Learning in Automotive Engines. *Ieee/asme Trans. Mechatron.* 25 (6), 2981–2991. doi:10.1109/tmech.2020.3000732

Shen, X., Zhang, Y., Shen, T., and Khajorntraidet, C. (2017). Spark advance Self-Optimization with Knock Probability Threshold for Lean-Burn Operation Mode of SI Engine. *Energy* 122, 1–10. doi:10.1016/j.energy.2017.01.065

Shi, Q., Guo, L., and Zhang, X. (2016). Research on Optimal Configuration of Distributed Generation Considering Economic Benefits of the Multi-Agent. *Power Syst. Prot. Control.* 44 (1), 85. doi:10.7667/j.issn.1674-3415.2016.01.012

Su, J., Zhang, P., and Liu, H. (2016). Cost-benefit Analysis of Distributed Generation and Optimization of Capacity Considering Different Stakeholders. *Power Syst. Techn.* 40 (4), 1128–1133. doi:10.13335/j.1000-3673.pst.2016.04.022

Wang, C., Mei, S., Yu, H., Cheng, S., Du, L., and Yang, P. (2021). Unintentional Islanding Transition Control Strategy for Three-/Single-phase Multimicrogrids Based on Artificial Emotional Reinforcement Learning. *IEEE Syst. J.* 15, 5464–5475. doi:10.1109/isvst.2021.307429610.1109/jsyst.2021.3074296

Wen, J., Zeng, B., and Zhang, J. (2016). Adjustable Robust Optimization for Distributed Wind Power Planning in Distribution. *Network Power System Technology*. 40, 227–233. doi:10.13335/j.1000-3673.pst.2016.01.031

Yang, N. (2021). A Comprehensive Review of Security-Constrained Unit Commitment. *J. Mod. Power Syst. Clean Energ.* doi:10.35833/MPCE.2021.000255

Yang, N., Qin, T., Wu, L., Huang, Y., Huang, Y., Xing, C., et al. (2022). A Multi-Agent Game Based Joint Planning Approach for Electricity-Gas Integrated Energy Systems Considering Wind Power Uncertainty. *Electric Power Syst. Res.* 204, 107673. doi:10.1016/j.epsr.2021.107673

Yang, N., Yang, C., Wu, L., Shen, X., Jia, J., Li, Z., et al. (2022). Intelligent Data-Driven Decision-Making Method for Dynamic Multisequence: An E-Seq2Seq-Based SCUC Expert System. *IEEE Trans. Ind. Inf.* 18, 3126–3137. doi:10.1109/tii.2021.3107406

Yang, N., Yang, C., Xing, C., Ye, D., and Jia, J. (2021). Deep Learning-Based SCUC Decision-Making: An Intelligent Data-Driven Approach with Self-Learning Capabilities. *IET Gener. Transm. Distrib* 16, 629–640. doi:10.1049/gtd2.12315

Zhang, L., Xie, Y., Ye, J., Xue, T., Cheng, J., Li, Z., et al. (2021). Intelligent Frequency Control Strategy Based on Reinforcement Learning of Multi-Objective Collaborative Reward Function. *Front. Energ. Res.* 9, 525. doi:10.3389/fenrg.2021.760525

Zhu, B., Ding, F., and Vilathgamuwa, D. M. (2020). Coat Circuits for DC-DC Converters to Improve Voltage Conversion Ratio. *IEEE Trans. Power Electron.* 35, 3679–3687. doi:10.1109/TPEL.2019.2934726

Conflict of Interest: Author BT is employed by Substation Transportation Inspection Branch State Grid Huangshi Power Supply Company. Authors XY, JY, and WX are employed by State Grid Yichang Electric Power Company. Author YR was employed by Economic and Technological Research Institute, State Grid Hubei Electric Power Company.

The remaining authors declare that the research was conducted in the absence of any commercial or financial relationships that could be construed as a potential conflict of interest.

Publisher's Note: All claims expressed in this article are solely those of the authors and do not necessarily represent those of their affiliated organizations, or those of the publisher, the editors, and the reviewers. Any product that may be evaluated in this article, or claim that may be made by its manufacturer, is not guaranteed or endorsed by the publisher.

GLOSSARY

C^{DG} objective function of the DG investment operator

C_S^{DG} DG electricity sale income

C_I^{DG} DG investment cost

C_{OM}^{DG} DG operation and maintenance cost

C_C^{DG} government subsidies for renewable energy generation

θ_{es1} unit electricity price of DG

θ_{es2} unit photovoltaic curtailment electricity price of DG

θ_{gc} subsidy cost per unit power generation of renewable energy

θ_{sg} investment cost per unit capacity DG

x_i variables of 0 or 1, when $x_i = 0$, meaning that the i candidate node does not access DG. Otherwise, the candidate node i accesses DG

P_t^{DG} total active power for DG at moment t

P_{qt}^{DG} photovoltaic curtailment of active power for DG at moment t

P_{sg}^{DG} rated power for a single DG

N_i number of DGs connected to the selected node i

r discount rates

LT life cycle of equipment

θ_{om} Unit power generation operation and maintenance costs of DG

C^{DN} objective function of distribution network company

C_S^{DN} income from electricity sales of the distribution network company

C_I^{DN} investment cost of new lines

C_L^{DN} cost of network loss

C_{B1}^{DN} cost of electricity purchase from the main network

C_{B2}^{DN} operator invested by DG

C_{B3}^{DES} operator invested by DES

ψ_{es} electricity price of distribution company;

P_t^{load} primary load at moment t;

P_t^{it} interruption power of interruptible load at moment t

P_t^{out} power transferred out of the load at moment t

P_t^{in} transfer into of the load at moment t

P_t^{DES} total active power for DES at moment t;

ψ_{sg} cost per unit length of the new line;

y_j variables of 0 or 1, when $y_j = 0$, meaning that the line j to be built is not selected. Otherwise, the line j to be built is selected.

l_j length of the new line.

P_t^{loss} active power loss at moment t.

ψ_{eb1} electricity price to the higher power grid.

ψ_{eb2} purchase electricity prices from the DG investment operator

ψ_{eb3} purchase electricity prices from the DES investment operator

ω_{eb} electricity price of consumers

ω_{gc} compensation cost of interruptible load

C_B^{US} reduced electricity cost of interruptible load after participating in the demand side response.

C_C^{US} compensation cost of interruptible load after participating in the demand side response C^{DES} the objective function of distributed energy storage investment operators

C_S^{DES} profit of energy price difference

C_C^{DES} government daily subsidy

C_I^{DES} investment cost of DES

C_{OM}^{DES} operation and maintenance cost of energy storage equipment

K_{in} coefficient of DES investment cost per unit capacity

K_p coefficient of DES power related cost

K_m coefficient of DES maintenance cost

K_o coefficient of DES annual operating cost

SOC_{min} minimum remaining capacity of lithium battery, 20–30% of the total battery capacity generally

SOC_{max} maximum remaining capacity of lithium battery, 80–100% of the total battery capacity generally

f^* planning strategies of DG investment operator under equilibrium state

y^* planning strategies of DN company under equilibrium state

p^* planning strategies of the DES investment operator under equilibrium state

$arg\ max(\cdot)$ set of variables when the objective is maximized

frontiers in Energy Research

BRIEF RESEARCH REPORT
published: 15 March 2022
doi: 10.3389/fenrg.2022.865069

Energy-Efficiency-Oriented Vision Feedback Control of QCSP Systems: Linear ADRC Approach

Shengming Li[1,2] *and Lin Feng*[1,2]*

[1]School of Computer Science and Technology, Dalian University of Technology, Dalian, China, [2]School of Innovation and Entrepreneurship, Dalian University of Technology, Dalian, China

How to save the energy of unmanned aerial vehicles (UAVs) and then enable long-distance transport is a very real and difficult task. However, for UAVs, the classic object detection algorithm, such as the deep convolutional neural network–based object detection algorithm and the classic flight control algorithm, such as the PID-based position control algorithm, require significant energy, which limits the application scenarios of the UAV system. In view of this problem, this paper proposes a lightweight object detection network and a linear active disturbance rejection controller (LADRC) for the quadrotor with the cable-suspended payload (QCSP) system to improve energy efficiency. The system uses a YOLOV3 network and embeds it into the Jesson NX mobile platform to accurately detect the target position. Furthermore, a nonlinear velocity controller with a cable-suspended structure to control the velocity of the payload, a LADRC algorithm is adopted to achieve fast and accurate control of the payload position. Simulations and real flight experiments show that the proposed object detection algorithm and the LADRC control strategy can save the energy of drone effectively.

Keywords: cable-suspended payload, quadrotor UAV, energy efficiency, object detection, linear active disturbance rejection controller, model compression

OPEN ACCESS

Edited by:
Xun Shen,
Tokyo Institute of Technology, Japan

Reviewed by:
Hongxu Zhang,
Harbin University of Science and Technology, China
Guoguang Wen,
Beijing Jiaotong University, China

***Correspondence:**
Lin Feng
fenglin@dlut.edu.cn

Specialty section:
This article was submitted to Smart Grids, a section of the journal Frontiers in Energy Research

Received: *29 January 2022*
Accepted: *08 February 2022*
Published: *15 March 2022*

Citation:
Li S and Feng L (2022) Energy-Efficiency-Oriented Vision Feedback Control of QCSP Systems: Linear ADRC Approach. Front. Energy Res. 10:865069. doi: 10.3389/fenrg.2022.865069

1 INTRODUCTION

With the development of unmanned aerial vehicle (UAV) technology (Wu et al., 2018), drone transport has become an important branch of UAV applications. The quadrotor with the cable-suspended payload (QCSP) (Lv et al., 2020; Lv et al., 2021) equipped with a camera and an embedded platform, is of great relevance to the realization of rescue and transport tasks. The QCSP actively adjusts the UAV's own attitude to quickly reduce the oscillation of the suspended load and then runs the vision algorithm through the embedded platform to process the images from the camera to obtain an accurate target position for the drone. Based on the target position information, the QCSP needs to reach the target position quickly and stably. However, in the transportation process, in addition to the energy required for drone flight, the object detection algorithm and the QCSP flight control strategy also consume great energy. Therefore, by considering the limited battery capacity of the drone, it is important to improve the energy efficiency of the QCSP systems.

Recent decades witness great progress in object detection with the development of convolutional neural networks (CNNs). To obtain a powerful network, numerous efforts are made to build large and complex architecture with high computation and energy consumption, which restricts its application on embedding devices such as a drone. To get the light network, Z. Liu *et al.* (Liu et al., 2017) utilize scaling factors to value the significance of connections and remove these under a

threshold. This efficient method works well for classification networks. However, it lacks effectiveness for detection networks. To make the network compression method suitable to detection network, Z. Xie *et al.* (Xie et al., 2020) introduce location-aware loss for network compression, which helps in preserving the comprehensive ability of the detection network. These methods are not optimal for saving energy because they do not adopt an energy-aware function during compressing.

To realize the path following for the QCSP, Qian, *et al.* (Qian and Liu, 2019) propose a controller based on uncertainty and an interference estimator. Hao, *et al.* (Hao et al., 2021) propose a nonlinear, robust, fault-tolerant, position-tracking, control law for a tilt tri-rotor UAV, thus avoiding rear servo's stuck fault together with parametric uncertainties and unknown external disturbances. To enable a multirotor UAV to achieve static hovering, Mochida, *et al.* (Mochida et al., 2021) propose a geometric method that reveals the relationship between the position of the center of mass (CoM) and the rotor placement of a multirotor UAV with upward-oriented rotors. These methods can effectively help UAVs accomplish their tasks, but they do not take into account the energy limitation of UAVs; the algorithm is complex and not applicable to the QCSP.

Although many researchers have done meaningful work and achieved results, there are still some challenges in vision processing and position control in the energy-efficiency-oriented QCSP, mainly as follows: 1) Object detection technique–based CNNs can obtain accurate target information for a UAV, but the improved detection performance of deep neural networks also brings huge energy consumption, which is not friendly to the QCSP. 2) The QCSP needs to control the load stably and reach the target position quickly, whereas the traditional PID controller usually needs a long adjustment time for the UAV to reach the target position, which is also not conducive to the QCSP system to save energy for long-distance transportation.

To improve the energy efficiency of the QCSP systems, we propose a lightweight object detection algorithm and an LADRC payload position control strategy for the QCSP. Specifically, the object detection model is compressed by network scaling factors and an energy-aware penalty, which enables the YOLOV3 network to run on the Jetson NX embedded platform of the QCSP with low energy consumption. In addition, an efficient control strategy in the form of a string stage is used to overcome the under-actuated characteristics of the QCSP, which includes attitude, swing angle, load velocity, and load position subcontrollers. The contributions of this paper to the energy saving of QCSP mainly include 1) a new QCSP experimental platform with embedded vision detection is constructed, and a lightweight object detection network is used to obtain position information; 2) an LADRC algorithm is used to control the payload position quickly and efficiently.

The remainder of this paper is structured as follows: **Section 2** introduces the dynamic model and object detection algorithm of the QCSP in detail; controller design, including the LADRC position control algorithm for the QCSP is introduced in **Section 3**; in **Section 4**, the effectiveness of the proposed QCSP system is verified through experiments. Conclusions are drawn in **Section 5**.

2 DYNAMIC MODEL AND OBJECT DETECTION ALGORITHM OF THE QCSP

There are three reference frames to describe the QCSP (Lv et al., 2020) system (see left of **Figure 1**): the inertial frame $\mathcal{I}\{X_i, Y_i, Z_i\}$, the quadrotor body frame $\mathcal{B}\{X_b, Y_b, Z_b\}$, and the payload body frame $\mathcal{B}_p\{X_p, Y_p, Z_p\}$. What needs to be mentioned is that the inertial frame follows the North-East-Down (NED) notation. For the quadrotor body frame, Z_b points down, the X_b toward the front direction, and the Y_b toward the right direction. Based on the reference frames, some variables are defined. The generalized coordinates $\boldsymbol{q} = [\boldsymbol{\xi}^\top\ \boldsymbol{\eta}^\top\ \boldsymbol{\sigma}^\top]^\top \in \mathbb{R}^8$, where $\boldsymbol{\xi} = [x\ y\ z]^\top \in \mathbb{R}^3$ denotes the coordinate of the quadrotor's CoG under the inertial frame $\mathcal{I}$; $\boldsymbol{\eta} = [\phi\ \theta\ \psi]^\top \in \mathbb{R}^3$ denotes the attitude angle of the quadrotor in the Euler coordinate system, and ϕ means the roll angle, θ means pitch angle, and ψ means yaw angle; $\boldsymbol{\sigma} = [\alpha\ \beta]^\top \in \mathbb{R}^2$ denotes the swing angle of the payload, where α and β are the roll and pitch angles of the cable, respectively. The boundaries of the quadrotor attitude and the swing angle are limited as

$$\phi, \theta, \alpha, \beta \in (-\pi/2, \pi/2). \tag{1}$$

The coordinate $\boldsymbol{\delta} = [x_p\ y_p\ z_p]^\top$ of the payload's CoG in inertial frame $\mathcal{I}$ can be given by $\boldsymbol{\xi}$ and $\boldsymbol{\sigma}$:

$$x_p = x + l\boldsymbol{c}\alpha\boldsymbol{s}\beta,\ \ y_p = y - l\boldsymbol{s}\alpha,\ \ z_p = z + l\boldsymbol{c}\alpha\boldsymbol{c}\beta, \tag{2}$$

and the velocity of the payload is expressed by $\dot{\boldsymbol{\delta}} = [\dot{x}_p\ \dot{y}_p\ \dot{z}_p]^\top$. In addition, $\boldsymbol{I}_n$ and $\boldsymbol{0}_{m\times n}$ represent the n-dimensional identity matrix and $m \times n$ dimensional null matrix, respectively. $\boldsymbol{c}\cdot$ and $\boldsymbol{s}\cdot$ are used to represent $\cos\cdot$ and $\sin\cdot$, respectively.

Following previous work (Lv et al., 2020), the dynamic model of the QCSP system is described by the following equations:

$$\ddot{\boldsymbol{\delta}} = \left(\boldsymbol{R}_G F_l - m_q\ddot{\boldsymbol{\xi}} + m_q\boldsymbol{g} + \boldsymbol{D}_\xi + \boldsymbol{D}_\delta\right)\Big/ m_p + \boldsymbol{g}, \tag{3a}$$

$$\ddot{\boldsymbol{\eta}} = \boldsymbol{J}_q^{-1}\left(\boldsymbol{\tau}_\eta + \boldsymbol{A} - \dot{\boldsymbol{J}}_q\dot{\boldsymbol{\eta}} + \boldsymbol{D}_\eta\right), \tag{3b}$$

$$\ddot{\boldsymbol{\sigma}} = -\boldsymbol{M}_1^{-1}\left(\boldsymbol{M}_2\ddot{\boldsymbol{\xi}} + \boldsymbol{V}_{d\sigma} - \boldsymbol{C} - \boldsymbol{D}_\sigma\right), \tag{3c}$$

where $\boldsymbol{F}_t = \boldsymbol{R}_G F_l - m_q\ddot{\boldsymbol{\xi}} + m_q\boldsymbol{g} + \boldsymbol{D}_\xi$ is the tensile force of the cable on the payload.

For dynamic model described by **Eq. 3a**, m_q is the mass of the quadrotor, m_p is the mass of the payload, $\boldsymbol{g}$ is the gravity acceleration, $\boldsymbol{D}_\xi$ and $\boldsymbol{D}_\delta$ are the air drag forces that act on the quadrotor and the payload, respectively. $\boldsymbol{R}_G$ is the projection vector in the inertial frame $\mathcal{I}$ of the unit vector on the axis Z_b.

For the dynamic submodel described by **Eq. (3b)**, $\boldsymbol{D}_\eta$ denotes the aerodynamic drag torque on the quadrotor. What needs to be mentioned is that $\boldsymbol{A} = [A_\phi\ A_\theta\ 0]^\top$ is given in Eq. 12a of (Lv et al., 2020), and the inertial matrix $\boldsymbol{J}_q$ is given in **Eq. 4** of (Lv et al., 2020).

For the dynamic model described by **Eq. 3c**, the drag torque $\boldsymbol{D}_\sigma$ on the payload is given by

$$\boldsymbol{D}_\sigma = \boldsymbol{I}_{2\times 3}\left(\boldsymbol{l} \times \boldsymbol{R}_i^{bp}\boldsymbol{D}_\sigma\right), \tag{4}$$

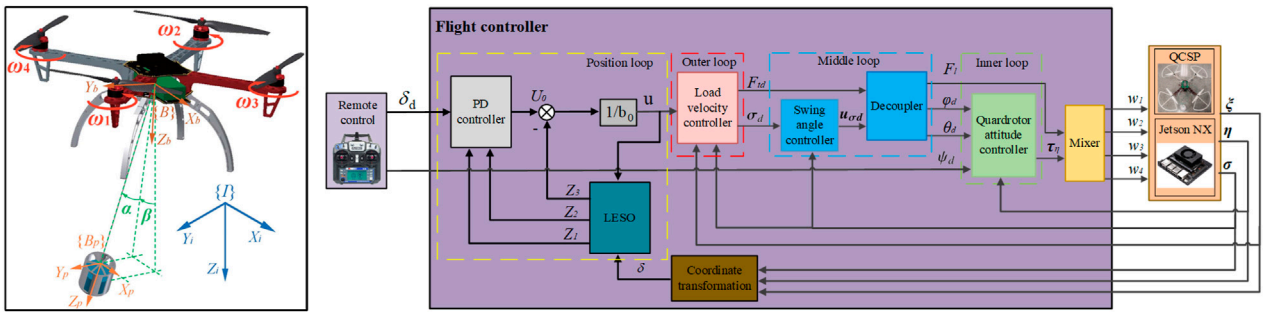

FIGURE 1 | The schematic diagram and the control block diagram of the QCSP.

where $\boldsymbol{I}_{2\times3} = \begin{bmatrix} 1 & 0 & 0 \\ 0 & 1 & 0 \end{bmatrix}$, $\boldsymbol{l} = [0\ 0\ l]^\top$, l is the length of cable. $\boldsymbol{M}_1 = m_p l^2 \ \text{diag}\ (1,\ \boldsymbol{c}^2\alpha)$, $\boldsymbol{M}_2 = -m_p l \begin{bmatrix} \boldsymbol{s}\alpha\boldsymbol{s}\beta & \boldsymbol{c}\alpha & \boldsymbol{s}\alpha\boldsymbol{c}\beta \\ -\boldsymbol{c}\alpha\boldsymbol{c}\beta & 0 & \boldsymbol{c}\alpha\boldsymbol{s}\beta \end{bmatrix}$, $\boldsymbol{V}_{d\sigma} = [m_p g l \boldsymbol{s}\alpha\boldsymbol{c}\beta\ m_p g l \boldsymbol{c}\alpha\boldsymbol{s}\beta]^\top$, $\boldsymbol{C} = [C_\alpha\ C_\beta]^\top$, with $C_\alpha = -m_p l^2 \boldsymbol{s}\alpha\boldsymbol{c}\alpha\dot{\beta}^2$, $C_\beta = 2m_p l^2 \boldsymbol{s}\alpha\boldsymbol{c}\alpha\dot{\alpha}\dot{\beta}$. To facilitate the controller design, the dynamic model (see **Eq. 3**)is rewritten as

$$\ddot{\boldsymbol{\delta}} = (\boldsymbol{F}_t + \boldsymbol{D}_\sigma) \Big/ m_p + \boldsymbol{g}, \tag{5a}$$

$$\ddot{\boldsymbol{\eta}} = \boldsymbol{J}_q^{-1} (\boldsymbol{\tau}_\eta + \boldsymbol{\tau}_{\eta e}), \tag{5b}$$

$$\ddot{\boldsymbol{\sigma}} = \boldsymbol{M}_\sigma \ddot{\boldsymbol{\xi}} + \boldsymbol{F}_{\sigma e} + \boldsymbol{M}_1^{-1} \boldsymbol{D}_\sigma, \tag{5c}$$

where $a = 1/m_p$, $\boldsymbol{\tau}_{\eta e} = \boldsymbol{A} - \dot{\boldsymbol{J}}_q \dot{\boldsymbol{\eta}} + \boldsymbol{D}_\eta$,

$$\boldsymbol{F}_{\sigma e} = \boldsymbol{M}^{-1} (\boldsymbol{C} - \boldsymbol{V}_{d\sigma}) = \begin{bmatrix} -\boldsymbol{s}\alpha\boldsymbol{c}\alpha\dot{\beta}^2 - \boldsymbol{s}\alpha\boldsymbol{s}\beta g \Big/ l \\ 2\boldsymbol{s}\alpha \Big/ \boldsymbol{c}\alpha\dot{\alpha}\dot{\beta} - \boldsymbol{s}\alpha\boldsymbol{s}\beta g \Big/ l \end{bmatrix},$$

$$\boldsymbol{M}_\sigma = -\boldsymbol{M}_1^{-1} \boldsymbol{M}_2 = \begin{bmatrix} \boldsymbol{s}\alpha\boldsymbol{s}\beta & \boldsymbol{c}\alpha & \boldsymbol{s}\alpha\boldsymbol{c}\beta \\ -\boldsymbol{c}\beta/\boldsymbol{c}\alpha & 0 & \boldsymbol{s}\beta/\boldsymbol{c}\alpha \end{bmatrix} \Big/ l.$$

It can be found that $\boldsymbol{M}_\sigma$, $\boldsymbol{F}_{\delta e}$, and $\boldsymbol{F}_{\sigma e}$ do not contain a.

Apart from dynamic model controlling the basic attitude of the quadrotor, the motion of the quadrotor depends on the guide of the object detection network (ODN). Currently, because of accuracy and effectiveness, YOLOV3 (Redmon and Farhadi, 2018) is adopted in a growing number of real-world situations. However, this ODN method is computationally expensive; hence, it creates huge energy consumption, which is not friendly to the QCSP system. Therefore, compressing the ODN to obtain a lightweight ODN is essential for deploying YOLOV3 on the quadrotor. As mentioned, preserving computational performance and saving energy cost simultaneously are challenging issues. For preserving performance of the network, we utilize the sparsity-induced penalty to retrain a sparsity network indicated by scaling factors. Then, these low-significance connections distinguished by scaling factors are removed to achieve network compression. Considering the energy consumption, we add an energy-aware penalty to supervise the compression process. Specifically, the retrain objective is given by

$$L = \sum_{\mathbf{X},\mathbf{Y}} l\big(f(\mathbf{X},\mathbf{W}),\mathbf{Y}\big) + \lambda \sum_{\gamma\in\Gamma} \|\gamma\|_1 + \alpha \sum_{i\in N} \big(E_{comp}^{(i)} + E_{data}^{(i)}\big), \tag{6}$$

where $l(\cdot)$ denotes the supervised training loss; for YOLOV3, $l(\cdot)$ is the detection loss proposed in (Redmon and Farhadi, 2018). ($\mathbf{X}$, $\mathbf{Y}$) denote the retrain input and label, $\mathbf{W}$ denotes the learnable weights, $\|\cdot\|_1$ denotes the L1-norm function, γ is a scaling factor and Γ is the scaling factors set, $\|\gamma\|_1$ is used as a sparsity-induced penalty. In practice, the learnable γ in batch normalization (Ioffe and Szegedy, 2015) is widely adopted as a scaling factor. $E_{comp}^{(i)}$ denotes the energy consumption for computation of the ith layer, whereas $E_{data}^{(i)}$ denotes the energy consumption for data access of the ith layer, N means the whole network consisting of N layers. $E_{comp}^{(i)} + E_{data}^{(i)}$ is utilized as the energy-aware penalty. λ and α balance three items. Following the principles of (Yang et al., 2018), the $E_{comp}^{(i)}$ of the normal convolutional layer is given by

$$\begin{cases} E_{comp}^{(i)} = e_{MAC} \cdot h' \cdot w' \cdot \|\mathbf{W}^{(i)}\|_0 \\ h' = \lfloor (h + 2p - r)/s \rfloor + 1 \\ w' = \lfloor (w + 2p - r)/s \rfloor + 1 \end{cases}, \tag{7}$$

where e_{MAC} denotes the energy consumption of one systolic array MAC (Kung, 1982) (a kind of hardware widely used in GPU or TPU) operation, whereas h and w denote the height and weight of the convolutional layer input, $\|\cdot\|_0$ denotes the L0-norm function, p, r, s denote the convolutional arguments, *i.e.*, padding, kernel size, and stride. Data access energy $E_{data}^{(i)}$ depends on the hardware architecture, *i.e.*, systolic array, which is complex and not helpful for understanding our method. We just describe it as a function of $\mathbf{X}^{(i)}$, h, w, p, r, s: $E_{data}^{(i)} = E_{data}^{(i)}(\mathbf{X}^{(i)}, h, w, p, r, s)$, where $\mathbf{X}^{(i)}$ denotes the input of the ith convolutional layer. The other omitted items depend on the specific architecture of the hardware, *e.g.*, bus bandwidth.

Obviously, **Eq. 6** gives a meaningful objective. However, it is hard to optimize because of $E_{data}^{(i)}$ and $E_{comp}^{(i)}$ are not functions of scaling factors γ. To make the energy-aware penalty influence γ, we redescribe **Eq. 6** as

$$L' = \sum_{\mathbf{X},\mathbf{Y}} l\big(f(\mathbf{X},\mathbf{W}),\mathbf{Y}\big) + \lambda \sum_{i\in N} \big(E_{comp}^{(i)} + E_{data}^{(i)}\big) \cdot \|\boldsymbol{\gamma}^{(i)}\|_1,$$

where $\boldsymbol{\gamma}^{(i)}$ is a scaling factor vector of the ith layer. Then, we optimize the above equation to obtain a sparsity distribution of

scaling factors and remove these low-significance connections. After that, the compact network is fine-tuned for several iterations to resume.

Finally, a network deployed on a computation and energy-limited platform could be accessed. We utilize this compact network to provide location and category information of the target object to the quadrotor as a basis for flight adjustment.

3 CONTROLLER DESIGN

Because of the underactuated character of the QCSP, the proposed controller mainly consists of two parts: the cascade controller for attitude self-stabilization and the active disturbance rejection controller for position control (see the right subfigure of **Figure 1**). Referring to (Lv et al., 2020), the design process of the cascade controller mainly consists of three parts: inner-loop attitude, middle-loop swing angle, and outer-loop velocity subcontrollers.

3.1 Tracking Errors

Errors associated with the dynamics of the QCSP are given as follows:

$$\boldsymbol{e}_{\boldsymbol{\eta},\boldsymbol{p}_{\boldsymbol{\eta}}} = \left[\boldsymbol{e}_{\boldsymbol{\eta}}^{\top} \ \boldsymbol{e}_{\boldsymbol{p}_{\boldsymbol{\eta}}}^{\top}\right]^{\top}, \tag{8}$$

$$\boldsymbol{e}_{\boldsymbol{\eta}} = \boldsymbol{\eta}_d - \boldsymbol{\eta}, \ \boldsymbol{e}_{\boldsymbol{p}_{\boldsymbol{\eta}}} = \dot{\boldsymbol{\eta}}_d - \dot{\boldsymbol{\eta}} + \boldsymbol{K}_{\boldsymbol{\eta}}\boldsymbol{e}_{\boldsymbol{\eta}}, \tag{9}$$

$$\boldsymbol{e}_{\boldsymbol{\sigma},\boldsymbol{p}_{\boldsymbol{\sigma}}} = \left[\boldsymbol{e}_{\boldsymbol{\sigma}}^{\top} \ \boldsymbol{e}_{\boldsymbol{p}_{\boldsymbol{\sigma}}}^{\top}\right]^{\top}, \tag{10}$$

$$\boldsymbol{e}_{\boldsymbol{\sigma}} = \boldsymbol{\sigma}_d - \boldsymbol{\sigma}, \ \boldsymbol{e}_{\boldsymbol{p}_{\boldsymbol{\sigma}}} = \dot{\boldsymbol{\sigma}}_d - \dot{\boldsymbol{\sigma}} + \boldsymbol{K}_{\boldsymbol{\sigma}}\boldsymbol{e}_{\boldsymbol{\sigma}}, \tag{11}$$

$$\boldsymbol{e}_{\dot{\boldsymbol{\delta}}} = \dot{\boldsymbol{\delta}}_d - \dot{\boldsymbol{\delta}}, \ \dot{\boldsymbol{e}}_{\dot{\boldsymbol{\delta}}} = \ddot{\boldsymbol{\delta}}_d - \ddot{\boldsymbol{\delta}}, \tag{12}$$

where $\dot{\boldsymbol{\delta}}_d = [\dot{x}_{pd} \ \dot{y}_{pd} \ \dot{z}_{pd}]^{\top}$, $\boldsymbol{\sigma}_d = [\alpha_d \ \beta_d]^{\top}$, and $\boldsymbol{\eta}_d = [\phi_d \ \theta_d \ \psi_d]^{\top}$ with the desired attitude $\boldsymbol{\eta}_d$, and the desired position $\boldsymbol{\delta}_d$, which can be determined by the object detection algorithm proposed in the above section. The positive definite diagonal matrixes $\boldsymbol{K}_{\boldsymbol{\sigma}} = \mathrm{diag}\,(k_\alpha, k_\beta)$ and $\boldsymbol{K}_{\boldsymbol{\eta}} = \mathrm{diag}\,(k_\phi, k_\theta, k_\psi)$. The attitude $\boldsymbol{\eta}$ in **(9)** and the velocity $\dot{\boldsymbol{\xi}}$ in **(12)** of the quadrotor are measured by the IMU integrated in the flight control system. The payload's velocity $\dot{\boldsymbol{\delta}}$ in **(12)** can be calculated by $\boldsymbol{\eta}$ and $\boldsymbol{\xi}$. From **Eq. 9**, the attitude error dynamic of the quadrotor is obtained as

$$\dot{\boldsymbol{e}}_{\boldsymbol{\eta}} = \boldsymbol{e}_{\boldsymbol{p}_{\boldsymbol{\eta}}} - \boldsymbol{K}_{\boldsymbol{\eta}}\boldsymbol{e}_{\boldsymbol{\eta}}, \ \dot{\boldsymbol{e}}_{\boldsymbol{p}_{\boldsymbol{\eta}}} = \ddot{\boldsymbol{\eta}}_d - \ddot{\boldsymbol{\eta}} + \boldsymbol{K}_{\boldsymbol{\eta}}\left(\boldsymbol{e}_{\boldsymbol{p}_{\boldsymbol{\eta}}} - \boldsymbol{K}_{\boldsymbol{\eta}}\boldsymbol{e}_{\boldsymbol{\eta}}\right). \tag{13}$$

The swing angle error dynamics of the payload are deduced from **Eq. 11**:

$$\dot{\boldsymbol{e}}_{\boldsymbol{\sigma}} = \boldsymbol{e}_{\boldsymbol{p}_{\boldsymbol{\sigma}}} - \boldsymbol{K}_{\boldsymbol{\sigma}}\boldsymbol{e}_{\boldsymbol{\sigma}}, \ \dot{\boldsymbol{e}}_{\boldsymbol{p}_{\boldsymbol{\sigma}}} = \ddot{\boldsymbol{\sigma}}_d - \ddot{\boldsymbol{\sigma}} + \boldsymbol{K}_{\boldsymbol{\sigma}}\left(\boldsymbol{e}_{\boldsymbol{p}_{\boldsymbol{\sigma}}} - \boldsymbol{K}_{\boldsymbol{\sigma}}\boldsymbol{e}_{\boldsymbol{\sigma}}\right). \tag{14}$$

3.2 Load Velocity Controller

3.2.1 Inner-Loop Attitude Controller

Considering the subsystem (see **Eq. 5b**), the inner-loop subcontroller (see the right of **Figure 1**) is used to control the attitude $\boldsymbol{\eta}$ of the quadrotor, which is measured by the inertial measurement unit (IMU) integrated in the flight control system of the quadrotor. The control torque $\boldsymbol{\tau}_{\boldsymbol{\eta}} \in \mathbb{R}^3$ of the inner-loop controller is given by

$$\boldsymbol{\tau}_{\boldsymbol{\eta}} = \boldsymbol{J}_q\left[\left(\boldsymbol{I}_3 - \boldsymbol{K}_{\boldsymbol{\eta}}^{\ 2}\right)\boldsymbol{e}_{\boldsymbol{\eta}} + \left(\boldsymbol{K}_{\boldsymbol{\eta}} + \boldsymbol{K}_{\boldsymbol{p}_{\boldsymbol{\eta}}}\right)\boldsymbol{e}_{\boldsymbol{p}_{\boldsymbol{\eta}}}\right] - \boldsymbol{\tau}_{\boldsymbol{\eta}\boldsymbol{e}}, \tag{15}$$

where $\boldsymbol{K}_{\boldsymbol{p}_{\boldsymbol{\eta}}} = \mathrm{diag}\,(k_{p\phi}, k_{p\theta}, k_{p\psi})$ denotes a constant positive definite matrix.

3.2.2 Middle-Loop Swing Angle Controller

Referring to **Eq. 16** in (Lv et al., 2020), the adaptive swing angle controller is applied to make $\boldsymbol{\sigma}$ follow the desired $\boldsymbol{\sigma}_d$. Noting **Eq. 5c**, $\boldsymbol{M}_{\boldsymbol{\sigma}}\ddot{\boldsymbol{\xi}}$ is taken as the visual control input. The desired visual control input is designed as

$$\boldsymbol{M}_{\boldsymbol{\sigma}}\ddot{\boldsymbol{\xi}}_{\boldsymbol{d}} = \left(\boldsymbol{I}_2 - \boldsymbol{K}_{\boldsymbol{\sigma}}^{\ 2}\right)\boldsymbol{e}_{\boldsymbol{\sigma}} + \left(\boldsymbol{K}_{\boldsymbol{\sigma}} + \boldsymbol{K}_{\boldsymbol{p}\boldsymbol{\sigma}}\right)\boldsymbol{e}_{\boldsymbol{p}\boldsymbol{\sigma}} - \boldsymbol{F}_{\boldsymbol{\sigma}\boldsymbol{e}} - \boldsymbol{M}_1^{-1}\boldsymbol{D}_{\boldsymbol{\sigma}}, \tag{16}$$

where $\boldsymbol{K}_{\boldsymbol{p}\boldsymbol{\sigma}} = \mathrm{diag}\ (k_{p\alpha}, k_{p\beta})$ is constant positive definite.

3.3.3 Decoupler

For the desired acceleration $\boldsymbol{M}_{\boldsymbol{\sigma}}\ddot{\boldsymbol{\xi}}_d$ in **Eq. 16** generated by the aforementioned adaptive swing angle controller, the quadrotor's lift force F_l and the desired attitude ϕ_d can be decoupled by $\boldsymbol{M}_{\boldsymbol{\sigma}}\ddot{\boldsymbol{\xi}}_d$ and F_{td}. Considering the constraint given in **(1)** and the mechanisms of the quadrotor maneuvers, we have $F_{lzd} > 0$, θ_d, $\phi_d \in (-\pi/2, \pi/2)$. The decoupling result is given by

$$\theta_d = arctan\left(\left(F_{lxd}\boldsymbol{c}\psi + F_{lyd}\boldsymbol{s}\psi\right)/F_{lzd}\right), \tag{17a}$$

$$\phi_d = -arctan\left(\left(-F_{lxd}\boldsymbol{s}\psi + F_{lyd}\boldsymbol{c}\psi\right)\boldsymbol{c}\theta_d/F_{lzd}\right), \tag{17b}$$

$$F_l = F_{lzd}/\left(\boldsymbol{c}\phi_d\boldsymbol{c}\theta_d\right). \tag{17c}$$

3.3.4 Outer-Loop Velocity Controller

As illustrated in the outer-loop part of the right subfigure in **Figure 1**, the outer-loop velocity controller is utilized to track the desired velocity $\dot{\boldsymbol{\delta}}_d$ for the translational dynamic (see **Eq. 5a**) of the payload. The desired tensile force $\boldsymbol{F}_{\boldsymbol{td}} = [F_{txd}, \ F_{tyd} \ F_{tzd}]^{\top}$ is designed as

$$\boldsymbol{F}_{\boldsymbol{td}} = \boldsymbol{K}_{\dot{\boldsymbol{\delta}}}\boldsymbol{e}_{\dot{\boldsymbol{\delta}}} - \boldsymbol{F}_{\boldsymbol{\delta}\boldsymbol{e}} - m_p\boldsymbol{g}, \tag{18}$$

with a constant positive definite diagonal matrix $\boldsymbol{K}_{\dot{\boldsymbol{\delta}}} = \mathrm{diag}\,(k_{\dot{x}_p}, k_{\dot{y}_p}, k_{\dot{z}_p})$. Considering the constraints in **(1)** and that the cable is always taut and there is tensile force on the cable, $F_{tzd} > 0$, α_d, $\beta_d \in (-\pi/2, \pi/2)$. Referring to Eq. 26 in (Lv et al., 2020), the desired magnitude F_{td} of tensile force and the desired swing angles α_d and β_d are given by

$$F_{td} = F_{tzd}/\left(\boldsymbol{c}\alpha_d\boldsymbol{c}\beta_d\right), \tag{19a}$$

$$\beta_d = arctan\left(F_{txd}/F_{tzd}\right), \tag{19b}$$

$$\alpha_d = -arctan\left(F_{tyd}\boldsymbol{c}\beta_d/F_{tzd}\right). \tag{19c}$$

3.3 LADRC Based Position Controller

LADRC is utilized for the position control of quadrotors. There are two parts in the LADRC, including the linear extended state observer (LESO) and PD controller. The LESO estimates the internal and external disturbances of the system through an extended state, which is called total disturbance, and compensates the control variables. Therefore, the integrator used in traditional PID to eliminate static error under

constant disturbance is no longer necessary. The system can be stabilized by PD controller.

Referring to the controller built by Gao in (Han, 2009) and taking δ_d as the expected input of the controller and δ as feedback, the designed LADRC block diagram is as follows:

3.3.1 LESO

Compared with ESO (Han, 2009), LESO introduces the frequency domain method. It connects the parameters with the observer bandwidth, making the parameter tuning more convenient.

The LESO for the position control of the QSCP is designed as

$$\dot{z} = [A - LC]\boldsymbol{z} - [B, L]\boldsymbol{u_c}, \tag{20a}$$

$$\boldsymbol{y_c} = \boldsymbol{z}, \tag{20b}$$

where $\boldsymbol{u_c} = [u\ \delta]^\top$ is the input of LESO, and $\boldsymbol{y_c}$ is the output. Besides this, $A = \begin{bmatrix} 0 & 1 & 0 \\ 0 & 0 & 1 \\ 0 & 0 & 0 \end{bmatrix}$, $B = \begin{bmatrix} 0 \\ b_0 \\ 0 \end{bmatrix}$, $C = [1\ 0\ 0]$, $L = [3\omega_0\ \ 3\omega_0^2\ \ \omega_0^3]^\top$. Here, b_0 can be adjusted according to the step response of the system. ω_0 is the observer bandwidth.

3.3.2 PD Controller

Under the action of LESO, the linear PD controller can stabilize the system. Besides this, the proportional coefficient and differential time constant are related to the controller bandwidth, which simplifies the tuning of the controller.

The PD controller is designed as

$$\boldsymbol{u_0} = k_p\,(\boldsymbol{\delta_d} - \boldsymbol{z_1}) - k_d\boldsymbol{z_2} \tag{21}$$

where δ_d is the expected input of the controller. $\boldsymbol{z_1}$ and $\boldsymbol{z_2}$ are observer states from LESO. k_p and k_d are the parameters of the controller gain matrix $K = [k_d\ k_p]^\top$ to be designed. We choose $k_p = \omega_c^2, k_d = 2\omega_c$ with the controller bandwidth ω_c.

Finally, the control quantity $\boldsymbol{u_0}$ with the total disturbance $\boldsymbol{z_3}$ has to be compensated, and the control quantity $\boldsymbol{u}$ is $\boldsymbol{u} = \frac{\boldsymbol{u_0} - \boldsymbol{z_3}}{\boldsymbol{b}}$, where $\boldsymbol{b}$ is the gain factor.

For the position control, it is necessary to obtain the position coordinates of the target point, but the camera feeds back the pixel coordinates, which should be compensated by attitude angle and height information. Besides this, due to the relative displacement between the quadcopter and the load, the coordinates of the target point collected by the camera relative to the quadcopter should be transformed into the coordinates relative to the load.

4 EXPERIMENT

To verify the effectiveness of the proposed algorithm, a QCSP experimental platform was created. The payload is connected to the bottom of the F450 quadcopter by a Cadan joint, and the Jetson NX board is fixed to the bottom plate with the camera as shown in **Figure 3A**.

Before the flight test, we simulated the designed LADRC control strategy and compared it with the conventional PID algorithm as shown in **Figure 2**. The parameters of LADRC and PID are obtained

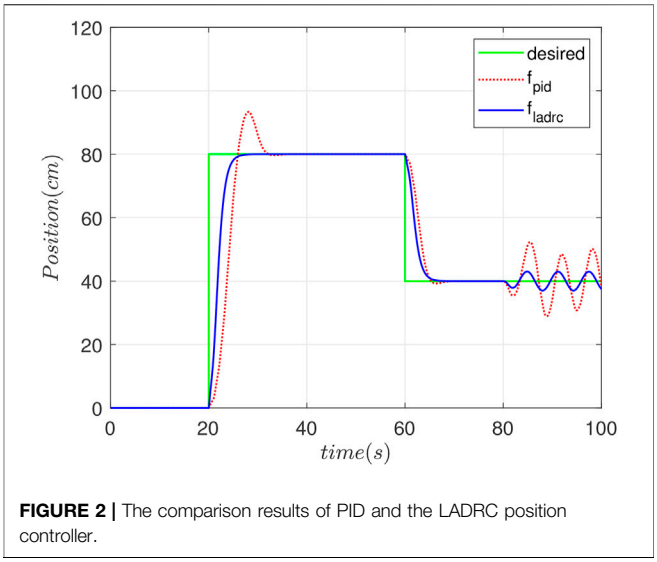

FIGURE 2 | The comparison results of PID and the LADRC position controller.

by many experiments according to overshoot and response time. Among them, "desired" is the target position curve after transformation, "f_{pid}" is the position curve of the payload under PID control. "f_{ladrc}" is the position curve of the payload under LADRC control. It can be seen that, at 20 s, given a target position of 80 cm, the payload achieved steady state in 7 s without overshoot under the LADRC control, while the state of the system oscillated and took more than three times as long to stabilize under the PID controller. When a sin disturbance signal is added in 80 s, the LADRC can obviously suppress the disturbance. As a result, it can be deduced that the LADRC controller is effective in saving QCSP energy.

The QCSP vision deployment hardware is Jetson NX, which runs aarch64 Ubuntu 18.04 as the operating system. PyTorch (Paszke et al., 2019) is used as the retraining, fine-tuning, and inference deep learning software. For efficient inference, popular object detection model YOLOV3(Redmon and Farhadi, 2018) is adopted, whose backbone is replaced by MobileNet (Howard et al., 2017) from DarkNet. The image size requires 416 × 416. The original network is retrained on a PASCAL VOC data set (Everingham et al., 2010) for 50,000 iterations and removes the connections whose scaling factors are lower than the threshold 0.01. Then, the compact network is fine-tuned for 12,000 iterations. The retraining and fine-tuning, which cost a large amount of computing power, are carried out on NVIDIA RTX 2080Ti, and only inference is done on the embedding Jetson NX platform. The target pattern is the helicopter landing area-"*H*", and the recognition effect is shown in part (b) of **Figure 3**, where four objects are detected with confidence 0.89, 0.95, 0.98, and 0.97.

Compression results are reported in **Table 1**. Through our method, we saved about 52% energy of the whole network with only 0.7 mean average precision (mAP) dropping. In addition, we also demonstrate the necessary of using sparsity-induced and energy-aware penalties simultaneously. In the case of only the sparsity-induced penalty used, the energy saved is not satisfactory (43% saved), but performance drops a lot (1.4) when only the energy-aware penalty is used.

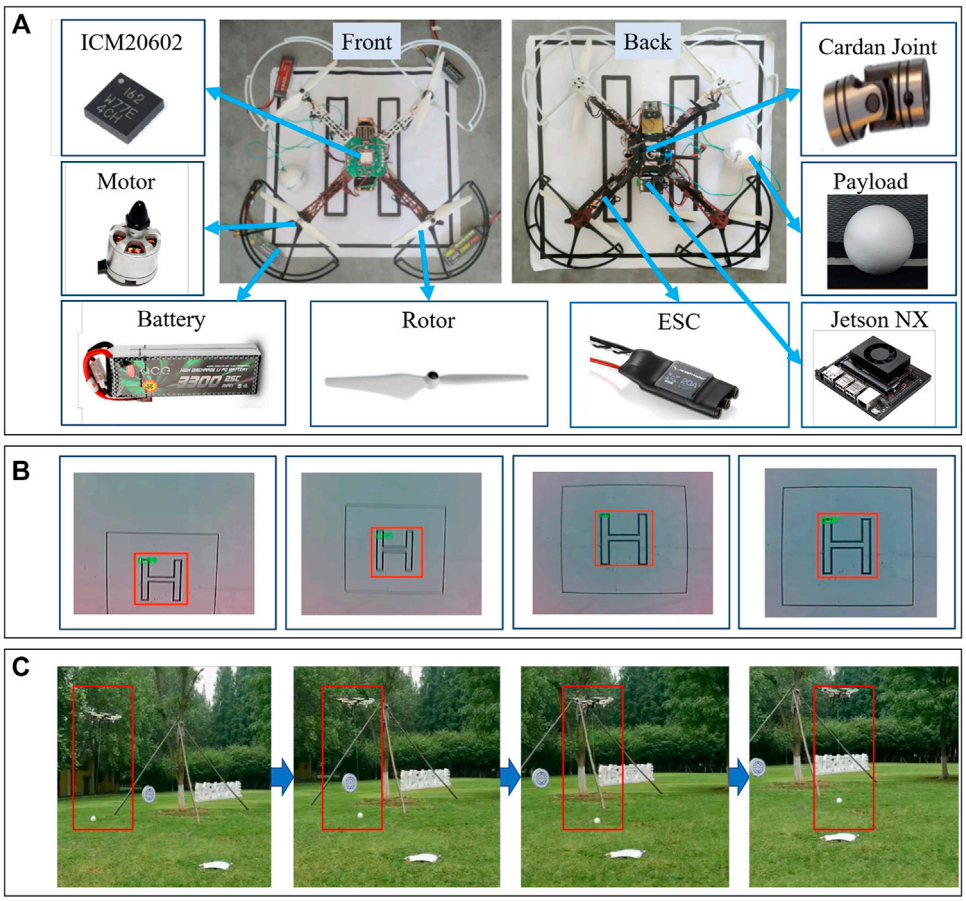

FIGURE 3 | Experimental platform of QCSP object detection and position control flight test.

TABLE 1 | Object detection performance on PASCAL VOC. *"Penalty"* denotes the penalty item that we added for training loss. *"Energy"* denotes the energy cost for detecting one image. *"Energy ↓"* denotes the energy saved comparing to original network whose backbone is MobileNet; *"mAP"* is a common indicator evaluating the performance of detection network.

Backbone	Penalty	Energy (J)	Energy ↓	mAP
DarkNet Redmon and Farhadi (2018)	—	6.61	—	76.1
MobileNet Howard et al. (2017)	—	0.21	—	76.8
MobileNet Howard et al. (2017)	saprsity-induced Liu et al. (2017)	0.12	43%	75.9
MobileNet Howard et al. (2017)	energy-aware Yang et al. (2018)	0.10	**52%**	75.4
MobileNet Howard et al. (2017)	Ours	0.10	**52%**	**76.1**

During the actual flight experiment, the quadcopter flew along the positive direction of the *X* axis at the speed of 20 cm/s. When the target point is identified by Jetson NX, it turn into position control mode as shown in **Figure 3C**. From the experiment, it can be seen that the QCSP system can control the payload stably, and when the target position is detected, it can reach the destination quickly and remain stable.

5 CONCLUSION

Energy-efficiency plays a crucial role in the development of UAVs. In this paper, a lightweight YOLOV3 object detection network with a LADRC-based position controller is proposed to reduce the energy consumption of the QCSP system. The experimental results show that the compressed network can save more than 50% of energy compared with the original network with little accuracy loss, and the LADRC controller has three times faster stabilization time and no overshoot compared with the classic PID controller and has a suppression effect on disturbing signals. Therefore, the work done in this paper can effectively save the energy of the QCSP and improve its range, anti-interference performance, and robustness.

DATA AVAILABILITY STATEMENT

The original contributions presented in the study are included in the article/Supplementary Material, further inquiries can be directed to the corresponding author.

AUTHOR CONTRIBUTIONS

SL contributed to the architecture, property, and training algorithm, and design of feedback controller of the QCSP systems. SL, and LF drafted the work and contributed to the experiments and conclusions. All authors agree to be accountable for the content of the work.

FUNDING

National Natural Science Foundation of China No. 61972064; LiaoNingRevitalizationTalentsProgram No. XLYC1806006.

REFERENCES

Everingham, M., Van Gool, L., Williams, C. K. I., Winn, J., and Zisserman, A. (2010). The Pascal Visual Object Classes (Voc) challenge. *Int. J. Comput. Vis.* 88 (2), 303–338. doi:10.1007/s11263-009-0275-4

Han, J. (2009). From Pid to Active Disturbance Rejection Control. *IEEE Trans. Ind. Electron.* 56 (3), 900–906. doi:10.1109/tie.2008.2011621

Hao, W., Xian, B., and Xie, T. (2021). Fault Tolerant Position Tracking Control Design for an Tilt Tri-rotor Unmanned Aerial Vehicle. *IEEE Trans. Ind. Electron.* 99, 1. doi:10.1109/TIE.2021.3050384

Howard, A. G., Zhu, M., Chen, B., Kalenichenko, D., Wang, W., Weyand, T., et al. (2017). *Mobilenets: Efficient Convolutional Neural Networks for mobile Vision Applications*. California: Google Inc. arXiv preprint arXiv:1704.04861. Available at: https://arxiv.53yu.com/pdf/1704.04861.pdf%EF%BC%89.

Ioffe, S., and Szegedy, C. (2015). "Batch Normalization: Accelerating Deep Network Training by Reducing Internal Covariate Shift," in International conference on machine learning (PMLR), Lille, France, July 7–9, 2015, 448–456.

Kung, H.-T. (1982). Why Systolic Architectures? *Computer* 15 (01), 37–46. doi:10.1109/mc.1982.1653825

Liu, Z., Li, J., Shen, Z., Huang, G., Yan, S., and Zhang, C. (2017). "Learning Efficient Convolutional Networks through Network Slimming," in Proceedings of the IEEE international conference on computer vision, Venice, Italy, October 22–29, 2017, 2736–2744. doi:10.1109/iccv.2017.298

Lv, Z.-Y., Li, S., Wu, Y., and Wang, Q.-G. (2021). Adaptive Control for a Quadrotor Transporting a cable-suspended Payload with Unknown Mass in the Presence of Rotor Downwash. *IEEE Trans. Veh. Technol.* 70 (9), 8505–8518. doi:10.1109/tvt.2021.3096234

Lv, Z.-Y., Wu, Y., and Rui, W. (2020). Nonlinear Motion Control for a Quadrotor Transporting a cable-suspended Payload. *IEEE Trans. Veh. Technol.* 69 (8), 8192–8206. doi:10.1109/tvt.2020.2997733

Mochida, S., Matsuda, R., Ibuki, T., and Sampei, M. (2021). A Geometric Method of Hoverability Analysis for Multirotor Uavs with Upward-Oriented Rotors. *IEEE Trans. Robotics* 99, 1–15. doi:10.1109/tro.2021.3064101

Paszke, A., Gross, S., Massa, F., Lerer, A., Bradbury, J., Chanan, G., et al. (2019). "PyTorch: An Imperative Style, High-Performance Deep Learning Library," in *Advances in Neural Information Processing Systems*. Editors Wallach, H., Larochelle, H., Beygelzimer, A., d\textquotesingle Alch\'{e}-Buc, F., Fox, E., and Garnett, R. (Curran Associates, Inc.) 32. Available at: https://proceedings.neurips.cc/paper/2019/file/bdbca288fee7f92f2bfa9f7012727740-Paper.pdf.

Qian, L., and Liu, H. (2019). Path Following Control of a Quadrotor Uav with a cable Suspended Payload under Wind Disturbances. *IEEE Trans. Ind. Electron.* 67, 1. doi:10.1109/TIE.2019.2905811

Redmon, J., and Farhadi, A. (2018). *Yolov3: An Incremental Improvement*. Washington D.C: University of Washington. Available at: https://arxiv.53yu.com/pdf/1804.02767.pdf.

Wu, Y., Hu, K., and Sun, X.-M. (2018). Modeling and Control Design for Quadrotors: A Controlled Hamiltonian Systems Approach. *IEEE Trans. Vehicular Tech.* 67 (12), 11 365. doi:10.1109/tvt.2018.2877440

Xie, Z., Zhu, L., Zhao, L., Tao, B., Liu, L., and Tao, W. (2020). Localization-aware Channel Pruning for Object Detection. *Neurocomputing* 403, 400–408. doi:10.1016/j.neucom.2020.03.056

Yang, H., Zhu, Y., and Liu, J. (2018). *Energy-constrained Compression for Deep Neural Networks via Weighted Sparse Projection and Layer Input Masking*. New York, NY: Cornell University. arXiv preprint arXiv:1806.04321.

Conflict of Interest: The authors declare that the research was conducted in the absence of any commercial or financial relationships that could be construed as a potential conflict of interest.

Publisher's Note: All claims expressed in this article are solely those of the authors and do not necessarily represent those of their affiliated organizations, or those of the publisher, the editors and the reviewers. Any product that may be evaluated in this article, or claim that may be made by its manufacturer, is not guaranteed or endorsed by the publisher.

frontiers in Energy Research

ORIGINAL RESEARCH
published: 16 March 2022
doi: 10.3389/fenrg.2021.820611

Multiterminal Hybrid DC Line Protection Based on Intrinsic Mode Energy Entropy

Chao Xing[1], *Pengsong Li*[1,2], *Guihong Bi*[2], *Shilong Chen*[2]*, *Junhao Chen*[1,2] *and Zihang Zhang*[1,2]

[1]Electric Power Research Institute of Yunnan Power Grid Co., Ltd., Kunming, China, [2]School of Electric Power Engineering, Kunming University of Science and Technology, Kunming, China

In view of the UHV multiterminal hybrid DC transmission system, the DC line protection with universal applicability, fast response speed, stability, and reliability is particularly important for its safe and economic operation. In this article, the boundary frequency characteristics of the UHV multiterminal hybrid DC transmission system are analyzed by considering the DC boundary of the rectifier side and inverter side, line frequency variation, and other factors. According to the fact that the boundary of the fault line has a strong attenuation effect on the high-frequency component of the transient current, a protection method based on the intrinsic mode energy entropy is proposed to distinguish the faults inside and outside. The criterion to initiate the protection is constructed by using the amplitude of the transient power; the fault direction criterion is constructed by using the positive and negative characteristics of the transient energy of the fault power detected by power direction elements on both sides of the T-zone; the fault pole selection criterion is constructed by using the ratio of low-frequency transient power changes of positive and negative poles. Finally, the Kun–Liu–Long line UHV three-terminal hybrid DC transmission system model is built on the PSCAD/EMTDC simulation platform, and a large number of simulation examples verify that the protection can operate reliably under different fault poles, fault positions, and transition resistances.

Keywords: the multiterminal hybrid DC, boundary frequency characteristics, the intrinsic mode energy entropy, the T-zone, the transient power

OPEN ACCESS

Edited by:
Xun Shen,
Tokyo Institute of Technology, Japan

Reviewed by:
Zhenhua Li,
China Three Gorges University, China
Xiaohua Li,
South China University of Technology, China

***Correspondence:**
Shilong Chen
chenshilong3@126.com

Specialty section:
This article was submitted to Smart Grids, a section of the journal Frontiers in Energy Research

Received: *23 November 2021*
Accepted: *23 December 2021*
Published: *16 March 2022*

Citation:
Xing C, Li P, Bi G, Chen S, Chen J and Zhang Z (2022) Multiterminal Hybrid DC Line Protection Based on Intrinsic Mode Energy Entropy. Front. Energy Res. 9:820611. doi: 10.3389/fenrg.2021.820611

1 INTRODUCTION

In recent years, large-scale new energy grid connection, regional power grid interconnection, and central load power supply have become hot issues at home and abroad, and it is urgent to build a DC network with higher power supply reliability on the basis of existing practical experience and theoretical research on DC transmission projects (Tang et al., 2013; He et al., 2017). Most of the traditional direct current transmission systems are two-terminal systems, which can only realize point-to-point power transmission whose remarkable feature is to realize AC collection–DC transmission–AC dispersion of electric energy (Wang et al., 2014). Compared with the traditional two-terminal DC transmission system, the UHV hybrid DC transmission system contains multiple sending terminals or receiving terminals, which can realize multipower supply and multi-drop power reception, and the operation mode is more flexible (Xu et al., 2013). The sending terminal is usually connected with a line-commutated converter (LCC), while the receiver is

usually connected in parallel with a modular multilevel converter (MMC) with fault self-clearing capability (He et al., 2020). This structure makes comprehensive use of the advantages of low loss and good economy of conventional DC power transmission as well as flexible and fast control of flexible DC power transmission without commutation failure, such as Kun–Liu–Long line UHV multiterminal hybrid DC transmission demonstration project planned and constructed in China (Li et al., 2019).

The long distance of DC transmission lines and the complex environment of transmission corridors lead to a high fault rate (Li et al., 2021; Liu et al., 2020). When the DC fault occurs, it develops very quickly. The superposition of fault output of multiple converter stations in the UHV multiterminal hybrid DC transmission system makes the fault hazards such as line overcurrent more prominent (Muniappan, 2021). At present, the main protection widely used for the DC transmission lines is traveling wave protection (Shen and Raksincharoensak, 2021a). However, in actual operation, traveling wave protection is easily affected by factors such as inaccurate extraction of wave head information, selection of setting value, and high resistance ground fault, while its protection reliability is poor (Zheng et al., 2018). Xia et al. (2018) use the longitudinal impedance at both ends of the transmission line to propose a multiterminal line differential current protection, but there is a problem of too many measured values, and the communication time required increases when the line is long. Zhou et al. (2017) put forward a multiterminal flexible DC line protection scheme based on the voltage amplitude of a current-limiting reactor by using the characteristics of DC reactors as line boundary elements. However, there is a problem of poor transient resistance, and the multiterminal DC lines are interconnected by DC buses, and the T-zone structure formed by interconnection can be used directly with relatively few line boundary elements. Li et al. (2019) study the unique structure of T-zone in the parallel multiterminal hybrid DC transmission system and propose a fault direction discrimination principle based on the comparison of wavelet energy of fault current on both sides of T-zone. When applied to the three-terminal hybrid DC system, there is no need for interstation communication, but the selection of its setting value depends on the result of wavelet decomposition. In reference (Zhang Y. et al., 2021), the transient current fault components at the three ends of the T-junction bus are measured, and the correlation coefficient is calculated to serve as the basis for fault zone identification of the hybrid multiterminal DC transmission system. No interstation communication is required, but the noise tolerance is poor. Therefore, it is necessary to further study the DC line protection which is suitable for the UHV multiterminal hybrid DC transmission system and has fast response, stability, and reliability. Yang and Liu (2018) take the current mutation of each phase in the AC distribution network as the characteristic quantity, calculate its inherent modal energy entropy, and use the maximum modal energy maximum value for fault line selection. It is less affected by grounding the resistance and system structure and is more suitable for systems with complex structures. This principle provides a certain idea for the study of multiterminal hybrid HVDC transmission line protection.

In this article, the Kun–Liu–Long line UHV three-terminal hybrid DC transmission system is selected as the research object, and the boundary frequency characteristics of the rectifier side and the inverter side are analyzed theoretically. On this basis, a protection method is proposed to distinguish faults, inside and outside, based on the intrinsic mode energy entropy. The amplitude of transient power is used as the criterion to initiate the protection; the positive and negative characteristics of transient energy of fault power detected by power direction elements on both sides of the T-zone are used to identify the fault direction; the ratio of the variable quantity of low-frequency transient power of positive and negative poles is used to select the fault poles. The model of the Kun–Liu–Long line UHV three-terminal hybrid DC transmission system is built on the PSCAD/EMTDC simulation platform, and the effectiveness of the protection scheme is verified by a large number of simulation examples.

2 THE ANALYSIS OF THE BOUNDARY FREQUENCY CHARACTERISTICS OF THE UHV MULTITERMINAL HYBRID DC TRANSMISSION LINE

Figure 1 shows the simulation model of the Kun–Liu–Long line UHV three-terminal hybrid DC transmission system. The system adopts the true bipolar connection mode, with independent converter equipment, transmission lines, and control systems for both positive and negative poles. The LCC is used in the Kunbei Converter Station on the rectifier side, while the bipolar MMC with fault self-clearing capability is used in the Liubei Converter Station and Longmen Converter Station on the inverter side. The sending terminal Kunbei Converter Station and the receiving terminal Longmen Converter Station are connected to the bus bar in the receiving terminal Liubei Converter Station by line L_1 and line L_2, respectively (Yu et al., 2020). The T-zone is formed by the DC line L_1 and L_2 connected in parallel with the bus bar, and the protection devices M1 and M2 are installed on the left and right sides of the T-zone, respectively.

2.1 The Analysis of Boundary Frequency Characteristics on the Kunbei Side Line

Because the rectifier side of the Kun–Liu–Long line UHV three-terminal hybrid DC transmission system adopts LCC, during the normal operation, due to the nonlinear characteristics of the converter, a large number of harmonic waves will be generated in the DC transmission line (Shen and Raksincharoensak, 2021b). Therefore, it is necessary to configure two smoothing reactors and two groups of triple-tuned DC filters at the head of the DC line L_1 to suppress the harmonic current generated by the converter and injected into the DC line (Shen et al., 2017, Shen et al., 2020a). The smoothing reactors and DC filters

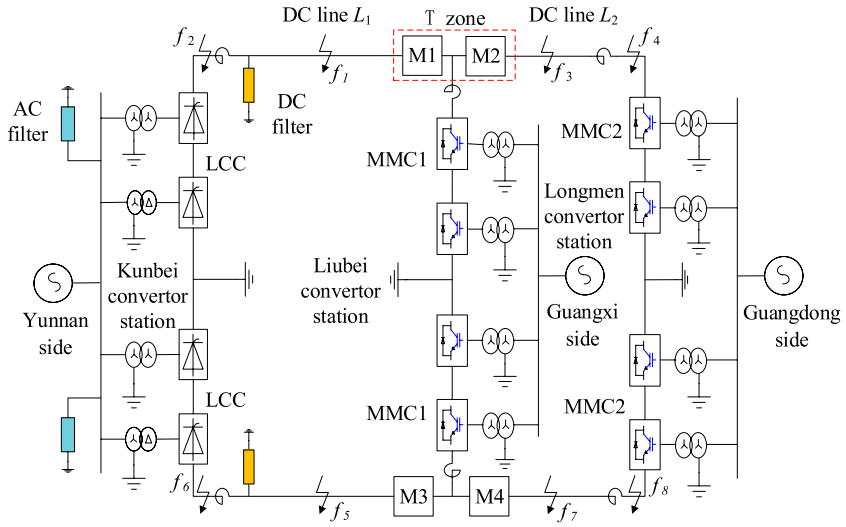

FIGURE 1 | Structure diagram of the UHV three-terminal hybrid DC transmission system.

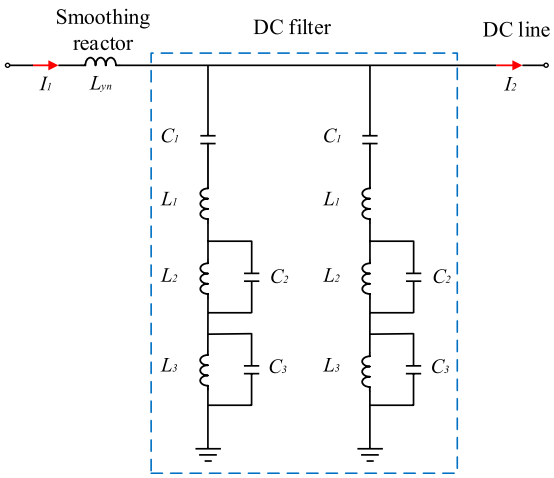

FIGURE 2 | Line boundary on the Kunbei side line.

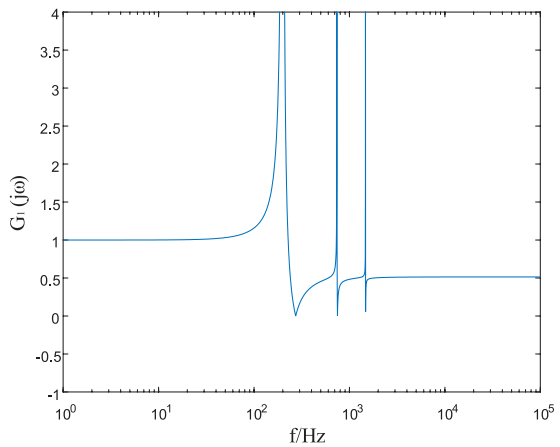

FIGURE 3 | Amplitude frequency characteristics of the line boundary transfer function on the Kunbei side line.

TABLE 1 | Parameters of the smoothing reactor and DC filter.

Smoothing reactor	***Lyn***	**150 mH**
DC filter	C_1	1.0 μF
	L_1	17.4 mH
	C_2	3.04 μF
	L_2	15.7 mH
	C_3	3.675 μF
	L_3	3.2 mH

together form the physical boundary on the rectifier side, as shown in **Figure 2**. The specific parameters of each component are shown in **Table 1**.

In **Figure 2**, the symbol (I_1) represents the transient current outside the protection zone of the DC line L_1, while the symbol (I_2) represents the transient current flowing into the DC line L_1 after attenuation by the line boundary on the Kunbei side line. According to the parameters in **Table 1**, the expressions of equivalent impedance of the smoothing reactor and DC filter can be obtained, respectively, as follows:

$$\boldsymbol{Z_1(j\omega) = j\omega L_{yn};} \tag{1}$$

$$\boldsymbol{Z_2(j\omega) = \frac{1}{2}\left(\frac{1}{j\omega C_1} + j\omega L_1 + \frac{j\omega L_2}{1-\omega^2 C_2 L_2} + \frac{j\omega L_3}{1-\omega^2 C_3 L_3}\right).} \tag{2}$$

In the formula, the symbol ($\boldsymbol{Z_2(j\omega)}$) represents the equivalent impedance of the smoothing reactor, while the symbol ($\boldsymbol{Z_2(j\omega)}$) represents the equivalent impedance of the DC filter. The expression defining the line boundary transfer function on the Kunbei side line is as follows (Chen et al., 2021):

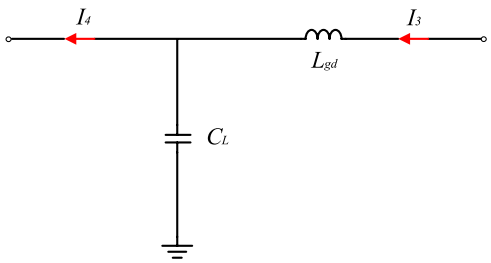

FIGURE 4 | Line boundary on the Longmen side.

$$G_1(j\omega) = \frac{I_2(j\omega)}{I_1(j\omega)}. \tag{3}$$

According to **Eqs 1–3**, the expression of the line boundary transfer function on the north side of Kunming can be further obtained as:

$$G_1(j\omega) = \frac{Z_1(j\omega) + Z_2(j\omega)}{2Z_1(j\omega) + Z_2(j\omega)}. \tag{4}$$

In order to quantitatively analyze the characteristics of $G_1(j\omega)$, the amplitude frequency characteristics of the boundary transfer function on the Kunbei side line can be obtained by substituting the parameters of each element in **Table 1**, as shown in **Figure 3**.

It can be seen from **Figure 3** that when 0 Hz < $f \leq$ 32 Hz $|G_1(j\omega)| = 1$, and it can be considered that the transient current has not decayed. When $f >$ 1472 H, $|G_1(j\omega)| \ll 1$. It can be seen that the line boundary on the Kunbei side line has a strong attenuation effect on the high-frequency component of the transient current.

2.2 The Analysis of Boundary Frequency Characteristics on the Longmen Side

The MMC is used in the inverter side of the Kun–Liu–Long line UHV three-terminal hybrid DC transmission system. Because MMC uses the sub-module cascade to output multilevel stepped waves and the output wave form is of high quality, then only one current-limiting reactor is required at the end of the DC line L_2 (Shen et al., 2020b, Shen et al., 2021a, Shen et al., 2021b). Because there is a ground capacitance between overhead lines and the ground, the current-limiting reactor and the ground capacitance of an overhead line at the end of the DC line L_2 constitute the realistic boundary on the Longmen side. The boundary equivalent circuit on the Longmen side is shown in **Figure 4**.

In **Figure 4**, the symbol (I_3) represents the transient current outside the protection zone of the DC line L_2, while the symbol (I_4) represents the transient current flowing into the DC line L_2 after being attenuated by the line boundary. The expression for defining the line boundary transfer function on the Longmen side is as follows:

$$G_2(j\omega) = \frac{I_4(j\omega)}{I_3(j\omega)} = \frac{Z_3(j\omega) + Z_4(j\omega)}{2Z_3(j\omega) + Z_4(j\omega)}. \tag{5}$$

In the formula, $Z_3(j\omega) = j\omega L_{gd}$ and $Z_4(j\omega) = 1/j\omega C_L$. By substituting the element parameters L_{gd} = 150 mH and C_L = 0.00124 μF, the amplitude frequency characteristics of the line boundary transfer function on the Longmen side can be obtained, as shown in **Figure 5**.

It can be seen from **Figure 5** that when 0Hz < $f \leq$ 434 Hz $|G_2(j\omega)| = 1$, it can be considered that the transient current has not decayed. When $f >$ 4,248 Hz, $|G_2(j\omega)| \ll 1$. Therefore, the line boundary on the Longmen side has a strong attenuation effect on the high-frequency component of the transient current.

From the aforementioned analysis of amplitude frequency characteristics of line boundary transfer functions on rectifier and inverter sides, it can be seen that high-frequency components of the transient current passing through boundary elements have obvious attenuation effect. When the fault occurs outside the DC line zone, the high-frequency energy of the fault transient current detected by the protection devices M1 and M2 is small due to the blocking effect of the line boundary. When the fault occurs in the DC line zone, the high-frequency signal is transmitted to the protection installation without obstruction, and the high-frequency energy of the fault transient current detected by the protection devices M1 and M2 is large. Therefore, the attenuation effect of high-frequency components of the transient current can be fully utilized, and the faults inside and outside the zone can be effectively distinguished.

3 THE PROTECTION ALGORITHM

3.1 The Complementary Ensemble Empirical Mode Decomposition

Because a certain wavelet base needs to be selected in the wavelet transform, the selection of the wavelet base has a great influence on the whole wavelet analysis result (Yang et al., 2018, Yang et al., 2019a). Once the wavelet base is determined, it cannot be replaced in the whole analysis process. Even though the wavelet base may be the best in the whole situation, it may

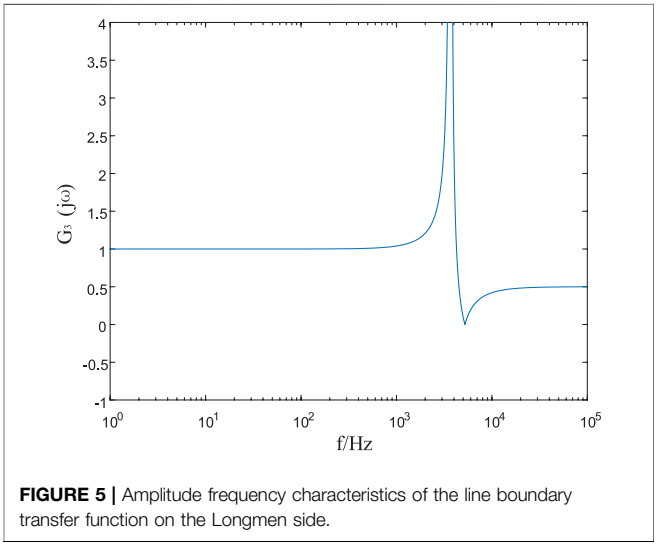

FIGURE 5 | Amplitude frequency characteristics of the line boundary transfer function on the Longmen side.

have poor effect in some parts (Yang et al., 2019b, Yang et al., 2021a).

In this article, complementary ensemble empirical mode decomposition (CEEMD) is selected as the signal processing method. CEEMD decomposes the line mode component of the fault transient current into several intrinsic mode functions (IMFs) and a residual margin according to the fluctuation or trend of different scales, and the intrinsic mode function reflects the fluctuation characteristics of the fault transient current in different time scales (Yang et al., 2021c, Yang et al., 2021b). The residual margin reflects the long-term trend characteristics of the fault transient current (Yeh et al., 2010). CEEMD does not need to predetermine or force a given basis function in advance but depends on the characteristics of the signal itself to decompose adaptively. The IMF components obtained generally have an obvious physical meaning, which is very suitable for the feature extraction of transient signals (Zhao, 2004).

Therefore, CEEMD is used to decompose the line mode component of the fault transient current inside and outside the DC line zone, and the decomposition result is shown in **Eq. 6** (Ye and Liu, 2011):

$$\boldsymbol{x}(\boldsymbol{t}) = \sum_{j=1}^{n} \boldsymbol{c}_j(\boldsymbol{t}) + \boldsymbol{r}_n(\boldsymbol{t}). \tag{6}$$

In the formula, the symbol $x(t)$ represents the original signal, $c_j(t)$ represents the intrinsic mode function, and $r_n(t)$ represents the residual term. $c_1(t)$, $c_2(t)$, ..., and $c_n(t)$ are obtained after multiple decomposition of $x(t)$, which have only a single frequency component at any time. They respectively represent n intrinsic mode function components which decrease from high frequency to low frequency, and the changing trend of $r_n(t)$ is similar to that of the original signal.

3.2 The Intrinsic Mode Energy Entropy

The intrinsic mode energy entropy is a measure that reflects the degree of energy distribution disorder of signals in various frequency bands (Zhu et al., 2020). It can be used to extract fault characteristics of the transient current. For the fault transient current, after CEEMD decomposition, the intrinsic mode energy of each frequency band in the decomposition scale on the i layer can be obtained as $E_c = E_{c_1}, E_{c_2}, \ldots, E_{c_i}$, and the energy of the i layer is defined as:

$$\boldsymbol{E}_{\boldsymbol{c}_i} = \int_{t1}^{t2} \boldsymbol{c}_i^2(\boldsymbol{t})\boldsymbol{dt}. \tag{7}$$

By dividing the intrinsic mode function of each layer obtained by decomposition into n parts on the time axis and combining it with information entropy, we can define the intrinsic mode energy entropy H as (Ning et al., 2017):

$$\boldsymbol{H} = -\sum_{i=1}^{n+1} \boldsymbol{p}_i \boldsymbol{ln}\, \boldsymbol{p}_i. \tag{8}$$

In the formula, $\boldsymbol{p_i} = \boldsymbol{E_{c_i}}/(\boldsymbol{E_{r_n}} + \sum_{i=1}^{n}\boldsymbol{E_{c_i}})$ $(\boldsymbol{i} = \boldsymbol{1, 2, \ldots, n})$; $\boldsymbol{p_{n+1}} = \boldsymbol{E_{r_n}}/(\boldsymbol{E_{r_n}} + \sum_{i=1}^{n}\boldsymbol{E_{c_i}})$.

The intrinsic mode energy entropy effectively combines complementary ensemble empirical mode decomposition, signal energy, and information entropy and effectively quantifies the discrete degree of energy distribution of the fault transient current with frequency (Guan and Zhang, 2011). It can be seen from **Eq. 8** that the more uneven the distribution of energy of the fault transient current with frequency is, the smaller the intrinsic mode energy entropy is, and the greater the energy entropy is.

4 The Criterion and Scheme of the Protection

4.1 The Criterion to Initiate the Protection

When the DC line L_1 or the DC line L_2 fails, the protection devices on both sides of the T-zone will detect larger transient current ($\boldsymbol{\Delta i}$) and voltage ($\boldsymbol{\Delta u}$); so, the amplitude of the transient power can be used to initiate the criterion of line protection. Amid the actual operation of the system, the current oscillation generally is allowed to be less than 10% of its rated value, and the voltage oscillation, less than 20% of its rated value. In this context, a certain margin should be reserved for the starting value of the protection device. In order to ensure the anti-interference performance of the protection device, the protection device operates after continuously detecting that the starting values of three data points are greater than the setting values since there are faults. The fault protection device at any position in the zone can be ensured to initiate. For that to happen, the reliability coefficient of the system, according to the analysis of the fault simulation data, is equal to 1.2, and the setting value is equal to 0.0028. By doing so, the starting is shown in the formula as follows (Zhang et al., 2016):

$$\boldsymbol{\Delta P_{star}} = \boldsymbol{K_{rel}}|\boldsymbol{\Delta u}(\boldsymbol{i})\boldsymbol{\Delta i}(\boldsymbol{i})| > \boldsymbol{\Delta P_{set}}. \tag{9}$$

4.2 The Criterion to Identify the Direction of the Fault

As there is the T-zone in the Kun–Liu–Long UHV three-terminal hybrid DC transmission system, protection devices are installed on the left and right sides of the zone; thus, directional components need to be added to identify where the faults are in an effective way. In this article, the power directional element as well as the positive and negative characteristics of the fault transient power is applied to identify the direction of faults. We select the time window of 2 ms after the protection is initiated, and we sum the transient power in the time window to form the transient energy. The formula is shown as follows:

$$\boldsymbol{\Delta E_M} = \sum_{i=1}^{N} \boldsymbol{\Delta P}(\boldsymbol{i}). \tag{10}$$

The positive direction of the current is specified as the DC bus flowing to the line. It is assumed when a grounding fault emerges from the line on the left side of the T-zone. That means the faulty power supply with a reversed polarity is accessed at the fault point, and the transient current of the line flows to the fault point.

The transient energy detected by the power directional element at the protection device (M1) is negative, while the one detected by the power directional element at the protection device (M2) is positive. When the grounding fault emerges from the line on the right side of the T-zone, the transient energy detected at the protection device (M1) is positive, but the one detected at the protection device (M2) is negative. Therefore, the specific discrimination results of the fault direction are as follows:

$$\begin{cases} \Delta E_{M_1} < 0 \cap \Delta E_{M_2} > 0 \textit{Faults on the left side of T zone} \\ \Delta E_{M_1} > 0 \cap \Delta E_{M_2} < 0 \textit{Faults on the right side of T zone} \end{cases}. \quad (11)$$

In the formula mentioned previously, the symbol (ΔE_{M_1}) represents the transient energy detected by the power directional element at the protection device (M1), while the symbol (ΔE_{M_2}) refers to the transient energy detected by the power direction element at the protection device (M2).

4.3 The Criterion to Identify Faults Inside and Outside the Left Side of the T-Zone

According to the analysis of the frequency characteristic at the boundary on the Kunbei side line in **Section 2.1**, it shows that the line boundary has a strong attenuation effect on the high-frequency component of the transient current. As a fault occurs outside the DC line L_2, the fault transient current reaches where the protection devices are installed after passing through the double attenuation of the boundary in the Kunbei side line and the DC line L_1. At this moment, the high-frequency energy of the fault transient current detected by the protection device M1 is smaller. However, when a fault occurs in the DC line L_1, the fault transient current reaches where the protection devices are installed only through the attenuation of the DC line. At this moment, the high-frequency energy of the fault transient current detected by the protection device (M1) is larger.

As a result, the line mode component of the fault transient current is decomposed by CEEMD (the Complementary Ensemble Empirical Mode Decomposition) before the intrinsic mode energy entropy of each frequency band is calculated, respectively. The energy entropy can be obtained through **Eq. 8**. When a fault occurs outside the DC line L_1, the intrinsic mode energy entropy of the fault transient current is smaller. However, when a fault occurs in the DC line L_2, the intrinsic mode energy entropy of the fault transient current is larger. In order to ensure the protection of the DC line L_1, the minimum intrinsic mode energy entropy of faults in the zone is supposed to be greater than the maximum one of faults outside the zone. Thus, the criterion to identify the faults, inside and outside, on the left side of the T-zone is as follows:

$$\textit{min}\{\boldsymbol{H_L}(\boldsymbol{K} - (\boldsymbol{N} - \boldsymbol{1})), \ldots, \boldsymbol{H_L}(\boldsymbol{K})\} > \boldsymbol{K_{rel}}\boldsymbol{H_{set1}}. \quad (12)$$

In the formula mentioned previously, the letter N represents the number of sampling points, collected within the 2-ms time window after the protection is initiated, the letter K stands for the number of sampling points at the current moment, the symbol K_{rel} refers to the reliable coefficient, and the symbol H_{set1} is the threshold value of the intrinsic mode energy entropy of the protection device (M1). Given the interference of the signal noise and sampling errors, the reliability coefficient is equivalent to 1.3. In order to distinguish the faults inside and outside of the zone in a reliable manner, the value of H_{set1} is selected with the most serious situation taken into account. The setting principle is that the high-resistance grounding fault in the DC line avoids the metallic grounding fault outside the line. The analysis of fault simulation data shows that, taking a certain margin into consideration, the threshold value of the intrinsic mode energy entropy is reasonably equivalent to 0.0008.

4.4 The Criterion to Identify Faults Inside and Outside the Right Side of the T-Zone

According to the frequency characteristic analysis of the boundary of the Longmen side line in **Section 2.2**, the boundary has a strong attenuation effect on the high-frequency component of the transient current. In the same way mentioned previously, the fault transient current line mode component on the right side of the T-zone is decomposed by CEEMD, thus calculating its intrinsic mode energy entropy. As there are faults emerging in and out of the DC line L_2, the intrinsic mode energy entropy detected by the protection device (M2) is used to distinguish the faults in and out of the DC-zone. The criterion to identify faults, inside and outside, in the right area of the T-zone is expressed in the following:

$$\textit{min}\{\boldsymbol{H_R}(\boldsymbol{K} - (\boldsymbol{N} - \boldsymbol{1})), \ldots, \boldsymbol{H_R}(\boldsymbol{K})\} > \boldsymbol{K_{rel}}\boldsymbol{H_{set2}}. \quad (13)$$

In the formula mentioned previously, the letter N represents the number of sampling points, collected within 2-ms time window after the protection is initiated, the letter K stands for the number of sampling points at the current moment, the symbol K_{rel} refers to the reliable coefficient, and the sign H_{set2} means the threshold value of the intrinsic mode energy entropy of the protection device (M2). Taking the interference of the signal noise and sampling errors into consideration, the reliable coefficient is equivalent to 1.3. In order to distinguish the faults inside and outside of the zone in a reliable manner, the value of H_{set2} is selected with the most serious situation taken into account. The setting principle is that the high-resistance grounding fault in the DC line L_2 avoids the metallic grounding fault outside the line. The analysis of fault simulation data shows that, reflecting a certain margin, the threshold value of the natural modal energy entropy is reasonably equivalent to 0.001.

4.5 The Criterion of Fault Pole Selection

Normally, the positive and negative poles of the DC power transmission system operate symmetrically. When a fault occurs in the line, a protection device is needed to quickly and accurately identify the fault line as a way of ensuring that the non-fault pole line can normally transmit power without interference from it. Due to the electromagnetic coupling between the positive and negative poles of the line, the non-

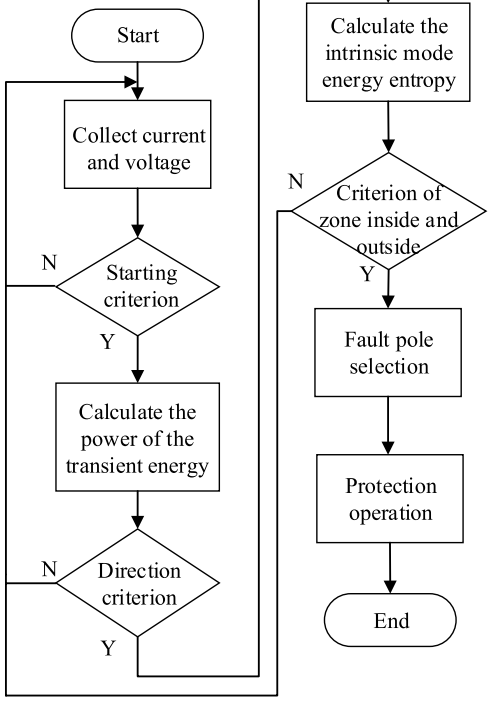

FIGURE 6 | Flow chart of the protection.

fault pole will produce an induced current when the grounding fault of the single pole occurs in the DC line. Amid the increase of the high-frequency component of the fault transient, the coupling effect between line poles is enhanced, narrowing the divide of high-frequency components between non-fault poles and fault ones. Therefore, the low-frequency component of the fault transient must be the option for the criterion of fault pole selection (Chu et al., 2017).

In this article, the fault transient power signal with a frequency below 1,000 Hz is extracted in a time window of 2 ms after the protection is operated. Also, the variation of the positive and negative transient power is viewed as the criterion of pole selection, and it is expressed in the following:

$$\boldsymbol{K} = \sum_{i=1}^{N} \left| \frac{\boldsymbol{\Delta P_1}(\boldsymbol{i})}{\boldsymbol{\Delta P_2}(\boldsymbol{i})} \right|. \tag{14}$$

In the formula mentioned previously, the letter N represents the number of sampling points, collected within the time window of 2 ms after the protection is initiated (the letter i is equal to 1, 2, and so on.). The symbols $\boldsymbol{\Delta P_1}(\boldsymbol{i})$ and $\boldsymbol{\Delta P_2}(\boldsymbol{i})$ stand for the amplitude variation of the fault transient power with positive and negative frequency below 1,000 Hz, respectively.

The analysis of fault simulation data suggests that, in order to make the protection devices against faults at any position in the zone, they can accurately select the poles; so, the setting value (K_{set1}) of the fault positive pole is equivalent to 150, while the value of the fault negative pole is equivalent to 60. Comparing the ratio (K) of the positive transient power variation to the negative one with both setting values K_{set1} and K_{set2}, the result of the criterion is as follows:

$$\begin{cases} \boldsymbol{K > K_{set1}} & \textbf{Positive pole fauls} \\ \boldsymbol{K < K_{set2}} & \textbf{Negative pole faults} \\ \boldsymbol{K_{set2} \le K \le K_{set1}} & \textbf{Faults between poles} \end{cases}. \tag{15}$$

4.6 The Protection Scheme

According to the aforementioned analysis, the transient scheme to protect the UHV multiterminal hybrid DC transmission line based on intrinsic mode energy entropy is introduced, by virtue of the criterion to initiate the protection, identify the direction of faults, to protect the criterion of fault pole selection inside and outside the zone. The scheme is shown in **Figure 6**. First, the protection device detects the transient current ($\boldsymbol{\Delta i}$) and voltage ($\boldsymbol{\Delta u}$) of the DC lines on both sides of the T-zone, which are substituted into **Eq. 9** to calculate the transient power. As the result, when ($\boldsymbol{\Delta P_{star}}$) is greater than its setting value ($\boldsymbol{\Delta P_{set}}$), the protection device works. By doing so, the power directional element is used to further identify the fault direction according to the positive and negative characteristics of the transient energy of the fault power:

1) Assuming that the transient energy detected by the power directional element at the protection device (M1) is negative and the one detected by the power directional element at the protection device M2 is positive, and there is a malfunction emerging on the left side of the T-zone. The line mode component of the fault transient current on the left side of the T-zone has undergone the decomposition through CEEMD as it seeks to calculate the intrinsic mode energy entropy of the fault transient current. The moment the minimum intrinsic mode energy entropy of the fault in the DC line L_1 is greater than the threshold value (H_{set1}), there is a fault occurring on the left side of the T-zone. That means the protection device (M1) works. On the contrary, when the maximum intrinsic mode energy entropy of the fault outside the DC line L_1 is less than the threshold value (H_{set1}), there is a fault outside the left side of the T-zone. Under this condition, the protection device (M1) does not operate.
2) Provided that the transient energy detected by the power directional element at the protection device (M1) is positive, and the one detected by the power direction element at the protection device (M2) is negative, and a fault must occur on the right side of the T-zone. The line mode component of the fault transient current on the right side of the T-zone is decomposed by CEEMD as a way of calculating its intrinsic mode energy entropy. When the minimum intrinsic mode energy entropy of potential faults in DC line L_2 is greater than the threshold value (H_{set2}), the right side of the T-zone is dysfunctional. That makes the protection device M2 to operate. On the contrary, when the maximum intrinsic mode energy entropy of the fault outside the DC line L_2 is less than the threshold value (H_{set2}), the fault occurs outside the right side of the T-zones. In this context, the protection device M2 does not operate.

TABLE 2 | Main parameters of the simulation model.

Parameter	Yunnan side	Guangxi side	Guangdong side
Rated voltage of the AC system	525 kV	525 kV	525 kV
Systematic rated power	8000 MW	3000 MW	5000 MW
Converter transformer ratio	525/172	525/216	525/243
Short-circuit impedance of the converter transformer	20%	16%	18%
Rated voltage of the converter station	±800 kV	±800 kV	±800 kV
Rated current of the converter station	5 kA	1.875 kA	3.125 kA
Converter valve type	Thyristor	IGBT	IGBT
Capacitance value of the sub-module	/	12 mF	18 mF
Rated voltage of the sub-module	/	4.5 kV	4.5 kV
Number of bridge arm sub-modules	/	200	200

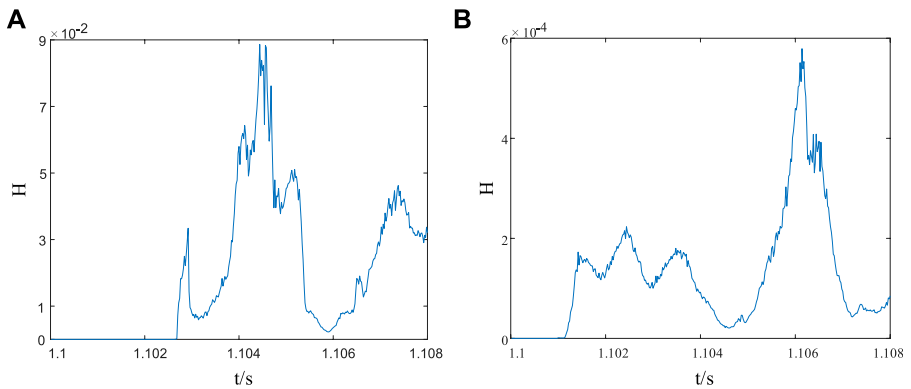

FIGURE 7 | Graph of intrinsic mode energy entropy changing with time. **(A)** Grounding fault of the point f_1 in the DC line L_1; and **(B)** grounding fault of the point f_2 outside the DC line L_2.

In the final analysis, the low-frequency component of the fault transient power is extracted to identify in which pole the malfunction appears through the ratio (K) of the positive transient power variation to the negative one.

5 THE SIMULATION MODEL AND VERIFICATION

5.1 The Simulation Model

In light of the engineering parameters of the Kun–Liu–Long line UHV three-terminal hybrid DC transmission system, the simulation model of the system as shown in **Figure 1** is established in the simulation platform PSCAD/EMTDC (Power Systems Computer-Aided Design/Electromagnetic Transients including DC). The main parameters of the simulation model are shown in **Table 2**.

In the Kunbei Converter Station, the main connection mode, featured by two unipolar 12-pulse converter units in series, is adopted. Each converter unit bears 400 kV voltage, and the unipolar series voltage is distributed according to (400 plus 400) kV. The constant current control is handled. The Liubei and Longmen converter stations are connected in series with two MMC units in a single pole. The two units are connected in series to form high- and low-valve groups, and the single-pole series voltage is distributed according to (400 plus 400) kV. Each converter chain unit inside the MMC applies the main connection mode that is mixing and cascading half-bridge and full-bridge in proportion. The upper and lower bridge arms are connected to 200 sub-modules at any time, with some left behind. The output voltage of a single converter valve is maintained at 400 kV.

In **Figure 1**, the total length of the DC line L_1 is 932 km, with an average soil resistivity of 1,750 along the line, whereas the total length of the DC line L_2 is 554 km, with an average soil resistivity of 2,500 along the line. Those where both adopt the frequency-dependent (Phase) model options f_1, f_3, f_5, and f_7 stand for the location of faults on the positive and negative DC line L_1 and the DC line L_2, the location of faults falls outside the positive and negative DC lines. The protection range of the protection device M1 includes the whole line L_1, whereas the protection device M2 responses to the whole line L_2.

5.2 The Simulation Verification

Under the amplitude frequency characteristics of the boundary transfer function gained from **Sections 2.1**, **2.2**, in this article, the sampling frequency of 50 kHz is

TABLE 3 | Result of protecting the positive pole from faults.

Fault location	Transition resistance (Ω)	K	ΔE_{M1}	ΔE_{M2}	H_L	H_R	M1 operation result	M2 operation result
0 km from M1	0.01	5,190.8	Negative	Positive	9.52e-2	/	Operation	No operation
	300	5,372.1	Negative	Positive	2.33e-2	/	Operation	No operation
	500	5,421.3	Negative	Positive	1.03e-2	/	Operation	No operation
466 km from M1	0.01	18,543	Negative	Positive	2.76e-2	/	Operation	No operation
	300	19,098	Negative	Positive	4.9e-3	/	Operation	No operation
	500	17,316	Negative	Positive	2.3e-3	/	Operation	No operation
932 km from M1	0.01	2,624.1	Negative	Positive	1.88e-2	/	Operation	No operation
	300	627.8	Negative	Positive	2.4e-3	/	Operation	No operation
	500	576.2	Negative	Positive	1.1e-3	/	Operation	No operation
f_2 outside the zone	0.01	/	Negative	Positive	5.24e-4	/	No operation	No operation
	300	/	Negative	Positive	2.62e-4	/	No operation	No operation
	500	/	Negative	Positive	1.21e-4	/	No operation	No operation
0 km from M2	0.01	7,337.3	Positive	Negative	/	5.05e-2	No operation	Operation
	300	7,308.7	Positive	Negative	/	2.37e-2	No operation	Operation
	500	7,400.5	Positive	Negative	/	1.58e-2	No operation	Operation
277 km from M2	0.01	1,539.0	Positive	Negative	/	1.75e-2	No operation	Operation
	300	12,672	Positive	Negative	/	5.5e-3	No operation	Operation
	500	19,963	Positive	Negative	/	4.9e-3	No operation	Operation
554 km from M2	0.01	15,375	Positive	Negative	/	1.03e-2	No operation	Operation
	300	14,063	Positive	Negative	/	4.5e-3	No operation	Operation
	500	5,963.3	Positive	Negative	/	3.3e-3	No operation	Operation
f_4 outside the zone	0.01	/	Positive	Negative	/	7.29e-4	No operation	No operation
	300	/	Positive	Negative	/	4.2e-4	No operation	No operation
	500	/	Positive	Negative	/	3.13e-4	No operation	No operation

TABLE 4 | Result of protecting the negative pole from faults.

Fault location	Transition resistance (Ω)	K	ΔE_{M1}	ΔE_{M2}	H_L	H_R	M1 operation result	M2 operation result
0 km from M1	0.01	2.12	Negative	Positive	2.96e-1	/	Operation	No operation
	300	1.99	Negative	Positive	1.68e-2	/	Operation	No operation
	500	1.95	Negative	Positive	9.2e-3	/	Operation	No operation
466 km from M1	0.01	10.35	Negative	Positive	5.64e-2	/	Operation	No operation
	300	10.73	Negative	Positive	7.2e-3	/	Operation	No operation
	500	10.83	Negative	Positive	4.1e-3	/	Operation	No operation
932 km from M1	0.01	19.95	Negative	Positive	3.13e-2	/	Operation	No operation
	300	26.38	Negative	Positive	2.6e-3	/	Operation	No operation
	500	26.86	Negative	Positive	1.1e-3	/	Operation	No operation
f_6 outside the zone	0.01	/	Negative	Positive	6.07e-4	/	No operation	No operation
	300	/	Negative	Positive	1.62e-4	/	No operation	No operation
	500	/	Negative	Positive	1.17e-4	/	No operation	No operation
0 km from M2	0.01	1.72	Positive	Negative	/	7.58e-2	No operation	Operation
	300	1.61	Positive	Negative	/	3.32e-2	No operation	Operation
	500	1.56	Positive	Negative	/	2.11e-2	No operation	Operation
277 km from M2	0.01	4.55	Positive	Negative	/	3.57e-2	No operation	Operation
	300	4.55	Positive	Negative	/	8.6e-3	No operation	Operation
	500	4.67	Positive	Negative	/	5.1e-3	No operation	Operation
554 km from M2	0.01	6.65	Positive	Negative	/	1.62e-2	No operation	Operation
	300	6.59	Positive	Negative	/	5.4e-3	No operation	Operation
	500	6.84	Positive	Negative	/	3.0e-3	No operation	Operation
f_8 outside the zone	0.01	/	Positive	Negative	/	6.86e-4	No operation	No operation
	300	/	Positive	Negative	/	4.3e-4	No operation	No operation
	500	/	Positive	Negative	/	2.9e-4	No operation	No operation

adopted, and the time window of 2 ms is taken after the protection is started. The fault appears at 1.1 s and lasts for 0.1 s.

The faults, inside and outside of the zone, can be distinguished by the value of intrinsic mode energy entropy in an effective way. For that to happen, the grounding fault at the point f_1, 932 km

away from the protection device on the left side of the T-zone, and another one at the point f_2, outside the DC line L_1 on the left side of the T-zone, are viewed as typical examples in this article. The intrinsic mode energy entropy that is calculated is made to slide in the sampling window of 2 ms. By doing so, the curve, showed in **Figure 7**, in which the intrinsic mode energy entropy changes with time, is accessible.

From **Figure 7**, the intrinsic mode energy entropy responses to the overall amplitude of the signal in a less sensitive manner. If faults occur inside and outside the DC line L_1, the intrinsic mode energy entropy at the position where the protection devices are installed will suddenly change. Due to the attenuation effect of the line boundary on the high-frequency component of the fault transient, the intrinsic mode energy entropy in the DC line is obviously larger than that of outside the line.

With regard to the transient protection scheme of the UHV multiterminal hybrid DC transmission line based on intrinsic mode energy entropy, the simulation verification of the protective principle is conducted, taking different positions of the fault anode and cathode (the points f_2 and f_6 outside the DC line L_1, the points f_1 and f_5 at 932, 466, and 0 km away from the protection device on the left of the T-zone, the points f_3 and f_7 at 0, 277, and 554 km away from the protection device on the right side of the T-zone, and the points f_4 and f_8 outside the DC line L_2) as well as various transition resistances (0.01 Ω, 300 Ω, and 500 Ω) into account. The setting values of the protection are shown as follows: K_{set1} is equivalent to 150, K_{set2}, 60, H_{set1}, 0.0008, and H_{set2}, 0.001.

From the simulation results in **Tables 3**, **4**, the location of faults and the transition resistance are expanding, and the energy entropy of the natural mode is decreasing. The entropy values, however, of faults inside and outside the zone are still quite different. That said, the protection is not affected and resistant to the transition resistance to some extent. In this article, the transient protection scheme of the UHV multiterminal hybrid DC transmission line based on the intrinsic mode energy entropy boasts a good performance on protection and high reliability. That means the protection devices (M1) and (M2) can operate in a reliable way as they are in face of different fault poles, positions, and transition resistances.

6 CONCLUSION

Regarding to the analysis and summary of boundary frequency characteristics of the Kun–Liu–Long UHV three-terminal hybrid DC transmission line, and on the basis of the complementary ensemble empirical mode decomposition (CEEMD), the intrinsic mode energy entropy, and the transient power polarity, a transient protection scheme, suitable for the UHV multiterminal hybrid DC transmission system, is put forward in this article. The protection scheme handles the positive and negative characteristics of transient energy of the fault power detected by power directional elements on both sides of the T-zone to identify the fault direction. As the boundary of the fault line is capable of reducing the high-frequency component of the transient current in a strong manner, the value of the intrinsic mode energy entropy is applied to further distinguish the faults inside and outside the zone. After the analysis mentioned previously, the following conclusions are attainable:

1) The transient current high-frequency component has obviously attenuated as it passes through the line boundary element, but the potential of the attenuation is supposed to be fully tapped to effectively distinguish the faults in and out of the zone.
2) The attenuation characteristics of high-frequency components of the transient current has limitation as it distinguishes the fault on the left and right sides of the T-zone of the UHV multiterminal hybrid DC transmission system; so, the power directional components can be used for identifying the direction of faults.
3) The protection scheme can quickly remove faults, without exchanging synchronous current information between converter stations.
4) A large amount of the simulation results show that the transient protection of UHV multiterminal hybrid DC transmission lines based on intrinsic mode energy entropy can operate reliably under different fault poles, fault positions, and transition resistances. That empowers it a fine value for practical application.

DATA AVAILABILITY STATEMENT

The original contributions presented in the study are included in the article/Supplementary Material; further inquiries can be directed to the corresponding author.

AUTHOR CONTRIBUTIONS

CX was responsible for providing ideas and methods and providing an experimental platform. SC was responsible for deriving formulas, reviewing, and verifying. PL was responsible for model building, simulation, data analysis, and manuscript writing. GB, JC, and ZZ wrote the sections of the manuscript. All authors participated in the reading and approved the submitted version.

FUNDING

The research is funded by the National Natural Science Foundation of China (52067009).

REFERENCES

Chen, S., Yang, H., Guihong, B., and Zhao, S. (2021). Boundary Frequency Characteristic Study of Traction Network in Continuous Co-phase at Traction Power Supply System [J]. *Electric Power Automation Equipment* 41 (06), 192. doi:10.16081/j.epae.202102026

Chu, X., Wang, L., Wang, H., and Song, G. (2017). Analysis of Inter-pole Coupling Effect and Faulty Pole Selection for HVDC Transmission Line [J]. *Electric Power Automation Equipment* 37 (04), 140. doi:10.16081/j.issn.1006-6047.2017.04.021

Guan, J., and Zhang, J. (2011). Weak Target Detection Based on Intrinsic Mode Energy Entropy. *J. Electro. Inf. Techn.* 33 (10), 2494–2499. doi:10.3724/sp.j.1146.2011.00147

He, J., Chen, K., Li, M., Luo, Y., Liang, X., and Xu, Y. (2020). Review of protection and Fault Handling for a Flexible DC Grid[J]. *Prot. Control. Mod. Power Syst.* 5 (1), 5–15. doi:10.1186/s41601-020-00157-9

He, J., Li, B., Li, Y., Qiu, H., Wang, C., and Dai, D. (2017). A Fast Directional Pilot Protection Scheme for the MMC-Based MTDC Grid [J]. *Proc. CSEE* 37 (23), 6878. doi:10.13334/j.0258-8013.pcsee.161573

Li, H., Zhang, K., Wang, G., Huang, D., Li, M., and Guo, Z. (2019). Fault Area Discrimination Method for Parallel Multi-Terminal Hybrid HVDC Line [J]. *Automation Electric Power Syst.* 43 (04), 119. doi:10.7500/AEPS20180615004

Li, Z., Jiang, W., Abu-Siada, A., Li, Z., Xu, Y., and Liu, S. (2021). Research on a Composite Voltage and Current Measurement Device for HVDC Networks. *IEEE Trans. Ind. Electron.* 68 (9), 8930–8941. doi:10.1109/tie.2020.3013772

Liu, Y., Yang, N., Dong, B., Wu, L., Yan, J., Shen, X., et al. (2020). "Multi-Lateral Participants Decision-Making: A Distribution System Planning Approach with Incomplete Information Game," in *IEEE Access*, 8, 88933–88950. doi:10.1109/access.2020.2991181

Muniappan, M. (2021). *A Comprehensive Review of DC Fault protection Methods in HVDC Transmission systems[J]*. Singapore: Springer Singapore PTE LTD.

Ning, L., Tai, N., Zheng, X., and Huang, W. (2017). Research on MMC-HVDC Transmission Line Protection Scheme Based on One Terminal Transient Current [J]. *Proc. CSEE* 37 (17), 5010

Shen, X., Ouyang, T., Khajorntraidet, C., Li, Y., Li, S., and Zhuang, J. (2021b). Mixture Density Networks-Based Knock Simulator. *Ieee/asme Trans. Mechatron.* 1, 1. doi:10.1109/TMECH.2021.3059775

Shen, X., Ouyang, T., Yang, N., and Zhuang, J. (2021a). Sample-based Neural Approximation Approach for Probabilistic Constrained Programs. *IEEE Trans. Neural Netw. Learn. Syst.*, 1–8. doi:10.1109/TNNLS.2021.3102323

Shen, X., and Raksincharoensak, P. (2021a). "Pedestrian-aware Statistical Risk Assessment," in IEEE Transactions on Intelligent Transportation Systems 99, 1–9. doi:10.1109/TITS.2021.3074522

Shen, X., and Raksincharoensak, P. (2021b). Statistical Models of Near-Accident Event and Pedestrian Behavior at Non-signalized Intersections. *J. Appl. Stat.*, 1–21. doi:10.1080/02664763.2021.1962263

Shen, X., Zhang, X., Ouyang, T., Li, Y., and Raksincharoensak, P. (2020b). Cooperative Comfortable-Driving at Signalized Intersections for Connected and Automated Vehicles. *IEEE Robot. Autom. Lett.* 5, 6247–6254. doi:10.1109/LRA.2020.3014010

Shen, X., Zhang, Y., Sata, K., and Shen, T. (2020a). Gaussian Mixture Model Clustering-Based Knock Threshold Learning in Automotive Engines. *Ieee/asme Trans. Mechatron.* 25 (6), 2981–2991. doi:10.1109/TMECH.2020.3000732

Shen, X., Zhang, Y., Shen, T., and Khajorntraidet, C. (2017). Spark advance Self-Optimization with Knock Probability Threshold for Lean-Burn Operation Mode of SI Engine. *Energy* 122, 1–10. doi:10.1016/j.energy.2017.01.065

Tang, G., and He, Z., and (2013). Research, Application and Development of VSC-HVDC Engineering Technology [J]. *Automation Electric Power Syst.* 37 (15), 3

Wang, J., Fu, C., Hu, M., Zhang, D., and Han, H. (2014). Discussion on the Protection in Parallel-type Multi-Terminal HVDC Systems [J]. *Proc. CSEE* 34 (28), 4923. doi:10.13334/j.0258-8013.pcsee.2014.28.020

Xia, J., Qin, R., Qian, H., Gao, S., Jiao, Z., and He, S. (2018). Study on Improved Algorithm in Differential protection of Multi-Terminal Line [J]. *Electric Power Automation Equipment* 38 (12), 140–147. doi:10.16081/j.issn.1006-6047.2018.12.021

Xu, Z., Hu, Y., and Fu, C. (2013). Control Strategy and Fault Characteristics of Parallel MTDC Transmission Systems [J]. *High Voltage Eng.* 39 (11), 2721. doi:10.3969/j.issn.1003-6520.2013.11.021

Yang, N., Huang, Y., and Hou, D. (2019b). Adaptive Nonparametric Kernel Density Estimation Approach for Joint Probability Density Function Modeling of Multiple Wind Farms[J]. *Energies* 12. doi:10.3390/en12071356

Yang, N., Ye, D., Zhou, Z., Cui, J., Chen, D., and Wang, X. (2018). Research on Modelling and Solution of Stochastic SCUC under AC Power Flow Constraints[J. *IET Generation, Transm. Distribution* 12 (15), 3618. doi:10.1049/iet-gtd.2017.1845

Yang, N., Huang, Y., Hou, D., Liu, S., Ye, D., Dong, B., et al. (2019a). Adaptive Nonparametric Kernel Density Estimation Approach for Joint Probability Density Function Modeling of Multiple Wind Farms. *Energies* 12, 1356. doi:10.3390/en12071356

Yang, N., Liu, S., Deng, Y., and Xing, C. (2021c). An Improved Robust SCUC Approach Considering Multiple Uncertainty and Correlation. *IEEJ Trans. Elec Electron. Eng.* 16, 21–34. doi:10.1002/tee.23265

Yang, N., Yang, C., Wu, L., Shen, X., Jia, J., Li, Z., et al. (2021a). "Intelligent Data-Driven Decision-Making Method for Dynamic Multi-Sequence: An E-Seq2Seq Based SCUC Expert System," in *IEEE Trans. Ind. Inf.*, doi:10.1109/TII.2021.3107406

Yang, N., Yang, C., Xing, C., Ye, D., Jia, J., Chen, D., et al. (2021b). Deep Learning-based SCUC Decision-making: An Intelligent Data-driven Approach with Self-learning Capabilities. *IET Gener. Transm. Distrib.* 1, 12. doi:10.1049/gtd2.12315

Yang, X., and Liu, W. (2018). A New Line Selection Method Based on Intrinsic Mode Energy of Phase Current Change [J]. *J. Electric Power Sci. Techn.* 33 (04), 147

Ye, L., and Liu, P. (2011). Combined Model Based on EMD-SVM for Short-Term Wind Power Prediction [J]. *Proc. CSEE* 31 (31), 102. doi:10.1016/S1872-5805(11)60064-4

Yeh, J. R., Shieh, J. S., and Huang, N. E. (2010). Complementary Ensemble Empirical Mode Decomposition: a Novel Noise Enhanced Data Analysis Method [J]. *Adv. Adaptive Data Anal.* 2 (2), 26. doi:10.1142/s1793536910000422

Yu, X., Wang, Y., Zhang, Q., Wang, Y., Dong, Y., and Gan, Z. (2020). Power Transfer Strategy of Parallel Three-Terminal Hybrid UHVDC Transmission System [J]. *Automation Electric Power Syst.* 44 (23), 150. doi:10.7500/AEPS20200601004

Zhang, Y., Ma, H., Li, T., Liu, Z., and Feng, K. (2016). HVDC Line Protection Based on the Mutant Power through Kaiser Window [J]. *High Voltage Eng.* 42 (01), 19. doi:10.13336/j.1003-6520.hve.2016.01.003

Zhang, L., Xie, Y., Ye, J., Xue, T., Cheng, J., and Li, Z. (2021). Intelligent Frequency Control Strategy Based on Reinforcement Learning of Multi-Objective Collaborative Reward Function [J]. *Front. Energy Res.* 9, 760525. doi:10.3389/fenrg.2021.760525

Zhang, Y., Chen, K., Luo, Y., Liang, C., Ning, J., and Nie, M. (2021). Hybrid Multi-Terminal HVDC Transmission Line Protection Based on Transient Current Correlation Coefficient [J]. *Electric Power Construction* 42 (05), 113–121. doi:10.12204/j.issn.1000-7229.2021.05.012

Zhao, W. (2004). *HVDC Transmission Engineering Technology [M]*. Beijing: China Electric Power Press.

Zheng, J., Wen, M., Qin, Y., Chen, Y., and Yu, B. (2018). A Novel Differential Protection Scheme with Fault Line Selection Capability for HVDC Transmission Line [J]. *Proc. CSEE* 38 (15), 4350. doi:10.13334/j.0258-8013.pcsee.171960

Zhou, J., Zhao, C., Li, C., Xu, J., and An, T. (2017). Boundary Protection Scheme for Multi-Terminal Flexible DC Grid Based on Voltage of DC Reactor [J]. *Automation Electric Power Syst.* 41 (19), 89. doi:10.7500/AEPS20170331005

Zhu, B., Ding, F., and Vilathgamuwa, D. M. (2020). Coat Circuits for DC-DC Converters to Improve Voltage Conversion Ratio. *IEEE Trans. Power Electron.* 35 (4), 3679–3687. doi:10.1109/TPEL.2019.2934726

Conflict of Interest: Author CX is employed by Electric Power Research Institute, Southern Power Grid Yunnan Electric Power Co., Ltd. Author SC works at Kunming University of Science and Technology.

All the authors declare that the research was conducted in the absence of any commercial or financial relationships that could be construed as a potential conflict of interest.

frontiers in Energy Research

ORIGINAL RESEARCH
published: 17 March 2022
doi: 10.3389/fenrg.2022.864211

Mechanism of Power Quality Deterioration Caused by Multiple Load Converters for the MVDC System

Heming Huang, Fei Liu and Xiaoming Zha*

School of Electrical Engineering and Automation, Wuhan University, Wuhan, China

Medium-voltage direct current (MVDC) systems are widely used to ship power-distributed systems, wind farms, and photovoltaic power plants. With the increase of load converters interfacing into the MVDC system, the power quality deteriorates. Few research studies focused on the factors affecting the MVDC power quality, and effects caused by multiple load converters are often neglected. In this study, the mechanism of power quality deterioration caused by interfacing multiple load converters on the MVDC system has been discussed. The impedance model of the MVDC system is developed with the state-space averaging method and the small-signal analysis method. A three-level H-bridge DC/DC converter is employed as the load converter. The results by the analysis of the impedance model show that the more the load converters connect to the MVDC system, the more fragile the MVDC system is to background harmonics. Simulation cases are implemented to verify this conclusion.

Keywords: MVDC, impedance modeling, multiple load converters, power quality, mechanism analysis

OPEN ACCESS

Edited by:
Yusen He,
Grinnell College, United States

Reviewed by:
Lu Wang,
National University of Singapore, Singapore
Shuang Zhao,
Hefei University of Technology, China

****Correspondence:***
Fei Liu
lf_dyj@whu.edu.cn

Specialty section:
This article was submitted to Wind Energy, a section of the journal Frontiers in Energy Research

Received: *28 January 2022*
Accepted: *08 February 2022*
Published: *17 March 2022*

Citation:
Huang H, Liu F and Zha X (2022) Mechanism of Power Quality Deterioration Caused by Multiple Load Converters for the MVDC System. Front. Energy Res. 10:864211. doi: 10.3389/fenrg.2022.864211

1 INTRODUCTION

In recent years, medium-voltage direct current (MVDC) systems have been gradually applied to ship power-distributed systems (Su et al., 2016; Mo and Li, 2017). The rated voltage levels of the MVDC system include 1.5, 3, 6, 12, 18, 24, and 30 kV. The power quality of the MVDC system starts to receive attention. The research on this field mainly focused on the measurement and evaluation of the power quality (Crapse et al., 2007; Ouyang and Li, 1646; Shin et al., 2004) and the way to improve it (Xie and Zhang, 2010; Puthalath and Bhuvaneswari, 2018; Arcidiacono et al., 2007). Few references discuss the factors that degrade the power quality. The reference by Steurer et al., (2007) explored the impact of the pulsed power charging loads on power quality. This study used high-precision modeling and simulation to analyze the problem without a deeper theoretical analysis. The reference by Sulligoi et al., (2017) mentioned that the multi-load converter connected to the MVDC system may lead to unstable bus voltage and deteriorate the power quality, yet the impact mechanism was not explained in detail. On this basis, this study discusses the mechanism of the multi-load converter's influence on power quality. In addition to the influence of the number of load converters on the power quality, the characteristics of the load converter itself are also considered.

At present, there are mainly three types of converters used in MVDC systems: the modular multilevel converter (MMC), three-level DC converter, and dual active bridge (DAB) converter. The power switches in the MMC structure withstand less voltage stress and generate less electromagnetic interference (Mo et al., 2015; Kenzelmann et al, 2011; Ferreira, 2013), which is conducive to better power quality. The application of wide bandgap devices such as SiC

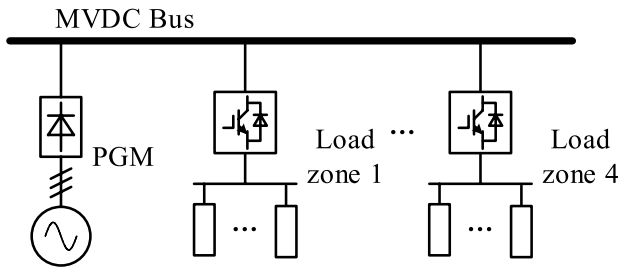

FIGURE 1 | MVDC distribution system network.

MOSFETs can reduce the stages of the MMC, thereby reducing the complexity of the MVDC system (Zhao et al., 2020; Zhao et al., 2021). The DAB has a good soft-switching performance and can achieve higher efficiency (Yanhui Xie et al., 2010; Zhao et al., 2017). The circuit topology of the three-level DC converter is relatively simple, easy to control, and more stable (Xiao et al., 2014; Xinbo Ruan et al., 2008). These three types of converters have their own characteristics. As for load converters, they can all be regarded as constant power loads with negative resistance, which introduce the system instability concern.

In prior to analyzing the influence of the network formed by the connection of multiple load converters on power quality, a suitable system model should be established. Many [references] have proposed modeling methods for MVDC systems. The reference by Khan et al., (2017) divided the MVDC system into three parts, including the power system, load system, and energy storage system, and established a detailed transient simulation model. The reference by Ji et al., (2018) described the system with an adjacency matrix and proposed a hierarchical control based on the system matrix. The reference by Tan et al., (2017) proposed a convex model for MVDC systems to study the transmission losses. The modeling methods mentioned in the studies by Khan et al., (2017); Tan et al., (2017); and Ji et al., (2018) were all for specific research purposes and could not be used to analyze the system state in general. References by Shi et al., (2015); Bosich et al., (2017); and Sulligoi et al., (2017) used the state-space averaging model and the small-signal analysis method to analyze the dynamic process of the system and then proposed a corresponding control strategy to maintain the stability of the bus voltage. Among them, the load converter model was taken as a constant power load model with a controlled current source connected in parallel with a capacitor. The parallel connection of multiple constant power load models is equivalent to a constant power load model, while this model is not appropriate for investigating the interactions of different load converters. The reference by Liu et al., (2017) utilized impedance modeling to analyze the stability and harmonics of the MVDC system including the power generation system and the motor drive system, while the influence of multiple load converters is also ignored. Although the models in references by Shi et al., (2015); Bosich et al., (2017); Liu et al., (2017); Sulligoi et al., (2017) cannot be used to describe the effects of multi-load converters, the modeling method can be used to analyze the system state.

In view of the above problems, this study explores the mechanism of the multi-load converter affecting the power quality based on the impedance network analysis method. An MVDC system with four load regions is taken as an example. A three-level H-bridge DC converter is used as the load converter. The state-space averaging method and the small-signal analysis method are used to establish the impedance model of the load converter; then, the impedance network of the system is established. Through comparing the system impedance spectrum under different numbers of load converters, the influence of the number of load converters on power quality is revealed.

The contribution of this study is as follows.

(1) This study reveals for the first time that an increase in the number of load converters will increase the probability of background harmonics being amplified in the MVDC system and make the system more susceptible to low-frequency background harmonics.
(2) The impedance model of the MVDC system is established by using the state-space averaging method and the small-signal analysis method to analyze the spectrum change of the system resonance point, and the mechanism of the power quality deterioration of the MVDC system caused by the multi-load converter is revealed.

The rest of this study is organized as follows. A modeling method of MVDC systems is proposed in **Section 2**. In **Section 3**, the input impedance model of the three-level H-bridge DC converter is introduced. On the basis, the influence of load converters on power quality is analyzed in **Section 4**, and the mechanism of the influence is verified in **Section 5**. **Section 6** concludes the full text.

2 MODELING OF AN MVDC SYSTEM

Figure 1 shows the network architecture of the MVDC system. Its configuration includes the following parts: 1) one power generation module (PGM); 2) one MVDC system bus; and 3) one to four load areas. The PGM is connected to the bus through a three-phase rectifier bridge, and the load area is connected to the bus through a three-level H-bridge DC converter. It is assumed that there are background harmonics on the output side of the three-phase rectifier

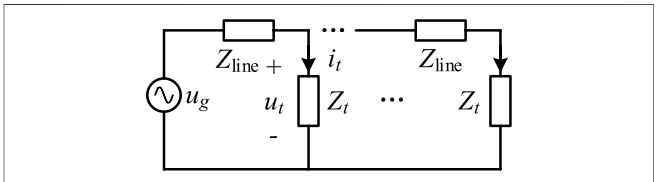

FIGURE 2 | Small-signal model of the MVDC system.

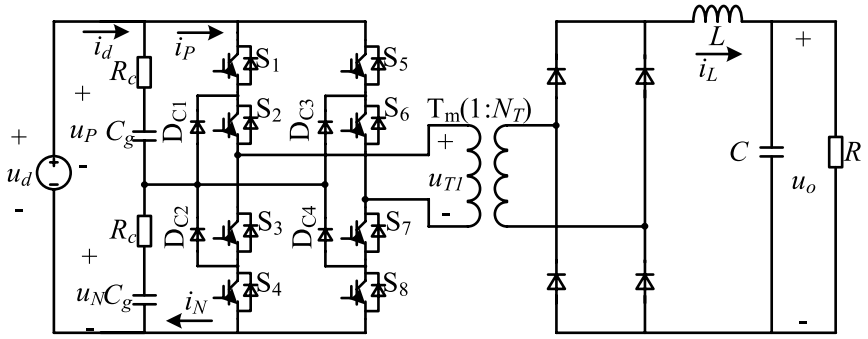

FIGURE 3 | Topology of the three-level H-bridge DC/DC converter.

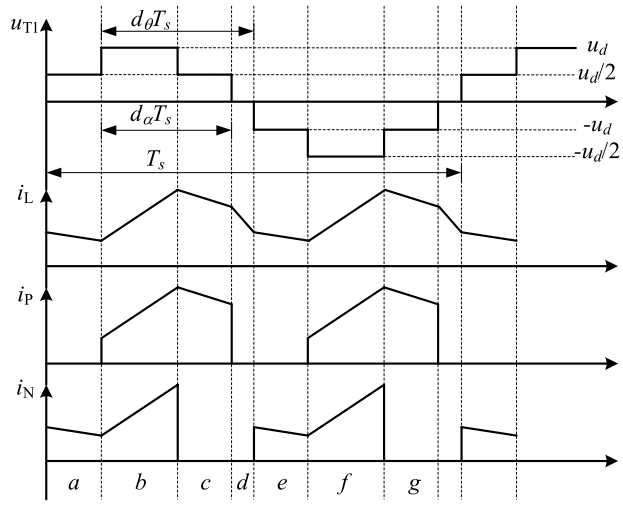

FIGURE 4 | Working waveforms of three-level H-bridge with phase-shift control.

bridge, which affects the power quality of the DC bus. To simplify the analysis, the output impedance of the PGM is ignored, and the load on the output side of the three-level H-bridge is replaced by a pure resistance. Finally, the small-signal model of the MVDC system shown in **Figure 2** is obtained. The inductance and the resistance are represented by a series of Z_{line} in **Figure 2**. The input impedance of the load converter can be derived from **equations 3** and **(4)**.

3 INPUT IMPEDANCE MODEL OF THE THREE-LEVEL H-BRIDGE DC CONVERTER

The topology of the three-level H-bridge DC converter is shown in **Figure 3**. C_g is the voltage equalizing capacitor on the output side. R_C is the equivalent resistance of the voltage equalizing capacitor. S_1~S_8 are the switching tubes on the inverter side. D_{c1}~D_{c4} are the clamping diodes. The transformation ratio of the intermediate frequency transformer T_m is $1{:}N_T$. L and C are the output filter parameters, and R is the load. u_d is the input voltage, and i_d is the input current. i_L is the current on L. u_o is the output voltage. u_P is the voltage of the upper-end equalizing capacitor. u_N is the voltage of the lower-end equalizing capacitor. u_{T1} is the primary side voltage of the transformer, and its direction is specified as the direction shown in **Figure 3**.

In this model, it is assumed that the frequency of the equalizing control loop is high; the influence of the control loop can be ignored. As a result, the switch devices in the figure are all ideal devices, and the transformer is an ideal transformer. Through the analysis, the working waveforms of the converter can be obtained, as shown in **Figure 4**, and the simplified model of **Figure 3** can be obtained, as shown in **Figure 5** (Zhao et al., 2017).

According to **Figures 4**, **5**, the state equations for the eight operating states (a~h) of the three-level H-bridge converter can be listed in **Table 1**.

Based on the previous assumptions, it can be obtained that

$$u_P = u_N = \frac{u_d}{2} - R_C C_g \frac{du_P}{dt}. \tag{1}$$

Assuming that the converter is controlled by a single voltage loop, the relationship between the conduction angle d_α and the output voltage u_o can be expressed as

$$d_\alpha = k_p\left(u_o^* - u_o\right) + k_i \int \left(u_o^* - u_o\right)dt, \tag{2}$$

where k_p and k_i are the parameters of the PI controller, and u_o^* is the reference of the output voltage. With the state-space averaging method and the small-signal analysis method, the transfer function from the input voltage to the input current can be obtained.

$$G_t(s) = \frac{C_g s}{2\left(R_C C_g s + 1\right)} + \frac{4CD_\alpha^2 N_T R s^2 + \left(4N_T D_\alpha^2 - 4I_L N_T R k_p D_\alpha\right)s - 4D_\alpha I_L N_T R k_i}{RLCs^3 + Ls^2 + \left(R + 2N_T U_d k_p R\right)s + 2N_T R U_d k_i}. \tag{3}$$

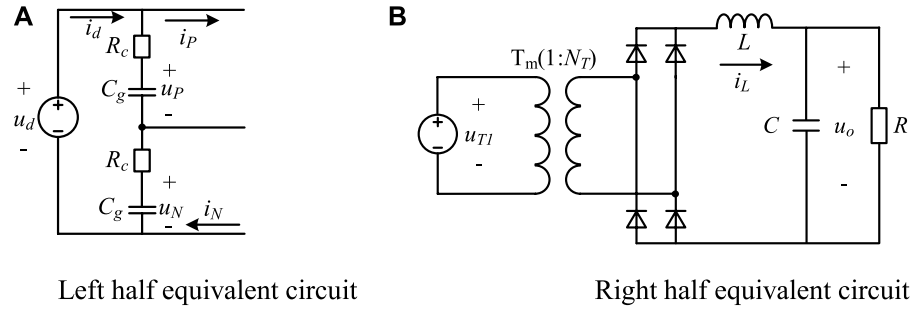

FIGURE 5 | Simplified circuit of the three-level H-bridge DC/DC converter. **(A)** Left half equivalent circuit **(B)** Right half equivalent circuit.

TABLE 1 | The equation of state for the converter.

Mode	Time	Equation of state
A	$(1/2\text{-}d_\theta)T_s$	$C_g\frac{du_P}{dt}=i_d\ C_g\frac{du_N}{dt}=i_d-N_Ti_L$
		$L\frac{di_L}{dt}=N_T\frac{u_d}{2}-u_o\ C\frac{du_o}{dt}=i_L-\frac{u_o}{R}$
B	$d_\alpha T_s$	$C_g\frac{du_P}{dt}=i_d-N_Ti_L\ C_g\frac{du_N}{dt}=i_d-N_Ti_L$
		$L\frac{di_L}{dt}=2N_T\frac{u_d}{2}-u_o\ C\frac{du_o}{dt}=i_L-\frac{u_o}{R}$
C	$(1/2\text{-}d_\theta)T_s$	$C_g\frac{du_P}{dt}=i_d-N_Ti_L\ C_g\frac{du_N}{dt}=i_d$
		$L\frac{di_L}{dt}=N_T\frac{u_d}{2}-u_o\ C\frac{du_o}{dt}=i_L-\frac{u_o}{R}$
d	$(d_\alpha\text{-}d_\theta)T_s$	$C_g\frac{du_P}{dt}=i_d\quad C_g\frac{du_N}{dt}=i_d$
		$L\frac{di_L}{dt}=-u_o\quad C\frac{du_o}{dt}=i_L-\frac{u_o}{R}$
e	$(1/2\text{-}d_\theta)T_s$	same as Mode a
f	$d_\alpha T_s$	same as Mode b
g	$(1/2\text{-}d_\theta)T_s$	same as Mode c
h	$(d_\alpha\text{-}d_\theta)T_s$	same as Mode d

Therefore, the input impedance of a three-level H-bridge converter can be expressed as

$$Z_t(s)=\frac{1}{G_t(s)}. \tag{4}$$

4 INFLUENCE OF THE LOAD CONVERTER ON POWER QUALITY

In order to analyze the influence of multi-load converters on power quality, the input voltage u_t and input current i_t of the load area closest to the PGM (hereinafter referred to as load area 1) are taken as an example for analysis. It is denoted that the equivalent input impedance of n load regions is Z_n. Thus, it can be deduced from **Figure 2** that the expression of Z_n is

$$Z_n(s)=\begin{cases} Z_t(s) & \text{n}=1 \\ \dfrac{1}{1/Z_t(s)+1/\left(Z_{n-1}(s)+Z_{\text{line}}(s)\right)} & \text{n}\geq 2 \end{cases}. \tag{5}$$

u_t and i_t can be expressed as

$$u_t(s)=\frac{Z_n(s)}{Z_n(s)+Z_{\text{line}}(s)}u_g, \tag{6}$$

$$i_t(s)=\frac{Z_n(s)}{Z_t(s)\left(Z_n(s)+Z_{\text{line}}(s)\right)}u_g(s), \tag{7}$$

where u_g is the background harmonic, and n ranges from 1 to 4.

Equations 6 and **7** reflect that the input voltage and current in load region 1 are affected by its self-impedance, impedance of other load regions, and the background harmonics. The transfer function from u_g to u_t is denoted by T_U(s), and the transfer function from u_g to i_t is denoted by T_I(s). Then, their expressions are shown in the following formulas.

$$T_U(s)=\frac{u_t(s)}{u_g(s)}=\frac{Z_n(s)}{Z_n(s)+Z_{\text{line}}(s)}, \tag{8}$$

$$T_I(s)=\frac{i_t(s)}{u_g(s)}=\frac{Z_n(s)}{Z_t(s)\left(Z_n(s)+Z_{\text{line}}(s)\right)}. \tag{9}$$

The spectral changes of T_U(s) and T_I(s) reflect the influence degree of multi-load converters on power quality. With different n, two transfer functions are calculated, and their Bode plots are shown in **Figure 6**. The parameters of the converter are listed in **Table 2**.

It can be seen from **Figure 6** that with the increase of the load converter number, the resonance point in the Bode diagram increases, and the original resonance peak frequency becomes lower. The resonance peak in the figure indicates that the background harmonics are amplified at this resonance point. The increase of resonance points means that the system is more susceptible to the influence of background harmonics. Lower resonant peak frequencies mean that the system is more susceptible to low-frequency disturbances, which are often difficult or expensive to filter out.

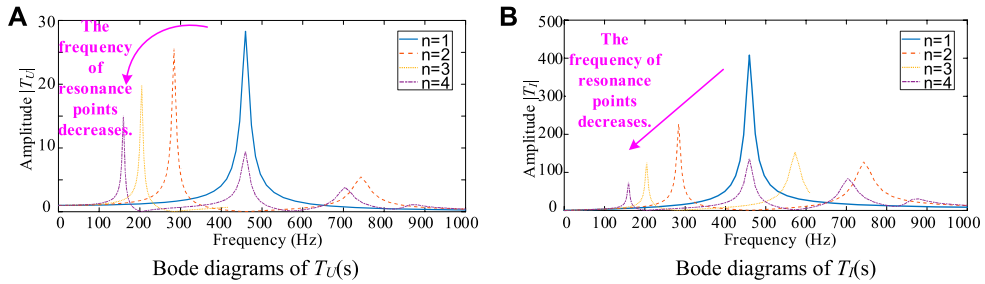

FIGURE 6 | Bode diagrams of T_U(s) and T_I(s) under different numbers of load zones **(A)** Bode diagrams of *TU*(s) **(B)** Bode diagrams of *TI*(s).

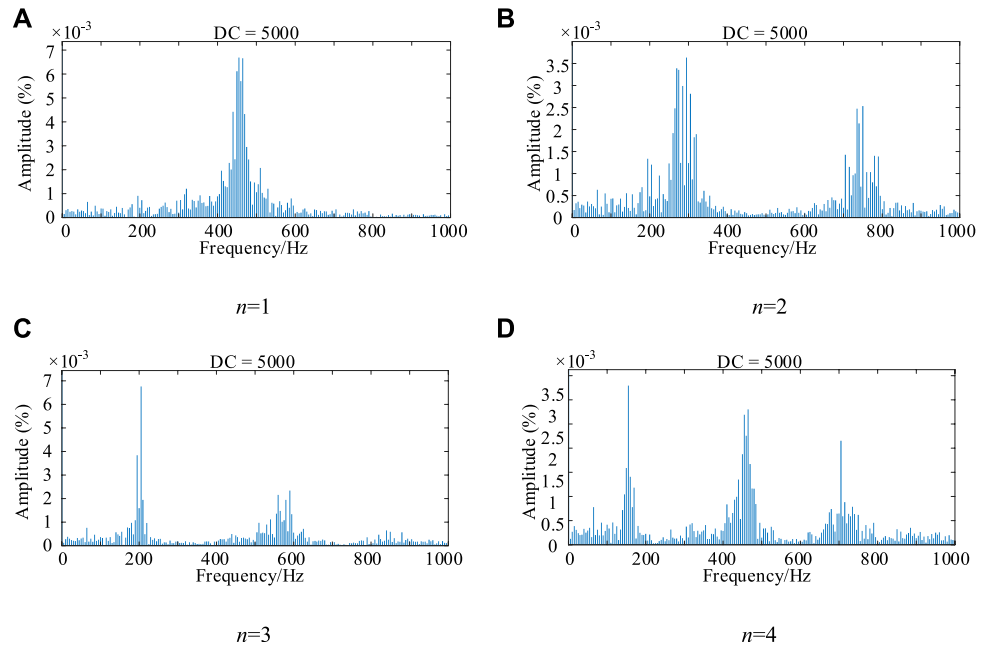

FIGURE 7 | FFT result of the input voltage for load zone 1 **(A)** *n*=1 **(B)** *n*=2 **(C)** *n*=3 **(D)** *n*=4.

5 CASE STUDY

In order to verify the above analysis results, a simulation model of the MVDC system based on the MATLAB/Simulink platform is established with an architecture shown in **Figure 1**. The PGM is replaced by an ideal voltage source, and a broad-spectrum white noise is superimposed on the ideal voltage source as background harmonics. The number of load zones varies from 1 to 4. The voltage and current on the input side of load area 1 are measured, and the measured data are subjected to fast Fourier transform (FFT) analysis (Li, 2021a; Li, 2021b; Li, 2022). The analysis results are shown in **Figures 7**,**8**.

TABLE 2 | Parameters of the converter.

Parameters	Value	unit
Equalizing capacitor C_g	10	mF
Transformer ratio 1:N_T	1:4	—
Filter capacitor *C*	10	MF
Filter inductor *L*	250	H
Load resistance *R*	0.5	—
Integration parameters k_i	0.01	—
Scale parameter k_p	0.001	
Input voltage U_d	5,000	V
Output voltage U_o	1,000	V

It can be seen from **Figures 7**,**8** that the high content of the ripple frequency in the simulation results is basically consistent with the resonance point frequency in the Bode plot obtained from T_U(s) and T_I(s). When one load zone is connected to the system, the ripple content at the frequency of 470 Hz is the highest. When two load areas are connected to the system, there are two frequencies with higher ripple content, and their frequencies are 270 and 750 Hz, respectively. As the number of load zones increases, the

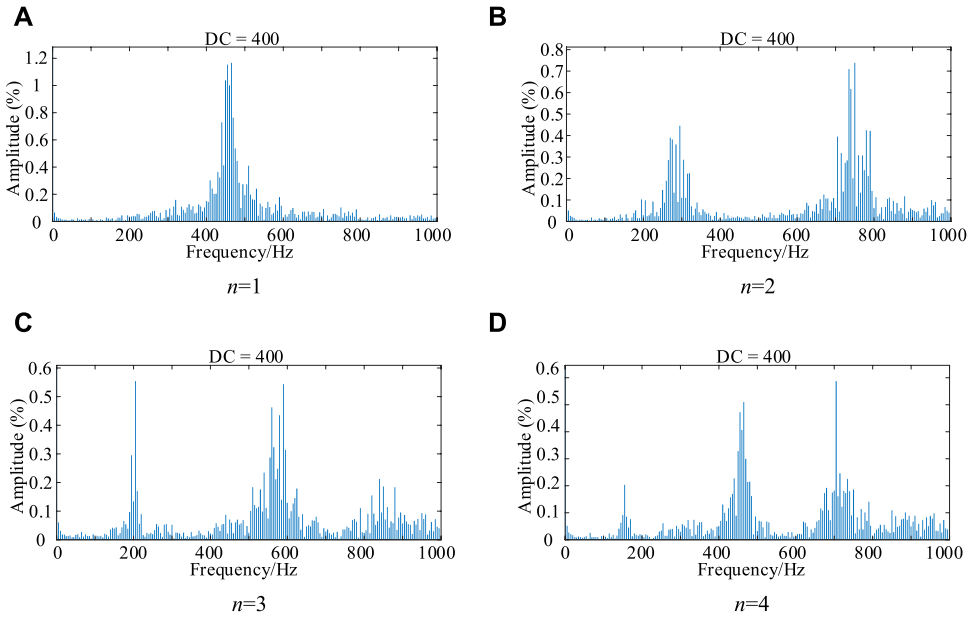

FIGURE 8 | FFT result of the input current for load zone 1 **(A)** *n*=1 **(B)** *n*=2 **(C)** *n*=3 **(D)** *n*=4.

types of ripples with higher content gradually increase, while the frequency of high-content ripples becomes lower.

6 CONCLUSION

This study analyzes the mechanism of power quality deterioration caused by the multi-load converter connected to the MVDC system. In this study, the load converter is modeled and analyzed by the state-space average method and the small-signal analysis method, and then, the impedance network model of the MVDC system is established. When the number of load converters changes, voltage and current on the input side of load area 1 are affected by the background harmonics. Finally, the influence of the number of load converters on power quality is analyzed. Two main conclusions are drawn:

(1) As the number of load converters increases, background harmonics are amplified in the MVDC system.
(2) The increase of load converters makes the MVDC system more susceptible to low-frequency background harmonics.

DATA AVAILABILITY STATEMENT

The raw data supporting the conclusions of this article will be made available by the authors, without undue reservation.

AUTHOR CONTRIBUTIONS

All authors listed have made a substantial, direct, and intellectual contribution to the work and approved it for publication.

REFERENCES

Arcidiacono, V., Menis, R., and Sulligoi, G. (2007). *Improving Power Quality in All Electric Ships Using a Voltage and VAR Integrated Regulator," Electric Ship Technologies Symposium*. Arlington, VA, USA: ESTS '07IEEE, 322

Bosich, D., Sulligoi, G., Mocanu, E., and Gibescu, M. (2017). Medium Voltage DC Power Systems on Ships: An Offline Parameter Estimation for Tuning the Controllers' Linearizing Function. *IEEE Trans. Energ. Convers.* 32 (2), 748–758. doi:10.1109/tec.2017.2676618

Crapse, P., Wang, J., Abrams, J., Shin, Y. J., and Dougal, R. (2007). *Power Quality Assessment and Management in an Electric Ship Power System," Electric Ship Technologies SymposiumESTS '07*. Arlington, VA, USA: IEEE, 328

Ferreira, J. A. (2013). The Multilevel Modular DC Converter. *IEEE Trans. Power Electron.* 28 (10), 4460–4465. doi:10.1109/tpel.2012.2237413

Ji, Y., Yuan, Z., Zhao, J., Lu, C., Wang, Y., Zhao, Y., et al. (2018). Hierarchical Control Strategy for MVDC Distribution Network under Large Disturbance. *IET Generation, Transm. Distribution* 12 (11), 2557–2565. doi:10.1049/iet-gtd.2017.1642

Kenzelmann, S., Rufer, A., Vasiladiotis, M., Dujic, D., Canales, F., and Novaes, Y. R. D. (2011). *A Versatile DC-DC Converter for Energy Collection and Distribution Using the Modular Multilevel Converter," - European Conference on Power Electronics and Applications*. Birmingham, UK: IEEE. 1

Khan, M. M. S., Faruque, M. O., and Newaz, A. (2017). *Fuzzy Logic Based Energy Storage Management System for MVDC Power System of All Electric Ship*, 99. IEEE Transactions on Energy Conversion, 1

Li, H. (2022). Detection and Segmentation of Loess Landslides via Satellite Images: a Two-phase Framework. *Landslides*, 1–14. doi:10.1007/s10346-021-01789-0

Li, H. (2021). Monitoring and Identifying Wind Turbine Generator Bearing Faults Using Deep Belief Network and EWMA Control Charts. *Front. Energ. Res.*, 770. doi:10.3389/fenrg.2021.799039

Li, H. (2021). Short-Term Nacelle Orientation Forecasting Using Bilinear Transformation and ICEEMDAN Framework. *Front. Energ. Res.*, 697. doi:10.3389/fenrg.2021.780928

Liu, H., Guo, H., Liang, J., and Qi, L. (2017). Impedance Based Stability Analysis and Harmonics Mitigation of MVDC Systems Using Generator-Thyristor Units and DTC Motor Drives. *IEEE J. Emerging Selected Top. Power Electro.* 99, 1

Mo, R., and Li, H. (2017). Hybrid Energy Storage System with Active Filter Function for Shipboard MVDC System Applications Based on Isolated Modular Multilevel DC/DC Converter (IM2DC). *IEEE J. Emerging Selected Top. Power Electro.* 99, 1

Mo, R., Li, R., and Li, H. (2015). *Isolated Modular Multilevel (IMM) DC/DC Converter with Energy Storage and Active Filter Function for Shipboard MVDC System Applications*. Electric Ship Technologies Symposium, 113

Ouyang, H., and Li, H. *The Ship Power Quality Monitoring System Based on Virtual Instrument and Configuration Software*. Chinese Automation Congress, 1646

Puthalath, S., and Bhuvaneswari, G. *Power Quality Enhancement and Renewable Energy Integration in Ship's Distribution Grid," 2018 IEEMA Engineer Infinite Conference (eTechNxT)*. 1

Shi, J., Amgai, R., and Abdelwahed, S. (2015). Modelling of Shipboard Medium-voltage Direct Current System for System Level Dynamic Analysis. *IET Electr. Syst. Transportation* 5 (4), 156–165. doi:10.1049/iet-est.2014.0033

Shin, Y. J., Monti, A., Ponci, F., Arapostathis, A., Grady, W. M., Powers, E. J., et al. (2004). Virtual Power Quality Analysis for Ship Power System Design, in" *Proceedings of the IEEE Instrumentation and Measurement Technology Conference Imtc 04*, 1758–1763.

Steurer, M., Andrus, M., Langston, J., Qi, L., Suryanarayanan, S., Woodruff, S., et al. (2007). *Investigating the Impact of Pulsed Power Charging Demands on Shipboard Power Quality," Electric Ship Technologies Symposium*. Arlington, VA, USA: ESTS '07IEEE, 315

Su, C.-L., Lin, K.-L., and Chen, C.-J. (2016). Power Flow and Generator-Converter Schemes Studies in Ship MVDC Distribution Systems. *IEEE Trans. Ind. Applicat.* 52 (1), 50–59. doi:10.1109/tia.2015.2463795

Sulligoi, G., Bosich, D., Giadrossi, G., Zhu, L., Cupelli, M., and Monti, A. (2017). Multiconverter Medium Voltage DC Power Systems on Ships: Constant-Power Loads Instability Solution Using Linearization via State Feedback Control. *IEEE Trans. Smart Grid* 5 (5), 2543

Tan, Y., Li, Y., Cao, Y., and Shahidehpour, M. (2017). Integrated Optimization of Network Topology and DG Output for MVDC Distribution Systems. *IEEE Trans. Power Syst.* 99, 1

Xiao, F., Yang, G., Fan, X., Xie, Z., Wang, R., and Han, X. (2014). *Design of an Isolated Medium-Frequency Medium-Voltage High-Power Three-Level H-Bridge DC/DC Converter*. Instrumentation and Measurement Technology Conference, 637–642.

Xie, C., and Zhang, C. (2010). *Research on the Ship Electric Propulsion System Network Power Quality with Flywheel Energy Storage," Asia-pacific Power & Energy Engineering Conference*. Chengdu, China: IEEE. 1

Xinbo Ruan, X., Bin Li, B., Qianhong Chen, Q., Siew-Chong Tan, S. C., and Tse, C. K. (2008). Fundamental Considerations of Three-Level DC-DC Converters: Topologies, Analyses, and Control. *IEEE Trans. Circuits Syst.* 55 (11), 3733–3743. doi:10.1109/tcsi.2008.927218

Yanhui Xie, Y., Jing Sun, J., and Freudenberg, J. S. (2010). Power Flow Characterization of a Bidirectional Galvanically Isolated High-Power DC/DC Converter over a Wide Operating Range. *IEEE Trans. Power Electron.* 25 (1), 54–66. doi:10.1109/tpel.2009.2024151

Zhao, B., Song, Q., Li, J., Xu, X., and Liu, W. (2017). Comparative Analysis of Multilevel-High-Frequency-Link and Multilevel-DC-Link DC-DC Transformers Based on MMC and Dual-Active-Bridge for MVDC Application. *IEEE Trans. Power Electro.* 99, 1

Zhao, S., Dearien, A., Wu, Y., Farnell, C., Rashid, A. U., Luo, F., et al. (2020). Adaptive Multi-Level Active Gate Drivers for SiC Power Devices. *IEEE Trans. Power Electron.* 35 (2), 1882–1898. doi:10.1109/tpel.2019.2922112

Zhao, S., Zhao, X., Wei, Y., Zhao, Y., and Mantooth, H. A. (2021). A Review of Switching Slew Rate Control for Silicon Carbide Devices Using Active Gate Drivers. *IEEE J. Emerg. Sel. Top. Power Electron.* 9 (4), 4096–4114. doi:10.1109/jestpe.2020.3008344

Conflict of Interest: The authors declare that the research was conducted in the absence of any commercial or financial relationships that could be construed as a potential conflict of interest.

Publisher's Note: All claims expressed in this article are solely those of the authors and do not necessarily represent those of their affiliated organizations, or those of the publisher, the editors, and the reviewers. Any product that may be evaluated in this article, or claim that may be made by its manufacturer, is not guaranteed or endorsed by the publisher.

frontiers in Energy Research

ORIGINAL RESEARCH
published: 17 March 2022
doi: 10.3389/fenrg.2021.825526

Fuzzy-Weighted Echo State Networks

Zhao Yao[1,2] *and Yingshun Li*[2]*

[1]Army Academy of Armored Forces, Changchun, China, [2]Dalian University of Technology, Dalian, China

A novel echo state network (ESN), referred to as a fuzzy-weighted echo state network (FWESN), is proposed by using the structural information of data sets to improve the performance of the classical ESN. The information is incorporated into the classical ESN via the concept of Takagi–Sugeno (TS) models/rules. We employ the fuzzy c-mean clustering method to extract the information based on the given data set. The antecedent part of the TS model is determined by the information. Then, we obtain new fuzzy rules by replacing the affine models in the consequent part of each TS rule with a classical ESN. Consequently, the output of the proposed FWESN is calculated through inferring these new fuzzy rules by a fuzzy-weighted mechanism. The corresponding reservoir is consisted of the sub-reservoirs of the new fuzzy rules. Furthermore, we prove that the FWESN has an echo state property by setting the largest spectrum radium of all the internal weight matrices in the sub-reservoirs less than one. Finally, a nonlinear dynamic system and five nonlinear time series are employed to validate the FWESN.

Keywords: echo state network, Takagi–Sugeno model, fuzzy, reservoir, time series prediction

OPEN ACCESS

Edited by:
Xun Shen,
Tokyo Institute of Technology, Japan

Reviewed by:
Datong Liu,
Harbin Institute of Technology, China

***Correspondence:**
Yingshun Li
leeys@dlut.edu.cn

Specialty section:
This article was submitted to Smart Grids, a section of the journal Frontiers in Energy Research

Received: *30 November 2021*
Accepted: *28 December 2021*
Published: *17 March 2022*

Citation:
Yao Z and Li Y (2022) Fuzzy-Weighted Echo State Networks. Front. Energy Res. 9:825526. doi: 10.3389/fenrg.2021.825526

1 INTRODUCTION

1.1 Summary of the Echo State Network

The recurrent network model describes the change process of the states of research object with time and space. Since the complexity of the problem increases and the computing power enhances, various recurrent networks have been successfully applied to different application fields, such as echo state networks in time series prediction (Jaeger and Haas, 2004), Boolean networks in games (Le et al., 2021; Le et al., 2020), and optimal control (Chen et al., 2019; Toyoda and Wu, 2021; Wu et al., 2021).

Echo state networks (ESNs) are a special case of recurrent neural networks (RNNs) proposed by Jaeger and Haas (2004). Unlike the traditional RNN, the recurrent layer of ESN uses a large number of neurons, and the connection weights between neurons are randomly generated and sparse. In an ESN, the recurrent layer is called a reservoir. The input signals drive the reservoir, and the trainable output neurons combine the output of the reservoir to generate task-special temporal patterns. This new RNN paradigm is referred to as reservoir computing. Similar to ESNs, liquid state machines (Maass et al., 2002), temporal recurrent neural networks (Steil, 2006), and decorrectation–backpropagation learning (LukošAevicius and Jaeger, 2009), and convolution and deep echo state networks (Ma et al., 2021; Wang et al., 2021) are all the instances of reservoir computing. The difference between ESNs and them is that the former employs analog neurons. The problem of traditional RNN is the lack of an effective supervised training algorithm. This problem is largely overcome by ESNs since only output weights are trained. ESNs have been successfully applied in a wide range of temporal tasks (Jaeger and Haas, 2004; Holzmann and Hauser, 2010; Song and Feng, 2010; Babinec and Pospichal, 2012; Xu et al., 2019; Yang and Zhao, 2020), especially in the prediction of nonlinear chaotic time series (Jaeger and Haas, 2004; Wang et al., 2021).

1.2 Summary of the Related Work and Motivation

The random and sparse connection weights between neurons in the reservoir bring much convenience for ESN applications. However, just simply creating at random is unsatisfactory for a specific modeling task (LukošAevicius and Jaeger, 2009). Recently, one of main streams for ESN research has been focused on developing a suitable reservoir to improve its performance (Jaeger, 2007; Holzmann and Hauser, 2010; Song and Feng, 2010; Babinec and Pospichal, 2012; Sheng et al., 2012). The fact shows that a specific architectural variant of the standard ESN leads to better results than that of a naive random creation. For examples, a new ESN with arbitrary infinite impulse response filter neurons is proposed for the task of learning multiple attractors or signal with different time scales. Then, the trainable delays in the synapse connection of output neurons are added to improve the memory capacity of ESNs (Holzmann and Hauser, 2010). Inspired by the simulation results of some nonlinear time series prediction, a complex ESN is proposed, in which the connection process of its reservoir is determined by five growth factors (Song and Feng, 2010). A complex prediction system is created by combining the local expert ESN with different memory length for solving the troubles of ESN with fixed memory length in applications (Babinec and Pospichal, 2012). A hierarchical architecture of ESN is presented for multi-scale time series. Its core ingredient of each layer is an ESN. This architecture as a whole is trained by a stochastic error gradient descent (Jaeger, 2007). An improved ESN is proposed to predict the noisy nonlinear time series, in which the uncertainties from internal states and outputs are meanwhile considered in accordance with the industrial practice (Sheng et al., 2012).

Note that uncertain information, noises, and structure information often exist in the systems (Liu and Xue, 2012; Shen et al., 2020; Shen and Raksincharoensak, 2021a,b). Thus, an extensive work has been carried out on designing a specific reservoir for a given modeling task as mentioned previously. However, the structure information for the input/output data is ignored when the reservoir is designed or revised. In fact, for many temporal tasks and pattern recognition problems, the data sets appear in homogenous groups, and this structural information can be exploited to facilitate the training process, so that the prediction accuracy can be further improved (Wang et al., 2007; Liu and Xue, 2012). Thus, it becomes a necessary requirement to consider the effects of data structure information on the ESN and then to design a suitable reservoir for a specific modeling task.

1.3 Main Idea and Contributions

This study aims at constructing a new type of ESN, referred to as a fuzzy-weighted echo state network (FWESN). The FWESN is able to incorporate the structural information of data sets into the classical ESN via the TS model. Actually, the FWESN can be regarded as a certain ESN, in which the output is calculated by a fuzzy-weighted mechanism, and the corresponding reservoir consists of sub-reservoirs corresponding to TS rules. Similar to the ESN, the echo state property for the FWESN is obtained when all weighted matrices of sub-reservoirs satisfy that their spectrums are less than one.

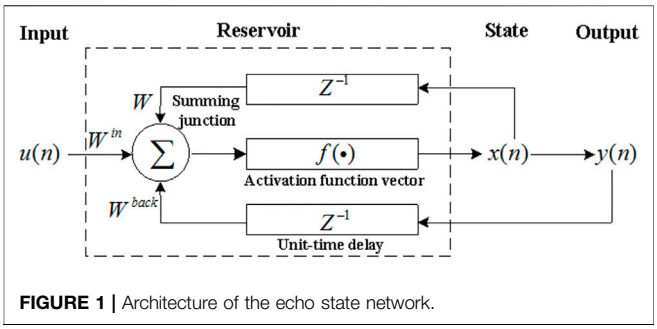

FIGURE 1 | Architecture of the echo state network.

The contribution of this article lies in the following aspects: first, the structural information of the data set is incorporated into the classical ESN to enhance its performance in applications.

Second, the structure of FWESN is parallel, which is distinguished from the hierarchical architecture of ESN. The FWESN is trained efficiently by a linear regression problem, which is the same as the training algorithms of the ESN and TS model. Thus, the FWESN avoids the problem of vanishing gradients, as the hierarchical ESN, deep feedforward neural networks, and fully trained recurrent neural networks based on gradient-descent methods.

The remaining article is structured as follows: preliminaries are given in **Section 2**. The architecture, echo state property, and training algorithm of FWESN are discussed in **Section 3**. Experiments are performed by comparing FWESN with the ESN and TS model in **Section 4**. Finally, conclusions are drawn in **Section 5**.

2 PRELIMINARIES

In this section, we give a brief introduction to typical ESNs and TS models. A more thorough treatments concerning them can be referred to Takagi and Sugeno (1985), Jaeger and Haas (2004), and Holzmann and Hauser (2010).

2.1 Echo State Networks

An ESN can be represented by state update and output equations. We formulate the ESN as shown in **Figure 1**.

The activation of internal units in a reservoir is updated according to the following equations:.

$$x(n) = f\left(W^{in}u(n) + Wx(n-1) + W^{back}y(n-1)\right). \quad (1)$$

Here, $x(n) = (x_1(n), \ldots, x_N(n))^T$ is a state vector of the reservoir, $u(n) = (u_1(n), \ldots, u_{N_{in}}(n))^T \in \mathbb{R}^{N_{in}}$ is an input vector, $y(n-1) = (y_1(n-1), \ldots, y_{N_{out}}(n-1))^T \in \mathbb{R}^{N_{out}}$ is an output vector, and $W^{in} \in \mathbb{R}^{N\times N_{in}}$, $W \in \mathbb{R}^{N\times N}$, and $W^{back} \in \mathbb{R}^{N\times N_{out}}$ are the input, internal, connection weight, and feedback matrices, respectively. $\mathbb{R}$ is the real number. $f(\cdot) = (f_1, \ldots, f_N)^T$ stands for an activation function vector. For example, $f_i(\cdot) = tanh(\cdot)$, $i = 1, 2, \ldots, N$. The full connection

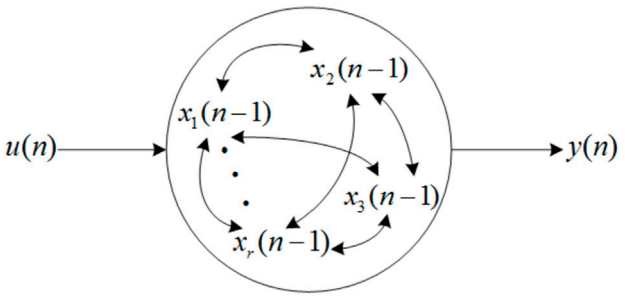

FIGURE 2 | Full connection of internal units in a reservoir.

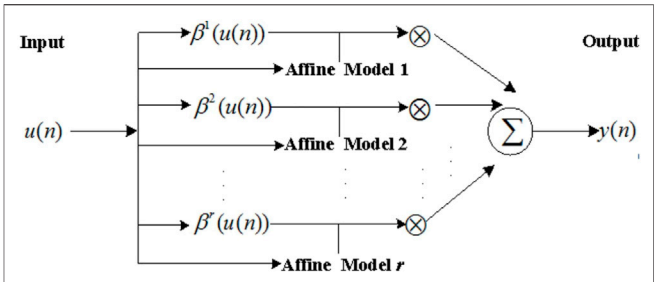

FIGURE 3 | Architecture of the TS model.

of internal units in the reservoir is shown in **Figure 2**. The output *y(n)* can be expressed as

$$y(n) = W^{out} S(n), \tag{2}$$

where

$$S(n) = \left[u^T(n), x^T(n), y^T(n-1)\right]^T \in \mathbb{R}^{N_{in}+N+N_{out}},$$

and

$$W^{out} \in \mathbb{R}^{N_{out}\times(N_{in}+N+N_{out})}$$

is the output weight matrix.

There are several notions of stability relevant to ESNs, where the echo state property is the most basic stability property (Jaeger and Haas, 2004).

Let $(u(n))_{n\in J} \in \mathcal{U}^J$ represent input sequences, where $\mathcal{U}$ is compact. $\bar{u}^{\pm\infty}$, $\bar{u}^{+\infty}$, $\bar{u}^{-\infty}$, and $\bar{u}^h$ denote left-right-infinite $J \in \mathbb{Z}$, right-infinite $J = k, k+1, \ldots$ for some $k \in \mathbb{Z}$, left-infinite, and finite h input sequences, respectively. $\mathbb{Z}$ is the integer. The network state update operator G is defined as follows (Jaeger and Haas, 2004):

$$x(n+h) = G\left(x(n), y(n), \bar{u}^h\right) \tag{3}$$

to denote the network state that results from an iterated application of **Eq. 1**. If the input sequence $\bar{u}^h = (u(n+1), \ldots, u(n+h))$ is fed into the network, the network is in state *x(n)* and has output *y(n)* at time *n*. In the network without output feedback, **Eq. 3** is simplified to

$$x(n+h) = G\left(x(n), \bar{u}^h\right).$$

Definition 1: Assume that the inputs are drawn from a compact input space $\mathcal{U}$, network states lie in a compact set $\mathcal{A}$, and the network has no output feedback connections. Let $\mathbb{N}$ be the natural numbers. Then, the network has echo states, if the network state *x(n)* is uniquely determined by any left-infinite input sequences $\bar{u}^{\infty}$. More precisely, this means that for every input sequence $\ldots, u(n-1), u(n) \in \mathcal{U}^{-\mathbb{N}}$, for all state sequences $\ldots$, *x (n − 1), x(n)* and $\tilde{x}(n-1), \tilde{x}(n) \in \mathcal{A}^{-\mathbb{N}}$ where *x(i) = G (x (i − 1), u(i))* and $\tilde{x}(i) = G(\tilde{x}(i-1), u(i))$, and it holds that $x(n) = \tilde{x}(n)$.

The condition of Def. 1 is hard to check in practice. Fortunately, a sufficient condition is given in Jaeger and Haas (2004), which is easily checked.

Proposition 1: Assume a sigmoid network with unit output functions $f_i = tanh$. Let the weight matrix W satisfy $\sigma_{\max} = \wedge < 1$, where $\sigma_{\max}$ is the largest singular value of W. Then, $d(G(x,u)), G(\tilde{x},u) < \wedge\, d(x,\tilde{x})$ for all inputs u, for all states $x, \tilde{x} \in [-1,1]^{\mathbb{N}}$, where d is an Euclidean distance on $\mathbb{R}^N$. This implies the echo states for all inputs u, for all states $x, \tilde{x} \in [-1,1]^{\mathbb{N}}$.

2.2 Takagi–Sugeno Models

Among various fuzzy modeling themes, the TS model (Takagi and Sugeno, 1985) has been one of the most popular modeling frameworks. A general TS model employs an affine model in the consequent part for every fuzzy rule. We formulate the TS model as shown in **Figure 3**.

A TS model can be represented with *r* fuzzy rules and each fuzzy rule has the following form:

$$\begin{aligned} &\text{If } u_1(n) \text{ is } M_1^i \text{ and } \ldots \text{ and } u_{N_{in}}(n) \text{ is } M_{N_{in}}^i \\ &\text{then } y(n) = h^i(u(n)),\ i = 1, 2, \ldots, r \end{aligned}, \tag{4}$$

where $u(n) = [u_1(n), \ldots, u_{N_{in}}]^T \in \mathbb{R}^{N_{in}}$ is the input vector of the antecedent part of the fuzzy rule at time *n*. *r* is the number of the rule. M_j^i are fuzzy sets.

$$y(n) = h^i(u(n)) = a^i u(n)$$

is the output from the *i*th fuzzy rule, where $a^i = (a_1^i, \ldots, a_{N_{in}}^i)$ is the vector of consequent parameters of the *i*th fuzzy rule.

Given an input *u(n)*, the final output of the fuzzy system is inferred as follows:

$$y(n) = \sum_{i=1}^{r} \beta^i(u(n)) h^i(u(n)), \tag{5}$$

where $\beta^i(u(n)) = \prod_{j=1}^{N_{in}} M_j^i(u_j(n)) / \sum_{i=1}^{r} \prod_{j=1}^{N_{in}} M_j^i(u_j(n))$, $M_j^i(u_j(n))$ is the membership grade of $u_j(n)$ in M_j^i and $i = 1, 2, \ldots, r$, $j = 1, 2, \ldots, N_{in}$.

3 FUZZY-WEIGHTED ECHO STATE NETWORKS

In this section, we propose a new framework based on the ESN and TS model, which is referred to as a fuzzy-weighted echo state network (FWESN). We further prove that an FWESN has the

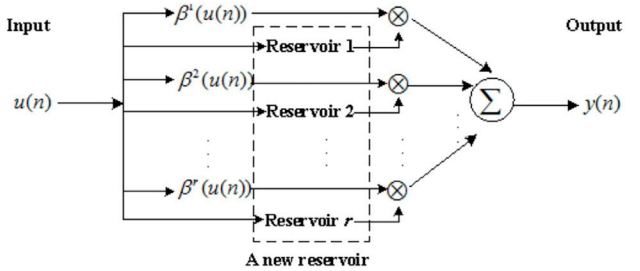

FIGURE 4 | Architecture of FWESN.

echo state property. Finally, we discuss the training algorithm of FWESN.

3.1 Architecture of Fuzzy-Weighted Echo State Networks

FWESNs are designed by taking advantage of TS models to improve ESN (1). The basic idea is to replace the affine model of each fuzzy rule (4) with ESN (1). FWESN is formulated as shown in **Figure 4**.

The FWESN can be represented by the fuzzy rules as follows:

$$\begin{aligned} &\text{If } u_1(n) \text{ is } M_1^i \text{ and } \ldots \text{ and } u_{N_{in}} \text{ is } M_{N_{in}}^i, \\ &\text{then } y(n) = W_i^{out} S^i(n), \ i = 1, 2, \ldots, r \end{aligned} \tag{6}$$

where $y(n)$ is the output for the ith fuzzy rule (6). $y(n)$ is determined by the following state update equations:

$$x^i(n) = f^i\left(W_i^{in} u(n) + W_i x^i(n-1) + W_i^{back} y(n-1)\right). \tag{7}$$

Here, $S^i(n) = (u^T(n), (x^i(n))^T, y^T(n-1))^T$, $x^i(n) \in \mathbb{R}^{N_i}$ is the state vector of the reservoir, $W_i^{in} \in \mathbb{R}^{N_i \times N_{in}}$, $W_i \in \mathbb{R}^{N_i \times N_i}$, $W_i^{back} \in \mathbb{R}^{N_i \times N_{out}}$, and $W_i^{out} \in \mathbb{R}^{N_{out} \times (N_{in}+N_i+N_{out})}$ are internal input, internal connection weight, and output weight matrices for the ith fuzzy rule (6), respectively. $f^i(\cdot) \in \mathbb{R}^{N_i}$ is the neuron activation function vector, applied element-wise for the ith fuzzy rule (6). Then, the corresponding output of FWESN is inferred by the fuzzy-weighted mechanism. From **Eqs. 5, 6**, it follows that

$$y(n) = \sum_{i=1}^{r} \beta^i(u(n)) W_i^{out} S^i(n). \tag{8}$$

Let

$$\begin{aligned} &W^{in} = \left(W_1^{in}, W_2^{in}, \ldots, W_r^{in}\right)^T \in \mathbb{R}^{\left(\sum_{i=1}^{r} N_i\right) \times N_{in}}, \\ &W^{back} = \left(W_1^{back}, W_2^{back}, \ldots, W_r^{back}\right)^T \in \mathbb{R}^{\left(\sum_{i=1}^{r} N_i\right) \times N_{out}}, \\ &F = \left(f^1, f^2 \ldots, f^r\right)^T \in \mathbb{R}^{\sum_{i=1}^{r} N_i}, \\ &W = diag(W_1, W_2, \ldots, W_r) \in \mathbb{R}^{\left(\sum_{i=1}^{r} N_i\right) \times \left(\sum_{i=1}^{r} N_i\right)}, \\ &X(n) = \left[(x^1(n))^T, (x^2(n))^T, \ldots, (x^r(n))^T\right] \in \mathbb{R}^{\sum_{i=1}^{r} N_i}. \end{aligned}$$

By **Eq. 6**, a new reservoir can be reformulated, where the state update equations are written as

$$X(n) = F\left(W^{in} u(n) + W X(n-1) + W^{back} y(n-1)\right). \tag{9}$$

Additionally, the same shorthand is used for the FWESN and ESN. Thus, from **Eqs. 3, 9**, it follows that

$$X(n+h) = G\left(X(n), y(n), \vec{u}^h\right), \tag{10}$$

which denotes the network state resulting from an iterated applications. For an FWESN without feedback, **Eq. 10** is simplified as

$$X(n+h) = G\left(x(n), \vec{u}^h\right). \tag{11}$$

For clarity, we use $(\beta, W^{in}, W, W^{back}, W^{out})$ to denote an FWESN, where $\beta = (\beta^1, \beta^2, \ldots, \beta^r)^T$. We use (W^{in}, W, W^{back}) to denote an untrained ESN.

3.2 Discussion on Several Special Cases for Fuzzy-Weighted Echo State Networks

Case 1: From the architecture of FWESN, the classical ESN can be regarded as a special case of FWESN. That is, let $r = 1$ and

$$M_j^1\left(u_j(n)\right) = \begin{cases} 1, & u_j = u_j(n), \\ 0, & \text{else}, \end{cases} \quad j = 1, 2, \ldots, N_{in} \tag{12}$$

in **Eq. 6**. Then, the final output of FWESN (8) is rewritten as

$$y(n) = \beta^1(u(n)) W_1^{out} S^1(n) = W_1^{out} S^1(n).$$

The corresponding update **Eq.7** is expressed as

$$x^1(n) = f^1\left(W_1^{in} u(n) + W_1 x(n-1) + W_1^{back} y(n-1)\right),$$

which is the same as ESN (1).

Case 2: The TS model (4) can be regarded as a special case of FWESN (6). That is, let $f^i = (1,0,\ldots,0)^T$ in **Eq. 6**. It follows that

$$x^i(n) = f^i = (1, 0, \ldots, 0)^T$$

and

$$S^i(n) = \left(u^T(n), 1, 0, \ldots, 0, y^T(n-1)\right)^T.$$

Let

$$W_i^{out} = \left(a_1^i, \ldots, a_{N_{in}}^i, a_0^i, 0, \ldots, 0, 0, \ldots, 0\right).$$

Then, we have the output of the ith fuzzy rule (6) as follows:

$$y(n) = W_i^{out} S^i(n) = a_0^i + a_1^i u_1(n) + \cdots + a_{N_{in}}^i u_{N_{in}}(n).$$

It is obvious that the fuzzy rule (6) has the same form as that of the fuzzy rule (4) based on the aforementioned conditions. Thus, the FWESN degrades into the TS model (4).

3.3 Echo State Property of Fuzzy-Weighted Echo State Networks

In this section, we will prove that the FWESN has the echo state property for the case of the network without output feedback.

Similar to Proposition 1, we give a sufficient condition for the echo state property of the FWESN.

Proposition 2: Let $\mathcal{U}$ and $\mathcal{X}$ be two compact sets. $\|\cdot\|_2$ is the operator norm on the space of matrices corresponding to 2-norms for vectors. Assume a sigmoid network (β, W^{in}, W, W^{back}, W^{out}) with unit output functions $f_j^i = tanh$, $i = 1, 2, \ldots, N_{in}$, $j = 1, 2, \ldots, N_{out}$. *Let* $\sigma(W_i) < 1$ for $i = 1, 2, \ldots, r$, where W = *diag* (W_1, W_2, …, W_r). Then,

$$\|G(X,u), G\left(\tilde{X},u\right)\|_2 < \sigma(W)\|X-\tilde{X}\|_2, \forall u \in \mathcal{U}, X, \tilde{X} \in \mathcal{X}.$$

This implies the echo states for all inputs $u \in \mathcal{U}$ and states $X, \tilde{X} \in \mathcal{X}$.

Proof: Considering $W = diag(W_1, W_2, \ldots, W_r)$ and $\sigma(W_i) < 1$, we have

$$\begin{aligned}\sigma(W) &= \left(\lambda_{max}\left(W^TW\right)\right)^{1/2} \\ &= \left[\lambda_{max}\left(\mathrm{diag}\left(W_1^TW_1,\ldots,W_r^TW_r\right)\right)\right]^{1/2}. \\ &= max_{1\le i\le r}\ \sigma\left(\left(W_i^TW_i\right)^{1/2}\right) < 1\end{aligned} \tag{13}$$

Here, $\lambda_{max}(\cdot)$ is the largest absolute value of an eigenvector of matrix. For two different states $X(n)$ and $\tilde{X}(n)$, by **Eqs. 9, 10**, we have

$$\begin{aligned}\|X(n)-\tilde{X}(n)\|_2 &= \|G(X(n-1),u(n)) - G\left(\tilde{X}(n-1),u(n)\right)\|_2 \\ &= \|F\left(W^{in}u(n)+WX(n-1)\right) \\ &\quad -F\left(W^{in}u(n)-W\tilde{X}(n-1)\right)\|_2\end{aligned} \tag{14}$$

For $f_j^i = tanh$, it follows that

$$\begin{aligned}\|X(n)-\tilde{X}(n)\|_2 &\le \|W^{in}u(n)+WX(n-1)-W^{in}u(n)-W\tilde{X}(n-1)\|_2 \\ &\le \|W\|_2\|X(n-1)-\tilde{X}(n-1)\|_2 \\ &= \delta(W)\|X(n-1)-\tilde{X}(n-1)\|_2,\end{aligned}$$

where

$$\|W\|_2 = \sup_{X\neq 0}\frac{\|WX\|_2}{\|X\|_2} = \delta(W).$$

That is, the Lipschitz condition obviously results in echo states for the FWESN.

Remark 1: From the proof of Proposition 2, we select that the updated **Eq. 1** is a special form based on the conditions $\sigma(W_i) < 1$ for $i = 1, 2, \ldots, r$.

3.4 Training Algorithm of Fuzzy-Weighted Echo State Networks

We state the training algorithm of FWESN based on the given training input/output pairs *(u(n), z(n))* ($n = 0, 1, 2, \ldots, k$). First, we employ a subtractive clustering approach (Bezdek, 1981) to determine the membership grade $M_j^i(u_j(n))$ for the *i*th fuzzy rule (6), where $i = 1, 2, \ldots, r$. Second, we randomly generate the untrained networks $(W_i^{in}, W_i, W_i^{back})$, which satisfy the echo state property. Third, we update the network states x^i(n) by **Eq. 7** and collect the concatenated input/reservoir/previous-output states ($u(n)$, $x^i(n)$, $y(n-1)$), $i = 1, 2, \ldots, r$. Fourth, we calculate W_i^{out} ($i = 1, 2, \ldots, r$) using the output y(n) of FWESN (8) to approximate $z(n)$ ($n = 0, 1, 2, \ldots, k$) by the mean square error. That is, the trained FWESN is obtained.

The procedure of the proposed training algorithm is described by four steps as follows:

Step 1 Calculate $\beta^i(u(n))$ ($i = 1, 2, \ldots, r$) in **Eq. 8** by the fuzzy c-mean clustering approach.

Step 2 Procure the untrained network $(W_i^{in}, W^i, W_i^{back})$ for $i = 1, 2, \ldots, r$.

1) Suppose the dimension of the state vector is N for r reservoirs corresponding to r fuzzy rules (5).
2) Initiate $i = 1$.
3) Randomly generate an input weight matrix W^{in}, an output backpropogation weight matrix W^{back}, and a matrix $W_0 \in \mathbb{R}^{N\times N}$. Normalize W^0 to a matrix W_1 by letting $W_1 = \frac{1}{\rho}W_0$, where ρ is the spectral radius of W_0. Scale W_1 to $W_2 = \gamma W_1$ ($\gamma < 1$).
4) Let $W_2 = W_i, W_Q^{in} = W_i^{in}, W_Q^{back} = W_i^{back}; i = i + 1$.
5) If $i > r$, end. Else go to Step 3.

Step 3 Sample network training dynamics for each fuzzy rule (4).

1) Let $i = 1$. Initial the state of the untrained network $(W_i^{in}, W^i, W_i^{back})$ arbitrarily, typically $x_i(0) = 0$ and $y(0) = 0$.
2) Drive the network $(W_i^{in}, W^i, W_i^{back})$ for time $n = 1, 2, \ldots, \mathcal{T}$, by presenting the teacher input $u(n)$, by presenting the teacher output $y(n-1)$, and by computing $x_i(n) = f_i(W_i^{in}u(n) + W_ix(n-1) + W_i^{back}y(n-1))$ for time $n = 1, 2, \ldots, \mathcal{T}$.
3) For each time equal or larger than an initial washout time $\mathcal{T}_1$, collect $x_i(n)$, $u(n)$, and $y(n)$ for $\mathcal{T}_1 \le n \le \mathcal{T}$. One has obtained $S^i(n) = (x_i^T, u^T(n), y^T(n-1))^T, \mathcal{T}_1 \le n \le \mathcal{T}$.
4) $i = i + 1$, if $i > r$, end; else go to Step 2.

Step 4 Calculate the output weights.

1) Let

$$Y = \left(y(\mathcal{T}_1), y(\mathcal{T}_1+1), \ldots, y(\mathcal{T})\right)^T \in \mathbb{R}^{N_{out}\times(\mathcal{T}-\mathcal{T}_1+1)},$$
$$W^{out} = \left(W_1^{out}, W_2^{out}, \ldots, W_r^{out}\right) \in \mathbb{R}^{N_{out}\times[r(N_{in}+N+N_{out})]}.$$

Collect $\beta^i(u(n))S^i(n)$ as a state matrix S for $n = \mathcal{T}_1, \mathcal{T}_1+1, \ldots, \mathcal{T}$, where $S \in \mathbb{R}^{[r(N_{in}+N+N_{out})]\times(\mathcal{T}-\mathcal{T}_1+1)}$. From **Eq. 8**, we have $y = \sum_{i=1}^r W_i^{out}[\beta^i u(n) S^i(n)]$.

2) By the least square method, the output weight W^{out} is calculated by $W^{out} = (SS^T)YS^T$.

Remark 2: By Step 2, we obtain untrained networks $(W_i^{in}, W^i, W_i^{back})$ for $i = 1, 2, \ldots, r$. Note that we limit the spectral radius of the internal weight matrix $W_i (i = 1, 2, \ldots, r)$ less than one, which guarantees that the network has the echo state property.

4 EXPERIMENTS

We have performed some experiments to validate the FWESN in this study. We have shown that the FWESN has better performance than the ESN owing to the incorporation of

structural information of data sets. The following terms are used in the experiments:

Data sets: A nonlinear dynamic system (Juang, 2002) and five nonlinear time series, i.e., Mackey-Class, Lorenz, ESTSP08(A), ESTSP08(B), and ESTSP08(C), are used in the experiments. Here, the nonlinear dynamic system is

$$y_p(k+1) = g\big(y_p(k), y_p(k-1), y_p(k-2), u(k), u(k-1)\big), \tag{15}$$

where

$$u(k) = \begin{cases} \sin(\pi k/25), & k < 250, \\ 1.0, & 250 \le k \le 500, \\ -1.0, & 500 \le k < 750, \\ 0.3\sin\left(\frac{\pi k}{25}\right) + 0.1\sin\left(\frac{\pi k}{32}\right) + 0.6\sin\left(\frac{\pi k}{10}\right), & 750 \le k < 1000, \end{cases}$$

$$g(x_1, x_2, x_3, x_4) = \frac{x_1 x_2 x_3 (x_3 - 1) + x_4}{1 + x_2^2 + x_3^2}.$$

$y_p(k)$ and $u(k)$ are the output and input, respectively. In the experiment, $(u(k), y_p(k-1))$ and $y_p(k)$ are the inputs and outputs of algorithms, respectively. The generate method of samples are the same with that in Juang (2002).

Algorithms: Three algorithms, i.e., FWESN, ESN, and TS model, are used in the experiments. The neurons in the form of hyperbolic tangent functions are used for the ESN and FWESN.

Parameters: r is the number of fuzzy rules. The main parameters of the reservoir are the scale of the reservoir N, the sparseness of the reservoir SD, the spectrum radium of the internal weight matrices in the reservoir SR, the input-unit scale IS, and shifting IT. In the experiments, FWESN and ESN use the same scale N, where $N = rN_i$ for FWESN, where N_i represents the scales of sub-reservoirs corresponding to **Eq. 6**, where $i = 1, 2, \ldots, r$. Moreover, $N_1 = N_2 = \ldots = N_r$. Additionally, SR, IS, IT, and SD in all sub-reservoirs of FWESN and the reservoir of ESN are the same. Thus, from **Eq. 13**, it follows that the spectra radius of W in **Eq. 9**) is the same as that in **Eq. 1**.

TABLE 1 | Experiment results for FWESN, ESN, and TS model.

Data set	Algorithm	Training error	Test error
Dynamic system (13)	FWESN	6.7 014e-6	**0.001 3**
	ESN	1.9 444e-4	0.217 3
	TS model	0.036 7	0.186 3
Mackey-Class	FWESN	3.7 599e-5	**3.6 374e-5**
	ESN	0.001 5	0.000 6
	TS model	0.035 7	0.032 8
Lorenz	FWESN	0.017 9	**0.021 4**
	ESN	0.189 6	0.226 7
	TS model	0.194 4	0.264 5
ESTSP08 (A)	FWESN	0.100 2	0.288 4
	ESN	0.420 0	0.610 0
	TS model	0.210 0	0.991 0
ESTSP08(B)	FWESN	0.254 9	**0.331 2**
	ESN	0.158 2	0.420 0
	TS model	0.865 8	1.112 8
ESTSP08(C)	FWESN	0.200 4	**0.227 6**
	ESN	0.425 9	0.852 3
	TS model	0.450 0	1.256 0

The bold values highlight the minimal test errors for each data set.

Finally for the FWESN and TS model, both the parameters in the antecedent part and the total number of fuzzy rules are the same.

Performance Indices: We choose the training and test errors as the performance indices. All the errors refer to the mean square errors in the experiment.

Experimental Results: The simulation results are summarized in **Table 1**.

From **Table 1**, the FWESN achieves better performance than the ESN and TS model under same conditions. The bold values in **Table 1** highlight the minimal test errors for each data set. For example, by the FWESN and dynamic system **Eq. 1**, the training and test errors are, respectively, 6.7 014e-6 and 0.001 3, which are far less than the errors based on the ESN and TS model. Thus, the

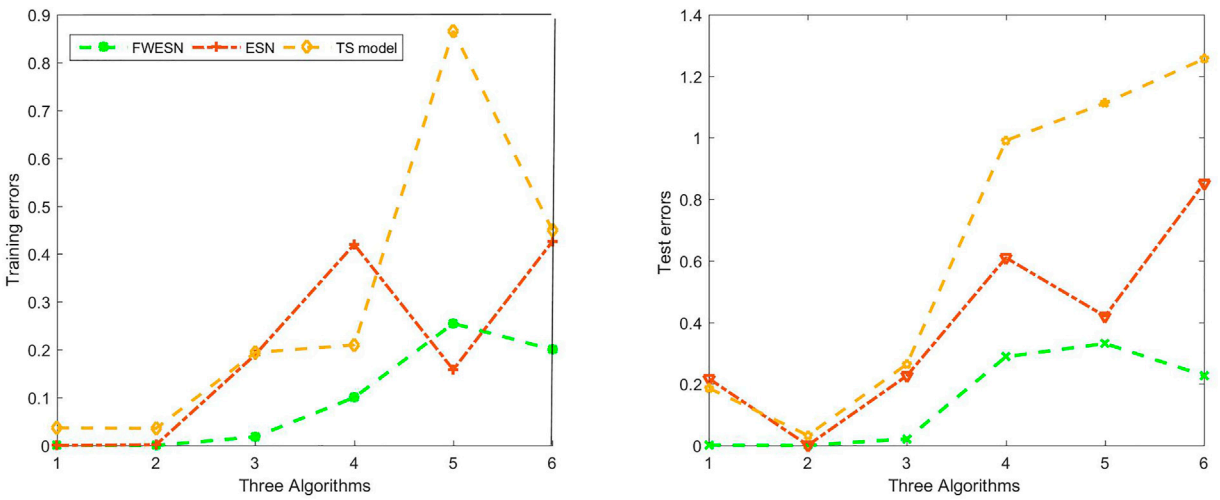

FIGURE 5 | Training and test errors for FWESN, ESN, and TS model.

learning ability and generalization ability are obviously better than the ESN and TS model. The similar results are obtained for the five nonlinear time series from **Figure 5**. On the one hand, the test errors of FWESN are less than those of ESN. The scale of FWESN and ESN are the same. The comparison indicates that the FWESN enhances the performance of ESN since we incorporate the structural information of the data sets into the ESN via the form of fuzzy weight. Additionally, the FWESN has better prediction ability, especially for nonlinear time series, than the TS model while their total number of fuzzy rules and the antecedent part of each fuzzy rule are the same.

5 CONCLUSION

In this work, a novel framework with the advantages of the ESN and TS model is proposed. As a generalization of both ESN and TS model, the ESN and TS model are improved and extended. Similar to the classical ESN, we prove that if the largest spectrum radium of the internal unit weight matrix is less than one, the FWESN has the echo state property. The FWESN shows higher accuracy than the TS model and ESN. For future work, we plan to continuously investigate the underlying theory problem of FWESN, such as the tighter stability conditions and approximation capability to a dynamical system or static function. We attempt to more different applications, for e.g., remaining useful life predictions. Additionally, we will consider hardware, for e.g., field-programmable gate array (FPGA) and implementation of FWESN oriented to real-time applications. Actually, with the development of computing power and access to big data, the convolutional neural networks are very popular owing to their obvious advantages. Thus, one further research will focus on the deep ESN based on the structural information of big data. We believe that some better results will be obtained through incorporating FWESN and deep-learning methods.

DATA AVAILABILITY STATEMENT

The raw data supporting the conclusions of this article will be made available by the authors, without undue reservation.

AUTHOR CONTRIBUTIONS

ZY contributed to the architecture, property, and training algorithm of fuzzy-weighted echo state networks. YL drafted the manuscript and contributed to the experiments and conclusions. All authors agree to be accountable for the content of the work.

FUNDING

This work was financially supported by the China Postdoctoral Science Foundation (Grant No. 2020M670785).

REFERENCES

Babinec, S., and Pospichal, J. (2012). Modular echo State Neural Networks in Time Series Prediction. *Comput. Inform.* 30, 321–334.

Bezdek, J. C. (1981). *Pattern Recognition with Fuzzy Objective Function Algorithms*. New YorkBoston, MA): Springer.

Chen, S., Wu, Y., Macauley, M., and Sun, X.-M. (2019). Monostability and Bistability of Boolean Networks Using Semitensor Products. *IEEE Trans. Control. Netw. Syst.* 6, 1379–1390. doi:10.1109/TCNS.2018.2889015

Chia-Feng Juang, C.-F. (2002). A TSK-type Recurrent Fuzzy Network for Dynamic Systems Processing by Neural Network and Genetic Algorithms. *IEEE Trans. Fuzzy Syst.* 10, 155–170. doi:10.1109/91.995118

Holzmann, G., and Hauser, H. (2010). Echo State Networks with Filter Neurons and a Delay∑ Readout. *Neural Networks* 23, 244–256. doi:10.1016/j.neunet.2009.07.004

Jaeger, H. (2007). *Discovering Multiscale Dynamical Features with Hierarchical echo State Networks*. (Bremen: Jacos University Breme).

Jaeger, H., and Haas, H. (2004). Harnessing Nonlinearity: Predicting Chaotic Systems and Saving Energy in Wireless Communication. *Science* 304, 78–80. doi:10.1126/science.1091277

Le, S., Wu, Y., Guo, Y., and Vecchio, C. D. (2021). Game Theoretic Approach for a Service Function Chain Routing in NFV with Coupled Constraints. *IEEE Trans. Circuits Syst.* 68, 3557–3561. doi:10.1109/TCSII.2021.3070025

Le, S., Wu, Y., and Toyoda, M. (2020). A Congestion Game Framework for Service Chain Composition in NFV with Function Benefit. *Inf. Sci.* 514, 512–522. doi:10.1016/j.ins.2019.11.015

Liu, F., and Xue, X. (2012). Design of Natural Classification Kernels Using Prior Knowledge. *IEEE Trans. Fuzzy Syst.* 20, 135–152. doi:10.1109/TFUZZ.2011.2170428

Lukoševičius, M., and Jaeger, H. (2009). Reservoir Computing Approaches to Recurrent Neural Network Training. *Comp. Sci. Rev.* 3, 127–149. doi:10.1016/j.cosrev.2009.03.005

Ma, Q., Chen, E., Lin, Z., Yan, J., Yu, Z., and Ng, W. W. Y. (2021). Convolutional Multitimescale echo State Network. *IEEE Trans. Cybern.* 51, 1613–1625. doi:10.1109/TCYB.2019.2919648

Maass, W., Natschläger, T., and Markram, H. (2002). Real-time Computing without Stable States: A New Framework for Neural Computation Based on Perturbations. *Neural Comput.* 14, 2531–2560. doi:10.1162/089976602760407955

Shen, X., and Raksincharoensak, P. (2021a). Pedestrian-aware Statistical Risk Assessment. *IEEE Trans. Intell. Transport. Syst.*, 1, 9. doi:10.1109/TITS.2021.3074522

Shen, X., and Raksincharoensak, P. (2021b). Statistical Models of Near-Accident Event and Pedestrian Behavior at Non-signalized Intersections. *J. Appl. Stat.*, 1, 21. doi:10.1080/02664763.2021.1962263

Shen, X., Zhang, X., and Raksincharoensak, P. (2020). Probabilistic Bounds on Vehicle Trajectory Prediction Using Scenario Approach. *IFAC-PapersOnLine* 53, 2385–2390. doi:10.1016/j.ifacol.2020.12.038

Sheng, C., Zhao, J., Liu, Y., and Wang, W. (2012). Prediction for Noisy Nonlinear Time Series by echo State Network Based on Dual Estimation. *Neurocomputing* 82, 186–195. doi:10.1016/j.neucom.2011.11.021

Song, Q., and Feng, Z. (2010). Effects of Connectivity Structure of Complex echo State Network on its Prediction Performance for Nonlinear Time Series. *Neurocomputing* 73, 2177–2185. doi:10.1016/j.neucom.2010.01.015

Steil, J. J. (2006). Online Stability of Backpropagation-Decorrelation Recurrent Learning. *Neurocomputing* 69, 642–650. doi:10.1016/j.neucom.2005.12.012

Takagi, T., and Sugeno, M. (1985). Fuzzy Identification of Systems and its Applications to Modeling and Control. *IEEE Trans. Syst. Man. Cybern.* SMC-15, 116–132. doi:10.1109/TSMC.1985.6313399

Toyoda, M., and Wu, Y. (2021). Mayer-type Optimal Control of Probabilistic Boolean Control Network with Uncertain Selection Probabilities. *IEEE Trans. Cybern.* 51, 3079–3092. doi:10.1109/TCYB.2019.2954849

Wang, D., Yeung, D. S., and Tsang, E. C. C. (2007). Weighted Mahalanobis Distance Kernels for Support Vector Machines. *IEEE Trans. Neural Netw.* 18, 1453–1462. doi:10.1109/TNN.2007.895909

Wang, Z., Yao, X., Huang, Z., and Liu, L. (2021). Deep echo State Network with Multiple Adaptive Reservoirs for Time Series Prediction. *IEEE Trans. Cogn. Dev. Syst.* 13, 693–704. doi:10.1109/TCDS.2021.3062177

Wu, Y., Guo, Y., and Toyoda, M. (2021). Policy Iteration Approach to the Infinite Horizon Average Optimal Control of Probabilistic Boolean Networks. *IEEE Trans. Neural Netw. Learn. Syst.* 32, 2910–2924. doi:10.1109/TNNLS.2020.3008960

Xu, M., Yang, Y., Han, M., Qiu, T., and Lin, H. (2019). Spatio-temporal Interpolated echo State Network for Meteorological Series Prediction. *IEEE Trans. Neural Netw. Learn. Syst.* 30, 1621–1634. doi:10.1109/TNNLS.2018.2869131

Yang, X., and Zhao, F. (2020). Echo State Network and echo State Gaussian Process for Non-line-of-sight Target Tracking. *IEEE Syst. J.* 14, 3885–3892. doi:10.1109/JSYST.2020.2982516

Conflict of Interest: The authors declare that the research was conducted in the absence of any commercial or financial relationships that could be construed as a potential conflict of interest.

frontiers in Energy Research

ORIGINAL RESEARCH
published: 18 March 2022
doi: 10.3389/fenrg.2022.865856

Simulation Study on Lightning Impulse Characteristics of Flexible Graphite Composite Grounding Materials Applied to Grounding Grid of Power System

Yuanchao Hu[1], Tao Huang[2], Yunzhu An[1], Jianyuan Feng[1], Meng Cheng[2], Hongping Xie[2], Wentao Shen[2] and Changqing Du[2]*

[1]School of Electrical and Electronic Engineering, Shandong University of Technology, Zibo, China, [2]Construction Branch of State Grid Jiangsu Electric Power Co., Ltd, Nanjing, China

The flexible graphite composite grounding electrode is a non-metallic grounding electrode with good electrical conductivity, corrosion resistance and non-ferromagnetic properties. In order to analyze the impulse characteristics of the graphite composite grounding electrode, this paper builds a frequency domain electrical network model and an equivalent radius iterative algorithm, considering skin effect, inductance effect, capacitance effect and spark discharge effect. The impulse characteristics of typical metal grounding electrodes and graphite composite grounding electrodes are analyzed by simulation. The research results show that: Compared with the traditional metal grounding electrode, the graphite composite grounding electrode has a smaller skin and inductance effect under the action of the impulse current, and a better current flowing capability; as the soil resistivity increases, the inductance effect and the skin effect are weakened, while the spark discharge effect is gradually enhanced and dominates. The spark discharge effect can effectively decrease the grounding resistance. The obtained critical value of the normalized parameter of 412 kA Ω, can be taken as the threshold to discriminate the conditions with dominate inductance effect from the conditions with dominant spark discharge effect.

Keywords: power system grounding electrode, graphite composite grounding electrode, impulse characteristics, spark discharge effect, inductance effect, electrical network model

OPEN ACCESS

Edited by:
Xun Shen,
Tokyo Institute of Technology, Japan

Reviewed by:
Hardeep Singh,
Sophia University, Japan
Vikram Kamboj,
Lovely Professional University, India

****Correspondence:***
Yunzhu An
anyunzhu2006@163.com

Specialty section:
This article was submitted to Smart Grids, a section of the journal Frontiers in Energy Research

Received: *30 January 2022*
Accepted: *21 February 2022*
Published: *18 March 2022*

Citation:
Hu Y, Huang T, An Y, Feng J, Cheng M, Xie H, Shen W and Du C (2022) Simulation Study on Lightning Impulse Characteristics of Flexible Graphite Composite Grounding Materials Applied to Grounding Grid of Power System. Front. Energy Res. 10:865856. doi: 10.3389/fenrg.2022.865856

INTRODUCTION

The grounding grid is the most basic lightning protection device in power system. Good impulse grounding performance is an important prerequisite for ensuring safe and reliable operation of power system. The grounding resistance of grounding device generated by lightning current is called impulse grounding impedance (Deng et al., 2013; He and Zhang, 2015; Zhang, 2018). Different from the power frequency current, the lightning current flows through the grounding electrode in a pulse manner in a very short time, resulting in that the impulse grounding impedance is different from the power frequency grounding resistance (Grcev, 2009a) (Tao et al., 2018). The lightning current flowing through grounding electrode and soil is a complex electromagnetic transient process accompanied by various physical effects such as inductance effect and spark discharge effect (Grcev, 2009b; Visacro and Rosado, 2009; Deng et al., 2012; Wen et al., 2016). The CDEGS, an international general grounding simulation software, can be used

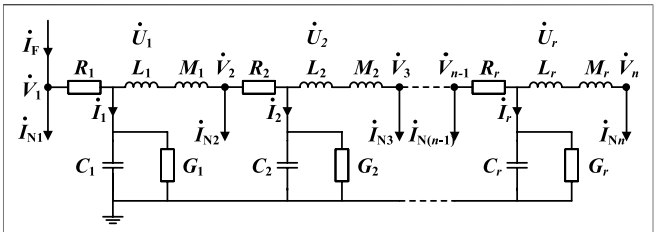

FIGURE 1 | Equivalent electrical network model of grounding electrode.

to calculate the impulse grounding impedance of grounding electrode. However, the calculation results of CDEGS do not consider the influence of soil ionization, which is called spark discharge effect in this paper, leading to a large error between the calculation results and the actual grounding impedance of the grounding electrode (Yang et al., 2021; Feng et al., 2015). At present, the numerical simulation algorithms for impulse characteristics of grounding devices considering the effect of soil spark discharge mainly include transmission line modeling method (TLM) and finite element method (FEM). The impulse response of grounding devices using TLM is equivalent to the wave propagation of transmission line. This method cannot consider the coupling between conductors (de Lima and Portela, 2007; Gazzana et al., 2014). The FEM method is more efficient, but the change of soil resistivity will lead to the occurrence of ill-conditioned matrix in the calculation, thus affecting the calculation accuracy (Nekhoul et al., 1996). It is difficult to consider all the physical processes like skin effect, inductance effect and spark discharge process when impulse current flew through the grounding electrode.

In recent years, flexible graphite composite grounding material as a new type of non-magnetic grounding electrode has been applied to the grounding grids of power system (Huang et al., 2019; Hu et al., 2014). Compared with traditional metal grounding materials, flexible graphite composite grounding materials have good electrical conductivity and natural corrosion resistance (Gong et al., 2016; Hu et al., 2016; Xiao et al., 2017). In order to study the impulse characteristics of graphite composite grounding electrode under the influence of skin effect, inductance effect and capacitance effect, the frequency domain electrical network model is established by MATLAB to simulate the current flow process of tower grounding electrode. Moreover, the iterative algorithm of equivalent radius is used to consider the influence of soil nonlinear ionization around the grounding electrode. The influences of various physical effects on the impulse characteristics of graphite composite grounding electrode are obtained by simulation. The research results can provide theoretical reference for optimizing the length of graphite composite grounding electrode.

SIMULATION MODELING METHOD

Frequency Domain Electrical Network Model of Grounding Electrode

In this section, the impulse process of grounding electrode in Earth is considered by frequency domain electrical network model. A simple horizontal grounding electrode is applied. In order to describe the grounding electrode more intuitively, this paper adopts the circuit modeling with lumped parameters. Firstly, the grounding electrode is gridded and each segment is equivalent to a circuit model composed of resistance, inductance, grounding capacitance and grounding conductance (Mentre and Grcev, 1994) (Lorentzou et al., 2003). The equivalent electrical network model of horizontal grounding rod is shown in **Figure 1**.

Suppose there are a total of r branches, n nodes, so that the branches $i = 1, 2, \cdots, r$, nodes $j = 1, 2, \cdots, n$, where R_i, L_i, M_i, C_i and G_i are the resistance, self-inductance, mutual-inductance, grounding capacitance, and grounding conductance of each branch after the grounding electrode meshing; $\dot{U}_i$ and $\dot{V}_j$ are the ground potential rises (GPR) of each segment of branch and each node relative to infinity; $\dot{I}_F$ is the external injection impulse current; $\dot{I}_i$ and $\dot{I}_{Nj}$ are the currents flowing into the Earth for each branch and each node.

Assuming that the GPR of each segment of the branch is equal to the average value of the GPR at both ends, as shown in **Eq. 1**.

$$\dot{\boldsymbol{U}}_i = \frac{\dot{\boldsymbol{V}}_i + \dot{\boldsymbol{V}}_{i+1}}{\mathbf{2}} \tag{1}$$

According to **Eq. 1**, the matrix relation between GPR vector $\dot{\mathrm{U}}$ of branch and GPR vector $\dot{\mathrm{V}}$ of node can be obtained.

$$\dot{\boldsymbol{U}} = \boldsymbol{K}\dot{\boldsymbol{V}} \tag{2}$$

where $\boldsymbol{K}$ is the relationship matrix between the branch and the node. When branch i is associated with node j, the corresponding value is 0.5, otherwise the value is 0.

Assuming that the current distribution on each branch is uniform, and the current at each node is equal to the average value of the branch current connected to it. Similarly, the vector relation of the current flowing into the Earth on nodes and branches can be obtained, as shown in **Eq. 3**.

$$\dot{\boldsymbol{I}}_{\mathbf{N}} = \boldsymbol{K}^{\boldsymbol{T}}\dot{\boldsymbol{I}} \tag{3}$$

where $\boldsymbol{K}^{\mathrm{T}}$ is the transposed matrix of $\boldsymbol{K}$.

The vector $\dot{I}$ of branch current flowing into the Earth and the vector $\dot{U}$ of branch GPR have the constraint relationship of **Eq. 4**.

$$\dot{\boldsymbol{U}} = \boldsymbol{Z}\dot{\boldsymbol{I}} \tag{4}$$

where $\boldsymbol{Z}$ is the impedance matrix of conductor grounding branch. The elements in $\boldsymbol{Z}$ are composed of the self-impedance of each branch and the mutual impedance between branches.

Inverse matrix $\boldsymbol{Z}$ and get **Eq. 5**.

$$\dot{\boldsymbol{I}} = \boldsymbol{Y}_{\mathbf{B}}\dot{\boldsymbol{U}} \tag{5}$$

According to the node voltage equation, **Eq. 6** is obtained.

$$\dot{\boldsymbol{I}}_{\mathbf{F}} - \dot{\boldsymbol{I}}_{\mathbf{N}} = \boldsymbol{Y}_{\mathbf{N}}\dot{\boldsymbol{V}} \tag{6}$$

where Y_N is the node admittance matrix composed of the resistance and inductance of each branch.

Eq. 7 can be obtained by **Eqs 2**, **3**, **5**, and **6**.

$$\dot{\boldsymbol{I}}_{\mathbf{F}} = \left(\boldsymbol{K}^{\mathrm{T}}\boldsymbol{Y}_{\mathbf{B}}\boldsymbol{K} + \boldsymbol{Y}_{\mathbf{N}}\right)\dot{\boldsymbol{V}} \tag{7}$$

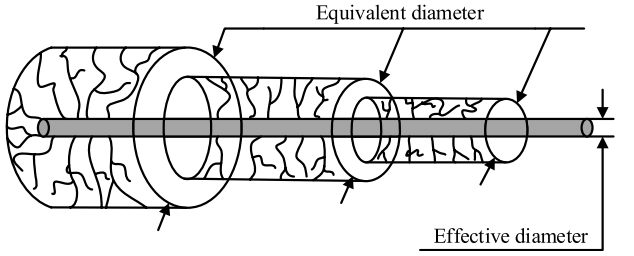

FIGURE 2 | Physical model of spark discharge field of soil around grounding electrode.

According to **Eq. 7**, the vector $\dot{V}$ of node GPR can be obtained, and the vector $\dot{U}$ of branch GPR and the vector $\dot{I}$ of branch current flowing into the Earth are obtained by **Eqs 2**, **5**.

It is required to solve the impulse response curve of grounding electrode in the time domain. Firstly, the pulse current in the time domain is decomposed into a plurality of sinusoidal alternating currents with different frequencies by fast Fourier transform (FFT). Under the action of current with different frequencies, the corresponding branch admittance matrix Y_B and node admittance matrix Y_N can be solved, thereby obtaining vector values of voltage and current. Finally, the frequency domain response is transformed into the corresponding time domain response through the inverse Fourier transform, and the impulse response curve of parameters such as branch GPR and current flowing into Earth can be obtained.

Iterative Algorithm Considering Spark Discharge Effect

In order to consider the influence of spark discharge effect on the impulse characteristics of grounding electrode, it is assumed that the spark discharge area generated around each branch of the grounding electrode is a cylinder with uniform ionization. The equivalent model of grounding electrode during discharge is shown in **Figure 2** (Shen and Raksincharoensak, 2021a; Shen and Raksincharoensak, 2021b).

Under the influence of sinusoidal alternating current at different frequencies, the grounding electrode surface and the surrounding soil will produce different electric field intensities $E_i(\omega)$ and current densities $J_i(\omega)$, as shown in **Eq. 8**.

$$\boldsymbol{J_i(\omega) = \frac{E_i(\omega)}{\rho} + j\omega\varepsilon E_i(\omega)} \tag{8}$$

where ρ is the soil resistivity; ω is the angular frequency of the sinusoidal alternating current; ε is the dielectric constant of the soil.

The current density of the grounding electrode surface can be determined by the branch current flowing into the Earth. According to **Eq. 8**, the relationship between the electric field intensity $E_i(\omega)$ and the equivalent radius r of spark discharge can be obtained as shown in **Eq. 9** (Shen et al., 2022).

$$\boldsymbol{E_i(\omega) = \frac{I_i(\omega)}{2\pi r l\left(1/\rho + j\omega\varepsilon\right)}} \tag{9}$$

The instantaneous value of electric field intensity in time domain is calculated by inverse Fourier transform of soil electric field intensity $E_i(\omega)$ around grounding electrode in frequency domain. By simplifying, the relationship between the equivalent radius $r_i(t)$ of the grounding electrode spark discharge and its surrounding soil electric field intensity $E_i(t)$ in the time domain is shown in **Eq. 10**.

$$\boldsymbol{\frac{r_i(t)}{r} = \frac{E_i(t)}{E_C}} \tag{10}$$

where $r_i(t)$ is the equivalent radius of the branch i; r is the real radius of the grounding electrode; E_c is the critical breakdown field strength of soil. If $E_i(t) > E_c$, the soil around the grounding electrode is broken down, resulting in spark discharge. The equivalent radius of the branch is calculated by **Eq. 10**. If $E_i(t) \le E_c$, it is calculated according to the real radius r.

With the change of equivalent radius $r_i(t)$, the self-admittance parameter in the grounding branch admittance matrix Y_B changes, thereby affecting the change of branch current flowing into the Earth. At the same time, the flowing current will change the value of the equivalent radius. The two interact, and the change of its value is an iterative process. The simulation calculation process is shown in **Figure 3**. The $k(t)$ is the ratio of the estimated branch GPR vector $\dot{U}$, which can be solved by the constraint condition that the sum of the currents $\dot{I}$ flowing into the Earth at each moment is equal to the sum of the node impulse currents $\dot{I}_F$. The e is the convergence criterion of the iterative algorithm, namely the difference $\Delta r_{i\max}(t)$ of the maximum radius between the equivalent radius $r_i(t)$ mth

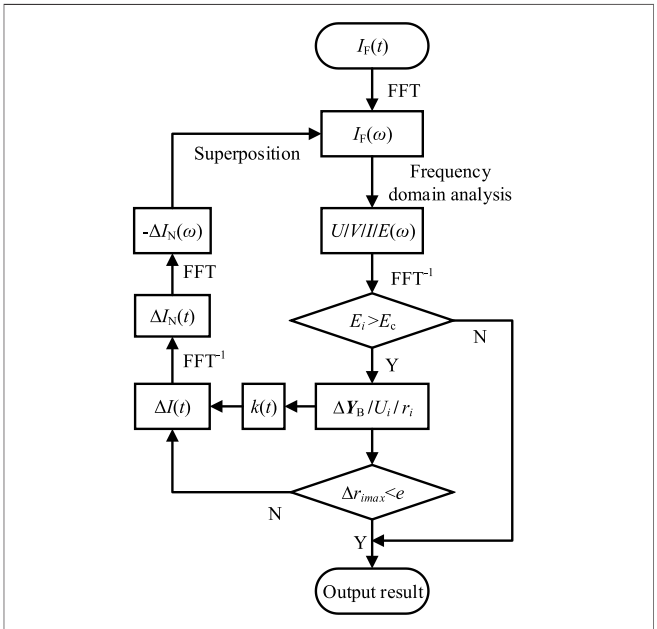

FIGURE 3 | Equivalent radius iterative algorithm flow chart.

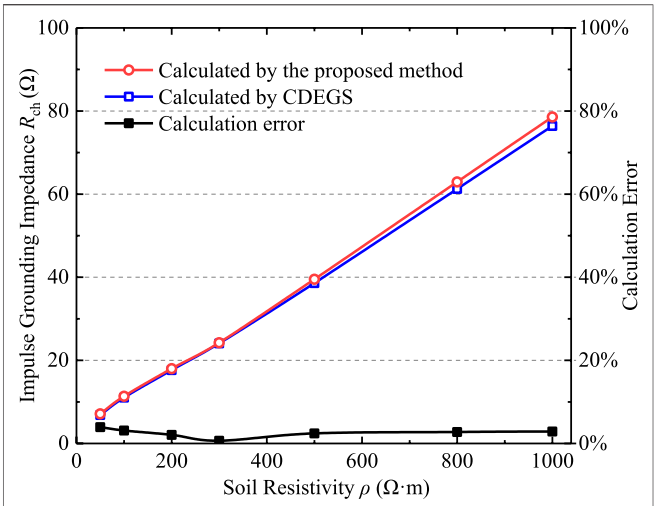

FIGURE 4 | Impulse grounding impedance curve without considering spark discharge effect.

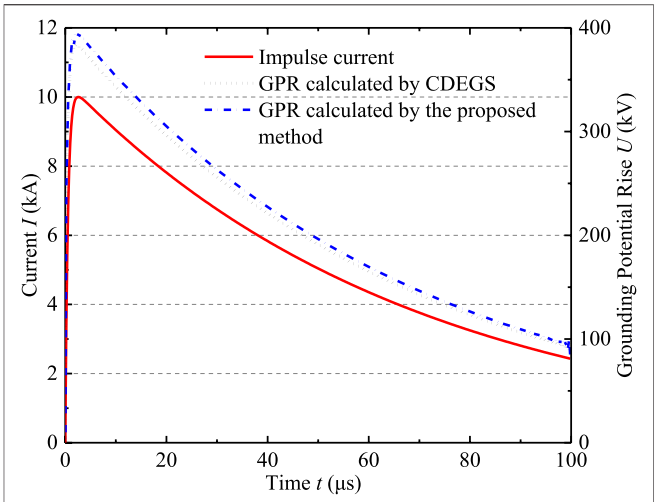

FIGURE 5 | Voltage response curve of grounding electrode when ρ is 500 Ω m.

iteration and the (m-1)th iteration. If the equivalent radius converges, the calculation result is directly output. Otherwise, the branch current variation $\Delta I_i(t)$ and node current variation $\Delta I_{Nj}(t)$ are obtained by the equivalent radius. The frequency domain value $\Delta I_{Nj}(\omega)$ is obtained by Fourier transform and superimposed into the reduction of external impulse current on the impulse current of the previous iteration. The simulation is continuously iteratively calculated until the equivalent radius converges.

VERIFICATION OF SIMULATION RESULTS

In order to verify the effectiveness of the frequency domain electrical network model and its iterative algorithm simulation results, the calculation results of this paper are compared with the calculation results of CDEGS grounding simulation software and the experimental results in the literature. Both simulations and experiments adopt round steel grounding electrodes. The grounding electrode radius is 10 mm, the length of grounding electrode is 20 m, the buried depth is 0.8 m, the impulse current waveform is 2.6/50 μs, the amplitude is 10 kA, the relative dielectric constant of sold is 9, and the soil critical breakdown field strength E_c is 400 kV/m (Mousa, 1994).

Without considering the effect of spark discharge, the variation curve of impulse grounding impedance R_{ch} of grounding electrode under different soil resistivities is obtained by frequency domain electrical network model simulation. The calculation results are compared with the simulation results of CDEGS, as shown in **Figure 4**.

The simulation results in this paper are basically consistent with the laws of CDEGS calculations, and the maximum error is less than 4%. **Figure 5** shows the time-domain voltage response curve of the grounding electrode when the soil resistivity ρ is 500 Ω m. It can be seen that the proposed method has good consistency with the calculation results of CDEGS, indicating that the calculation method of frequency domain electrical network model proposed in this paper is correct.

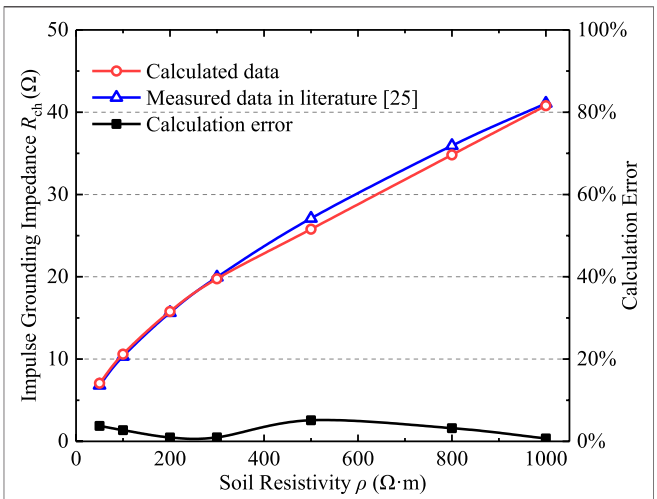

FIGURE 6 | Impulse grounding impedance curve considering spark discharge effect.

Moreover, this paper uses the equivalent radius iterative algorithm to simulate the soil discharge process, and compares its calculation results with the simulation results in literature (He et al., 2003), as shown in **Figure 6**. Affected by different soil resistivity, the impulse grounding impedance calculated by the equivalent radius iterative algorithm proposed in this paper is similar to the simulation experiment in literature (He et al., 2003), and the maximum error is less than 6%.

The calculated results of 20 m horizontal grounding electrode in soil with resistivity of 1,000 Ω m are compared with the results obtained from the full-scale experiments by Wen *et al* (Yang et al., 2022) in **Table 1**, where α is the impulse

TABLE 1 | Comparison with the impulse coefficient α of the experiment.

Impulse current	2 kA	4 kA	6 kA	8 kA
He et al. (2003)	0.63	0.59	0.57	0.55
Wen *et al.* (Yang et al., 2022)	0.68	0.59	0.55	0.52
calculated data	0.72	0.62	0.56	0.52

TABLE 2 | Material parameters of the steel and graphite grounding electrode.

Material	Diameter Φ(mm)	Resistivity δ(Ω·m)	Relative permeability ε_r
Steel	12	1.92×10^{-6}	636
Graphite	28	3.25×10^{-5}	1

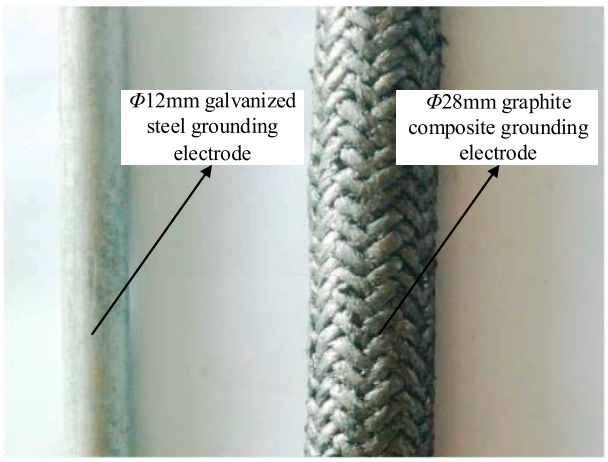

FIGURE 7 | Physical picture of the grounding electrode.

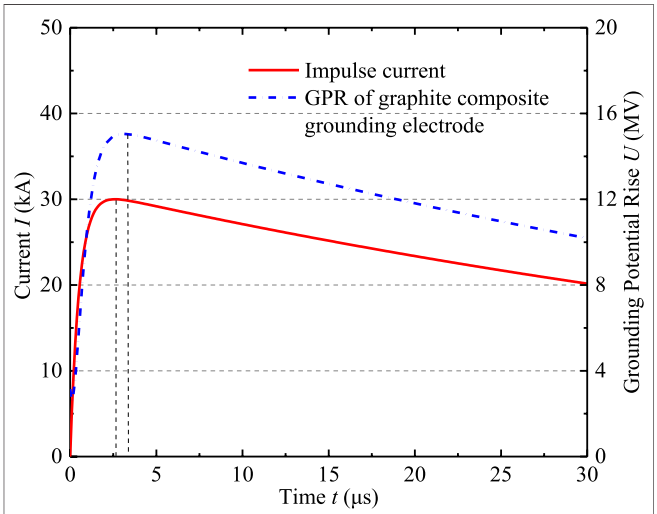

FIGURE 8 | Waveform of grounding potential rise when capacitance effect is dominant.

coefficient, which is equal to the ratio of impulse grounding impedance R_{ch} to power frequency grounding resistance R_g. It can be seen that the calculated results are in good agreement with the experiment results of Wen *et al* (Yang et al., 2022). In general, the proposed simulation models and algorithms are correct, and the results are credible.

EFFECT OF VARIOUS PHYSICAL EFFECTS ON IMPULSE CHARACTERISTICS OF GRAPHITE COMPOSITE GROUNDING ELECTRODES

Under the action of high frequency lightning current and fault current, the grounding grid presents impedance characteristics, including resistance component and reactance component. Therefore, in order to analyze the grounding characteristics of graphite composite grounding materials, the grounding impedance characteristics should be analyzed under the action of alternating current. The physical processes affecting the grounding impedance include skin effect, inductance effect, capacitance effect and spark discharge effect. In this paper, the influence of four physical effects on graphite composite grounding materials is analyzed and calculated. The results are compared with traditional metal grounding materials (galvanized steel). The physical picture and measured parameters of grounding electrode of two materials are shown in **Figure 7** and **Table 2**.

In the simulation, the length of grounding electrode is 10, 30, 60 m, the buried depth is 0.8m, the critical breakdown field strength of soil is 400 kV/m, the lightning current parameter is 2.6/50 μs, and the amplitude is 30 kA. In **Table 2**, Φ is the diameter of grounding electrode; δ is the grounding material resistivity, Ω·m; ε_r is the relative permeability of grounding material.

Capacitance Effect

When only capacitance effect is considered, inductance effect, skin effect and spark discharge effect should be ignored. That is, in the simulation calculation process, the grounding electrode inductance, high frequency resistance and iterative algorithm are not involved in the simulation calculation. The α_C is defined as the impulse coefficient of different soil resistivity. It is found that the impulse coefficients α_C of both materials are less than the value 1, and the maximum error between α_C and value 1 is not more than 0.6%. It shows that capacitance effect can reduce impulse grounding impedance under the impulse current, but the effect is very small.

The capacitance effect will not only reduce the impulse grounding impedance, but also cause the grounding potential rise waveform on the grounding electrode lagging behind the impulse current waveform. **Figure 8** shows the impulse current waveform and grounding potential rise waveform of graphite composite grounding electrode with soil resistivity ρ of 4,000 Ω m and length l of 10 m.

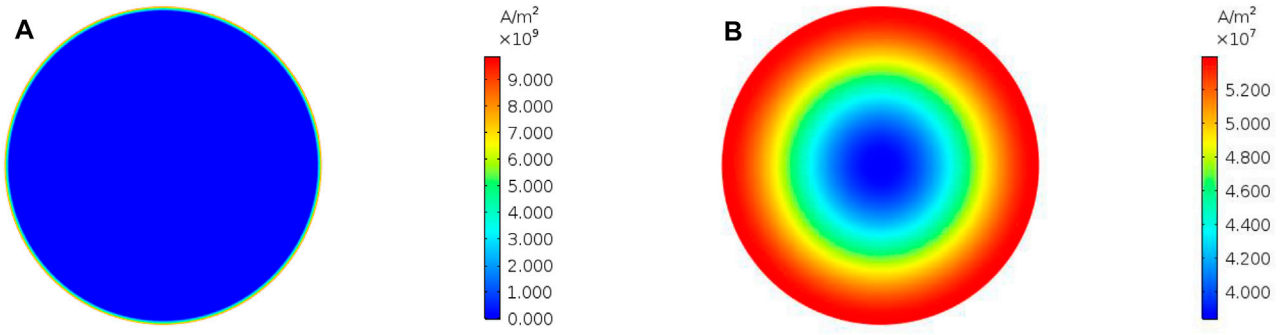

FIGURE 9 | Skin effect of grounding electrodes. **(A)** Current density of Φ12 mm galvanized steel grounding electrode cross section. **(B)** Current density of Φ28 mm graphite composite grounding electrode cross section.

Skin Effect

Finite element numerical calculation method is used to compare and analyze the skin effect of grounding electrodes of different materials in the flow of high frequency current. Galvanized steel grounding electrode of diameter Φ = 12 mm and graphite composite grounding electrode of diameter Φ = 28 mm are applied during simulation according to practical grounding engineering. The current frequency is 100 kHz, and the length l of grounding electrode is 1 m. The simulation results are shown in **Figure 9**.

It can be seen that the current density distribution of galvanized steel grounding electrode is extremely uneven due to skin effect, and the current is mostly concentrated on the external surface of the grounding electrode. This results in a significant reduction in the actual area of current flowing through the grounding electrode. On the contrary, the current density distribution of graphite composite grounding electrode is relatively uniform.

Due to the influence of high frequency current, the cross-sectional area of the actual current flowing through the grounding electrode decreases, thereby increasing the resistance of the grounding electrode. In order to compare and analyze the influence of skin effect on the grounding characteristics of two grounding materials, the resistance R of grounding electrode under different frequencies is used as the influencing factor of skin effect, which can be calculated according to **Eq. 11**.

$$R = \begin{cases} \dfrac{l}{\pi\sigma r^2}, & \delta \geq r \\ \dfrac{l}{\pi\sigma\delta(2r-\delta)}, & \delta < r \end{cases} \tag{11}$$

where σ is the conductivity of the conductor; δ is the radial depth that the current flowing through the grounding electrode can reach due to the skin effect, and is calculated by **Eq. 12**.

$$\delta = \sqrt{\frac{2}{\omega\mu_r\mu_0\sigma}} \tag{12}$$

where μ_0 is vacuum permeability; μ_r the relative permeability of grounding material. The actual lightning current frequency is mostly concentrated in 0–200 kHz. The resistance R of graphite composite grounding electrode and galvanized steel grounding electrode in the unit length can be obtained by calculation. As shown in **Figure 10**, as the frequency increases, the resistance R of galvanized steel grounding electrode increases greatly. In contrast, the increase in resistance of graphite composite grounding electrode is small, which indicates that the graphite composite grounding electrode has less affected by the skin effect under the action of high frequency current.

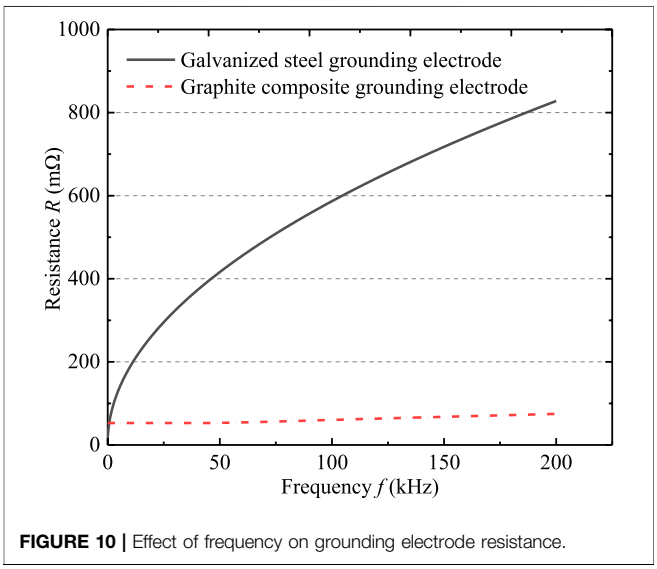

FIGURE 10 | Effect of frequency on grounding electrode resistance.

Considering the capacitance effect, the impulse coefficient α_{sc} and α_c of the grounding electrode at different materials are calculated with and without the skin effect. In order to facilitate the analysis of the influence of skin effect on the grounding electrode impulse characteristics, the influence rate η_s of skin effect on the impulse coefficient is defined. The effect of skin effect on the impulse characteristics of grounding electrode can be solved by **Eq. 13**.

$$\eta_s = (\alpha_{SC} - \alpha_C) \times 100\% \tag{13}$$

TABLE 3 | Influence rate η_s of skin effect (%).

Soil resistivity ρ (Ω·m)	Galvanized steel grounding electrode			Graphite composite grounding electrode		
	10 m	30 m	60 m	10 m	30 m	60 m
50	7.07	42.91	90.68	0.05	0.36	0.92
200	1.81	14.09	41.65	0.01	0.11	0.34
500	0.73	5.88	20.12	0.01	0.04	0.16
1,000	0.35	2.93	10.54	0	0.02	0.06
2000	0.18	1.43	5.22	0	0.01	0.06
4,000	0.02	0.56	2.44	0	0	0.01

The effect rate of skin effect on the grounding electrodes is shown in **Table 3**. It can be seen that the change of impulse coefficient of galvanized steel grounding electrode is greater than that of graphite composite grounding electrode affected by lightning current. The influence of graphite composite grounding electrode is less than 1%.

On the whole, the resistance R of the grounding electrode is related to its length l, and the longer the length l, the larger the resistance R. Therefore, when the length of the grounding electrode is long, the skin effect has a great influence. In high soil resistance area, the lightning grounding current flows through the grounding electrode, and the current flowing to the surrounding soil is small, resulting in large impulse grounding impedance. At this time, the proportion of GPR of grounding electrode in the total GPR is small, so the skin effect is weak.

Inductance Effect

In order to fully consider the influence of the inductance effect, this paper divides the inductance of the grounding electrode into self-inductance and mutual inductance, and the mutual inductance can be obtained by the Neumann equation (Ma et al., 2015). Since the magnetic flux generated by the current through the conductor is respectively closed inside and outside the conductor, the self-inductance is equal to the sum of external self-inductance and inner self-inductance. The external self-inductance L_e can ignore the influence of frequency and it is calculated by **Eq. 14**.

$$L_e = \frac{\mu_0 l}{2\pi}\left(\ln\frac{2l}{r} - 1\right) \tag{14}$$

where μ_0 is vacuum permeability; l is the length of grounding electrode; r is the radius of the grounding electrode. The internal self-inductance L_i is calculated by the low frequency current, as shown in **Eq. 15**.

$$L_i = \frac{\mu_r \mu_0 l}{8\pi} \tag{15}$$

where μ_0 is vacuum permeability; μ_r the relative permeability of grounding material; l is the length of grounding electrode. When the current frequency is high, the internal self-inductance of grounding electrode changes due to skin effect, and is solved according to **Eq. 16**.

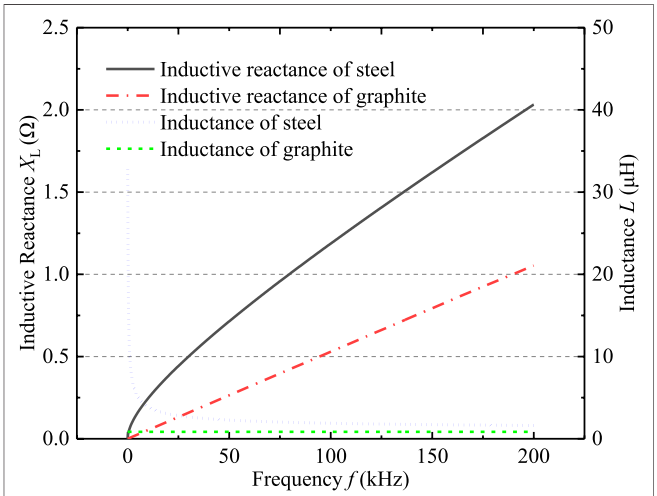

FIGURE 11 | Effect of frequency on the inductance of the grounding electrode.

$$L_i = \frac{l}{2\pi r}\sqrt{\frac{\mu_r \mu_0}{2\omega\sigma}} \tag{16}$$

where μ_0 is vacuum permeability; μ_r the relative permeability of grounding material; l is the length of grounding electrode; r is the radius of the grounding electrode; σ is the conductivity of the grounding electrode. As the sinusoidal alternating current at different frequencies changes, the self-inductance and inductive reactance per unit length of graphite composite grounding electrode and galvanized steel grounding electrode are shown in **Figure 11**.

Under the influence of 0–200 kHz AC current, the inductive reactance of graphite composite grounding electrode is smaller than that of galvanized steel grounding electrode. This is because the galvanized steel grounding electrode is the paramagnetic material, and its magnetic permeability is much larger than that of the graphite composite grounding electrode, resulting in a larger inductance of galvanized steel grounding electrode.

Considering the capacitance effect, skin effect and inductance effect simultaneously, the impulse coefficient α_{SLC} of grounding electrode is calculated, and the influence rate η_L of inductance effect is obtained by **Eq. 17**.

$$\eta_L = (\alpha_{SLC} - \alpha_{SC}) \times 100\% \tag{17}$$

TABLE 4 | Influence rate η_L of inductance effect (%).

Soil resistivity ρ (Ω·m)	Galvanized steel grounding electrode			Graphite composite grounding electrode		
	10 m	30 m	60 m	10 m	30 m	60 m
50	22.83	117.88	194.07	12.51	107.19	164.29
200	1.69	55.6	126.42	0.12	44.53	114.74
500	0.43	18.49	78.21	0.1	8.17	67.76
1,000	0.26	3.56	46.05	0.05	0.22	35.89
2000	0.18	1.02	17.22	0.02	0.08	8
4,000	0.1	0.38	1.88	0.01	0.02	0.13

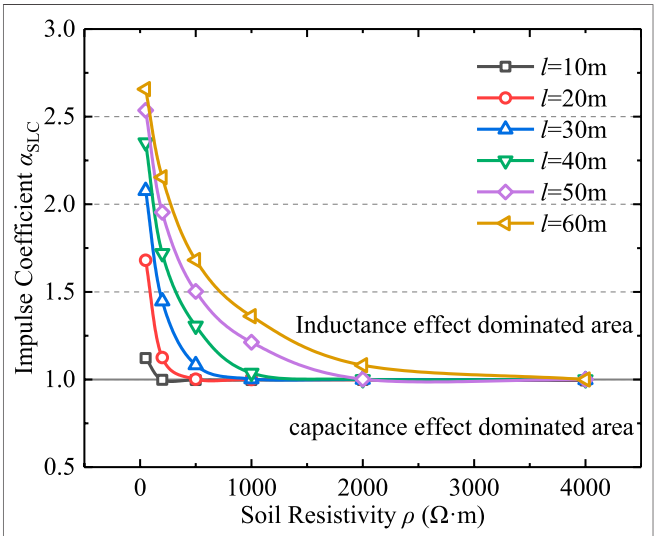

FIGURE 12 | Impulse coefficient of graphite composite grounding electrode without spark discharge effect.

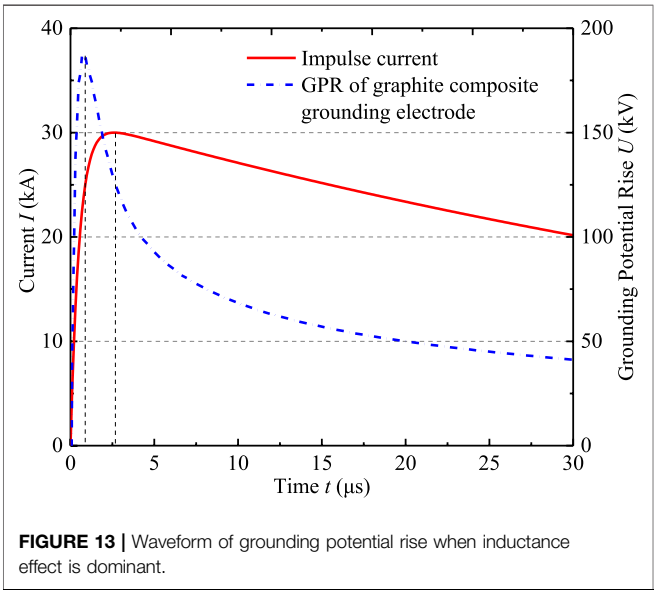

FIGURE 13 | Waveform of grounding potential rise when inductance effect is dominant.

As shown in **Table 4**, the galvanized steel grounding electrode is more affected than graphite composite grounding electrode due to the inductance effect. Overall, the longer the length l of grounding electrode, the stronger the inductance effect, and the greater the obstruction of current flowing to the far position of grounding electrode. With the increase of soil resistivity, the proportion of GPR generated by the inductance of grounding electrode in total GPR decreases. Therefore, the inductance effect of grounding electrode has little effect on its impulse grounding characteristics in the areas with high soil resistivity.

Without considering the spark discharge effect, the variation of impulse coefficient of calculated graphite composite grounding electrode with soil resistivity is shown in **Figure 12**. In most cases, the impulse coefficient α_{SLC} is greater than the value 1. As skin effect has little effect on graphite composite grounding material, it is mainly caused by the inductive effect of grounding electrode. **Figure 13** shows the impulse response curve when the soil resistivity ρ is 50 Ω m and the grounding electrode length l is 60 m. It can be seen that the grounding impedance of grounding electrode presents inductance characteristics, and the GPR waveform is ahead of the impulse current. When the grounding electrode is short or the soil resistivity is high, the impulse coefficient α_{SLC} appears to be less than the value 1. This is because the conductivity of soil is poor, and the influence of inductance effect and skin effect are small. At this time, the grounding capacitance of grounding electrode is involved in the diffusion of high frequency current, resulting in significant capacitance characteristic of impulse grounding impedance, and the impulse grounding impedance is less than power frequency grounding resistance.

Spark Discharge Effect

Under the effect of the impulse current, when the electric field intensity E of the soil around the grounding electrode reaches the critical breakdown electric field intensity E_c of the soil, the soil ionization occurs due to the breakdown. The soil resistivity around the grounding electrode is greatly reduced. An iterative algorithm of equivalent radius of grounding electrode is used to simulate the spark discharge process and calculate the impact grounding impedance of grounding electrode. The influence rate η_D of spark discharge effect is calculated by **Eq. 18**, as shown in **Table 5** and **Table 6**.

$$\eta_D = (\alpha - \alpha_{SC}) \times 100\% \tag{18}$$

TABLE 5 | Influence rate η_D of spark discharge effect (%).

Soil resistivity ρ (Ω·m)	Galvanized steel grounding electrode			Graphite composite grounding electrode		
	10 m	30 m	60 m	10 m	30 m	60 m
50	−33.22	−56.54	−76.1	−19.8	−28.63	−33.33
200	−51.42	−50.36	−75.16	−47.51	−33.37	−45.94
500	−64.68	−43.97	−66.04	−60.51	−31.82	−46.03
1,000	−72.04	−48.11	−58.40	−68.64	−43.44	−44.28
2000	−77.95	−61.24	−50.08	−75.32	−60.52	−40.17
4,000	−82.42	−71.89	−53.09	−79.8	−67.98	−51.8

TABLE 6 | Impulse grounding impedance R_{ch} of different material grounding electrodes (Ω).

Soil resistivity ρ (Ω·m)	Galvanized steel grounding electrode			Graphite composite grounding electrode		
	10 m	30 m	60 m	10 m	30 m	60 m
50	6.77	6.2	5.95	5.96	5.56	5.45
200	14.48	13.9	13.12	13.26	12.32	11.79
500	25.26	23.22	21.82	24.77	20.6	19.53
1,000	39.4	33.6	32.05	39.25	30.34	28.48
2,000	61.35	47.28	46.96	61.58	41.92	41.47
4,000	95.44	66.23	66.01	99.23	67.53	58.34

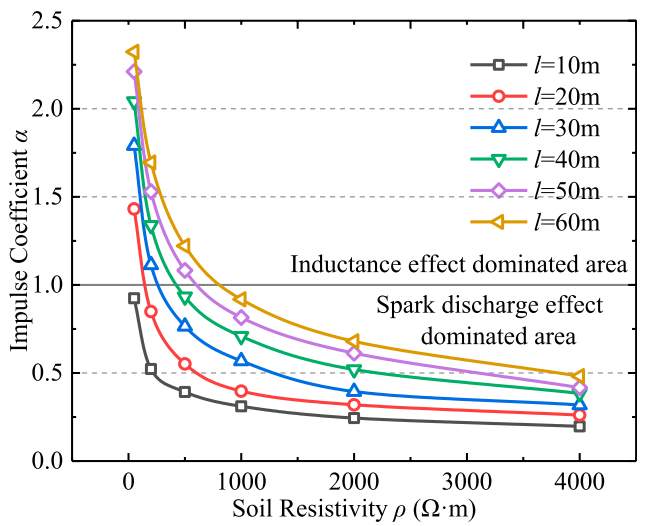

FIGURE 14 | Curve of impulse coefficient of graphite composite grounding electrode.

Where the impulse coefficient α_{SLC} considering capacitance effect, skin effect and inductance effect; the impulse coefficient α considering capacitance effect, skin effect, inductance effect and spark discharge. The spark discharge effect of galvanized steel grounding electrode is slightly better than that of graphite composite grounding electrode, but graphite composite grounding electrode is less affected by inductance effect and skin effect, so it has better current flowing capability. Comparing the impulse grounding impedance, the inductance effect is less affected when the soil resistivity is high and the grounding electrode length is short, and the galvanized steel grounding electrode is greatly affected by the spark discharge effect, resulting in its impulse grounding impedance R_{ch} is smaller than graphite. But as a whole, the impulse grounding impedance of graphite composite grounding electrode is mostly smaller than that of steel. In the actual engineering design of tower grounding engineering, large-size square grounding electrodes with elongated conductors are usually used. The grounding electrode is more affected by inductance effect and skin effect. Therefore, the impulse grounding characteristic of graphite composite grounding electrode is better than that of galvanized steel grounding electrode.

In summary, the inductance effect and skin effect will increase the grounding impedance of the grounding electrode. Conversely, the capacitance effect and sparking discharge effect can reduce the impulse grounding impedance. For graphite composite grounding electrode, the capacitance effect and skin effect have little effect, so this paper only analyzes the influence of inductance effect and spark discharge effect. It can be seen from **Figure 14** that in the low soil resistivity area and the grounding electrode is long, the grounding electrode impulse coefficient α is greater than the value 1. The GPR generated by inductance effect accounts for a large proportion of the total GPR, leading to the inductance effect being dominant. However, as the soil resistivity ρ increases, the impulse coefficient α decreases and the spark discharge effect increases. When α is less than the value 1, the spark discharge effect is more dominant than inductance effect.

OPTIMIZATION OF LENGTH OF FLEXIBLE GRAPHITE COMPOSITE GROUNDING ELECTRODE

In practical engineering applications, in order to improve the current dispersion characteristics of tower grounding grid, the effect of inductance effect should be minimized or the effect of spark discharge effect should be increased to make the spark discharge effect of grounding electrode dominant. According to

TABLE 7 | Computation parameters of lightning current impulse waveform.

Waveform parameter	Front time T_1 (μs)	Time to half value T_2 (μs)	Peak value I_m (kA)
Waveform 1	0.8	48	12
Waveform 2	2.6	50	30
Waveform 3	8	69	30

TABLE 8 | Soil resistivity critical value on which dominant inductance effect switch to spark discharge effect.

Waveform parameter	Critical value of soil resistivity ρ_c (Ω·m)					
	10 m	20 m	30 m	40 m	50 m	60 m
Waveform 1	144	455	824	1,237	1,638	2039
Waveform 2	41	138	263	428	624	824
Waveform 3	12	53	97	164	238	318

TABLE 9 | Critical value of normalized parameters on which dominant inductance effect switch to dominant spark discharge effect.

Waveform parameter	Normalized parameters S (kA·Ω)					
	10 m	20 m	30 m	40 m	50 m	60 m
Waveform 1	173	273	330	371	393	408
Waveform 2	122	207	263	321	374	412
Waveform 3	35	80	97	123	143	159

the field measurement results of lightning current, this paper selects three kinds of the most common lightning current, the waveforms are shown in **Table 7**.

Waveform 1 is a typical initial waveform of lightning impulse current, which is mainly used to simulate the significant inductance effect. Waveform 2 is the standard lightning current waveform recommended for lightning protection calculation. Waveform 3 is a typical secondary waveform of lightning impulse current, which is mainly used to simulate the significant spark discharge effect.

The impulse coefficient α of graphite composite grounding electrode is calculated under different lightning current waveforms.

According to the fitting of the result curve, the soil resistivity critical value ρ_c was estimated, which is the soil resistivity when the pulse characteristic is converted from the dominance of inductance effect to the dominance of spark discharge effect. As shown in **Table 8**, the inductance effect dominates when the soil resistivity is less than the corresponding critical value, otherwise the spark discharge effect dominates.

In order to facilitate the optimal design of grounding electrode, it is necessary to make a general quantitative description of the dominant range of inductance effect and spark effect. Therefore, the normalization parameter S is defined as the quantitative criterion of conversion, which can be calculated by **Eq. 19**.

$$S = \frac{\rho_C I_m}{l} \tag{19}$$

According to **Table 9**, when the soil resistivity ρ and the lightning impulse current front waveform time T_1 and the peak value I_m are known, the appropriate grounding electrode length l can be selected to ensure that the impulse characteristics are always dominated by spark discharge effect, so as to reduce the impulse impedance. For example, when the soil resistivity ρ is 500 Ω m and the lightning current is waveform 2, the grounding electrode length l is selected as 40 m, and the corresponding normalized parameter S is 375 kA Ω, which is larger than the 321 kA Ω in **Table 9**. The spark discharge effect dominates, and the impulse grounding impedance R_{ch} is smaller than the power frequency grounding resistance R_g. Meanwhile, in order to facilitate engineers to conservatively estimate the impulse characteristics of graphite composite grounding electrode, the maximum value of 412 kA Ω in **Table 9** is taken as the critical value of normalized parameter for converting inductance effect into spark discharge effect. It should be pointed out that the above conclusion is determined according to the soil critical breakdown field strength E_c of 400 kV/m, which has a certain deviation from the actual E_c value. When E_c>400 kV/m, the corresponding normalized parameter S is larger than the values listed in **Table 9**, and when E_c<400 kV/m, S is smaller than the values in **Table 9**.

CONCLUSION

This paper presents a frequency domain electrical network analysis method to simulate the impulse characteristics of grounding electrodes. The impulse characteristics of typical metal grounding electrode and graphite composite grounding electrode are calculated, and the following conclusions are obtained.

1) Compared with the galvanized steel grounding electrode, the graphite composite grounding electrode has little effect on skin effect and inductance effect, and the graphite composite grounding electrode has better current dispersion ability under the impulse current.
2) The inductance effect and skin effect can increase the grounding impedance of grounding electrode, while the capacitance effect and spark discharge effect can reduce it. However, the capacitance effect is very small compared with the spark discharge effect, which can be ignored.
3) The longer the grounding electrode length, the more obvious the effect of inductance and skin effect. However, with the increase of soil resistivity, the influence of the two decreases, and the spark discharge effect increases and gradually dominates.
4) The normalized parameter S is defined to quantitatively distinguish the influence range of inductance effect and

spark discharge effect. The length of graphite composite grounding electrode can be optimized by critical value *S*, so as to ensure that the impulse characteristics are always dominated by spark effect, and finally the purpose of reducing impulse grounding impedance is achieved. To conservatively estimate the impulse characteristics of grounding electrode, the recommended *S* value is 412 kA Ω as the critical value to convert inductive effect into spark discharge effect (Shen and Raksincharoensak, 2021b).

DATA AVAILABILITY STATEMENT

The original contributions presented in the study are included in the article/Supplementary Material, further inquiries can be directed to the corresponding author.

AUTHOR CONTRIBUTIONS

YH: conceptualization, writing-original draft preparation, software; TH: software; YA: funding acquisition, validation; JF: Simulation and figures; MC: project administration; HX: supervision; WS: supervision; CD: validation.

FUNDING

This manuscript was supported in part by the Natural Science Foundation of China under Grant 51807113, in part by the Natural Science Foundation of Shandong Province under Grant ZR202103040796 and the Natural Science Foundation of Jiangsu Province under Grant SBK2020042717.

REFERENCES

de Lima, A. C. S., and Portela, C. (2007). Inclusion of Frequency-dependent Soil Parameters in Transmission-Line Modeling. *IEEE Trans. Power Deliv.* 22 (1), 492–499. doi:10.1109/tpwrd.2006.881582

Deng, C., Yang, Y., Tong, X., Dong, X., and Peng, Q. (2012). Impulse Characteristics Analysis of Grounding Devices. *High Voltage Eng.* 38 (9), 1–8. doi:10.3969/j.issn.1003-6520.2012.09.044

Deng, C., Yang, Y., Dong, X., Ma, S., Peng, Q., and Wang, X. (2013). Development of Impulse High Current Testing System of Grounding Devices and Testing of tower Grounding Impulse Characteristics. *High Voltage Eng.* 39 (6), 1527–1535. doi:10.3969/j.issn.1003-6520.2013.06.035

Feng, Z., Wen, X., Tong, X., Lu, H., Lan, L., and Xing, P. (2015). Impulse Characteristics of Tower Grounding Devices Considering Soil Ionization by the Time-Domain Difference Method. *IEEE Trans. Power Deliv.* 30 (4), 1906–1913. doi:10.1109/tpwrd.2015.2425419

Gazzana, D. S., Bretas, A. S., Dias, G. A. D., Telló, M., Thomas, D. W. P., and Christopoulos, C. (2014). The Transmission Line Modeling Method to Represent the Soil Ionization Phenomenon in Grounding Systems. *IEEE Trans. Magn.* 50 (2), 103–107. doi:10.1109/tmag.2013.2283714

Gong, R., Ruan, J., Hu, Y., Wu, Y., and Jin, S. (2016). "Research on Flexible Graphite-Copper Composited Electrical Grounding Material," in Proceeding of the 12th IET International Conference on AC and DC Power Transmission (ACDC 2016), Beijing, China (IEEE), 1–6. doi:10.1049/cp.2016.0403

Grcev, L. (2009). Time- and Frequency-dependent Lightning Surge Characteristics of Grounding Electrodes. *IEEE Trans. Power Deliv.* 24 (4), 2186–2196. doi:10.1109/tpwrd.2009.2027511

Grcev, L. (2009). Impulse Efficiency of Ground Electrodes. *IEEE Trans. Power Deliv.* 24 (1), 441–451. doi:10.1109/tpwrd.2008.923396

He, J., Zeng, R., Tu, Y., Zou, J., Guan, S., and Guan, Z. (2003). Laboratory Investigation of Impulse Characteristics of Transmission tower Grounding Devices. *IEEE Trans. Power Deliv.* 18 (3), 994–1001. doi:10.1109/tpwrd.2003.813802

He, J., and Zhang, B. (2015). Progress in Lightning Impulse Characteristics of Grounding Electrodes with Soil Ionization. *IEEE Trans. Ind. Applicat.* 51 (6), 4924–4933. doi:10.1109/tia.2015.2427124

Hu, Y., An, Y., Xian, R., Li, H., Ruan, J., Huang, D., et al. (2016). "Study on Magnetic Properties of Flexible Graphite Composite Grounding Material," in Proceeding of the 2016 IEEE International Conference on High Voltage Engineering and Application, Chengdu, China, Sept. 2016 (IEEE), 1–4. doi:10.1109/ICHVE.2016.7800753

Hu, Y., Ruan, J., Gong, R., Liu, Z., Wu, Y., and Wen, W. (2014). Flexible Graphite Composite Electrical Grounding Material and its Application in tower Grounding Grid of Power Transmission System. *Power Syst. Technol.* 38 (10), 2851–2857. doi:10.13335/j.1000-3673.pst.2014.10.037

Huang, D., Xia, J., Ruan, J., Wu, Y., and Quan, W. (2019). Characteristics of the Flexible Graphite Grounding Material and its Engineering Application. *IEEE Access* 7, 59780–59787. doi:10.1109/access.2019.2913558

Lorentzou, M. I., Hatziargyriou, N. D., and Papadias, B. C. (2003). Time Domain Analysis of Grounding Electrodes Impulse Response. *IEEE Trans. Power Deliv.* 18 (2), 517–524. doi:10.1109/tpwrd.2003.809686

Ma, Z., Zhou, X., Shang, Y., and Zhou, L. (2015). Form and Development Trend of Future Distribution System. *Proc. CSEE* 35 (6), 1289–1298. doi:10.13334/j.0258-8013.pcsee.2015.06.001

Mentre, F. E., and Grcev, L. (1994). EMTP-based Model for Grounding System Analysis. *IEEE Trans. Power Deliv.* 9 (4), 1838–1849. doi:10.1109/61.329517

Mousa, A. M. (1994). The Soil Ionization Gradient Associated with Discharge of High Currents into Concentrated Electrodes. *IEEE Trans. Power Deliv.* 9 (3), 1669–1677. doi:10.1109/61.311195

Nekhoul, B., Labie, P., Zgainski, F. X., Meunier, G., Morillon, F., and Bourg, S. (1996). Calculating the Impedance of a Grounding System. *IEEE Trans. Magn.* 32 (3), 1509–1512. doi:10.1109/20.497536

Shen, X., Ouyang, T., Khajorntraidet, C., Li, Y., Li, S., and Zhuang, J. (2022). Mixture Density Networks-Based Knock Simulator. *Ieee/asme Trans. Mechatron.* 27, 159–168. doi:10.1109/TMECH.2021.3059775

Shen, X., and Raksincharoensak, P. (2021a). Pedestrian-aware Statistical Risk Assessment. *IEEE Trans. Intell. Transport. Syst.*, 1–9. doi:10.1109/TITS.2021.3074522

Shen, X., and Raksincharoensak, P. (2021b). Statistical Models of Near-Accident Event and Pedestrian Behavior at Non-signalized Intersections. *J. Appl. Stat.*, 1–21. doi:10.1080/02664763.2021.1962263

Tao, S., Zhang, X., Wang, Y., and Yang, J. (2018). Transient Behavior Analysis of Offshore Wind Turbines during Lightning Strike to Multi-Blade. *IEEE Access* 6, 22070–22083. doi:10.1109/access.2018.2828043

Visacro, S., and Rosado, G. (2009). Response of Grounding Electrodes to Impulsive Currents: An Experimental Evaluation. *IEEE Trans. Electromagn. Compat.* 51 (1), 161–164. doi:10.1109/temc.2008.2008396

Wen, X., Feng, Z., Lu, H., Tong, X., Lan, L., Chen, W., et al. (2016). Sparkover Observation and Analysis of the Soil under the Impulse Current. *IET Sci. Meas. Tech.* 10 (3), 228–233. doi:10.1049/iet-smt.2015.0082

Xiao, W., Hu, Y., Ruan, J., Zhan, Q., and Huang, D. (2017). Flexible Graphite Composite Electrical Grounding Material and its Grounding Application Features. *Power Syst. Technol.* 32 (2), 85–94. doi:10.19595/j.cnki.1000-6753.tces.2017.02.010

Yang, N., Yang, C., Xing, C., Ye, D., Jia, J., Chen, D., et al. (2021). Deep Learning-based SCUC Decision-making: An Intelligent Data-driven Approach with Self-learning Capabilities. *IET Generation Trans. Dist* 16, 629–640. doi:10.1049/gtd2.12315

Yang, N., Yang, C., Wu, L., Shen, X., Jia, J., Li, Z., et al. (2022). Intelligent Data-Driven Decision-Making Method for DynamicMultisequence: An

E-Seq2Seq-Based SCUC Expert System. *IEEE Trans. Ind. Inf.* 18, 3126–3137. doi:10.1109/TII.2021.3107406

Zhang, X. (2018). Computation of Lightning Transients in Large Scale Multiconductor Systems. *IEEE Access* 6, 76573–76585. doi:10.1109/access.2018.2883385

Conflict of Interest: TH, MC, HX, WS and CD are employed by Construction Branch of State Grid Jiangsu Electric Power Co., Ltd.

The remaining authors declare that the research was conducted in the absence of any commercial or financial relationships that could be construed as a potential conflict of interest.

Publisher's Note: All claims expressed in this article are solely those of the authors and do not necessarily represent those of their affiliated organizations, or those of the publisher, the editors and the reviewers. Any product that may be evaluated in this article, or claim that may be made by its manufacturer, is not guaranteed or endorsed by the publisher.

frontiers in Energy Research

BRIEF RESEARCH REPORT
published: 18 March 2022
doi: 10.3389/fenrg.2022.873602

Data-Driven Traction Substations' Health Condition Monitoring via Power Quality Analysis

Jingyi Xie *

College of Electrical Engineering and New Energy, China Three Gorges University, Yichang, China

Electrified railway traction substations are an important part of the transportation system, the health of its operation condition indirectly affects the national economy. Generally, traction substations' conditions are studied from their power quality, while the nonlinearity of loads and effects from the outside environment are factors mainly affecting the accuracy of condition monitoring. In order to recognize the status of traction substations intelligently and govern them with fast measurements, this paper proposed a data-driven approach for recognizing types of power quality problems, and developed a system with intelligent governance strategies. The proposed approach contains two parts. Firstly, a double discrete Fourier transform (DDFT) algorithm was developed to extract valid feature vectors from power data. Then, a well-known data-driven method, support vector machine (SVM), was applied to build classifiers. Finally, based on classification results, a strategy library for power quality problems was built. Industrial data of a real traction substation in Wuhan, China, was tested for the experiment. Compared with traditional methods, the proposed approach is validated to be useful in improving the classification performance of power quality problems, and fast and effective for governance in traction substations.

Keywords: data-driven, condition monitoring, traction substation system, power quality analysis, DDFT

OPEN ACCESS

Edited by:
Zhenhao Tang,
Northeast Electric Power University, China

Reviewed by:
Zhe Wang,
North China Electric Power University, China
Heming Huang,
Wuhan University, China

****Correspondence:***
Jingyi Xie
jingyiyxie@gmail.com

Specialty section:
This article was submitted to Smart Grids, a section of the journal Frontiers in Energy Research

Received: *11 February 2022*
Accepted: *15 February 2022*
Published: *18 March 2022*

Citation:
Xie J (2022) Data-Driven Traction Substations' Health Condition Monitoring via Power Quality Analysis. Front. Energy Res. 10:873602. doi: 10.3389/fenrg.2022.873602

INTRODUCTION

As the major infrastructure in transportation systems, electrified railway traction substations are a powerful guarantee for national economic development and social progress (Hu et al., 2017). Due to the electric locomotive being a type of nonlinear load, it has nonlinearity, impact, and asymmetric distribution features in three phases of power electricity. Currently, there are serious challenges in the process of maintaining the power quality traction substation, guaranteeing the safe and stable operation of electrified railway (Hu et al., 2016). For example, the major power quality problems faced by traction substations include harmonics, voltage fluctuations, flicker, as well as negative-sequence current (Bitoleanu et al., 2016). These problems seriously reduced the power quality of both traction substations and superior power systems, and subsequently impact the safety and economic operation of the power system (Liu and Hu, 2017). Therefore, to ensure the stable power supply of traction substation systems and the safe operation of electrified railway, monitoring their health status and making targeted compensation measures are very important.

Power quality problems are dangerous not only to the traction power system but also to other power systems. Currently, the study of power quality problem analyses in literature are mainly based on voltage signals (Khadkikar et al., 2017), for example, voltage analysis via Fourier transformation, wavelet analysis, and so on. Considering the particularity of traction

substations, higher computation speed is required to guarantee the real-time decision-making. It is not feasible to analyze the entire signal sequence as the object. Currently, according to global research, mathematical transformations were commonly used in power quality detection, such as the short-time Fourier transform, wavelet transform, s-transform, and bilinear time-frequency transform (De Yong et al., 2015; Mahela et al., 2015; Shen et al., 2022). Then, the transformed features have been utilized for fast and effective analysis. These transformation methods achieve some positive results to a certain extent. However, taking the actual requirements of rapid compensation in traction power quality into account, these methods still have some restrictions in practical applications, e.g. their complex calculations. On the other hand, according to the results of power quality analysis, how to make timely and effective control measures is also essential to traction substation systems. In power quality governance measures, the mixed compensation methods are usually applied, namely the coordinated control of fixed units and dynamic compensation devices (Mikkili and Panda, 2015; Lam et al., 2017). However, the power quality governance of traction substations is different from that of traditional power systems. It has something to do with the real-time operation status, and is related to factors such as weather, geographical distribution and so on, so it is a typical non-stationary random process. As the intelligent scheduling requirements have been proposed in recent years, when and what types of compensation methods are the major questions. Therefore, an intelligent governance system for a traction substation is required to solve power quality problems.

Aiming to tackle the mentioned issues above, in order to solve power quality problems in electrified railway traction substations intelligently, fast, and effectively, an intelligent system for substations' power quality problems is proposed based on data-driven method in this paper. It is mainly based on Double Discrete Fourier Transform (DDFT) with a sliding window and intelligent classification methods. Contributions of the proposed method are summarized as follows. First, considering power quality problems vary with time, only the latest period of data is used to analyze the power quality problem in this paper, instead of using a long sequence of historic data to extract features in traditional transformation methods. Meanwhile, a sliding window is proposed to guarantee the analysis process in real time. Second, in order to ensure less information is lost in the sliding window, DDFT is applied in the features analysis. DDFT can not only extract the basic physical characteristics of power quality at the first level as other transformation methods do, but also analyze the historical variation characteristics at the second level. In this way, less information will be lost, and the dimension of analyzed variables will not be increased dramatically. So DDFT could facilitate the rapid detection of power quality problems in traction substations. Third, advanced machine learning models are built for multi-category classification, they can be used to establish the power quality governance system combined with the expert system model. Then, in the power quality governance of real traction substations, the proposed system could analyze the power quality problems rapidly, then make a fast decision automatically based on the strategies library, and finally realize the effective governance of traction substation's power quality problems intelligently.

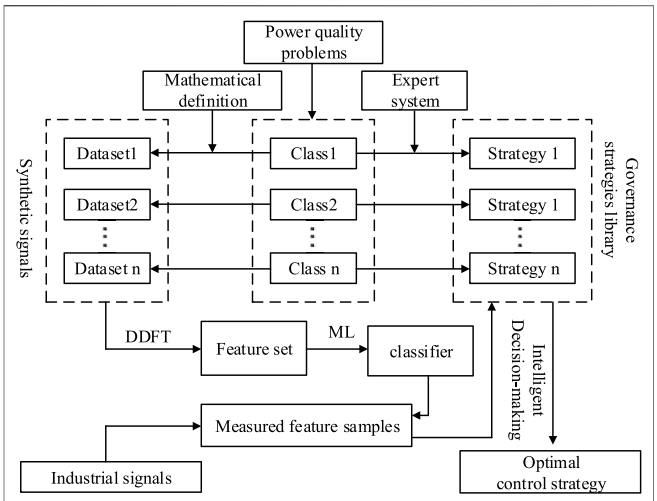

FIGURE 1 | The framework of intelligent governance system.

FRAMEWORK OF THE PROPOSED APPROACH

According to the description above, to maintain the safe and stable operation of electrified railway, the main purpose existing in a traction substation's power quality problems is to build a system for rapid analysis and intelligent governance. This paper proposed an intelligent system based on DDFT and machine learning (ML) algorithms, which mainly consists of two parts: fast detection of power quality problems based on a DDFT algorithm, and intelligent control and targeted governance based on ML. The framework of the main idea of the proposed approach is shown in **Figure 1**.

It can be seen from **Figure 1** that the intelligent governance system can be divided into two parts: the training part and testing part. In the training part, in order to achieve the intelligent and rapid governance system for traction substation, some typical signals of power quality problems are generated firstly based on their mathematical definition models. The frequency-domain features of these power quality samples are extracted through the DDFT algorithm. On the other hand, based on the classes of different power quality problems, the expert system is used to determine their effective control measures or governance strategies, and these strategies consist of the governance library. Finally, taking the extracted features as inputs and the strategies library as the outputs, classification models are built based on ML algorithms. The optimal classifier is applied for the intelligent governance of power quality problems. In the testing part, the application

objects are practical electric railways. The industrial data is often voltage signals of traction substation. The same as the training process, the frequency-domain features of industrial data should be extracted by DDFT at first. Then the feature vectors are input as the optimal classifier for decision-making. The results are the effective strategies based on the classifier and strategies library. Ignoring the classification process of determining what exact types of power quality problems the industrial signal belongs to, the optimal governance strategies can be given out directly according to the proposed system. In this way, it realizes intelligent governance of the traction substation's power quality problems, and keeps the safe operation of electric railways.

INTELLIGENT SYSTEM AND METHODOLOGY

Notion of Power Quality Problems

The operation of electric railway causes several power quality problems to traction substations and outlet substations of power systems, including voltage fluctuation, voltage unbalance, voltage harmonics, and so on (Shen et al., 2021). In order to quantify these problems in practice, models of some common power quality problems including voltage rise, voltage drop, voltage flicker, and transient impact are defined (Singh et al., 2014; Wong et al., 2014; Shi et al., 2016), as expressed in (1–3).

1) Signal of voltage rise and drop

$$f(t) = \begin{cases} \sin(\omega t) & t < t_1, t > t_2 \\ \alpha \sin(\omega t) & t_1 < t < t_2 \end{cases} \tag{1}$$

Where, t_1 and t_2 represent the start and end time of disturbance respectively; ω is the angle frequency of carrier voltage on power frequency; α is the normalized voltage amplitude, when α> 1, $f(x)$ represents the voltage rise signal, when α< 1, $f(x)$ represent the voltage drop signal.

2) Signal of voltage flicker

$$f(t) = \begin{cases} \sin(\omega t) & t < t_1, t > t_2 \\ (A + m\cos\Omega t)\sin(\omega t) & t_1 < t < t_2 \end{cases} \tag{2}$$

Where, m is the amplitude of amplitude-modulated (AM) wave, Ω is the angle frequency of AM wave.

3) Signal of transient voltage

$$f(t) = \begin{cases} \sin(\omega t) & t < t_1, t > t_2 \\ \sin(\omega t) + \sum_{i=2}^{N} A_i \sin(i\omega t + \varphi_i) + Ae^{-\lambda t} & t_1 < t < t_2 \end{cases} \tag{3}$$

It can be seen that the transient voltage consists of multi-frequency signals, such as mutations with damping attenuation $Ae^{-\lambda t}$ and transient high-frequency signals $\sum_{i=2}^{N} A_i \sin(i\omega t + \varphi_i)$, A represents the amplitude and φ_i represents the phase deviation of the ith high-frequency signal. All these components lead to the power quality problems.

Double Discrete Fourier Transformation

According to the analysis of formula (1-3), the definition of power quality problems mainly considers the harmonics in the frequency domain and amplitude characteristics of the time domain. Conventional Fourier transform mainly analyzes signal characteristics from the perspective of frequency domain (Boashash, 2015). However, it has limitation in rapid detection of the traction substation's power quality problems in real-time. Wavelet transformation has the ability to express both time-domain and frequencydomain characteristics (Shen et al., 2020), but it is not easy to choose a suitable mother wavelet. After a comprehensive comparison, on the basis of discrete Fourier transform (DFT), this paper proposed the double discrete Fourier transform (DDFT) as the major tool to solve the electric power quality detection problems of traction substations.

To satisfy the real-time analysis of traction power quality, the DDFT algorithm is developed based on sliding-window iterative DFT (Zhan et al., 2016). Results of DFT usually reflect real-time information in the frequency domain, but they cannot distinguish all the power quality problems, which have an impact on the amplitude of fundamental frequency signals, e.g. voltage rise, voltage drop, and voltage flicker. Therefore, the proposed DDFT algorithm tries to extract fundamental sequences {X (k,t)} from the historical results of DFT transformation. The sequence is then used for Fourier transform for the second time. The purpose of this process is to obtain fundamental frequency information, which can be used to distinguish between temporary voltage rise, drop, and flicker problems.

Figure 2 shows the technological process of DDFT. It can be seen that the original signal is analyzed based on Fourier transformation by taking sliding windows as units. In this way, the computational cost is reduced, and the calculation is speeded up for real-time analysis. After that, the fundamental sequence in the historical windows is extracted at the same size of sliding window, and processed with DFT algorithm once again. Therefore, the DDFT algorithm can not only extract the variation of the fundamental signal and other frequency information, but also maintain the real-time signal analysis, both of which are essential for the power quality analysis in traction substations.

Multi-Classes Classification Based on Machine Learning Models

For a given voltage signal in the traction substation $\{x_n\}$, a series of transformed features are obtained through the DDFT algorithm. To determine the class that the power quality signal belongs to is a must for the decision-making of selecting appropriate control strategies and power compensation devices. This paper generated some typical power quality signals, and extracted their characteristics by DDFT. By regarding the mechanism of identifying power quality problems as the process of choosing a classifier, and collecting feature samples to be used to train the classifier, the classifier would complete the recognition of power quality

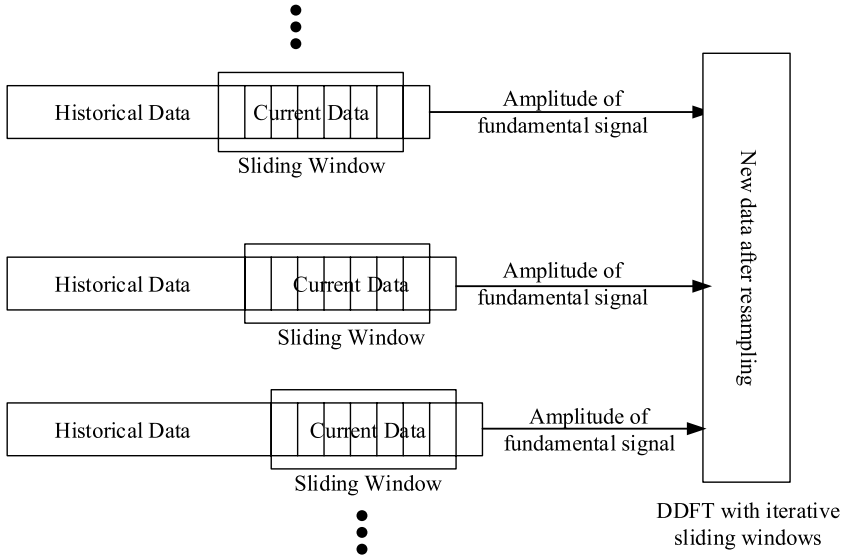

FIGURE 2 | The technological flow of double discrete Fourier transform algorithm.

TABLE 1 | Feature values of different power quality signals.

Feature label	Normal voltage	Voltage rise (20%)	Voltage drop 20%	Voltage flicker	Transient voltage
X0	19.9848	22.4087	17.5729	19.6173	19.9848
X1	0.0194	1.2042	1.2085	0.4559	0.0194
X2	0.0265	0.3623	0.3821	1.2708	0.0265
X3	0.0115	0.2228	0.2498	0.5574	0.0115
X4	0.0195	0.2696	0.2423	0.2507	0.0195

problems. According to the above analysis, this paper applied ML-based algorithms to build the classifier.

EXPERIMENTS AND DISCUSSION

Training Part

1) synthetic power quality signals.

To train an optimal mechanism for power quality governance in a traction substation, the first task is to obtain the training dataset. In this paper, the training data is generated through the definitions of typical power quality problems. According to the definitions in (1-3), 10 sets of power quality signals with different parameters are constructed based on each mathematical definition.

2) Features extraction.

For different types of power quality problems, it is subjective and not applicable to determine the classes that each power quality signal belongs to through by observation directly. It absolutely does not work in the analysis of actual operation of electric railways. In order to discriminate different types of power quality problems quantitatively, the DDFT algorithm is proposed to extract features of voltage signal for fast analysis, instead of the original signal sequences. Due to the amplitude of high-frequency harmonics always being low, to reduce the dimension and computation cost, only the DC component and 5–50 Hz harmonic components are taken as the main feature variables. **Table 1** gives out the feature values of four typical power quality signals.

In **Table 1**, feature values of four typical power quality signals are presented, features of the corresponding original signals are also extracted and displayed. Here, X0 represents the DC component, and X1-X5 represent the 5–50 Hz harmonic components, respectively. It is seen that voltage rise and drop signals mainly reflect difference with other signals on the DC component and 5 Hz harmonics component. The voltage flicker signals mainly have some influence on the 10 Hz harmonics component. For more thorough feature analysis, a nonlinear model is required.

3) Establishing classifiers and strategies library.

To build a suitable classification model for analyzing power quality problems, the DDFT algorithm is applied to extract feature vectors x_i at first. Taking feature vectors x_i = [X (0,t), X (1,t), ⋯X (N-1,t)] as inputs, the class labels of power quality problems as outputs, different ML classification models are established, such as SVM, ELM, NN (Ouyang, 2021; Ouyang

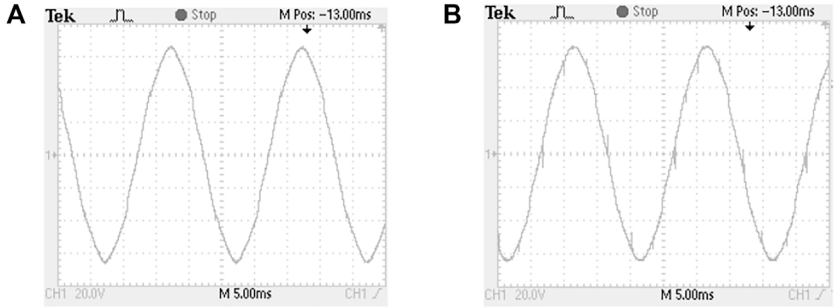

FIGURE 3 | Two signals with typical power quality problems in an actual traction substation.

et al., 2021; Tang et al., 2021). Finally, the optimal ML model is selected. The essence of the proposed method is to construct classifiers based on ML algorithms, and to the constructed classifier to distinguish *power quality* problems automatically.

Testing and Validation Part

According to the above description, some typical power quality signals are generated as training data, and used to build classification models. Meanwhile, the governance strategies are given out according to expert systems and form the strategies library. Then, the intelligent governance system for traction substations' power quality problems is completed by combining classifiers and strategies libraries. In order to validate performance of the proposed system, including how effective it is to use the DDFT algorithm to extract features of power quality problems, the performance of using ML to classify different power quality problems, and the effectiveness and feasibility of the intelligent governance system in traction substation are discussed.

For analyzing the effectiveness of the proposed approach quantitatively, this paper introduces the confusion matrix (Xiong et al., 2017) in performance evaluation. Here, four commonly used indicators are defined in (4), such as Recall (R), Precision (P), Accuracy (Acc), and Error Rate (ER) (Ohsaki et al., 2017).

$$\begin{cases} Acc = \dfrac{TP + \mathrm{T}N}{\mathrm{T}P + \mathrm{F}P + TN + FN} \\ R = TP/(\mathrm{T}P + FN) \\ P = TP/(TP + FP) \\ ER = 1 - Acc \end{cases} \tag{4}$$

In this paper, taking an actual traction substation in Wuhan China as an example, there are in total 1,000 voltage signals collected as the testing dataset. The frequency of these signals is 50Hz, and each signal has a period of 50 ms. First, necessary data preprocessing is needed, and the dataset is normalized. Then the power quality problems of the collected signals are tested according to the given intelligent governance system. According to the records of operators in traction substations, the distribution of these signals is displayed as 43 voltage variation, 16 voltage flicker, 19 voltage transient singles and 922 other signals. In other signals, most of the signals are normal signals, and a few of the signals are other undefined signals in this paper. Two typical signals collected from actual traction substations are shown in **Figure 3**.

In **Figure 3**, the variation of voltage signals for two typical power quality problems are shown. **Figure 3A** shows the signal of voltage flicker, and **Figure 3B** shows the impact of transient voltage signal. It is known that it is difficult for operators to determine what power quality problems a collected signal belongs to, and the period of a set of signals is too fast to capture. This is also the reason why an intelligent system is required to be developed for governing the power quality problems in traction substations.

To evaluate the performance of the proposed approach in the classification of power quality problems, 120 sets of actual signals are used for validation. Since normal signals take up more than 90% of the testing datasets, for classifying different types of power quality problems effectively, only 42 sets of normal signals are selected, and combined with other typical signals as the validation dataset. According to the description in **Figure 1**, the validation data is processed by DDFT to extracted feature vectors, then feature vectors are input into the obtained classifier. Based on the classification results, the suitable governance strategies could be determined according to the strategies library to control the harmful effects of power quality problems. In other words, the performance of classifying power quality problems of voltage signals of traction substation is directly related to the performance of the proposed intelligent governance system. Therefore, statistical analysis is completed to discuss the performance of the proposed approach. According to the definitions in **(Eq. 4)**, values of four indicators are shown in **Table 2**.

In **Table2**, the performance of four indicators are presented. For comparison, three ML models using feature vectors extracted from DFT are also analyzed. From the results of **Table 2**, it is seen that all these methods have values of almost 85% on Recall, Precision, and Accuracy indicators, and the classifier based on ELM in power quality problems classification performs the best. Therefore, ELM could be selected for the construction of final intelligent system. On the other hand, comparing the feature vectors from DFT and DDFT, it is seen that the performance has

TABLE 2 | Performance of classification of power quality problems.

	Recall (R)	Precision (P)	Accuracy (Acc)	Error Rate (ER)
DFT + SVM	0.8975	0.8469	0.9249	0.0751
DDFT + SVM	0.9237	0.8705	0.9509	0.0491
DFT + ELM	0.9107	0.8722	0.9433	0.0567
DDFT + ELM	0.9294	0.8903	0.9526	0.0474
DFT + NN	0.9039	0.8688	0.9335	0.0665
DDFT + NN	0.9277	0.8831	0.9494	0.0506

been improved. Therefore, it is validated that the proposed approach has better performance on classification of power quality problems. While, for the governance of traction substations in the real world, the proposed system combined the advanced approach with the control strategies library, therefore it not only achieves a fast and accurate identification of power quality problems, but also makes a fast decision to govern traction substations' power quality by taking the corresponding measures from the strategies library. In this way, the proposed system can realize the intelligent governance of power quality in traction substations and guarantee the safety operation of electrified railways.

CONCLUSION

In this paper, an intelligent system based on data-driven and DDFT is proposed to govern the power quality problems of traction substations. First, definitions of several typical power quality problems are given out, and synthetic voltage signals based on these definitions are generated. By using the proposed DDFT algorithm to extract feature vectors of these signals, it shows that DDFT has advantages at extract features distinguishing different power quality problems. Using the extracted feature vectors as inputs, three ML-based classifiers are built to discriminate three types of power quality problems, and finally ELM is selected. Combined with the control strategies library from an expert system, the intelligent governance of power quality problems in traction substation is completed. The industrial data of actual traction substations were tested with the proposed approach and traditional approach, the numerical results validated the proposed approach improved the performance of classifying power quality problems. It is validated that the proposed system can realize the intelligent and fast governance of power quality problems in traction substations, and can guarantee the safe operation of electricity railways.

DATA AVAILABILITY STATEMENT

The original contributions presented in the study are included in the article/supplementary material, further inquiries can be directed to the corresponding author.

AUTHOR CONTRIBUTIONS

All authors listed have made a substantial, direct, and intellectual contribution to the work and approved it for publication.

REFERENCES

Bitoleanu, A., Popescu, M., and Suru, V. (2016). "Optimal Controllers Design in Indirect Current Control System of Active DC-Traction Substation," in *Power Electronics and Motion Control Conference (PEMC), 2016 IEEE International* (IEEE), 912–917. doi:10.1109/epepemc.2016.7752115

Boashash, B. (2015). *Time-frequency Signal Analysis and Processing: A Comprehensive Reference*. Academic Press.

De Yong, D., Bhowmik, S., and Magnago, F. (2015). An Effective Power Quality Classifier Using Wavelet Transform and Support Vector Machines. *Expert Syst. Appl.* 42 (15), 6075–6081. doi:10.1016/j.eswa.2015.04.002

Hu, H., Gao, S., Shao, Y., Wang, K., He, Z., and Chen, L. (2017). Harmonic Resonance Evaluation for Hub Traction Substation Consisting of Multiple High-Speed Railways. *IEEE Trans. Power Deliv.* 32 (2), 910–920. doi:10.1109/tpwrd.2016.2578941

Hu, K., Liu, Z., Huang, K., Dai, C., and Gao, S. (2016). Improved Differential Evolution Algorithm of Model-based Diagnosis in Traction Substation Fault Diagnosis of High-speed Railway. *IET Electr. Syst. Transportation* 6 (3), 163–169. doi:10.1049/iet-est.2015.0003

Khadkikar, V., Xu, D., and Cecati, C. (2017). Emerging Power Quality Problems and State-Of-The-Art Solutions. *IEEE Trans. Ind. Electron.* 64 (1), 761–763. doi:10.1109/tie.2016.2619663

Lam, C.-S., Wang, L., Ho, S.-I., and Wong, M.-C. (2017). Adaptive Thyristor-Controlled LC-Hybrid Active Power Filter for Reactive Power and Current Harmonics Compensation with Switching Loss Reduction. *IEEE Trans. Power Electron.* 32 (10), 7577–7590. doi:10.1109/tpel.2016.2640304

Liu, Z., and Hu, K. (2017). A Model-Based Diagnosis System for Traction Power Supply System. *IEEE Trans. Ind. Inform.* 13 (6), 2834–2843. doi:10.1109/tii.2017.2735480

Mahela, O. P., Shaik, A. G., and Gupta, N. (2015). A Critical Review of Detection and Classification of Power Quality Events. *Renew. Sustain. Energ. Rev.* 41, 495–505. doi:10.1016/j.rser.2014.08.070

Mikkili, S., and Panda, A. K. (2015). *Power Quality Issues: Current Harmonics*. Taylor & Francis.

Ohsaki, M., Wang, P., Matsuda, K., Katagiri, S., Watanabe, H., and Ralescu, A. (2017). Confusion-matrix-based Kernel Logistic Regression for Imbalanced Data Classification. *IEEE Trans. Knowledge Data Eng.* 29 (9), 1806–1819. doi:10.1109/tkde.2017.2682249

Ouyang, T. (2021). Feature Learning for Stacked ELM via Low-Rank Matrix Factorization. *Neurocomputing* 448, 82–93. doi:10.1016/j.neucom.2021.03.110

Ouyang, T., Marco, V. S., Isobe, Y., Asoh, H., Oiwa, Y., and Seo, Y. (2021). Improved Surprise Adequacy Tools for Corner Case Data Description and Detection. *Appl. Sci.* 11 (15), 6826. doi:10.3390/app11156826

Shen, X., Ouyang, T., Khajorntraidet, C., Li, Y., Li, S., and Zhuang, J. (2022). Mixture Density Networks-Based Knock Simulator. *Ieee/asme Trans. Mechatron.*, 27. 159–168. doi:10.1109/TMECH.2021.3059775

Shen, X., Ouyang, T., Yang, N., and Zhuang, J. (2021). Sample-Based Neural Approximation Approach for Probabilistic Constrained Programs. *IEEE Trans. Neural Netw. Learn. Syst.*, 1–8. doi:10.1109/TNNLS.2021.3102323

Shen, X., Ouyang, T., Zhang, Y., and Zhang, X. (2020). Computing Probabilistic Bounds on State Trajectories for Uncertain Systems. *IEEE Trans. Emerg. Top. Comput. Intell.*, 1–6. doi:10.1109/TETCI.2020.3019040

Shi, S., Xiao, J., Liu, S., Tu, L., Cao, Q., Liang, Y., Zhang, G., and Mao, C. (2016). A Scheme of Dynamic Voltage Restorer to Improve Power Quality in Large Scale Industrial Enterprises. *Jpee* 04 (02), 19–26. doi:10.4236/jpee.2016.42003

Singh, B., Chandra, A., and Al-Haddad, K. (2014). *Power Quality: Problems and Mitigation Techniques*. John Wiley & Sons.

Tang, Z., Zhao, G., and Ouyang, T. (2021). Two-phase Deep Learning Model for Short-Term Wind Direction Forecasting. *Renew. Energ.* 173, 1005–1016. doi:10.1016/j.renene.2021.04.041

Wong, J., Lim, Y. S., Tang, J. H., and Morris, E. (2014). Grid-connected Photovoltaic System in Malaysia: A Review on Voltage Issues. *Renew. Sustain. Energ. Rev.* 29, 535–545. doi:10.1016/j.rser.2013.08.087

Xiong, Y., Zha, X., Qin, L., Ouyang, T., and Xia, T. (2017). Research on Wind Power Ramp Events Prediction Based on Strongly Convective Weather Classification. *IET Renew. Power Generation* 11 (8), 1278–1285. doi:10.1049/iet-rpg.2016.0516

Zhan, J., Cheng, X., Xu, Q., Wu, L., and Chen, G. (2016). "Design of Comprehensive Motor Protector Based on Improved Sliding-Window Iterative DFT Algorithm," in *Power Electronics and Motion Control Conference (IPEMC-ECCE Asia)* (IEEE 8th InternationalIEEE), 3658–3662. doi:10.1109/ipemc.2016.7512881

Conflict of Interest: The author declares that the research was conducted in the absence of any commercial or financial relationships that could be construed as a potential conflict of interest.

Publisher's Note: All claims expressed in this article are solely those of the authors and do not necessarily represent those of their affiliated organizations, or those of the publisher, the editors and the reviewers. Any product that may be evaluated in this article, or claim that may be made by its manufacturer, is not guaranteed or endorsed by the publisher.

frontiers in Energy Research

ORIGINAL RESEARCH
published: 18 March 2022
doi: 10.3389/fenrg.2022.865902

Two-Stage Optimal Location Allocations of DPFC Considering Wind and Load Uncertainty

*Xuedong Zhu, Liu Dichen and Jun Wu**

School of Electrical Engineering and Automation, Wuhan University, Wuhan, China

Distributed power flow controller (DPFC) has a considerable potential to regulate the power flow and generator rescheduling continuously. This study presents a novel two-stage stochastic model for optimal location allocations of the DPFC coupled with the interactions of DPFC to search for the optimal solutions. The Benders decomposition is utilized to reformulate the two-stage problem into the master problem and the subproblem. The optimal solution can be easily obtained with the master problem and subproblem iteratively. The relaxed DC power flow with a DPFC in the master problem accelerates the efficiency of optimal locations under a base condition. Slack variables are incorporated in the subproblem to check the feasibility of relaxed AC power flow. The optimal compensation levels of DPFC at different load/wind scenarios are optimized in the subproblem. The IEEE 118 bus system is conducted to verify the performance of the proposed procedure. The DPFC has positive impacts on unit costs, voltage performance, wind absorption, and power losses. Detailed simulation results illustrate the effect of the proposed approach.

Keywords: distributed power flow controller, relaxed AC-SOCP, Benders decomposition, uncertainty, optimal FACTS

OPEN ACCESS

Edited by:
Xun Shen,
Tokyo Institute of Technology, Japan

Reviewed by:
Hardeep Singh,
Sophia University, Japan
Sahil Sardana,
Indian Institute of Technology Dhanbad, India

****Correspondence:***
Jun Wu
byronwu@whu.edu.cn

Specialty section:
This article was submitted to Wind Energy, a section of the journal Frontiers in Energy Research

Received: *30 January 2022*
Accepted: *11 February 2022*
Published: *18 March 2022*

Citation:
Zhu X, Dichen L and Wu J (2022) Two-Stage Optimal Location Allocations of DPFC Considering Wind and Load Uncertainty. Front. Energy Res. 10:865902. doi: 10.3389/fenrg.2022.865902

1 INTRODUCTION

The existing transmission network can be challenging under the increasing growth of load. There is a congestion problem of power flow that should be mitigated because of the transfer capability limit of transmission lines (Hemmati et al., 2013). Transmission expansion planning (TEP) is one of the effective ways to alleviate congestions (Jabr, 2013). However, there are the characteristics of higher investment and occupation of transmission corridors (Ugranli et al., 2016). It is well known that the flexible AC transmission system (FACTS) can significantly influence the performance of power flow. With the rapid development of electronic technology, the FACTS is considered a strongly effective device to manage power flow (Yuan et al., 2010). It has the capability to control the voltage magnitude or phase angle and provide controllable active or reactive power compensation independently (Khanchi and Garg, 2013). The DPFC (Dai et al., 2019; Tang et al., 2020; Li et al., 2021; Zhang et al., 2021) is derived from the UPFC, which has the same external characteristics, such as voltage support, control of real power flow, and other functions. Compared to the UPFC device, the DPFC shows a great superiority in economy and reliability.

The optimal location and allocations of FACTS have been studied extensively. This research focused on three topics: equivalent injection model, optimization goals, and solution approach. The equivalent injection model is the key to implementing control strategies and improving the solution efficiency. Many exertions have been made in the last few years to establish effective injection models

of FACTS. Based on the voltage source model of unified power flow controller (UPFC), two approaches have been proposed to solve the optimal problem combined with the power injection model (Orfanogianni and Bacher, 2003; Tripathy et al., 2006; Shen et al., 2021a; Shen and Raksincharoensak, 2021a; Shen et al., 2021b; Shen and Raksincharoensak, 2021b), sensitivity analysis–based methods are the first choice to be employed to obtain the candidate of location, and another choice is the optimal power flow (OPF) method. Muwaffaq (Alomoush, 2004) proposed the Π-model of UPFC to maintain the diagnose features of Jacobian matrix based on the port equivalent. A direct model has been proposed (Bhowmick et al., 2008) to simplify the difficulties of UPFC, the existing power system–installed UPFC is transformed into an augmented equivalent network without any UPFC, and the difficulty of Newton Raphson power flow diminishes dramatically due to the absence of UPFC. Many optimization goals with the FACTS injected have been researched intensively. Alomoush (2003), Alomoush (2004), Yang et al. (2021a), Yang et al. (2021b), Yang et al. (2021c), and Yang (2021) leveraged DC power flow to minimize the operating cost with the injection Π-model of UPFC. Sarker and Goswami (2014) minimized the operating cost combined with sensitivity analysis–based methods, and the control values of UPFC and SVC can be directly obtained under the location of PI sensitivity. Several researchers (Verma and Gupta, 2006; Tiwari and Sood, 2012; Tiwari and Sood, 2013; Dawn and Tiwari, 2016) optimized the location allocations of FACTS into social welfare; this goal is to maximize the benefits of all anticipants, that is, to maximize the benefit of power sales and minimize the operating cost of the generator. Furthermore, some researchers use the FACTS to improve the performance of power flow, such as voltage stability (Singh, 2016; Zhang et al., 2020), power loss (Tripathy and Mishra, 2007; Sarker and Goswami, 2014), and transfer capability enhancement (Prasad et al., 2011; Rajabi-Ghahnavieh et al., 2015).

The mathematical formulations of FACTS location allocation are originally non-linear and non-convex because of its mixed integer non-linear programming (MINLP) model. The OPF method is the first approach to solving the MINLP problem. It can be solved by MATPOWER iteratively with the changing Jacobian matrix based on matrix block decompose technology and the injection model of FACTS. Noroozian et al. (1997) reconstructed the modified Jacobian matrix by correlating Jacobian's matrix elements with the control variables of the UPFC load injection model. Pereira and Zanetta (2012) proposed the OPF approach with the control modes based on the voltage source model and power injection model of UPFC. Ebeed et al. (2019) and Vo Tien et al. (2019) established the modified matrix with installing variables of STATCOM or TCSC based on its shunt or series reactance model. The speed of the OPF method is questionable because of iteratively updating the Jacobian matrix. Another popular procedure is the heuristic method of solving the MINLP problem. Saravanan et al. (2007) presented the particle swarm optimization (PSO) technique to search the optimal solution of MINLP with a minimum investment cost of FACTS devices. Hooshmand et al. (2015) proposed a hybrid method that combines the bacterial foraging algorithm with a Nelder–Mead method to solve the MINLP problem. Ranganathan et al. (2016) proposed the self-adaptive firefly algorithm (SAFA) to optimize the power flow performance, such as voltage stability and power loss. However, the difficulties of FACTS injected into the system still exist, and its solving accuracy is difficult to guarantee because of the non-linear and non-convex characteristics of AC power flow. Linear approximation of AC power flow also has been utilized for the MISOCP problem of FACTS. Nikoobakht et al. (2018) proposed a PWL approximation method to transform the MISOCP problem to the MILP problem. Ding et al. (2015), Sahraei-Ardakani and Hedman (2015), and Sang and Sahraei-Ardakani (2017) developed an MILP model due to the robustness and high speed efficiency of the DC power flow. Second-order conic programming (SOCP) (Tang et al., 2018) is another method to solve the MISOCP problem, and the optimal solution of convex optimization is easily obtained despite its non-linearity. However, the characteristic of reactive power is ignored in the DC power flow, whereas the SOCP model (Tang et al., 2018) with the DPFC hardly obtains the optimal solution whose decision variables belong to the open interval.

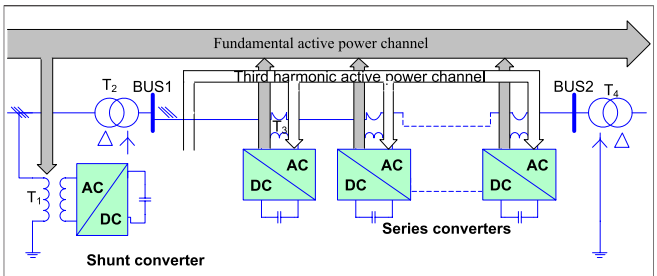

FIGURE 1 | Configuration and principle of the DPFC.

This article develops an equivalent power injection model (PIM) of DPFC considering its active compensation, which not only holds the external characteristic but also can be easily injected to the system. A two-stage MISOCP problem consisting of the operating cost and investment of DPFC is formulated to optimize the location and compensation level of DPFC. The main contributions of this paper can be summarized as follows:

1) The optimization method holds the internal characteristics of DPFC, maintaining the interactions and increasing the consistent performance of scheduling planning.
2) A nested method consisting of the reactive model and the PIM has been developed to optimize the locations and allocations of DPFC simultaneously, where the efficiency and accuracy have been increased.

We demonstrate the effectiveness of the proposed two-stage stochastic problem in the IEEE 118 bus system and insight into the influence on the performance of DPFC. This paper is organized as follows. **Section 2** introduces the equivalent reactive model of DPFC and its operating principle. **Section 3**

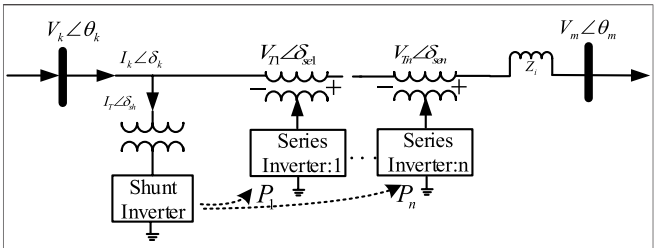

FIGURE 2 | Simplified DPFC circuit diagram.

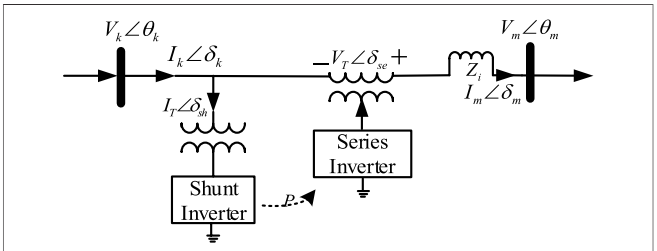

FIGURE 3 | Simplified DPFC model.

presents the two-stage stochastic model of optimal location-allocation problem. **Section 4** describes the two-stage procedure of Benders decomposition method. **Section 5** shows the results and discussion, while the conclusion is presented in **Section 6**.

2 DPFC STEADY-STATE MODEL

A. DPFC Configuration and Principle

The general configuration of the DPFC device includes a shunt converter and multiple series converters, as shown in **Figure 1**. The shunt converter is similar to the shunt component of UPFC, injection power flow into the linked bus. Unlike the unified series component of UPFC with a larger rated capacity, the independent distributed lower capacity series converters of DPFC can provide similar effects based on the superposition theorem. Furthermore, there is a huge difference between the third harmonic characteristics of DPFC and the fundamental wave of UPFC on the principle of power flow control. The UPFC absorbs the fundamental frequency power flow on the shunt side and directly injects it into the series side through VSC1 and VSC2. However, the shunt converter of DPFC absorbs the fundamental frequency power flow and converts it into the third harmonic and then converts it back to the fundamental frequency power flow through the series converters, injected into the system.

Based on the configuration and principle of DPFC, the independent capacity of a single series converter is small, and only after multiple series converters are added, power system requirements can be satisfied. A simplified DPFC circuit diagram can be derived, composed of a shunt inverter and multiple series inverters, as shown in **Figure 2**.

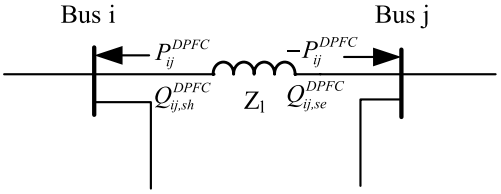

FIGURE 4 | PIM of the DPFC.

Figure 3 illustrates the cascade series inverters of DPFC superimposed into equivalent unified inverters based on the superposition theorem. The cascade DPFC on the series side can be modeled as an independent voltage source. The third harmonic power is nested in the operating condition, and only the base power flow is reflected in the static perspective. Referring to the equivalent voltage source model of UPFC, the following equation describes the equivalent process clearly for the DPFC series side:

$$V_T\angle\theta_{se} = V_{T1}\angle\theta_{se1} + \cdots V_{Tn}\angle\theta_{sen} = \sum_{i=1}^{n} V_{Ti}\angle\theta_{sei}. \tag{1}$$

As shown in **Figure 3**, the equivalent variables $\vec{V}_T$, $\vec{I}_m$, $\vec{I}_T$ are the injected series voltage, the series current, and the shunt current. They can be decomposed into an in-phase voltage/current and quadrature voltage/current as follows:

$$\begin{aligned} \vec{V}_T &= \left(V_p + jV_q\right)e^{j\theta_m}, \\ \vec{I}_T &= \left(I_p + jI_q\right)e^{j\theta_k}. \end{aligned} \tag{2}$$

For the KCL and KVL, the terminal voltage and current can be explained as follows:

$$\begin{aligned} \vec{V}_m &= \vec{V}_k + \vec{V}_T = V_k e^{j\theta_k} + V_p e^{j\delta_m} + V_q e^{j\delta_0}, \\ \vec{I}_m &= \vec{I}_k - \vec{I}_T = I_k e^{j\delta_k} - I_p e^{j\theta_k} - I_q e^{j\theta_k}. \end{aligned} \tag{3}$$

The complex power of both DPFC series inverters and shunt inverts from **Figure 3** is illustrated in **Eqs 6–7**:

$$\begin{aligned} S_{se} &= \vec{V}_T \cdot \vec{I}_m^* = V_p \cdot I_m + jV_q \cdot I_m, \\ S_{sh} &= \vec{V}_k \cdot \vec{I}_T^* = V_k \cdot I_p + jV_k \cdot I_q, \end{aligned} \tag{4}$$

where S_{se} and S_{sh} are the complex power of series/shunt side of the DPFC device.

There is a common similarity between UPFC and DPFC with its external feature of active power balance (Dai et al., 2019), and the active power flow from the shunt side to the series side holds conservation characteristics, as shown by

$$V_k I_p = V_p I_m. \tag{5}$$

Together with **Eqs (4)**, **(5)**.

Combined with the complex power of the DPFC, in both the shunt and the series side with conservative characteristics, reactive power complies with the following equation, reflecting that the DPFC may generate or absorb reactive power after its injection into the power system.

$$S_{sh} - S_{se} = j\left(V_k I_q - V_q I_m\right). \tag{6}$$

Due to the conservation characteristic of active power in the DPFC device, a power injection model (PIM) can be conducted as depicted in **Figure 4**:

$$\begin{aligned} P^*_{ij} &= P_{ij} - P^{DPFC}_{ij}, \\ P^*_{j,rev} &= P_{ij,rev} + P^{DPFC}_{ij}, \end{aligned} \tag{7}$$

where $P_{ij}, P_{ij,rev}$ are the line power and reverse line power and P^{DPFC}_{ij} is the DPFC compensation level.

3 PROBLEM FORMULATION

A. The Relaxed AC-SOCP Model

The AC power flow model can be represented as

$$\begin{aligned} P_{ij}(\theta, V) &= V_i^2 g_{ij} - V_i V_j\left(g_{ij}\cos\left(\theta_i - \theta_j\right) + b_{ij}\sin\left(\theta_i - \theta_j\right)\right), \\ Q_{ij}(\theta, V) &= -V_i^2 b_{ij} - V_m V_n\left(g_{ij}\sin\left(\theta_i - \theta_j\right) - b_{ij}\cos\left(\theta_i - \theta_j\right)\right). \end{aligned} \tag{8}$$

The above traditional model is non-linear. Therefore, the equivalent transformation is introduced to cope with the difficulties of the non-linear problem. Several variables are defined in the following equations:

$$U_i = V_i^2; U_j = V_j^2, \tag{9}$$

$$R_{ij} = U_i U_j cos\left(\theta_i - \theta_j\right); R_{ij} \geq 0, \tag{10}$$

$$T_{ij} = U_i U_j sin\left(\theta_i - \theta_j\right). \tag{11}$$

The combined AC power flow model with **Eqs 8**, **9–11** is relaxed as follows:

$$\begin{aligned} P_{ij} &= g_{ij}U_i - g_{ij}R_{ij} - b_{ij}T_{ij}, \\ Q_{ij} &= -b_{ij}U_i - g_{ij}T_{ij} + b_{ij}R_{ij}, \\ P_{ij,rev} &= g_{ij}U_j - g_l R_{ij} + b_{ij}T_{ij}, \\ Q_{ij,rev} &= -b_{ij}U_j + g_{ij}T_{ij} + b_{ij}R_{ij}. \end{aligned} \tag{12}$$

According to **Eqs 10–11**, a constraint between R_{ij} and T_{ij} must be satisfied as follows:

$$R_{ij}^2 + T_{ij}^2 = V_i^2 V_j^2 = U_i U_j. \tag{13}$$

The above equation is still non-linear due to the quadratic form, and we relax the equality constraint to inequality format which can be transformed into an SOCP form:

$$\left\| \begin{matrix} 2R_{ij} \\ 2T_{ij} \\ U_i - U_j \end{matrix} \right\|_2 \leq U_i + U_j. \tag{14}$$

Thus, the relaxed AC-SOCP model is transformed into an SOCP model with **Eqs 12**, **14**, which can be solved by the commercial solvers such as CPLEX.

B. Two-Stage Stochastic MISOCP Model

The power system planners aim to determine the location allocations of DPFC, which can enhance the management efficiency of power flow and decrease the investment of DPFC. However, the operators desire to minimize the operation cost of injected DPFCs. Therefore, optimal location allocations of DPFC in the power system must consider the operational cost and investment of installing DPFCs. The optimal model is represented by

$$min \sum_{i\in G(i)} c_i P_i^G + \sum_{ij} \pi_{ij}^{DPFC} P_{ij}^{DPFC}, \tag{15}$$

$$\begin{aligned} &\sum_{i\in WG} P_{Wi} + \sum_{i\in G_m} P_{Gi} + \sum_{j\in\xi(i)} P_{ij}^{DPFC} - \sum_{j\in\psi(i)} P_{ij}^{DPFC} - \sum_{i\in G_D} P_{Di} \\ &= \sum P_{ij}(\theta, V, \lambda), \end{aligned} \tag{16}$$

$$0.95* \sum_{i\in WG} P_{Wi} + \sum_{i\in G_m} Q_{Gi} - \sum_{i\in G_D} Q_{Di} = \sum Q_{ij}(\theta, V, \lambda), \tag{17}$$

$$P_{Gi}^{min} \leq P_{Gi} \leq P_{Gi}^{max}, \tag{18}$$

$$Q_{\mathrm{Gi}}^{\min} \leq Q_{Gi} \leq Q_{\mathrm{Gi}}^{\max}, \tag{19}$$

$$V_i^{\min} \leq V_i \leq V_i^{\max}, \tag{20}$$

$$\theta_i^{\min} \leq \theta_i \leq \theta_i^{\max}, \tag{21}$$

$$\begin{aligned} &\begin{cases} P_{ij} = g_{ij}U_i - g_{ij}R_{ij} - b_{ij}T_{ij}, \\ Q_{ij} = -b_{ij}U_i - g_{ij}T_{ij} + b_{ij}R_{ij}, \\ P_{ij,rev} = g_{ij}U_j - g_l R_{ij} + b_{ij}T_{ij}, \\ Q_{ij,rev} = -b_{ij}U_j + g_{ij}T_{ij} + b_{ij}R_{ij}, \end{cases} \\ &T \approx \theta_i - \theta_j, \\ &\left\| \begin{matrix} 2R_{ij} \\ 2T_{ij} \\ U_i - U_j \end{matrix} \right\|_2 \leq U_i + U_j, \end{aligned} \tag{22}$$

$$\left\| \begin{matrix} P_{ij} - P_{ij}^{DPFC} \\ Q_{ij} \end{matrix} \right\|_2 \leq S_{ij}, \tag{23}$$

$$\left\| \begin{matrix} P_{ij,rev} + P_{ij}^{DPFC} \\ Q_{ij,rev} \end{matrix} \right\|_2 \leq S_{ij}, \tag{24}$$

$$0 \leq P_{ij}^{DPFC} \leq \delta_{ij} P_{ij,max}^{DPFC}, \tag{25}$$

$$N^{DPFC} \in \alpha_L. \tag{26}$$

The objective function is to minimize the generation cost and investment cost of DPFC in **Eq. 15**. **Equations 16**, **17** hold the bus balance of active and reactive power. **Equations 18–21** represent the upper bound and lower bound of active power, reactive power, voltage magnitude, voltage angle, and line power, respectively. The active power and reactive power of line with relaxed SOCP power flow are reformulated in **Eq. 22**, and we set the line apparent power constraints with the DPFC in **Eqs 23**, **24**. **Equations 25**, **26** constrain the installation capacity and number of DPFCs.

The formulated MISOCP problem aims to optimize the location and ratings of DPFC under the base level. Once the DPFC is injected into the grid, the device should offer functions under different load–wind conditions with its fixed locations, and the above MISOCP model must cover different scenarios. We develop a two-stage stochastic approach to determine the optimal locations and ratings with a hybrid model of DPFC to accelerate its efficiency.

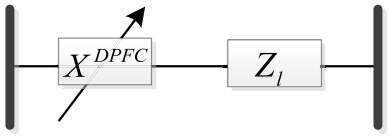

FIGURE 5 | Reactance model of the DPFC.

4 SOLUTION APPROACH

A. DC Power Flow With Reactance Model of DPFC

Based on the conservation of active power and unbalance of reactive power in the DPFC, a reactance model of DPFC can be shown in **Figure 5**.

The equivalent reactance x_{ij}^{DPFC} can be transformed into a function of the connected line's reactance where the DPFC is located:

$$x_{ij}^{\bullet} = x_{ij} + x_{ij}^{DPFC}, \tag{27}$$

$$x_{ij}^{DPFC} = \gamma_{ij} x_{ij}, \tag{28}$$

where γ_{ij} is the compensation level of line between buses i and j and $\gamma_{ij} = \lambda_{ij}/(1-\lambda_{ij})$. Therefore, the reactance with DPFC between buses i and j can be updated as follows:

$$x_{ij}^{\bullet} = x_{ij} \big/ \left(1 - \lambda_{ij}\right). \tag{29}$$

According to **Eq. 6**, the DPFC can absorb or generate reactive power, and the equivalent compensation level of the series reactance of the DPFC bounds the value between −0.2 and 0.7. Consequently, the corresponding linear interval is between −0.17 and 2.33.

The DC power flow approximation is widely used in power planning, which supposes voltage magnitude equal to 1 p.u. and ignores reactive power and resistance of lines because of $r_{ij} \ll x_{ij}$. This can be shown as

$$P_{ij} = \theta_{ij} \big/ x_{ij}. \tag{30}$$

Once the DPFC is injected to the system, the reactance of two adjacent buses is changed from x_{ij} to $x_{ij}^{\bullet}$. Furthermore, all the phase angles θ and injected compensation level λ are decision variables; once $x_{ij}^{\bullet}$ is substituted to form the DC active power with DPFCs, both θ and x_{ij}/ are incorporated in a multiplied form, which is still non-linear.

The active power of the transmission line can be varied with DPFC injection with the updated reactance $x_{ij}^{\bullet}$. The DC power flow with the DPFC is illustrated as follows:

$$P_{ij}(\theta, \lambda, \delta) = \theta_{ij} \big/ x_{ij}^{\bullet} = \theta_{ij} \big/ x_{ij} - \delta_{ij}\lambda_{ij}\theta_{ij} \big/ x_{ij}, \tag{31}$$

$$\lambda_{ij}^{\min} \le \lambda_{ij} \le \lambda_{ij}^{\max}. \tag{32}$$

There is a non-linear variable term $\delta_{ij}\lambda_{ij}\theta_{ij}/x_{ij}$ in **Eq. 31**, and a virtual variable ϕ_{ij} is introduced to linearize the non-linear term:

$$\phi_{ij} = \delta_{ij}\lambda_{ij}\theta_{ij} \big/ x_{ij}. \tag{33}$$

The active power in **Eq. 31** can be rewritten as

$$P_{ij}(\theta, \lambda, \delta) = \theta_{ij} \big/ x_{ij} - \phi_{ij}. \tag{34}$$

Combining **Eqs 32**, **33**, we multiply both sides of the equation with a voltage angle difference of δ_{ij}:

$$\delta_{ij}\lambda_{ij}^{min} \le \phi_{ij} x_{ij} \big/ \theta_{ij} = \delta_{ij}\lambda_{ij} \le \delta_{ij}\lambda_{ij}^{max}. \tag{35}$$

The feasible range of variables ϕ_{ij} is only valid when a phase angle difference θ_{ij} is positive. A binary variable y_{ij} is used to depict the direction of power flow, and a big-M relax constraint is introduced to linearize **Eq. 35**:

$$-M_{ij}y_{ij} + \delta_{ij}\lambda_{ij}^{\min}\theta_{ij} \le \phi_{ij}x_{ij} \le \delta_{ij}\lambda_{ij}^{\max}\theta_{ij} + M_{ij}y_{ij}, \tag{36}$$

$$-M_{ij}\left(1 - y_{ij}\right) + \delta_{ij}\lambda_{ij}^{\max}\theta_{ij} \le \phi_{ij}x_{ij} \le \delta_{ij}\lambda_{ij}^{\min}\theta_{ij} + M_{ij}\left(1 - y_{ij}\right). \tag{37}$$

In the optimization process, one of **Eqs 36**, **37** is valid, and another one is always useful because of the large number M_{ij}.

Note that the bilinear term $\delta_{ij}\theta_{ij}$ is still non-linear and another dummy variable U_{ij} is introduced and linearized by applying the big-M method repeatedly as follows:

$$U_{ij} = \delta_{ij}\theta_{ij}, \tag{38}$$

$$-\delta_{ij}\theta_{ij}^{\max} \le U_{ij} \le \delta_{ij}\theta_{ij}^{\max}, \tag{39}$$

$$\theta_{ij} - \left(1 - \delta_{ij}\right)\theta_{ij}^{\max} \le U_{ij} \le \theta_{ij} + \left(1 - \delta_{ij}\right)\theta_{ij}^{\max}. \tag{40}$$

Combining **Eqs 36**–**37** with the dummy variable U_{ij}, the active power of line can be replaced as follows:

$$\begin{aligned} &-M_{ij}y_{ij} + U_{ij}\lambda_{ij}^{\min} \le \phi_{ij}x_{ij} \le U_{ij}\lambda_{ij}^{\max} + M_{ij}y_{ij}, \\ &-M_{ij}\left(1 - y_{ij}\right) + U_{ij}\lambda_{ij}^{\max} \le \phi_{ij}x_{ij} \le U_{ij}\lambda_{ij}^{\min} + M_{ij}\left(1 - y_{ij}\right). \end{aligned} \tag{41}$$

Hence, the DC power flow with the DPFC, including **Eqs 31**, **39**–**41**, is reformulated into an MILP problem.

B. Two-Stage Stochastic Optimal Location Allocations of DPFC

Due to the unrepeated features of DPFC planning, we develop a two-stage optimization method based on Benders decomposition to solve the MISOCP problem under different wind–load scenarios. The original MISOCP problem can be decomposed into an MILP master problem and an SOCP subproblem. The MILP problem is to solve the optimal locations of DPFC under the baseload case, and the relaxed DC power flow based on the reactance model of DPFC accelerates its efficiency. In contrast, the optimal ratings of DPFC with various scenarios are obtained in the SOCP subproblem.

The master problem is represented as

$$\begin{aligned} &min\ \Phi^{down} = \sum_{i\in G(i)} c_i P_i^G + \alpha \\ &\begin{cases} (18) - (26) \\ \alpha \geq z + \sum_{ij} \mu_{ij}\left(\delta_{ij} - \delta_{ij}^*\right) + \sum_{i=1}^{NG} \sigma_i \left(P_{Gi} - P_i^{G,*}\right) \end{cases} \end{aligned} \tag{42}$$

Equation 42 is the objective function of master problem, which is explicitly reflected in the lower bound. In the objective function, the first term is the generation cost, while the latter is the investment cost of DPFC. The relax DC active power balance is constrained in the second column of **Eq. 42**, whose non-linearized term is linearized using the big-M method. The second column in **Eq. 42** is the Benders cuts generated in the subproblem to accelerate the solution efficiency.

The active power balance of the SOCP subproblem may be challenging because of wind–load uncertainty. Slack variables are incorporated into the power balance equations to relax and ensure the feasibility of the subproblem. The stochastic SOCP subproblem is represented by **Eq. 44**.

The subproblem is as follows:

$$min\ z = \sum_s \rho_s \left[\sum_{ij} \pi_{ij}^{DPFC} P_{ij,s}^{DPFC} + c_i \sum_{i\in G(i)} \left(\Delta k_{p,ij}^+ + \Delta k_{p,ij}^-\right) \right], \tag{43}$$

$$\begin{cases} \sum_{i\in G(i)} P_{i,s}^G - \sum_{i\in D(i)} P_{i,s}^D + \sum_{j\in \xi(i)} P_{ij,s}^{DPFC} - \sum_{j\in \psi(i)} P_{ij,s}^{DPFC} + \Delta k_{p,ij}^+ \\ \quad - \Delta k_{p,ij}^- = \sum_{j\in \delta(i)} P_{ij}(\theta, V, \lambda), \\ \sum_{i\in G(i)} Q_{i,s}^G - \sum_{i\in D(i)} Q_{i,s}^D = \sum_{j\in \delta(i)} P_{ij}(\theta, V, \lambda), \\ P_i^{G,min} - \Delta k_{p,ij}^- \leq P_{i,s}^G \leq P_i^{G,max} + \Delta k_{p,ij}^+, \\ Q_i^{G,min} \leq Q_{i,s}^G \leq Q_i^{G,max}, \\ \Delta k_{p,ij}^+ \geq 0, \Delta k_{p,ij}^- \geq 0, \forall l \in \Omega_l, \\ (16) - (17), \\ (20 - 24), \\ 0 \leq P_{ij,s}^{DPFC} \leq \delta_{ij} P_{max}^{DPFC}, \\ P_{is}^G = P_i^{G,*} \ : \mu_{ij,s}, \\ \delta_{ij,s} = \delta_{ij}^* \ : \sigma_{i,s}. \end{cases} \tag{44}$$

Equation 44 represents the subproblem objective function, which consists of the investment cost of DPFC and the sum of relaxing slack variables. The constraints are updated under various scenarios, and some slack variables are introduced into the power flow constraints to ensure the convergence of power flow. Hence, the constraints of active and reactive power are also rewritten with the slack variables. The dual of Benders cuts is obtained from the latter columns of **Eq. 44**. However, the duals of cuts need to be reconstructed because of load/wind uncertainty. We reformulate the expected value of duals associated with numerous scenarios, as shown in the following equations:

$$\mu_{ij} = \sum_s \rho_s \mu_{ij,s}, \tag{45}$$

$$\sigma_i = \sum_s \rho_s \sigma_{i,s}. \tag{46}$$

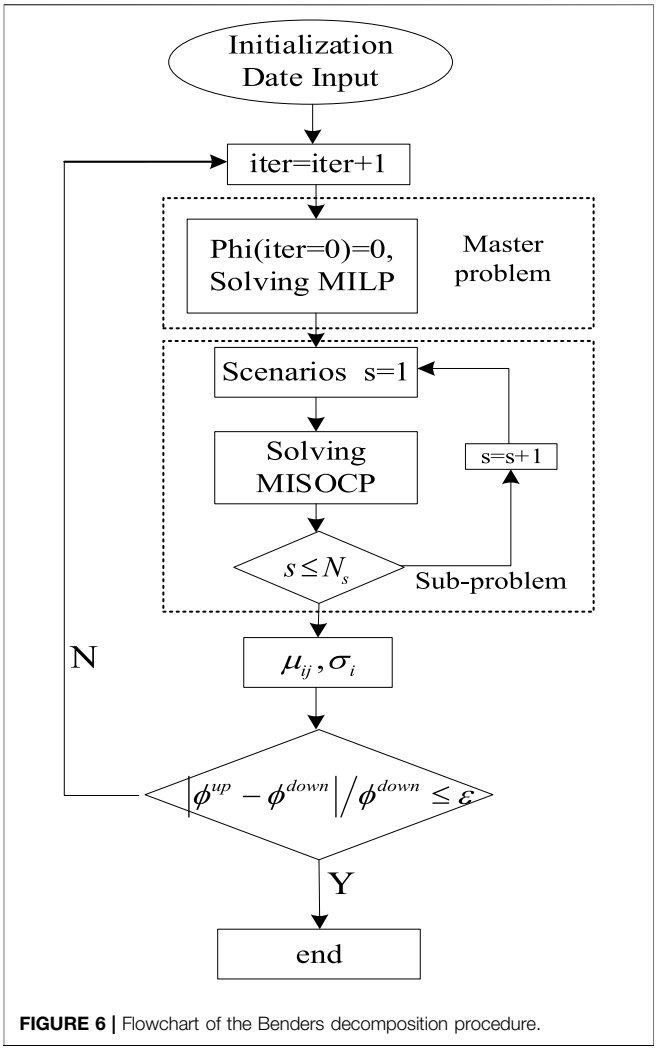

FIGURE 6 | Flowchart of the Benders decomposition procedure.

Based on the Benders decomposition method, the two-stage problem has a lower bound and upper bound. The Benders cuts accelerate the optimization efficiency iteratively and move the solution toward optimality. A stop criterion is justified as the optimal solution to the original problem. The upper bound of MISOCP and stop criterion is established, as shown in the following equations:

$$\Phi^{up} = z + \sum_{i\in G(i)} c_i P_i^G, \tag{47}$$

$$\frac{\left|\Phi^{up} - \Phi^{down}\right|}{\left|\Phi^{down}\right|} \leq \varepsilon. \tag{48}$$

The flowchart of two-stage stochastic optimization is depicted in **Figure 6**.

For a given gap ε, the complete procedure of solving the two-stage stochastic can be described as follows:

Step 1: Let $\Phi^{down} = -\infty$, $\Phi^{up} = +\infty$, iter=0;
Step 2: Solve the MP which is modeled in **Eq. 42**,

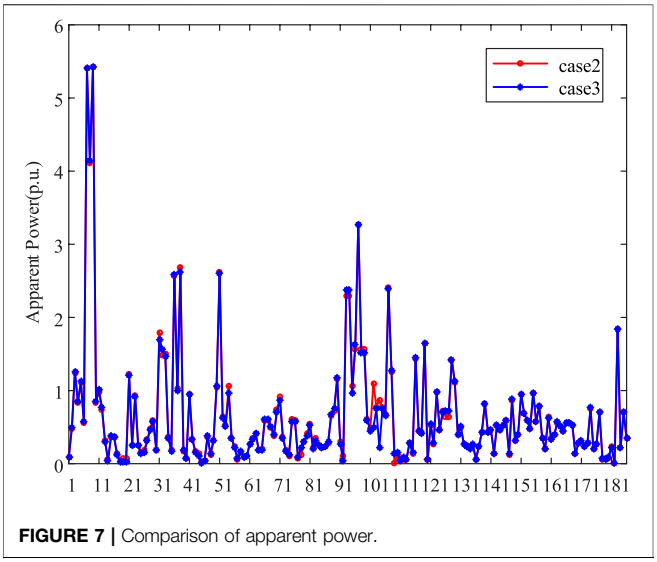

FIGURE 7 | Comparison of apparent power.

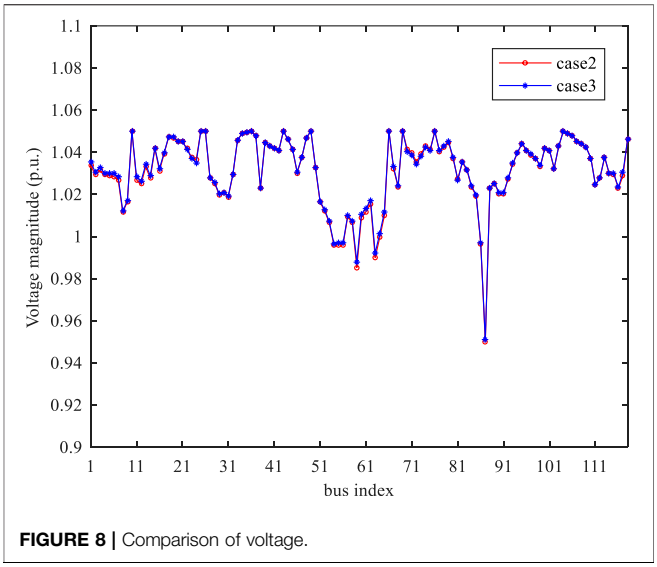

FIGURE 8 | Comparison of voltage.

Obtain the output of generators P_i^{G*} and location of DPFC δ_{ij}^* under the base case,

Update the lower bound Φ^{down};

Step 3: Fix the location of DPFC and output of thermal units and solve the SP considering various wind–load scenarios,

Obtain compensation levels $P_{ij,s}^{DPFC}$ and slack variables $\Delta k_{p,ij}^+, \Delta k_{p,ij}^-$ under each scenario,

Update the upper bound Φ^{up};

Step 4: If $\frac{|\Phi^{up}-\Phi^{down}|}{|\Phi^{down}|} \le \varepsilon$, return the optimal solutions and stop. Otherwise, add the Benders cut into a master problem and go to step 2.

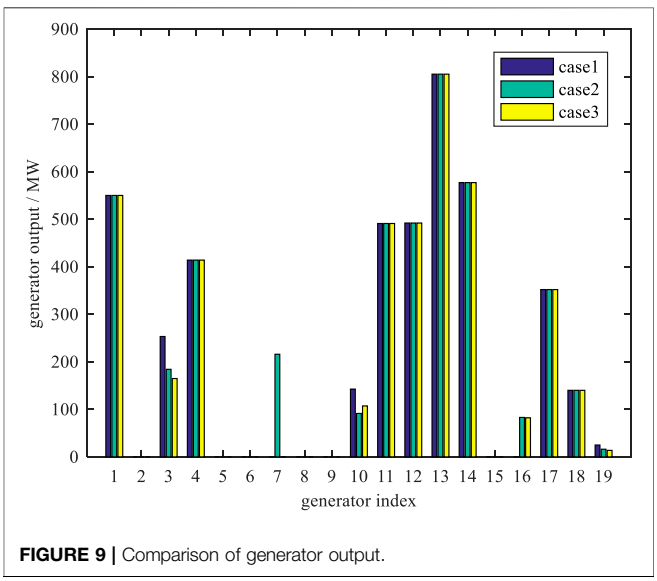

FIGURE 9 | Comparison of generator output.

5 CASE STUDY

A. Verification of the Relaxed AC-SOCP Model

In this section, several power flow cases are utilized to illustrate the effectiveness of the proposed model. The numerical cases are tested on the IEEE 118 bus system. The data of IEEE 118 are obtained from MATPOWER 6.0.

Case 1: the proposed relaxed DC power flow in **Section 3.1A**, which is solved by GAMS/CPLEX.

Case 2: the traditional non-linear power flow in **Eq. 8**, which is solved by GAMS/CONOPT.

Case 3: the proposed SOCP model in **Eq. 22**, which is solved by GAMS/CPLEX.

As for the power flow analysis, we only consider the original power flow without DPFC. Compared to Case 2 and Case 3, Case 1 cannot simulate the AC power characteristic. **Figure 7** depicts apparent power of lines in Case 2 and Case 3, and the difference of the two solutions is less than 1%. **Figure 8** also compares the bus voltage performance between Case 2 and Case 3, and the voltage magnitude of the two cases is fairly close. **Figure 9** shows significant differences of generation output in the three cases. The generation dispatch solution of Case 1 shows a different trend because of ignoring reactive power constraints, whereas the dispatch solutions show highly consistent characteristics between Case 2 and Case 3.

To illustrate the accuracy of the relaxed AC-SOCP model, we define a deviation index stated in (), which depicts the gap of line constraints between the non-linear AC power flow and the relaxed AC-SOCP model. **Figure 10** shows the gap performance, which is almost zero for all lines:

$$DI = U_i U_j - R_{ij}^2 - T_{ij}^2. \tag{49}$$

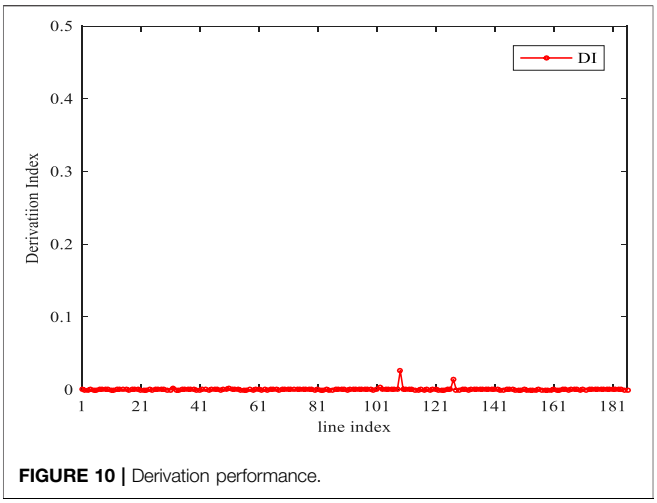

FIGURE 10 | Derivation performance.

B. Effect of the Optimal DPFC With High Penetration of Wind Power

To verify the proposed method, we conducted case studies on the modified IEEE 118 bus system. The baseload is 4242 MW, and the capacity of the total generator is 5,859.2 MW. The load uncertainty is statistically based on the Latin hypercube sampling (LHS) (Le and Wu, 2021) and K-means clustering method (Toyoda and Wu, 2021; Wu, 2021), as shown in **Table 1**. There is an artificially decreased capacity to create congestion with the thermal limits of transmission lines. GAMS implements the procedure, the MILP master problem is solved by GAMS/CPLEX, and GAMS/CPLEXD solves the SOCP subproblem. The threshold values of the stop criterion are set to be 1e-4.

A. The Performance With Different Numbers and Ratings of DPFCs

There are three huge impacts with different numbers of optimal DPFCs' planning. **Table 2** shows the total operation cost with different numbers of optimal location allocation. The operating cost of power systems shows a downward trend as the numbers of installed DPFCs increase because of their power flow management of DPFC. Compared to the optimal locations, there is a continuous trend, which verifies the robustness of the optimal planning program and overcomes the drawbacks of the iterative planning method. The level of wind absorption has also been improved. However, the increment level is not obvious between the two-DPFC and three-DPFC planning, which closely achieves the extreme in the system (**Table 3**):

$$V_{vio} = \sum_{i \in G(i)} \left\| V_i - V_{ref} \right\|. \tag{50}$$

With different installing numbers of DPFCs, the voltage violation and power loss of the system are shown in **Figure 11**. The system voltage fluctuations gradually decrease as the number of DPFCs increases, whereas the increment of power loss has a positive trend.

Figure 12 shows a great advantage of voltage stability with three DPFCs installed over the others.

TABLE 1 | Load and wind scenarios and probabilities.

Scenarios	$P_{W,s}$	$P_{D,s}$	ρ_s	Scenarios	$P_{W,s}$	$P_{D,s}$	ρ_s
s1	0.3023	0.4858	0.0555	s11	0.7927	0.5323	0.0406
s2	0.8007	0.6916	0.0446	s12	0.1858	0.8558	0.0231
s3	0.6263	0.7338	0.0412	s13	0.5018	0.6266	0.0773
s4	0.0825	0.5919	0.0788	s14	0.4203	0.4948	0.0529
s5	0.1846	0.4796	0.064	s15	0.5088	0.9065	0.0137
s6	0.5815	0.487	0.0516	s16	0.4031	0.7437	0.0483
s7	0.26	0.7026	0.0468	s17	0.2117	0.5897	0.0938
s8	0.3488	0.6036	0.0868	s18	0.1213	0.7087	0.0502
s9	0.0844	0.4701	0.0574	s19	0.184	1	0.0001
s10	0.653	0.5936	0.0732	s20	0.867	0.4915	0.0001

TABLE 2 | Solution of optimal location allocations of DPFC.

DPFC number	Optimal DPFC planning		Wind output (MW)				Generation cost value	Wind penetration
	Location	Capacity (MW)	5	26	61	95		
0	-	-	2	3.25	2.39	1.20	60070	27.6%
1	L147	0.45	2.28	3.25	2.86	1.61	57722	32.9%
2	L89	45.5	2.27	3.46	3.03	1.76	58623	35.19%
	L147	0.6						
3	L89	42.5	2.26	3.44	2.99	1.89	56124	35.33%
	L147	3.03						
	L150	86.5						

A voltage violation index is established to evaluate the stability, as is shown.

TABLE 3 | Solution of optimal DPFC with the constant capacity of DPFC.

DPFC number	Optimal DPFC planning		Wind output (MW)				Generation cost value	Wind penetration
	Location	Capacity (MW)	5	26	61	95		
0		-	2	3.25	2.39	1.20	60070	27.6%
1		L147	2.01	3.24	2.41	1.22	59830	27.7%
2		L89 L147	2.01	3.24	2.47	1.19	59902	27.9%
3		L89 L147 L150	2.01	3.24	2.44	1.22	59589	27.9%

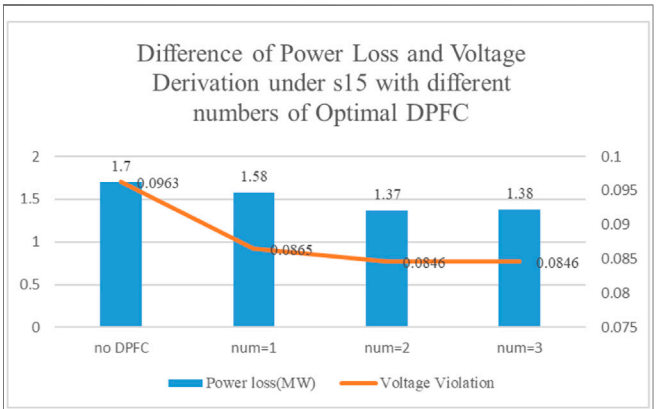

FIGURE 11 | Performance of power flow w/o DPFC.

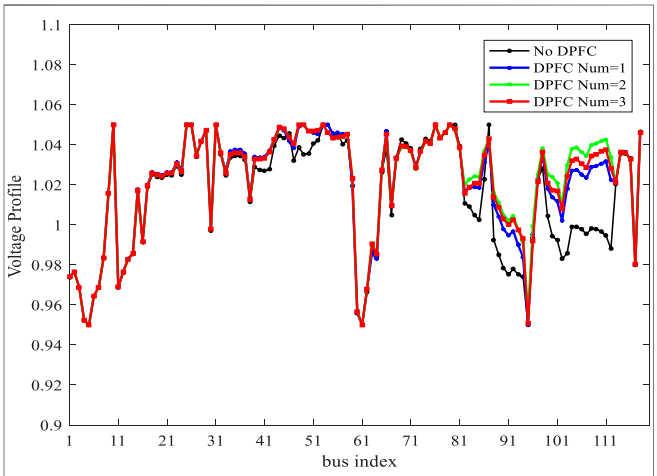

FIGURE 12 | Voltage profile w/o DPFC under s15 scenario.

To evaluate the effects of DPFC on generator rescheduling, the output of generators under a loading operation with scenario s15 is shown in **Figure 13**. The generator dispatch has a considerable difference from the DPFC under the load level. Comparing the no-DPFC and one-DPFC solutions, the absorption of wind power in this scenario has little change. However, the output of thermal unit is significantly different because more economical units participate in more dispatch plans, which verifies the management efficiency of DPFC to the dispatch solution of thermal generators. Once two or three DPFCs are injected into the system, the wind absorption has an obvious increment, which illustrates the power flow shiftable capability of DPFC.

The Performance With Certain Compensation Level of DPFC

When the compensation level of DPFC is equal to 5 MW, the performance is different from that in **Table 2**. It is observed that the expected cost decreases slightly as the number of DPFCs increases. The wind penetration also shows little changes. This result also confirms the superiority of the planning method, in which the location and allocation are optimized simultaneously.

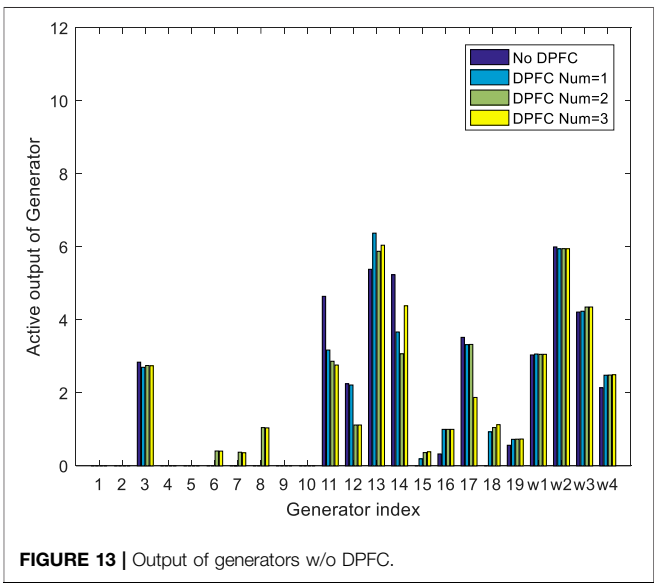

FIGURE 13 | Output of generators w/o DPFC.

TABLE 4 | Solution of optimal DPFC with variable wind power.

DPFC number	Optimal DPFC planning		Wind output (MW)				Generation cost value	Wind penetration
	Location	Capacity (MW)	3	50	80	118		
0	-	-	1.48	1.47	3.76	1.37	63287	27.3%
1	L120	74.5	1.53	1.54	3.86	1.50	62023	29.1%
2	L106	99.67	1.55	1.59	3.87	1.51	62372	29.5%
	L120	87.51						
3	L106	13.13	1.52	1.59	3.84	1.47	61610	29.2%
	L120	64.18						
	L150	29.69						

C. The Performance With Variable Wind Location With Optimal DPFC

To assess the impact of optimal DPFC solutions with varied wind locations, we transfer the wind location to bus [3,50,80,118]. Comparing **Tables 2**, **4**, the overall decline in wind power penetration is relatively obvious, which only can illustrate the manage ability of DPFC is subjected to the structure of generators. At the same time, it can be observed that the operating cost and wind penetration also show a positive trend when DPFC numbers increased.

6 CONCLUSION

This work presents a novel two-stage stochastic optimization model, which simultaneously optimizes the location and compensation level of DPFCs considering various wind–load scenarios. Case studies are performed to demonstrate the effectiveness of the proposed method. The conclusions are summarized as follows:

1) The relaxed AC-SOCP model can easily simulate the non-linear AC power flow and has an advantage of solving speed and difficulties.
2) The proposed two-stage method has a consistent scheduling plan of DPFC, which maintains the non-linear internal characteristics of DPFC and overcomes the drawback of iterative scheduling planning.
3) The power flow management of DPFC on the network side plays an important role in system operation. The operating cost, power flow performance, and wind absorption have a positive trend as the numbers of DPFCs increased.

In addition, the methodology proposed in this paper is applicable to the areas of strengthening the management efficacy on the network side. Also in the future work, we will test the DPFC in more scenarios to check its control capability.

DATA AVAILABILITY STATEMENT

The original contributions presented in the study are included in the article/Supplementary Material, and further inquiries can be directed to the corresponding author.

AUTHOR CONTRIBUTIONS

XZ wrote the manuscript and performed the method. LD provided the financial support for this research. JW provided the support for solving method.

FUNDING

This research was supported by the State Grid Corporation of China (No. 52150016000Y).

REFERENCES

Alomoush, M. I. (2003). Derivation of UPFC DC Load Flow Model with Examples of its Use in Restructured Power Systems. *IEEE Trans. Power Syst.* 18 (3), 1173–1180. doi:10.1109/tpwrs.2002.805002

Alomoush, M. I. (2004). Impacts of UPFC on Line Flows and Transmission Usage. *Electric Power Syst. Res.* 71 (3), 223–234. doi:10.1016/j.epsr.2004.01.017

Bhowmick, S., Das, B., and Kumar, N. (2008). An Indirect UPFC Model to Enhance Reusability of Newton Power-Flow Codes. *IEEE Trans. Power Deliv.* 23 (4), 2079–2088. doi:10.1109/tpwrd.2008.923105

Dai, J., Tang, Y., Liu, Y., Ning, J., Wang, Q., Zhu, N., et al. (2019). Optimal Configuration of Distributed Power Flow Controller to Enhance System Loadability via Mixed Integer Linear Programming. *J. Mod. Power Syst. Clean. Energ.* 7 (6), 1484–1494. doi:10.1007/s40565-019-0568-8

Dawn, S., and Tiwari, P. K. (2016). Improvement of Economic Profit by Optimal Allocation of TCSC & UPFC with Wind Power Generators in Double Auction Competitive Power Market. *Int. J. Electr. Power Energ. Syst.* 80, 190–201. doi:10.1016/j.ijepes.2016.01.041

Ding, T., Bo, R., and Li, F. (2015). Optimal Power Flow with the Consideration of Flexible Transmission Line Impedance[J]. *IEEE Trans. Power Syst.* 31 (2), 1655–1656. doi:10.1109/tpwrs.2015.2412682

Ebeed, M., Kamel, S., Yu, J., and Jurado, F. (2019). Development of UPFC Operating Constraints Enforcement Approach for Power Flow Control. *IET Generation, Transm. Distribution* 13 (20), 4579–4591. doi:10.1049/iet-gtd.2018.5609

Hemmati, R., Hooshmand, R. A., and Khodabakhshian, A. (2013). Comprehensive Review of Generation and Transmission Expansion

Planning. *IET Generation, Transm. Distribution* 7 (9), 955–964. doi:10.1049/iet-gtd.2013.0031

Hooshmand, R.-A., Morshed, M. J., and Parastegari, M. (2015). Congestion Management by Determining Optimal Location of Series FACTS Devices Using Hybrid Bacterial Foraging and Nelder-Mead Algorithm. *Appl. Soft Comput.* 28, 57–68. doi:10.1016/j.asoc.2014.11.032

Jabr, R. A. (2013). Optimization of AC Transmission System Planning. *IEEE Trans. Power Syst.* 28 (3), 2779–2787. doi:10.1109/tpwrs.2012.2228507

Khanchi, S., and Garg, V. K. (2013). Unified Power Flow Controller (FACTS Device): A Review[J]. *system* 5, 6.

Le, Shuting., and Wu, Yuhu. (2021). Game Theoretic Approach for a Service Function Chain Routing in NFV with Coupled Constraints. *IEEE Trans. Circuits Syst.*.68:3557 doi:10.1109/TCSII.2021.3070025

Li, Z., Jiang, W., Abu-Siada, A., Li, Z., Xu, Y., and Liu, S. (2021). Research on a Composite Voltage and Current Measurement Device for HVDC Networks. *IEEE Trans. Ind. Electron.* 68 (9), 8930–8941. doi:10.1109/tie.2020.3013772

Nikoobakht, A., Aghaei, J., Parvania, M., and Sahraei-Ardakani, M. (2018). Contribution of FACTS Devices in Power Systems Security Using MILP-based OPF. *IET Generation, Transm. Distribution* 12 (15), 3744–3755. doi:10.1049/iet-gtd.2018.0376

Noroozian, M., Angquist, L., Ghandhari, M., and Andersson, G. (1997). Use of UPFC for Optimal Power Flow Control. *IEEE Trans. Power Deliv.* 12 (4), 1629–1634. doi:10.1109/61.634183

Orfanogianni, T., and Bacher, R. (2003). Steady-state Optimization in Power Systems with Series Facts Devices. *IEEE Trans. Power Syst.* 18 (1), 19–26. doi:10.1109/tpwrs.2002.807110

Pereira, M., and Zanetta, L. C. (2012). A Current Based Model for Load Flow Studies with UPFC[J]. *IEEE Trans. Power Syst.* 28 (2), 677–682.doi:10.1109/tpwrs.2012.2206409

Prasad, J. V., Ram, I. S., and Jayababu, B. (2011). Genetically Optimized FACTS Controllers for Available Transfer Capability Enhancement[J]. *Int. J. Comp. Appl.* 975, 8887.doi:10.5120/2349-3072

Rajabi-Ghahnavieh, A., Fotuhi-Firuzabad, M., and Othman, M. (2015). Optimal Unified Power Flow Controller Application to Enhance Total Transfer Capability[J]. IET Generation. *Transm. Distribution* 9 (4), 358–368.doi:10.1049/iet-gtd.2014.0110

Ranganathan, S., Surya Kalavathi, M., and Asir Rajan C., C. (2016). Self-adaptive Firefly Algorithm Based Multi-objectives for Multi-type FACTS Placement. *IET Generation, Transm. Distribution* 10 (11), 2576–2584. doi:10.1049/iet-gtd.2015.0905

Sahraei-Ardakani, M., and Hedman, K. W. (2015). A Fast LP Approach for Enhanced Utilization of Variable Impedance Based FACTS Devices[J]. *IEEE Trans. Power Syst.* 31 (3), 2204–2213.doi:10.1109/pesgm.2016.7741200

Sang, Y., and Sahraei-Ardakani, M. (2017). The Interdependence between Transmission Switching and Variable Impedance Series FACTS Devices [J]. *IEEE Trans. Power Syst.* 33 (3), 2792–2803. doi:10.1109/tpwrs.2017.2756074

Saravanan, M., Slochanal, S. M. R., and Venkatesh, P. (2007). Application of Particle Swarm Optimization Technique for Optimal Location of FACTS Devices Considering Cost of Installation and System Loadability[J]. *Electric Power Syst. Res.* 77 (3-4), 276–283. doi:10.1016/j.epsr.2006.03.006

Sarker, J., and Goswami, S. K. (2014). Solution of Multiple UPFC Placement Problems Using Gravitational Search Algorithm. *Int. J. Electr. Power Energ. Syst.* 55, 531–541. doi:10.1016/j.ijepes.2013.10.008

Shen, Xun., Ouyang, Tinghui., Li, Yuanchao., and Khajorntraidet, Chanyut. (2021). "Mixture Density Networks-Based Knock Simulator". *IEEE/ASME Trans. Mechatronics, Early Access*. doi:10.1109/TMECH.2021.3059775

Shen, Xun., Ouyang, Tinghui., Yang, Nan., and Zhuang, Jiancang. (2021). "Sample-based Neural Approximation Approach for Probabilistic Constrained Programs". *IEEE Trans. Neural Networks Learn. Syst. Early Access*. doi:10.1109/TNNLS.2021.3102323

Shen, Xun., and Raksincharoensak, Pongsathorn. (2021). "Pedestrian-aware Statistical Risk Assessment". *IEEE Trans. Intell. Transportation Syst. Early Access*, 1. doi:10.1109/TITS.2021.3074522

Shen, Xun., and Raksincharoensak, Pongsathorn. (2021). "Statistical Models of Near-Accident Event and Pedestrian Behavior at Non-signalized Intersections. *J. Appl. Stat. Early Access*. 1.doi:10.1080/02664763.2021.1962263

Singh, S. P. (2016). Congestion Mitigation Using UPFC[J]. IET Generation. *Transm. Distribution* 10 (10), 2433–2442.doi:10.1049/iet-gtd.2015.1199

Tang, A., Lu, Z., and Yang, H. (2020). Digital/analog Simulation Platform for Distributed Power Flow Controller Based on ADPSS and dSPACE[J]. *CSEE J. Power Energ. Syst.* 7 (1), 181–189.

Tang, A., Shao, Y., Huang, Y., and Xu, Q. (2018). A New Topology of the Distributed Power Flow Controller and its Electromagnetic Transient Characteristics. *Electric Power Syst. Res.* 163, 280–287. doi:10.1016/j.epsr.2018.07.002

Tiwari, P. K., and Sood, Y. R. (2013). An Efficient Approach for Optimal Allocation and Parameters Determination of TCSC with Investment Cost Recovery under Competitive Power Market. *IEEE Trans. Power Syst.* 28 (3), 2475–2484. doi:10.1109/tpwrs.2013.2243848

Tiwari, P. K., and Sood, Y. R. (2012). Efficient and Optimal Approach for Location and Parameter Setting of Multiple Unified Power Flow Controllers for a Deregulated Power Sector. *IET Gener. Transm. Distrib.* 6 (10), 958–967. doi:10.1049/iet-gtd.2011.0722

Toyoda, M., and Wu, Y. (2021). Mayer-type Optimal Control of Probabilistic Boolean Control Network with Uncertain Selection Probabilities. *IEEE Trans. Cybern.* 51, 3079–3092. doi:10.1109/tcyb.2019.2954849

Tripathy, M., and Mishra, S. (2007). Bacteria Foraging-Based Solution to Optimize Both Real Power Loss and Voltage Stability Limit. *IEEE Trans. Power Syst.* 22 (1), 240–248. doi:10.1109/tpwrs.2006.887968

Tripathy, M., Mishra, S., Lai, L. L., and Zhang, Q. P. (2006). *Transmission Loss Reduction Based on FACTS and Bacteria Foraging algorithm[M]// Parallel Problem Solving from Nature-PPSN IX*. Springer, Berlin, Heidelberg.

Ugranli, F., Karatepe, E., and Nielsen, A. H. (2016). MILP Approach for Bilevel Transmission and Reactive Power Planning Considering Wind Curtailment[J]. *IEEE Trans. Power Syst.* 32 (1), 652–661.

Verma, K. S., and Gupta, H. O. (2006). Impact on Real and Reactive Power Pricing in Open Power Market Using Unified Power Flow Controller. *IEEE Trans. Power Syst.* 21 (1), 365–371. doi:10.1109/tpwrs.2005.857829

Vo Tien, D., Goňo, R., and Leonowicz, Z. (2019). *Load Flow Analysis in Power System Network Incorporating Statcom: A Comparison of the Direct and Indirect Algorithm of the newton-raphson method[J]*.

Wu, Y. (2021). Yuqian Guo, Mitsuru Toyoda, Policy Iteration Approach to the Infinite Horizon Average Optimal Control of Probabilistic Boolean Networks. *IEEE Trans. Neural Networks Learn. SystemsVol* 32 (6), 2910–2924. doi:10.1109/tnnls.2020.3008960

Yang, N. (2021). A Comprehensive Review of Security-Constrained Unit Commitment. *J. Mod. Power Syst. Clean Energ.*. doi:10.35833/MPCE.2021.000255

Yang, N., Qin, T., Wu, L., Huang, Y., Huang, Y., and Xing, C. (2021). A Multi-Agent Game Based Joint Planning Approach for Electricity-Gas Integrated Energy Systems Considering Wind Power Uncertainty. *Electric Power Syst. Res.*, 107673. doi:10.1016/j.epsr.2021.107673

Yang, N., Yang, C., Wu, L., Shen, X., Jia, J., Li, Z., et al. (2021). Intelligent Data-Driven Decision-making Method for Dynamic Multi-Sequence: An E-Seq2Seq Based SCUC Expert System. *IEEE Trans. Ind. Inform.* doi:10.1109/TII.2021.3107406

Yang, N., Yang, C., Xing, C., Ye, D., Jia, J., Chen, D., et al. (2021). Deep Learning-Based SCUC Decision-Making: An Intelligent Data-Driven Approach With Self-Learning Capabilities. *IET Gener. Transm. Distrib.*, 1–12. doi:10.1049/gtd2.12315

Yuan, Z., de Haan, S. W. H., Ferreira, J. B., and Cvoric, D. (2010). A FACTS Device: Distributed Power-Flow Controller (DPFC). *IEEE Trans. Power Electron.* 25 (10), 2564–2572. doi:10.1109/tpel.2010.2050494

Zhang, L., Xie, Y., Ye, J., Xue, T., Cheng, J., Li, Z., et al. (2021). Intelligent Frequency Control Strategy Based on Reinforcement Learning of Multi-Objective Collaborative Reward Function. *Front. Energ. Res.* 9. 760525.doi:10.3389/fenrg.2021.760525

Zhang, T., Xu, X., and Li, Z. (2020). Optimum Location and Parameter Setting of STATCOM Based on Improved Differential Evolution Harmony Search Algorithm[J]. *IEEE Access*.8:87810. doi:10.1109/access.2020.2993066

Conflict of Interest: The authors declare that the research was conducted in the absence of any commercial or financial relationships that could be construed as a potential conflict of interest.

Publisher's Note: All claims expressed in this article are solely those of the authors and do not necessarily represent those of their affiliated organizations, or those of the publisher, the editors, and the reviewers. Any product that may be evaluated in this article, or claim that may be made by its manufacturer, is not guaranteed or endorsed by the publisher.

GLOSSARY

Sets and indices

i/j Bus index

ij Line index connected bus i and j

s Load scenario index

$G(i)$ Sets of generator located bus i

$D(i)$ Sets of load located bus i

$\delta(i)$ Sets of lines connected bus i DPFC variables

V_T/V_{Ti} Unified/distributed series voltage magnitude of DPFC

θ_{se}/θ_{sei} Unified/distributed series voltage angle phase of DPFC

S_{se}/S_{sh} Complex power of series or shunt side

x_{ij}^{DPFC} Equivalent reactance of DPFC located line ij

π_{ij}^{DPFC} Amortized cost of DPFC located line ij

λ_{ij} Compensation level of DPFC

N^{DPFC} Total numbers of DPFC Variables

r_{ij}/x_{ij} Resistance or reactance of line ij

P_i^G/Q_i^G Active or reactive power of generator located at bus i

P_i^D/Q_i^D Active or reactive load located at bus i

$\Delta k_{p,ij}^{+}/\Delta k_{p,ij}^{-}$ Positive slack variable

δ_{ij} Binary variable indicating DPFC located

y_{ij} Binary variable indicating the direction of power flow of line ij

c_i Coefficient of generator cost located bus i

P_{ij} Active power of line ij

V_i Voltage magnitude of bus i

θ_i Voltage angle of bus i

θ_{ij} Angle difference between bus i and j

α_L Constant variable

$P_{ij}^{\max}$ Thermal limit of line ij

$\lambda_{ij}^{min}/\lambda_{ij}^{max}$ Lower or upper bound of compensation level

$\theta_i^{\min}/\theta_i^{\max}$ Lower or upper bound of voltage angle

$V_i^{\min}/V_i^{\max}$ Lower or upper or lower bound of voltage magnitude

$P_i^{G,min}/P_i^{G,max}$ Lower or upper and lower bound of active power supplied by generator

$Q_i^{G,min}$ / $Q_i^{G,max}$ Lower or upper bound of reactive power

Φ^{down} Lower bound of original problem

Φ^{up} Upper bound of original problem

M_{ij} Penalty coefficient

ρ_s probability of scenarios.

frontiers in Energy Research

ORIGINAL RESEARCH
published: 18 March 2022
doi: 10.3389/fenrg.2022.820137

Accurate Modeling Simulation and Experimental Study of Hybrid Multi-Terminal UHVDC Transmission System

Chao Xing[1,2], *Wang Cai*[2,3], *Yanbo Che*[1], *Guihong Bi*[3], *Shilong Chen*[3]*, *Jingye Gao*[2,3] *and Long Wang*[2,3]

[1]Key Laboratory of Smart Grid of Education Ministry, Tianjin University, Tianjin, China, [2]Institute of Electric Power Science and Research, Yunnan Power Grid Corporation, Kunming, China, [3]Faculty of Electric Power Engineering, Kunming University of Science and Technology, Kunming, China

This study researches on the Wudongde hybrid multi-terminal Ultra High-Voltage Direct Current Transmission (UHVDC) project (referred to as Wudongde transmission project in short) from the electromagnetic transient model and simulation and establishes an accurate simulation model of the hybrid multi-terminal UHVDC transmission system with the Power Systems Computer-Aided Design (PSCAD). The hybrid multi-terminal UHVDC transmission system consists of the primary system and the control system. The simulation model of the primary system adopts the parameters of the Wudongde transmission project, and the simulation model of the control system refers to the control system benchmark model of HVDC transmission and 9-terminal DC grid in the International Council on Large Electric Systems (CIGRE). According to the characteristics of the hybrid multi-terminal UHVDC control system, the benchmark model of HVDC transmission and 9-terminal DC grid control system in the CIGRE is modified accordingly, and a simulation model of the control system applicable to the hybrid multi-terminal UHVDC transmission system is established. The accuracy and credibility of the model are verified through the comparison of the recording waveform and the simulating waveform of the steady-state and transient operation. The simulating and field recording waveforms show that the model can accurately simulate the Wudongde transmission project and be used as an effective tool for further studying the electromagnetic transient characteristics of the hybrid multi-terminal UHVDC transmission system.

Keywords: PSCAD/EMTDC, hybrid multi-terminal UHVDC, CIGRE, accurate simulation model, recording waveform classification

OPEN ACCESS

Edited by:
Mohd Hasan Ali,
University of Memphis, United States

Reviewed by:
Narottam Das,
Central Queensland University, Australia
Mehdi Firouzi,
Islamic Azad University, Abhar, Iran

***Correspondence:**
Shilong Chen
chenshilong3@126.com

Specialty section:
This article was submitted to Smart Grids, a section of the journal Frontiers in Energy Research

Received: *22 November 2021*
Accepted: *31 January 2022*
Published: *18 March 2022*

Citation:
Xing C, Cai W, Che Y, Bi G, Chen S, Gao J and Wang L (2022) Accurate Modeling Simulation and Experimental Study of Hybrid Multi-Terminal UHVDC Transmission System. Front. Energy Res. 10:820137. doi: 10.3389/fenrg.2022.820137

INTRODUCTION

With the implementation of the strategy of "West-East electricity transmission and nationwide interconnection" (Dan et al., 2020; He et al., 2020; Huaqiang et al., 2020; Zehong et al., 2021), several UHVDC projects have been put into operation. UHVDC is an important means to solve the problem of hydropower transmission in Southwest China and the collection and transmission of new energy in Northwest China (Benfeng et al., 2021; Xichun et al., 2021; Yuankang et al., 2021). As the world's first hybrid multi-terminal UHVDC to solve the outward transmission of hydropower from

southwest China, the Wudongde hybrid multi-terminal UHVDC transmission project has been completed and put into operation (Hong et al., 2017), which is a significant breakthrough of UHVDC technology in China. The Wudongde transmission project combines the advantages of traditional high-voltage direct current (HVDC) and flexible DC (Chao et al., 2017; Liu et al., 2020; Li et al., 2021; Muniappan, 2021), with the Kunbei converter station using the Line commutated converter (LCC) and the converter station of Liubei and Longmen using the Modular multilevel converter (MMC) of the Voltage source converter (VSC). Meanwhile, the half-bridge submodule (HBSM) and full-bridge submodule (FBSM) of the MMC are mixed in proportional cascade, which makes the structure of the whole system more complex and the control mode more flexible and brings difficulties to the modeling of the hybrid multi-terminal UHVDC transmission system.

As for DC transmission technologies, there is much research on traditional DC and flexible DC, and the findings are also very rich. On the contrary, there is some research on hybrid multi-terminal DC, although some findings have been made, and they are mainly focusing on topology, control strategy, modeling simulation, and line protection. A few studies have been conducted specifically on hybrid multi-terminal UHVDC (Shan et al., 2018). Shan et al. (2018) studied the topology of the DC system combined with LCC, VSC, overhead line, and cable and proposed a control strategy suitable for the system. Weihuang et al. (2017) designed a control strategy for the hybrid multi-terminal UHVDC to achieve the purpose of coordinating the control of each terminal. Song et al. (2019) and Zhi-da and Qing-song (2019) studied the topology and working principle of the hybrid multi-terminal DC and designed a control strategy suitable for the system. A general small-signal modeling method of hybrid multi-terminal DC is proposed in Anran et al. (2019), and the simulation results are compared in MATLAB and PSCAD. Weihuang et al. (2020) studied the parameters of hybrid multi-terminal HVDC and proposed an optimization method of small-disturbance stability parameters. In Yuansheng et al. (2021), taking the three-section hybrid DC line as the research object, the equivalent circuit of transient traveling wave is derived, and a line protection scheme using traveling wave phase is proposed. Although the above-mentioned references have made some achievements in the study of hybrid multi-terminal DC, it is not entirely for the hybrid multi-terminal UHVDC system, and the parameters of the simulation model are not the actual engineering one, which makes the credibility of the research findings applied to the actual engineering in need for further verification.

The current DC transmission system modeling is mainly studied based on the standard DC test system published by the International Council on Large Electric Systems (CIGRE), but the system lacks a standard simulation model for hybrid DC transmission. In the standard test system, LCC-HVDC is a unipolar structure, the converter valve is composed of one 12-pulse converter, and the output DC voltage level is +500 kV. MMC-HVDC has true and pseudo bipolar structures, the single converter station or unipolar converter valve has only one MMC converter, and the converter bridge arm is composed of a single bridge sub-module. There are two modulation modes for the control of the converter valve: the Pulse Width Modulation (PWM) and the Nearest Level Control (NLC). The output DC voltage level of PWM-MMC-HVDC is ±320 kV, and the output DC voltage level of NLC-MMC-HVDC is ±400 kV. While the output DC voltage of the Wudongde transmission project is ±800 kV. The LCC converter station is composed of double 12-pulse converters in series, and VSC converter station is composed of double MMC converters in series (Yan et al., 2017). It can be seen that the primary system structure of LCC-HVDC and MMC-HVDC in CIGRE is no longer applicable to the hybrid multi-terminal UHVDC transmission system, while the control systems of LCC-HVDC and MMC-HVDC are also different, which needs to be modified on the basis of the standard test system to construct a suitable hybrid multi-terminal UHVDC control system and primary system structure in order to build an accurate simulation model of hybrid multi-terminal UHVDC for the study of electromagnetic transient characteristics (Shen et al., 2017; Shen et al., 2020a; Shen et al., 2020b; Shen and Raksincharoensak, 2021a; Shen and Raksincharoensak, 2021b; Shen et al., 2021a).

This research studies the Wudongde transmission project and establishes an accurate simulation model of the hybrid multi-terminal UHVDC transmission system with the PSCAD/EMTDC simulation software (Yang et al., 2018; Yang et al., 2019a; Yang et al., 2019b; Shen et al., 2021b; Yang et al., 2021a; Yang et al., 2022). Based on the actual parameters of the Wudongde transmission project, a detailed simulation model of the primary system is established. Based on the LCC-HVDC and NLC-MMC-HVDC control systems in CIGRE, the control system is modified, and the necessary additional control links are added to establish a suitable simulation model of the control system. The primary and the control systems are combined to build an accurate simulation model of the hybrid multi-terminal UHVDC transmission system. Compared with the recording waveforms, the simulating waveforms show that the model can simulate the Wudongde transmission project accurately and can be used as an effective tool for further studying the electromagnetic transient characteristics of the hybrid multi-terminated UHVDC transmission system (Yang et al., 2021b; Zhang et al., 2021; Zhu et al., 2020).

SIMULATION MODEL OF THE PRIMARY SYSTEM

An accurate simulation model of the hybrid multi-terminal UHVDC system directly determines the accuracy of the actual engineering simulation. This study takes the Wudongde transmission project as the research object and establishes the primary equipment simulation model of the hybrid multi-terminal UHVDC transmission system based on the actual design parameters and primary system structure of the Wudongde transmission project, which fully reflects the actual

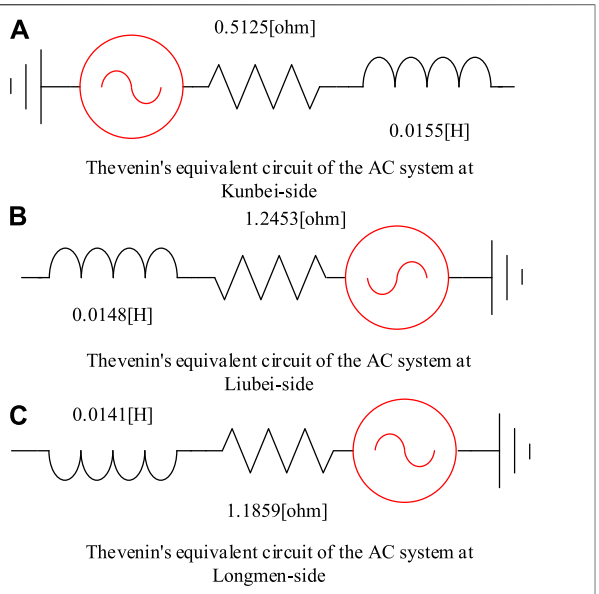

FIGURE 1 | Thevenin's equivalent circuit of the AC system.

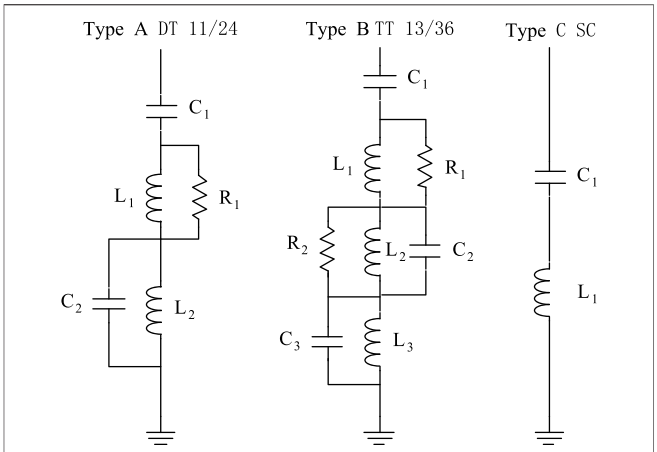

FIGURE 2 | Grouping wiring diagram of the AC filter.

parameters of the primary system of the Wudongde transmission project and has high accuracy and credibility.

Simulation Model of the AC System Module

Simulation Model of the AC System

In this study, according to the AC system voltage and maximum three-phase short-circuit current of the Wudongde transmission project, Thevenin's equivalent models of AC systems at Kunbei-side, Liubei-side, and Longmen-side are established, respectively. The rated voltages of the AC systems at Kunbei-side, Liubei-side, and Longmen-side are 535, 525, and 500 kV, respectively, and the maximum three-phase short-circuit currents of the AC systems at all three sides are 63 kA. The maximum short-circuit capacity and Thevenin's equivalent impedance of the AC systems can be calculated according to the following equations:

$$SC = \sqrt{3} \times U \times I, \tag{1}$$

$$Z_{st} = \frac{V_C^2}{SC}. \tag{2}$$

SC is the maximum short-circuit capacity of the AC system, U is the rated voltage of the converter bus, I is the maximum three-phase short-circuit current of the AC system, and Z_{st} is Thevenin's equivalent impedance of the AC system. The parameters of the AC system at each terminal of the Wudongde transmission project are brought in to obtain the equivalent parameters of the AC system at each terminal. Simultaneously, the simulation models established by the AC system on the Kunbei-side, Liubei-side, and Longmen-side are shown in **Figure 1**.

Simulation Model of the AC Filter

As LCC converter is adopted at the Kunbei converter station, in order to ensure that reactive power compensation and harmonic level meet engineering requirements, six groups of type A filters DT 11/24, six groups of type B filters TT 3/13/36, and eight groups of type C filters SC are configured, with a total of 20 groups. The wiring diagrams of types A, B, and C of filters are shown in **Figure 2**. The 20 groups are divided into four groups. The grouping scheme is as follows:

ACF1: 2DT 11/24 + TT 3/13/36 + 2SC,
ACF2: DT 11/24 + 2TT 3/13/36 + 2SC,
ACF3: 2DT 11/24 + TT 3/13/36 + 2SC,
ACF4: DT 11/24 + 2TT 3/13/36 + 2SC.

For Liubei and Longmen converter stations, MMC converter is adopted, and the harmonic content of the introduced system is lower than the standard of configuring AC filter (Zheng, 2016). At the same time, an MMC converter can be used as a STATCOM device, capable of emitting and absorbing reactive power. Therefore, the AC filter only needs to be configured at the Kunbei converter station.

Simulation Model of the Converter Station Module

The converter station module contains converter transformer, converter valve, smoothing reactor, DC filter, current limiting reactor, and converter valve control module, whose function is to realize the mutual conversion of AC and DC, which is the core part of the whole DC transmission system, among which the simulation model of converter valve control module is described in the next section.

Simulation Model of the Converter Transformer

The parameters of the converter transformer of the Wudongde transmission project are shown in **Table 1**. It shows the parameters of a single-phase two-winding transformer (Lingyun et al., 2018). The actual project usually combines three single-phase transformers to form a three-phase transformer, and the simulation model can use a three-phase

TABLE 1 | Converter transformer parameters.

Items	Yunnan-side	Guangxi-side	Guangdong-side
Network side rated voltage of winding (kV)	525	525	525
Valve-side rated voltage of winding (kV)	172.2	196	217
Wiring form	Y0/Y and Y0/△	Y0/Y	Y0/Y
Rated capacity (MVA)	405.8	290	480
Short circuit impedance	0.2	0.16	0.18

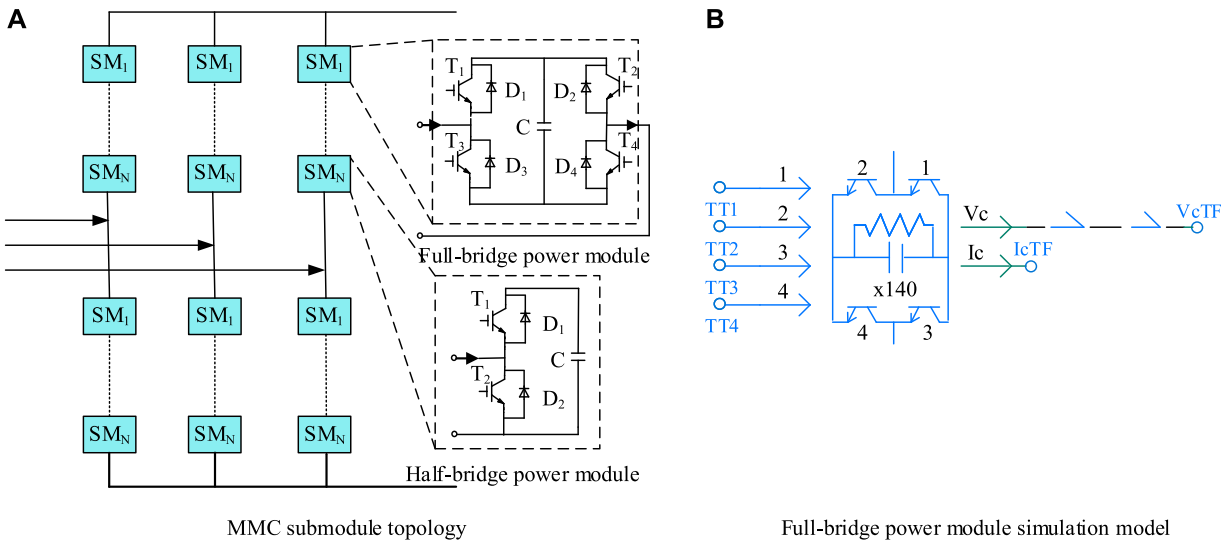

FIGURE 3 | MMC submodule topology and full-bridge power module simulation model.

two-winding transformer instead, but the capacity is changed. The capacity of the Kunbei-side becomes 1,217.4 MVA, that of Liubei-side becomes 870 MVA, and that of Longmen-side becomes 1440 MVA, while other parameters and wiring methods remain unchanged.

Simulation Model of the Converter Valve

The rated voltage of the hybrid multi-terminal UHVDC is ±800 kV. In order to make the output voltage of the converter station reach the design value, two 12-pulse converter units are connected in series to form the simulation model of the unipolar converter valve of the Kunbei converter station, two LCCs are connected in series to form the high-low valve, each converter unit is subjected to 400kV, and the voltage is distributed according to (400 + 400) kV. Two MMC converter units are connected in series to form a simulation model of unipolar converter valve at the Liubei and Longmen converter stations. Two MMCs are connected in series to form a high-low valve, a single MCC converter is subjected to 400 kV, and the series voltage is distributed according to (400 + 400) kV. The single MMC is composed of half-bridge submodules and full-bridge submodules in a mixed cascade of 3:7 to form each bridge arm, with a total of 200 submodules conducting at any moment in the upper and lower bridge arms with some redundancy. The output voltage of the single MMC converter is maintained at 400 kV. The sub-module topology is shown in **Figure 3A**, and the simulation model of the full-bridge sub-module is shown in **Figure 3B**.

Simulation Model of DC Filter

Among the three converter stations, the MMC voltage source converter is adopted in Liubei and Longmen converter station, and the harmonic content of output direct flow satisfies the specifications. Therefore, a DC filter is not required, but only in the Kunbei converter station. The Kunbei converter station is configured with unipolar two groups of three tuned filters, and its parameters are as follows: C_1 = 1.0 μF, L_1 = 17.4 mH, C_2 = 3.04 μF, L_2 = 15.7 mH, C_3 = 3.675 μF, and L_3 = 3.2 mH.

Simulation Model of Smoothing Reactor and Current Limiting Reactor

Two 75 mH smoothing reactors are installed at the unipolar neutral bus and DC pole, respectively, in the Kunbei Converter Station, with a total of four.

One 200 mH current limiting reactor is installed at the unipolar neutral bus of the Liubei converter station, and two 50 mH current limiting reactors are installed at the DC pole line,

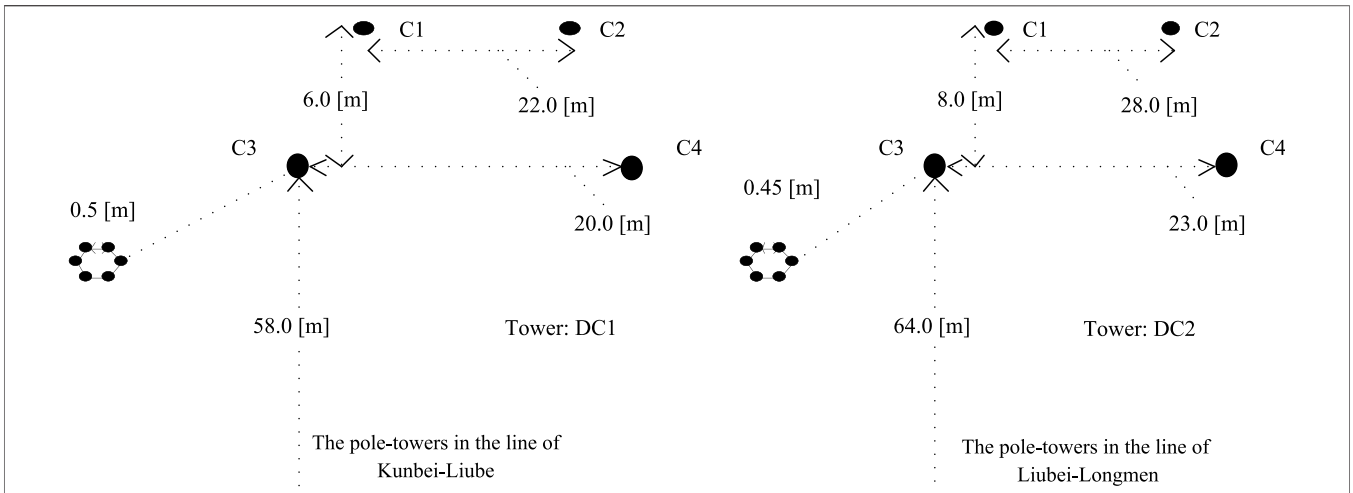

FIGURE 4 | Model and parameters of transmission line towers of Wudongde transmission project.

with a total of three. One 150 mH current limiting reactor is installed at each unipolar neutral bus and DC pole at Longmen converter station, two in total.

Simulation Model of Transmission Line Module

Wudongde transmission project starts from Kunbei converter station in Kunming, Yunnan province in the west, to the Liubei converter station in Liuzhou, Guangxi province, and Longmen converter station in Huizhou, Guangdong province in the East, with a total length of 1,489 km, of which the length of the Kunbei-Liubei section is 932 km, and the average soil resistivity along the line is 1750 Ω · m. The length of the Liubei Longmen section is 557 km, and the average soil resistivity along the line is 2,500 Ω · m. The parameters of the line tower are shown in **Figure 4**.

CONTROL SYSTEM MODELING

A CIGRE standard HVDC test system has been published, which is an effective and convenient research tool to study HVDC technology. At present, two types of simulation models of LCC-HVDC and VSC-HVDC are provided in the system. Among them, the MMC-HVDC control system of VSC-HVDC has two modulation modes of PWM and NLC to choose from. However, CIGRE does not provide a standard HVDC model for mixing the LCC converter station with VSC converter stations. Moreover, the Wudongde transmission project adopts constant DC and constant α control at the Kunbei-side, constant active and reactive power control at the Liubei-side, and constant DC voltage and reactive power control at the Longmen-side.

Therefore, based on the LCC-HVDC and NLC-MMC-HVDC control systems in CIGRE, this study establishes a simulation model of the control system suitable for hybrid multi-terminal UHVDC transmission by making necessary modifications to the control system and adding some auxiliary control links.

Control System Model of LCC Converter Station

The LCC-HVDC in CIGRE is a unipolar system. The converter station is connected in series with two 6-pulse converters to form a single 12-pulse converter, with rated DC, voltage, and power of 2 kA, 500 kV, and 1000 MW, respectively. While the Wudongde transmission project is a bipolar system. The Kunbei converter station adopts the LCC converter, and the single-pole consists of high-low valves through two 12-pulse converter in series. The output rated DC, voltage, and power are 5 kA, 800 kV, and 4000 MW, respectively (Jingjing et al., 2018). The output of voltage, DC, and DC power of the whole converter station is ±800 kV DC, ±5 kA, and 8000 MW, respectively. It can be seen that the existing control system in CIGRE cannot meet the actual needs of the project. For this reason, the standard control system of LCC-HVDC is modified to meet the control requirements of the converter valve in the Kunbei converter station, and the modified control system is shown in **Figure 5A**.

As can be seen from **Figure 5A**, the main modifications are as follows:

1) The same measured voltage and current values are selected as the control signals for the unipolar converter valve at the Kunbei converter station.
2) The same triggering angle α generated by constant current control is used to control the conduction of all converters of the unipolar converter valve simultaneously.
3) The measurement links at the Kunbei-side and Longmen-side are simulated with the first-order inertial link. The measured current gain of the Kunbei-side is modified to 0.2, and the measured current and voltage gains of the Longmen-side are modified to 0.32 and 0.00125, respectively. Then, the measured current of the Longmen-side after the first-order inertia link is multiplied by 0.04 and adds with the measured voltage of the Longmen-side after the first-order inertia link as the voltage value at the midpoint of the line, which is

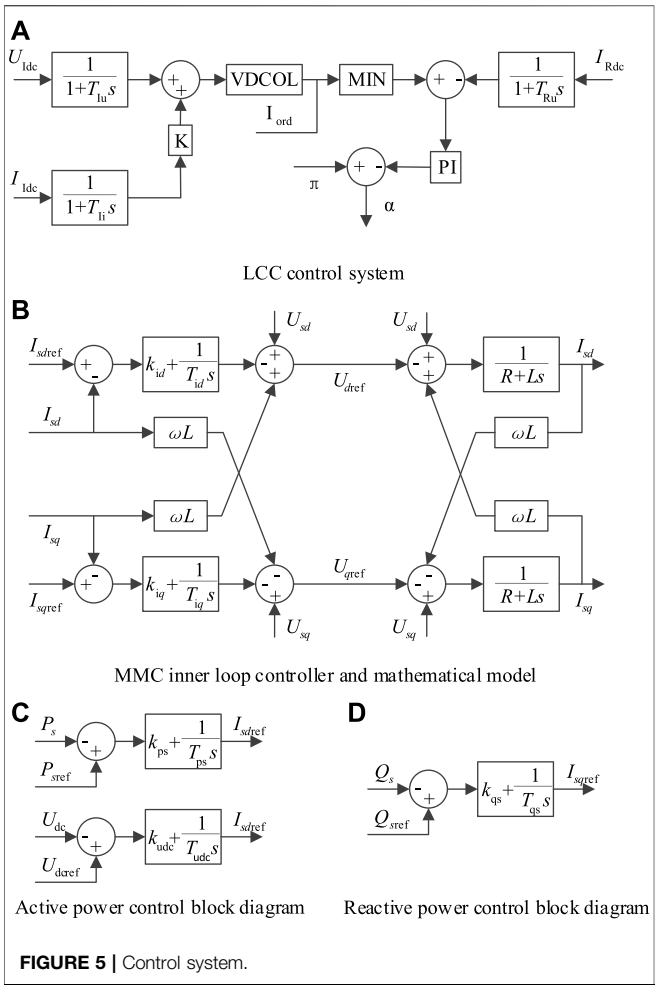

FIGURE 5 | Control system.

converted to current value after the limiting link, and the inertia time constant is not modified.

In addition, the unipolar converter valve adds a forced phase-shifting and unlocking control module to realize the purpose of unlocking conduction after establishing a stable DC voltage at the MMC side and forced phase-shifting after DC system fault. The control models of the positive electrode and the negative electrode are basically the same. After multiplying the measured voltage at the gantry side by −1, it can be used as the input value of the measured voltage of the negative electrode control system at the Kunbei-side.

Control System Model of MMC

The NLC-MMC-HVDC in CIGRE has both true and pseudo-bipolar structures. However, a single converter station or unipolar converter valve has only one MMC converter, and the output rated DC voltage is ±400 kV. In contrast, the Wudongde transmission project is a true bipolar multi-terminal system, with MMC converters at Liubei and Longmen converter station and a unipolar converter valve with two MMCs connected in series to form a high-low valve. The output rated DC, voltage, and power are ±1.875 kA, ±800 kV, and 3000 MW at the Liubei converter station and ±3.125 kA, ±800 kV, and 5000 MW at the Longmen converter station. In addition, the MMC converter of the standard flexible DC test system in CIGRE has a single bridge structure, while the MMC converter of the Wudongde transmission project has a hybrid bridge structure, which shows that the existing control system cannot meet the actual needs of the project. Therefore, the standard control system of NLC-MMC-HVDC is modified to meet the converter valve control requirements of the Liubei and Longmen converter station. The MMC converter has two kinds of controllers, the outer loop and the inner loop (Ligang et al., 2017), and the combination of the two constitutes the control system of the MMC. The inner loop controller and the mathematical model are shown in **Figure 5B**, and the outer loop controller is shown in **Figure 5C** and **Figure 5D**.

Based on the MMC converter control system, the main modifications are as follows:

1) The same measured current value and the measured voltage values of both high-low valves are selected as the control signals for the unipolar converter valves at the Liubei and Longmen converter stations.
2) The same active or reactive command value is adopted as the input command signal for both unipolar high-low valves.
3) An unlocking module on failure is added to achieve transient fault self-clearing capability for the full-bridge submodule.

Moreover, the MMC submodule of the Wudongde transmission project adopts a hybrid bridge structure, so the full-bridge submodule is added to the half-bridge type MMC to form a hybrid bridge structure, using the same measured signal as the input signal of the full-bridge and half-bridge submodule control systems, the output signal of the half-bridge submodule control system controls the on/off of the half-bridge submodule, and the output signal of the full-bridge submodule control system controls the on/off of the full-bridge module. The simulation models of the half-bridge submodule and the full-bridge submodule control system are shown in **Figure 6** and **Figure 7**.

SIMULATION MODEL OF HYBRID MULTI-TERMINAL UHVDC

According to the parameters, the main wiring diagram, the simulation model of each component, and the control system of the Wudongde transmission project, the simulation model of the Wudongde transmission system is established as shown in **Figure 8**.

The Wudongde transmission project is designed with a rated voltage of ±800 kV, the Kunbei converter station is designed to output ±5 kA rated current and 8000 MW rated DC power, the Liubei converter station is designed to output ±1.875 kA rated current and 3000 MW rated DC power, and the Longmen converter station is designed to output ±3.125 kA rated current and 5000 MW rated DC power. The Kunbei-side is controlled with constant current, the Liubei-side is controlled with constant active and reactive power, and the Longmen-side is controlled with

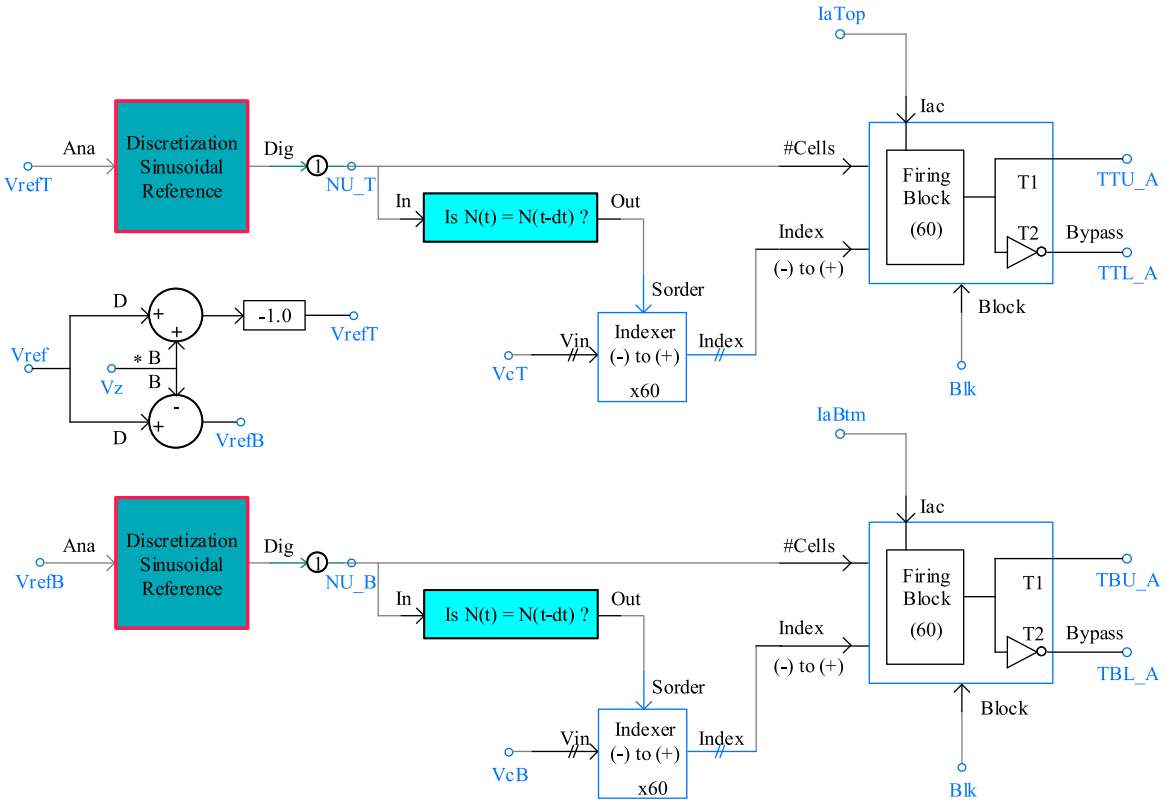

FIGURE 6 | Simulation model of half-bridge power module control system.

constant DC voltage and constant reactive power. The rated voltage of the AC system is 535, 525, and 500 kV at Kunbei, Liubei, and Longmen converter station, respectively, and the maximum short-circuit current of all three phases is 63 kA. Four large groups of AC filters are installed at the AC bus of the Kunbei converter station, two groups of triple tuned filters at the positive and negative electrode outlet of the converter station, and two sets of 75 mH smoothing reactors are installed at the positive and negative neutral bus and the DC pole, respectively. At the positive and negative neutral bus of the Liubei converter station, one 200 mH current limiting reactor is installed, respectively, and two 50 mH current limiting reactors are installed, respectively, at the DC pole. A 150 mH current limiting reactor is installed at the positive and negative neutral bus and DC pole, respectively, in the Longmen converter station. The transformer adopts a three-phase double-winding structure, with the capacity of a single set of 1,217.4 MVA at the Kunbei-side, wired in two ways, Y0/Y and Y0/△; 870 MVA at the Liubei-side, wired in Y0/Y; and 1440 MVA at the Longmen-side, wired in Y0/Y. The unipolar converter valve of the Kunbei converter station uses two 12-pulse LCC converters connecting in series to form a high-low valve, the voltage distribution is according to (400 + 400) kV, the two MMC converter units are connecting in series to form the unipolar converter valve of the Liubei converter station and Longmen converter station, and the voltage distribution is according to (400 + 400) kV. The MMC converter valve bridge arm is composed of a half-bridge submodule and full-bridge submodule in a mixed cascade ratio of 3:7. The upper and lower bridge arms are connected to 200 submodules at any time with certain redundancy, and the output voltage of a single converter is maintained at 400 kV. The total length of the Wudongde transmission project is 1,489 km, of which the Kunming–Liuzhou section is 932 km, the average soil resistivity along the line is 1750 Ω · m, the Liuzhou–Longmen section is 557 km, and the average soil resistivity along the line is 2,500 Ω · m. The frequency correlation model is adopted. Based on the LCC-HVDC and NLC-MMC-HVDC control systems in CIGRE, modifications are made to add some necessary auxiliary control links to establish a simulation model of the control system applicable to the Wudongde transmission project.

SIMULATION RUNNING

In this study, a simulation model of hybrid multi-terminal UHVDC transmission is established in PSCAD/EMTDC with the Wudongde transmission project as the object. Under the full-voltage ground return operation mode, steady-state simulation experiments are conducted for three basic DC operation modes, namely, positive, negative, and bipolar operation, and the transient process of faults occurring on the DC line during bipolar operation is simulated to verify the accuracy and credibility of the simulation model built in this study, in which the measurement points are located at the outlet of the smoothing

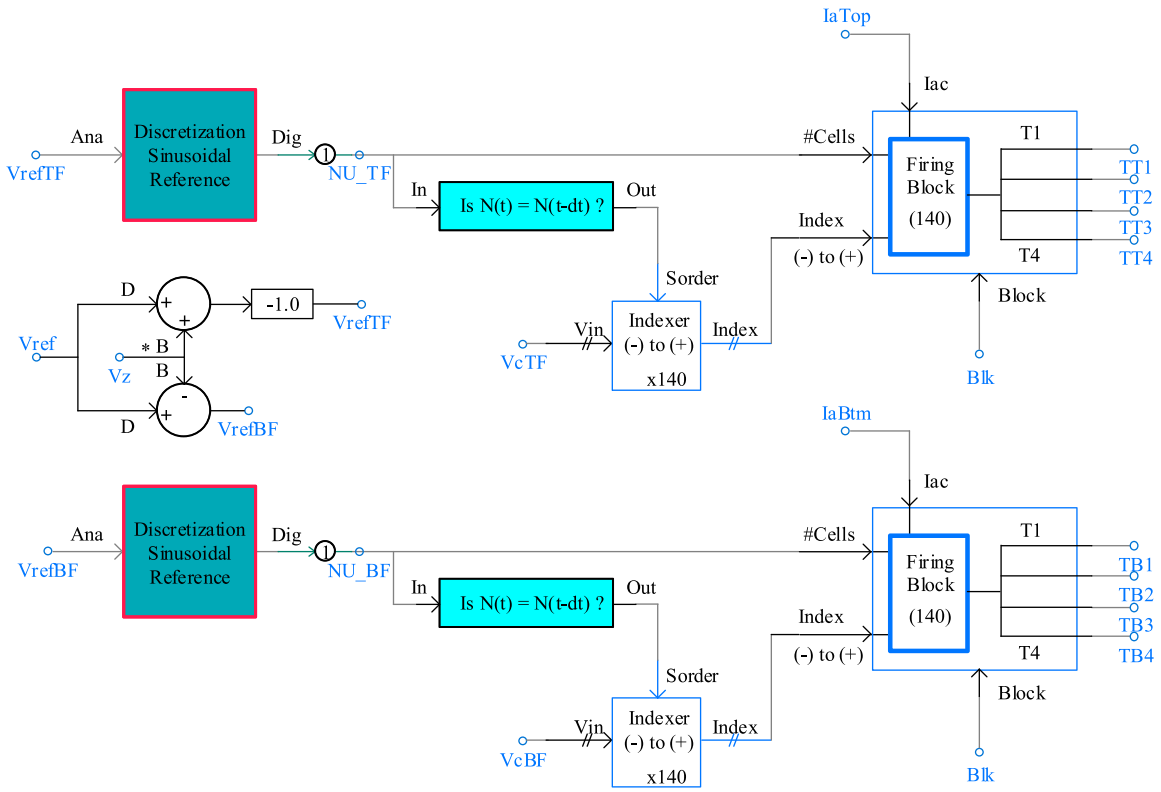

FIGURE 7 | Simulation model of full-bridge power module control system.

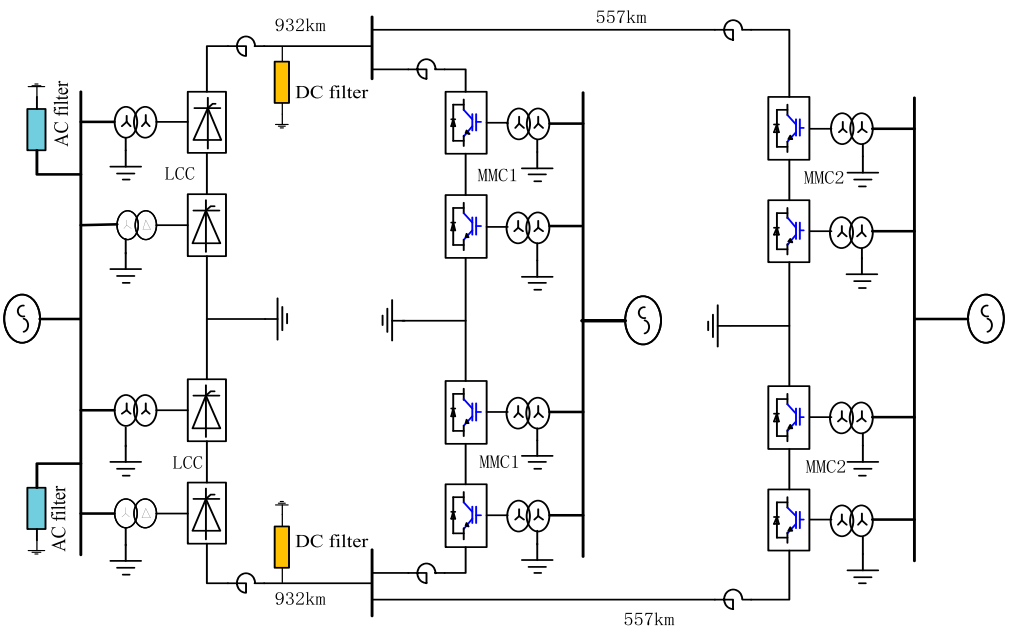

FIGURE 8 | Simulation model of the Wudongde transmission project.

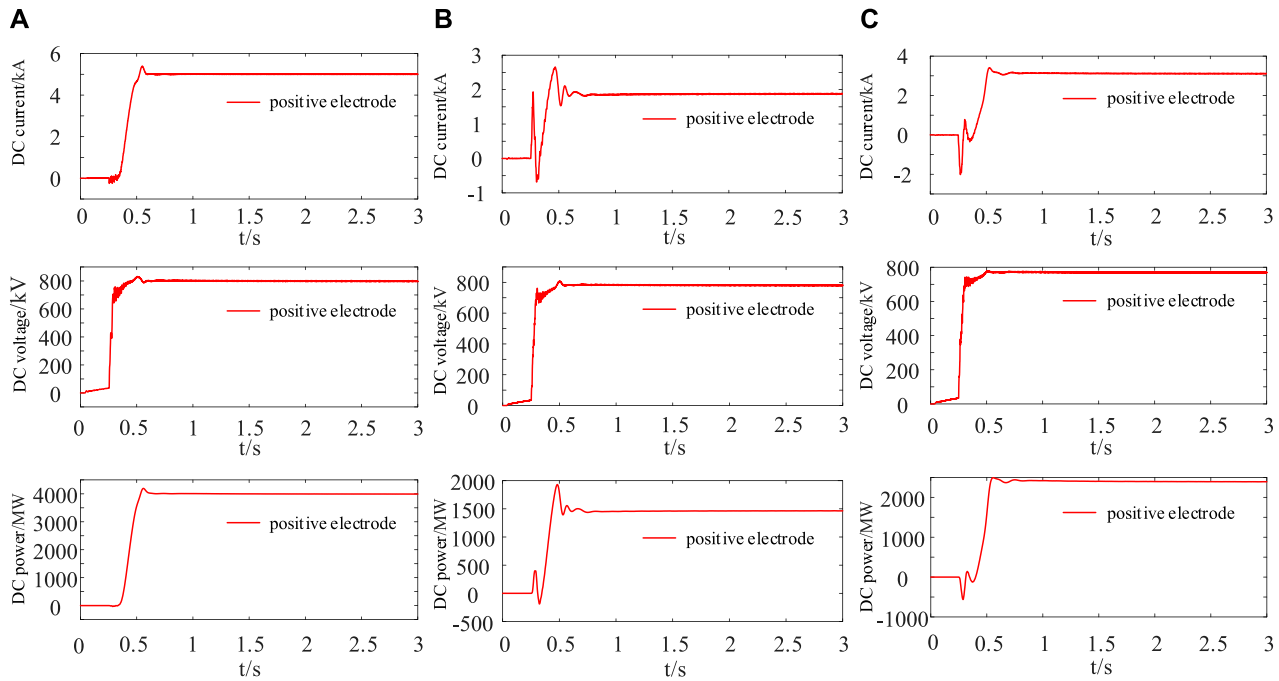

FIGURE 9 | Simulated waveform of positive full voltage ground return operation.

reactor of Kunbei converter station and the outlet of the current limiting reactor of Liubei and Longmen converter station outlet.

Steady-State Operation

Simulation of Positive Full-Voltage Ground Return Operation

The DC, voltage, and power waveforms at the outlet of the positive smoothing reactor of the Kunbei converter station and the outlet of the positive limit current reactor of the Liubei and Longmen converter station under the positive full-voltage ground return operation are shown in **Figure 9**.

From **Figure 9**, it can be seen that the DC, voltage, and power at the outlet of the smoothing reactor of Kunbei converter station are +5 kA, +800 kV, and 4000 MW, respectively; the DC, voltage, and power at the outlet of the current limiting reactor at Liubei converter station are around +1.875 kA, +780 kV, and 1445 MW, respectively; and the DC at the outlet of the current limiting reactor at the Longmen converter station are around +3.125 kA, +765 kV, and 2375 MW, respectively. The DC, voltage, and power at the Kunbei-side are consistent with the design rating of the Wudongde transmission project, and the DC at the Liubei-side and Longmen-side are consistent with the design rating of the project, while the DC voltage and power are lower than the design rating, which is caused by the transmission line losses. It can be seen that the output DC, voltage, and power of the hybrid multi-terminal UHVDC transmission system established in this study for positive full-voltage operation are basically the same as the design values of rated current, voltage, and power during the positive operation of the Wudongde transmission project.

Simulation of Negative Ground Return Operation Mode in Full Voltage

Under the negative ground return operation mode in full voltage, the DC, voltage, and power waveforms at the outlet of the negative smoothing reactor of the Kunbei converter station, the DC, voltage, and power waveforms at the outlet of the negative limiting current reactor of the Liubei converter station and the DC, voltage, and power waveforms at the outlet of the negative limiting current reactor of Longmen converter station are shown in **Figure 10**.

From **Figure 10**, it can be seen that the DC, voltage, and power at the outlet of the smoothing reactor at Kunbei converter station are −5 kA, −800 kV, and 4000 MW, respectively; the DC, voltage, and power at the outlet of the current limiting reactor at the Liubei converter station are around −1.875 kA, −780 kV, and 1445 MW, respectively; and the DC, voltage, and power at the outlet of the current limiting reactor at the Longmen converter station are around −3.125 kA, −765 kV, and 2375 MW, respectively. The DC, voltage, and power at the Kunbei-side are highly consistent with the design rating of the Wudongde transmission project; the DC at the Liubei-side and Longmen-side are consistent with the design rating of the Wudongde transmission project; and the DC voltage and power are lower than the design rating, which is caused by the transmission line losses. It can be seen that the output DC, voltage, and power of the

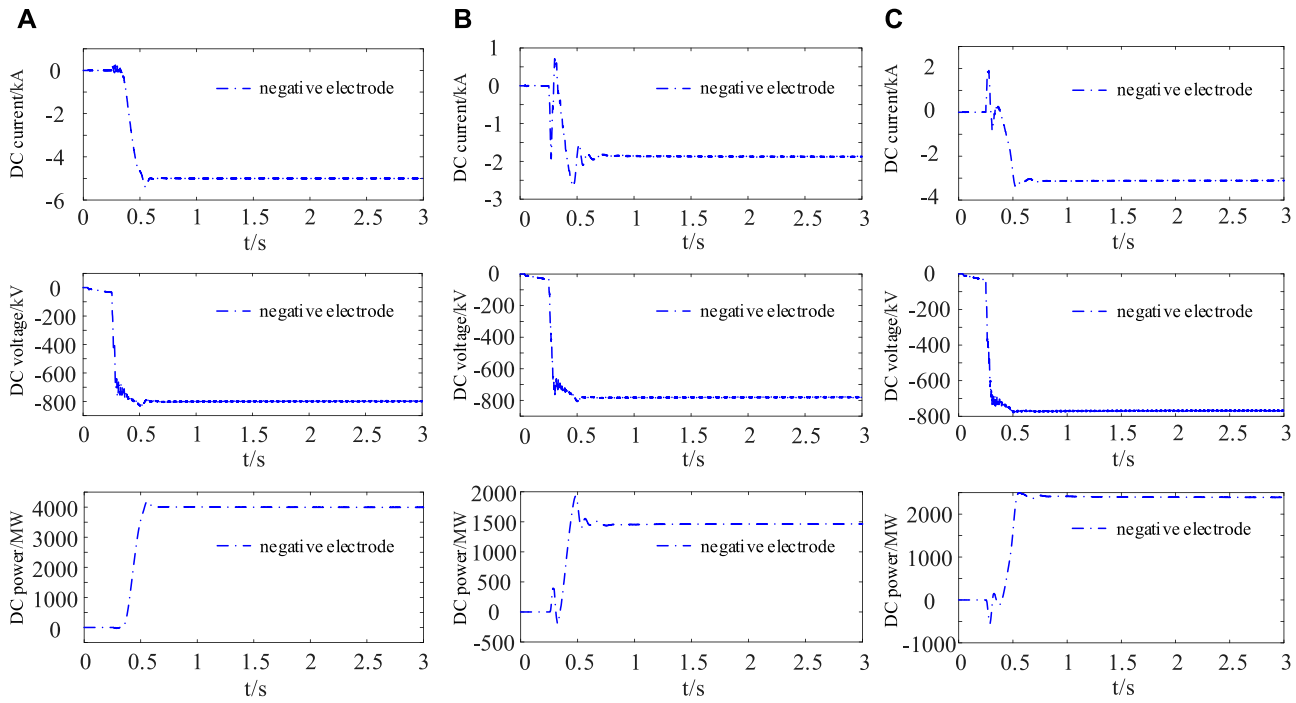

FIGURE 10 | Simulated waveform of negative full voltage ground return operation.

hybrid multi-terminal UHVDC transmission system established in this study for negative full-voltage operation are basically the same as the design values of rated current, voltage, and power for negative operation of the Wudongde transmission project.

Simulation of Bipolar Ground Return Operation Mode in Full Voltage

The DC, voltage, and power waveforms at the outlet of the smoothing reactors of the positive electrode and the negative electrode at the Kunbei converter station; the DC, voltage, and power waveforms at the outlet of the limiting current reactors of the positive electrode and the negative electrode at the Liubei converter station; and the DC, voltage, and power waveforms at the outlet of the limiting current reactors of the positive electrode and the negative electrode at the Longmen converter station under the bipolar ground return operation mode in full voltage are shown in **Figure 11**.

From **Figure 11**, it can be seen that the DC, voltage, and power at the outlet of the smoothing current reactor of the positive electrode at the Kunbei converter station are +5 kA, +800 kV, and 4000 MW, respectively, and the DC, voltage, and power at the outlet of the smoothing current reactor of the negative electrode are −5 kA, −800 kV, and 4000 MW, respectively. The DC, voltage, and power at the outlet of the limiting reactor of the positive electrode at the Liubei converter station are around +1.875 kA, +780 kV, and 1445 MW, respectively. The DC, voltage, and power at the outlet of the limiting reactor of the negative electrode are around −1.875 kA, −780 kV, and 1445 MW, respectively. The DC, voltage, and power at the outlet of the limiting reactor of the positive electrode at the Longmen converter station are around +3.125 kA, +765 kV, and 2375 MW, respectively. The DC, voltage, and power at the outlet of the limiting reactor of the negative electrode are around −3.125 kA, −765 kV, and 2375 MW, respectively. The DC, voltages, and powers of the positive electrode and the negative electrode at the Kunbei-side are consistent with the design rating of the Wudongde transmission project; the DC of the positive electrode and the negative electrode at the Liubei-side and Longmen-side are consistent with the design rating of the Wudongde transmission project; and the DC voltages and powers are lower than the design rating, which is caused by the transmission line losses. It can be seen that the output DC, voltage, and power of the bipolar operation in full voltage of the hybrid multi-terminal UHVDC transmission system established in this study are basically the same as the design rated current, voltage, and power of the bipolar operation in full-voltage of the Wudongde transmission project.

Waveform Comparison in Steady-State Operation

The simulating and recording waveforms of the Wudongde transmission project are shown in **Figure 12** under the operations of bipolar ground return in full voltage.

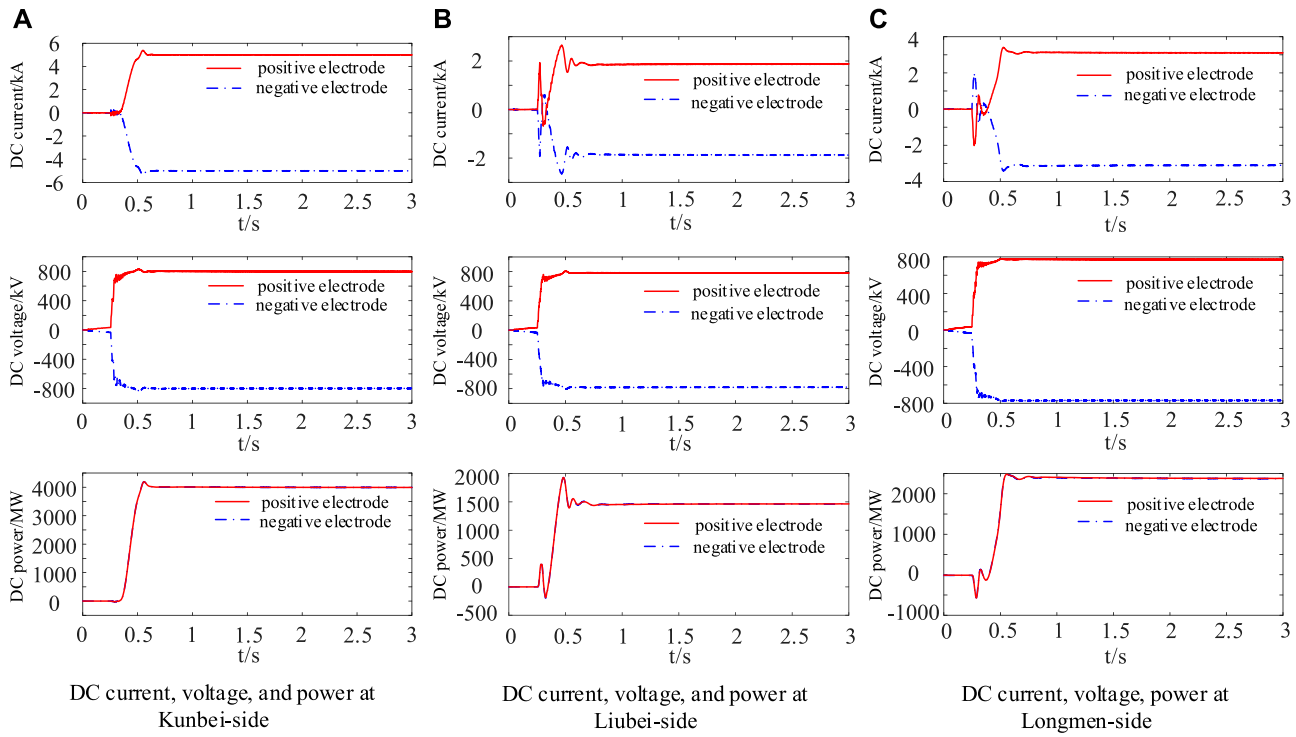

FIGURE 11 | Simulation waveform of full voltage bipolar ground loop operation mode.

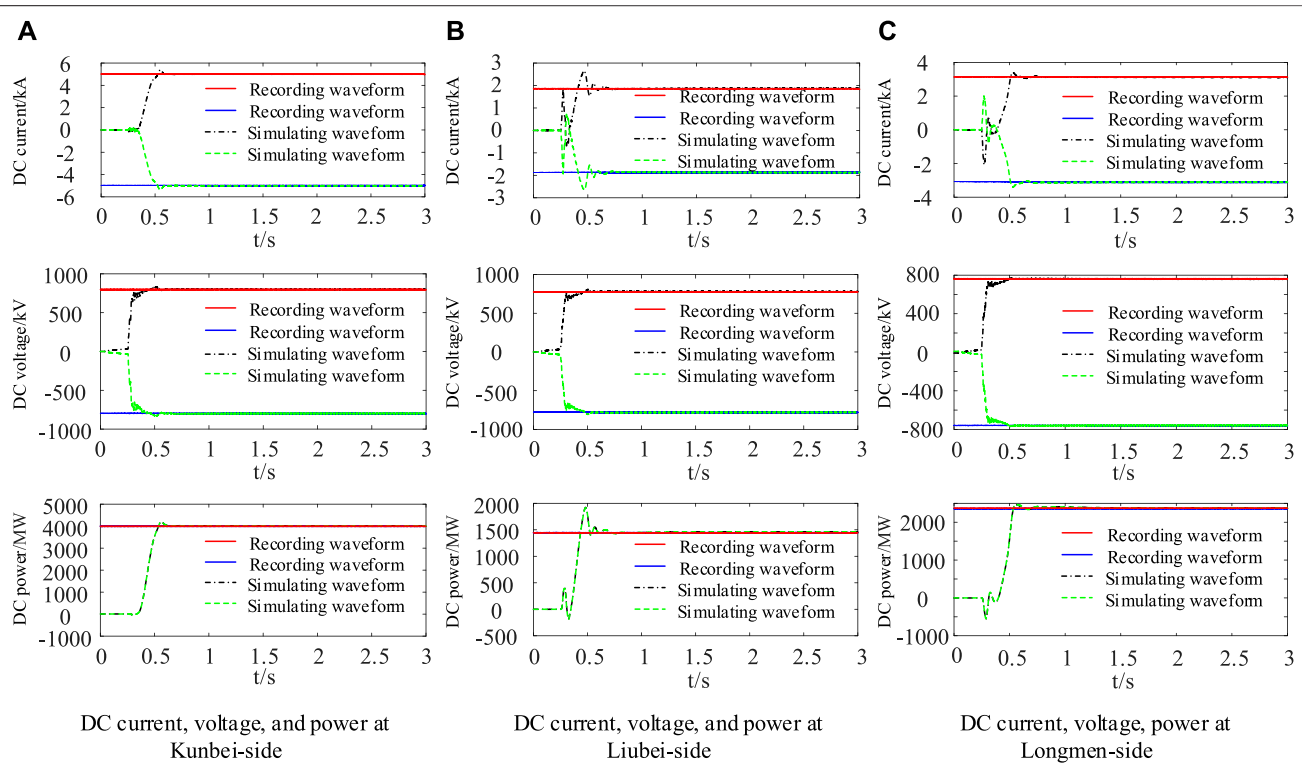

FIGURE 12 | Comparison of simulated waveforms and recorded waveforms in steady-state operation.

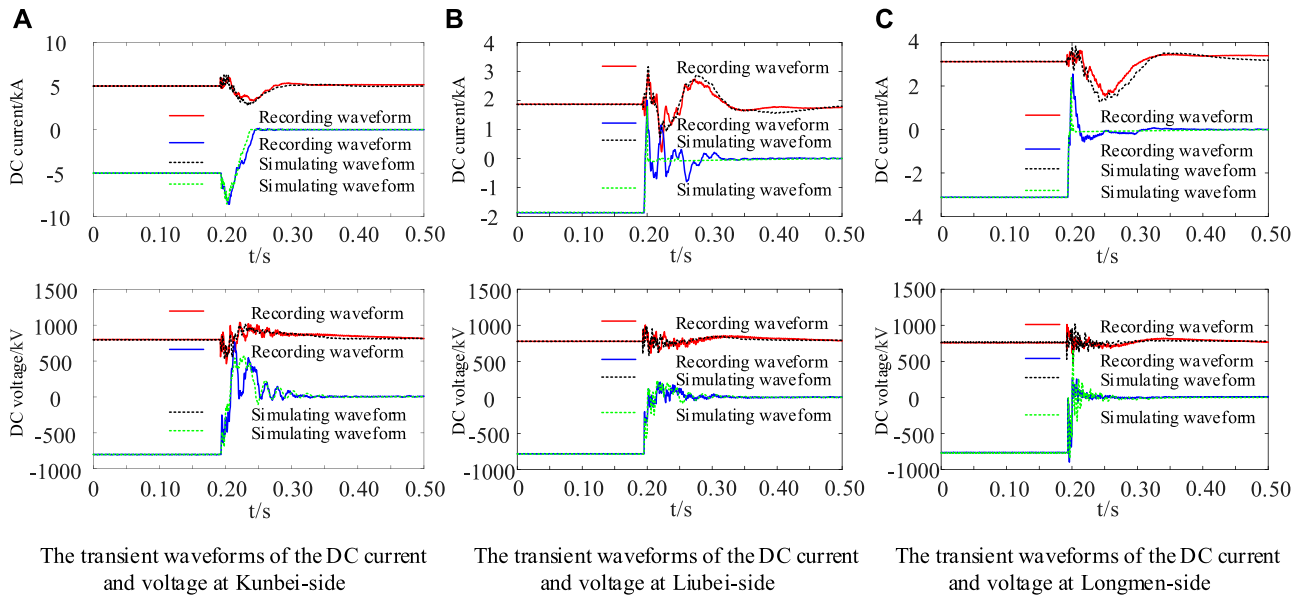

FIGURE 13 | Comparison of transient waveforms of negative electrode midpoint faults in the DC line from Liuzhou to Longmen.

From **Figure 12**, it can be seen that the output DC, voltage, and power simulation waveforms at the outlet of the smoothing reactor of the Kunbei converter station of the hybrid multi-terminal UHVDC transmission system are highly consistent with the recording waveforms under the operations of bipolar ground return in full voltage. Moreover, the output DC, voltage, and power simulating waveforms at the outlet of the limiting reactor of the Liubei and Longmen converter stations are highly consistent with the recording waveforms, which shows that the simulation model of the hybrid multi-terminal UHVDC transmission system built in this study can accurately simulate the steady-state operation of the Wudongde DC transmission project.

Waveform Comparison of Transient Operation

Overhead DC transmission lines are prone to failure due to complex terrain and climate, and transient response is an important means to test the accuracy of the simulation model. Therefore, taking the grounding fault of the transmission line as an example, this study compared the simulating waveforms with the actual recording waveforms to further verify the accuracy and credibility of the simulation model of the hybrid multi-terminated UHVDC transmission system built in this study.

Midpoint Fault of the Negative Electrode of the DC Line From Liuzhou to Longmen Converter Station

Assume that the grounding fault of the negative electrode occurs at the midpoint of the Liuzhou–Longmen transmission line, with the grounding resistance of 0.4 Ω and the fault duration of 0.1 s. A comparison of the simulating and recording waveforms of the DC and voltage is shown in **Figure 13**.

From **Figure 13**, it can be seen that when a grounding fault occurs at the negative electrode midpoint of the transmission line of the Wudongde transmission project, the DC at the fault pole of the Kunbei-side increases rapidly to 1.7 times the rated value and then gradually decreases to 0. The DC at the non-fault pole increases slightly, fluctuates sharply, and then tends to normal values. The fault pole voltage rapidly decreases, increases anyway, and then gradually decreases to 0, and the non-fault pole voltage fluctuates violently and then tends to normal value. At the Liubei-side, the fault pole DC rapidly decreases and increases in reverse to near the rated value and then gradually decreases to 0. The non-fault pole current fluctuates violently and then gradually tends to normal value. The fault pole voltage decreases rapidly and then gradually tends to 0, and the non-fault pole voltage fluctuates and then gradually tends to the normal value. The fault pole DC at the Longmen-side decreases rapidly and increases in reverse to near the rated value and then gradually decreases to 0. The non-fault pole current fluctuates violently and then gradually tends to the normal value. The fault pole voltage decreases rapidly and then gradually tends to 0. The non-fault pole voltage fluctuates and then gradually tends to the normal value. The trend of the simulating waveform at the three terminals after the fault is basically the same as that of the recording waveform, especially in the first 5 ms after the fault and after a period of time. The incomplete consistency between the recording and the simulating waveforms after the fault is caused by the difference in control strategies between the CIGRE standard control system and the actual engineering control system during the fault.

Fault at 25% of the Positive Electrode of the DC Transmission Line From Liuzhou to Longmen Converter Station

Assume that the grounding fault occurs at 25% of the positive electrode of the transmission line from Liuzhou to Longmen, with

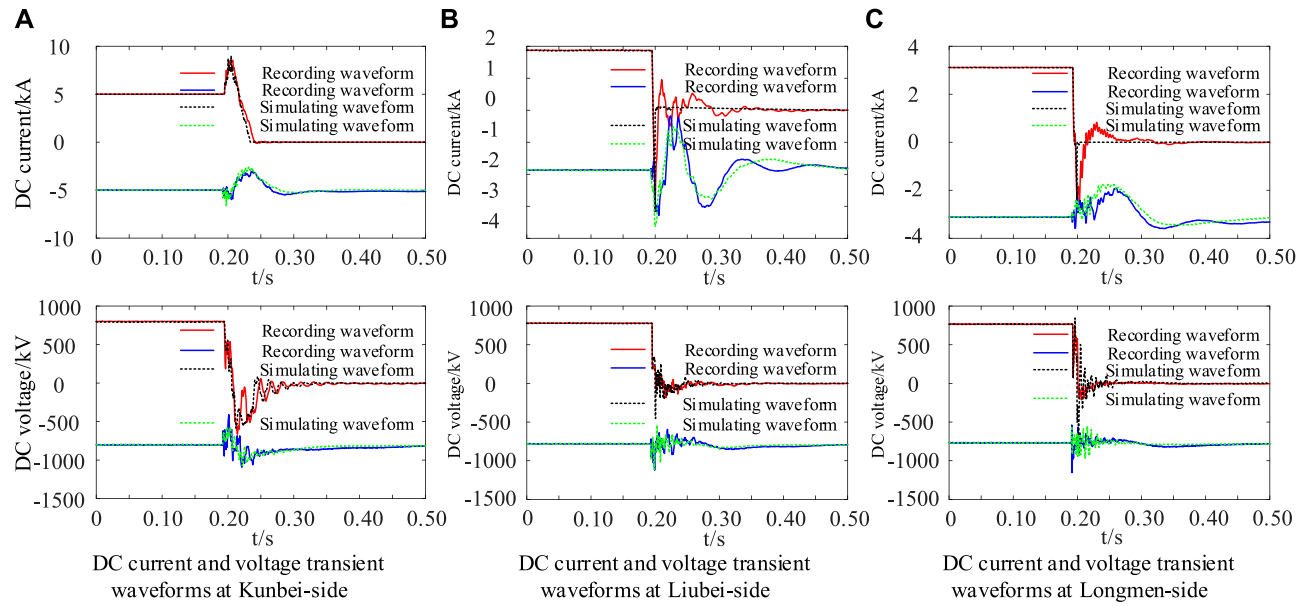

FIGURE 14 | Comparison of transient waveforms at the positive electrode 25% of the DC line from Liuzhou to Longmen.

a ground resistance of 0.4 Ω and a fault duration of 0.1 s. A comparison of the simulating and recording waveforms of the DC and voltage is shown in **Figure 14**.

From **Figure 14**, it can be seen that when a ground fault occurs at the positive electrode of the transmission line of the Wudongde transmission project, the DC at the fault pole of the Kunbei-side increases rapidly to 1.7 times the rated value and then gradually decreases to 0. The DC at the non-fault pole fluctuates after a slight increase and then tends to the normal value. The voltage at the fault pole rapidly decreases and increases anyway and then gradually decreases to 0. The non-fault pole voltage fluctuates drastically and then tends to a normal value. The DC of the fault pole at the Liubei-side rapidly decreases, increases in reverse to near the rated value, and then gradually decreases to 0. Non-fault pole current fluctuates violently and then gradually tends to normal value. The fault pole voltage decreases rapidly and then gradually tends to 0. The non-fault pole voltage fluctuates and then gradually tends to the normal value. The fault pole DC of the Longmen-side decreases rapidly, increases in reverse to near the rated value, and then gradually decreases to 0. The non-fault pole current fluctuates violently and then gradually tends to the normal value. The fault pole voltage decreases rapidly and then gradually tends to 0. The non-fault pole voltage fluctuates and then gradually tends to the normal value. The trend of the simulating waveforms at the three terminals after the fault is basically the same as that of the recording waveforms, especially in the first 5 ms after the fault and after a period of time. The incomplete consistency between the recording and simulating waveforms after the fault is caused by the difference in control strategies between the CIGRE standard control system and the actual engineering control system during the fault.

From the above analysis, it can be seen that the DC, voltage, and power of the simulated model of the hybrid multi-terminal UHVDC transmission system in full-voltage operation are consistent with the design rating of the Wudongde transmission project, and the simulating waveforms of DC, voltage, and power in steady-state operation of the model are highly consistent with the actual recording waveforms of the project. The trends of DC and voltage waveforms during the transient process are basically consistent with the trends of recording waveforms, especially in the first 5 ms after the fault occurs, and the simulating and recording waveforms are highly consistent. It can be seen that the simulation model of the hybrid multi-terminal UHVDC transmission system established in this study can accurately simulate the operation of the Wudongde transmission project.

CONCLUSION

This research studied the Wudongde transmission project. Based on the design parameters and system control mode of the Wudongde transmission project, a detailed simulation model of the hybrid multi-terminal UHVDC transmission system is built by PSCAD/EMTDC. The steady-state operation simulation of the positive electrode, negative electrode, and bipolar DC power transmission is carried out under full-voltage ground return operation mode, and the steady-state simulation waveform of bipolar full-voltage operation mode is compared with the actual recording waveforms. The grounding fault of the DC line is simulated, and the trend of simulating waveform and recording waveform in the transient process is compared. Results show the following:

1) The hybrid multi-terminal UHVDC transmission system simulation model established based on the primary system

parameters of the Wudongde transmission project has high accuracy and reliability.
2) The control system model modified based on the HVDC transmission and 9-terminal DC grid control benchmark model of the CIGRE is suitable for the Wudongde transmission project.
3) Under the steady-state operation, the simulating waveforms of the hybrid multi-terminal UHVDC transmission system are highly consistent with those at the same points during the steady-state operation of the actual project.
4) Under transient operation, the trend of simulated waveforms of the hybrid multi-terminal UHVDC transmission system is consistent with the trend of recording waveforms at the Wudongde transmission project.
5) It provides accurate, credible, and effective tools for the study of the electromagnetic transient characteristics in the hybrid multi-terminal UHVDC transmission system.
6) It provides accurate and credible fault simulation data for the research of the hybrid multi-terminal UHVDC transmission line protection.
7) It provides some guidance for the inversion analysis of the Wudongde transmission project accident.

DATA AVAILABILITY STATEMENT

The original contributions presented in the study are included in the article/supplementary material, further inquiries can be directed to the corresponding author.

AUTHOR CONTRIBUTIONS

CX was responsible for providing ideas, methods, and an experimental platform. SC and YC were responsible for deriving formulas, reviewing, and verifying. WC was responsible for model building, simulation, data analysis, and manuscript writing. GB, JG, and LW wrote sections of the manuscript. All authors participated in the reading and approved the submitted version.

FUNDING

Research on traveling wave boundary protection of UHV multi-terminal hybrid HVDC transmission lines 52067009.

REFERENCES

Anran, Z. H. E. N. G., Chunyi, G. U. O., and Zihan, Y. I. N. (2019). Small-signal Modeling Method of Hybrid Multi-Terminal HVDC System[J]. *Power Syst. Tech.* 43 (11), 4087–4096.

Benfeng, G. A. O., Jian, Y. A. N. G., and Shengli, S. O. N. G. (2021). Coordinated Control Strategy of Hydropower Units for Mitigating Overvoltage of Renewable Energy Generation System Integrated with HVDC[J]. *Proc. CSEE*, 1–14. [2021-07-11].

Chao, H. O. N. G., Bonian, S. H. I., and Gang, S. U. N. (2017). Fault Characteristics and Control & Protection Strategy of Three-TerminalLCC-MMC Hybrid HVDC Transmission System[J]. *Electric Pow er Construction* 28 (08), 73–79.

Dan, Y. A. N. G., Jie, D. A. N. G., and Wei, Q. I. U. (2020). Study on Voltage Stability of Hunan Power Grid Integrated with Qi-Shao UHVDC Transmission Line[J]. *J. Electric Power Sci. Tech.* 35 (06), 163–170.

He, J., Chen, K., Li, M., Luo, Y., Liang, C., and Xu, Y. (2020). Review of protection and Fault Handling for a Flexible DC Grid. *Prot. Control. Mod. Power Syst.* 5, 15. doi:10.1186/s41601-020-00157-9

Hong, R. A. O., Chao, H. O. N. G., and Baorong, Z. H. O. U. (2017). Study on Improvement of VSC-HVDC at Inverter Side of Wudongde Multi-Terminal UHVDC for the Problem of Centralized Multi-Infeed HVDC[J]. *South. Power Syst. Tech.* 11 (03), 1–5.

Huaqiang, X. I. O. N. G., Chengxiang, Y. A. N. G., and Liang, M. A. (2020). Electromechanical-electromagnetic Transient Hybrid Simulation of an AC/DC Hybrid Power Grid with UHVDC Hierarchical Connection Mode[J]. *Power Syst. Prot. Control.* 48 (24), 145–153.

Jingjing, L. I., Weihuang, H. U. A. N. G., and Tao, L. I. U. (2018). Research on Control Strategy of Multi-Terminal Hybrid UHVDC Transmission System[J]. *South. Power Syst. Tech.* 12 (02), 47–55.

Li, Z., Jiang, W., Abu-Siada, A., Li, Z., Xu, Y., and Liu, S. (2021). Research on a Composite Voltage and Current Measurement Device for HVDC Networks. *IEEE Trans. Ind. Electron.* 68 (9), 8930–8941. doi:10.1109/tie.2020.3013772

Ligang, Z. H. A. O., Chao, H. O. N. G., and Liang, T. U. (2017). Research and Realization of Electromechanical Transient Modeling of Multi-Terminal DC Transmission System[J]. *South. Power Syst. Tech.* 11 (07), 26–31.

Lingyun, C. H. E. N., Gaihong, C. H. E. N. G., and Chong, S. H. A. O. (2018). Research on Control Strategy for a 3-terminal LCC-MMC HVDC Transmission System[J]. *High Voltage Apparatus* 54 (07), 146–152.

Liu, Yi., Yang, Nan., and Dong, Bangtian. (2020). Multi-Lateral Participants Decision-Making: A Distribution System Planning Approach with Incomplete Information Game," *in IEEE Access* 8, 88933–88950.

Muniappan, Mohan. (2021). A Comprehensive Review of DC Fault protection Methods in HVDC Transmission Systems. *Prot. Control. Mod. Power Syst.* 6, 2. doi:10.1186/s41601-020-00173-9

Shan, L. I. U., Jun, Y. U., and Zhiyuan, H. E. (2018). Research on the Topology and Characteristic of Multi-Terminal HVDC Based on VSC and LCC[J]. *Proc. CSEE* 38 (10), 2980–2988+3148.

Shen, X., Ouyang, T., Khajorntraidet, C., Li, Y., Li, S., and Zhuang, J. (2021a). Mixture Density Networks-Based Knock Simulator. *Ieee/asme Trans. Mechatron.*, 1. doi:10.1109/TMECH.2021.3059775

Shen, X., Ouyang, T., Yang, N., and Zhuang, J. (2021b). Sample-Based Neural Approximation Approach for Probabilistic Constrained Programs. *IEEE Trans. Neural Netw. Learn. Syst.*, 1–8. doi:10.1109/TNNLS.2021.3102323

Shen, X., and Raksincharoensak, P. (2021b). Pedestrian-Aware Statistical Risk Assessment. *IEEE Trans. Intell. Transport. Syst.*, 1–9. doi:10.1109/TITS.2021.3074522

Shen, X., and Raksincharoensak, P. (2021a). Statistical Models of Near-Accident Event and Pedestrian Behavior at Non-signalized Intersections. *J. Appl. Stat.*, 1–21. doi:10.1080/02664763.2021.1962263

Shen, X., Zhang, X., Ouyang, T., Li, Y., and Raksincharoensak, P. (2020a). Cooperative Comfortable-Driving at Signalized Intersections for Connected and Automated Vehicles. *IEEE Robot. Autom. Lett.* 5, 6247–6254. doi:10.1109/lra.2020.3014010

Shen, X., Zhang, Y., Sata, K., and Shen, T. (2020b). Gaussian Mixture Model Clustering-Based Knock Threshold Learning in Automotive Engines. *Ieee/asme Trans. Mechatron.* 25, 2981–2991. doi:10.1109/TMECH.2020.300073210.1109/tmech.2020.3000732

Shen, X., Zhang, Y., Shen, T., and Khajorntraidet, C. (2017). Spark advance Self-Optimization with Knock Probability Threshold for Lean-Burn Operation Mode of SI Engine. *Energy* 122, 1–10. doi:10.1016/j.energy.2017.01.065

Song, Huang., Yingping, Yi., and Longzhen, Zhu. (2019). Research on Control Strategy of Positive and Negative Bipolar Hybridmulti-Terminal HVDC Transmission System[J]. *Electr. Meas. & Instrumentation* 56 (13), 51–57+96.

Xichun, W. A. N. G., Chun, L. I. U., and Weifang, L. I. N., (2021) Influence of Wind Turbine Fault Ride through Characteristics on Transient Overvoltage of Large-Scale Wind Power DC Transmission Systems and Parameters Optimization[J].

Weihuang, H. U. A. N. G., Ming, L. I., and Guo Zhu (2020). Control Parameter Analysis and Optimization Method of Multi-Terminal Hybrid HVDC

Transmission System Based on Small Signal Stability[J]. *Power Syst. Tech.* 44 (08), 2941–2949.

Weihuang, H. U. A. N. G., Shukai, X. U., and Huang Ying (2017). Steady-State Control Strategy of Multi-Terminal Hybrid UHVDC[J]. *South. Power Syst. Tech.* 11 (07), 5–10.

Yan, Y. A. N. G., Yong, L. I. N., and We, X. U. (2017). Influnce of Wudongde Multi-Terminal HVDC on Security and Stability of Guangdong Power Grid[J]. *Guangdong Electric Power* 30 (11), 44–50.

Yang, N., Huang, Y., and Hou, D. (2019a). Adaptive Nonparametric Kernel Density Estimation Approach for Joint Probability Density Function Modeling of Multiple Wind Farms[J]. *Energies*, 12.

Yang, N., Ye, D., Zhou, Z., Cui, J., Chen, D., and Wang, X. (2018). Research on Modelling and Solution of Stochastic SCUC under AC Power Flow Constraints[J].IET Generation. *Transm. Distribution* 12 (15), 3618–3625.

Yang, N., Huang, Y., Hou, D., Liu, S., Ye, D., Dong, B., et al. (2019b). Adaptive Nonparametric Kernel Density Estimation Approach for Joint Probability Density Function Modeling of Multiple Wind Farms. *Energies* 12, 1356. doi:10.3390/en12071356

Yang, N., Liu, S., Deng, Y., and Xing, C. (2021b). An Improved Robust SCUC Approach Considering Multiple Uncertainty and Correlation. *IEEJ Trans. Elec Electron. Eng.* 16, 21–34. doi:10.1002/tee.23265

Yang, N., Yang, C., Wu, L., Shen, X., Jia, J., Li, Z., et al. (2022). Intelligent Data-Driven Decision-Making Method for Dynamic Multisequence: An E-Seq2Seq-Based SCUC Expert System. *IEEE Trans. Ind. Inf.* 18, 3126–3137. doi:10.1109/TII.2021.3107406

Yang, N., Yang, C., Xing, C., Ye, D., Jia, J., Chen, D., et al. (2021a). Deep Learning-based SCUC Decision-making: An Intelligent Data-driven Approach with Self-learning Capabilities. *IET Generation Trans. Dist* 16, 629–640. doi:10.1049/gtd2.12315

Yuankang, H. E., Ruifeng, L. I. U., and Tian'en, C. H. E. N. (2021). Exploration of Bundled Transaction Model for All Clean Energy Transmission of Qing-Yu UHV DC Project[J]. *Electric Power*, 1–9. [2021-07-11].

Yuansheng, L. I. A. N. G., Zejie, H. U. A. N. G., and Haifeng, L. I. (2021). Phase Characteristics Based Travelling Wave Protection for Transmission Line of Three-Terminal Hybrid HVDC System. *Proc. CSEE* 41 (13), 4525–4543.

Zehong, L. I. U., Weimin, M. A., and Wang Shaowu (2021). Schematic Design of Hybrid Cascaded Ultra HVDC and its Modification in Dynamic Model Experiment[J]. *Power Syst. Tech.* 45 (03), 1214–1222.

Zhang, L., Xie, Y., Ye, J., Xue, T., Cheng, J., Li, Z., et al. (2021). Intelligent Frequency Control Strategy Based on Reinforcement Learning of Multi-Objective Collaborative Reward Function. *Front. Energ. Res.*, 9. SCI. doi:10.3389/fenrg.2021.760525Frontiers in Energy Research, Early Access

Zheng, Xu. (2016). *Flexible DC Transmission System[M]*. Beijing: Machinery Industry Press.

Zhi-da, H. U. A. N. G., and Qing-song, H. U. A. N. G. (2019). Control Strategy of Hybrid Multi-Terminal HVDC Transmission System[J]. *Control Eng. China* 26 (09), 1738–1744.

Zhu, B., Ding, F., and Vilathgamuwa, D. M. (2020). Coat Circuits for DC-DC Converters to Improve Voltage Conversion Ratio. *IEEE Trans. Power Electron.* 35, 3679–3687. doi:10.1109/TPEL.2019.2934726

Conflict of Interest: Author CX is employed by Electric Power Research Institute, Southern Power Grid Yunnan Electric Power Co., Ltd. Author SC works at Kunming University of Science and Technology.

All the authors declare that the research was conducted in the absence of any commercial or financial relationships that could be construed as a potential conflict of interest.

frontiers in Energy Research

ORIGINAL RESEARCH
published: 18 March 2022
doi: 10.3389/fenrg.2022.848209

Prediction of the 3D Distribution of NOx in a Furnace *via* CFD Data Based on ELM

Manli Lv[1,2†], *Jianping Zhao*[2*], *Shengxian Cao*[2] *and Tao Shen*[3]

[1]College of Computer Science and Technology, Changchun University of Science and Technology, Changchun, China, [2]School of Automation Engineering, Northeast Electric Power University, Jilin, China, [3]Harbin Boiler Company Limited, Harbin, China

A novel method for the prediction of three-dimensional (3D) spatial distribution of NOx in a furnace is proposed and evaluated. Computational fluid dynamics (CFD) simulations are conducted to generate the data sets of 3D NOx spatial distribution. The data sets are partitioned based on NOx generation mechanisms to improve the model accuracy. Combining the Pearson coefficient and mutual information (PMI), the model input variables are optimized by feature selection. The prediction model of 3D NOx spatial distribution in the furnace is established based on extreme learning machine (ELM). The experiments are conducted considering a 350 MW coal-fired boiler with a change in the burner tilt angles under a rated load. The experimental results show that the data-driven method based on PMI-ELM can realize the rapid prediction of the 3D spatial distribution of NOx in the furnace with 12.84% mean absolute percentage error.

Keywords: three dimensional(3D) distribution of NOx, computational fluid dynamics simulation, coal-fired boiler, Pearson coefficient and mutual information, extreme learning machine

OPEN ACCESS

Edited by:
Tinghui Ouyang,
National Institute of Advanced Industrial Science and Technology, Japan

Reviewed by:
Jun Zhang,
Civil Aviation University of China, China
Yuan Yuan,
Shenyang Aerospace University, China

****Correspondence:***
Jianping Zhao
zjp@cust.edu.cn

†ORCID ID:
Manli Lv
orcid.org/0000-0003-0824-538X

Specialty section:
This article was submitted to Smart Grids, a section of the journal Frontiers in Energy Research

Received: *04 January 2022*
Accepted: *24 January 2022*
Published: *18 March 2022*

Citation:
Lv M, Zhao J, Cao S and Shen T (2022) Prediction of the 3D Distribution of NOx in a Furnace via CFD Data Based on ELM. Front. Energy Res. 10:848209. doi: 10.3389/fenrg.2022.848209

1 INTRODUCTION

Nitrogen oxides (NOx), released by coal-fired power plants, are one of the most harmful air pollutants that tend to seriously impact the air quality and human health. New NOx emission standards in coal-fired power plants list them to be below 100 mg of NO_2/Nm3 at 6% O_2 (dry-basis) (Ministry of Environmental Protection of the PRC, 2011). There are two primary methods to decrease NOx emissions: 1) flue gas denitration and 2) low nitrogen combustion (Fang Wang et al., 2018). Flue gas denitration is a post-treatment method that is performed by adding denitration devices at the tail flue. On the other hand, the low nitrogen combustion method utilizes low NOx burners or fuel/air at the combustion stage. The essence of low nitrogen combustion is to change the temperature field and component distribution in the furnace to reduce NOx formation. However, a lack of means for effective on-line observation of temperature and component distribution hinders the understanding of NOx formation. Rapid and accurate prediction of 3D spatial distribution of NOx has become a necessity in order to control NOx emissions and optimize the combustion process.

Two methods are usually used to obtain the NOx concentration in emissions of the coal-fired power plants: 1) the mechanism-based method and 2) the data-driven method. Computational fluid dynamics (CFD), a mechanism-based method, involves solving the partial differential equations governing the combustion process to simulate it under the given boundary and initial conditions (Dindarloo and Hower, 2015; Boyd and Kent, 1988; Xu et al., 2001). The calculation of NOx emissions through CFD can be divided into two stages. The first stage includes evaluating the 3D spatial distribution of the temperature field, velocity field, and products of combustion in the furnace.

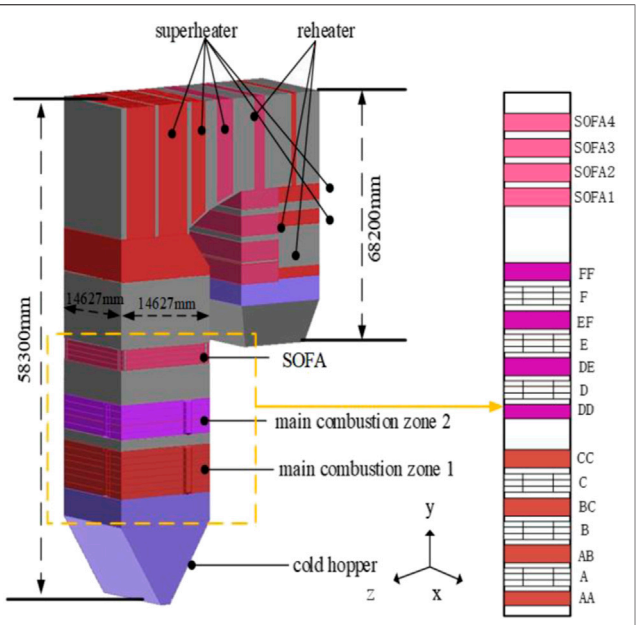

FIGURE 1 | Schematic structure and burner arrangement of the studied 350 MW boiler. **(A)** Boiler structure **(B)** Arrangement of the burner and the secondary wind.

The second stage involves NOx distribution evaluation by means of post-processing the already obtained combustion product data. CFD simulations with regards to the NOx spatial distribution mostly investigate the effects of a certain change in the working conditions of a furnace. This may include variations in boiler loads (Dindarloo and Hower, 2015; Boyd and Kent, 1988), swirl arrangements and coal injection modes (Choi et al., 2020), air staging combustion (Zhang et al., 2015; Wang and Zhou, 2020), separated over-fire air (SOFA) ratio and location (Ma et al., 2015), and tilt angles of the burner (Tan et al., 2017). CFD methods can analyze the change in NOx spatial distribution based on different input conditions and the relationships between various parameters. There have also been some improvements over the years with regards to the CFD combustion simulation methods .Zhang et al. (2019) proposed a semi-empirical modeling strategy with the large eddy simulation in which the concentration of CO + H2 substituted CHi, which is difficult to calculate to quantify NO homogenous reduction. The new model can accurately predict different NOx evolution characteristics under various conditions. Secco et al. (2015) coupled a genetic algorithm with CFD calculations to automatically generate optimal boiler configurations for minimizing NOx emissions. CFD simulations can also be used to optimize the combustion process. A drawback of using CFD simulations, however, is that they involve a plethora of complicated calculations which consume a large amount of time.

Another method to predict the NOx distribution is the data-driven method. This method is mainly focused on the NOx emission of the exhaust gas. In this regard, numerous algorithms, including statistical regression (Li et al., 2004; Chunlin Wang et al., 2018), support vector machine (Wei et al., 2013; Zhou et al., 2012; Ahmed et al., 2015; Lv et al., 2013), artificial neural network (ANN) (Chu et al., 2003; Ilamathi et al., 2013; Preeti and Sharad, 2013; Jacob and Tuttll, 2019), and deep learning (Li and Hu, 2020; Yang et al., 2020; Tan et al., 2019; Xie et al., 2020; Kang et al., 2017; Wang et al., 2017) are often used to predict the NOx concentration. Although remarkable achievements have been obtained in this area, the time complexity of support vector machines increases exponentially as the sample size increases. This problem may be attributed to quadratic programming problems. Moreover, the ANN is easy to fall into the local minimum and has the risk of over-fitting. The required data of data-driven modeling are usually collected from the operation and experimental data of power plants. In this regard, scholars have tried to combine CFD techniques with experimental data to predict the NOx distribution in engineering applications (Fang Wang et al., 2018; Yan et al., 2019). Currently, CFD data are mainly used as the supplement of operation data, or it is combined with historical data to obtain comprehensive data on the working conditions. However, it is a challenge to analyze a huge amount of 3D data obtained from CFD simulation. On the other hand, simple NOx prediction of the exhaust gas is not conducive to optimizing combustion parameters and fault analysis.

In this study, a data-driven method is proposed to obtain the 3D NOx distribution based on the extreme learning machine (ELM) method. Then, NOx distribution in the furnace is obtained using CFD simulation. The obtained data are partitioned based on the formation mechanism of NOx in the furnace. Meanwhile, the Pearson coefficient and mutual information (PMI) is used to obtain optimal inputs. Finally, the ELM is applied to establish a 3D NOx distribution model in the furnace, and the feasibility of the method is verified through experiments. The proposed model is expected to obtain the 3D distribution of NOx at any burner tilt angle quickly and accurately and provide a guideline for combustion optimization and NOx emission reduction.

2 DESCRIPTION OF THE PROPOSED SYSTEM

2.1 Boiler Description

In the present study, a 350 MW once-through supercritical boiler is selected as the research object. **Figure 1** illustrates the schematic layout of the boiler. The boiler is 58,300 mm high and has a 14,627 × 14.627 mm cross section. Moreover, the depth of the horizontal and tail flue gas duct is 53,200 mm and

TABLE 1 | Main boiler operating parameters at the rated power.

Parameter	unit	Values
Pulverized coal	*kg/s*	53.75
Total air	*kg/s*	370.64
Average excess air coefficient	—	1.20
Primary air	*kg/s*	110.07
Second air	*kg/s*	260.54
SOFA	*kg/s*	111.18
Primary air temperature	*°C*	65.0
Secondary air temperature	*°C*	356.0
Ambient temperature	*°C*	30

TABLE 2 | Proximate and ultimate analyses of pulverized coal.

Coal properties	Parameter	Value
Ultimate analysis (%)	Carbon	44.82
	Hydrogen	2.68
	Oxygen	10.26
	Nitrogen	0.52
	Sulfur	0.13
Proximate analysis (%)	Moisture	31.75
	Ash	9.84
	Volatile	24.78
	Fixed carbon	33.63
Low calorific value (kJ/kg)	Qnet	16,310

68,200 mm, respectively. The boiler adopts a new type of tangential combustion. The main combustion area contains six layers of pulverized coal air chambers and eight layers of auxiliary air chambers. Each pulverized coal–air chamber has four nozzles, which are arranged on the four planes of the water-cooled wall. Four secondary air nozzles are arranged in each auxiliary air chamber to surround it. Moreover, four SOFA layers are installed in the corner above the main combustion area to replenish the required air in the next stage of combustion.

The main operating parameters at the rated power of the boiler are shown in **Table 1**. **Table 2** shows the chemical composition of the coal.

2.2 Overall Modeling of Modeling

Obtaining the 3D distribution of NOx concentration in the furnace mainly consists of four steps, including CFD simulation, data preprocessing, feature selection, and ELM modeling. The overall modeling process is shown in **Figure 2**.

Step 1: Input parameters and boundary conditions are set according to the type of the boiler and unit load, and then, CFD simulation is carried out.

Step 2: The 3D distribution data obtained from CFD simulation are preprocessed; then, the data are partitioned into multiple subsets based on the formation mechanism of NOx.

Step 3: Primary data are selected based on the formation mechanism; then, the PMI is combined for feature selection. Finally, variables with high correlation are selected as modeling inputs.

Step 4: Prediction models of the NOx distribution of each subset are established based on the ELM concept. It is worth noting that different subsets have different optimal inputs. Accordingly, multiple NOx prediction models can be obtained for different conditions. Hence, all partial models should be integrated into the final prediction model.

3 COMPUTATIONAL FLUID DYNAMICS SIMULATION

Generally, CFD simulation consists of three steps, including pre-processing, solving governing equations, and post-processing. The main objective of pre-processing is to prepare the computational domain and generate an appropriate mesh. **Figure 1** shows that the calculation domain includes the furnace and horizontal and rear passes. In the present study, structured hexahedral meshes are used

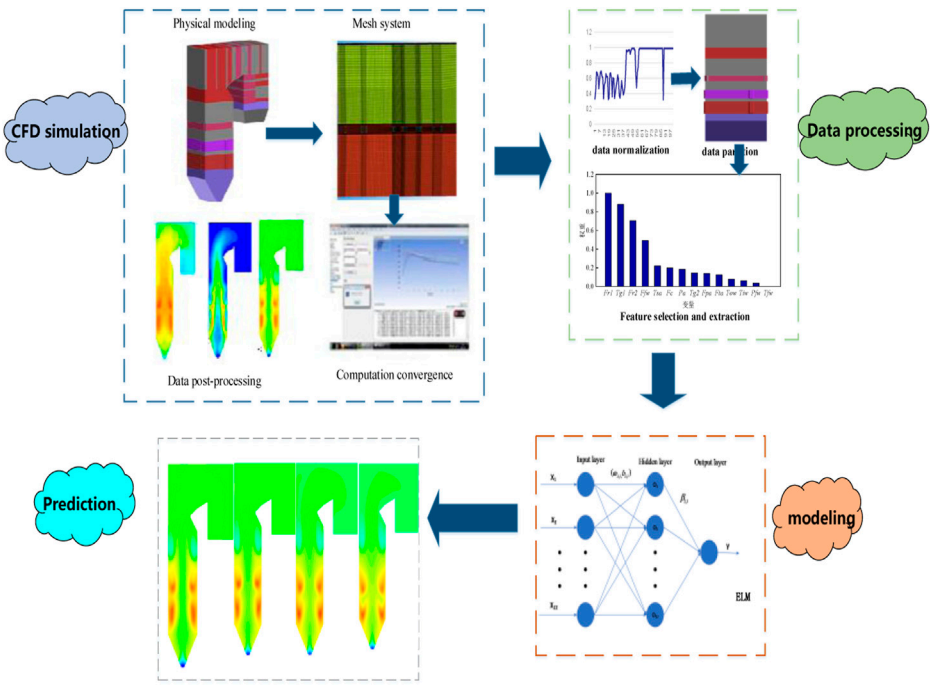

FIGURE 2 | Modeling framework to obtain the 3D NO_X distribution in the furnace.

TABLE 3 | The comparison between CFD results and experimental plant values.

	CFD prediction	Plant values	Relative error
T1 (°C)	1,000	994	0.6%
T2 (°C)	1,297	1,329	−2.4%
O2 (%)	4.35	4.12	5.5%

T1: Furnace outlet gas temperature, T2: gas temperature of platen superheater bottom.

for the furnace body, while refined unstructured meshes are used in the combustion zone to ensure the accuracy of calculations. Three mesh resolutions, containing $2.82*10^6$, $3.18*10^6$, and $3.43*10^6$ meshes, are used to perform the grid independence test. Trading off between simulation accuracy and the computational expense, $3.18*10^6$ meshes are used in all simulations.

In this article, Fluent 15.0 software is used to study the behavior of gas-solid two-phase flow and coal combustion. Moreover, the k–ε model is used to solve the gas-phase turbulent equations. Meanwhile, the stochastic tracking model is used in the Euler–Lagrange method to simulate the two-phase flow. In the combustion model, the volatile pyrolyzation model adopts the two-step competitive reaction model, and the diffusion/kinetics model is used to describe char combustion. The discrete ordinates (DO) model is selected to model radiant heat transfer in the furnace. The load, excess air coefficient, coal quality, primary and secondary air distribution, and SOFA are important and affecting parameters in the furnace. The imposed boundary conditions are presented in **Table 2**.

To verify the CFD model, the simulation results of the 0°tilt angle are compared with plant data at the rated point. **Table 3** reveals that the absolute error of the outlet gas temperature (T1) is 6°C, which is equivalent to a relative error of less than 1%. Furthermore, the absolute error of the gas temperature of the platen superheater bottom is 32°C, which is equivalent to a relative error of less than 3%. The relative error of O_2 concentration at the boiler outlet is 5.5%. The performed analyses demonstrate that the CFD model can be applied to simulate combustion accurately.

CFD simulations are carried out for constant operating conditions and different burner tilt angles. In this regard, seven tilt angles (−30°, −20°, −10°, 0°, 10°, 20°, and 30°) are considered, and the concentration of combustion products and the flow field are obtained.

4 3D NOX EMISSION PREDICTION USING EXTREME LEARNING MACHINE

4.1 Data Preprocessing

4.1.1 Data Acquisition and Normalization

First, the outliers should be processed. Based on the physical mechanism, when an abnormal value of temperature or species concentration is achieved, it is set to zero. On the other hand, when an individual node has an extremely higher or lower value than the surrounding nodes, the mean value of surrounding nodes is used for it.

Meanwhile, different variables have different orders of magnitude. The influence of data with high orders can be highlighted in the modeling process, while other data with low numerical values but great influence, such as O_2 concentration, may be ignored. In order to ensure the reliability of the model and training speed, it is necessary to perform a Min-Max data normalization process. This can be mathematically expressed as follows:

$$x_i^* = \frac{x_i - x_{min}}{x_{max} - x_{min}}, \tag{1}$$

where x_i is the original value, x_i^* is the normalized value, and x_{max} and x_{min} denote maximum and minimum values, respectively.

4.1.2 Data Partition Based on the NOx Formation Mechanism

The formation of NOx in the furnace is a complex process that involves numerous chemical reactions and thermal phenomena. In a large-scale coal-fired boiler, more than 90% of the total NOx originates from NO (Diez et al., 2017). On the other hand, NO can be divided into three categories, including thermal NOx, fuel NOx, and prompt NOx, according to different formation mechanisms. Studies show that the concentration of prompt NO in conventional burners and furnaces is very low so that it can be ignored in calculations.

Thermal NOx refers to the nitrogen oxide generated by the oxidation of N_2 molecules of the combustion air at high temperatures. In this reaction, NOx is created based on the extended Zeldovich mechanism. The net formation rate of NO can be calculated from the following expression:

$$\frac{d[NO]}{dt} = k_1[O][N_2] + k_2[N][O_2] + k_2[N][OH] - k_{-1}[NO][N] - k_{-2}[NO][O] - k_{-3}[NO][H]. \tag{2}$$

To calculate the formation rate of NOx, the concentrations of affecting radicals such as N, O, H, and OH should be determined first. The partial equilibrium method can be used to determine the concentrations of these radicals (United States: Fluent Inc., 2006). In this method, it is assumed that the generation rate and dissipation rate of radicals in a short period of time are equal.

Fuel NOx refers to the oxidation of molecular nitrogen that exists in the fuel structure (e.g., coal here). In this regard, the De Soete mechanism is widely used to determine the formation and depletion of fuel NOx. According to this mechanism, fuel-based N can be classified into volatile N and char N. The formation of fuel NOx is presented in **Figure 3**. It should be indicated that HCN and NH3 are the main intermediates of volatile N and char N. It is observed that the formation of fuel NOx is mainly affected by the O_2 concentration, fuel type, and char surface density.

The origin of coordinates of the geometric model is located at the center of the furnace bottom. Axes of coordinates are shown in **Figure 1**. In order to improve the accuracy of the results and reduce the computational expenses, the data were divided into 11 subsets along the *y*-direction according to the combustion mechanism. **Table 4** indicates that subset 1 refers to the cold ash hopper area. There are two main combustion areas, which are

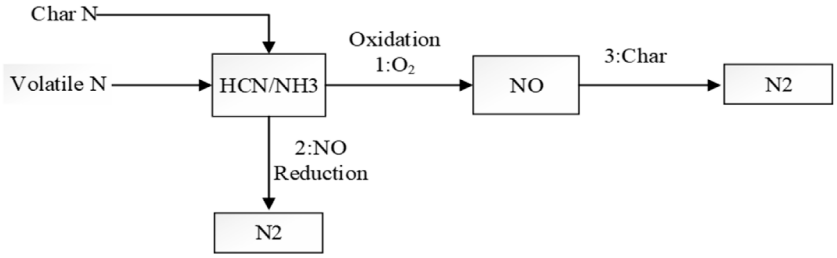

FIGURE 3 | Chemical reactions that lead to the formation of fuel NOx.

TABLE 4 | Partitioned data in the furnace.

Subset	y-coordinate (m)	Number of meshes	Subset	y-coordinate (m)	Number of meshes
1	[6.5, 19.5)	77,631	7	[27.0,28.3)	286,240
2	[19.5, 21.0)	345,750	8	[28.3,29.8)	356,409
3	[21.0, 22.4)	305,256	9	[29.8,34.2)	326,907
4	[22.4, 23.7)	311,906	10	[34.2,40.0)	275,240
5	[23.7, 25.5)	250,035	11	[40.0,64.8)	265,371
6	[25.5, 27.0)	383,153			

divided into seven burner subsets. Subsets 9 and 10 denote the transition zone and SOFA area, respectively. Moreover, subset 11 refers to the furnace top and the horizontal and tail flue heat transfer zone.

4.2 Feature Selection Based on the Pearson Correlation and MI

The selection of input variables directly affects the prediction accuracy, computational expenses, and generalization of the model. In the present study, 21 relevant variables are preselected from CFD simulation data according to the NOx formation mechanism. The input variables of 11 subsets are reselected from 21 relevant variables based on the Pearson coefficient and mutual information (PMI).

In the first step, the PMI variables are determined using **Eq. 3**. When the correlation coefficient between the two variables is $\rho_{x_i,x_j} > 0.9$, one of them can be removed to reduce the dimension of input variables.

$$\boldsymbol{\rho}_{\boldsymbol{x_i},\boldsymbol{x_j}} = \frac{\sum x_i, x_j - \frac{1}{n}\sum x_i \sum x_j}{\sqrt{\left(\sum (x_i)^2 - \frac{1}{n}(\sum x_i)^2\right)\left(\sum \left(x_j\right)^2 - \frac{1}{n}\left(\sum x_j\right)^2\right)}}. \quad (3)$$

The MI-based feature selection method can be applied to obtain the optimal feature by maximizing the joint MI between the input features and the target variable. The joint MI of NOx and related inputs can be defined as follows:

$$\boldsymbol{I}(\boldsymbol{x_1}, \boldsymbol{x_2}, \cdots, \boldsymbol{x_m}; \boldsymbol{NO_x}) = \sum_{\boldsymbol{x}\in \boldsymbol{X}} \sum_{\boldsymbol{y}\in \boldsymbol{Y}} \boldsymbol{p}(\boldsymbol{x_1}, \boldsymbol{x_2}, \cdots, \boldsymbol{x_m}; \boldsymbol{NO_x}) \log \frac{\boldsymbol{p}(\boldsymbol{x_1}, \boldsymbol{x_2}, \cdots, \boldsymbol{x_m}, \boldsymbol{NO_x})}{\boldsymbol{p}(\boldsymbol{x_1}, \boldsymbol{x_2}, \cdots, \boldsymbol{x_m})\boldsymbol{p}(\boldsymbol{NO_x})}, \quad (4)$$

where $p(x_1, x_2, \cdots, x_m, NO_x)$ is the variable joint distribution, $p(x_1, x_2, \cdots, x_m)$ is the marginal distribution of input variables, and $p(NO_x)$ denotes the marginal distribution of NOx.

According to the PMI feature selection, except for three variables (x-, y-, and z-coordinates), seven variables have a relatively high correlation with NOx concentration. These variables are listed in **Table 5**, according to the correlation intensity. In addition to three coordinate variables, 10 CFD variables of each subset are retained.

4.3 Obtaining the NO_X Distribution

4.3.1 Extreme Learning Machine

ELM (Huang et al., 2017) is a single hidden layer feedforward neural network (SLFN), which has remarkable properties such as simple structure, fast learning, and superior generalization performance. Accordingly, ELM is widely used in different kinds of dimensional reduction or regression problems. **Figure 4** shows the structural block diagram of the ELM network.

In an ELM model, (X_i, t_i), $X_i = [\boldsymbol{x_{i1}}, \boldsymbol{x_{i2}}, \cdots, \boldsymbol{x_{im}}]^T \in R^n$, and $t_i = [\boldsymbol{t_{i1}}, \boldsymbol{t_{i2}}, \cdots, \boldsymbol{t_{im}}]^T \in R^m$, are train sets, and $g(x)$ is the activation function. The output of the ELM can be expressed as follows:

$$\sum_{i=1}^{L} \boldsymbol{\beta_i} \boldsymbol{g_i}\left(\boldsymbol{\omega_i} \cdot \boldsymbol{x_j} + \boldsymbol{b_i}\right) = \boldsymbol{o_j}, \quad (5)$$

where $j = 1, 2, \cdots, L$, and L refers to hidden nodes; $\boldsymbol{\omega_i}$ is the connection weight between the hidden and the input layers; $\boldsymbol{\beta_i}$ is the connection weight between the hidden and output layers; $\boldsymbol{b_i}$ denotes the offset of the i^{th} hidden layer, and $\boldsymbol{\omega_i} \cdot \boldsymbol{x_j}$ is the inner product. When the optimal $\boldsymbol{\beta}$, $\boldsymbol{\omega}$, and $\boldsymbol{b}$, are optimized, then the error reaches zero ($\sum_{j=1}^{N} o_j - t_j = 0$). Consequently, **Eq. 5** can be rewritten in the form below:

TABLE 5 | Feature selection of each subject.

Correlation rank	Subsets 1	Subset2- subset 9	Subsets 10	Subsets 11
1	velocity-magnitude	temperature	molef-o2	molef-o2
2	y-velocity	molef-o2	velocity-magnitude	molef-n2
3	temperature	molef-co	temperature	pressure
4	molef-o2	molef-n2	y-velocity	y-velocity
5	heat-of-reaction	velocity-magnitude	molef-n2	temperature
6	dpm-concentration	y-velocity	molef-co	molef-co
7	dpm-burnout	pressure	pressure	z-velocity

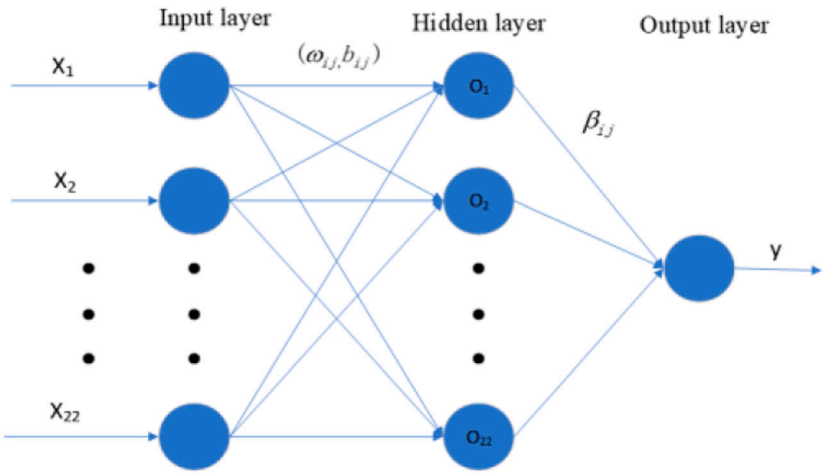

FIGURE 4 | Structural diagram of the ELM network.

$$\sum_{i=1}^{L} \boldsymbol{\beta}_i \boldsymbol{g}_i\left(\boldsymbol{\omega}_i \cdot \boldsymbol{x}_j + \boldsymbol{b}_i\right) = \boldsymbol{t}_j. \tag{6}$$

Eq. 6 can also be expressed in the following matrix form:

$$\boldsymbol{H\beta} = \boldsymbol{T}, \tag{7}$$

where $\boldsymbol{H}$ is the neuron output matrix, $\boldsymbol{\beta}$ is the output weight, and T is the output of the neural network. In the ELM algorithm, minimum norm least-squares (LS) are used to solve the SLFN. When the activation function $g(x)$ is infinitely differentiable, the input weight $\boldsymbol{\omega_i}$ and hidden layer bias $\boldsymbol{b_i}$ can be randomly set to t (Huang et al., 2017). The training process of ELM consists of two steps, including random feature mapping and linear parameter solution. In ELM, the hidden layer is initialized randomly through nonlinear mapping functions, and the data are mapped to the feature space. Accordingly, the output weight matrix $\hat{\beta}$ can be obtained based on the least-squares regression.

$$\hat{\boldsymbol{\beta}} = \boldsymbol{H}^{+}\boldsymbol{T}, \tag{8}$$

where $\boldsymbol{H}^{+}$ is the Moore–Penrose generalized inverse of the matrix $\boldsymbol{H}$.

4.3.2 Computational Environment and Parameter Setting

All calculations are carried out in the *Python* 3.5 environment, installed. Configurations of the PC o Sun program are Windows7 (64 bit) and an Intel Core i5-9400F processor with 2.9 GHz processor speed.

The input weight and bias value are randomly selected according to the performed ELM analysis. “tanh” function is selected as the activation function of ELM, and 100 neurons are considered in the hidden layer.

4.3.3 Description of the Data Set

In this section, CFD simulation is carried out to study variations of the tilt angle of a typical burner at rated power. In order to investigate the NOx distribution at an arbitrary angle, training and test data sets should be constructed. According to PMI correlation analysis, NOx distribution is mainly affected by seven factors. Moreover, there are 22 variables as the inputs of the training set.

TABLE 6 | Construction of the training set and test set.

Data set	Data set of the input variables	Data set of the output variable
Training set 1	−30°, −10°	−20°
Training set 2	−20°, 0°	−10°
Training set 3	−10°, 10°	0°
Training set 4	10°, 30°	20°
Test set	0°, 20°	10°

TABLE 7 | Performance indicators in different subsets.

	R^2	MAPE	RMSE	Train Time (s)	Test Time(s)
Subset1	0.49	8.19	36.20	3.03	0.22
Subset2	0.79	18.85	46.68	14.36	1.18
Subset3	0.82	20.55	61.25	15.35	1.37
Subset4	0.81	22.52	59.35	15.46	1.40
Subset5	0.73	12.12	58.35	12.18	1.09
Subset6	0.86	10.51	42.88	18.61	1.56
Subset7	0.85	20.24	51.59	14.12	1.18
Subset8	0.67	10.20	47.46	14.73	1.45
Subset9	0.75	4.62	25.39	13.48	1.13
Subset10	0.73	4.89	23.92	11.38	0.95
Subset11	0.86	2.56	10.23	11.27	0.91
Mean	0.76	12.29	40.49	13.00	1.00

The construction rules of the data set are shown in **Table 6**. Four cases are combined to train the model, and one is used to test it. In this study, the NOx distribution of the upward 10° tilt angle will be predicted.

4.3.4 Performance Metrics

In order to evaluate the prediction performance of models, the mean absolute percentage error (MAPE), root-mean-squared error (RMSE), and correlation coefficient R-square (R^2) are used as evaluation indicators. These indicators are defined as follows:

$$MAPE = \frac{1}{m}\sum_{i=1}^{m}\left|\frac{y_p(i) - y_c(i)}{y_c(i)}\right| \times 100\%, \tag{9}$$

$$RMSE = \sqrt{\frac{1}{m}\sum_{i=1}^{m}\left(y_p(i) - y_c(i)\right)^2}, \tag{10}$$

$$R^2 = 1 - \frac{\left[\sum_{i=1}^{m}\left(y_p(i) - y_c(i)\right)^2\right]/m}{\left[\sum_{i=1}^{m}\left(\bar{y}_p(i) - y_c(i)\right)^2\right]/m}, \tag{11}$$

where m is the number of samples in the test set, and $\bar{y}_p(i)$ denotes the average value of NO_X distribution. Furthermore, y_c and y_p are the calculated and predicted NOx concentrations, respectively.

4.3.5 Prediction of NOx Distribution Based on Extreme Learning Machine

3D distribution of NOx in 11 subsets are modeled respectively adopting the aforementioned ELM model and then are tested by the working condition of the upward 10° burner tilt angle. The predicted results are shown in **Table 6**.

In this section, it is intended to model the NOx distribution in 11 subsets adopting the ELM model. Then, the results are verified by the experimental data of the upward 10° burner tilt angle. The performance indicators of the predicted results are shown in **Table 7**.

Considering the required computational time for CFD simulation, ELM can be applied to rapidly model the flow and obtain the NOx distribution at an arbitrary tilt angle.

Compared with other subsets, R^2 of subset 1 is relatively small, indicating that the predicted value deviates from the real value. This subset locates in the cold hopper area. Accordingly, the NOx distribution is mainly affected by the ash fall and the combustion in the upper zones. Meanwhile, cold air blowing to the bottom of the furnace affects the field distribution and species concentration. Accordingly, it is an enormous challenge to predict the NOx distribution in this region.

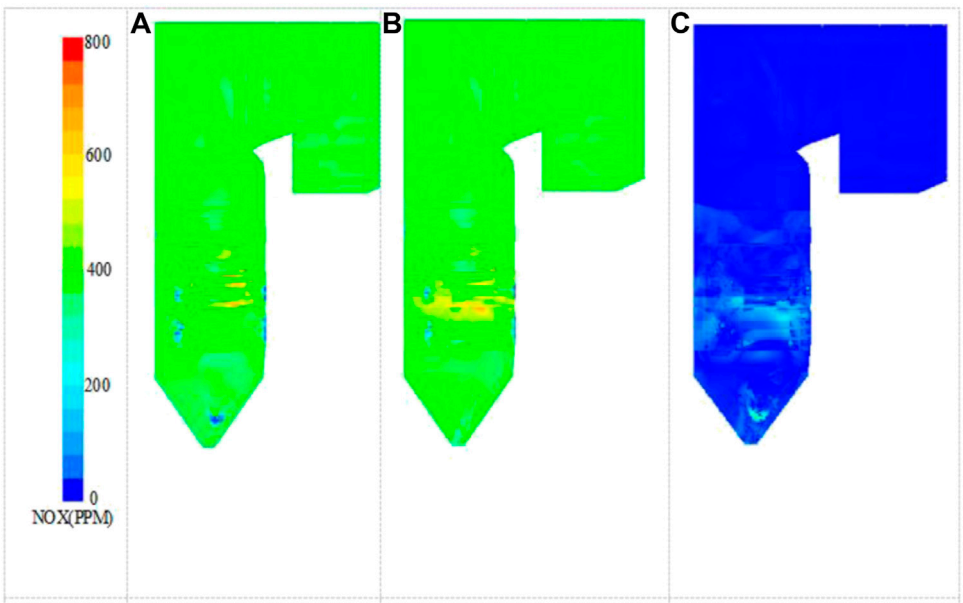

FIGURE 5 | Contour of 3D distribution of NO_X. **(A)** NO_X concentration obtained from CFD simulation **(B)** NO_X concentration obtained from ELM prediction **(C)** Prediction error

TABLE 8 | Statistical indicators of the prediction using different methods.

	MR^2	*MMAPE*	*MRMSE*	Mean Train Time (s)
PMI-ELM	0.76	12.29	40.49	13.09
ELM	0.65	15.55	48.89	16.99

Table 7 indicates that the *MAPE* of subsets 3, 4, and 7 is about 20%, which is much larger than that of other subsets. These three subsets locate in burner B, burner C, and burner E, respectively. When the burner tilt angle is 10° upward, the combustion center of the lower main combustion zone locates in subsets 3 and 4, and the combustion center of the upper main combustion zone locates in subset 7. Under this circumstance, large turbulent flow and flame fluctuation decreases the prediction accuracy. **Figure 5** shows the overall contours of NOx distribution in the studied furnace. It is observed that the NOx concentration in the main combustion zone is relatively high, and the range of variation is large. Consequently, the prediction error is relatively large.

In subsets 9, 10, and 11, the MAPE and RMSE of the model are small. This is because at the top of the furnace and the horizontal flue, the combustion reaction has ended, and the turbulence disappears. As a result, the distribution of the material composition is stable.

5 VERIFICATION OF THE ALGORITHM

5.1 Analysis of Feature Selection

To verify the influence of PMI feature selection on the modeling accuracy and efficiency, a comparative study is carried out on the NOx distribution of 11 subspaces. There are 42 input variables before feature selection, including 3 coordinates (x-, y-, and z-coordinates), 19 variables in each known working condition and the burner tilt angle of an unknown working condition. The output is NOx distribution in the desired working condition. Furthermore, there are 22 input variables after PMI feature selection. Three evaluation indicators are used to analyze the modeling effect.

Table 8 shows the mean index indicators of 11 subspaces. It is observed that after feature selection, the mean R^2 (MR^2) increases by 14.5%, while the mean MAPE (MMAPE) and mean RMSE (MRMSE) decrease by 20.9% and 17.2%, respectively. Moreover, mean training time decreases by 3.9 s. It is concluded that predicting

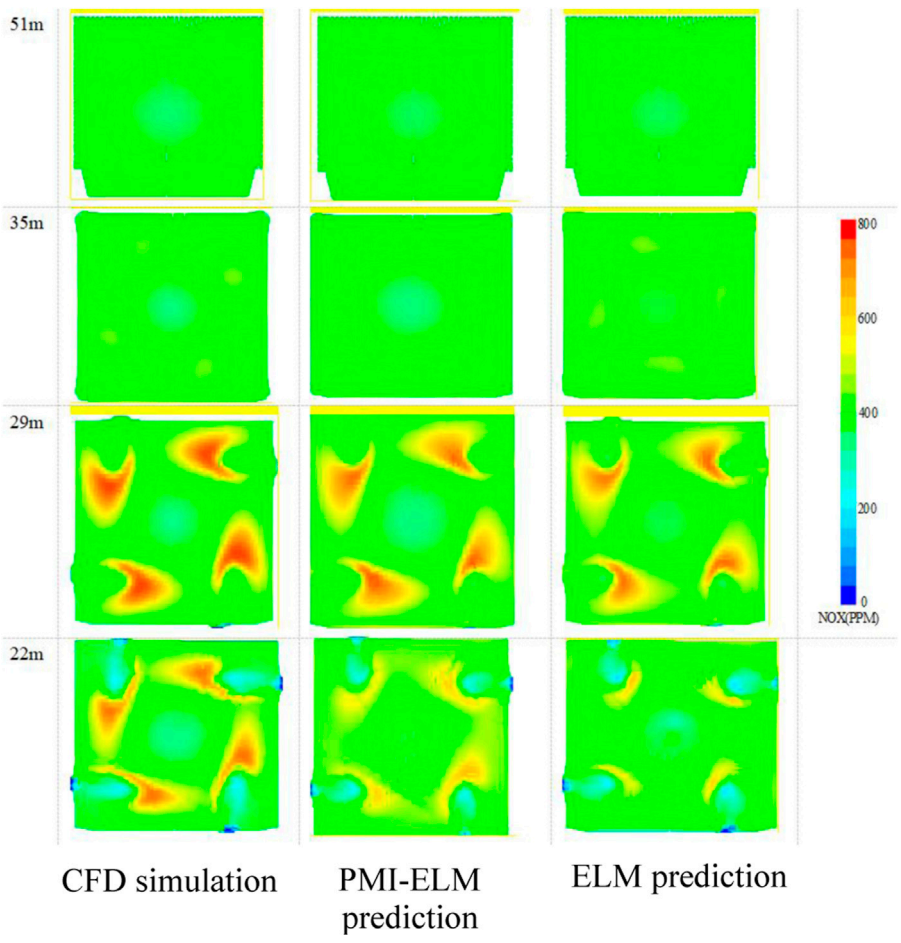

FIGURE 6 | Contours of NO_X concentration along the height of the furnace obtained from different methods.

TABLE 9 | Mean performance indices of different algorithms.

	DNN	*DBN*	*MLR*	*ESN*	*ELM*
R^2	0.70	0.65	0.51	0.59	0.76
MAPE	17.09	15.28	22.28	20.75	12.30
RMSE	47.08	50.71	48.36	48.64	42.12
Average Train Time (s)	25684.97	7919.24	0.46	24.81	13.22

the NOx distribution using the PMI feature decreases the prediction data dimension and improves the prediction performance.

Considering the high temperature in the combustion zone and the high-temperature gradient around the flame, it is a challenge to simulate the flow accurately. The flue gas flow at the top and tail of the furnace is relatively steady, so the predicted value of NOx distribution is relatively accurate. **Figure 6** shows the NOx distribution in the horizontal cross section at four heights of the furnace with an upward burner tilt angle of 10°. It is observed that at the height of 22 m (burner region B), firing circles appear clearly, and the predicted values using the feature extraction are more consistent with the experimental data. At the height of 29 m, airflow rotates and the deviation of the NOx concentration in the furnace center is smaller than that of the case where this feature is not selected. For the SOFA area at 35 m, the prediction accuracy of PMI-ELM is high. At the top of the furnace, the NOx distribution can be accurately predicted regardless of the feature selection. It is inferred that prediction errors mainly appear in the high-temperature zone and the bottom of the furnace. Except for the top region, the prediction performance can be significantly improved using feature extraction.

5.2 Comparative Analysis of Different Algorithms

To verify the effectiveness of the ELM algorithm on predicting the NOx distribution in the studied furnace, 11 subsets are modeled using different algorithms, including the deep belief network (DBN), deep neural network (DNN), multiple linear regression (MLR), and echo state network (ESN). The average prediction performances of different algorithms are compared in **Table 9**. It is observed that the smallest prediction error and the largest R^2 can be achieved from the ELM model. Moreover, the ELM has a higher prediction speed than DBN and DNN models. The comparison of error evaluation indices demonstrates that the ELM model outperforms other models in predicting the NOx distribution in the studied furnace.

Figure 7 shows the absolute error boxplot of the studied algorithms. It is observed that the lowest absolute error can be achieved from the ELM algorithm, while it has a tighter variation bandwidth than the other algorithms. The variation of the predicted results using the ELM algorithm is consistent with that of the CFD simulation. It is concluded that the ELM-based model has a reasonable fitting effect and prediction ability.

6 CONCLUSION

The ELM model has been established to predict the 3D NOx distribution in the furnace using CFD simulation data at different burner tilt angles. Based on the obtained results and performed analyses, the main conclusions of this research can be summarized as follows:

The mean R^2, MAPE, and RMSE of the ELM-based data-driven method are 0.76, 12.29%, and 40.49, respectively, indicating that the proposed method can be used to accurately predict the NOx distribution in the furnace.

1) Due to a large amount of CFD data, the data are partitioned based on the combustion mechanism. PMI feature extraction is used to select optimal variables of each subset. This technique increased MR^2 and MMAPE by 14.5 and 20.9%, respectively, while reducing the MRMSE by 17.2%. It is

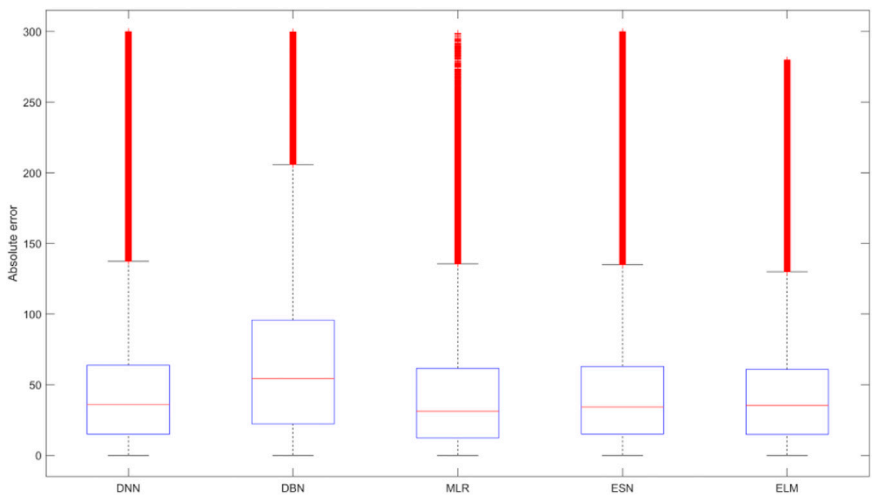

FIGURE 7 | Absolute error box plot of different algorithms.

concluded that data partition and PMI feature selection can effectively improve the prediction performance.

2) CFD simulation results at typical burner tilt angles are used as the training set. Then, NOx distributions are predicted at arbitrary tilt angles. It is found that the proposed data-driven method can predict the NOx distribution in the furnace online based on offline modeling Xu et al., 2001.

DATA AVAILABILITY STATEMENT

The raw data supporting the conclusion of this article will be made available by the authors, without undue reservation.

AUTHOR CONTRIBUTIONS

JZ provided administrative and technical support. ML designed experiments, carried out research, analyzed the experimental results and wrote articles. SC made the research obtain financial support and gave technical guidance. TS validated of field data and compared the experimental data with the actual operation of the power plant.

FUNDING

This work was supported in part by the Jilin Science and Technology Project under Grant 20200401085GX.

REFERENCES

Ahmed, F., Cho, H. J., Kim, J. K., Seong, N. U., and Yeo, Y. K. (2015). A Real-Time Model Based on Least Squares Support Vector Machines and Output Bias Update for the Prediction of NOx Emission from Coal-Fired Power Plan. *Korean J. Chem. Eng.* 32 (6), 1029e36. doi:10.1007/s11814-014-0301-2

Boyd, R. K., and Kent, J. H. (1988). "Three-Dimensional Furnace Computer Modelling," in *Twenty-First Symposium on Combustion* (Twenty-First Symposium (International) on Combustion/The 382 Combustion Institute), 265–274. doi:10.1016/s0082-0784(88)80254-6

Choi, M., Park, Y., Li, X., Kim, K., Sung, Y., Hwang, T., et al. (2020). Numerical Evaluation of Pulverized Coal Swirling Flames and NOx Emissions in a Coal-Fired Boiler: Effects of Co- and Counter-swirling Flames and Coal Injection Modes. *Energy* 217, 119439. doi:10.1016/j.energy.2020.119439

Chu, J., Shieh, S., Jang, S., Chien, C. I., Wan, H. P., and Ko, H. H. (2003). Constrained Optimization of Combustion in a Simulated Coal-Fired Boiler Using Artificial Neural Network Model and Information Analysis. *Fuel* 82 (6), 693–703. doi:10.1016/s0016-2361(02)00338-1

Chunlin Wang, C., Liu, Y., Zheng, S., and Jiang, A. (2018). Optimizing Combustion of Coal Fired Boilers for Reducing NOx Emission Using Gaussian Process. *Energy* 153, 149–158. doi:10.1016/j.energy.2018.01.003

Dal Secco, S., Juan, O., Louis-Louisy, M., Lucas, J.-Y., Plion, P., and Porcheron, L. (2015). Using a Genetic Algorithm and CFD to Identify Low NOx Configurations in an Industrial Boiler. *Fuel* 158, 672–683. doi:10.1016/j.fuel.2015.06.021

Diez, L. I., Corte´s, C., and Pallare´s, J. (2017). Numerical Investigation of NOx Emissions from a Tangentially-Fired Utility Boiler under Conventional and Overfire Air Operation. *Fuel* 87 (7), 1259–1269. doi:10.1016/j.fuel.2007.07.025

Dindarloo, S. R., and Hower, J. C. (2015). Prediction of the Unburned Carbon Content of Fly Ash in Coal-Fired Power Plants. *Coal Combustion Gasification Prod.* 7, 19–29. doi:10.4177/ccgp-d-14-00009.1

Fang Wang, F., Ma, S., Wang, H., Li, Y., and Zhang, J. (2018). Prediction of NOX Emission for Coal-Fired Boilers Based on Deep Belief Network. *Control. Eng. Pract.* 80, 26–35. doi:10.1016/j.conengprac.2018.08.003

Fluent Inc (2006). *Fluent User's Guid.*. USA: Fluent Inc.

Huang, G. B., Zhu, Q. Y., and Siew, C. K. (2017). Extreme Learning Machine: Theory and Applications. *Neurocomputing* 70 (1-3), 489–501.

Ilamathi, P., Selladurai, V., Balamurugan, K., and Sathyanathan, V. T. (2003). ANN-GA Approach for Predictive Modeling and Optimization of NOx Emission in a Tangentially Fired Boiler Clean. *Technol. Environ.* 15 (1), 125e31. doi:10.1007/s10098-012-0490-5

Kang, J. K., Niu, Y. G., Hu, B., Li, H., and zhou, Z. H. (2017). Dynamic Modeling of SCR Denitration Systems in Coal-Fired Power Plants Based on a Bi-directional Long Short-Term Memory Method. *Process Saf. Environ. Prot.* 148, 867–878. doi:10.1016/j.psep.2021.02.009

Li, K., Thompson, S., and Peng, J. (2004). Modelling and Prediction of NOx Emission in a Coal-Fired Power Generation Plant. *Control. Eng. Pract.* 12 (6), 707–723. doi:10.1016/s0967-0661(03)00171-0

Li, N., and Hu, Y. (2020). The Deep Convolutional Neural Network for NOx Emission Prediction of a Coal-Fired Boiler. *IEEE Access* 8 (8), 85912–85922. doi:10.1109/access.2020.2992451

Lv, Y., Liu, J., Yang, T., and Zeng, D. (2013). A Novel Least Squares Support Vector Machine Ensemble Model for NOx Emission Prediction of a Coal-Fired Boiler. *Energy* 55, 319–329. doi:10.1016/j.energy.2013.02.062

Ma, L., Fang, Q., Lv, D., Zhang, C., Chen, G., Chen, Y., et al. (2015). Influence of Separated Overfire Air Ratio and Location on Combustion and NOx Emission Characteristics for a 600 MWe Down-Fired Utility Boiler with a Novel Combustion System. *Energy Fuels* 29, 7630–7640. doi:10.1021/acs.energyfuels.5b01569

Ministry of Environmental Protection of the PRC (2011). *Emissions Standard of Air Pollutants for thermal Power Plants*.

Preeti, M., and Sharad, T. (2013). Artificial Neural Network Based Nitrogen Oxides Emission Prediction and Optimization in thermal Power Plant. *Int. J. Comput. Eng. &Technol. (IJCET)* 4, 491–502.

Tan, P., He, B., Zhang, C., Rao, D., Li, S., Fang, Q., et al. (2019). Dynamic Modeling of NOX Emission in a 660 MW Coal-Fired Boiler with Long Short-Term Memory. *Energy* 176, 429–436. doi:10.1016/j.energy.2019.04.020

Tan, P., Tian, D., Fang, Q., Ma, L., Zhang, C., Chen, G., et al. (2017). Effects of Burner Tilt Angle on the Combustion and NOX Emission Characteristics of a 700 MWe Deep-Air-Staged Tangentially Pulverized-Coal-Fired Boiler. *Fuel* 196 (MAY15), 314–324. doi:10.1016/j.fuel.2017.02.009

Tuttle, J. F., Vesel, R., Alagarsamy, S., Blackburn, L. D., and Powell, K. (2019). Sustainable NO_X Emission Reduction at a Coal-Fired Power Station through the Use of Online Neural Network Modeling and Particle Swarm Optimization. *Control. Eng. Pract.* 93, 104167. doi:10.1016/j.conengprac.2019.104167

Wang, Y., Liu, H., Liu, K., Li, X., Yang, G., and Xie, R. (2017). An Ensemble Deep Belief Network Model Based on Random Subspace for NOx Concentration Prediction[J]. *ACS Omega* 6, 7655–7668. doi:10.1021/acsomega.0c06317

Wang, Y., and Zhou, Y. (2020). Numerical Optimization of the Influence of Multiple Deep Air-Staged Combustion on the NOx Emission in an Opposed Firing Utility Boiler Using Lean Coal. *Fuel* 269, 116996. doi:10.1016/j.fuel.2019.116996

Wei, Z., Li, X., Xu, L., and Cheng, Y. T. (2013). Comparative Study of Computational Intelligence Approaches for NOx Reduction of Coal-Fired Boiler. *Energy* 55, 683–692. doi:10.1016/j.energy.2013.04.007

Xie, P., Gao, M., Zhang, H., Niu, Y., and Wang, X. (2020). Dynamic Modeling for NO_X Emission Sequence Prediction of SCR System Outlet Based on Sequence to Sequence Long Short-Term Memory Network. *Energy* 190, 116482. doi:10.1016/j.energy.2019.116482

Xu, M., Azevedo, J. L. T., and Carvalho, M. G. (2001). Modeling of a Front wall Fired Utility Boiler for Different Operating Conditions. *Comput. Methods Appl. Mech. Eng.* 190 (28), 3581–3590. doi:10.1016/s0045-7825(00)00287-5

Yan, S., Wza, B., and Xi, C. (2019). Combustion Optimization of Ultra Supercritical Boiler Based on Artificial Intelligence[J]. *Energy* 170, 804–817. doi:10.1016/j.energy.2018.12.172

Yang, G. T., Wang, Y. N., and Li, X. L. (2020). Prediction of the NO_X Emissions from thermal Power Plant Using Long-Short Term Memory Neural Network. *Energy* 192, 116597. doi:10.1016/j.energy.2019.116597

Zhang, X., Zhou, J., Sun, S., Sun, R., and Qin, M. (2015). Numerical Investigation of Low NOx Combustion Strategies in Tangentially-Fired Coal Boilers. *Fuel* 142, 215–221. doi:10.1016/j.fuel.2014.11.026

Zhang, Z., Wu, Y., Chen, D., Shen, H., Li, Z., Cai, N., et al. (2019). A Semi-empirical NOx Model for LES in Pulverized Coal Air-Staged Combustion. *Fuel* 241, 402–409. doi:10.1016/j.fuel.2018.12.036

Zhou, H., Pei Zhao, J., Gang Zheng, L., Lin Wang, C., and Fa Cen, K. (2012). Modeling NOx Emissions from Coal-Fired Utility Boilers Using Support Vector Regression with Ant colony Optimization. *Eng. Appl. Artif. Intelligence* 25 (1), 147–158. doi:10.1016/j.engappai.2011.08.005

Conflict of Interest: TS was employed by the Harbin Boiler Company Limited. The remaining authors declare that the research was conducted in the absence of any commercial or financial relationships that could be construed as a potential conflict of interest.

Publisher's Note: All claims expressed in this article are solely those of the authors and do not necessarily represent those of their affiliated organizations, or those of the publisher, the editors, and the reviewers. Any product that may be evaluated in this article, or claim that may be made by its manufacturer, is not guaranteed or endorsed by the publisher.

frontiers in Energy Research

ORIGINAL RESEARCH
published: 22 March 2022
doi: 10.3389/fenrg.2022.860707

Analysis of Abnormal Detection Data of Fire Accident in Power Cable Tunnel and Field Test Study on Characteristic Parameters of Tunnel Fire

Wei Guo[1], *Ziheng Pu*[2]*, *Zhigang Ren*[1], *Shiyi Zhou*[1], *Lang Quan*[2], *Yekun Men*[1] *and Zehua Pan*[1]

[1]State Grid Beijing Electric Power Research Institute, Beijing, China, [2]College of Electrical Engineering and New Energy, China Three Gorges University, Yichang, China

With the continuous expansion of urban cable scale and the increase in service time, the fire accident risk of cable tunnels also increases. Defects in the configuration of fire prevention measures lead to many fire accidents and seriously affect the reliability of power supply. First, the detection data of a typical tunnel fire accident are analyzed in this study. The results show that the main problems are the unreasonable installation position of fire extinguishers, the lack of fire prevention measures between intermediate joints, and the insufficient fire prevention performance of interlayer fire barriers. Then, the field test of cable tunnel fire is carried out in a cable tunnel to be put into operation. The test data show that the high-temperature area is mainly concentrated on the top of the tunnel, and the insufficient suspension height of the fire extinguisher will affect the trigger time. The energy of a short circuit accident is large, the cable burns and spreads rapidly, and the delayed triggering may lead to large fire to extinguish effectively. Comparing the simulation and test results of abnormal characteristic parameters in fire, the temperature error is less than 4%. The fire power development curve is obtained through simulation, and the burner power is set to test the fire prevention and extinguishing devices. Finally, the optimal configuration scheme of the fire anomaly data detection equipment and fire-extinguishing products is proposed. The temperature drop rate increases by 135%.

Keywords: power cable tunnel, fire accident, anomaly detection, field test, detection data analysis, fire development

OPEN ACCESS

Edited by:
Xun Shen,
Tokyo Institute of Technology, Japan

Reviewed by:
Gaurav Sachdeva,
DAV University, India
Hardeep Singh,
Sophia University, Japan

***Correspondence:**
Ziheng Pu
pzhdq@ctgu.edu.cn

Specialty section:
This article was submitted to Smart Grids, a section of the journal Frontiers in Energy Research

Received: *23 January 2022*
Accepted: *25 February 2022*
Published: *22 March 2022*

Citation:
Guo W, Pu Z, Ren Z, Zhou S, Quan L, Men Y and Pan Z (2022) Analysis of Abnormal Detection Data of Fire Accident in Power Cable Tunnel and Field Test Study on Characteristic Parameters of Tunnel Fire. Front. Energy Res. 10:860707. doi: 10.3389/fenrg.2022.860707

INTRODUCTION

In recent years, the cable utilization rate in the core area of megacities has reached 100%. Cables of multiple transmission circuits in key areas are laid in the same tunnel. If one cable is on fire, other lines will be directly exposed to the fire. Even flame-retardant cables will produce insulation deterioration and breakdown under long-term burning and then become a new fire source (Yan et al., 2018). At the same time, non-flame-retardant distribution power cables or optical cables are often laid in the main cable tunnels. It will also be ignited and cause the fire to burn continuously. Therefore, in case of fire in the tunnel, it is very easy to cause all cables and optical cables in the same channel to burn. The load of the whole transmission channel is lost, which may lead to large-scale power failure in the city. In order to monitor the tunnel fire, optical fiber temperature measurement, smoke sensor, and other detection devices are installed. Some new important cable tunnels are also equipped with intelligent inspection devices and video monitoring (Shen et al., 2021; Yang et al.,

2021a; Yang et al., 2021b). With the application of the artificial intelligence algorithm in the power system, some fire prediction methods have also been proposed. The cable tunnel is long and narrow, the entrance is small, and the space is sealed. In case of fire, firefighters cannot enter to carry out routine firefighting. Therefore, firefighting products such as fire extinguishers, fire barriers, and fireproof tapes are used in cable tunnels. However, due to the lack of research on the combustion characteristics of tunnel fire, the configuration of some tunnel firefighting products built in the early stage is unreasonable. Moreover, the short circuit energy of high-voltage cables is huge, the fire develops rapidly, and the performance of some firefighting products is not enough to deal with it. It is necessary to analyze the abnormal data of typical tunnel fire accidents to determine the causes of accidents and the deficiencies of fire prevention and extinguishing measures, and to further put forward improvement schemes.

The main causes of fire in cable tunnels are high temperature caused by excessive line load or excessive short circuit current; partial insulation damage and discharge arc ignition caused by overvoltage; and the fault of cable grounding system leads to sheath suspension potential breakdown and long-term small current discharge (Dong et al., 2017). After the fire accident in the cable tunnel, due to the long and narrow seal and the accumulation of a large amount of toxic smoke, it is difficult for personnel to enter and extinguish the fire from the outside (Wang et al., 2017; Liang et al., 2019; Song et al., 2020). It is easy to spread and causes great economic losses. The alarm time of different detectors is obtained by tests (Liu X et al., 2021). The alarm characteristics of fire detectors with different sensitivities are simulated and analyzed, which provide a reference for selecting sensors with extra sensitivity and designing fire-monitoring systems in cable tunnels. Zhang and Zhao (2020) combined test and simulation and concluded that closing the fire door after a fire and adopting mechanical ventilation can effectively control the fire. The establishment of a test platform confirmed the feasibility of liquid nitrogen fire extinguishing in a cable tunnel (Guo et al., 2020). Liu Y et al. (2021) conducted water mist fire-extinguishing tests and found that the greater the flow or velocity, the stronger the inhibition effect on the total firepower of cable tunnel. Li et al. (2018) analyzed the fire development law of cable tunnels under different fire spacing and found that a fire spacing of no more than 500 m is conducive to controlling the fire development and ventilation after fire extinguishing. Mi et al. (2020) simulated different combinations of ventilation modes, automatic fire-extinguishing systems, and fire doors to effectively control the smoke propagation in the tunnel and help people evacuate immediately. However, the aforementioned studies mostly analyzed a single fire prevention measure and did not consider the characteristics of a high-voltage cable channel. Due to the lack of comprehensive configuration of various fire-extinguishing measures, the fire risk of the high-voltage cable tunnel is still high.

In order to configure fire prevention and extinguishing measures more reasonably, it is necessary to obtain the development characteristics of high-voltage cable tunnel fire. The research of tunnel fire is mostly simulation analysis. However, because it is difficult to determine the relevant combustion parameters, there are some differences between the simulated data and the actual combustion data of the high-voltage cable tunnel. The research on the fire prevention effect of fire prevention and extinguishing measures needs experimental verification. Zhu et al. (2019) conducted the fire test of reduced size cable tunnels. It was found that within 200–600 s, the combustion time of the cable was 23%, the mass loss was 75%, and the transverse temperature distribution in the range of 0–90 degrees of the tunnel was obtained. An et al. (2020) studied the effects of layer spacing and cable spacing on flame characteristics and the risk of multilayer cables. It was found that the flame height increased with the increase in layer spacing, and the flame width decreased with the increase in cable spacing. Fire tests were carried out in a reduced cable tunnel under different oxygen concentrations (Xu et al., 2021). It was found that different combustion parameters changed under different oxygen concentrations, and there were two temperature peaks on the section, which were directly above the fire source. It is found that in the case of fire in a cable tunnel, the highest position of ceiling temperature has nothing to do with the cable inclination (An et al., 2021). When the cable inclination is less than 15°, the highest ceiling temperature further increases. However, the aforementioned research is mostly carried out in a laboratory or a reduced scale platform, which is different from the actual high-voltage cable tunnel. If the test is carried out in a typical actual tunnel, more reference test data can be provided.

First, combined with the monitoring data of typical cable tunnel fire accidents, this study analyzes the causes and development of fire. More targeted studies pointed out the shortcomings of fire prevention and extinguishing measures of high-voltage cable tunnels. Then, in order to obtain the characteristics of cable combustion spread and detection data in the cable tunnel, the field test of cable fire is carried out in a cable tunnel to be put into operation. The obtained data are more real and effective, and the simulation model can be verified and modified. At the same time, the fire test of firefighting products such as fire extinguishers and fire barriers were carried out in the tunnel. Finally, the optimal configuration scheme of fire anomaly data detection equipment and firefighting products is proposed according to the test and simulation data. The comprehensive effects of various fire prevention and extinguishing products are considered.

ABNORMAL DATA ANALYSIS OF TUNNEL FIRE ACCIDENTS

Cause Analysis of Fire Accident in Cable Tunnel

According to incomplete statistics, about 200 cable lines have been tripped due to cable tunnel fires in the past 4 years. Most of the tunnel fires are caused by joint failure. In particular, cables with a voltage of 110 kV and above cause huge economic losses after failure. This study takes a fire accident caused by a 220 kV intermediate joint fault as an example. The scene of the cable combustion accident is shown in **Figure 1**. In case of breakdown, the copper shell of the intermediate joint has burst and the

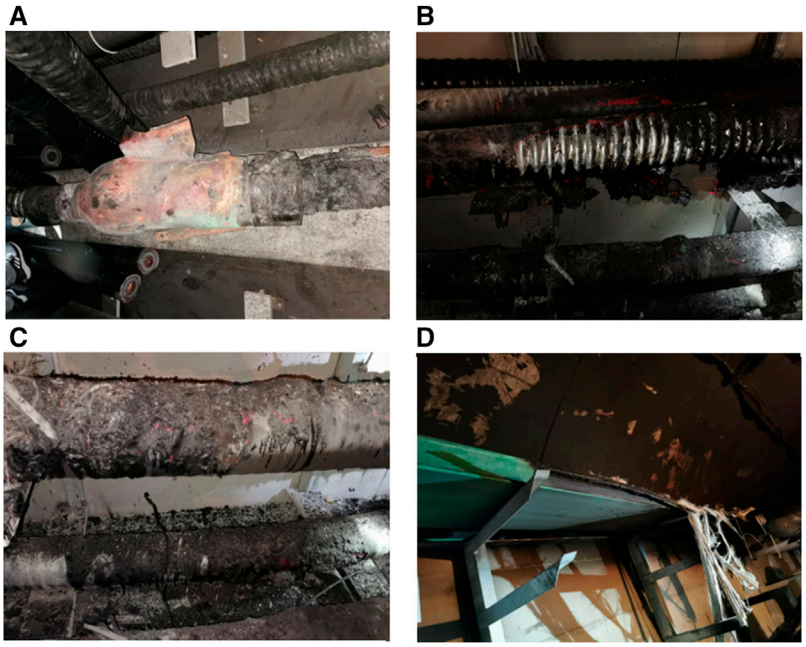

FIGURE 1 | Field conditions of cable tunnel with fire accident **(A)** accident intermediate joint **(B)** adjacent phase cables in the same circuit **(C)** another circuit cable in the lower layer **(D)** fire barrier above.

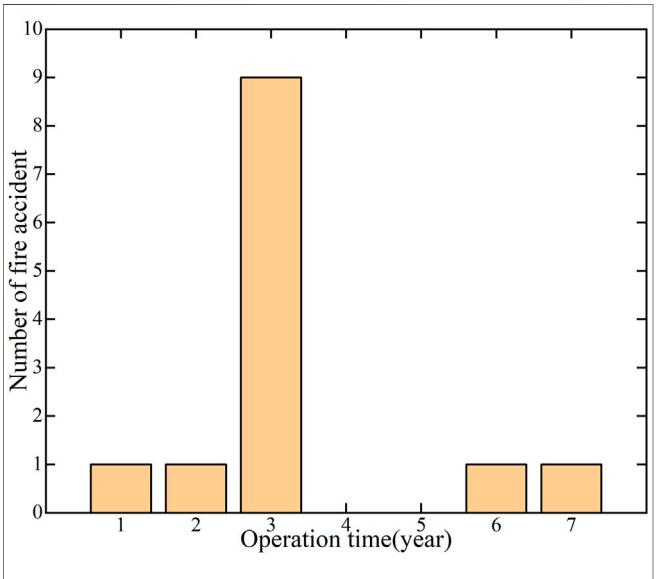

FIGURE 2 | Statistical analysis of operation time of typical accident cables.

intermediate joint has been seriously burnt. Although the outer sheaths of the other two phases of cables in the same circuit adjacent to them are flame-retardant materials, they are still seriously ablated, and the aluminum sheaths of the inner layer are exposed to varying degrees. The cross-linked polyethylene material inside the failed intermediate joint started to melt after combustion and dropped onto the 220 kV cable of another circuit below, which damaged the outer sheath, but did not cause open fire, and the inner aluminum sheath was not exposed and damaged. The fire barrier above the intermediate joint was burnt out for about 6 m, and all the communication cables laid inside were burnt out. The fire barrier has not played its due role, and the fireproof performance needs to be tested.

The cable intermediate joint is disassembled for analysis. There are 33-cm-long cracks in the copper shell of the cable intermediate joint. The exposed insulating rubber parts have obvious breakdown holes. After the metal copper shell was cut off, it was found that the insulating rubber parts were ablated in a large area, and the length of the ablation area was up to 50 cm. The insulating rubber parts are cut to observe the breakdown position of the cable body and the breakdown position of the corresponding insulating rubber parts. The fault breakdown is the radial breakdown of insulating rubber parts, and the starting position of high voltage is the end of the wire core shield. After the semiconductive tape outside the shield at the cable core is stripped, obvious ablation can be found at the edge of the shield. When insulating rubber part is cut along the axial direction of the fault breakdown position, the breakdown path can be observed. It can be seen that the diameter of the breakdown hole is about 10 mm, and the position of the breakdown path is consistent with the position of the mold joint of the semiconductive layer in the insulating rubber part. There are impurities on the surface of the semiconductive layer in some insulating rubber parts, which may cause partial discharge.

According to the statistical analysis of similar faults, there have been 13 breakdown faults of silicone rubber intermediate joints of 110 kV and above voltage levels of the same manufacturer since 2014. There are 11 breakdown faults during power transmission and closing, and 2 breakdown faults during voltage withstand

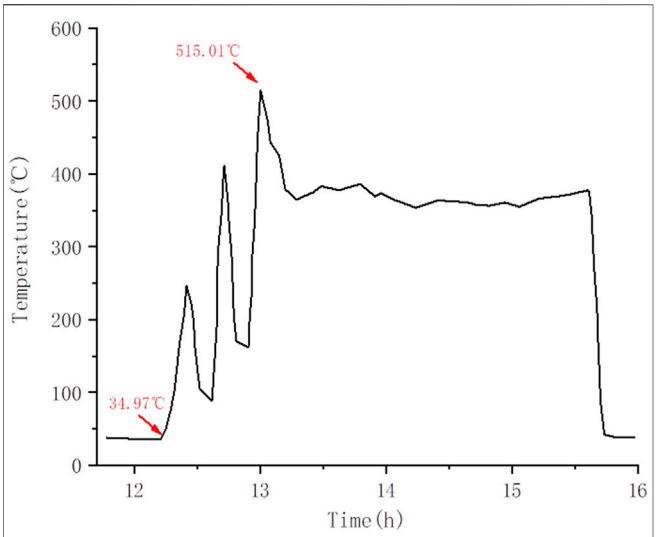

FIGURE 3 | Optical fiber temperature measurement data of cable tunnel fire accident.

tests. The causes of the breakdown faults were analyzed. There are 10 failures caused by the breeding of electric trees in insulating rubber parts. There are 2 failures caused by construction quality problems. The cause of another accident is unknown. The operation time of cable joints in these 13 accidents is counted, as shown in **Figure 2**. The operation time of the 69.2% faulty cable is 3 years. This is consistent with the development law of actual cable insulation defects. During the initial operation of 1–2 years, insulation defects continue to develop. To a certain extent in the third year, breakdown accidents are prone to occur with overvoltage. For cables without obvious defects, the insulation aging does not gradually produce defects until 6 years of operation, resulting in breakdown. The investigation and analysis show that the cable intermediate joint faults all occur in the power transmission and closing stage. The main reasons are insulation defects of insulating rubber parts, insufficient insulation margin, and breakdown caused by operating overvoltage during closing. It is necessary to improve the process of intermediate joints of similar manufacturers to avoid insulation defects of intermediate joints.

Analysis of Monitoring Data in Tunnel

First, the fault time is determined according to the voltage and current waveform of fault recording. The fault is a phase C short circuit fault, which occurred at 12:08:51 and lasted for 0.04 s. During the fault, the phase C voltage drops to 16.61 kV and the maximum fault current is 13.37 kA. The system returns to normal after an oscillation of 0.04 s. Due to the short fault duration, the monitoring system did not collect the grounding current value at the time of fault occurrence. The grounding current of each phase of the fault circuit collected by the monitoring system before and after the fault is within 13 A. According to the simulation calculation of the induced current of the metal sheath of 220 kV double circuit cable, the grounding current is about 10 A under different loads and laying methods. The monitored grounding current data are normal.

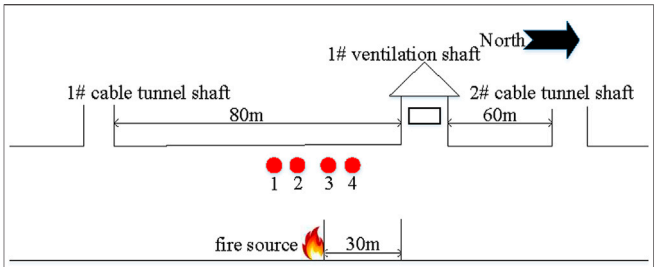

FIGURE 4 | Tunnel structure and overall layout for field test.

The optical fiber temperature data within 5 h before and after the fault are shown in **Figure 3**. The sampling rate of the optical fiber temperature measurement on-line monitoring system is about 5 min/time. The system does not collect the instantaneous temperature rise process at the time of fault discharge (12:08). The temperature before (12:05) and after (12:10) the time of fault is 35°C, and the measured temperature data are normal. From the time of failure (12:08) to the starting time of temperature rise displayed by optical fiber temperature measurement (12:15), the temperature measurement data are normal. It is judged that this stage is the ignition stage of the phase C cable, and the phase B cable has not been ignited. The temperature measurement optical fiber is arranged in the phase B cable, so the temperature data are unchanged. During the period when the optical fiber temperature measurement data increased from 34.97°C (12:15) to 515.01°C (13:01), the temperature value generally showed a sharp upward trend. It is judged that this stage is the combustion stage of the phase C cable, and the peaks occurred successively during this stage. In the following 156 min (to 15:36), the optical fiber temperature measurement value was maintained at 360°C, and it was judged that the combustion of the phase C cable was extinguished at this time. Combined with the field analysis, the upper fireproof slot box of the cable is ignited during the cable combustion, and the high temperature measured by the optical fiber is caused by the slot box combustion. After 15:36, the oxygen content in the tunnel space was insufficient to maintain the continuous combustion of the tank box, all the flames in the tunnel were extinguished, and the temperature measurement data returned to normal. The two temperature drop areas are due to the action of fire extinguishers separated by a certain distance, which has a certain cooling effect. However, due to the long trigger time of fire extinguishers and insufficient distance, the flame is not completely extinguished. The area near the middle joint of the cable is reignited. This indicates that the layout of fire extinguishers needs to be optimized.

FIELD TEST OF SIMULATED FIRE IN CABLE TUNNEL

Test Equipment Layout and Test Method

A tunnel to be put into operation was selected for the cable fire test. The tunnel section is 2.1 m high and 2 m wide. The cable

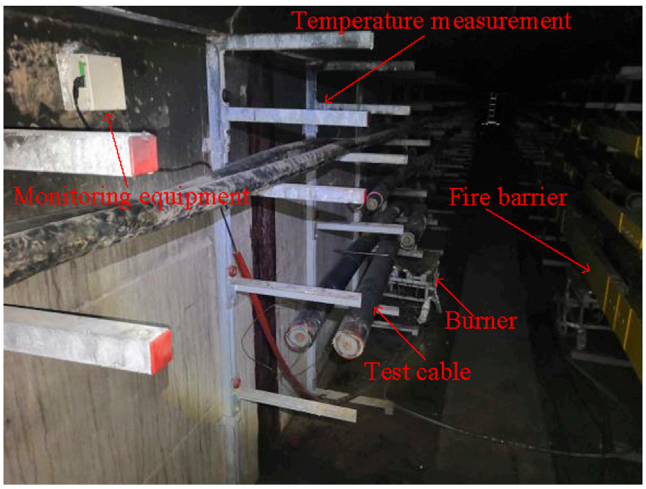

FIGURE 5 | Specific layout inside the tunnel.

tunnel area for testing is between two cable tunnel shafts, with a total length of 140 m, and there is a ventilation shaft in the middle, as shown in **Figure 4**. The fire source is arranged 30 m to the south of the ventilation shaft. It mainly tests the monitoring data of intermediate joint in case of fire. Four monitoring points are set at 3 m and 6 m on both sides of the fire source for the measurement of CO, CO_2, and flue gas concentration data. The temperature data need to analyze the difference in different heights. Four monitoring points are arranged on both sides of the fire source, and the height of the monitoring points is from 1.5 to 1.9 m. The specific layout inside the tunnel is shown in **Figure 5**. It can also be seen that there are six layers of supports in the tunnel, including 220 kV cables placed for the second time and 110 kV cables placed on the third and fourth layers. The left side of the figure shows the test layout without fire prevention measures. On the right side is a comparative test arrangement with fire barriers.

The main equipment of the test includes a simulated fire source system and characteristic data monitoring system. Combined with relevant standards, a set of fire source device with remote control ignition and adjustable power is developed in this study. The fire source system mainly includes propane gas supply device, flowmeter, control valve, anti-backfire device, fireproof metal pipe, burner, and wireless ignition device. The power regulation of fire source is feedback controlled by a flowmeter and control valve. At the same time, the ignition source can be controlled off after the cable ignition is completed. In order to ensure the signal acceptance of the wireless ignition device in the underground tunnel, signal repeaters are installed at the tunnel shaft and in the tunnel. The characteristic data of cable combustion mainly include temperature, CO, CO_2, and flue gas concentration. CO concentration in gas is one of the effective characteristic quantities of fire gas in fire detection. CO_2 is the main product of most polymer combustion, and its concentration can characterize the scale of fire. The fire smoke particles vary in size, and the diameter range generated by complete combustion is concentrated below 1 um. Here, the cable combustion is incomplete combustion, and the particles are large. The PM10 sensor is used to monitor the smoke concentration. The main technical parameters of the sensor used are as follows: CO sensor, range 0–1000 ppm, resolution 0.1 ppm; CO_2 sensor, range 0–5000 ppm, resolution 50 ppm; and PM10 sensor, range 0–1999 ug/m^3, resolution 0.3–10 um. CO, CO_2, and PM10 sensors are integrated. Three prevention treatments and sheet metal shells are installed to adapt to the harsh environment of the cable tunnel. The shell opening channel can effectively collect tunnel data. There are many temperature acquisition points, and the K-type thermocouple matrix is used for acquisition. All collected characteristic data are monitored online through the RS485 communication module and uploaded to supporting software. All data can be displayed and stored in real time.

Considering the fire caused by the simulated cable discharge fault, the test method is as follows: the burner is placed under the lowest support, the cable is cut off, the insulating layer is exposed; the ventilation is adjusted to simulate different arc power to ignite the cable; the fire source is turned off after igniting for a period of time, the cable continues to burn; the combustion situation is video-recorded; the characteristic parameters such as temperature and gas are collected and recorded through a monitoring device; the tunnel is filled with dry ice to extinguish the fire after completing the combustion test, and air extraction and tail gas treatment are carried out to ensure that the air in the tunnel meets the entry requirements of personnel before going down the well.

Monitoring Data Analysis of Tunnel Fire Test

The development of cable combustion in the tunnel is shown in **Figure 6**. After the burner is ignited, the 220 kV cable on the second layer support is ignited within 5S. The outer sheath begins to undergo pyrolysis under the influence of high temperature, resulting in a variety of gas products such as alkanes, olefins, and chlorinated products. These products are mixed with air for

FIGURE 6 | Development of cable combustion in tunnel.

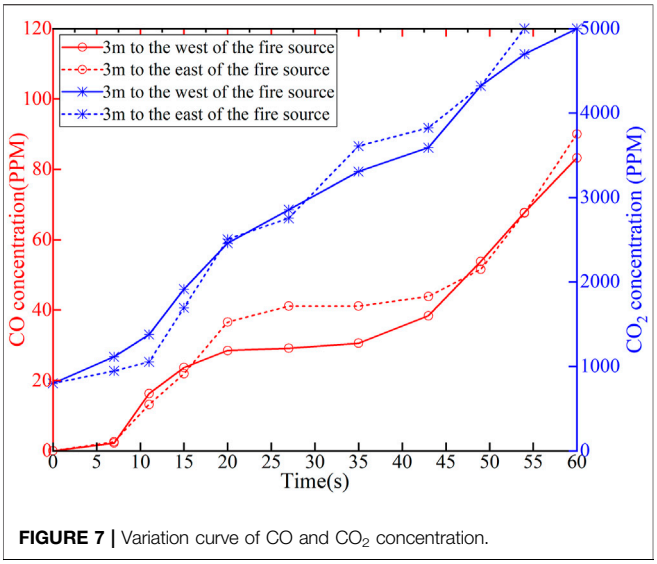

FIGURE 7 | Variation curve of CO and CO_2 concentration.

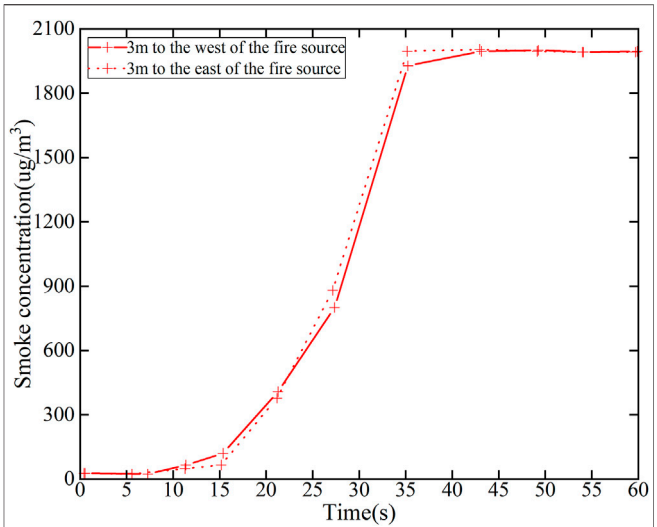

FIGURE 8 | Variation curve of flue gas particle concentration.

combustion, and the flame height increases rapidly. The insulating layer is cut and exposed to simulate the joint breakdown fault. The insulating layer is made of XLPE, which is flammable. At high temperature, the XLPE will melt and fall, resulting in obvious flame on the ground. A large amount of heat and flue gas are generated by combustion and gradually diffused. After the 220 kV cable is completely burned, the 110 kV cable on the upper layer is further ignited. Finally, the test cables are fully burned to form a stable flame area.

The relevant data of the fire test are collected in real time. The gas monitoring data of two monitoring points, which are 3 m away from the fire source, are analyzed as an example. The variation curve of CO and CO_2 concentration is shown in **Figure 7**. The CO_2 gas concentration increased continuously in the initial stage and exceeded 5,000 ppm in 55 s. CO_2 in the initial stage is mainly produced by a propane burner. After the 220 kV cable is ignited, the burner is closed. At this time, CO_2 is mainly generated by the combustion of the cable. In the initial stage, oxygen is sufficient, and the propane burner burns completely to produce very little CO. CO is mainly produced by pyrolysis combustion of the cable outer sheath and insulating layer. After the cable is ignited, insufficient initial pyrolysis will produce a large amount of CO. The CO content increased to 20 ppm in 15 s. Then the temperature increases rapidly, the pyrolysis of CO is fully burnt, and the CO content enters the slow growth stage. The combustion range expanded in about 45 s, more cables were not fully pyrolyzed, and the CO content increased rapidly again, reaching 90 ppm in 60 s. The variation curve of flue gas particle concentration is shown in **Figure 8**. In the first 10 s, the combustion causes the temperature in the fire source area to increase sharply, forming a local high-temperature area. With the acceleration of air flow, some stationary particles begin to diffuse under the action of thermal convection. The flame-retardant characteristics of the cable sheath led to a large number of smoke particles, the diameter of which is greater than 2.5 μm accounting for the main proportion. These particles form a layer of hot smoke at the top of the tunnel. The measured concentration quickly exceeds 1800 ug/m^3, and the smoke concentration reaches the maximum range of the sensor within 45 s.

The temperature variation curve at different heights of each monitoring point is shown in **Figure 9**. The temperature of monitoring points 2 and 3, 3 m away from the fire source, began to increase from 18 s. There are obvious differences in the maximum temperature at different heights. For example, the temperature at the height of 1.9 m of measuring point 2 can reach more than 160°C, while the temperature at the height of 1.5 m is about 100°C. The monitoring temperature of measuring point 3 is higher than that of measuring point 2. Since measuring point 3 is close to the side of the ventilation shaft, the air flow is easier to supplement oxygen, burn more fully, and generate more heat. As shown in the monitoring data of measuring point 1, it can be seen that the temperature difference between different heights below 1.8 m height is greater than that of measuring point 2. However, the temperature data of 1.8 m height and 1.9 m height are close. This indicates that the hot gas flow diffuses at the top, and the farther away from the fire point, the more the temperature is concentrated at the top of the tunnel. The maximum temperature at the height of 1.5 at measuring point 1 is only about 70°C, so the fire extinguisher may not be triggered. In the accident analyzed before, the fire extinguisher was placed on the cable support near the middle of the channel. The suspension height is about 1.6 m and is not in the area directly above the fire source but in the middle of the tunnel. It is placed about 3 m away from the ignition point. This leads to the late triggering time, and the limited fire-extinguishing range of the fire extinguisher also limits the fire-extinguishing effect. The layout of the fire extinguisher equipment needs to be optimized.

Fire Performance Test Results of Fire Barrier

As shown in **Figure 5**, a fire barrier is arranged on the support on the right side of the tunnel for test. The area with the fire barrier

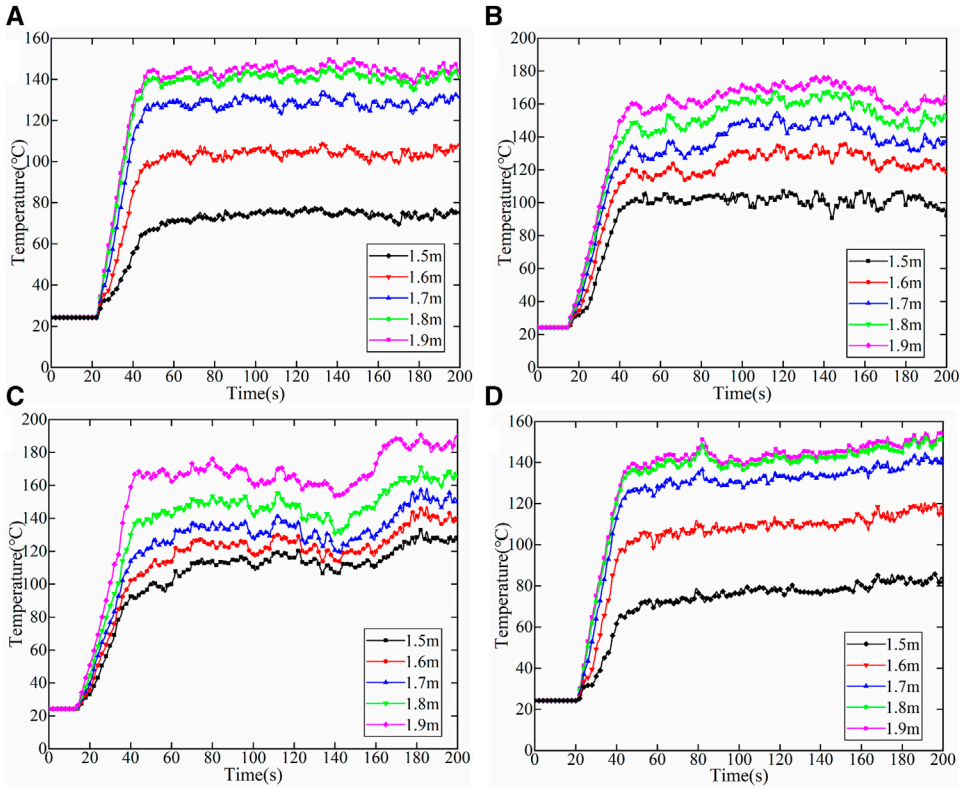

FIGURE 9 | Temperature variation curve at different heights of each monitoring point **(A)** 1, **(B)** 2, **(C)** 3, and **(D)** 4

protects the upper cable from ignition, as shown in **Figure 6**. When the fire barrier is tested, the fire source power of the burner needs to be set based on the actual cable tunnel fire. However, the fire source power of the actual cable tunnel cannot be obtained directly. The simulation analysis of cable fire needs to be used and then compared with the experimental temperature monitoring data. A high-voltage XLPE cable is composed of multilayer materials. The complex pyrolysis method is used to simulate the combustion spread of the multilayer cable structure. The reaction rate formula of combustion is as given follows:

$$W_i = A_i\left(\frac{\rho_i(x,t)}{\rho o}\right)^N \exp\left(-\frac{E_i}{RT_S(x,t)}\right)X_{O_2}^{n_{o_2,i}}, \quad (1)$$

where W_i is the i-th pyrolysis reaction rate; A_i is the i-th pre-exponential factor; E_i is the activation energy of the i-th reaction; R is the general gas constant, with a value of 8.314 kJ/kmol•K; T_s is the reaction temperature (K); N is the reaction order; ρ_i is the mass concentration of the current solid phase type; ρ_o is the initial density of the solid surface at the boundary; and X_{O2} is a simulated reaction rate, which is affected by local oxygen concentration.

During the combustion process of the power cable, the combustion of the outer sheath and insulating layer needs to be determined according to the test. Combined with the combustion calorific value of solid materials obtained from the test, the mass of gas fuel required for the corresponding gas-phase reaction is converted. According to the ratio of the outer sheath and insulating layer of the high-voltage cable, the gas-phase reaction equation is shown in **formula 2**.

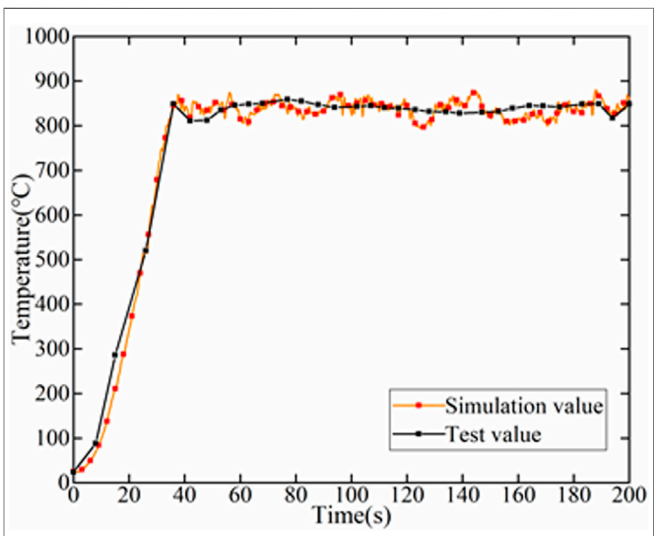

FIGURE 10 | Temperature comparison of test and simulation above fire source.

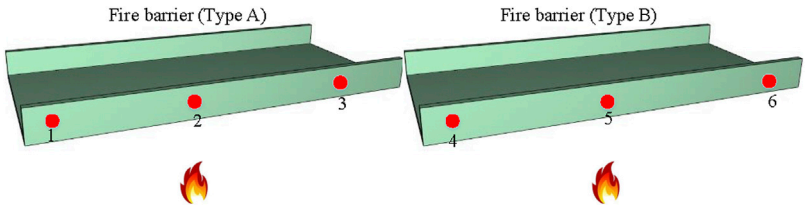

FIGURE 11 | Layout of the temperature measuring points.

TABLE 1 | Comparative combustion test data of two kinds of fire barrier.

Temperature (°C)	0.5 min	State	1 min	State	1.5 min	State	3 min	State	5 min	State
Point 1	40.2	Intact	45.4	Intact	54.1	Intact	72	Ignite	104.6	Ignite
Point 2	48.4	Intact	101.7	Intact	150	Intact	291	Ignite	556	Violent combustion
Point 3	39.6	Intact	45.9	Intact	57.1	Intact	70	Ignite	90	Ignite
Point 4	33.7	Intact	36.4	Intact	40.1	Intact	44	Intact	47.5	Ignite
Point 5	42.5	Intact	54.4	Intact	66.6	Intact	92	Intact	147	Ignite
Point 6	44.1	Intact	42.8	Intact	50.2	Intact	61	Intact	80.6	Ignite

$$C_2H_{3.6}Cl_{0.4} + 2.39O_2 \rightarrow 1.42CO_2 + 0.34CO + 1.6H_2O + 0.4HCl + 0.24C. \quad (2)$$

The simulation model is established based on the field test cable and tunnel structure size. Simulation is carried out with the previous settings. The comparison between the monitoring data of the temperature sensor above the fire source and the simulation data is shown in **Figure 10**. After the cable is ignited, the temperature increases rapidly. After about 40 s, the temperature oscillates around 840°C, and the oscillation amplitude of the simulation value is slightly higher than that of the test value. The change trend of temperature is very close between the test and simulation. The maximum error is about 4%. The effectiveness of the simulation model is verified.

Comparative tests were carried out on the type A fire barrier (using the pultrusion process) and the type B fire barrier (using new high-flame-retardant molding plastic process). The temperature sensor is used to measure the temperature at three different positions of the fireproof partition sample. The layout of the measuring points is shown in **Figure 11**. The flame temperature is about 1,000°C, and the combustion time is 6 min. The test results are shown in **Table 1**.

In the first 1.5 min, neither sample was ignited. The temperature of sample B was up to 66.6°C and that of the sample A was up to 150°C. At 3 min, sample A begins to burn obviously, and the maximum temperature of the measuring point reaches 291°C. At 3.5 min, sample B began to burn sporadically. At 4 min, the combustion fire of sample A becomes larger, the smoke is thick and black, and the combustion fire of sample B is smaller. At 6 min, the combustion fire and smoke of sample A are very large. The temperature in the tank box reaches more than 500°C, while the maximum temperature of sample B is only 147°C. When the fire source is turned off, the combustion flame of sample B will extinguish itself within 5 s, while the combustion flame of sample A will not extinguish for 40 s. It will not be extinguished until it is sprayed many times by the fire-extinguishing device. The fire barrier in the accident is type A. Its fire protection performance obviously cannot meet the fire protection requirements of the high-voltage cable tunnel. The type A fire barrier in the existing high-voltage cable tunnel needs to be replaced. Type B fire barrier can meet the fire isolation requirements at the joint.

OPTIMAL CONFIGURATION SCHEME OF FIRE PREVENTION AND EXTINGUISHING PRODUCTS

Based on the aforementioned accident data analysis and field fire test, the existing firefighting measures for cable joints in high-voltage cable tunnels mainly have the following problems: 1) The trigger time of fire-extinguishing bomb from fire to action is long, resulting in longer fire development time and expanded influence range; 2) in case of severe fire, the fire extinguisher can temporarily suppress the fire situation after spraying fire-extinguishing agent, but then it will rekindle; 3) fire will spread to the part outside the protection area of the fire protection tape, and the flame will directly burn the cable body, resulting in cable damage; and 4) when the cable intermediate joint is arranged in the middle, the molten medium caused by high temperature will drip to the lower cable after the failure of the cable intermediate joint, affecting the normal operation of the lower cable. In view of the aforementioned problems, improvements are made from the layout position and configuration quantity of fire extinguishers, the winding range of fireproof tapes, and the optimization of fireproof diaphragms.

Through tests, when the fire extinguisher is placed at the top of the middle of the tunnel, about 30 s after the fire source is turned

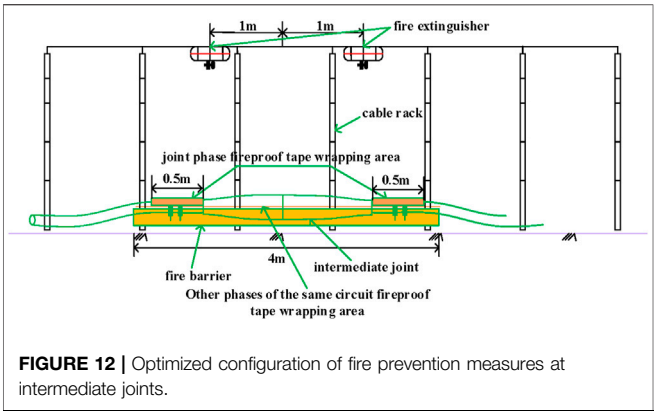

FIGURE 12 | Optimized configuration of fire prevention measures at intermediate joints.

on, the temperature at the temperature-sensing glass ball of the fire extinguisher reaches the trigger temperature of the fire extinguisher, the fire extinguisher starts to act, ejects fire-extinguishing agent, and the fire is controlled. When the fire extinguisher is placed on the uppermost support directly above the cable joint, the fire-extinguishing conditions can be triggered earlier, and the fire can be extinguished before the fire develops completely. The optimized trigger time is about 20 s, which is about 30°C lower at the maximum temperature. At the same time, the ignition point is uncertain due to the long middle joint of the high-voltage cable. The actual fire-extinguishing device may not be directly above the intermediate joint. The test is conducted at 1 and 1.5 m on both sides of the center line of the cable joint of the upper support. When the distance is 1.5 m, it reaches the trigger temperature of the fire extinguisher in about 33 s. However, due to the late start-up time and the spread of the fire, the cables outside the fire envelope are still ablated. When the distance is 1 m, the trigger temperature of the fire extinguisher is reached in about 25 s. After the combustion test, there are slight ablation marks on the outer sheath of the cable, and the fire prevention effect is better than the that in aforementioned methods, but it is still possible to damage the upper cable in extreme fire. Consider arranging one fire extinguisher on both sides of the intermediate joint. The test results show that the trigger temperature is reached in about 25 s. The ultra-fine dry powder in the fire area maintains a high concentration, and oxygen is seriously insufficient, so it cannot be reignited. The temperature drop rate is about 135% faster than that of a single fire extinguisher.

In the current fire protection layout scheme for the middle joint area of the high-voltage cable tunnel, the cables on both sides of the joint of the whole line are wrapped with the fireproof tape about 3 m. The test results show that the cable 3 m away from the burning place of the middle joint of the cable is still ablated, and the length of the cable body not covered with the fireproof tape is not more than 1 m. The length of the cable covered with the fireproof tape is optimized to be 4 m.

The optimized configuration of fire protection measured at the intermediate joint of the high-voltage cable is shown in **Figure 12**. The installation position and dosage of ultra-fine dry powder fire-extinguishing device have an obvious influence on the extinguishing effect. According to the comparative analysis of the test, a 4-kg ultra-fine dry powder fire-extinguishing device is installed at the top support 0.8~1 m from both sides of the center line of the cable joint. In order to prevent the high-temperature molten medium in the faulty joint from affecting the lower cable, the high-flame-retardant, non-toxic, and low-smoke plastic cable fireproof partition is installed at the lower part of the cable intermediate joint. In order to prevent the fault arc or open fire from affecting the surrounding cables, the cables on both sides of the cable intermediate joint and within 4 m on both sides are wrapped with the fireproof wrapping tape. The fire test was carried out after improving the layout of fire-extinguishing measures. After the fire is formed at 19 s, the fire-extinguishing bomb acts, and the fire extinguishing is completed when the fire is not fully developed. At the same time, fire barriers and fire belts also effectively inhibit the development of cable fire.

CONCLUSION

The abnormal monitoring data of typical high-voltage cable tunnel fire accidents are analyzed in this study. Combined with the field tunnel fire test, the shortcomings of the existing fire prevention and extinguishing measures are analyzed. The optimal configuration scheme of the fire anomaly data detection equipment and fire-extinguishing products is proposed. The main conclusions are as follows:

1) The statistical data of typical accidents show that the joint breakdown fault is the main cause of cable tunnel fire. The main problems existing in the existing tunnel fire prevention measures are the unreasonable installation position of fire extinguishers, the lack of fire prevention measures between intermediate joints, and the insufficient fire prevention performance of interlayer fire barriers.
2) The field test shows that the high temperature of the high-voltage cable is mainly concentrated at the top of the tunnel near the ignition point. If the layout is unreasonable, it is difficult to trigger the fire extinguisher in time. The melting drop of the insulating layer is easy to cause fire below. Comparing the simulation and test results of abnormal characteristic parameters in fire, the temperature error is less than 4%. The fire power curve of the cable tunnel is obtained through simulation, and then the burner power is set. It can conveniently and effectively test the performance of different fire prevention and extinguishing devices.
3) The fire prevention and extinguishing configuration of the cable tunnel is improved from the aspects of the layout position and configuration quantity of fire extinguishers, winding range of the fireproof tape, and optimization of fireproof partition. The temperature drop rate increased by about 135%, and can effectively prevent re-ignition.

DATA AVAILABILITY STATEMENT

The original contributions presented in the study are included in the article/supplementary material; further inquiries can be directed to the corresponding author.

AUTHOR CONTRIBUTIONS

ZP put forward research ideas. WG guided the research methods. ZP wrote the original draft and he is the corresponding author. ZR reviewed the manuscript. YM and ZeP conducted field tests. SZ edited figures and tables. ZeP did the data analysis. All authors have read and approved the submitted version of the manuscript.

REFERENCES

An, W., Wang, T., Liang, K., Tang, Y., and Wang, Z. (2020). Effects of Interlayer Distance and cable Spacing on Flame Characteristics and Fire hazard of Multilayer Cables in Utility Tunnel. *Case Stud. Therm. Eng.* 22, 100784. doi:10.1016/j.csite.2020.100784

An, W., Wang, X., Tang, Y., Wang, T., and Lu, J. (2021). Influence of cable Inclination Angle and Longitudinal Ventilation on Temperature Distribution during cable Fire in Utility Tunnel. *Case Stud. Therm. Eng.* 27, 101304. doi:10.1016/j.csite.2021.101304

Dong, X., Yang, Y., Zhou, C., and Hepburn, D. M. (2017). Online Monitoring and Diagnosis of HV cable Faults by Sheath System Currents. *IEEE Trans. Power Deliv.* 32 (5), 2281–2290. doi:10.1109/TPWRD.2017.2665818

Guo, D., Zhang, G., Zhu, G., Jia, B., and Zhang, P. (2020). Applicability of Liquid Nitrogen Fire Extinguishing in Urban Underground Utility Tunnel. *Case Stud. Therm. Eng.* 21, 100657. doi:10.1016/j.csite.2020.100657

Li, J., Shi, C., Chen, C., Zhang, Y., Xu, X., and Shi, J. (2018). "October)Fire Smothering and Post-fire Ventilation Strategy for Cable Compartment in Urban Utility Tunnel," in *Asia-Oceania Symposium on Fire Science and Technology* (Singapore: Springer), 1047–1059.

Liang, K., Hao, X., An, W., Tang, Y., and Cong, Y. (2019). Study on cable Fire Spread and Smoke Temperature Distribution in T-Shaped Utility Tunnel. *Case Stud. Therm. Eng.* 14, 100433. doi:10.1016/j.csite.2019.100433

Liu, X., Hou, D., Ji, J., and Zhu, H. (2021). Experiment and Numerical Simulation of cable Trench Fire Detection. *Case Stud. Therm. Eng.* 28, 101338. doi:10.1016/j.csite.2021.101338

Liu, Y., Fang, Z., Tang, Z., Beji, T., and Merci, B. (2021). The Combined Effect of a Water Mist System and Longitudinal Ventilation on the Fire and Smoke Dynamics in a Tunnel. *Fire Saf. J.* 122, 103351. doi:10.1016/j.firesaf.2021.103351

Mi, H., Liu, Y., Jiao, Z., Wang, W., and Wang, Q. (2020). A Numerical Study on the Optimization of Ventilation Mode during Emergency of cable Fire in Utility Tunnel. *Tunnelling Underground Space Technology.* 100, 103403. doi:10.1016/j.tust.2020.103403

Shen, X., Ouyang, T., Khajorntraidet, C., Li, Y., Li, S., and Zhuang, J. (2022). Mixture Density Networks-Based Knock Simulator. *Ieee/asme Trans. Mechatron.* 27, 159–168. doi:10.1109/TMECH.2021.3059775

Song, Z., Wang, X., Tan, Z., Miao, X., and Zou, L. (2020). "Analysis of Distribution Law of Fire Gas Concentration in Underground Cable Tunnel of Substation," in 2020 IEEE International Conference on High Voltage Engineering and Application (ICHVE) (IEEE), 1–4.

Wang, Y., Rui, D., Qingyun, L., and Fang, G. (2017). Review of Urban High-Voltage cable Tunnel Monitoring Techniques," in *2017 EPTC Power Transmission and Transformation Technology Conference (PTTTC)*, 8. doi:10.1049/cp.2017.0552

Xu, G., Zhu, G., Pan, R., and Liu, X. (2021). Experimental Study on Combustion Parameters and Temperature Distribution of Linear Fire under Different Oxygen Concentration in Tunnel. *Results Eng.* 11, 100272. doi:10.1016/j.rineng.2021.100272

Yan, B., Ren, G., Huang, X., Chi, J., Zheng, L., Luo, H., et al. (2018). "Study on Early Fire Behavior Detection Method for Cable Tunnel Detection Robot," in *Intelligent Computing and Internet of Things* (Singapore: Springer), 215–224.

Yang, N., Dong, Z., Wu, L., Zhang, L., Shen, X., Chen, D., et al. (2021a). A Comprehensive Review of Security-Constrained Unit Commitment. *J. Mod. Power Syst. Clean Energ.* doi:10.35833/MPCE.2021.000255

Yang, N., Yang, C., Wu, L., Shen, X., Jia, J., Li, Z., et al. (2021b). Intelligent Data-Driven Decision-Making Method for Dynamic Multi-Sequence: An E-Seq2Seq Based SCUC Expert System. *IEEE Trans. Ind. Inform.* doi:10.1109/TII.2021.3107406

Zhang, H., and Zhao, Y. (2020). Study on Underground Utility Tunnel Fire Characteristics under Sealing and Ventilation Conditions. *Adv. Civil Eng.* 2020. doi:10.1155/2020/9128704

Zhu, H., Chi, Q., Sun, H., and Zhao, X. (2019). "Study on Temperature Field of Cable Tunnel Fire," in 2019 9th International Conference on Fire Science and Fire Protection Engineering (ICFSFPE) (IEEE), 1–5. doi:10.1109/icfsfpe48751.2019.9055804

Conflict of Interest: The authors declare that the research was conducted in the absence of any commercial or financial relationships that could be construed as a potential conflict of interest.

frontiers in Energy Research

ORIGINAL RESEARCH
published: 24 March 2022
doi: 10.3389/fenrg.2022.865620

Research on Battery Energy Storage STATCOM Suppressing HVDC Commutation Failure

Chao Xing[1], *Junhao Chen*[1,2], *Zhi Xu*[1], *Xinze Xi*[1], *Xin He*[1] *and Shilong Chen*[2]*

[1]Electric Power Research Institute of Yunnan Power Grid Co., Ltd., Kunming, China, [2]School of Electric Power Engineering, Kunming University of Science and Technology, Kunming, China

Due to the poor performance of traditional STATCOM in DC engineering, a compensation method using battery energy storage STATCOM (STATCOM/BESS) to suppress commutation failure of the weak receiving-end high voltage direct current transmission system is proposed, and its effect is better than traditional STATCOM. First, the mechanism and influencing factors of commutation failure are analyzed; the extinction angle of the converter valve is taken as the decision index of commutation failure; the relationship between various electrical parameters and extinction angle is studied under the condition of the single-phase grounding fault on the inverter side. Second, according to the differences between the positive and negative sequence reactive current output by STATCOM/BESS when a fault occurs in single-phase grounding, a compensation method is proposed to suppress commutation failure by STATCOM/BESS, which increases the proportion of positive sequence reactive current output by STATCOM/BESS under the condition of constant output so as to reduce the probability of commutation failure. At last, STATCOM/BESS is added into the standard model of LCC-HVDC for the simulation experiment and compared with conventional running characteristics of STATCOM in order to verify the effect of STATCOM/BESS in suppressing commutation failure.

Keywords: high voltage direct current (HVDC) transmission, battery energy storage STATCOM, commutation failure, positive and negative sequence reactive current, single-phase grounding fault

OPEN ACCESS

Edited by:
Xun Shen,
Tokyo Institute of Technology, Japan

Reviewed by:
Hardeep Singh,
Sophia University, Japan
Varun Nayyar,
Lovely Professional University, India

***Correspondence:**
Shilong Chen
chenshilong3@126.com

Specialty section:
This article was submitted to Smart Grids, a section of the journal Frontiers in Energy Research

Received: *30 January 2022*
Accepted: *14 February 2022*
Published: *24 March 2022*

Citation:
Xing C, Chen J, Xu Z, Xi X, He X and Chen S (2022) Research on Battery Energy Storage STATCOM Suppressing HVDC Commutation Failure. Front. Energy Res. 10:865620. doi: 10.3389/fenrg.2022.865620

INTRODUCTION

High voltage direct current (HVDC) transmission technology can not only meet the demand of large capacity and long distance transmission of electric energy but also reduce the loss of electric energy in transmission lines; (Shen et al., 2021) thus, it becomes an important means of electric energy transmission between long distance and large area power grids (Peng et al., 2017). When the power at the receiving end of the HVDC transmission system is weak, the AC system at the inverter side breaks down, which easily leads to the commutation failure of the HVDC system, resulting in the increase of DC current amplitude, the decrease of DC voltage amplitude, and voltage waveform distortion, etc., which seriously threatens the safety and reliability of the power grid (Huang, 2006). The fundamental condition of inverter commutation failure is that the extinction angle γ of a certain commutation valve is less than its intrinsic limit extinction angle γmin (Zhao et al., 2015). The factors causing converter commutation failure include internal factors and external factors of the inverter system,

(Zhenhua et al., 2021) among which one of the most common factors of commutation failure is caused by commutation voltage drop raised by AC grid fault.

At present, in order to support the grid voltage and restrain the commutation failure of the HVDC system, reactive compensation equipment has been put into many weak receiving-end system inverter stations, among which the dynamic response of STATCOM is pretty fast during operation, and the effect of restraining commutation failure is remarkable. Guo et al. (2013) has modeled the whole connection of STATCOM into the doubly-fed HVDC system and pointed out that STATCOM can effectively support the receiving-end bus of the doubly-fed system within a reasonable electrical distance so as to improve the system performance and avoid commutation failure within a certain range. In Zhang (2011), the apparent short-circuit ratio increment (ASCRI) is defined to reflect the change of the strength of the receiving-end system after adding STATCOM. The theoretical and simulation results show that the ASCRI index of the system after adding STATCOM is greater than 0, and the ASCRI is positively correlated with the capacity of the added STATCOM within a certain range, which indicates that STATCOM can support the voltage of the receiving-end AC power grid, and can avoid the commutation failure of the HVDC system to a certain extent. However, when traditional STATCOM performs large-capacity reactive power compensation, it will affect the control accuracy of DC side voltage and lead to large fluctuations of DC side voltage. The energy storage STATCOM combining energy storage technology with reactive power compensation technology makes up for the shortcomings of traditional STATCOM in HVDC system application. In Virtanen et al. (2013), energy storage STATCOM is used to increase the voltage of the parallel connection point with an electric arc furnace load, and the voltage drop of the parallel connection point was reduced from 15% to 2%. In Liang (2014), the whole switch function model of STATCOM/BESS is established, and the power feedforward control is introduced, and a prototype of STATCOM/BESS with a capacity of 10kVA is built. The simulation and experiment show that the proposed topology and control method can enhance the stability of the system and restrain the power fluctuation of the wind farm.

Compared with traditional STATCOM, (Guobing et al., 2020) STATCOM/BESS has more advantages in improving the stability of the power system. The traditional way to maintain the stability of the power system is to strengthen the network structure, improve the performance of the prime mover and the excitation system, cut off the machine, cut the load, and use the STATCOM device to provide dynamic reactive power to support the system voltage, but it cannot perform active power regulation to dampen. Apart from the power oscillation of the system, these methods inevitably have their own limitations. As a new type of FACTS device, STATCOM/BESS is composed of a high-power power electronic converter and an energy storage system. He et al. (2020) A large-capacity energy storage device is added to the DC side of the converter and is connected to the power grid in parallel. It absorbs and releases active and reactive power quickly and has the ability of four-quadrant operation. At present, there is less application research in the field of DC transmission, especially in the suppression of commutation failure. Therefore, this article studies the commutation failure suppression of the HVDC system and puts forward the compensation method to suppress commutation failure by STATCOM/BESS under single-phase grounding fault. The STATCOM/BESS is added in the HVDC system during the experiment, which shows that the effect of STATCOM/BESS on suppression of commutation failure is better than that of traditional STATCOM.

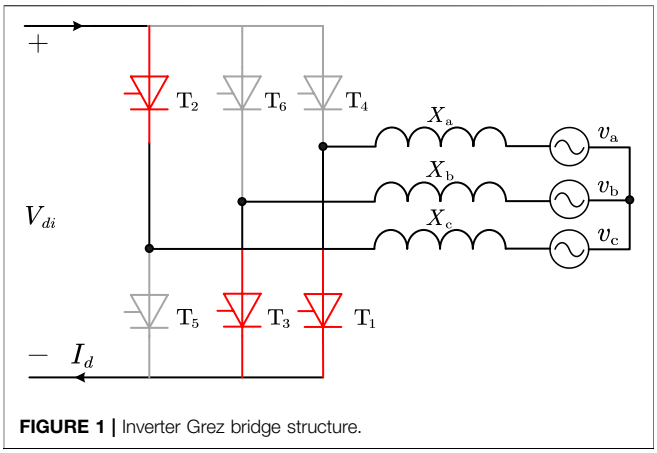

FIGURE 1 | Inverter Grez bridge structure.

HVDC COMMUTATION FAILURE AND ITS INFLUENCING FACTORS

HVDC Commutation Failure

Thyristor converter valves are used in the HVDC transmission system. During the process of commutation, if the process is not completed or the blocking ability is not restored within a period of time under the action of reverse voltage, the commutated valves will switch phases to the valves scheduled to be turned off when the voltage on the valve side becomes positive. This phenomenon is called commutation failure. Lei et al. (2021) From the thyristor device level, it takes a certain time for the thyristor to complete the carrier recombination and restore the blocking ability. γmin represents the recovery time of the thyristor valve, expressed by the electrical angle, which is about 10. It reflects the shortest time for the thyristor to bear the reverse voltage when restoring the blocking ability. When the extinction angle γ < γmin is calculated, the commutation is considered to be failed.

Figure 1 is the topology of the inverter, in which T_1~T_6 are thyristors, and Xa ~ Xc are commutation reactive resistances of each phase. Id represents direct current; and v_a, v_b, and v_c are the three-phase voltages of the AC system bus. **Eq. 1** represents the extinction angle-related commutation (Cai et al., 2019):

$$\gamma = \arccos\left(\frac{\sqrt{2}kI_dX_c}{E} + \cos\beta\right). \quad (1)$$

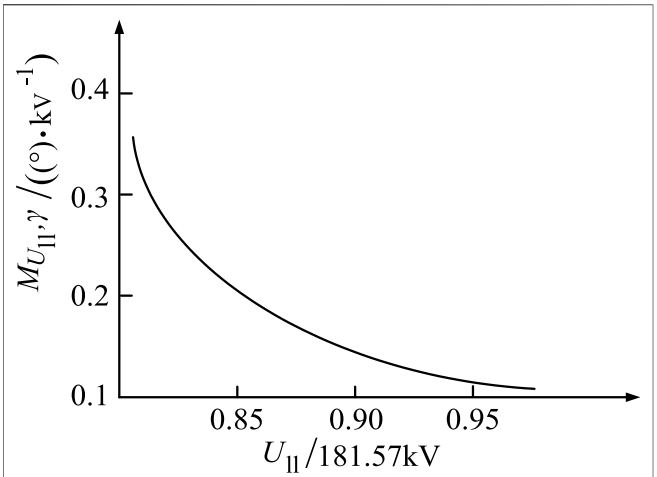

FIGURE 2 | Sensitivity of U_{ll} to γ.

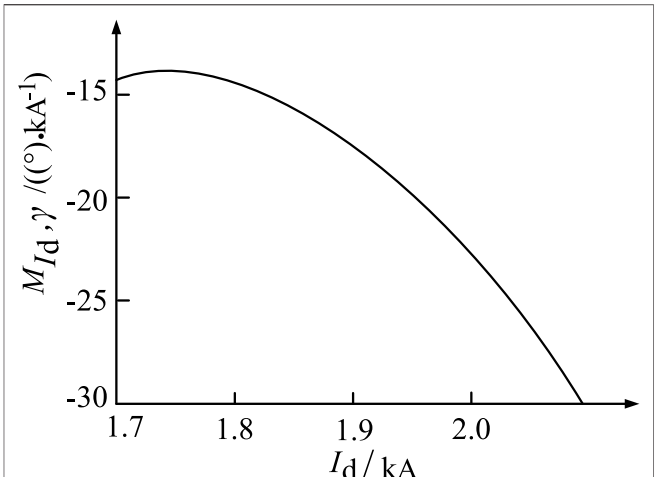

FIGURE 3 | Sensitivity of I_d to γ.

If the fault causes commutation voltage asymmetry, the offset of this voltage crossing the zero point should be considered in the aforementioned formula, then the offset of commutation voltage crossing the zero point should be written as φ, and the expression of γ at this time can be shown (Li et al., 2017) as:

$$\gamma = \arccos\left(\frac{\sqrt{2}kI_dX_c}{E} + \cos\beta\right) - \varphi. \quad (2)$$

In **Eqs 1**, **2**, k represents the commutation ratio, I_d represents the direct current, Xc represents the commutation reactive resistance, E represents the effective value of the commutation bus line voltage, and β represents the leading trigger angle.

The Influencing Factors of Commutation Failure

It can be seen from **Eq. 2** that the occurrence of commutation failure depends on many factors, including electrical factors such as AC bus voltage, DC current, commutation reactive resistance, and commutation voltage offset angle, and control factors such as trigger angle. The following mainly analyzes the influence of AC bus voltage and DC current on commutation failure when the AC system at the receiving end fails.

The Influence of Bus Voltage Amplitude Drop on Commutation Failure

When a short-circuit fault occurs in an AC system, it is assumed that the leading trigger angle β and the change ratio k are unchanged in a short time. Mitsuru and Yuhu (2021) In order to analyze the influence of the AC bus voltage U_{ll} on the commutation failure on the inverter side, the sensitivity of its extinction angle γ can be used. The deviation of γ on the bus voltage U_{ll} can be obtained by using **Eq. 2**:

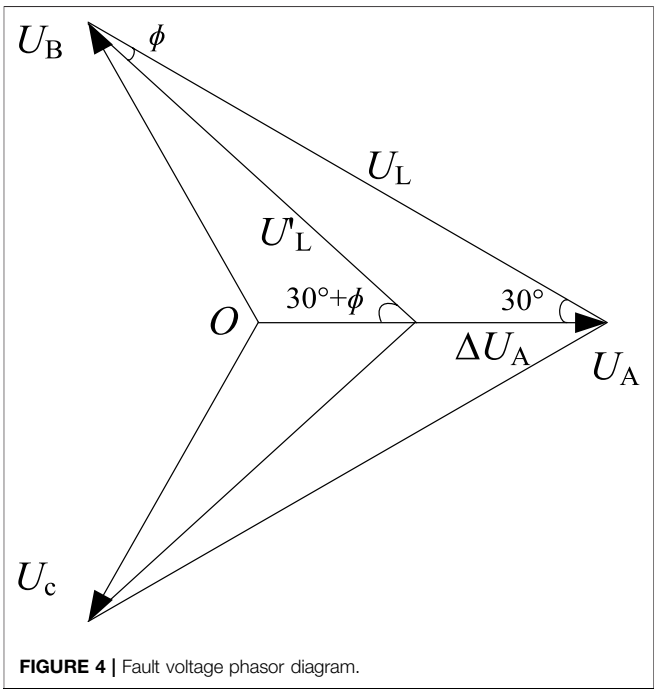

FIGURE 4 | Fault voltage phasor diagram.

$$M_{U_{11},\gamma} = \frac{\partial\gamma}{\partial U_{11}} = \frac{1}{\sqrt{1-\left(\frac{\sqrt{2}kI_dX_c}{U_{11}} + \cos\beta\right)^2}} = \frac{\sqrt{2}kI_dX_c}{U_{11}^2}. \quad (3)$$

When other parameters are unchanged, the relationship between bus voltage and sensitivity of the extinction angle is shown in **Figure 2**. The smaller the converter bus voltage is, the greater its sensitivity to extinction angle is, that is, the smaller the converter bus voltage is, the faster the extinction angle decreases, and the more likely it is to have commutation failure.

The Influence of DC Current Surge on Commutation Failure

The AC voltage drop usually causes the DC current to rise, and the DC current rise will have a certain limit. When the AC voltage on the valve side drops to a certain value, the system will start the link of "low voltage and current limit," thus controlling the continuous rise of DC current, and ensuring the stable operation of the DC transmission system (Zhu, 2008). In order to analyze the influence of DC current Id on the extinction angle, the deviation of extinction angle γ on DC current I_d is calculated according to **Eq. 2**:

$$M_{Id,\gamma} = \frac{\partial \gamma}{\partial I_d} = \frac{-1}{\sqrt{1-\left(\frac{\sqrt{2}kI_dX_c}{U_{11}}+\cos\beta\right)^2}}\frac{\sqrt{2}kX_c}{U_{11}}. \tag{4}$$

Under other conditions unchanged, the relationship between DC current and sensitivity of the extinction angle is shown in **Figure 3**. Yang (2021) The sensitivity of DC current I_d to extinction angle γ is negative, and the greater the I_d is, the greater its sensitivity to γ will be, so the increase of I_d will also lead to the decrease of extinction angle γ, and the greater the I_d is, the faster the γ will decrease, which will easily lead to commutation failure.

Analysis of the Single-Phase Grounding Fault in the AC System on the Inverter Side

A single-phase grounding fault is the most common asymmetric fault in the power system, characterized by the voltage drop, and phase shift of one phase on the bus line after the fault, which will affect the other two phases in the weak receiving end of the AC system, and the influence on the extinction angle is relatively complex. Take the single-phase grounding short-circuit fault in phase A of the AC power grid as an example, and the fault phase voltage is shown in **Figure 4** (Mohan, 2021).

It can be seen from **Figure 4** that when the grounding short-circuit fault occurs in phase A and the amplitude of phase voltage decreases by ΔU_A, the amplitude of line voltages U_{AB} and U_{CA} will decrease then the zero point of line voltage will shift. According to the trigonometric function theorem (all expressed in standard values) (Muniappan, 2021):

$$U'_L = \sqrt{1-\sqrt{3}\Delta U_A+\Delta U_A^2}; \tag{5}$$

$$\varphi = \arctan\frac{\Delta U_A}{\sqrt{3}\,(2-\Delta U_A)}. \tag{6}$$

Therefore, when an asymmetric fault occurs on the AC side of the system, the calculation formula of the extinction angle γ becomes:

$$\gamma = \arccos\left(\frac{\sqrt{2}kI_dX_c}{U'_L}+\cos\beta\right)-\varphi. \tag{7}$$

In the formula, U'_L represents the voltage value of the commutation line after the fault, and φ represents the angle value of zero crossing point of commutation line voltage caused by the asymmetric fault. Shen and Raksincharoensak (2021) It can be seen that when an asymmetric fault occurs in the AC system on the inverter side, the change of commutation voltage affects the extinction angle, and the phase shift caused by the zero crossing of commutation line voltage also changes the extinction angle. In addition, (Yu et al., 2020) the influence of the single-phase fault on different line voltages is different. Taking the A-phase short-circuit fault as an example, the influence of the single-phase fault on the valve commutation process among A-phase, B-phase, and C-phase bridge arms will be discussed as follows:.

1) Valve 1 commutates to valve 3, and valve 4 commutates to valve 6, that is, the valve on the A-phase bridge arm commutates to the valve on the B-phase bridge arm. When A-phase is grounded in a single phase, the extinction angle γ is:

$$\gamma' = \arccos\left(\frac{\sqrt{2}kI_dX_c}{\sqrt{1-\sqrt{3}\Delta U_A+\Delta U_A^2}}+\cos\beta\right) - \arctan\frac{\Delta U_A}{\sqrt{3}\,(2-\Delta U_A)}. \tag{8}$$

It can be seen from **Eq. 8** that under the condition of certain system parameters, the change of the evalve extinction angle is related to the degree of voltage drop of A-phase. According to CIGRE standard system parameters (**Table 1** below), the function graph of the extinction angle can be drawn in MATLAB as shown in **Figure 5**.

It can be seen from the aforementioned figure that when A-phase is grounded in a single phase, (Yuhu et al., 2021) the extinction angles of valves 1 and 4 decrease monotonously with the increase of ΔU_A. When ΔU_{Amax} = 0.10pu, γ < γmin, it is judged that commutation failure occurs, while when $\Delta U_A < \Delta U_{Amax}$, it is considered that commutation failure will not occur.

2) Valve 2 commutates to valve 4, and valve 5 commutates to valve 1, that is, the valve on the C-phase bridge arm commutates to the valve on the A-phase bridge arm. When the A-phase is grounded in a single phase, the function image of the extinction angle γ is also obtained in MATLAB as shown in **Figure 6**.

It can be seen from the variation curve in **Figure 6** that the extinction angle of valves 2 and 5 is not monotonic with ΔU_A. It can be obtained from the intersection point with the straight line γmin = 10° that when A-phase is grounded in a single phase, the interval of commutation failure of valves 2 and 5 is 0.18pu < ΔU_A < 0.46pu. In other intervals, it is considered that commutation failure will not occur.

3) Valve 3 commutates to valve 5, and valve 6 commutates to valve 2, that is, the valve on the B-phase bridge arm commutates to the valve on the C-phase bridge arm. It can be seen from **Figure 5** that the single-phase grounding of A-phase has no effect on the line voltage between B-phase and C-phase, so it has no effect on

TABLE 1 | CIGRE standard system parameters.

System-rated parameter		
500 kV, 100 MW, 50 Hz		
Rectifier side		
AC system	Reactive power compensation capacity	Single converter transformer
382.87 kV	626Mvar	603.7 MV A
47.65∠84°Ω		XT = 0.18p.u.
SCR = 2.5		345/213.5 kV
Inverter side		
DC system	Reactive power compensation capacity	Single converter transformer
215.05 kV	626Mvar	591.8 MV A
21.2∠75°Ω		XT = 0.18p.u.
SCR = 2.5		230/209.2kV
DC side		
Rd = 2.5Ω, Ld = 0.6H		

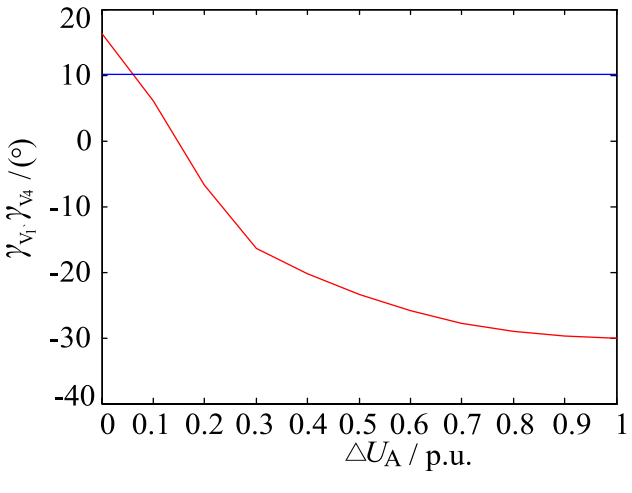

FIGURE 5 | Function diagram of the extinction angle of valves 1 and 4.

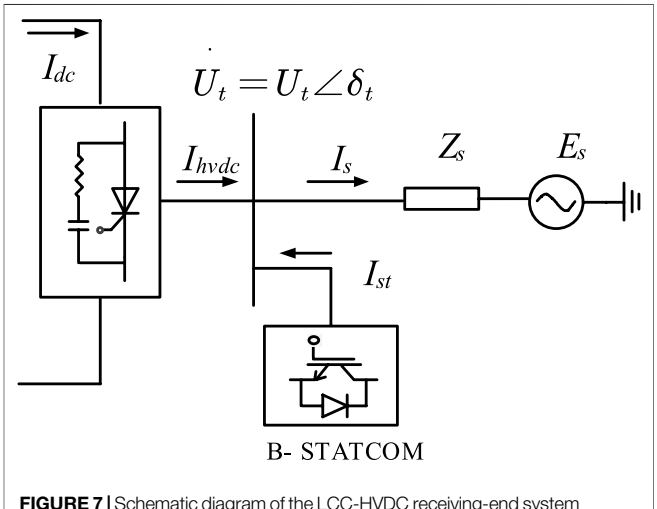

FIGURE 7 | Schematic diagram of the LCC-HVDC receiving-end system with STATCOM/BESS.

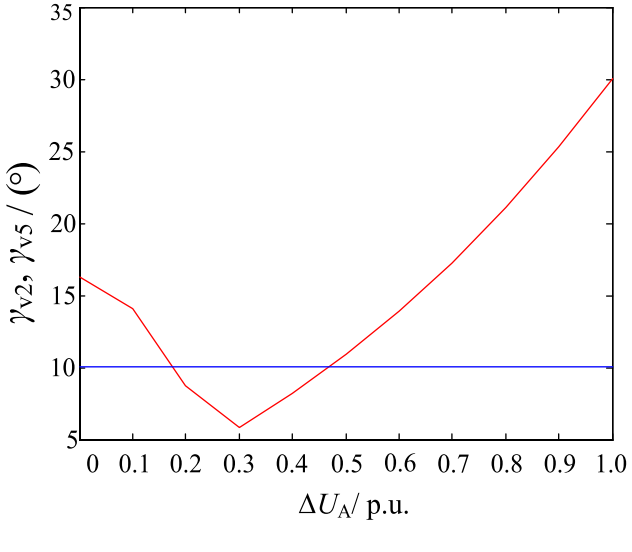

FIGURE 6 | Function diagram of the extinction angle of valves 2 and 5.

the extinction angles of valves 3 and 6. Theoretically, it is considered that the γ values of the two valves are unchanged in this type of the single-phase grounding fault.

Similarly, the influence of single-phase grounding of phases B and C on the commutation process can be analyzed.

COMPENSATION METHOD OF STATCOM/BESS SUPPRESSION COMMUTATION FAILURE UNDER THE SINGLE-PHASE GROUNDING FAULT

According to the analysis of the single-phase grounding fault in the previous section, the short-circuit fault of A-phase has the least influence on the commutation voltage between B-phase and C-phase, (Yang et al., 2021b) while it has the greatest negative influence on the commutation voltage between A-phase and B-phase, and the probability of commutation failure is also the largest. Therefore, under

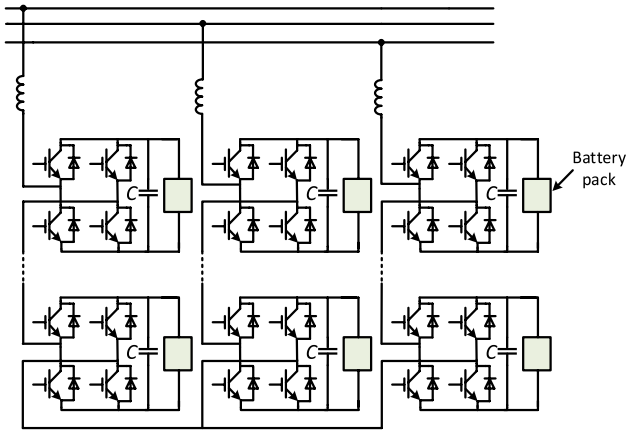

FIGURE 8 | STATCOM/BESS topology.

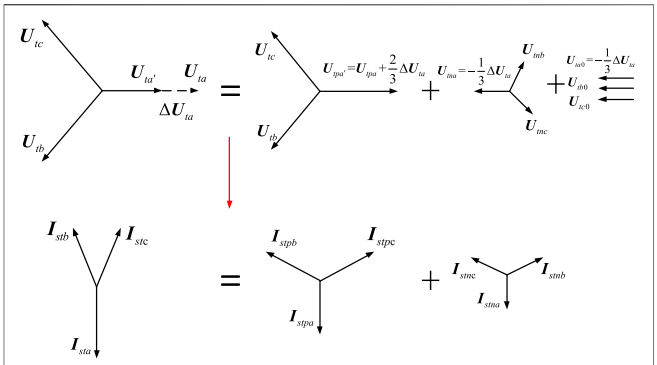

FIGURE 9 | Schematic diagram of decomposition of positive and negative sequence reactive current.

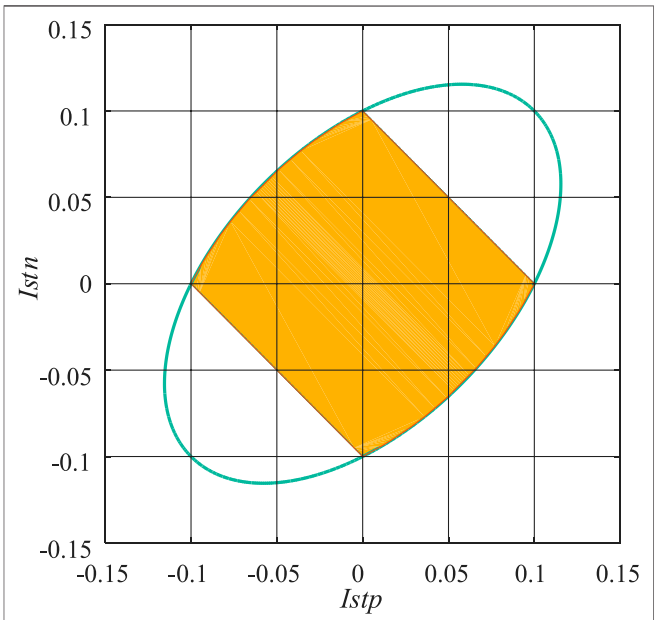

FIGURE 10 | Feasible region of STATCOM/BESS output current.

the single-phase fault condition, the ratio and capacity of positive and negative sequence components of STATCOM/BESS reactive current are controlled to reduce the probability of commutation failure.

The Influence of STATCOM/BESS Positive and Negative Sequence Reactive Power Compensation Components on the Extinction Angle

Figure 7 shows the schematic diagram of the LCC-HVDC receiving-end system including STATCOM/BESS. Le et al. (2021) In the figure, *I*dc represents DC current of the inverter station, *I*hvdc represents output current of the inverter station, U_t represents phase voltage of the converter bus, I_{st} represents reactive current output by STATCOM/BESS, I_s represents AC grid current, Z_s represents line resistance, and Es represents AC power supply voltage. STATCOM/BESS adopts an angular chain structure, and each phase includes three H-bridge sub-modules, as shown in **Figure 8**.

For the convenience of analysis, taking the voltage phasor of the converter bus as the reference coordinate, (Shen et al., 2022) according to the circuit principle, the voltage coordinates of each phase of the converter bus can be obtained when the system is in stable operation (assuming that STATCOM/BESS does not output reactive current at this time):

$$\begin{cases} U_{ta,0} = (U, 0) \\ U_{tb,0} = (U\cos 240°, \mathrm{U}\sin 240°) \\ U_{tc,0} = (U\sin 120°, \mathrm{U}\cos 240°) \end{cases}. \tag{9}$$

U_{t0} represents the steady-state phasor before fault, and U represents the voltage amplitude before fault. According to **Eq. 9**, the commutation voltages corresponding to the converter valves are:

$$\begin{cases} U_{tab0} = U_{ta0} - U_{tb0} = \left(\frac{3}{2}U, \frac{\sqrt{3}U}{2}\right) \\ U_{tbc0} = U_{tb0} - U_{tc0} = \left(0, \sqrt{3}\,U\right) \\ U_{tca0} = U_{tc0} - U_{ta0} = \left(-\frac{3}{2}U, \frac{\sqrt{3}U}{2}\right) \end{cases}. \tag{10}$$

When the A-phase short-circuit fault occurs in the AC system at the receiving end, the phase voltage U_{ta} of the converter bus becomes the original (1-d), (Yang et al., 2019) and the reactive current output by STATCOM is $I_{st} = I_{stp} + I_{stn}$, where I_{stp} and I_{stn} are positive and negative reactive currents, respectively. Assuming that the phasor of positive and negative sequence reactive current is perpendicular to the phasor of

TABLE 2 | Comparison of commutation failure suppression effects.

t Istp:Istn	1.001 s (H)	1.002 s (H)	1.003 s (H)	1.004 s (H)	1.005 s (H)
1:1	0.86	0.78	0.75	0.70	0.65
2:1	0.77	0.75	0.70	0.68	0.60
1:0	0.68	0.67	0.63	0.60	0.51

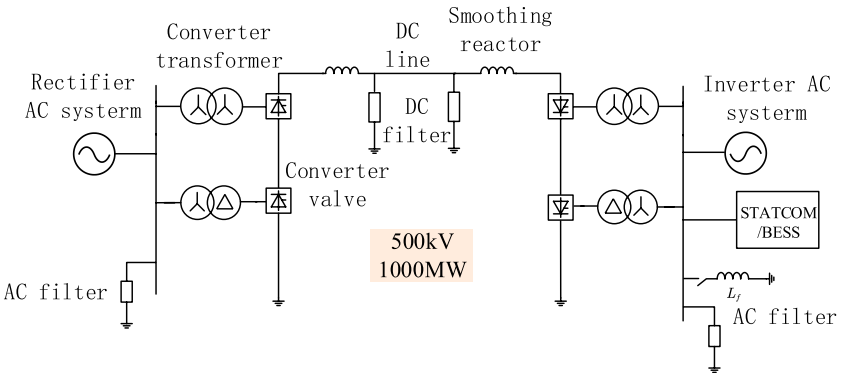

FIGURE 11 | LCC-HVDC standard model with STATCOM/BESS.

TABLE 3 | Main parameters of the CIGRE HVDC model simulation circuit.

Electrical parameter	Parameter on the rectifier side	Parameter on the inverter side
Rated value of AC voltage	345 kV	230 kV
Capacity of the commutation transformer	603.7 MVA	591.8 MVA
Ratio of the commutation transformer	345:213.5	230:209.2
Leakage reactance of the commutation transformer	0.18p.u.	0.18p.u.
Connection type of the commutation transformer	Y-△/Y-Y	△-Y/Y-Y

converter bus voltage, the positional relationship of I_{stp} and I_{stn} is shown in **Figure 9**.

The corresponding commutation voltage is Yang et al. (2022):

$$\begin{cases} U_{tab} = \sqrt{3}\sqrt{\left(U + XI_{stp}\right)^2 + \left(XI_{stp} - dU\right)\left[X\left(I_{stn} + I_{stp}\right) + U\right] + (dU)^2}/3 \\ \delta_{tab} = \arctan\dfrac{\sqrt{3}\left[U + X\left(I_{stn} + I_{stp}\right)\right]}{(3-2d)U + 3X\left(I_{stn} + I_{stp}\right)} \\ U_{tab} = \sqrt{3}\left[U + X\left(I_{stn} + I_{stp}\right)\right] \\ \delta_{tab} = -90° \\ U_{tcb} = \sqrt{3}\sqrt{\left(U + XI_{stp}\right)^2 + (XI_{stn} - dU)\left[X\left(I_{stn} + I_{stp}\right) + U\right] + (dU)^2}/3 \\ \delta_{tca} = 180° - \arctan\dfrac{\sqrt{3}\left[\mathrm{U} + \mathrm{X}\left(\mathrm{I_{stn}} - \mathrm{I_{stp}}\right)\right]}{(3-2\mathrm{d})\mathrm{U} + 3\mathrm{X}\left(\mathrm{I_{stn}} + \mathrm{I_{stp}}\right)} \end{cases} . \quad (11)$$

By substituting **Eq. 11** into the calculation formula of the extinction angle, the extinction angle of each converter valve after STATCOM/BESS that compensates positive and negative reactive power is:

$$\gamma_m = \arccos\left(\frac{\sqrt{2}I_{dc}X_t}{U_{tm}} + \cos\beta_o\right) - (\delta_{tm} - \delta_{tm0}), \quad (12)$$

where m = (ab,bc,ca), in which X_t represents the reactance of the commutation transformation phase, δtm represents the voltage phase after fault, and δtm0 represents the voltage phase before fault (Yang et al., 2021a).

The reference capacity S_B of the LCC-HVDC system with STATCOM/BESS is taken as 1000 MVA; the reference voltage V_B is taken as 230 kv, and the rated power of STATCOM/BESS is taken as 100 MVA. Xun and Pongsathorn (2021) In order to prevent reactive power compensation equipment from burning out due to over-current, the output current of each phase of STATCOM/BESS should not exceed its rated current. According to **Figure 9**, the output current of STATCOM/BESS needs to meet the following constraints:

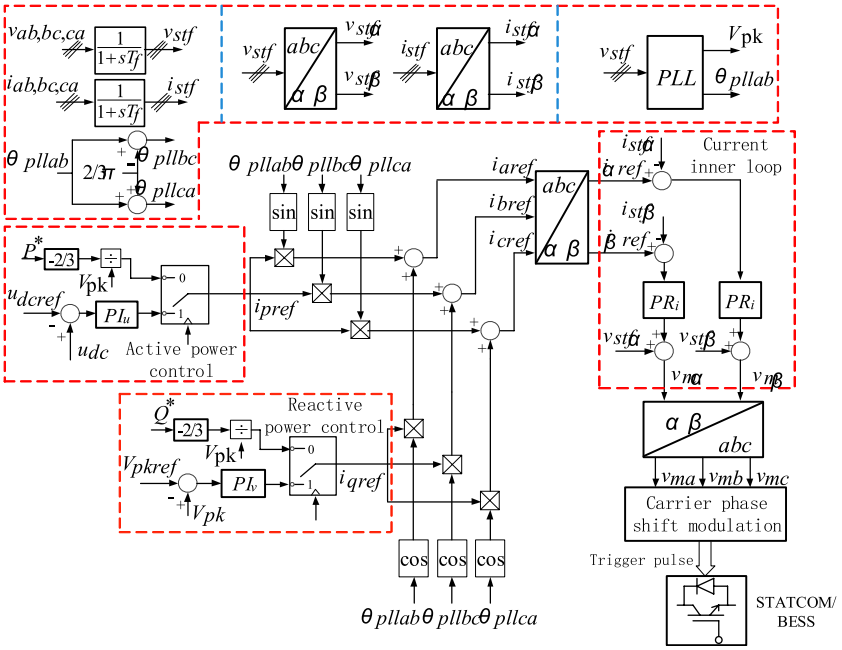

FIGURE 12 | Control structure of the three-module angle chain energy storage STATCOM.

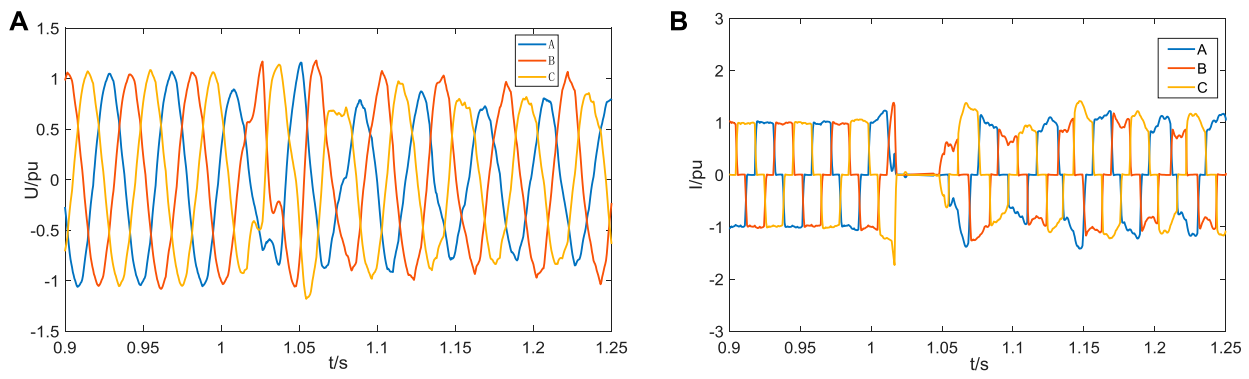

FIGURE 13 | Simulation waveform diagram after installing conventional STATCOM. **(A)** AC voltage on the inverter side; **(B)** inverter current of the converter valve.

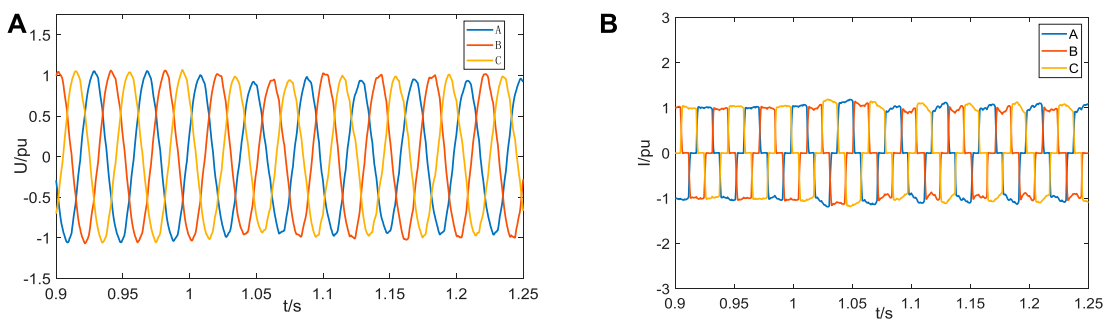

FIGURE 14 | Experimental waveform diagram of installing STATCOM/BESS. **(A)** AC voltage on the inverter side; **(B)** inverter current of the converter valve.

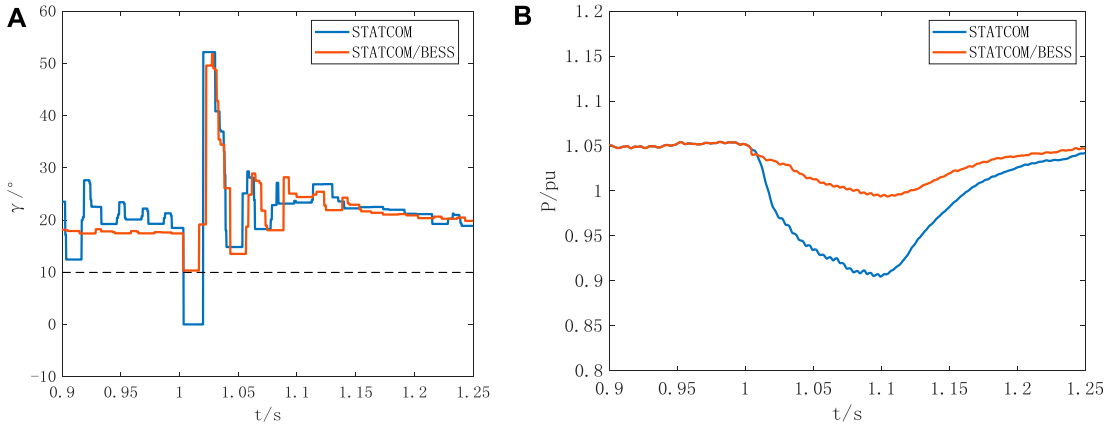

FIGURE 15 | Comparison diagram of the system transmission power and extinction angle. **(A)** Comparison diagram of extinction angle; and **(B)** Comparison diagram of transmission power.

$$\begin{cases} |I_{stp}| + |I_{stn}| \le I_m \\ \sqrt{I_{stp}^2 + I_{stn}^2 - I_{stp}I_{stn}} \le I_m \end{cases}. \tag{13}$$

In the formula, I_m is rated current of STATCOM/BESS and I_m = 0.1p.u. According to **Eq. 13**, the feasible region of reactive current can be obtained as shown in the yellow area in **Figure 10**.

Substituting the positive and negative sequence reactive current values in the feasible region into **Eqs 12**, **13** (Xun et al., 2017), it can be concluded that there is a larger positive gradient between the minimum value in the extinction angle of each converter valve and the positive sequence reactive current, that is, the positive sequence current compensated by STATCOM/BESS has a more obvious effect on increasing the extinction angle.

Therefore, after a single-phase grounding fault, (Shen et al., 2020a) in order to get better suppression effect of commutation failure, the compensation component of STATCOM/BESS positive sequence reactive current should be increased.

Simulation of Suppression Effect of Positive and Negative Sequence Reactive Power Compensation Components on Commutation Failure

In order to verify the theoretical analysis in Section 3.1, (Shen et al., 2020b) this section compares the effects of STATCOM/BESS on suppressing commutation failure under different positive and negative sequence reactive current compensation ratios based on the CIGRE HVDC standard test model. Starting from 1.0 s, the A-phase-inductive grounding fault is set at the inverter side converter bus at 1 ms intervals so as to simulate the single-phase fault at different closing angles of the receiving-end power grid in practical engineering. Yang et al. (2018) When STATCOM/BESS compensates the positive and negative sequence currents by 1:1, 2: 1, and 1:0, respectively, after detecting the fault (the sum of the positive and negative sequence output currents is 0.1pu), the critical inductance value of commutation failure of the inverter station is shown in **Table 2**. In **Table 2**, when the fault occurs at the same time, the green frame to the red frame sequentially indicate that the critical fault inductance gradually increases, that is, the commutation failure suppression effect gradually weakens. With the increase of the proportion of positive sequence reactive power commands, the number of green frames gradually increases, indicating that the commutation failure suppression effect is enhanced, (Zhu et al., 2020) which is consistent with the theoretical analysis in Section 3.1.

STATCOM/BESS SIMULATION EXPERIMENT

Figure 11 shows the LCC-HVDC standard model with STATCOM/BESS built in this article. The rectifier converter station and inverter converter station contain high and low valve sets, respectively. The rated DC voltage of the CIGRE HVDC model is ±500 kV, and the rated transmission capacity is 1000MW. Other main circuit parameters are shown in **Table 3**.

The control system adopts double-loop control, in which the inner loop is current control and the outer loop reactive power control can be selected as constant AC voltage control and constant reactive power control, and the active control part can be selected as active control or constant DC voltage control. The control block diagram is shown in **Figure 12**.

In order to compare the commutation failure suppression effect between STATCOM/BESS and conventional STATCOM, a serious single-phase grounding fault is set at 1s in this experiment. **Figure 13A** and **Figure 13B** show the AC voltage and inverter current at the inverter side of the HVDC system when a A-phase at the inverter side suddenly has a grounding fault after a period of normal operation. At this time, the system is equipped with conventional STATCOM. After the fault occurred, the A-phase voltage begin to drop, and the AC voltage on the inverter side is greatly distorted. The inverter current dropped to 0 at the

same time in the vicinity of 1s, indicating that commutation failure occurred.

When STATCOM/BESS is installed in the system, the grounding fault occurs in A-phase in 1s. It can be seen from **Figure 14A** and **Figure 14B** that the AC voltage distortion on the inverter side is relatively small, and the phenomenon that the three-phase current is zero at the same time during the fault period does not occur, which indicates that STATCOM/BESS has restrained the occurrence of commutation failure under the single-phase fault condition.

Comparing the extinction angle and system transmission power under the two conditions; it can be seen from **Figure 15A** that the extinction angle drops to 0 after the fault occurs when installing conventional STATCOM and never drops below 10 after installing STATCOM/BESS, which effectively inhibits the commutation failure at the inverter side. It can be seen from **Figure 15B** that STATCOM/BESS compensates active power and reactive power at the same time in case of failure. Compared with conventional STATCOM, the transmission power oscillation of the system is smaller, which can quickly stabilize the transmission of system power in case of failure.

CONCLUSION

The purpose of this article is to suppress commutation failure at the weak receiving end of the LCC-HVDC system and propose a compensation method for STATCOM/BESS to suppress commutation failure under the single-phase grounding fault. The design and comparison simulation verify the ability of STATCOM/BESS to suppress commutation failure and draw the following conclusions:

(1) Under the single-phase grounding condition of the AC system on the inverter side, the commutation failure conditions of each phase of the converter valve are different.
(2) Increasing the proportion of the positive sequence reactive power compensation component of STATCOM/BESS output under the single-phase grounding fault of the AC system on the inverter side can better restrain commutation failure.
(3) The STATCOM/BESS device is installed in the single-pole 12-pulse HVDC transmission system, and a single-phase ground fault was set, and a comparison experiment was carried out with the traditional STATCOM system; by comparing the four typical electrical quantities of AC voltage, inverter current, turn-off angle, and system transmission power, which verifies the effectiveness of the STATCOM/BESS designed in this article in suppressing commutation failure.

DATA AVAILABILITY STATEMENT

The original contributions presented in the study are included in the article/Supplementary Material, further inquiries can be directed to the corresponding author.

AUTHOR CONTRIBUTIONS

CX was responsible for providing ideas and methods and providing an experimental platform. SC was responsible for deriving formulas, reviewing, and verifying. JC was responsible for model building, simulation, data analysis, and manuscript writing. All authors participated in the reading and approved the submitted version.

FUNDING

The research is funded by the National Natural Science Foundation of China (52067009).

REFERENCES

Cai, W., Yang, G., Du, D., and Wang, X. (2019). Commutation Failure Prediction and Identification Method Considering Multiple Factors. *Power Syst. Technology.* 43 (10), 3477–3487. doi:10.13335/j.1000-3673.pst.2019.1098

Guo, C., Zhang, Y., and Zhao, C. (2013). Influence of STATCOM on the Operating Characteristics of Dual-Infeed DC Systems. *Proc. Chin. Soc. Electr. Eng.* 33 (25), 99–106. doi:10.13334/j.0258-8013.pcsee.2013.25.006

Guobing, S., Junjie, H., and Bing, G. (2020). Pilot protection of Hybrid MMC DC Gridbased on Active Detection. *Prot. Control. Mod. Power Syst.* V5 (1), 82–96. doi:10.13335/j.1000-3673.pst.2020.0200a

He, J., Chen, K., and Li, M. (2020). Review of protection and Fault Handling for a Flexible DC Grid. *Prot. Control. Mod. Power Syst.* 5 (1), 15. doi:10.1186/s41601-020-00157-9

Huang, Y. (2006). *Research on Commutation Failure of HVDC transmission[D].* Beijing: North China Electric Power University.

Le, S., Wu, Y., Guo, Y., and Vecchio, C. D. (2021). Game Theoretic Approach for a Service Function Chain Routing in NFV with Coupled Constraints. *IEEE Trans. Circuits Syst.* 68, 3557–3561. Published online. doi:10.1109/TCSII.2021.3070025

Lei, Z., Yumiao, X., and Jing, Y. (2021). Intelligent Frequency Control Strategy Based on Reinforcement Learning of Multi-Objective Collaborative Reward Function. *Front. Energ. Res. Early Access* 9. doi:10.3389/fenrg.2021.760525

Li, Z., Wang, J., Li, Y., Wang, Z., Huang, M., and Fu, C. (2017). Modeling of Switching Function of HVDC Converter Based on the Zero Crossing point of Actual Commutation Voltage. *Proc. Chin. Soc. Electr. Eng.* 37 (18), 5389–5398+5538. doi:10.13334/j.0258-8013.pcsee.161788

Liang, S. (2014). *Research on Static Synchronous Compensator with Battery Energy Storage device[D].* Harbin: Harbin Institute of Technology.

Mitsuru, T., and Yuhu, W. (2021). Mayer-Type Optimal Control of Probabilistic Boolean Control Network With Uncertain Selection Probabilities. *IEEE Trans. Cybernetics.* 51, 3079–3092. doi:10.1109/TCYB.2019.2954849

Mohan, M. (2021). A Comprehensive Review of DC Faultprotection Methods in HVDC Transmissionsystems. *Prot. Control. Mod. Power Syst.* V6 (1), 1–20.

Muniappan, S. (2021). *A Comprehensive Review of DC Fault protection Methods in HVDC Transmission Systems.* Singapore: Singapore Springer Pte Ltd.

Peng, L., He, J., and Xie, K. (2017). Comparison of Reliability and Economy of UHVAC and DC Transmission Systems. *Power Syst. Technology.* 41 (4), 1098–1107. doi:10.13335/j.1000-3673.pst.2016.2503

Shen, X., Ouyang, T., Khajorntraidet, C., Li, Y., Li, S., and Zhuang, J. (2022). Mixture Density Networks-Based Knock Simulator. *Ieee/asme Trans. Mechatron.* 27, 159–168. doi:10.1109/TMECH.2021.3059775

Shen, X., Ouyang, T., Yang, N., and Zhuang, J. (2021). Sample-based Neural Approximation Approach for Probabilistic Constrained Programs. *IEEE Trans. Neural Netw. Learn. Syst.*, 1–8. doi:10.1109/TNNLS.2021.3102323

Shen, X., and Raksincharoensak, P. (2021). Pedestrian-aware Statistical Risk Assessment. *IEEE Trans. Intell. Transport. Syst.*, 1–9. doi:10.1109/TITS.2021.3074522

Shen, X., Zhang, X., Ouyang, T., Li, Y., and Raksincharoensak, P. (2020a). Cooperative Comfortable-Driving at Signalized Intersections for Connected and Automated Vehicles. *IEEE Robot. Autom. Lett.* 5 (4), 6247–6254. doi:10.1109/LRA.2020.3014010

Shen, X., Zhang, Y., Sata, K., and Shen, T. (2020b). Gaussian Mixture Model Clustering-Based Knock Threshold Learning in Automotive Engines. *Ieee/asme Trans. Mechatron.* 25 (6), 2981–2991. doi:10.1109/TMECH.2020.3000732

Virtanen, A., Tuusa, H., and Aho, J. (2013). "Performance Analysis of Conventional STATCOMs and STATCOMs with Energy Storage in Electric Arc Fumace Applications," in 28th Annual IEEE Applied Power Electronics Conference and Exposition, Long Beach. USA, 1623–1629.

Xun, S., and Pongsathorn, R. (2021). Statistical Models of Near-Accident Event and Pedestrian Behavior at Non-signalized Intersections. *J. Appl. Stat.* doi:10.1080/02664763.2021.1962263

Xun, S., Yahui, Z., Tielong, S., and Chanyut, K. (2017). Spark advance Self-Optimization with Knock Probability Threshold for Lean-Burn Operation Mode of SI Engine. *Energy.* 122, 1–10. doi:10.1016/j.energy.2017.01.065

Yang, N., Huang, Y., and Hou, D. (2019). Adaptive Nonparametric Kernel Density Estimation Approach for Joint Probability Density Function Modeling of Multiple Wind Farms. *Energies* 12, 1356. doi:10.3390/en12071356

Yang, N., Ye, D., Zhou, Z., Cui, J., Chen, D., and Wang, X. (2018). Research on Modelling and Solution of Stochastic SCUC under AC Power Flow Constraints. *IET Generation, Transm. Distribution.* 12 (15), 3618–3625. doi:10.1049/iet-gtd.2017.1845

Yang, N. (2021). A Comprehensive Review of Security-Constrained Unit Commitment. *J. Mod. Power Syst. Clean Energ.* doi:10.35833/MPCE.2021.000255

Yang, N., Liu, S., Deng, Y., and Xing, C. (2021a). An Improved Robust SCUC Approach Considering Multiple Uncertainty and Correlation. *IEEJ Trans. Elec Electron. Eng.* 16, 21–34. doi:10.1002/tee.23265

Yang, N., Yang, C., Xing, C., Ye, D., Jia, J., Chen, D., et al. (2021b). Deep Learning-based SCUC Decision-making: An Intelligent Data-driven Approach with Self-learning Capabilities. *IET Generation Trans. Dist* 16, 629–640. doi:10.1049/gtd2.12315

Yang, N., Yang, C., Wu, L., Shen, X., Jia, J., Li, Z., et al. (2022). Intelligent Data-Driven Decision-Making Method for Dynamic Multisequence: An E-Seq2Seq-Based SCUC Expert System. *IEEE Trans. Ind. Inf.* 18, 3126–3137. doi:10.1109/TII.2021.3107406

Yu, X., Wang, Y., Zhang, Q., Wang, Y., Dong, Y., and Gan, Z. (2020). Power Transfer Strategy of Parallel Three-Terminal Hybrid UHVDC Transmission System. *Automation Electric Power Syst.* 44 (23), 150–156. doi:10.7500/AEPS20200601004

Yuhu, W., Yuqian, G., and Toyoda, M. (2021). Policy Iteration Approach to the Infinite Horizon Average Optimal Control of Probabilistic Boolean Networks. *IEEE Trans. Neural Networks Learn. Syst.* 32 (6), 2910–2924.

Zhang, Y. (2011). *Investigation of Reactive Power Control and Compensation for HVDC system[D]*. Winnipeg: The University of Manitoba.

Zhao, T., Lu, M., and Lou, J. (2015). Research on Abnormal Commutation Failure of Multi-Feed HVDC Transmission System. *Power Syst. Technology.* 39 (3), 705–711. doi:10.13335/j.1000-3673.pst.2015.03.018

Zhenhua, L., Weihui, J., and Abu-Siada, A. (2021). Research on a Composite Voltage and Current Measurement Device for HVDC Networks. *IEEE Trans. Ind. Electronics* 69 (9), 8930–8941. doi:10.1109/TIE.2020.3013772

Zhu, B., Ding, F., and Vilathgamuwa, D. M. (2020). Coat Circuits for DC-DC Converters to Improve Voltage Conversion Ratio. *IEEE Trans. Power Electron.* 35 (4), 3679–3687. doi:10.1109/TPEL.2019.2934726

Zhu, J. (2008). *Cause Analysis and Simulation Research on Commutation Failure of HVDC Transmission[D]*. North China Electric Power University Hebei.

Conflict of Interest: Authors CX, JC, ZX, XX, and XH were employed by the Electric Power Research Institute of Yunnan Power Grid Co., Ltd.

The remaining author declares that the research was conducted in the absence of any commercial or financial relationships that could be construed as a potential conflict of interest.

frontiers in Energy Research

ORIGINAL RESEARCH
published: 24 March 2022
doi: 10.3389/fenrg.2021.812367

Numerical Simulation of Galloping Characteristics of Multi-Span Iced Eight-Bundle Conductors

Ding Shunli[1†], *Cai Mengqi*[2,3*†], *Tian Bowen*[1†], *Liang Junhao*[1†], *Zhou Linshu*[4†], *Wu Chuan*[5†], *Huang Hanjie*[6†] *and Liu Jun*[7†]

[1]School of Mechanical Engineering, Chengdu University, Chengdu, China, [2]School of Architecture and Civil Engineering, Chengdu University, Chengdu, China, [3]Failure Mechanics and Engineering Disaster Prevention Key Laboratory of Sichuan Province, Sichuan University, Chengdu, China, [4]State Grid Sichuan Integrated Energy Service Co., Ltd., Chengdu, China, [5]Henan Electric Power Research Institute, Zhengzhou, China, [6]China Aerodynamics Research and Development Center, Mianyang, China, [7]School of Mechanical and Electrical Engineering, Southwest Petroleum University, Chengdu, China

In this article, the numerical model of the multi-span iced eight-bundle conductor is established using the nonlinear finite element method, the galloping of the line under different parameters is simulated, and the tension in the galloping process is analyzed. Based on the aerodynamic characteristics and galloping characteristics of conductors, the galloping modes, frequency characteristics, vibration amplitudes, and galloping orbits of multi-span lines under different wind velocities, span lengths, ice shape, and number of spans are analyzed, compared with those of single-span lines. It is demonstrated that there are differences in galloping characteristics between multi-span transmission lines and single-span lines. Each span of the transmission line is different, so it should be fully considered in the research of galloping prevention and control technology.

Keywords: iced eight-bundle conductors, multi-span transmission line, galloping characteristic, numerical simulation, conductor tension

OPEN ACCESS

Edited by:
Yusen He,
Grinnell College, United States

Reviewed by:
Yang Zhao,
Chongqing University of Posts and Telecommunications, China
Jiahao Deng,
DePaul University, United States
Jirong Yi,
Hologic, Inc., United States

****Correspondence:***
Cai Mengqi
mq.cai@foxmail.com

†These authors have contributed equally to this work

Specialty section:
This article was submitted to Wind Energy, a section of the journal Frontiers in Energy Research

Received: *10 November 2021*
Accepted: *06 December 2021*
Published: *24 March 2022*

Citation:
Shunli D, Mengqi C, Bowen T, Junhao L, Linshu Z, Chuan W, Hanjie H and Jun L (2022) Numerical Simulation of Galloping Characteristics of Multi-Span Iced Eight-Bundle Conductors. Front. Energy Res. 9:812367. doi: 10.3389/fenrg.2021.812367

INTRODUCTION

Aiming at solving the problem of unbalanced power supply and demand, the 1,000 kV ultra-high voltage (UHV) bundle conductor transmission line has been launched (Jafari et al., 2020; Cai et al., 2019a). The so-called galloping refers to the phenomenon of self-excited vibration of low frequency and large amplitude generated by the wind load when the conductor forms an asymmetric circular section after freezing in winter (Li et al., 2021a; Min et al., 2021). Conductor galloping usually occurs for an extended period. Therefore, it is harmful for the operation of the power transmission system, and it is liable to cause major accidents such as alternating flashover, power failure, failure of conductors or even conductor disconnection, metal damage, and tower toppling (Liu et al., 2021a). In recent years, serious cases of iced transmission tower lines collapsing under wind load have been reported in Hunan and Anhui provinces, China (Liu et al., 2019). Therefore, anti-galloping is a hot issue in the field of electrical and civil engineering.

In recent years, many experts have studied the problem of galloping transmission lines. Yan et al. (2016) proposed the numerical method to investigate the galloping characteristics of iced-quad bundle conductors. Cai et al. (2015) studied the variation of aerodynamic coefficients varying with angle of wind attack by the finite element method (FEM). The effectiveness of the aerodynamic coefficients determined by numerical simulation in the study of galloping characteristics and anti-galloping technology of overhead transmission lines is verified. By using ABAQUS software, Hu et al.

(2012) defined a new unit by the pneumatic loading unit for ice conductors, the being studied by the numerical method under different wind velocities and line structure parameters of quad-bundle conductor ice galloping. Lu et al. (2019) simulated the galloping of the iced quad-bundle conductor according to the wind tunnel test results. They concluded the impact of wind velocity, ice thickness, conductor type, bundle spacing, and bundle number on the aerodynamic parameters and conductor galloping. Matsumiya et al. (2018) conducted aeroelastic tests in a wind tunnel by using a rigid-body section model of quad-bundle conductors. Liu et al. (2020a) and Liu X. H. et al. (2021) obtained the aerodynamic coefficients of the conductor through a wind tunnel test and studied the stability and galloping characteristics of the iced quad-bundle conductor. Cai et al. (2019b) used nonlinear FEM to analyze the galloping of the sector-shape iced eight-bundle conductor under different wind velocities, span length, and angles of wind attack. Zhou et al. (2018) studied the effects of interphase spacer on the galloping of the iced eight-bundle conductor. Zhou et al. (2016) conducted wind tunnel tests to simulate the galloping of iced eight-bundle conductor segment and studied the galloping behaviors under different parameters. Cai et al. (2020) numerically simulated the galloping behaviors of a D-shape iced six-bundle conductor in the test line under a random wind field. Lou et al. (2021) studied the effects of ice shape and roughness on iced conductors galloping. Liu et al. (2009) studied the nonlinear numerical simulation method of galloping of iced conductors, proved the effectiveness of this method, and found a new possible galloping mode. Liu et al. (2020) compared and analyzed the stability of the iced conductor under the action of uniform and turbulent wind. Kim and Sohn. (2018) simulated the galloping of elliptical and triangular iced sections through wind tunnel tests. Talib et al. (2019) proposed a new dynamic model for the simulation of power-transmission-line galloping. Due to the continual presence of the galloping phenomenon and the great harm which could cause, Oh and Sohn. (2020) analyzed conductor galloping through the study of stability of transmission line. Furthermore, because of the complex aerodynamic characteristics of the eight-bundle conductor and the high cost of the tests required to simulate the galloping, there is no research on the multi-span eight-bundle conductor in the available literature.

In this article, the galloping law of a 1000 kV multi-span iced eight-bundle conductor and the characteristics of the galloping are analyzed. The difference between a multi-span iced eight-bundle conductor and a single-span iced eight-bundle conductor is compared. The research results provide the important basis for the research of transmission line anti-galloping technology.

TYPICAL LINE SECTION AND FINITE ELEMENT MODEL

Wind-driven wet snow may pack onto the windward sides of conductors, forming a hard, tenacious deposit with a fairly sharp leading edge. The resulting ice shape may permit galloping. Combined with actual observation, a crescent shape can be generalized with respect to the great variety of the natural heavy ice shape (Hu et al., 2012; Yan et al., 2016). The aerodynamic forces of bundle conductors are the foundations of the analysis of the galloping of transmission lines (Liu et al., 2009). Herein, the aerodynamic coefficients of crescent-shape iced eight-bundle conductors are experimentally measured by wind tunnel tests.

The three-span and five-span iced eight-bundle lines are the main research objects. The two lines with the span length of 200 and 400 m and the sub-spans of each span are the same. The conductor model is 8 × LGJ-400/50, and the diameter of the sub-conductor is 30 mm. The model of the spacer is FJZ-400, each with a mass of 8.5 kg. The length of the suspension insulator string is set to be 3 m. Assuming that the conductor ice is a 12 mm crescent-shape ice, the initial angle of wind attack is 60°.

The physical parameters of conductors and ice are listed in **Supplementary Table S1**. The cross section of the iced conductor is simplified as a circular section when the galloping of the iced conductor is simulated by ABAQUS software. It is noted that the axial rigidity, torsional rigidity, mass per unit length, moment of inertia of the equivalent cable and those of the original cable should be equal, which can be expressed as follows:

$$\begin{aligned} E'\pi d'^2/4 &= EA; \quad G'\pi d'^2/32 = GI \\ \rho'\pi d'^2/4 &= \mu; \quad \rho'\pi d'^4/32 = J \end{aligned} \tag{1}$$

where E', G', ρ', and d' are, respectively, the elastic modulus, the shear modulus, the density, and the diameter of the equivalent cable, which can be obtained by solving **Eq. 1** whose right hands are the corresponding quantities of the original iced conductor. The physical parameters of the conductors and ice are listed in **Supplementary Table S1**.

In the FEM model, according to the previous research results (Hu et al., 2012), the accuracy requirement can be met when the length of the conductor element is about 0.5 m, and the conductor is selected as the cable element, which is obtained by releasing the bending degrees of freedom of the nodes of the spatial Euler beam element (Yan et al., 2016). The spacer can be simplified into a regular octagonal frame, simulated by spatial beam elements, and the suspension insulator string is also simulated by beam elements.

The upper end of the suspension insulator string in the model is suspended on the tower, and the lower end of the suspension insulator string is connected only to the sub-conductor. The influence of the tower on the suspension insulator string is ignored. Meanwhile, the constraints of three rotational degrees of freedom and sets of three planes are released by the upper end of the suspension insulator string. A fixed constraint with six degrees of freedom is set at both ends of the conductor. The established FEM model of the three-span and five-span iced eight-bundle conductor of 200 m span lines is shown in **Supplementary Figure S1**. For the convenience of comparison and analysis, the galloping characteristics of single-span lines are also simulated and analyzed.

The influence of the initial axial tension in the main and side cables on the element stiffness matrix cannot be ignored. In

addition, the cable sags due to its own weight, resulting in a certain decrease or loss of its elastic modulus. In order to consider the influence of cable sag, the concept of equivalent elastic modulus is used to modify the elastic modulus of cable. The equivalent modulus of elasticity generally adopts the E_{Ernst} formula:

$$E_{\mathrm{Ernst}} = \frac{E}{1 + \frac{(ql)^2}{12T^3}AE} \tag{2}$$

where E_{Ernst} is the equivalent elastic modulus of the material; E is the elastic modulus of the material; q is the weight of the unit length of the cable; l is the projection length of the cable element in the horizontal direction; A is the cross-sectional area of the cable, and T is cable tension.

The numerical simulations were carried out on a personal computer Dell Studio Desktop D540, and each job took about 5 hours to arrive at a steady result. To speed up the efficiency, several jobs were submitted simultaneously. The dynamic implicit analysis is used in the numerical method. The dynamic responses of the transmission line with different damping ratios in different directions are analyzed by ABAQUS with the user-defined cable element. The damping ratios ξ_{z1}, ξ_{y1}, and $\xi_{\theta 1}$, in horizontal, vertical, and torsional directions, are set to 0, 0.5, and 2%, respectively, determined and verified by Zhou et al. (2018). Considering the efficiency of the numerical simulation, the time step is set to 0.01.

ANALYSIS OF DYNAMIC CHARACTERISTICS OF ICED CONDUCTORS

For the sake of understanding the galloping characteristics of the iced conductor, the ABAQUS software is used to calculate the dynamic characteristics of each line. The vibration directions are the frequencies corresponding to the low-order modes in the vertical, horizontal, and torsional directions. The typical low-order modes of the three-span iced eight-bundle conductor with a span length of 200 m are shown in **Supplementary Figure S2**. The low-order natural frequency values summarized by the modes and corresponding frequencies are listed in **Supplementary Tables S2, S3**. From **Supplementary Figure S2**, it can be found that the multi-span line has the phenomenon of double frequency, and the wave number of conductors increases with the increasing of frequency.

The galloping characteristics depend on the mode and natural frequency of the transmission line, which can be obtained from the results in **Supplementary Tables S2, S3**. Compared with the single-span line, the natural frequency of the multi-span line is lower, which is less than or equal to the natural frequency of the single-span line, and the phenomenon of repeated frequency appears. In addition, the low-order natural frequencies of the third span and the fifth span multi-span line are very close. In addition, it can be found from **Supplementary Table S3** that the vertical galloping of the 400 m single-span line starts directly from the double half-wave, which is related to the structure of the conductor. Based on the results of the dynamic characteristics of multi-span line, combined with spectrum response analysis, the galloping mode of the multi-span lines can be judged.

ANALYSIS OF GALLOPING CHARACTERISTICS OF MULTI-SPAN ICED CONDUCTORS

This section studies the characteristic analysis of multi-span iced conductors-galloping. Firstly, a theoretical analysis of the galloping of the line is carried out. Because the iced conductors are mostly of irregular shapes, not only resistance but also lift and moment are generated by the wind load. The force F_D, lift F_L, and moment M acting on a unit length of the non-circular cross section iced conductor can be determined by the following formula (Cai et al., 2020b):

$$F_D = \frac{1}{2}C_D(\alpha)\rho U^2 d;\ F_L = \frac{1}{2}C_L(\alpha)\rho U^2 d;\ M = \frac{1}{2}C_M(\alpha)\rho U^2 d^2 \tag{3}$$

where ρ is the air density, U is the wind velocity, and d is the diameter of the conductor. $C_D(\alpha)$ is the drag coefficient, $C_L(\alpha)$ is lift coefficient, and $C_M(\alpha)$ is moment coefficient of the iced conductor, which are related to the angle of wind attack α. The change of angle of wind attack during the movement of the iced conductor can be determined by the following formula:

$$\alpha \approx \theta - \left(\frac{R\dot{\theta} + \dot{V}}{U}\right) \tag{4}$$

where θ, R, $\dot{\theta}$, and $\dot{V}$ are, respectively, the torsion angle, characteristic radius, torsion angular velocity, and vertical velocity of the iced conductor. In the numerical simulation of this article, the aerodynamic coefficients of each sub-conductor of the iced eight-bundle conductor measured by the wind tunnel test varies with the angle of wind attack.

Galloping Characteristics of the Conductor

The wind velocity of 8 m/s, the thickness of crescent-shaped ice is 12 mm, the initial angle of wind attack is 60°, and each span length is 200 m. The corresponding numerical simulation of the galloping process of the three-span iced eight-bundle conductor is carried out. The motion state of the three-span multi-span iced eight-bundle conductor at different times is shown in **Supplementary Figure S3**. According to **Supplementary Figure S3**, the three-span iced eight-bundle conductor with a span of 200 m has a single-half-wave galloping model for each sub-span, and galloping occurs in each sub-span.

The displacement time and galloping trace of the midpoint of sub-conductor 1 in each span are shown in **Supplementary Figures S4, S5**. The galloping amplitude is listed in **Supplementary Table S4**. It can be seen from **Supplementary Figure S4** that the galloping displacement of each span is different and slight fluctuations. Referring to **Supplementary Figure S5**, the traces of the midpoints of each span are close

to an elliptical limit cycle. In the 200 m multi-span line, the vibration of the conductors of each span under the wind velocity of 8 m/s is all vertical galloping. It can be seen intuitively from **Supplementary Table S4** that there are also significant differences in the galloping amplitudes of the conductors in each span in the 200 m span multi-span line. The third span of vertical displacement is the largest, but the middle span of the torsional angle is the largest (Hung et al., 2014).

Galloping Mode and Frequency Characteristics

The galloping mode and frequency characteristics of the conductor in the galloping process are important parameters for the research of galloping prevention and control technology. Through the displacement response spectrum of the conductor, combined with the mode and natural frequency of the line (**Supplementary Tables S2, S3**), the vibration mode and frequency characteristics of galloping are analyzed. The displacement spectrum analysis is carried out according to the displacement time history response of **Supplementary Figure S4**, and the data results are shown in **Supplementary Figure S6**. It can be seen that the spectra of vertical displacement, horizontal displacement, and torsional angle of each conductor all have peaks at the first-order natural frequency of 0.286 Hz, in which the vibration frequency of torsion angle has four peaks, which are close to 0.286, 0.411, 0.697, 0.858 Hz, which correspond to the low-order natural frequencies of (**Supplementary Table S2**) the 200 m multi-span and single-span iced eight-bundle conductors.

THE INFLUENCE OF DIFFERENT PARAMETERS ON THE GALLOPING OF MULTI-SPAN ICED CONDUCTOR

Effect of Span on Galloping

In this section, the effect of galloping of the iced eight-bundle conductor under different span lengths is studied. The span condition of conductors in *Galloping Characteristics of the Conductor* is changed to 400 m. The remaining parameters are in accordance with those of the previous conductors. The galloping of the three-span iced eight-bundle conductor is numerically simulated. The galloping shape of an iced eight-bundle conductor of three-span at different times with a span length of 400 m is shown in **Supplementary Figure S7**. Compared with the motion state of Section 4.1 200 m three-span iced eight-bundle conductor, the conductor galloping mode has changed, and the whole span galloping and sub-span vibration have taken place on the line. The three-span iced eight-bundle galloping with a span of 400 m has a double half-wave, which is no longer a single half-wave galloping mode**.**

The time history of midpoint displacement of each sub-conductor 1 is shown in **Supplementary Figure S8**, and the galloping amplitude is listed in **Supplementary Table S5**. As can be seen from **Supplementary Figure S8**, the horizontal displacement of the midpoint of each sub-conductor 1 remains basically unchanged, and the vertical displacement of the middle span is larger than that of both sides, indicating that the galloping of the middle span is more intense. Compared with **Supplementary Figure S4**, the galloping of the conductor with span length of 400 m is not as stable as that of 200 m. As can be seen from the results in **Supplementary Table S5**, the vertical amplitude, horizontal amplitude, and torsional angle are all large in the middle span, and the galloping amplitudes of the first span and the third span are similar.

It shows the mid-point displacement spectrum of the wind velocity of 8 m/s span 400 m three-span iced eight-bundle conductor 1 in **Supplementary Figure S9**. Combined with the results of **Supplementary Table S3** and **Supplementary Figure S9**, it can be found that the in-plane vibration frequency and out-of-plane vibration frequency of each span have a peak near the natural frequency 0.153 Hz of one half-wave, it is indicated that the vibration mode is one half-wave. The torsional vibration frequency of each span has the maximum peak near the natural frequency 0.269 Hz of the single half-wave; that is, the vibration mode is dominated by the one half-wave. Moreover, there is also a small peak value in the plane of the two spans, which is close to the natural frequency of 0.285 Hz, and its corresponding mode is double half-wave. According to the motion form of conductor galloping, the galloping mode on both sides of the three 400 m multi-span transmission line is mainly double half-wave, and there is an obvious single half-wave, while the middle span is mainly one half-wave. It is galloping mode has changed compared with the 200 m three-span line, which indicates that the larger the span, the more complex the conductor galloping mode. As can be seen from **Supplementary Figure S9C**, the horizontal angle spectrum is more complex, and the galloping will excite multiple frequencies.

Effect of Wind Velocity on Galloping

Wind excitation is the direct cause of conductor galloping, which will cause galloping under the stable action of wind velocity of 4 m/s~20 m/s. In this section, the influence of wind velocity on galloping is studied, and the galloping response of the 200 m three-span iced eight-bundle conductor at wind velocity 12 m/s is simulated and compared with the galloping response at 8 m/s wind velocity given in *Galloping Characteristics of the Conductor*.

The galloping pattern of the three-span iced eight-bundle conductor with a wind velocity of 12 m/s and a span of 200 m at different times is given in **Supplementary Figure S10**. Compared with **Supplementary Figure S3** in *Galloping Characteristics of the Conductor*, the galloping mode of the conductor has changed. The galloping mode on both sides of the 200 m multi-span changes from a single half-wave to one half-wave or double half-wave, while the middle span is still one half-wave.

Supplementary Figure S11 shows the time history of midpoint displacement of each sub-conductor of the three-span iced eight-bundle conductor with span length of 200 m in 12 m/s. Compared to the lower wind velocity length of 8 m/s, it is obvious that the galloping is unstable, and there are wave in the upper and lower limits of vertical amplitude, horizontal amplitude, and torsion angle of each span, which demonstrates that the galloping of the conductor is more

unstable with the increasing of wind velocity. In addition, it can be seen that the greater the wind velocity, the greater the vertical amplitude, horizontal amplitude, and torsion angle of the conductor, which shows that the effect of wind velocity on galloping is very significant and intense.

The spectrum at the midpoint displacement of each span at 12 m/s wind velocity is illustrated in **Supplementary Figure S12**. The peak value of the displacement spectrum of each span appears near 0.358 Hz, and there are multiple peaks. According to the results of **Supplementary Table S2**, the wind velocity is changed, and the galloping is still dominated by a single half-wave. However, the increasing of wind velocity will increase the galloping amplitude and make the circuit more unstable.

Effect of Initial Angle of Wind Attack on Galloping

Wind excitation is another necessary condition for transmission line galloping. Different wind velocities will affect the aerodynamic state, thus affecting the conductor galloping. Meanwhile, the size and shape of the galloping of a section of the line are also determined by the angle between the wind and the conductor axis, that is, the initial angle of wind attack. The galloping amplitudes of a 200 m three-span iced eight-bundle conductor under several typical angles of wind attack are depicted in **Supplementary Table S6**. It can be seen from the table that, with the increasing of angle of wind attack, the greater the galloping amplitude, the greater the vertical displacement, horizontal displacement, and torsional angle. When the included angle is 0°, that is, when the wind direction is parallel to the axis of the conductor, the possibility of galloping is the least, and there is basically no vibration. When the initial angle of wind attack is 90°, the lift coefficient of the conductor decreases and tends to 0, so it is difficult to cause galloping. The difference between the amplitudes of 30°and 60°is obvious. Therefore, the initial angle of wind attack has a great influence on the galloping of the conductor. Referring to the aerodynamic curve of an iced eight-bundle conductor obtained in reference (Hartog, 1932; Nigol et al., 1977), it is known that galloping may occur in the range of 60° using Den Hartog theory.

Effect of the Number of Spans on Galloping

This section studies the effect of the number of spans on galloping, simulates the galloping of the five-span iced eight-bundle conductor with 200 m at the wind velocity of 8 m/s, and compares it with the galloping of the three-span iced conductor with the span length of 200 m in *Galloping Characteristics of the Conductor*.

Supplementary Figure S13 shows the galloping pattern of the five-span iced eight-bundle conductor under wind velocity of 8 m/s at different times. Compared with the results of the three consecutive spans in *Galloping Characteristics of the Conductor*, the galloping pattern of the conductor is the same, and each span is a single half-wave.

Supplementary Figure S14 shows the time history of the mid-point displacement of each sub-conductor 1 of the five-span iced eight-bundle conductor with a wind velocity of 8 m/s and a span of 200 m, and the displacement spectrum of the middle point of each sub-conductor 1 is shown in **Supplementary Figure S15**. From this, we can know that the vibration amplitude of the five-span transmission line is slightly smaller than that of the third span transmission line. Compared with the displacement time history of the third span, it can be seen clearly that the vibration amplitude of the fifth span is more unstable, the upper and lower limits are unstable, and there are slight fluctuations. Meanwhile, the vertical displacement of the middle span is larger than that of the two sides. It can be seen clearly from the displacement spectrum that the vertical displacement of each span has many peaks, which are concentrated near 0.286 Hz. Compared with the third span, the fifth span is still dominated by a one half-wave, but the galloping is more chaotic.

Supplementary Figure S16 shows the galloping trace of the midpoint of each sub-conductor 1. It can be seen that the motion trace is still close to the oval limit cycle, and the ellipse trace on both sides is fuller, indicating that the horizontal galloping on both sides is larger, and the galloping trace in the middle span is slender, indicating that the galloping in the middle span is more complex. The vertical displacement of the middle span is also larger.

Effect of Ice Shape on Galloping

Different ice types will cause aerodynamic differences. When the temperature is low (−8°C ~ −11°C) and the rainfall is low (Liu et al., 2020b), the typical crescent-shape ice is easy to form because the small water droplets coagulate upon contact with the conductor surface. When the temperature is high and the rainfall is high, the water droplets cannot reach the contact point when they reach the surface of the conductor. In this case, if the wind velocity is low, it is easy to form typical sector-shape ice.

In order to investigate the galloping of iced eight-bundle conductors under different ice shapes, the wind velocity is 8 m/s, the sector-shape ice thickness is 18 mm, the initial angle of attack of ice is 140° (Cai et al., 2020b), the 200 m three-span conductor is discussed, and the galloping characteristics are numerically simulated. The galloping state of a 200 m three-span iced eight-bundle conductor at different times is shown in **Supplementary Figure S17**. Compared with the motion state of a 200 m three-span crescent-shape ice eight-bundle conductor in *Galloping Characteristics of the Conductor*, the galloping mode of the conductor is mainly single half-wave, and there are double half-waves. There are galloping among each span of sub-conductors, and the galloping form is also different, which demonstrates that the sector-shape ice galloping under the same conditions is more disordered.

The time history of displacement and the response spectrum of the midpoint of each span of sub-conductor 1 are shown in **Supplementary Figures S18, S19**. Compared with the crescent crescent-shape, the galloping tends to be stable. However, the upper and lower limits of the vertical amplitude, horizontal amplitude, and torsional angle of each span fluctuate slightly, which is not as regular as the galloping amplitude of the crescent-shape shape. Compared with the crescent-shape ice eight-bundle conductors, it can be found that the vertical amplitude, horizontal

amplitude, and torsional angle of the sector-shape ice conductor are larger than those of crescent-shape ice, and the torsional angle changes violently. It can also be seen from the spectrum that the frequency of torsional angle excites multiple peaks, which shows that sector-shape ice is more prone to galloping than crescent-shape ice, and the destructive force of galloping is stronger.

The galloping trace of the midpoint of each span sub-conductor 1 is presented in **Supplementary Figure S20**. It can be seen that the galloping trace is still close to the elliptical limit cycle. The change of the three-span galloping trace is the same as that of the crescent-shape, but it can be clearly compared that the sector-shape trace is rougher, and there is no smoothness of the crescent-shape, which also shows that the sector-shape ice galloping is more intense and irregular. In addition, the difference in galloping amplitude between sub-conductors of each span is small, which is due to the whole span oscillation of the line due to the reinforcement of spacers during conductor galloping.

The existing research on iced conductor galloping shows that the wind velocity has an obvious influence on conductor galloping. In this section, the FEM is used to compare the influence of wind velocity on the galloping of the sector-shape ice eight-bundle conductor. **Supplementary Table S7** compares in detail the galloping amplitude at the midpoint of the span line under the different wind velocities (4 m/s and 8 m/s) of the sector-shape ice eight-bundle conductor with angle of wind attack 140° under the 200 m span (Cai et al., 2020a). It can be seen from the table that, with the increasing of wind velocity, the galloping mode of the conductor changes significantly, and the vertical amplitude and horizontal vibration amplitude increase gradually. This is consistent with the conclusion of crescent-shape under the influence of wind velocity. The greater the wind velocity, the greater the galloping amplitude and the more complex the galloping mode.

ANALYSIS OF CONDUCTOR TENSION

Tension Change in the Process of Conductor Galloping

Conductor galloping seriously threatens the safe and stable operation of transmission lines. The main threats of galloping to the transmission lines are mechanical damage and electrical faults of the line, which are closely related to the mechanical strength and electrical performance of the line itself (Zhang et al., 2000). In terms of mechanical strength, the additional tension caused by galloping on the conductor must be tested. Therefore, the study of dynamic tension important to include in the study of galloping.

The tension analysis of the two terminals of the three-span iced eight-bundle conductor under the 8 m/s wind velocity is shown in **Supplementary Table S8**. Because the position of each sub-conductor has a certain offset, there is a slight difference in the tension of the eight sub-conductors. Meanwhile, the tension of each conductor at the left and right ends is not the same but also has a certain deviation. The longitudinal comparison shows little difference in the average value of the eight sub-conductors between the left and right ends, indicating that the tension between the two ends is balanced. **Supplementary Figure S21** shows the tension analysis of each sub-conductor at the left end in different periods. It can also be seen from the figure that the tension of the eight sub-conductors in different periods is very similar, with slight changes, but the overall difference is small. This shows that the damage of line galloping to the tower comes from long-term fatigue damage.

Adaptability Analysis of Simplified Formula for Galloping Amplitude Traverse

This section contains a comparative analysis and analyzes the existing theoretical simplification and formula correction for calculating the galloping amplitude of conductors based on the results of numerical simulation (Liu et al., 2021c). The comparison between the calculated values of the vertical amplitude of the improved formula and the results of numerical simulation are illustrated in **Supplementary Table S9**.

Based on the energy balance method, Hunt and Richards gave a simplified formula for calculating the amplitude (peak-peak) of conductor galloping (Hunt and Richards, 1969):

$$A_{max} = \frac{0.26V}{f} \tag{5}$$

where V is the wind velocity and f is the natural frequency of the conductor.

Equation 5 shows that the galloping amplitude of the conductor is directly proportional to the wind velocity. However, it is inversely proportional to the natural frequency of the conductor. The natural frequency of the conductor decreases with the increasing of the number and length of the span, so the result shows that, in **Supplementary Table S8**, the vertical amplitude of the conductor with the span length of 400 m is larger than that of the conductor with the span length of 200 m. The modified formula of reference is defined as (Zhao, 2014)

$$A_{max} = \frac{0.18V}{f} + 0.34 \tag{6}$$

As can be seen from the table below (**Supplementary Table S9**), the modified formula greatly improves the calculated value of the vertical amplitude of the conductor galloping (Rossi et al., 2020). However, from the relative error, it can be seen that there is still a big gap between the amplitude calculated by the individually modified formula and the numerical simulation. As the galloping of transmission lines is very complex and there are many factors affecting galloping (Liu et al., 2021d; Liu et al., 2021e), it is very difficult to obtain a formula to accurately calculate the vertical amplitude of galloping in order to be consistent with the actual numerical simulation (Li et al., 2021b).

CONCLUSION

In this article, the galloping process of the conductor is simulated and analyzed under different span lengths, span numbers, wind

velocities, and initial angle of wind attacks using FEM. Finally, the tension at both ends of the conductor is numerically simulated. Based on the dynamic analysis and dynamic response results of the line, the galloping mode, frequency characteristic, vibration amplitude, galloping trace, and tension analysis of the line are studied, and the following conclusions are obtained. Those conclusions are as follows:

1) Compared with single-span transmission lines, the natural frequency of multi-span transmission lines is lower, and the number of span has less effects on the natural frequency. The initial angle of wind attack has a significant influence on the conductor galloping, and the large amplitude galloping is most likely to occur under the angle of wind attack of 60°.
2) As span length increasing the galloping half-wave number of the multi-span line increases, the galloping becomes more complex. The galloping mode of the two sides of the multi-span line changes, with the wind velocity increasing, in which the galloping amplitude also increases.
3) With the increasing of the number of spans, the difference of the galloping mode between each span decreases, the vertical displacement has multiple peaks, and the galloping is more disordered. The vertical vibration amplitude of the middle span of the multi-span transmission line is larger than that of the two sides, and the horizontal displacement and torsion angle of each span has little difference.
4) Under the same conditions, sector-shape ice conductors are more prone to galloping than crescent-shape ice conductors. Because the tension at both ends of the conductor is similar, the galloping modes on both sides of the multi-span line are similar.

DATA AVAILABILITY STATEMENT

The original contributions presented in the study are included in the article/**Supplementary Material**. Further inquiries can be directed to the corresponding author.

AUTHOR CONTRIBUTIONS

All authors listed have made a substantial, direct, and intellectual contribution to the work and approved it for publication. Among them, DS is mainly responsible for numerical simulation and article writing; CM is responsible for providing ideas for project implementation; TB and LJ participate in processing some data; ZL and HH provide technical consulting services, and WC and LJ provide article modification opinions.

FUNDING

This work was in part financially supported by the National Natural Science Foundation of China (Grant No. 515107106), China Postdoctoral Foundation (2021M702371) and Chengdu International Science and Technology Cooperation Support Funding (2020-GH02-00059-HZ).

SUPPLEMENTARY MATERIAL

The Supplementary Material for this article can be found online at: https://www.frontiersin.org/articles/10.3389/fenrg.2021.812367/full#supplementary-material

REFERENCES

Cai, M.-q., Zhou, L.-s., Xu, Q., Yang, X.-h., and Liu, X.-h. (2020b). Galloping Response of Sector-Shape Iced Eight Bundle Conductors. *Can. J. Civ. Eng.* 47 (10), 1201–1213. doi:10.1139/cjce-2018-0114

Cai, M., Xu, Q., Zhou, L., Liu, X., and Huang, H. (2019b). Aerodynamic Characteristics of Iced 8-bundle Conductors under Different Turbulence Intensities. *KSCE J. Civ Eng.* 23 (11), 4812–4823. doi:10.1007/s12205-019-0359-9

Cai, M., Yan, B., Lu, X., and Zhou, L. (2015). Numerical Simulation of Aerodynamic Coefficients of Iced-Quad Bundle Conductors. *IEEE Trans. Power Deliv.* 30 (4), 1669–1676. doi:10.1109/TPWRD.2015.2417890

Cai, M., Yang, X., Huang, H., and Zhou, L. (2020a). Investigation on Galloping of D-Shape Iced 6-Bundle Conductors in Transmission Tower Line. *KSCE J. Civ Eng.* 24 (6), 1799–1809. doi:10.1007/s12205-020-0595-z

Cai, M., Zhou, L., Lei, H., and Huang, H. (2019a). Wind Tunnel Test Investigation on Unsteady Aerodynamic Coefficients of Iced 4-Bundle Conductors. *Adv. Civil Eng.* 2019, 1–12. doi:10.1155/2019/2586242

Hartog, J. P. D. (1932). Transmission Line Vibration Due to Sleet. *Trans. Am. Inst. Electr. Eng.* 51 (4), 1074–1076. doi:10.1109/T-AIEE.1932.5056223

Hu, J., Yan, B., Zhou, S., and Zhang, H. (2012). Numerical Investigation on Galloping of Iced Quad Bundle Conductors. *IEEE Trans. Power Deliv.* 27 (2), 784–792. doi:10.1109/TPWRD.2012.2185252

Hung, P. V., Yamaguchi, H., Isozaki, M., and Gull, J. H. (2014). Large Amplitude Vibrations of Long-Span Transmission Lines with Bundled Conductors in Gusty Wind. *J. Wind Eng. Ind. Aerodynamics* 126, 48–59. doi:10.1016/j.jweia.2014.01.002

Hunt, J. C. R., and Richards, D. J. W. (1969). Overhead-line Oscillations and the Effect of Aerodynamic Dampers. *IEEE Proc.* 116 (11), 1869–1874. doi:10.1049/piee.1969.0344

Jafari, M., Hou, F., and Abdelkefi, A. (2020). Wind-Induced Vibration of Structural Cables. *Nonlinear Dyn.* 100 (1), 351–421. doi:10.1007/s11071-020-05541-6

Kim, J.-W., and Sohn, J.-H. (2018). Galloping Simulation of the Power Transmission Line under the Fluctuating Wind. *Int. J. Precis. Eng. Manuf.* 19 (9), 1393–1398. doi:10.1007/s12541-018-0164-2

Li, H., Deng, J., Feng, P., Pu, C., Arachchige, D. D. K., and Cheng, Q. (2021a). Short-Term Nacelle Orientation Forecasting Using Bilinear Transformation and ICEEMDAN Framework. *Front. Energ. Res.* 9, 780928. doi:10.3389/fenrg.2021.780928

Li, H., Deng, J., Yuan, S., Feng, P., and Arachchige, D. D. K. (2021b). Monitoring and Identifying Wind Turbine Generator Bearing Faults Using Deep Belief Network and EWMA Control Charts. *Front. Energ. Res.* 9, 799039. doi:10.3389/fenrg.2021.799039

Liu, X.-h., Yan, B., Zhang, H.-y., and Zhou, S. (2009). Nonlinear Numerical Simulation Method for Galloping of Iced Conductor. *Appl. Math. Mech.-Engl. Ed.* 30 (4), 489–501. doi:10.1007/s10483-009-0409-x

Liu, X. H., Min, G. Y., Sun, C., and Cai, M. Q. (2021b). Investigation on Stability and Galloping Characteristics of Iced Quad Bundle Conductor. *Jafm* 14 (1), 117–129. doi:10.47176/jafm.14.01.31417

Liu, X., Hu, Y., and Cai, M. (2019). Free Vibration Analysis of Transmission Lines Based on the Dynamic Stiffness Method. *R. Soc. Open Sci.* 6 (3), 181354. doi:10.1098/rsos.181354

Liu, X. H., Zou, M., Wu, C., Yan, B., and Cai, M. Q. (2020c). Galloping Stability and Aerodynamic Characteristic of Iced Transmission Line Based on 3-DOF. *Shock and Vibration* 2020, 8828319. doi:10.1155/2020/8828319

Liu, X., Liang, H., Min, G., Wu, C., and Cai, M. (2021a). Investigation on the Nonlinear Vibration Characteristics of Current-Carrying Crescent Iced Conductors under Aerodynamic Forces, Ampere's Forces, and Forced Excitation Conditions. *Discrete Dyn. Nat. Soc.* 2021, 1–22. doi:10.1155/2021/5009209

Liu, X., Min, G., Cai, M., Yan, B., and Wu, C. (2021c). Two Simplified Methods for Galloping of Iced Transmission Lines. *KSCE J. Civ Eng.* 25 (1), 272–290. doi:10.1007/s12205-020-0693-y

Liu, X., Min, G., Wu, C., and Cai, M. (2020a). Investigation on Influences of Two Discrete Methods on Galloping Characteristics of Iced Quad Bundle Conductors. *Adv. Civil Eng.* 2020, 1–17. doi:10.1155/2020/8818728

Liu, X., Yang, S., Min, G., Cai, M., Wu, C., and Jiang, Y. (2021d). Investigation on the Accuracy of Approximate Solutions Obtained by Perturbation Method for Galloping Equation of Iced Transmission Lines. *Math. Probl. Eng.* 2021, 1–18. doi:10.1155/2021/6651629

Liu, X., Yang, S., Wu, C., Zou, M., Min, G., Sun, C., et al. (2021e). Planar Nonlinear Galloping of Iced Transmission Lines under Forced Self-Excitation Conditions. *Discrete Dyn. Nat. Soc.* 2021, 1–20. doi:10.1155/2021/6686028

Liu, X., Zou, M., Wu, C., Cai, M., Min, G., and Yang, S. (2020b). Galloping Stability and Wind Tunnel Test of Iced Quad Bundled Conductors Considering Wake Effect. *Discrete Dyn. Nat. Soc.* 2020, 1–15. doi:10.1155/2020/8885648

Liu, Z. H., Ding, C. H., Qin, J., and Lei, Y. (2020). The Nonlinear Galloping of Iced Transmission Conductor under Uniform and Turbulence Wind. *Struct. Eng. Mech.* 75 (4), 465–475. doi:10.12989/sem.2020.75.4.465

Lou, W., Chen, S., Wen, Z., Wang, L., and Wu, D. (2021). Effects of Ice Surface and Ice Shape on Aerodynamic Characteristics of Crescent-Shaped Iced Conductors. *J. Aerosp. Eng.* 34 (3), 04021008. doi:10.1061/(ASCE)AS.1943-5525.0001246

Lu, J., Wang, Q., Wang, L., Mei, H., Yang, L., Xu, X., et al. (2019). Study on Wind Tunnel Test and Galloping of Iced Quad Bundle Conductor. *Cold Regions Sci. Tech.* 160, 273–287. doi:10.1016/j.coldregions.2018.12.009

Matsumiya, H., Nishihara, T., and Yagi, T. (2018). Aerodynamic Modeling for Large-Amplitude Galloping of Four-Bundled Conductors. *J. Fluids Structures* 82, 559–576. doi:10.1016/j.jfluidstructs.2018.08.003

Min, G., Liu, X., Wu, C., Yang, S., and Cai, M. (2021). Influences of Two Calculation Methods about Dynamic Tension on Vibration Characteristics of Cable-Bridge Coupling Model. *Discrete Dyn. Nat. Soc.* 2021, 1–11. doi:10.1155/2021/6681954

Nigol, O., Clarke, G. J., and Havard, D. G. (1977). Torsional Stability of Bundle Conductors. *IEEE Trans. Power Apparatus Syst.* 96 (5), 1666–1674. doi:10.1109/T-PAS.1977.32496

Oh, Y.-J., and Sohn, J.-H. (2020). Stability Evaluation of the Transmission Line by Using Galloping Simulation. *Int. J. Precis. Eng. Manuf.* 21 (11), 2139–2147. doi:10.1007/s12541-020-00399-5

Rossi, A., Jubayer, C., Koss, H., Arriaga, D., and Hangan, H. (2020). Combined Effects of Wind and Atmospheric Icing on Overhead Transmission Lines. *J. Wind Eng. Ind. Aerodynamics* 204, 104271. doi:10.1016/j.jweia.2020.104271

Talib, E., Shin, J.-H., Kwak, M. K., and Koo, J. R. (2019). Dynamic Modeling and Simulation for Transmission Line Galloping. *J. Mech. Sci. Technol.* 33 (9), 4173–4181. doi:10.1007/s12206-019-0812-1

Yan, B., Liu, X., Lv, X., and Zhou, L. (2016). Investigation into Galloping Characteristics of Iced Quad Bundle Conductors. *J. Vibration Control.* 22 (4), 965–987. doi:10.1177/1077546314538479

Zhang, Q., Popplewell, N., and Shah, A. H. (2000). Galloping of Bundle Conductor. *J. Sound Vibration* 234 (1), 115–134. doi:10.1006/jsvi.1999.2858

Zhao, L. (2014). *Research on Galloping Simulation of 500 KV Transmission Tower-Line System*. Chongqing, China: Chongqing University.

Zhou, A., Liu, X., Zhang, S., Cui, F., and Liu, P. (2018). Wind Tunnel Test of the Influence of an Interphase Spacer on the Galloping Control of Iced Eight-Bundled Conductors. *Cold Regions Sci. Tech.* 155, 354–366. doi:10.1016/j.coldregions.2018.08.026

Zhou, L., Yan, B., Zhang, L., and Zhou, S. (2016). Study on Galloping Behavior of Iced Eight Bundle Conductor Transmission Lines. *J. Sound Vibration* 362, 85–110. doi:10.1016/j.jsv.2015.09.046

Conflict of Interest: ZL was employed by State Grid Sichuan Integrated Energy Service Co., Ltd. WC was employed by Henan Electric Power Research Institute.

The remaining authors declare that the research was conducted in the absence of any commercial or financial relationships that could be construed as a potential conflict of interest.

Publisher's Note: All claims expressed in this article are solely those of the authors and do not necessarily represent those of their affiliated organizations, or those of the publisher, the editors, and the reviewers. Any product that may be evaluated in this article, or claim that may be made by its manufacturer, is not guaranteed or endorsed by the publisher.

frontiers in Energy Research

ORIGINAL RESEARCH
published: 31 March 2022
doi: 10.3389/fenrg.2022.865602

Traction Network Protection Based on Similarity of Transient Current Waveform

*Shilong Chen[1], Zihang Zhang[1], Hao Liu[2], Guihong Bi[1], Chao Xing[3], Pengsong Li[1] and Wenying Zhang[1]**

[1]Department of Electrical Engineering, Kunming University of Science and Technology, Kunming, China, [2]Kunming Power Supply Bureau in Yunnan Power Grid Co., Ltd., Kunming, China, [3]Electric Power Research Institute, Yunnan Power Grid Co., LTD., Kunming, China

In this paper, a protection scheme for the traction network of the penetrating co-phase traction direct power supply system based on the waveform similarity at both ends of line is proposed. Besides, research on the transmission characteristics of fault current is also carried out. This article, from the perspectives of the reflection and refraction process, attenuation degree, and polarity of fault current, analyzes the correlation and difference of current waveforms at both ends when interior line faults and adjacent line faults emerge. The correlation of waveforms can be proved by cosine similarity after the process of synchronous squeezes wavelet transformation of fault current. The conclusions are as follows: when the interior line faults occur, the sequence, reflection and refraction process, and attenuation degree reaching both ends are roughly the same, the polarity change direction is the same, and the waveform similarity is high; when the adjacent line faults occur, the sequence, reflection and refraction process, and attenuation degree reaching at both ends are greatly different, the polarity change direction is opposite, and the waveform similarity is low. When a protection scheme is based on using cosine similarity, it can quickly and accurately identify internal or external current faults. Simulation results show that the proposed algorithm can meet the requirements of rapidity, selectivity, and reliability and is not affected by transition resistance and fault inception angles, so it has an application prospect to a certain degree.

Keywords: penetrating co-phase traction direct power supply system, synchronous squeezed wavelet transformation, cosine similarity, traction network, transient protection

OPEN ACCESS

Edited by:
Xun Shen,
Tokyo Institute of Technology, Japan

Reviewed by:
Sandeep Kumar Duran,
Lovely Professional University, India
Sahil Sardana,
Indian Institute of Technology, Dhanbad, India

****Correspondence:***
Wenying Zhang
kmzwying@sina.com

Specialty section:
This article was submitted to Smart Grids, a section of the journal Frontiers in Energy Research

Received: *30 January 2022*
Accepted: *03 March 2022*
Published: *31 March 2022*

Citation:
Chen S, Zhang Z, Liu H, Bi G, Xing C, Li P and Zhang W (2022) Traction Network Protection Based on Similarity of Transient Current Waveform. Front. Energy Res. 10:865602. doi: 10.3389/fenrg.2022.865602

1 INTRODUCTION

The traction direct power supply system is a unique branch of the power system, but suffers high failure frequency due to its complicated deployment environment, such as bad geographic environment, complex weather conditions, locomotive load, and lightning stroke. At the same time, traction network has high requirements for power supply reliability. For this reason, its relay protection scheme must have specific capabilities to quickly and accurately identify the faults.

Relay protection schemes and fault location methods based on traveling wave and transient signals have achieved great success in the deployment of transmission and distribution lines. Deng et al. (2018), Biswas and Milanfar, (2016) and Li et al. (2019) based on time–frequency correlation of fault waveform characteristics put forward a time–frequency matrix constructed by fault waveform of continuous

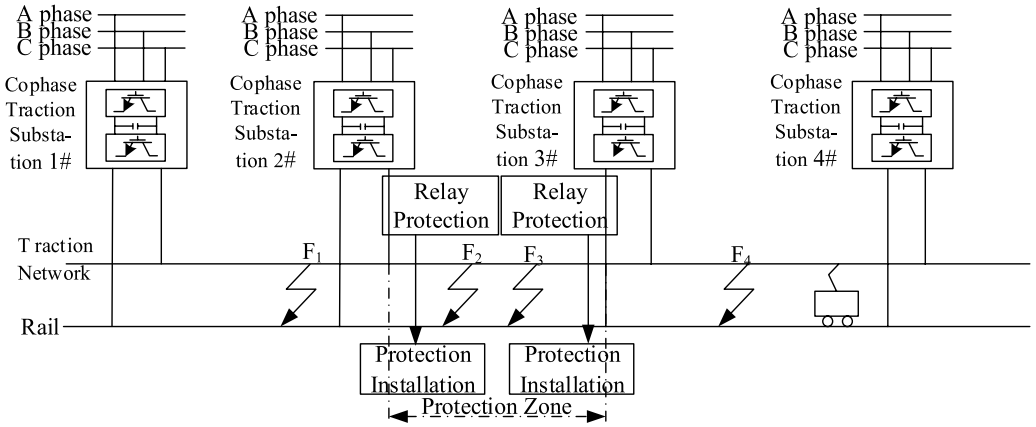

FIGURE 1 | Penetrating co-phase traction direct power supply system.

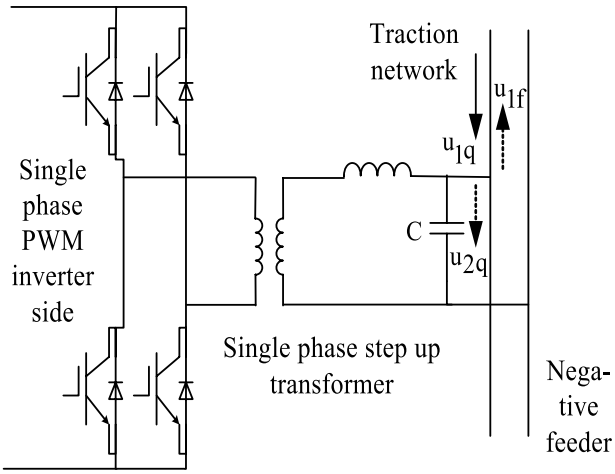

FIGURE 2 | Connection method of co-phase traction substation and traction network.

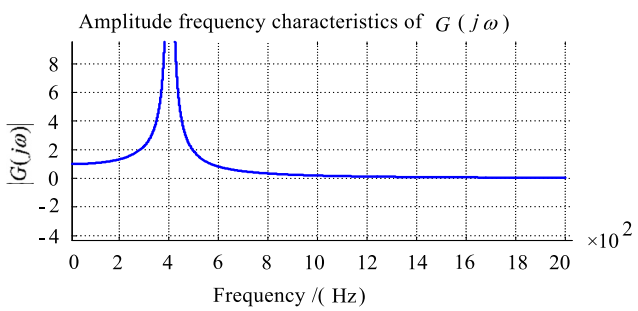

FIGURE 3 | Amplitude–frequency characteristics of the traction network boundary.

wavelet transform and S-transform, and by it, they believe that the internal and external faults of transmission line could be distinguished; Wang et al. (2019) and Zhen et al. (2019), with

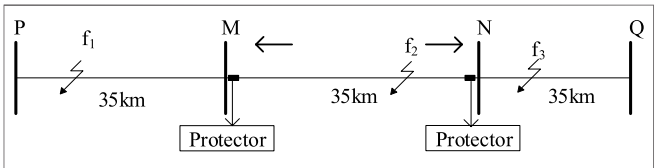

FIGURE 4 | Schematic diagram of the traction network line structure.

the help of cosine similarity of transient current waveform to construct a flexible DC distribution system, give a scheme for outgoing feeder protection of new energy station. Based on the correlation characteristics of fault waveforms, Li Z. et al. (2018) and Hongchun et al. (2012) propose using waveform coefficient to distinguish internal and external faults; Li et al. (2019), based on the waveform similarity of forward and reverse differential currents, state that the fault location information can be accessed by analysis of the Pearson coefficient. In recent years, many researchers in this field have analyzed the propagation characteristics of fault traveling wave in the traction network line and appealed that the research of fault traveling wave and fault located of traction network should be conducted as a whole (Xue et al., 2012; Xiong et al., 2019; Pan et al., 2014). However, fault traveling wave and fault transient signal have not been widely used in the protection of traction network. As transient protection is of the advantages of stability, reliability, and rapidity, it would be a new attempt to apply it to traction network.

The penetrating co-phase traction direct power supply system and capacitance are paralleled at every outlet of traction substations for filtering, and the paralleled capacitance would create wave impedance discontinuity. The waveform detected at the relay location is the transient signal generated by the fault point, and after repeated folding, reflection, (Shen et al., 2021; Shen and Raksincharoensak, 2021a) and refraction, it is superimposed according to a certain time sequence. The traction network and line boundary exert a certain attenuation effect on the fault transient signal, which is why the amplitude of waveform (Shen et al., 2020a; Shen et al., 2020b; Zhang et al., 2021) at both ends of the line is different when the fault location is different. The polarity of the signal detected at both ends of the device is different (Shen and Raksincharoensak, 2021b; Shen et al., 2022) when the fault

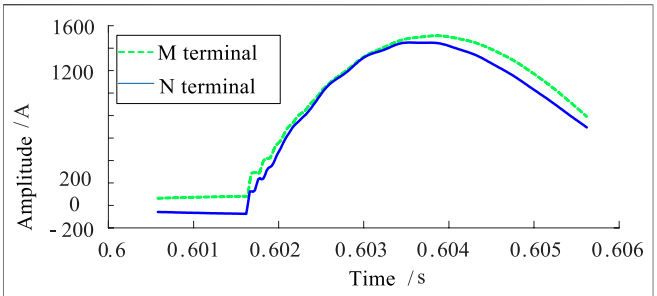

FIGURE 5 | Line mode waveform in M and N at the fault in the zone (f_2). (**A**) Forward zone out of fault (f_3). (**B**) Reverse zone out of fault (f_1).

location is different. The cosine similarity is used to represent the difference of waveform at both ends of the line. When the information about the reflection and refraction, arrival time sequence, attenuation degree, polarity, and other relevant factors of waveforms at both ends of the line are roughly the same, the waveform similarity is high, and the cosine similarity is large. Otherwise, the cosine similarity is small. Taking advantage of the (Han et al., 2016; Li B. et al., 2018) abovementioned characteristics, the pilot protection of traction network in the traction direct power supply system could be constructed on the basis of the similarity of current waveform.

Synchronous squeeze wavelet transform (SWT) compresses the time–frequency map after wavelet transform in the frequency domain direction (Li et al., 2021; Liu et al., 2020), and its time–frequency curve is clearer and the decomposition result remains approximately unchanged, which is conducive to solving the mode mixing problem and is more accurate than taking wavelet transform, S-transform, and other methods (Duan et al., 2019; Yu et al., 2017a).

This study studies the unique structure of the traction direct power supply system. Based on the transmission characteristics and attenuation function of transient waveform, it analyzed the similarity of the current waveforms at both ends of the traction network interior line faults and adjacent line faults and proposed a new method of the line protection based on synchronous squeeze wavelet and waveform similarity, whereby the internal and external faults can be quickly and accurately identified. The scheme uses cosine similarity of waveform at both ends of the line to form the protection criterion, making effective use of the waveform characteristics and making the protection more reliable, and is not affected by the transition resistance and the initial angle of the fault. It is the first time this method and the traction system have been combined. With the help of simulation software PSCAD/EMTDC, the model of the penetrating co-phase traction direct power supply system could be constructed for effective algorithm verification.

2 STRUCTURE AND BOUNDARY OF THE PENETRATING CO-PHASE TRACTION DIRECT POWER SUPPLY SYSTEM

2.1 Penetrating Co-Phase Traction Direct Power Supply System

The structure of the penetrating co-phase traction direct power supply system is shown in **Figure 1**. The system is mainly

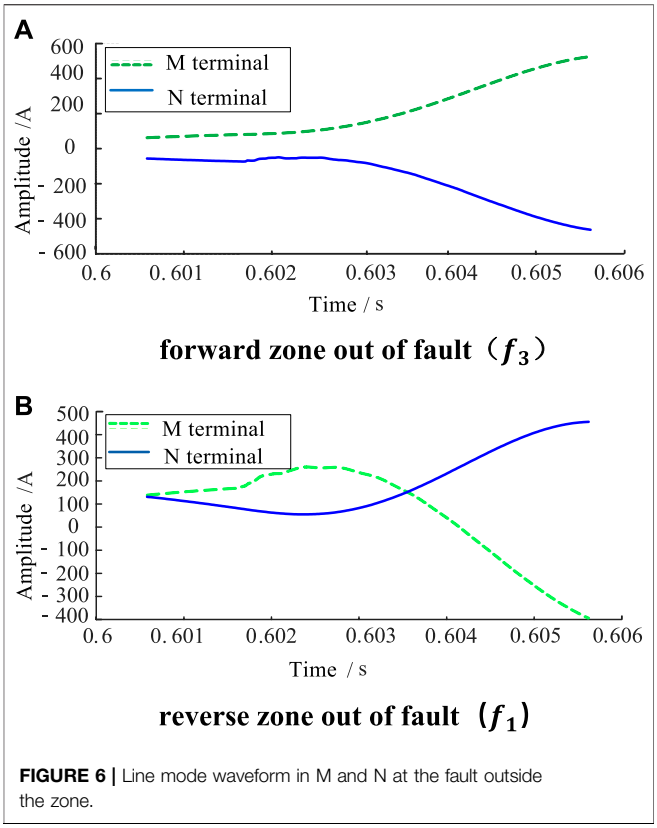

FIGURE 6 | Line mode waveform in M and N at the fault outside the zone.

composed of public power grid, traction substation, traction network, and electric locomotive. The three-phase alternating current of the public power grid outputs a single-phase alternating current with equal amplitude and same phase through rectifier operation and inverter operation of traction substation (Li, 2014). Usually, the length of the line between two traction substations is 30–35 km. In this study, 35 km is adopted.

2.2 Boundary of Traction Network

Connection method of co-phase traction substation and traction network is shown in **Figure 2**. The capacitors at the outlet are connected in parallel with the traction network to reduce the harmonic content entering the traction network and improve the power quality of the traction network lines.

The capacitance connected in parallel with traction network shows low impedance to high frequency current. Thus, it is of certain boundary characteristics. When the fault current passes through the boundary of the traction network, a part of the fault current flows into the capacitors, which leads to a sharp difference with the fault current detected at the relay location where internal and external fault appears. According to the method from Song et al., 2014, the capacitance at the outlet of traction substation plus-2 meters contact line is set as the line boundary.

According to the composition of traction network boundary of co-phase traction power supply system, the frequency characteristics are analyzed, as shown in **Figure 3**.

It can be seen from **Figure 3** that fault signals with different frequencies show unequal passage characteristics after passing through the boundary. When the signal frequency is greater than

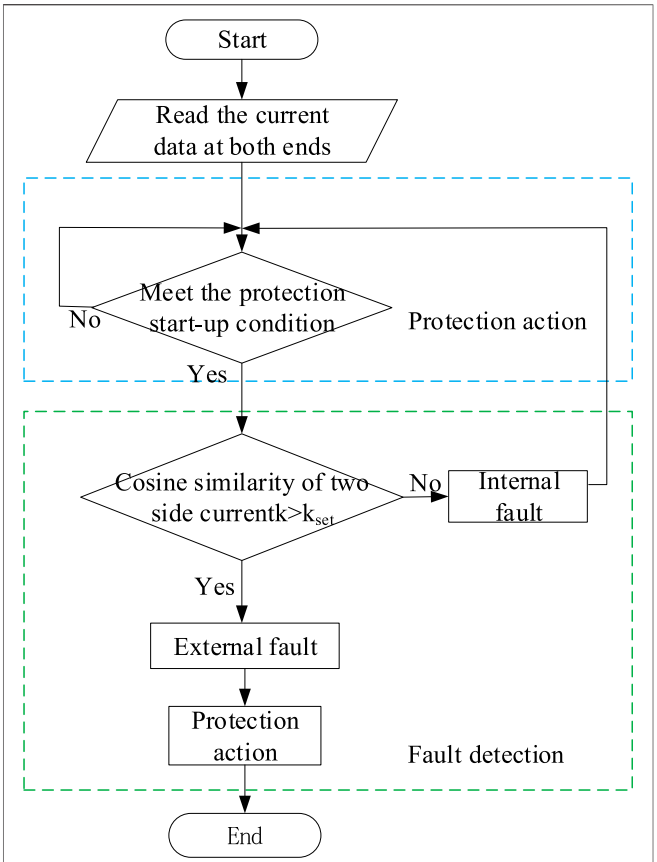

FIGURE 7 | Protection scheme flowchart.

600Hz, the amplitude of amplitude–frequency characteristic is far less than 1, which indicates that the boundary has a strong attenuation effect on high frequency signal (Shen et al., 2017; Yang et al., 2018; Song et al., 2020).

3 THE ANALYSIS OF THE FAULT CURRENT OF THE PENETRATING CO-PHASE TRACTION DIRECT POWER SUPPLY SYSTEM

Figure 4 is the typical schematic diagram of the traction network line structure, and P、Q、M、N is where the traction substation is located, also known as the fault detecting point. In this study, the traction network between M, N is taken as the research object, which is also in the zone. The faults are set in f_1, f_2, and f_3. After the fault occurs in the traction network, the fault transient current signal propagates along the line at the fault point at high speed to both sides, and produces reflection and refraction where the wave impedance is discontinuous. The transient signal detected by the detecting point, M, N, is related to attenuation function, reflection and refraction coefficient and fault location. The positive directions of M、N are shown in **Figure 3**.

3.1 Internal Line Fault

When the fault occurs in f_2 (in the zone), the transient current from the fault point flows to both ends of the line, and the traction network has an attenuation effect on the transient signal of the fault. The polarity changes of the transient current detected by the protection devices at both ends of the line are the same, and the transient current only passes through the line, so the attenuation characteristics, reflection process, and transmission sequence are basically consistent, and the waveform shape of the transient current is basically the same. However, when the fault point is relatively far from the midpoint of the line, the waveform shape is different due to the different arrival time sequence of the fault transient current; at the same time, due to the attenuation effect of the traction network on the fault transient signal, the attenuation degree of the transient current with different frequency is different in the transmission process, so the amplitude is different.

When a metallic short-circuit fault occurs, a distance of 15 km form M, its mode component is obtained by decoupling and transforming the fault transient current of M and N, as shown in **Figure 5**.

It can be seen from **Figure 5** that the waveform of mode component of fault transient current at both ends of the line is basically the same when the fault occurs in the zone.

3.2 Adjacent Line Fault

In case of fault occurring in f_1 (outside the reverse zone) and f_3 (outside the forward zone), the transient current will flow through the boundary of the traction network line, and the waveform of the transient current will be reflected, and the high frequency component will be strongly attenuated when passing through the boundary. The polarity change direction of the current waveform detected by the detecting point, M, N, will be opposite; the reflection and refraction process, attenuation degree, and transmission sequence of the transient current waveform will be completely different. Therefore, the waveform of fault transient current will be completely different.

When a metallic short-circuit fault occurs, a distance of 35 km forms the forward zone of N, that is f_3, its mode component is obtained by decoupling and transforming the fault transient current of M and N, as shown in **Figure 6A**. When a metallic short-circuit fault occurs, a distance of 20 km forms the reverse zone of M, that is f_1, its mode component is shown in **Figure 6B**.

It can be seen from **Figure 6** that the waveform of mode component of fault transient current at both ends of the line is opposite and in sharp difference when the fault occurs outside the zone.

To sum up, the waveform of fault current is related to transmission characteristics (refraction and reflection process, attenuation degree, arrival time sequence, change direction) and transmission function. When the fault occurs in the zone, the refraction and reflection process and attenuation characteristics of the transient current are basically the same, the polarity change direction is the same, and the transmission sequence is slightly different, all resulting in local differences in waveform. But generally speaking, the fault transient current waveforms detected at both ends of the line are basically similar. When the fault occurs outside the area, the transient current attenuates through the boundary, the

TABLE 1 | Cosine similarity at different fault locations.

Fault location	Fault distance/km	K	Result
f_2 in the zone	0	0.9097	In the zone
	5	0.9214	In the zone
	10	0.9880	In the zone
	15	0.9960	In the zone
	20	0.9967	In the zone
	25	0.9826	In the zone
	30	0.8996	In the zone
	35	0.8749	In the zone
$f_3$outside the forward zone	0	–0.8343	Outside the zone
	5	–0.9011	Outside the zone
	10	–0.9816	Outside the zone
	15	–0.9927	Outside the zone
	20	–0.9955	Outside the zone
	25	–0.9965	Outside the zone
	30	–0.9964	Outside the zone
	35	–0.9974	Outside the zone
f_1 outside the reverse zone	0	–0.7751	Outside the zone
	5	–0.8349	Outside the zone
	10	–0.9455	Outside the zone
	15	–0.9683	Outside the zone
	20	–0.9763	Outside the zone
	25	–0.9821	Outside the zone
	30	–0.9885	Outside the zone
	35	–0.9867	Outside the zone

frequency components are different, the refraction and reflection process, the transmission sequence are completely different, and the polarity change direction is opposite. The waveform of fault transient current detected at both ends of the line is significantly different.

4 THE PILOT PROTECTION BASED ON SYNCHRONOUS SQUEEZED WAVELET AND WAVEFORM SIMILARITY

Based on the above analysis, this article puts forward the transmission line protection principle based on the theoretical basis of the change characteristics of current waveform at both ends and the similarity of transient current waveform.

4.1 Similarity Theory

Cosine similarity is widely applied for information retrieval and data mining. In recent years, many scholars have studied, with cosine similarity, the fault line detection, fault location, and line protection (Li B. et al., 2019; Wang et al., 2019; Li Z. et al., 2018). The cosine value of the angle between two vector inner spaces is used to characterize their similarity, which is known as the follows:

$$\cos(\theta) = \frac{\vec{a} \bullet \vec{b}}{\|a\| \times \|b\|} \tag{1}$$

From **Eq. 1**, it can be concluded that when the direction of two vectors, $\vec{a}$ and $\vec{b}$ are same, cosine similarity is 1; when $\vec{a}$ and $\vec{b}$ are vertical, cosine similarity is 0; when the direction of two vectors, $\vec{a}$ and $\vec{b}$, are opposite, cosine similarity is -1.

If $x = \{x_1, x_2, \cdots, x_n\}$ and $y = \{y_1, y_2, \cdots, y_n\}$ are two independent variables, and n is sampling point, their cosine similarity can be expressed as follows:

$$R(x, y) = \frac{\sum_{i=1}^{n} x_i y_i}{\sqrt{\sum_{i=1}^{n} x_i^2} \sqrt{\sum_{i=1}^{n} y_i^2}}. \tag{2}$$

In the formula, $R(x, y)$ represents cosine similarity, and x_i, y_i ($i = 1, 2, \cdots, n$) are the No. i element of independent variable, x and y, respectively.

The value range of $R(x, y)$ is [- 1,1], and the sign indicates the relevant direction. For $R(x, y)$, the higher the value, higher the similarity of the waveform of the two signals. When $R(x, y) = -1$, it means that the two signals are completely negatively correlated; when $R(x, y) = 1$, it means that the two signals are completely positively correlated; when $R(x, y) = 0$, the two signals are quite different and uncorrelated (Deng et al., 2018; Li Z. et al., 2018).

4.2 The Method Based on Synchronous Squeezed Wavelet Transformation

4.2.1 Basic Principles of SWT

Daubechies et al., 2011 and Thakur et al., 2013 proposed when obtained by SWT, the time–frequency curve is of higher clearness, the component precision is higher, and the time–frequency energy is more concentrated (Duan et al., 2019; Yu et al., 2017a). In this case, the composite signal, $f(t)$, is as follows:

$$f(t) = \sum_{k=1}^{n} f_k(t) = \sum_{k=1}^{n} A_k(t) e^{-\lambda t} \cos(2\pi\omega_k t + \varphi_k). \tag{3}$$

TABLE 2 | Cosine similarity under different transition resistances.

Fault location	Transition resistances/ Ω	Fault distance/km	K	Result
f_2 in the zone	0.1	0	0.9097	In the zone
		15	0.9960	In the zone
		35	0.8749	In the zone
	10	0	0.9010	In the zone
		15	0.9954	In the zone
		35	0.8130	In the zone
	50	0	0.8721	In the zone
		15	0.9926	In the zone
		35	0.7980	In the zone
	100	0	0.7542	In the zone
		15	0.9826	In the zone
		35	0.7827	In the zone
f_3 outside of forward zone	0.1	0	–0.9943	Outside the zone
		15	–0.9927	Outside the zone
		35	–0.9974	Outside the zone
	10	0	–0.9078	Outside the zone
		15	–0.9437	Outside the zone
		35	–0.9790	Outside the zone
	50	0	–0.7193	Outside the zone
		15	–0.6853	Outside the zone
		35	–0.6828	Outside the zone
	100	0	–0.7033	Outside the zone
		15	–0.6615	Outside the zone
		35	–0.6553	Outside the zone
f_1 outside the reverse zone	0.1	0	–0.9751	Outside the zone
		15	–0.9683	Outside the zone
		35	–0.9867	Outside the zone
	10	0	–0.7438	Outside the zone
		15	–0.8475	Outside the zone
		35	–0.8359	Outside the zone
	50	0	–0.5858	Outside the zone
		15	–0.5486	Outside the zone
		35	–0.6437	Outside the zone
	100	0	–0.4599	Outside the zone
		15	–0.4235	Outside the zone
		35	–0.4373	Outside the zone

The synchronous squeezed wavelet changes on the basis of continuous wavelet, and $f(t)$ is the change of continuous wavelet transforms into $W_f(a,b)$, in which a, b are the scale and shift factor. The initial estimated instantaneous frequency of $W_f(a,b)$, as a result, is

$$\omega_f(a,b) = \begin{cases} \dfrac{-i}{W_f(a,b)} \cdot \dfrac{\partial\left(W_f(a,b)\right)}{\partial b} \neq 0\, W_f(a,b) \neq 0 W_f(a,b) = 0 \\ W_f(a,b) = 0 \end{cases} \tag{4}$$

After synchronous squeezing of wavelet coefficient, $W_f(a,b)$, where $\tilde{\varepsilon}$ is the threshold value and accuracy is δ, the result is

$$S^{\delta}_{f,\tilde{\varepsilon}}(b,\omega) = \int_{A_{\tilde{\varepsilon},f}(b)} W_f(a,b) \frac{1}{\delta} h\left(\frac{\omega - \omega_f(a,b)}{\delta}\right) a^{-3/2} da. \tag{5}$$

In this formula, $\tilde{\varepsilon} = 1.4826\sqrt{2\ln N} \bullet MAD(|W_f|_{n_v})$ and N are the signal length. $MAD(|W_f|_{n_v})$ is the median value of wavelet coefficients in the minimum scale layer; $A_{\tilde{\varepsilon},f}(b) = \{a \in R^+; |W_f(a,b)| > \tilde{\varepsilon}\}$.

If $Z_k = \{(a,b): |a\omega_k^{'}(b) - 1| < \Delta\}$, when $(a,b) \in Z_k$, there would be

$$\left|\omega_f(a,b) - \omega_k^{'}(b)\right| \leq \tilde{\varepsilon}. \tag{6}$$

After the reconstruction of the component, $f_k(t)$ turns into $\tilde{f}_k(b)$, and the result is as follows:

$$\tilde{f}_k(b) = \lim_{\delta \to 0}\left(R_{\psi}^{-1} \int_{\left|\omega - \omega^{'}(b) < \tilde{\varepsilon}\right|} S^{\delta}_{f,\tilde{\varepsilon}}(b,\omega) d\omega \right). \tag{7}$$

For constant C, if $\forall b \in R$, there would be

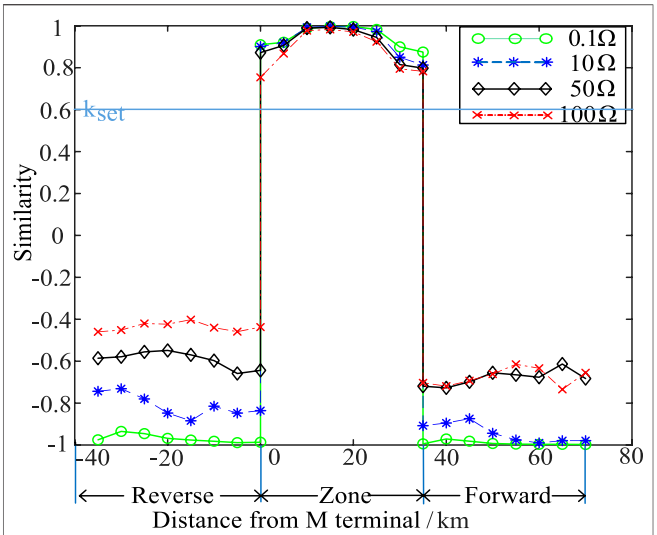

FIGURE 8 | Similarity under different transition resistances.

$$\left|\tilde{f}_k(b) - A_k(b)e^{-\lambda b}\cos\left(2\pi\omega_k b + \varphi_k\right)\right| \le C\tilde{\varepsilon}. \tag{8}$$

According to (**8**), the SWT reconstructed component, $\tilde{f}_k(b)$, is very accurately close to composite signal ($f(t)$) 's k^{th} component, $f_k(t)$.

4.2.2 The Signal of Synchronous Squeezed Wavelet Transformation Processing

When SWT is used to process fault transient signal, the steps are as follows:

(1) The result of the continuous wavelet transform processing for composite (Yang et al., 2021a; Yang et al., 2021b; Yang et al., 2022) signal, $f(t)$is as follows:

$$W_f(a,b) = \int_{-\infty}^{+\infty} f(t)a^{-\frac{1}{2}}\bar{\psi}\left(\frac{t-b}{a}\right)dt. \tag{9}$$

(2) Division of frequency interval: if the length of $f(t)$ is $n = 2^{L+1}$, the sampling interval is Δt, n_v is taken as 32. We assume $n_a = Ln_v$, $\Delta\omega = \frac{1}{n_a - 1}\log_2\left(\frac{n}{2}\right)$, and dividing $f(t)$ into different frequency intervals, the l^{th} frequency component of center frequency (ω_l) is as shown in **formula (10)**.

(2) Division of frequency interval: if the length of $f(t)$ is $n = 2^{L+1}$, the sampling interval is Δt, n_v takes 32, $n_a = Ln_v$, $\Delta\omega = \frac{1}{n_a - 1}\log_2\left(\frac{n}{2}\right)$ and $f(t)$ is divided into different frequency intervals, as shown in **formula (10)**, the l^{th} frequency component of center frequency (ω_l) would be

$$W_l = \left(\frac{\omega_{l-1} + \omega_l}{2}, \frac{\omega_l + \omega_{l+1}}{2}\right). \tag{10}$$

(3) Computing the coefficient of synchronous squeezed wavelet $(T_f(a,b))$,

$$T_f(\omega_l, b) = (\Delta\omega)^{-1} \sum_{a_k:\ \left|\omega_f(a,b) - \omega_l\right| \le \frac{\Delta\omega}{2}} W_f(a,b)a_k^{-\frac{3}{2}}(\Delta a)_k, \tag{11}$$

where ω_l represents the l^{th} central frequency. a_k is the discrete value of wavelet changing scale, a. $(\Delta a)_k = a_k - a_{k-1}$; $\Delta\omega = \omega_l - \omega_{l-1}$.

(4) After inverse transform, the reconstructed signal, $f(t)$, can be achieved by

$$\begin{aligned} f(t) &= \mathrm{Re}\left[C_\psi^{-1}\left(\int_0^{+\infty} W_f(a,b)a^{-3/2}da\right)\right] \\ &= \mathrm{Re}\left[C_\psi^{-1}\left(\sum_i W_f(a,b)a_i^{-3/2}(\Delta a)_i\right)\right] \\ &= \mathrm{Re}\left[C_\psi^{-1}\left(\sum_i T_f(\omega_l, b)(\Delta\omega)\right)\right] \end{aligned} \tag{12}$$

where $C_\psi^{-1} = \int_0^{+\infty} \varphi^*(\xi)\frac{d\xi}{\xi}$ and $\varphi^*(\xi)$ are the conjugated Fourier transform of wavelet function; a_i is the discrete scale; and i is the scale of discreteness.

4.3 Protection Scheme

The basic flow chart of traction network protection algorithm using synchronous squeezed wavelet transformation and waveform similarity is shown in **Figure 7**.

(1) Start

(2) After the procedure has started, the fault transient current under the data window at both ends of the line is collected and decoupled. Selecting a mode component, the reconstructed signal $f(t)$ can be collected after preprocessing of line mode component of current by synchronous squeezed wavelet transformation and then the similarity of waveform at both ends,k is calculated by using the reconstructed signal.

(3) If the similarity between the two ends is greater than the set threshold, $k > k_{set}$, an internal line fault occurs, and protective measures is adopted immediately; otherwise, it is an external line fault and no action is required.

Considering the influence of test error, communication delay, noise and other factors, the constant is set as 0.6, that is, $k_{set} = 0.6$.

5 SIMULATION VERIFICATION AND ANALYZING

With the help of simulation software PSCAD/EMTDC, the model of the penetrating co-phase traction direct power supply system can be constructed, as shown in **Figure 1**.

The line between No.1 and two of traction substation, that is the section of M、N in **Figure 4**, is taken as the research object. As the traction network schematic diagram shown in **Figure 4**, the fault of f_2 (in the zone), f_1 (outside the reverse zone) and f_3, the adjacent line fault (outside the forward zone), are taken into consideration, and the simulation test is carried out, respectively, at different fault locations, different transition

TABLE 3 | Cosine similarity under different fault initial angles.

Fault location	Fault initial angle/(◦)	Fault distance/km	K	Result
f_2 in the zone	5	0	0.8078	In the zone
		15	0.9709	In the zone
		35	0.8940	In the zone
	30	0	0.8088	In the zone
		15	0.9920	In the zone
		35	0.8931	In the zone
	45	0	0.8191	In the zone
		15	0.9955	In the zone
		35	0.8630	In the zone
	90	0	0.9051	In the zone
		15	0.9975	In the zone
		35	0.8935	In the zone
f_3 outside the forward zone	5	0	–0.9893	Outside the zone
		15	–0.9950	Outside the zone
		35	–0.9854	Outside the zone
	30	0	–0.9544	Outside the zone
		15	–0.9942	Outside the zone
		35	–0.9919	Outside the zone
	45	0	–0.8802	Outside the zone
		15	–0.9928	Outside the zone
		35	–0.9903	Outside the zone
	90	0	–0.8810	Outside the zone
		15	–0.9780	Outside the zone
		35	–0.9902	Outside the zone
f_3 outside the forward zone	5	0	–0.8670	Outside the zone
		15	–0.9976	Outside the zone
		35	–0.9666	Outside the zone
	30	0	–0.8596	Outside the zone
		15	–0.9879	Outside the zone
		35	–0.9978	Outside the zone
	45	0	–0.8995	Outside the zone
		15	–0.9642	Outside the zone
		35	–0.9919	Outside the zone
	90	0	–0.8862	Outside the zone
		15	–0.9176	Outside the zone
		35	–0.9680	Outside the zone

resistances, and different fault inception angles. The sampling frequency is set at 50 KHz and the data window, 5 ms.

5.1 The Analysis of Internal and External Faults in Different Locations

In order to simulate and analyze the effectiveness of the protection scheme at different fault locations, assuming metal grounding short-circuit faults occur at f_1 (outside the reverse zone), f_2 (in the zone), and f_3 (outside the forward zone), respectively, with the initial fault angle of 60°. Among them, for f_2, starting from 0km, simulated fault points are set every 5 km away from the positive direction of M; for f_3, the right exit of N end is taken as the reference point outside the positive zone, and starting from 0km, simulated fault points are set every 5 km from the positive direction of N; for f_1, the left exit of Mend is taken as the reference point outside the negative zone, and starting from 0km, simulated fault points are set every 5 km from the negative direction of M. After computing the current waveform similarity of M、 N at both ends, the results are shown in **Table 1**.

As shown in **Table 1**, in case of fault in the zone, the waveform similarity of both sides of the line is close to 1, indicating that the current waveform on both sides of the line is highly correlated; when the fault occurs outside the zone, value of waveform similarity is close to -1, indicating that the current waveform on both sides is negatively correlated. It can be seen from **Table 1** that the internal and external faults can be accurately identified by the calculation results of cosine similarity.

5.2 The Identification of Internal and External Faults Under Different Transition Resistances

As simulated analysis of effectiveness of the protection scheme, the transition resistances are 0.1Ω, 10Ω, 10Ω, and 100Ω,respectively,

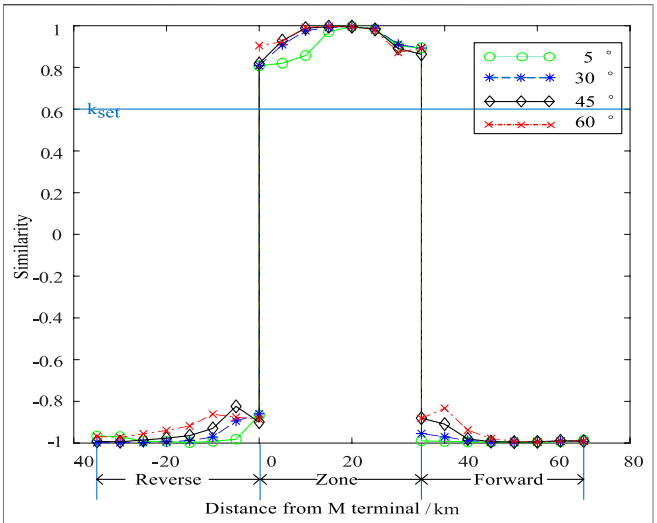

FIGURE 9 | Similarity at different initial fault angles.

and the initial fault angle is $\theta = 60^{\circ}$. The setting of fault point is the same as that in **Section 5.1**. The fault current in and outside the zone is detected, and the mode component after phase-mode transformation is taken for synchronous squeezed wavelet transformation, and the similarity of the reconstructed signal can be calculated. Due to limited space, this article provides only the calculation results of waveform similarity at the beginning, midpoint, and end of outside the reverse zone, in the zone, and outside of forward zone under different transition resistance in **Table 2**.

The waveform similarity calculation results of different fault locations under different transition resistances are shown in **Figure 8**.

In **Figure 8**, the abscissa is the distance from the fault point to the protection device, M, and the negative sign indicates the reverse fault; the ordinate is the calculation result of the current waveform similarity of M、N at both ends; the calculation results under different transition resistances are represented by different line types; those parallel to the abscissa are the thresholds (k_{set}) set in this article. It can be seen from **Table 2** and **Figure 8** that under different transition resistances, the similarity of current waveforms at both ends is greater than 0.6 in the case of internal fault, and much less than 0.6 in the case of external fault.

5.3 The Identification of Internal and External Faults at Different Fault Inception Angles

The effectiveness of the protection scheme is analyzed when the fault inception angles are5°,30°,45°, and 90°, respectively, and the transition resistance is 5Ω. Due to limited space, this article only gives the calculation results of waveform similarity at the beginning, midpoint, and end of outside the reverse zone, in the zone, and outside of forward zone at different fault inception angles, as shown in **Table 3**.

The waveform similarity calculation results of different fault locations at different fault inception angles are shown in **Figure 9**.

It can be seen from **Table 3** and **Figure 8** that, at different fault inception angles, the similarity of current waveforms at both ends is greater than 0.6 in the case of internal fault, and much less than 0.6 in the case of external fault.

It can be seen from **Figures 8**, **9** that the similarity value of the fault in the zone is greater than the threshold value, and that of the fault outside the zone is less than the threshold value. When the fault occurs at different initial fault angles, faults can be correctly identified by the protection scheme, which shows that the protection scheme is less affected by the initial fault angle.

From the above simulation results, it can be seen that this protection scheme based on synchronous squeezed wavelet and waveform similarity can accurately identify the internal and external faults when they occur at different fault locations, under different transition resistances, and at different fault initial angles, so as to reliably protect the line.

6 CONCLUSION

In this article, the propagation characteristics of fault transient current in the penetrating co-phase traction power supply system during internal and external faults are analyzed, and a protection scheme for the co-phase traction direct power supply system based on synchronous squeezed wavelet transformation and waveform similarity is proposed. The theoretical analysis and simulation results show the following:

(1) The scheme has the advantages of short time window, easy calculation, and good rapidity
(2) The waveform of fault transient current detected at both ends is basically the same and the polarity change direction is the same as well in the case of internal fault; as for external fault, the waveform of fault transient current detected at both ends is quite different, and the polarity change direction is opposite
(3) The synchronous squeezed wavelet transform can achieve lossless and invertible transformation, and the processed fault transient current can accurately represent the fault information
(4) A large number of simulation experiments show that the protection scheme based on synchronous squeezed wavelet transform and waveform similarity can quickly and accurately distinguish the internal and external faults and can act reliably at different fault locations, under different transition resistances and at different initial fault angles

DATA AVAILABILITY STATEMENT

The original contributions presented in the study are included in the article/Supplementary Material; further inquiries can be directed to the corresponding author.

AUTHOR CONTRIBUTIONS

SC was responsible for methodology, formal analysis, and validation. WZ was responsible for review and supervision and contributed to the conception and design of the study. ZZ was responsible for simulation, data analysis, and manuscript writing. HL and PL wrote sections of the manuscript. GB and CX were responsible for the derivation of the formula. All authors have read and approved the final version.

FUNDING

This work was supported by the National Natural Science Funds of China (No. 51767012).

REFERENCES

Biswas, S. K., and Milanfar, P. (2016). One Shot Detection with Laplacian Object and Fast Matrix Cosine Similarity. *IEEE Trans. Pattern Anal. Mach. Intell.* 38 (3), 546–562. doi:10.1109/tpami.2015.2453950

Daubechies, I., Lu, J., and Wu, H.-T. (2011). Synchrosqueezed Wavelet Transforms: An Empirical Mode Decomposition-like Tool. *Appl. Comput. Harmonic Anal.* 30 (2), 243–261. doi:10.1016/j.acha.2010.08.002

Deng, F., Li, X., Zeng, X., Leng, Y., Ni, J., Ma, S., et al. (2018). Research on Single-End Traveling Wave Based Protection and Fault Location Method Based on Waveform Uniqueness and Feature Matching in the Time and Frequency Domain[J]. *Proc. CSEE* 38 (05), 1475–1487. doi:10.13334/j.0258-8013.pcsee.170899

Duan, J., Li, H., Yang, L., and Zhao, Z. (2019). Transient-based Directional Protection Using Synchrosqueezing Wavelet Transforms for AC Transmission Lines in HVAC/DC Hybrid System[J]. *Proc. CSEE* 39 (13), 3833–3842. doi:10.13334/j.0258-8013.pcsee.180669

Han, L., Zhang, J., and Huang, Z. (2016). Surface Wave Removal with Synchrosqueezing Wavelet Transform[J]. *Oil Geophys. Prospecting* 51 (01), 71–79+19. doi:10.13810/j.cnki.issn.1000-7210.2016.01.010

Hongchun, S., Xincui, T., Jun, D., Guangbin, Z., Yi, Y., and Shiyun, S. (2012). Identification between Internal and External Faults of ±800kV HVDC Transmission Lines Based on Voltage Correlation[J]. *Proc. CSEE* 32 (04), 151–160+5. doi:10.13334/j.0258-8013.pcsee.2012.04.022

Li, B., Zhang, J., Liu, H., and Li, H. (2019). Fault Location of HVDC Transmission Lines Based on Waveform Similarity Analysis[J]. *Electric Power Automation Equipment* 39 (09), 27–32+53. doi:10.16081/j.epae.201909001

Li, B., Qiu, H., Chao, H., Zhang, Y., and Jiang, Y. (2018). High-speed Direction protection of Flexible DC System Based on Voltage Source Converter[J]. *Electric Power Automation Equipment* 38 (02), 1–8. doi:10.16081/j.issn.1006-6047.2018.02.001

Li, Q. (2014). On New Generation Traction Power Supply System and its Key Technologies for Electrification Railway[J]. *J. Southwest Jiaotong Univ.* 49 (04), 559–568. doi:10.3969/j.issn.0258-2724.2014.04.001

Li, Z., He, Z., Guo, T., et al. (2019). Transient Protection Method for Transmission Lines Based on Similarity of Time-Frequency Matrix[J]. *Automation Electric Power Syst.* 43 (05), 121–134. doi:10.7500/AEPS20180806002

Li, Z., Guo, T., Zeng, X., Fan, C., and Xiong, Y. (2018). Wave Correlation Analysis Based Transient Protection Method for Transmission Lines[J]. *Proc. CSU-EPSA* 30 (08), 44–50. doi:10.3969/j.issn.1003-8930.2018.08.008

Li, Z., Jiang, W., Abu-Siada, A., Li, Z., Xu, Y., and Liu, S. (2021). Research on a Composite Voltage and Current Measurement Device for HVDC Networks. *IEEE Trans. Ind. Electron.* 68 (9), 8930–8941. doi:10.1109/tie.2020.3013772

Liu, Y., Yang, N., Dong, B., Wu, L., Yan, J., Shen, X., et al. (2020). Multi-Lateral Participants Decision-Making: A Distribution System Planning Approach with Incomplete Information Game. *IEEE Access* 8, 88933–88950. doi:10.1109/access.2020.2991181

Pan, D., Tian, L., and Zhou, H. (2014). Characteristics of Travelling Wave Propagation in Catenary of High-Speed Railway[J]. *J. China Railway Soc.* 36 (02), 25–30. doi:10.3969/j.issn.1001-8360.2014.02.004

Shen, X., Ouyang, T., Khajorntraidet, C., Li, Y., Li, S., and Zhuang, J. (2022). Mixture Density Networks-Based Knock Simulator. *Ieee/asme Trans. Mechatron.* 27, 159–168. doi:10.1109/TMECH.2021.3059775

Shen, X., Ouyang, T., Yang, N., and Zhuang, J. (2021). Sample-based Neural Approximation Approach for Probabilistic Constrained Programs. *IEEE Trans. Neural Netw. Learn. Syst.*, 1–8. doi:10.1109/TNNLS.2021.3102323

Shen, X., and Raksincharoensak, P. (2021a). Pedestrian-aware Statistical Risk Assessment. *IEEE Trans. Intell. Transport. Syst.*, 1–9. doi:10.1109/TITS.2021.3074522

Shen, X., and Raksincharoensak, P. (2021b). Statistical Models of Near-Accident Event and Pedestrian Behavior at Non-signalized Intersections. *J. Appl. Stat* doi:10.1080/02664763.2021.1962263

Shen, X., Zhang, Y., Sata, K., and Shen, T. (2020a). Gaussian Mixture Model Clustering-based Knock Threshold Learning in Automotive Engines. *IEEE/ASME Trans. Mechatron.* 25 (6), 2981–2991. doi:10.1109/TMECH.2020.3000732

Shen, X., Zhang, X., Ouyang, T., Li, Y., and Raksincharoensak, P. (2020b). Cooperative Comfortable-Driving at Signalized Intersections for Connected and Automated Vehicles. *IEEE Robot. Autom. Lett.* 5 (4), 6247–6254. doi:10.1109/LRA.2020.3014010

Shen, X., Zhang, Y., Shen, T., and Khajorntraidet, C. (2017). Spark advance Self-Optimization with Knock Probability Threshold for Lean-Burn Operation Mode of SI Engine. *Energy* 122, 1–10. doi:10.1016/j.energy.2017.01.065

Song, G., Hou, J., Guo, B., and Chen, Z. (2020). Pilot protection of Hybrid MMC DC Gridbased on Active Detection. *J. Prot. Control. Mod. Power Syst.* V5 (1), 82–96. doi:10.1186/s41601-020-0152-2

Song, G., Ran, M., Xu, C., Jin, X., Liu, T., and Ma, Z. (2014). A New Single-End Current Based Whole-Line Quick-Action Protection for VSC-HVDC Transmission Lines[J]. *Power Syst. Techn.* 38 (05), 1402–1407. doi:10.13335/j.1000-3673.pst.2014.05.043

Thakur, G., Brevdo, E., Fučkar, N. S., and Wu, H.-T. (2013). The Synchrosqueezing Algorithm for Time-Varying Spectral Analysis: Robustness Properties and New Paleoclimate Applications. *Signal. Process.* 93 (5), 1079–1094. doi:10.1016/j.sigpro.2012.11.029

Wang, C., Jia, K., Bi, T., Zhao, Q., and Zhu, R. (2019). Protection for Flexible DC Distribution System Based on Transient Current Waveform Similarity Identification[J]. *Power Syst. Techn.* 43 (10), 3823–3832. doi:10.13335/j.1000-3673.pst.2018.2163

Xiong, L., Wu, G., and Wang, Z. (2019). Study on Fault Location of Multi Measuring Points Traveling Wave Method Based on IHHT in All Parallel at Traction Network[J]. *Trans. China Electrotechnical Soc.* 34 (15), 3244–3252. doi:10.19595/j.cnki.1000-6753.tces.180834

Xue, Y., Duan, J., Xu, B., and Li, J. (2012). Characteristic Analysis of Fault Generated Traveling Waves in Direct Feeding Traction Network[J]. *Power Syst. Techn.* 36 (04), 167–173. doi:10.13335/j.1000-3673.pst.2012.04.041

Yang, N., Ye, D., Zhou, Z., Cui, J., Chen, D., and Wang, X. (2018). Research on Modelling and Solution of Stochastic SCUC under AC Power Flow Constraints. *IET Generation, Transm. Distribution* 12 (15), 3618–3625. doi:10.1049/iet-gtd.2017.1845

Yang, N., Huang, Y., Hou, D., Liu, S., Ye, D., Dong, B., et al. (2019). Adaptive Nonparametric Kernel Density Estimation Approach for Joint Probability Density Function Modeling of Multiple Wind Farms. *Energies* 12, 1356. doi:10.3390/en12071356

Yang, N., Liu, S., Deng, Y., and Xing, C. (2021b). An Improved Robust SCUC Approach Considering Multiple Uncertainty and Correlation. *IEEJ Trans. Elec Electron. Eng.* 16, 21–34. doi:10.1002/tee.23265

Yang, N., Yang, C., Wu, L., Shen, X., Jia, J., Li, Z., et al. (2022). Intelligent Data-Driven Decision-Making Method for Dynamic Multisequence: An E-Seq2Seq-Based SCUC Expert System. *IEEE Trans. Ind. Inf.* 18, 3126–3137. doi:10.1109/TII.2021.3107406

Yang, N., Yang, C., Xing, C., Ye, D., Jia, J., Chen, D., et al. (2021a). Deep Learning-based SCUC Decision-making: An Intelligent Data-driven Approach with Self-learning Capabilities. *IET Generation Trans. Dist* 16, 629–640. doi:10.1049/gtd2.12315

Yu, M., Wang, B., Chen, X., Wang, W., and Jin, J. (2017b). Application of Synchrosqueezed Wavelet Transform for Extraction of the Oscillatory

Parameters of Low Frequency Oscillation in Power Systems[J]. *Trans. China Electrotechnical Soc.* 32 (06), 14–20. doi:10.19595/j.cnki.1000-6753.tces.2017.06.003

Yu, B., Wang, B., Wang, W., Zhang, L., Cheng, Y., et al. (2017a). Power System Time-Varying Transient Harmonics Detection Based on SWT[J]. *Trans. China Electrotechnical Soc.* 32 (S1), 50–57. doi:10.19595/j.cnki.1000-6753.tces.L70483

Zhang, L., Xie, Y., Ye, J., Xue, T., Cheng, J., Li, Z., et al. (2021). Intelligent Frequency Control Strategy Based on Reinforcement Learning of Multi-Objective Collaborative Reward Function. *Front. Energ. Res* doi:10.3389/fenrg.2021.760525

Zhen, L., Jia, K., Bi, T., Fang, Y., and Yang, Z. (2019). Cosine Similarity Based Pilot Protection of Teed Transmission Line Connected to Renewable Energy Power Plants[J]. *Automation Electric Power Syst.* 43 (18), 111–124. doi:10.7500/AEPS20181008011

Conflict of Interest: Authors HL and CX were employed by the company Yunnan Power Grid Co., Ltd.

The remaining authors declare that the research was conducted in the absence of any commercial or financial relationships that could be construed as a potential conflict of interest.

Publisher's Note: All claims expressed in this article are solely those of the authors and do not necessarily represent those of their affiliated organizations, or those of the publisher, the editors, and the reviewers. Any product that may be evaluated in this article, or claim that may be made by its manufacturer, is not guaranteed or endorsed by the publisher.

frontiers | Frontiers in Energy Research

ORIGINAL RESEARCH
published: 04 April 2022
doi: 10.3389/fenrg.2022.862795

Improved Electrogeometric Model of UHV Transmission Line Based on Long Gap Discharge and Its Application

Yuanchao Hu[1], Minghao Yang[1], Lu Qu[2], Yunzhu An[1], Jing Wang[1], Yan Cheng[1], Xiao Sha[1], Qingchen Wang[1], Chenghui Ma[3], Bingchen An[3] and Dan Chen[3]*

[1]School of Electrical and Electronic Engineering, Shandong University of Technology, Zibo, China, [2]Electric Power Research Institute, China Southern Power Grid, Guangzhou, China, [3]Jining Huayuan Thermal Power Plant, Jining, China

Based on long air gap discharge test data and lightning return stroke observation data, an improved electrogeometric model (EGM) considering terrain conditions is established and verified to analyze the lightning shielding performance of UHV transmission lines. The striking distance formula is modified as $r_s = 0.13\,(I^2 + 40I)^{0.814}$. In this paper, the lightning shielding failure rate of three-phase conductors of EHV and UHV transmission lines calculated by the improved EGM model is consistent with the lightning observation data of actual transmission lines in Japan and the scaled lightning discharge simulation experimental results of UHV transmission lines in plains and mountainous areas of China, which verifies the applicability of the improved EGM model to evaluate the lightning shielding performance of large-scale UHV transmission lines. The improved EGM model is applied to evaluate the influence of tower type and slope steepness on the shielding failure tripping rate of UHV transmission lines. The shielding failure tripping rate of the SZ322 tower is higher than that of the SZT1 tower, and the shielding failure tripping rate of UHV transmission lines is greatly affected by slope gradient and increases with the increase of slope gradient.

Keywords: UHV transmission line, lightning shielding, electrogeometric model, striking distance formula, long air gap discharge

OPEN ACCESS

Edited by:
Xun Shen,
Tokyo Institute of Technology, Japan

Reviewed by:
Hardeep Singh,
Sophia University, Japan
Sandeep Kumar,
Lovely Professional University, India

****Correspondence:***
Yunzhu An
anyunzhu2006@163.com

Specialty section:
This article was submitted to Smart Grids, a section of the journal Frontiers in Energy Research

Received: *26 January 2022*
Accepted: *14 February 2022*
Published: *04 April 2022*

Citation:
Hu Y, Yang M, Qu L, An Y, Wang J, Cheng Y, Sha X, Wang Q, Ma C, An B and Chen D (2022) Improved Electrogeometric Model of UHV Transmission Line Based on Long Gap Discharge and Its Application. Front. Energy Res. 10:862795. doi: 10.3389/fenrg.2022.862795

1 INTRODUCTION

In the context of achieving the goal of carbon peaking and carbon neutralization, China is accelerating the construction of UHV to meet the needs of large-scale development and consumption of clean energy such as wind and solar energy. Large-scale transmission lines are exposed to the natural environment and are vulnerable to lightning strike during thunderstorm season (Hengxin et al., 2016). The lightning shielding failure of Durong line of the 1,000 kV transmission line in China occurred in 2015 and 2017. In addition, the lightning shielding failure of Binjin line, Fufeng line, and Jinsu line of the ±800 kV transmission line in China has occurred more than 10 times since 2010 (Chongyu et al., 2015). The UHV transmission line has large transmission capacity and low loss, but it is more prone to lightning shielding failure than 220 kV and below transmission lines, and the harm and loss caused by the accident are even greater. The operation experience of relevant industries has also shown that the current lightning tripping fault of UHV transmission lines is mainly caused by lightning shielding failure (Shen et al., 2021; Shen and Raksincharoensak, 2021). One of the reasons is that the current design of the lightning shielding system of UHV transmission lines draws on the calculation model of low-voltage transmission lines,

resulting in large calculation errors. Therefore, it is necessary to study the lightning shielding performance evaluation model for large-scale UHV transmission lines.

The electrogeometric model (EGM) method is mainly used to study the shielding failure performance of transmission lines, which is widely used by power enterprises IEC and IEEE. Since Wagner proposed the concept of lightning return stroke model in 1961 (Wagner and Hileman, 1961), many scholars have tried to improve the striking distance formula in various ways. In 1968, Whitehead and Armstrong firstly proposed the typical EGM model by using the 1–3 m gap discharge test (Armstrong and Whitehead, 1968). Since then, many scholars have further improved the typical EGM model on this basis to make the evaluation of lightning shielding performance of transmission lines more applicable. In 1985, the IEEE working group proposed the general striking distance formula and the striking distance coefficient based on various factors (Grant et al., 1985). These improved striking distance formulas based on the discharge test data of 1–4 m gap distance played an important guiding role in the lightning shielding performance of low-voltage transmission lines. With the improvement of the voltage level of transmission lines, especially the rapid development of UHV AC and DC transmission technology, the air gap is further lengthened, and the shielding failure of UHV transmission lines is too high and some fully shielded lines in the theoretical model cannot be well explained by the typical EGM model method.

In recent years, scholars have begun to try to combine the practical operation experience of transmission lines with the experimental data of longer gap discharge to improve the striking distance formula and striking distance coefficient in the EGM model (Wang et al., 2014; Yu et al., 2017). The striking distance formula of the EGM model is derived from the gap discharge test results and lightning observation empirical formula. Thus, the accuracy of the lightning empirical formula also affects the accuracy of the model. Taniguchi et al. conducted the gap discharge test with the maximum gap distance of 6 m in 2008, and improved the EGM model combined with the probability formula of return stroke velocity (Taniguchi et al., 2010). In 2014, Wang et al. carried out negative impulse discharge tests on 1–10 m long air gaps with two kinds of voltage waveforms of −20/2,500 μs and −80/2,500 μs (Wang et al., 2014; Yu et al., 2014). Then, they conducted lightning shielding simulation tests of UHV AC transmission lines with a scale of 1:12.5, and obtained the lightning shielding performance of scaled UHV transmission lines (Yunzhu, 2015). The above large-scale discharge test provides basic data for the correction of the striking distance formula and the striking distance coefficient in the EGM model suitable for UHV transmission lines. In addition, the relationship between the primary lightning stroke current I and the primary lightning discharge speed v_1 is the empirical formula $I = 2{,}400v_1^3$ estimated by a large number of theoretical analysis (Shen et al., 2021). In 1984, Idone et al. found that the speed of subsequent return strokes had a good nonlinear correlation with the peak lightning current through an artificial lightning experiment (Idone et al., 1984). Yu et al. (2017) combined the large-scale long air gap discharge data with the probability distribution of the return stroke velocity of the artificial lightning pilot channel of Idone, and proposed an improved stroke distance formula related to the lightning return stroke velocity. Since the striking distance formula is related to the dispersion probability of the return stroke velocity, the striking distance formula is a dispersion form related to the return stroke velocity. However, the actual lightning process is random, and the lightning return stroke speed does not only consist the limited lightning return stroke speed considered in its dispersion form. The relevant research by Idone et al. (1984) shows that the probability distribution law of Idone's return stroke velocity in the pilot channel of an artificially induced mine conforms to the relationship between return stroke velocity and current peak recommended by Lundholm (1957). Since the relationship between return stroke velocity and lightning current peak value proposed by Lundholm can be verified with the experimental data of artificial lightning induction in laboratory, the formula of striking distance in the EGM model can be modified to a formula only related to the amplitude of return stroke current (Yang et al., 2021a; Yang et al., 2021b).

In this paper, the data of large-scale long air gap negative discharge characteristics with the relationship between return stroke velocity and lightning current peak proposed by Lundholm (1957) modify the striking distance formula and the striking distance coefficient in the EGM model and use a calculation method to consider the incidence angle of lightning leader. The lightning shielding failure rate of ultra-high-voltage transmission lines in Japan is calculated by the improved EGM model in this paper, and the results are compared with the lightning observation data to verify the adaptability of the improved EGM model to the evaluation of lightning shielding failure rate of large-scale transmission lines. Combined with the simulation test of lightning shielding performance of UHV transmission lines, the influence of terrain conditions on the lightning shielding performance of UHV transmission lines is analyzed and compared with the calculation results of the improved EGM model in this paper. Finally, considering that the tower structure of 1,000 kV transmission lines in China is diverse, and the lightning shielding performance of transmission lines is greatly affected by terrain conditions, the improved EGM model is used to calculate and analyze the influence of tower structure and slope gradient on the lightning shielding performance of UHV transmission lines.

2 IMPROVED ELECTROGEOMETRIC MODEL BASED ON LONG GAP DISCHARGE RESULTS AND NATURAL LIGHTNING DATA

2.1 Relationship Between Natural Lightning Return Stroke Current and Return Stroke Velocity

At the beginning of the 1950s, some researchers found that the lightning return stroke speed was not stable (Lundholm, 1957). When the lightning leader falls, the leader head potential V_s is proportional to the primary lightning current I, and inversely

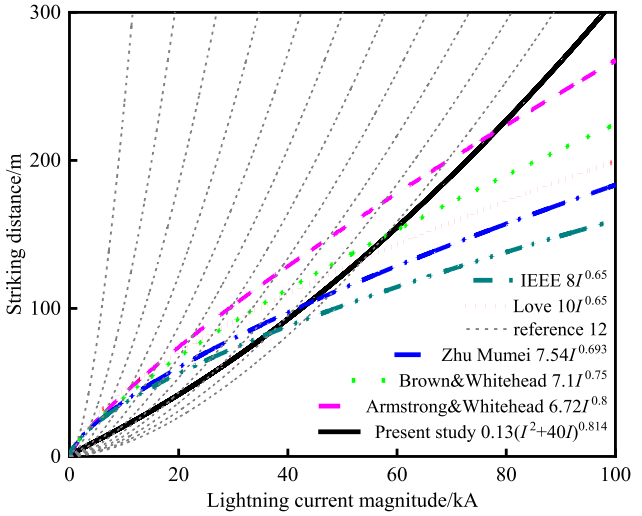

FIGURE 1 | Comparison of different striking distance formulas.

proportional to the primary lightning speed v_1. In 1963, Wagner established the relationship between lightning current amplitude I and lightning leader head potential V_s as shown in **Eq. 1** (Wagner, 1963):

$$V_s = 60\,(I/v_1) \times \ln(2r'/d') \tag{1}$$

where I is the primary lightning current, kA; v_1 is the lightning discharge speed with the speed of light as the unit value, p.u.; r' is the distance between the lightning leader head and the ground at the last jump, m; d' is the corona radius of the leader head, m. The long-term observation results show that r' and d' increase with lightning current I, while the variation of logarithm $\ln(2r'/d')$ is small. Taking $\ln(2r'/d')$ as 4.6, **Eq. 2** can be obtained.

$$V_s = 276\,(I/v_1) \tag{2}$$

Idone et al. (1984) found that there is a good nonlinear correlation between the speed of the subsequent return stroke and the peak lightning current through the artificial lightning experiment. Their research results basically verify the relationship between the return stroke speed recommended by Lundholm and the peak current as shown in **Eq. 3** (Lundholm, 1957):

$$v_{rs} = c\left(1 + W/I_p\right)^{-0.5} \tag{3}$$

where v_{rs} is the pilot return stroke speed, km/s. c is the speed of light, km/s. I_p is the peak return stroke current, kA. W is a constant. Idone et al. used the least square method to fit the experimental data and got $W = 40$.

2.2 Striking Distance Formula Based on Long Gap Discharge Results

The relationship between 50% negative switching impulse breakdown voltage (U50%) of the 1–10 m rod–rod gap and gap distance d is shown in **Eq. 4**.

$$U_{50\%} = 0.9667d^{0.614} \tag{4}$$

where $U_{50\%}$ is 50% negative switching impulse breakdown voltage, kV; d is gap distance, m.

By substituting **Eq. 3** into **Eq. 2**, the relationship between lightning current I and lightning leader tip potential V_s can be obtained as **Eq. 5**.

$$V_s = 276I\,(1 + 40/I)^{0.5} \tag{5}$$

Assuming that the $U_{50\%}$ of the rod–rod gap is equal to the tip potential of the lightning leader, the striking distance formula can be derived as **Eq. 6**.

$$r_s = 0.13\left(I^2 + 40I\right)^{0.814} \tag{6}$$

Comparison of different striking distance is shown in **Figure 1**. As the peak lightning current is less than 40 kA, the present striking distance in this paper is less than that of most scholars. When the peak lightning current exceeds 80 kA, the present striking distance is larger.

2.3 Striking Distance Coefficient

In the typical EGM model, the striking distances between lightning leader tip and the lightning conductor, each phase conductor, and the earth are the same (Anderson et al., 1993). However, factors such as terrain condition, operation voltage, and the upward leader process of the earth surface object will affect the striking distance. Subsequent scholars introduced the concept of striking distance coefficient to distinguish the striking distance difference between lightning leader tip and phase conductors, lightning conductor, and earth (Golde, 1977), as shown in **Eqs 7**, **8**.

$$r_g = K_g r_c \tag{7}$$

$$r_{gw} = K_{gw} r_c \tag{8}$$

where r_c, r_{gw}, and r_g are the striking distances of lead to conductor, ground line, and earth, respectively. K_g and K_{gw} are respectively the striking distance coefficient against ground and the striking distance coefficient against ground line.

Since the $U_{50\%}$ of the 1–4 m rod–plane gap is slightly higher than that of the rod–rod gap, previous scholars believe that the ground striking distance coefficient K_g should be less than 1 (Qian et al., 2010; Wenxia et al., 2015). Experimental results of longer air gap negative switching impulse discharge show that the $U_{50\%}$ of the rod-plane gap is lower than that of the rod–rod gap as gap distance exceeds 4 m (Grant et al., 1985). Thus, the coefficient K_{gw} was revised to 1.1. However, optical observation results of the physical discharge process (Wang et al., 2014) show that the downward streamer-leader discharge process of rod-plane gap is more obvious than that of rod–rod gaps under the negative switching impulse as the gap distance exceeds 4 m. It indicates that the final discharge length of rod–plane gaps is smaller than that of rod–rod gaps. Hence, taking the coefficient K_{gw} as 1.1 may overestimate the lightning attractive ability of the earth. In the present study, the striking distance coefficient K_g = 1.05 and K_{gw} = 1.

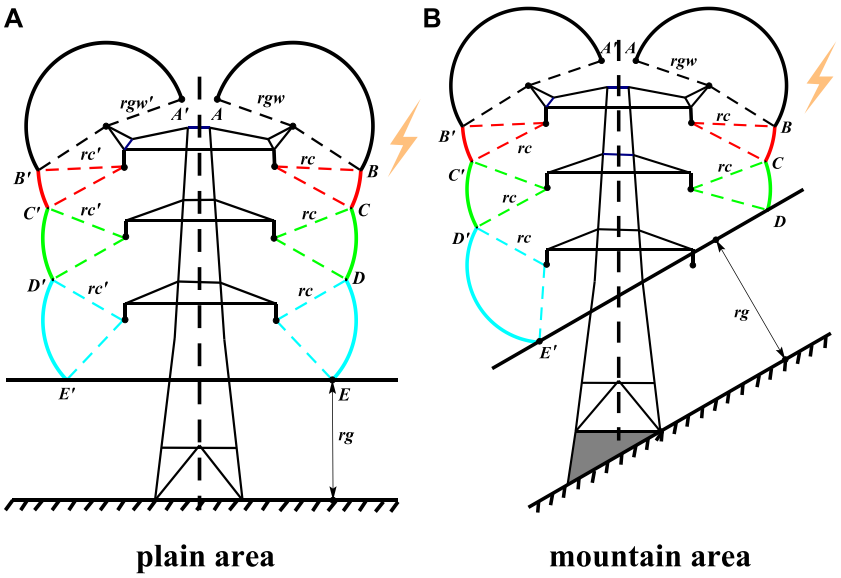

FIGURE 2 | Diagram of the EGM model for transmission lines in plains and mountainous areas. **(A)** Plains area. **(B)** Mountain area.

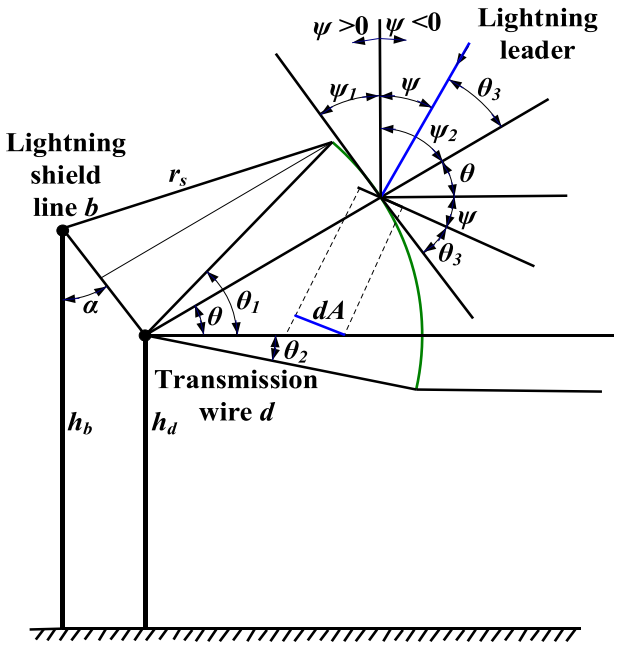

FIGURE 3 | Diagram of the EGM model calculation method.

2.4 Calculation Method of the Improved Electrogeometric Model

In the EGM model, it is considered that the development of the lightning downward leader is stochastic before reaching the critical striking distance of the stroke object. Hence, the probability distribution of lightning leader incidence in the range of −π/2 to π/2 angle has been considered as **Eq. 9**.

$$p(\psi) = 0.75\cos^3\psi \tag{9}$$

A schematic diagram of the EGM model under plains and mountainous terrain conditions is shown in **Figure 2**.

As shown in **Figure 2A**, arcs are made with the center of the lightning conductor and the three-phase conductor, respectively, and the radius of their respective striking distances. At this point, a curved surface is formed by arc AB, arc BC, arc CD, arc DE, and line EE′ along the direction of the transmission line. Only when the lightning downward leader falls into the positioning surface of the corresponding object is it believed that the lightning will strike the object. Thus, the arc BC, arc CD, and arc DE are also called the shielding arc. As the lightning return stroke current varies, the grounding conductors, phase conductors, and earth will be changed. For transmission lines in mountainous areas, as shown in **Figure 2B**, the shielding arc of the lines on both sides of the tower is not symmetrical due to the angle of the hillside. This is due to the inclination of the striking distances of earth line DE, which makes the shielding arc of the line facing the slope side decrease, while the other side increases. Besides, only when the lightning return stroke leader current exceeds the lightning current withstand level of transmission line $I_{\min}$ can insulation flashover occur on the transmission line.

The detailed calculation method of the EGM model used in this paper is shown in **Figure 3**. At a certain angle θ and ψ, the unit area of the shielding arc per unit length of the line perpendicular to the leading incident direction dA is

$$dA = r_s d\theta \cos\theta_3 = r_s d\theta \sin(\theta + \psi) \tag{10}$$

The corresponding exposure area of a lightning leader with a certain amplitude and incident angle perpendicular to the incident direction of the leader is

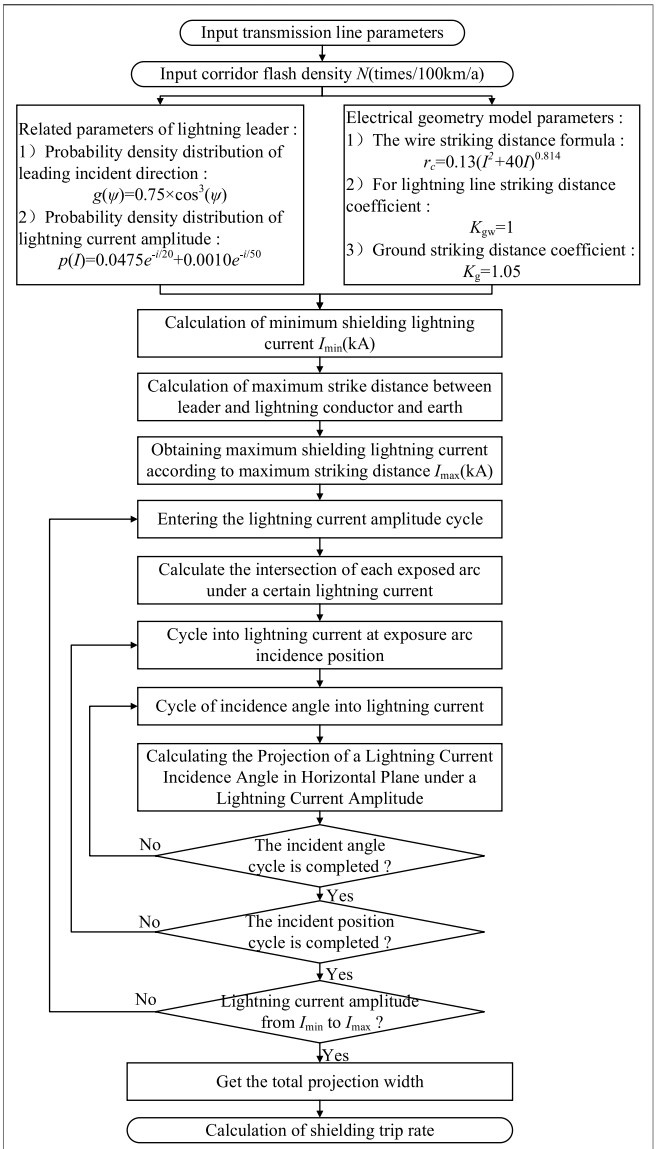

FIGURE 4 | Improved EGM model calculation flow chart.

$$X = \int_{-\theta_2}^{\theta_1} \int_{-\psi_2}^{\psi_1} r_s \sin(\theta + \psi) g(\psi) d\psi d\theta \tag{11}$$

where $g(\psi)$ is the probability density function of the incident direction of the lightning leader, $-\pi/2 < \psi < \pi/2$.

The number of unit length line shielding strike fault is

$$n = N \int_{r_{min}}^{r_{max}} Xp(r_s) dr_s = N \int_{I_{min}}^{I_{max}} Xp(I) dI \tag{12}$$

where N is the number of falling thunders per year per unit area, strokes/km^2/a; $p(r_s)$ and $p(I)$ are the probability distribution density function of r_s and I, respectively; r_{max} is the maximum striking distance that can cause shielding failure; r_{min} is the minimum striking distance that can cause shielding failure tripping, m; I_{max} is the maximum shielding current; I_{min} is the minimum shielding trip lightning current, namely, line lightning withstand level, kA. The calculation process of the present EGM model is shown in **Figure 4**. It is mainly used to calculate the maximum and minimum shielding trip lightning current of the line, and then according to **Eqs 11**, **12**, concurrency points in turn, the angle of lightning incident and lightning incident position and amplitude of lightning current are circulated. Finally, the total projection width is calculated and the shielding tripping rate is obtained.

3 VERIFICATION AND ANALYSIS OF THE IMPROVED EGM MODEL WITH OBSERVATION AND EXPERIMENTAL RESULTS

3.1 Comparison With Observation Data of 500 kV and UHV Transmission Lines in Japan

In order to verify the applicability of the present EGM model, the present EGM model in this paper is applied to calculate the lightning stroke rate to power lines of 500 kV and UHV transmission lines in Japan. The specific parameters of 500 kV and UHV double-circuit transmission lines on the same tower in Japan are shown in **Table 1**.

For the lightning density N_g, the typical EGM model is 3.0 strokes/km^2/a, the 500 kV line area in Japan is 4.9 strokes/km^2/a, and the UHV line area is 5.2 strokes/km^2/a (Taniguchi et al., 2010).

The probability density of lightning current amplitude is

$$P(i) = 0.0475e^{-\frac{i}{20}} + 0.001e^{-\frac{i}{50}} \tag{13}$$

In this paper, the improved EGM model results are compared with the typical EGM model results, Taniguchi et al. (2010) and Yu et al. (2017) improved EGM model results, and long-term lightning observation results in Japan (Taniguchi et al., 2009) are shown in **Figure 5**.

In order to facilitate accurate comparison, the lightning stroke rate of each phase p_A, p_B, p_C in each model is divided by their total P to obtain the proportion of each phase P_A, P_B, P_C in each model as shown in **Eq. 14**.

$$P_A = \frac{p_A}{P}, P_B = \frac{p_B}{P}, P_C = \frac{p_C}{P}, \tag{14}$$

As shown in **Figure 5A**, for 500 kV transmission lines, the total lightning stroke rate of the improved EGM model in this paper and the improved EGM model in Taniguchi et al. (2010) is slightly different from the actual observation data, which is 7% larger and 6% smaller, respectively, and the lightning stroke rate of each phase calculated by the two models is 45%:30%:25% and 30%:32%:38%, respectively. Compared with the typical EGM model and the improved EGM model in Yu et al. (2017), the two models are closer to the 36%:40%:24% of

TABLE 1 | Size parameters of double-circuit AC transmission lines on the same tower in Japan.

Voltage level of transmission line (kV)	Lines	Average height (m)	Horizontal distance (m)
500	Phase A	64.00	8.00
	Phase B	53.00	8.40
	Phase C	42.00	8.80
	Grounding line	93.33	11.30
1,000	Phase A	94.67	15.50
	Phase B	75.67	16.00
	Phase C	56.67	16.50
	Grounding line	128.00	19.00

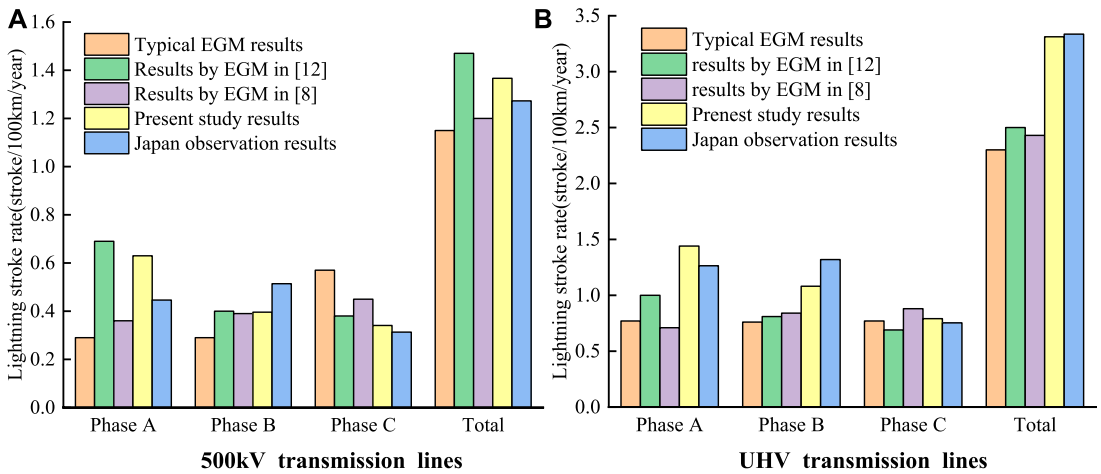

FIGURE 5 | Comparison of different lightning stroke rate calculation methods with actual observation data. **(A)** 500 kV transmission lines. **(B)** UHV transmission lines.

the actual operation observation results in Japan (Taniguchi et al., 2009).

As shown in **Figure 5B**, for UHV transmission lines, the lightning stroke rate calculated by the present EGM model is closer to the observation results in Japan with a deviation of −0.73%. The calculated shielding failure ratio of each phase is 43: 33:24, which is closest to the 38:39:23 observed in Japan (Taniguchi et al., 2009) compared to the other three models. This also reflects that the improved EGM model in this paper is more suitable for the calculation of lightning shielding performance of large-scale UHV transmission lines.

3.2 Comparison With Lightning Discharge Simulation Test Results With Scaled UHV Transmission Line

In the past few years, a series of lightning discharge tests of scaled UHV transmission line have been carried out under different terrain conditions in China (Yu, 2012; Wang et al., 2014; Yu et al., 2014; Yunzhu et al., 2014; Yunzhu, 2015; Zongxi et al., 2016; Yu et al., 2017). In these tests, a 10-m-long steel rod with a spherical tip was applied to simulate the downward leader. The scaled ratio of UHV transmission line was 1:12.5. In Yunzhu (2015), Yu et al. (2017), Yunzhu et al. (2014), and Zongxi et al. (2016), the gap distance between the high voltage rod tip and the scaled line was 5 m. According to the ratio of 1:12.5, the striking distance of the actual line can be calculated to be 62.5 m. According to the improved striking distance formula as **Eq. 6**, the lightning return stoke current can be deduced as 28.7 kA.

To compare calculation results of the present EGM model with lightning discharge simulation test results, the ratio of each phase line effective shielding arcs *l*a, *l*b, *l*c to total effective shielding arc *L* under a lightning current of 28.7 kA is calculated by the present EGM model as shown in **Eq. 15**.

$$P_a = \frac{l_a}{L}, P_b = \frac{l_b}{L}, P_c = \frac{l_c}{L} \tag{15}$$

In the calculation, the tower type is SZ322, which is the same as that in simulation tests in Yunzhu (2015), Yu et al. (2017), Yunzhu et al. (2014), and Zongxi et al. (2016). The protection angle of UHV transmission line is 1.5°. The slope angle of mountain ground is 30°. The ratio of each phase line shielding

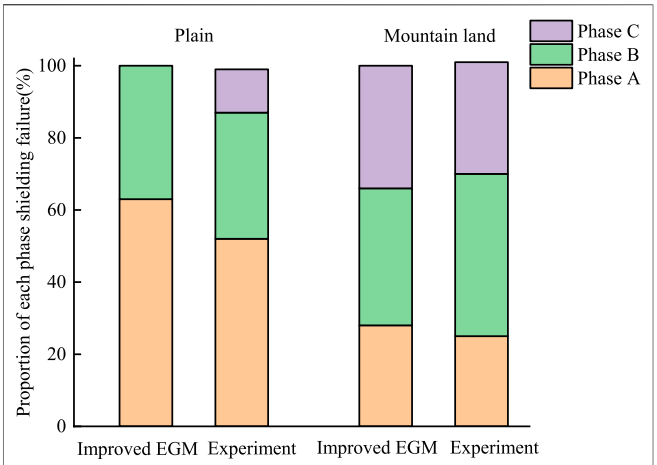

FIGURE 6 | Comparison chart of shielding failure proportion of each phase line.

failure calculated by the improved EGM model is compared with the lightning discharge test results of UHV transmission lines (Yunzhu, 2015), as shown in **Figure 6**.

As shown in **Figure 6**, in a plains area, the ratio of the ABC three-phase line shielding failure rate calculated by the improved EGM model in this paper is 63%:37%:0, and the probability of the ABC three-phase conductor being attacked in the test is 52%:35%:12%. Both show that the shielding failure probability of phase A is the highest, followed by phase B and phase C. Considering the dispersion of the discharge direction in the lightning discharge simulation experiment, there is a certain deviation between the improved EGM model and the test data. In mountainous areas, the ratio of the ABC three-phase line shielding failure calculated by the improved EGM model is 28%:38%:34%, which is in good agreement with those results in lightning discharge tests of the scaled UHV transmission line of 25%:44%:31%.

According to the comparison results in **Section 2.1** and **Section 2.2**, the calculation results of shielding failure ratio of three-phase lines of large-scale transmission lines by the present improved EGM model in this paper are consistent with observation results of lightning shielding failure of EHV and UHV transmission lines in Japan and the lightning discharge tests of scaled UHV transmission lines in plains and mountainous areas in China. The above results indicate that the present EGM model proposed in this paper is more appropriate for lightning shielding performance evaluation of large-scale transmission lines.

4 THE EFFECT OF TERRAIN AND TOWER STRUCTURE ON LIGHTNING SHIELDING PERFORMANCE OF UHV TRANSMISSION LINES

To study the effect of terrain and tower structure on lightning shielding performance of UHV transmission lines, two tower structures, SZT1 and SZ322, are applied to calculate the lightning shielding failure tripping out rate of UHV transmission lines in plains and mountainous areas. The terrain slope angle is set between 0° and 70° to simulate different terrains. The two tower structures, SZT1 and SZ322, are shown in **Figure 7**. The detailed transmission line parameters are shown in **Table 2**.

The calculation lightning shielding failure tripping out rate by the present EGM model is shown in **Figure 8**. The lightning shielding failure tripping out rate of UHV transmission lines increases with the terrain slope angle. Because the terrain slope angle is 0°, the shielding failure tripping out rate of the line is close to 0. Because the terrain slope angle is 30°, the shielding failure tripping out rates of the SZT1-type tower line and the SZ322-type tower line are 0.12 strokes/(100 km·a) and 0.13 strokes/(100 km·a), respectively. When the terrain slope reaches 70°, the shielding failure trip rates of the two tower lines reach 0.38 strokes/(100 km·a) and 0.41 strokes/(100 km·a), respectively. Besides, under the same terrain condition, the shielding failure tripping out rate of the SZ322 tower line is higher than that of the SZT1 tower line. It is due to the fact that the height of the SZ322 tower line is significantly higher than that of the SZT1 tower line. The grounding line of the SZ322 tower line is much higher than that of the SZT1 tower line, but the height of the C phase conductor is not much different. The lightning protection effect of grounding line in the SZ322 tower line on the conductor is weaker than that of the SZT1 tower line. Therefore, the probability of lightning shielding failure tripping out rate of the SZ322 tower line is higher than that of SZT1 in a mountainous area.

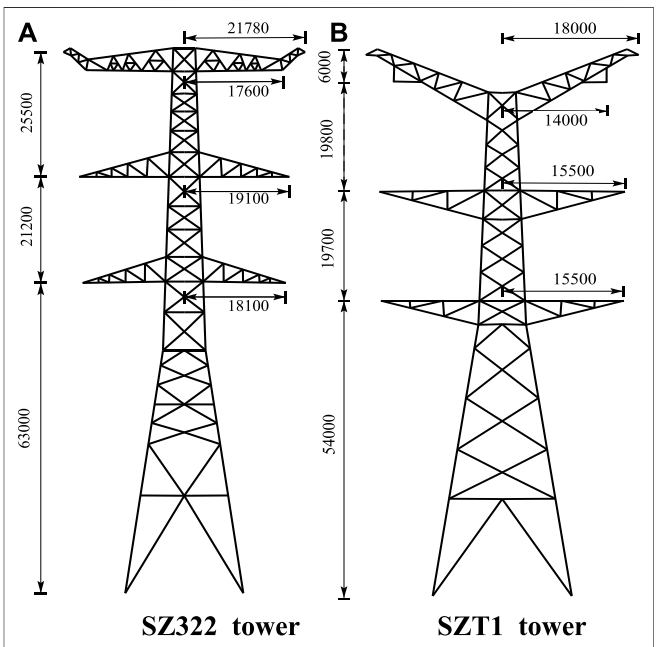

FIGURE 7 | Structure diagram of SZT1 and SZ322 double-circuit tower on the same tower. **(A)** SZ322 tower, **(B)** SZT1 tower.

TABLE 2 | Practical size parameters of SZT1 and SZ322 tower lines.

Tower type	Lines	Average height (m)	Horizontal distance (m)
SZ322	Phase A	83.7	17.6
	Phase B	62.2	19.1
	Phase C	41	18.1
	Grounding line	104	21.78
SZT1	Phase A	68.17	14
	Phase B	48.37	15.5
	Phase C	38.67	15.5
	Grounding line	85.2	18

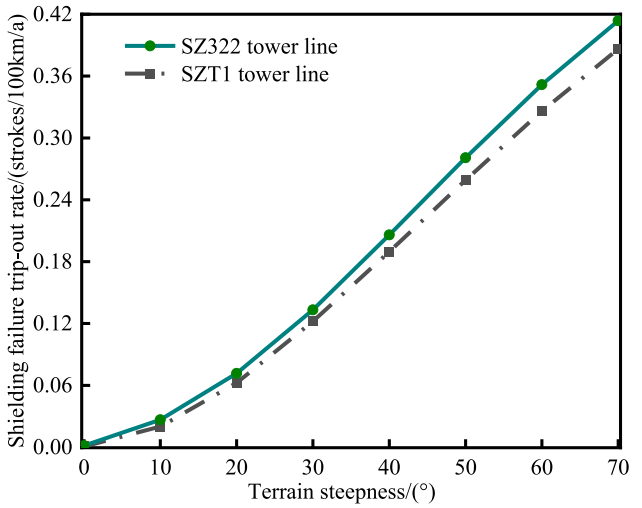

FIGURE 8 | Influence of slope steepness under different tower models on shielding failure tripping out rate of 1,000 kV lines in China.

5 CONCLUSION

In order to analyze the lightning shielding performance of UHV transmission line more accurately, based on the long gap discharge test data and the lightning current return stroke current formula verified by researchers, this paper modifies the existing striking distance formula and uses the improved EGM model and the lightning simulation test of UHV transmission lines to analyze the influence of topography on the lightning tripping out rate of large-scale transmission lines.

(1) Based on the long air gap discharge test data of rod–rod gaps and lightning current return stroke velocity formula, the proposed striking distance formula is $r_c = 0.13\ (I^2 + 40I)^{0.814}$, the earth striking distance coefficient is 1.05, and the ground wire striking distance correction coefficient is 1.0.

(2) The calculation results of lightning shielding failure rate of UHV transmission lines by the present EGM model consist of the lightning observation data of the UHV transmission line in Japan and the lightning discharge simulation test results of scaled UHV transmission lines in plains and mountainous areas in China. which verifies the applicability of the improved EGM model in large-scale transmission lines.

(3) The tower configuration and terrain steepness have a significant impact on the shielding failure tripping out rate of 1,000 kV lines in China. The shielding failure tripping rate of the SZ322 tower UHV line is higher than that of the SZT1 tower line. With the increase of terrain steepness, line shielding failure trip rate is also increasing rapidly.

DATA AVAILABILITY STATEMENT

The original contributions presented in the study are included in the article/Supplementary Material, further inquiries can be directed to the corresponding author.

AUTHOR CONTRIBUTIONS

YH: Conceptualization and writing—original draft preparation; MY: software and analysis; LQ: project administration; YA: software; JW: funding acquisition and validation; YC: Drawing; XS: supervision; QW: revision; CM: figures; BA: supervision; DC: figures.

FUNDING

This work was supported in part by the National Natural Science Foundation of China under Grant 51807113 and in part by the Natural Science Foundation of Shandong Province under Grant ZR202103040796.

REFERENCES

Anderson, J. G., Clayton, R., and Elahi, H. (1993). Estimating Lightning Performance of Transmission Lines. II. Updates to Analytical Models[J]. *IEEE Trans. Power Deliv.* 8 (3), 1254–1267. doi:10.1109/61.252647

Armstrong, H., and Whitehead, E. (1968). Field and Analytical Studies of Transmission Line Shielding. *IEEE Trans. Power Apparatus Syst.* PAS-87 (1), 270–281. doi:10.1109/tpas.1968.291999

Chongyu, X., Haiyue, W., and Feifei, D. (2015). Typical Cases Analysis of ±800kV UHV DC Transmission Line. *Hunan Electr. Power* 36 (1), 55–59. doi:10.3969/j.issn.1008-0198.2016.01.016

Golde, R. H. (1977). Lightning, (Vol. 1). London: Academic Press.

Grant, I. S., Anderson, J. G., and Hileman, A. R. (1985). A Simplified Method for Estimating Lightning Performance of Transmission Lines[J]. *IEEE Trans. Power Apparatus Syst.* PAS-104 (4), 918–932. doi:10.1109/TPAS.1985.319093

Hengxin, H., Weijiang, C., and Yu, Y. N. (2016). Lightning Shielding Failure protection of the Strained Angled tower of Double Circuit UHV AC Transmission Lines[J]. *High Voltage Eng.* 42 (11), 3448–3455. doi:10.13336/j.1003-6520.hve.20161031011

Idone, V. P., Orville, R. E., Hubert, P., Barret, L., and Eybert-Berard, A. (1984). Correlated Observations of Three Triggered Lightning Flashes. *J. Geophys. Res.* 89 (D1), 1385–1394. doi:10.1029/jd089id01p01385

Lundholm, R. (1957). Calculation of Transmission Line Lightning Voltages by Field Concepts. *Trans. Am. Inst. Electr. Eng. Part III Power App. Syst.* 76 (3), 1271–1281. doi:10.1109/AIEEPAS.1957.4499772

Yang, N., Qin, T., Wu, L., Huang, Y., Huang, Y., Xing, C., et al. (2021). A Multi-Agent Game Based Joint Planning Approach for Electricity-Gas Integrated Energy Systems Considering Wind Power Uncertainty, *Electric Power Syst. Res.* 204, 107673. doi:10.1016/j.epsr.2021.107673

Qian, P., Jun, L., and Peng, B. (2010). Application of Improved Electrical Geometry Model Method in Calculation of Lightning Tripping Rate of 1000kv Transmission Line[J]. *Power Syst. Technology* 34 (9), 155–159. doi:10.1109/CCECE.2010.5575154

Shen, X., Ouyang, T., Li, Y., Khajorntraidet, C., Li, S., and Zhuang, J. (2021). Mixture Density Networks-Based Knock Simulator. *IEEE/ASME Trans. Mechatronics* 27, 159–168. Early Access. doi:10.1109/TMECH.2021.3059775

Shen, X., and Raksincharoensak, P. (2021). Pedestrian-aware Statistical Risk Assessment. *IEEE Trans. Intell. Transportation Syst.* Early Access. doi:10.1109/TITS.2021.3074522

Taniguchi, S., Tsuboi, T., Okabe, S., Nagaraki, Y., Takami, J., and Ota, H. (2010). Improved Method of Calculating Lightning Stroke Rate to Large-Sized Transmission Lines Based on Electric Geometry Model. *IEEE Trans. Dielect. Electr. Insul.* 17 (1), 53–62. doi:10.1109/tdei.2010.5412002

Taniguchi, S., Tsuboi, T., and Okabe, S. (2009). Observation Results of Lightning Shielding for Large-Scale Transmission Lines. *IEEE Trans. Dielect. Electr. Insul.* 16 (2), 552–559. doi:10.1109/tdei.2009.4815191

Wagner, C. F., and Hileman, A. R. (1961). The Lightning Stroke-II. *Trans. Aiee, Part. Power Appar. Syst.* 80 (3), 622–636. doi:10.1109/aieepas.1961.4501104

Wagner, C. (1963). The Relation between Stroke Current and the Velocity or the Return Stroke. *IEEE Trans. Power Apparatus Syst.* 82 (68), 609–617. doi:10.1109/tpas.1963.291375

Wang, Y., Zhijun, L., and Min, D. (2014). Research on Typical Long Air Gaps with Negative Switching impulses(I)—Experiments[J]. *Proc. CSEE* 34 (21), 3534–3540. doi:10.13334/j.0258-8013.pcsee.2014.36.020

Wenxia, S., Qing, Y., Yongfu, L., and Fan, S. (2015). Analysis and prospect of Lightning Shielding Failure Evaluation Methods of Transmission Lines[J]. *High Voltage Eng.* 41 (8), 2500–2513. doi:10.13336/j.1003-6520.hve.2015.08.004

Yang, N., Yang, C., Xing, C., Ye, D., Jia, J., et al. (2021). Deep Learning-Based SCUC Decision-Making: An Intelligent Data-Driven Approach with Self-Learning Capabilities. *IET Gener. Transm. Distrib* 16, 629–640. doi:10.1049/gtd2.12315

Yu, W. (2012). Experimental Study of Breakdown Characteristics of Long Air Gaps and Their Applications in Lightning Protection[D]. *Wuhan Univ.*

Yu, W., Xishan, W., and Lei, L. (2014). Breakdown Characteristics of Long Air gap with Negative Polarity Switching Impulse[J]. *IEEE Trans. Dielectrics Electr. Insul.* 21 (2), 603–611. doi:10.1109/TDEI.2013.003627

Yu, W., Yeqiang, D., Xishan, W., and Ma, Y. (2017). An Improved Electric Geometry Model Based on Breakdown Test of Long Air Gaps and Suited for Large-Sized Transmission Lines[J]. *Proc. Csee* 37 (12), 3654–3661. doi:10.13334/j.0258-8013.pcsee.161081

Yunzhu, A., Lei, L., and Xishan, W. (2014). Impacting Factors of Large-Sized Model Test for Lightning Shielding Performance of UHV Transmission Lines [J]. *Power Syst. Technology* 38 (05), 1385–1389. doi:10.13335/j.1000-3673.pst.2014.05.040

Yunzhu, A. (2015). Study on Lightning Stroke Characteristics Based on Negative Impulse Discharge Characteristics of Long Air Gap[D]. *Wuhan Univ.*

Zongxi, L., Lei, L., Yu, W., et al. (2016). Effect of Terrains on Lightning Shielding Performance of UHV Common-tower Double-Transmission Lines [J]. *High Voltage Eng.* 42 (9), 2950–2955. doi:10.13336/j.1003-6520.hve.20160907034

Conflict of Interest: Authors CM, BA, and DC are employed by Jining Huayuan Thermal Power Plant.

The remaining authors declare that the research was conducted in the absence of any commercial or financial relationships that could be construed as a potential conflict of interest.

Publisher's Note: All claims expressed in this article are solely those of the authors and do not necessarily represent those of their affiliated organizations, or those of the publisher, the editors, and the reviewers. Any product that may be evaluated in this article, or claim that may be made by its manufacturer, is not guaranteed or endorsed by the publisher.

frontiers | Frontiers in Energy Research

ORIGINAL RESEARCH
published: 08 April 2022
doi: 10.3389/fenrg.2022.877042

Robust Unit Commitment for Minimizing Wind Spillage and Load Shedding With Optimal DPFC

Xuedong Zhu, Jun Wu and Dichen Liu**

School of Electrical Engineering and Automation, Wuhan University, Wuhan, China

The distributed power flow controller (DPFC) has a positive effect of UC problem on the network side based on its ability to manage capacity of power flow. This study presents a novel two-stage robust model to optimize the status of the generator and location–allocation of the DPFC, while simultaneously considering wind and load uncertainties. The column-and-constraint generation (CCG) method is utilized to solve the two-stage problem into the master problem and the subproblem iteratively. The optimal status of the generator and location of the DPFC can be easily obtained with the master problem, and the dispatch solution and compensation level of the DPFC are solved in the subproblem. We conduct the IEEE 24 bus system to verify the performance of the proposed procedure. There are effects on wind spillage/load shedding and generator dispatch scheduling planning once the DPFC is injected. Detailed simulation results illustrate the effect of the proposed approach.

Keywords: column-and-constraint generation (CCG) algorithm, optimal FACTS planning, distributed power flow controller, relaxed AC-SOCP$_2$, robust optimization

OPEN ACCESS

Edited by:
Xun Shen,
Tokyo Institute of Technology, Japan

Reviewed by:
Gaurav Sachdeva,
DAV University, India
Vikram Kamboj,
Lovely Professional University, India

****Correspondence:***
Jun Wu
byronwu@whu.edu.cn
Dichen Liu
2014202070048@qq.com

Specialty section:
This article was submitted to Wind Energy, a section of the journal Frontiers in Energy Research

Received: *16 February 2022*
Accepted: *03 March 2022*
Published: *08 April 2022*

Citation:
Zhu X, Wu J and Liu D (2022) Robust Unit Commitment for Minimizing Wind Spillage and Load Shedding With Optimal DPFC. Front. Energy Res. 10:877042. doi: 10.3389/fenrg.2022.877042

1 INTRODUCTION

Over the last decade, the penetration of wind power is gradually increasing as the load diversity changes (Yang et al., 2021a). However, the inherent fluctuation of wind power and load also constrains the operating economy and safety of the unit commitment problem (UC) with the long-distance power transmission (Milligan et al., 2009). On the other hand, the flexible AC transmission system (FACTS) device can enhance the flexibility of the network side, which also affects the operating conditions (Yuan et al., 2010). The DPFC is derived from the UPFC, which will be the most powerful tools in the FACTS. It has the same external characteristics as that of the UPFC and has advantage over the transmission corridors, investment, and replaceability (Khanchi and Garg, 2013; Dai et al., 2019; Tang et al., 2020).

Generally, the flexible operating principle of the major UC problem is divided into three categories: source side, demand side, and network side. In the source and demand sides, various research methods have been studied in the UC problem to enhance the operating flexibility by tackling uncertain parameters such as stochastic optimization (SO), robust optimization (RO), and information gap decision theory (IGDT). All these methods focus on tackling the uncertainty parameters such as wind or load uncertainties. The SO optimizes the dispatch problem with various scenarios considering uncertainty samples, which can enforce the dispatch scheduling feasibility. Wang et al. (2012) and Nandi et al. (2022a) present a stochastic UC model considering the uncertainty of demand response (DR) to improve the overall social welfare, where the uncertainty of DR is functioned as the chance constrained form. Zhao et al. (2014); Nandi and Kamboj (2021);

Nandi et al. (2022b); and Kamboj et al. (2022) evaluate the wind utilization in the UC problems, where the wind uncertainty is also solved by the stochastic chance constraint. Wu et al. (2019) formulated a two-stage dispatch model considering network congestion with the chance-constrained forms of wind and DR uncertainties. Dvorkin et al. (2014) presented a stochastic rolling UC model to evaluate the operating cost, considering wind spillage and load not served, where the wind is constrained by the chance-constrained form and the load is depicted as its stochastic interval form. Obviously, there are two drawbacks: the computational efficiency decreases rapidly as the scenarios increase, and the probability distribution function (PDF) is hard to obtain accurately (Shen and Raksincharoensak, 2021a; Shen and Raksincharoensak, 2021b; Shen et al., 2021; Shen et al., 2022). There is no need to obtain the exact PDF of uncertain parameters in the RO method, and only its uncertainty boundary is offered to describe the fluctuation of the uncertain parameters. An and Zeng (2014) explore the wind uncertainty by formulating a "min–max–min" robust model to research the dispatch problem, and the result verifies the effectiveness of optimal scheduling to incorporate the wind. In the work carried out by Gangammanavar et al. (2015), the worst scenarios of uncertain wind is well-distinguished with the deterministic load. In the study by Zhang et al. (2017), the authors researched the coordination of DG and elastic-price DR scheduling with uncertainty in the microgrid, which is solved by the CCG algorithm. Wang et al. (2016) propose an adjustable robust model of the building energy system to optimize the social welfare, where the PV output and load demands are uncertain. Zhao et al. (2013) assumed that the connection between elastic electricity price and load demand fluctuates within a certain range, derived the uncertainty set for demand response, and then proposed a two-stage robust model with interval sets to depict the uncertain parameters. Zhang et al. (2016) developed a robust model coordinating the energy storage system and direct-load control (DLC) considering uncertainties, which the generation/wind/PV/ESS and DLC scheduling planning satisfy for any realization of uncertainty. Based on the aforementioned research, the two-stage model for the RO method to deal with the uncertainty is mainly important in two directions. On the one hand, the reserve capacity in the first stage is optimized to adapt to the fluctuation of the uncertain parameters in the second stage, and on the other hand, the uncertain parameters are directly optimized in the second stage to ensure power balance. The conservation of the RO method challenges the operating cost of the system dispatch, where the extreme worst scenario hardly appears (Yang et al., 2021a; Yang et al., 2021b; Li et al., 2021; Yang et al., 2022a; Yang et al., 2022b). The IGDT method aims to search for the adjustable bound of uncertain parameters based on its stochastic model and robust model, which satisfy the objective function in the predefined interval. The IGDT overcomes the difficulties of acquiring distribution function in the SO problem and reduces the conservation of the RO problem. Thus, the computational time of IGDT is much lower than that of the RO and SO methods, and the conservation is also improved obviously. This approach is widely used in dealing with the uncertainty of renewable energy (Nikoobakht and Aghaei, 2017; Ahmadi et al., 2018), energy system (Ahmadi et al., 2019; Khajehvand et al., 2021), electrical vehicles (Rabiee et al., 2014), and other loads (Ahrabi et al., 2021). Nikoobakht and Aghaei (2017 present a robust model to solve the SCUC problem considering wind uncertainty; the wind absorption is optimized with flexible resources. Ahmadi et al. (2019) formulate the UC problems with the ESS uncertainty to improve the optimal capacity of ESS. A linear model by Rabiee et al. (2014); Ahrabi et al. (2021) is established to evaluate the effect of load uncertainty to the dispatch scheduling based on its stochastic model.

Although the FACTS has an advantage over the flexibility of the network side, few studies have been proposed to investigate its impacts on operating performance. Ziaee et al. (2017) optimized the TCSC device to improve the absorption of wind based on the stochastic method, evaluating the positive effect of wind spillage and considering optimal location and allocation of TCSC simultaneously. Nasri et al. (2014) formulate a two-stage model to minimize wind spillage and load shedding considering optimal TCSC with a fixed scenario. All these research studies focus on a single-time phase sample, which only indicates the aspects of improving operating safety considering the optimization of the FACTS. There are several studies which focus on the areas of the UC problem, where the FACTS location is predefined. Li et al. (2018) investigate the effect of the UPFC to the operating cost with a fixed wind scenario. Sang et al. (2017) reduced the wind spillage by optimizing the location–allocation of TCSC considering various wind scenarios. Considering the past research studies, there is no evidence of evaluating the inter-connection between the generator status and optimal FACTS. At the same time, there is no research study on the robust UC problem considering the optimal FACTS, which may be the best way to locate the FACTS successfully.

This study develops a two-stage robust model with optimal DPFC based on its PIM model considering wind and load uncertainties, which can not only hold the internal characteristics of multiple DPFCs but also enforce the feasible horizon with the uncertain parameters. We solve the status of generators and location of the DPFC in the master problem and obtain the dispatch solution and compensation level of the DPFC in the subproblem. The main contribution in this study can be summarized as follows:

1) The DPFC scheduling planning maintains the consistence, which is easy to adopt for the uncertain environments based on the proposed model.
2) A robust UC model with a flexible FACTS on the network side is presented, which is solved by the CCG algorithm.
3) A detailed experiment with different numbers of DPFCs has been presented to evaluate the impacts of the DPFC to the generator scheduling, wind absorption, and load supplies.

We demonstrate the effectiveness of the proposed two-stage robust dispatch problem in the IEEE 24 bus system and provide insight into the influence on the performance of the DPFC. This article is organized as follows: **Section 2** introduces the power injection model of the DPFC and a relaxed AC-SOCP power flow

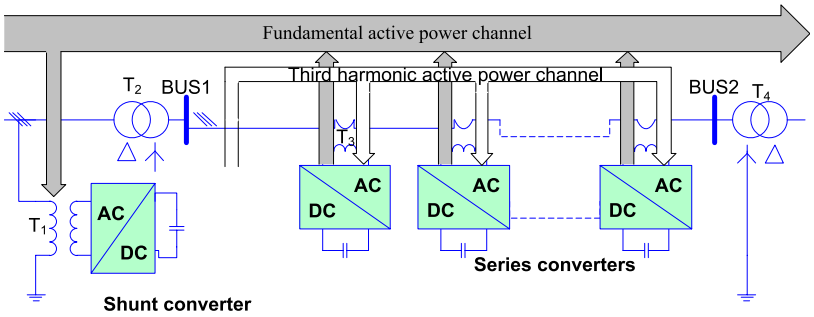

FIGURE 1 | Configuration and principle of the DPFC

model. **Section 3** presents the two-stage robust model of the optimal location–allocation problem. **Section 4** describes the procedure of the CC&G method. **Section 5** shows the results and discussion, while the conclusion is represented in **Section 6**.

2 POWER INJECTION MODEL OF DISTRIBUTED POWER FLOW CONTROLLER

2.1 Distributed Power Flow Controller Configuration and Principle

The general structure of the DPFC device includes the series side and shunt side. In the series side, there are many distributed converters cascaded to offer its control capabilities to manage the power flow on the network side. There are huge capacity shunt converters injected in the bus. There is power flow exchange by the fundamental wave and third harmonic wave through the series/shunt converters. The structure and operating principle is shown in **Figure 1**.

There is high similarity in the external characteristics between the UPFC and DPFC. However, the DPFC involves only active power transferable from the shunt side to the series side, which can reduce the power loss. Thus, a power injection model (PIM), which is introduced by the UPFC, can be modified as depicted in **Figure 2**

$$\begin{aligned} P^{*}_{ij} &= P_{ij} - P^{DPFC}_{ij}, \\ P^{*}_{ij,rev} &= P_{ij,rev} + P^{DPFC}_{ij}, \\ Q^{DPFC}_{ij,sh} &= 0;\ Q^{DPFC}_{ij,se} = 0; \end{aligned} \tag{1}$$

where P_{ij}, $P_{ij,rev}$ is the line power or reverse line power and P^{DPFC}_{ij} is the DPFC compensation level.

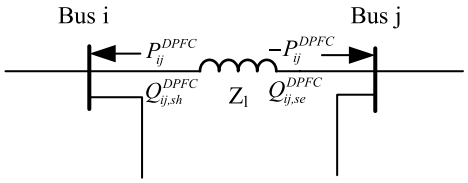

FIGURE 2 | PIM model of the DPFC.

2.2 Relaxed AC-SOCP Model

The traditional line flow (Le et al., 2021; Toyoda and Wu*, 2021; Wu et al., 2021) is modeled as shown in **Eq. 2**. Obviously, the nonlinear model is nonconvex.

$$\begin{aligned} P_{ij}(\theta, V) &= V_i^2 g_{ij} - V_i V_j\left(g_{ij}\cos\left(\theta_i - \theta_j\right) + b_{ij}\sin\left(\theta_i - \theta_j\right)\right). \\ Q_{ij}(\theta, V) &= -V_i^2 b_{ij} - V_m V_n\left(g_{ij}\sin\left(\theta_i - \theta_j\right) - b_{ij}\cos\left(\theta_i - \theta_j\right)\right). \end{aligned} \tag{2}$$

To tackle the nonconvex and nonlinear difficulties of the traditional model, we introduce several relax variables to the convex model, which are shown in **Eqs 3–5**

$$U_i = V_i^2;\ U_j = V_j^2. \tag{3}$$

$$R_{ij} = U_i U_j cos\left(\theta_i - \theta_j\right);\ R_{ij} \geq 0. \tag{4}$$

$$T_{ij} = U_i U_j sin\left(\theta_i - \theta_j\right). \tag{5}$$

Hence, the traditional model can be rewritten as shown in **Eq. 6**, which is a linear model and easily solved.

$$\begin{aligned} P_{ij} &= g_{ij}U_i - g_{ij}R_{ij} - b_{ij}T_{ij} \\ Q_{ij} &= -b_{ij}U_i - g_{ij}T_{ij} + b_{ij}R_{ij} \\ P_{ij,rev} &= g_{ij}U_j - g_l R_{ij} + b_{ij}T_{ij} \\ Q_{ij,rev} &= -b_{ij}U_j + g_{ij}T_{ij} + b_{ij}R_{.ij} \end{aligned} \tag{6}$$

However, there are connections between R_{ij} and T_{ij} in the original model, which can represented as

$$R_{ij}^2 + T_{ij}^2 = V_i^2 V_j^2 = U_i U_j. \tag{7}$$

There are bilinear variable terms in the aforementioned equation, which is still nonlinear. By relaxing the tight equality constraint into an inequality one, we can transform the representation into an SOCP form.

$$\left\| \begin{matrix} 2R_{ij} \\ 2T_{ij} \\ U_i - U_j \end{matrix} \right\|_2 \leq U_i + U_j. \tag{8}$$

An SOCP power flow model can be easily constructed by **Eqs 6**, **8**, which can be easily solved by CPLEX due to its convexity.

3 ROBUST MODEL WITH THE OPTIMAL DISTRIBUTED POWER FLOW CONTROLLER

The power system planners aim to determine the location–allocation of the DPFC considering wind and load uncertainties, which can enhance the management efficiency of power flow and decrease the investment of the DPFC. However, the operators desire to minimize the operation cost of injected DPFCs and improve the operating level of the system. Therefore, optimal location–allocation of the DPFC in the power system must consider the operational cost, investment of installing the DPFC, curtailment of wind spillage, and load shedding. The optimal model is represented by **Eqs 9–23**

$$\begin{aligned} &min \sum_{t}\sum_{i\in G_i}\left[SU_i + SD_i + c_{g,i}P_{i,t}^{G}\right] + \sum_{t}\sum_{ij\in G_{ij}} \pi^{DPFC} P_{ij}^{DPFC} \\ &+ \sum_{t}\sum_{i\in G_w} M^{Curt} P_{i,t}^{W,curt} + \sum_{t}\sum_{i\in G_{nb}} M^{shed} P_{i,t}^{D,shed} \end{aligned} \tag{9}$$

$$\begin{cases} SU_i \geq C_i^{su} u_{i,t} \\ SD_i \geq C_i^{sd} v_{i,t} \end{cases} \tag{10}$$

$$\begin{cases} u_{i,t} - v_{i,t} = I_{i,t} - I_{i,t-1} \\ u_{i,t} + v_{i,t} \leq 1 \end{cases} \tag{11}$$

$$\begin{cases} \sum_{h=0}^{T_i^{on}+h-1} I_{i,t} \geq T_i^{on}\left(I_{i,t} - I_{i,t-1}\right) \\ \sum_{h=0}^{T_i^{off}+h-1} I_{i,t} \geq T_i^{off}\left(I_{i,t-1} - I_{i,t}\right) \end{cases} \tag{12}$$

$$\begin{aligned} I_{i,t}P_{i,t}^{G,min} \leq P_{i,t}^{G} \leq I_{i,t}P_{i,t}^{G,max} \\ I_{i,t}Q_{i,t}^{G,min} \leq Q_{i,t}^{G} \leq I_{i,t}Q_{i,t}^{G,max} \end{aligned} \tag{13}$$

$$\begin{aligned} P_{i,t}^{G} - P_{i,t-1}^{G} \leq \left(2 - I_{i,t} - I_{i,t-1}\right)I_{i,t}P_{i,t}^{G,min} + \left(1 + I_{i,t-1} - I_{i,t}\right)RU_i \\ P_{i,t-1}^{G} - P_{i,t}^{G} \leq \left(2 - I_{i,t} - I_{i,t-1}\right)I_{i,t}P_{i,t}^{G,min} + \left(1 - I_{i,t-1} + I_{i,t}\right)RD_i \end{aligned} \tag{14}$$

$$\begin{aligned} &P_{i,t}^{G} - \sum_{j\in\psi(i)} P_{ij} - \sum_{j\in\phi(i)} P_{ij,rev} + \sum_{l\in\psi(i)} P_{ij}^{DPFC} - \sum_{l\in\phi(i)} P_{ij}^{DPFC} - P_{i,t}^{W,shed} \\ &+P_{i,t}^{D,curt} = P_{i,t}^{D} + P_{i,t}^{D,u} - P_{i,t}^{W} \quad Q_{i,t}^{G} - \sum_{j\in\psi(i)} Q_{ij} - \sum_{j\in\phi(i)} Q_{ij,rev} - Q_{i,t}^{W,curt} \\ &+Q_{i,t}^{D,curt} = Q_{i,t}^{D} + Q_{i,t}^{D,u} - Q_{i,t}^{W} \end{aligned} \tag{15}$$

$$\begin{aligned} 0 \leq P_{i,t}^{D,shed} \leq P_{i,t}^{D} + P_{i,t}^{D,u} \\ 0 \leq Q_{i,t}^{D,shed} \leq Q_{i,t}^{D} + Q_{i,t}^{D,u} \end{aligned} \tag{16}$$

$$\begin{aligned} 0 \leq P_{i,t}^{W,curt} \leq P_{i,t}^{W} \\ 0 \leq Q_{i,t}^{W,curt} \leq 0.95 * P_{i,t}^{W} \end{aligned} \tag{17}$$

$$\begin{aligned} 0 \leq P_{ij,t}^{DPFC} \leq \delta_{ij,t} P_{DPFC}^{max} \\ \sum_{ij} \delta_{ij,t} \leq \alpha_L \end{aligned} \tag{18}$$

$$\left\| \begin{matrix} P_{ij} - P_{ij}^{DPFC} \\ Q_{ij} \end{matrix} \right\|_2 \leq S_{ij} \tag{19}$$

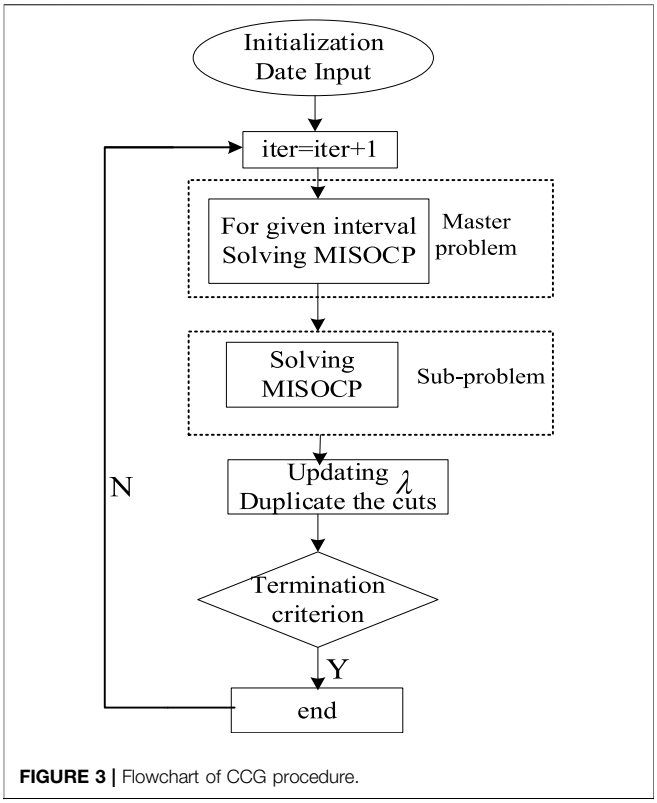

FIGURE 3 | Flowchart of CCG procedure.

$$\left\| \begin{matrix} P_{ij,rev} + P_{ij}^{DPFC} \\ Q_{ij,rev} \end{matrix} \right\|_2 \leq S_{ij} \tag{20}$$

$$\begin{aligned} &T_{ij} \approx \theta_i - \theta_j \\ &\begin{cases} P_{ij} = g_{ij}U_i - g_{ij}R_{ij} - b_{ij}T_{ij} \\ Q_{ij} = -b_{ij}U_i - g_{ij}T_{ij} + b_{ij}R_{ij} \\ P_{ij,rev} = g_{ij}U_j - g_lR_{ij} + b_{ij}T_{ij} \\ Q_{ij,rev} = -b_{ij}U_j + g_{ij}T_{ij} + b_{ij}R_{ij} \end{cases} \\ &\left\| \begin{matrix} 2R_{ij} \\ 2T_{ij} \\ U_i - U_j \end{matrix} \right\|_2 \leq U_i + U_j \end{aligned} \tag{21}$$

$$\theta_i^{min} \leq \theta_i \leq \theta_i^{max} \tag{22}$$

$$\left(V_i^{min}\right)^2 \leq U_i \leq \left(V_i^{max}\right)^2. \tag{23}$$

The objective function is to minimize the generation cost, investment cost of the DPFC, and curtailment of wind spillage and load shedding as shown in **Eq. 9**. **Eq. 10** constrains the start-up and shut down cost of the thermal unit; **Eq. 11** distinguishes the operating state from the start-up and shut down state of generators. The minimum ON/OFF time limits are shown in **Eq. 12**, the active and reactive output of generators is limited in **Eqs 13**, **14** and shows the ramp-up and ramp-down limitation of thermal units. The active and reactive power balance is depicted in **Eq. 15**. **Eqs 16–18** constrain wind spillage, load shedding, and location–allocation of the DPFC. The transmission network security constraint is formulated in **Eqs 19–20** with line

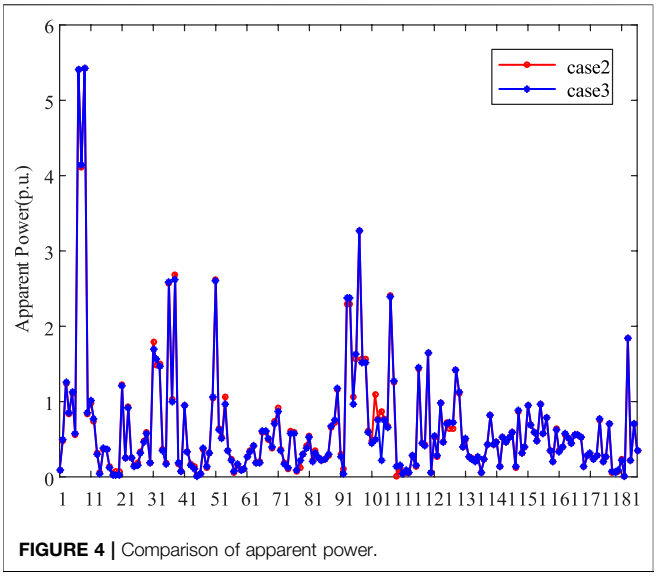

FIGURE 4 | Comparison of apparent power.

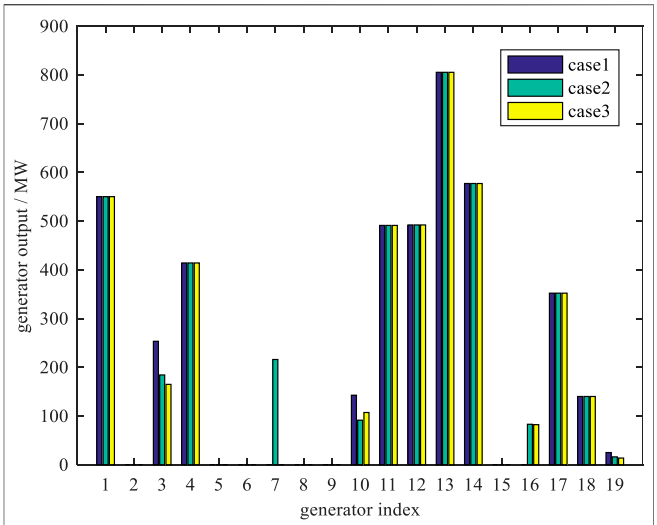

FIGURE 6 | Comparison of generator output.

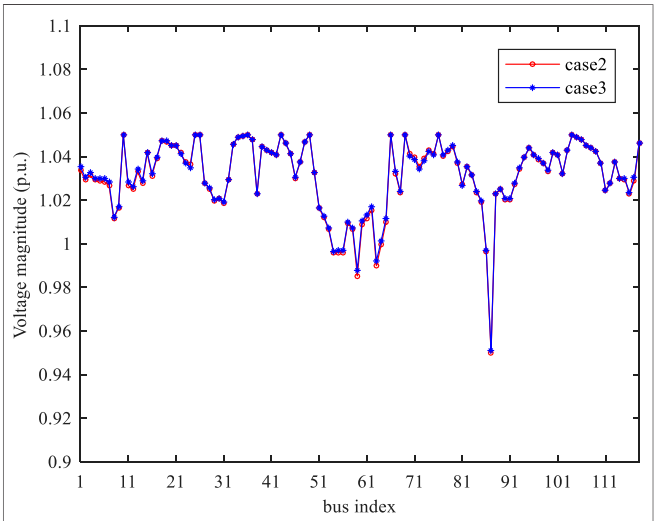

FIGURE 5 | Comparison of voltage.

forward and reverse power flow. The relaxed AC-SOCP power flow model is introduced in **Eqs 21–23**.

The formulated MISOCP problem aims to improve the operating level with optimal location and ratings of the DPFC. However, there are uncertainties of wind and load, as shown in **Eqs 24–25**.

$$P_{i,t}^{DR} = \left\{ P_{i,t}^{DR} \middle| P_{i,t}^{DR} \in \left[P_{i,t}^{DR,F} - \mu_{i,t}^{DR} \triangle P_{i,t}^{DR}, P_{i,t}^{DR,F} + \mu_{i,t}^{DR} \triangle P_{i,t}^{DR} \right], \mu_{i,t}^{DR} \in \{0,1\} \right\}. \tag{24}$$

$$P_{i,t}^{W} = \left\{ P_{i,t}^{W} \middle| P_{i,t}^{W} \in \left[P_{i,t}^{W,F} - \mu_{i,t}^{W} \triangle P_{i,t}^{W}, P_{i,t}^{W,F} + \mu_{i,t}^{W} \triangle P_{i,t}^{W} \right], \mu_{i,t}^{W} \in \{0,1\} \right\}. \tag{25}$$

Once the DPFC is injected into the grid, the device should offer its functions considering the uncertainty circumstance of wind-load with fixed locations. We developed a two-stage robust approach to obtain the robust dispatch solutions with the PIM model of the DPFC, which can easily adapt to the uncertain environment. The robust model is shown as

$$\begin{aligned} &min \sum_t \sum_{i \in G_i} [SU_{i,t} + SD_{i,t}] + max\, min [\sum_t \sum_{i \in G_i} c_{g,i} P_{i,t}^{G} + \sum_t \sum_{i \in G_i} \pi^{DPFC} P_{ij}^{DPFC} . \\ &+ \sum_t \sum_{i \in G_i} M^{Curt} P_{i,t}^{W,curt} + \sum_t \sum_{i \in G_i} M^{shed} P_{i,t}^{D,shed}]. \\ &s.t. \begin{cases} (10) - (23) \\ (24) - (25) \end{cases} \end{aligned} \tag{26}$$

4 TWO-STAGE ROBUST UNIT COMMITMENT AND COLUMN-AND-CONSTRAINT GENERATION METHOD

The column-and-constraint generation method is introduced to solve the proposed two-stage robust problem (Zeng and Zhao, 2013). For simplicity, the robust problem can be reformulated in the following compact matrix form:

$$\begin{aligned} &\min_x \; c^T x + \max_\lambda \; \min_y \; d^T y + e^T \lambda. \\ &s.t. \; Ax \le b, x \in \{0,1\}. \\ &Y = \left\{ y \middle| \begin{array}{l} Cy \le f \\ Gx + Dy \le g \\ Ey = \lambda \\ \left\| Q_i y + q_i \right\|_2 \le h_i y + d_i, i = 1, \ldots, n \end{array} \right\}. \end{aligned} \tag{27}$$

The objective described in **(27)** corresponds to constraint (26), which is modeled in a "min–max–min" optimization form. The outer "min" is to minimize the start-up and shut down costs of generators considering the optimal locations of the DPFC; the decision variable $\{x\}$ is a binary variable, which

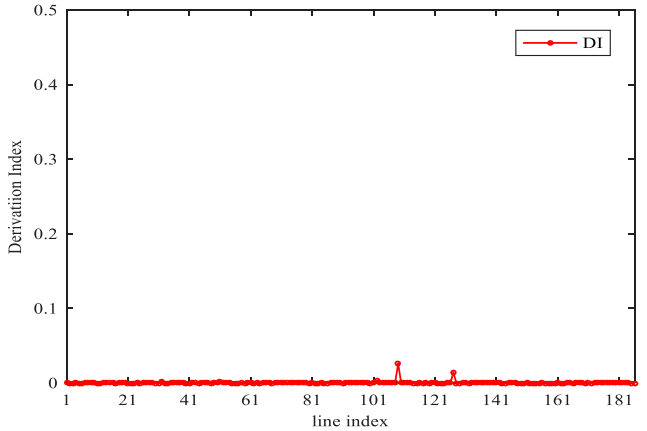

FIGURE 7 | Derivation performance.

represents the state variables including the thermal generator operating state and optimal locations of the DPFC. The "max" is to find the worst uncertainty scenario under the uncertainty circumstance; the decision variable $\{\lambda\}$ refers the wind and load operating level, which is shown in **Eqs 24–25**. The inner "min" is to obtain the solutions under the worst uncertainty case; the decision variable $\{y\}$ represents the continuous variables in the second stage, which is described in **Eqs 13–23**. It can be observed that the decision variable $\{\lambda\}$ is optimized in the second stage by maximizing the minimal second stage costs, which can easily improve the robustness.

The details of the CC&G method are shown as follows:

Master Problem

$$\begin{min}_{x}\ c^T x + \eta. \\ \begin{cases} Ax \le b \\ \eta \ge d^T y_l^* + e^T \lambda_l^*. \\ Cy_l^* \le f \\ Dy_l^* \le g - Gx^* \\ Ey_l^* = \lambda_l^* \\ \left\| Q_i y_l^* + q_i \right\|_2 \le h_i y + d_i, i = 1, \ldots, n \\ l \in \{1, \ldots, m\} \end{cases} \tag{28}$$

The master problem is optimized to obtain the first-stage decision under various worst-case scenarios, which is duplicated from the subproblem. Obviously, the master problem provides the lower bound of the original problem.

For a given first-stage decision variable $\{x\}$, the subproblem can be formulated as follows. The SP is aimed to obtain the optimal dispatch solutions with uncertainty. This can provide an upper bound of the original problem.

Subproblem

$$\begin{max}_{\lambda}\ \begin{min}_{y}\ d^T y + e^T \lambda. \\ \begin{cases} Cy \le f \quad (\gamma_1) \\ Gx + Dy \le g \quad (\gamma_2) \\ Ey = \lambda \quad (\gamma_3) \\ \left\| Q_i y + q_i \right\|_2 \le h_i y + d_i, i = 1, \ldots, n \quad (\gamma_4, \gamma_5) \end{cases} \end{max} \tag{29}$$

The aforementioned "max–min" problem can be transformed by the dualization method, which can be easily solved. The convert procedure is shown in **Eq. 30**.

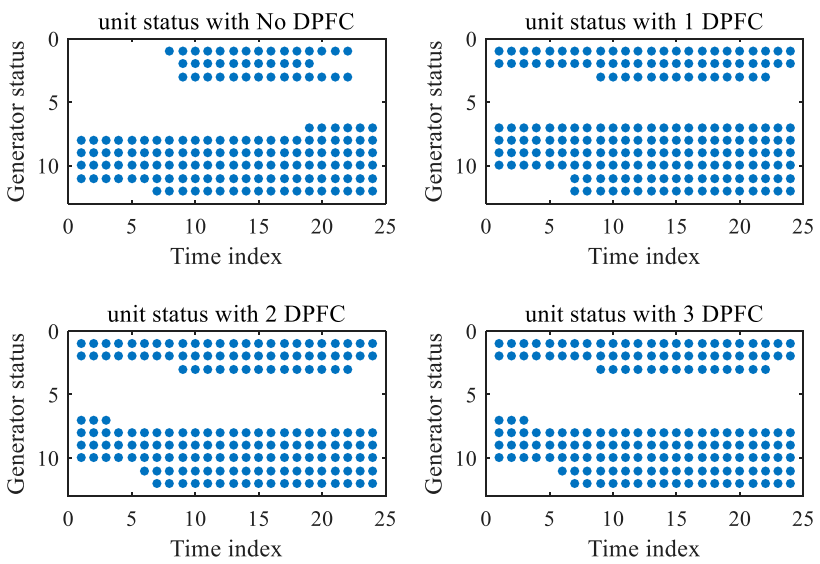

FIGURE 8 | Thermal generator state with different numbers of the DPFC.

TABLE 1 | Dispatch performance with different numbers of the DPFC.

Case no.		Objective value	SD/SU cost($)
A		563,219	15889
B	NL5	535,301	7,931
C	NL5	527,238	8,243
	NL15		
D	NL5	527,176	8,243
	NL15		
	NL26		

$$\max\ f^T\gamma_1 + \left(g^T - G^T x^*\right)\gamma_2 + \lambda^T\gamma_3 - \sum_{i=1}^{n}\left(q_i^T\gamma_4 + d_i^T\gamma_5\right).$$
$$\begin{cases} C^T\gamma_1 + D^T\gamma_2 + E^T\gamma_3 + \sum_{i=1}^{n}\left(Q_i^T\gamma_4 + h_i^T\gamma_5\right) = d \\ \left\|\gamma_4\right\|_2 \le \gamma_5 \\ \gamma_1 \le 0;\ \gamma_2 \le 0;\ \gamma_4 \le 0;\ \gamma_3:\ free;\ \gamma_5 \ge 0; \\ \lambda \in \left\{ \begin{matrix} d_{i,t} \\ g_{i,t} \end{matrix} \middle| \begin{matrix} d_{i,t}^{min} \le d_{i,t} \le d_{i,t}^{max} \\ g_{i,t}^{min} \le g_{i,t} \le g_{i,t}^{max} \end{matrix} \right\} \end{cases} \tag{30}$$

It is clearly observed that there is a bilinear term $\{\lambda^T\gamma_3\}$ in the subproblem, which is hard to solve. According to Li et al. (2018), all the optimal solutions with uncertainties can be obtained at its extreme points. This reminds us to convert the bilinear term to linear ones by introducing the Big-M method. We can introduce a binary variable, which can easily convert the uncertainty interval optimization into boundary point optimization.

The extreme points of uncertainty can be formulated as follows:

$$\lambda^T\gamma_3 = \lambda_{i,t}^{min}\gamma_3 + \left(\lambda_{i,t}^{max} - \lambda_{i,t}^{min}\right)\mu_{i,t}\gamma_3. \tag{31}$$

We introduce a dummy variable $\{\omega_{i,t} = \mu_{i,t}\gamma_3\}$ and based on the Big-M method, we can obtain the following linear constraints:

$$\begin{gathered} \left(\lambda_{i,t}^{max} - \lambda_{i,t}^{min}\right)\omega_{i,t} = \left(\lambda_{i,t}^{max} - \lambda_{i,t}^{min}\right)\mu_{i,t}\gamma_3. \\ -M\mu_{i,t} \le \omega_{i,t} \le M\mu_{i,t} \\ -M\left(1-\mu_{i,t}\right) + \gamma_3 \le \omega_{i,t} \le \gamma_3 + M\left(1-\mu_{i,t}\right). \end{gathered} \tag{32}$$

Combining **Eqs 30–32**, a linear single-stage model is successfully reformulated to obtain its maximum solution, which is easily solved by commercial software such as CPLEX.

The flowchart of two-stage robust optimization is depicted in **Figure 3**.

For a given gap ε , the complete procedure of CCG can be described as

Step 1: Let $\Phi^{down} = -\infty$, $\Phi^{up} = +\infty$, iter = 0;
Step 2: Solve the MP which is modeled in **Eq. 28**,

Obtain the status of generators $I_{i,t}$ and location of the DPFC $\delta_{ij,t}$ with the uncertainty λ^*,
Update the lower bound Φ^{down};

Step 3: Fix the location of the DPFC and status of thermal units. Solve the SP considering wind-load uncertainties.

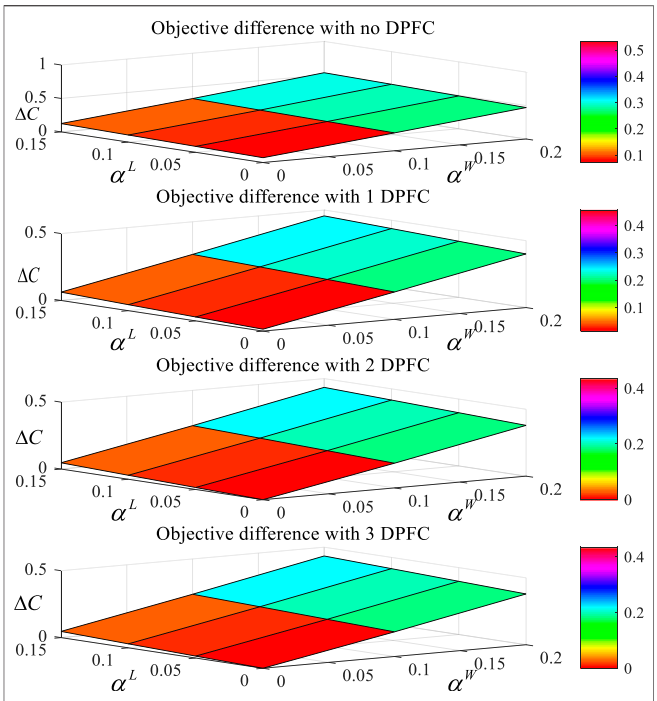

FIGURE 9 | Objective difference with different numbers of the DPFC.

Obtain decision variable solution $P_{i,t}^G/Q_{i,t}^G/P_{i,t}^{W,curt}/P_{i,t}^{D,shed}/P_{ij,s}^{DPFC}$ and uncertainty parameters α^L, α^W under each scenario.
Update the upper bound Φ^{up};

Step 4: If $\frac{|\Phi^{up}-\Phi^{down}|}{|\Phi^{down}|} \le \varepsilon$, return the optimal solutions and stop. Otherwise, duplicate the cuts into the master problem, update the uncertainty parameters, and go to step.

5 CASE STUDY

5.1 Verification of the Relaxed AC-SOCP Model

In this section, three cases are presented to check the characteristics of the power flow to illustrate the effectiveness of the proposed model. All cases are conducted on the IEEE-118 bus system.

Case 1: DC power flow
Case 2: the nonlinear power flow model
Case 3: the proposed model in **Eq. 27**

To evaluate the performance of the three power flow models, we conducted the simulation on apparent power of lines, generator outputs, and voltage magnitude, as is shown in **Figures 4**, **5**, **6**. We can easily find that the apparent power of lines has little difference in case 2 and case 3; only four lines have a little fluctuation. Similarly, voltage magnitude also conforms to the trend. In the aspect of generator output, there is an obvious

TABLE 2 | Objective values under different intervals considering the optimal DPFC.

DPFC no.	Objective value				
	?^{L}?^{W}	0	0.05	0.1	0.15
0	0	399,105	405,222	411,648	418,525
	0.1	471,743	478,216	484,835	492,136
	0.2	547,254	555,226	563,219	570,626
1	0	377,613	383,188	388,956	395,432
	0.1	448,383	454,950	461,332	467,730
	0.2	521,626	528,422	535,301	542,181
2	0	372,290	377,742	383,399	389,663
	0.1	441,059	447,551	453,916	460,283
	0.2	513,641	520,407	527,238	534,085
3	0	372,290	377,742	383,350	389,562
	0.1	440,885	447,332	453,854	460,210
	0.2	513,600	520,356	527,176	534,012

difference between case 1 and case 2/3 on the G3/G7/G19, which is due to the absence of reactive power. Comparing the output of generators in case 2 and case 3, the dispatch solutions show highly consistent characteristics (**Figures 4**, **5**, **6**, **7**).

To quantify the exactness of the relaxed AC-SOCP model, a deviation index stated in **(39)** is introduced to describe the gap difference between case 2 and case 3, as shown in **Figure 7**. It is clearly shown that the gap difference is almost zero for the system.

$$DI = U_i U_j - R_{ij}^2 - T_{ij}^2. \tag{39}$$

5.2 Effects of the Optimal Distributed Power Flow Controller With High Penetration of Wind Power

To verify the proposed method, we conducted case studies on the modified IEEE-24 bus system. The wind power is located at bus 6/8. The rating of wind power is 4 MW. There are three loads with uncertainties, which are located at bus 4/5/6. The interval of wind and load is 0.2 and 0.1, respectively. The proposed method is solved by GAMS/CPLEX. The threshold values of the stop criterion are set to be 1e-4.

In order to evaluate the impacts of optimal DPFC planning, four cases have been set up to quantify the specific control effects of the DPFC to the scheduling of the thermal generator.

Case (a): the proposed robust model with no DPFC.

Case (b): the proposed robust model with one optimal DPFC.

Case (c): the proposed robust model with two optimal DPFC.

Case (d): the proposed robust model with three optimal DPFC.

A. Comparison of Unit States With Different Optimal Distributed Power Flow Controller Solutions

As shown in **Figure 8**, there is a huge difference in the start–stop scheduling planning of the units. Compared to the generator statuses of case (a), there are huge differences of scheduling planning with four units; the SD/SU costs have decreased from 15,889$ to 7,931$, which is shown in **Table 1**. Once 2/3 DPFC devices are injected into the system, the unit state is exactly the same, which illustrates that the control capacity of the DPFC has reached its extreme effects on the scheduling state of the system. Furthermore, the status of G7 and G11 show a different planning solution between case (b) and case (c)/(d); the SD/SU costs have a little increment from 7,931$ to 8,243$. Hence, there is a positive trend of dispatch state scheduling considering the optimal DPFC injected.

Table 1 shows the objective performance with different numbers of the DPFC; the value keeps decreasing as the number of DPFCs increase. Comparing the performance between case (c) and case (d) , the objective values change very little, which indicates that the management of power flow is approaching its limit.

In order to more clearly depict the performance difference between the robust model and deterministic model considering the optimal DPFC, we introduce an index ΔC, which denotes the objective difference.

$$\Delta C = \frac{C_{RO} - C_{DM,3}}{C_{DM,3}}, \tag{40}$$

where C_{RO} is the objective value of the robust model and $C_{DM,3}$ is the objective value for the deterministic model with three DPFCs injected. The differences of objective values for the IEEE 24 bus system under different wind and load intervals are shown in **Figure 9**.

As shown in **Table 2** and **Figure 9**, it is easily observed that the robust model has a high property improvement, which is due to the robust conversation of dispatch solution. The system operators only sacrifice the economy effects to tackle with the uncertainties of wind/load. Furthermore, the difference ΔC shows the downward directions as the numbers of DPFC increased. There is a similar trend with **Figure 9**. The objective difference ΔC is almost the same when comparing the 2 and 3 DPFCs injected, which indicates that optimal location and allocations of 2 DPFC has reached its limitation for the IEEE 24 bus system.

B. Comparison of the Last Worst Wind-Load Scenario with Different Optimal Distributed Power Flow Controller Solutions

With the uncertainties of wind and load, the optimal solution is obtained at the extreme points of uncertain parameters. However, there is an inconsistent trend while the uncertain parameters reach its extreme values with different numbers in the last worst case scenario, as shown in **Figure 10**. Obviously, there is only one difference of wind extreme values at a single time phase ($t = 23$). However, it can be easily found that the load reaches its upper values once 1/2/3 DPFC is injected, which indicates that optimal DPFC planning can enforce the resistance level of power supply considering the uncertainty.

To evaluate the effects of wind spillage and load shedding with the optimal DPFC in the last worst-case scenario,

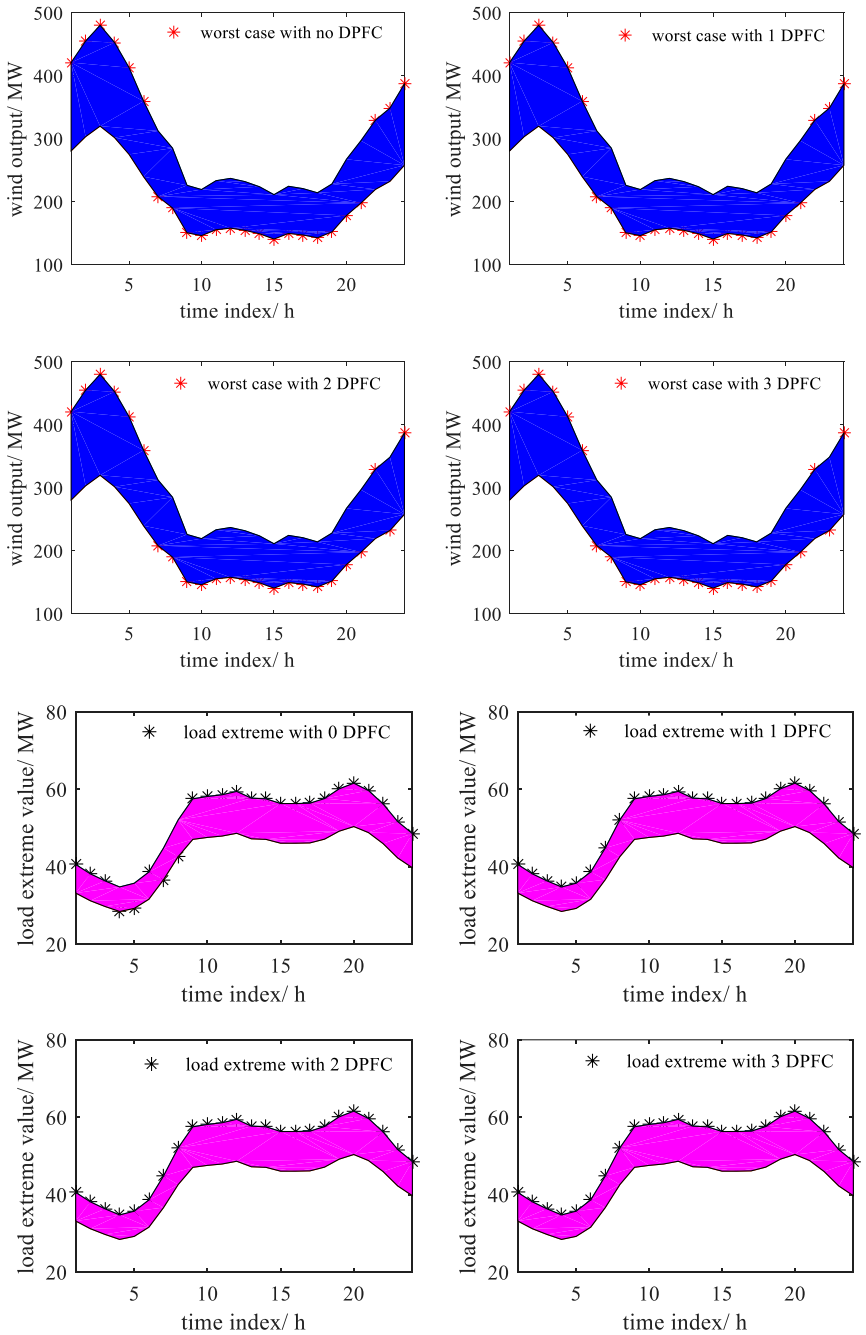

FIGURE 10 | Wind/load upper/lower bound and its worst-case scenario with different numbers of the DPFC.

considering its extreme value inconsistence with wind/load uncertainties, we conducted the simulation of wind absorption and actual load supplies, which is shown in **Figure 11**. For the wind aspect, the overall trend of wind absorption is positive, and the amount outputs of wind absorption are 94.06/96.24/96.32/96.32 MW as the numbers of DPFC are 0/1/2/3, respectively. For the actual load aspect, there is a drop difference at time phase (t = 23 h) considering different numbers of the DPFC optimized. However, the amounts of actual load supplies are 43.89/44.20/45.13/45.13 MW from case (a) to case (d). Hence, the dispatch effects with the DPFC optimized the wind spillage and load shedding move in a positive direction.

For the consistence of DPFC optimal scheduling planning, **Table 3** shows advantages of the location and allocation of the optimized DPFC simultaneously. Once the DPFC is injected, the unit cost has a great positive effect, and the wind spillage and load shedding also conform to the positive trend with the

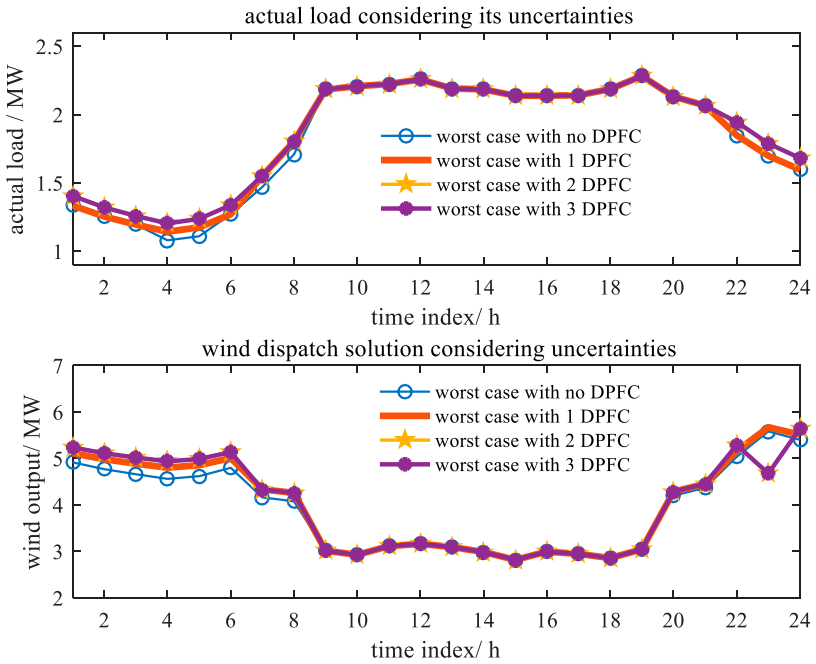

FIGURE 11 | Wind upper/lower bound and its worst-case scenario with different numbers of the DPFC.

TABLE 3 | Optimal dispatch performance with the optimal DPFC under the worst-case scenario.

Case no.		Generation cost	DPFC investment	Wind spillage (MW)	Load shedding(MW)
A		249,949	---	31.15	1.75
b	NL5	240,857	2,921	28.97	0.03
c	NL5 NL15	241,424	6,426	27.76	0
d	NL5 NL15 NL26	241,185	6,603	27.76	0

increased numbers of the DPFC. In cases (c) and (d), the amounts of load shedding are 0, and the wind spillage also has no changes, which indicates that the robust planning of the DPFC has reached its extreme repeatedly.

6 CONCLUSION

This work presents a two-stage robust dispatch method with optimal location–allocations of the DPFC considering wind-load uncertainties. In the model, we mainly optimize the scheduling state of thermal units and location–allocation of the DPFC to tackle the uncertainties. Case studies are performed to demonstrate the effectiveness of the proposed method. The conclusions are summarized as follows:

1) The relaxed AC-SOCP model can easily simulate the nonlinear AC power flow and has an advantage of solving speed and difficulties.
2) The robust dispatch with the optimal DPFC has an economic advantage and load supplies, which also reduce the wind spillage and load shedding.
3) The proposed model can be easily solved by the CCG method, which efficiently checks the worst-case scenario, optimizes the dispatch solution, and DPFC consistent scheduling planning with uncertainties.

However, the robust dispatch with the optimal DPFC may face a conservative challenge because of the overall intervals of uncertainties. Some studies have developed a distributed robust optimization to overcome the conservation, which combine the priorities between stochastic and robust optimization. In addition, the DPFC has shown great advantages over the management on the network side. We will conduct more research studies on the control capabilities of the DPFC in the future. Such advantages may be effective in dispatching and operating the principle of integrated energy system (IES) due to the electric characteristics; we can relieve the couple conjunction in the gas turbine (GT) and CCHP with the energy storage system (ESS) by optimal coordination of

the control capabilities of the DPFC. Another coordinate research on the TEP and DPFC has been in process to tackle the high wind-load conditions to improve robustness and flexibilities in the network side, which render more capability of available transfer power. Obviously, there is an advantage of the DPFC to be adopted in N-k contingency analysis, which may be the best performance in the application areas of the DPFC.

DATA AVAILABILITY STATEMENT

The original contributions presented in the study are included in the article/Supplementary Material, further inquiries can be directed to the corresponding authors.

AUTHOR CONTRIBUTIONS

XZ contributed to the simulation and writing. JW contributed to the model and method. DL offered financial support.

FUNDING

This study received funding from the State Grid Corporation of China (No. 52150016000Y) and National Key Research and Development Program of China (No.2018YFB0904800). The funders were not involved in the study design, collection, analysis, interpretation of data, the writing of this article, or the decision to submit it for publication.

REFERENCES

Ahmadi, A., Nezhad, A. E., and Hredzak, B. (2018). Security-constrained Unit Commitment in Presence of Lithium-Ion Battery Storage Units Using Information-gap Decision Theory[J]. *IEEE Trans. Ind. Inform.* 15 (1), 148–157.

Ahmadi, A., Nezhad, A. E., Siano, P., Hredzak, B., and Saha, S. (2019). Information-gap Decision Theory for Robust Security-Constrained Unit Commitment of Joint Renewable Energy and Gridable Vehicles[J]. *IEEE Trans. Ind. Inform.* 16 (5), 3064–3075.

Ahrabi, M., Abedi, M., Nafisi, H., Mirzaei, M. A., Mohammadi-Ivatloo, B., and Marzband, M. (2021). Evaluating the Effect of Electric Vehicle Parking Lots in Transmission-Constrained AC Unit Commitment under a Hybrid IGDT-Stochastic Approach. *Int. J. Electr. Power Energ. Syst.* 125, 106546. doi:10.1016/j.ijepes.2020.106546

An, Y., and Zeng, B. (2014). Exploring the Modeling Capacity of Two-Stage Robust Optimization: Variants of Robust Unit Commitment Model[J]. *IEEE Trans. Power Syst.* 30 (1), 109–122.

Dai, J., Tang, Y., Liu, Y., Ning, J., Wang, Q., Zhu, N., et al. (2019). Optimal Configuration of Distributed Power Flow Controller to Enhance System Loadability via Mixed Integer Linear Programming. *J. Mod. Power Syst. Clean. Energ.* 7 (6), 1484–1494. doi:10.1007/s40565-019-0568-8

Dvorkin, Y., Pandžić, H., Ortega-Vazquez, M. A., and Kirschen, D. S. (2014). A Hybrid Stochastic/interval Approach to Transmission-Constrained Unit Commitment[J]. *IEEE Trans. Power Syst.* 30 (2), 621–631.

Gangammanavar, H., Sen, S., and Zavala, V. M. (2015). Stochastic Optimization of Sub-hourly Economic Dispatch with Wind Energy[J]. *IEEE Trans. Power Syst.* 31 (2), 949–959.

Kamboj, V. K., Kumari, C. L., Bath, S. K., Prashar, D., Rashid, M., Alshamrani, S. S., et al. (2022). A Cost-Effective Solution for Non-convex Economic Load Dispatch Problems in Power Systems Using Slime Mould Algorithm. *Sustainability* 14 (5), 2586. doi:10.3390/su14052586

Khajehvand, M., Fakharian, A., and Sedighizadeh, M. (2021). A Risk-Averse Decision Based on IGDT/stochastic Approach for Smart Distribution Network Operation under Extreme Uncertainties. *Appl. Soft Comput.* 107, 107395. doi:10.1016/j.asoc.2021.107395

Khanchi, S., and Garg, V. K. (2013). Unified Power Flow Controller (FACTS Device). *A. Review[j]. System* 5, 6.

Le, S., Wu, Y., Guo, Y., and Vecchio, C. D. (2021). Game Theoretic Approach for a Service Function Chain Routing in NFV with Coupled Constraints. *IEEE Trans. Circuits Syst.* 68, 3557–3561. doi:10.1109/TCSII.2021.3070025

Li, J., Liu, F., Li, Z., Mei, S., and He, G. (2018). Impacts and Benefits of UPFC to Wind Power Integration in Unit Commitment. *Renew. Energ.* 116, 570–583. doi:10.1016/j.renene.2017.09.085

Li, Z., Jiang, W., Abu-Siada, A., Li, Z., Xu, Y., and Liu, S. (2021). Research on a Composite Voltage and Current Measurement Device for HVDC Networks. *IEEE Trans. Ind. Electron.* 68 (9), 8930–8941. doi:10.1109/tie.2020.3013772

Milligan, M., Porter, K., DeMeo, E., Denholm, P., Holttinen, H., Kirby, B., et al. (2009). Wind Power Myths Debunked. *IEEE Power Energ. Mag.* 7 (6), 89–99. doi:10.1109/mpe.2009.934268

Nandi, A., and Kamboj, V. K. (2021). A Meliorated Harris Hawks Optimizer for Combinatorial Unit Commitment Problem with Photovoltaic Applications[J]. *J. Electr. Syst. Inf. Technol.* 8 (1), 1–73. doi:10.1186/s43067-020-00026-3

Nandi, A., Kamboj, V. K., and Khatri, M. (2022). Hybrid Chaotic Approaches to Solve Profit Based Unit Commitment with Plug-In Electric Vehicle and Renewable Energy Sources in winter and Summer[J]. *Mater. Today Proc.* doi:10.1016/j.matpr.2021.12.525

Nandi, A., Kamboj, V. K., and Khatri, M. (2022). Metaheuristics Approaches to Profit Based Unit Commitment for GENCOs[J]. *Mater. Today Proc.* doi:10.1016/j.matpr.2021.12.526

Nasri, A., Conejo, A. J., Kazempour, S. J., and Ghandhari, M. (2014). Minimizing Wind Power Spillage Using an OPF with FACTS Devices. *IEEE Trans. Power Syst.* 29 (5), 2150–2159. doi:10.1109/tpwrs.2014.2299533

Nikoobakht, A., and Aghaei, J. (2017). IGDT-based Robust Optimal Utilisation of Wind Power Generation Using Coordinated Flexibility Resources. *IET Renew. Power Generation* 11 (2), 264–277. doi:10.1049/iet-rpg.2016.0546

Rabiee, A., Soroudi, A., and Keane, A. (2014). Information gap Decision Theory Based OPF with HVDC Connected Wind Farms[J]. *IEEE Trans. Power Syst.* 30 (6), 3396–3406.

Sang, Y., Sahraei-Ardakani, M., and Parvania, M. (2017). Stochastic Transmission Impedance Control for Enhanced Wind Energy Integration[J]. *IEEE Trans. Sustain. Energ.* 9 (3), 1108–1117.

Shen, X., Ouyang, T., Khajorntraidet, C., Li, Y., Li, S., and Zhuang, J. (2022). Mixture Density Networks-Based Knock Simulator. *Ieee/asme Trans. Mechatron.* 27, 159–168. doi:10.1109/TMECH.2021.3059775

Shen, X., Ouyang, T., Yang, N., and Zhuang, J. (2021). Sample-based Neural Approximation Approach for Probabilistic Constrained Programs. *IEEE Trans. Neural Netw. Learn. Syst.*, 1–8. doi:10.1109/TNNLS.2021.3102323

Shen, X., and Raksincharoensak, P. (2021). Pedestrian-aware Statistical Risk Assessment. *IEEE Trans. Intell. Transport. Syst.*, 1–9. doi:10.1109/TITS.2021.3074522

Shen, X., and Raksincharoensak, P. (2021). Statistical Models of Near-Accident Event and Pedestrian Behavior at Non-signalized Intersections. *J. Appl. Stat.*, 1–21. doi:10.1080/02664763.2021.1962263

Tang, A., Lu, Z., Yang, H., Zou, X., Huang, Y., and Zheng, X (2020). Digital/analog Simulation Platform for Distributed Power Flow Controller Based on ADPSS and dSPACE[J]. *CSEE J. Power Energ. Syst.* 7 (1), 181–189.

Toyoda, M., and Wu*, Y. (2021). Mayer-type Optimal Control of Probabilistic Boolean Control Network with Uncertain Selection Probabilities. *IEEE Trans. Cybern.* 51, 3079–3092. doi:10.1109/tcyb.2019.2954849

Wang, C., Jiao, B., Guo, L., Tian, Z., Niu, J., and Li, S. (2016). Robust Scheduling of Building Energy System under Uncertainty. *Appl. Energ.* 167, 366–376. doi:10.1016/j.apenergy.2015.09.070

Wang, Q., Wang, J., and Guan, Y. (2012). Stochastic Unit Commitment with Uncertain Demand Response[J]. *IEEE Trans. Power Syst.* 28 (1), 562–563.

Wu, J., Zhang, B., Jiang, Y., Bie, P., and Li, H. (2019). Chance-constrained Stochastic Congestion Management of Power Systems Considering

Uncertainty of Wind Power and Demand Side Response. *Int. J. Electr. Power Energ. Syst.* 107, 703–714. doi:10.1016/j.ijepes.2018.12.026

Wu, Y., Guo, Y., and Toyoda, M. (2021). Policy Iteration Approach to the Infinite Horizon Average Optimal Control of Probabilistic Boolean Networks. *IEEE Trans. Neural Netw. Learn. Syst.* 32 (6), 2910–2924. doi:10.1109/TNNLS.2020.3008960

Yang, N., et al. (2021). A Comprehensive Review of Security-Constrained Unit Commitment. *J. Mod. Power Syst. Clean Energ.*, 1–14. doi:10.35833/MPCE.2021.000255

Yang, N., Qin, T., Wu, L., Huang, Y., Huang, Y., Xing, C., et al. (2022). A Multi-Agent Game Based Joint Planning Approach for Electricity-Gas Integrated Energy Systems Considering Wind Power Uncertainty. *Electric Power Syst. Res.* 204, 107673. doi:10.1016/j.epsr.2021.107673

Yang, N., Yang, C., Wu, L., Shen, X., Jia, J., Li, Z., et al. (2022). Intelligent Data-Driven Decision-Making Method for Dynamic Multisequence: An E-Seq2Seq-Based SCUC Expert System. *IEEE Trans. Ind. Inf.* 18, 3126–3137. doi:10.1109/TII.2021.3107406

Yang, N., Yang, C., Xing, C., Ye, D., Jia, J., Chen, D., et al. (2021). Deep Learning-based SCUC Decision-making: An Intelligent Data-driven Approach with Self-learning Capabilities. *IET Generation Trans. Dist* 16, 629–640. doi:10.1049/gtd2.12315

Yuan, Z., de Haan, S. W. H., Ferreira, J. B., and Cvoric, D. (2010). A FACTS Device: Distributed Power-Flow Controller (DPFC). *IEEE Trans. Power Electron.* 25 (10), 2564–2572. doi:10.1109/tpel.2010.2050494

Zeng, B., and Zhao, L. (2013). Solving Two-Stage Robust Optimization Problems Using a Column-And-Constraint Generation Method. *Operations Res. Lett.* 41 (5), 457–461. doi:10.1016/j.orl.2013.05.003

Zhang, C., Xu, Y., Dong, Z. Y., and Wong, K. P. (2017). Robust Coordination of Distributed Generation and price-based Demand Response in Microgrids[J]. *IEEE Trans. Smart Grid* 9 (5), 4236–4247.

Zhang, C., Xu, Y., Dong, Z. Y., and Ma, J. (2016). Robust Operation of Microgrids via Two-Stage Coordinated Energy Storage and Direct Load Control[J]. *IEEE Trans. Power Syst.* 32 (4), 2858–2868.

Zhao, C., Wang, J., Watson, J.-P., and Guan, Y. (2013). Multi-Stage Robust Unit Commitment Considering Wind and Demand Response Uncertainties. *IEEE Trans. Power Syst.* 28 (3), 2708–2717. doi:10.1109/tpwrs.2013.2244231

Zhao, C., Wang, Q., Wang, J., and Guan, Y. (2014). Expected Value and Chance Constrained Stochastic Unit Commitment Ensuring Wind Power Utilization. *IEEE Trans. Power Syst.* 29 (6), 2696–2705. doi:10.1109/tpwrs.2014.2319260

Ziaee, O., Alizadeh-Mousavi, O., and Choobineh, F. F. (2017). Co-optimization of Transmission Expansion Planning and TCSC Placement Considering the Correlation between Wind and Demand Scenarios[J]. *IEEE Trans. Power Syst.* 33 (1), 206–215.

Conflict of Interest: The authors declare that the research was conducted in the absence of any commercial or financial relationships that could be construed as a potential conflict of interest.

Publisher's Note: All claims expressed in this article are solely those of the authors and do not necessarily represent those of their affiliated organizations, or those of the publisher, the editors, and the reviewers. Any product that may be evaluated in this article, or claim that may be made by its manufacturer, is not guaranteed or endorsed by the publisher.

GLOSSARY

Indices

i/j Indices of busesIndices of lines

ij Indices of busesIndices of lines

Sets

G_i Sets of generators

G_w Sets of wind generator

G_{ij} Sets of lines

G_{nb} Sets of buses

Constants

g_{ij}/b_{ij} Line parameters

C_i^{su}/C_i^{sd} Coefficients of start-up/shut down cost of generator i

$c_{g,i}$ Cost coefficient of generator

π^{DPFC} Cost coefficients of DPFC investment

T_i^{on}/T_i^{off} Minimum up-time and down time of generator

$P_i^{G,min}/P_i^{G,max}$ Lower and upper bound of generator active output

$Q_i^{G,min}/Q_i^{G,max}$ Lower and upper bound of generator reactive output

RU_i/RD_i Ramp-up and ramp-down values of generator

SU_i/SD_i Start-up/shut down cost of generator i

S_{ij} Apparent power limitation of line ij

$\theta_i^{min}/\theta_i^{max}$ Lower and upper bound of voltage angle

V_i^{min}/V_i^{max} Lower and upper bound of voltage magnitude

M^{Curt} Curtailment coefficient of wind spillage

M^{shed} Curtailment coefficient of load shedding

Variables

P_{ij}/Q_{ij} Active/reactive power flow of line ij

$P_{ij,rev}/Q_{ij,rev}$ Reverse active/reactive power flow of line ij

V_i Voltage magnitude

θ_i Voltage angle

R_{ij}/T_{ij} Slack variables

$P_{i,t}^G/Q_{i,t}^G$ Active/reactive power of generator

P_{ij}^{DPFC} Compensation level of the DPFC on line ij

$\delta_{ij,t}$ Binary variables indicating the location of the DPFC

α Scalar indicating the amount of DPFC numbers

$P_{i,t}^{W,curt}$ Wind spillage value

$P_{i,t}^{D,shed}$ Load shedding value

$u_{i,t}/v_{i,t}/I_{i,t}$ Binary variable indicating start-up/shut down/operating state.

$P_{i,t}^{W,curt}/Q_{i,t}^{W,curt}$ Active/reactive power spillage of wind

$P_{i,t}^{D,shed}/Q_{i,t}^{D,shed}$ Active/reactive load shedding

$P_{i,t}^{D,u}/Q_{i,t}^{D,u}$ Active/reactive power of load considering uncertainty.

frontiers | Frontiers in Energy Research

ORIGINAL RESEARCH
published: 11 April 2022
doi: 10.3389/fenrg.2022.851299

Acoustic-Electrical Joint Localization Method of Partial Discharge in Power Transformer Considering Multi-Path Propagation Impact

Jun Jia[1,2], Hui Fu[3], Bo Wang[4], Yong Li[5], Yue Yu[6], Yuan Cao[7] and Di Jiang[7]*

[1]School of Electrical Engineering, Southeast University, Nanjing, China, [2]Research Institute, State Grid Jiangsu Electric Power Co., Ltd., Nanjing, China, [3]State Grid Jiangsu Electric Power Co., Ltd., Nanjing, China, [4]School of Electrical Engineering and Automation, Wuhan University, Wuhan, China, [5]State Grid Taizhou Power Supply Company, Taizhou, China, [6]State Grid Lianyungang Power Supply Company, Lianyungang, China, [7]College of Electrical Engineering, Zhejiang University, Hangzhou, China

Efficient and accurate localization of partial discharge (PD) is of paramount importance to ensure the safe operation of power transformers. However, the multi-path propagation effect introduced by the reflection, refraction and diffraction of the ultrasonic signal may add significant computational complexity to the localization process and degrade the localization accuracy. This paper proposes an acoustic- electrical joint method for partial discharge location in the power transformer with the full consideration of the multi-path propagation impact. Unlike the conventional error analysis methods, a partial discharge localization model is proposed for characterizing the multipath propagation impact without the prior knowledge of the transcendental error probability. Based on the matrix inequality transformation and relaxation, the high-dimensional nonlinear localization equations are transformed into a set of second-order convex optimization equations that can be solved using the convex second-order cone program (SOCP). The proposed solution can significantly reduce the computational complexity and improve the localization accuracy as well as avoid the local optimum and slow convergence. The solution is assessed through extensive experiments based on simulations, testbed and trial deployment in comparison with the existing solutions with the localization error of about 0.1 m.

Keywords: power transformer, partial discharge, localization algorithm, convex second-order cone program, acoustic-electrical joint, acoustic-electrical joint localization

OPEN ACCESS

Edited by:
Xun Shen,
Tokyo Institute of Technology, Japan

Reviewed by:
Hardeep Singh,
Sophia University, Japan
Vikram Kamboj,
Lovely Professional University, India

****Correspondence:***
Jun Jia
jiajuntec@163.com

Specialty section:
This article was submitted to Smart Grids, a section of the journal Frontiers in Energy Research

Received: *09 January 2022*
Accepted: *08 February 2022*
Published: *11 April 2022*

Citation:
Jia J, Fu H, Wang B, Li Y, Yu Y, Cao Y and Jiang D (2022) Acoustic-Electrical Joint Localization Method of Partial Discharge in Power Transformer Considering Multi-Path Propagation Impact. Front. Energy Res. 10:851299. doi: 10.3389/fenrg.2022.851299

INTRODUCTION

It is well known that the insulation of large transformers is one of the fundamental and stringent requirements to ensure the safe and reliable operation of electric power substations. In the past decades, the timely detection and analysis of partial discharge (PD) have been widely investigated for fault detection and diagnosis of the internal insulation deterioration of power transformers (e.g., Tarimoradi and Gharehpetian, 2017; Wang et al., 2017; Chen, 2019; Ganguly et al., 2020; Karami et al., 2020). This enables the determination of fault type and location at the early stage, and hence the field maintenance can be timely carried out to prevent the power transformers from failures or outages.

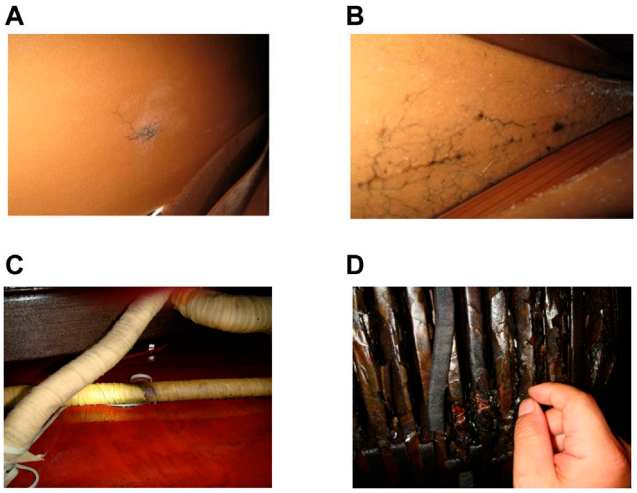

FIGURE 1 | Insulation discharge phenomena of transformers. **(A)** Insulation paperboard at the outer enclosure of transformer **(B)** Insulation paperboard at the lower end of the winding **(C)** Winding cable discharge **(D)** Internal discharge of winding.

In general, the partial discharge can make the insulation being destroyed and gradually expand due to the direct bombardment of the discharge particles, resulting in insulation breakdown; In addition, the chemical action of the active gases (e.g., heat, ozone and nitrogen oxide) produced by the discharge can lead to corrosion of the partial insulation, which increases the dielectric loss and finally leads to thermal breakdown (Kallberg, 1980; Naderi et al., 2007). More specifically, the partial discharge can introduce the following impacts:

1) Partial discharge can lead to the separation and cleavage of chemical bonds and the destruction of the insulating material's molecular structure. This may introduce discharge at the concentration of the electric field and leads to dendritic discharge traces and insulation breakdown.
2) The thermal effect of discharge point leads to the thermal cracking of insulation or promotes oxidative cracking. This may increase the conductivity and dielectric loss that accelerates the aging process.
3) The generated ozone and nitrogen oxides during the discharge can lead to a nitric acid chemical reaction. Such a reaction can corrode the insulator when meet with the water, resulting in the deterioration of insulation performance.

In addition, the high-energy radiation phenomenon during partial discharge can potentially degrade the insulating materials. The X wax (a waxy substance produced by overheating) deposited on the solid insulation makes it difficult to dissipate heat, resulting in overheating and damages to the solid insulation. The examples of insulation discharge phenomena in the transformers are illustrated in **Figure 1**.

At present, the partial discharge localization of power transformers is mainly based on electrical (mainly in ultra-high frequency) and ultrasonic detection methods (e.g., (Luo Yongfen et al., 2006; Moore et al., 2006; Markalous et al., 2008; Coenen and Tenbohlen, 2012; Tarimoradi and Gharehpetian, 2017)). The electrical method mainly detects the UHF (Ultra High Frequency) electromagnetic wave generated by partial discharge sources. Considering that the propagation speed of the electrical signal is the speed of light, the electrical method requires a high sampling frequency reaching the nanosecond level or even sub-nanosecond level. Moreover, the electrical wave signal is shielded and attenuated by the power *trans*-former borne (Kweon et al., 2005).

The ultrasonic detection method detects and analyses the arrival time of the PD pulse signal to determine the location of partial discharge sources. Due to the advantages of non-destructive, robust and high precision, the ultrasonic detection method is one of the most widely used location technologies of power transformers (Howells and Norton, 1978; Han-Lee Song, 1994; Cakir et al., 2013; Hekmati and Hekmati, 2017; Wang et al., 2017; Chen, 2019). The location solutions can be classified into the pure acoustic-based method, the pure electrical-based method

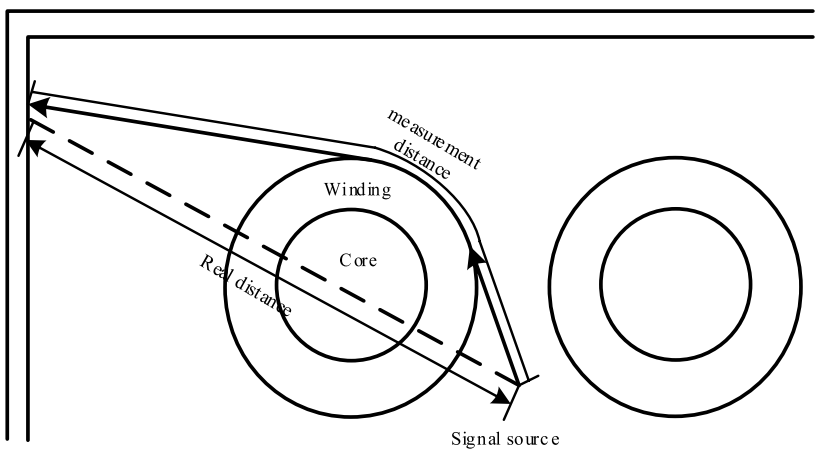

FIGURE 2 | Diagram of the relationship between measurement distance and real distance.

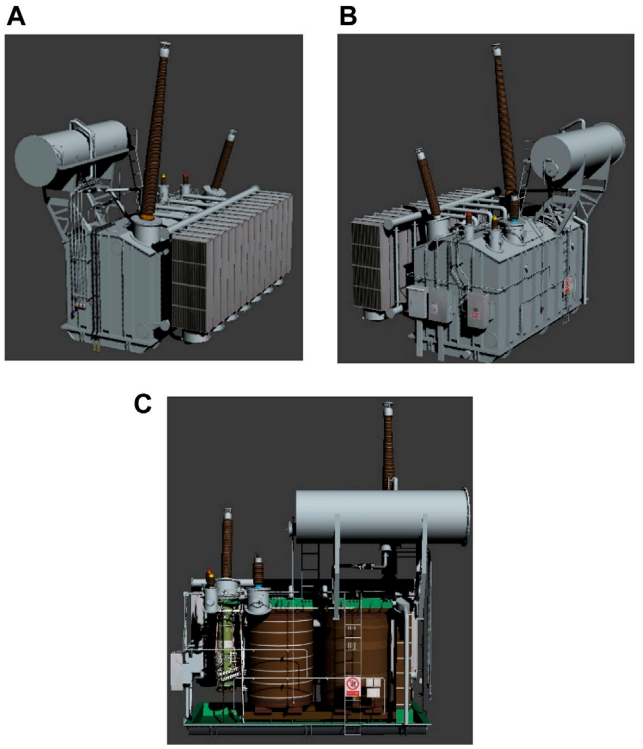

FIGURE 3 | Simulated power transformer.

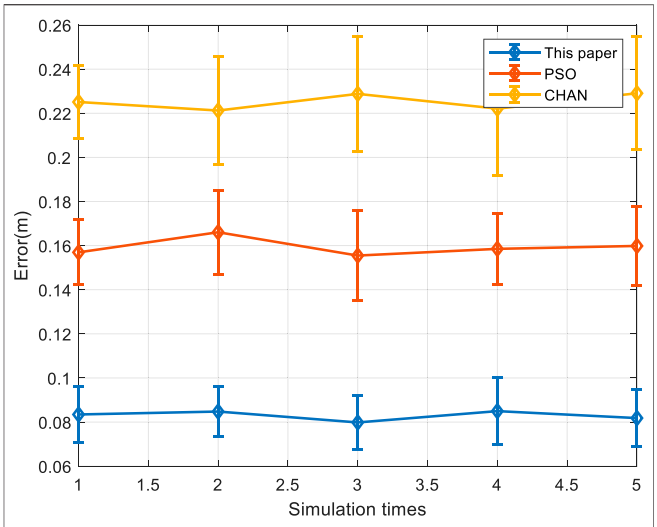

FIGURE 4 | Performance comparison of the proposed solution against the CHAN and PSO algorithms.

and the acoustic electrical joint method (e.g., Markalous et al., 2008; Coenen and Tenbohlen, 2012; Rubio-serrano et al., 2012). The pure acoustic localization method and the pure electrical-based localization method select the arrival time of one ultrasonic sensor or UHF sensor signal as the reference time and then measure the time delay of other signals relative to the reference time for partial discharge localization. The acoustic electrical joint method is considered as the arrival time of the electric pulse signal of the partial discharge as the reference time since the electric signal delay is very tiny and can be ignored compared with the ultrasonic signals. Through using a set of ultrasonic synchronized sensors to measure the ultrasonic time delay and multiplying the equivalent sound velocity, the distance of discharge source to individual sensors can be calculated, as suggested in (Meka et al., 2018). The ultrasonic wave propagation speed within the transformer is close to that of sound wave speed, and the electromagnetic wave speed is about two-thirds of that of lightwave speed. Therefore, the time error of the pure electrical-based localization method is much larger than other methods. The existing study (Coenen and Tenbohlen, 2012) confirmed that the positioning accuracy of the electric acoustic joint method is higher than that of the pure acoustic method. Since the time arrival time of the acoustic signal is not easy to be accurately measured, a larger error can be introduced between the acoustic and acoustic signals. Moreover, for multiple PD sources, the acoustic-electrical joint method is expected to provide improved performance in terms of distinguishing the signals from different PD sources in practical deployment compared with the acoustic-based method.

The main factors affecting the accuracy of the partial discharge localization are the nonlinear localization equation solving method and the elimination method of various errors in the localization process. In the existing studies, many optimization algorithmic solutions, e.g., the particle swarm optimization and its extensions (Hooshmand et al., 2013; Wang et al., 2017; Meka et al., 2018), genetic algorithm (Chang et al., 2014; Li and Luan, 2018), fuzzy clustering (Contin et al., 2002; Homaei et al., 2014), have been adopted attempting to obtain the optimal solution of the nonlinear localization problem. However, there are many problems in the practical application, e.g., falling into local optimum, slow convergence speed, and premature nature. It is difficult to ensure the robustness and accuracy of the solved results. Also, the existing literature mainly focuses on the influence of sensor measurement error rather than the error caused by multi-path propagation.

Unlike our previous work (Jia et al., 2021) that presented an acoustic-based method for PD location, this paper proposes an acoustic-electrical joint method for locating the partial discharge sources in a power transformer considering the influence of the multi-path propagation effect. In this paper, the following contributions are made:

1) The proposed acoustic-electrical joint localization method fully considered the impact of multipath propagation errors to accurately describe the phenomenon of PD signal propagation in the power transformer.
2) The acoustic-electrical joint localization is formulated as a second-order cone program (SOCP) that can efficiently obtain the accurate PD source locations whilst avoiding the local optimum and slow convergence.
3) The proposed algorithmic solution of PD localization is extensively assessed and validated by a range of experiments based on simulations, experimental testbed and field test against a set of existing solutions.

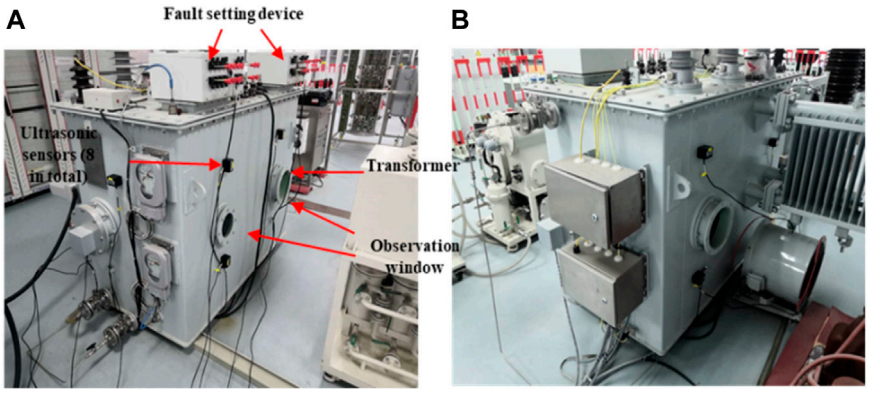

FIGURE 5 | TWCP-0.5/50 transformer and deployment of the installed ultrasonic partial discharge sensors. **(A)** Front view **(B)** Back view.

TABLE 1 | Spatial coordinate of ultrasonic sensor of TWCP-0.5/50.

No	X	Y	Z
1	0.850	0.000	0.800
2	1.700	0.225	0.900
3	1.700	0.225	0.300
4	1.700	0.675	0.900
5	0.850	0.900	0.800
6	0.000	0.225	0.900

The remainder of this work is as follows: the analysis of the partial discharge propagation path in the transformer is presented in *Analysis of Partial Discharge Propagation Path in Transformer*. *SOCP Localization Model* formulates the PD location problem and adopts the SOCP to solve the localization model. *Performance Evaluation and Numerical Result* carries out a range of experiments to validate the proposed method. Finally, the conclusions and future work are discussed in *Conclusive Remarks*.

ANALYSIS OF PARTIAL DISCHARGE PROPAGATION PATH IN TRANSFORMER

When the internal medium of the power transformer is affected by dampness, aging, breakdown, or other reasons, the power transformer may cause insulation weakness points. When the applied voltage exceeds the weakness point threshold voltage, it will emit electric and ultrasonic signals. Due to the complexity of the internal structure of the power transformer, the propagation process of electric and ultrasonic signals can be divided into four categories, as shown in **Figure 2**.

1) Internal reflection process of power transformer: when the ultrasonic wave touches the winding or borne, it will be reflected, thus prolonging the time delay to reach the sensor;
2) The internal refraction process of power transformer: when the ultrasonic wave travels through the winding or borne, it will be refracted, thus also prolonging the time delay to reach the sensor;
3) The diffraction process in power transformer: under the condition that the ultrasonic wave wavelength is close to the shelter width, the direction of the ultrasonic wave may change when it touches the winding;
4) Refraction process of power transformer borne: when the ultrasonic wave touches the power transformer borne, it will continue to spread in the borne. However, the wave propagating in the border decays very fast, it can be filtered by the threshold method.

SOCP LOCALIZATION MODEL

Suppose synchronized one electric PD sensor and n ultrasonic PD sensors are arranged around the power transformer. The time delay between the measurement sensor and the PD source can be formulated as **Eq. 1**:

$$t_i = \frac{r_i}{v} = \frac{1}{v}(d_i + n_i + e_i) \tag{1}$$

In **Eq. 1**, r_i is the measured distance from the PD to the i th sensor $(i = 1, 2, \cdots, n)$. v is the ultrasonic wave propagation velocity within the transformer. d_i is the real distance between the i th sensor and the PD source (all variables units in this paper are in meters). n_i denotes the sensor measurement error that follows the normal distribution $N(0, \sigma^2)$ (Chan and Ho, 1994) with the mean value of 0 and variance of σ^2, and $|n_i| \ll d_i$. e_i is the error caused by the velocity affected by the composite path in the process of signal propagation.

$$r_i = t_i v \tag{2}$$

$$d_i = \|x - s_i\| \tag{3}$$

In **Eq. 3**, x and s_i denotes the three-dimensional coordinates of the PD source and the i th sensor, i.e. (x_x, y_x, z_x) and $(x_{s_i}, y_{s_i}, z_{s_i})$, respectively. Here, **Figure 2** illustrates the relationship between measurement distance and real distance.

By square the two sides of **Eq. 1** and substituting formulas **Eqs 2**, **3**,

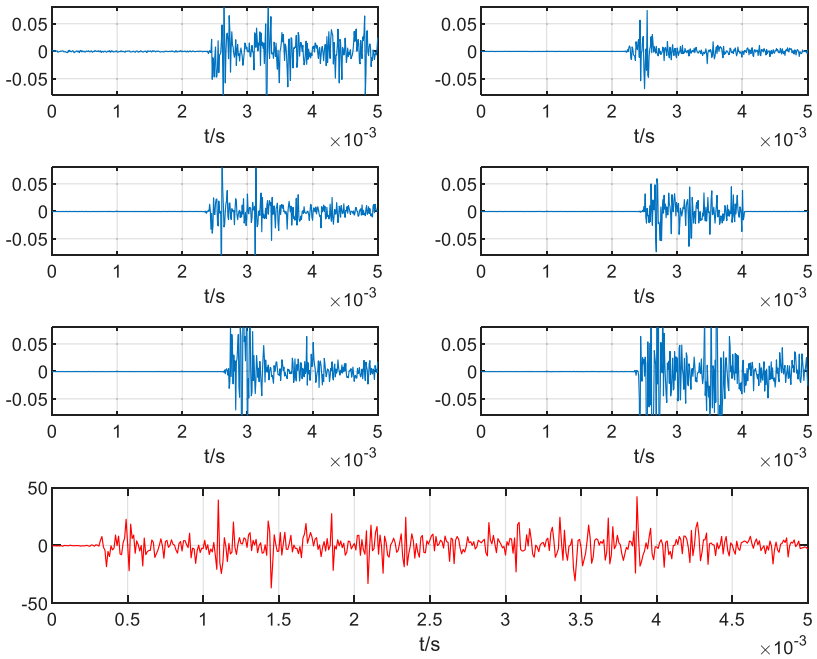

FIGURE 6 | The ultrasonic localization result using TWCP-0.5/50 transformer testbed

$$r_i^2 - 2r_i e_i + e_i^2 - \|x - s_i\|^2 = 2n_i\|x - s_i\| + n_i^2 \tag{4}$$

Considering $|n_i| \ll d_i$, n_i^2 can be omitted as a high-order small quantity,

$$n_i \approx \frac{r_i^2 - 2r_i e_i + e_i^2 - \|x - s_i\|^2}{2\|x - s_i\|} \tag{5}$$

So, the localization model can be formulated as

$$\min_x \max_{e_i} \sum_{i=1}^{N} \left(\frac{r_i^2 - 2r_i e_i + e_i^2 - \|x - s_i\|^2}{2\|x - s_i\|} \right)^2 \tag{6}$$

Eq. 6 can be reformed as:

$$\min_x \sum_{i=1}^{N} \left[\max_{e_i} \left(\frac{r_i^2 - 2r_i e_i + e_i^2 - \|x - s_i\|^2}{2\|x - s_i\|} \right) \right]^2 \tag{7}$$

Considering $0 \le e_i \le \rho_i$, which ρ_i is the upper bound of e_i.

$$\begin{aligned} &\max_{e_i} \left(\frac{r_i^2 - 2r_i e_i + e_i^2 - \|x - s_i\|^2}{2\|x - s_i\|} \right) \\ &= \max \left(\frac{r_i^2 - \|x - s_i\|^2}{2\|x - s_i\|}, \frac{r_i^2 - 2r_i\rho_i + \rho_i^2 - \|x - s_i\|^2}{2\|x - s_i\|} \right) \end{aligned} \tag{8}$$

Define ξ_i:

$$\xi_i = \frac{r_i^2 - 2r_i e_i + e_i^2 - \|x - s_i\|^2}{2\|x - s_i\|} \tag{9}$$

So, according to SCOP, **Eq. 7** can be rewritten as

$$\begin{aligned} &\min_{x,\xi} \sum_{i=1}^{N} \xi_i \\ &\left(\frac{r_i^2 - 2r_i\rho_i + \rho_i^2 - \|x - s_i\|^2}{2\|x - s_i\|} \right)^2 \le \xi_i \\ &\left(\frac{r_i^2 - \|x - s_i\|^2}{2\|x - s_i\|} \right)^2 \le \xi_i \end{aligned} \tag{10}$$

Considering $\|x\|^2$ is a non-convex parameter, the second-order relaxing parameter is defined as $\|x\|^2 \le y$. So $\|x - s_i\|^2$ can be converted to $y - 2s_i x + \|s_i\|^2$ and the following can be obtained:

$$\begin{aligned} &\min_{x,\xi} \sum_{i=1}^{N} \xi_i \\ &\frac{\left(r_i^2 - 2r_i\rho_i + \rho_i^2 - y + 2s_i x - \|s_i\|^2\right)^2}{4\left(y - 2s_i x + \|s_i\|^2\right)} \le \xi_i \\ &\frac{\left(r_i^2 - y + 2s_i x - \|s_i\|^2\right)^2}{4\left(y - 2s_i x + \|s_i\|^2\right)} \le \xi_i \\ &\|x\|^2 \le y \end{aligned} \tag{11}$$

Here, **Eq. 11** is a convex second-order cone program (SOCP)and the PD source localization can be implemented

TABLE 2 | Performance comparison of Pd location algorithm in power transformer of twcp-0.5/50.

No	Coordinate	CHAN		PSO		Proposed solution	
		Location result	Error (m)	Location result	Error (m)	Location result	Error (m)
1	(0.75, 0.485, 0.81)	(0.753, 0.466, 0.937)	0.128	(0.904, 0.45, 0.895)	0.18	(0.754, 0.484, 0.91)	0.101
2	(0.61, 0.485, 0.56)	(0.635, 0.516, 0.717)	0.162	(0.572, 0.624, 0.578)	0.145	(0.557, 0.473, 0.588)	0.061
3	(0.66, 0.772, 0.875)	(0.716, 0.888, 0.997)	0.177	(0.708, 0.733, 0.992)	0.132	(0.65, 0.737, 0.879)	0.037
4	(0.72, 1.0760, 0.403)	(0.841, 1.112, 0.443)	0.132	(0.693, 1.002, 0.524)	0.144	(0.734, 1.079, 0.474)	0.073
5	(0.675, 1.02, 0.610)	(0.664, 1.136, 0.698)	0.146	(0.657, 1.021, 0.714)	0.106	(0.686, 1.062, 0.652)	0.06

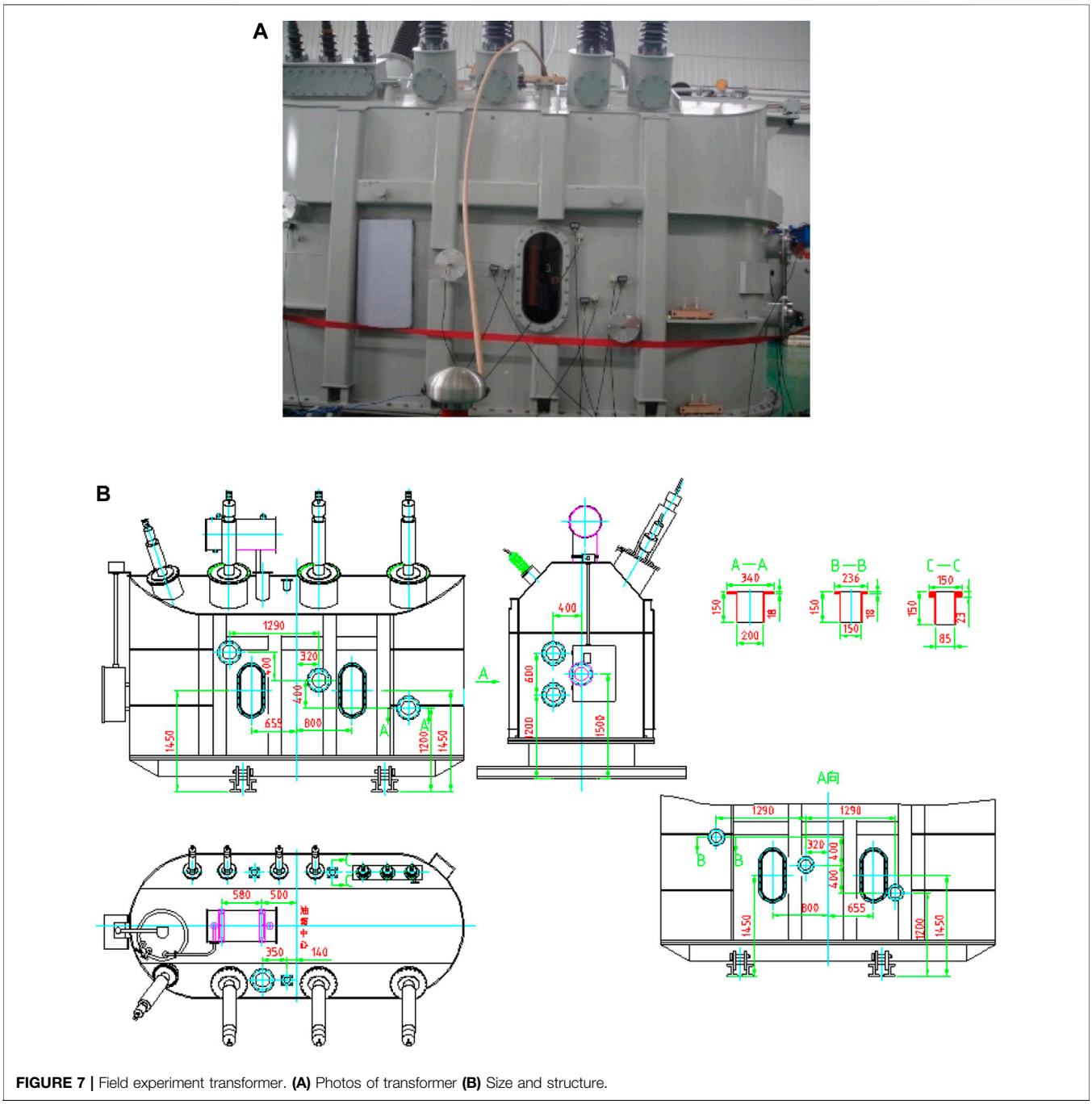

FIGURE 7 | Field experiment transformer. **(A)** Photos of transformer **(B)** Size and structure.

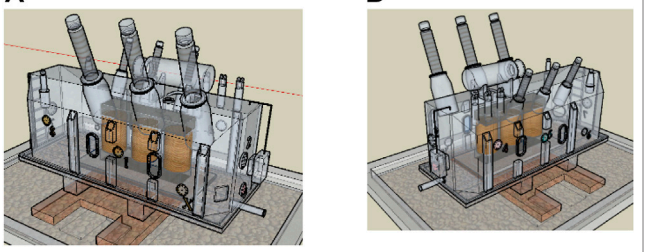

FIGURE 8 | Schematic diagram of transformer sensor location. **(A)** Front view **(B)** Back view.

through solving **Eq. 11** using the toolbox (CVX toolbox) in MATLAB (ver. R2019b).

PERFORMANCE EVALUATION AND NUMERICAL RESULT

Simulation Experiment

This section firstly carries out the performance evaluation of the proposed PD location solution through simulations. The simulated ODFS-334MVA/500kV transformer (8.6 m × 6.7 m × 7.6 m) in **Figure 3**. The propagation process of the ultrasonic wave within the studied transformer is simulated using the Edge-diffraction-toolbox (MATLAB ver. R2019b). In simulations, the ultrasonic wave propagation speed in the core, winding and oil are set as 5200 m/s, 3750 m/s and 1450 m/s, respectively, as suggested in (Harrold, 1979; Yang et al., 2021; Yang et al., 2022b). In this work, the errors of individual sensors follow the normal distribution described as $\mu = 0$, $\sigma = 3 \times 10^{-5}$.

Through MATLAB, randomly select the position of discharge source in different media of core, winding and oil, repeat the above simulation experiment for 10,000 times, and get the positioning error statistics of different positioning methods, as shown in **Figure 4**.

Figure 4 gives the simulation results of the proposed PD localization method against the existing CHAN and PSO algorithmic solutions (Yang et al., 2022a; Shen and Raksincharoensak, 2021; Xun et al., 2021; Yang, 2021). Since the refraction and diffraction errors are not considered in the CHAN algorithm, a significant PD source localization error can be produced. On the other hand, the PSO algorithm may fall into the local optimum in the iterative search process. As a result, the proposed method provides better performance compared with the comparison benchmarks with the overall positioning error within the range of 0.05–0.1 M.

Testbed Validation

The TWCP-0.5/50 transformer testbed is used for further validation (Wu et al., 2017; Han, 2019; Le et al., 2021). In the testbed, different forms of discharge models, e.g., oil gap discharge and tip discharge, are implemented. **Figure 5** illustrates the TWCP-0.5/50 transformer testbed from both the front and back view with the deployed ultrasonic partial discharge sensors as well as the fault setting devices. **Table 1** gives the

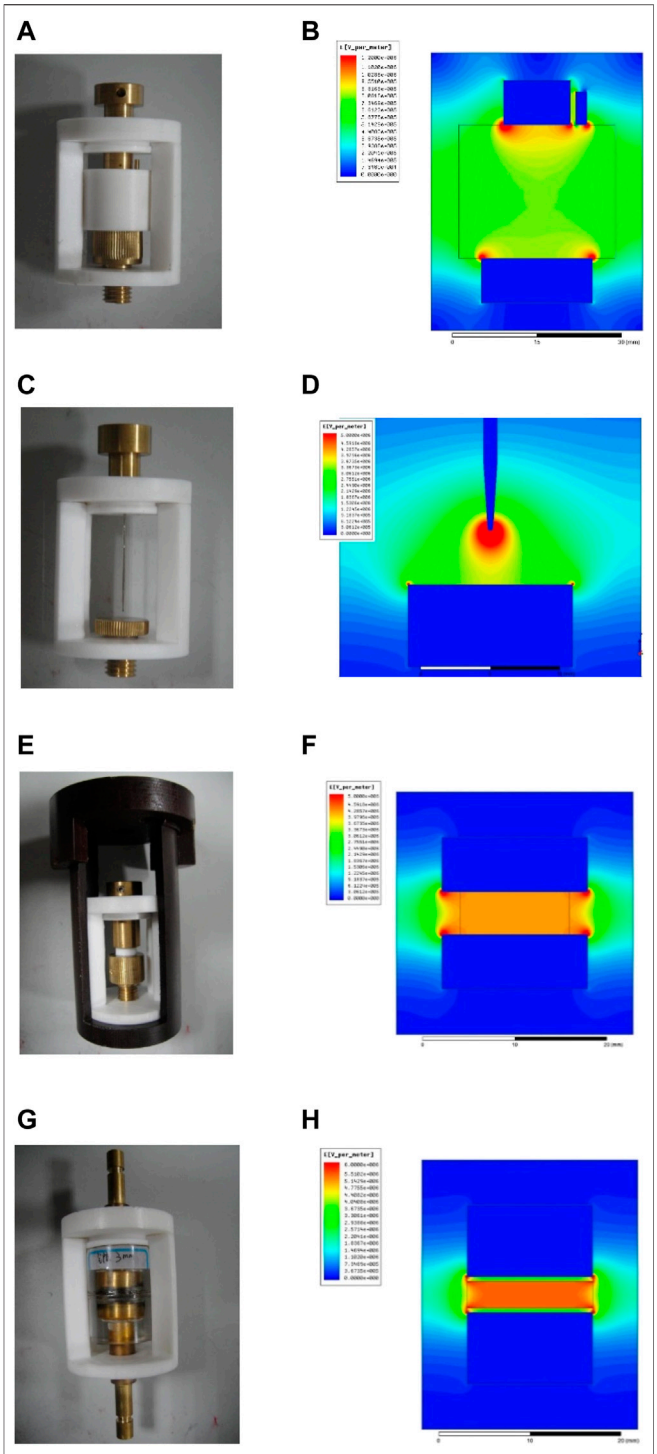

FIGURE 9 | Discharge models. **(A)** Suspension discharge model **(B)** Analysis simulation of suspension discharge model **(C)** Tip discharge model **(D)** Analysis simulation of tip discharge model **(E)** Surface discharge model **(F)** Analysis simulation of surface discharge model **(G)** Oil gap discharge model **(H)** Analysis simulation of oil gap discharge model.

FIGURE 10 | Discharge model in transformer.

locations of the deployed ultrasonic sensors in terms of spatial coordinates in the testbed.

In the testbed, the transformer is operated with the rated voltage. Here, the ultrasonic testing equipment bandwidth is 100 kHz with a sampling frequency of 20 MHz. The ultrasonic localization result based on the TWCP-0.5/50 transformer testbed is presented in **Figure 6**. In addition, the developed PD localization method is assessed against the existing solutions in the TWCP-0.5/50 testbed. **Table 2** presents the numerical results.

Table 2 presents the numerical results of the proposed solution against the CHAN and PSO algorithms.

The numerical results demonstrate that the proposed solution outperforms the comparison benchmarks, i.e., Chan and PSO algorithm, in terms of localization accuracy.

Field Test

The specifications and technical parameters of the 110kV transformer are as follows (Toyoda and Wu, 2021; Wu et al., 2021):

1) Type: S10-6300/110
2) Capacity: 6300/6300KVA
3) Rated voltage ratio: 110/35 kV/10.5 kV
4) Insulation level: LI480AC200/LI200AC95-LI75AC25
5) Connection group: YNd11
6) Short circuit impedance: 9%
7) Cooling mode: ONAN

The size of the transformer is 5.8 × 2.300 × 2 m, and the drawing is shown in **Figure 7**.

Eight ultrasonic sensors (No. 1–8) and one UHF sensor (No. x) are arranged around the transformer to form a three-dimensional sensor array, as shown in **Figure 8**.

In this work, the suspension discharge, tip discharge, surface discharge, and oil gap discharge models are developed. The electrodes at both ends of the model are made of brass, and the insulating material in the middle is polytetrafluoroethylene. The corresponding finite element models are established for analysis, and the electric fields of the discharge models are simulated, respectively, as illustrated in **Figure 9**.

The discharge defects in **Figure 9** relate to the electrical glue stick and put into the transformer, and the high voltage line that is corona free (red wire) and ground wire are appropriately tied to the electrical glue stick. This can pressurize the two poles of the discharge point defects to ensure the occurrence of partial discharge, as illustrated in **Figure 10**.The acoustic-electrical joint localization results are presented in **Figure 11**.

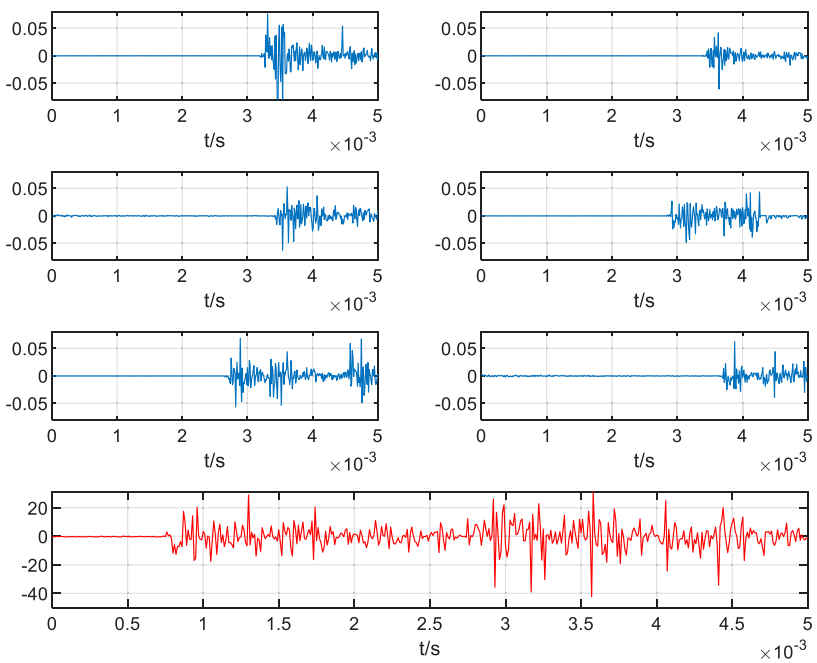

FIGURE 11 | Recording results of ultrasonic localization experiment of Field experiment transformer.

TABLE 3 | Performance Comparison of PD localization algorithm in power transformer.

No	Phase/ location	Discharge model type	Capacity (pC)	Coordinate	CHAN		PSO		Proposed solution	
					Location result	Error (m)	Location result	Error (m)	Location result	Error (m)
1.	Phase C (Top)	Suspended discharge	73.5	(4.213, 1.226, 1.702)	(4.242, 1.405, 1.907)	0.274	(4.298, 1.213, 1.911)	0.226	(4.187, 1.173, 1.737)	0.068
2.		Tip discharge	982.5	(4.457, 1.464, 1.618)	(4.707, 1.355, 1.714)	0.29	(4.461, 1.467, 1.773)	0.155	(4.517, 1.418, 1.642)	0.079
3.		Surface discharge	164.3	(4.34, 1.5, 1.206)	(4.475, 1.551, 1.331)	0.192	(4.376, 1.575, 1.357)	0.173	(4.383, 1.502, 1.219)	0.045
4.	Phase B (Middle)	Oil gap discharge	18,326.2	(3.1, 1.474, 0.841)	(3.17, 1.526, 1.083)	0.257	(2.943, 1.477, 0.947)	0.19	(3.171, 1.419, 0.882)	0.098
5.		Tip discharge	1,213.7	(3.486, 1.474, 1.039)	(3.279, 1.576, 1.101)	0.238	(3.408, 1.402, 1.237)	0.224	(3.427, 1.416, 1.133)	0.125
6.		Surface discharge	120.4	(3.601, 1.306, 0.863)	(3.642, 1.235, 1.109)	0.259	(3.661, 1.205, 1.05)	0.221	(3.585, 1.308, 0.967)	0.105
7.	Phase A (Bottom)	Tip discharge	1,036.3	(2.157, 1.449, 0.582)	(2.083, 1.38, 0.799)	0.24	(2.153, 1.452, 0.797)	0.215	(2.216, 1.439, 0.681)	0.115
8.		Surface discharge	183.4	(2.702, 1.223, 0.745)	(2.722, 1.515, 0.788)	0.295	(2.742, 1.173, 0.861)	0.132	(2.697, 1.179, 0.802)	0.072
9.		Suspension discharge	61.8	(0.913, 0.102, 0.2)	(1.023, 0.172, 0.437)	0.27	(0.898, 0.123, 0.369)	0.171	(0.929, 0.169, 0.234)	0.077

The proposed solution is further assessed in the field transformer that is operated at the rated voltage. The same sampling frequency is adopted in this experiment as in the testbed validation. The performance of the solution is evaluated against the CHAN algorithm and PSO-based algorithm. The numerical results are presented in detail in **Table 3**.

CONCLUSIVE REMARKS

This work presented an acoustic-electrical joint PD source localization solution that fully considered the multi-path propagation effect within the transformers. The SOCP algorithm is exploited and designed for PD source localization. The developed method has been extensively assessed and validated through simulations, testbed and field deployment. The obtained experimental results clearly demonstrated the effectiveness of the developed method and its benefit over the existing CHAN algorithm and PSO-based localization solution with the localization error of about 0.1 m.

For future work, a set of directions are considered worth further research exploitation. The proposed method needs to be evaluated through extensive experiments considering the cases of multiple partial discharge sources. Also, the advanced modeling techniques need to be further investigated for accurate characterization of multi-media refraction and diffraction.

DATA AVAILABILITY STATEMENT

The original contributions presented in the study are included in the article/supplementary material, further inquiries can be directed to the corresponding author.

AUTHOR CONTRIBUTIONS

JJ, HF and BW contributed to conception and design of the study. YL and YY organized the database. YC and DJ performed the statistical analysis.

REFERENCES

Cakir, O., Kaya, I., Yazgan, A., and Cakir, Ö. (2013). Dynamic Orientation of Receiver Arrays Using Particle Swarm Optimisation. *Electron. Lett.* 49, 1313–1315. doi:10.1049/el.2013.2165

Chan, Y. T., and Ho, K. C. (1994). A Simple and Efficient Estimator for Hyperbolic Location. *IEEE Trans. Signal. Process.* 42, 1905–1915. doi:10.1109/78.301830

Chang, Y.-T., Wu, C.-L., and Cheng, H.-C. (2014). The Enhanced Locating Performance of an Integrated Cross-Correlation and Genetic Algorithm for Radio Monitoring Systems. *Sensors* 14, 7541–7562. doi:10.3390/s140407541

Chen, Z. (2019). Review of Direction of Arrival Estimation Algorithms for Partial Discharge Localisation in Transformers. *IET Sci. Meas. Tech.* 13, 529–535. doi:10.1049/iet-smt.2018.5297

Coenen, S., and Tenbohlen, S. (2012). Location of PD Sources in Power Transformers by UHF and Acoustic Measurements. *IEEE Trans. Dielect. Electr. Insul.* 19, 1934–1940. doi:10.1109/TDEI.2012.6396950

Contin, A., Cavallini, A., Montanari, G. C., Pasini, G., and Puletti, F. (2002). Digital Detection and Fuzzy Classification of Partial Discharge Signals. *IEEE Trans. Dielect. Electr. Insul.* 9, 335–348. doi:10.1109/TDEI.2002.1007695

Ganguly, B., Chaudhury, S., Biswas, S., Dey, D., Munshi, S., Chatterjee, B., et al. (2020). Wavelet Kernel Based Convolutional Neural Network for Localization of Partial

Discharge Sources within a Power Apparatus. *IEEE Trans. Ind. Inf.* 17, 1. doi:10.1109/TII.2020.2991686

Han, J. (2019). A Novel Low Voltage Ride through Strategy for Cascaded Power Electronic Transformer. *Prot. Control. Mod. Power Syst.* 4, 1. doi:10.1186/s41601-019-0137-1

Han-Lee Song, S. (1994). Automatic Vehicle Location in Cellular Communications Systems. *IEEE Trans. Veh. Technol.* 43, 902–908. doi:10.1109/25.330153

Harrold, R. (1979). Acoustic Waveguides for Sensing and Locating Electrical Discharges in High Voltage Power Transformers and Other Apparatus. *IEEE Trans. Power Apparatus Syst.* 98, 449–457. doi:10.1109/TPAS.1979.319381

Hekmati, A., and Hekmati, R. (2017). Optimum Acoustic Sensor Placement for Partial Discharge Allocation in Transformers. *IET Sci. Meas. Tech.* 11, 581–589. doi:10.1049/iet-smt.2016.0417

Homaei, M., Moosavian, S. M., and Illias, H. A. (2014). Partial Discharge Localization in Power Transformers Using Neuro-Fuzzy Technique. *IEEE Trans. Power Deliv.* 29, 2066–2076. doi:10.1109/TPWRD.2014.2339274

Hooshmand, R. A., Parastegari, M., and Yazdanpanah, M. (2013). Simultaneous Location of Two Partial Discharge Sources in Power Transformers Based on Acoustic Emission Using the Modified Binary Partial Swarm Optimisation Algorithm. *IET Sci. Meas. Tech.* 7, 119–127. doi:10.1049/iet-smt.2012.0029

Howells, E., and Norton, E. T. (1978). Detection of Partial Discharges in Transformers Using Acoustic Emission Techniques. *IEEE Trans. Power Apparatus Syst.* 97, 1538–1549. doi:10.1109/TPAS.1978.354646

Jia, J., Hu, C., Yang, Q., Lu, Y., Wang, B., and Zhao, H. (2021). Localization of Partial Discharge in Electrical Transformer Considering Multimedia Refraction and Diffraction. *IEEE Trans. Ind. Inf.* 17, 5260–5269. doi:10.1109/TII.2020.3023883

Kallberg, B. (1980). Location of Partial Discharges in Power Transformers by Computation and Measurement of Capacitively Transmitted Voltage Pulses. *IEEE Trans. Power Apparatus Syst.* PAS-99, 589–596. doi:10.1109/TPAS.1980.319705

Karami, H., Tabarsa, H., Gharehpetian, G. B., Norouzi, Y., and Hejazi, M. A. (2020). Feasibility Study on Simultaneous Detection of Partial Discharge and Axial Displacement of HV Transformer Winding Using Electromagnetic Waves. *IEEE Trans. Ind. Inf.* 16, 67–76. doi:10.1109/TII.2019.2915685

Kweon, D.-J., Chin, S.-B., Kwak, H.-R., Kim, J.-C., and Song, K.-B. (2005). The Analysis of Ultrasonic Signals by Partial Discharge and Noise from the Transformer. *IEEE Trans. Power Deliv.* 20, 1976–1983. doi:10.1109/TPWRD.2004.833923

Le, Shuting., Wu, Yuhu., Guo, Yuqian., and Del Vecchio, Carmen. (2021). Game Theoretic Approach for a Service Function Chain Routing in NFV with Coupled Constraints. *IEEE Trans. Circuits Syst.* 68, 3557. doi:10.1109/tcsii.2021.3070025

Li, A., and Luan, F. (2018).An Improved Localization Algorithm Based on CHAN with High Positioning Accuracy in NLOS-WGN Environment. in 10th International Conference on Intelligent Human-Machine Systems and Cybernetics, 332–335.

Luo Yongfen, Y., Ji Shengchang, S., and Li Yanming, Y. (2006). Phased-ultrasonic Receiving-Planar Array Transducer for Partial Discharge Location in Transformer. *IEEE Trans. Ultrason. Ferroelect., Freq. Contr.* 53, 614–622. doi:10.1109/TUFFC.2006.1610570

Markalous, S., Tenbohlen, S., and Feser, K. (2008). Detection and Location of Partial Discharges in Power Transformers Using Acoustic and Electromagnetic Signals. *IEEE Trans. Dielect. Electr. Insul.* 15, 1576–1583. doi:10.1109/TDEI.2008.4712660

Meka, K., Giridhar, A. V., and Siva Sarma, D. V. S. S. (2018). PD Source Location Utilizing Acoustic TDOA Signals in Power Transformer by Fuzzy Adaptive Particle Swarm Optimization. *Radioengineering* 27, 1119–1127. doi:10.13164/re.2018.1119

Moore, P. J., Portugues, I. E., and Glover, I. A. (2006). Partial Discharge Investigation of a Power Transformer Using Wireless Wideband Radio-Frequency Measurements. *IEEE Trans. Power Deliv.* 21, 528–530. doi:10.1109/TPWRD.2005.848438

Naderi, M., Vakilian, M., Blackburn, T. R., Phung, B. T., Naderi, M., and Nasiri, A. (2007). A Hybrid Transformer Model for Determination of Partial Discharge Location in Transformer Winding. *IEEE Trans. Dielect. Electr. Insul.* 14, 436–443. doi:10.1109/TDEI.2007.344625

Rubio-serrano, J., Rojas-moreno, M. V., Posada, J., Martínez-tarifa, J. M., Robles, G., and Garcia-souto, J. A. (2012). Electro-acoustic Detection, Identification and Location of Partial Discharge Sources in Oil-Paper Insulation Systems. *IEEE Trans. Dielect. Electr. Insul.* 19, 1569–1578. doi:10.1109/TDEI.2012.6311502

Shen, Xun., and Raksincharoensak, Pongsathorn. (2021). Statistical Models of Near-Accident Event and Pedestrian Behavior at Non-signalized Intersections. *J. Appl. Stat.*, 1–21. doi:10.1080/02664763.2021.1962263

Tarimoradi, H., and Gharehpetian, G. B. (2017). Novel Calculation Method of Indices to Improve Classification of Transformer Winding Fault Type, Location, and Extent. *IEEE Trans. Ind. Inf.* 13, 1531–1540. doi:10.1109/TII.2017.2651954

Toyoda, M., and Wu, Y. (2021). Mayer-type Optimal Control of Probabilistic Boolean Control Network with Uncertain Selection Probabilities. *IEEE Trans. Cybern.* 51, 3079–3092. doi:10.1109/tcyb.2019.2954849

Wang, Y.-B., Chang, D.-G., Fan, Y.-H., Zhang, G.-J., Zhan, J.-Y., Shao, X.-J., et al. (2017). Acoustic Localization of Partial Discharge Sources in Power Transformers Using a Particle-Swarm-Optimization-Route-Searching Algorithm. *IEEE Trans. Dielect. Electr. Insul.* 24, 3647–3656. doi:10.1109/TDEI.2017.006857

Wu, Y., Guo, Y., and Toyoda, M. (2021). Policy Iteration Approach to the Infinite Horizon Average Optimal Control of Probabilistic Boolean Networks. *IEEE Trans. Neural Netw. Learn. Syst.* 32 (6), 2910–2924. doi:10.1109/TNNLS.2020.3008960

Wu, Y. H., Dong, X. Z., and Mirsaeidi, S. (2017). Modeling and Simulation of Air-Gapped Current Transformer Based on Preisach Theory. *Prot. Control. Mod. Power Syst.* 2, 11. doi:10.1186/s41601-017-0046-0

Xun, S., Tinghui, O., Nan, Y., and Jiancang, Z. (2021). Sample-based Neural Approximation Approach for Probabilistic Constrained Programs. *IEEE Trans. Neural Networks Learn. Syst.*, 1–8. doi:10.1109/tnnls.2021.3102323

Yang, N. (2021). "A Comprehensive Review of Security-Constrained Unit Commitment," in *Journal of Modern Power Systems and Clean Energy*. doi:10.35833/MPCE.2021.000255

Yang, N., Qin, T., Wu, L., Huang, Y., Huang, Y., Xing, C., et al. (2022a). A Multi-Agent Game Based Joint Planning Approach for Electricity-Gas Integrated Energy Systems Considering Wind Power Uncertainty. *Electr. Power Syst. Res.* 204, 107673. doi:10.1016/j.epsr.2021.107673

Yang, N., Yang, C., Wu, L., Shen, X., Jia, J., Li, Z., et al. (2022b). Intelligent Data-Driven Decision-Making Method for Dynamic Multisequence: An E-Seq2Seq-Based SCUC Expert System. *IEEE Trans. Ind. Inf.* 18, 3126–3137. doi:10.1109/TII.2021.3107406

Yang, N., Dong, Z., Wu, L., Zhang, L., Shen, X., Chen, D., et al. (2021). A Comprehensive Review of Security-Constrained Unit Commitment. *J. Mod. Power Syst. Clean Energy*, 1–14. doi:10.35833/MPCE.2021.000255

Conflict of Interest: Author JJ was employed by the company State Grid Jiangsu Electric Power Co., Ltd. Author HF was employed by the company State Grid Jiangsu Electric Power Co., Ltd. Author YL was employed by the company State Grid Taizhou Power Supply Company. Author YY was employed by the company State Grid Lianyungang Power Supply Company.

The remaining authors declare that the research was conducted in the absence of any commercial or financial relationships that could be construed as a potential conflict of interest.

Publisher's Note: All claims expressed in this article are solely those of the authors and do not necessarily represent those of their affiliated organizations, or those of the publisher, the editors and the reviewers. Any product that may be evaluated in this article, or claim that may be made by its manufacturer, is not guaranteed or endorsed by the publisher.

frontiers | Frontiers in Energy Research

BRIEF RESEARCH REPORT
published: 13 April 2022
doi: 10.3389/fenrg.2022.830628

A New Grounding Resistance Reduction Method for Wind Turbines by Grounding Grid Connection in Limited Areas

Yuanchao Hu[1], Zhixiang Liu[1], Tao Huang[2], Yunzhu An[1], Wentao Shen[2], Shangmao Hu[3], Chenghui Ma[4], Bingchen An[4] and Dan Chen[4]*

[1]School of Electrical and Electronic Engineering, Shandong University of Technology, Zibo, China, [2]Construction Branch of State Grid Jiangsu Electric Power Co., Ltd., Nanjing, China, [3]Electric Power Research Institute, China Southern Power Grid, Guangzhou, China, [4]Jining Huayuan Thermal Power Plant, Jining, China

Restricted by cultivated land vegetation, road construction, and land acquisition compensation costs, the grounding electrode extension method is not applicable for grounding resistance reduction of some wind turbines in limited areas. A new grounding resistance reduction method is proposed and verified for wind turbines by connecting nearby wind turbine grounding grids. To study the efficiency of the proposed method, the grounding characteristics of connected grounding grids are calculated. Simulation results indicate that the grounding resistance of connected grounding grids is smaller than that of box extension grounding grids. The grounding characteristics of the grounding grid connection are affected by grounding current frequency and material parameters. The grounding grid connection increases the current dispersion area and reduces the ground potential rise of the grounding conductor.

Keywords: wind turbine, grounding grid connection, grounding resistance, ground potential rise, grounding resistance reduction

OPEN ACCESS

Edited by:
Xun Shen,
Tokyo Institute of Technology, Japan

Reviewed by:
Xiaohan Shi,
Shandong University, China
Ming-Xiao Zhu,
China University of Petroleum Huadong, China

****Correspondence:***
Yunzhu An
anyunzhu2006@163.com

Specialty section:
This article was submitted to Wind Energy, a section of the journal Frontiers in Energy Research

Received: *07 December 2021*
Accepted: *14 March 2022*
Published: *13 April 2022*

Citation:
Hu Y, Liu Z, Huang T, An Y, Shen W, Hu S, Ma C, An B and Chen D (2022) A New Grounding Resistance Reduction Method for Wind Turbines by Grounding Grid Connection in Limited Areas. Front. Energy Res. 10:830628. doi: 10.3389/fenrg.2022.830628

INTRODUCTION

Lightning discharge is an important factor affecting the stability of power systems. The lightning back flashover is the main reason for lightning accidents in wind turbines (Zhang et al., 2015; Kuklin, 2016; Shen et al., 2020). Reducing the grounding resistance is an effective measure to improve the lightning withstanding level of wind turbines and power systems (Wu et al., 2014; Shen et al., 2017; Taha et al., 2020). However, the grounding construction of a wind turbine is restricted by cultivated land vegetation, road construction, and land acquisition compensation costs in practical grounding engineering, which affect the current dissipation and resistance reduction of the grounding grid.

In recent years, a lot of research studies were conducted on the grounding resistance reduction of grounding grids. Li et al. (2013) conducted a comparison simulation test on the horizontal star grounding grid with and without spicules. The results show that the local structure change of the grounding grid can expand the spark discharge area and reduce the impulse grounding impedance. Yuan et al., 2012; Zhu et al., 2015 conducted a systematic study to analyze the effect of the spicule's length, the spicule's location, and the distance between adjacent spicules on the grounding characteristics of the grounding grid. Caetano et al. (2018) proposed the arrangement method of connecting the tower foundation to a set of additional grounding grids by using overhead lines to increase the dispersion length and reduce the grounding impedance. Alipio et al., 2021 show that when the wind turbine grounding systems are connected by a bare

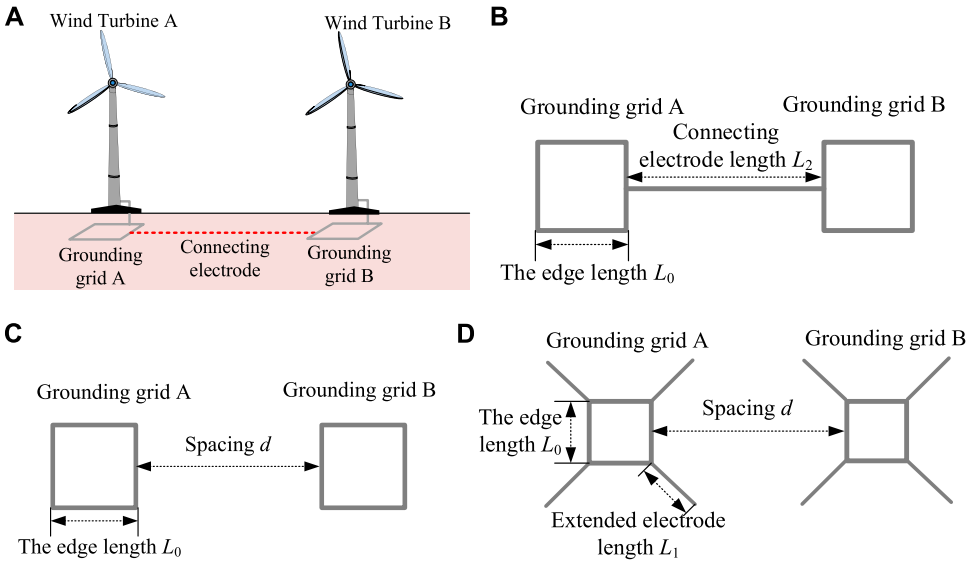

FIGURE 1 | Schematic diagram of the nearby wind turbine grounding grid. **(A)** Nearby wind turbine grounding grid connection. **(B)** Grounding grid connection. **(C)** Box grounding grid. **(D)** Box extension grounding grid.

conductor, the ground potential rise (GPR) peak reduction is due to the connecting electrode, and when the connection is made through an insulated electrode, the GPR reduction is related to the current that is partly diverted to the adjacent grounding grid, especially for high-resistivity soils. Gao et al., 2018 conducted a series of calculations based on a typical tower grounding grid model to study the influence of length and number of vertical grounding electrodes on grounding resistance reduction. In recent years, non-metallic grounding material has been applied to the tower grounding grid (Hu et al., 2016; Shen and Pongsathorn, 2021; Sun et al., 2021) Compared with galvanized steel, the flexible graphite composite grounding material can effectively reduce the grounding resistance under a high-frequency current.

Currently, there are few studies on the current dispersion and resistance reduction of the wind turbine grounding grid under a limited construction area. A new grounding resistance reduction method is proposed in this article for wind turbines by connecting nearby wind turbine grounding grids together. Two grounding resistance reduction methods are compared in detail, including grounding grids with the traditional extension electrode method and the proposed grounding grid connection method. Factors such as extension length, soil resistivity, current frequency, and grounding material are analyzed to study the grounding resistance reduction efficiency. Besides, the GPR of the grounding conductor of the grounding grid connection is calculated to verify the safety of the proposed method.

DIFFERENT MODELS OF THE WIND TURBINE GROUNDING GRID

In order to reduce the grounding resistance of nearby wind turbines under the limited construction area, box extension grounding grid models are commonly applied in practical cases. In this article, the nearby grounding grid connection method is proposed for grounding resistance reduction, as shown in **Figure 1A**. To illustrate the effectiveness of the grounding grid connection method, three models of the wind turbine grounding grid are established as shown in **Figures 1B–D**, including the box grounding grid, the box extension grounding grid, and the grounding grid connection.

In the grounding grid, the edge length L_0 of the box grounding electrode is 10 m. For the traditional box extension grounding grid model, extended grounding electrodes with a length of L_1 are located at the four corners of the grounding grid. For the proposed grounding grid connection model, the grounding grids of two wind turbines are connected by grounding the electrode with a length of L_2. It should be noted that the connecting electrode in **Figure 1B** and the extended grounding electrode in **Figure 1D** belong to the extended grounding electrode of the grounding grid. When setting the simulation parameters, the total length L of extended grounding electrodes of different grounding grids should be kept equal, that is, $L = L_2 = 8^*L_1$. The grounding electrodes are buried in soil with a depth of 0.8 m. To simulate the practical lightning impulse grounding characteristics of the abovementioned three grounding grids, a current of 40 kA is applied to the grounding grid for the amplitude of most lightning currents in nature is between 16 and 40 kA.

Metallic materials are commonly applied in the grounding grid. Owing to their high magnetoconductivity, the skin effect and inductance effect will be intense, resulting in a high impulse grounding impedance. Compared with metal grounding materials, flexible graphite composite materials have stable physical and chemical properties, low magnetoconductivity, and good electrical conductivity (Hu et al., 2014). The impulse

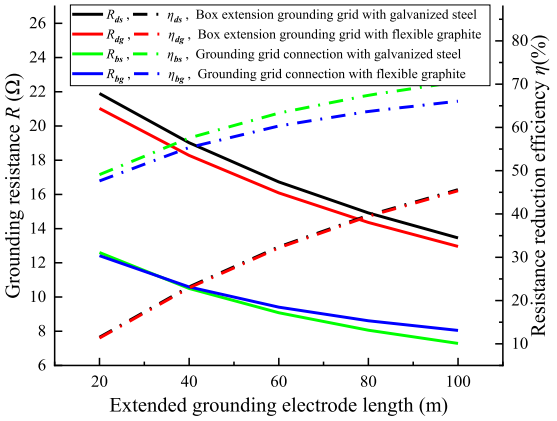

FIGURE 2 | Grounding resistance and resistance reduction efficiency under different extended grounding electrode lengths.

grounding impedance can be smaller. To compare their grounding characteristics, galvanized steel and flexible graphite composite grounding materials are selected. The diameter of galvanized steel and the flexible graphite electrode is 16 and 28 mm, respectively. The relative resistivity of galvanized steel and the flexible graphite electrode is 109.7 and 1857.1, respectively, while the relative permeability is 636 and 1, respectively. As a 10 kHz current flows through the abovementioned two grounding electrodes, their skin depths are 0.277 and 28.692 mm, respectively.

SIMULATION AND ANALYSIS ON THE GROUNDING RESISTANCE REDUCTION METHOD OF THE WIND TURBINE

The grounding characteristics of the wind turbine grounding grid are related to many factors, such as the grounding material, extended grounding electrode length, soil resistivity, and grounding current frequency. In order to characterize the influence of a certain factor on wind turbine grounding resistance, the resistance reduction efficiency η is introduced. Resistance reduction efficiency η is defined as **Eq.1**

$$\eta = \frac{R_0 - R_i}{R_0} \times 100\%, \tag{1}$$

where R_0 is the primary grounding resistance with no resistance reduction method, Ω, and R_i is the grounding resistance with the resistance reduction method, Ω.

The grounding grids of different structures are composed of galvanized steel or flexible graphite. According to the number of grounding grids in **Figure 1** and the grounding material, the grounding resistance R and the resistance reduction coefficient η are expressed in different forms. Among them, the grounding resistances of the grounding grid connection with galvanized steel and flexible graphite are respectively represented by R_{bs} and R_{bg}, and the corresponding resistance reduction efficiencies are represented by η_{bs} and η_{bg}; the grounding resistances of the box grounding grid with galvanized steel and flexible graphite are respectively represented by R_{cs} and R_{cg}, and the corresponding resistance reduction efficiencies are represented by η_{cs} and η_{cg}; the grounding resistances of the box extension grounding grid with galvanized steel and flexible graphite are respectively represented by R_{ds} and R_{dg}, and the corresponding resistance reduction efficiencies are represented by η_{ds} and η_{dg}.

Effect of Extended Grounding Electrode Length

To study the effect of extended grounding electrode length on grounding resistance reduction of the wind turbine grounding grid, the extended grounding electrode length L is taken as 0–100 m. The soil resistivity is 500 Ω m, and the grounding current frequency is 50 Hz. Both the traditional box extension grounding grid model and the proposed grounding grid connection model are applied with galvanized steel and the flexible graphite material. The grounding resistance and resistance reduction efficiency calculation results are shown in **Figure 2**.

The grounding resistances of galvanized steel and the flexible graphite box grounding grid are 24.75 and 23.72Ω, respectively. As shown in **Figure 3**, the wind turbine grounding resistance decreases gradually with the increase of extended length. With the same extended length, the grounding resistance of the grounding grid connection method is smaller.

When the box extension grounding grid scheme is adopted or the grounding electrode length L_2 of the grounding grid connection is less than 40m, the grounding resistance of the flexible graphite grounding grid is smaller. However, when the grounding electrode length L_2 of the grounding grid connection is more than 40 m, the grounding resistance of the galvanized steel grounding grid is lower. This is because when the size of the grounding grid is relatively small, the volume of the grounding conductor occupies a large proportion of the entire grounding system. A larger-diameter flexible graphite grounding electrode is

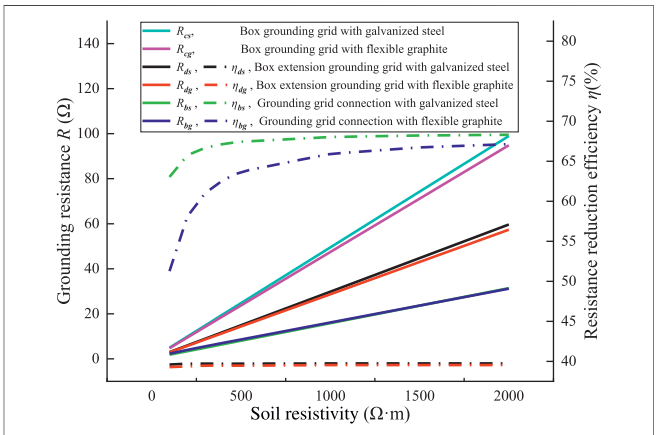

FIGURE 3 | Grounding resistance and resistance reduction efficiency under different soil resistivities.

conducive to current dispersion to the soil. In a large grounding grid, the volume of the grounding conductor accounts for a small proportion of the entire grounding system, and the low-resistivity galvanized steel is more conducive to current dispersion to the soil.

It can also be seen from **Figure 2** that the grounding resistance reduction efficiency of the grounding grid connection method is higher than that of the box extension grounding grid method. Besides, the grounding resistance reduction efficiency increases with the extended grounding electrode length but shows a saturated tendency. When the connecting grounding electrode length is 100 m, the resistance reduction efficiency of the galvanized steel grounding grid and flexible graphite grounding grid is 70.55 and 66.06%, respectively. However, as the connecting grounding electrode length is increased from 80 to 100 m, the resistance reduction efficiency of the galvanized steel grounding grid and flexible graphite grounding grid is increased by less than 5%. This is mainly because the current dispersion length of the connecting grounding electrode has a certain limit. As the effective current dispersion length is reached, a longer connecting electrode length cannot significantly improve the resistance reduction efficiency.

Effect of Soil Resistivity

There are great differences in soil resistivity under different geological terrain areas. The corresponding requirements for wind turbine grounding resistance are also different (Alipio et al., 2019; Salarieh et al., 2020). In order to study the effect of soil resistivity on the grounding resistance reduction of the wind turbine, the soil resistivity is set to 100–2000 Ω m. Moreover, the extended grounding electrode length L is 80m, and the current frequency is 50 Hz. The grounding resistance and resistance reduction efficiency of grounding grids under different soil resistivities are shown in **Figure 3**.

As the soil resistivity is 100 Ω m, there is little difference between the grounding resistance of the traditional box extension grounding grid and the proposed grounding grid connection for good current dispersion characteristics in the soil. With the increase of soil resistivity, the current dispersion in soil becomes difficult. Under the same high-soil resistivity conditions, the grounding resistance of the grounding grid connection is about 50% of that of the box extension grounding grid.

The resistance reduction efficiency of the box extension grounding grid is constant at about 40%, while the resistance reduction efficiency of the grounding grid connection increases from 51 to 68% with a soil resistivity of 100–2000 Ω m. Under the same soil conditions, the resistance reduction efficiency of the grounding grid connection is obviously higher than that of the box extension grounding grid.

In the connected grounding grids, the resistance reduction efficiency of the galvanized steel grounding grid is higher than that of the flexible graphite grounding grid, but the difference gradually decreases with the increasing soil resistivity. Under a soil resistivity of 100–1500 Ω m, the grounding grid made of low-resistivity galvanized steel has a larger current dispersion ability to the far end. However, high soil resistivity can intensify the end effect of the grounding electrode, which makes more current tend to disperse from the far end into the soil. Thus, the effect of the grounding material on grounding resistance reduction decreases in areas with high soil resistivity.

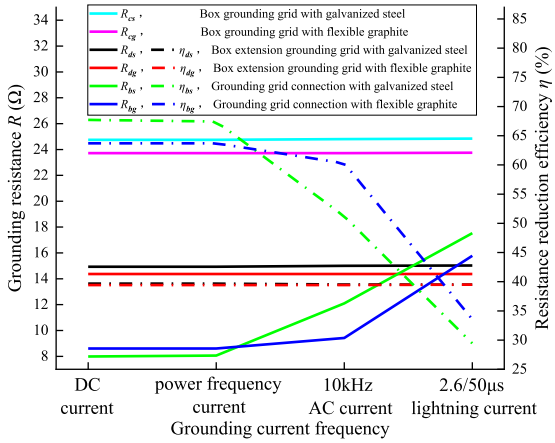

FIGURE 4 | Grounding resistance and resistance reduction efficiency under different grounding current frequencies.

Effect of Grounding Current Frequency

In nature, more than 90% of lightning current energy is concentrated within 20 kHz. In order to study the effect of grounding current frequency on wind turbine grounding characteristics (Chen and Du, 2019; Sekioka, 2019), a DC current, a power frequency current, an AC current of 10 kHz, and a standard lightning current of 2.6/50 μs were applied. The current amplitude is 40 kA, the soil resistivity is 500 Ω m, and the extended grounding electrode length L is 80 m. The grounding resistance of two grounding grids under different grounding current frequencies is calculated, as shown in **Figure 4**.

As shown in **Figure 4**, under different grounding current frequencies, the grounding resistance of the box grounding grid composed of galvanized steel and flexible graphite is constant at 24.8 and 23.7 Ω, respectively, and the grounding resistance of the box extension grounding grid composed of galvanized steel and flexible graphite is constant at 15 and 14.4 Ω, respectively. This is because the size of the grounding grid is relatively small so that the current at different frequencies can be fully dispersed in the grounding grid.

With an increase in grounding current frequency, the grounding resistance of connected ground grids increases. The flexible graphite grounding grid has lower grounding resistance than the steel one. It is caused by the weaker inductance effect, the skin effect, and better dispersion properties of the flexible graphite grounding electrode with lower magnetoconductivity.

It can also be seen from **Figure 4** that the resistance reduction efficiency of the box extension grounding grid is constant at 40% under different grounding current frequencies. The resistance reduction efficiency of connected grounding grids varies with the grounding material and

TABLE 1 | Grounding resistance of three grounding grids.

Grounding grid	Power frequency ground resistance R/Ω	Standard value R/Ω
Box grounding grid	24.76	15
Box extension grounding grid	14.92	15
Grounding grid connection	8.03	15

grounding current frequency. As the grounding current frequency increases, the resistance reduction efficiency of connected grounding grids decreases. Under DC or power frequency current, the resistance reduction efficiency of the grounding grid is greater than 62%, which is higher than that of the box extension grounding grid; under the AC current of 10 kHz, the resistance reduction efficiency of the flexible graphite grounding grid is higher than that of the galvanized steel grounding grid; under the standard lightning current of 2.6/50 μs, the large high-frequency component of lightning current causes a great inductance effect and skin effect of the grounding electrode, leading to a smaller resistance reduction efficiency of connected grounding grids.

GROUND POTENTIAL RISE OF THE GROUNDING CONDUCTOR OF THE GROUNDING GRID CONNECTION

The current dispersion in the grounding grid determines the potential distribution of the grounding conductor. In order to analyze the grounding characteristics and GPR of the grounding conductor of the three grounding grids shown in **Figure 1**, the edge length of the grounding grid L_0 is 10 m, and the quad-angle extended grounding electrode L_1 is 10 m. The connecting grounding electrode L_2 and the grounding grid spacing d are 80 m. Galvanized steel grounding grids are buried in the soil with a resistivity of 500 Ω m. The power frequency grounding current of 40 kA is applied to wind turbine A. The grounding resistance results are shown in **Table 1**.

As shown in **Table 1**, with the increasing grounding grid area, the grounding resistance decreases. The grounding resistance of the box grounding grid with the smallest grounding current dispersion area is 24.76 Ω, which is higher than the standard value of 15 Ω. The grounding resistance of the box extension grounding grid and the grounding grid connection is less than the standard value, and the minimum grounding resistance of the grounding grid connection is only 8.03 Ω. Due to more current flowing into the soil, the GPR of the grounding conductor decreases with the increasing grounding grid area. The maximum GPR of the box grounding grid is 995 kV. By adding an auxiliary extended grounding electrode, the maximum GPR value can be reduced to 598 kV, with a decrease of 39.9%. Meanwhile, the induced voltage of the wind turbine B grounding grid is 35.7 kV. The grounding grid connection further increases the current dispersion area so that the maximum GPR of the wind turbine A grounding grid is 322 kV, and the maximum GPR of the wind turbine B grounding grid is 302 kV. Therefore, the GPR of the wind turbine B grounding grid does not exceed the insulation level of the wind turbine at the same voltage level.

According to the abovementioned analysis, we can infer that when the voltage level or insulation level of wind turbines is close, the current dispersion from the lightning-struck wind turbine will not cause the back flashover of the connected wind turbine. With the increase of distance between adjacent wind turbines and the decrease of soil resistivity, the influence will be further reduced. Therefore, the grounding grid connection structure is conducive to reducing the GPR of the grounding grid and the lightning potential at the wind turbine top.

CONCLUSION

In this article, the grounding characteristics of the grounding grid connection and the box extension grounding grid are compared. The current dispersion effect of galvanized steel and the flexible graphite composite grounding electrode is analyzed. The GPRs of the grounding grid connection are studied. The conclusions are as follows:

1) Under the power frequency current, the grounding resistance of the grounding grid connection is smaller than that of the box and box extension grounding grid. The grounding resistance of the grounding grid decreases with the increase of the extended grounding electrode length and the decrease of soil resistivity. As the connecting grounding electrode length L_2 exceeds 80m, the resistance reduction of the grounding grid gradually slows down; as the soil resistivity exceeds 1000 Ω m, the resistance reduction efficiency of the grounding grid connection is nearly saturated and constant at about 68%.
2) The higher the grounding current frequency, the more obvious the advantage of the flexible graphite composite grounding grid dispersing current to the far end. Meanwhile, the high-frequency grounding current limits the grounding reduction efficiency of the grounding grid connection.
3) The grounding grid connection increases the current dispersion area, making the GPR of the grounding conductor lower than that of the box extension grounding grid. When the voltage level or insulation level of wind turbines is close, the current dispersion of the lightning-struck wind turbine will not cause the back flashover of connected wind turbines.

DATA AVAILABILITY STATEMENT

The original contributions presented in the study are included in the article/Supplementary Material, and further inquiries can be directed to the corresponding author.

AUTHOR CONTRIBUTIONS

YH: conceptualization, writing—original draft preparation, and simulation; ZL: software and grounding test; TH: software and grounding test; YA: project administration and data arrangement; WS: supervision; SH: supervision and proofreading; CM: drawing; BA: figures; DC: revision.

FUNDING

This work was supported by the Natural Science Foundation of China under Grant 51807113, the Shandong Provincial Natural Science Foundation, China (ZR2021ME092), the Jiangsu Provincial Natural Science Foundation, China (SBK2020042717), and the China Southern Power Grid Science and Technology Project(CSGULAEMEST-2021-KF-05).

REFERENCES

Alipio, R., Conceição, D., De Conti, A., Yamamoto, K., Dias, R. N., and Visacro, S. (2019). A Comprehensive Analysis of the Effect of Frequency-dependent Soil Electrical Parameters on the Lightning Response of Wind-Turbine Grounding Systems. *Electric Power Syst. Res.* 175, 105927. doi:10.1016/j.epsr.2019.105927

Alipio, R., De Conti, A., Duarte, N., and Correia de Barros, M. T. (2021). Bare versus Insulated Conductors for Improving the Lightning Response of Interconnected Wind Turbine Grounding Systems. *Electric Power Syst. Res.* 197, 107320. doi:10.1016/j.epsr.2021.107320

Caetano, C. E. F., Lima, A. B., Paulino, J. O. S., Boaventura, W. C., and Cardoso, E. N. (2018). A Conductor Arrangement that Overcomes the Effective Length Issue in Transmission Line Grounding. *Electric Power Syst. Res.* 159, 31–39. doi:10.1016/j.epsr.2017.09.022

Chen, H., and Du, Y. (2019). Lightning Grounding Grid Model Considering Both the Frequency-dependent Behavior and Ionization Phenomenon. *IEEE Trans. Electromagn. Compat.* 61 (1), 157–165. doi:10.1109/TEMC.2017.2789210

Gao, Z., Cao, X., and Du, J. (2018). Study on the Effect of Vertical Rod on Reducing Tower's Impulse Grounding Resistance[J]. *High Voltage Apparatus* 54 (04), 182–187. doi:10.13296/j.1001-1609.hva.2018.04.027

Hu, Y., Ruan, J., Gong, R., et al. (2014). Flexible Graphite Composite Electrical Grounding Material and its Application in tower Grounding Grid of Power Transmission System[J]. *Power Syst. Tech.* 38 (10), 2851–2857. doi:10.13335/j.1000-3673.pst.2014.10.037

Hu, Y., Ruan, J., Xiao, W., et al. (2016). Study on Flexible Graphite Composite Material for Electrical Grounding and its Correlation Experimentations[J]. *High Voltage Eng.* 42 (06), 1879–1889. doi:10.13336/j.1003-6520.hve.20160616028

Kuklin, D. (2016). Choosing Configurations of Transmission Line tower Grounding by Back Flashover Probability Value. *Front. Energ.* 10 (2), 213–226. doi:10.1007/s11708-016-0398-6

Li, J., Jiang, J., and Li, L. (2013). Simulation and experiment Study on Resistance-Reducing Mechanism of Grounding Device with Spicules[J]. *Power Syst. Tech.* 37 (01), 211–217. doi:10.13335/j.1000-3673.pst.2013.01.037

Salarieh, B., De Silva, H. M. J., and Kordi, B. (2020). Electromagnetic Transient Modeling of Grounding Electrodes Buried in Frequency Dependent Soil with Variable Water Content. *Electric Power Syst. Res.* 189, 106595. doi:10.1016/j.epsr.2020.106595

Sekioka, S. (2019). Frequency and Current-dependent Grounding Resistance Model for Lightning Surge Analysis. *IEEE Trans. Electromagn. Compat.* 61, 419–425. doi:10.1109/temc.2018.2829923

Shen, X., and Pongsathorn, R. (2021). Pedestrian-aware Statistical Risk Assessment. *IEEE Trans. Intell. Transportation Syst.*, 1-9. doi:10.1109/tits.2021.3074522

Shen, X., Zhang, Y., and Kota, S. (2020). Gaussian Mixture Model Clustering-Based Knock Threshold Learning in Automotive Engines. *IEEE/ASME Trans. Mechatronics* 25(6):2981-2991. doi:10.1109/tmech.2020.3000732

Shen, X., Zhang, Y., and Tielong, S. (2017). Spark advance Self-Optimization with Knock Probability Threshold for Lean-Burn Operation Mode of SI Engine. *Energy* 122 (MAR.1), 1–10. doi:10.1016/j.energy.2017.01.065

Sun, J., Tian, X., Li, Y., Wu, Y., Duan, Y., Chen, J., et al. (2021). Lightning Strike-Induced Dynamic Conduction Characteristics and Damage Behavior of Carbon Fiber-Reinforced Polymer Composites. *Compos. Structures* 275, 114391. doi:10.1016/j.compstruct.2021.114391

Taha, M. A., Li, L., and Wang, P. (2020). Estimation Performance of the Lightning protection System in an Urban 110 kV Grounding Grid Substation. *Results Eng.* 6, 100140. doi:10.1016/j.rineng.2020.100140

Wu, J., Zhang, B., He, J., and Zeng, R. (2014). Optimal Design of tower Footing Device with Combined Vertical and Horizontal Grounding Electrodes under Lightning. *Electric Power Syst. Res.* 113, 188–195. doi:10.1016/j.epsr.2014.03.021

Yuan, T., Lei, C., and Sima, W. (2012). Analysis of Grounding Resistance Reduction Effect Based on Enhancing Impulse Current Leakage Efficiency [J]. *Trans. China Electrotechnical Soc.* 27 (11), 278–284. doi:10.19595/j.cnki.1000-6753.tces.2012.11.037

Zhang, B., He, J., and Zeng, R. (2015). State of Art and Prospect of Grounding Technology in Power System[J]. *High Voltage Eng.* 41 (8), 2569–2582. doi:10.13336/j.1003-6520.hve.2015.08.010

Zhu, B., Sima, W., and Yuan, T. (2015). Structure Parameter Optimization of Grounding Device with Needle-Shaped Conductors Based on Electric Field Distribution in Soil[J]. *Power Syst. Tech.* 39 (10), 2907–2914. doi:10.13335/j.1000-3673.pst.2015.10.034

Conflict of Interest: TH and WS were employed by the company State Grid Jiangsu Electric Power Co., Ltd. SH was employed by the company China Southern Power Grid.

The remaining authors declare that the research was conducted in the absence of any commercial or financial relationships that could be construed as a potential conflict of interest.

Publisher's Note: All claims expressed in this article are solely those of the authors and do not necessarily represent those of their affiliated organizations or those of the publisher, the editors, and the reviewers. Any product that may be evaluated in this article or claim that may be made by its manufacturer is not guaranteed or endorsed by the publisher.

frontiers | Frontiers in Energy Research

ORIGINAL RESEARCH
published: 26 April 2022
doi: 10.3389/fenrg.2022.888327

Numerical Analysis on the Sub-Span Oscillation of Iced Eight-Bundle Conductors During Galloping

Liu Yu[1], *Cai Mengqi*[2,3]*, *Wang Qingyuan*[1,2,3]*†, *Zhou Linshu*[4], *Xu Qian*[3], *Ding Shunli*[1], *Liu Jun*[5] *and Huang Chunlin*[1]

[1]School of Mechanical Engineering, Chengdu University, Chengdu, China, [2]Failure Mechanics and Engineering Disaster Prevention Key Laboratory of Sichuan Province, Sichuan University, Chengdu, China, [3]School of Architecture and Civil Engineering, Chengdu University, Chengdu, China, [4]State Grid Sichuan Integrated Energy Service Co. Ltd, Chengdu, China, [5]School of Mechanical and Electrical Engineering, Southwest Petroleum University, Chengdu, China

Under the excitement of wind loads, UHV transmission lines are subject to two types of vibration phenomena, namely, sub-span oscillation and galloping. This phenomenon can easily lead to conductor breakage, interphase flashover, fatigue damage to fittings, and even lead to tower collapse and disconnection accidents. The numerical analysis method is used to analyze the sub-span oscillation characteristics of the eight-bundle conductor during galloping. The results of the numerical simulation are compared to explore the influence of wind speed, span length, initial angle of wind attack, and turbulence intensity on the galloping line, looking for movement characteristics between each sub-conductor. The results provide a reference for research on the galloping principle of UHV transmission line and anti-oscillation to further improve the resistance of the power grid against disaster ability.

Keywords: galloping characteristic, iced eight-bundle conductors, multi-span transmission line, numerical simulation, sub-span oscillation

OPEN ACCESS

Edited by:
Yusen He,
Grinnell College, United States

Reviewed by:
Cheng Liu,
Shanghai Jiao Tong University, China
C. Lu,
Columbia University, United States

****Correspondence:***
Wang Qingyuan
wangqy@scu.edu.cn
Cai Mengqi
mq.cai@foxmail.com

†This author have contributed equally to this work

Specialty section:
This article was submitted to Wind Energy, a section of the journal Frontiers in Energy Research

Received: *02 March 2022*
Accepted: *17 March 2022*
Published: *26 April 2022*

Citation:
Yu L, Mengqi C, Qingyuan W, Linshu Z, Qian X, Shunli D, Jun L and Chunlin H (2022) Numerical Analysis on the Sub-Span Oscillation of Iced Eight-Bundle Conductors During Galloping. Front. Energy Res. 10:888327. doi: 10.3389/fenrg.2022.888327

INTRODUCTION

In recent years, there has been the problem of imbalance between power supply and demand (EPRI 2009; Li et al., 2021a; Li et al., 2021b; Li et al., 2022). Therefore, it is necessary to address ultra-long distance and cross-regional energy transmission. Of course, the safe operation of UHV transmission lines will be affected by the working environment. Due to the sudden change and complexity of the external environment, the normal operation of transmission lines faces serious challenges (Jafari et al., 2020). Aerodynamic instability of iced conductors with asymmetric cross-section area would cause iced conductors to gallop. This phenomenon is typical self-excited fluid–solid coupling vibration, which may cause breakage and short-circuit of transmission lines, or even tower toppling (Nigol et al., 1977; Cai et al., 2019a; Cai et al., 2019b). Research on the galloping phenomenon of UHV transmission lines is very limited, which cannot yet meet the actual engineering needs. In recent years, domestic scholars have begun to study the galloping mechanism of UHV transmission lines and its prevention and control technology, but much research work is still in the exploratory stage.

Numerical models for sub-span oscillation analysis of subconductors are usually dependent on quasi-stationary theory (QST). Since it is very difficult to design a corresponding small-scale model of transmission lines in a long-span length wind tunnel, numerical simulation is an effective method for studying wake-induced oscillation phenomena. Most researchers focused

on the wake-induced oscillation responses of twin bundle conductors. Rawlins (1976) and Rawlins (1977) expressed the dynamic properties of twin conductors in the normal propagation mode using the transfer matrix method. Tsui and Tsui (1980) used the 2D and 3D finite element method (FEM) to study sub-span oscillation. Williams and Suaris (2006) presented an interference model to discuss the effects of space on aerodynamic response, and they highlighted that there were three dominant regions: the proximity interference region, induced sub-span oscillation region, and wake interference region. With the wide use of quad-bundle conductors, the sub-span oscillation of quad bundle conductors attracts the interest of researchers. Diana et al. (2014a) and Diana et al. (2014b) proposed a numerical approach to reproduce sub-span oscillation and investigated the quad spacer damper for controlling sub-span oscillations using aerodynamic coefficients obtained in wind tunnel tests. Although there are some studies on the oscillation of bundle conductors, the effects of complicated meteorological conditions of sub-span oscillation behaviors of bundle conductor transmission lines, especially eight-bundle conductors, require further investigation.

TABLE 1 | Parameters of the iced eight-bundle conductor.

Section	Size (mm)	ρ (kg/M^3)	*E* (MPa)	*G* (MPa)
Conductor	30	1735.9	63,000	24,230.7
Ice	18	900	0.6	0.6

In recent years, lots of experts have studied the problem of galloping of transmission lines by numerical methods. Cai et al. (2015) studied the variation of the aerodynamic coefficient varying with the angle of wind attack by using the finite element method (FEM). Zhou et al. (2018) carried out a wind tunnel simulation to simulate the galloping of iced eight-bundle conductors and investigated different galloping behaviors of the parameters. Cai et al. (2019b) used the nonlinear FEM to analyze the galloping morphology of a

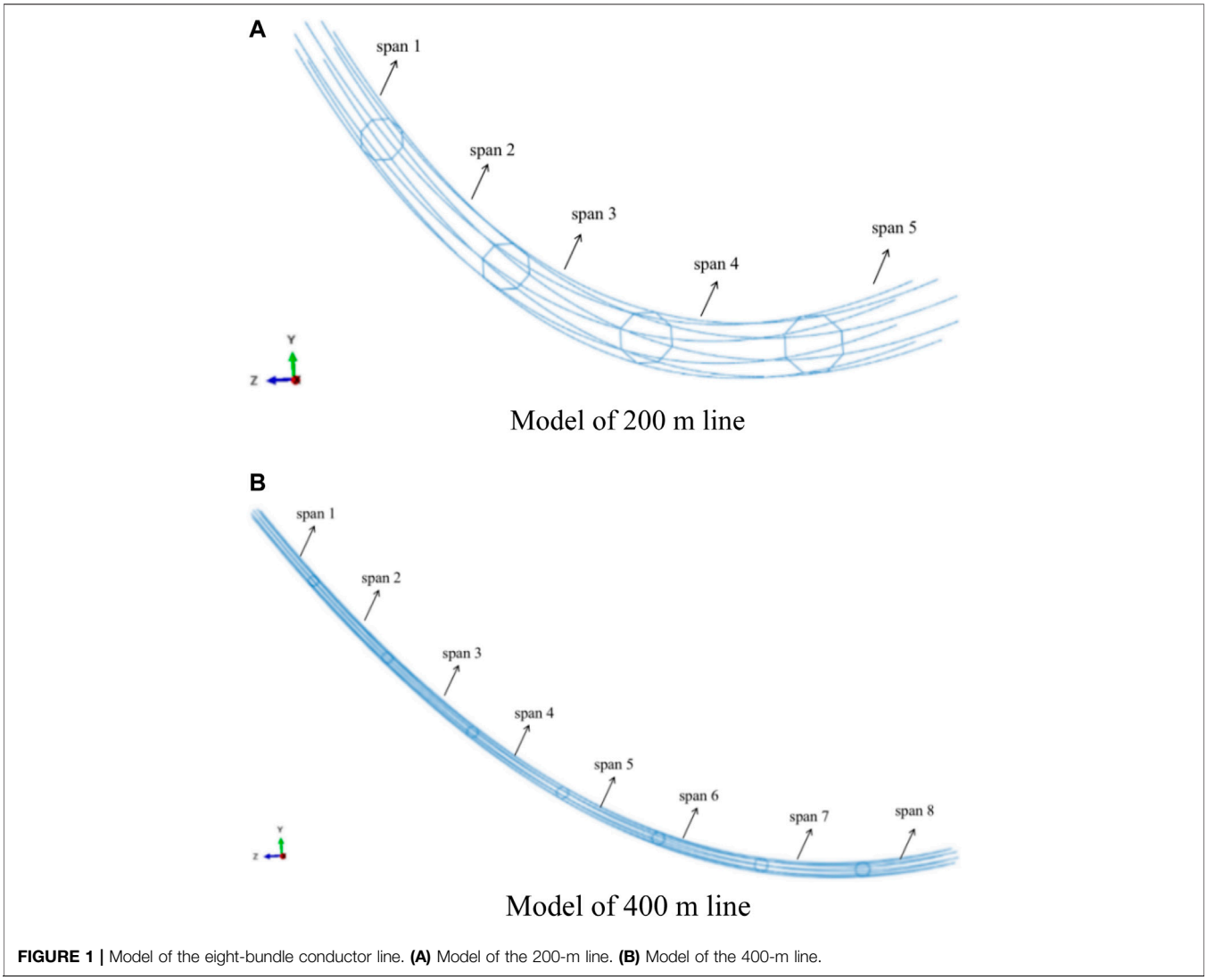

FIGURE 1 | Model of the eight-bundle conductor line. **(A)** Model of the 200-m line. **(B)** Model of the 400-m line.

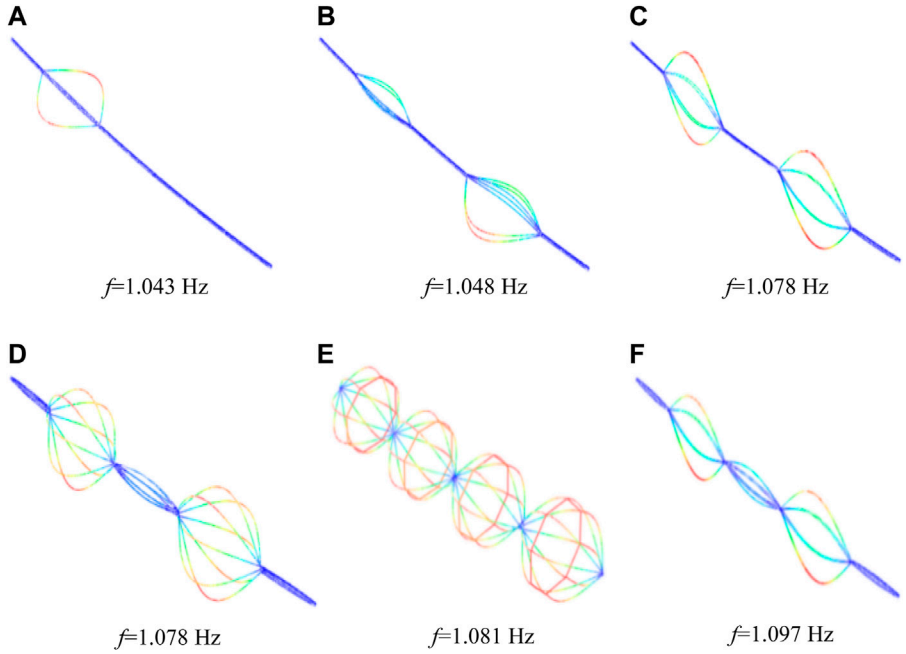

FIGURE 2 | Typical partial mode 200-m span. **(A)** *f*=1.043 Hz. **(B)** *f*=1.048 Hz. **(C)** *f*=1.078 Hz. **(D)** *f*=1.078 Hz. **(E)** *f*=1.081 Hz. **(F)** *f*=1.097 Hz.

TABLE 2 | Physical and mechanical parameters of the iced conductor.

EA (×10^{6}N)	*GI* (N m^2/rad)	*μ* (kg/M)	*J* (×10^{-4} kg m)
31.7	1,057	1.733	2.69

sector-shaped eight-bundle conductor with different wind speeds, span lengths, and initial angle of wind attack. Talib et al. (2019) proposed a new dynamic model for the simulation of transmission line galloping. Liu et al. (2019), Liu et al. (2020a), Liu et al. (2020b), Liu et al. (2020c), Liu et al. (2021a), Liu et al. (2021b), Liu et al. (2021c), Liu et al. (2021d) and Liu et al. (2021e) and Min et al. (2021) obtained the aerodynamic coefficients of the conductor by applying the wind tunnel test and examined the stability and galloping characteristics of the iced conductor. The galloping behaviors of D-shape six bundles in the random wind test line are numerically simulated. Due to the continued existence of the galloping phenomenon and great harm, Oh and Sohn (2020) analyzed conductor galloping through the study of transmission line stability. Cai et al. (2020a) analyzed sector-shape eight-bundle conductor galloping through the FEM; furthermore, Cai et al. (2020b) analyzed galloping behaviors results of the test transmission tower-line.

Recently, there is still a lack of the influence of sub-span oscillation of iced eight-bundle conductors during galloping, especially the parameter analysis of UHV transmission lines under different turbulence intensity. In this article, the conductor galloping process of iced eight-bundle conductors is simulated by the numerical simulation method, the influence of wind speed and span length on sub-span oscillation during the conductor galloping process is analyzed, and the effects of wind speed, the angle of wind attack and the wind turbulence intensity are studied. Therefore, the follow-up research on galloping and anti-galloping characteristics of the frozen eight-bundle conductor has significant reference meaning.

NUMERICAL METHODS FOR TYPICAL EIGHT-BUNDLE LINES

Wind-driven wet snow may pack onto the windward sides of conductors, forming a hard, tenacious deposit with a sharp leading edge. The resulting ice shape may permit galloping. Combined with actual observation, the crescent shape can be generalized with respect to the great variety of natural heavy ice shapes (Hu et al., 2012; Yan et al., 2016). The aerodynamic forces of bundle conductors are the foundations of the analysis of the galloping of transmission lines (Liu et al., 2019). Here, the aerodynamic coefficients of crescent-shaped iced eight-bundle conductors are experimentally measured by wind tunnel tests.

Eight-bundle iced transmission lines are major research objects. The sub-spans of each span are the same. The conductor model is 8×LGJ-400/50, and the diameter of the sub-conductor is 30 mm. The model of the sub-spacer is FJZ-400, each with a mass of 17.5 kg. Its parameters are given in **Table 1**, and the model diagrams of 200- and 400-m lines are shown in **Figures 1**, **2**.

The physical parameters of conductors and ice are listed in **Table 2**. The cross section of the iced conductor is simplified as a circular section when the galloping of the iced conductor is simulated by ABAQUS software. It is noted that the axial

TABLE 3 | Spacer arrangement.

Span (m)	Spacer number (N)	Sub-span length (m)
200	4	31 m–50 m – 47 m–46 m – 26 m
400	7	40 m–50 m – 55 m–55 m – 55 m–55 m – 50 m–40 m

TABLE 4 | Modes and natural frequencies of the iced eight-bundle conductor.

Direction	Modal shape	Natural frequency (Hz)	
		200 m	400 m
In-plane	One loop	0.26	0.14
	Two loops	0.52	0.29
	Three loops	0.77	0.37
Out-of-plane	Two loops	0.52	0.29
	Three loops	0.80	0.43
	Four loops	1.02	0.57
Torsion	One loop	0.43	0.31
	Two loops	0.60	0.36
	Three loops	0.83	0.48

rigidity, torsional rigidity, mass per unit length, and moment of inertia of the equivalent cable and those of the original cable should be equal, which can be expressed as

$$\begin{array}{ll} E'\pi d'^2/4 = EA; & G'\pi d'^2/32 = GI \\ \rho'\pi d'^2/4 = \mu; & \rho'\pi d'^4/32 = J \end{array}, \quad (1)$$

where E', G', ρ', and d' are, respectively, the elastic modulus, shear modulus, density, and diameter of the equivalent cable, which can be obtained by solving (1) whose right hand sides are the corresponding quantities of the original iced conductor. The physical parameters of the conductors and ice are listed in **Table 2**.

The influence of the initial axial tension in the main cable and side cable on the element stiffness matrix cannot be ignored. In addition, the cable sags due to its own weight, resulting in a certain decrease or loss of its elastic modulus. In order to consider the influence of cable sag, the concept of equivalent elastic modulus is used to modify the elastic modulus of the cable. The equivalent modulus of elasticity generally adopts the E_{Ernst} formula:

$$E_{\mathrm{Ernst}} = \frac{E}{1 + \frac{(ql)^2}{12T^3}AE}, \quad (2)$$

where E_{Ernst} is the equivalent elastic modulus of the material; E is the elastic modulus of the material; q is the weight of the unit length of the cable; l is the projection length of the cable element in the horizontal direction; A is the cross-sectional area of the cable; and T is cable tension.

The numerical simulations were carried out on a personal computer Dell Studio Desktop D540, and each process to arrive at a steady result took about 5 h. To speed up the efficiency, several simulations were submitted at the same time. The dynamic implicit analysis is used in the numerical method. The dynamic responses of the transmission line with different damping ratios in different directions are analyzed by ABAQUS with the user-defined cable element. The damping ratios ξ_{z1}, ξ_{y1}, and $\xi_{\theta 1}$, in the horizontal, vertical, and torsional directions are set to be 0, 0.5, and 2%, respectively, determined and verified by the reference (Zhou et al., 2016). The time step is set to be 0.01; we have already calculated that the step is set to be 0.005, and the error of the vertical amplitude is 2.74%. Considering the efficiency of the numerical simulation, the time step is set to be 0.01.

In the research, the aerodynamic parameters of the iced UHV transmission line are analyzed using the results of wind tunnel experiments (Yan et al., 2016). The aerodynamic forces are applied to the conductor to numerically simulate the galloping of the conductor. In the stiffness and massless user-defined element, the torsion angle, velocity, and displacement under the condition of applying aerodynamic force could help obtain the node of the cable element used in ABAQUS software (Zhou et al., 2016). The arrangement of the spacers is shown in **Table 3**.

The Rayleigh attenuation model is general for cable attenuation, shown in **Eq. 3**:

$$\mathrm{C} = \alpha G + \beta \mathrm{K}. \quad (3)$$

C, **M,** and **K** are damping matrices, quality matrices, and stiffness matrices, respectively. α and β is the Rayleigh damping coefficient, which are determined by the natural frequency and damping ratio. In order to improve the accuracy of the galloping characteristics, according to the previous literature (Hu et al., 2012, Cai et al., 2015) the calculation repetition time step is set to 0.01.

WHOLE-SPAN AND SUB-SPAN MODELS

When the transmission conductor galloping occurs, the line is often accompanied by the vibration between the sub-spans in addition to the whole-span galloping. The natural frequency and mode affect the characteristics of conductor galloping (Zhang et al., 2000; Liu et al., 2021e). The natural frequency and whole-span mode are obtained, shown in **Table 4**. In the case of a transmission line with a distance of 200 m, the natural frequency of the in-plane single and half-wave 0.26 Hz is less than the natural frequency of the in-plane double half-wave 0.52 Hz, and the frequency of the in-plane single-half-wave is almost the natural frequency of the double half-wave; the natural frequency of the out-of-plane double–half-wave 0.52 Hz is less than the natural frequency of the out-of-plane four-half wave, and the natural frequency of the out-of-plane double half-wave is almost half of the natural frequency of the out-of-plane four-half wave; the natural frequency of the twist three-half wave is 0.83 Hz. It is nearly equal to the natural frequency of 0.80 Hz for the out-of-plane three-half-wave; for a line with a span of

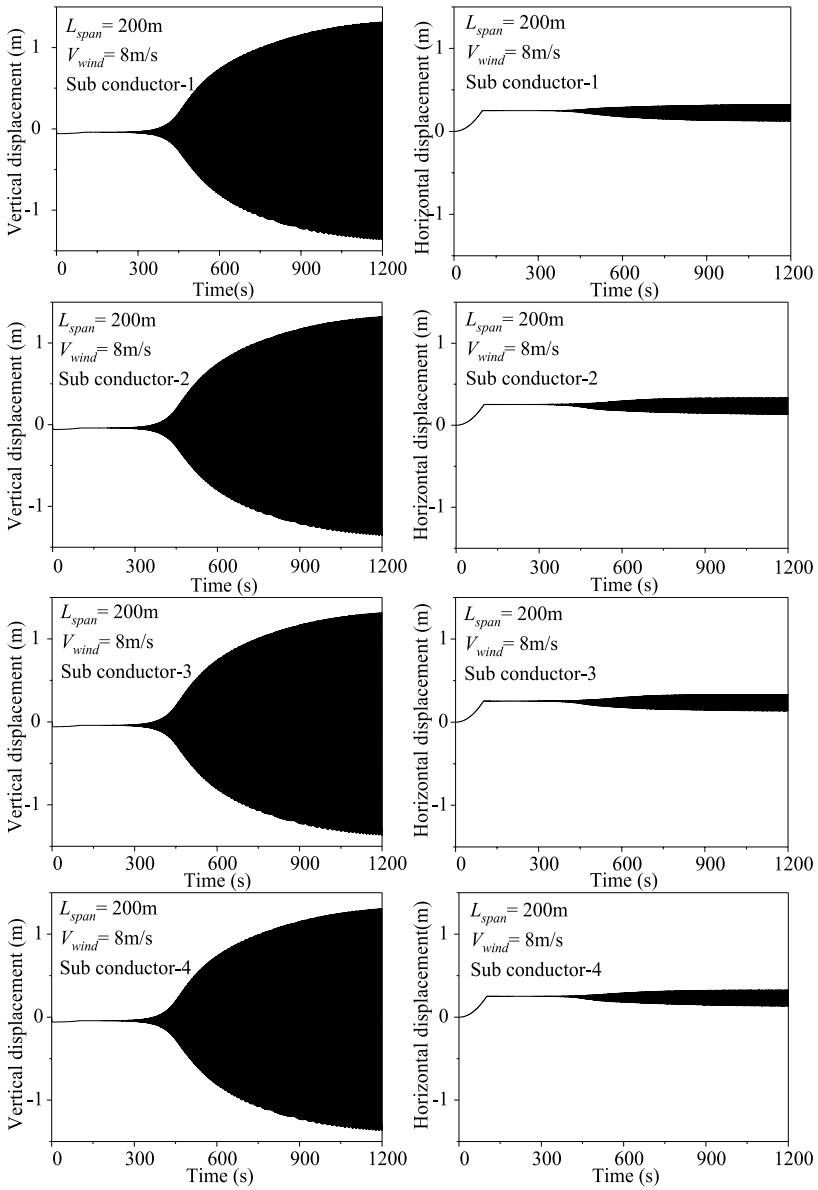

FIGURE 3 | Time history of midpoint displacement of the iced eight-bundle conductor under a wind velocity of 8 m/s (200 m span).

400 m, the natural frequency of the in-plane single half-wave of 0.14 Hz is less than the natural frequency of the in-plane double half-wave 0.29 Hz, and the frequency of the in-plane single half-wave is nearly half of the natural frequency of the double half-wave. The natural frequency of the out-of-plane three-half-wave 0.43 is almost equal to the natural frequency of the torsional three-half-wave 0.48 Hz. The natural frequency of the in-plane double half-wave 0.52 Hz is the same as the natural frequency of the out-of-plane double half-wave 0.52 Hz. It is not difficult to find that in this case, there are 1:2 and 1:1 internal resonance conditions by analyzing the modal and natural frequencies of the 200- and 400-m spans.

It can be observed from the figure that a relatively dense natural frequency is concentrated in the frequency range of 1.043–1.138 Hz, with three directions of in-plane, out-of-plane and torsion, single half-wave, double half-wave, three-half-wave, four-half-wave wave, and several other modes [67]. For example: f = 1.043 Hz and f = 1.045 Hz are single half-waves, f = 1.048 Hz, f = 1.052 Hz, f = 1.138 Hz are double half-waves, f = 1.058 Hz and f = 1.097 Hz are three half-waves, and f = 1.081 Hz is four half-waves.

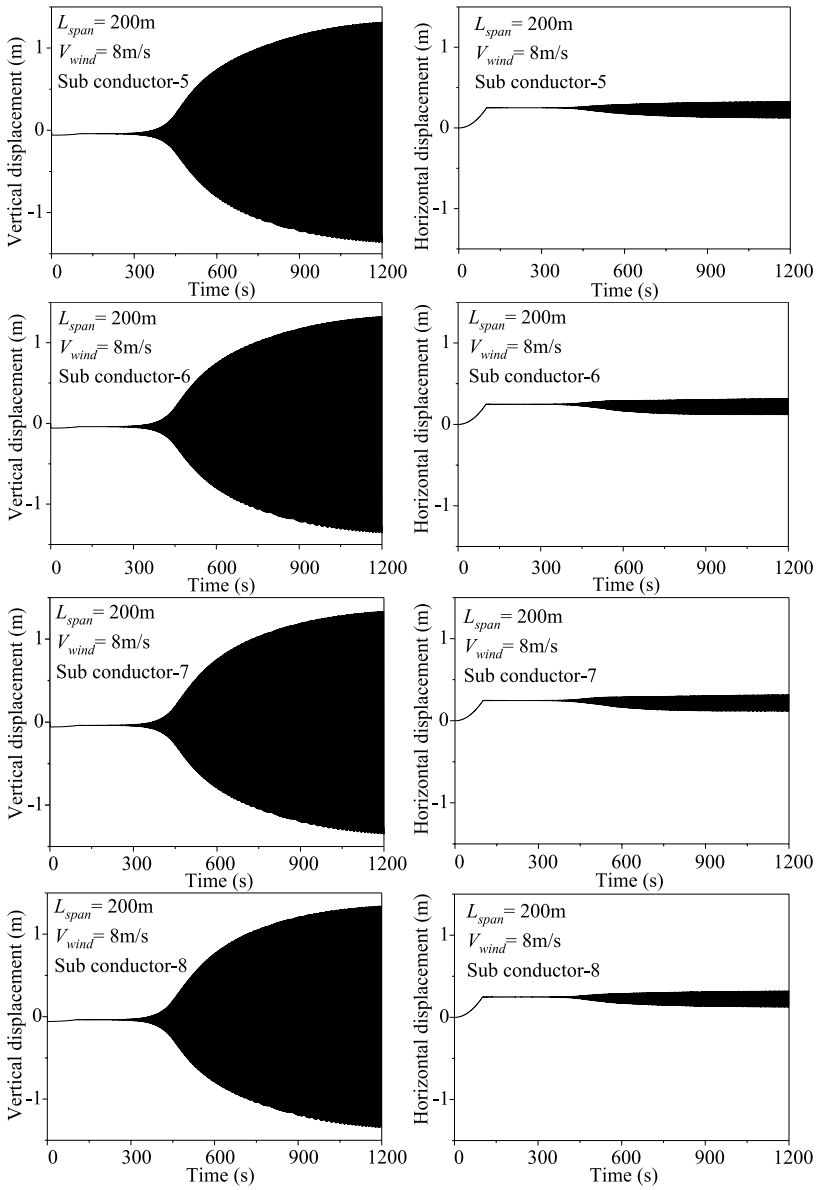

FIGURE 3 | Continued.

THE SUB-SPAN OSCILLATION OF ICED EIGHT-BUNDLE CONDUCTORS DURING GALLOPING

The Sub-Span Oscillation of the Characteristic of Each SubConductor

The galloping process of iced UHV transmission lines under a given wind velocity is analyzed by numerical simulation. The time history of the average displacement of the sub-conductor to iced eight conductors under the wind speed of 8 m/s with a span length of 200 m has been shown in **Figure 3**. At a wind speed of 8 m/s, because of the different aerodynamic forces between the conductors, the amplitude of the vibration in the vertical direction is more evident than the amplitude of the vibration in the horizontal direction. Among them, at a period of time after the beginning of the galloping, the galloping of the conductor tends to be stable, and the efficiency at which the horizontal galloping tends to stabilize is faster than the efficiency at which the vertical galloping tends to stabilize.

Compared with the galloping dynamic response analysis (**Table 3**), the first prominent peak frequency in the secondary range is 0.45 Hz, which is close to the 0.52 Hz natural frequency of

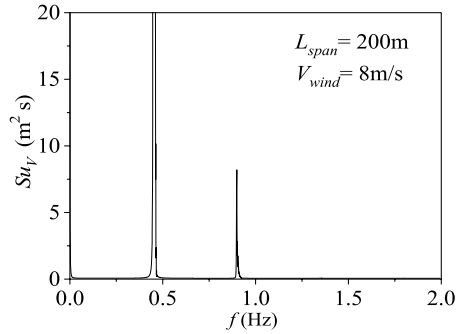

FIGURE 4 | Displacement spectrum analysis of the midpoint displacement of the subconductor of the first span of the iced eight-bundle conductor of 200 m span length.

the in-plane double half-waves (**Figure 4**). The second apparent peak frequency is 0.82 Hz, which is close to the natural frequency of 0.80 Hz of the third out-of-plane half-waves (**Table 2**).

Research on Sub-Span Vibration of the Conductor During Galloping Under Different Wind Velocities

Under different wind velocities the vertical and horizontal amplitude of each subconductor during the line galloping process increased, and the amplitude of vertical vibration increases significantly, reaching 11 m. When the wind speed is 8 m/s, the vertical and horizontal displacement between the subconductors is approximately the same. When the typical wind speed is 12 m/s, the aerodynamic load of each iced subconductor is significantly different due to the interference of the wake. The amplitude of the vibration of each subconductor in the bundle is obviously different. As shown in **Table 5**, as the wind speeds increase, the horizontal vibration amplitude of the subconductors also increases correspondingly, but the increase rate is relatively slow compared to the vertical vibration amplitude.

Research on the Sub-Span Oscillation Conductor During Galloping Under Different Subconductors

Figure 5 shows the change in the galloping distance of the subconductor at the intermediate point of the sub-span 3. The vertical vibration amplitude of the subconductor 5, subconductor 6, conductor 7, and subconductor 8 on the leeward side is greater than the vertical vibration amplitude of the subconductor 1, subconductor 2, conductor 3, and subconductor 4 at the leeward side. In the case of the wind speed of 12 m/s, the change of the galloping distance between the subconductors in the middle point of the sub-span 3 is shown in **Figure 5**. From the table, it can be found that at 400 s, the interval between the subconductors reaches the maximum, and then with the passage of time, the distance between the subconductors fluctuates closer; among them, conductor 1 and 2, conductor 5 and 6 is relatively long, and the distance between conductors 6 and 7 is relatively close.

GALLOPING BEHAVIORS UNDER DIFFERENT TURBULENT FLOW

In the wind tunnel experiment, it can be found that different turbulence intensities will lead to different aerodynamic coefficients of UHV transmission lines, and the Den Hartog and Nigol coefficients determined by the aerodynamic coefficients are also different (Den Hartog 1932; Nigol et al., 1977). The effect of different parameters on the galloping of UHV transmission lines is discussed, and the law of influence of wind speed, angle of wind attack, and span length on conductor galloping under the action of the turbulent wind is obtained.

Effects of Wind Velocity on Galloping Behaviors Under Turbulent Flow

Based on the aerodynamic coefficients obtained from the wind tunnel test (Cai et al., 2019b), the finite element method was used to study the effect of wind speed on the galloping of UHV transmission lines. **Figure 6** compares the movement traces of each subconductor at the midpoint of the line span under the action of different wind speeds under the turbulence degree of 8.41% of the 300-m span and angle of wind attack of 20°.

Under higher wind velocity, a shorter time will be needed to reach the wake-induced oscillation state. It also increases the amplitude of vertical displacement, indicating that galloping can occur at high wind speeds (**Figure 6**). As the wind speed increases, the amplitude of the galloping vertical amplitude of the subconductor decreases, but the amplitude of the horizontal vibration gradually increases.

TABLE 5 | Vibration amplitude of each subconductor during line galloping under different wind velocities.

Wind Velocity	Direction	Subconductor number							
		1	2	3	4	5	6	7	8
8 m/s	Vertical	2.741	2.741	2.733	2.728	2.730	2.731	2.734	2.734
	Horizontal	0.330	0.336	0.333	0.328	0.327	0.319	0.318	0.322
12 m/s	Vertical	9.355	9.360	9.390	9.454	9.489	9.461	9.401	9.367
	Horizontal	1.631	1.798	1.787	1.718	1.875	1.894	1.868	1.729
16 m/s	Vertical	11.267	11.041	11.129	11.469	11.695	11.270	11.126	11.318
	Horizontal	4.562	4.486	4.470	4.604	4.881	4.762	4.836	4.876

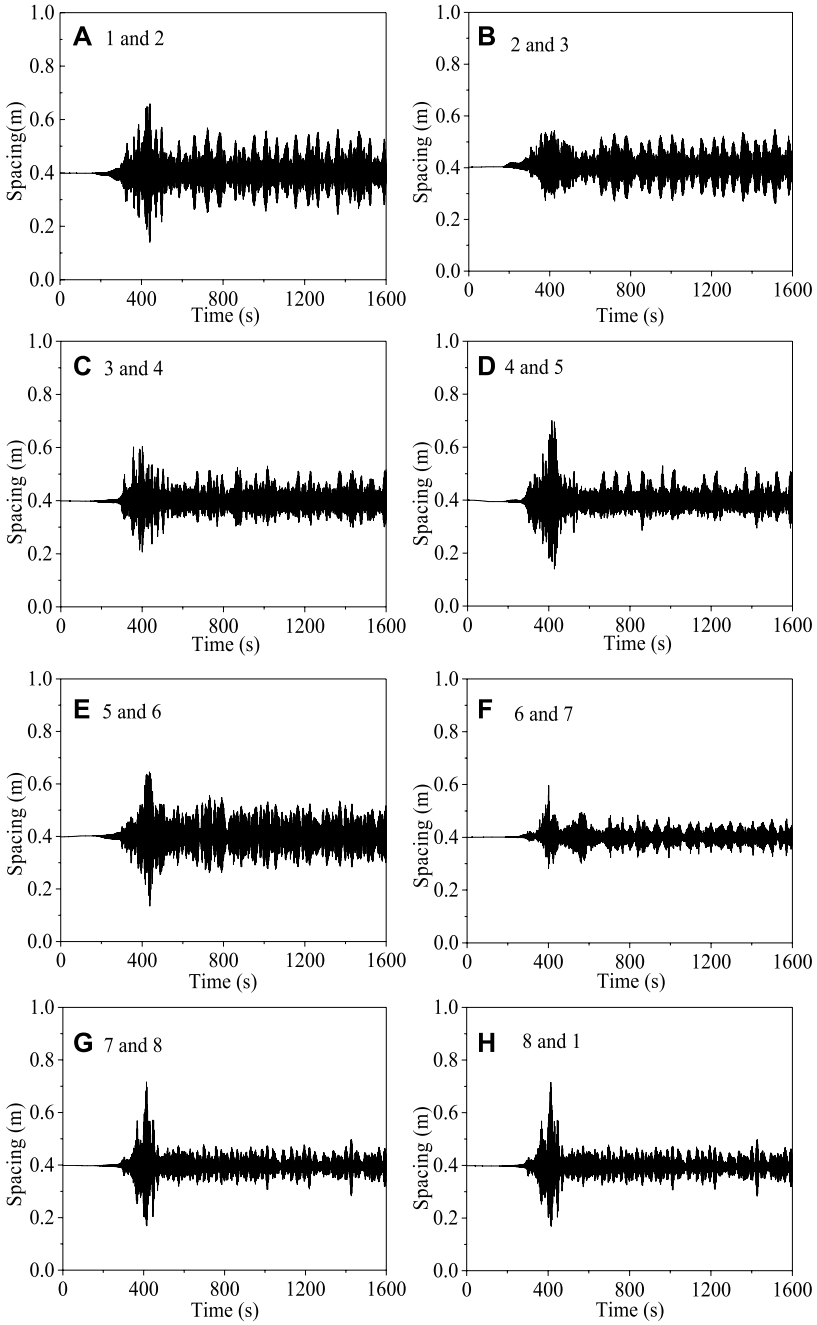

FIGURE 5 | Variation of the galloping distance of the respective conductors at the midpoint varying with time when the wind velocity is 12 m/s.

Figure 7 is the spectrum analysis diagram of the midpoint of the subconductor of the UHV transmission line under different wind speeds. Compared with the vertical displacement response spectrum analysis part, when the wind speed is 6 m/s, the first prominent peak frequency is 0.38 Hz, which is close to the natural frequency of 0.39 Hz of the in-plane single half-wave. The second prominent peak frequency appears (0.67 Hz), which is close to the natural frequencies of the in-plane and out-of-plane half-waves. In this case, the UHV transmission line has in-gear oscillation during the galloping process. On the other hand, when the wind speed is 12 m/s, the vertical displacement response spectrum has a special peak frequency of 0.41 Hz. It can be found that when the wind speed is high, the high-order vibration modes of the line vibration will be excited.

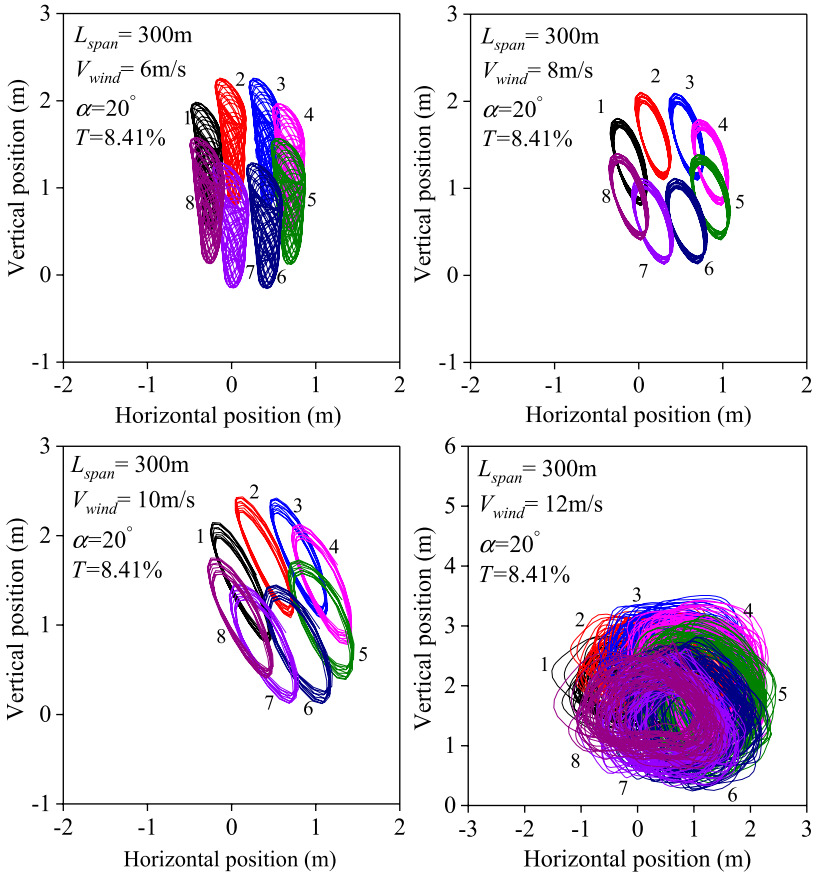

FIGURE 6 | Galloping traces of the midpoint of eight-bundle conductors under different wind velocities.

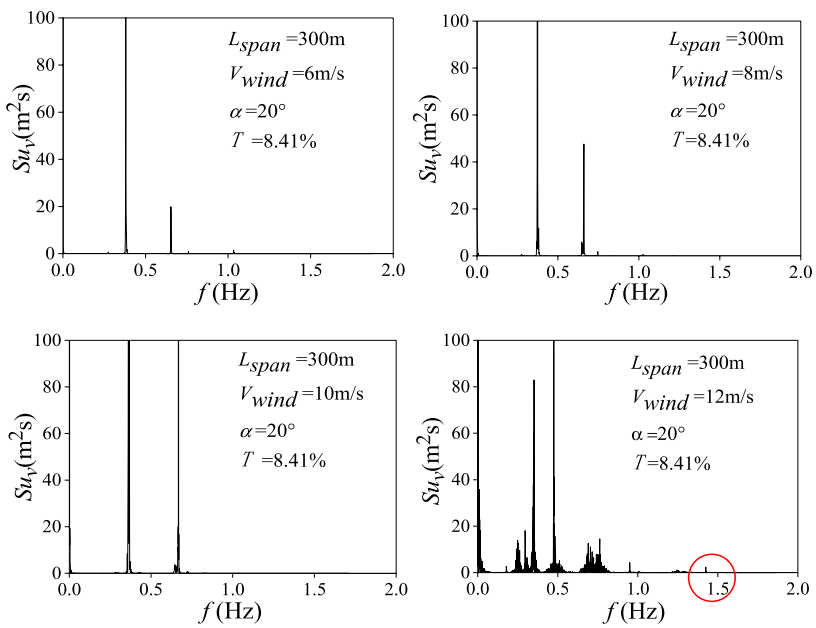

FIGURE 7 | Displacement spectrum under different wind velocities.

TABLE 6 | RMS amplitude of galloping behaviors under different span lengths.

Span length (m)	Turbulence Intensity (%)	V_{amp} (m)	H_{amp} (m)
300	0	0.31	0.18
	8.41	3.55	2.27
400	0	1.01	0.75
	8.41	4.66	5.39

TABLE 7 | RMS amplitude of galloping behaviors under different turbulence intensity.

V_{wind} (m/s)	Turbulence intensity (%)	α (°)	V_{amp} (m)	H_{amp} (m)
12	0	20	4.38	4.46
		60	17.35	6.80
	8.41	20	4.58	3.29
		60	16.76	6.21

Effects of Span Length on Galloping Behaviors Under Turbulent Flow

According to the relevant research on the influence of span length on the UHV transmission line, it can be known that the difference in span length can lead to the change of the galloping amplitude of the UHV transmission line. **Table 6** shows the maximum galloping amplitudes of UHV transmission lines with 300- and 400-m span length when the wind speed is 12 m/s; the initial wind angle of attack is selected to be 20°, and the turbulence intensities are 0 and 8.41%. It can be seen that the galloping amplitude in the vertical and horizontal directions increases correspondingly with increase of span length.

Effects of Initial Angle of Wind Attack on Galloping Behaviors Under Turbulent Flow

According to the existing research on the conductor galloping phenomenon, it can be known that the difference of the initial attack of the wind angle will lead to the difference of the aerodynamic coefficients (Cai et al., 2019b). When the ice of the UHV transmission line is crescent-shaped, when the initial angle of wind attack is 15°–60° and 120°–180°, it presents an unstable state, and in actual conditions, the initial angle of wind attack being greater than 90° is rare. **Table 7** shows the maximum galloping amplitude of the line when the wind speed is 12 m/s, and the initial angle of wind attack is 20° and 60°. The comparison shows that the vertical and horizontal amplitude of the UHV transmission line when the initial angle of wind attack is 60° is much larger than the vertical and horizontal amplitude when the initial angle of wind attack is 20°. Meanwhile, it can also be found that when other parameters are constant, the greater the turbulence intensity, the greater its horizontal and vertical amplitude.

CONCLUSION

The sub-span oscillation of iced eight-bundle conductors during galloping under different wind velocities, span length, initial angle of wind attack, and turbulence intensity is simulated and analyzed by using the FEM. The following conclusions can be obtained as follows:

1) The subconductors of the iced eight-bundle transmission line gallop in the same direction under different wind velocities, and the main oscillation direction is the vertical direction. Meanwhile, there is an oscillation in the sub-span during the galloping of the iced eight-bundle conductor, which may cause the subconductor to vibrate.
2) Due to the influence of wake disturbance and aerodynamic load, the amplitude of the oscillation of each subconductor is different. Under the same wind velocity, the vertical oscillation amplitude of the subconductor on the leeward side is greater than that on the upwind side.
3) The vertical and horizontal amplitudes of line galloping increase obviously with the increasing of wind velocity and span length; there are obvious differences in the galloping amplitude of the conductors, and the difference of the initial angle of wind attack will lead to a significant difference.
4) Under the influence of turbulence intensity, the line is more likely to gallop, the galloping trace of the conductor is elliptical, and the vibration amplitude of each subconductor has a difference under higher turbulence intensity. The amplitude of galloping increases significantly with the increase of wind velocity, and high wind velocity will excite higher-order vibration modes of line vibration under higher turbulence intensity.

DATA AVAILABILITY STATEMENT

The original contributions presented in the study are included in the article/Supplementary Material; further inquiries can be directed to the corresponding authors.

AUTHOR CONTRIBUTIONS

All authors listed have made a substantial, direct, and intellectual contribution to the work and approved it for publication.

FUNDING

This work was in part financially supported by the National Natural Science Foundation of China (Grant No. 515107106), Postdoctoral Research Foundation of China (2021M702371), Chengdu International Science and Technology Cooperation Support Funding (2020-GH02-00059-HZ), and Open Research Fund of Failure Mechanics and Engineering Disaster Prevention, Key Laboratory of Sichuan Province, Sichuan University (FMEDP202201).

REFERENCES

Cai, M., Yan, B., Lu, X., and Zhou, L. (2015). Numerical Simulation of Aerodynamic Coefficients of Iced-Quad Bundle Conductors. *IEEE Trans. Power Deliv.* 30 (4), 1669–1676. doi:10.1109/TPWRD.2015.2417890

Cai, M., Zhou, L., Lei, H., and Huang, H. (2019a). Wind Tunnel Test Investigation on Unsteady Aerodynamic Coefficients of Iced 4-Bundle Conductors. *Adv. Civil Eng.* 2019, 1–12. doi:10.1155/2019/2586242

Cai, M., Xu, Q., Zhou, L., Liu, X., and Huang, H. (2019b). Aerodynamic Characteristics of Iced 8-bundle Conductors under Different Turbulence Intensities. *KSCE J. Civ Eng.* 23 (11), 4812–4823. doi:10.1007/s12205-019-0359-9

Cai, M., Yang, X., Huang, H., and Zhou, L. (2020a). Investigation on Galloping of D-Shape Iced 6-Bundle Conductors in Transmission Tower Line. *KSCE J. Civ Eng.* 24 (6), 1799–1809. doi:10.1007/s12205-020-0595-z

Cai, M.-q., Zhou, L.-s., Xu, Q., Yang, X.-h., and Liu, X.-h. (2020b). Galloping Response of Sector-Shape Iced Eight Bundle Conductors. *Can. J. Civ. Eng.* 47 (10), 1201–1213. doi:10.1139/cjce-2018-0114

Diana, G., Belloli, M., Giappino, S., Manenti, A., Mazzola, L., Muggiasca, S., et al. (2014a). A Numerical Approach to Reproduce Subspan Oscillations and Comparison with Experimental Data. *IEEE Trans. Power Deliv.* 29 (3), 1311–1317. doi:10.1109/TPWRD.2014.2315444

Diana, G., Belloli, M., Giappino, S., Manenti, A., Mazzola, L., Muggiasca, S., et al. (2014b). Wind Tunnel Tests on Two Cylinders to Measure Subspan Oscillation Aerodynamic Forces. *IEEE Trans. Power Deliv.* 29 (3), 1273–1283. doi:10.1109/TPWRD.2014.2313455

EPRI (2009). *Transmission Line Reference Book: Wind-Induced Conductor Motion*. Palo Alto, CA: EPRI.

Hartog, J. P. D. (1932). Transmission Line Vibration Due to Sleet. *Trans. Am. Inst. Electr. Eng.* 51 (4), 1074–1076. doi:10.1109/T-AIEE.1932.5056223

Hu, J., Yan, B., Zhou, S., and Zhang, H. (2012). Numerical Investigation on Galloping of Iced Quad Bundle Conductors. *IEEE Trans. Power Deliv.* 27 (2), 784–792. doi:10.1109/TPWRD.2012.2185252

Jafari, M., Hou, F., and Abdelkefi, A. (2020). Wind-Induced Vibration of Structural Cables. *Nonlinear Dyn.* 100 (1), 351–421. doi:10.1007/s11071-020-05541-6

Li, H., Deng, J., Feng, P., Pu, C., Arachchige, D. D. K., and Cheng, Q. (2021a). Short-Term Nacelle Orientation Forecasting Using Bilinear Transformation and ICEEMDAN Framework. *Front. Energ. Res.* 9, 780928. doi:10.3389/fenrg.2021.780928

Li, H., Deng, J., Yuan, S., Feng, P., and Arachchige, D. D. K. (2021b). Monitoring and Identifying Wind Turbine Generator Bearing Faults Using Deep Belief Network and EWMA Control Charts. *Front. Energ. Res.* 9, 799039. doi:10.3389/fenrg.2021.799039

Li, H., He, Y., Xu, Q., Deng, J., Li, W., and Wei, Y. (2022). Detection and Segmentation of Loess Landslides via Satellite Images: a Two-phase Framework. *Landslides* 19, 673–686. doi:10.1007/s10346-021-01789-0

Liu, X., Hu, Y., and Cai, M. (2019). Free Vibration Analysis of Transmission Lines Based on the Dynamic Stiffness Method. *R. Soc. Open Sci.* 6 (3), 181354. doi:10.1098/rsos.181354

Liu, X., Min, G., Wu, C., and Cai, M. (2020a). Investigation on Influences of Two Discrete Methods on Galloping Characteristics of Iced Quad Bundle Conductors. *Adv. Civil Eng.* 2020, 1–17. doi:10.1155/2020/8818728

Liu, X., Zou, M., Wu, C., Cai, M., Min, G., and Yang, S. (2020b). Galloping Stability and Wind Tunnel Test of Iced Quad Bundled Conductors Considering Wake Effect. *Discrete Dyn. Nat. Soc.* 2020, 1–15. doi:10.1155/2020/8885648

Liu, X., Zou, M., Wu, C., Yan, B., and Cai, M. (2020c). Galloping Stability and Aerodynamic Characteristic of Iced Transmission Line Based on 3-DOF. *Shock and Vibration* 2020, 1–15. doi:10.1155/2020/8828319

Liu, X., Liang, H., Min, G., Wu, C., and Cai, M. (2021a). Investigation on the Nonlinear Vibration Characteristics of Current-Carrying Crescent Iced Conductors under Aerodynamic Forces, Ampere's Forces, and Forced Excitation Conditions. *Discrete Dyn. Nat. Soc.* 2021, 1–22. doi:10.1155/2021/5009209

Liu, X. H., Min, G. Y., Sun, C., and Cai, M. Q. (2021b). Investigation on Stability and Galloping Characteristics of Iced Quad Bundle Conductor. *J. Appl. Fluid Mech.* 14 (1), 117–129. doi:10.47176/jafm.14.01.31417

Liu, X., Min, G., Cai, M., Yan, B., and Wu, C. (2021c). Two Simplified Methods for Galloping of Iced Transmission Lines. *KSCE J. Civ Eng.* 25 (1), 272–290. doi:10.1007/s12205-020-0693-y

Liu, X., Yang, S., Min, G., Cai, M., Wu, C., and Jiang, Y. (2021d). Investigation on the Accuracy of Approximate Solutions Obtained by Perturbation Method for Galloping Equation of Iced Transmission Lines. *Math. Probl. Eng.* 2021, 1–18. doi:10.1155/2021/6651629

Liu, X., Yang, S., Wu, C., Zou, M., Min, G., Sun, C., et al. (2021e). Planar Nonlinear Galloping of Iced Transmission Lines under Forced Self-Excitation Conditions. *Discrete Dyn. Nat. Soc.* 2021, 1–20. doi:10.1155/2021/6686028

Min, G., Liu, X., Wu, C., Yang, S., and Cai, M. (2021). Influences of Two Calculation Methods about Dynamic Tension on Vibration Characteristics of Cable-Bridge Coupling Model. *Discrete Dyn. Nat. Soc.* 2021, 1–11. doi:10.1155/2021/6681954

Nigol, O., Clarke, G. J., and Havard, D. G. (1977). Torsional Stability of Bundle Conductors. *IEEE Trans. Power Apparatus Syst.* 96 (5), 1666–1674. doi:10.1109/T-PAS.1977.32496

Oh, Y.-J., and Sohn, J.-H. (2020). Stability Evaluation of the Transmission Line by Using Galloping Simulation. *Int. J. Precis. Eng. Manuf.* 21 (11), 2139–2147. doi:10.1007/s12541-020-00399-5

Rawlins, C. B. (1976). Fundamental Concepts in the Analysis of Wake-Induced Oscillation of Bundled Conductors. *IEEE Trans. Power Apparatus Syst.* 95 (4), 1377–1393. doi:10.1109/T-PAS.1976.32233

Rawlins, C. B. (1977). Extended Analysis of Wake-Induced Oscillation of Bundled Conductors. *IEEE Trans. Power Apparatus Syst.* 96 (5), 1681–1689. doi:10.1109/T-PAS.1977.32498

Talib, E., Shin, J.-H., Kwak, M. K., and Koo, J. R. (2019). Dynamic Modeling and Simulation for Transmission Line Galloping. *J. Mech. Sci. Technol.* 33 (9), 4173–4181. doi:10.1007/s12206-019-0812-1

Tsui, Y. T., and Tsui, C. C. (1980). Two Dimensional Stability Analysis of Two Coupled Conductors with One in the Wake of the Other. *J. Sound Vibration* 69 (3), 361–394. doi:10.1016/0022-460X(80)90478-2

Williams, R. G., and Suaris, W. (2006). An Analytical Approach to Wake Interference Effects on Circular Cylindrical Structures. *J. Sound Vibration* 295 (1-2), 266–281. doi:10.1016/j.jsv.2006.01.023

Yan, B., Liu, X., Lv, X., and Zhou, L. (2016). Investigation into Galloping Characteristics of Iced Quad Bundle Conductors. *J. Vibration Control.* 22 (4), 965–987. doi:10.1177/1077546314538479

Zhang, Q., Popplewell, N., and Shah, A. H. (2000). Galloping of Bundle Conductor. *J. Sound Vibration* 234 (1), 115–134. doi:10.1006/jsvi.1999.2858

Zhou, L., Yan, B., Zhang, L., and Zhou, S. (2016). Study on Galloping Behavior of Iced Eight Bundle Conductor Transmission Lines. *J. Sound Vibration* 362, 85–110. doi:10.1016/j.jsv.2015.09.046

Zhou, A. Q., Liu, X. J., Zhang, S. X., Cui, F. J., and Liu, P. (2018). Wind Tunnel Test of the Influence of an Interphase Spacer on the Galloping Control of Iced Eight-Bundled Conductors. *Cold Regions Sci. Technology* 155, 354–366. doi:10.1016/j.coldregions.2018.08.026

Conflict of Interest: Author ZL is employed by State Grid Sichuan Integrated Energy Service Co. Ltd.

The remaining authors declare that the research was conducted in the absence of any commercial or financial relationships that could be construed as a potential conflict of interest.

frontiers | Frontiers in Energy Research

ORIGINAL RESEARCH
published: 26 April 2022
doi: 10.3389/fenrg.2022.874351

Power Quality Data Compression and Disturbances Recognition Based on Deep CS-BiLSTM Algorithm With Cloud-Edge Collaboration

Xin Xia[1†], *Chuanliang He*[1†], *Yingjie Lv*[2], *Bo Zhang*[2], *ShouZhi Wang*[2], *Chen Chen*[3] and *Haipeng Chen*[4*]

[1]State Grid Laboratory of Power Line Communication Application Technology, Beijing Smart-Chip Microelectronics Technology Co., Ltd., Beijing, China, [2]Beijing Electric Power Science and Smart Chip Technology Company Limited, Beijing, China, [3]College of Instrumentation and Electrical Engineering, Jilin University, Changchun, China, [4]Department of Electrical Engineering, Northeast Electric Power University, Jilin, China

OPEN ACCESS

Edited by:
Tinghui Ouyang,
National Institute of Advanced Industrial Science and Technology (AIST), Japan

Reviewed by:
Jiang Li,
Shanghai University of Electric Power, China
Chunxu Qin,
Inner Mongolia University of Technology, China

***Correspondence:**
Haipeng Chen
haipeng0704@126.com

[†]These authors have contributed equally to this work and share first authorship

Specialty section:
This article was submitted to Smart Grids, a section of the journal Frontiers in Energy Research

Received: 12 February 2022
Accepted: 14 March 2022
Published: 26 April 2022

Citation:
Xia X, He C, Lv Y, Zhang B, Wang S, Chen C and Chen H (2022) Power Quality Data Compression and Disturbances Recognition Based on Deep CS-BiLSTM Algorithm With Cloud-Edge Collaboration. Front. Energy Res. 10:874351. doi: 10.3389/fenrg.2022.874351

The current disturbance classification of power quality data often has the problem of low disturbance recognition accuracy due to its large volume and difficult feature extraction. This paper proposes a hybrid model based on distributed compressive sensing and a bi-directional long-short memory network to classify power quality disturbances. A cloud-edge collaborative framework is first established with distributed compressed sensing as an edge-computing algorithm. With the uploading of dictionary atoms of compressed sensing, the data transmission and feature extraction of power quality is achieved to compress power quality measurements. In terms of data transmission and feature extraction, the dictionary atoms and measurements uploaded at the edge are analyzed in the cloud by building a cloud-edge collaborative framework with distributed compressed sensing as the edge algorithm so as to achieve compressed storage of power quality data. For power disturbance identification, a new network structure is designed to improve the classification accuracy and reduce the training time, and the training parameters are optimized using the Deep Deterministic Policy Gradient algorithm in reinforcement learning to analyze the noise immunity of the model under different scenarios. Finally, the simulation analysis of 10 common power quality disturbance signals and 13 complex composite disturbance signals with random noise shows that the proposed method solves the problem of inadequate feature selection by traditional classification algorithms, improves the robustness of the model, and reduces the training time to a certain extent.

Keywords: distributed compressed sensing, power quality disturbance classification, bidirectional long-short memory network, edge algorithm and cloud edge collaboration, parameter optimization, DDPG algorithm

1 INTRODUCTION

The emergence of new communication technologies has led to an increase in the size and complexity of the power quality data that must be processed by power companies when implementing information systems and intelligent interconnection technologies (Jin et al., 2019). Therefore, advanced technologies and algorithms are needed to provide support for the storage, transmission, and management of power quality data in the era of the energy Internet (Elphick

et al., 2017a). However, the existing measuring instruments are difficult to identify the disturbance accurately, so the power system's relay protection and automatic devices may have false-action, which threatens the stable operation of the power system. Managing and storing massive power quality data, digging the intrinsic value contained in the power quality data, and utilizing the collected power quality data to analyze and identify the disturbances have become urgent problems to be solved (Yin et al., 2017). Efficient collection and evaluation of power quality data are significant to load prediction, operation status evaluation and early warning, power quality monitoring, and evaluation, effective operation of the power network, and distribution network planning (Negnevitsky et al., 2000; Chen, 2003).

When the sampling of power quality data still follows the Nyquist-Shannon sampling theorem (Elphick et al., 2017b), in conjunction with the acquisition-compression-storage-transmission-detection-identification process (Song et al., 2012), it will naturally result in a large amount of sampled data, and as the amount of data increases, the processing time for the data also increases, significantly increasing the cost of storage and transmission (Noland, 2016). The Fourier transform method for power quality data acquisition and analysis has advantages in the frequency domain analysis of signals but lacks the ability of time-domain analysis (Pei et al., 2006). The compression performance of the Fourier transform method is therefore not optimal. Power quality signal compression is proposed in reference (Bravo-Rodríguez et al., 2020) based on the One-Class Support Vector Machine (OCSVM) and normalized distance measure, which has excellent compression performance and has a low compression ratio for different kinds of signals. In reference (Berutu and Chen, 2020), the method of multi-wavelet threshold transformation combined with lossless and lossy compression is adopted for power-quality data compression. Meanwhile, the Set Partitioning in Hierarchical Trees (SPIHT) lossy compression algorithm is used for the high-frequency wavelet coefficient matrix, and the LZ77 lossless compression algorithm is used for the low-frequency part of the wavelet coefficient matrix. However, wavelet transforms have a problem selecting a wavelet basis, and the algorithm is not particularly adaptable. The Compressed Sensing (CS) method (Li et al., 2020) can sample the signal with much fewer observations than the Nyquist sampling theorem and preserve the original characteristics as much as possible. However, the basic compressed sensing theory can only handle a single signal; it cannot exploit correlations between signals to optimize the reconstruction accuracy or speed of the compression model. To take advantage of the correlation between data and within data, the distributed compressed sensing (DCS) theory is proposed based on CS theory. DCS can be regarded as a theory that combines distributed source coding (DSC) and compressed sensing (Pei et al., 2006). This theory compresses different signals separately but performs joint reconstruction. When the same parts of different signals account for a large proportion, DCS can significantly reduce the number of observations, so the complexity of recovering signals on the decoding side is significantly reduced. This feature is essential for distributed applications with low complexity requirements at the decoder. DCS theory has been widely used in the fields of audio and video processing, image fusion, and multi-transmitter multi-receiver channel estimation (von Gladiß et al., 2015), laying a good research foundation for its application in the field of electrical engineering data processing.

The power quality disturbance classification method extracts feature of power quality signal as the input of a recognizer through digital signal processing methods and machine learning algorithms (Gibbon et al., 2009). Currently, the recognition methods mainly include: neural network (Cai et al., 2019), support vector machine (Tang et al., 2020), decision tree (Zhao et al., 2019) etc. (Xin et al., 2020) converts the input of Power Quality Disturbances (PQDs) data into a two-dimensional matrix which is similar to image data, and then uses a two-dimensional Convolutional Neural Network (CNN) to identify the type of PQDs. However, PQDs data is a one-dimensional time series, and two-dimensional CNN is made for image recognition. Therefore, it is not completely appropriate for PQDs. In (Lu et al., 2020), several common CNNs and RNNs are examined in the context of PQDs classification, but the training time, parameter numbers, model size, and anti-noise ability of these CNNs are not considered. PQDs classification by deep learning neural network is prone to long network training time and limited classification accuracy for a large amount of power quality data (Uçkun et al., 2020). The combination of neural networks and compressed sensing significantly minimizes the amount of processed data, effectively shortens the recognition time, achieves or even exceeds the original recognition accuracy, and reduces hardware performance requirements.

The combination of traditional methods utilizing digital signal processing to extract features and machine learning as classifiers to achieve disturbance classification becomes unsuitable for generalization; For another thing, the rise of deep learning methods provides new ideas for power quality disturbance identification by directly utilizing raw data to extract and classify disturbance signal features. Deep learning methods combine feature extraction and classification into a single model, which compensates for traditional methods' relatively independent feature extraction and classification. As a result, the application of deep learning methods to detect disturbances will gradually become a research focus for academics. Deep learning methods automatically extract features from the original signal, and traditional Nyquist sampling used to obtain electrical energy signal data is too large, putting excessive strain on transmission and storage, obtaining the signal via CS theory and combining it with deep learning methods to achieve disturbance classification is critical for practical applications.

Meanwhile, the power system put forward new requirements for the classification of disturbances that affect the power quality of the distribution network. The classification of PQDs needs higher timeliness and accuracy. These conditions serve as a scenario-based basis for applying the PQD classification method proposed in this article.

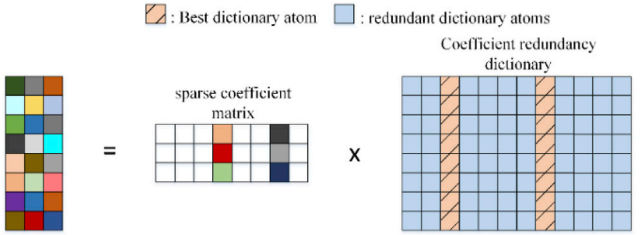

FIGURE 1 | Sparse decomposition.

As a consequence of the advent of new scenarios, the traditional disturbance recognition method employing digital signal processing to extract features and machine learning to recognize disturbances has shown its limitations (Zhang et al., 2021; Li et al., 2022). Emerging artificial intelligence methods such as deep learning offer a new direction for PQD classification. Deep learning methods based on compressed sensing theory can ensure the safe operation of the system and quickly and accurately classify PQDs. This is an important step in solving power quality problems. Through the gradual development of communication technology, the proposed combination of compressed sensing and deep learning can also serve as technical support for edge computing in cloud edge collaborations. The research on PQD classification based on compressed sensing and deep learning, therefore, has both theoretical and practical significance.

The main contributions of this paper are as follows: 1) a distributed compression storage method of power quality is proposed, which can be used for cloud edge collaboration, and the design of its dictionary matrix. 2) a combined method of compressed sensing and deep learning for power quality data disturbance recognition is proposed, which reduces the model's training speed and improves the accuracy of PQD recognition. 3) The Deep Deterministic Policy Gradient (DDPG) is employed to optimize the neural network parameters so that the constructed neural network can maintain good convergence ability in different scenarios. 4) The proposed method is aimed at a forward-looking new power system with a high proportion of renewable energy.

2 DISTRIBUTED COMPRESSED SENSING

2.1 Distributed Compressed Sensing Theory

DCS is developed to deal with the set of related signals. The model can take into account the internal correlations among power quality signals as well as the correlations between signals. When the signal aggregation is highly correlated, joint sparse and joint reconstruction can be performed.

Assuming that there are j signals, x represents the joint signal composed of multiple target signals $x_j \in R^N$, and y represents the joint signal composed of the observed values $y_j \in R^M$ corresponding to each target signal, the joint signal can be expressed as follows:

$$x = \left[x_1, x_2 \cdots x_j\right]^T \tag{1}$$

$$y = \left[y_1, y_2 \cdots y_j\right]^T \tag{2}$$

$$\Phi = \begin{bmatrix} \Phi_1 & 0 & \cdots & 0 \\ 0 & \Phi_2 & \cdots & 0 \\ \vdots & \vdots & \ddots & \vdots \\ 0 & 0 & \cdots & \Phi_j \end{bmatrix} \tag{3}$$

Then y can be expressed as:

$$y = \Phi x \tag{4}$$

Due to the fact that compressed sensing is the foundation of DCS, the premise of both two methods is that the signals must be sparse. Although many power quality signals do not have sparsity, the sparsity of these signals can be reflected in a certain sparse base. Assuming that ψ_j is a sparse matrix and θ_j is a sparse coefficient vector, $x_j = \psi_j \theta_j$ the signal acquisition model of DCS is as follow:

$$y_j = \Phi_j \psi_j \theta_j \tag{5}$$

2.2 Construction Steps of Learning Dictionary for Distributed Compressed Sensing

DCS of power quality data relies heavily on sparse representation of the signal, and the key factor is the design of an efficient and simple sparse matrix. The continuous updating and optimization of dictionary learning methods is the main reason for the superior performance of sparse representation in compressive reconstruction and type recognition. The sparse decomposition and construction steps of the learning dictionary of distributed compressed sensing are shown in **Figure 1**.

1) The model of power quality signals' training sample set $E \in R^{M_1 \times W_1}$ and $G \in R^{M_2 \times W_2}$ are established, where E means the public sample set, G means the feature sample set, W stands for the number of training samples and M denotes the number of sampling points for training sample. The training sample is expressed as follows:

$$E_i = [e_{i1}, e_{i2}, \cdots, e_{in}] \in R^{M_1 \times W_1} \tag{6}$$

$$G_i = [g_{i1}, g_{i2}, ..., g_{in}] \in R^{M_2 \times W_2} \tag{7}$$

Where $e_{ij} \in R^{M \times 1}$ represents class i, j training samples in a common sample set, $g_{ij} \in R^{M \times 1}$ represents class i, j training samples in feature sample sets, $i = 1, 2, ..., k$, $j = 1, 2, ..., n$, M represents the sample dimension, R represents the set of real numbers.

2) Initialize the public and the feature dictionaries, respectively. For example, in feature dictionary, Q training samples of the feature sample set G is randomly selected to initialize the dictionary $D_{t0} \in R^{M \times Q}$, then two—norm normalization is executed for each column of D_{t0}: $\|D_{t0}^j\|_2 = 1$, among

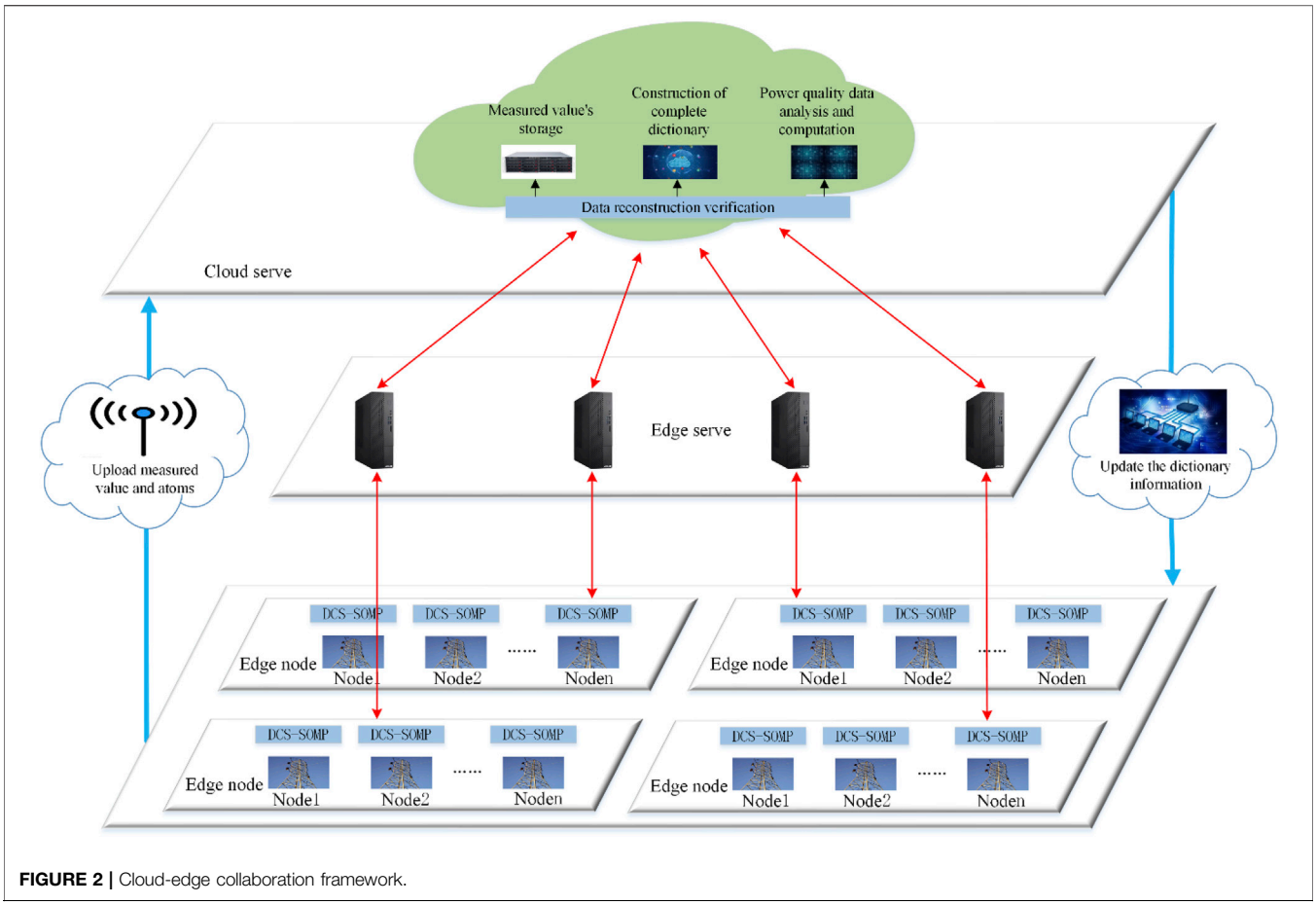

FIGURE 2 | Cloud-edge collaboration framework.

$j = 1, 2, ..., Q$, the objective function of dictionary initialization is:

$$J_{D_{t0},T_0} = \arg\min_{D_{t0},T_0} \left(\|G - D_{t0}T_0\|_2^2 + \lambda \|T_0\|_0 \right) \tag{8}$$

$$G_0^{jL} G_0^j = 1 \tag{9}$$

Where T_0 is the sparse representation matrix found by optimizing the objective function on the initial feature dictionary D_{t0} in the sample set G, and λ is the regularization parameter to balance the reconstruction error and the sparsity of the sparse matrix; the iterations' initial value is set to $L = 1$. In terms of the basic atomic characteristics of the initialized dictionary and the experimental simulation, the total iteration number m and the tolerance of error J_s are selected.

3) Finally, the KSVD algorithm is employed to optimize the objective function. It firstly holds the feature dictionary D_{ti} constant after the i^{th} iteration:

$$J_{T_i} = \arg\min_{T_i} \left(\|G - D_{ti}T_i\|_2^2 + \lambda \|T_i\|_0 \right) \tag{10}$$

Then, hold the sparse representation matrix T_i constant after the last iteration and optimize the base atom in the feature dictionary D_{ti} separately. And the objective function can still be simplified. The update can be made as follows:

$$\begin{aligned} J_{D_{ti}} &= \arg\min_{D_{ti}} \left(\left\| G - \sum_{j=1}^{k} G_i^j T_i^{jL} \right\|_2^2 \right) \\ &= \left(\left\| \left(G - \sum_{j \neq k} G_i^j T_i^{jL} \right) - D_{ti}^k T_i^{kL} \right\|_2^2 \right) = \left(\left\| G_k - G_i^k T_i^{kL} \right\|_2^2 \right) \end{aligned} \tag{11}$$

Where $k = 1, 2, ..., N$, G_k are real error items, the SVD algorithm is used to decompose G_k, and the base atom d_k that needs to be updated is the feature vector corresponding to the maximum eigenvalue, which can be computed by the least-square method. Then, the optimal feature dictionary D_t is obtained, and the public dictionary D_g is attained by the same method. The DCS learning dictionary D is obtained by cascading D_g and D_t together. Therefore, the DCS learning dictionary can be expressed as follow:

$$D = \begin{bmatrix} D_g & D_t & 0 & \cdots & 0 \\ D_g & 0 & D_t & \cdots & \\ \cdots & \cdots & \cdots & \cdots & 0 \\ D_g & 0 & \cdots & 0 & D_t \end{bmatrix} \tag{12}$$

2.3 Data Storage Based on Cloud Edge Collaboration

Under the cloud-edge collaborative architecture (Ning et al., 2021), the DCS-OMP edge algorithm is used to compress and collect the power quality data of *s* nodes in a distribution system at the same time, the power quality data of each node in the distribution system share the same dictionary atoms, set the data length of each node as n and the number of uploaded dictionary atoms as τ, the corresponding formula is as follow:

$$[\boldsymbol{Y}_{m\times s} \quad \boldsymbol{D}_{\tau\times n}] = DCS\_SOMP(\boldsymbol{X}_{n\times s}, \boldsymbol{\Psi}_{m\times n}, \boldsymbol{\Phi}_{n\times n}, \tau, SNR_{\text{def?}}) \tag{13}$$

$Y_{m\times s}$ is the measured value of each node; $X_{n\times s}$ is the original signal of each node, $D_{\tau\times n}$ is the uploaded dictionary atoms to the cloud. By reducing the length *m* of the measurement matrix and the number τ of the uploaded cloud dictionary atoms, the memory capacity of the measured values uploaded to the cloud, and the dictionary atoms can be reduced. In addition, in order to ensure that cloud data can be called accurately and quickly, the cloud integrates the dictionary atoms uploaded by each edge to generate a complete dictionary $D_{k\times n}$, where *k* is the total number of atoms in the complete dictionary. When calling data in this partition, the sparse representation coefficient corresponding to the partition data is calculated by the **Eq. 13**.

$$\boldsymbol{\theta}_{n\times s} = SOMP(\boldsymbol{Y}_{m\times s}, \boldsymbol{D}_{k\times n}, \boldsymbol{\Psi}_{m\times n}) \tag{14}$$

Then the original signal $X'_{n\times s}$ of the partition is recovered through **Eq. 13** as follow:

$$\boldsymbol{X}'_{n\times s} = real(\boldsymbol{\Phi}_{n\times n}\boldsymbol{\theta}_{n\times s}) \tag{15}$$

By establishing a complete dictionary in the cloud center, each edge only needs to upload the measurement values to realize compression storage of power quality data, which reduces the storage space of cloud data. The steps for constructing a complete dictionary are as follows:

1) Calculate the correlation $r_{i,k}$ between the newly uploaded dictionary atom $\boldsymbol{d}i$ of the edge node and the *k*th atom D_k in the initial sparse dictionary $D_{k\times n}$ in the cloud. The formula is as follow:

$$r_{i,k} = \frac{\operatorname{cov}(\boldsymbol{d}_i, D_k)}{\sqrt{\operatorname{var}[\boldsymbol{d}_i]\operatorname{var}[D_k]}} \tag{16}$$

Suppose the value of each generated is lower than a certain threshold. In that case, the overall correlation between the dictionary atom $\boldsymbol{d}i$ uploaded to the cloud and the cloud dictionary $D_{k\times n}$ is relatively weak. Therefore, the dictionary atom is added to the sparse cloud dictionary.

2) Combine the dictionary atoms uploaded in each partition into an over-complete sparse dictionary, and regularization is performed to reduce the correlation between the dictionary atoms.

$$\boldsymbol{D}_{k\times n} = \{\boldsymbol{d}_1, \boldsymbol{d}_2, \cdots, \boldsymbol{d}_k\} \tag{17}$$

$$\boldsymbol{d'}_k = \boldsymbol{d}_k - \frac{\boldsymbol{d}_k, \boldsymbol{d'}_1}{\boldsymbol{d'}_1, \boldsymbol{d'}_1}\boldsymbol{d'}_1 - \frac{\boldsymbol{d}_k, \boldsymbol{d'}_2}{\boldsymbol{d'}_2, \boldsymbol{d'}_2}\boldsymbol{d'}_2 - \cdots - \frac{\boldsymbol{d}_k, \boldsymbol{d'}_{k-1}}{\boldsymbol{d'}_{k-1}, \boldsymbol{d'}_{k-1}}\boldsymbol{d'}_{k-1} \tag{18}$$

3) Normalizes the over-complete dictionaries to update dictionary atoms.

$$\boldsymbol{d}_k = \frac{\boldsymbol{d'}_k}{\boldsymbol{d'}_k} \tag{19}$$

4) Combined with the over-complete sparse dictionary, recover the original data from the measured values uploaded by the DCS algorithm to verify the recoverability of the stored data and the corresponding sparse coefficient $\boldsymbol{\theta}_j$, $j\in[1,s]$ of each node is obtained. Finally, the compressed storage of power quality data of each node is realized.

Cloud computing is a type of technology that enables the analysis of large amounts of data (Luo, 2022). It is not required to maintain computing hardware, data storage, or associated software on-premises. However, because of the physical separation between the cloud platform and each terminal, response times are frequently slow.

Edge computing is introduced as a novel technique for augmenting cloud computing systems (Ma et al., 2021). Because the edge is located close to the terminal equipment, it can reduce not only the network delay associated with data processing, but also the bandwidth required to transfer the original data to the storage center. As a result of the cloud platform and edge platform collaborating, the system's performance will be significantly improved.

In this paper, based on the cloud-edge collaboration framework shown in **Figure 2**, the edge acquisition algorithm based on DCS-SOMP algorithm is compiled on the MATLAB simulation platform to collect the power quality data generated in PSCAD, and the sparse dictionary atoms and measured values generated in the reconstruction process are uploaded to the cloud server by establishing a connection with the remote cloud. There are three main operations in the cloud: 1) compressed storage of power quality data of distribution network; 2) Construction of complete sparse dictionary; 3) Analysis and calculation of power quality data. The cloud server sends the result of dynamic partition to the edge in time. The edge algorithm obtains the new partition information, adjusts the computing resources, and collects the power quality contained in the new partition, and uploads it to the cloud server again. So as to realize the mutual cooperation between "cloud" and "edge".

3 POWER QUALITY DATA CLASSIFICATION

3.1 Classification of Power Quality Disturbance Signals

The PQD classification model first extracts the characteristics of the disturbance signals and then designs a classifier to recognize different disturbances. According to the different characteristics of amplitude, frequency, and phase of the disturbance signal, the

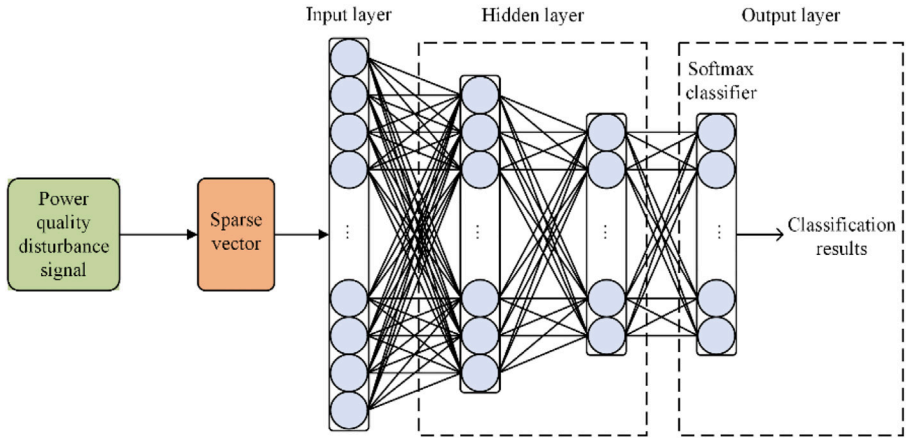

FIGURE 3 | Structure of CS-DL network.

single disturbance is defined as voltage sag, voltage swell, short interruption, harmonic, transient oscillation, pulse, and flicker. The three disturbances of voltage sag, voltage swell, and short interruption are short-term root mean square fluctuations. And the harmonic, transient oscillation, pulse, and flicker are long-term root mean square fluctuation or high-frequency impact disturbance. In addition to the above single disturbance, disturbance usually occurs simultaneously in the actual situation, which is called composite disturbance. The composite disturbance is compounded by two or more single disturbances, which is difficult to analyze. Referring to the IEEE standard and previous literature, six types of single disturbances and four types of composite disturbances are analyzed in this paper.

3.2 Basic Principle of Power Disturbance Classification Based on CS-DL

3.2.1 The Framework of CS-DL Network

A Deep Neural Network (DNN) is the basis of deep learning, which is a multi-layer expression algorithm for learning the implicit distribution of data. Specifically, DNN first employs unsupervised learning to pre-train each layer to learn the characteristics of layers. Training one layer at a time, using the results as the input to the next layer, and then using supervised learning to fine-tune the model from top to bottom. The feature learning process is illustrated in **Figure 3**.

The feature of the constructed CNN is the feature extractor composed of the convolution layer and the sub-sampling layer. The CS-DL network uses a local connection, which only connects one neuron with a few peripheral neurons. The convolution layer of CNN contains multiple differentiated feature planes, each of which consists of some rectangularly arranged neurons, and the neurons on the same feature plane share weight with each other. CNN sub-sampling is a special convolution process and reduces the number of model parameters. In summary, CNN uses the convolution layer and sub-sampling layer, as well as the corresponding local connection and weight sharing rules to enhance feature extraction's self-learning and characterization capacity and finally realizes the classification of direct power quality signal inputs.

3.2.2 Structures of CNN-BiLSTM and CS-BiLSTM Networks

PQD signal is a typical time-series signal, but CNN does not consider the timing characteristics of the signals in the process of feature extraction. Meanwhile, the bidirectional long short-term memory (BiLSTM) model is a kind of Recurrent Neural Network (RNN) suitable for time-series signal analysis. Therefore, a mixed CNN-BiLSTM model based on the classification of PQD signals by the CNN model is proposed. Firstly, features of disturbing signals are extracted automatically by CNN. Then, the features are further processed by BiLSTM. The proposed CNN-BiLSTM model enhances the feature extraction ability of the model, speeds up the convergence rate of training, further improves the accuracy of disturbance classification, and has high noise immunity. In order to deal with the time-consuming defect and classification problem of composite disturbance, an improved CS-BiLSTM is proposed, which utilizes the CS method to transmit signal characteristics quickly, accurately, and effectively so as to improve the efficiency and timeliness of the PQD classification process.

The Structures of CS-BiLSTM Networks are illustrated in **Figure 4**.

3.3 Parameter Optimization Based on DDPG

3.3.1 Concept of Reinforcement Learning

Reinforcement learning achieves global optimization of the objective function through the feedback of the reward function. The main parts of the DDPG reinforcement learning algorithm are as follows:

Agent: The agent that needs to be controlled, corresponding to the parameter optimizer in this paper.

State s: The agent's current state, corresponding to the current value of the key parameters such as learning rate, minibatch number, etc.

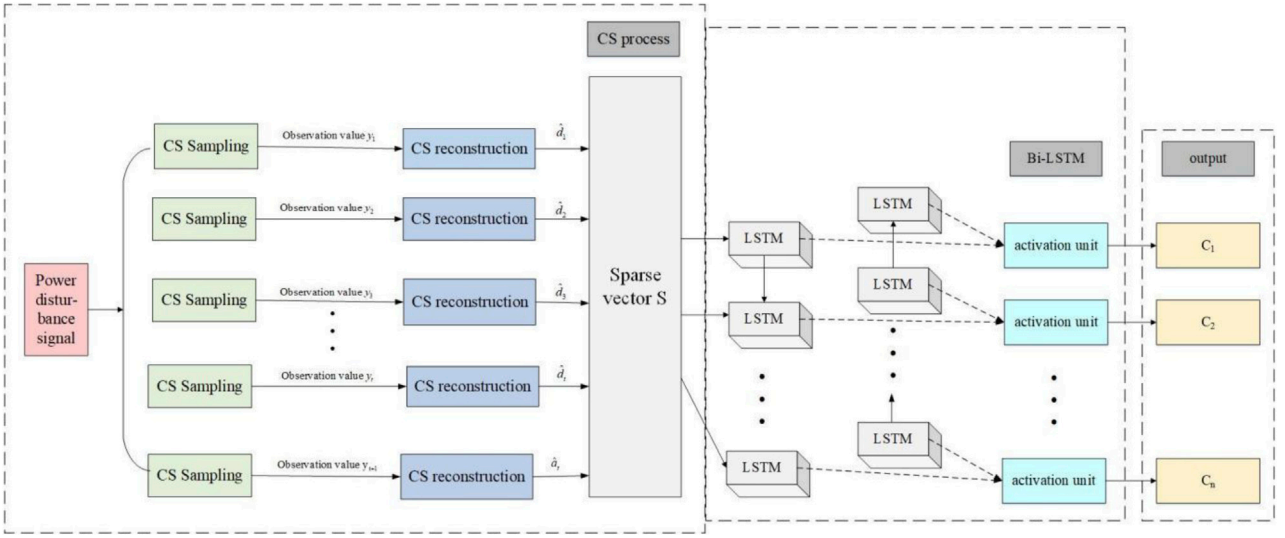

FIGURE 4 | Structure of CS-BiLSTM.

Action a: The actions that the agent can take, corresponding to the variation of the parameters.

Reward r: The feedback value of the environment, and the evaluation value of the previous action, corresponding to the accuracy in this paper.

π The agent's action to move from the current state to the next state.

Value: The reward value of the agent's long-term actions, as distinguished from the short-term reward represented by Reward r.

Environment: The environment in which the agent is placed.

3.3.2 Concept of Deterministic Policy Gradient

Deterministic Policy Gradient (DPG) is an improved algorithm based on AC (Action and Critic) structure. It utilizes the PG (Policy Gradient)'s advantage in continuous space and changes the randomized strategy to a deterministic strategy. The corresponding formula is shown in (20):

$$a_t \sim \pi_\theta(s_t|\theta^\pi) \tag{20}$$

The DPG method can reduce the sampling size of data. For randomized strategy, policy gradient needs to integrate state and action simultaneously, and determine strategy only needs to integrate the state, which greatly improves the algorithm's efficiency. The formulas of deterministic strategy and the gradient expression are as follows:

$$J_\beta(\mu) = E_{S\sim\rho^\beta}\left[Q^\mu(s,\mu(s))\right] \tag{21}$$

$$\nabla_\theta J(\mu_\theta) = E_{S\sim\rho^\beta}\left[\nabla\theta\mu_\theta(s)Q^\mu(s,a)\big|_{a=\mu_\theta}\right] \tag{22}$$

Where: μ represents the determined strategy adopted by DDPG, ρ^β represents the distribution of a balanced exploration and utilization process. In the DPG algorithm, the Critic network is a linear function approximator, and the Actor updates the parameters in the direction of the Critic's action-value function.

The DDPG algorithm is improved by the following details: the updating methods of the target network's parameters, the regularization method of the samples, and the exploration noise of action. Compared with DQN (Deep Q network), which updates the parameters of the target network at regular time intervals, DDPG adopts a soft update method, which transfers the parameters both before and after updating to the target network. In order to prevent gradient disappearance or exploding gradient, the input and output of ANN are normalized in batches. Moreover, the DDPG algorithm adds a Gaussian noise to the determined action to improve the diversity of samples.

3.4 CS-BILSTM Model Based on DDPG Optimization

The complexity of PQD classification is prone to result in no convergence and poor training effects for the classification model. Therefore, the DDPG method is introduced to optimize the parameters during the training process. The DDPG algorithm based on artificial intelligence has the characteristics of self-organization, self-adaptation, and self-learning, has high robustness, and is easy to parallel. The detailed parameter of the DDPG network is set as follows. The inputs of the Actor network are normally $N \times 2$ sequences with two hidden layers which has 256 and 32 neurons respectively. The activation function of the Actor network is tanh, the loss function is MSE, and the optimization method RMSprop is introduced here. The input of Critic network consists of two parts: the first part is the state observed by the agent; The second part is the corresponding actions taken by the agent. The hidden layer includes two layers, the number of neurons is 256 and 32 respectively, and the number of neurons in the output layer is 1, which indicates the Q value obtained by the critical network

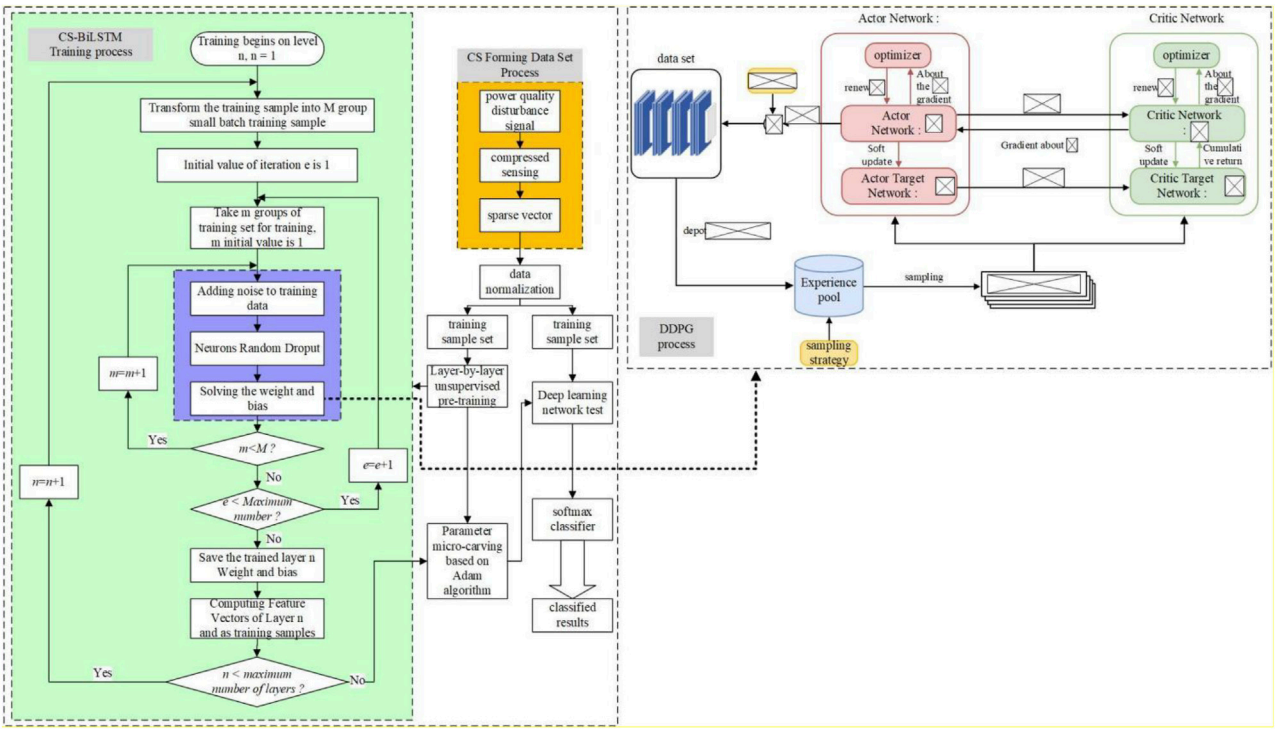

FIGURE 5 | Schematic diagram of the CS-BILSTM model optimized by DDPG algorithm.

taking some action in this state. Except for the output layer, other activation functions use tanh, and the activation function of the output layer is Relu. After obtaining the Q value, the probability of generating random action is ε Strategy, i.e., probability 1- ε chooses $\pi^*(s) = \arg\max Q(s,a)$. Meanwhile, the value of random action follows the normal distribution , $\sigma = (Q(s,a) - \arg\max(Q(s,a)))^2$. The related Param-eter setting and description of DDPG algorithm is shown in **APPENDIX** part.

It is widely used in the optimization of multimodal functions. The traditional stacked denoising autoencoder adopts SGD in the fine-tuning stage. The SGD updates each sample with a fast update rate, which can automatically pick out the inferior local optimtbal points. However, on account of the many update times, the cost function may experience acute fluctuation with inferior convergence performance, which affects the classification effect of the encoder. Therefore, this paper improves the traditional DAE. Adam is used to updating the network weights and bias during the fine-tuning stage instead of SGD. The flow chart of PQD classification by the improved CS-BiLSTM algorithm based on DDPG parameter optimization is illustrated in **Figure 5**.

4 SIMULATION RESULTS AND ANALYSIS

The proposed power quality signal compression technique and PQD classification are evaluated in this section via the comparative experiments with four simulation tests. The simulation software are respectively Matlab2019b and Python3.6.5 with its advanced tool pytorch1.2.0. As for the computer configuration, the Intel Core CPU i3-8100 and internal storage 16G with the 1T hard disk storage device.

This paper uses the WAMS (Wide Area Measurement System) data collected from the actual power grid in a province of China in 2020 to form a data set. The data set is the power quality data that has been manually verified, including 2000 pieces of data. In order to form the enough training set, some power quality data is generated with the MATLAB simulation.

A series of power quality signals are generated by mathematical modeling simulation, and the sampling frequency is set to 3200 Hz based on the actual sampling frequency of power equipment in the power system. Also, the power quality signal sampling length is 18 cycles.

Then, the Gaussian white noise is added in the generation of the PQD signal to simulate the random noise in the power system. The signal-to-noise ratio (SNR) ranges from 20 dB to 40 dB.

The generated power quality signals include six categories of single disturbance and four types of composite disturbance such as voltage sag, harmonic, voltage flicker, harmonic with voltage sag, harmonic with voltage interruption, voltage sag with voltage flicker, etc. They are all labeled with the number from 1 to 10, respectively.

MATLAB is used to generate 20,000 sets of PQD signals, where 18,000 sets are chosen as the training set, and the last 2000 sets are selected as the testing set. The 10-fold cross-validation is adopted to select the suitable training set and validation set in this step. **Figure 7** demonstrates the experiment result.

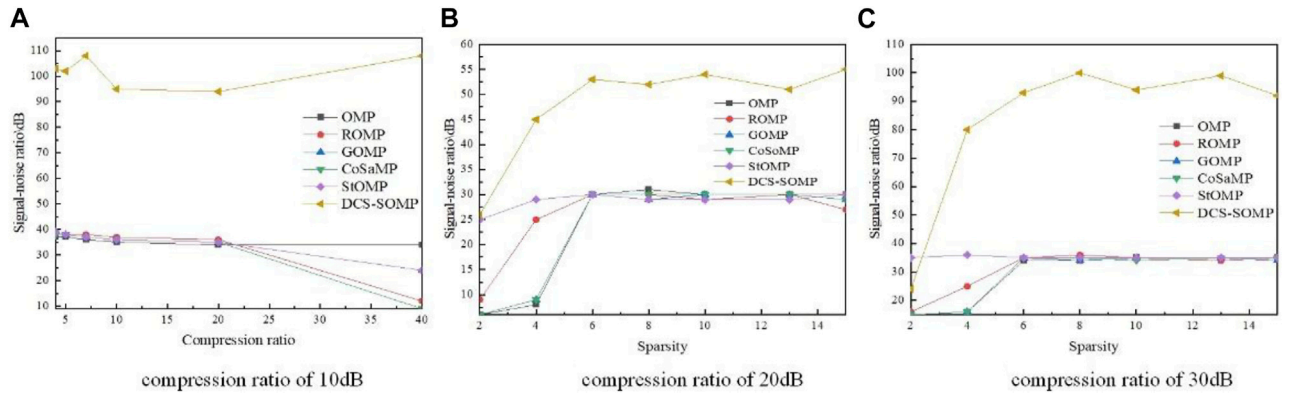

FIGURE 6 | Comparison of reconstruction effects. **(A)** Compression ratio of 10 dB, **(B)** Compression ratio of 20 dB, and **(C)** Compression ratio of 30 dB.

4.1 Comparison Results of Reconstruction Algorithms

As shown in **Figure 6**, Orthogonal Matching Pursuit, Generalized Orthogonal Matching Pursuit (Generalized OMP, GOMP), Regularized Matching Pursuit (Regularized OMP, ROMP), and Stage Orthogonal Matching Pursuit (StagewiseOMP, StOMP), Compressive Sampling Matching Pursuit (CompressiveSamplingMP, CoSaMP), and DCS-SOMP algorithms are adopted to perform compressive sampling of PQD signals in the power grid, while the sparsity of the PQD signal of each node is assumed as 10. The comparison of the signal-to-noise ratios (SNR) of reconstructed power quality signals under different compression ratios is carried out between the above algorithms. **Figure 5** demonstrates that except for the DCS-SOMP algorithm, the signal-to-noise ratio of other algorithms' reconstructed power quality signals decreases with the increase of compression ratio. In the subfigure (a) of **Figure 5**, the reconstructed power quality signals of the ROMP and CoSaMP algorithms show distortion when the compression ratio rises to 40. Additionally, in the process of power quality data compression and storage, the sparsity of PQD signals under the sparse dictionary has an important impact on the power quality data's upload speed to the cloud. The sparser the data, the fewer sparse dictionary atoms, thus, the smaller data sizes. By contrast, the DCS-SOMP reconstruction algorithm overperform other algorithms, like OMP, ROMP, etc. It is clearly more accurate for the compressed acquisition of power quality data.

4.2 Reconstruction and Demonstration of Different Power Quality Disturbances

After determining the transform domain, the measurement matrix, and the reconstruction algorithm, the compression-reconstruction simulation of 6 types of PQD signals is carried out, and the compression rate represents the ratio of the observation points' number to the signal length, which is set as 25%. In order to reduce the reconstruction error, the sparsity value of different disturbance signals in **Table 1** is determined through a large number of experiments. Moreover, **Table 1** shows the error values between the original signal and the reconstructed PQD signal obtained by compressed sensing and reconstructing of randomly generated PQD signals. **Figure 7** shows the simulation diagrams of the original signals, the reconstruction signals, and the error waveform of the two kinds of PQD signals. Finally, we use mean square error to evaluate the reconstruction signals.

TABLE 1 | Reconstruction error of power quality disturbance signal.

Power quality disturbance	Sparsity (K)	Reconstruction error (%)
Voltage sag	10	1.12
Voltage swell	10	1.47
Harmonic	10	3.29
Voltage flicker	10	3.99
Pulse	10	1.02
Transient oscillation	10	6.15

4.3 Comparison of Application of CS-DL in Power Quality Disturbance Classification

4.3.1 Results of Power Quality Disturbance Classification

It can be seen from **Figure 8** that the classification accuracy of PQD signals is still relatively low in the initial stage of training. Then, the loss value is quickly reduced to less than 0.1 after about 850 epochs of training. Also, the classification accuracy is improved to about 94% and remains stable, which indicates that the network converges after about 850 training epochs. Moreover, the training accuracy and test accuracy are almost equal after about 950 epochs of training, and the total classification accuracy of PQD signals in the test set is 99.7%. In order to obtain better network performance, the setting of the network parameters is necessary, in which the setting of the learning rate is critical. In this paper, the dynamic setting method of learning rate is adopted. The initial learning rate is set to 0.001; after 200 iterations, it drops to 0.0001. This setting can further improve the classification accuracy of PQD signals.

It can be seen from **Figure 9**, **Figure 10**, and **Table 2** that the CS-BiLSTM method we proposed has a superior performance

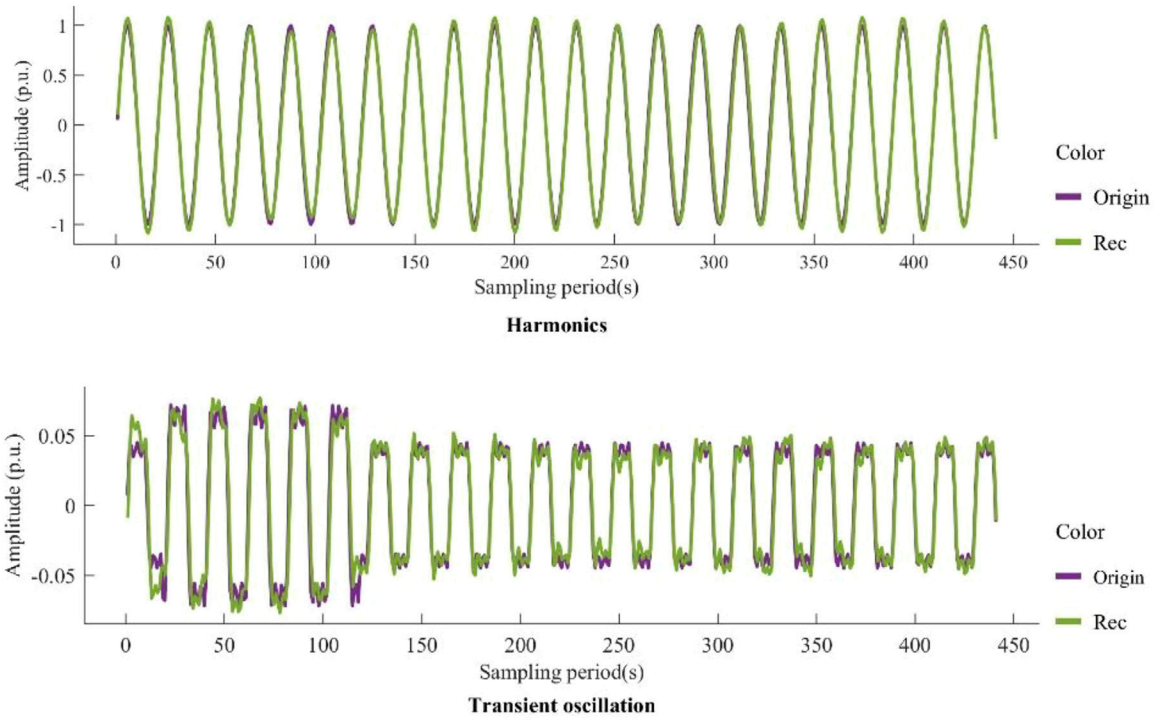

FIGURE 7 | Simulation waveform of the original signal and reconstructed signal.

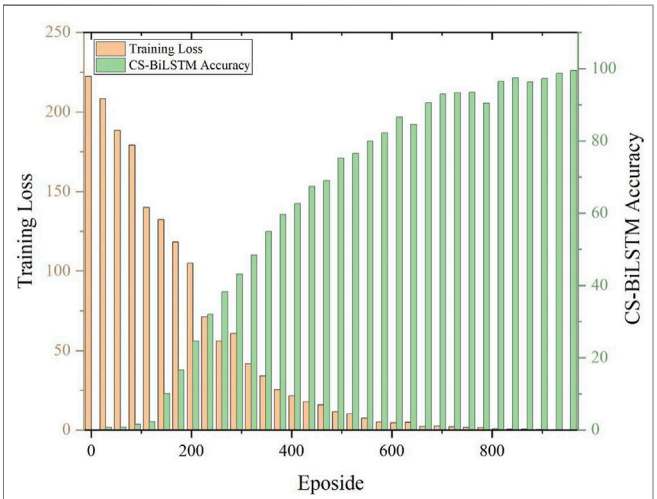

FIGURE 8 | Training loss and classification accuracy of CS-BiLSTM model.

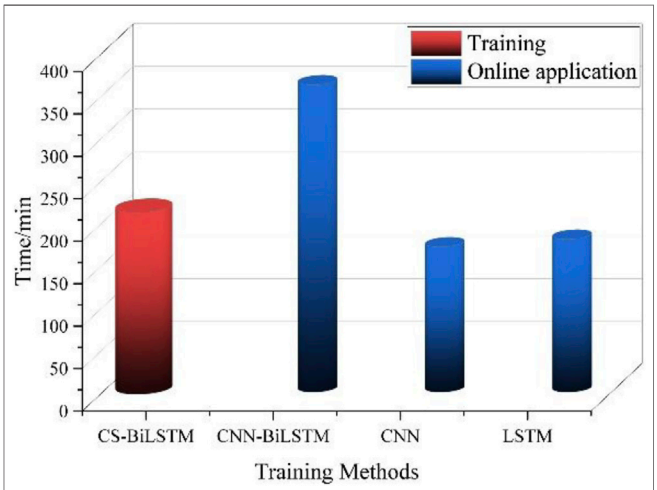

FIGURE 9 | Comparison of training time.

compared with the CNN-BiLSTM method in the classification of PQD. Although the CS-BiLSTM model has lower classification accuracy for voltage flicker and transient oscillation than the CNN-BiLSTM model, the CS-BiLSTM has higher classification accuracy in the other eight types of PQD and average classification accuracy. Meanwhile, the CS-BiLSTM model's training time is only 59.12% of the CNN-BiLSTM model's training time. Since the voltage sags, voltage swells, and harmonics account for more than 70% of the PQD types, in reality, the ten types of PQD samples are also created in proportion.

In the case of identifying 1,000 groups of voltage sag disturbance data, 730 groups are classified as voltage sags, 80 groups are identified as oscillation with voltage sags, 20 groups are identified as voltage flicker with voltage sags, and 180 groups are identified as harmonic with voltage sags. Furthermore, we analyze the 180 groups of signals that are identified as composite

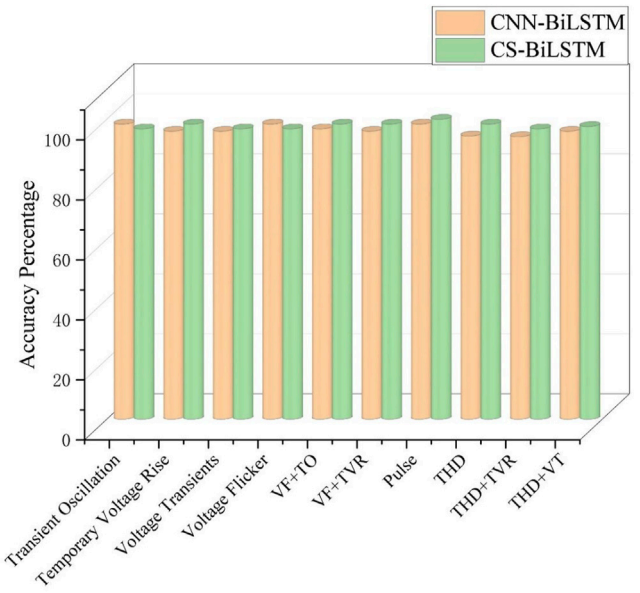

FIGURE 10 | Classification results of non-noise power quality disturbance signals.

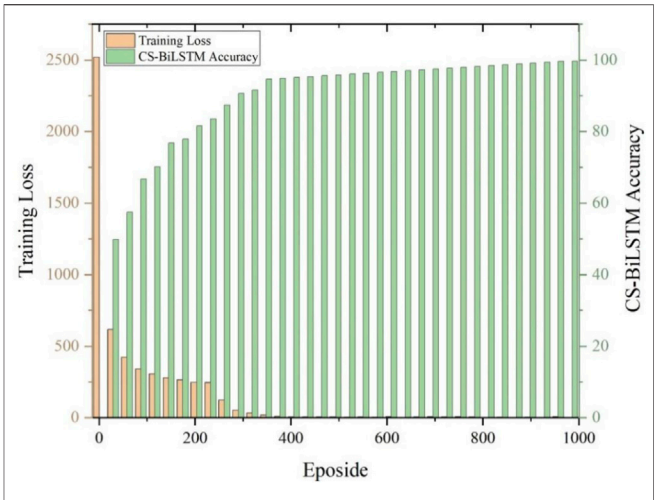

FIGURE 11 | Training loss and classification accuracy of the optimized CS-BiLSTM model.

TABLE 2 | Classification accuracy of the reconstructed signal.

Power quality disturbance	Classification accuracy (%)	
	CNN-BiLSTM	CS-BiLSTM
Voltage sag	96.0	96.8
Voltage swell	96.0	98.4
Harmonic	94.4	98.4
Voltage flicker	98.4	96.8
Pulse	98.4	100
Transient oscillation	98.4	96.8
Harmonic + voltage sag	96.0	97.6
Harmonic + voltage swell	94.2	96.8
Voltage flicker + transient oscillation	96.8	98.4
Voltage flicker + voltage sag	96.0	98.4
Average value	96.43	97.6

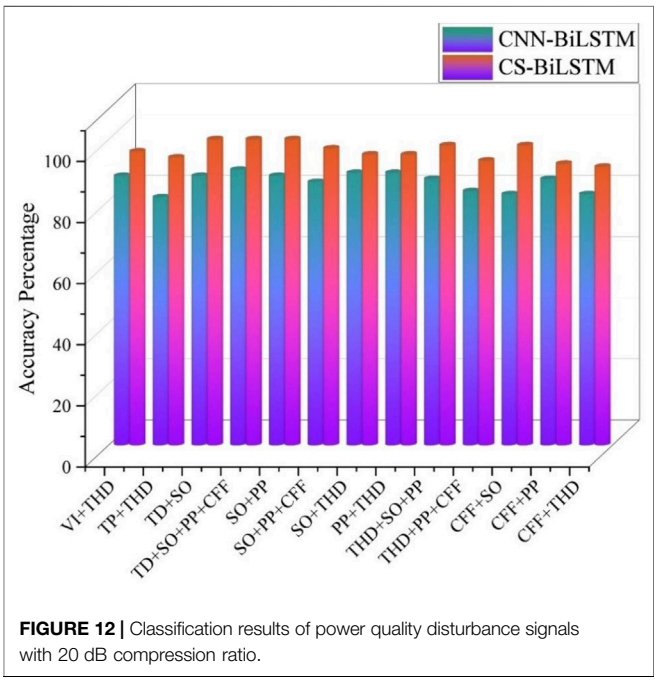

FIGURE 12 | Classification results of power quality disturbance signals with 20 dB compression ratio.

disturbances of harmonic with voltage sags. The analysis shows that there exist harmonic components in these signals, which meet the requirements of IEEE standard for harmonic definition. In addition, it indicates that the label of some original data is inaccurate. Meanwhile, the result demonstrates that the proposed method has high classification accuracy for composite disturbances, which is normally neglected in the previous study. The total classification time of the CS-BiLSTM model for the 1,000 groups of voltage sags data is 15 s, with an average classification time of 0.15 s per sample.

4.3.2 Results of Parameter Optimization Based on DDPG Method

Three Gaussian white noises were added to the initial signal to verify the noise immunity of the algorithm before training, and the SNR is 20 dB, 30 dB, and 40 dB, respectively, after adding the Gaussian noise. As shown in **Figure 11**, the accuracy rate of PQD classification increases rapidly in the initial stage of training. After about 400 rounds of training and learning, the loss value decreases rapidly to less than 0.2. The classification accuracy rate increases to about 95% and then remains stable, indicating that the network has converged. Compared with the traditional method, the proposed method has a superior performance of PQD classification both under simple situations and in the case of complex PQD.

It can be seen from **Figure 12** and **Table 3** that with the increase of noise, the average classification accuracy of the two methods for PQD is gradually reduced. When the noise intensity is 40 and 30 dB, the average classification accuracy of the CS-BiLSTM model

TABLE 3 | Classification results of multiple disturbances.

Power quality disturbance	SNR			
	20 dB	30 dB	40 dB	Non-noise
Voltage interruption and harmonic	96 (88)	97 (86)	97 (87)	98 (88)
Voltage swell and harmonic	94 (81)	94 (80)	93 (83)	95 (81)
Voltage sag and transient oscillation	100 (88)	100 (89)	99 (90)	100 (88)
Pulse and harmonic	95 (89)	99 (86)	97 (87)	97 (89)
Transient oscillation and harmonic	95 (89)	96 (88)	93 (82)	95 (89)
Voltage flicker and harmonic	91 (82)	93 (81)	95 (82)	93 (82)
Transient oscillation and pulse	100 (88)	98 (89)	100 (90)	100 (88)
Voltage flicker and pulse	92 (87)	98 (88)	100 (90)	100 (87)
Voltage flicker and transient oscillation	98 (82)	96 (89)	100 (88)	100 (82)
Harmonic and transient oscillation and pulse	98 (87)	96 (90)	99 (90)	99 (87)
Harmonic and pulse and voltage flicker	93 (83)	94 (83)	94 (84)	95 (83)
Transient oscillation and pulse and voltage flicker	97 (86)	99 (89)	100 (89)	100 (86)
Voltage sag and transient oscillation and pulse and voltage Flicker	100 (92)	98 (89)	100 (90)	100 (93)
Average value	96.07 (86.15)	96.76 (86.77)	97.49 (87.15)	97.85 (87.69)

(The recognition rate of traditional methods in parentheses).

is 97.49 and 96.76%, respectively. When the noise intensity is further strengthened to 20 dB, the classification accuracy is significantly reduced to 96.07% but remains high. Compared with the CNN-BiLSTM model, the CS-BiLSTM hybrid model performs a higher classification accuracy obviously for all types of PQDs. The experimental results fully prove that the proposed hybrid model possesses a good classification ability of PQD signals and has promising anti-noise capability.

5 CONCLUSION

This paper presents a power quality disturbance classification and classification method based on DCS and deep learning. Through this method, the efficient compression and accurate reconstruction of power quality data of each node in the power grid can be realized. Moreover, the identification and classification of PQDs in the power grid can be realized, which provides a new reference for the governance of power grid harmonics and the storage of power quality data. The main conclusions of this paper are as follows:

1) Based on the SOMP algorithm and K-SVD dictionary learning algorithm, a DCS algorithm called DCS-OMP is proposed, which realizes efficient compression and accurate reconstruction of power quality data in distribution network under low measurement value and high compression ratio.
2) Based on the CNN-BiLSTM model, a CS-BiLSTM hybrid model is built, and a comparison is carried out between the two models. The average recognition rate of CS-BiLSTM hybrid model is 97.85% without noise, and 97.49, 96.76, and 96.07% with 40, 30, and 20 dB noise, respectively. Compared with the CNN-BiLSTM model, the recognition rate of the CS-BiLSTM hybrid model is increased by 10.15, 10.30, 10.00, and 9.23% in the case of no noise, 40 dB noise, 30 dB noise, and 20 dB noise, respectively. The recognition rate in high-intensity noise interference is improved significantly. According to the results, the proposed CS-BiLSTM hybrid model has a higher recognition rate and better noise immunity.
3) DDPG algorithm is employed to optimize the parameters in the training process of the CS-BiLSTM hybrid model, which ensures the convergence of training and the effectiveness of results.

The proposed method CS-BiLSTM is more efficient to solve the problems of high sampling rate, high cost of hardware implementation when performing the disturbance recognition of power quality data. It helps improve the related theory and algorithm of power quality analysis and detection. However, the application of parameters optimization via reinforcement learning will inevitably encounter spending much time training the network. In the future, we would like to further adjust the parameters to make the experiment converge, speed up the convergence speed of the network, reduce the time spent on training and improving the computing efficiency of the algorithm.

DATA AVAILABILITY STATEMENT

The original contributions presented in the study are included in the article/Supplementary Material, further inquiries can be directed to the corresponding author.

AUTHOR CONTRIBUTIONS

XX: Drafting the manuscript, CH: experimental analysis, HC: Review and Supervision, YL: Methodology and Formal analysis, BZ: Conceptualization and Revised, SW: Data Curation and Resources, CC: Software.

FUNDING

This work is supported by The Laboratory Open Fund of Beijing Smart-chip Microelectronics Technology Co., Ltd.

REFERENCES

Berutu, S. S., and Chen, Y. C. (2020). "Power Quality Disturbances Classification Based on Wavelet Compression and Deep Convolutional Neural Network," in 2020 International Symposium on Computer, Consumer and Control (IS3C).IEEE, Taichung City, Taiwan, 13-16 Nov. 2020, 327–330.

Bravo-Rodríguez, J. C., Torres, F. J., and Borrás, M. D. (2020). Hybrid Machine Learning Models for Classifying Power Quality Disturbances: A Comparative Study. *Energies* 11 (13), 2761–2768. doi:10.3390/en13112761

Cai, K., Cao, W., Aarniovuori, L., Pang, H., Lin, Y., and Li, G. (2019). Classification of Power Quality Disturbances Using Wigner-Ville Distribution and Deep Convolutional Neural Networks. *IEEE Access* 7 (1), 119099–119109. doi:10.1109/ACCESS.2019.2937193

Chen, S. (2003). A Quantitative Analysis of the Data Acquisition Requirements for Measuring Power Quality Phenomena. *IEEE Trans. Power Deliv.* 18 (4), 1575–1577. doi:10.1109/TPWRD.2003.817521

Elphick, S., Ciufo, P., Drury, G., Smith, V., Perera, S., and Gosbell, V. (2017). Large Scale Proactive Power-Quality Monitoring: An Example from Australia. *IEEE Trans. Power Deliv.* 32 (2), 881–889. doi:10.1109/TPWRD.2016.2562680

Elphick, S., Gosbell, V., Smith, V., Perera, S., Ciufo, P., and Drury, G. (2017). Methods for Harmonic Analysis and Reporting in Future Grid Applications. *IEEE Trans. Power Deliv.* 32 (2), 989–995. doi:10.1109/TPWRD.2016.2586963

Gibbon, T. B., Yu, X., and Monroy, I. T. (2009). Photonic Ultra-wideband 781.25-Mb/s Signal Generation and Transmission Incorporating Digital Signal Processing Detection. *IEEE Photon. Technol. Lett.* 21 (15), 1060–1062. doi:10.1109/LPT.2009.2022503

Jin, L., Haosong, L., Zhongping, X., Ting, W., Shuai, W., Yutong, W., et al. (2019). "Research on Wide-Area Distributed Power Quality Data Fusion Technology of Power Grid," in 2019 IEEE 4th International Conference on Cloud Computing and Big Data Analysis (ICCCBDA), Chengdu, China, 12-15 April 2019, 185–188. doi:10.1109/icccbda.2019.8725668

Li, L., Liu, P., Wu, J., Wang, L., and He, G. (2020). Spatiotemporal Remote-Sensing Image Fusion with Patch-Group Compressed Sensing. *IEEE Access* 8, 209199–209211. doi:10.1109/ACCESS.2020.3011258

Li, Y., Zhang, M., and Chen, C. (2022). A Deep-Learning Intelligent System Incorporating Data Augmentation for Short-Term Voltage Stability Assessment of Power Systems. *Appl. Energ.* 308, 118347. doi:10.1016/j.apenergy.2021.118347

Lu, W., Wei, Y., Yuan, J., Deng, Y., and Song, A. (2020). Tractor Assistant Driving Control Method Based on EEG Combined with RNN-TL Deep Learning Algorithm. *IEEE Access* 8, 163269–163279. doi:10.1109/ACCESS.2020.3021051

Luo, F. (2022). Data-Driven Energy Demand Side Management Techniques. *Front. Energ. Res.*, 24. doi:10.3389/fenrg.2022.849031

Ma, F., Wang, B., Li, M., Dong, X., Mao, Y., Zhou, Y., et al. (2021). Edge Intelligent Perception Method for Power Grid Icing Condition Based on Multi-Scale Feature Fusion Target Detection and Model Quantization. *Front. Energ. Res.* 9, 591. doi:10.3389/fenrg.2021.754335

Negnevitsky, M., Faybisovich, V., Santoso, S., Powers, E. J., Grady, W. M., and Parsons, A. C. (2000). Discussion of "Power Quality Disturbance Waveform Recognition Using Wavelet-Based Neural Classifier-Part 1: Theoretical Foundation. *IEEE Trans. Power Deliv.* 15 (4), 1347–1348. doi:10.1109/61.891571

Ning, L., Si, L., Nian, L., and Fei, Z. (2021). Network Reconfiguration Based on Edge-Cloud-Coordinate Framework and Load Forecasting. *Front. Energ. Res.* 9, 525. doi:10.3389/fenrg.2021.679275

Noland, K. C. (2016). High Frame Rate Television: Sampling Theory, the Human Visual System, and Why the Nyquist–Shannon Theorem Does Not Apply. *SMPTE Motion Imaging J.* 125 (3), 46–52. doi:10.5594/JMI.2016.2531998

Pei, S., Hsue, W., and Ding, J. (2006). Discrete Fractional Fourier Transform Based on New Nearly Tridiagonal Commuting Matrices. *IEEE Trans. Signal Process.* 54 (10), 3815–3828. doi:10.1109/TSP.2006.879313

Song, Z., Liu, B., Pang, Y., Hou, C., and Li, X. (2012). An Improved Nyquist–Shannon Irregular Sampling Theorem from Local Averages. *IEEE Trans. Inf. Theor.* 58 (9), 6093–6100. doi:10.1109/TIT.2012.2199959

Tang, Q., Qiu, W., and Zhou, Y. (2020). Classification of Complex Power Quality Disturbances Using Optimized S-Transform and Kernel SVM. *IEEE Trans. Ind. Electro.* 67 (61), 9715–9723. doi:10.1109/TIE.2019.2952823

Uçkun, F. A., Özer, H., Nurbaş, E., and Onat, E. (2020). "Direction Finding Using Convolutional Neural Networks and Convolutional Recurrent Neural Networks," in 2020 28th Signal Processing and Communications Applications Conference (SIU), Gaziantep, Turkey, 5-7 Oct. 2020, 1–4. doi:10.1109/SIU49456.2020.9302448

von Gladiß, A., Ahlborg, M., Knopp, T., and Buzug, T. M. (2015). Compressed Sensing of the System Matrix and Sparse Reconstruction of the Particle Concentration in Magnetic Particle Imaging. *IEEE Trans. Magnetics* 51 (2), 1–4. doi:10.1109/TMAG.2014.2326432

Xin, R., Zhang, J., and Shao, Y. (2020). Complex Network Classification with Convolutional Neural Network. *Tsinghua Sci. Technol.* 25 (4), 447–457. doi:10.26599/TST.2019.9010055

Yin, M., Xu, Y., Shen, C., Liu, J., Dong, Z. Y., and Zou, Y. (2017). Turbine Stability-Constrained Available Wind Power of Variable Speed Wind Turbines for Active Power Control. *IEEE Trans. Power Syst.* 32 (3), 2487–2488. doi:10.1109/TPWRS.2016.2605012

Zhang, M., Li, J., Li, Y., and Xu, R. (2021). Deep Learning for Short-Term Voltage Stability Assessment of Power Systems. *IEEE Access* 9, 29711–29718. doi:10.1109/access.2021.3057659

Zhao, W., Shang, L., and Sun, J. (2019). Power Quality Disturbance Classification Based on Time-Frequency Domain Multi-Feature and Decision Tree. *Prot. Control. Mod. Power Syst.* 4 (1), 1–6. doi:10.1186/s41601-019-0139-z

Conflict of Interest: Authors XX and CH were employed by Beijing Smart-Chip Microelectronics Technology Co., Ltd Authors YL, BZ, and SW were employed by Beijing Electric Power Science and Smart Chip Technology Company Limited.

The authors declare that this study received funding from The Laboratory Open Fund of Beijing Smart-chip Microelectronics Technology Co., Ltd. The funder had the following involvement in the study: data collection, experiment analysis.

APPENDIX

TABLE A1 | Parameter setting and description of DDPG algorithm.

Parameter	Definition	Value
Tau_1	Smoothing coefficient of target network in the actor and critic networks	0.001
Tau_2	The smoothing coefficient of exploring network	0.002
α_1	Learning rate of actor and critic network	0.001
α_2	Learning rate of ε control network	0.002
Batch_size	Number of samples drawn from the experience pool per training	64
Capacity	Size of experience pool	10,000
Σ	Control the initial value of the variance of the exploration range	1
Γ	Discount factor	95

frontiers | Frontiers in Energy Research

BRIEF RESEARCH REPORT
published: 26 April 2022
doi: 10.3389/fenrg.2022.882818

Power Grid Material Demand Forecasting Based on Pearson Feature Selection and Multi-Model Fusion

Zhou Dai[1,2], *Gang Wang*[1]*, *Ruien Bian*[2] *and Chaozhi Deng*[2]

[1]School of Electric Power Engineering, South China University of Technology, Guangzhou, China, [2]China Southern Power Grid Materials Co., Ltd, Guangzhou, China

The demand projection of power grid materials can furnish an effective support for the management of power grid materials. Due to variations in the data distribution of individual districts and diversity of materials, a single forecasting model is incapable of accurately predicting the demand for all types of materials. Moreover, for the data-driven network model, the effect of the model has a strong correlation with the quality of its input parameters. To address these problems, this study proposes a power grid material demand forecasting model based on feature selection and multi-model fusion. The first step in this regard is the usage of Pearson coefficient in the selection of main characteristic parameters from original parameters and using them as the input of the network model. Then, stacking fusion algorithm is used to fuse multiple basic models. At last, the proposed method mentioned in this study is tested on a real dataset. The results depict that the proposed method can fully integrate the advantages of various basic models with higher accuracy and generalization ability.

Keywords: power grid materials, demand prediction, feature selection, fusion algorithm, gradient boosting decision tree, eXtreme gradient boosting tree, long- and short-term memory network

OPEN ACCESS

Edited by:
Xun Shen,
Tokyo Institute of Technology, Japan

Reviewed by:
Gaurav Sachdeva,
DAV University, India
Sandeep Kumar Duran,
Lovely Professional University, India

***Correspondence:**
Gang Wang
wangg@scut.edu.cn

Specialty section:
This article was submitted to Smart Grids, a section of the journal Frontiers in Energy Research

Received: *24 February 2022*
Accepted: *11 March 2022*
Published: *26 April 2022*

Citation:
Dai Z, Wang G, Bian R and Deng C (2022) Power Grid Material Demand Forecasting Based on Pearson Feature Selection and Multi-Model Fusion. Front. Energy Res. 10:882818. doi: 10.3389/fenrg.2022.882818

INTRODUCTION

A power grid system is one of the preeminent pillars for national economic development. Any sort of issue in power equipment might cause large-scale power outage of the power grid, thus leading to huge negative impacts. At present, the material management of power grid has several problems including "the material data fragmentation, material reserves mechanization, and main responsibility ambiguity." The accuracy, correctness, and integrity problems existing in most of the historical demand data of electric power materials, which leads to the demand of material, cannot be predicted (Lai et al., 2016; Oliveira et al., 2021), thereby causing inadequate refinement of material management. Therefore, in order to achieve higher efficiency and precision of material management, the material demand forecasting has been researched deeply throughout the world.

According to the references (Pan et al., 2016; Wang and Gu, 2016; Zhao et al., 2017; Wang et al., 2019; Dong et al., 2020; Ming et al., 2021), most of the prediction models for power grid materials are presently using a single model structure having the problem of either over-fitting or under-fitting and also have poor generalization for different scenarios. However, the data model requires a high quality of input parameter information. As a result, the input parameter information should be screened. According to the reference (Yang et al., 2022a), this research is a pioneer study for SCUC problems

that proposes an expanded sequence-to-sequence (E-Seq2Seq) based data-driven SCUC expert system for dynamic multiple-sequence mapping samples; it can accommodate the mapping samples of SCUC and consider the various input factors that affect SCUC decision-making, possessing strong generality, high solution accuracy, and efficiency over the traditional method.

Aiming at the aforementioned problems, this study proposes a power grid material prediction model based on feature selection and multi-model fusion. First, the Pearson coefficient will be used to calculate the relevant characteristic parameters. After removing the irrelevant parameters, the important characteristic parameters related to the problem will be extracted as the input of the subsequent network model. Afterward, the multiple base models will be fused using stacking fusion. The basic model will utilize gradient boosting decision tree (GBDT), extreme gradient boosting tree (XgBoost), and long- and short-term memory network (LSTM), portraying excellent regression learning ability. The multi-model fusion network is able to fulfill the advantages of each basic model, through high prediction accuracy as well as improvement in the generalization ability.

STATISTICAL ANALYSIS OF POWER GRID MATERIAL FAULTS AND DEFECTS

First of all, this study presents a statistical analysis of the defect levels of a certain bureau of China Southern Power Grid Corporation from 2015 to 2019. The defect levels can be categorized into four types: emergency, major, general, and others accounting for 46, 9, 42, and 3%, respectively. Based on various types of defects, the current material demand can be bifurcated into three categories, namely, daily materials (defect level is general), major defect materials, and emergency defect materials (Gong, 2013; Ke et al., 2017; Dong, 2018; Chai, 2020; Shen and Raksincharoensak, 2021; Yang et al., 2022b).

The main factors responsible for these defects include the quality of the product design, the quality of construction, the quality of operation and maintenance, the service time of products, the overload state of equipment, and the natural environment.

THE MODEL OF POWER GRID MATERIAL DEMAND

Gradient Boosting Decision Tree Algorithm

The gradient boosting decision is made to superimpose M sub-trees to achieve regression prediction:

$$F(x,w)=\sum_{m=0}^{M}\alpha_m h_m(x,w_m)=\sum_{m=0}^{M}f_m(x,w_m). \tag{1}$$

In the formula shown previously, x represents the input sample, w_m represents the model parameter, h represents the classification regression tree, and α signifies the weight of each tree. The core concept of GBDT algorithm is based on the weighted sum of multiple weak learners (Chen et al., 2015; Son et al., 2015; Sheridan et al., 2016; Rao et al., 2019; Wu et al., 2020; Yang et al., 2021a; Yang et al., 2021b; Shen et al., 2021). This study initializes several weak learners in the beginning:

$$F_0(x)=\arg\min_c\sum_{i=1}^{N}L(y_i,c). \tag{2}$$

Then, building M trees, $m=1,2,\ldots,M$:

1) For the sample $i=1,2,\ldots,N$, the negative gradient corresponding to the number M tree is calculated by pseudo-residual:

$$r_{m,i}=-\left[\frac{\partial L(y_i,F(x_i))}{\partial F(x)}\right]_{F(x)=F_{m-1}(x)}. \tag{3}$$

2) For the sample $i=1,2,\ldots,N$, the number M regression tree is obtained by using data $(x_i,r_{m,i})$, and its corresponding leaf node region is $R_{m,j}$, and $j=1,2,\ldots,J_m$.
3) For J_m leaf nodes region $j=1,2,\ldots,J_m$, the best fitting value is calculated as follows:

$$C_{m,j}=\operatorname*{argmin}_c\sum_{x_i\in R_{m,j}}L(y_i,F_{m-1}(x_i)+c). \tag{4}$$

4) Renewing the learner $F_m(x)$, we get:

$$F_m(x)=F_{m-1}(x)+\sum_{j=1}^{J_m}c_{m,j}I\left(x\in R_{m,j}\right). \tag{5}$$

5) The final expression of the strong learner $F_M(x)$ is:

$$F_M(x)=F_0(x)+\sum_{m=1}^{m}\sum_{j=1}^{J_m}c_{m,j}I\left(x\in R_{m,j}\right). \tag{6}$$

The model of GBDT has many parameters, such as the number of base learners, the learning rate, the number of subsamples, and the maximum depth of each base learner (decision tree). Due to the limited number of defect data samples, the maximum depth of the tree should not be too deep.

Extreme Gradient Boosting Tree

Extreme gradient boosting algorithm is an ensemble learning algorithm based on gradient boosting. It calculates the final regression result by integrating multiple basic trees. It has advantages pertaining to high efficiency and accuracy in regression tasks. On the basis of GBDT, XgBoost introduces the loss function of the second derivative of the predicted results. It adds the tree model complexity into the objective function as a regular term. This can prevent over-fitting and improve the generalization performance of the model. In this study, the XgBoost prediction function is constructed as follows (Malhotra et al., 2015; Sikora and Al-Laymoun, 2015; Xu et al., 2015):

$$\hat{y}_i = \phi(x_i) = \sum_{k=1}^{K} f_k(x_i), f_k \in F. \tag{7}$$

Since the model is additive, the current prediction results need to be added to calculate in each iteration.

$$L^{(t)} = \sum_{i=1}^{n} l\left(y_i, \hat{y}_i^{t-1} + f_t(x_i)\right) + \Omega(f_t). \tag{8}$$

The overall objective function is:

$$L_\phi = \sum_i l(\hat{y}_i, y_i) + \sum_k \Omega(f_k). \tag{9}$$

The $\Omega(f)$ is the regular term, which is expressed as:

$$\Omega(f) = \gamma T + \frac{1}{2}\lambda \|w\|^2. \tag{10}$$

.

Taylor expansion of $L^{(t)}$is:

$$\begin{aligned} \bar{L}^t &= \sum_{i=1}^{n}\left[g_i f_t(x_i) + \frac{1}{2}h_i f_t^2(x_i)\right] + \gamma T + \frac{1}{2}\lambda\sum_{j=1}^{T} w_j^2 \\ &= \sum_{j=1}^{T}\left[\left(\sum_{i\in I_j} g_j\right)w_j + \frac{1}{2}\left(\sum_{i\in I_j} h_j + \lambda\right)w_j^2\right] + \gamma T. \end{aligned} \tag{11}$$

Then, the ideal weight of leaf node j in round t should be

$$w_j^* = -\frac{\sum_{i\in I_j} g_i}{\sum_{i\in I_j} h_i + \lambda}. \tag{12}$$

The quality score of the tree in round t is marked by the following formula:

$$\bar{L}^t(q) = -\frac{1}{2}\sum_{j=1}^{T}\frac{\left(\sum_{i\in I_j} g_i\right)^2}{\sum_{i\in I_j} h_i + \lambda} + \gamma T. \tag{13}$$

For all leaf nodes to be split in this round, I_L and I_R represent the set of assumed leaf nodes after splitting, so the loss reduction after splitting can be measured by the following formula illustrated as:

$$L_{\text{split}} = \frac{1}{2}\left[\frac{\left(\sum_{i\in I_L} g_i\right)^2}{\sum_{i\in I_L} h_i + \lambda} + \frac{\left(\sum_{i\in I_R} g_i\right)^2}{\sum_{i\in I_R} h_i + \lambda} - \frac{\left(\sum_{i\in I} g_i\right)^2}{\sum_{i\in I} h_i + \lambda}\right] - \gamma. \tag{14}$$

Compared to GBDT, XgBoost algorithm is a further optimization design, which can reduce model variance through row sampling. Also, it reduces over-fitting through learning rate setting. Moreover, it controls the tree growth through early stopping to avoid over-fitting.

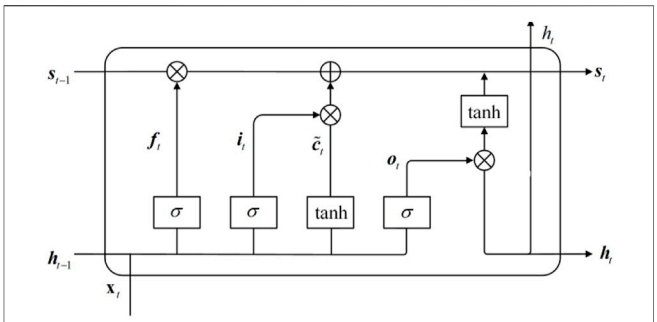

FIGURE 1 | Unit structure of LSTM.

Long- and Short-Term Memory Network

Figure 1 illustrates the unit structure of LSTM. At every moment t, the weight calculated by LSTM is linked back to itself. The input to the LSTM unit is the previous state h_{t-1} and the current input x_t. The function of storing and forgetting information is realized through four fully connected neurons, namely, f_t, i_t, $\tilde{c}_t$, and o_t. Specifically, the forgetting gate f_t determines how much previous information is transmitted forward; input gate i_t controls the input information level; the forgetting gate o_t determines the output of this time step (Singh, 2017; Hu et al., 2018). The formula for calculation is described as follows:

1) Input the sequence value x_t at time t and the hidden layer state h_{t-1} at time t-1, and determine the discarded information through activation function. At this time, the output is as follows:

$$f_t = \sigma\left(W_f \cdot h_{t-1} + W_f \cdot x_t + b_f\right). \tag{15}$$

In the previously stated formula, f_t is the result of the forgetting gate state, and W_f and b_f are the residual weight matrix and bias, respectively. σ is the activation function, usually the tanh or sigmoid function.

2) The input gate state formula is illustrated as follows:

Confirm that the Data Availability statement is accurate. Note that we have used the statement provided at Submission. If this is not the latest version, please let us know

$$i_t = \sigma(W_i \cdot h_{t-1} + W_i \cdot x_t + b_i); \tag{16}$$

$$\tilde{c}_t = \tanh(W_c \times h_{t-1} + W_c \times x_t + b_c); \tag{17}$$

$$c_t = i_t \circ \tilde{c}_t + f_t \circ c_{t-1}. \tag{18}$$

In the aforementioned formula, i_t is the result of the input gate state, and $\tilde{c}_t$ is the input unit state at time t. W_i and W_c are input gate weight matrix and input unit state weight matrix, repectively, and b_i and b_c are the corresponding input gate bias and input unit state bias, respectively. tanh is activation function, and $\circ$ stands for multiplying by elements.

3) Output information of LSTM is determined by the output gate and unit state as shown in the following equation:

$$o_t = \sigma(W_o \cdot h_{t-1} + W_o \cdot x_t + b_o); \quad (19)$$

$$h_t = o_t \circ \tanh(c_t). \quad (20)$$

In the formula, o_t is the output gate state result, and W_o and b_o are the weight matrix and output bias, respectively.

Stacking Fusion Algorithm

Stacking fusion algorithm reduces the generalization error of the whole model and improves the classification accuracy of the model via building a two-layer learner. This makes the second-layer model to learn the classification results of the first-layer model. Among them, T basic classification models are first used in the first layer. After inputting the original data, a result with the same data size is outputted as the input of the second-layer network. The output of each basic learner is used as input when training the second-layer learner, and the function of the second-layer learner is to integrate the output of the basic learner.

Power Grid Material Prediction Based on Pearson Feature Selection and Multi-Model Fusion

In this study, the integrated feature scoring model is used to evaluate, and the total score is averaged to avoid the limitations of single feature selection and finally optimizes the effect of feature selection. With the help of classical Pearson correlation coefficient analysis and selecting high linear correlation attributes, we can roughly find out the relevant attribute categories that have a great impact on material defects. The Pearson correlation coefficient formula is shown in **Eq. 21** and **Eq. 22**. Through this formula, Pearson correlation coefficient can be obtained by dividing the covariance by the standard deviation of two related variables, which is used to make up for the weak performance of the covariance value in the correlation degree of random variables.

.

$$cov(x, y) = \frac{\sum_n^{i=1}(x_i - x)(y_i - y)}{n-1}; \quad (21)$$

$$Pearson = corr(x, y) = \frac{cov(x, y)}{\sigma_x \sigma_y} = \frac{E\left[(x - \mu_x)(y - \mu_y)\right]}{\sigma_x \sigma_y}. \quad (22)$$

The range of the Pearson coefficient is $[-1, 1]$. The larger the absolute value is, the more linearly related the two random variables are. Pearson = 1 means that the random variables are completely positively correlated, Pearson = −1 means that the random variables are completely negatively correlated, and Pearson = 0 means that there is almost no linear correlation between the two variables [Feng et al., 2019; Li et al., 2021a; Li et al., 2021b].

TABLE 1 | Comparison of different basic models and fusion model algorithms for emergency defective material prediction.

Model and method	*RMSE*	*Err* (%)
XgBoost	11.2	41.2
GBRT	8.9	33.4
LSTM-1	13.4	29.9
LSTM-2	15.6	38.4
LSTM-3	9.7	43.1
LSTM-4	7.8	40.7
Multi-model fusion	6.6	27.5
Multi-model fusion with feature optimization	4.7	18.3

EXAMPLES ANALYSIS

The sample dataset provided by the power supply bureau of China Southern Power Grid Corporation was selected for training and testing. The defect data from 2015 to 2019 were initially used to train the model, and then the data from 2020 were tested to verify the prediction effect of the model.

The Method of Model Evaluation

In order to comprehensively evaluate the validity and accuracy of the proposed method in power grid material forecasting, the following two evaluation indexes are selected:

The value of the root mean square error (RMSE) between the real value of the test set and the predicted value of the model is expressed as follows:

$$RMSE = \sqrt{\frac{\sum_{i=1}^{T}(\tilde{x}_i - x_i)^2}{T}}. \quad (23)$$

The average relative error between the real value and the predicted value, *Err*, is expressed as:

$$Err = \frac{1}{T}\sum_{i=1}^{T}\left|\frac{\tilde{x}_i - x_i}{x_i}\right| \times 100\%. \quad (24)$$

The Result of Examples Analysis

In this study, the prediction results of emergency defect materials are compared and analyzed, taking overhead wire as an example.

The number of sub-trees of XgBoost is set at 300, and the learning rate is kept at 0.04, while the penalty factors γ and λ of tree model complexity are taken as 0.01 and 0.9, respectively. Furthermore, the number of sub-trees of GBDT too is set at 300 along with the learning rate at 0.04. The network layers of four kinds of LSTM networks (LSTM-1, LSTM-2, LSTM-3, and LSTM-4) are set at 3, 3, 4, and 4, respectively; the number of corresponding neurons is set to 128, 128, 256, and 256, respectively, and the learning rate is set at 0.01.

Table 1 shows the prediction results of different base models, multi-model fusion, and multi-model fusion with feature optimization for emergency materials. The results of the basic model are obtained directly from their own network without the second layer fusion of the proposed network.

The results of the evaluation index reveal that a single model cannot achieve the best effects. After using the multi-model fusion algorithm, it can make full use and give full play to the prediction advantages of each basic model in one aspect. Moreover, it improves the overall prediction accuracy of the algorithm. It also avoids the phenomenon of over-fitting along with enhanced stability of prediction. On the basis of multi-model fusion, this study also uses Pearson coefficient to optimize the input parameters and selects the most important characteristic parameters as the input of the network. Therefore, after the feature optimization of the original input parameters, the main influencing feature parameters can be selected. Following this, the feature parameters of irrelevant factors can be eliminated, so that the subsequent learning model can better fit the historical data. Therefore, based on the aforementioned observations, it can be concluded that the multi-model fusion algorithm of feature optimization proposed in this study has high accuracy in the prediction of power grid materials.

CONCLUSION

Focusing at the problem of material prediction in the power system, a prediction method based on feature selection and multi-model fusion is proposed in this study. Starting by calculating the Pearson coefficient, the irrelevant parameters are removed from the original parameters. The main characteristic parameters are then selected as the input of the subsequent network model. Furthermore, three excellent data-driven models are identified as the basic model followed by the application of the stacking method for fusion. The fusion algorithm can not only make full use of the advantages of each basic model to improve the prediction accuracy but also improve the generalization ability of the model. Hence, the predicted power grid material demand can provide an effective data support for the management of power grid materials.

DATA AVAILABILITY STATEMENT

The original contributions presented in the study are included in the article/Supplementary Material, further inquiries can be directed to the corresponding author.

AUTHOR CONTRIBUTIONS

ZD put forward the research technical route of the manuscript; GW reviewed the scientificity of the manuscript; and RB and CD completed the data analysis of the manuscript.

REFERENCES

Chai, Q. (2020). *Research on Forecasting Method of Emergency Materials for Meteorological Disasters in Power Grid[D]*. Jinan, China: Shandong University.

Chen, T., He, T., Benesty, M., and Khotilovich, V. (2015). *Xgboost: Extreme Gradient boosting[J]*, 1. R package version 0.4-2.4

Dong, Wei. (2018). *Research on Grid Materials Warehousing Dispatch Optimization Decision-Making Model and Decision Support system[D]*. Beijing: North China Electric Power University.

Dong, Y., Shen, S., and Lu, X. (2020). Prediction of the Duration of Electricity Material in Stock Based on Gradient Boosting Decision Tree[J]. *Electric Power Inf. Commun. Tech.* 18 (9), 50–56. doi:10.16543/j.2095-641x.electric.power.ict.2020.09.008

Feng, W., Zhu, Q., Zhuang, J., and Yu, S. (2019). An Expert Recommendation Algorithm Based on Pearson Correlation Coefficient and FP-Growth[J]. *Cluster Comput.* 22, S7401–S7412. doi:10.1007/s10586-017-1576-y

Gong, W. (2013). *Research on Inventory Control and Demand Forecast of Power Supplies Based on Demand Features Classification[D]*. Shenyang, China: Northeastern University.

Hu, Z., Tong, H., Zeng, Y., Luo, X., Wang, J., Huang, S., et al. (2018). Fast Image Recognition of Transmissiontower Based on Big Data[J]. *Prot. Control. Mod. Power Syst.* V3 (2), 149–158. doi:10.1186/s41601-018-0088-y

Ke, G. L., Meng, Q., Finley, T., Wang, T. F., Chen, W., Ma, W. D., et al. (2017). "Lightgbm: A Highly Efficient Gradient Boosting Decision Tree[J]", in Proceeding of 31st Annual Conference on Neural Information Processing Systems (NIPS), Long Beach, CA, December, 2017 30.

Lai, W., Li, R., Xie, L., and Qi, M. (2016). "The Vehicle Routing for Power Grid Material Distribution: A Case Study in China[C]," in Proceeding of the 2016 13th International Conference on Service Systems and Service Management (ICSSSM), Kunming, June 2016 (IEEE), 1–5.

Li, H., Deng, J., Feng, P., Pu, C., Arachchige, D., and Cheng, Q. (2021a). Short-Term Nacelle Orientation Forecasting Using Bilinear Transformation and ICEEMDAN Framework. *Front. Energy Res.* 9, 780928. doi:10.3389/fenrg.2021.780928

Li, H., Deng, J., Yuan, S., Feng, P., and Arachchige, D. (2021b). Monitoring and Identifying Wind Turbine Generator Bearing Faults using Deep Belief Network and EWMA Control Charts. *Front. Energy Res.* 9, 799039. doi:10.3389/fenrg.2021.799039

Malhotra, P., Vig, L., Shroff, G., and Agarwal, P. (2015). "Long Short Term Memory Networks for Anomaly Detection in Time Series[C]," in Proceedings. Presses universitaires de Louvain, Bruges, Belgium, April 2015, 89–94.

Ming, L., Zheng, Y., and Gao, Z. (2021). Electric Power Materials Demand Forecasting Based on Influencing Factors Multi-Dimensional Fusion and Bayesian Probability Updating[J]. *Logistics Tech.* 40 (3), 71. doi:10.3969/j.issn.1005-152X.2021.03.014

Oliveira, T., Caseiro, L., Mendes, A., Cruz, S., and Perdigão, M. (2021). Model Predictive Control for Paralleled Uninterruptible Power Supplies with an Additional Inverter Leg for Load-Side Neutral Connection. *Energies* 14 (8), 2270. doi:10.3390/en14082270

Pan, W., Zhong, S., Huang, S., and Wu, D. (2016). "Online Power Grid Emergency Material Demand Forecasting Model in Typhoon Disaster Based on Relevance Vector Machine[C]," in Proceeding of the 2016 9th International Symposium on Computational Intelligence and Design (ISCID), Hangzhou, China, Dec. 2016 (IEEE), 402–405.

Rao, H., Shi, X., Rodrigue, A. K., Feng, J., Xia, Y., Elhoseny, M., et al. (2019). Feature Selection Based on Artificial Bee colony and Gradient Boosting Decision Tree. *Appl. Soft Comput.* 74, 634–642. doi:10.1016/j.asoc.2018.10.036

Shen, X., Ouyang, T., Yang, N., and Zhuang, J. (2021). Sample-based Neural Approximation Approach for Probabilistic Constrained Programs. *IEEE Trans. Neural Netw. Learn. Syst.*, 1–8. doi:10.1109/TNNLS.2021.3102323

Shen, X., and Raksincharoensak, P. (2021). Pedestrian-aware Statistical Risk Assessment. *IEEE Trans. Intell. Transport. Syst.*, 1–9. doi:10.1109/TITS.2021.3074522

Sheridan, R. P., Wang, W. M., Liaw, A., Ma, J., and Gifford, E. M. (2016). Extreme Gradient Boosting as a Method for Quantitative Structure-Activity Relationships. *J. Chem. Inf. Model.* 56 (12), 2353–2360. doi:10.1021/acs.jcim.6b00591

Sikora, R., and Al-Laymoun, O. l. (2015). A Modified Stacking Ensemble Machine Learning Algorithm Using Genetic Algorithms. *IGi Glob.* 23, 43–53. doi:10.4018/978-1-4666-7272-7.ch004

Singh, M. (2017). Protection Coordination in Distributionsystems with and without Distributedenergy Resources- a Review. *J].Protection Control. Mod. Power Syst.* V2 (3), 294–310. doi:10.1186/s41601-017-0061-1

Son, J., Jung, I., Park, K., and Han, B. (2015). "Tracking-by-segmentation with Online Gradient Boosting Decision Tree[C]," in Proceedings of the IEEE International Conference on Computer Vision, Santiago, Chile, Dec. 2015 (IEEE), 3056–3064.

Wang, J., and Gu, Y. (2016). Design of Combined Demand Forecasting System for Electric Power Supplies[J]. *Enterprise Manag.* S1, 130–131. CNKI:SUN:QIGL.0.2016-S1-062.

Wang, Z-J., Zhu, Y-Q., and Sun, J-P. (2019). Prediction of Power Grid Material Demand Based on Matrix Decomposition[J]. *J. Sichuan Univ. (Natural Sci. Edition)* 56 (4), 639–644. doi:10.3969/j.issn.0490-6756.2019.04.010

Wu, Z., Wang, X., and Jiang, B. (2020). Fault Diagnosis for Wind Turbines Based on ReliefF and eXtreme Gradient Boosting. *Appl. Sci.* 10 (9), 3258. doi:10.3390/app10093258

Xu, H., and Deng, Y. (2018). Dependent Evidence Combination Based on Shearman Coefficient and Pearson Coefficient[J]. *IEEE ACCESS* 6, 11634–11640. doi:10.1109/ACCESS.2017.2783320

Xu, Y., Mou, L., Li, G., Chen, Y., Peng, H., and Jin, Z. (2015). "Classifying Relations via Long Short Term Memory Networks along Shortest Dependency Paths[C]," in Proceedings of the 2015 conference on empirical methods in natural language processing, 1785–1794.

Yang, N., Dong, Z., Wu, L., Zhang, L., Shen, X., Chen, D., et al. (2021). A Comprehensive Review of Security-Constrained Unit Commitment. *J. Mod. Power Syst. Clean Energ.*, 1–14. doi:10.35833/MPCE.2021.000255

Yang, N., Qin, T., Wu, L., Huang, Y., Huang, Y., Xing, C., et al. (2022). A Multi-Agent Game Based Joint Planning Approach for Electricity-Gas Integrated Energy Systems Considering Wind Power Uncertainty. *Electric Power Syst. Res.* 204, 107673–107796. doi:10.1016/j.epsr.2021.107673

Yang, N., Yang, C., Wu, L., Shen, X., Jia, J., Li, Z., et al. (2022). Intelligent Data-Driven Decision-Making Method for Dynamic Multisequence: An E-Seq2Seq-Based SCUC Expert System. *IEEE Trans. Ind. Inf.* 18, 3126–3137. doi:10.1109/TII.2021.3107406

Yang, N., Yang, C., Xing, C., Ye, D., Jia, J., Chen, D., et al. (2021). Deep Learning-Based SCUC Decision-Making: An Intelligent Data-Driven Approach with Self-Learning Capabilities. *IET Generation Trans. Dist* 16, 629–640. doi:10.1049/gtd2.12315

Zhao, Y-P., Ding, Y-F., and Yao, K-F. (2017). Time Series Prediction of Power Supplies Based on BP Neural Network Error Correction[J]. *Comp. Syst. Appl.* 26 (10), 196–200.

Conflict of Interest: Authors ZD, RB, and CD were employed by China Southern Power Grid Materials Co., Ltd.

The remaining author declares that the research was conducted in the absence of any commercial or financial relationships that could be construed as a potential conflict of interest.

frontiers | Frontiers in Energy Research

ORIGINAL RESEARCH
published: 05 May 2022
doi: 10.3389/fenrg.2022.870253

Recognition of Bird Nests on Power Transmission Lines in Aerial Images Based on Improved YOLOv4

Zhaoyun Zhang and Guanfeng He*

School of Electronic Engineering and Intelligence, Dongguan University of Technology, Dongguan, China

Bird nests on transmission line towers pose a serious threat to the safe operation of power systems. Exploring an effective method to detect bird nests taken by drone inspection is crucial. However, the images taken by drones have problems such as drastic changes in the size of the object, occlusion of the object, and inconsistency in the characteristics of the object in relation to the background. The original YOLOv4 model has difficulty solving these problems. Therefore, this article improves the original YOLOv4 model by adding a Swin transformer block to its backbone network, fusing the attention mechanism into the neck of the original model, implementing classification and regression tasks for head decoupling, and using an anchor-free frame strategy and the SimOTA sample allocation method. The improved model was trained and tested on a bird nest dataset, and the detection accuracy reached 88%. Finally, the method was compared and evaluated against Faster R-CNN, RetinaNet, SSD, and the original YOLOv4, four of the other mainstream object detection models. The results showed that the accuracy obtained by the algorithm was better than the other models; the algorithm could effectively detect difficult objects such as multiple angles, occlusions, and small objects, and the detection speed could meet the real-time requirements.

Keywords: bird nest, YOLO, object detection, power inspection, smart grid

OPEN ACCESS

Edited by:
Yahui Zhang,
Yanshan University, China

Reviewed by:
Yongxin Liu,
Embry–Riddle Aeronautical University, United States
Dazhong Ma,
Northeastern University, China

****Correspondence:***
Zhaoyun Zhang
18927491998@163.com

Specialty section:
This article was submitted to Smart Grids, a section of the journal Frontiers in Energy Research

Received: *06 February 2022*
Accepted: *22 March 2022*
Published: *05 May 2022*

Citation:
Zhang Z and He G (2022) Recognition of Bird Nests on Power Transmission Lines in Aerial Images Based on Improved YOLOv4. Front. Energy Res. 10:870253. doi: 10.3389/fenrg.2022.870253

INTRODUCTION

Birds are indispensable and important members of nature. They play a vital role in the global ecosystem and directly affect the human health, economic development, and food production, as well as millions of other species. However, their nesting behavior has always been one of the main sources of transmission line faults (Li et al., 2020a). Bird nests on the transmission lines can easily cause the lines to trip or insulators to be broken down, causing major losses to the operation of the distribution network. To ensure the safe operation of the transmission network and reduce the potential safety hazards to the transmission lines caused by bird activities, it is necessary to monitor the behavior of bird nests on the overhead line towers.

Traditional manual inspection methods are labor-intensive and have low inspection efficiency and personal safety. In some dangerous terrains, inspections cannot even be carried out (Ding et al., 2021). To this end, power grid companies have introduced new technologies at a large scale in recent years, using robots, drones, and helicopters to perform fault inspection on the overhead lines (Dai et al., 2020). With the popularization of a new generation of inspection methods, the difficulty of field inspections has been greatly reduced, but massive amounts of visualized data have been produced. Faced with a large number of inspection images and videos, the use of naked eyes to detect the

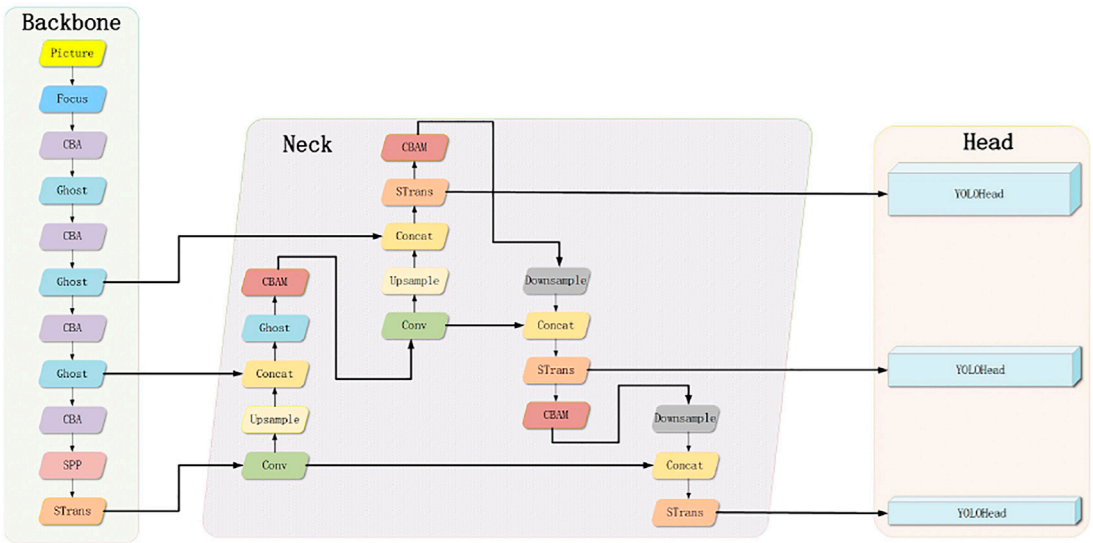

FIGURE 1 | Architecture of the improved YOLOv4 model.

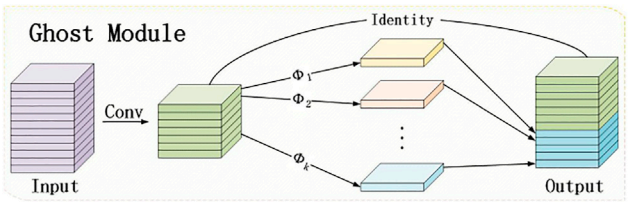

FIGURE 2 | Ghost module structure.

inspection images is not efficient and has greatly increased the burden on the staff (Li et al., 2020b). As a result, currently, the analysis and the processing of power inspection images mainly involve uploading all the inspection data to the backend server through network transmission, using the powerful computing power of the server to store and perform object detection. Chen et al. performed CenterNet-based bird nest detection of overhead lines in power grids and introduced the anchor-free mechanism to overcome the disadvantages of excessive preselection frame calculations in the existing object detection algorithms. Wang et al., (2019) used the Faster R-CNN algorithm to detect a bird nest on a tower, with a multiscale algorithm alleviating the difficult detection problem under a complex background. Ding et al., (2021) proposed a dual-scale bird nest detection algorithm based on YOLOv3, which not only took into account the accuracy and efficiency of the detection algorithm but also had strong antinoise performance and improved the robustness of the detection algorithm. Liu et al., (2020) proposed an algorithm based on RetinaNet, which improved the detection accuracy of small-sized bird nests by increasing the number of feature layers and expanding the range of the network's receptive field. Liu et al., (2020) improved the spatial pyramid module of YOLOv4 to reduce the loss of object information due to pooling. It also improved the loss function to enhance the model's ability to distinguish similar objects.

However, most of the existing object detection algorithms have been designed for images of natural scenes. Because of the randomness of the position of bird nests, it is impossible to shoot at a fixed position, in contrast to the fixed position of the insulator on the overhead line. The direct application of an existing detection algorithm to deal with the object detection task in the UAV capture scene has the following main problems (Li et al., 2021). First, drastic changes in the flying height of the drones drastically change the proportion of the detected bird nests. Second, the overhead line images taken by the drones contain high-density objects (such as towers), which can cause the bird nests to be obscured (Tian et al., 2021). Third, due to the large coverage area, images taken by the drones always contain confusing geographic elements, forming the illusion that bird nests blend with the background (Zhang et al., 2021). The abovementioned three problems make the automatic detection of bird nests based on drone photography very challenging. In terms of the problems of the original YOLOv4 model for detecting small and dense objects, it requires a strong prior knowledge to set the size of the preselection box (Wang et al., 2021); the Swin transformer block (Wang et al., 2020) module is added to the backbone network, and the Swin transformer block is used. The module makes up for the lack of global information extraction capabilities of the convolutional network and further improves the feature extraction capabilities of the model. The Swin transformer block module and convolutional block attention module (CBAM) are also added to the neck to further strengthen the neck multiscale feature map spatial information and semantic information fusion ability and convert the information output by the backbone network into a feature map with a more contextual information input to the detection head. A decoupled head operation is performed in the detection head part, and the classification and regression tasks are processed separately. This enables the model to achieve better accuracy and convergence speed during the classification and regression and introduces an

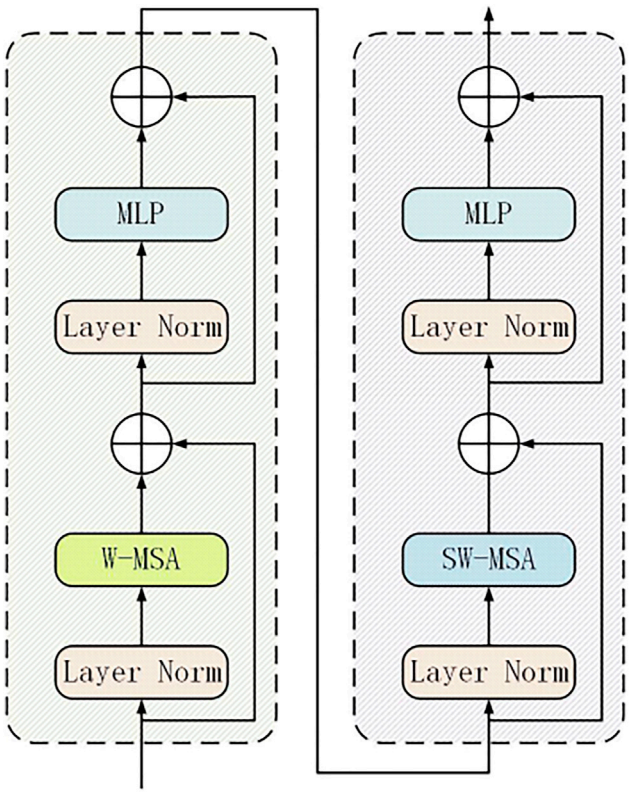

FIGURE 3 | Two successive Swin transformer blocks.

anchor-free frame mechanism, eliminating the need for design. It can obtain the detection accuracy comparable to an anchor-based mechanism and uses SimOTA for positive and negative sample matching, while determining the priori box step, which greatly alleviates the problem of the positive and negative sample mismatch. The improved model architecture is shown in **Figure 1**. Our contributions are listed as follows:

- We integrated the ghost module into YOLOv4, which can significantly decrease the amount of model parameters and computation.
- We integrated the decoupled head into YOLOv4, which can slightly accelerate the training speed.
- We integrated the CBAM into YOLOv4, which can help the network to find the region of interest in images that have a large region coverage.
- We integrated the Swin transformer block into YOLOv4, which can accurately localize the objects in high-density scenes.

BACKBONE

The backbone network is used as a feature extraction network to extract the image information for generating a feature map and then detecting the location and the category of the object. The existing object detection models often use classification networks with powerful feature extraction capabilities such as ResNet, MobileNet, EfficientNet, and Darknet as the backbone network, but the parameters of the backbone network need to be fine-tuned according to specific detection tasks. Based on the original YOLOv4 backbone network CSPDarknet, the CSP module is replaced with a ghost module, the original convolutional downsampling layer is replaced with a ghost convolution, and finally, the Swin transformer block is added to the end of the backbone network.

Ghost Module

Based on the YOLOv4 backbone network CSPDarknet-53, the original backbone network of CSPDarknet is optimized. First, three ghost layer modules and four ghost convolutional downsampling modules are added to the backbone network. Each ghost layer module is based on the residual module of Darknet53 and is produced by the improvement of the structure of CSPNet (Han et al., 2020). It consists of three ghost convolution modules and n ghost bottleneck modules that are superimposed. A ghost module first uses a small number of convolution kernels to extract the features of the input feature map, then further performs cheaper linear change operations on this part of the feature map, and generates the final feature map through the splicing operation, as shown in **Figure 2**.

Dosovitskiy et al., (2020) pointed out that rich feature information could be captured by stacking the convolutional layers containing redundant information, which would be conducive to a more comprehensive understanding of the data by the network. Therefore, the rich feature information is extracted through the conventional convolution operation, and the redundant feature information is generated by a cheaper linear transformation operation. This can effectively reduce the computing resources required by the model, and the design is simple and easy to implement, allowing for a plug-and-play execution.

Swin Transformer Block

Inspired by the vision transformer (ViT) (Liu et al., 2021), the last CSP module in the original YOLOv4 version of CSPDarknet is replaced with a transformer encoder block. Compared with the original CSP module, the transformer encoder block can capture global information and richer contextual information. However, the introduction of the transformer module greatly increases the number of calculations and parameters of the model. In contrast to the direct multi-head self-attention of the global feature map in the ViT, the Swin transformer uses the concept of window multi-head self-attention (W-MSA) to divide the feature map into multiple disjoint windows. As shown in **Figure 3**. Multi-head self-attention is performed only within each window. It can reduce the amount of calculation significantly, especially when the shallow feature map is large. Although this reduces the amount of calculation, it also isolates the transfer of information between different windows, thereby giving rise to the shifted window multi-head self-attention (SW-MSA) operation in the Swin transformer. Since W-MSA and SW-MSA are used in pairs, this solves the problem of information exchange between different windows.

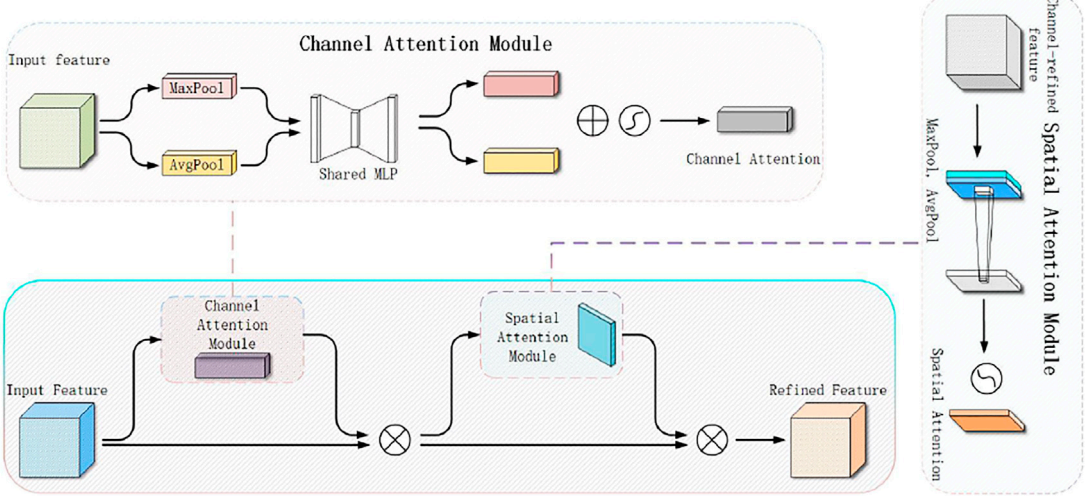

FIGURE 4 | Convolutional block attention module.

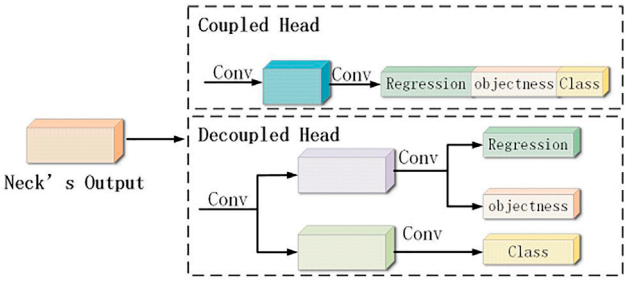

FIGURE 5 | Comparison between the decoupled head and the coupled head.

The Swin transformer block increases the ability to capture different local information while using the self-attention mechanism to explore the potential of feature representation. In addition, it performs better on the high-density occluded objects. Due to the trade-off among the amount of calculation, the number of parameters, and the accuracy, the Swin transformer block is applied only to the neck and the end of the backbone network based on YOLOv4. Because the resolution of the feature map at the end of the network is low, applying the Swin transformer block to the low-resolution feature map can reduce the expensive calculation and storage costs, while allowing the model to pay more attention to the extraction of bird nest features.

NECK

To make better use of the features extracted by the backbone network, the feature maps of different stages extracted by the backbone are reprocessed and used rationally. The following three main improvements are made: 1) the ghost module replaces the CSPLayer module; 2) the convolution block attention module is added to the upsampling and downsampling path of the neck; and 3) the Swin transformer block is added to the output of the neck module. The ghost module is the same as that in the backbone network. Therefore, no special introduction is given in this section.

CBAM

The convolutional block attention module is simple but effective. It is a lightweight module that can be integrated and is used for plug-and-play execution in any convolutional neural network and thus can be trained end-to-end. Given an intermediate feature map, the convolutional block attention module sequentially infers the attention map along the two independent dimensions of channel and space and then multiplies the attention map with the input feature map to perform the adaptive feature optimization. The structure of the convolution block attention module is shown in **Figure 4**. According to the experiment in (Woo et al., 2018), after integrating the convolution block attention module into different models on different classification and detection datasets, the performance of the model is greatly improved. This proves the effectiveness of this module. According to the images taken by drones, large coverage areas always contain complex background elements. Using the convolution block attention module, we can extract the attention regions, help the model resist chaotic information, and focus on the detection of bird nests.

Swin Transformer Block

The fusion of multiscale features has always been difficult in object detection. The image contains rich visual semantic information in space and scale. This semantic information is continuously obtained through the convolution operations, and only the information within the size range of the convolution

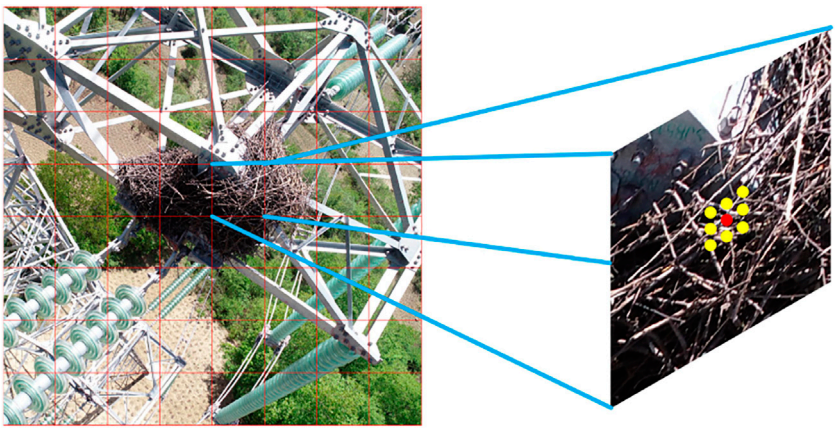

FIGURE 6 | Positive sample candidate area.

TABLE 1 | SimOTA algorithm.

SimOTA algorithm process
1. Identify positive sample candidate areas.
2. The regression loss and category loss of each sample and the GT are calculated to generate the cost matrix M.
3. According to the sum of the IoU values of the top ten samples of the current GT, the number of positive samples k is determined.
4. In M, the first K samples with the minimum loss are taken for each GT as positive samples.

kernel can be extracted each time. To obtain global information, it is necessary to stack multiple convolutional layers. In this regard, some researchers have proposed a nonlocal neural network (NLN), which matches the nonlocal information in the convolutional layer. Wang et al., (2018) believed that the NLN does not cross-scale and only extracts information across space, unable to capture the nonlocal context of objects at different scales. Because the neck itself is a multiscale feature fusion module, the cross-scale feature interaction can effectively locate and identify the local details of semantics. Zhang et al., (2020) believed that the existing methods cannot achieve the cross-scale feature interaction and have proposed the feature pyramid transformer (FPT) to make full use of the mutual fusion of the cross-space and cross-scale features. The advantage of introducing the Swin transformer block module is to connect the low-resolution, high-semantic information and low-level features of the high-resolution, low-semantic information output from the different stages of the backbone network, from top to bottom and vice versa. Therefore, the features at different scales' output by the neck have rich semantic information.

HEAD

As a classification network, the backbone network cannot complete the positioning task, and the head is responsible for detecting the location and the category of the object through the feature map extracted from the backbone network. Detectors are generally divided into two categories: one-stage object detectors and two-stage object detectors. The two-stage detector has long been the dominant method in the field of object detection, and the most representative one is the RCNN series. In contrast to the two-stage detector, the one-stage detector can predict the boundary regression and the object category at the same time. The single-stage detector has obvious advantages in speed but has a lower accuracy. To improve the capabilities to detect and position small objects, based on the original YOLOv4 detection head, the classification and regression tasks are decoupled, the anchor-free mechanism is introduced, and the SimOTA sample allocation algorithm is used.

Decoupled Head

In object detection, the conflict between classification tasks and regression tasks is a long-standing problem. However, the coupled heads for classification and positioning are widely used in most one- and two-stage detectors. Song et al., (2020) proposed that the positioning and classification tasks of object detection have a spatial misalignment problem. In other words, the two tasks have different focuses and places of interest, and the classification pays more attention to the similarity between the extracted features and the existing categories, while the positioning pays more attention to the coordinate position of the real frame. Therefore, to make the

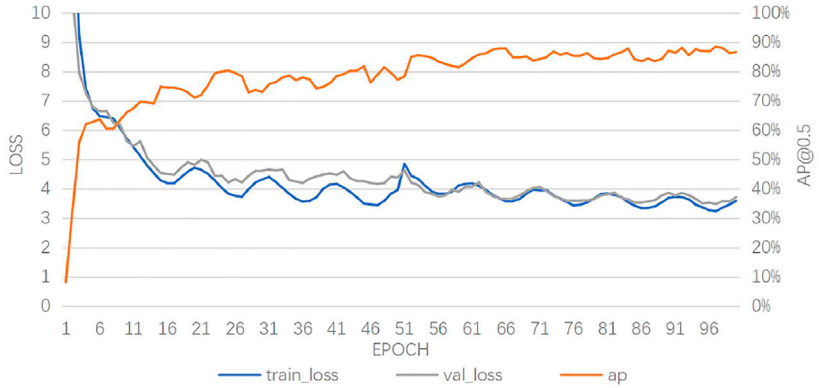

FIGURE 7 | Loss curve and AP curve during the training.

TABLE 2 | Test results of the different detection algorithms.

Model	Precision (%)	Recall (%)	AP@0.5 (%)	Params (M)	Flops (G)	Fps (rtx3090)
Faster R-CNN	52.80	77.09	74.49	28	473	25f/s
RetinaNet	93.94	67.93	76.19	36	81	49f/s
SSD	93.47	74.10	83.32	23	136	67f/s
YOLOv4	86.34	83.07	87.31	63	70	43f/s
Proposed	92.11	83.67	88.56	30	40	43f/s

detection head more efficient, the method of decoupling the head is introduced, that is, the detection head is changed from one branch to three branches using a convolution operation, as shown in **Figure 5**. Decoupling the head leads to an improved detection accuracy of the model and a faster convergence speed. Although the 1 × 1 convolutional dimensionality reduction operation is performed on the feature map output by the neck, decoupling the head does slightly slow the inference speed of the model. In general, however, head decoupling has more advantages than disadvantages.

Anchor-Free Mechanism

Due to the variation in the shooting angle and the distance of drones and the size of bird nests, the sizes of bird nests in different images are quite varied, and artificially set anchor frames cannot always match the real frames in the dataset. The anchor frame mechanism needs to set the size and the scale parameters in advance, which requires a strong prior knowledge. To address this problem, the traditional YOLO series uses the K-means method to cluster the dataset and calculate the size of the anchor frame. The use of K-means does increase the detection performance, but the generated anchor frame can only apply to a specific dataset, and it increases the complexity of the detection head and the number of potential object predictions. In addition, the traditional anchor-free frame method uses only the center position of each grid as a positive sample (the red dot in **Figure 6**), ignoring other high-quality prediction samples away from the center. Optimizing those high-quality prediction samples is not only beneficial to the convergence speed but also alleviates the imbalance of the positive and negative samples during the training (Ge et al., 2021). In addition, for discontinuous objects such as bird nests, only a positive sample is taken at the center of the object, which is likely to cause errors and affect the final detection performance. Therefore, multiple samples of the 3 × 3 area in the object center are selected as the positive sample candidates (the red and yellow dots in **Figure 6**).

SimOTA

The traditional object detection algorithm allocates the positive and negative samples according to the IoU of the anchor frame and the real frame. However, the division of the positive and negative samples under different sizes, shapes, and occlusion conditions should be different, and the context information also needs to be considered. An excellent sample matching algorithm can effectively solve the dense object detection problem and optimize the detection effect when there are extreme proportions of objects or imbalanced positive samples of extreme size objects (Tian et al., 2019). Therefore, SimOTA treats sample matching as an optimal

FIGURE 8 | Test results of different detection models.

transportation problem in a linear programming problem. The specific process is shown in **Table 1**.

EXPERIMENT

The experiment selected a real UAV line patrol dataset containing bird nests. The proposed model and the four mainstream models of YOLOv4, Faster R-CNN, SSD, and RetinaNet were trained, tested, compared, and evaluated on the selected dataset.

Description

The bird nest dataset comes from the data obtained by a power grid company conducting live-line inspections with unmanned aerial vehicles on its overhead lines. The dataset for this study had a total of 4,514 bird nest pictures, and the original dataset was divided into non-test and test sets at a

TABLE 3 | Ablation study result.

Model	AP@0.5 (%)	Params (M)	Flops (G)	Fps (rtx3090)
YOLOv4	87.31	63	70	43f/s
YOLOv4+ghost	82.54	35	39	65f/s
YOLOv4+ghost + decoupled head	80.22	29	42	51f/s
YOLOv4+ghost + decoupled head + CBAM	84.54	29	42	47f/s
Proposal (previous + Swin transformer)	88.56	30	40	43f/s

ratio of 9:1. The non-test set was divided 9:1 into training and validation sets. The training set, the validation set, and the test set included 3,655, 407, and 452 images, respectively. Because the bird nest detection model requires a large number of data samples to train the network, this study performed random mosaic data enhancement and a series of random processing of color gamut and size before inputting each picture in the original dataset.

Training and testing on the experimental data were carried out on the same deep learning server with the Ubuntu 18.04 operating system, an Intel Xeon W-2245 CPU, a single GeForce RTX 3090 24 GB GPU, and 64-GB DDR4 RAM. The training and testing were implemented using the PyTorch 1.8.0 framework, and the detection effect of a single picture or a video was visualized through the OpenCV tool library.

Analysis

At the beginning of the training, the weights of the model were randomly initialized, and the coco dataset was used to pre-train the model and to let the model learn the ability to extract features. This can extract the potential features or common structures between the original problem dataset and the object dataset, thereby accelerating the training and improving the performance of the model. The training process was optimized by batch normalization. Each batch has trained 16 samples, and each iteration has trained 228 batches. Since the bird nest dataset was relatively small, only 100 epochs were trained. The initial learning rate of the model was set to the cosine annealing learning rate, the Adam optimizer was used, the weight attenuation was 0.0005, and the size of the input image was 640 × 640. The parameters of the backbone network were not updated in the first 50 epochs, and the entire parameters of the network were updated in the rest of the 50 epochs. The training results are shown in **Figure 7**.

Result

To verify the effectiveness of the improved model, Faster R-CNN, RetinaNet, SSD, YOLOv4, and the improved model were evaluated experimentally on the same bird nest dataset, and the experimental results were compared (all the models were trained under the same conditions). Evaluation indicators included the calculation accuracy (precision), average precision (AP) with a detection threshold of 0.5 (IoU), model parameters (Params), model calculations (Flops), and detection speed (FPS). Among them, AP is an important indicator for evaluating the detection effect, which can be obtained by calculating the area enclosed by the curves for the accuracy rate P and recall rate R. **Table 2** shows the test results of the five models. Among them, the improved model had an AP value of 88.56% and a detection speed of 43 f/s when the threshold was 0.5. The analysis is as follows: the improved model was superior to the other models in detection accuracy and recall rate. Among the models, RetinaNet achieved the highest accuracy due to the lower regression rate. However, overall, the detection effect of the improved model was better than the other types of detection. In addition, while the introduction of head decoupling into the improved model resulted in a slower detection speed than that of the SSD algorithm and RetinaNet, it still met the requirements of real-time detection.

Figure 8 shows the detection results of the improved model and the four other mainstream detection models on the test set. The test set included a small-sized bird nest object, multiple bird nest objects in a single image, a bird nest being severely obscured by a tower, and a bird nest blending with the background. These are the common situations for a variety of power inspections. The improved model maintained a good detection performance under the above mentioned conditions. Other models had good detection capabilities for bird nests (as shown in **Figure 8A**). However, the following situations were also observed. 1) Insufficient detection capabilities for the small objects: as shown in **Figures 8B,E**, the SSD algorithm, RetinaNet algorithm, Faster R-CNN algorithm, and YOLOv4 algorithm failed to detect the third bird nest at the bottom right. Each of the above mentioned algorithms also missed the detections in **Figures 8C,D,F,G**. 2) They were prone to false detection: as shown in **Figure 8C**, YOLOv4 recognized the bamboo frame on the left as a bird nest. As shown in **Figure 8F**, Faster R-CNN recognized the tower on the right as a bird nest. 3) The detection capability for complex backgrounds was insufficient. As shown in **Figure 8H**, all the four mainstream models missed the detection. The aforementioned results show that the improved model can maintain the detection accuracy and robustness in different scenarios and is suitable for the power inspection of the UAV aerial photography.

Ablation Study

The importance of each proposed component was analyzed on the test set. The impact of each component is listed in **Table 3**.

CONCLUSION

The classic object detection algorithm is not suitable for the detection of aerial images, and it has disadvantages such as poor detection accuracy, high rates of missed detection, and excessive model scale. Based on YOLOv4, improvements were made from the backbone network, neck, and detection head. The ghost module, the CBAM module, the transform module, the anchor-free mechanism, and SimOTA were added based on YOLOv4 to form an improved bird nest detection algorithm of drone aerial photography. The improved model was tested on a bird nest dataset from the aerial photographs of an electric power inspection drone. The experiments showed that compared with the other mainstream algorithms, the improved algorithm had advantages in the recall rate and simultaneously obtained a higher accuracy rate. Therefore, the improved model can help power inspectors to obtain a better experience in UAV power inspection. Although the proposed algorithm presently meets the requirements for real-time bird nest detection, the detection speed still needs to be improved compared with the SSD algorithm. In the future, by reducing the scale of the weight parameters of the network, the model will be lightened, and the detection speed will be improved.

DATA AVAILABILITY STATEMENT

The original contributions presented in the study are included in the article/Supplementary Material, further inquiries can be directed to the corresponding author.

AUTHOR CONTRIBUTIONS

ZZ and GH contributed to conception and design of the study. ZZ performed the statistical analysis. GH wrote the first draft of the manuscript. All authors contributed to manuscript revision, read, and approved the submitted version.

REFERENCES

Chen, Z. Y., Li, Y., Wang, D. H., and Zhang, S-J. (2021). A Device Anomaly Detection Method Based on CenterNet [J]. *Comp. Appl.* 41 (S1), 304.

Dai, Z., Yi, J., Zhang, Y., Zhou, B., and He, L. (2020). Fast and Accurate Cable Detection Using CNN. *Appl. Intell.* 50 (12), 4688–4707. doi:10.1007/s10489-020-01746-9

Ding, J., Huang, L., and Zhu, D. (2021). High Tower as the Bird's Nest Detection Oriented Double Scale YOLOv3 Network Study [J]. *J. Xi 'an Polytechnic Univ.* (02), 253–260. doi:10.19322/j.carolcarroll

Dosovitskiy, A., Beyer, L., and Kolesnikov, A. (2020). *An Image Is Worth 16x16 Words: Transformers for Image Recognition at Scale[J]*. arXiv preprint arXiv: 2010.11929.

Ge, Z., Liu, S., and Wang, F. (2021). *Yolox: Exceeding yolo Series in 2021*. [J]arXiv preprint arXiv:2107.08430.

Han, K., Wang, Y., Tian, Q., Guo, J., Xu, C., and Xu, C. (2020). "Ghostnet: More Features from Cheap Operations[C]," in Proceedings of the IEEE/CVF Conference on Computer Vision and Pattern Recognition, 1580–1589.

Li, F., Xin, J., Chen, T., Xin, L., Wei, Z., Li, Y., et al. (2020). An Automatic Detection Method of Bird's Nest on Transmission Line Tower Based on Faster_RCNN. *IEEE Access* 8, 164214–164221. doi:10.1109/access.2020.3022419

Li, J., Yan, D., Luan, K., Li, Z., and Liang, H. (2020). Deep Learning-Based Bird's Nest Detection on Transmission Lines Using UAV Imagery. *Appl. Sci.* 10 (18), 6147. doi:10.3390/app10186147

Li, X., Li, Z., and Wang, H. (2021). Unmanned Aerial Vehicle for Transmission Line Inspection: Status, Standardization, and Perspectives[J]. *Front. Energ. Res.* 9, 336. doi:10.3389/fenrg.2021.713634

Liu, G. W., Zhang, C. X., and Li, B. (2020). An Improved RetinaNet Model for Catenary Bird Nest Detection. *Data Acquisition Process.* 35 (03), 563–571. doi:10.16337/j.1004-9037.2020.03.018

Liu, Z., Lin, Y., and Cao, Y. (2021). *Swin Transformer: Hierarchical Vision Transformer Using Shifted Windows[J]*. arXiv preprint arXiv:2103.14030.

Song, G., Liu, Y., and Wang, X. (2020). "Revisiting the Sibling Head in Object Detector[C]," in Proceedings of the IEEE/CVF Conference on Computer Vision and Pattern Recognition, 11563–11572.

Tian, G., Liu, J., Zhao, H., and Yang, W. (2021). Small Object Detection via Dual Inspection Mechanism for UAV Visual Images[J]. *Applied Intelligence*, 1–14.

Tian, Z., Shen, C., Chen, H., and He, T. (2019). "Fcos: Fully Convolutional One-Stage Object Detection[C]," in Proceedings of the IEEE/CVF International Conference on Computer Vision, 9627–9636.

Wang, C. Y., Bochkovskiy, A., and Liao, H. Y. M. (2021). "Scaled-yolov4: Scaling Cross Stage Partial Network[C]," in Proceedings of the IEEE/CVF Conference on Computer Vision and Pattern Recognition, 13029–13038.

Wang, C. Y., Liao, H. Y. M., Wu, Y. H., Chen, P. Y., Hsieh, J. W., and Yeh, I. H. (2020). "CSPNet: A New Backbone that Can Enhance Learning Capability of CNN[C]," in Proceedings of the IEEE/CVF Conference on Computer Vision and Pattern Recognition Workshops (Seattle, USA, 390–391.

Wang, J. W., Luo, H. B., and Yu, P. F. (2019). Multi-Scale Bird Nest Detection for High Pressure Tower Based on Faster R-Cnn [J]. *Beijing Jiaotong Univ.* 43 (05), 37. doi:10.11860/j.issn.1673-0291.20180168

Wang, X., Girshick, R., Gupta, A., and He, K. (2018). "Non-Local Neural Networks [C]," in Proceedings of the IEEE Conference on Computer Vision and Pattern Recognition, 7794–7803.

Woo, S., Park, J., Lee, J.-Y., and Kweon, I. S. (2018). "Cbam: Convolutional Block Attention Module[C]," in Proceedings of the European Conference on Computer Vision (ECCV) (Cham: Springer), 3–19. doi:10.1007/978-3-030-01234-2_1

Zhang, D., Zhang, H., Tang, J., Wang, M., Hua, X., and Sun, Q. (2020). "Feature Pyramid Transformer[C]," in European Conference on Computer Vision (Cham: Springer), 323–339.

Zhang, X., Wan, T., Wu, Z., and Du, B. (2021). *Real-Time Detector Design for Small Targets Based on Bi-Channel Feature Fusion Mechanism[J]. Applied Intelligence,* 1–10.

Conflict of Interest: The authors declare that the research was conducted in the absence of any commercial or financial relationships that could be construed as a potential conflict of interest.

frontiers | Frontiers in Energy Research

BRIEF RESEARCH REPORT
published: 20 May 2022
doi: 10.3389/fenrg.2022.878810

An Improved Solution to Generation Scheduling Problem Using Slime Mold Algorithm

Zixuan Zhu *

China Three Gorges University, Yichang, China

The slime mold algorithm (SMA) is a novel meta-heuristic search that replicates the characteristics of slime mold during oscillation. This is presented in a novel mathematical formulation that employs changeable weights to modify the sequence of both negative and positive propagation waves in order to build a mechanism for linking food availability with intensive exploration capacity and exploitation affinity. The study demonstrates how to solve a non-convex and cost-effective load dispatch issue (ELD) in an electric power system using the SM method. The efficacy of SMA is explored for a single-area economic load dispatch on small-scale power systems, using 3-, 5-, and 6-unit test systems, and the results are validated by comparing the results to those of other well-known meta-heuristic algorithms.

Keywords: slime mold algorithm, non-convex optimization, electric power system, metaheuristic algorithms, load dispatch

OPEN ACCESS

Edited by:
Xun Shen,
Tokyo Institute of Technology, Japan

Reviewed by:
Surya Deo Choudhary,
Aryabhatta Knowledge University, India
Bhagwan Shree Ram,
Saharsa College of Engg., India

***Correspondence:**
Zixuan Zhu
2945196605@qq.com

Specialty section:
This article was submitted to Smart Grids, a section of the journal Frontiers in Energy Research

Received: *18 February 2022*
Accepted: *08 March 2022*
Published: *20 May 2022*

Citation:
Zhu Z (2022) An Improved Solution to Generation Scheduling Problem Using Slime Mold Algorithm. Front. Energy Res. 10:878810. doi: 10.3389/fenrg.2022.878810

INTRODUCTION

In the actual functioning of power systems, economic load dispatch (ELD) is a crucial problem to solve. The role of the power system is to deliver continuous power to the consumers at an affordable price which is its main feature (Panigrahi et al., 2006), (Jadoun et al., 2015). The objective is to reduce energy-generating costs while fulfilling load needs and ensuring equality and in-quality constraints. This fact results in a higher degree of pollution awareness in thermal plants and a lower cost of diagnosing the problem. Because they operate in conjunction with a collection of viable alternatives, evolutionary methods are now perfectly suited for discovering answers to optimization problems. All optimization approaches, including evolutionary ones, are known to be influenced by constraints (Salcedo-Sanz, 2009). Since the traditional procedure of an evolutionary approach, employing operators for individuals in a population may violate the constraint rules. The way evolutionary approaches deal with constraint rules of challenges is a significant aspect that is directly connected to the quality of solutions created for such problems. By converting the present solution that opposes the constraints into a viable one, a redesigned method eliminates unattainable solutions.

Wind, solar, thermal, nuclear, renewable, hydro, and other power-producing facilities are used in most power generation systems. In the case of renewable energy systems, the operational cost will not change as much as the production. In thermal systems, however, the running cost varies with the total power output. As a result, the ELD issue, which includes the use of thermal systems as generators, is considered a critical optimization issue in electric power systems. Maintaining an economical operation is a difficult challenge for both traditional and smart grid systems. When power systems are exposed to operational and a transmission imperative, the ELD limits the optimal outcome for an electric power generation to sustain the load demand with a minimum generation price. The ELD problem is usually solved by sophisticated computerized approaches that meet the

operational and power system imperatives *via* minute-to-minute monitoring. A little increase in the ELD demonstrates its long-term reaction to the declining price of the total power output. As a result, a variety of optimization methods have been developed to address cost-effective load dispatch issues while producing high-quality results. Traditional optimization approaches were the sole option to address ELD concerns for many years. Because of the limitations of conventional methods, system operators have a chance to fail to notice the realistic and technological imperatives of the system's units. There are two types of simplifications in this category: first, combined with the accuracy of the generating unit's pricing model, particularly for different types of fuels or taking the valve-point loading impact into account (Cai et al., 2012; Zhong et al., 2013). Multi-valve steam turbines are widely seen in real-world generating units. The valve point of the generating unit is drawn when the steam turbine's intake valve opens abruptly, pushing the energy consumption curve upward.

LITERATURE SURVEY

The economic load dispatch problem is a major concern for the cost-effective operation of electric power systems as it concentrates on basically assembling the power outputs of the units by establishing time intervals to decrease generating costs while still meeting other system requirements. In general, the traditional ELD problem is reduced to solve the convex quadratic programming problem (Reid and Hasdorff, 1973), which may now be handled effectively using MOSEK (Babonneau et al., 2019). Furthermore, the system becomes non-smoothed, non-convex, and non-continuous when the valve-point loading effect, transmission loss, and prohibited operating zones are considered. The objective function arises as multiples of the local minimum because of these features, making global minima exceedingly difficult to attain. Aside from that, the non-smooth nature of the function makes the derivate-based mathematical programming technique challenging to apply directly.

Traditional optimization techniques often look at linear, piece-wise linear, and price functions of generators in quadratic functions, with just network loss being considered. These classic techniques include lambda iteration (Zhan et al., 2014), gradient descent method (Dibangoye et al., 2015), linear programming (Torreglosa et al., 2016), Newton's technique (Wang et al., 2014), dynamic programming (Al-Kalaani, 2009), gradient search (Subathra et al., 2015), and the Lagrangian relaxation algorithm (Li et al., 2013; Mohammadi-Ivatloo et al., 2013). Because of the persistence of severe non-linear characteristics in real-world practical networks, while dealing with high-dimensional economic dispatch difficulties, these suffer disadvantages such as failure to meet imperatives and lengthy time calculations.

This time-consuming calculation in optimization methods prompted researchers to develop meta-heuristic optimization strategies to solve large-scale problems. The meta-heuristic method (Gjorgiev and Čepin, 2013) takes into consideration non-convex pricing functions and non-smooth operating functions as well as other imperatives. This includes techniques such as synergic predator–prey optimization (SPPO) (Singh et al., 2016), seeker optimization algorithm (SOA) (Shaw et al., 2012), genetic algorithm (GA) (Amjady and Nasiri-Rad, 2010), (Elsayed et al., 2014), evolutionary programming (EP) (Sinha et al., 2003), firefly algorithm (FA) (Yang et al., 2012), particle swarm optimization (PSO) (Neyestani et al., 2010), (Safari and Shayeghi, 2011), (Wang and Singh, 2009), artificial bee colony (ABC) (Aydın and Özyön, 2013), colonial competitive differential algorithm (CCDE) (Ghasemi et al., 2016), bacterial foraging algorithm (BFA) (Farhat and El-Hawary, 2010), improved Tabu search algorithm (ITS) (Whei-Min Lin et al., 2002), ant colony optimization (ACO) (Pothiya et al., 2010), group search optimizer (GSO) (Zare et al., 2012), harmony search algorithm (HAS) (Jeddi and Vahidinasab, 2014), biogeography-based optimization (BBO) (Bhattacharya and Chattopadhyay, 2010), and differential evolution (DE) (Jiang et al., 2013). Many researchers used slime mould algorithm to bring better results and few such algorithms are Dispersed Foraging Slime Mould Algorithm (DFSMA) (Hu et al., 2022), Chaos-opposition-enhanced slime mould algorithm (CO-SMA) (Rizk, 2022), Opposition based learning slime mould algorithm (OBLSMA) (Houssein et al., 2022), Multi-objective slime mould algorithm (MOSMA) (Houssein et al., 115870), Equilibrium optimizer slime mould algorithm (EOSMA) (Yin et al., 2022). In this work, SMA is used to identify solutions to economic load dispatch problems on a variety of test systems. Other new and popular approaches outcomes are compared to analyze the results.

MATHEMATICAL FORMULATION FOR SINGLE-AREA ECONOMIC LOAD DISPATCH

The goal of the ELD problem is to lower the entire fuel cost of power systems by finding the optimum combination of power outputs from all generating units while congregating load demand and operational constraints (Dubey et al., 2013).

Single-Area Economic Load Dispatch

The fuel cost for unit generation is represented as a quadratic function, with the assumption that the collective cost curves of the generating units develop as linear functions over time. The mathematical equation for the single-area ELD for an hour is as follows in **Eq. 1**:

$$fc\left(p^{g}\right)=\sum_{n=1}^{ng}\left[a_{n}\left(p_{n}^{g}\right)^{2}+b_{n}p_{n}^{g}+c_{n}\right], \tag{1}$$

where n ∈ ng.

The dispatching of power-generating units for "Hr" hours can be represented as follows:

$$fc\left(p^{g}\right)=\sum_{hr=1}^{Hr}\sum_{n=1}^{ng}\left[a_{n}\left(p_{n}^{g}\right)^{2}+b_{n}p_{n}^{g}+c_{n}\right], \tag{2}$$

where $n \in ng$; $hr \in Hr$.

The right mathematics for ED is **Eq. 2**. Because the load demand changes over time, "hr" is changed from a single hour to "Hr" hours.

The aforementioned objective functions are subjected to the following equality and inequality constraints:

Power Balance Constraint

The total power generation is equal to total power demand plus system power loss.

$$\sum_{n=1}^{ng} p_n^g = p^d + p^l, \tag{3}$$

where p^d indicates the requirement of power, and the power loss p^l can be written as follows:

$$p^l = \sum_{n=1}^{ng} \sum_{m=1}^{ng} p_n^g B_{nm} P_m^g, \tag{4}$$

In presence of loss coefficients B_{i10} and B_{010} matrices, **Eq. 4** can be written as follows:

$$p^l = p_n^g B_{nm} P_m^g + \sum_{n=1}^{ng} p_n^g \times B_{i0} + B_{00}. \tag{5}$$

The extension of **Eq. 5** is as follows:

$$p^l = \begin{bmatrix} p_1 p_2 \ldots\ldots\ldots p_{ng} \end{bmatrix} \begin{bmatrix} B_{11} & B_{12} & B_{1n} \\ B_{21} & B_{22} & B_{2n} \\ B_{n1} & B_{n2} & B_{nn} \end{bmatrix} \begin{bmatrix} p_1 \\ p_2 \\ p_{ng} \end{bmatrix} + \begin{bmatrix} p_1 & p_2 & p_{ng} \end{bmatrix} \begin{bmatrix} B_{01} \\ B_{02} \\ B_{0ng} \end{bmatrix} + B. \tag{6}$$

Generator Limit Constraint

The true power output of each generator is controlled by the upper and lower operational limits.

$$p^y_{n(\min imum)} \le p_n^y \le p^y_{n(\max imum)}, \mathrm{n} = 1, 2, 3, ., \mathrm{ng} \tag{7}$$

where $p^y_{n(\min imum)}$ implies the lowest real power allocated at unit and $p^y_{n(\max imum)}$ announces the highest real power allotted at until n.

Ramp Rate Limits

The output power of the generating unit is boosted between the lower and higher limits of active power generation.

1) By increasing the generated power,

$$p_n^g \le p_0^{g0} \le ur_n, \mathrm{n} = 1, 2, 3, .., \mathrm{ng} \tag{8}$$

2) By reducing the amount of generated power

$$p_n^g \le p_0^{g0} \le ur_n, \mathrm{n} = 1, 2, 3, \ldots\ldots, \mathrm{ng} \tag{9}$$

Therefore, the generator ramp rate is shown in the following equation:

$$\begin{aligned} &\max imum\left[\max imum\left[p^g_{n(\max imum)}, (ur_n - p_n^g)\right]\right. \\ &\left. \le \min imum\left[p^g_{n(\min imum)}, (p_n^{g0} - dr_n)\right]\right], \end{aligned} \tag{10}$$

where n = 1,2, 3, . . ., ng, and p_n^{g0} is the current active power of the nth generation unit.

Prohibited Operating Zones

Prohibited operating zones (POZ) are allocated to the graph for input–output powers in the generating unit, which may be discontinuous due to functional constraints of the generator produced by a defective mistake in the machine parts or the machine itself. The discontinuous input–output power limitations are as follows in **Eq. 11**:

$$\begin{cases} p_{n(\min imum)} \le p_n \le p_n^{poz}(\min imum), 1 \\ p^{poz}_{n(\max imum),m-1} \le p_n \le p^{poz}(\min imum), m \\ p^{poz}_{n(\max imum),m} \le n_i \le p_n(\max imum); m = n_{poz} \end{cases}. \tag{11}$$

SLIME MOLD ALGORITHM

It is known that the behavior of the organism can be imitated and molded to tackle the mathematics of unconstrained and non-convex characteristics. Researchers have framed to imitate the guiding principles to develop computations and algorithms. The slime molds have received significant courteousness for the past few years. Scientifically, slime mold is titled as *Physarum polycephalum* (Howard, 1931). The slime mold undergoes few changes in its structure, that is, it repositions its front position into a fan-shaped model, and its interconnected venous network allows the cytoplasm to flow inside at some level in relocation series. This stretchable venous network helps in searching for food in multiple places and grabs the food from food points. The slime mold has the ability to creep up to 900 sq.m if it finds rich food points in the environment.

Mathematical Modeling of Slime Mold Algorithm

The mathematical modeling of SMA is discussed in three stages, namely, approaching food, wrapping food, and food grabble (Li et al., 2020).

Technique of Approaching Food

Step 1: The slime mold identifies the food based on the smell present in the air. The mathematics to explicate the contraction phase and update its position during the food search process is presented in the following expression which depends on x and p:

$$\overrightarrow{Y(\tau+1)} = \overrightarrow{Y_b(\tau)} + \overrightarrow{vb} \times \left(\vec{w} \times \overrightarrow{Y_A(\tau)} - \overrightarrow{Y_B(\tau)}\right), x > p \tag{12}$$

$$\overrightarrow{Y(\tau+1)} = \overrightarrow{vc} \times Y(\tau), x > p, \tag{13}$$

where $\overrightarrow{vb}$ is the parameter which ranges from $[-d, d]$.

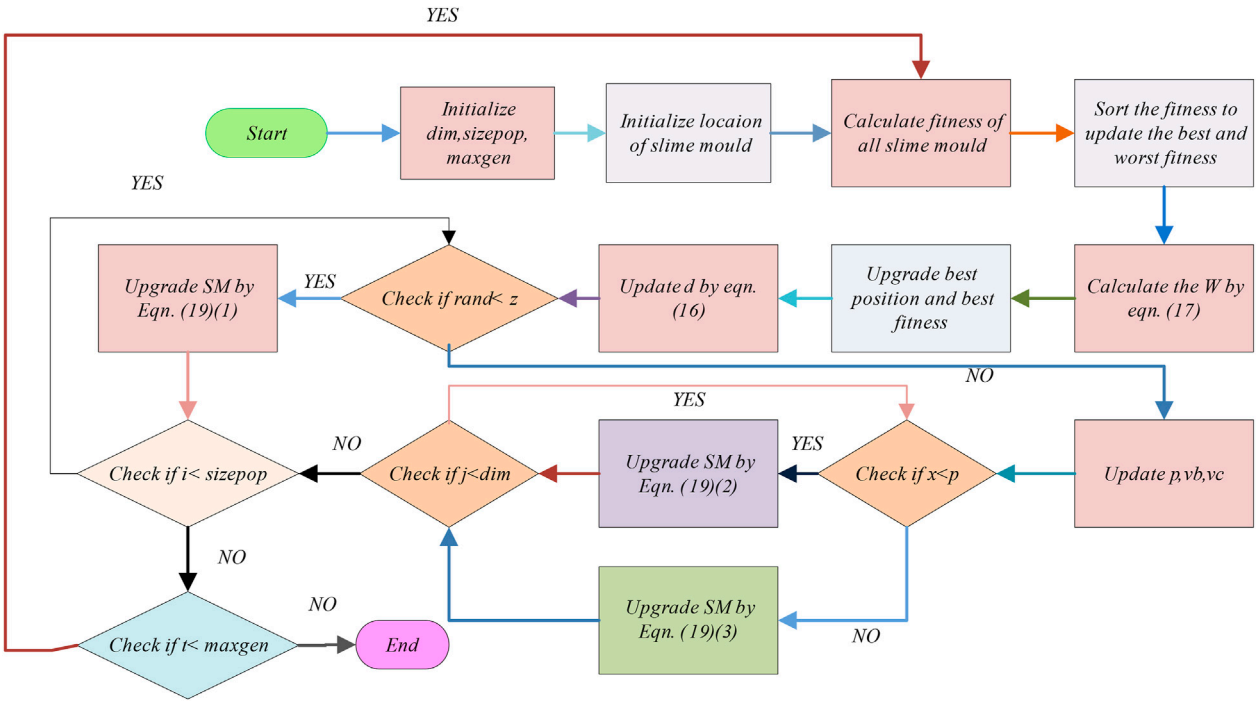

FIGURE 1 | Flow Chart of SMA Algorithm.

The maximum limit p is as follows:

$$p = \tanh\left|F(t) - bf\right|, \tag{14}$$

where t = 1, 2,.n, $F(t)$ is the fitness of the slime mold's location and bf is the fitness value from all the steps. **Eq. 4** describes the range of the parameter $\vec{vb}$.

$$\vec{vb} = [-d, d], \tag{15}$$

$$d = \arctan h\left[-\left(\frac{\tau}{\max_{\tau}}\right) + 1\right]. \tag{16}$$

The equation $\vec{W}$ is expressed as follows:

$$\overrightarrow{W\left[Stenchindex(\tau)\right]} = \begin{cases} 1 + x\log\left(\dfrac{OpF - F(t)}{OpF - lF} + 1\right) \\ 1 - x\log\left(\dfrac{OpF - F(t)}{OpF - lF} + 1\right) \end{cases}, \tag{17}$$

$$Stenchindex = sort(F), \tag{18}$$

where $F(t)$ ranks first half of the population and random value x lies in the interval [0,1].

Technique of Wrapping Food

The slime mold's updated location is numerically given as follows:

$$\vec{Y^{l}} = \begin{cases} rand \times (U_{ub} - U_{lb}) + U_{ub}, rand < z \\ \overrightarrow{Y_b(\tau)} \end{cases} + \vec{vb} \times \left(\vec{W} \times \overrightarrow{Y_A(\tau)} - \times \overrightarrow{Y_B(\tau)}, x > p\right) \overrightarrow{vc} \times \overrightarrow{Y_A(\tau)}, x > p. \tag{19}$$

The upper and lower bounds of search ranges are given as U_{ub} and U_{lb}, respectively, and $rand$ and x indicate the random values in the interval [0,1].

Technique of Food Grabble

The slime mold's location gets upgraded in the search process and the value varies within the limits and fluctuates between [-1, 1] and falls to zero. The flowchart of the proposed optimizer is shown in **Figure 1**.

TEST SYSTEM RESULTS AND DISCUSSIONS

In this section of the article, the IEEE bus systems in small size test systems were considered, and comparison was done with other methods, to see how well the slime mold optimization algorithm performed on the ELD issue.

TABLE 1 | (Case I) Slime mold algorithm results for economic dispatch of 3-unit system (without valve-point effect).

Method	Transfer of Power Generating units					
	Fuel price (Rs./hr)	Required power in demand(MW)	G1	G2	G3	Loss in power, P_{Loss}(MW)
Grey Wolf optimizer (Kamboj et al. (2016))	1597.4815	150	30.4998	64.6208	54.8994	2.3444
Quadratic programming (Zaraki and Othman (2009))	1596	150	32.8116	64.5973	54.9329	2.3419
Lambda method (Sharma and Moses (2016))	1599.98	150	33.4701	64.0974	55.1011	2.6686
Particle swarm optimization (Sharma and Moses (2016))	1597.48	150	32.8101	64.595	54.9369	2.342
Genetic algorithm (Sharma and Moses (2016))	1600	150	34.4895	64.0299	54.1534	2.6728
Slime mold algorithm	**1590.627083**	150	10	76.42812	64.24508	0.336600019

Bold values represent the best cost.

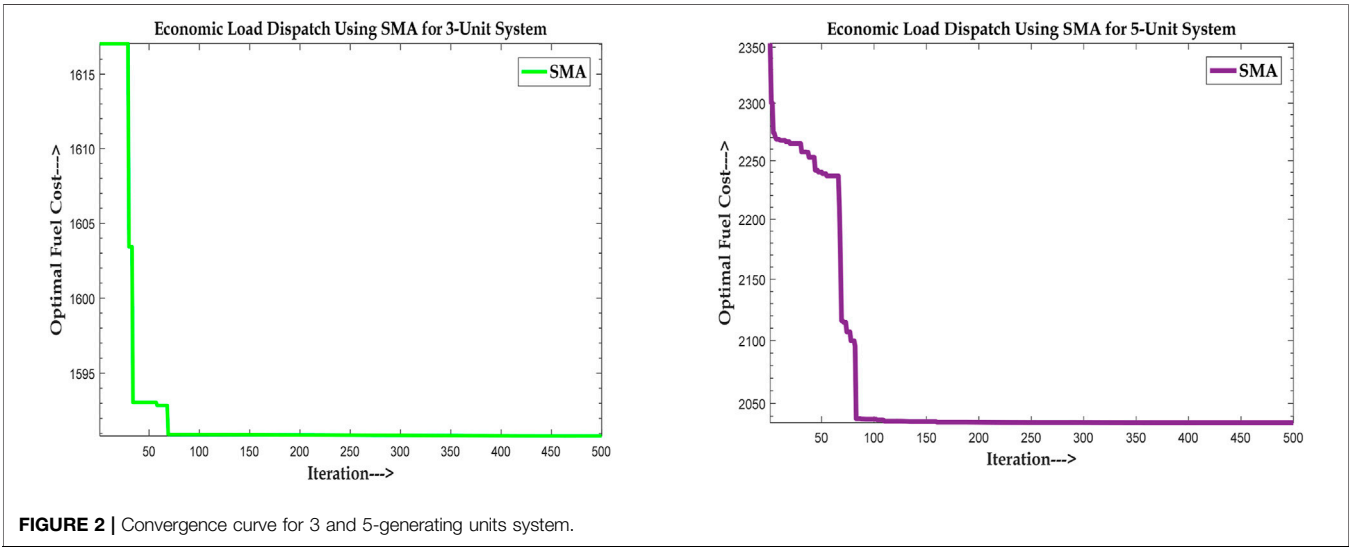

FIGURE 2 | Convergence curve for 3 and 5-generating units system.

TABLE 2 | Slime mold algorithm results for economic dispatch of 5-unit system (with valve-point effect).

Method	Transfer of power-generating units							
	Fuel price (Rs./h)	Required power in demand (MW)	G1	G2	G3	G4	G5	Loss in power, P_{Loss} (MW)
Genetic algorithm (Coelho and Lee (2008))	2412.538	730	218.0184	109.0092	147.5229	28.37844	227.0275	NR
Particle swarm optimization (Coelho and Lee (2008))	2252.572	730	229.5195	125	175	75	125.4804	NR
Lambda (Coelho and Lee (2008))	2412.709	730	218.028	109.014	147.535	28.380	272.042	NR
APSO (Coelho and Lee (2008))	2140.97	730	225.3845	113.020	109.4146	73.11176	209.0692	NR
Slime mold algorithm	**2034.972427**	730	229.5195832	102.9830227	112.6813882	74.9999977	209.816008	0

Bold values represent the best cost.

Case Study

The input test data and loss coefficient matrices were obtained from Sharma and Moses (2016), which shows a three-generator test system with a power requirement of 150 MW assessed. The input test data are displayed in appendix. In this case, the ELD issue was cracked without a valve-point effect. **Table 1** indicates that the slime mold algorithm's fuel price is 1590.627083 Rs./h, which was the lowest of all the algorithms satisfying the system constraints. The convergence curve of the SMA obtained by simulation which was stable is shown in **Figure 2A**.

Case Study

With a power demand of 730MW, a five-unit test system with a valve-point loading effect was used, and its input test information

was taken from Coelho and Lee (2008) with the loss coefficient matrix set to zero, which is given in appendix. **Table 2** shows that the slime mold algorithm obtained a fuel price of 2034.972427 R/h, satisfying all the constraints and was the best fuel price among all algorithms. The convergence curve of SMA obtained by simulation which was stable is shown in **Figure 2B**.

In order to intuitively analyze the location and fitness changes of the slime mold during foraging, the qualitative analysis findings of the SMA in lowering the fuel cost in ELD are provided in **Figures 2A,B**. During the iteration phase, the convergence curve reveals the ideal fitness value of the slime mold. The convergence curve shows how the average fitness of the slime mold's ideal fitness value changes over time. We can see the slime mold's convergence rate and the moment when it transitions between exploration and exploration gradation by looking at the decline of the curve.

CONCLUSION

In this study, the slime mold optimization approach was used to solve economic load dispatch problems in electric power networks. This method's effectiveness was tested on conventional IEEE bus systems with 3 and 5 producing units in small, medium, and large power systems. According to the statistics, the slime mold optimizer was clearly the best choice for dealing with economic load dispatch issues since it contributes reduced fuel costs and less transmission loss. It has a higher rate of convergence than other well-known optimizers. By establishing a balance between exploration and exploitation, the slime mold optimizer achieved maximal avoidance in the local optimum. As a result, this algorithm provided improved solutions for load dispatch difficulties that were cost-effective.

DATA AVAILABILITY STATEMENT

The original contributions presented in the study are included in the article/Supplementary Material, further inquiries can be directed to the corresponding author.

AUTHOR CONTRIBUTIONS

The author confirms being the sole contributor of this work and has approved it for publication.

REFERENCES

Al-Kalaani, Y. (2009). Power Generation Scheduling Algorithm Using Dynamic Programming. *Nonlinear Anal. Theor. Methods Appl.* 71 (12), e641–e650. doi:10.1016/j.na.2008.11.082

Amjady, N., and Nasiri-Rad, H. (2010). Solution of Nonconvex and Nonsmooth Economic Dispatch by a New Adaptive Real Coded Genetic Algorithm. *Expert Syst. Appl.* 37 (7), 5239–5245. doi:10.1016/j.eswa.2009.12.084

Aydın, D., and Özyön, S. (2013). Solution to Non-convex Economic Dispatch Problem with Valve point Effects by Incremental Artificial Bee colony with Local Search. *Appl. Soft Comput.* 13 (5), 2456–2466. doi:10.1016/j.asoc.2012.12.002

Babonneau, F., Corcos, G., Drouet, L., and Vial, J.-P. (2019). Neatwork: A Tool for the Design of Gravity-Driven Water Distribution Systems for Poor Rural Communities. *INFORMS J. Appl. Analytics* 49 (3), 129–136. doi:10.1287/inte.2018.0983

Bhattacharya, A., and Chattopadhyay, P. K. (2010). Solving Complex Economic Load Dispatch Problems Using Biogeography-Based Optimization. *Expert Syst. Appl.* 37 (5), 3605–3615. doi:10.1016/j.eswa.2009.10.031

Cai, J., Li, Q., Li, L., Peng, H., and Yang, Y. (2012). A Hybrid CPSO-SQP Method for Economic Dispatch Considering the Valve-point Effects. *Energ. Convers. Manag.* 53 (1), 175–181. doi:10.1016/j.enconman.2011.08.023

Coelho, L. d. S., and Lee, C.-S. (2008). Solving Economic Load Dispatch Problems in Power Systems Using Chaotic and Gaussian Particle Swarm Optimization Approaches. *Int. J. Electr. Power Energ. Syst.* 30 (5), 297–307. doi:10.1016/j.ijepes.2007.08.001

Dibangoye, J., Doniec, A., Fakham, H., Colas, F., and Guillaud, X. (2015). Distributed Economic Dispatch of Embedded Generation in Smart Grids. *Eng. Appl. Artif. Intelligence* 44, 64–78. doi:10.1016/j.engappai.2015.05.007

Dubey, H. M., Pandit, M., Panigrahi, B. K., and Udgir, M. (2013). Economic Load Dispatch by Hybrid Swarm Intelligence Based Gravitational Search Algorithm. *Ijisa* 5 (8), 21–32. doi:10.5815/ijisa.2013.08.03

Elsayed, S. M., Sarker, R. A., and Essam, D. L. (2014). A New Genetic Algorithm for Solving Optimization Problems. *Eng. Appl. Artif. Intelligence* 27, 57–69. doi:10.1016/j.engappai.2013.09.013

Farhat, I. A., and El-Hawary, M. E. (2010). Dynamic Adaptive Bacterial Foraging Algorithm for Optimum Economic Dispatch with Valve-point Effects and Wind Power. *IET Gener. Transm. Distrib.* 4 (9), 989–999. doi:10.1049/iet-gtd.2010.0109

Ghasemi, M., Taghizadeh, M., Ghavidel, S., and Abbasian, A. (2016). Colonial Competitive Differential Evolution: An Experimental Study for Optimal Economic Load Dispatch. *Appl. Soft Comput.* 40, 342–363. doi:10.1016/j.asoc.2015.11.033

Gjorgiev, B., and Čepin, M. (2013). A Multi-Objective Optimization Based Solution for the Combined Economic-Environmental Power Dispatch Problem. *Eng. Appl. Artif. Intelligence* 26 (1), 417–429. doi:10.1016/j.engappai.2012.03.002

Houssein, E. H., Mahdy, M. A., Shebl, D., Manzoor, A., Sarkar, R., and Mohamed, W. M. (1158). An Efficient Slime Mould Algorithm for Solving Multi-Objective Optimization Problems. *Expert Syst. Appl.* 187, 2022. doi:10.1016/j.eswa.2021.115870

Houssein, E. H., Helmy, B. E.-d., Rezk, H., and Nassef, A. M. (2022). An Efficient Orthogonal Opposition-Based Learning Slime Mould Algorithm for Maximum Power point Tracking. *Neural Comput. Applic* 34 (5), 3671–3695. doi:10.1007/s00521-021-06634-y

Howard, F. L. (1931). The Life History Ofphysarum Polycephalum. *Am. J. Bot.* 18 (2), 116–133. doi:10.1002/j.1537-2197.1931.tb09577.x

Hu, J., Gui, W., Heidari, A. A., Cai, Z., Liang, G., Chen, H., et al. (2022). Dispersed Foraging Slime Mould Algorithm: Continuous and Binary Variants for Global Optimization and Wrapper-Based Feature Selection. *Knowledge-Based Syst.* 237, 107761. doi:10.1016/j.knosys.2021.107761

Jadoun, V. K., Gupta, N., Niazi, K. R., Swarnkar, A., and Bansal, R. C. (2015). Improved Particle Swarm Optimization for Multi-Area Economic Dispatch with Reserve Sharing Scheme. *IFAC-PapersOnLine* 48 (30), 161–166. doi:10.1016/j.ifacol.2015.12.371

Jeddi, B., and Vahidinasab, V. (2014). A Modified harmony Search Method for Environmental/economic Load Dispatch of Real-World Power Systems. *Energ. Convers. Manag.* 78, 661–675. doi:10.1016/j.enconman.2013.11.027

Jiang, X., Zhou, J., Wang, H., and Zhang, Y. (2013). Dynamic Environmental Economic Dispatch Using Multiobjective Differential Evolution Algorithm with Expanded Double Selection and Adaptive Random Restart. *Int. J. Electr. Power Energ. Syst.* 49 (1), 399–407. doi:10.1016/j.ijepes.2013.01.009

Kamboj, V. K., Bath, S. K., and Dhillon, J. S. (2016). Solution of Non-convex Economic Load Dispatch Problem Using Grey Wolf Optimizer. *Neural Comput. Applic* 27 (5), 1301–1316. doi:10.1007/s00521-015-1934-8

Li, S., Chen, H., Wang, M., Heidari, A. A., and Mirjalili, S. (2020). Slime Mould Algorithm: A New Method for Stochastic Optimization. *Future Generation Comp. Syst.* 111, 300–323. doi:10.1016/j.future.2020.03.055

Li, Z., Wu, W., Zhang, B., Sun, H., and Guo, Q. (2013). Dynamic Economic Dispatch Using Lagrangian Relaxation with Multiplier Updates Based on a Quasi-Newton Method. *IEEE Trans. Power Syst.* 28, 4516–4527. doi:10.1109/TPWRS.2013.2267057

Mohammadi-Ivatloo, B., Rabiee, A., and Soroudi, A. (2013). Nonconvex Dynamic Economic Power Dispatch Problems Solution Using Hybrid Immune-Genetic Algorithm. *IEEE Syst. J.* 7 (4), 777–785. doi:10.1109/JSYST.2013.2258747

Neyestani, M., Farsangi, M. M., and Nezamabadi-Pour, H. (2010). A Modified Particle Swarm Optimization for Economic Dispatch with Non-smooth Cost Functions. *Eng. Appl. Artif. Intelligence* 23 (7), 1121–1126. doi:10.1016/j.engappai.2010.06.006

Panigrahi, C. K., Chattopadhyay, P. K., Chakrabarti, R. N., and Basu, M. (2006). Simulated Annealing Technique for Dynamic Economic Dispatch. *Electric Power Components Syst.* 34 (5), 577–586. doi:10.1080/15325000500360843

Pothiya, S., Ngamroo, I., and Kongprawechnon, W. (2010). Ant colony Optimisation for Economic Dispatch Problem with Non-smooth Cost Functions. *Int. J. Electr. Power Energ. Syst.* 32 (5), 478–487. doi:10.1016/j.ijepes.2009.09.016

Reid, G., and Hasdorff, L. (1973). Economic Dispatch Using Quadratic Programming. *IEEE Trans. Power Apparatus Syst.* PAS-92 (6), 2015–2023. doi:10.1109/TPAS.1973.293582

Rizk, M.Rizk-Allah, Aboul Ella Hassanien, Dongran Song, "Chaos-Opposition-Enhanced Slime Mould Algorithm for Minimizing the Cost of Energy for the Wind Turbines on High-Altitude Sites". *ISA Trans.* 121, 2022191–2022205. doi:10.1016/j.isatra.2021.04.011

Safari, A., and Shayeghi, H. (2011). Iteration Particle Swarm Optimization Procedure for Economic Load Dispatch with Generator Constraints. *Expert Syst. Appl.* 38 (5), 6043–6048. doi:10.1016/j.eswa.2010.11.015

Salcedo-Sanz, S. (2009). A Survey of Repair Methods Used as Constraint Handling Techniques in Evolutionary Algorithms. *Comp. Sci. Rev.* 3 (3), 175–192. doi:10.1016/j.cosrev.2009.07.001

Sharma, U., and Moses, B. (2016). Analysis and Optimization of Economic Load Dispatch Using Soft Computing Techniques. *Int. Conf. Electr. Electron. Optim. Tech. ICEEOT*, 4035–4040. doi:10.1109/ICEEOT.2016.7755472

Shaw, B., Mukherjee, V., and Ghoshal, S. P. (2012). Solution of Economic Dispatch Problems by Seeker Optimization Algorithm. *Expert Syst. Appl.* 39 (1), 508–519. doi:10.1016/j.eswa.2011.07.041

Singh, N. J., Dhillon, J. S., and Kothari, D. P. (2016). Synergic Predator-Prey Optimization for Economic thermal Power Dispatch Problem. *Appl. Soft Comput.* 43, 298–311. doi:10.1016/j.asoc.2016.02.042

Sinha, N., Chakrabarti, R., and Chattopadhyay, P. K. (2003). Evolutionary Programming Techniques for Economic Load Dispatch. *IEEE Trans. Evol. Computat.* 7 (1), 83–94. doi:10.1109/TEVC.2002.806788

Subathra, M. S. P., Selvan, S. E., Victoire, T. A. A., Christinal, A. H., and Amato, U. (2015). A Hybrid with Cross-Entropy Method and Sequential Quadratic Programming to Solve Economic Load Dispatch Problem. *IEEE Syst. J.* 9 (3), 1031–1044. doi:10.1109/JSYST.2013.2297471

Torreglosa, J. P., García-Triviño, P., Fernández-Ramirez, L. M., and Jurado, F. (2016). Control Based on Techno-Economic Optimization of Renewable Hybrid Energy System for Stand-Alone Applications. *Expert Syst. Appl.* 51, 59–75. doi:10.1016/j.eswa.2015.12.038

Wang, L., and Singh, C. (2009). Reserve-constrained Multiarea Environmental/economic Dispatch Based on Particle Swarm Optimization with Local Search. *Eng. Appl. Artif. Intelligence* 22 (2), 298–307. doi:10.1016/j.engappai.2008.07.007

Wang, M. Q., Gooi, H. B., Chen, S. X., Lu, S., Lu, S., and Variables, A. (2014). A Mixed Integer Quadratic Programming for Dynamic Economic Dispatch with Valve Point Effect. *IEEE Trans. Power Syst.* 29 (5), 2097–2106. doi:10.1109/APPEEC.2014.706614710.1109/tpwrs.2014.2306933

Whei-Min Lin, W., Fu-Sheng Cheng, F., and Ming-Tong Tsay, M. (2002). An Improved Tabu Search for Economic Dispatch with Multiple Minima. *IEEE Trans. Power Syst.* 17 (1), 108–112. doi:10.1109/59.982200

Yang, X.-S., Sadat Hosseini, S. S., and Gandomi, A. H. (2012). Firefly Algorithm for Solving Non-convex Economic Dispatch Problems with Valve Loading Effect. *Appl. Soft Comput.* 12 (3), 1180–1186. doi:10.1016/j.asoc.2011.09.017

Yin, S., Luo, Q., and Zhou, Y. (2022). EOSMA: An Equilibrium Optimizer Slime Mould Algorithm for Engineering Design Problems. *Arab. J. Sci. Eng.*doi:10.1007/s13369-021-06513-7

Zaraki, A., and Othman, M. F. B. (2009). Implementing Particle Swarm Optimization to Solve Economic Load Dispatch Problem. SoCPaR 2009 - Soft Comput. Pattern Recognit, 60–65. doi:10.1109/SoCPaR.2009.24

Zare, K., Haque, M. T., and Davoodi, E. (2012). Solving Non-convex Economic Dispatch Problem with Valve point Effects Using Modified Group Search Optimizer Method. *Electric Power Syst. Res.* 84 (1), 83–89. doi:10.1016/j.epsr.2011.10.004

Zhan, J. P., Wu, Q. H., Guo, C. X., and Zhou, X. X. (2014). Fast λ-Iteration Method for Economic Dispatch with Prohibited Operating Zones. *IEEE Trans. Power Syst.* 29 (2), 990–991. doi:10.1109/TPWRS.2013.2287995

Zhong, H., Xia, Q., Wang, Y., and Kang, C. (2013). Dynamic Economic Dispatch Considering Transmission Losses Using Quadratically Constrained Quadratic Program Method. *IEEE Trans. Power Syst.* 28 (3), 2232–2241. doi:10.1109/TPWRS.2013.2254503

Conflict of Interest: The author declares that the research was conducted in the absence of any commercial or financial relationships that could be construed as a potential conflict of interest.

Publisher's Note: All claims expressed in this article are solely those of the authors and do not necessarily represent those of their affiliated organizations, or those of the publisher, the editors, and the reviewers. Any product that may be evaluated in this article, or claim that may be made by its manufacturer, is not guaranteed or endorsed by the publisher.

frontiers | Frontiers in Energy Research

ORIGINAL RESEARCH
published: 30 May 2022
doi: 10.3389/fenrg.2022.861563

Sequential Detection of Microgrid Bad Data *via* a Data-Driven Approach Combining Online Machine Learning With Statistical Analysis

Heming Huang[1,2], *Fei Liu*[1]*, *Tinghui Ouyang*[1] *and Xiaoming Zha*[1]

[1]School of Electrical Engineering, Wuhan University, Wuhan, China, [2]Engineering College, The University of Iowa, Iowa City, IA, United States

Bad data is required to be detected and removed from the microgrid data stream because it misleads the decision-making of the Energy Management Systems (EMS) and puts the microgrid at risk of instability. In this paper, the authors propose a sequential detection method that combines three data mining algorithms, that is the Online Sequential Extreme Learning Machine (OSELM), statistical analysis within a sliding time window, and the Density-Based Spatial Clustering of Applications with Noise (DBSCAN). After sequential data training, OSELM is used to construct an online updated error-filtering map to extract the electrical feature of the microgrid data sequence. Meanwhile, the statistical features, i.e. the surge of the variance and the corresponding correlation coefficients under a sliding time window are first proposed as another two complementary feature dimensions. The three-dimensional features are finally analyzed by DBSCAN to discriminate the bad data. The detection performance of this approach is verified by the data sequence collected from a four-terminal ring-shaped DC microgrid prototype. Compared with bad data detection using a single electrical feature or only statistical features, this approach shows the best performance. Moreover, it can be further applied to the online detection of microgrid bad data in the future.

Keywords: bad data detection, microgrid anomaly, OSELM, DBSCAN, statistical analysis

OPEN ACCESS

Edited by:
Haris M. Khalid,
Higher Colleges of Technology, United Arab Emirates

Reviewed by:
Dazhong Ma,
Northeastern University, China
Alex Jung,
Aalto University, Finland

***Correspondence:**
Fei Liu
lf_dyj@whu.edu.cn

Specialty section:
This article was submitted to Smart Grids, a section of the journal Frontiers in Energy Research

Received: *24 January 2022*
Accepted: *21 April 2022*
Published: *30 May 2022*

Citation:
Huang H, Liu F, Ouyang T and Zha X (2022) Sequential Detection of Microgrid Bad Data via a Data-Driven Approach Combining Online Machine Learning With Statistical Analysis. Front. Energy Res. 10:861563. doi: 10.3389/fenrg.2022.861563

1 INTRODUCTION

In the concept of the future smart grid, the information and communication system should be highly integrated with the energy distribution infrastructure in the microgrid. Data is the key element between these two layers of the infrastructure. The reliability of the microgrid electrical data is the premise of many energy dispatching and system control functions of the EMS, such as real-time operation plan adjustment, operating mode switching, and emergency response to large disturbances. With the application of big data in the smart grid, data quality becomes much more important in improving both the economy and sustainability of the energy utilization in the microgrid (Rana et al., 2015; Rana and Li., 2015). However, due to the uncertainties of the microgrid data acquisition system, such as sensor failure, asynchronous measurement, communication interruption, error coding, storage exception, the abnormal shutdown of the data acquisition program, data injection attack from the external network, etc. (Zhao et al., 2014; Anwar et al., 2017; Wu et al., 2017), normal data is mixed with a small amount of outliers, known as bad data. Bad data misleads the EMS in decision-making on economic operation when the

microgrid is in a steady state. It also impacts the emergency decision on system security when the microgrid is under large disturbances. These factors further affect the economy of microgrid operation, even causes disastrous consequences such as system collapse (Shahnia et al., 2010). Therefore, it is particularly necessary to detect and eliminate these bad data. With the future integration of the information system and the physical infrastructure as well as the high penetration of power electronic devices, the 4V (volume, velocity, variety, and veracity) features of the microgrid data are becoming more and more obvious. As a result, the types and contents of bad data in the microgrid are more complicated than that of the utility grid (Qiu et al., 2017), which calls for a more rapid and effective bad data detection method.

Power system bad data detection has been researched for over 40 years. Most of the research aims at the utility grid. Through the survey of much-related literature, bad data detection is divided into two steps, features extraction, and features analysis. The first task is to obtain the quantitative features containing the differences between the normal data and the bad data from single or multiple dimensions. The next step is to analyze the features and approximate the dividing boundary between normal data and bad data. Traditional bad data detection methods use electrical features to identify bad data, based on the idea that bad data stems from various uncertainties and does not comply with the electrical mechanism of the power system. The electrical features can be obtained from either the power system model or the vast historical data. According to these two feature-acquiring means, the research methods of bad data detection are divided into the traditional method based on the power system analytical model and the modern method based on the data-driven model.

The traditional power system analytical model based on the bad data detection method relies on either the estimation or prediction of the operating state of the power system. According to the features differences, it is mainly divided into the residual method and surge method. The residual method uses the state estimator to estimate the real-time power flow of the power system and extracts the residual (the difference between the measured value and the estimation of the true value) as the feature. Next, based on the probability distribution of the residuals, the outliers located outside of certain confidence intervals are detected as bad data (Bretas and Bretas, 2015; Zhao et al., 2017). This method is limited by the huge computational cost because the state estimation process should be repeated many times to avoid the residual pollution and residual flooding effect (Liu et al., 2011). The surge method (Huang and Lin, 2004; Do Coutto Filho and de Souza, 2009) treats the power system as a dynamic model and takes the surge (difference between the present measured value and the predicted value at the previous sampling time) as the feature. Next, the bad data is detected based on the statistical hypothesis test of the surge. This method overcomes the formerly mentioned disadvantage of huge computational cost. But it assumes that the topology and the parameters of the utility grid are not changed during the adjacent sampling time, which restricts its application.

Traditional bad data detection methods have a long way to go before being applied in the microgrid. Due to the high penetration of Distributed Energy Resources (DERs) in the microgrid, the operating modes and operating states are more complicated than that of the utility grid (Hu et al., 2011). At the same time, as a hybrid AC-DC multi-converter system, the static operating point of the microgrid often migrates. It is difficult to establish a dynamic analytical model for the microgrid (Xia et al., 2016), while the analytical model is the basis of the traditional bad data detection methods. Reference (Gu et al., 2017) proposed a state estimation method based on a dynamic large-signal model of the microgrid to realize the distributed control of microgrid voltage. However, the influence of the inter-converter coordinated control scheme on the model parameters is not considered. Authors in (Beg et al., 2017) proposed a bad data detection method based on the hybrid numeral and physical simulation model of the microgrid. The main idea is the use of a microgrid dynamic simulation model to verify whether the data conforms with the electrical laws. This method is very instructive, but the traditional power system analytical model is not used.

On the contrary, the modern bad data detection methods based on data-driven models do not need to analyze the power system model (Wu et al., 2013; Huang et al., 2016). They use the machine learning method to extract the electrical features out of the vast historical data, which are used for the prediction of the measurement error. Next, clustering analysis is used to automatically assort normal data and bad data in different clusters (Shyh-Jier and Jeu-Min, 2002; Cramer et al., 2015; Yang et al., 2017). In our previous work (Huang et al., 2018), the machine learning algorithm ELM is used to extract the electrical feature, and the feature is analyzed by the clustering algorithm DBSCAN to realize the fast and effective detection of the bad data in the microgrid. To the best of our knowledge, this method is the first application of bad data detection in microgrids based on the data-driven model. The combining of ELM and DBSCAN can achieve faster and more accurate detection than the previous methods (Shyh-Jier and Jeu-Min, 2002; Cramer et al., 2015; Yang et al., 2017). However, there are still some drawbacks. The research adopts the idea of offline training, the prediction model is only trained once, and its accuracy depends on the completeness of the information contained in the historical data. Inspired by the sequential detection idea in reference (Li et al., 2015), we introduce the OSELM algorithm to improve our previous work. Using the method of online training to update the prediction model sequentially is more conducive to the realization of the online detection of bad data in the future. However, there is still a problem in the sequential learning of OSELM. The accuracy and generalization ability of such supervised machine learning models still heavily depend on prior knowledge. They are not sensitive enough to some unfamiliar operating modes or states. Therefore, it is necessary to introduce some other dimensions of features together with a new unsupervised detection method to complement the shortcomings of the single electrical feature extracted by the supervised OSELM algorithm.

Recently, bad data detection methods based on statistical analysis have been widely used in the field of network security

(Bosman et al., 2017; Ren et al., 2017). Its main idea is to use the statistical property of the continuous data stream to determine whether an observation value is beyond the statistical range of normal data (Almalawi et al., 2014; Mohammadpourfard et al., 2017). The external appearance of bad data is an outlier that is too large or too small. So, it has a statistically significant surge feature, and lower correlation with other normal data. Therefore, the surge of variance and the correlation coefficient of the measurement data sequence within a sliding time window [inspired by (Araya et al., 2017)] can be used as two feature dimensions to distinguish the bad data. As mentioned earlier, the operating conditions of the microgrid are more complex than that of the utility grid. Due to the lack of prior knowledge of the intrinsic electrical relationship between the data, the statistical features of microgrid measurement data can be flooded by the noise of the data itself. Therefore, a single statistical method is not sufficient for the microgrid bad data detection. On the contrary, the electrical features of microgrid measurement data use prior knowledge of the microgrid electrical laws. The combining of the above two supervised and unsupervised methods, i.e. the use of both electrical features and statistical features, can achieve a better detection performance of bad data.

Guided by the above idea, this paper presents a sequential detection method of microgrid bad data based on machine learning and statistical analysis. Based on our previous research work, this paper takes the microgrid simulation data as the prior knowledge and builds the error-filtering map in the training process of the OSELM algorithm which has the sequential learning ability. The online updated error-filtering map is used to obtain the electrical feature of the microgrid measurement. Meanwhile, the statistical analysis method is used to obtain the surge of the variance and the correlation coefficient of the microgrid measurement data sequence in a sliding time window. Finally, we use the clustering algorithm DBSCAN to analyze the features in the above three dimensions and identify the bad data. The contribution of this paper is as follows.

1) On the basis of our previous bad data detection method ELM + DBSCAN, an online training and sequential detection method for microgrid bad data via the combination of OSELM and DBSCAN is proposed for the first time.
2) A statistical method that uses the surge of the variance and the correlation coefficient of the data sequence in a sliding time window is first proposed and applied in microgrids for bad data detection.
3) The above two types of methods are combined by using electrical features and statistical features at the same time. This hybrid method can not only avoid being flooded by system noise but also recognize the sudden change of the microgrid operating states. The detection performance is better than that of the OSELM + DBSCAN method using the single electrical feature or the statistical method using only statistical features. More importantly, it can realize the sequential detection of bad data (both point anomaly and contextual anomaly), while the existing methods can only achieve the detection of point anomaly.

The rest of this paper is organized as follows. The basic theory and our new idea of microgrid bad data detection are introduced in **section 2**. In **section 3**, the sequential detection method combining the OSELM, statistical analysis, and DBSCAN algorithm is proposed. And the detection performance of the method is verified by the data sequence from a real microgrid prototype in **section 4**. **Section 5** concludes the full text.

2 BASIC THEORY AND NEW IDEA

Figure 1 shows the entire path of data from measuring to transmission to processing in the microgrid which adopts the commonly used hierarchical control structure. Data in the microgrid are mainly divided into two categories, the upward system status information, and downward control commands. The status information includes voltage, current, active and reactive power, switch status, port status, protection action instructions, etc. Among them, the electrical measurements, i.e. the voltage, current, and power are the objects for bad data detection in this paper.

The electrical data on each Distributed Energy Resource (DER) port, grid port, and load port of the microgrid are collected by the sensors and finally enter the local controller and the host computer *via* the communication network. These electrical data are used to guide the host computer to issue control commands including the operating mode of each port, input control command value of the converter, and switch on/off command, to realize energy dispatching and system control of the microgrid. However, due to the uncertainties of the data acquisition and communication systems, this electrical data is inevitably mixed with noise and even gross error. In order to improve the reliability of the data, state estimation is needed to reduce noise. At the same time, the bad data detection method is required to clear out the gross error.

2.1 Bad Data in Microgrid

" An outlier is an observation that deviates so much from other observations as to arouse suspicion that it was generated by a different mechanism" By Douglas M. Hawkins in 1980. The appearance of abnormal data can be seen as a random, sporadic phenomenon relative to the large amount of normal data present, which is largely deviated from normal data and comes from different mechanisms. Therefore, abnormal data often does not have a strong correlation with normal data. This correlation is reflected in two aspects, one is the relevance of the data attribute, the other is the correlation of the data structure. The normal data generally comes from the same mechanism, and the structure is relatively compact, often showing a spherical or band-like structure. The abnormal data does not conform to the intrinsic structure of normal data, and the structural correlation is weak.

According to these characteristics of bad data and normal data, there are two premises in detecting bad data.

Premise 1: Normal data instances occur in dense neighborhoods, while anomalies occur far from their closest neighbors.

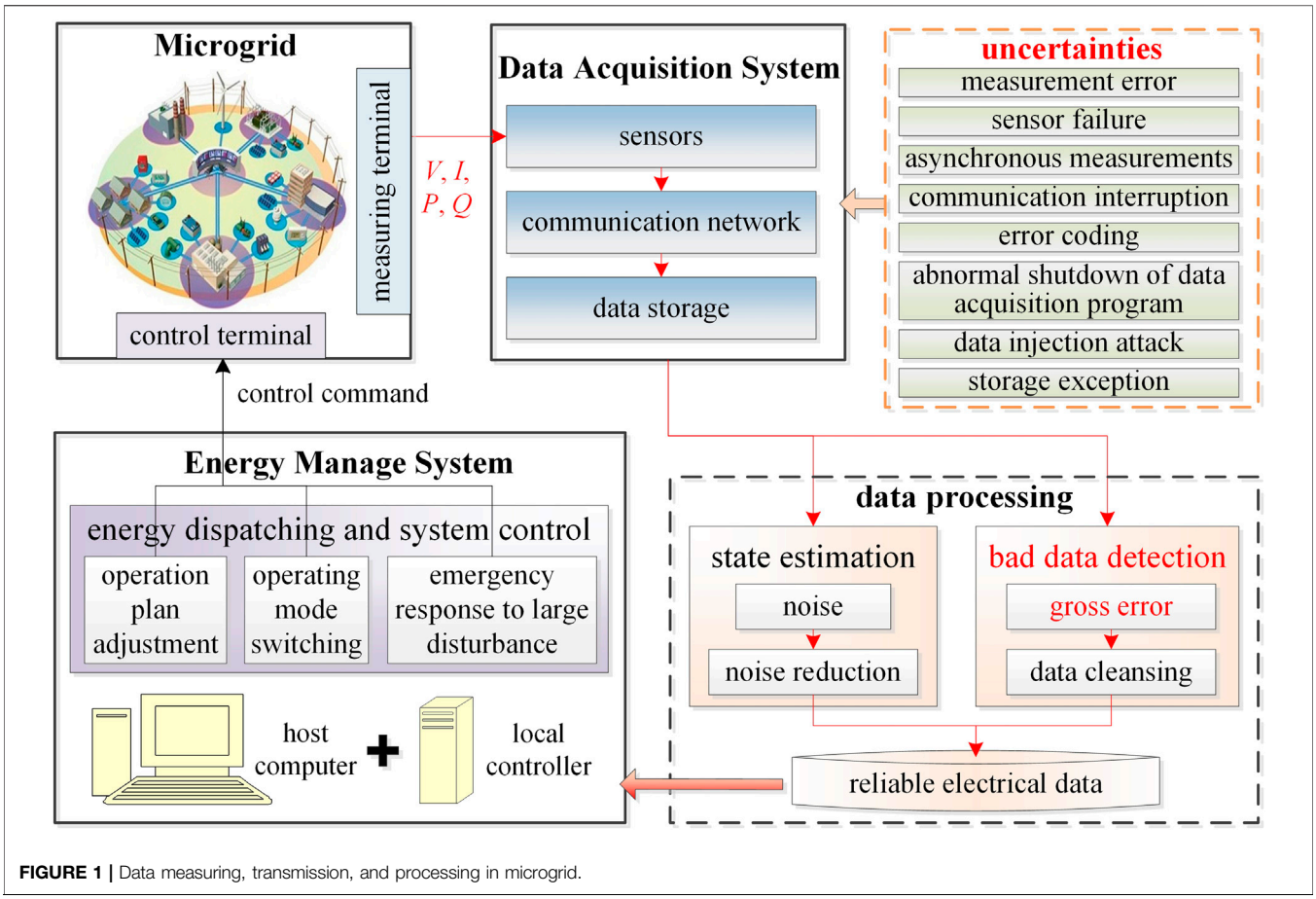

FIGURE 1 | Data measuring, transmission, and processing in microgrid.

Premise 2: Normal data is the majority and is relevant because it arises from the expected mechanism. While abnormal data is generated by sporadic mechanisms and is therefore partially or completely uncorrelated.

Based on the above two premises, the data attributes in the microgrid are shown in **Figure 2**.

We can see from **Figure 2** that there are four kinds of attributes of microgrid data, i.e. spatial attribute, graph attribute, sequential attribute, and profile attribute.

1) Spatial attribute refers to different electrical features of the discrete electrical data points formed by the readings of the sensors. As a single data point in the network topology, the data itself contains noise.
2) Graph attribute refers to the neighbor relationship of the sensor in space. At each time interval, the electrical measurements in each column conform to the microgrid measurement equation $\mathbf{z} = h(\mathbf{x})+\mathbf{v}$. The electrical data is spatially correlated.
3) Sequential attribute refers to the neighbor relationship of the data sequence in time series. When the topology and parameters of the microgrid keep unchanged, the microgrid is a dynamic time-invariant system. The electrical data sequence $\mathbf{z}$ conforms to the state transition equation $\mathbf{z}_{k+1} = f(\mathbf{x}_k)+\mathbf{q}_k$, and the data is also time-dependent.
4) Profile attribute is the scene feature of anomaly defined at the system level in the dimensions of time, space, etc. In the space-time dimension, because different operating scenarios often change periodically, there is a similarity between data sequences.

Based on these four kinds of attributes, three kinds of the anomaly are classified.

1) Point anomaly refers to bad data points in the spatial dimension.
2) Contextual anomaly refers to bad data points or sequences in the time dimension.
3) Collective anomaly refers to abnormal states or patterns in the space-time dimension.

The microgrid bad data discussed in this paper belong to both point anomaly and contextual anomaly, as a result, both spatial correlation and timing correlation can be used to distinguish good data and bad data.

1) bad data in spatial correlation.

The electrical measurements in the microgrid can be expressed as a linear combination of the true values and the measurement

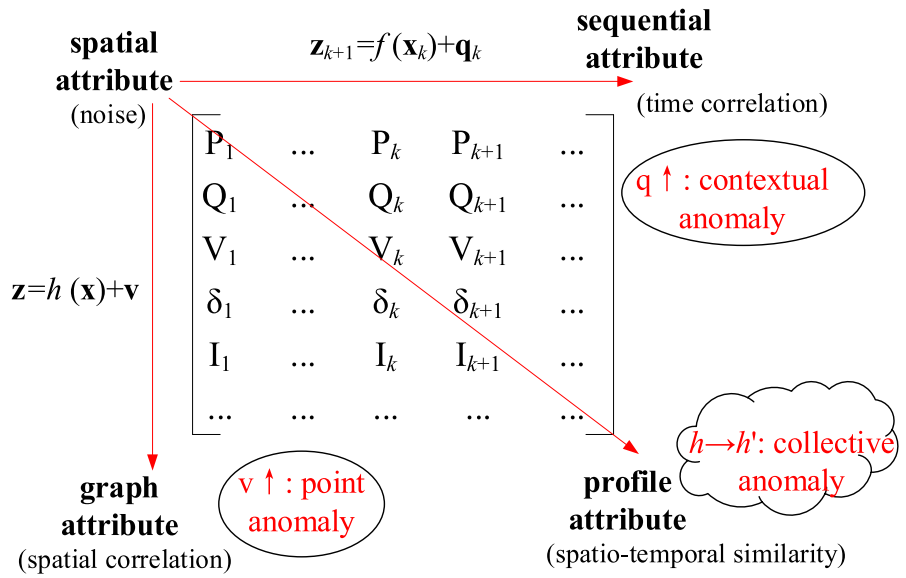

FIGURE 2 | Data attribute in microgrid.

errors, as shown in **Eq. 1**. Note that all the variables are in matrix form.

$$\mathbf{z} = h(\mathbf{x}) + \mathbf{v} \tag{1}$$

where z is the measurement, $h(x)$ is the true value, x is the state variable which ensures the observability of the microgrid, $h(\cdot)$ is the equation expression of the microgrid model, v is the measurement error.

Rewrite **Eq. 1** into the time series form.

$$\mathbf{z}(t) = \mathbf{h}[x(t)] + \mathbf{v} \tag{2}$$

where, t is the time stamp, $\mathbf{z}(t)$, $\mathbf{x}(t)$, and $\mathbf{v}$ are all in vector form.

When $z(t)$ only contains normal data, the corresponding v stands for the Gaussian white noise.

$$\mathbf{v} \sim N(\mathbf{0}, \boldsymbol{\sigma}) \tag{3}$$

where σ is the standard deviation of the measurement error v.

When $z(t)$ contains bad data $z_b(t)$,

$$\mathbf{z}(t) = \begin{bmatrix} \mathbf{z}_g(t) \\ \mathbf{z}_b(t) \end{bmatrix} = h[\mathbf{x}(t)] + \begin{bmatrix} \mathbf{v}_g \\ \mathbf{v}_b \end{bmatrix} \tag{4}$$

where v_b is the gross error, which deviates beyond a certain statistical confidence interval of the normal measurement errors. The confidence interval is usually determined as ±(6–7) σ in industrial applications (Clewer Bernard, 1986).

2) bad data in timing correlation.

The microgrid electrical data sequence in time series can also be expressed as

$$\mathbf{z}_{k+1} = f(\mathbf{x}_k) + \mathbf{q}_k \tag{5}$$

where k is the time stamp, $f(\cdot)$ is the equation expression of the microgrid model mapping in time series, and $\mathbf{q}_k$ is the surge of electrical measurement.

When $\mathbf{q}_k$, i.e. the difference between the present measured value and the predicted value at the previous sampling time, is very big, there comes an outlier. This outlier may represent bad data. It can also be caused by the sudden change of the microgrid operating state. A further timing correlation method is needed to distinguish the two situations, which will be described later in **section 3**.

The key to bad data detection lies in the processing of data features. The process is divided into two main steps.

1) Features extraction: the procedure of estimating or predicting the features of bad data. The features include both electrical features and statistical features. The electrical features represent the distance between the measurement z and the true value $h(x)$. The statistical features represent the distance between the measurement z_{k+1} in sampling time k+1 and the true value $f(x_k)$ in sampling time k.
2) Features analysis: using mathematical statistics, data clustering, or other unsupervised methods to approach the interface between normal data and bad data in certain feature dimensions.

The traditional bad data detection method is based on State Estimation.

The diagram of bad data detection based on State Estimation is shown in **Figure 3**.

When the model of the power system can be analytically resolved as expression $h(\cdot)$, the estimated values $\hat{X}$ of x can be obtained through a State Estimator according to the measurement vector z and the prior knowledge σ from the

data acquisition system. The electrical features, i.e., residuals $r = z - h(\hat{X})$ are obtained.

Then, the probability distribution $f(\mathbf{r}\mathbf{r}^{\mathrm{T}})$ of the residuals $\mathbf{r}$ is used as a hypothesis test to detect bad data. The existence of bad data $\mathbf{z}_b$ can affect the results of the State Estimation, i.e., residuals $\mathbf{r}$, leading $f(\mathbf{r}\mathbf{r}^{\mathrm{T}})$ to change. Therefore, in the vicinity of the boundary where the threshold γ is located, a false or miss detection may occur.

2.2 Bad Data Detection Based on Online Sequential Machine Learning

The electrical features of microgrid measurements have the most abundant prior knowledge for bad data detection. The analytical model $h(\cdot)$ of the microgrid can be approximately fitted as $\hat{h}(\cdot)$ by supervised online sequential machine learning, as long as plenty of microgrid historical measurements and simulation data (e.g. data from the SIMULINK model of the microgrid in (Beg et al., 2017)) are given. The schematic of the online sequential machine learning based bad data detection is shown in **Figure 4**.

Learning from historical data, the online sequential machine learning based bad data detection method constructs an online updating error-filtering map between the historical electrical data sequence and the historical power flow first and then the updated map predicts the true value $\hat{h}(x)$ out of the present measurement z. Subsequently, the electrical feature $z - \hat{h}(x)$ can be obtained.

Since it is hard to discover the statistical properties of the prediction of the machine learning method, the analysis of the feature $z - \hat{h}(x)$ cannot be carried out by statistical hypothesis testing. Thus, the unsupervised machine learning method, clustering is used to do the job. Based on the similarity of the data itself, clustering analysis can automatically sort normal data and bad data in different clusters without any prior knowledge. Due to the uncertainty of the boundary between normal data and bad data, a false or missed detection will occur in the vicinity of the interface.

2.3 Bad Data Detection Based on Statistical Analysis in Time Series

Micro-grid is a strong nonlinear time-varying system. Every measurement of the microgrid is not independent but restricted to the electrical mechanism. Therefore, the statistical features of the data in time series indirectly reflect the electrical features and can be used for bad data detection. The schematic of the bad data detection based on the statistical analysis in time series is illustrated in **Figure 5**.

When an outlier (data point p+1) occurs in the microgrid electrical data series, the variance and correlation coefficient of the data sequence in a sliding window with enough width N shows different degrees of the surge. Note that the surge of the variance is $\Delta D(p+1)$ and the surge of the correlation coefficient is $\Delta\rho(p+1)$. The $\Delta D(p+1)$ reflects the continuity of a single-dimensional data sequence, which can be used to recognize outliers. But the outliers can not only be caused by the bad data, but also by the sudden change of the microgrid operating state. When there exists a sudden change of the microgrid operating state, the $\Delta D(p+1)$ is also significant. Under such a situation, the $\Delta\rho(p+1)$,

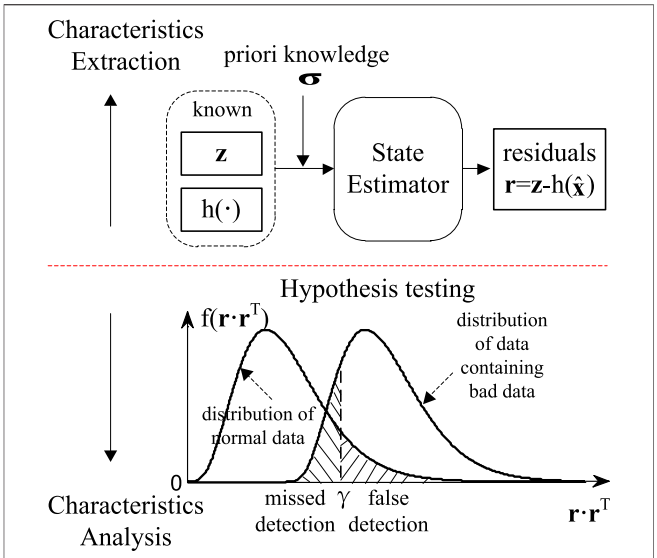

FIGURE 3 | Bad data detection based on state estimation.

reflecting the correlation between the multi-dimensional data sequences, can be used to further distinguish the bad data based on the correlation between different electrical measurements.

Since the operating state of the microgrid changes very often, the threshold of $\Delta D(p+1)$ and $\Delta\rho(p+1)$ cannot be determined by a fixed statistical hypothesis testing. So, clustering is used to analyze the two statistical features and sort normal data, outliers, and bad data in different clusters. A false or missed detection can also happen near the boundary of different clusters.

2.4 OSELM Algorithm

A combination of two machine learning algorithms, the supervised ELM and unsupervised DBSCAN, is used for bad data detection in our previous work. Compared to other machine learning algorithms, ELM is well known for its unmatched training speed and great potential for algorithm evolution. Detailed information on ELM and DBSCAN can be referred to (Huang et al., 2018). The OSELM (Liu et al., 2015) which is used in this paper is briefly introduced on the basis of ELM. The network structure and parameters of ELM are shown in Figure A1 in the appendix. Through sequential learning, OSELM can update the machine learning model online, which makes the model more adaptive in the application of time-series data.

3 SEQUENTIAL DETECTION *VIA* DATA-DRIVEN APPROACH

According to **section 2**, OSELM is a brand-new online sequential machine learning algorithm that can quickly approximate and update the error-filtering map between the measurements and the true values by recursive linear regression. DBSCAN is very suitable for distinguishing outliers with non-Gaussian distributions, e.g. bad data.

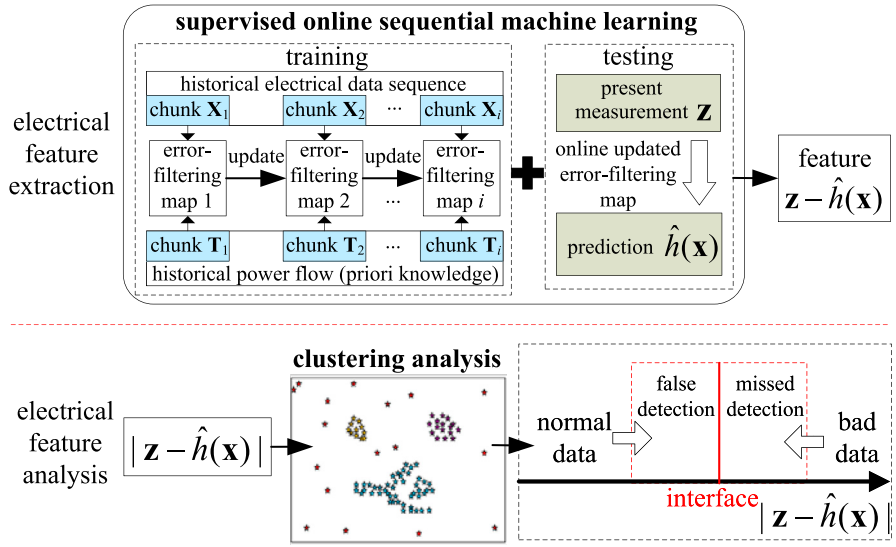

FIGURE 4 | Bad data detection based on online sequential machine learning.

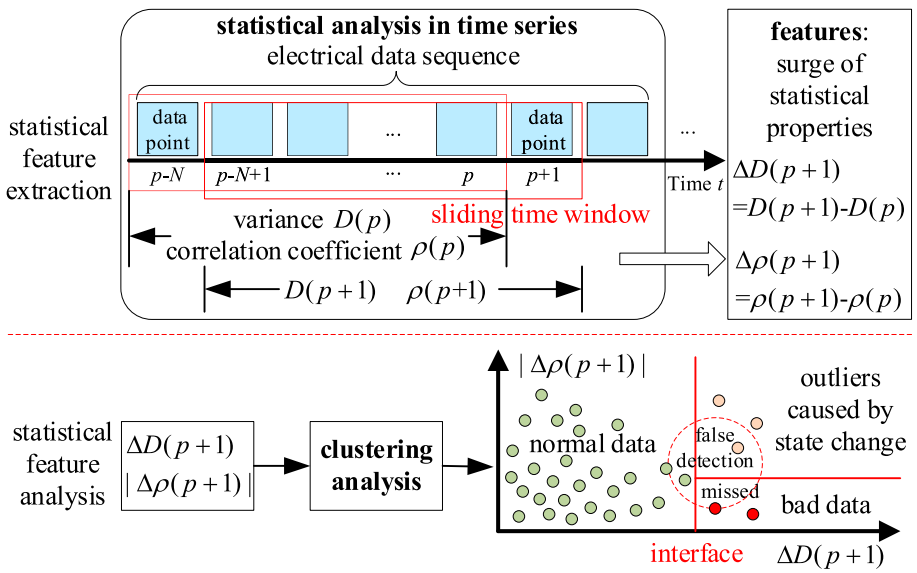

FIGURE 5 | Bad data detection based on statistical analysis in time series.

Therefore, the combination of OSELM and DBSCAN can quickly realize the sequential detection of the micro-grid bad data. But such a supervised machine learning method, relying on data training, is not sensitive enough to some unfamiliar operating modes or states.

The unsupervised statistical analysis in the time series method, which uses the statistical features (the surge of the variance and the correlation coefficient) in a sliding time window, is proposed to recognize the sudden change of the microgrid operating states.

On this basis, a sequential bad data detection method is proposed by using both the electrical features and the statistical features. The proposed sequential bad data detection method is described as follows. The application details of the proposed statistical analysis in the time series method are explained later.

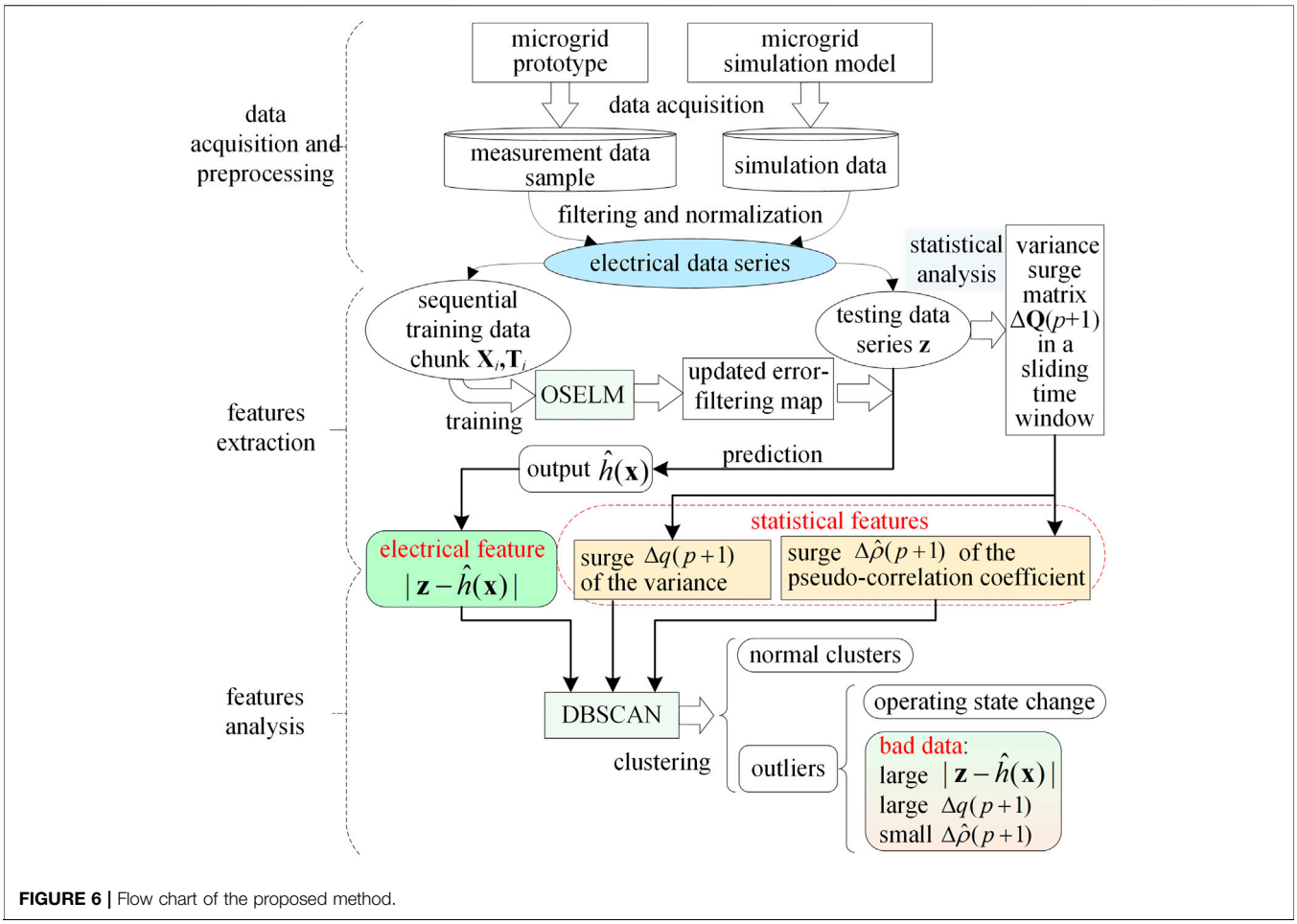

FIGURE 6 | Flow chart of the proposed method.

3.1 Sequential Bad Data Detection

Guided by the previously mentioned two detection ideas, a sequential detection method using a data-driven approach is proposed. It combines the OSELM, the statistical analysis in time series, and the DBSCAN. The flow chart of this method is illustrated in **Figure 6**.

The process of the method is mainly divided into the following steps.

1) Data acquisition and preprocessing.

Collect, screen, and normalize the measurement data of the microgrid prototype and the simulation data of the corresponding microgrid simulation model to form an electrical data series. Next, this processed data series is split into the sequential training data chunks $\mathbf{X}_i$ and $\mathbf{T}_i$, (i = 1, 2, . . .) and the testing data series z. The sequential training data chunks, input matrix $\mathbf{X}_i$ come from the old measurement data, and the other sequential training data chunks, target matrix $\mathbf{T}_i$ is from the simulation data corresponding to X_i. Meanwhile, the testing data series z is acquired from the current measurement data.

2) Features extraction.

Based on the recursive training method of the OSELM algorithm, the OSELM model is trained by $\mathbf{X}_i$ and $\mathbf{T}_i$, (i = 1, 2, . . .) to build an online updating error-filtering map. Using the updated error-filtering map to predict the testing data series z, the output matrix $\hat{h}(x)$ is obtained, and then $|z - \hat{h}(x)|$ is extracted as the electrical feature, i.e. the error (including the gross error) in z.

At the same time, the statistical analysis method is developed to calculate the variance surge matrix ΔQ (p+1) of the testing data series z in a sliding time window, where p+1 is the time stamp. The surge of the variance $\Delta q(p+1)$ and the surge of the pseudo-correlation coefficient $\Delta\hat{\rho}(p+1)$ are extracted as the statistical features sequentially.

3) Features analysis.

The aforementioned three features are clustered by DBSCAN to obtain normal clusters and outliers. Outliers with large $|z - \hat{h}(x)|$, large $\Delta q(p+1)$, and small $\Delta\hat{\rho}(p+1)$ are identified

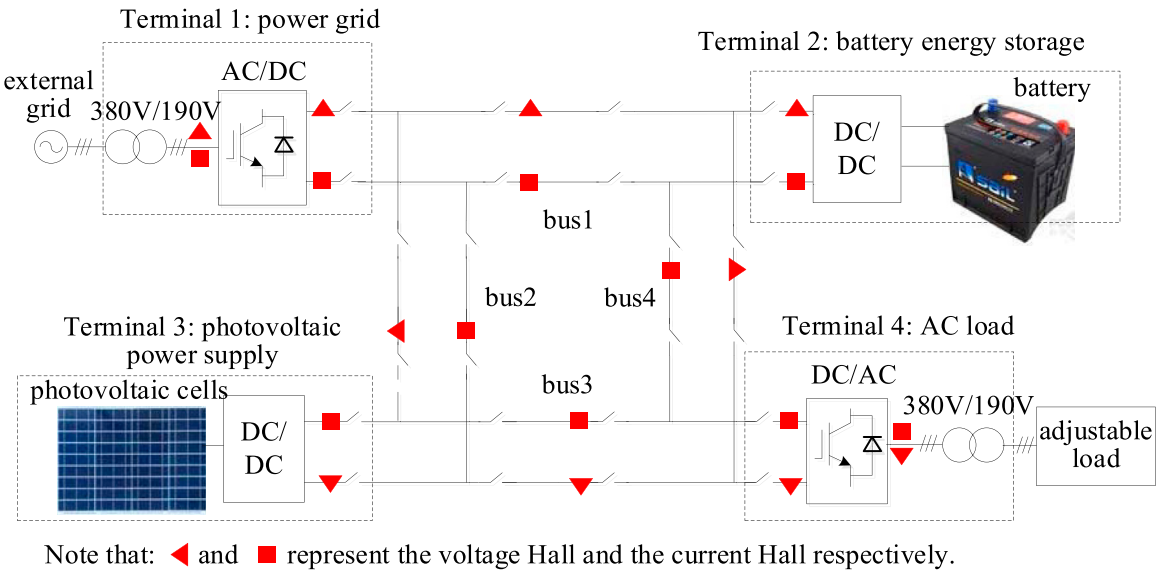

FIGURE 7 | Topology of the DC microgrid prototype.

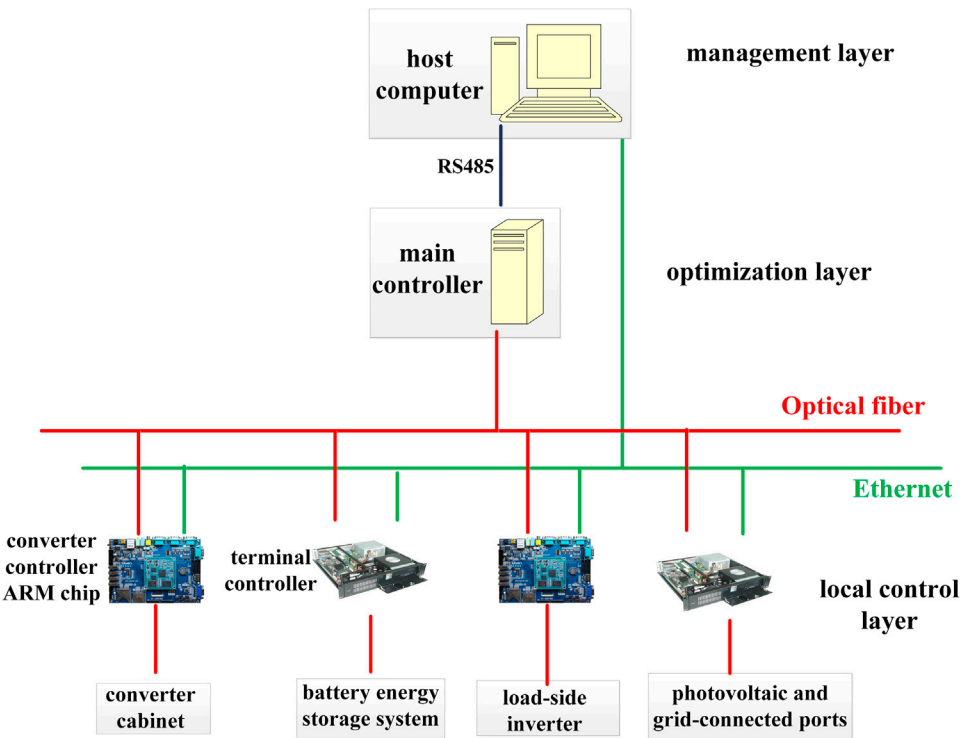

FIGURE 8 | Control structure of the DC microgrid prototype.

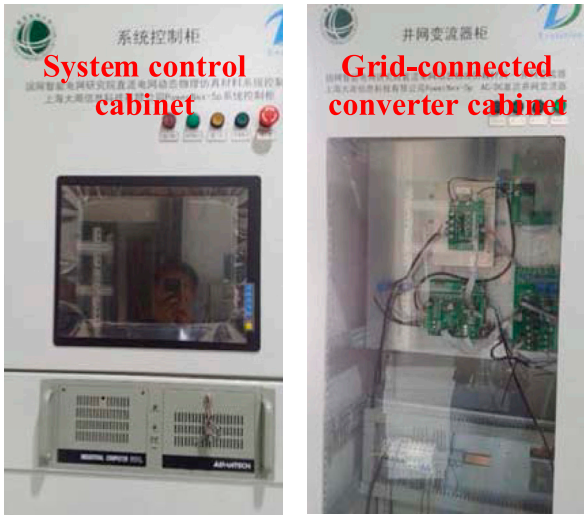

FIGURE 9 | Partial components display of the DC microgrid prototype.

as bad data. The other outliers are recognized as the change of the microgrid operating state.

3.2 Statistical Analysis in Time Series

1) Statistical property of data sequence.

Take the data sequence $z^{M\times N}(p)$ out of the microgrid measurement matrix z within the fixed time window width N at the pth sampling time. According to **Eq. 2**, we can see

$$\mathbf{z}^{M\times N}(p) = \mathbf{h}[x(t)] + \mathbf{v}(t), t = p - N + 1, p - N + 2, ..., p \quad (6)$$

where t is the time stamp, M is the dimension of the electrical measurements in z.

Calculate the covariance matrix $\mathbf{Q}(p)$ of the data sequence $z^{M\times N}(p)$.

$$\mathbf{Q}(p) = Cov(\mathbf{z}^{M\times N}(p)) = E\left\{[\mathbf{z}^{M\times N}(p)][\mathbf{z}^{M\times N}(p)]^T\right\} \quad (7)$$

where E is the expectation function.

The entries of matrix $\mathbf{Q}(p)$ are

$$\begin{cases} q_{ii}(p) = E[z_i(p) - \bar{z}_i(p)]^2 \\ q_{ij}(p) = E\left\{[z_i(t) - \bar{z}_i(p)][z_j(t) - \bar{z}_j(p)]\right\} \end{cases} \quad (8)$$
$$i, j = 1, 2, ..., M; i \neq j; t = p - N + 1, p - N + 2, ..., p$$

where $z_i(t)$ is the ith electrical measurement at sampling time t, $\bar{z}_i(p)$ is the average of the ith electrical measurement sequence over the time window of width N, the diagonal entry $q_{ii}(p)$ is the variance of the ith electrical measurement in the data sequence at the sampling time p, $q_{ij}(p)$ is the covariance of the ith electrical measurement and the jth electrical measurement, and $q_{ij}(p) = q_{ji}(p)$.

2) Statistical features in sliding time window.

Slide the time window with fixed width N forward by one data point. During this process, the surge of the variance matrix $\mathbf{Q}$ is

$$\Delta\mathbf{Q}(p+1) = \mathbf{Q}(p+1) - \mathbf{Q}(p) \quad (9)$$

The entries of $\Delta\mathbf{Q}$ $(p+1)$, i.e. the surge of the variance $\Delta q_{ii}(p+1)$ and covariance $\Delta q_{ij}(p+1)$ at the $(p+1)$th sampling time is derived as **Eq. 10** under the approximation that $\bar{z}_i(p+1) \approx \bar{z}_i(p)$ (marked as $\bar{z}_i$) when N is large enough. At the same time, we assume that the surges before the sampling time $(p+1)$ have been already detected and eliminated. That is to say, $z_i(p - N + 1) \approx \bar{z}_i$. Under such conditions, the following equation can be deprived.

$$\begin{cases} \Delta q_{ii}(p+1) = q_{ii}(p+1) - q_{ii}(p) \approx \frac{1}{N}[z_i(p+1) - \bar{z}_i]^2 \\ \Delta q_{ij}(p+1) = q_{ij}(p+1) - q_{ij}(p) \approx \frac{1}{N}\left\{[z_i(p+1) - \bar{z}_i][z_j(p+1) - \bar{z}_j]\right\} \end{cases}$$
$$i, j = 1, 2, ..., M; i \neq j \quad (10)$$

According to **Eq. 10**, if the new arrived electrical measurement $z_i(p+1)$ is a normal data, it is in the vicinity of $\bar{z}_i$, and then $\Delta q_{ii}(p+1)$ will be quite small. On the contrary, if $z_i(p+1)$ is an outlier, $\Delta q_{ii}(p+1)$ is large enough to be defined as a surge. So, $\Delta q_{ii}(p+1)$ can be used for outlier detection. The outlier may be caused by the bad data. But, it can also be caused by the sudden change of the microgrid operating state. Therefore, the single statistical feature $\Delta q_{ii}(p+1)$ is not enough for bad data detection.

When the outlier $z_i(p+1)$ is bad data, the other statistical feature $\Delta q_{ij}(p+1)$ is also obvious to be defined as a surge. And it is quite smaller than $\Delta q_{ii}(p+1)$, because $z_j(p+1)$ is very close to $\bar{z}_j$. But, when the outlier $z_i(p+1)$ is caused by the sudden change of the microgrid operating state, the change of $z_i(p+1)$ will result in the change of other electrical measurements $z_j(p+1)$ because they have strong electrical relationships with each other. Thus, some of $z_j(p+1)$ are

TABLE 1 | Operation modes of the DC microgrid prototype.

Mode	Grid-Connected Converter	Battery Energy Storage Terminal	Photovoltaic Terminal
1	Voltage control	Droop control	Lockout
2	Lockout	Voltage control	MPPT
3	Voltage control	Droop control	MPPT
4	Constant power control	Voltage control	MPPT

TABLE 2 | Confusion matrix.

		Observation		Total
		1	0	
Classification	1	TP	FP	Positive
	0	FN	TN	Negative
Total		Positive	Negative	NN = TP + FP + TN + FN

much larger than $\bar{z}_j$, which makes these $\Delta q_{ij}(p+1)$ very close to $\Delta q_{ii}(p+1)$.

Concerning the concept of the correlation coefficient $\rho_{ij}(p+1) = \frac{q_{ij}(p+1)}{\sqrt{q_{ii}(p+1)}\sqrt{q_{jj}(p+1)}}$, we define $\Delta\hat{\rho}_{ij}(p+1)$ the surge of the pseudo-correlation coefficient as **Eq. 11**.

$$\Delta\hat{\rho}_{ij}(p+1) = \frac{\Delta q_{ij}(p+1)}{\Delta q_{ii}(p+1)} = \frac{z_j(p+1) - \bar{z}_j}{z_i(p+1) - \bar{z}_i}, i \neq j \tag{11}$$

If the outlier $z_i(p+1)$ is caused by the bad data, $\Delta\hat{\rho}_{ij}(p+1) \to 0$. If it is caused by the sudden change of the microgrid operating state, $z_j(p+1)$ has an electrical relationship with $z_i(p+1)$, $|\Delta\hat{\rho}_{ij}(p+1)| \in [0, 1]$.

For the application of $|\Delta\hat{\rho}_{ij}(p+1)|$, we average it in the dimension j as follows.

$$\left|\Delta\hat{\rho}_i(p+1)\right| = \frac{1}{M-1}\sum_{j=1, i\neq j}^{M}\left|\Delta\hat{\rho}_{ij}(p+1)\right| \tag{12}$$

So, $|\Delta\hat{\rho}_{ij}(p+1)|$ can be used as another statistical feature to further distinguish bad data from outliers caused by the sudden change of microgrid operating states.

4 CASES STUDY

4.1 Acquisition and Preprocessing of Data

The data sequence of the microgrid is obtained from a four-terminal ring-shaped DC microgrid prototype and its simulation model. The topology, control structure, and partial components of the prototype are illustrated respectively in **Figures 7–9**.

According to its control strategy, the microgrid has four operation modes, which are shown in **Table 1**.

There are 24 kinds of electrical measurements collected from the microgrid prototype, namely: terminal voltage and terminal current of the four terminals [U_{p1}, U_{p2}, U_{p3}, U_{p4}, I_{p1}, I_{p2}, I_{p3}, I_{p4}], four DC buses voltage [U_{dc1}, U_{dc2}, U_{dc3}, U_{dc4}], the current flowing through the four positive DC bus [I_{dc1}, I_{dc2}, I_{dc3}, I_{dc4}], the power output of the four terminals [P_1, P_2, P_3, P_4], the active power and reactive power of the grid side [P_{grid}, Q_{grid}], the active power and reactive power of the load side [P_{load}, Q_{load}].

The microgrid prototype can be switched between the four operating modes in **Table 1** by issuing control commands from the host computer. The data sequence is obtained from the microgrid prototype and its SIMULINK simulation program in the above four control models in a month's operation. Six sets of testing data were randomly selected. The sampling frequency was 10 Hz, and the sampling time was 13 min 20 s. The Transient processes between different operating modes are removed. The reasons are as follows. First, the physical mechanism of the transient process is clear, rather than caused by uncertainty or unfamiliar mechanisms. Second, the transient process can be detected by the microgrid operation mode switching control signal to know the time of its occurrence, and according to the end of the wide fluctuation of the data to know the time of its end. Therefore, it is not the target of point anomaly detection and contextual anomaly detection in this paper. Each row of the testing data matrix is sorted by electrical quantities order [P_1, P_2, P_3, P_4, P_{grid}, P_{load}, Q_{grid}, Q_{load}, U_{dc1}, U_{dc2}, U_{dc3}, U_{dc4}, U_{line1}, U_{line2}, U_{line3}, U_{line4}, I_{dc1}, I_{dc2}, I_{dc3}, I_{dc4}, I_{line1}, I_{line2}, I_{line3}, I_{line4}].

All testing data input and output are scaled, taking the reference value p = 6 kW, Q = 0.5 kVar, U = 550 V, I = 10 A.

4.2 Simulation Cases Design

Parameters Design.

1) The number k of hidden layer nodes in OSELM is set to 80, and the excitation function g (·) is the sigmoid function.
2) The neighborhood radius *Eps* and the density threshold *MinPts* of the neighborhood in DBSCAN are set to 0.005 and 4, respectively.

TABLE 3 | Detection Performance Comparison between the Three Methods in case 1.

Testing Data	Method A		Method B		Method C		Performance Sorting	
	R_r (%)	Time (s)	R_r (%)	Time (s)	R_r (%)	Time (s)	R_r	Time
Dataset 1	76.4	7.4	68.7	16.3	84.5	21.7	B < A < C	A < B < C
Dataset 2	72.6	6.9	69.0	15.2	83.4	20.3	B < A < C	A < B < C
Dataset 3	78.2	8.3	71.2	14.6	85.3	21.1	B < A < C	A < B < C
Dataset 4	73.0	7.5	66.3	15.4	79.8	20.6	B < A < C	A < B < C
Dataset 5	74.3	7.8	74.5	15.9	88.6	22.4	A < B < C	A < B < C
Dataset 6	78.6	6.2	72.7	14.7	85.9	19.3	B < A < C	A < B < C

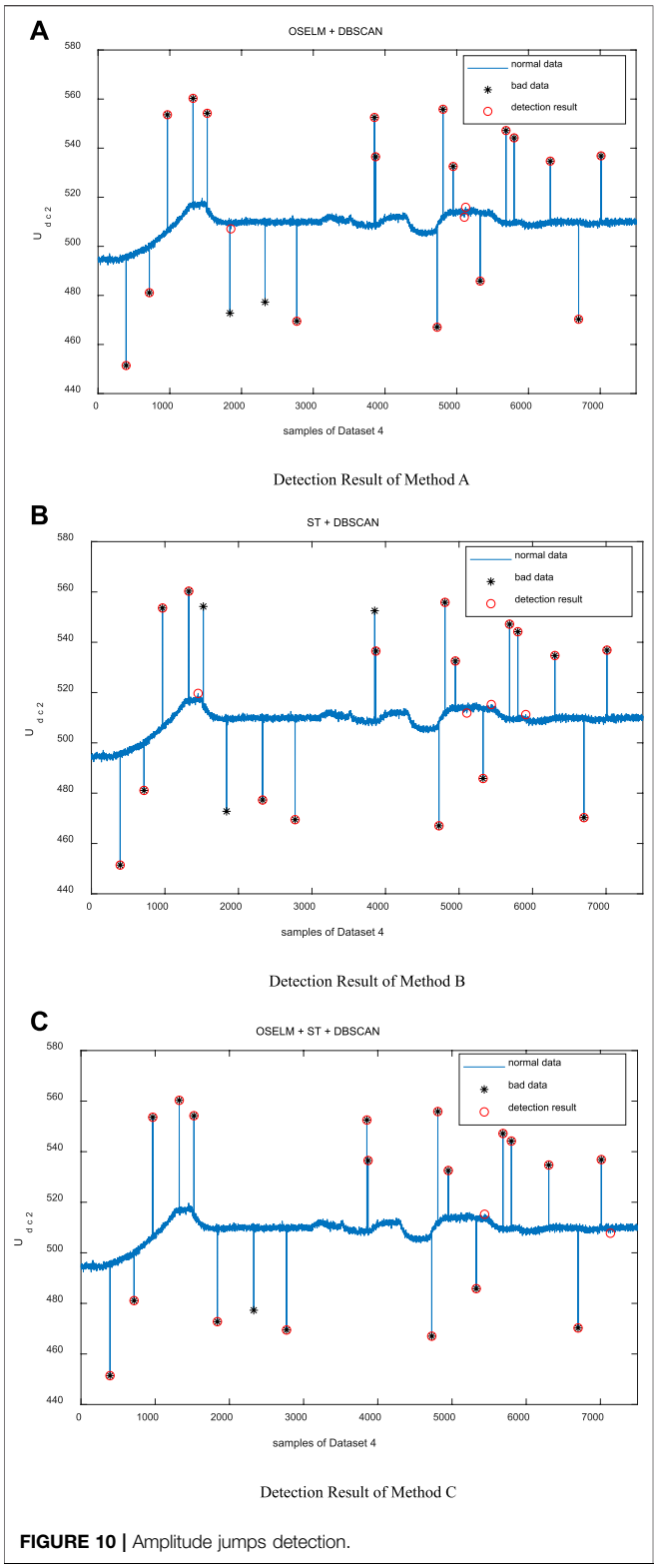

FIGURE 10 | Amplitude jumps detection.

Simulation Environment.

1) The simulation software is MATLAB R2018b.

2) The computer configuration for simulation is core i5 processor with 2.4 GHz frequency plus DDRIII memory bank with 8 Gbps memory

4.2.1 Simulation Cases

According to the normal distribution characteristics of the measurement error, the bad data with a gross error of 7–10 times the standard deviation of the measurement error were randomly preset in the six sets of testing data with a content of 5%. The measurement accuracies of the voltage Halls (Type: VSM500D) and the current Halls (Type: LA150-P) used in the micro-grid prototype in the simulation section of this paper are 0.008 and 0.01 respectively. The formula for calculating the standard deviation of errors can be found in reference (Huang et al., 2018).

The bad data preset in this paper includes cases of amplitude jumps (point anomalies), amplitude deviations, and amplitude shifts (contextual anomalies) (Xu et al., 2021). The simulation cases verify the effectiveness of the proposed method by comparing the detection performances of the three algorithms, including the OSELM + DBSCAN method, the ST (statistical analysis) + DBSCAN method, and the OSELM + ST + DBSCAN method. For point anomaly, the detection performance indicators include the right detection rate and calculation time. The right detection rate R_r is calculated by the correct detection times N_r, false detection times N_f, and missed detection times N_m. $R_r = N_r/(N_r + N_f + N_m)$. N_r, N_f, and N_m are confirmed by contrasting the detection results of bad data with the preset location of bad data. For contextual anomaly, the detection performance is quantified by the confusion matrix in **Table 2** (Hu et al., 2020; Li et al., 2021a; Li et al., 2021b; Hu et al., 2021; Jung, 2022).

In **Table 2**, TP (True Positive) represents true positive events, FN (False Negative) represents false negative events, FP (False Positive) represents false positive events, TN (True Negative) represents true negative events, and NN represents all events. Based on these events, indicators such as Recall (R), Precision (P), Accuracy (Acc), and Error (Err) are chosen to evaluate the detection performance. Their definitions are shown below

$$\begin{cases} R = card\,(\mathrm{TP})/card\,(\mathrm{TP} + \mathrm{FN}) \\ P = card\,(\mathrm{TP})/card\,(\mathrm{TP} + \mathrm{FP}) \\ Acc = card\,(\mathrm{TP} + \mathrm{TN})/card\,(\mathrm{NN}) \\ Err = 1 - Acc \end{cases} \tag{13}$$

where $card\,(\bullet)$ is the counting function. Large values of R, P, and Acc with a small value of Err represent good detection performance.

The OSELM + DBSCAN method, ST + DBSCAN method, and OSELM + ST + DBSCAN method are denoted respectively as methods A, B, and C. The bad data detection results are carried out by using methods A, B, and C for simulation in each case. Each simulation case repeats 10 times, and the average detection performances are calculated.

TABLE 4 | Detection Performance Comparison between the Three Methods in case 2. The bold values mean the best detection performance among the three detection methods (Method A, Method B, and Method C).

Testing Data	Methods	*R*	*P*	*Acc*	*Err*
Dataset 1	Method A	**0.983**	0.736	0.734	0.236
	Method B	0.962	0.823	0.810	0.190
	Method C	0.980	**0.845**	**0.838**	**0.162**
Dataset 2	Method A	0.959	0.701	0.692	0.308
	Method B	0.958	0.768	0.747	0.253
	Method C	**0.982**	**0.808**	**0.803**	**0.197**
Dataset 3	Method A	0.961	0.732	0.717	0.283
	Method B	0.965	0.813	0.794	0.206
	Method C	**0.966**	**0.841**	**0.821**	**0.179**
Dataset 4	Method A	0.959	0.694	0.687	0.313
	Method B	**0.971**	0.770	0.759	0.241
	Method C	0.966	**0.804**	**0.792**	**0.208**
Dataset 5	Method A	0.976	0.746	0.742	0.258
	Method B	0.979	0.844	0.835	0.165
	Method C	**0.980**	**0.895**	**0.883**	**0.117**
Dataset 6	Method A	0.949	0.692	0.673	0.327
	Method B	0.954	0.767	0.744	0.256
	Method C	**0.957**	**0.812**	**0.787**	**0.213**

TABLE 5 | Detection Performance Comparison between the Three Methods in case 3. The bold values mean the best detection performance among the three detection methods (Method A, Method B, and Method C).

Testing Data	Methods	*R*	*P*	*Acc*	*Err*
Dataset 1	Method A	0.952	0.738	0.717	0.283
	Method B	0.954	0.769	0.746	0.254
	Method C	**0.957**	**0.819**	**0.793**	**0.207**
Dataset 2	Method A	0.974	0.677	0.675	0.325
	Method B	0.976	0.731	0.728	0.272
	Method C	**0.977**	**0.775**	**0.770**	**0.230**
Dataset 3	Method A	0.961	0.695	0.684	0.316
	Method B	0.964	0.764	0.749	0.251
	Method C	**0.967**	**0.823**	**0.805**	**0.195**
Dataset 4	Method A	0.964	0.677	0.669	0.331
	Method B	**0.969**	**0.776**	0.754	0.246
	Method C	0.968	0.775	**0.772**	**0.228**
Dataset 5	Method A	0.993	0.723	0.733	0.267
	Method B	0.993	0.801	0.807	0.193
	Method C	**0.994**	**0.856**	**0.859**	**0.141**
Dataset 6	Method A	0.931	0.687	0.656	0.344
	Method B	0.936	0.744	0.710	0.290
	Method C	**0.940**	**0.798**	**0.761**	**0.239**

4.3 Simulation Results and Analysis

1) **Case 1**: amplitude jumps (point anomaly).

The amplitude jumps are those discrete data points that deviate far from normal data. The detection performances are shown in **Table 3**.

As can be seen from **Table 3**, for point anomalies, the three methods have good detection results (R_r is between 66% and 89%). Except for Dataset 5, the detection accuracy of Method C is better than that of Method A and Method B, but the calculation time is sacrificed. Relatively speaking, Method B has the worst detection performance.

Randomly select an electrical measurement U_{dc2} from Dataset four in Case 1 to visually display the detection effects of the three methods as shown in **Figure 10**.

Through **Figure 10**, it is seen that all three methods can detect point anomaly quite well with a few false detections and missed detections. Method C shows the best performance.

2) **Case 2**: amplitude deviations (contextual anomaly).

The amplitude deviations are those data sequences that deviate far from normal data series in a stepwise way. The detection performances are shown in **Table 4**.

In **Table 4**, the indicators corresponding to the best detection performance in each dataset are bolded. It can be seen that Method C shows the best performance when detecting the amplitude deviations, except for *R* in Dataset 1 and Dataset 4.

Randomly select the electrical measurement P_4 from Dataset 1 in Case 2 to visually display the detection effects of the three methods as shown in **Figure 11**.

Through **Figure 11**, it is seen that all three methods can detect the amplitude deviation quite well with a few false detections and missed detections. Method C shows the best performance.

3) **Case 3**: amplitude shifts (contextual anomaly).

The amplitude shifts are those data sequences that slowly shift and continuously deviate from normal data series. The detection performances are shown in **Table 5**.

Through **Table 5**, it can be seen that Method C shows the best performance when detecting the amplitude shifts, except for *R* and *P* in Dataset 4.

Randomly select the electrical measurement I_{line1} from Dataset 5 in Case 3 to visually display the detection effects of the three methods as shown in **Figure 12**.

Through **Figure 12**, it is seen that all three methods can detect the amplitude shift quite well with a few false detections and missed detections. Method C shows the best performance.

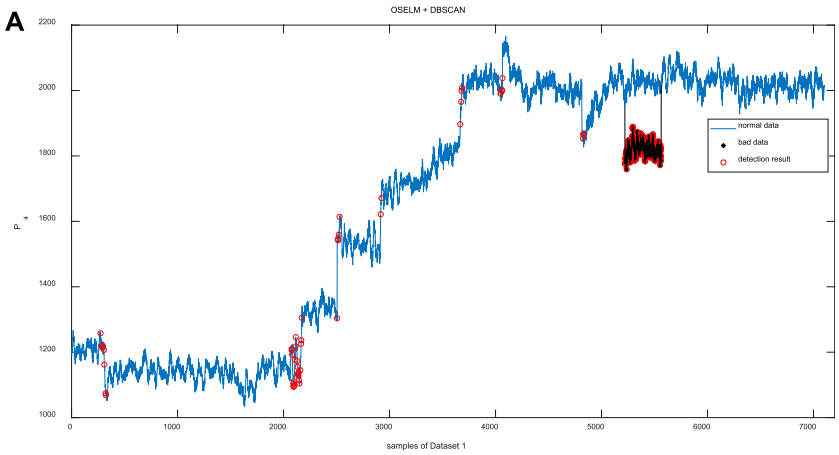

(a) Detection Result of Method A

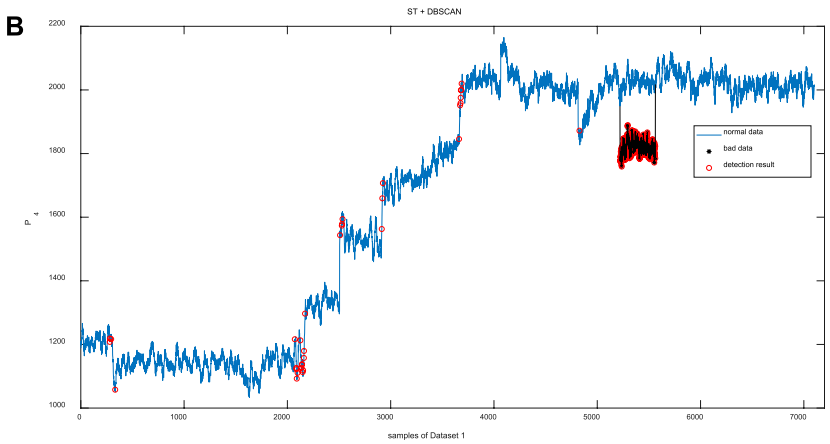

(b) Detection Result of Method B

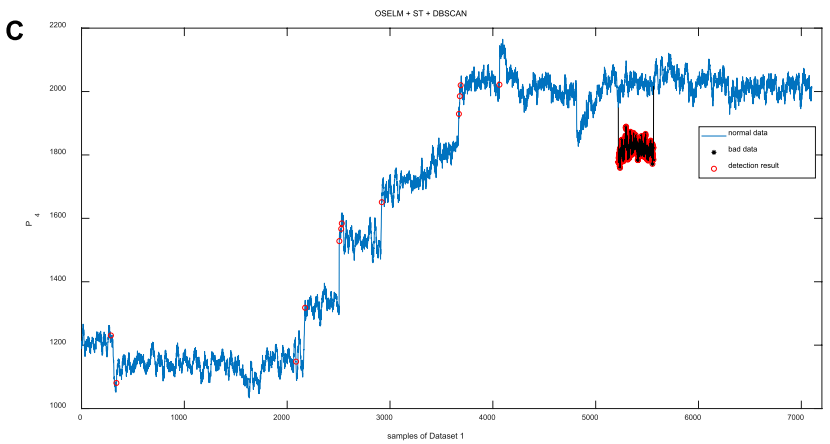

(c) Detection Result of Method C

FIGURE 11 | Amplitude deviations detection.

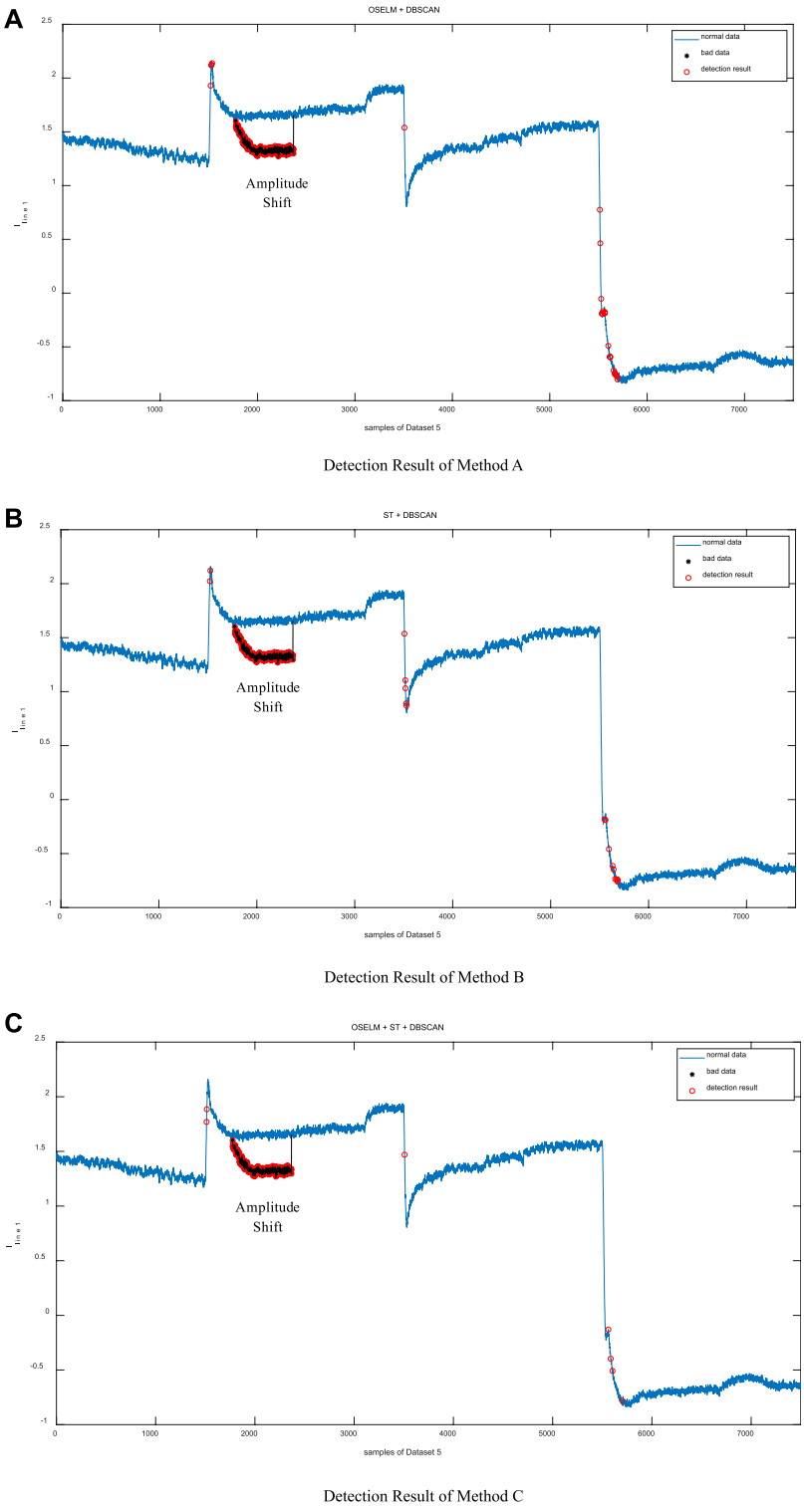

FIGURE 12 | Amplitude shifts detection.

5 CONCLUSION

In this paper, the statistical surge feature (ST) is first used for bad data detection, including point anomaly detection and contextual anomaly detection. On this basis, a sequential detection method that combines OSELM, ST, and DBSCAN is proposed for micro-grid bad data detection. The performance of this method is verified by a four-terminal ring-shaped DC

micro-grid prototype. By comparing with the existing OSELM + DBSCAN method and the ST + DBSCAN method, it is demonstrated that the proposed OSELM + ST + DBSCAN method has the best detection performance. To be more specific, 1) The OSELM + ST + DBSCAN can detect both point anomaly and contextual anomaly, such as amplitude jumps, amplitude deviations, and amplitude shifts. 2) The OSELM + ST + DBSCAN method can realize the best bad data detection accuracy at the cost of a small increase of computation.

DATA AVAILABILITY STATEMENT

The original contributions presented in the study are included in the article/**Supplementary Material**, further inquiries can be directed to the corresponding author.

AUTHOR CONTRIBUTIONS

All authors listed have made a substantial, direct, and intellectual contribution to the work and approved it for publication.

ACKNOWLEDGMENTS

The authors would like to thank Professor Andrew Kusiak at the University of Iowa for his academic support on this paper.

SUPPLEMENTARY MATERIAL

The Supplementary Material for this article can be found online at: https://www.frontiersin.org/articles/10.3389/fenrg.2022.861563/full#supplementary-material

REFERENCES

Almalawi, A., Yu, X., Tari, Z., Fahad, A., and Khalil, I. (2014). An Unsupervised Anomaly-Based Detection Approach for Integrity Attacks on SCADA Systems. *Comput. Secur.* 46, 94–110. doi:10.1016/j.cose.2014.07.005

Anwar, A., Mahmood, A. N., and Pickering, M. (2017). Modeling and Performance Evaluation of Stealthy False Data Injection Attacks on Smart Grid in the Presence of Corrupted Measurements. *J. Comput. Syst. Sci.* 831, 58–72. doi:10.1016/j.jcss.2016.04.005

Araya, D. B., Grolinger, K., ElYamany, H. F., Capretz, M. A. M., and Bitsuamlak, G. (2017). An Ensemble Learning Framework for Anomaly Detection in Building Energy Consumption. *Energy Build.* 144, 191–206. doi:10.1016/j.enbuild.2017.02.058

Beg, O., Johnson, T., and Ali, D. (2017). Detection of False-Data Injection Attacks in Cyber-Physical Dc Microgrids. *IEEE Trans. Industrial Inf.* 13, 2693. doi:10.1109/tii.2017.2656905

Bosman, H. H., Iacca, G., Tejada, A., Wörtche, H. J., and Liotta, A. (2017). Spatial Anomaly Detection in Sensor Networks Using Neighborhood Information. *Inf. Fusion* 33, 41–56. doi:10.1016/j.inffus.2016.04.007

Bretas, N. G., and Bretas, A. S. (2015). A Two Steps Procedure in State Estimation Gross Error Detection, Identification, and Correction. *Int. J. Electr. Power & Energy Syst.* 73, 484–490. doi:10.1016/j.ijepes.2015.05.044

Clewer and Bernard, C. (1986). *State Estimation and Bad Data Detection in Electrical Power System*. Diss. Durham University.

Cramer, M., Goergens, P., and Schnettler, A. (2015). "Bad Data Detection and Handling in Distribution Grid State Estimation Using Artificial Neural Networks," in 2015 IEEE Eindhoven PowerTech, Eindhoven, Netherlands, 29 June-2 July 2015. doi:10.1109/ptc.2015.7232655

Do Coutto Filho, M. B., and de Souza, J. C. S. (2009). Forecasting-Aided State Estimation-Part I: Panorama. *IEEE Trans. Power Syst.* 24, 1667–1677. doi:10.1109/tpwrs.2009.2030295

Gu, W., Lou, G., Tan, W., and Yuan, X. (2017). A Nonlinear State Estimator-Based Decentralized Secondary Voltage Control Scheme for Autonomous Microgrids. *IEEE Trans. Power Syst.* 32, 4794. doi:10.1109/tpwrs.2017.2676181

Hu, X., Huaguang, Z., Dazhong, M., and Rui, W. (2020). A tnGAN-Based Leak Detection Method for Pipeline Network Considering Incomplete Sensor Data. *IEEE Trans. Instrum. Meas.* 70, 1–10. doi:10.1109/TIM.2020.3045843

Hu, X., Zhang, H., Dazhong, M., and Rui, W. (2021). Hierarchical Pressure Data Recovery for Pipeline Network via Generative Adversarial Networks. *IEEE Trans. Automation Sci. Eng.* 99, 1–11. doi:10.1109/tase.2021.3069003

Hu, Y., Kuh, A., Kavcic, A., and Nakafuji, D. (2011). "Real-time State Estimation on Micro-grids," in The 2011 International Joint Conference on Neural Networks, San Jose, CA, USA, 31 July-5 Aug. 2011. doi:10.1109/ijcnn.2011.6033385

Huang, H., Liu, F., Zha, X., Xiong, X., Ouyang, T., Liu, W., et al. (2018). Robust Bad Data Detection Method for Microgrid Using Improved ELM and DBSCAN Algorithm. *J. Energy Eng.* 144, 04018026. doi:10.1061/(asce)ey.1943-7897.0000544

Huang, S.-J., and Lin, J.-M. (2004). Enhancement of Anomalous Data Mining in Power System Predicting-Aided State Estimation. *IEEE Trans. Power Syst.* 19, 610–619. doi:10.1109/tpwrs.2003.818726

Huang, Y., Tang, J., Cheng, Y., Li, H., Campbell, K. A., and Han, Z. (2016). Real-time Detection of False Data Injection in Smart Grid Networks: an Adaptive CUSUM Method and Analysis. *IEEE Syst. J.* 10, 532–543. doi:10.1109/jsyst.2014.2323266

Jung, A. (2022). *Machine Learning: The Basics*. Singapore: Springer. Available at: http://mlbook.cs.aalto.fi.

Li, H., Deng, J., Feng, P., Pu, C., Arachchige, D. K., and Cheng, Q. (2021). Short-Term Nacelle Orientation Forecasting Using Bilinear Transformation and ICEEMDAN Framework. *Front. Energy Res.* 9, 780928. doi:10.3389/fenrg.2021.780928

Li, H., Deng, J., Yuan, S., Feng, P., and Arachchige, D. K. (2021). Monitoring and Identifying Wind Turbine Generator Bearing Faults Using Deep Belief Network and EWMA Control Charts. *Front. Energy Res.* 9, 799039. doi:10.3389/fenrg.2021.799039

Li, S., Yilmaz, Y., and Wang, X. (2015). Quickest Detection of False Data Injection Attack in Wide-Area Smart Grids. *IEEE Trans. Smart Grid* 6, 2725–2735. doi:10.1109/tsg.2014.2374577

Liu, Y., He, B., Dong, D., Shen, Y., Yan, T., Nian, R., et al. (2015). "ROS-ELM: A Robust Online Sequential Extreme Learning Machine for Big Data Analytics," in *Proceedings of ELM-2014* (Cham: Springer International Publishing), 325–344.

Liu, Y., Ning, P., and Reiter, M. K. (2011). False Data Injection Attacks against State Estimation in Electric Power Grids. *ACM Trans. Inf. Syst. Secur. (TISSEC)* 14, 13. doi:10.1145/1952982.1952995

Mohammadpourfard, M., Sami, A., and Seifi, A. R. (2017). A Statistical Unsupervised Method against False Data Injection Attacks: A Visualization-Based Approach. *Expert Syst. Appl.* 84, 242–261. doi:10.1016/j.eswa.2017.05.013

Qiu, R., Lei, C., Xing, H., Zenan, L., and Haichun, L. (2017). *Spatio-Temporal Big Data Analysis for Smart Grids Based on Random Matrix Theory: A Comprehensive Study*. Ithaca, NY: arXiv preprint of Cornell University. *arXiv preprint arXiv:1708.04935*.

Rana, M., Li, L., and Li, Li. (2015). An Overview of Distributed Microgrid State Estimation and Control for Smart Grids. *Sensors* 15, 4302–4325. doi:10.3390/s150204302

Rana, M. M., and Li., L. (2015). Microgrid State Estimation and Control for Smart Grid and Internet of Things Communication Network. *Electron. Lett.* 512, 149–151. doi:10.1049/el.2014.3635

Ren, H., Liu, M., Li, Z., and Pedrycz, W. (2017). A Piecewise Aggregate Pattern Representation Approach for Anomaly Detection in Time Series. *Knowledge-Based Syst.* 135, 29–39. doi:10.1016/j.knosys.2017.07.021

Shahnia, F., Majumder, R., Ghosh, A., Ledwich, G., and Zare, F. (2010). Operation and Control of a Hybrid Microgrid Containing Unbalanced and Nonlinear Loads. *Electr. Power Syst. Res.* 808, 954–965. doi:10.1016/j.epsr.2010.01.005

Shyh-Jier, H., and Jeu-Min, L. (2002). Enhancement of Power System Data Debugging Using GSA-Based Data-Mining Technique. *IEEE Trans. Power Syst.* 17, 1022–1029. doi:10.1109/tpwrs.2002.804992

Wu, Y., Onwuachumba, A., and Musavi, M. (2013). "Bad Data Detection and Identification Using Neural Network-Based Reduced Model State Estimator," in 2013 IEEE Green Technologies Conference (GreenTech), Denver, CO, USA, 4-5 April 2013. doi:10.1109/greentech.2013.35

Wu, Y., Xiao, Y., Hohn, F., Nordstorm, L., Wang, J., and Zhao, W. (2017). Bad Data Detection Using Linear WLS and Sampled Values in Digital Substations. *IEEE Trans. Power Deliv.* 99, 1–8. doi:10.1109/TPWRD.2017.2669110

Xia, N., Gooi, H. B., Chen, S., and Hu, W. (2016). Decentralized State Estimation for Hybrid AC/DC Microgrids. *IEEE Syst. J.* 12, 434. doi:10.1109/JSYST.2016.2615428

Xu, F., Xue, A., Chang, N., Kong, H., and Xu, J. (2021). Research Status and Prospects of Detection, Correction and Recovery for Abnormal Synchrophasor Data in Power System. *Proc. CSEE* 41 (20), 6869–6886. doi:10.13334/j.0258-8013.pcsee.202180

Yang, L., Li, Y., and Li, Z. (2017). Improved-ELM Method for Detecting False Data Attack in Smart Grid. *Int. J. Electr. Power & Energy Syst.* 91, 183–191. doi:10.1016/j.ijepes.2017.03.011

Zhao, J., Liu, K., Wang, W., and Liu, Y. (2014). Adaptive Fuzzy Clustering Based Anomaly Data Detection in Energy System of Steel Industry. *Inf. Sci.* 259, 335–345. doi:10.1016/j.ins.2013.05.018

Zhao, J., Zhang, G., Scala, M. L., and Wang, Z. (2017). Enhanced Robustness of State Estimator to Bad Data Processing through Multi-Innovation Analysis. *IEEE Trans. Ind. Inf.* 134, 1610–1619. doi:10.1109/tii.2016.2626782

Conflict of Interest: The authors declare that the research was conducted in the absence of any commercial or financial relationships that could be construed as a potential conflict of interest.

Publisher's Note: All claims expressed in this article are solely those of the authors and do not necessarily represent those of their affiliated organizations, or those of the publisher, the editors and the reviewers. Any product that may be evaluated in this article, or claim that may be made by its manufacturer, is not guaranteed or endorsed by the publisher.

frontiers | Frontiers in Energy Research

METHODS
published: 17 June 2022
doi: 10.3389/fenrg.2022.889273

Series Arc Fault Diagnosis Based on Variational Mode Decomposition and Random Forest

Luyao Zhao[1], *Changchun Chi*[1]*, *Qiangqiang Zhao*[1] *and Haifeng Mao*[2]

[1]School of Electrical Engineering, Shanghai Dianji University, Shanghai, China, [2]Suzhou Future Electric Co., Ltd., Suzhou, China

In order to improve the accuracy of series arc fault detection and prevent fire accidents caused by series arc fault, a series arc fault simulation experiment circuit was built to obtain the low-frequency and high-frequency current waveform of series arc fault under different loads. The kurtosis, waveform factor, crest factor, pulse factor, and margin factor of low-frequency current waveform are extracted in the time domain. In the frequency domain, a method based on variational mode decomposition and energy entropy is proposed to extract the characteristic quantity of series arc faults. It was found that the energy entropy of the intrinsic mode function component with the largest variance contribution ratio will increase when a series of arc faults occur, and it was used as a characteristic quantity. Characteristic vectors were constructed based on time–frequency characteristic quantities, and the characteristic vector was trained based on the random forest algorithm to obtain the diagnosis model and analyze the series arc fault diagnosis. The analysis showed that the diagnostic accuracy of the model trained by the proposed method was above 97%, and the fault recognition effect was remarkable, which provides an important reference for the improvement of the series arc fault detection technology.

Keywords: series arc fault, IMF component, variational modal decomposition, energy entropy, random forest algorithm

OPEN ACCESS

Edited by:
Yahui Zhang,
Yanshan University, China

Reviewed by:
Srete Nikolovski,
Josip Juraj Strossmayer University of Osijek, Croatia
Ahmad Farid Abidin,
Faculty of Electrical Engineering UiTM, Malaysia

***Correspondence:**
Changchun Chi
changchun_chi@126.com

Specialty section:
This article was submitted to Smart Grids, a section of the journal Frontiers in Energy Research

Received: *04 March 2022*
Accepted: *02 May 2022*
Published: *17 June 2022*

Citation:
Zhao L, Chi C, Zhao Q and Mao H (2022) Series Arc Fault Diagnosis Based on Variational Mode Decomposition and Random Forest. Front. Energy Res. 10:889273. doi: 10.3389/fenrg.2022.889273

1 INTRODUCTION

According to the Fire Statistics Annual Report of China Fire Protection Association (CFPA) Shao (2020), the number of electrical fires in China has been on the rise in recent years, and the proportion of electrical fires ranks first among all types of fires, accounting for about 30%. Arc faults are one of the leading causes of electrical fires. In low-voltage distribution lines, series of arc faults may occur due to aging and damage of insulation of wires, poor connection of wires, or loose connection of electrical equipment (Xiong et al., 2016). A large amount of heat will be generated when the series of arc faults occurs in the line, which is easy to ignite combustible materials and lead to fire [Liu G. et al. (2017), Lin et al. (2021), Liu G. G. et al. (2017)]. In serious cases, explosions will occur, endangering personal safety. Therefore, in order to protect the safety of production and the safety of residents, effectively solving low-voltage series of arc faults has become a research hotspot for scholars at home and abroad.

The current series of arc fault detection technology has the problems of low detection ratio and ineffective identification under mixed loads. In the field of series arc fault detection and diagnosis, the detection methods for low-voltage series arc are mainly divided into two categories: 1) the arc is detected by the radiation, energy, and temperature changes of the arc. 2) Detect series arc faults by current and voltage waveform changes. Wang et al. (2019) and Xiong et al. (2017) used third-order

and fourth-order Hilbert fractal antennas to detect electromagnetic radiation (EMR) signals generated by DC arcs. The experimental results show that EMR can be used as a characteristic quantity to characterize a series of arc faults. The Hilbert transform can parse the signal into an analytic signal containing the instantaneous frequency and amplitude, but the disadvantage is that the Hilbert transform is only suitable for part of the frequency band of the electromagnetic radiation signal, and the method is greatly affected by environmental factors, and the positioning range is limited. Lala and Subrata, (2020), Jiang et al. (2021), Chen et al. (2015), Jingjing and Zhihong (2019), Miao et al. (2019) and Liu et al. (2019) took the empirical mode decomposition (EMD) energy entropy as the characteristic quantity of series arc fault. Although good results are obtained, the EMD energy entropy is used as a characteristic quantity, and there are end-point effects and modal aliasing. The methods of arc fault detection using radiation, temperature, and energy have great limitations, so the mainstream research methods are still based on current and voltage waveforms for arc identification. In the article by Chen et al. (2019),Qi et al. (2017),Yu et al. (2020),Ma et al. (2021), Zhang et al. (2018), and Gao et al. (2021), the wavelet transform is used to decompose the current and voltage waveform, and the energy in different frequency bands, the maximum value of detail signal in each frequency band, and the low-frequency approximation coefficient of adjacent periodic current are calculated as the characteristic quantities of series arc faults. The wavelet transform is based on the Fourier transform to refine the signal at multiple scales, and at the same time overcomes the shortcomings such as the window does not change with the frequency during local refinement; however, the wavelet transform is not ideal for the situation where the frequency bands of the useful signal and the noise overlap each other, and the problem of spectral aliasing is prone to occur. Karakose et al. (2018) and Cui and Tong. (2021) used S-transform and generalized S-transform to detect pantograph–catenary system arc faults and aviation arc faults, respectively. The S-transform uses a Gaussian window function, and the window width is proportional to the inverse of the frequency and do not need to select window functions. The selection of the function improves the defect of fixed window width, but the feature quantity extracted by S-transform has the problem of insensitivity to noise. This method is inaccurate in the frequency domain resolution in the higher frequency range, and the resolution is lower than that of the Fourier transform. The series current is an electrical parameter that is easily obtained in the traditional distribution line protection system. The currents in the series loop are equal in magnitude. In principle, the arc detection device can be installed at any point in the loop, and the sampling position is not restricted by the position of the arc in the loop. However, when the load terminal voltage is used as the detection signal, the power terminal voltage and the load terminal voltage are likely to introduce harmonic interference, resulting in misjudgment. So most scholars abandon the voltage and use the current signal as the target quantity for feature extraction. In the article by Syafi'i et al. (2018),Zhang et al. (2016), Karakose et al. (2018), Khafidli et al. (2018) and Wang et al. (2017), characteristic quantities in the frequency domain are extracted by fast Fourier transform, and the amplitude of the harmonic component and the all-phase spectrum is taken as characteristic quantities. However, the disadvantage is that the amount of calculation is large, and the Fourier transform has defects in the analysis of non-stationary time-varying signals, extracting feature quantities in the time domain is good for fault arc diagnosis of a single load line but not very good for circuits with mixed loads. In the article by Lin et al. (2020) and Cui et al. (2021), the series arc fault current waveform is analyzed in the time domain, and the periodic amplitude, the correlation, and the continuity between adjacent periodic current samples, the zero-rest time of the current, and the zero-rest time proportional coefficient of the two periodic currents are calculated as the characteristic quantity. However, it is not good to extract characteristic quantities in the time domain for circuits with different load mixtures. EMD energy entropy as a characteristic quantity has a modal aliasing problem.

In view of the above shortcomings and considering the actual low-voltage series arc fault detection requirements and the realization of the method application in the protection device, this article proposes an arc fault detection method based on time–frequency feature fusion. The specific contributions are as follows:

1) Simulate the series arc fault of different load types and mixed load types, and extract the low-frequency and high-frequency current waveforms when the load is working normally and when the series arc fault occurs. Feature quantities are extracted for low-frequency current components in the time domain.
2) Aiming at the extraction of high-frequency current component features, a series of arc fault feature extraction method based on VMD and energy entropy is studied.
3) Use the random forest algorithm to train and diagnose the extracted feature quantities.
4) Optimize the random forest algorithm to train the diagnostic model to improve its recognition rate and correct rate.

This article is organized as follows: **Section 2** conducts low-voltage series arc fault experiments, collects low-voltage AC current data, and performs waveform analysis; **Section 3** introduces the extraction method of arc time-domain feature quantity and the feature extraction method based on VMD to extract energy entropy; in **Section 4**, we build a random forest algorithm training diagnosis model, propose an arc fault diagnosis algorithm, and conduct sum simulation verification; the final conclusions are summarized in **Section 5**.

2 SERIES ARC FAULT SIMULATION EXPERIMENT

2.1 Experimental Environment

It is difficult to obtain the current waveform of series arc faults from actual distribution wires because of the uncertainty of the occurrence time and location of series arc faults. This article sets up a series of arc fault simulation experiment environments,

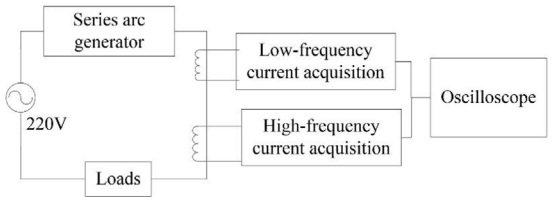

FIGURE 1 | Schematic diagram of the series arc fault simulation experiment circuit.

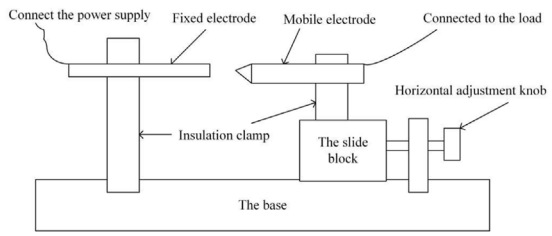

FIGURE 2 | Schematic diagram of the series arc fault generator.

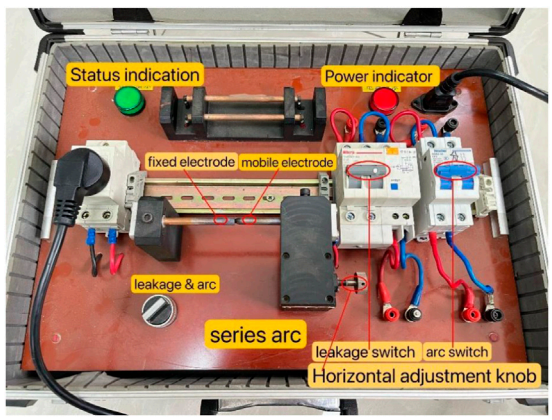

FIGURE 3 | Physical map of the arc fault generator.

which are composed of a power supply, series arc generator, signal acquisition module, and loads inspection (General Administration of Quality Supervision, 2014). The schematic diagram of the series arc fault simulation experiment is shown in **Figure 1**.

In this article, an arc generator is chosen to simulate the generation of arc faults. The series of arc generator is mainly composed of two electrodes. One electrode which is regarded as a mobile electrode is a carbon-graphite rod with a diameter of 6 ± 0.5 mm. The arc burning end of the electrode is made into a tip and equipped with a sliding block. The clearance between the two electrodes can be controlled by adjusting the horizontal adjusting knob. The other can be a 6 ± 0.5-mm-diameter copper rod set as a fixed electrode. The arc ends of both electrodes should be kept clean

TABLE 1 | Main hardware configuration of the series arc fault experiment.

Name	Model and parameter
The power supply	220 AC
The base	70 cm*60 cm*5 cm
Copper rod	φ6 mm
Low-frequency current transformer	DL-CT1005 APL 2000/1
High-frequency current transformer (custom)	Ratio 2000/1
Resistance	220 V/0–50 Ω
Vacuum cleaner	ZL100-TA 220 V/1000 W
Electric kettle	220 V 1500 W
Electric drill	220 V/700 W 50/60 Hz
Oscilloscope	Tektronix/TBS2000B

to allow for repeatability of arcing. The two electrodes are connected in series by wire, with one end connected to a load and the other to the power supply. A stable arc can be formed by adjusting the horizontal adjustment knob so that the two electrodes are separated at proper distances. The schematic diagram of the device is shown in **Figure 2**. The physical map is shown in **Figure 3**.

The signal acquisition module is composed of a current transformer and a filter amplifying circuit and is responsible for collecting arc current signals. The current is converted into a voltage signal through a current transformer and a sampling resistor, then filtered and amplified by the circuit, and finally, the current signal is sampled using an oscilloscope. For the acquisition of the current signal, the low-frequency and high-frequency mutual inductors are used to collect the low-frequency and high-frequency current waveforms, respectively. The low-frequency mutual inductor collects the low-frequency current and outputs the low-frequency current component signal through the low-pass filtering and amplifying circuit. The low-pass filtering circuit consists of an RC low-pass filter. The cut-off frequency is configured according to $1/2\pi RC$ to about 1 kHz. The high-frequency mutual inductor collects the high-frequency current and outputs the high-frequency current component signal through the high-pass filtering and amplifying circuit. The high-pass filtering circuit consists of an RC high-pass filter, and the cut-off frequency is configured to be about 1 kHz.

According to GB/T31143-2014 “General Requirements for Series Arc Fault Detection Device (AFDD)" issued by the General Administration of Quality Supervision, Inspection and Quarantine of the People’s Republic of China in 2014, it is stipulated that AFDD must meet the inhibitory load shielding test. Seven shielded loads are specified in the standard; they are vacuum cleaners, switching power supplies, motor loads with capacitive start (such as vacuum cleaners and compressors), electronic light regulators, resistive loads, electric drill loads, and halogen lamps. Therefore, resistance, electric kettle, electric drill, and vacuum cleaner are taken as the loads. The main hardware configuration required for the experiment is shown in **Table 1**.

2.2 Experimental Process

Experiments were carried out at room temperature, the power supply is connected to the arc generator through the isolated power supply, the other end of the arc generator is connected to the load,

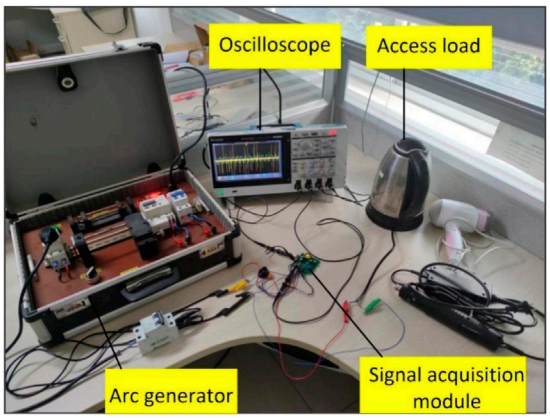

FIGURE 4 | Field diagram of the series arc fault simulation experiment.

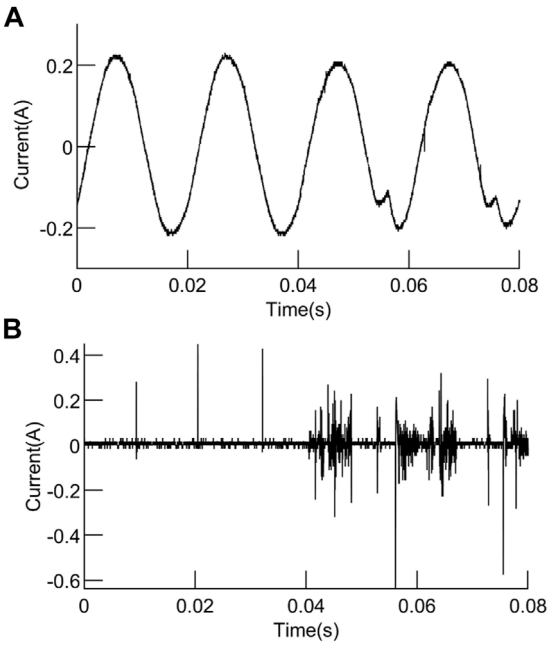

FIGURE 5 | Current waveform of the electric kettle: **(A)** low-frequency waveform. **(B)** High-frequency waveform.

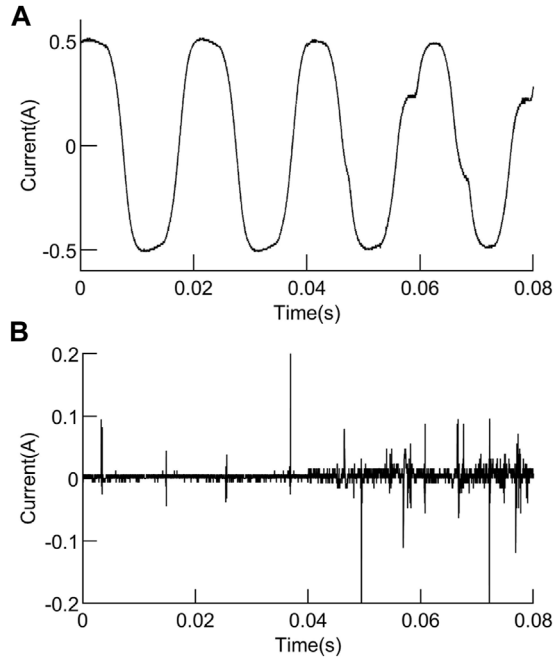

FIGURE 6 | Current waveform of the resistance: **(A)** low-frequency waveform. **(B)** High-frequency waveform.

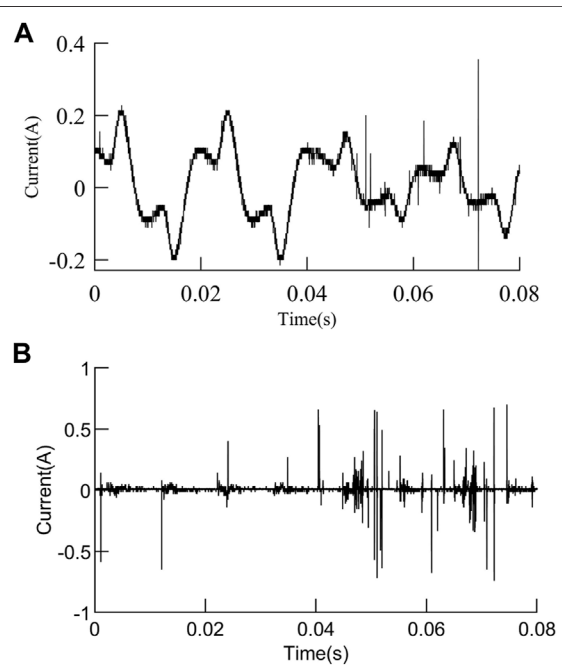

FIGURE 7 | Current waveform of the vacuum cleaner: **(A)** low-frequency waveform. **(B)** High-frequency waveform.

and the wire of the load end passes through the mutual inductor. The current signal enters the signal acquisition module through the sampling resistor, and the output end of the signal acquisition module is connected to the oscilloscope. The waveform displayed by the oscilloscope is the voltage value, which actually reflects the current waveform in the line. The field diagram of the series arc fault simulation experiment is shown in **Figure 4**.

The horizontal adjustment knob of the arc generator is adjusted to control the generation of the arc. The sampling frequency of the oscilloscope is set at 62.5 kHz, and the sampling time of each group of waveforms is 320 ms, with a total of 16 cycles. The experiment obtains the low-frequency and high-frequency current waveforms of resistors, electric kettles, electric drills, and vacuum cleaners during normal operation and arc faults, as well as the current waveforms of switching power supplies and electric drills at the

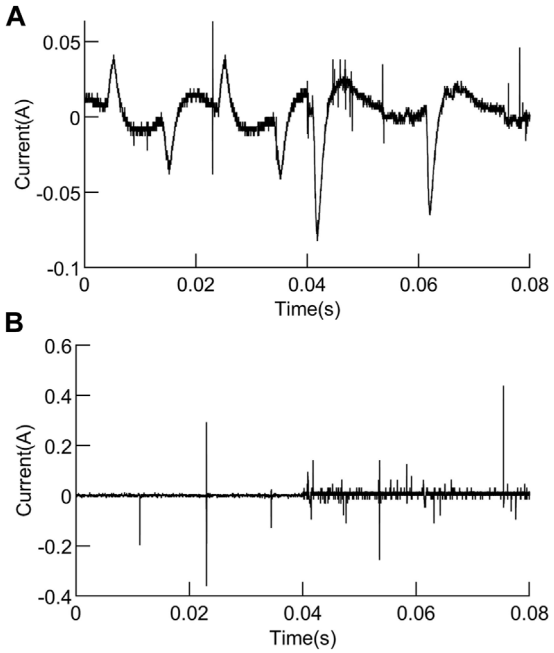

FIGURE 8 | Current waveform of the electric drill: **(A)** low-frequency waveform. **(B)** High-frequency waveform.

TABLE 2 | Time-domain characteristic expressions.

time-domain characteristic quantity	Expression
Kurtosis	$X_1 = \frac{E(x_i-\mu)^4}{\sigma^4}$
Waveform factor	$X_2 = \frac{1}{N}\frac{\sqrt{\frac{1}{N}\sum_{i=1}^{N}\lvert x_i\rvert^2}}{\sum_{i=1}^{N}\lvert x_i\rvert}$
Crest factor	$X_3 = \frac{x_{max}-x_{min}}{\sqrt{\frac{1}{N}\sum_{i=1}^{N}\lvert x_i\rvert^2}}$
Pulse factor	$X_4 = \frac{1}{N}\frac{x_{max}-x_{min}}{\sum_{i=1}^{N}\lvert x_i\rvert}$
Margin factor	$X_5 = \frac{x_{max}-x_{min}}{(\frac{1}{N}\sqrt{\lvert x_i\rvert})^2}$

TABLE 3 | Average time-domain characteristic values of low-frequency current waveform.

Load	State	X_1	X_2	X_3	X_4	X_5
Electric kettle	Normal	1.493	1.111	2.912	3.237	3.556
	Fault	1.463	1.102	3.065	3.387	3.697
Resistance	Normal	1.533	1.125	3.065	3.450	3.902
	Fault	1.541	1.119	3.336	3.728	4.181
Electric drill	Normal	4.516	1.349	6.467	7.943	12.151
	Fault	3.680	1.327	6.676	8.845	12.353
Vacuum cleaner	Normal	1.995	1.213	4.062	4.590	4.990
	Fault	2.297	1.151	5.213	6.062	6.725

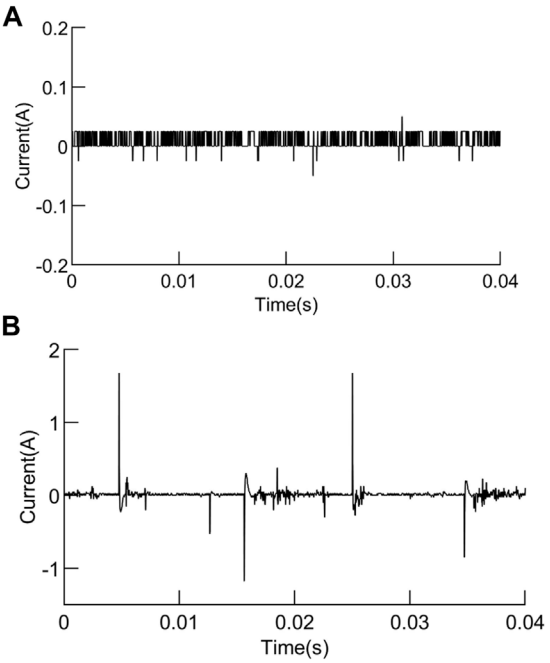

FIGURE 9 | High-frequency current component of the electric kettle: **(A)** normal. **(B)** Series arc fault.

moment of startup. For the convenience of subsequent data analysis, the collected data are normalized in MATLAB. **Figures 5–8** show the low-frequency and high-frequency arc current waveform of four cycles under different loads.

At 0.04 s, the series arc generator simulates the occurrence of series arc faults, that is, the waveform of the first two cycles is in a normal working state, and the series arc faults occur in the last two cycles. It can be seen from the waveform figure that when the electric kettle and resistance work normally, the low-frequency current waveform is a sine wave of 50 Hz, and the high-frequency current signal waveform has a small number of high-frequency pulses. When a series of arc faults occurs, the low-frequency waveform appears and has burrs at the peak, while the high-frequency waveform changes obviously and there are a large number of high-frequency pulses. When the electric drill and vacuum cleaner work normally, the low-frequency current waveform has the "flat shoulder," which is similar to the low-frequency waveform when the series arc fault occurs between the electric kettle and the resistance. At the same time, the high-frequency current signal waveform also has a small number of high-frequency pulses. When a series of arc faults occurs, the low-frequency waveform changes dramatically, burrs increase, waveform amplitude decreases, waveform distortion is serious, the high-frequency waveform amplitude increases, and there are a large number of high-frequency pulses.

3 CHARACTERISTIC EXTRACTION OF SERIES ARC FAULTS

3.1 Analysis of Time Domain Characteristics of Series Arc Faults

Time domain characteristics refer to the description of signal waveform with time as a variable, which is an important indicator

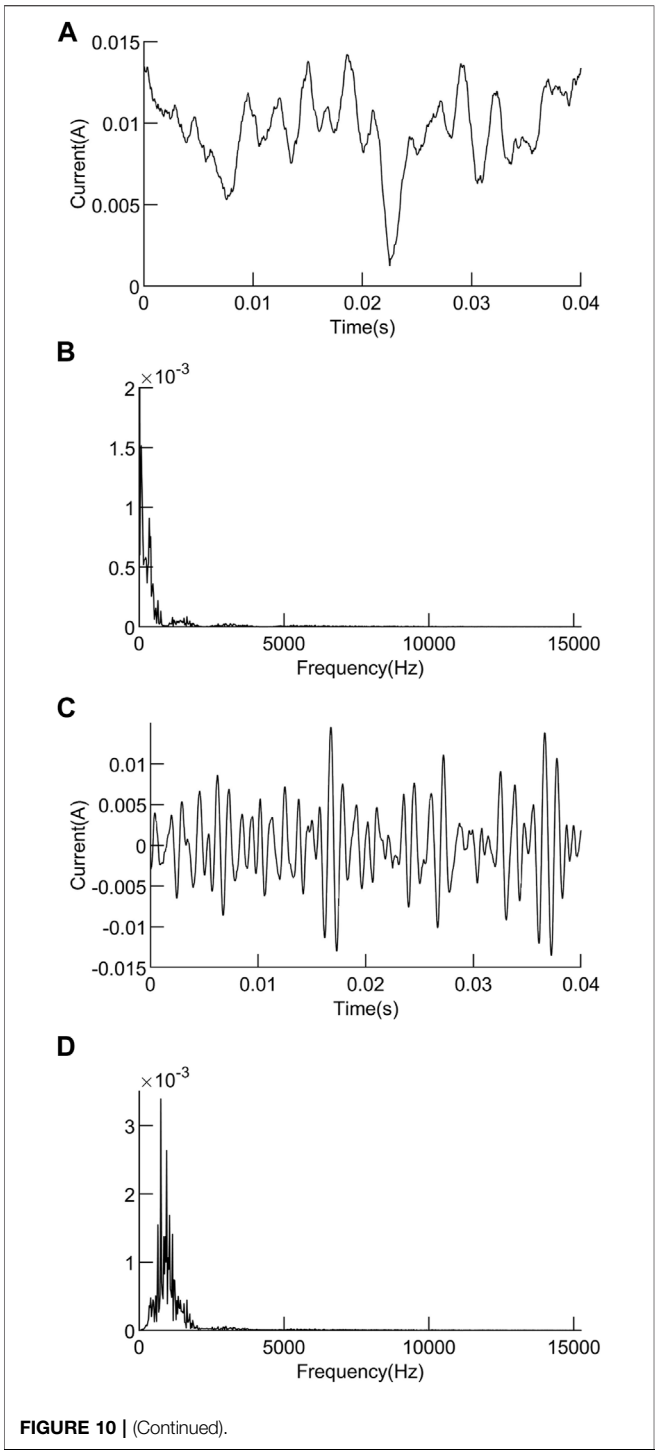

FIGURE 10 | (Continued).

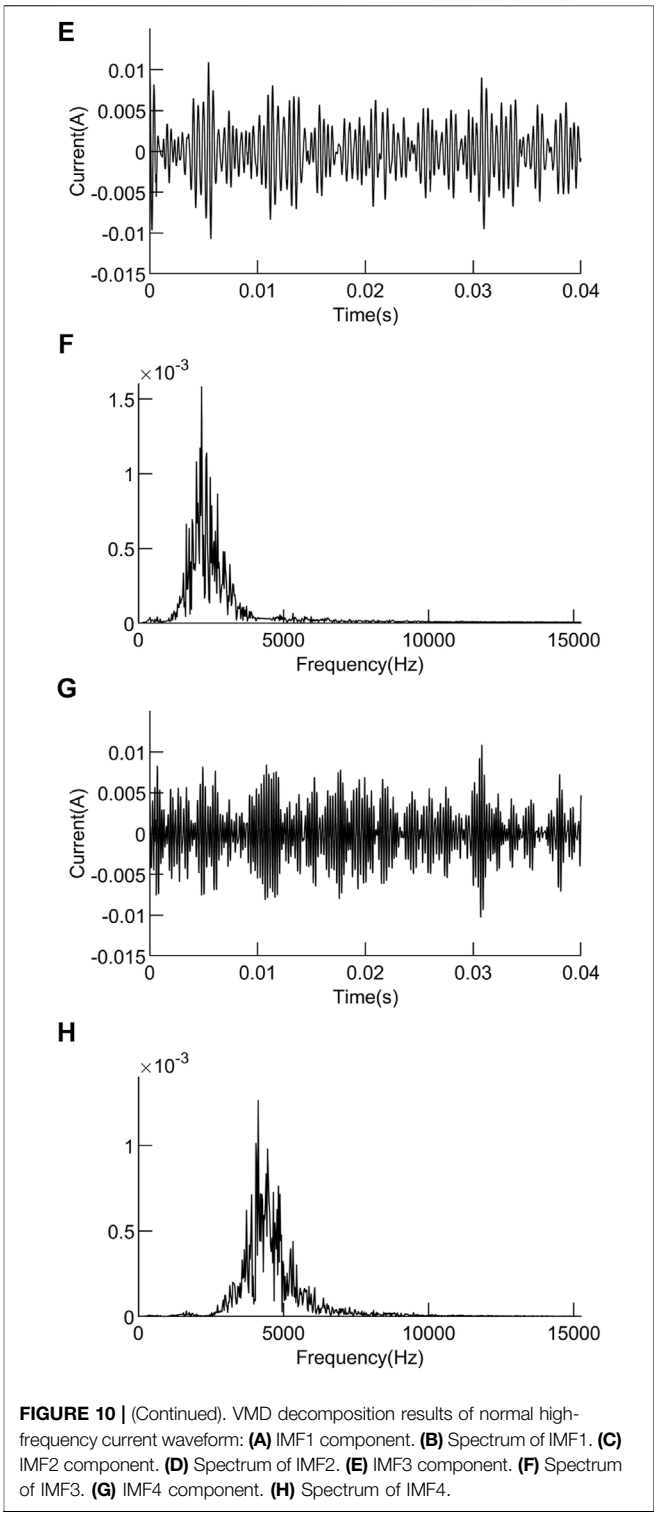

FIGURE 10 | (Continued). VMD decomposition results of normal high-frequency current waveform: **(A)** IMF1 component. **(B)** Spectrum of IMF1. **(C)** IMF2 component. **(D)** Spectrum of IMF2. **(E)** IMF3 component. **(F)** Spectrum of IMF3. **(G)** IMF4 component. **(H)** Spectrum of IMF4.

to measure signal characteristics. Characteristic quantities in the time domain are usually divided into dimensionless and dimensional characteristic quantities. Dimensionless characteristics are not sensitive to the change of load and can more intuitively represent the status information of normal operation and fault of load. Kurtosis is often used in the field of bearing fault diagnosis. It has nothing to do with bearing speed and size, etc. It is sensitive to impact signals and is suitable for the description of surface damage faults. It can be seen from the arc fault current waveform diagram in **Figures 3–6** that the current waveform will be distorted and high-frequency pulses will appear when an arc fault occurs. These signals are similar to impulse

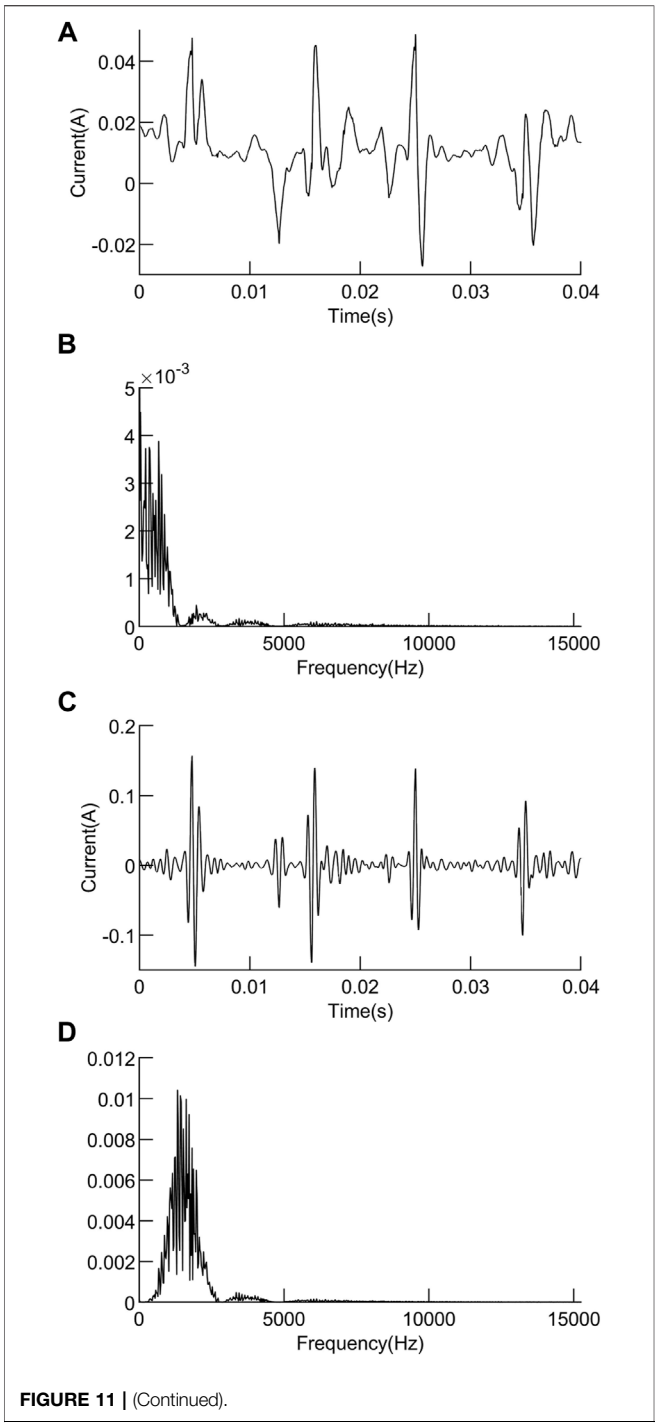

FIGURE 11 | (Continued).

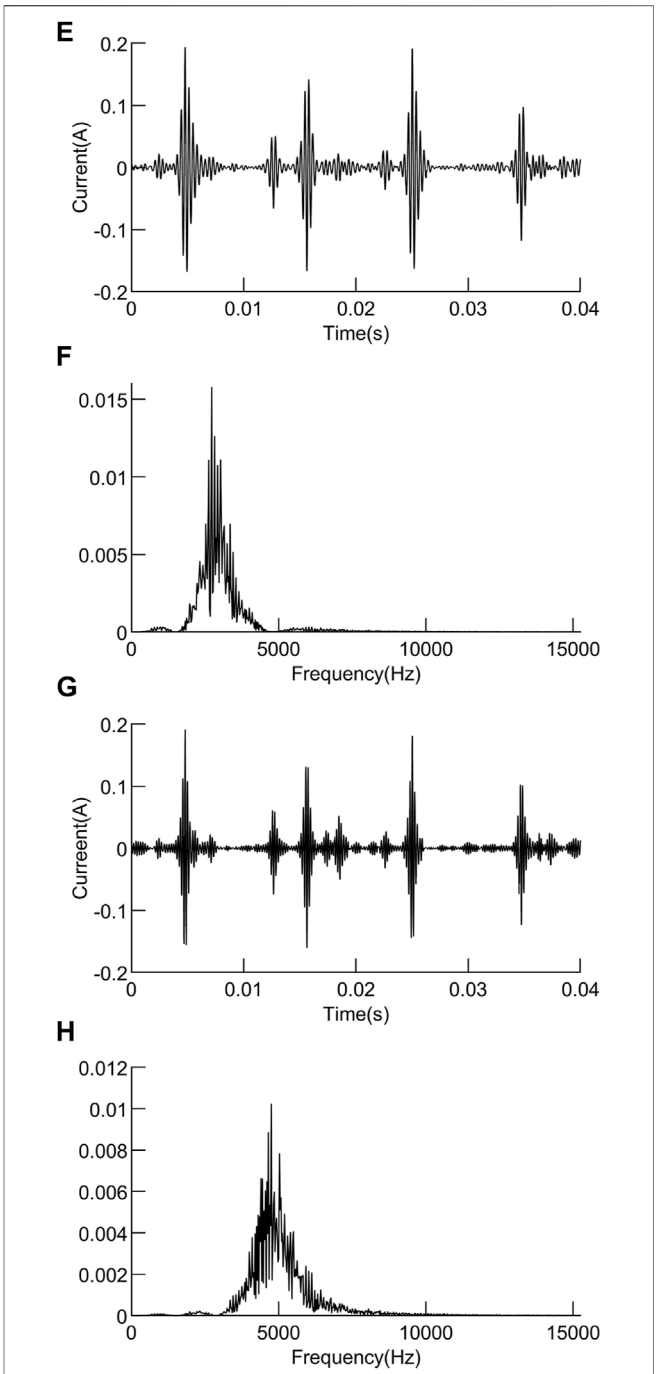

FIGURE 11 | (Continued). VMD decomposition results of high-frequency current components of series arc fault: **(A)** IMF1 component. **(B)** Spectrum of IMF1. **(C)** IMF2 component. **(D)** Spectrum of IMF2. **(E)** IMF3 component. **(F)** Spectrum of IMF3. **(G)** IMF4 component. **(H)** Spectrum of IMF4.

signals. Therefore, this article uses kurtosis as a waveform time domain feature to calculate. The waveform factor is the ratio of the effective value to the rectified average value. When an arc fault occurs, the waveform of the low-frequency current component will be distorted, the periodicity will be destroyed, and both the effective value and the rectified average value will change, so its shape factor can be calculated. The crest factor is defined as the ratio of the peak-to-peak value to the effective value of a signal. When an arc fault occurs, the low-frequency current component will appear "burr," and its peak-to-peak value will become larger, so the arc fault can be described by calculating the change in the value of the crest factor. The impulse factor refers to the ratio of the peak value of the signal to the rectified average value. Similar

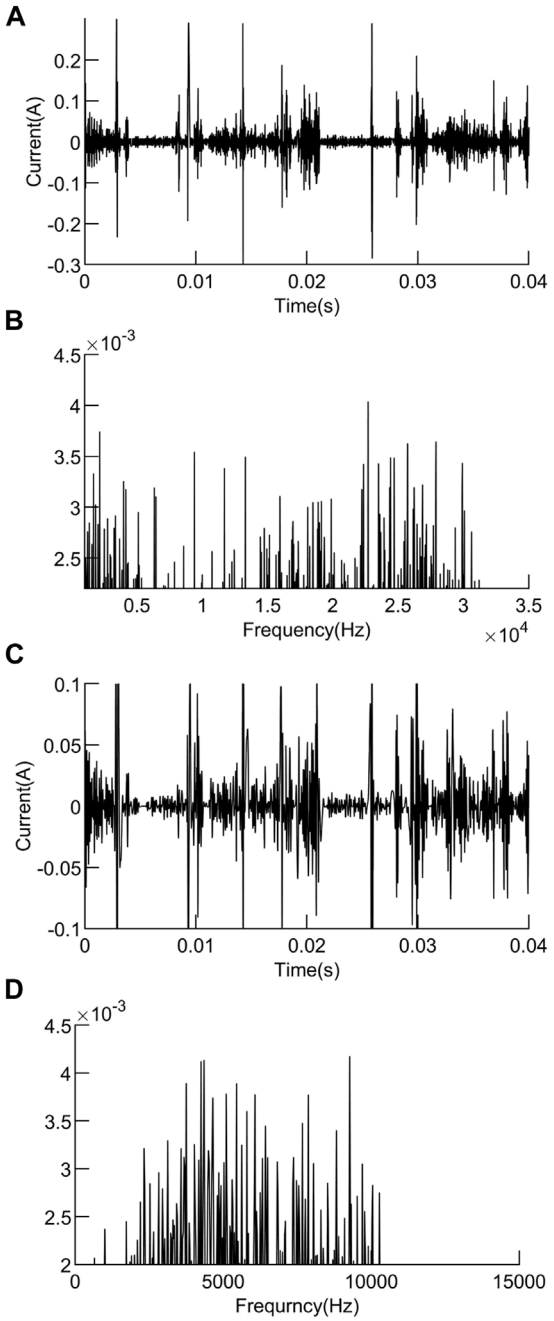

FIGURE 12 | (Continued).

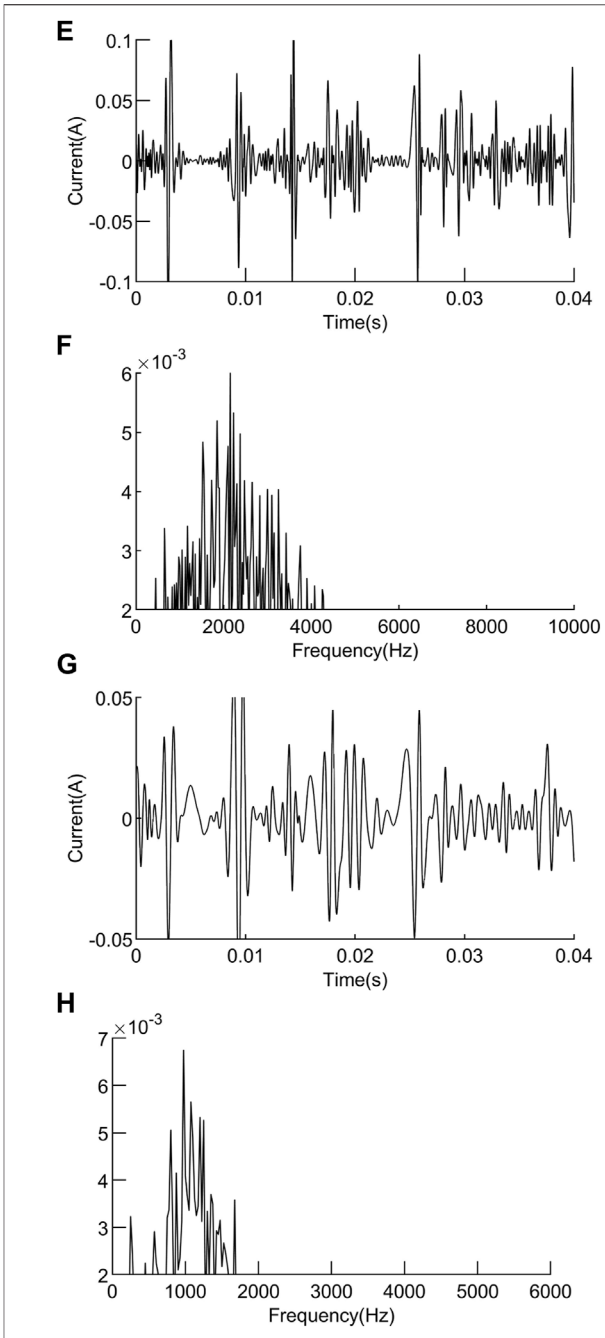

FIGURE 12 | EMD decomposition results of high-frequency current components of series arc fault: **(A)** IMF1 component. **(B)** Spectrum of IMF1. **(C)** IMF2 component. **(D)** Spectrum of IMF2. **(E)** IMF3 component. **(F)** Spectrum of IMF3. **(G)** IMF4 component. **(H)** Spectrum of IMF4. **(I)** IMF5 component. **(J)** Spectrum of IMF5. **(K)** IMF6 component. **(L)** Spectrum of IMF6. (**M**) IMF7 component. **(N)** Spectrum of IMF7. **(O)** IMF8 component. **(P)** Spectrum of IMF8. **(Q)** IMF9 component. **(R)** Spectrum of IMF9.

to the crest factor, arc faults can also be described by the pulse factor. The margin factor is the ratio of the peak value of the signal to the rms amplitude. Crest factor, impulse factor, and margin factor, like kurtosis, are all indicators used to detect whether there is a shock in a signal. In this article, kurtosis, waveform factor, crest factor, pulse factor, and margin factor are selected as five dimensionless indexes for time domain characteristic extraction. Low-frequency current waveform of two cycles, i.e., 20 ms, and 2,500 points of sampling points N were selected as an analysis sample. Kurtosis, waveform factor, crest factor, pulse factor, and margin factor of low-frequency current waveform were calculated in the time domain, and the five characteristic quantities were marked as X_1, X_2, X_3, X_4, and

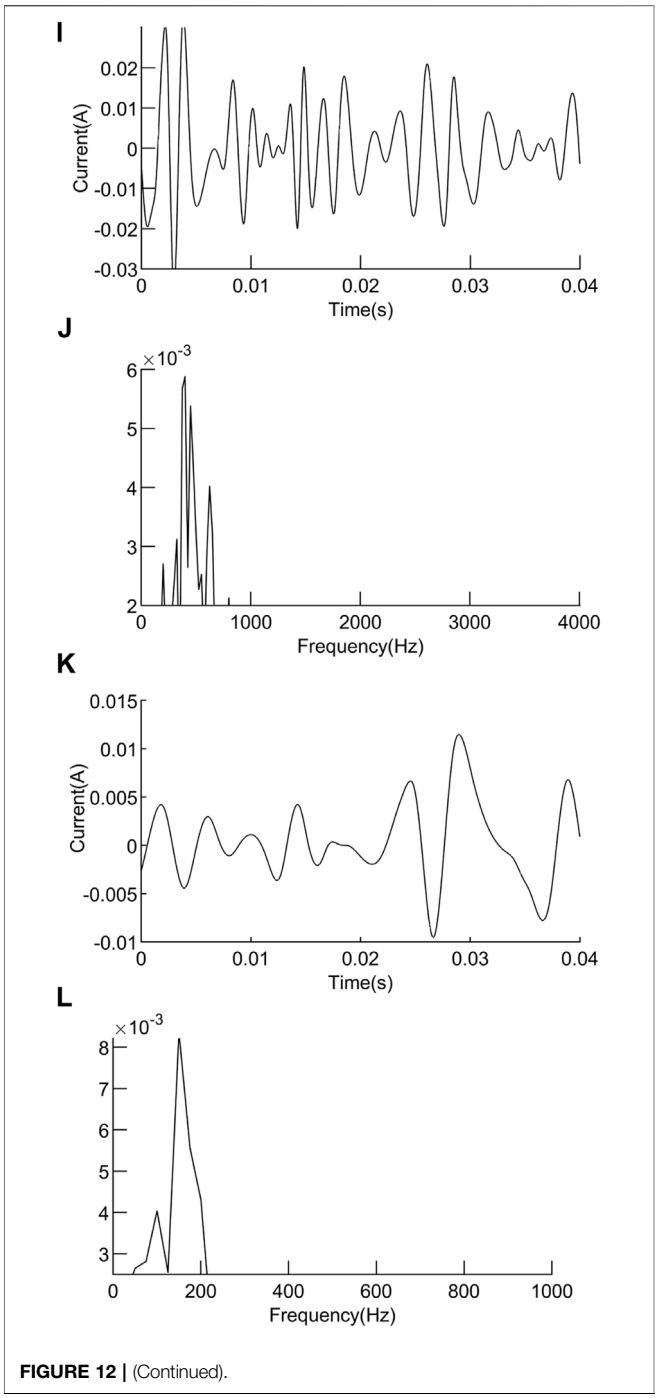

FIGURE 12 | (Continued).

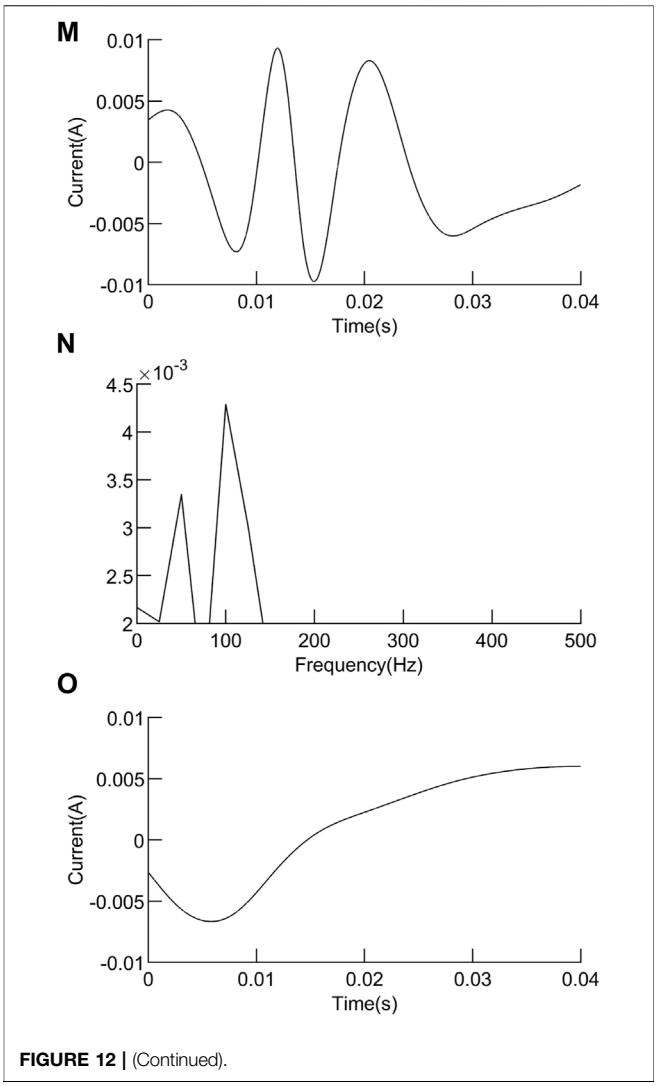

FIGURE 12 | (Continued).

X_5 in turn. The expression of each time domain characteristic quantity is shown in **Table 2**.

In **Table 2**, x_i represents the current sample at the ith sampling point, i = 1,2,3..., N; μ is the mean of x_i, σ is the standard deviation of x_i, and E represents the mathematical expectation. The time domain characteristic quantities of 100 samples were calculated for each load. **Table 3** shows the average time domain characteristics values of different loads.

It can be seen from **Table 2** that the crest factor, pulse factor, and margin factor of each load increase when a series of arc faults occurs compared with normal operation. The value of the waveform factor decreases when a series of arc faults occurs. For kurtosis, the values of electric kettles and electric drills will decrease in the event of a series of arc faults, and the values of resistance and vacuum cleaners will increase. Under the condition of a single load, the threshold value can be set to determine whether the series of arc faults occurs. But in the actual line, load condition cannot be determined in advance, and threshold setting will be difficult. It can be seen that the high-frequency current waveform changes dramatically when series arc faults occur, and more series arc fault characteristics can be obtained in the high-frequency waveform, so it is necessary to analyze the high-frequency current waveform.

3.2 Analysis of Frequency Domain Characteristics of Series Arc Faults

It is impossible to calculate the characteristic values of the high-frequency current waveform in the time domain because the waveform of the high-frequency current waveform is very drastic.

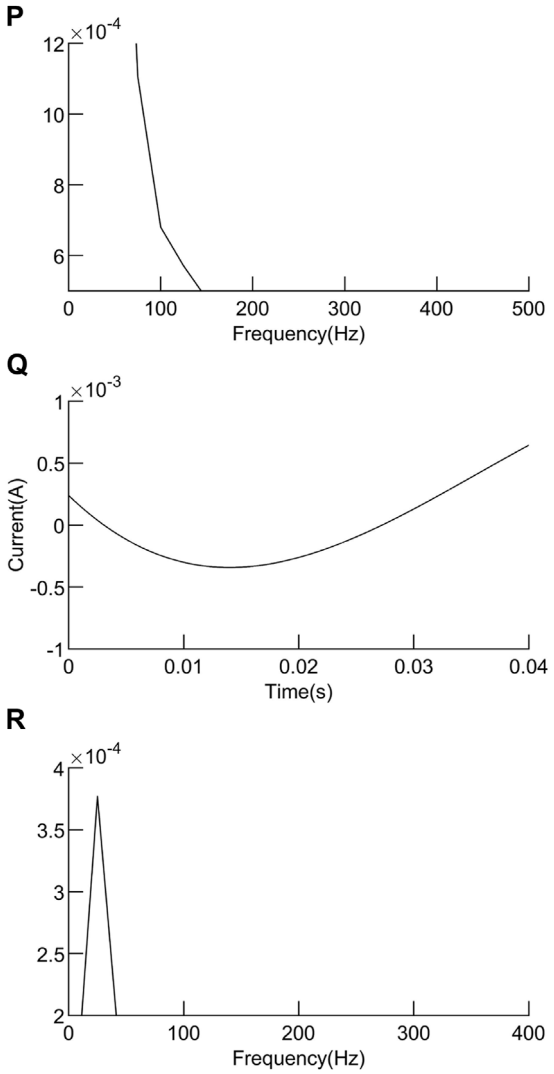

FIGURE 12 | (Continued). EMD decomposition results of high-frequency current components of series arc fault: (A) IMF1 component. (B) Spectrum of IMF1. (C) IMF2 component. (D) Spectrum of IMF2. (E) IMF3 component. (F) Spectrum of IMF3. (G) IMF4 component. (H) Spectrum of IMF4. (I) IMF5 component. (J) Spectrum of IMF5. (K) IMF6 component. (L) Spectrum of IMF6. (M) IMF7 component. (N) Spectrum of IMF7. (O) IMF8 component. (P) Spectrum of IMF8. (Q) IMF9 component. (R) Spectrum of IMF9.

Therefore, characteristic extraction is carried out in the frequency domain.

VMD is a novel adaptive and completely non-recursive signal analysis method provided by Dragomiretskiy and Zosso. (2014) for EMD's sensitivity to noise and signal sampling. To establish and solve the variational problem as the core, based on the classical Wiener filter, Hilbert transform and mixes as the basis of expansion solution, intrinsic mode function, and their respective central frequencies are obtained through each intrinsic mode function to reconstruct the signal. The reconstructed signal can smoothly reproduce the input signal. VMD is the sum of the input signal

TABLE 4 | Central frequencies of IMF components.

IMF component	Central frequency (kHz)	
	Normal	Series arc fault
IMF1	0.075	0.675
IMF2	1.050	1.425
IMF3	2.175	2.725
IMF4	4.450	4.450

f(t) decomposed into K sub-signals (i.e., IMF components) and the remainder:

$$f(t) = u_r(t) + \sum_{k=1}^{K} u_k(t), \tag{1}$$

where $u_k(t)$ is the kth IMF component, and $u_r(t)$ is the remainder.

The IMF component is a function of amplitude and frequency modulation:

$$u_k(t) = A_k(t)\cos(\varphi_k(t)), \tag{2}$$

where $\varphi_k(t)$ is a non-decreasing function, that is, $\varphi'_k(t) \geq 0, k \leq K$; $A_k(t)$ represents the envelope $A_k(t) \geq 0$; $k \leq K$.

The VMD algorithm requires the bandwidth and minimum of all IMF components. The solution of the constrained variational problem is constructed as follows:

$$\min_{\{u_k(t)\},\{\omega_k\}} \left\{ \sum_{k=1}^{K} \left\| \partial_t \left[\left(\delta(t) + \frac{j}{\pi t} \right) * u_k(t) \right] e^{-j\omega_k t} \right\|_2^2 \right\}, \tag{3}$$

where ω_k is the central frequency of the kth IMF component, $\omega_k = \varphi'_k(t)$; $\delta(t)$ is the Dirac function.

In **Formula (3)**, quadratic penalty term and Lagrange multiplier are introduced to solve the variational problem, making it unconstrained. The augmented Lagrange function is obtained as follows:

$$\begin{aligned} L\{[u_k(t)], [\omega_k], \lambda(t)\} = \alpha \sum_{k=1}^{K} \left\| \partial_t \left[\left(\delta(t) + \frac{j}{\pi t} \right) * u_k(t) \right] e^{-j\omega_k t} \right\|_2^2 \\ + \left\| f(t) - \sum_{k=1}^{K} u_k(t) \right\|_2^2 + \langle \lambda(t), f(t) \\ - \sum_{k=1}^{K} u_k(t) \rangle, \end{aligned} \tag{4}$$

where $\lambda(t)$ is the Lagrange multiplier and α is the penalty factor.

The detailed iterative solution steps of modal components $u_k(t)$, central frequency ω_k, and $\lambda_k(t)$ in **Formula (4)** can be referred to as the solution steps in the article by Dragomiretskiy K and Zosso D (2014). According to the aforementioned principle, the VMD algorithm is used in MATLAB for waveform decomposition. According to the study of K and α in an article by Ma et al. (2020), the number of decomposition and the penalty factors were set at K = 4 and α = 2000, respectively. Other parameters in the VMD algorithm are set as the default values of the algorithm in an article by Liu et al. (2021). The high-frequency current waveform is taken as an example when an electric kettle works normally and a series of arc faults occurs. For the convenience of analysis, the waveform data were

TABLE 5 | Energy entropy and variance contribution ratio.

IMF component	Normal		Series arc fault	
	Energy entropy	Variance contribution ratio	Energy entropy	Variance contribution ratio
IMF1	0.115	22.753	0.128	25.155
IMF2	0.112	19.142	0.155	22.099
IMF3	0.101	15.769	0.148	18.548
IMF4	0.101	15.858	0.123	11.618

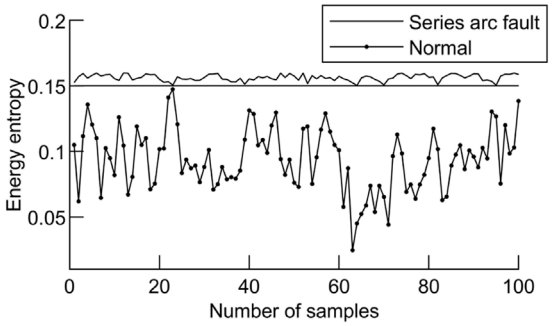

FIGURE 13 | Energy entropy of normal operation and series arc fault.

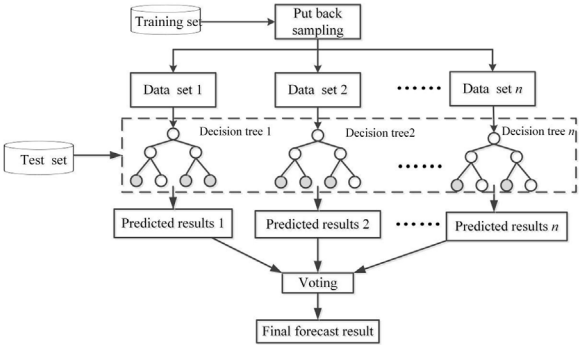

FIGURE 14 | Diagnostic flow chart of random forest algorithm.

TABLE 6 | Characteristic vectors of some experimental samples.

X_1	X_2	X_3	X_4	X_5	X_6	X_7
1.457	1.103	2.910	3.210	3.699	0.159	1
1.484	1.105	3.995	4.417	4.828	0.157	1
1.464	1.105	2.893	3.198	3.600	0.157	1
1.495	1.112	2.878	3.201	3.520	0.118	0
1.490	1.110	2.878	3.197	3.509	0.111	0
1.653	1.105	3.976	4.397	4.740	0.159	1
1.591	1.125	3.291	3.703	4.143	0.159	1
1.521	1.105	3.274	3.621	3.975	0.157	1
1.498	1.112	2.964	3.298	3.634	0.140	0
1.500	1.114	3.103	3.458	3.836	0.129	0
7.919	1.648	5.409	8.915	12.354	0.157	1
8.482	1.654	5.901	9.761	13.624	0.154	1
7.035	1.494	6.430	9.610	12.305	0.153	1
3.601	1.258	5.744	7.230	8.6078	0.143	0
3.256	1.214	7.293	8.855	10.028	0.137	0
1.677	1.138	4.328	4.929	5.444	0.158	1
3.675	1.209	9.878	11.94	13.518	0.156	1
16.951	1.238	9.686	16.956	19.847	0.158	1
1.891	1.119	3.740	4.189	4.520	0.136	0
1.886	1.118	3.815	4.269	4.607	0.142	0

normalized, and then VMD decomposition was carried out to obtain four IMF components, and the corresponding spectrum of each component was obtained by Fast Fourier Transformation in MATLAB. The decomposition results are shown in **Figures 9–11**. At the same time, the EMD algorithm was used for the same series arc fault waveform to obtain each IMF component and its spectrum after decomposition, as shown in **Figure 12**.

Figure 9 shows the original current waveform when the electric kettle is in normal operation and series arc fault occurs; **Figure 10** shows the decomposition result of VMD algorithm when the electric kettle is in normal operation; **Figures 11**, **12**, respectively, show the decomposition result of VMD and EMD algorithms of the same high-frequency component of the series arc fault. As can be seen from **Figure 12**, the EMD algorithm decomposes the high-frequency signal into nine components, and the IMF1–9 components are arranged according to the central frequency from large to small. Among them, both IMF1 and IMF2 appear in the frequency band around 5 kHz, with an over-decomposition phenomenon. The center frequency distribution of the IMF2 component is not obvious, including the frequency band [5000 Hz and 10000 Hz], and there is the phenomenon of mode aliasing. In addition, it can be seen from the amplitude–frequency diagram of IMF5–9 components that the component is lower than 1kHz, which is due to the frequency band attenuation of the RC high-pass filter, but it is not needed for the high-frequency component analysis in this article. It can be seen from **Figure 11** that the high-frequency current component is decomposed into four IMF components by the VMD algorithm, which are independent of each other without modal aliasing, and the decomposition effect is significantly better than that of the EMD algorithm. The center frequency of each IMF based on the VMD algorithm is shown in **Table 4**.

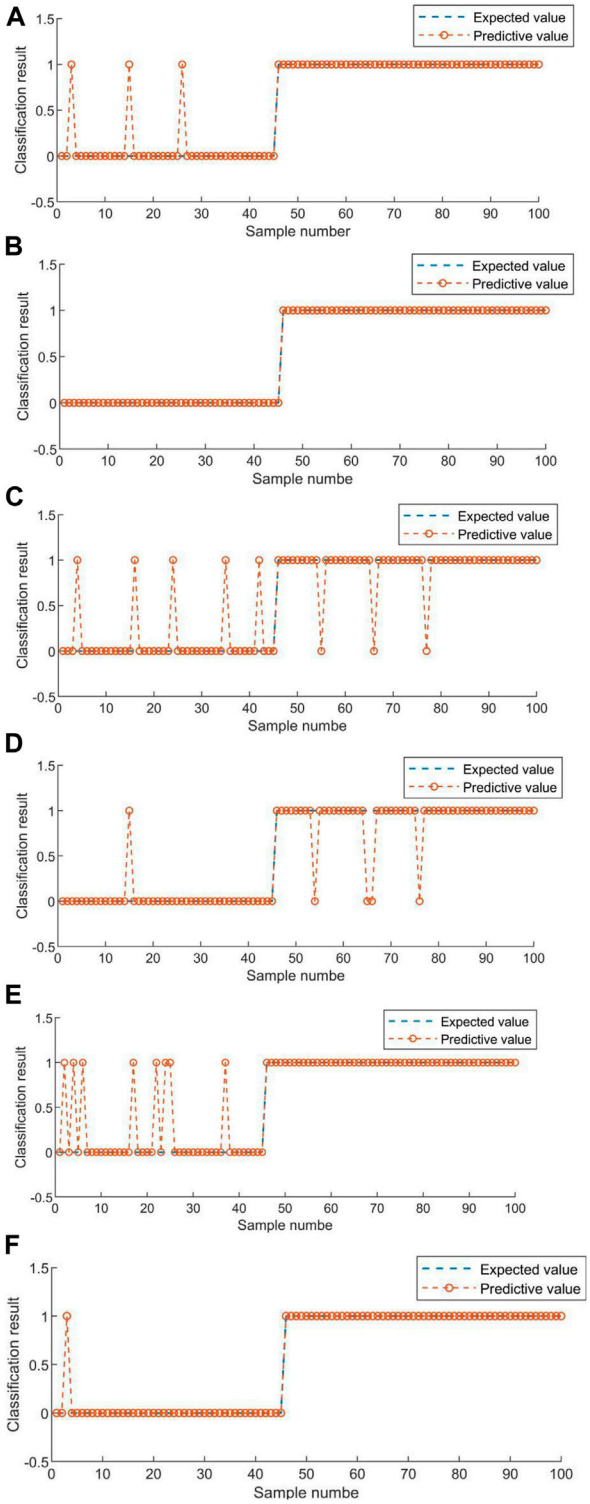

FIGURE 15 | Diagnostic results of different types of loads based on random forest algorithm. **(A)** Effect of random forest algorithm on electric kettle arc fault diagnosis. **(B)** Effect of random forest algorithm on resistance arc fault diagnosis. **(C)** Effect of random forest algorithm on electric drill arc fault diagnosis. **(D)** Effect of random forest algorithm on switching power supply arc fault diagnosis. **(E)** Effect of random forest algorithm on vacuum cleaner arc fault diagnosis. **(F)** Effect of random forest algorithm on hair dryer arc fault diagnosis.

TABLE 7 | Detection accuracy of the random forest diagnostic model.

Load	Number of samples		Correct ratio		
	Normal	Fault	Normal sample (%)	Fault sample (%)	Comprehensive testing (%)
Electric kettle	100	300	100	98.67	99
Electric drill	208	320	98.56	96.88	97.53
Vacuum cleaner	176	240	99.43	97.08	98.08
Resistance	160	208	96.88	99.04	98.64

TABLE 8 | Diagnostic results of switching power supply, hair dryer, and mixed load.

Load	Original sample diagnostic model		New sample diagnostic model	
	Number of samples	Correct ratio (%)	Number of samples	Correct ratio (%)
Switching power supply	432	94.91	282	98.93
Hair dryer	464	92.67	214	97.66
Electric kettle + electric drill	448	93.75	198	97.47
Switching power supply + electric drill	400	92.50	150	98.67
Resistance + vacuum cleaner	480	91.67	230	97.82
Resistance + hair dryer	496	91.13	246	97.56

Energy entropy can measure the regularity of time series and the energy characteristics of signals in different frequency bands (Jin et al., 2021). When the series arc fault occurs, the current will change and the energy will also change. The energy entropy of mth IMF component is calculated as:

$$HE_m = \frac{\sum_{i=1}^{N}(x_m(i))^2}{\sum_{m=1}^{K}\sum_{i=1}^{N}(x_m(i))^2} lg \frac{\sum_{i=1}^{N}(x_m(i))^2}{\sum_{m=1}^{K}\sum_{i=1}^{N}(x_m(i))^2}, \quad (5)$$

where $x_m(i)$ is the value of the ith point of the mth IMF component, m = 1,2,3, . . . ,K.

$$s_m = \frac{var_m}{var_r + \sum_{k=1}^{K} var_k}, \quad (6)$$

where var_m is the variance of mth IMF component, m = 1,2,3, . . . , K and var_r is the variance of the remainder.

The energy entropy and variance contribution ratio of each IMF in **Figures 8**, **9** were calculated according to the aforementioned formula. **Table 5** shows the calculation results.

It can be seen from **Tables 4**, **5** that the IMF1 component has a center frequency of less than 1 kHz, which is due to the frequency band attenuation of the high-pass filter, but it is not needed for the high-frequency waveform analysis in this article. The frequency of the high-frequency current waveform in this article is set above 1 kHz, so only the IMF component larger than 1 kHz needs to be studied. When the center frequency of the IMF component is greater than 1KHZ, the IMF2 variance contribution rate of the normal operating current is the largest, and the energy entropy is 0.122. When a series of arc faults occur, the variance contribution ratio of IMF1 is the largest, and the energy entropy is 0.155, which increases obviously. The corresponding energy entropy of IMF with the largest variance contribution ratio was calculated for 100 groups of normal working and 100 groups of series arc fault samples, as shown in **Figure 13**.

As can be seen from **Figure 11**, the corresponding energy entropy of IMF with the largest variance contribution ratio in normal operation is less than 0.15, and the corresponding energy entropy of IMF with the largest variance contribution ratio in series arc fault is greater than 0.15. Therefore, the energy entropy corresponding to IMF with the largest variance contribution ratio can be taken as a characteristic value and denoted as X_6.

4 SERIES ARC FAULT DIAGNOSIS

4.1 Construction of a Series Arc Fault Characteristic Vector

In order to improve the diagnosis ratio of series arc fault and realize the diagnosis under different load conditions, the load working state is marked as X_7, "0" means normal operation, "1" means series arc fault, and the series arc fault characteristic vector is constructed with the six time–frequency characteristic quantities in this article. The characteristic vectors of some experimental samples are shown in **Table 6**.

4.2 Series Arc Fault Diagnosis Based on Random Forest

Random forest algorithm is an algorithm that integrates multiple decision trees through the idea of ensemble learning (Li et al., 2020). Its basic unit is the decision tree. In this article, the decision tree algorithm selects CART [Jiang et al. (2021), Ali et al. (2012)], and the Gini coefficient minimization criterion is used for characteristic selection in CART. The series arc fault diagnosis flow chart based on random forest algorithm is shown in **Figure 14**:

In this article, 1000 training samples were selected with 250 for each load, including 100 normal samples and 150 series of arc fault samples. Characteristic quantities n = 6. The number of decision trees is T = 100. The diagnosis model was trained, and the untrained load samples were tested. **Figures 15A–F** shows the diagnostic results of different types of loads based on the random

forest algorithm. From **Figures 15A–F**, the information shown in **Table 7** can be obtained. The random forest algorithm has ideal fault diagnosis effects and high diagnosis accuracy for electric kettles, hair dryers, electric drills, switching power supplies, and vacuum cleaners.

It can be seen from **Table 7** that in the series arc fault detection model based on random forest, the accuracy ratio of load detection under a normal working state is higher than 96%. The fault detection accuracy of load in a series arc fault state is higher than 96%. The comprehensive detection ratio was above 97%. The detection effect is very good.

In the actual distribution lines, the loads are varied and mixed. In order to verify the validity of the aforementioned diagnostic model, series arc fault simulation experiments of switching power supply, hair dryer, and mixed load are added in this article. Switching power supply parameters: BSD-36 P-60 W, input 220 VAC 50 Hz, and output 36 VDC 60 W. Hair dryer parameters: 220 VAC 1600 W. According to the time domain and frequency domain characteristic extraction methods proposed in this article, the time–frequency characteristic values are extracted, the characteristic vector is constructed, and a new load training sample diagnosis model is added based on the random forest algorithm training, and then the fault diagnosis is carried out. The diagnosis results are shown in **Table 8**.

As can be seen from **Table 8**, in the diagnosis of the new loads and mixed load types, the accuracy of the original diagnosis model decreases to 94.91% and 91.13%, respectively, and the detection effect is lower than that of the original four loads. Therefore, new loads and mixed loads were added to the original training samples to optimize the diagnostic model. The results in **Table 8** show that the recognition efficiency of the new diagnostic model has reached more than 97%, and the recognition effect is significant. For more load cases, new training samples can be added to improve the diagnosis model for diagnosis.

5 CONCLUSION

Aiming at the problem of low-voltage series arc faults that are difficult to identify and cause great harm, this article proposes a series of arc fault feature extraction method based on VMD and energy entropy. First, a series arc fault simulation experimental circuit is built, and the series of arc fault current waveform data under different loads are obtained, and the arc characteristic quantity is extracted by VMD decomposition and Fourier transform. Then, the random forest algorithm model for training is established, and the random forest algorithm is used to train the diagnostic model to identify arc faults. Finally, the feasibility of the method is verified by MATLAB simulation, and the conclusions of this article are as follows:

1) The energy entropy corresponding to the IMF component with the largest variance contribution rate extracted based on VMD decomposition can effectively characterize the arc fault feature quantity.
2) The random forest algorithm training diagnosis model based on five time-domain feature quantities and one IMF component corresponding to energy entropy as the frequency-domain feature quantity has good generalization performance for arc fault identification.
3) The training process of random forest uses a decision tree as the basic unit to perform simple two-class classification. The training results show that the recognition rate of series arc faults has reached more than 97%, and the recognition effect is remarkable, which can provide analytical ideas for the improvement of series arc fault diagnosis algorithms and the research on the safety of people's livelihood.

DATA AVAILABILITY STATEMENT

The raw data supporting the conclusion of this article will be made available by the authors, without undue reservation.

AUTHOR CONTRIBUTIONS

LZ and CC contributed to the conception and design of the study. QZ and LZ organized case studies. CC was responsible for program compilation and writing–original draft. HM was responsible for laboratory and supervision. LZ completed the substantial revision. All authors contributed to manuscript revision and read, and approved the submitted version.

ACKNOWLEDGMENTS

All authors are acknowledged for their contributions to the article and experiments.

REFERENCE

Ali, J., Khan, R., Ahmad, N., and Maqsood, I. (2012). Random Forests and Decision Trees. *Int. J. Comput. Sci. Issues (IJCSI).* 9 (5), 272.

Chen, C. K., Guo, F., Liu, Y., Wang, Z., Chen, Y., and Liang, H. (2015). "Recognition of Series Arc Fault Based on the Hilbert Huang Transform," in 2015 IEEE 61st Holm Conference on Electrical Contacts (Holm) (IEEE). doi:10.1109/holm.2015.7355116

Chen, S., Li, X., Meng, Y., and Xie, Z. (2019). Wavelet-based Protection Strategy for Series Arc Faults Interfered by Multicomponent Noise Signals in Grid-Connected Photovoltaic Systems. *Sol. Energy* 183, 327–336. doi:10.1016/j.solener.2019.03.008

Cui, R. H., Tong, D., and Li, Z. (2021). Aviation Arc Fault Detection Based on Generalized S Transform. *Chin. J. Electr. Eng.* 41 (23), 8241–8250. doi:10.13334/j.0258-8013.pcsee.201626

Cui, R., and Tong, D. (2021). Aeronautical AC Series Arc Fault Detection Based on Levene Test. *Chin. J. Electrotech. Technol.* 36 (14), 3034–3042.

Dragomiretskiy, K., and Zosso, D. (2014). Variational Mode Decomposition. *IEEE Trans. Signal Process.* 62 (3), 531–544. doi:10.1109/tsp.2013.2288675

Gao, H., Wang, Z., and Tang, A. (2021). Research on Series Arc Fault Detection and Phase Selection Feature Extraction Method. *IEEE Trans. Instrum. Meas.* 70, 1–8. doi:10.1109/tim.2021.3080376

General Administration of Quality Supervision (2014). *Inspection and Quarantine of the People's Republic of China GB/T31143-2014. General Requirements of Series Arc Fault Detection Device (AFDD)*. Beijing: Standards Press of China.

Jiang, J., Li, W., Wen, Z., Bie, Y., Schwarz, H., and Zhang, C. (2021). Series Arc Fault Detection Based on Random Forest and Deep Neural Network. *IEEE Sensors J.* 21 (15), 17171–17179. doi:10.1109/jsen.2021.3082294

Jin, J. T., Xu, Z., Li, C., Miu, W., and Li, G. (2021). Bearing Fault Diagnosis Based on VMD Energy Entropy and Optimized Support Vector Machine. *J. Metrology* 42 (7), 898–905.

Jingjing, S. U., and Zhihong, X. U. (2019). Diagnosis Method of Multi-Variable Criterion Based on EMD and PNN for Arc Fault Diagnosis. *Electr. Power Autom. Equip.* 39 (4), 106–113.

Karakose, E., Gencoglu, M. T., and Karakose, M. (2018). A New Arc Detection Method Based on Fuzzy Logic Using S-Transform for Pantograph–Catenary Systems. *J. Intell. Manuf.* 29, 839–856. doi:10.1007/s10845-015-1136-3

Khafidli, M. K. (2018). "Implementation AC Series Arc Fault Recognition Using Mikrokontroller Based on Fast Fourier Transform," in 2018 International Electronics Symposium on Engineering Technology and Applications (IES-ETA) (IEEE). doi:10.1109/elecsym.2018.8615529

Lala, H., and Subrata, K. (2020). Detection and Experimental Validation of High Impedance Arc Fault in Distribution System Using Empirical Mode Decomposition. *IEEE Syst. J.* 14 (3), 3494–3505. doi:10.1109/jsyst.2020.2969966

Li, S., Bai, X., Dong, H., Lu, H., and Guo, C. (2020). Early Fault Identification Method of Cable Based on Stationary Wavelet Transform and Random Forest. *New Technol. Electr. Power Eng.* 39 (3), 40–48.

Lin, J., Wang, Y., Li, K., and Tian, M. (2020). Series Arc Fault Detection Method Based on Self-Organizing Feature Mapping Network. *Electr. Power Autom. Equip.* 40 (08), 210–219.

Lin, J., Luan, W., and Liu, B. (2021). "A Novel Non-intrusive Arc Fault Detection Method for Low-Voltage Customers," in 2021 6th Asia Conference on Power and Electrical Engineering (ACPEE), 84–88. doi:10.1109/ACPEE51499.2021.9437035

Liu, G., Du, S., Su, J., and Han, X. (2017). Research and Development Trend of Low Voltage Arc Fault Protection Technology. *Power grid Technol.* 1, 321–329.

Liu, G. G., Du, H. S., Su, J., and Han, X. H. (2017). Research and Development Trend of Low Voltage Arc Fault Protection Technology. *Power Syst. Technol.* 41 (01), 305–313. doi:10.13335/j.1000-3673.pst.2016.0804

Liu, J., Zhou, K., and Hu, Y. (2018). "EMD-WVD Method Based High-Frequency Current Analysis of Low Voltage Arc," in 2018 Condition Monitoring and Diagnosis (CMD) (IEEE). doi:10.1109/cmd.2018.8535969

Liu, S., Liu, Z., Liu, Y., Cao, Y., and Li, J. (2021). "Arc Fault Recognition Based on VMD and ELM," in The Proceedings of the 9th Frontier Academic Forum of Electrical Engineering (Singapore: Springer). doi:10.1007/978-981-33-6609-1_47

Ma, T., Tian, E., Liu, Z., Liu, S., Guo, T., Wang, T., et al. (2020). Detection of DC Series Arc Fault Based on VMD and ELM. *J. Phys. Conf. Ser.*, 1486 (6), doi:10.1088/1742-6596/1486/6/062037

Ma, Y., Maqsood, A., Oslebo, D., and Corzine, K. (2022). Wavelet Transform Data-Driven Machine Learning-Based Real-Time Fault Detection for Naval DC Pulsating Loads. *IEEE Trans. Transp. Electrific.* 8 (2), 1956–1965. doi:10.1109/TTE.2021.3130044

Miao, W., Xu, Q., and Lam, K. H. (2020). DC Arc-Fault Detection Based on Empirical Mode Decomposition of Arc Signatures and Support Vector Machine. *IEEE Sensors J.* 21 (5), 7024–7033.

Qi, P., Jovanovic, S., and Lezama, J. (2017). Discrete Wavelet Transform Optimal Parameters Estimation for Arc Fault Detection in Low-Voltage Residential Power Networks. *Electr. Power Syst. Res.* 143, 130–139. doi:10.1016/j.epsr.2016.10.008

Shao, X. L. (2020). Analysis of the Importance of Fire Prevention to the Safety of High-Rise Residential Buildings. *China Fire Prot.* 41 (05), 53–54.

Syafi'i, M. H. R. A., Prasetyono, E., Khafidli, M. K., Anggriawan, D. O., and Tjahjono, A. (2018). "Real Time Series DC Arc Fault Detection Based on Fast Fourier Transform," in 2018 International Electronics Symposium on Engineering Technology and Applications (IES-ETA) (IEEE).

Wang, Y., Li, Y., and Ge, L. (2017). Fault Identification of Series DC Arc Based on Sliding Discrete Fourier Transform. *J. Electrotech.* 32 (19), 118–124.

Wang, Y., Zhang, Y. F., and Niu, F. (2019). Characterization and Measurement Method of DC Arc Electromagnetic Radiation for Photovoltaic Systems. *Trans. China Electrotech. Soc.* 34 (14), 2913–2921.

Xiong, Q., Chen, W. J., Ji, C. C., and Zhu, L. Y. (2016). Review of Research Progress on Arc Fault Characteristics Detection and Location Methods in Low-Voltage DC Systems. *Proc. CSEE* 36 (19), 5236–5244.

Xiong, Q., Ji, S. C., and Lu, W. F. (2017). Amplitude and Frequency Characteristics of Electromagnetic Radiation of Series DC Arc Faults under Low Pressure. *Proc. CSEE* 37 (4), 1071–1079.

Yu, Q., Hu, Q., and Yang, Y. (2020). Arc Fault Detection Based on Wavelet Features and Deep Learning. *J. Electron. Meas. Instrum.* 34 (03), 100–108.

Zhang, G. Y., Zhang, X. L., Liu, H., and Zhang, Y. H. (2016). On-line Detection Method of Series Arc Fault in Low Voltage System. *J. Electrotech. Technol.* 31 (08), 109–115.

Zhang, Z., Nie, Y., and Lee, W. J. (2018). Approach of Voltage Characteristics Modeling for Medium-Low-Voltage Arc Fault in Short Gaps[J]. *IEEE Trans. Industry Appl.* 55 (3), 2281–2289.

Conflict of Interest: Author HM is employed by Suzhou Future Electric Co., Ltd.

The remaining authors declare that the research was conducted in the absence of any commercial or financial relationships that could be construed as a potential conflict of interest.

Publisher's Note: All claims expressed in this article are solely those of the authors and do not necessarily represent those of their affiliated organizations, or those of the publisher, the editors, and the reviewers. Any product that may be evaluated in this article, or claim that may be made by its manufacturer, is not guaranteed or endorsed by the publisher.

NOMENCLATURE

X_1 kurtosis
X_2 waveform factor
X_3 crest factor
X_4 pulse factor
X_5 margin factor
X_6 energy entropy
X_7 arc fault status
x_i current sampling sample
E expectation
σ standard deviation
$\lambda(t)$ Langrange multiplier
α penalty factor
$\delta(t)$ Dirac delta function
ω_k IMF component center frequency
$uk(t)$ modal components
K the number of modal decompositions
HE_m energy entropy
S_m variance contribution rate
var_m variance of IMF components
var_r variance of remainder

Abbreviations

EMD empirical mode decomposition
IMF intrinsic modal function
CART classification and regression tree
VMD variational mode decomposition

frontiers | Frontiers in Energy Research

ORIGINAL RESEARCH
published: 23 June 2022
doi: 10.3389/fenrg.2022.827914

Research on the STATCOM Mathematical Model of Battery Storage in HVDC Transmission System

Chao Xing[1], *Junhao Chen*[1,2], *Xinze Xi*[1], *Zhi Xu*[1], *Xin He*[1], *Shengnan Li*[1] *and Shilong Chen*[2]*

[1]Electric Power Research Institute, Yunnan Power Grid Co., Ltd., Kunming, China, [2]School of Electric Power Engineering, Kunming University of Science and Technology, Kunming, China

When traditional STATCOM (Static Synchronous Compensator) performs large-capacity reactive power compensation, the control accuracy of the DC side voltage will be affected and the DC side voltage will fluctuate greatly. Therefore, this study proposes to use battery energy storage STATCOM (STATCOM/BESS) and gives the main circuit topology of STATCOM/BESS. By analyzing the working principle of STATCOM/BESS, the mathematical model and control method are derived and modeled, in which the Shepherd model is used as the energy storage battery in STATCOM/BESS. Aiming at the possible imbalance of the battery state of charge (SOC) in STATCOM/BESS, the phase-to-phase SOC balance control and phase control are proposed. At last, in PSCAD/EMTDC simulation software, STATCOM/BESS is tested for dynamic response and steady-state response performance of active power control, reactive power control, and transformation failure suppression test, which verifies the effectiveness and superiority of STATCOM/BESS commutation failure.

Keywords: HVDC, STATCOM/BESS, mathematical model, commutation failure, SOC

OPEN ACCESS

Edited by:
Chia-Chi Chu,
National Tsing Hua University, Taiwan

Reviewed by:
Binxin Zhu,
China Three Gorges University, China
Jiyong Li,
Guangxi University, China
Jian-Hong Liu,
Yuan Ze University, Taiwan

***Correspondence:**
Shilong Chen
chenshilong3@126.com

Specialty section:
This article was submitted to Smart Grids, a section of the journal Frontiers in Energy Research

Received: *02 December 2021*
Accepted: *26 April 2022*
Published: *23 June 2022*

Citation:
Xing C, Chen J, Xi X, Xu Z, He X, Li S and Chen S (2022) Research on the STATCOM Mathematical Model of Battery Storage in HVDC Transmission System. Front. Energy Res. 10:827914. doi: 10.3389/fenrg.2022.827914

INTRODUCTION

High Voltage Direct Current (HVDC) plays an important role in China's strategy of "West-East electricity transmission project and national network" by virtue of its advantages in long-distance and large-capacity power transmission and grid interconnection (Zhang et al., 2010). In HVDC transmission projects put into operation in China, the characteristics of "strong HVDC and weak AC, multi-infeed DC" are increasingly prominent, which leads to the safety, stability, and reliability of the power grid (Wang et al., 2018). When a fault occurs at the receiving end of the HVDC system, it is easy to cause the voltage sag of the AC busbar at the inverter side, leading to commutation failure of the HVDC system. STATCOM can realize dynamic reactive power compensation, suppress the bus voltage flicker, and improve the voltage transient stability of the system. When the traditional STATCOM performs high-capacity reactive power compensation, the control accuracy of the outer DC side voltage will be affected, leading to the DC side voltage oscillation and large amounts of harmonic components in the output current. At this time, the traditional STATCOM only compensates for the reactive power, and its supporting effect on the grid voltage will be not ideal (Li et al., 2014).

STATCOM by itself has no ability to control and compensate active power, and the energy-storage STATCOM combined with reactive power compensation technology can make up for the deficiency of traditional STATCOM in HVDC system applications (Authors Anonymous, 2016). At present, the energy storage in the field of power systems mainly includes pumped storage, flywheel

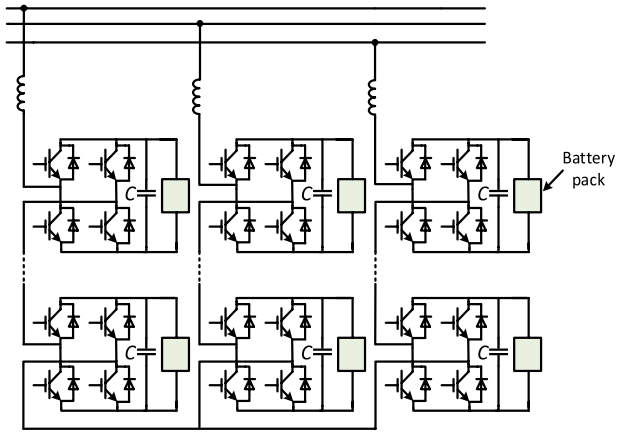

FIGURE 1 | STATCOM/BESS topology.

energy storage, supercapacitor, and battery energy storage (Cheng et al., 2007). In the study of Castaneda et al. (2010), energy-storage STATCOM was applied to the grid-connected wind power planning, which effectively avoids voltage collapse in case of sudden failure and shorts the voltage recovery time. Yang et al. (2001) proposed a STATCOM/BESS device with parallel batteries on the DC side of STATCOM to improve the dynamic and transient stability and power transmission capacity of the system. Xie et al. (2009) studied the effect of energy-storage STATCOM on suppressing voltage phase change in the weak power grid. Through experiments and simulations, it is found that when the system fails, compared with traditional STATCOM, energy-storage STATCOM can suppress voltage phase transformation and reduce voltage sag by 7%. For the study of the topology and control method of energy storage type STATCOM, a static reactive generator/battery energy storage (STATCOM/BESS) integrated system consisting of high-pressure-resistant, high-power, and low-switching switching devices such as GTO, IGBT, and so on is designed (Fei et al., 2005), which can compensate for the power loss of the system itself while improving the system's compensation capacity, thus damping oscillation and improving the system's temporary stability. Compared with traditional STATCOM, STATCOM/BESS integrated system can effectively reduce fault voltage landing and significantly suppress oscillations during voltage recovery.

In this study, according to the existing research results and the actual system requirements, a STATCOM/BESS with an angle cascaded H-bridge structure is carried out, and the performance of the designed STATCOM/BESS is verified by simulation.

STATCOM/BESS TOPOLOGY AND MATHEMATICAL MODEL

DC/DC Section

Energy storage batteries are connected to the DC side in direct parallel connection, non-isolated two-way DC/DC connection, isolated two-way DC/DC connection, and so on. Isolated two-way DC/DC connection requires a low- or high-frequency transformer for boost, which is large in volume and high in cost (Fei et al., 2005; Xie et al., 2009; He, 2016). The non-isolated bi-directional DC/DC connection has a simple structure, is of low cost, and has good energy conversion efficiency. Its disadvantages are that the adjustment range of input and output is small and there is no electrical isolation between the battery pack and the power grid (Li et al., 2021).

The actual STATCOM/BESS phase contains 36/42 cascade H bridge modules, which is a large number. Therefore, considering the cost and technical difficulty of the device, the parallel capacitor of the energy storage battery is directly connected to the DC side of STATCOM, in which the parallel capacitor plays the role of energy buffer and flattens the power difference between the H bridge module and energy storage battery module.

DC/AC Section

In the conventional low-voltage distribution network, the DC/AC part of STATCOM usually adopts the low-voltage two-level topology. However, due to its low-voltage grade, high switching device frequency, and large loss, the multi-level topology is usually adopted in the HVDC transmission system (Shen and Raksincharoensak, 2021a). STATCOM/BESS uses the multilevel topology to make the output waveform have a better harmonic spectrum, and the voltage stress borne by each switching device is smaller, effectively reducing the capacity and voltage level of each battery pack (Li et al., 2014).

Figure 1 shows the angle-cascaded H-bridge STATCOM/BESS topology (Shen et al., 2022). There is a zero-sequence current in the angle structure, which can exchange active

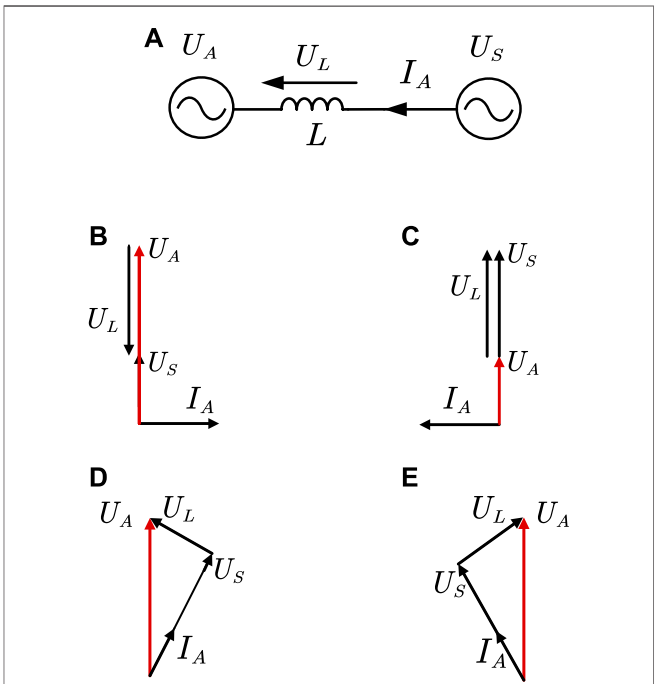

FIGURE 2 | Schematic diagram of power regulation.

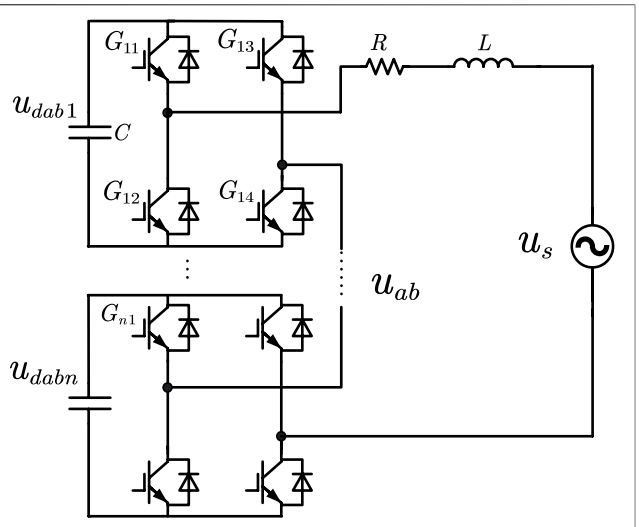

FIGURE 3 | Single-phase circuit structure diagram.

power between three-phase bridge chains. Several H-bridge submodules are cascaded to form a bridge chain. Each H-bridge submodule can output three levels of voltage, and the bridge chain series reactor can be directly integrated into the grid and withstand the gridline voltage. When the number of H-bridge sub-modules is n, $2n$+1 levels can be output through modulation, and the AC side output of the converter is a multi-level waveform, so changing the number of H-bridge sub-modules can change the output voltage of the converter (He, 2016). Compared with the diode clamp three-level topology and capacitor clamp three-level topology, the cascaded H-bridge topology has a simple structure and convenient maintenance, requiring only the minimum number of components in the case of the same number of output levels (Cui et al., 2011), and avoiding the problem of unbalanced charge and discharge when multiple battery groups are connected in series.

Based on the above considerations, this study adopts the angle-cascaded H-bridge topology.

STATCOM/BESS Working Principle

The H-bridge-cascaded STATCOM/BESS each phase bridge chain can be directly integrated into the power grid after series reactor L. The network between each phase bridge chain and the connection point is equivalent to the two-terminal network as shown in **Figure 2A**; Yang et al., 2022. Each phase bridge chain can be regarded as a controllable voltage source, with output voltage U_A, connection point grid U_S, and internetwork current I_A. By controlling the amplitude and phase angle of the output voltage U_A, mutual compensation of the active and reactive power between STATCOM/BESS and the power grid is realized.

In **Figure 2B**, the grid voltage at the U_S grid-connected point controls U_A and U_S in the same direction and makes U_A amplitude greater than U_S amplitude. At this point, STATCOM/BESS sends perceptual reactive power to the grid. In **Figure 2C**, the U_A is controlled in the same direction as the U_S, and the U_A amplitude is smaller than the U_S amplitude. At this time, the STATCOM/BESS sends capacitive reactive power to the grid. In **Figure 2D**, the U_A phase is controlled to lead the U_S phase, and the STATCOM/BESS sends active power to the grid at this time. In **Figure 2E**, the U_A phase is controlled to lag BEHIND U_S phase, at which time STATCOM/BESS absorbs active power from the grid. By controlling the amplitude and phase angle of the output voltage U_A, STATCOM/BESS, and the power grid can complement each other with active and reactive power.

The STATCOM/BESS Mathematical Model

Assuming that the parameters of each phase of the angle cascade STATCOM/BESS are completely consistent, one three-phase STATCOM can be decomposed into three single-phase STATCOM to facilitate the analysis and derivation of the mathematical model. Taking the AB phase as an example, its single-phase equivalent circuit is shown in **Figure 3**; Shen et al., 2020.

According to Kirchhoff's voltage theorem, The single-phase bridge chain voltage drop under the angle-cascaded structure is the grid-connected point line voltage u_s, u_{ab} is the bridge chain output voltage, and i_{ab} is the grid-connected phase current.

$$\boldsymbol{u_{ab} = u_s - L\frac{di_{ab}}{dt} - Ri_{ab}} \tag{1}$$

The H-bridge sub-module is composed of four switching devices in parallel with a DC capacitor(Yang et al., 2019). Suppose that the switch state of G_{j1} is 1 when it is on and 0 when it is off. The same is true for G_{j3}. At this time, the difference between the switch states of G_{j1} and G_{j3} is used to define the switch state H_j of the entire H-bridge module; then H_j is

$$\boldsymbol{H_j = \begin{cases} 1 & G_{j1} = 1, G_{j3} = 0 \\ 0 & G_{j1} = 0, G_{j3} = 0 \\ & G_{j1} = 1, G_{j3} = 1 \\ -1 & G_{j1} = 0, G_{j3} = 1 \end{cases} (j = 1 \ldots n)} \tag{2}$$

Eq. 3 can be used to obtain the current i_{cj} of the DC container in parallel with the jth H bridge sub-module:

$$\boldsymbol{i_{cj} = H_j i_{ab} \quad (j = 1 \ldots n)} \tag{3}$$

According to **Eq. 3**, the state equation of the capacitor voltage can be obtained, where u_{dabj} is the capacitor voltage of the jth H bridge module on the AB bridge chain:

$$\boldsymbol{C\frac{du_{dabj}}{dt} = i_{cj} = H_j i_{ab} \quad (j = 1 \ldots n)} \tag{4}$$

Define the sum of the switching states of the H bridge at all levels as the switching state N of the phase converter, then

$$\boldsymbol{N = H_1 + H_2 + \cdots + H_j + \cdots + H_n} \tag{5}$$

Using **Eq. 6**, one can obtain the output voltage of the jth H bridge sub-module u_{abj}:

$$\boldsymbol{u_{abj} = H_j u_{dabj}} \tag{6}$$

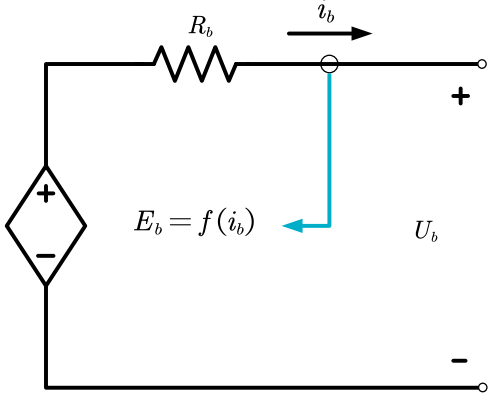

FIGURE 4 | Shepherd model circuit diagram.

Assume that the capacitor voltages of all modules in the bridge chain are equal; then, u_{dab} is the sum of capacitor voltages of all modules in the bridge chain, and the output voltage u_{ab} of the bridge chain can be obtained by combining **Eq. 5**:

$$u_{ab} = \sum_{j=1}^{n} H_j u_{dabj} = N\frac{u_{dab}}{n} \tag{7}$$

Combining **Eq. 4**, we can get

$$C\frac{du_{dab}}{dt} = \sum_{j=1}^{n} H_j i_{ab} = N i_{ab} \tag{8}$$

After substituting **Eq. 7** into **Eq. 1**, we can get

$$L\frac{di_{ab}}{dt} = u_{sab} - Ri_{ab} - N\frac{u_{dab}}{n} \tag{9}$$

Assume that the grid-connected current i_{ab} and the total capacitor voltage u_{dab} are state variables, and establish their state equation by combining **Eqs 8** and **9**; Shen and Raksincharoensak, 2021b. After discretization, the discrete state equation can be obtained as

$$\begin{cases} i_{ab}(k+1) = \left(1 - \dfrac{RT_k}{L}\right) i_{ab}(k) - \dfrac{T_k}{nL} N(k) u_{dab}(k) \\ \qquad\qquad + \dfrac{T_k}{L} u_{sab}(k) \\ u_{dab}(k+1) = u_{dab}(k) + \dfrac{T_k}{C} N(k) i_{ab}(k) \end{cases} \tag{10}$$

where $i_{ab}(k+1)$ and $u_{dab}(k+1)$ indicate the AB-phase grid-connected current and bridge-chain capacitor voltage value at time $(k+1)$, and $N(k)$ and $u_{sab}(k)$ indicate the AB bridge-chain switch at time k and state and grid-connected point line voltage, respectively and, T_k is the sampling period (Shen et al., 2021).

ENERGY STORAGE ELEMENT AND SOC EQUALIZATION CONTROL

Parameter Extraction of the Shepherd Model

The Shepherd model directly describes the electrochemical behavior of batteries including the port voltage, open-circuit voltage, internal resistance, discharge current, and state of charge (SOC) through an equation. The model can be used to describe the charging and discharging process of the battery. The circuit diagram of the Shepherd model is shown in **Figure 4**, where E_b is the no-load voltage of the battery, U_b is the output voltage of the battery, R_b is the internal resistance of the battery and i_b is the output current of the battery.

The nonlinear function shown in **Eq. 11** describes the relationship between battery no-load voltage and output current (Zhu et al., 2020):

$$E_b = f(i_b) = E_0 - K\frac{Q}{Q - it} + Ae^{(-B \cdot it)} \tag{11}$$

In **Eq. 11**, E_0 is the voltage constant (V), K is the polarization voltage (V), Q is the battery capacity (Ah), A is the voltage constant in the exponential discharge zone (V), B is the time constant in the exponential discharge zone (Ah^{-1}) (Zhou et al., 2016), and $it = \int i_b dt$ is the actual cumulative output charge of the battery.

Figure 5 shows the charge and discharge waveform of the battery(Shen et al., 2017). It can be seen that the change in the battery terminal voltage can be roughly divided into three areas: exponential change area, relatively stable area, and rapid change area. The terminal voltage of the battery in the area of exponential change rises or falls with the change of charge in the form of exponential, and the corresponding voltage value of the battery in the state of full charge is E_{full}. When the battery runs in the relatively stable region, the terminal voltage changes slowly with the charge quantity, and the critical voltage corresponding to the transition from the exponential changing region to the relatively stable region is E_{exp}. In the rapidly changing region, the battery terminal voltage changes rapidly with the amount of charge, and

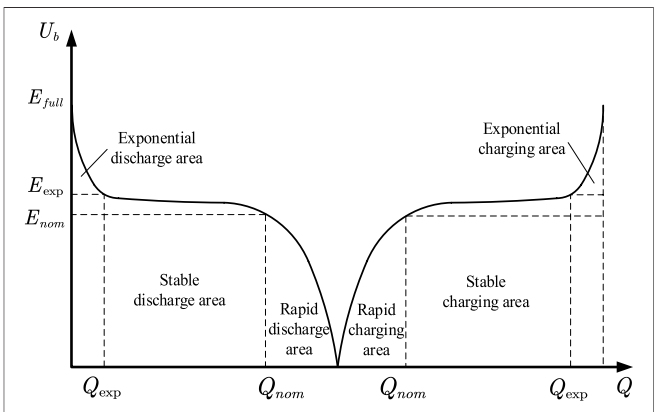

FIGURE 5 | Typical charge and discharge waveform of a battery.

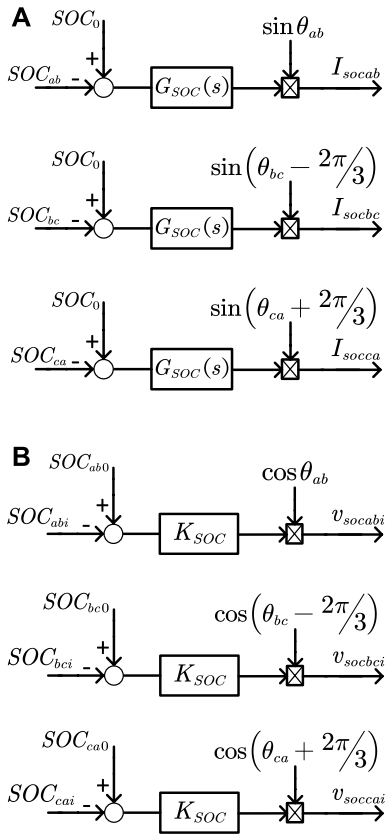

FIGURE 6 | STATCOM/BESS SOC equalization control: **(A)** phase-to-phase SOC equalization control and **(B)** in-phase sub-module SOC equalization control.

the critical voltage corresponding to the transition from the relatively stable region to the rapidly changing region is E_{nom}.

Estimation of battery internal resistance R: The internal resistance R affects the output voltage of the battery and then affects the working efficiency of the battery. Therefore, the internal resistance of the battery can be estimated by measuring the working efficiency of the battery. The working efficiency of the battery η can be easily calculated as follows (Liu et al., 2020):

$$\eta = 1 - \frac{I_{nom}^2 R}{V_{nom} I_{nom}} = 1 - \frac{RI_{nom}}{V_{nom}} \tag{12}$$

where I_{nom} is the nominal discharge current of the battery and V_{nom} is the nominal voltage. Typical values of the working efficiency of batteries can be obtained by statistical methods in the practical project, and the calculation equation of internal resistance R can be obtained from **Eq.** 13:

$$R = V_{nom}\frac{1-\eta}{I_{nom}} \tag{13}$$

To determine the remaining parameters of the model, three sets of data can be obtained from the measured discharge curve given by the manufacturer: full charge voltage E_{full}, exponential area boundary voltage E_{exp}, discharge capacity Q_{exp}, stable discharge area boundary voltage E_{nom} ,and boundary capacity Q_{nom}.

The exponential zone discharge voltage time constant A can be determined by **Eq. 14**:

$$A = E_{full} - E_{\exp} \tag{14}$$

The exponential zone discharge voltage time constant B can be determined by **Eq. 15**:

$$B = \frac{3}{Q_{\exp}} \tag{15}$$

After extracting the parameters A and B, the polarization voltage K can substitute the first group of data and the third group of data in **Eq. 11** to obtain **Eq. 16**:

$$K = \frac{E_{full} - E_{nom} + A\left(e^{-B\cdot Q_{nom}-1}\right)}{Q_{nom}} \cdot (Q - Q_{nom}) \tag{16}$$

Finally, the voltage time constant E_0 can be derived from the full charge voltage E_{full} to obtain **Eq. 17**:

$$E_0 = E_{full} + K + Ri - A \tag{17}$$

SOC Equalization Control

There are many chained STATCOM/BESS modules, which may lead to different charge and discharge times of each phase energy storage battery and sub-module batteries in the phase. Especially when the grid-connected voltage is not symmetrical, the disequilibrium of charge and discharge between energy storage batteries will be more serious, reducing the efficiency of energy storage batteries. Therefore, a state of charge (SOC) equalization control strategy for STATCOM/BESS is proposed, as shown in **Figure 6**; Yang et al., 2021a.

In **Figure 6A**, SOC_{ab}-SOC_{ca} is the SOC of each phase, SOC_0 is the average SOC of the phase, and are calculated using **Eqs 18** and **19**, respectively:

$$SOC_m = \sum SOC_{mi} \quad (m = ab, bc, ca) \tag{18}$$

$$SOC_0 = \frac{SOC_{ab} + SOC_{bc} + SOC_{ca}}{3} \tag{19}$$

The basic idea of phase-to-phase SOC equalization control is as follows: the difference between each phase SOC_m and the phase average SOC_0 passes through the PI controller $G_{soc(s)}$ to obtain the phase SOC equalization active current command I_{socm} (Yang et al., 2021b), which is then sent to the current inner loop control. If the SOC_m is less than SOC_0, a positive active power command is obtained, and the energy storage battery of this phase is in the state of charge as a whole so that the SOC_m increases and the SOC balance of the phase is achieved, and vice versa.

In **Figure 6B**, SOC_{mi} is the SOC of the sub-module battery in the phase and SOC_{m0} is the average SOC of the sub-module battery in the phase. The basic idea of SOC control of sub-module in phase is as follows (Yang et al., 2018): If SOC_{mi} is greater than SOC_{m0}, then the difference value is proportionally controlled to

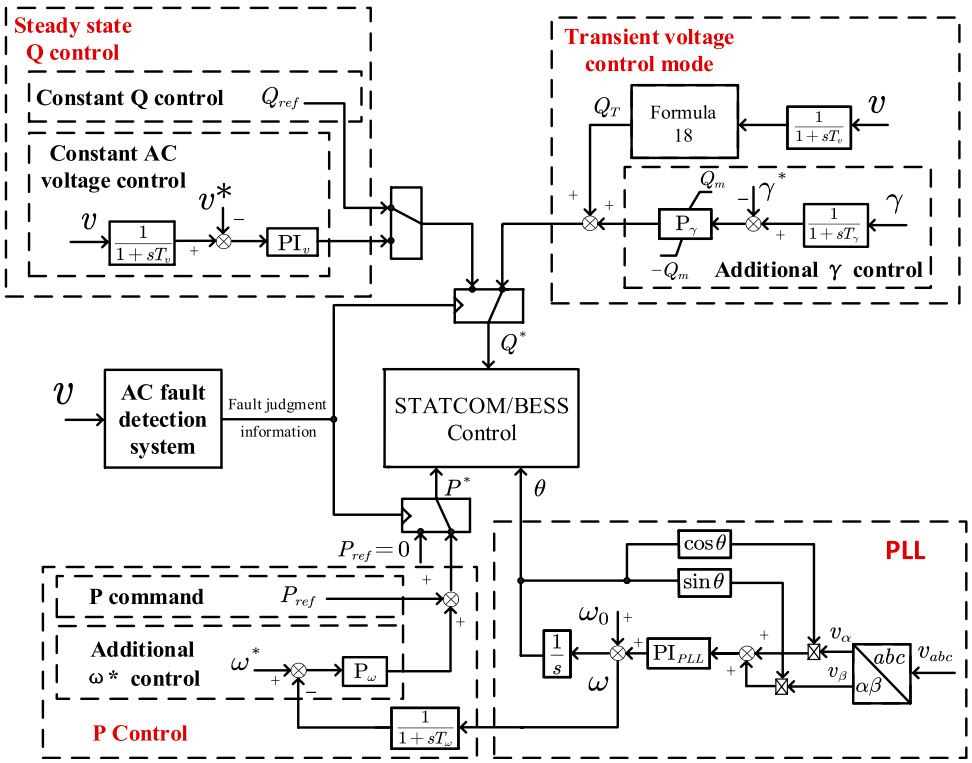

FIGURE 7 | Power coordinated control system.

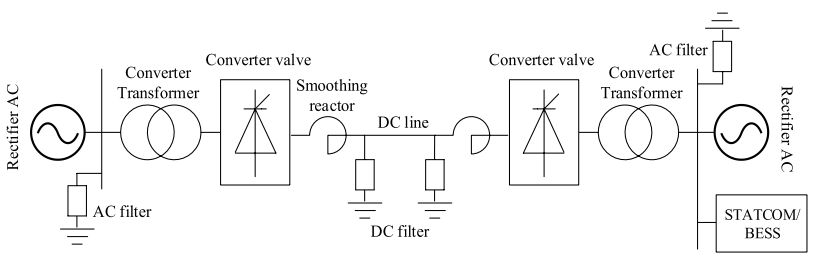

FIGURE 8 | LCC-HVDC simulation system.

TABLE 1 | LCC-HVDC system parameters.

Parameter	Rectifier side	Inverter side
AC system voltage	525 kV	525 kV
Volume	1500 MW	1500 MW
SCR	3	2.5
Transformer	890MVA, X_T = 0.16pu, 525/209 kV	869 MVA, X_T = 0.16 pu, 525/204 kV

obtain the submodule SOC to adjust the additional modulation signal v_{socmi}. Since v_{socmi} is ahead of the line voltage corresponding to the link, the submodule will output active power to the grid and SOC_{mi} decreases so as to achieve the SOC balance of the submodule, and vice versa.

SYSTEM CONTROL STRATEGY

The goal of the STATCOM/BESS control system is to maintain a stable phase transformation voltage and reduce the probability of its occurrence when it detects that the commutation failure of the

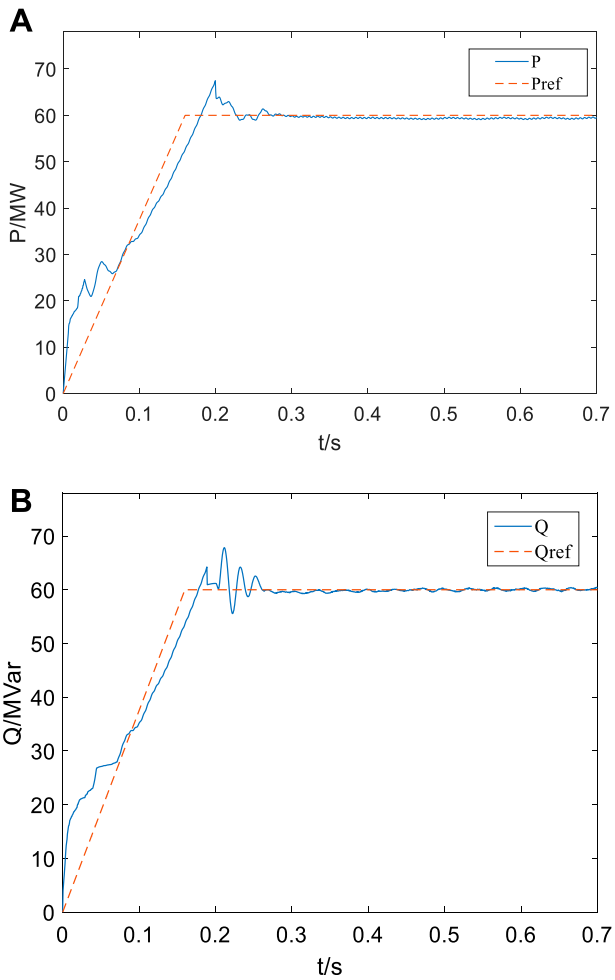

FIGURE 9 | Power output response diagram: **(A)** active power output response diagram and **(B)** reactive power output response diagram.

DC transmission system may occur (Zhang et al., 2021). In order to suppress commutation failure of the DC transmission system, after STATCOM/BESS detects the AC system failure, it switches the corresponding control strategy according to the severity of the failure and proposes the STATCOM/BESS power coordinated control method. When the AC system fails, STATCOM/BESS performs fast with reasonable compensation of reactive and active power, provides effective voltage support to the receiving end power grid, and effectively suppresses the occurrence of commutation failure. The power coordination control system is shown in **Figure 7**, Feng et al., 2021.

On the basis of receiving the upper active power command, the active power control module adds active power adjustment control based on frequency deviation, which can enhance the damping of the interconnected system and suppress power oscillation (Qi et al., 2006); the active power command is set to 0 under fault conditions and reactive power control The module starts to work, including steady-state constant reactive power control and constant AC voltage control, while the transient voltage control mode is based on the dynamic

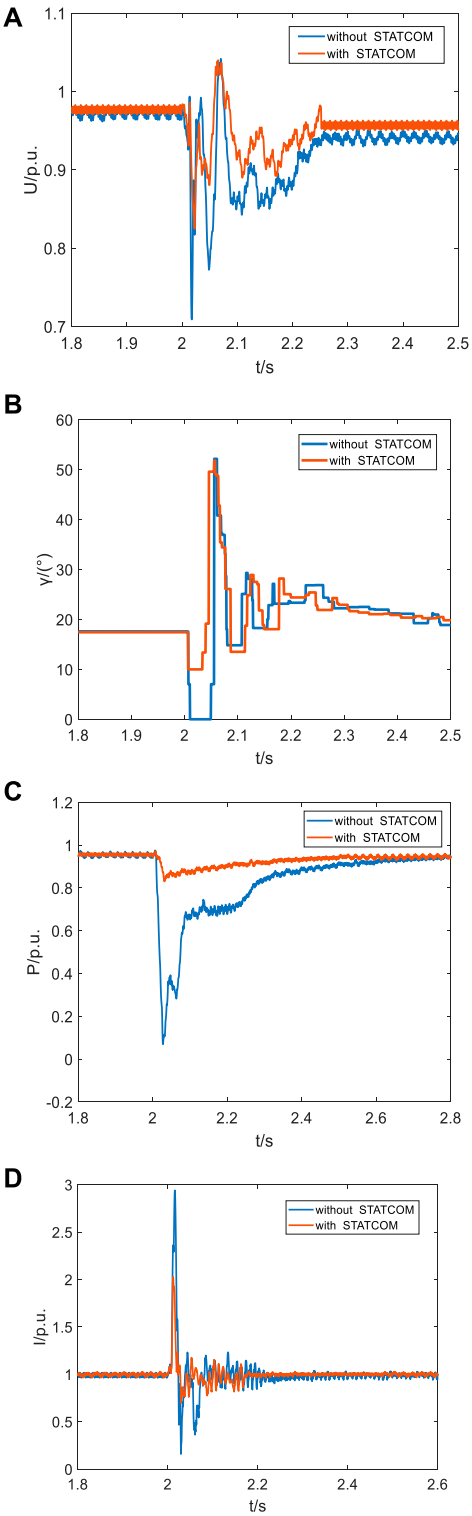

FIGURE 10 | Typical characteristic quantities of single-phase faults. **(A)** Effective value of AC voltage on inverter side in single-phase fault. **(B)** Extinction angle of commutation failure in single-phase fault. **(C)** System transmission power in single-phase fault. **(D)** System DC current in single-phase fault.

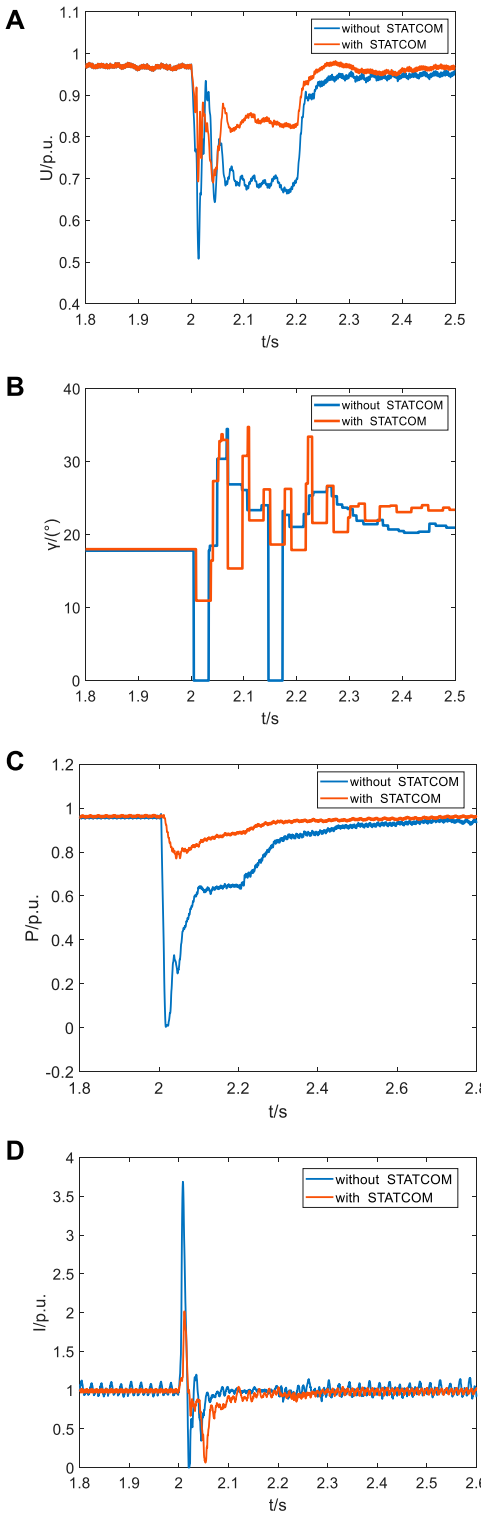

FIGURE 11 | Typical Characteristic quantities of three-phase fault. **(A)** Effective value of the AC voltage on the inverter side in three-phase fault. **(B)** Extinction angle of commutation failure in three-phase fault. **(C)** System transmission power in three-phase fault. **(D)** System DC in three-phase fault.

reactive power support based on voltage sag, with additional DC transmission system inverter station shutting-off the angle control.

It can provide more reactive power compensation for the grid under fault conditions to ensure the normal progress of the phase transformation process. The dynamic reactive power QT injected into the grid by STATCOM/BESS should track the voltage changes at the grid-connected point in real time, and satisfy the following equation (Oghorada et al., 2021):

$$\begin{cases} \boldsymbol{Q_T \geq k_{TI}\,(v_{\max} - v) I_N v\,(v_{\min} \leq v \leq v_{\max})} \\ \boldsymbol{Q_T \geq I_N v\,(v < v_{\min})} \\ \boldsymbol{Q_T = 0\,(v > v_{\max})} \end{cases} \tag{20}$$

In the equation, v represents the STATCOM/BESS grid-connected point voltage per unit value, I_N represents the STATCOM/BESS rated current, $v_{\max}$ and $v_{\min}$, respectively, represent the upper and lower limits of the bus voltage at the grid-connected point during the dynamic reactive power support process, and k_{TI} represents the reactive power proportional coefficient in the process of dynamic reactive power compensation.

SIMULATION ANALYSIS

In this study, PSCAD/EMTDC software is used to build the electromagnetic transient simulation model. The overall framework of the electromagnetic transient model is shown in **Figure 8**. In the model, the main circuit of the LCC-HVDC system adopts the single-pole 12 pulse structure, and the main parameters are selected by referring to Yongfu DC Project, as shown in **Table 1**. The DC control system is the same as the controller in the CIGRE standard model.

Limited by the simulation speed, the STATCOM/BESS electromagnetic transient simulation model in this article is equipped with three H-bridge modules per phase, with a total capacity of 150 Mvar, which is connected to the LCC-HVDC inverter side AC bus through a 35/525 kV transformer.

Active and Reactive Power Control

The response performance of STATCOM/BESS is simulated. The STATCOM output active power instruction is set as 60 MW and reactive power instruction as 60 Mvar, respectively, and the output power changes are observed. **Figure 9A** shows the constant active power control power response graph. During the dynamic response process, the active power output by STATCOM quickly follows the active command; the rise time is about 0.18 s, the maximum output is 66 MW, and the overshoot is less than 11%. In the steady-state process, the active power output by STATCOM fluctuates between 59 and 61.5 MW, and the steady-state response error is less than 3%. **Figure 9B** shows the power response diagram of constant reactive control. Its dynamic response process is also good, with a rising time of 0.178 s, a maximum output value of 67.6 Mvar, and an overshoot of less than 13%. It enters the

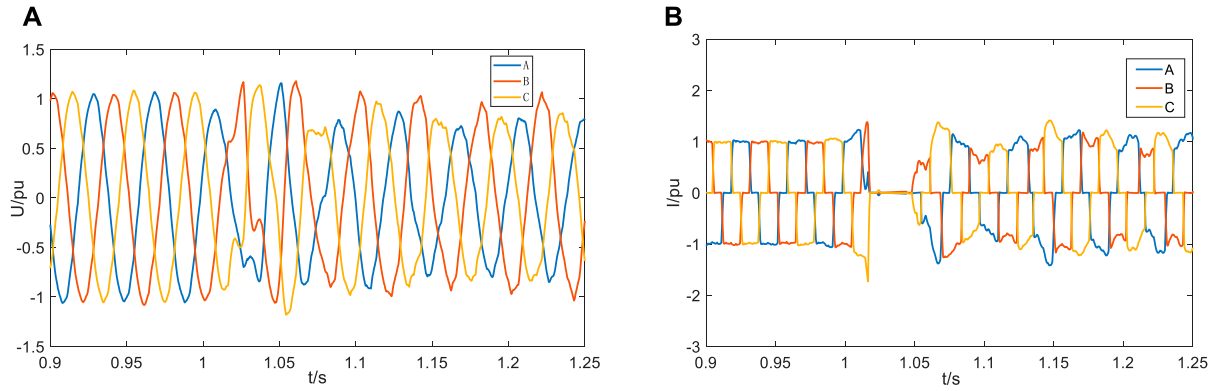

FIGURE 12 | Simulation waveform diagram after installing conventional STATCOM: **(A)** AC voltage on the inverter side and **(B)** inverter current of the converter valve.

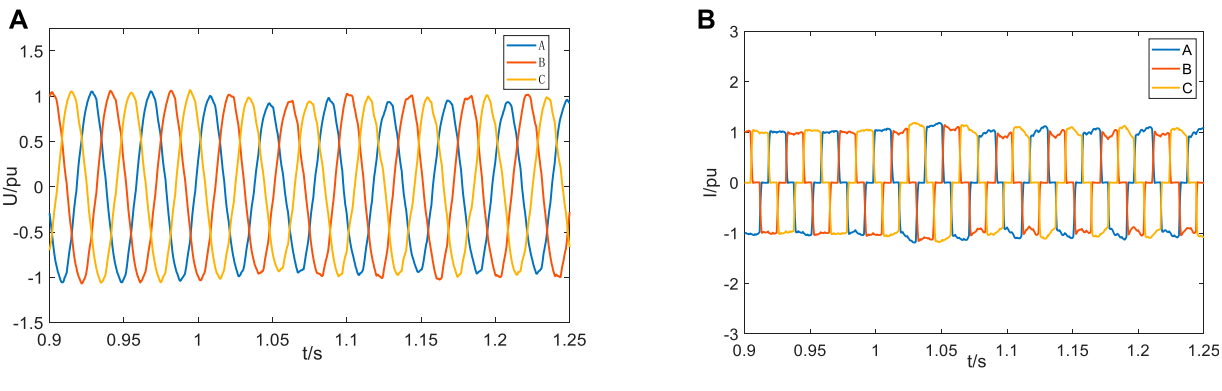

FIGURE 13 | Experimental waveform diagram of installing STATCOM/BESS: **(A)** AC voltage on the inverter side and **(B)** inverter current of the converter valve.

steady state at 0.24 s. The STATCOM output reactive power fluctuates between 58 Mvar and 62.5, and the steady-state response error is less than 5%. The simulation results show that the STATCOM/BESS used in this study has good output performance and can respond quickly to a given power command.

Single-Phase Ground Fault

When the setting is 2 s, a single-phase ground fault occurs in the AC system on the inverter side and the fault lasts for 0.2 s. **Figure 10** shows the effective value of the AC voltage on the inverter side before and after the fault, the extinction angle of commutation failure, the transmission power of the system, and the DC. In **Figure 10A**, when STATCOM is not connected, the AC voltage on the inverter side drops to 0.7 pu after the fault occurs and basically recovers to 0.96 pu after 2.5 s. After STATCOM is connected, the voltage sag is reduced to 0.83 pu, and the recovery is increased to 0.96 pu, reducing the impact of faults on the AC system. In **Figure 10B**, when STATCOM is not connected, the extinction-angle γ decreases to 0° after the fault occurs, indicating that the first commutation failure occurs. After STATCOM access, the extinction-angle γ is about 10°, and commutation failure is inhibited. In **Figures 10C,D**, when STATCOM is not connected, the power transmitted by the system drops dramatically and the DC increases sharply, seriously affecting the system operation and equipment safety. After STATCOM is connected, the transmission power and DC voltage of the system are less affected by the fault and will be stabilized in a short time. According to this group of simulation, when a single-phase grounding short-circuit occurs on the inverter side, voltage sag will occur, which will lead to commutation failure. After STATCOM/BESS is connected, the terminal voltage can be effectively supported, constant-extinction-angle can be improved, and the commutation failure and subsequent chain reaction caused by the fault can be inhibited.

Three-Phase Ground Fault

When the setting is 2 s, a three-phase ground fault occurs in the AC system on the inverter side, and the fault lasts for 0.2 s. **Figure 11** shows the effective value of the AC voltage on the inverter side before and after the fault, the extinction angle of commutation failure, the transmission power of the system, and the DC current. As shown in **Figure 11A**, when STATCOM is not connected, AC voltage sag on the inverter

side is obvious after the fault occurs, and the lowest drops to 0.5 pu, which basically recovers to 0.96 pu after 2.5 s. After STATCOM is connected, the voltage sag is reduced to 0.7 pu, and the power supply is restored more quickly. As shown in **Figure 11B**, when STATCOM is not connected, the extinction-angle γ decreases to 0° after the fault occurs and the first commutation failure occurs, and again to 0° at 2.15 s, indicating that continuous commutation failure occurs during the fault process.

With/Without BESS Simulation Verification

In order to compare the commutation failure suppression effect between STATCOM/BESS and conventional STATCOM, a serious single-phase grounding fault is set at 1 s in this experiment. **Figures 12A,B** show the AC voltage and inverter current at the inverter side of the HVDC system when an A-phase at the inverter side suddenly has a grounding fault after a period of normal operation. At this time, the system is equipped with conventional STATCOM. After the fault occurred, the A-phase voltage begin to drop, and the AC voltage on the inverter side is greatly distorted. The inverter current dropped to 0 at the same time in the vicinity of 1 s, indicating that commutation failure occurred.

When STATCOM/BESS is installed in the system, the grounding fault occurs in A-phase in 1 s. It can be seen from **Figures 13A,B** that the AC voltage distortion on the inverter side is relatively small, and the phenomenon that the three-phase current is zero at the same time during the fault period does not occur, which indicates that STATCOM/BESS has restrained the occurrence of commutation failure under the single-phase fault condition.

CONCLUSION

In this study, the mathematical model of STATCOM/BESS is established, a suitable battery model is selected as its energy storage element, and a SOC equilibrium control strategy is put forward. The model is built in PSCAD/EMTDC simulation software and its function is tested and the following conclusions are obtained:

1) STATCOM/BESS adopts coordinated power control, which is divided into two modules: active power control and reactive power control. It can compensate active power and reactive power quickly and reasonably in case of fault.
2) Shepherd model is selected as the energy storage element, and the SOC equilibrium control strategy is proposed to improve the working efficiency of the energy storage battery.
3) Compared with the traditional STATCOM that can only compensate for reactive power, STATCOM/BESS can track active power commands and respond quickly when the active power output is required. At the same time, it can also compensate reactive power quickly when a serious fault occurs, thereby supporting the grid voltage by suppressing the commutation failure, which is of great significance in improving the operation stability of the AC/DC system with a weak receiving end.
4) The STATCOM/BESS device is installed in the single-pole 12-pulse HVDC transmission system, a single-phase ground fault is set, and a comparison experiment is carried out with the traditional STATCOM system; by comparing the two typical electrical quantities of AC voltage and inverter current, the effectiveness of the STATCOM/BESS designed in this study is verified in suppressing commutation failure.

DATA AVAILABILITY STATEMENT

The raw data supporting the conclusion of this article will be made available by the authors, without undue reservation.

AUTHOR CONTRIBUTIONS

CX was responsible for providing ideas and methods and providing an experimental platform. SC was responsible for deriving formulas, reviewing, and verifying. JC was responsible for model building, simulation, data analysis, and manuscript writing. XX, ZX, XH, and SL wrote sections of the manuscript. All authors participated in the reading and approved the submitted version.

FUNDING

This work was supported by the National Natural Science Foundation of China (52067009).

REFERENCES

Authors Anonymous (2016). *Research on Control Strategy and Application for STATCOM/BESS.* Harbin, China: Harbin Institute of Technology.

Castaneda, J., Enslin, J., Elizondo, D., Abed, N., and Teleke, S. (2010). "Application of STATCOM with Energy Storage for Wind Farm Integration," in IEEE Transmission and Distribution Conference and Exposition, New Orleans, USA, 19-22 April 2010, 1–6.

Cheng, S., Yu, W., and Wen, J. (2007). Energy Storage Technology and its Application in Power System Stability Control[J]. *Power Syst. Technol.* 31 (20), 97–108. doi:10.13335/j.1000-3673.pst.2007.20.009

Cui, Y., Yang, R., Gao, Q., and Xu, D. (2011). Design and Simulation of Cascaded SVG Control System[J]. *High-power Convert. Technol.* 5, 45–49. doi:10.13889/j.issn.2095-3631.2011.05.002

Fei, W., Zhang, Y., and Lu, Z. (2005). Integration of Large-Capacity Static Reactive Power Generator and Battery Energy Storage[J]. *Automation Electr. Power Syst.* 29 (10), 41–44.

Feng, S., Wu, X., Wang, Z., Niu, T., and Chen, Q. (2021). Damping Forced Oscillations in Power System via Interline Power Flow Controller with Additional Repetitive Control. *Prot. Control Mod. Power Syst.* 6, 21. doi:10.1186/s41601-021-00199-7

Hailian Xie, H., Angquist, L., and Nee, H.-P. (2009). Investigation of StatComs with Capacitive Energy Storage for Reduction of Voltage Phase Jumps in Weak

Networks. *IEEE Trans. Power Syst.* 24 (1), 217–225. doi:10.1109/tpwrs.2008.2008611

He, Z. (2016). *Research on the Key Technology and Application of Cascaded Multilevel Static Synchronous Compensator*. Changsha, China: Hunan University.

Li, N., Yanchao, J., and Wang, J. (2014). Overview of Static Synchronous Compensator (STATCOM/BESS) with Battery Energy Storage Device[J]. *New Technol. Electr. Eng. Energy* 33 (4), 48–53.

Li, Z., Jiang, W., Abu-Siada, A., Li, Z., Xu, Y., and Liu, S. (2021). Research on a Composite Voltage and Current Measurement Device for HVDC Networks. *IEEE Trans. Ind. Electron.* 68 (9), 8930–8941. doi:10.1109/tie.2020.3013772

Liu, Y., Yang, N., Dong, B., Wu, L., Yan, J., Shen, X., et al. (2020). Multi-Lateral Participants Decision-Making: A Distribution System Planning Approach with Incomplete Information Game. *IEEE Access* 8, 88933–88950. doi:10.1109/access.2020.2991181

Oghorada, O. J. K., Zhang, L., Han, H., Esan, A. B., and Mao, M. (2021). Inter-cluster Voltage Balancing Control of a Delta Connected Modular Multilevel Cascaded Converter under Unbalanced Grid Voltage. *Prot. Control Mod. Power Syst.* 6, 23. doi:10.1186/s41601-021-00203-0

Qi, X., Zeng, D., Shi, D., Fang, X., Lan, L., Su, H., et al. (2006). Research on the Impact of UHV DC Transmission on System Security and Stability. *Power Syst. Technol.* 30 (02), 1–6.

Shen, X., and Raksincharoensak, P. (2021b). Statistical Models of Near-Accident Event and Pedestrian Behavior at Non-signalized Intersections. *J. Appl. Statistics*. doi:10.1080/02664763.2021.1962263

Shen, X., Ouyang, T., Khajorntraidet, C., Li, Y., Li, S., and Zhuang, J. (2022). Mixture Density Networks-Based Knock Simulator. *IEEE/ASME Trans. Mechatron.* 27, 159–168. doi:10.1109/TMECH.2021.3059775

Shen, X., Ouyang, T., Yang, N., and Zhuang, J. (2021). Sample-based Neural Approximation Approach for Probabilistic Constrained Programs. *IEEE Trans. Neural Netw. Learn. Syst.*, 1–8. doi:10.1109/TNNLS.2021.3102323

Shen, X., and Raksincharoensak, P. (2021a). Pedestrian-aware Statistical Risk Assessment. *IEEE Trans. Intell. Transp. Syst.* 2021, 1–9. doi:10.1109/TITS.2021.3074522

Shen, X., Zhang, X., Ouyang, T., Li, Y., and Raksincharoensak, P. (2020). Cooperative Comfortable-Driving at Signalized Intersections for Connected and Automated Vehicles. *IEEE Robot. Autom. Lett.* 5 (4), 6247–6254. doi:10.1109/LRA.2020.3014010

Shen, X., Zhang, Y., Sata, K., and Shen, T. (2020). Gaussian Mixture Model Clustering-Based Knock Threshold Learning in Automotive Engines. *IEEE/ASME Trans. Mechatron.* 25 (6), 2981–2991. doi:10.1109/TMECH.2020.3000732

Shen, X., Zhang, Y., Shen, T., and Khajorntraidet, C. (2017). Spark Advance Self-Optimization with Knock Probability Threshold for Lean-Burn Operation Mode of SI Engine. *Energy* 122, 1–10. doi:10.1016/j.energy.2017.01.065

Wang, X., Hong, W., Ou, Z., Fu, Y., and Yu, J. (2018). A STATCOM Compensation Scheme to Suppress HVDC Commutation Failure[J]. *Power Syst. Prot. Control* 46 (05), 135–142. doi:10.7667/PSPC170230

Yang, N., Huang, Y., Hou, D., and Liu, S. (2019). Adaptive Nonparametric Kernel Density Estimation Approach for Joint Probability Density Function Modeling of Multiple Wind Farms[J]. *Energies* 12. doi:10.3390/en12071356

Yang, N., Ye, D., Zhou, Z., Cui, J., Chen, D., and Wang, X. (2018). Research on Modelling and Solution of Stochastic SCUC under AC Power Flow Constraints. *IET Generation Transm. Distribution* 12 (15), 3618–3625. doi:10.1049/iet-gtd.2017.1845

Yang, N., Huang, Y., Hou, D., Liu, S., Ye, D., Dong, B., et al. (2019). Adaptive Nonparametric Kernel Density Estimation Approach for Joint Probability Density Function Modeling of Multiple Wind Farms. *Energies* 12, 1356. doi:10.3390/en12071356

Yang, N., Liu, S., Deng, Y., and Xing, C. (2021b). An Improved Robust SCUC Approach Considering Multiple Uncertainty and Correlation. *IEEJ Trans. Elec Electron Eng.* 16, 21–34. doi:10.1002/tee.23265

Yang, N., Yang, C., Wu, L., Shen, X., Jia, J., Li, Z., et al. (2022). Intelligent Data-Driven Decision-Making Method for Dynamic Multisequence: An E-Seq2Seq-Based SCUC Expert System. *IEEE Trans. Ind. Inf.* 18, 3126–3137. doi:10.1109/TII.2021.3107406

Yang, N., Yang, C., Xing, C., Ye, D., Jia, J., Chen, D., et al. (2021a). Deep Learning-based SCUC Decision-making: An Intelligent Data-driven Approach with Self-learning Capabilities. *IET Generation Trans Dist* 16, 629–640. doi:10.1049/gtd2.12315

Yang, Z., Shen, C., Zhang, L., Crow, M. L., and Atcitty, S. (2001). Integration of a StatCom and Battery Energy Storage. *IEEE Trans. Power Syst.* 16 (2), 254–260. doi:10.1109/59.918295

Zhang, L., Xie, Y., Ye, J., Xue, T., Cheng, J., Li, Z., et al. (2021). Intelligent Frequency Control Strategy Based on Reinforcement Learning of Multi-Objective Collaborative Reward Function[J]. *Front. Energy Res.* 9 doi:10.3389/fenrg.2021.760525

Zhang, W., Tang, Y., and Zeng, N. (2010). Multi-terminal HVDC Transmission Technologies and its Application Prospects in China[J]. *Power Syst. Technol.* 34 (9), 1–6. doi:10.13335/j.1000-3673.pst.2010.09.001

Zhou, R., Lu, J., Long, X., Zhang, X., and Chao, L. (2016). Research on the Optimization of the Discharge Balance of Hybrid Energy Storage Battery Packs. *J. Nav. Univ. Eng.* 28 (S1), 105–109. doi:10.7495/j.issn.1009-3486.2016.03(z).022

Zhu, B., Ding, F., and Vilathgamuwa, D. M. (2020). Coat Circuits for DC-DC Converters to Improve Voltage Conversion Ratio. *IEEE Trans. Power Electron.* 35 (4), 3679–3687. doi:10.1109/TPEL.2019.2934726

Conflict of Interest: CX, JC, XX, ZX, XH, and SL are employed by Yunnan Power Grid Co., Ltd.

The remaining authors declare that the research was conducted in the absence of any commercial or financial relationships that could be construed as a potential conflict of interest.

Publisher's Note: All claims expressed in this article are solely those of the authors and do not necessarily represent those of their affiliated organizations, or those of the publisher, the editors, and the reviewers. Any product that may be evaluated in this article, or claim that may be made by its manufacturer, is not guaranteed or endorsed by the publisher.

Advantages of publishing in Frontiers

OPEN ACCESS
Articles are free to read for greatest visibility and readership

FAST PUBLICATION
Around 90 days from submission to decision

HIGH QUALITY PEER-REVIEW
Rigorous, collaborative, and constructive peer-review

TRANSPARENT PEER-REVIEW
Editors and reviewers acknowledged by name on published articles

Frontiers
Avenue du Tribunal-Fédéral 34
1005 Lausanne | Switzerland

Visit us: www.frontiersin.org
Contact us: frontiersin.org/about/contact

REPRODUCIBILITY OF RESEARCH
Support open data and methods to enhance research reproducibility

DIGITAL PUBLISHING
Articles designed for optimal readership across devices

FOLLOW US
@frontiersin

IMPACT METRICS
Advanced article metrics track visibility across digital media

EXTENSIVE PROMOTION
Marketing and promotion of impactful research

LOOP RESEARCH NETWORK
Our network increases your article's readership